

International Association of Geodesy Symposia

154

Jeffrey T. Freymueller  
Laura Sánchez *Editors*

# Geodesy for a Sustainable Earth

Proceedings of the 2021 Scientific Assembly  
of the International Association of Geodesy, Beijing,  
China, June 28 – July 2, 2021

OPEN ACCESS

 Springer

# International Association of Geodesy Symposia

*Jeffrey T. Freymueller, Series Editor*  
*Laura Sánchez, Series Assistant Editor*

---

**Series Editor**

Jeffrey T. Freymueller  
Endowed Chair for Geology of the Solid Earth  
Department of Earth and Environmental Sciences  
Michigan State University  
East Lansing, MI, USA

**Assistant Editor**

Laura Sánchez  
Deutsches Geodätisches Forschungsinstitut  
Technische Universität München  
München, Germany

# International Association of Geodesy Symposia

*Jeffrey T. Freymueller, Series Editor*  
*Laura Sánchez, Series Assistant Editor*

---

- Symposium 112: Geodesy and Physics of the Earth: Geodetic Contributions to Geodynamics
  - Symposium 113: Gravity and Geoid
  - Symposium 114: Geodetic Theory Today
- Symposium 115: GPS Trends in Precise Terrestrial, Airborne, and Spaceborne Applications
  - Symposium 116: Global Gravity Field and Its Temporal Variations
  - Symposium 117: Gravity, Geoid and Marine Geodesy
  - Symposium 118: Advances in Positioning and Reference Frames
  - Symposium 119: Geodesy on the Move
- Symposium 120: Towards an Integrated Global Geodetic Observation System (IGGOS)
  - Symposium 121: Geodesy Beyond 2000: The Challenges of the First Decade
  - Symposium 122: IV Hotine-Marussi Symposium on Mathematical Geodesy
  - Symposium 123: Gravity, Geoid and Geodynamics 2000
  - Symposium 124: Vertical Reference Systems
  - Symposium 125: Vistas for Geodesy in the New Millennium
- Symposium 126: Satellite Altimetry for Geodesy, Geophysics and Oceanography
  - Symposium 127: V Hotine-Marussi Symposium on Mathematical Geodesy
  - Symposium 128: A Window on the Future of Geodesy
  - Symposium 129: Gravity, Geoid and Space Missions
  - Symposium 130: Dynamic Planet - Monitoring and Understanding . . .
- Symposium 131: Geodetic Deformation Monitoring: From Geophysical to Engineering Roles
- Symposium 132: VI Hotine-Marussi Symposium on Theoretical and Computational Geodesy
  - Symposium 133: Observing our Changing Earth
  - Symposium 134: Geodetic Reference Frames
  - Symposium 135: Gravity, Geoid and Earth Observation
  - Symposium 136: Geodesy for Planet Earth
- Symposium 137: VII Hotine-Marussi Symposium on Mathematical Geodesy
  - Symposium 138: Reference Frames for Applications in Geosciences
  - Symposium 139: Earth on the Edge: Science for a Sustainable Planet
- Symposium 140: The 1st International Workshop on the Quality of Geodetic Observation and Monitoring Systems (QuGOMS'11)
  - Symposium 141: Gravity, Geoid and Height Systems (GGHS2012)
- Symposium 142: VIII Hotine-Marussi Symposium on Mathematical Geodesy
- Symposium 143: Scientific Assembly of the International Association of Geodesy, 150 Years
  - Symposium 144: 3rd International Gravity Field Service (IGFS)
- Symposium 145: International Symposium on Geodesy for Earthquake and Natural Hazards (GENAH)
  - Symposium 146: Reference Frames for Applications in Geosciences (REFAG2014)
  - Symposium 147: Earth and Environmental Sciences for Future Generations
  - Symposium 148: Gravity, Geoid and Height Systems 2016 (GGHS2016)
  - Symposium 149: Advancing Geodesy in a Changing World
- Symposium 150: Fiducial Reference Measurements for Altimetry
- Symposium 151: IX Hotine-Marussi Symposium on Mathematical Geodesy
  - Symposium 152: Beyond 100: The Next Century in Geodesy
- Symposium 153: Terrestrial Gravimetry: Static and Mobile Measurements (TG-SMM 2019)
  - Symposium 154: Geodesy for a Sustainable Earth

# Geodesy for a Sustainable Earth

Proceedings of the 2021 Scientific Assembly of the  
International Association of Geodesy, Beijing, China, June  
28 – July 2, 2021

Edited by

Jeffrey T. Freymueller, Laura Sánchez

*Series Editor*

Jeffrey T. Freymueller  
Endowed Chair for Geology of the Solid Earth  
Department of Earth and Environmental Sciences  
Michigan State University  
East Lansing, MI, USA

*Assistant Editor*

Laura Sánchez  
Deutsches Geodätisches Forschungsinstitut  
Technische Universität München  
München, Germany

ISSN 0939-9585                      ISSN 2197-9359 (electronic)  
International Association of Geodesy Symposia  
ISBN 978-3-031-29506-5              ISBN 978-3-031-29507-2 (eBook)  
<https://doi.org/10.1007/978-3-031-29507-2>

© The Editor(s) (if applicable) and The Author(s) 2023. This book is an open access publication.

**Open Access** This book is licensed under the terms of the Creative Commons Attribution 4.0 International License (<http://creativecommons.org/licenses/by/4.0/>), which permits use, sharing, adaptation, distribution and reproduction in any medium or format, as long as you give appropriate credit to the original author(s) and the source, provide a link to the Creative Commons license and indicate if changes were made.

The images or other third party material in this book are included in the book's Creative Commons license, unless indicated otherwise in a credit line to the material. If material is not included in the book's Creative Commons license and your intended use is not permitted by statutory regulation or exceeds the permitted use, you will need to obtain permission directly from the copyright holder.

The use of general descriptive names, registered names, trademarks, service marks, etc. in this publication does not imply, even in the absence of a specific statement, that such names are exempt from the relevant protective laws and regulations and therefore free for general use.

The publisher, the authors, and the editors are safe to assume that the advice and information in this book are believed to be true and accurate at the date of publication. Neither the publisher nor the authors or the editors give a warranty, expressed or implied, with respect to the material contained herein or for any errors or omissions that may have been made. The publisher remains neutral with regard to jurisdictional claims in published maps and institutional affiliations.

This Springer imprint is published by the registered company Springer Nature Switzerland AG  
The registered company address is: Gewerbestrasse 11, 6330 Cham, Switzerland

## Preface

The 2021 Scientific Assembly of the International Association of Geodesy (IAG) was hosted by the Chinese Society for Geodesy, Photogrammetry and Cartography (CSGPC) in Beijing, China from June 28 to July 2, 2021. Due to the COVID-19 pandemic, the Assembly was organized as a hybrid conference with in-person and online attendants. The total number of registered participants was 1,269, being 146 in-person participants.



Steering and local organizing committees of the IAG2021 Scientific Assembly

The theme of the Assembly was *Geodesy for a Sustainable Earth*. 613 contributions (255 oral presentations and 358 poster presentations) covered all topics of the broad spectrum considered by the IAG. The topics were classified in the following symposia:

Symposium 1: *Reference Frames* (Chairs: Christopher Kotsakis, Jean-Paul Boy, Urs Hugentobler, Xavier Collilieux, Carine Bruyninx, Zinovy Malkin). It covered:

- International Terrestrial Reference Frame: strengths, weaknesses, and strategies for future improvements
- Advancements and open problems in global reference frame theory and methodology (joint session with Symposium 6)
- Terrestrial and space geodetic ties for multi-technique combinations
- Regional reference frames and networks
- Comparison and combination of space geodesy techniques for improving consistency between TRF, CRF, and EOPs

- Vertical reference systems: methodologies, realization, and new technologies (joint session with Symposia 2a and 6)

Symposium 2a: *Earth's Static Gravity Field* (Chairs: Mirko Reguzzoni, Derek van Westrum, George Vergos, Cheinway Hwang, Roland Pail). It covered:

- Terrestrial, marine, and airborne gravimetry (joint session with Symposium 6)
- Vertical reference systems: methodologies, realization, and new technologies (joint session with Symposia 1 and 6)
- Local and regional geoid and gravity modelling
- Global gravity field modelling
- Satellite altimetry and oceanography (joint session with Symposia 2b and 6)
- Gravity inversion for Solid Earth (joint session with Symposia 2b and 6)
- Topography and bathymetry gravity modelling (joint session with Symposium 6)

Symposium 2b: *Earth's Time-variable Gravity Field* (Chairs: Adrian Jäggi, Frank Flechtner, Wei Feng, Srinivas Bettadpur). It covered:

- Analysis techniques
- Spaceborne and terrestrial gravimetry for hydrology (joint session with Symposium 6)
- Cryospheric changes from gravity data (joint session with Symposium 6)
- Satellite altimetry and oceanography (joint session with Symposia 2a and 6)
- Gravity inversion for Solid Earth (joint session with Symposia 2a and 6)
- Future gravity mission concepts (joint session with Symposium 6)

Symposium 3: *Earth Rotation and Geodynamics* (Chair: Janusz Bogusz), with the contribution of the International Association of Seismology and Physics of the Earth's Interior (IASPEI), the International Association of Volcanology and Chemistry of the Earth's Interior (IAVCEI), the International Association of Cryospheric Sciences (IACS), and International Astronomical Union (IAU). It covered:

- Earth rotation, low-degree gravitational change, and mass transport in geophysical fluids (joint session with Symposium 6)
- Observations and modeling of deformation related to changing ice loads
- Geodetic observations in volcanic and tectonically active areas (joint session with Symposium 6)

Symposium 4: *Positioning and applications* (Chairs: Allison Kealy, Vassilis Gikas). It covered:

- Geodetic remote sensing (joint session with Symposium 6)
- Next generation positioning
- Techniques and applications in high precision GNSS

Symposium 5: *The Global Geodetic Observing System (GGOS): the metrological basis for the monitoring of the System Earth* (Chairs: Basara Miyahara, Mike Pearlman, Detlef Angermann, Laura Sánchez). It covered:

- Geodetic infrastructure for Earth System monitoring
- Gravity observations and networks in the framework of GGOS (joint session with Symposia 2a, 2b, and 6)
- Standardized geodetic products for a reliable System Earth observation
- Geodetic space weather research
- Assimilation of geodetic observations in the modelling of the Atmosphere, Cryosphere, and Hydrosphere (joint session with Symposium 6)
- Geodesy contributions to address societal challenges
- Advances in geodesy for geohazard monitoring and disaster risk reduction (joint session with Symposium 6)

Symposium 6: *Inter-Commission Committees' and IAG Project's Symposium* (Chairs: Pavel Novák, Annette Eicker, YY Yang, Jürgen Müller). It covered:

- Geodetic Theory
- Geodesy for Climate Research
- Seafloor geodesy, marine positioning, and undersea navigation
- Novel Sensors and Quantum Technology for Geodesy



Some online attendees to the IAG2021 Scientific Assembly

This volume contains 45 selected papers from the all Symposia of the IAG2021 Scientific Assembly. All published papers were peer-reviewed, and we warmly recognize the contributions and support of the Associate Editors and Reviewers (see the list in later pages). We have organized these papers according to the broad themes covered in all of the Symposia.

East Lansing, MI, USA  
München, Germany

J. T. Freymueller  
L. Sánchez



---

# Contents

## Part I Geometric Reference Frames

<b>Combined IVS Contribution to the ITRF2020</b> .....	3
Hendrik Hellmers, Sadegh Modiri, Sabine Bachmann, Daniela Thaller, Mathis Bloßfeld, Manuela Seitz, and John Gipson	
<b>An Experimental Combination of IGS repro3 Campaign’s Orbit Products Using a Variance Component Estimation Strategy</b> .....	15
Pierre Sakic, Gustavo Mansur, Benjamin Männel, Andreas Brack, and Harald Schuh	
<b>The Correlations of the Helmert Transformation Parameters as an Additional Auxiliary Diagnostic Tool for Terrestrial Reference Frames Quality Assessment</b> ...	25
D. Ampatzidis, D. Thaller, and L. Wang	
<b>Shimosato Co-Location of the SLR and GNSS Stations</b> .....	31
Yuto Nakamura, Shun-ichi Watanabe, Yusuke Yokota, Akira Suzuki, Haruka Ueshiba, and Noritsune Seo	
<b>Local Ties at SLR Station Riga</b> .....	39
Kalvis Salmins, Viesturs Sprogis, Imants Biļinskis, and Jorge del Pino	
<b>Datum Problem Handling in Local Tie Surveys at Wettzell and Metsähovi</b> .....	45
Ulla Kallio, Thomas Klügel, Simo Marila, Svetlana Mähler, Markku Poutanen, Timo Saari, Torben Schüler, and Heli Suurmäki	
<b>Close Range Photogrammetry for High-Precision Reference Point Determination</b> .....	57
Michael Lösler, Cornelia Eschelbach, and Thomas Klügel	
<b>Frame Accuracy of Combined EPN Weekly Coordinate Solutions</b> .....	67
Christopher Kotsakis and Miltiadis Chatzinikos	
<b>The Atlantic Network of Geodynamic and Space Stations (RAEGE)</b> .....	77
José A. López-Pérez, João S. Ferreira, Javier González-García, Francisco J. Beltrán-Martínez, Carlos Albo-Castaño, Beatriz Vaquero-Jiménez, Abel García-Castellano, Javier López-Ramasco, Esther Azcue-Infanzón, Pablo de Vicente-Abad, José A. López-Fernández, Francisco M. Wallenstein, Luís R. Santos, and Sara Pavão	
<b>ITRF Densification in Cyprus</b> .....	83
Chris Danezis, Miltiadis Chatzinikos, and Christopher Kotsakis	
<b>Geodetic Analyses at the National Geographic Institute of Spain</b> .....	95
José C. Rodríguez, Esther Azcue, Víctor Puente, José A. López-F., José A. López-P., Elena Martínez, José A. Sánchez Sobrino, Marcelino Valdés, Beatriz Vaquero, and Pablo de Vicente	

<b>Large-Scale Dimensional Metrology for Geodesy—First Results from the European GeoMetre Project</b> .....	105
Florian Pollinger, Clément Courde, Cornelia Eschelbach, Luis García-Asenjo, Joffray Guillory, Per Olof Hedekvist, Ulla Kallio, Thomas Klügel, Pavel Neyezhmakov, Damien Pesce, Marco Pisani, Jeremias Seppä, Robin Underwood, Kinga Wezka, and Mariusz Wiśniewski	
<b>GGOS Bureau of Products and Standards: Description and Promotion of Geodetic Products</b> .....	111
D. Angermann, T. Gruber, M. Gerstl, R. Heinkelmann, U. Hugentobler, L. Sánchez, P. Steigenberger, R. Gross, K. Heki, U. Marti, H. Schuh, M. Sehnal, and M. Thomas	
<b>Part II Physical Height Systems</b>	
<b>Can an Earth Gravitational Model Augmented by a Topographic Gravity Field Model Realize the International Height Reference System Accurately?</b> .....	123
Jianliang Huang, Marc Véronneau, John W. Crowley, Bianca D’Aoust, and Goran Pavlic	
<b>Assessing Molodensky’s Heights: A Rebuttal</b> .....	131
R. Kingdon, P. Vaníček, M. Santos, Z. Martinec, and I. Foroughi	
<b>On the Accuracy of Geoid Heights Derived from Discrete GNSS/Levelling Data Using Kriging Interpolation</b> .....	139
Emanuele Alcaras, Pier Paolo Amoroso, Ugo Falchi, and Claudio Parente	
<b>Gravimetric Geoid Modeling by Stokes and Second Helmert’s Condensation Method in Yogyakarta, Indonesia</b> .....	147
Brian Bramanto, Kosasih Prijatna, Muhammad Syahrullah Fathulhuda, and Arisauna Maulidyan Pahlevi	
<b>A Geodetic Determination of the Gravitational Potential Difference Toward a 100-km-Scale Clock Frequency Comparison in a Plate Subduction Zone</b> .....	155
Yoshiyuki Tanaka and Yosuke Aoki	
<b>Validation of the Hellenic Gravity Network in the Frame of the ModernGravNet Project</b> .....	165
Vassilios N. Grigoriadis, Vassilios D. Andritsanos, and Dimitrios Natsiopoulou	
<b>Part III Global Gravity Field Modeling</b>	
<b>Combined Gravity Solution from SLR and GRACE/GRACE-FO</b> .....	175
Zhigui Kang, John Ries, Srinivas Bettadpur, Himanshu Save, and Byron Tapley	
<b>Contribution of LARES SLR Data to Co-estimated Earth Geopotential Coefficients</b> .....	183
Linda Geisser, Ulrich Meyer, Daniel Arnold, and Adrian Jäggi	
<b>Determination and Combination of Monthly Gravity Field Time Series from Kinematic Orbits of GRACE, GRACE-FO and Swarm</b> .....	191
Thomas Grombein, Martin Lasser, Daniel Arnold, Ulrich Meyer, and Adrian Jäggi	
<b>Topographic Gravity Field Modelling for Improving High-Resolution Global Gravity Field Models</b> .....	203
E. Sinem Ince, Christoph Förste, Oleh Abrykosov, and Frank Flechtner	

<b>The Benefit of Accelerometers Based on Cold Atom Interferometry for Future Satellite Gravity Missions</b> .....	213
Annike Knabe, Manuel Schilling, Hu Wu, Alireza HosseiniArani, Jürgen Müller, Quentin Beaufiles, and Franck Pereira dos Santos	
<b>Kalman-Filter Based Hybridization of Classic and Cold Atom Interferometry Accelerometers for Future Satellite Gravity Missions</b> .....	221
Alireza HosseiniArani, Benjamin Tennstedt, Manuel Schilling, Annike Knabe, Hu Wu, Steffen Schön, and Jürgen Müller	
<b>Gravimetry by Nanoscale Parametric Amplifiers Driven by Radiation-Induced Dispersion Force Modulation</b> .....	233
Fabrizio Pinto	
<b>Part IV Earth Rotation</b>	
<b>On the Improvement of Combined EOP Series by Adding 24-h VLBI Sessions to VLBI Intensives and GNSS Data</b> .....	245
Lisa Lengert, Daniela Thaller, Claudia Flohrer, Hendrik Hellmers, and Anastasiia Girdiuk	
<b>Investigating the Relationship Between Length of Day and El-Niño Using Wavelet Coherence Method</b> .....	253
Shrishail Raut, Sadegh Modiri, Robert Heinkelmann, Kyriakos Balidakis, Santiago Belda, Chaiyaporn Kitpracha, and Harald Schuh	
<b>Estimation of Earth Rotation Parameter UT1 from Lunar Laser Ranging Observations</b> .....	259
Liliane Biskupek, Vishwa Vijay Singh, and Jürgen Müller	
<b>Part V Surface Deformation Monitoring</b>	
<b>Determination of a GNSS-Based Velocity Field of the African Continent</b> .....	269
Saturday E. Usifoh, Benjamin Männel, Pierre Sakic, Joseph D. Dodo, and Harald Schuh	
<b>Vertical Land Motion at Tide Gauges Observed by GNSS: A New GFZ-TIGA Solution</b> .....	279
Benjamin Männel, Tilo Schöne, Markus Bradke, and Harald Schuh	
<b>CyCLOPS: A National Integrated GNSS/InSAR Strategic Research Infrastructure for Monitoring Geohazards and Forming the Next Generation Datum of the Republic of Cyprus</b> .....	289
Chris Danezis, Dimitris Kakoullis, Kyriaki Fotiou, Marina Pekri, Miltiadis Chatzinikos, Christopher Kotsakis, Ramon Brcic, Michael Eineder, Marios Nikolaidis, Georgios Ioannou, Andreas Christofe, Nicholas Kyriakides, George Melillos, Michalakis Christoforou, Marios Tzouvaras, Sylvana Pilidou, Kyriacos Themistocleous, and Diofantos Hadjimitsis	
<b>Part VI GNSS Positioning</b>	
<b>Dilution of Precision (DOP) Factors for Evaluating Observations to Galileo Satellites with VLBI</b> .....	305
Helene Wolf, Johannes Böhm, Matthias Schartner, Urs Hugentobler, Benedikt Soja, and Axel Nothnagel	

<b>On the Limits of State-of-the-Art GNSS Receivers in Frequency Transfer</b> . . . . .	313
Thomas Krawinkel and Steffen Schön	
<b>On the Effect of Antenna Calibration Errors on Geodetic Estimates</b> . . . . .	321
Tobias Kersten, Grzegorz Krzan, Karol Dawidowicz, and Steffen Schön	
<b>Estimation and Validation of Codephase Center Correction Using the Empirical Mode Decomposition</b> . . . . .	333
Yannick Breva, Johannes Kröger, Tobias Kersten, and Steffen Schön	
<b>On the Potential of Image Similarity Metrics for Comparing Phase Center Corrections</b> . . . . .	345
Johannes Kröger, Tobias Kersten, Yannick Breva, and Steffen Schön	
<b>Multipath Characterization Using Ray-Tracing in Urban Trenches</b> . . . . .	359
Lucy Icking, Fabian Ruwisch, and Steffen Schön	
<b>Bounding the Residual Tropospheric Error by Interval Analysis</b> . . . . .	367
Jingyao Su and Steffen Schön	
<b>Precise Orbit Determination of CubeSats Using Proposed Observations Weighting Model</b> . . . . .	377
Amir Allahviridi-Zadeh, Ahmed El-Mowafy, and Kan Wang	
<b>Part VII Geodetic Atmospheric and Remote Sensing</b>	
<b>Optimal TEC Forecast Models Based on Machine Learning and Time Series Analysis Techniques: A Preliminary Study on the Ring of Fire</b> . . . . .	387
Nhung Le, Benjamin Männel, Pierre Sakic, Chinh Thai Nguyen, Hoa Thi Pham, and Harald Schuh	
<b>Sensitivity of Shipborne GNSS Troposphere Retrieval to Processing Parameters</b> . . .	397
Aurélie Panetier, Pierre Bosser, and Ali Khenchaf	
<b>Application of the Total Variation Method in Near Real-Time GNSS Tropospheric Tomography</b> . . . . .	405
Zohreh Adavi and Robert Weber	
<b>Comparison of the Effective Isotropic Radiated Power Parameter in CYGNSS v2.1 and v3.0 Level 1 Data and Its Impact on Soil Moisture Estimation</b> . . . . .	417
Paulo T. Setti Jr. and Tonie van Dam	
<b>Cross-polarization Correction for Soil Moisture Retrieval Using GNSS SNR Data</b> . . . . .	423
M. Han, D. Yang, B. Zhang, X. Hong, and F. Wang	
<b>Correction to: Dilution of Precision (DOP) Factors for Evaluating Observations to Galileo Satellites with VLBI</b> . . . . .	C1
Helene Wolf, Johannes Böhm, Matthias Schartner, Urs Hugentobler, Benedikt Soja, and Axel Nothnagel	
<b>Associate Editors</b> . . . . .	431
<b>List of Reviewers</b> . . . . .	433
<b>Author Index</b> . . . . .	435
<b>Subject Index</b> . . . . .	439

---

**Part I**

**Geometric Reference Frames**



# Combined IVS Contribution to the ITRF2020

Hendrik Hellmers, Sadegh Modiri, Sabine Bachmann, Daniela Thaller,  
Mathis Bloßfeld, Manuela Seitz, and John Gipson

## Abstract

The ITRF2020 is the upcoming official solution of the International Terrestrial Reference Frame and is the successor to the currently used ITRF2014. The global ITRF2020 solution is based on an inter-technique combination of the four space-geodetic techniques VLBI, GNSS, SLR, and DORIS. In this context, the Combination Centre of the IVS (International VLBI Service for Geodesy and Astrometry) operated by the Federal Agency for Cartography and Geodesy (BKG, Germany) in close cooperation with the Deutsches Geodätisches Forschungsinstitut at TUM (DGFI-TUM, Germany) generates the final VLBI contribution of the IVS. This is achieved by an intra-technique combination utilizing the individual contributions of multiple IVS Analysis Centres (ACs). For the IVS contribution to the ITRF2020, sessions containing 24 h VLBI observations from 1979 until the end of 2020 were re-processed by 11 different ACs and submitted to the IVS Combination Centre. As a result, datum-free normal equations containing station coordinates and source positions as well as full sets of Earth Orientation Parameters (EOP) are delivered. In order to ensure consistency of the combined solution, time series of EOP and station coordinates were generated and further investigated for validation. Finally, the IVS contribution to the ITRF2020 comprises session-wise normal equations including EOP and station coordinates provided in SINEX format. In order to assess the quality of the contributions by the individual IVS ACs, internal as well as external comparisons of the estimated EOP are carried out, with the combined solution as well as external time series (e.g., IERS Bulletin A) serving as a reference. Additionally, the scale of the IVS contribution is investigated as VLBI is one of the space geodetic techniques realizing the scale of the ITRF. The evaluation of the contributions by the ACs, the combination procedure, and the results of the combined solution for station coordinates and EOP will be presented.

## Keywords

Combination of normal equations · Earth orientation parameters · ITRF2020 · IVS · Station coordinate · Terrestrial reference frame

H. Hellmers (✉) · S. Modiri · S. Bachmann · D. Thaller  
Federal Agency for Cartography and Geodesy (BKG), Department  
Geodesy, Frankfurt am Main, Germany  
e-mail: [Hendrik.Hellmers@bkg.bund.de](mailto:Hendrik.Hellmers@bkg.bund.de)

M. Bloßfeld · M. Seitz  
Deutsches Geodätisches Forschungsinstitut (DGFI-TUM), Technische  
Universität München, Munich, Germany

J. Gipson  
Planetary Geodynamics Laboratory, Goddard Space Flight Center,  
Greenbelt, MD, USA

## 1 Introduction

The International Terrestrial Reference Frame (ITRF) represents the realization of the International Terrestrial Reference System (ITRS) and, thus, represents the official global terrestrial reference frame. Containing positions and velocities of globally distributed geodetic observing stations, the ITRF is the basis for various topics of scientific research as well as applications in geoscience. Climate change, global sea-level rise, or earthquakes are common examples (Métivier et al. 2014).

An updated ITRF solution is usually computed every five to six years considering up-to-date models, parameterizations, and data evaluation. Considering systematic errors within the individual technique solutions, new stations, and geophysical processes ensure a high quality of the current ITRF. For the upcoming ITRF2020 new models have been applied concerning galactic aberration, pole tides, gravitational deformation of the VLBI antennas, and high-frequency Earth rotation. The ITRF product is finally provided by the ITRS Centre of the International Earth Rotation and Reference Systems Service (IERS) and is based on mathematical foundations, physical constants, and conventional models provided by the IERS 2010 Conventions (Petit and Luzum 2010).

The ITRF2020 will replace the current ITRF2014 as the succeeding official realization of the ITRS (Altamimi et al. 2016). For covering the individual strengths in the context of geodetic parameter determination, the ITRF computation is based on an inter-technique combination of the four space-geodetic observation techniques (e.g., Thaller 2008). Satellite-based space geodetic observations such as Global Navigation Satellite System (GNSS), Satellite Laser Ranging (SLR), and Doppler Orbitography and Radiopositioning Integrated by Satellite (DORIS) provide solutions w.r.t. an Earth-centered, Earth-fixed reference system. Very Long Baseline Interferometry (VLBI), however, as the only space technique observing extra-galactic objects (radio sources), enables the determination of the movement of the Earth in inertial space. Consequently, VLBI is able to provide the full set of Earth Orientation Parameters (EOP).

The Combination Centre of the International VLBI Service for Geodesy and Astrometry (IVS; Nothnagel et al. 2017) is responsible for the VLBI contribution to the ITRF. It is located at the Federal Agency of Cartography and Geodesy (BKG, Germany) and is working in close cooperation with the Deutsches Geodätisches Forschungsinstitut (DGFI-TUM, Germany; cf. Bachmann et al. 2017). Within the IVS combination the individual contributions of multiple IVS Analysis Centres (ACs) are combined on the level of normal equations (NEQs; Vennebusch et al. 2007; Böckmann et al. 2010). The intra-technique combination is realized by

using the software DOGS-CS. Finally, the combined IVS contribution to the ITRF2020 is delivered as session-wise SINEX files (Bachmann et al. 2016).

For assessing the quality and consistency of the combination and the individual AC solutions, the accuracy of the obtained EOP and station coordinate time series has been evaluated. For this purpose, internal as well as external comparisons of the estimated EOP were carried out, with the combined solution as well as external products (IERS Bulletin A time series; Stamatakos et al. 2020) serving as a reference. In addition, the scale of the IVS contribution is compared to the current reference frame, i.e., ITRF2014.

This paper presents the evaluation of the individual contributions by the IVS ACs, the combination procedure, and the results of the combined solution for station coordinates, EOP, and scale including internal and external accuracy.

---

## 2 Contributions by Individual IVS Analysis Centers

New and improved analysis models as well as new observing stations cause the necessity of a regular update of the ITRF. In comparison to the ITRF2014, the IVS contribution to ITRF2020 includes Galactic Aberration (MacMillan et al. 2019), a new secular pole model, gravitational deformation for some VLBI antennas,<sup>1</sup> and an updated high-frequency EOP model.<sup>2</sup> Moreover, sessions based on observations of the VLBI Global Observing System (VGOS) became available in the most recent years and will be included in the ITRF2020 for the first time. This newly established station network focuses on increasingly demanding requirements for improved VLBI solutions. Figure 1 shows the global distribution of the IVS station network and the cooperating VLBI sites.

The IVS ACs re-processed 24-h sessions for the time span 1979 until the end of 2020. The guidelines for the homogeneous re-processing were provided by the IVS Analysis Coordinator.<sup>3</sup> Each of the 11 ACs provided session-wise SINEX files containing datum-free normal equations including station coordinates, EOP and source positions. Fortunately, the variety of software packages used by the ACs increased since ITRF2014 (see Table 1).

Almost 6,600 sessions have been contributed to the IVS Combination Centre by the different ACs. The submissions undergo several quality checks concerning SINEX format requirements, numerical stability of the normal equation and

<sup>1</sup>[https://ivscc.gsfc.nasa.gov/IVS\\_AC/apriori/gravity\\_deform\\_model\\_v2019Nov21.txt](https://ivscc.gsfc.nasa.gov/IVS_AC/apriori/gravity_deform_model_v2019Nov21.txt).

<sup>2</sup>[https://ivscc.gsfc.nasa.gov/hfeop\\_wg/](https://ivscc.gsfc.nasa.gov/hfeop_wg/).

<sup>3</sup>[https://ivscc.gsfc.nasa.gov/IVS\\_AC/IVS-AC\\_contact.htm](https://ivscc.gsfc.nasa.gov/IVS_AC/IVS-AC_contact.htm).

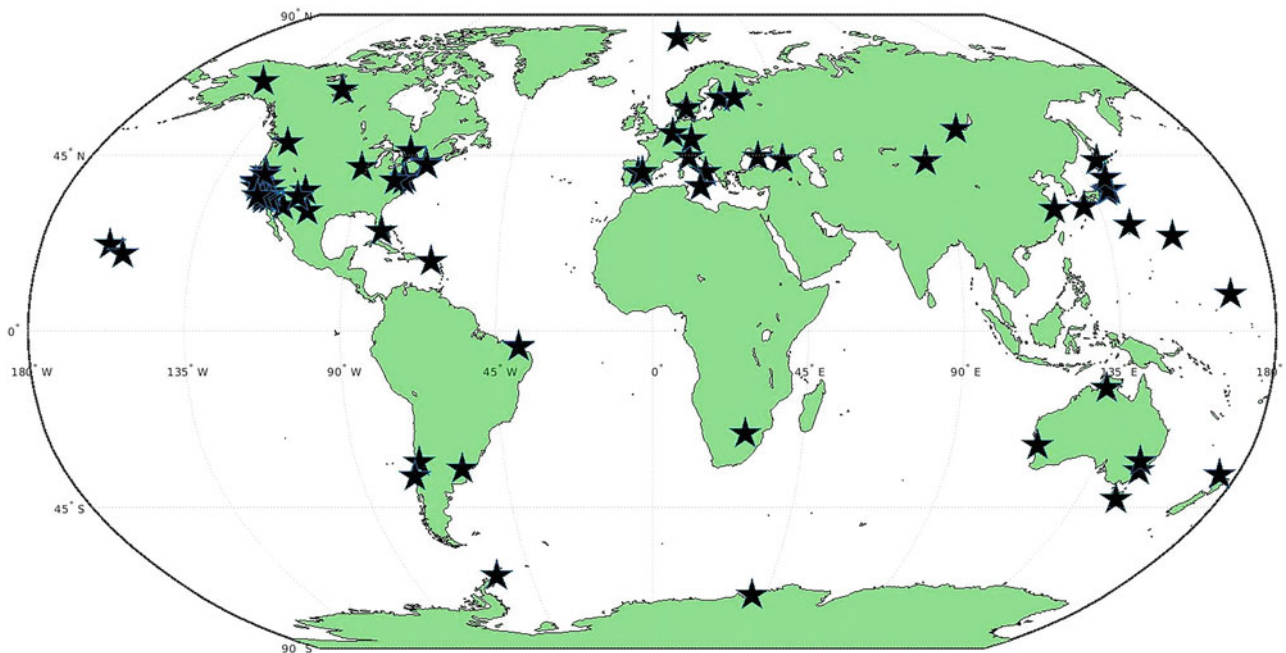


**Fig. 1** Global distribution of VLBI station network

**Table 1** Software packages used by the different IVS ACs

AC	Name	Software
ASI	Italian Space Agency	CALC/SOLVE
BKG	Federal Agency for Cartography and Geodesy	CALC/SOLVE
DGFI-TUM	Deutsches Geodätisches Forschungsinstitut	DOGS-RI
GFZ	German Research Centre for Geosciences	PORT
GSFC	Goddard Space Flight Center	CALC/SOLVE
IAA	Institute of Applied Astronomy	QUASAR
NMA	Norwegian Mapping Authority	Where
OPA	Observatoire de Paris	CALC/SOLVE
OSO	Onsala Space Observatory	ivg::ascot
USNO	United States Naval Observatory	CALC/SOLVE
VIE	Vienna University of Technology	VieVS

the quality of estimated parameters. In order to ensure that the data setup of each AC’s contribution is set properly, completeness and format of the delivered SINEX files are checked, including for instance the existence of all station IDs, station eccentricities or applied precession and nutation models. In addition, an outlier detection is responsible for rejecting contributions with low quality. As a result, a number of almost 350 sessions had to be excluded from the contribution to ITRF due to errors of the required data format or numerical uncertainties (e.g. not invertible matrices). These 5.5% of the sessions are not submitted to the ITRF Combination Centres.

Finally, 94.5% of the submitted sessions could be successfully combined and station coordinates as well as the full sets of EOP had been estimated for almost 99% of the combined sessions. Due to the poor station configuration – most sessions in the early 1980s consist of only three or four stations – less than 100 sessions (1%) are only invertible if the EOP are slightly constrained. Therefore, for reliable constraint-free estimation of the full set of EOP, an adequate station network (minimum of five globally distributed stations) is required. Further investigations will focus on such kind of sessions characterized by a poor geometry in order to establish an optimal procedure for including them into future ITRF computations.

Figure 2 summarizes the number of submitted sessions by each AC. BKG and USNO miss approximately 500 sessions, especially sessions in the early years and sessions with a weak station network (i.e., only 3–4 stations). These sessions are not designed for global parameter estimation (see explanations above), and are, hence, not well-suited for TRF and EOP determination. As a consequence, these sessions are often anyway excluded from the combination. In this context, the estimation of station coordinates becomes possible solely by fixing EOP, which are correlated with the TRF. However, these sessions increase the density of the long-term time series in the early years and are therefore necessary, especially for velocity determination.

In addition to the successfully combined sessions, about 5–10% of the submitted SINEX files per AC had been excluded from combination process due to not processible data (green part in Fig. 2) or outlier detection (yellow part



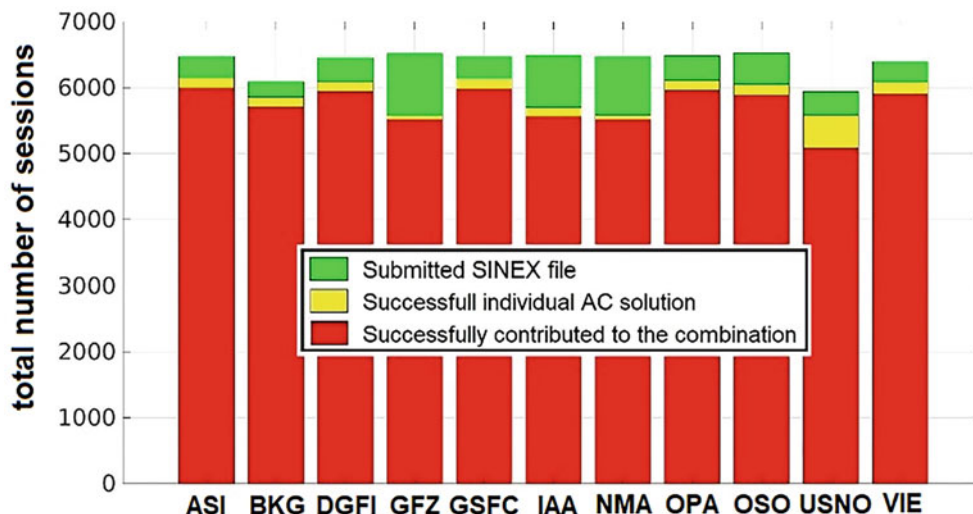


**Fig. 2** Number of VLBI sessions contributed to the ITRF2020 reprocessing by each IVS AC

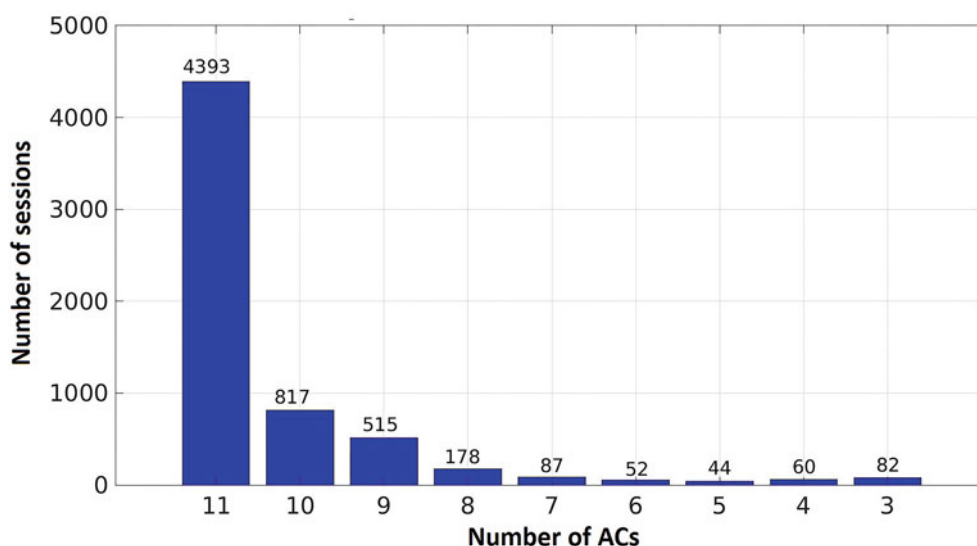


**Fig. 3** Number of ACs per session that contributed to the IVS combination

in Fig. 2). While the processability of each file is checked as described above, the outlier detection utilizes a *three-sigma range test* for each parameter taking into account station coordinates and EOP. Thus, the variance of each estimation defines a threshold for rejecting the corresponding parameter. Detailed information about the outlier detection and the underlying *Least Median of Squares* method is described in general in Rousseeuw and Leroy (2005), as well as in Bachmann et al. (2012) regarding the specific application within the IVS combination. Finally, the number of sessions successfully contributed by each AC to the IVS combination reduces to about 5,000–6,000 (red bars in Fig. 2).

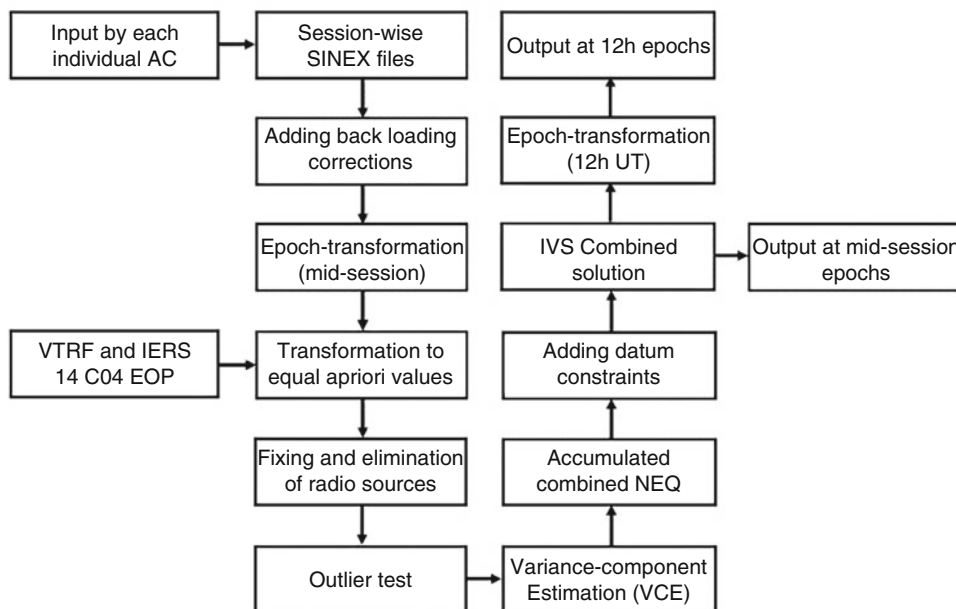
As a supplement, Fig. 3 shows a histogram of the number of ACs contributing to the successful combined solutions per session. It is evident, that almost 92% of the combined ses-

sions (i.e., 5725) include the contributions of 9 or more ACs. On the other hand, 122 sessions are submitted by 3–4 ACs only, which is especially the case for local network sessions (e.g., Onsala tie sessions or dedicated VGOS sessions). As the combination requires contributions by at least 3 ACs, this limited number is critical.

### 3 IVS Combination Procedure

The main goal of an intra-technique combination is the reduction of the so-called analysis noise, and, thus, improved precision and accuracy compared to the individual solutions delivered by the ACs. The combination on the level of normal equations leads – in addition – to more stable equation sys-

**Fig. 4** Combination procedure for the session-wise IVS combination



tems and the correct consideration of correlations between the individual parameters. Due to the utilization of different software packages for the VLBI analysis, the single AC solutions use different assumptions, leading to a wide variety of the combination input data.

Figure 4 shows a sketch of the combination procedure. For achieving session-wise consistency between the available individual contributions, a transformation to equal epochs and equal a priori values for all parameters is carried out. The reference epoch is thereby the middle of the 24-h observation interval. The a priori TRF is chosen as the VLBI-based Terrestrial Reference Frame (VTRF) of the latest IVS Quarterly solution (which is 2020/Q2 in the case of the studies presented hereafter). The IVS Quarterly solution represents an update of the current official terrestrial reference frame, i.e., the ITRF2014. In order to be consistent with the ITRF2014, the datum definition for the IVS Quarterly solution is realized by applying No-Net-Rotation (NNR) and No-Net-Translation (NNT) conditions based on a subset of stable core stations, which are consequently well suited for datum definition. Alternatively, the datum could be defined by the TRF realizations DTRF2014 (Seitz et al. 2022) and JTRF2014 (Abbondanza et al. 2017). However, they represent no official solutions, and hence are usually used in the context of research studies rather than for generating an official product as the IVS combined contribution to ITRF2014. The a priori values of the EOP are transformed to the IERS 14 C04 values (Bizouard et al. 2019). The source coordinates are fixed to the ICRF3 (Charlot et al. 2020) and are subsequently eliminated from the equation system.

In the standard IVS procedure, the non-tidal atmospheric loading (NTAL) is corrected by applying geophysical mod-

els in order to prevent seasonal signals to be present in the estimated station coordinates. However, the requirement for ITRF2020 stipulates no correction of non-tidal loading deformation within the data analysis. Therefore, those ACs that applied NTAL corrections to the observations provided these corrections as normal equations within their SINEX file. Then, these corrections are added back to the normal equations during the IVS combination procedure in order to fulfill the requirements set by the IERS ITRS Product Center for ITRF2020.

For realizing individual solutions for each AC, the station coordinates are constrained by NNR and NNT conditions w.r.t. the a priori TRF. The EOP are estimated as free parameters (exceptions see Sect. 2). In the next step, the outlier detection is performed for detecting inadequate contributions or sessions that do not fit well within the time series, and, thus, should be excluded from the combination. The remaining contributions are then subject to a variance-component estimation (VCE), which leads to AC-specific weighting factors by respecting the corresponding global variance factor.

Finally, the combined normal equation consists of the accumulated, weighted individual NEQs, where station coordinates and EOP are stacked. The final IVS contribution to the ITRF combination consists of two series: one series with parameters given at the mid-epoch of each VLBI session (i.e., representing the best VLBI-only solutions), and a second series with all parameters transformed to noon epochs (UTC) in order to be consistent with the other space-geodetic techniques. However, this weakens the VLBI contributions within the inter-technique combination.

## 4 IVS Combination Results

An evaluation of the resulting station coordinates and EOP has been carried out in order to assess the quality of the combination product. Comparisons of the combined and the individual AC solutions with external products (e.g., ITRF2014, IERS Bulletin A) and the current VTRF are performed, leading to Mean and Weighted-Root-Mean-Square (WRMS) values of the differences as a measure of the accuracy. The IERS Bulletin A time series is an official product which contains EOPs on a daily interval based on all space-geodetic techniques and augmented by geophysical models (Stamatakos et al. 2020): The polar motion is characterized by every space-geodetic technique, whereas dUT1 is a product of VLBI only. But the latter is highly correlated to the LOD series which is based on VLBI, GNSS and SLR contributions, and additionally supported by excitation functions from geophysical models.

Figure 5 shows the comparison “estimated-reference” for the coordinates of the best-performing stations. These 22 stations are characterized by a small number of outliers as well as a stable corresponding time series, i.e., with low noise level. The illustration is limited to the height component and the reference TRF is given by the IVS Quarterly 2020/Q2 solution. The mean values and the corresponding deviations are calculated using the station coordinate estimations from 1979 until 2020. It is evident that the combined solution for every station is well within the range spanned by the individual solutions so that the combination mathematically

represents a weighted mean of the AC contributions. Consequently, the combination benefits from the variety of the utilized software packages.

In addition, Fig. 6 illustrates the enhanced precision of the combination. The color scheme indicates which combined solution could improve the station’s height component compared to the corresponding individual solution. Thereby, the percentage of the enhancement is given by:

$$\alpha[\%] = \frac{\sigma_{AC} - \sigma_{COMBI}}{\sigma_{AC}} \cdot 100, \quad (1)$$

where  $\sigma_{AC}$  is the standard deviation of the individual estimation and  $\sigma_{COMBI}$  is the standard deviation of the combination. Almost 90% are characterized by a green shade, which illustrates an improvement of the precision due to the combination. Only a few stations do not benefit from a combination, like Owens Valley (OVRO 30) which was solely included in sessions during the late 80s, and, thus are consequently characterized by a poor station network.

In order to get a more detailed insight into the station coordinate repeatability, Fig. 7 shows the WRMS deviations in all three components for the station Wettzell as one example. The dashed lines illustrate the accuracy level of the combination. As all individual AC solutions show values above the dashed lines for all three components, the benefit of the combined product compared to the individual solutions is confirmed for all three components.

For completing the evaluation of the parameter estimates, the external evaluation of the EOP estimation is shown. The

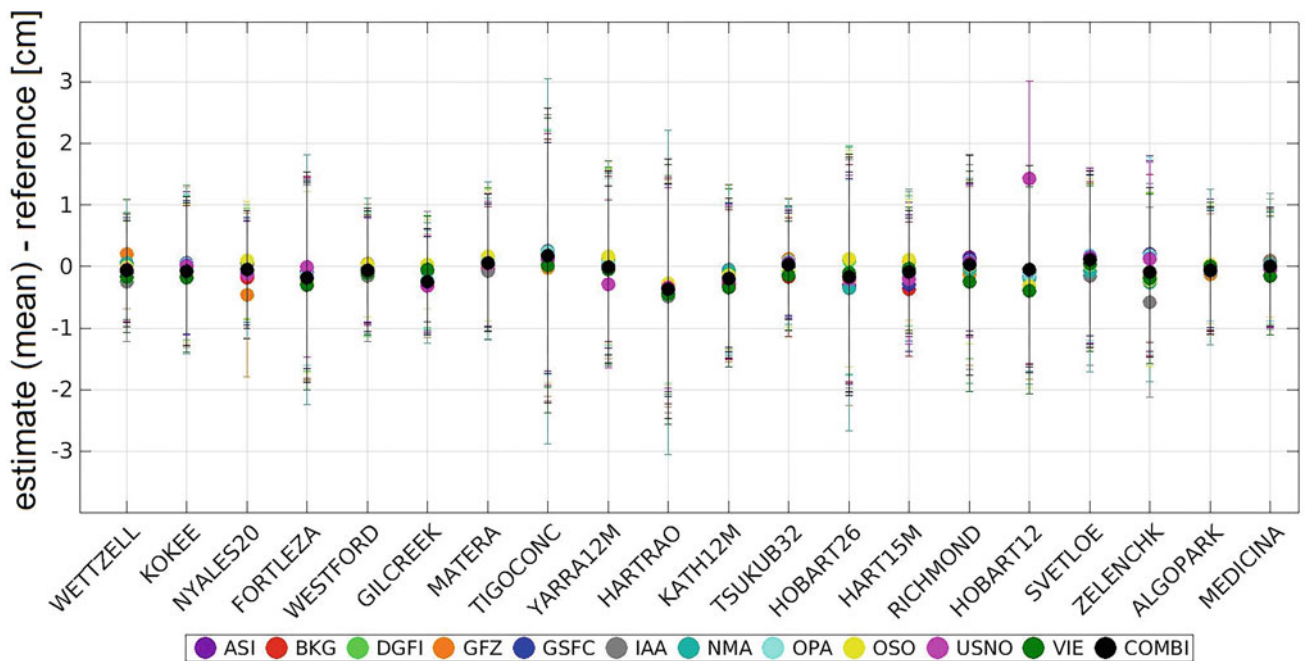
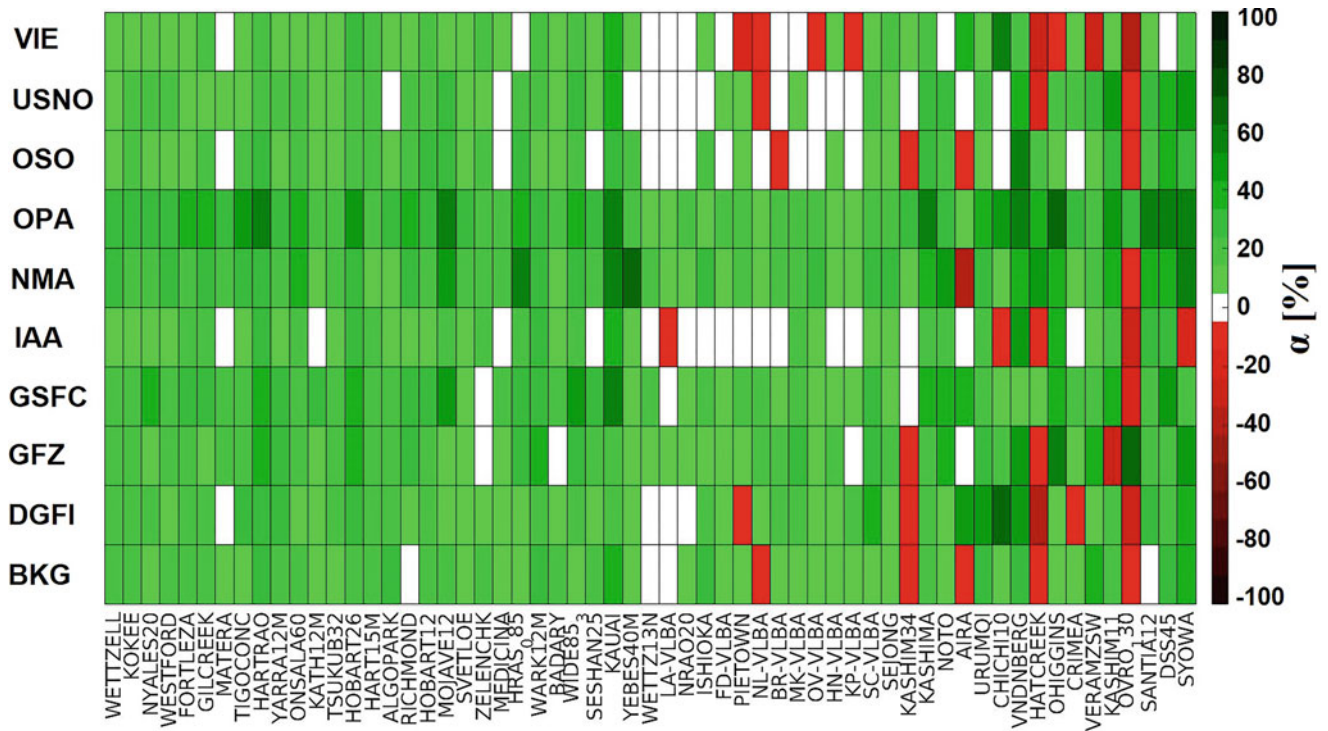
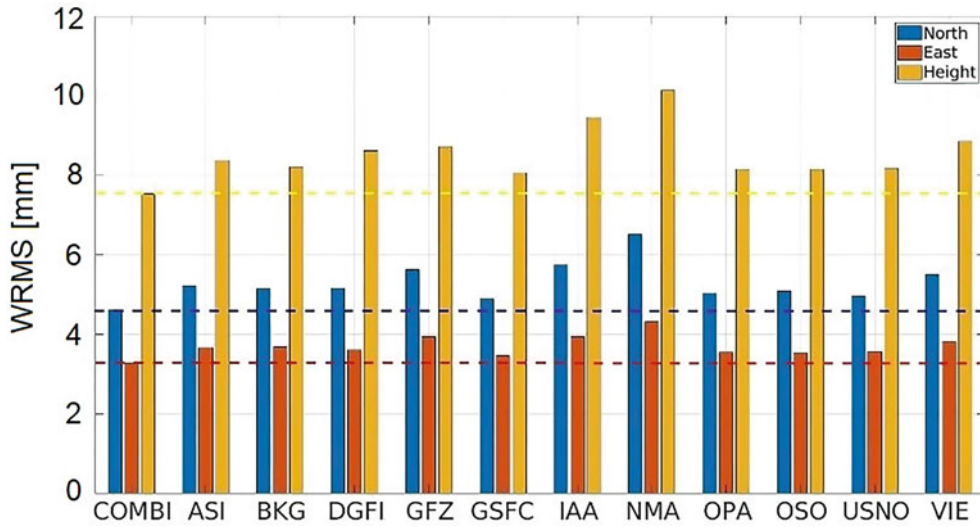


Fig. 5 Accuracy of the IVS station height components evaluated w.r.t. the IVS Quarterly solution 2020/Q2



**Fig. 6** Improvement (green) and degradation (red) of the height components’ standard deviation by the combination (in percentage compared to the individual AC solutions)



**Fig. 7** WRMS of the station coordinate differences w.r.t. the IVS Quarterly solution for the station Wettzell

difference w.r.t. the IERS Bulletin A time series (see Fig. 8 for dUT1 as an example) is used to compute the WRMS values of all individual AC solutions and the IVS combination (see Fig. 9). The axes of polar motion and dUT1 are scaled in such a way that the angles are commensurate (10  $\mu$ s of dUT1 corresponds to the same angular displacement as 150  $\mu$ as of Polar Motion). The WRMS values of the IVS combination is below the WRMS level of the individual solutions for all three ERPs, so that the external comparison confirms the

accuracy enhancement through the combination. It is also visible that the external agreement for the polar motion is slightly better than for dUT1.

Figure 10 illustrates the agreement of the ERPs estimated by the individual ACs with those derived from the IVS combination. It becomes visible that the VLBI-internal consistency is clearly better – up to a factor 2 – than the agreement with external series (shown in Fig. 9). Furthermore, we see for most of the ACs a slightly better agreement for dUT1 than

**Fig. 8** Difference of dUT1 w.r.t. IERS Bulletin A time series

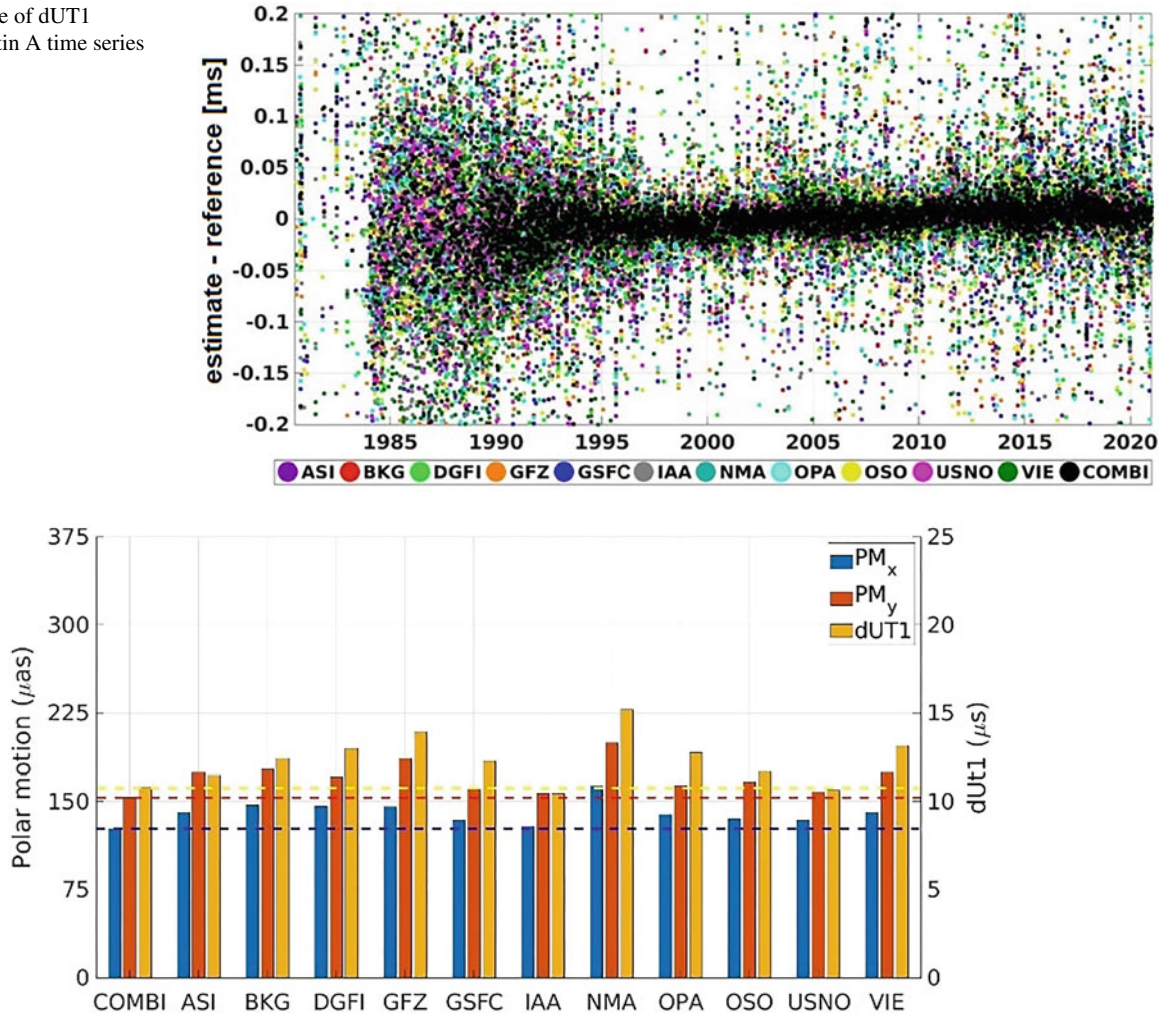


**Fig. 9** External validation of ERP estimates: WRMS of the differences w.r.t. IERS Bulletin A at the mid-epochs of each VLBI session. The horizontal lines represent the WRMS values of the IVS combination of the respective ERP

for polar motion. This behaviour is opposite to the behaviour recognized for the external comparison, and demonstrates the potential of VLBI to determine dUT1 at the level of about 5 micro-seconds or even better. Although almost half of the ACs use the CALC/Solve software, meaning that these contributions cannot be denoted as completely independent, the combination does not seem to be dominated by those ACs which might be due to the broader variety of software packages reached nowadays compared to earlier IVS combinations. However, the influence of the different software packages on the combination will be further investigated in the near future in order to confirm this positive development.

Finally, Fig. 11 illustrates the mean scale of the combined and the individual AC solutions w.r.t. the ITRF2014. The dots represent the raw session-wise scale parameters of the combination, whereas the solid lines result from applying a moving median filter of 90 days. The scale differences between the VLBI solutions and the ITRF2014 are derived

by a session-wise seven-parameter Helmert-transformation using a predefined network of 155 good performing VLBI stations for datum definition. These stations are characterized by an adequate number of observations over a time period of several years, which prevents uncertainties in the scale affected by the station network. Similar to the results seen for the station coordinates (Fig. 5), the combination mathematically describes a weighted mean of the individual solutions also for the global scale. The larger variations in the early years (i.e., roughly until the early 90s) are caused by the weak network configurations that are typical during this time. In addition, a seasonal signal can be recognized. This is most likely caused by non-tidal loading deformations that are not corrected within the ITRF2020 contribution, and, thus, causing a seasonal oscillation within the scale time series.

In addition Fig. 12 shows the unweighted mean scale offsets for each solution. It is evident that the scale offsets of all solutions are in the range of 0.3 to 0.5 ppb, except

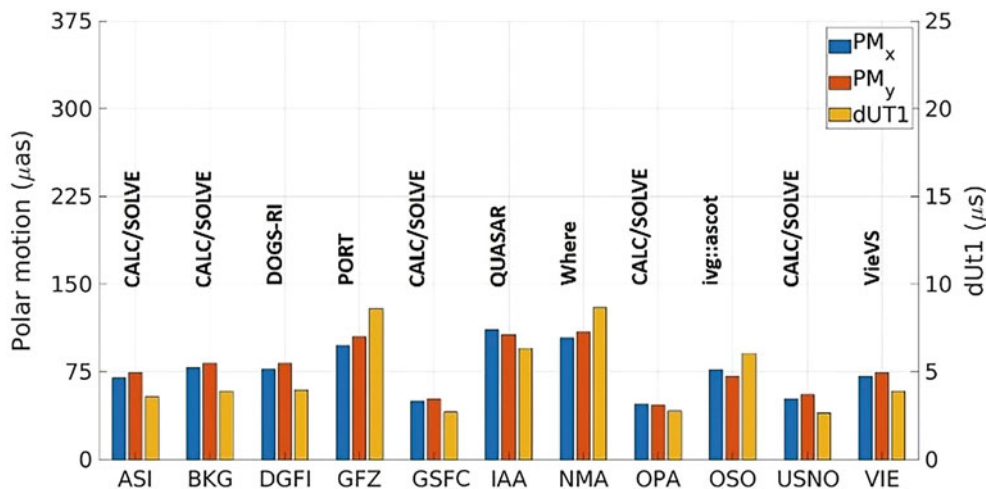


Fig. 10 VLBI-internal validation of ERP estimates: WRMS of the differences between individual AC solutions and the IVS combination

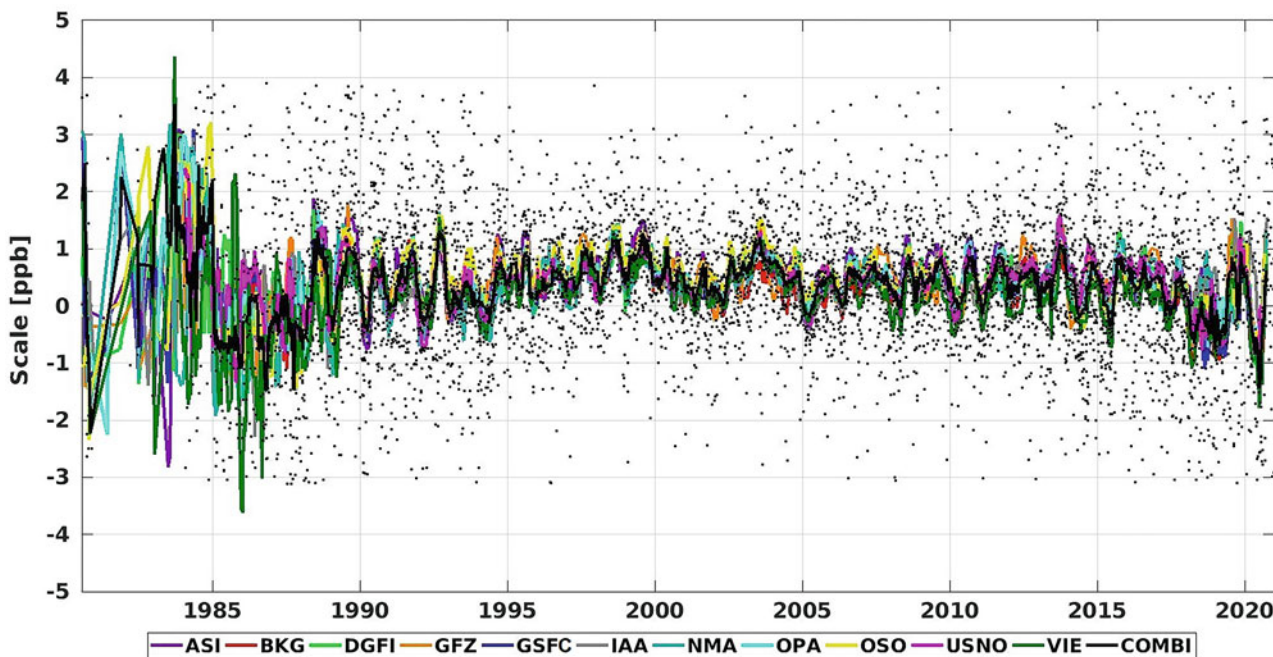


Fig. 11 Scale difference of individual and combined solutions w.r.t. ITRF2014. The solid lines represent a moving median filter of 90 days

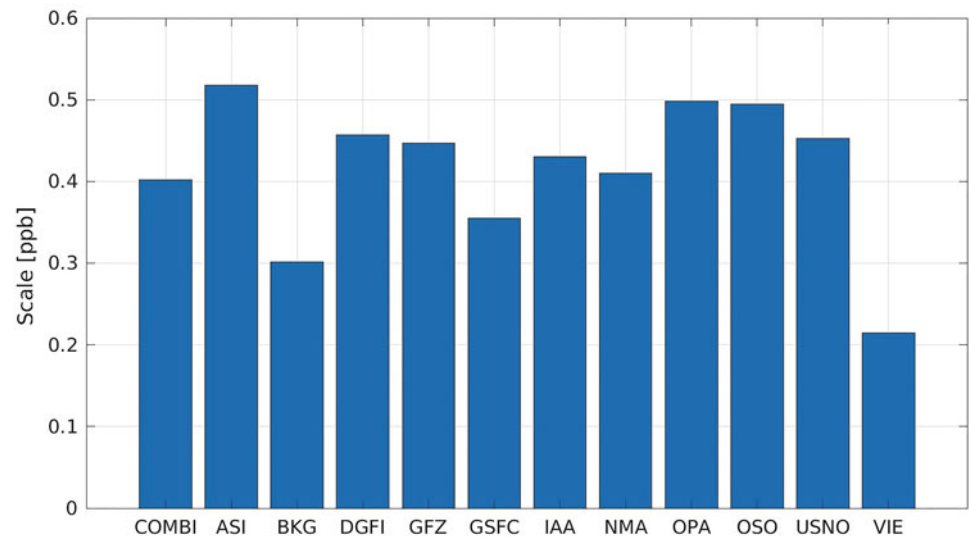
for the solution of the AC VIE which shows a mean scale difference of only 0.2 ppb. The IVS combination shows a scale difference of 0.40 ppb w.r.t. ITRF2014 which confirms the assumption of a weighted mean effect of a combined solution.

## 5 Conclusions and Outlook

In this paper, the IVS contribution to the ITRF2020 is presented. The IVS Combination Centre carried out a session-wise combination of the individual contributions by 11 Analysis Centres on the level of normal equations. The

EOP and the station coordinates of all AC contributions are transformed to equal epochs and equal a priori values for consistency. The source coordinates are fixed to the ICRF3 and are eliminated from the equation system. In contrast to the operational IVS solutions, the non-tidal atmospheric loading corrections are not applied in the final IVS combined contribution, and for those AC contributions originally containing loading corrections, these corrections are added back to the NEQ before entering the combination. The applied variance component estimation yields individual weighting factors for ensuring an unbiased combination with improved accuracy w.r.t. the single solutions (cf. Bähr et al. 2007). Using the complete normal equation matrices ensures that

**Fig. 12** Mean scale offsets of individual and combined solutions w.r.t. ITRF2014 (from 1995 until 2020)



all correlations between the parameters (including the pre-reduced ones) are correctly taken into account. Because VLBI delivers observations w.r.t. the inertial space, the full set of EOP can be estimated as free parameters without applying any constraints. In this context, the geodetic datum is defined by No-Net-rotation and No-Net-translation conditions for a subset of good and stable stations w.r.t. the VTRF realized by the current IVS Quarterly solution (2020/Q2). By applying this procedure, the solutions are consistent with the ITRF2014.

The session-wise solutions for station coordinates and EOPs as well as the terrestrial scale are further investigated in view of consistency between the individual ACs, quality of the AC contributions, and quality of the IVS combined solution. Regarding the investigations of estimated EOP and station coordinates, a significant improvement of the combination compared to the individual AC solutions was achieved for all parameters.

Within the validations w.r.t. external references (i.e., IVS 2020/Q2 solution, IERS Bulletin A) a decreased WRMS of the station coordinates and the ERPs, respectively, could be achieved. The variance component estimation and the outlier detection deliver realistic weighting factors for unbiased parameter estimations.

At the end, almost 6,200 sessions could be combined successfully with high-quality results, and the session-wise combined SINEX files are submitted as IVS contribution to the IERS as input for ITRF2020. A number of almost 100 sessions are submitted with constrained EOP due to small and regional networks that requires special handling as they are not suited for EOP estimation but valuable for densification of the station coordinate time series, and consequently for good position and velocity estimation within ITRF2020.

For all sessions, two different series of SINEX files are provided: one SINEX file where the parameters refer to the mid-epoch of each session, i.e., yielding to the optimal estimates for VLBI solutions, and a second SINEX file, where all parameters are transformed to noon epochs (UTC) in order to be consistent with the other space-geodetic techniques used for the ITRF2020 combination. It must be emphasized that the latter SINEX files do not represent the best contribution by VLBI, but is needed for consistency reasons with the other space-geodetic techniques. This dilemma could only be solved if VLBI sessions would cover standard 24-h intervals in UTC.

Future work will focus on the optimal handling of the source coordinates together with the TRF and EOP within the combination process in order to get a fully consistent set of parameters. Additionally, a long-term VTRF solution will be generated. This is of special importance as the data set generated for ITRF2020 contains VGOS sessions as well as mixed-mode sessions for the first time. Additionally, further investigations related to an optimal weighting strategy in view of handling dependencies due to identical software packages in the ACs' contributions will be carried out. Nevertheless, one must admit that the variety of software packages contributing to the IVS products already increased significantly in the recent years and also for the ITRF2020 contributions, so that it is expected that this dependency is not as big as in the early years of the IVS.

## Conflict of Interest

The authors declare that they have no conflict of interest.

## References

- Abbondanza C, Chin TM, Gross RS, Heflin MB, Parker JW, Soja BS, van Dam T, Wu X (2017) JTRF2014, the JPL Kalman filter and smoother realization of the international terrestrial reference system. *J Geophys Res Solid Earth* 122(10):8474–8510
- Altamimi Z, Rebischung P, Métivier L, Collilieux X (2016) ITRF2014: A new release of the international terrestrial reference frame modeling nonlinear station motions. *J Geophys Res Solid Earth* 121(8):6109–6131. <https://doi.org/10.1002/2016JB013098>
- Bachmann S, Lösler M, Messerschmitt L, Schmid R, Bloßfeld M, Thaller D (2012) IVS combination center at BKG-robust outlier detection and weighting strategies. In: International VLBI service for geodesy and astrometry, pp 266–270
- Bachmann S, Thaller D, Roggenbuck O, Lösler M, Messerschmitt L (2016) IVS contribution to ITRF2014. *J Geodesy* 90(7):631–654. <https://doi.org/10.1007/s00190-016-0899--4>
- Bachmann S, Messerschmitt L, Schmid R, Bloßfeld M, Thaller D (2017) BKG/DGFI-TUM combination center biennial report 2015+2016. In: Bayer KD, Behrend D, Armstrong KL (eds) International VLBI service for geodesy and astrometry 2015+2016 biennial report, NASA/TP-2017-219021
- Bähr H, Altamimi Z, Heck B (2007) Variance component estimation for combination of terrestrial reference frames. Tech. Rep. 6, Karlsruhe Institut für Technologie (KIT). <https://doi.org/10.5445/KSP/1000007363>
- Bizouard C, Lambert S, Gattano C, Becker O, Richard JY (2019) The IERS EOP 14C04 solution for earth orientation parameters consistent with ITRF 2014. *J Geodesy* 93(5):621–633
- Böckmann S, Artz T, Nothnagel A (2010) VLBI terrestrial reference frame contributions to ITRF2008. *J Geodesy* 84(3):201–219. <https://doi.org/10.1007/s00190-009-0357-7>
- Charlot P, Jacobs C, Gordon D, Lambert S, de Witt A, Böhm J, Fey A, Heinkelmann R, Skurikhina E, Titov O, et al. (2020) The third realization of the international celestial reference frame by very long baseline interferometry. *Astron Astrophys* 644:A159. <https://doi.org/10.1051/0004-6361/202038368>
- MacMillan D, Fey A, Gipson J, Jacobs C, Kásná H, Lambert S, Malkin Z, Titov O, Wang G, Xu H (2019) Galactocentric acceleration in VLBI analysis - Findings of IVS WG8. *Astron Astrophys* 630:A93. <https://doi.org/10.1051/0004-6361/201935379>
- Métivier L, Collilieux X, Altamimi Z, Lercier D (2014) The ITRF and its scientific applications. In: Proceedings of the Journées 2013 “Systèmes de référence spatio-temporels”, pp 3–6
- Nothnagel A, Artz T, Behrend D, Malkin Z (2017) International VLBI service for geodesy and astrometry. *J Geodesy* 91(7):711–721. <https://doi.org/10.1007/s00190-016-0950-5>
- Petit G, Luzum B (2010) IERS conventions (2010), IERS technical note no. 36, version 1.3.0. International Earth Rotation and Reference Systems Service, Frankfurt, Germany
- Rousseeuw PJ, Leroy AM (2005) Robust regression and outlier detection. Wiley
- Seitz M, Bloßfeld M, Angermann D, Seitz F (2022) DTRF2014: DGFI-TUM’s ITRS realization 2014. *Adv Space Res* 69(6):2391–2420
- Stamatakos N, Davis M, Shumate N (2020) IERS rapid service/prediction center products and services: improvements, changes, and challenges, 2017 to 2019. In: Astrometry, earth rotation, and reference systems in the GAIA era, pp 99–105
- Thaller D (2008) Inter-technique combination based on homogeneous normal equation systems including station coordinates, Earth orientation and troposphere parameters. PhD thesis, Technische Universität München
- Vennebusch M, Böckmann S, Nothnagel A (2007) The contribution of very long baseline interferometry to ITRF2005. *J Geodesy* 81(6-8):553–564. <https://doi.org/10.1007/s00190-006-0117-x>

**Open Access** This chapter is licensed under the terms of the Creative Commons Attribution 4.0 International License (<http://creativecommons.org/licenses/by/4.0/>), which permits use, sharing, adaptation, distribution and reproduction in any medium or format, as long as you give appropriate credit to the original author(s) and the source, provide a link to the Creative Commons license and indicate if changes were made.






The images or other third party material in this chapter are included in the chapter’s Creative Commons license, unless indicated otherwise in a credit line to the material. If material is not included in the chapter’s Creative Commons license and your intended use is not permitted by statutory regulation or exceeds the permitted use, you will need to obtain permission directly from the copyright holder.







# An Experimental Combination of IGS repro3 Campaign's Orbit Products Using a Variance Component Estimation Strategy

Pierre Sakic , Gustavo Mansur , Benjamin Männel , Andreas Brack , and Harald Schuh 

## Abstract

Over the past years, the International GNSS Service (IGS) has put efforts into reprocessing campaigns, reanalyzing the entire data collected by the IGS network since 1994. Using state-of-the-art models and software, the goal is to provide a consistent set of orbits, station coordinates, and earth rotation parameters. Unlike the previous campaigns—namely: repro1 and repro2—the repro3 includes not only GPS and GLONASS but also the Galileo constellation. The main repro3 objective is the contribution to the next realization of the International Terrestrial Reference Frame (ITRF2020). To achieve this goal, several Analysis Centers (AC) submitted their own products to the IGS, which are combined to provide the final solutions for each product type. In this contribution, we focus on the combination of the orbit products. We present a consistent orbit solution based on a newly developed combination strategy, where the weights are determined by a Least-Squares Variance Component Estimation (LSVCE). The orbits are intended to be combined in an iterative processing: firstly, by aligning all the products via a Helmert transformation, secondly by defining which satellites will be used in the LSVCE, and finally by normalizing the inverse of the variances as weights that are used to compute a weighted mean. The combination results show an agreement between the different AC's input orbits around 10 mm for GPS, 30 mm for GLONASS. The combination also highlights the improvement of the Galileo orbit determination over the past decade, the internal precision decreasing from around 35 mm to 16 mm for the most recent weeks. We used Satellite Laser Ranging (SLR) observations for external validation. The combined orbit has one of the best RMS agreements with respect to the SLR measurements (9.1 mm for GLONASS, and 8.3 mm over the last five years of the processed period).

## Keywords

GNSS · IGS · Orbit combination · Repro3 · Variance components estimation

---

P. Sakic (✉)  
GFZ German Research Centre for Geosciences, Potsdam, Germany  
Institut de Physique du Globe de Paris, Paris-Cité University, Paris,  
France  
e-mail: [sakic@ipgp.fr](mailto:sakic@ipgp.fr)

---

G. Mansur · H. Schuh  
GFZ German Research Centre for Geosciences, Potsdam, German  
Technische Universität Berlin, Institute for Geodesy and  
Geoinformation Technology, Faculty VI, Berlin, Germany  
B. Männel · A. Brack  
GFZ German Research Centre for Geosciences, Potsdam, German

## 1 Introduction

Over the past years, the International GNSS Service (IGS) has put efforts into reprocessing campaigns reanalyzing the full data collected by the IGS network since 1994. The goal is to provide a consistent set of orbits, station coordinates, and earth rotation parameters using state-of-the-art models. Since the end of 2020, the IGS has completed the *reprocessing 3* campaign (abbreviated as repro3). It differs from the previous campaigns (namely repro1 achieved in 2009 and repro2 in 2015) by the fact that repro3 includes not only GPS and GLONASS but also the Galileo constellation. The main repro3 objective is to provide the GNSS contribution to the next realization of the International Terrestrial Reference Frame (ITRF2020, Altamimi et al. 2021). To achieve this goal, 12 Analysis Centers (AC) joined the effort and submitted their own products to the Analysis Center Coordinator (ACC). Each product type is then combined at the solution or at the normal equation level to provide to the final user an “IGS-labeled” solution with the best accuracy possible. In this contribution, we mainly focus on the combination of the orbit products.

The strategy of combining orbits and clock offsets was developed during the early age of the IGS for two main reasons (Kouba et al. 1994):

1. to provide to the users the most reliable of all the submitted solutions and
2. to offer a feedback tool to evaluate the consistency between ACs.

The initial developments of such combination were performed by Springer and Beutler (1993) and Beutler et al. (1995), and then slightly modified by Kouba et al. (2001). However, it has evolved very little for more than 25 years. The major limitation of the current algorithm used operationally by the IGS’s ACC is that it is not adapted to a multi-GNSS environment (Mansur et al. 2020b), while the new generation of satellite positioning constellations (Galileo, Beidou, QZSS, IRNSS) are coming to maturity. Therefore, an update of the combination procedure is necessary.

Thus, our research group has started to study a new combination strategy compatible with the new constellations, initially based on the legacy IGS software (Sakic et al. 2020), then by designing an *ad hoc* strategy optimised for a multi-GNSS configuration (Mansur et al. 2020b,a). These activities are carried out in parallel with the orbit combination studies performed by the ACC in the context of the IGS’s Multi-GNSS Experiment (MGEX) pilot project (Sošnica et al. 2020), and the ones regarding integer clocks (Banville et al. 2020).

The present paper presents the results obtained for an orbit combination of the IGS’s repro3 orbit products based on the new strategy we developed. We describe hereafter

the input products integrated and the processing method. We present the results of the orbit combination results compared with each individual AC, for all satellites and for each separated constellation. We provide also a Satellite Laser Ranging (SLR) validation for an external assessment of the combination.

## 2 Material and Methods

The new combination strategy elaborated by our working group, based on a Least-Squares Variance Component Estimation (LSVCE) weighting, is described in detail in Mansur et al. (2020a). It is developed within the framework of the Python *GeodeZYX Toolbox* software (Sakic et al. 2019).

General workflow can be summarized as follow:

1. A simple arithmetic mean of all the input AC’s orbits is computed.
2. Helmert transformations are performed between this mean and the ACs’ solutions.
3. A set of so-called “core satellites” is defined. The goal is to get the common satellites present in all the input AC’s solutions. During this step, an improved outlier detection scheme is applied: a Modified Z-Score approach (Iglewicz and Hoaglin 1993) is used to test the radial, along-track, and cross-track components of each set of AC coordinates for all satellites. If one satellite’s component is detected as outlier, the satellite is excluded from the set of core satellites.
4. The variance components are estimated based on the theory of Amiri-Simkooei et al. (2007), using only the set of core satellites as defined before. The detailed mathematical development is available in Mansur et al. (2020a).
5. The variance components  $\sigma^2$  are normalized and used as weights using the formula:

$$\hat{\mathbf{X}}_c = \frac{1}{\sum_{ac=1}^{AC} \frac{1}{\sigma_{ac}^2}} \cdot \sum_{ac=1}^{AC} \frac{1}{\sigma_{ac}^2} \cdot \bar{\mathbf{X}}_{ac}, \quad (1)$$

where  $\bar{\mathbf{X}}_{ac}$  are the input coordinate vectors of the ACs,  $\sigma_{ac}^2$  is the variance for each AC, and  $\hat{\mathbf{X}}_c$  is the combined coordinate vector.

The process is repeated iteratively until the 3D-RMS difference between two iterations is bellow 1 mm. This occurs usually at the fifth iteration.

The algorithm has been designed to realize a weighting based on the different AC only, or based on both the ACs and the different constellations. For the present study, we adopted the so-called *AC plus constellation* strategy.

We considered all the orbit products provided by the different ACs which participated to the repro3 efforts. The

**Table 1** Summary of the different input orbit products. *Abrev.* stands for the AC abbreviation, *Const.* for the GNSS constellations computed by each AC: G for GPS, R for GLONASS, E for Galileo

Analysis center	Abrev.	Const.	First epoch (calendar)	First epoch (GPS week)	Products and/or software
Center for orbit Determination in Europe	cod	GRE	1994-01-02	730	Selmke et al. (2020) Dach et al. (2015)
European Space Agency	esa	GRE	1995-01-01	782	Schoenemann et al. (2021)
GeoForschungsZentrum	gfz	GRE	1994-01-02	730	Männel et al. (2020, 2021)
Groupe de Recherche en Géodésie Spatiale	grg	GRE	2000-05-03	1060	Katsigianni et al. (2019)
Jet Propulsion Laboratory	jpl	G	1994-01-01	729	Bertiger et al. (2020)
Massachusetts Institute of Technology	mit	GE	2000-01-02	1043	Herring et al. (2018)
National Geodetic Survey	ngs	G	1994-01-02	730	Damiani and Freeman (2019)
Graz University of Technology	tug	GRE	1994-01-01	729	Strasser and Mayer-Gürr (2021) Mayer-Gürr et al. (2021)
Wuhan University	whu	GR	2008-01-01	1460	Guo et al. (2016)

campaign period ranges from GPS week 730 (1994-01-02) to 2138 (2020-12-31). Table 1 summarizes the different AC products used and their contribution period.

The orbits are described in the SP3d format (Hilla 2016) and were retrieved from the Crustal Dynamics Data Information System (CDDIS) server (Noll 2010).

### 3 Results

To evaluate the compatibility between the combination and the input orbit products, we compute the Root Mean Square (RMS) differences using the formulas described in Kouba et al. (1994):

$$RMS_{ac} = \sqrt{\frac{1}{N_{sat_{ac}}} \sum_{sat}^{N_{sat_{ac}}} (RMS_{ac}^{sat})^2} \quad (2)$$

$$RMS_{ac}^{sat} = \sqrt{\frac{\sum_i^{N_{epoch_{ac}^{sat}}} \|\bar{\mathbf{X}}_{ac}^{sat} - \hat{\mathbf{X}}_c^{sat}\|_i^2}{3 \cdot N_{epoch_{ac}^{sat}} - 7}} \quad (3)$$

where  $RMS_{ac}$  is the center's RMS,  $RMS_{ac}^{sat}$  is the satellite's RMS per center,  $N_{sat_{ac}}$  is the number of satellites per center and  $N_{epoch_{ac}^{sat}}$  is the number of determined orbit positions per center per satellite.

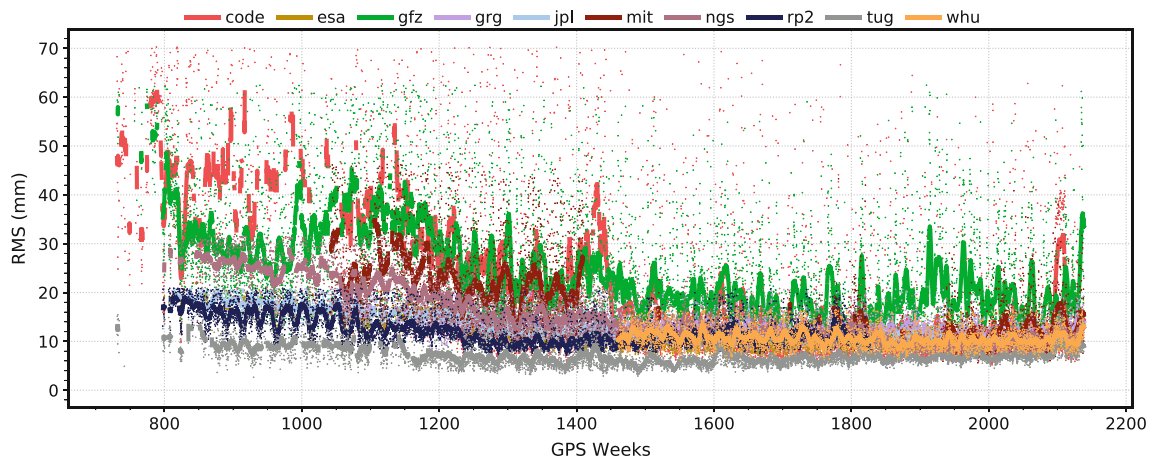
The results are shown in Fig. 1. We also adopt a similar graphical representation as the one usually presented by the IGS's ACC (e.g. Griffiths 2019): dots representing the daily RMS, and a smoothing curve based on a 14-day window Gaussian filter. We perform also a comparison with respect to the previous combined orbits generated at the end of the previous repro2 campaign (Griffiths 2019). The repro2 products, used only for comparison purposes and based on GPS-only orbits, are identified as *rp2* in Fig. 1. We also

indicate in Table 2 the mean RMS for each AC for the three processed constellations, and subdivided into two columns, one for the full-time range and the other for the last year (2020) only.

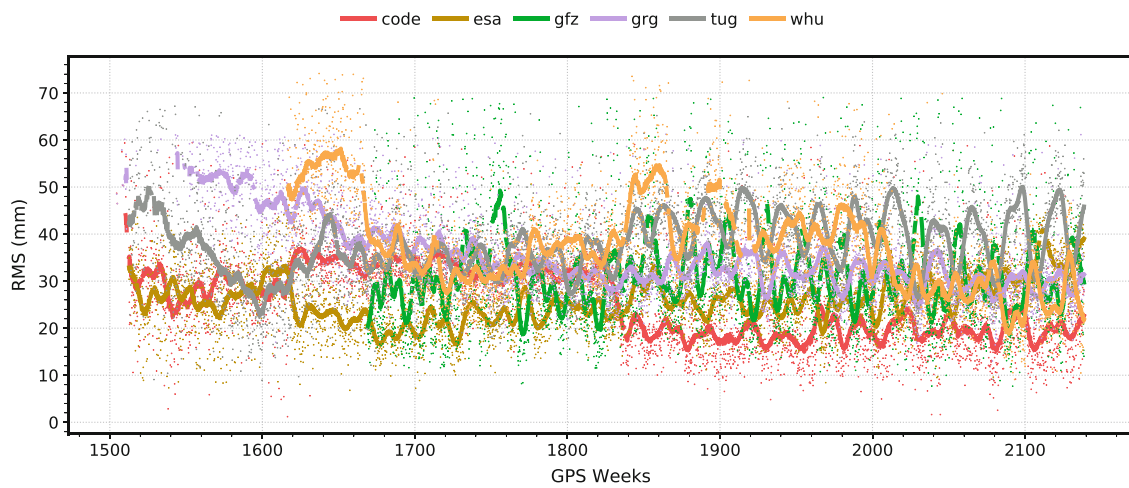
For GPS, the differences of individual ACs with respect to the combination reach 60 mm for the early weeks of the repro3 period. It stabilizes after GPS week 1400 at around 25 mm for the ACs with the highest RMS, and around 10 mm for the majority of the ACs. The best RMS values along with the best stability is achieved by the TUG solution around 6 mm. A noticeable difference with the repro2 solution is visible, ranging from 18 mm for the early weeks to 10 mm after GPS week 1250. This difference can be seen as a general improvement in the accuracy of the repro3 orbits compared to the previous reprocessing campaign.

For GLONASS, the differences are centered around 30 mm for the complete period, with a dispersion between 55 mm and 20 mm, with the latter achieved by CODE. Regarding Galileo, the differences range from about 35 mm from GPS week 1745 (date of the first Galileo satellite activation) to a stabilized value of 16 mm after GPS week 1900. For the European constellation, it is also remarkable that half of the ACs (namely CODE, ESA and TUG) have the same level of agreement for their provided orbits, since their RMS differences with respect to the combination are similar (to the level of 5 mm).

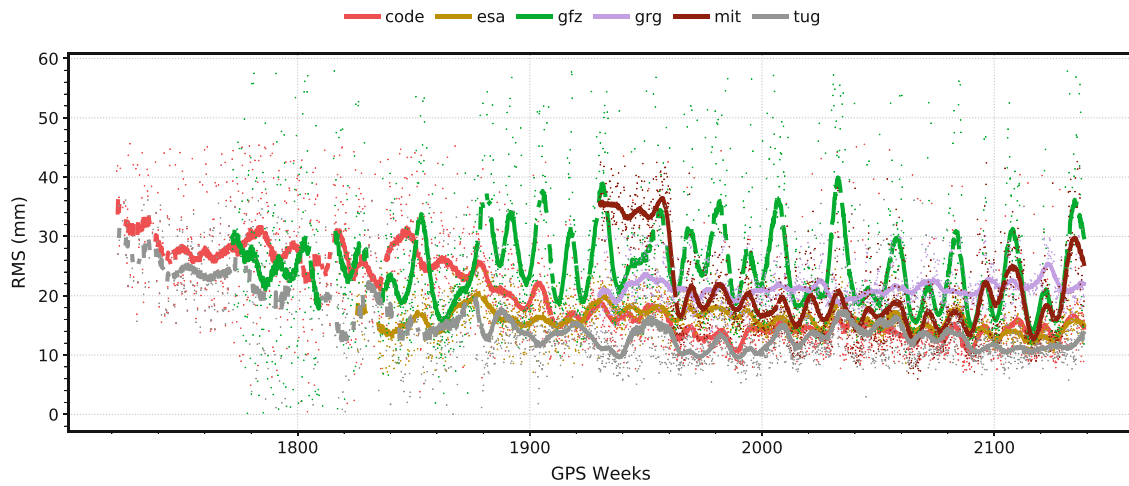
The weights derived from the LSVCE are represented on Fig. 2. They are the corollary of the RMS difference plots, since the ACs with the smallest RMS present the highest weights. For GPS, the values of the weights obtained for the different ACs are reasonably equivalent: they range from 7% (GFZ and GRG) to 17% (TUG), with an average value of 11% (all the ACs, i.e. 9 provide their solutions). For GLONASS, the differences are more pronounced, ranging from 9% (TUG) to 30% (COD), with an average value of



(a) GPS



(b) GLONASS



(c) Galileo

**Fig. 1** 3D-RMS difference of individual AC orbit solutions w.r.t the combined solution. Please note that the y-axis scales are different for each figure. (a) GPS. (b) GLONASS. (c) Galileo

**Table 2** Mean RMS for each AC for the three processed constellations, for the full period (*full* column) and the last year (*2020* column)

	G (full)	G (2020)	R (full)	R (2020)	E (full)	E (2020)
cod	66.88	22.14	35.08	23.18	37.85	16.39
esa	25.42	18.91	27.74	34.34	16.80	13.78
gfz	48.09	20.19	56.80	37.51	154.41	33.55
grg	30.47	16.82	52.50	30.96	22.79	23.25
jpl	18.72	11.51	N/A	N/A	N/A	N/A
mit	28.66	13.85	N/A	N/A	24.69	21.64
ngs	41.84	11.67	N/A	N/A	N/A	N/A
tug	18.96	8.96	48.07	41.59	36.69	12.24
whu	11.48	14.76	198.74	25.75	N/A	N/A

16% (6 solutions provided). For Galileo, the mean weight value is also around 16% for 6 solutions provided, with noticeable discrepancies ranging from 11% (GFZ and GRG) to 24% (TUG). For most AC's the weights are stable over time as expected for a consistent re-processing. Short-term (periodic) fluctuation represents differences related to the individual orbit modeling approaches.

#### 4 SLR External Validation

To perform an independent quality assessment of the combination, we performed an external validation using SLR observations. Indeed, all Galileo and the most of the GLONASS satellites (GLONASS-M and GLONASS-K generations) are equipped with Laser Retroreflector Arrays (LRA, Dell'Agnello et al. 2011) and thus are suited for such operation. We use as observation input the normal points provided by the International Laser Ranging Service (ILRS, Pearlman et al. 2002). The processing is performed with GFZ's EPOS-P8 software (Uhlemann et al. 2015), designed for GNSS precise orbit determination, precise point positioning, and orbit validation using SLR. SLR station coordinates are fixed to the SLRF2014 (Luceri et al. 2015). Ocean tidal loading is corrected from the station positions using the FES2004 model (Lyard et al. 2006). An outlier threshold for residuals over 0.5 m is applied. Daily averaged residuals and a smoothing curve based on a 14-day window Gaussian filter for each AC are shown in Fig. 3. The validation is performed starting from GPS week 1745, when the first Galileo satellites were available. Table 3 summarizes the mean residuals and the associated standard deviation for each AC and both constellations.

The combined solution shows one of the best agreements with the SLR measurement ( $-2.63$  mm mean residuals for Galileo,  $0.84$  mm for GLONASS). It shows also the sec-

ond smallest dispersion for GLONASS (std. =  $9.10$  mm for GLONASS). For Galileo, the combination dispersion is not significantly reduced over the whole tested period ("E, full" in Table 3) due to the input solutions' high residuals during the early weeks. But if we consider the residuals on a reduced period only after the GPS week 1890 ("E, red." in Table 3), the combination shows the second smallest dispersion (std. =  $8.15$  mm). This external validation illustrates that the combination provides both the best accuracy and precision level out of the individual input solutions.

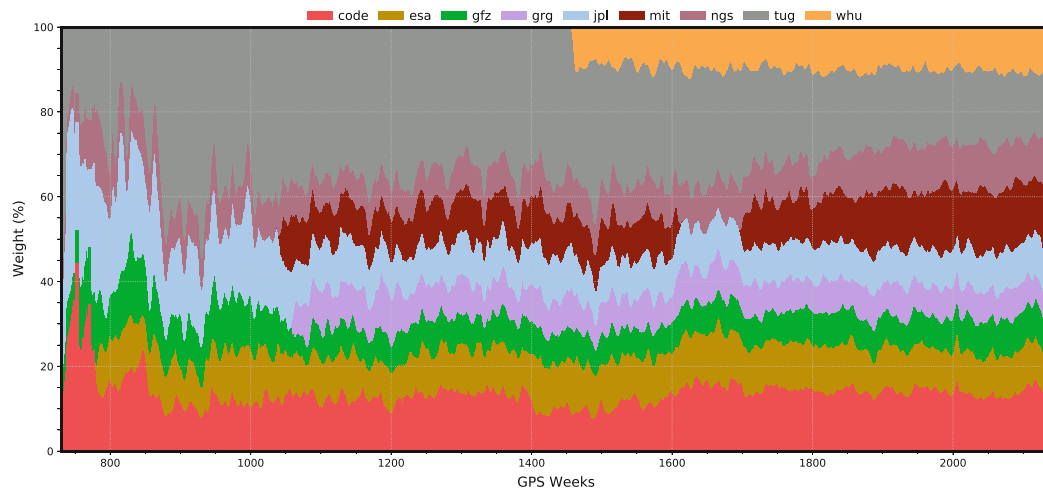
#### 5 Discussion and Perspectives

We developed a new GNSS orbit combination strategy based on a Least-Squares Variance Component Estimation, and an improved detection for outlier satellites (Mansur et al. 2020a). This algorithm can also handle the different constellations separately. It corrects the weaknesses of the legacy software used routinely by the IGS's ACC, which have been raised during a preliminary study investigating the possibilities to improve it for a multi-GNSS environment (Sakic et al. 2020). We tested this new algorithm with the recent set of orbit products generated by the different IGS ACs in the framework of the repro3 reprocessing campaign. A 10 mm internal precision is achieved for GPS, 30 mm for GLONASS, and 16 mm for Galileo at the end of the reprocessed period (2020-12-31). The SLR validation shows that the combination has one of the best agreements with the laser measurements and also the smallest residual dispersion, then confirming its robustness with an external technique. The results can be a useful tool for the ACs to identify potential weaknesses in their processing. The present work can also be a support for cross-comparison and validation of the orbit combination currently performed by the IGS's ACC (Masoumi and Moore 2021).

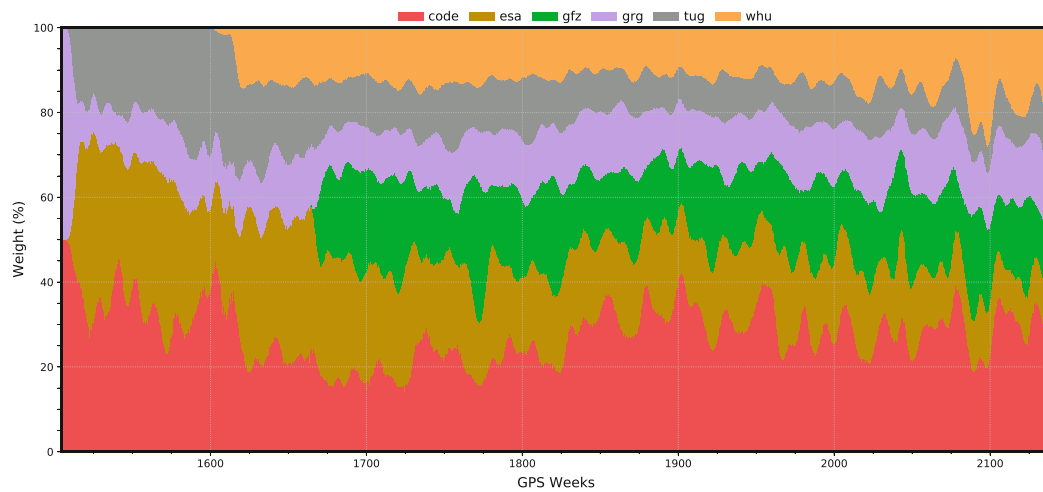
#### Data Availability

The data used for this work are publicly and freely available on the CDDIS server. The combined products described in this study can be provided for free on demand.

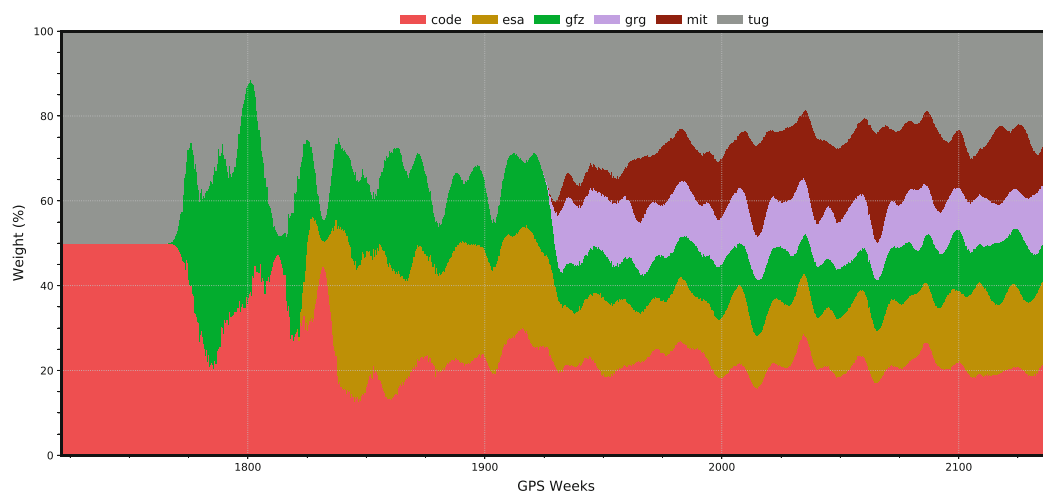
**Acknowledgements** We would like to thank the International Laser Ranging Service (ILRS), the International GNSS Service and more particularly its Analysis Centers for providing their products. The PhD of Gustavo Mansur is funded by the Deutscher Akademischer Austauschdienst (DAAD, German Academic Exchange Service).



(a)



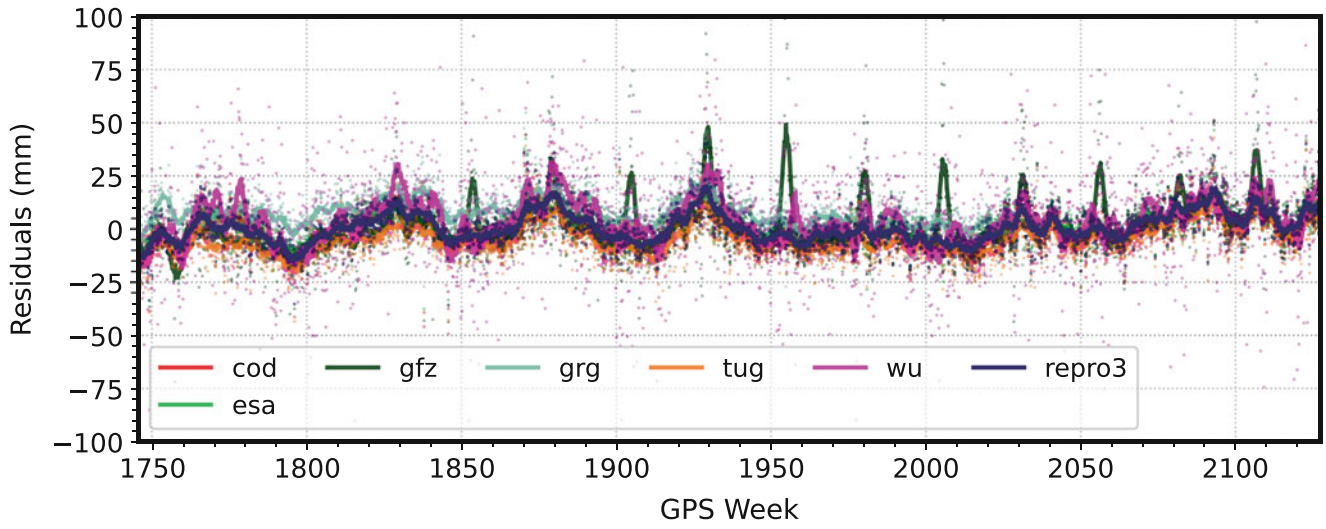
(b)



(c)

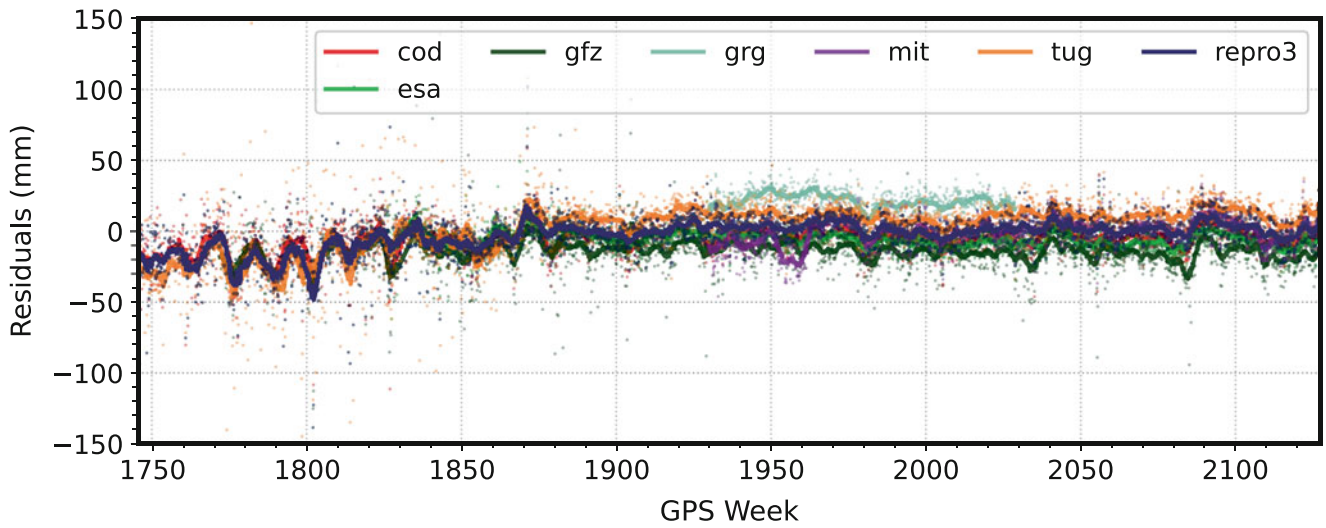
**Fig. 2** Weights derived from the LSVCE for each AC solution per constellation. (a) GPS. (b) GLONASS. (c) Galileo

### SLR Residuals for GLONASS



(a)

### SLR Residuals for Galileo



(b)

**Fig. 3** Average SLR Residuals per constellation for each AC solution and the combination. (a) GLONASS. (b) Galileo

**Table 3** Mean residuals, standard deviation, and Root Mean Square w.r.t. 0 in mm for each input AC for GLONASS (R) and Galileo (E). For Galileo, the statistics are split into two ranges: a full period ("E, full" column) and a reduced period ("E, red." column) starting from GPS week 1890.

Const.	AC	Mean	Std.	RMS
R	cod	0.04	9.61	9.61
R	esa	1.26	8.89	8.97
R	gfz	0.79	16.47	16.48
R	grg	7.67	9.15	11.94
R	tug	-5.03	9.14	10.43
R	whu	3.54	23.13	23.40
R	rp3	0.84	9.10	9.14
E,full	cod	-6.31	13.08	14.52
E,full	esa	-5.84	8.58	10.38
E,full	gfz	-14.37	14.69	20.55
E,full	grg	21.34	8.53	22.98
E,full	mit	-0.12	10.97	10.97
E,full	tug	2.37	22.87	22.99
E,full	rp3	-2.63	14.56	14.79
E,red.	cod	-4.26	8.42	9.43
E,red.	esa	-6.58	7.15	9.71
E,red.	gfz	-14.16	12.25	18.73
E,red.	grg	21.34	8.53	22.98
E,red.	mit	-0.12	10.97	10.97
E,red.	tug	10.84	8.65	13.87
E,red.	rp3	1.55	8.15	8.30

## References

- Altamimi Z, Rebischung P, Métivier L, Collilieux X, Chanard K (2021) Highlights of IGS contribution to ITRF2020. In: Tour de l'IGS 1st stop online conference. <https://files.igs.org/pub/resource/pubs/workshop/2021/03-Altamimi.pdf>
- Amiri-Simkooei AR, Tiberius CC, Teunissen PJ (2007) Assessment of noise in GPS coordinate time series: Methodology and results. *J Geophys Res Solid Earth* 112(7):1–19. <https://doi.org/10.1029/2006JB004913>
- Banville S, Geng J, Loyer S, Schaer S, Springer T, Strasser S (2020) On the interoperability of IGS products for precise point positioning with ambiguity resolution. *J Geodesy* 94(1):10. <https://doi.org/10.1007/s00190-019-01335-w>
- Bertiger W, Bar-Sever Y, Dorsey A, Haines B, Harvey N, Hemberger D, Heflin M, Lu W, Miller M, Moore AW, Murphy D, Ries P, Romans L, Sibois A, Sibthorpe A, Szilagy B, Vallisneri M, Willis P (2020) GipsyX/RTGx, a new tool set for space geodetic operations and research. *Adv Space Res* 66(3):469–489. <https://doi.org/10.1016/j.asr.2020.04.015>. 2004.13124
- Beutler G, Kouba J, Springer T (1995) Combining the orbits of the IGS analysis centers. *Bull Géodésique* 69(4):200–222. <https://doi.org/10.1007/BF00806733>
- Dach R, Lutz S, Walser P, Fridez P (2015) Bernese GNSS Software Version 5.2. <https://doi.org/10.7892/BORIS.72297>
- Damiani T, Freeman W (2019) Strengthening the NOAA CORS Network: Foundation CORS, orbit analysis, and other initiatives. In: AGU fall meeting abstracts, vol 2019, pp G11A–07
- Dell'Agnello S, Delle Monache GO, Currie DG, Vittori R, Cantone C, Garattini M, Boni A, Martini M, Lops C, Intaglietta N, Tauraso R, Arnold DA, Pearlman MR, Bianco G, Zerbini S, Maiello M, Berardi S, Porcelli L, Alley CO, McGarry JF, Sciarretta C, Luceri V, Zagwodzki TW (2011) Creation of the new industry-standard space test of laser retroreflectors for the GNSS and LAGEOS. *Adv Space Res* 47(5):822–842. <https://doi.org/10.1016/j.asr.2010.10.022>
- Griffiths J (2019) Combined orbits and clocks from IGS second reprocessing. *J Geodesy* 93(2):177–195. <https://doi.org/10.1007/s00190-018-1149-8>
- Guo J, Xu X, Zhao Q, Liu J (2016) Precise orbit determination for quad-constellation satellites at Wuhan University: strategy, result validation, and comparison. *J Geodesy* 90(2):143–159. <https://doi.org/10.1007/s00190-015-0862-9>
- Herring TA, King RW, Floyd MA, McClusky SC (2018) GAMIT reference manual - release 10.7. Department of Earth, Atmospheric, and Planetary Sciences Massachusetts Institute of Technology
- Hilla S (2016) The extended standard product 3 orbit format (SP3-d). Tech. rep., National Geodetic Survey, Silver Spring. <ftp://ftp.igs.org/pub/data/format/sp3d.pdf>
- Iglewicz B, Hoaglin DC (1993) How to detect and handle outliers, vol 16. Asq Press
- Katsigianni G, Loyer S, Perosanz F, Mercier F, Zajdel R, Sońnica K (2019) Improving Galileo orbit determination using zero-difference ambiguity fixing in a Multi-GNSS processing. *Adv Space Res* 63(9):2952–2963. <https://doi.org/10.1016/j.asr.2018.08.035>
- Kouba J, Mireault Y, Lahaye F (1994) IGS orbit/clock combination and evaluation, Appendix 1 of the analysis coordinator report, international GPS service for geodynamics 1994 annual report. Jet Propulsion Laboratory Publication, pp 18–95
- Kouba J, Springer T, Héroux P (2001) New IGS station and satellite clock combination. *GPS Solutions* 4(4):31–36. <https://doi.org/10.1007/PL00012863>
- Luceri V, Pavlis EC, Pace B, König D, Kuzmich-Cieslak M, Bianco G (2015) Overview of the ILRS contribution to the development of ITRF2013. In: International association of geodesy symposia. Springer International Publishing Switzerland, pp 101–108. [https://doi.org/10.1007/1345\\_2015\\_153](https://doi.org/10.1007/1345_2015_153)
- Lyard F, Lefevre F, Letellier T, Francis O (2006) Modelling the global ocean tides: Modern insights from FES2004. *Ocean Dynamics* 56(5–6):394–415. <https://doi.org/10.1007/s10236-006-0086-x>
- Männel B, Brandt A, Bradke M, Sakic P, Brack A, Nischan T (2020) Status of IGS reprocessing activities at GFZ. In: International association of geodesy symposia. Springer, Berlin, Heidelberg. [https://doi.org/10.1007/1345\\_2020\\_98](https://doi.org/10.1007/1345_2020_98)
- Männel B, Brandt A, Bradke M, Sakic P, Brack A, Nischan T (2021) GFZ repro3 product series for the International GNSS service (IGS). <https://dataservices.gfz-potsdam.de/panmetaworks/showshort.php?id=c7c804cc-6644-11eb-9603-497c92695674>
- Mansur G, Sakic P, Brack A, Männel B, Schuh H (2020a) Combination of GNSS orbits using variance component estimation. In review in *J Geodesy*, preprint available on EarthArXiv, pp 1–12. <https://doi.org/10.31223/X5MK64>. <https://eartharxiv.org/repository/view/1932/>
- Mansur G, Sakic P, Männel B, Schuh H (2020b) Multi-constellation GNSS orbit combination based on MGEX products. *Adv Geosci* 50:57–64. <https://doi.org/10.5194/adgeo-50-57-2020>. <https://www.adv-geosci.net/50/57/2020/https://adgeo.copernicus.org/articles/50/57/2020/>
- Masoumi S, Moore M (2021) Multi-GNSS orbit solutions from the third IGS Reprocessing. In: Tour de l'IGS 1st stop online conference. <https://files.igs.org/pub/resource/pubs/workshop/2021/04-Masoumi.pdf>
- Mayer-Gürr T, Behzadpour S, Eicker A, Ellmer M, Koch B, Krauss S, Pock C, Rieser D, Strasser S, Süsser-Rechberger B, Zehentner N, Kvas A (2021) GROOPS: A software toolkit for gravity field recovery and GNSS processing. *Comput Geosci* 155(December 2020):104864. <https://doi.org/10.1016/j.cageo.2021.104864>
- Noll CE (2010) The crustal dynamics data information system: A resource to support scientific analysis using space



- geodesy. *Adv Space Res* 45(12):1421–1440. <https://doi.org/10.1016/j.asr.2010.01.018>. <https://linkinghub.elsevier.com/retrieve/pii/S0273117710000530>
- Pearlman M, Degnan J, Bosworth J (2002) The international laser ranging service. *Adv Space Res* 30(2):135–143. [https://doi.org/10.1016/S0273-1177\(02\)00277-6](https://doi.org/10.1016/S0273-1177(02)00277-6). [https://ebooks.worldscinet.com/ISBN/9789812836182/9789812836182\\_0009.htmlhttps://linkinghub.elsevier.com/retrieve/pii/S0273117702002776](https://ebooks.worldscinet.com/ISBN/9789812836182/9789812836182_0009.htmlhttps://linkinghub.elsevier.com/retrieve/pii/S0273117702002776)
- Sakic P, Mansur G, Kitpracha C, Ballu V (2019) The geodeZyX toolbox: a versatile Python 3 toolbox for geodetic-oriented purposes. <https://doi.org/10.5880/GFZ.1.1.2019.002>. <https://dataservices.gfz-potsdam.de/panmetaworks/showshort.php?id=escidoc:4754924>
- Sakic P, Mansur G, Mannel B (2020) A prototype for a Multi-GNSS orbit combination. In: 2020 European navigation conference (ENC). IEEE, pp 1–11. <https://doi.org/10.23919/ENC48637.2020.9317316>. <https://ieeexplore.ieee.org/document/9317316/>
- Schoenemann E, Dilssner F, Mayer V, Gini F, Otten M, Springer T, Bruni S, Enderle W, Zandbergen R (2021) ESA's efforts for more consistent geodetic products. EGU General Assembly 2021. <https://doi.org/10.5194/egusphere-egu21-8899>. <https://doi.org/10.5194/egusphere-egu21-8899>
- Selmke I, Dach R, Arnold D, Prange L, Schaer S, Sidorov D, Stebler P, Villiger A, Jäggi A, Hugentobler U (2020) CODE repro3 product series for the IGS. <https://doi.org/10.7892/BORIS.135946>. <https://boris.unibe.ch/135946/>
- Sošnica K, Zajdel R, Bury G, Bosy J, Moore M, Masoumi S (2020) Quality assessment of experimental IGS multi-GNSS combined orbits. *GPS Solutions* 24(2):54. <https://doi.org/10.1007/s10291-020-0965-5>
- Springer T, Beutler G (1993) Towards an official IGS orbit by combining the results of all IGS processing centers. In: Proceedings of the 1993 IGS workshop, held March, pp 24–26
- Strasser S, Mayer-Gürr T (2021) Satellite orbits. <https://doi.org/10.3217/DATASET-7012-6314-1426>. <https://repository.tugraz.at/records/ebamh-r3860>
- Uhlemann M, Gendt G, Ramatschi M, Deng Z (2015) GFZ global Multi-GNSS network and data processing results. In: International association of geodesy symposia. Springer, vol 12, pp 673–679. [https://doi.org/10.1007/1345\\_2015\\_120](https://doi.org/10.1007/1345_2015_120)

**Open Access** This chapter is licensed under the terms of the Creative Commons Attribution 4.0 International License (<http://creativecommons.org/licenses/by/4.0/>), which permits use, sharing, adaptation, distribution and reproduction in any medium or format, as long as you give appropriate credit to the original author(s) and the source, provide a link to the Creative Commons license and indicate if changes were made.

The images or other third party material in this chapter are included in the chapter's Creative Commons license, unless indicated otherwise in a credit line to the material. If material is not included in the chapter's Creative Commons license and your intended use is not permitted by statutory regulation or exceeds the permitted use, you will need to obtain permission directly from the copyright holder.





# The Correlations of the Helmert Transformation Parameters as an Additional Auxiliary Diagnostic Tool for Terrestrial Reference Frames Quality Assessment

D. Ampatzidis, D. Thaller, and L. Wang

## Abstract

In the present study, we estimate the correlations of the Helmert transformation's parameters for various Terrestrial Reference Frame realizations (TRFs). The correlations can be served as an auxiliary diagnostic tool on assessing the quality of the Helmert transformation parameters (origin, scale, orientation and associated rates, respectively). Possible high correlations between the pair of parameters are signs of strong dependency of each other, hence their estimation can lead to misinterpretations. We compute the Helmert correlation coefficients of global TRFs for the following cases: (a) the SLR and VLBI intra-technique combinations contributing to the DTRF2014 construction and the associated SLR and VLBI inter-technique combinations and (b) the DORIS-related TRFs computed by the International DORIS Service (IDS) and the ITRF2014 (International TRF 2014). The results verify the good quality of DTRF2014 (DGFI-TUM TRF 2014) in terms of the Helmert parameters quality, for both SLR- and VLBI-related TRFs. For the case of the DORIS solutions, we find that the correlations are severely increased for the solution that includes 5 more years of observations than the ITRF2014 one.

## Keywords

Correlations · Datum definition · DORIS · Helmert transformation parameters · SLR · TRF assessment · VLBI

## 1 Introduction

The assessment of the global TRFs is a matter of great importance in the direction of their consistent realization. The TRFs assessment is mainly done via extensive reanalysis of observations from all contributing techniques and a comparison of the results, e.g. station position and velocity

residuals, orbital fits, etc. Another tool for TRF assessment is the well-known Helmert transformation (e.g. Altamimi et al. 2008; Liu et al. 2021). Helmert transformation quantifies the consistency (or more practically, the level of similarity) between two frames). E.g., the technique-only solution is compared to the (final) solution derived from combining the technique-only solution, respectively, in terms of the 7 or 14 Helmert transformation parameters (e.g., Altamimi et al. 2002, 2007). The assessment can also be realized through the comparison between a technique-only and combined solution(s) with external sources (Collilieux et al. 2014). The magnitude of the estimated Helmert transformation parameters between two solutions is an indication of their consistency. Relatively large Helmert parameters are a sign of inconsistency between two solutions. For example, the scale between SLR and VLBI of the ITRF2014 estimated at the level of 1.37 ppb (Altamimi et al. 2016), implying the presence of systematic errors that could exist in either or both

---

D. Ampatzidis (✉)  
German Federal Agency for Cartography and Geodesy, Frankfurt am Main, Germany

Present Address: Department of Surveying and Geomatics Engineering, International Hellenic University, Serres, Greece  
e-mail: [dimitrios.ampatzidis@bkg.bund.de](mailto:dimitrios.ampatzidis@bkg.bund.de); [dampatzi@teicm.gr](mailto:dampatzi@teicm.gr)

D. Thaller · L. Wang  
German Federal Agency for Cartography and Geodesy, Frankfurt am Main, Germany

techniques. For ITRF2020 (preliminary results), the scale discrepancies between SLR and VLBI seems to be significantly mitigated, mostly because the SLR analysis scheme include the station-wise range biases estimation (Altamimi et al. 2021).

However, it is possible that two or more parameters are associated with high correlations (larger than 0.7, see e.g. Frost 2020), and thus, degrade their independent estimation. The correlations are mostly depended on the network's geometry. The correlations can serve as an additional diagnostic tool in the direction of the quality assessment of the Helmert transformation. In contrast to the application of the Helmert transformation that compares two different TRFs, the correlations focus on each technique's ability to provide qualitative information regarding the origin, scale and orientation (and their rates) for a single TRF. The purpose of this study is to verify the differences between the correlations among the 14 Helmert parameters (a) for the intra- and inter- SLR and VLBI technique combinations, respectively of the DTRF2014 (Seitz et al. 2016) solution and (b) the difference of the parameters correlations among different IDS (International DORIS Service) TRFs and the ITRF2014, respectively. The term intra-technique refers to the internal combination of each space technique (technique-only), while inter-technique combination corresponds to the final combined solution using all the space techniques, local and space ties (ERPs), respectively (Angermann et al. 2004).

## 2 Mathematical Model

The Covariance Matrix (CV matrix) of a TRF consists of two different types of uncertainty (e.g., Kotsakis 2013; Sillard and Boucher 2001): the so-called Reference System Effect (RSE) and the observational one. The correlations among the Helmert parameters are estimated using the so-called CV matrix (often provided in SINEX format, Blewitt et al. 1994) of the Datum Noise Effect (DNE see Sillard and Boucher 2001; Kelm 2003; Rebischung 2014):

$$\mathbf{C}_\theta = (\mathbf{E}^T \mathbf{C}_x^{-1} \mathbf{E})^{-1} \quad (1)$$

where  $\mathbf{C}_\theta$  the CV matrix of the datum noise,  $\mathbf{E}$  the design matrix of the 14 Helmert transformation parameters and  $\mathbf{C}_x$  the CV matrix of the initial solution (derived directly from the SINEX file). The correlation coefficient  $k_{ij}$  between two Helmert parameters  $i$  and  $j$  are calculated from the elements of  $\mathbf{C}_\theta$  as follows:

$$k_{ij} = \frac{\sigma_{ij}}{\sigma_i \sigma_j} \quad (2)$$

where  $\sigma_{ij}$  the covariance between two Helmert parameters  $i$  and  $j$  and  $\sigma_i, \sigma_j$  the standard deviations of the Helmert parameters  $i$  and  $j$ , respectively (derived from  $\mathbf{C}_\theta$ ). We should point out that in our experiments we only include the core stations of each TRF. We should also address here that for the present paper we investigate the correlations for the core stations, not only because of the better stability, but also for the good spatial distribution. There are number of non-core stations belong to global TRFs which their uncertainties are relatively large (e.g., larger than few cm and few mm/year). This fact could distort the significance of the estimated correlation coefficients.

The derivation of Eq. (1) is based on the separation between datum and observational datum effects, adopting the least-squares principle (Sillard and Boucher 2001). This method (used also herein) can be called as covariance matrix orthogonal projection and was introduced by Blewitt et al. (1992). Some interesting issues regarding this fact is addressed by Rebischung (2014, Chapter 3), offering some elegant approaches on the problem of datum noise investigations.

Regarding the application of Eq. (1) we should point out that the inversion of the  $\mathbf{C}_x$  could present some issues with respect the stability of the inverted matrix (extremely high condition number). This can be overcome by adding really small number to the diagonal of the covariance matrix, according to Sillard and Boucher (2001).

## 3 Results

### 3.1 DTRF2014

We compare the correlations of the intra- and inter-technique for (a) the SLR and (b) for the VLBI combinations, respectively. The Helmert transformation parameters are defined as: origin per axis  $t_x, t_y, t_z$ , scale  $D$  and orientation per axis  $r_x, r_y, r_z$ . The dot signs refer to their rates.

#### 3.1.1 The SLR-only TRF

Figure 1 visualizes the SLR core stations, while Table 1 refers to the correlations of some characteristic Helmert transformation. The correlations for the intra-technique and inter-technique combinations of DTRF2014 for the SLR stations, respectively.

The comparison of the correlations of the SLR intra- and inter-technique combinations, respectively, shows a depletion of major correlations, hence it demonstrated a reduction of dependency after the combination and this confirm the improved quality of the DTRF2014 solution versus SLR-only solution. We chose translations and scale related param-



**Fig. 1** The SLR core stations

**Table 1** The correlations for the intra-technique (second column) and inter-technique combinations, respectively, of DTRF2014 for the SLR stations (third column)

Parameters	SLR intra-technique	DTRF2014 (inter-technique)
$t_x, \dot{t}_x$	0.068	0.055
$t_y, \dot{t}_y$	0.070	0.052
$t_z, \dot{t}_z$	0.048	0.038
$D, \dot{D}$	0.072	0.047
$t_x, t_y$	-0.061	-0.047
$t_x, t_z$	-0.140	-0.128
$t_x, D$	-0.133	-0.136
$t_y, t_z$	0.152	0.125
$t_y, D$	-0.121	-0.102
$t_z, D$	-0.162	-0.158
$t_z, \dot{D}$	-0.302	-0.330

eters, since SLR provides both of for the DTRF2014 datum realization. The origin and the origin rates correlations are low (lower than 0.5, Frost 2020). The correlations among the fundamental parameters are slightly improved. In addition, there is a perfect agreement between the signs of the two solutions. The largest correlation is found between the z-axis origin rate and the scale rate (found at the level of  $-0.3$ ), while in the case of inter-technique combination it is slightly worsened, reaching  $-0.33$ .

### 3.1.2 The VLBI-only TRF

Figure 2 visualizes the VLBI core stations, while Table 2 summarizes the correlations of some characteristic Helmert transformation parameters for the intra-technique and inter-

technique combinations of DTRF2014 for the VLBI stations, respectively.

Table 2 shows the great importance of the combination for the VLBI network. The extremely high correlations (larger than 0.9) among the Helmert transformations parameters (the VLBI technique senses only the scale and its rate) after the combination. Since the correlation is limited within  $[-1,1]$ , whereas 0 means no linear dependency, 1 with full linear dependency and  $-1$  with a full linear dependency but with the opposite phase. The correlation between the scale and its rate remains low in both VLBI-only and DTRF2014 product. However, the correlation between the scale parameters increases in the case of inter-technique combination (0.117 versus 0.069). Their comparisons to the SLR case demonstrate that both techniques demonstrate low correlations between the scale and its rates. Although, the SLR seems to give slightly better results (for scale and its rate). Scale and scale rate are better separated in DTRF2014 with the inclusion of independent information from the other techniques. The fact that in the case of VLBI this is opposite indicates the erroneous information introduced.

## 3.2 IDS and ITRF2014 Comparison

The IDS solutions (Moreaux et al. 2016; DORIS cumulative solutions n.d.) are the official DORIS-only TRFs. IDS provide five different TRFs which are aligned to the ITRF2014 solutions. We analyze the following TRFs: (a) the IDS17-d1



**Fig. 2** The VLBI core stations

**Table 2** The correlations for the intra-technique (second column) and inter-technique combinations, respectively, of DTRF2014 for the VLBI stations (third column)

Parameters	VLBI-intra-technique	DTRF2014 (inter-technique)
$t_x, \dot{t}_x$	0.941	0.192
$t_y, \dot{t}_y$	0.929	0.216
$t_z, \dot{t}_z$	0.901	0.146
$D, \dot{D}$	0.069	0.117
$r_x, \dot{r}_x$	0.937	0.084
$r_y, \dot{r}_y$	0.939	0.056
$r_z, \dot{r}_z$	0.949	0.247
$t_y, \dot{r}_x$	-0.823	-0.591
$t_x, \dot{r}_y$	-0.762	-0.081
$t_z, \dot{r}_x$	-0.714	0.238
$t_x, \dot{r}_y$	-0.807	-0.540

TRF (b) the IDS19-d4 TRF and (c) ITRF2014 exclusively for the DORIS core stations. Figure 3 depicts the DORIS core stations, while Table 3 refers to the correlations of some characteristic Helmert transformation parameters for the IDS and for the final ITRF2014 solutions, respectively.

The results of Table 3 show that the IDS17-d1 correlations are ultra-low, almost all the correlations are lower than 0.1. For the ITRF2014 we observe that, although they remain

low, they are increased. On the other hand, the IDS19-d4 correlations are severely increased among the origin and their rates, respectively. One possible explanation for this behavior is the fact that the IDS19-d4 comprises 5 more years of observations than the ITRF2014. Thus, after the alignment to ITRF2014 there is an impact on the network's reference frame uncertainty (constrained network's geometry).

The DORIS series are a conglomerate of computed Normal Equations (NEQs) that span different space segment contributions. Thus, they refer to numerous different satellite constellations entering the picture depending on the time period and with each such entry or exit of contributing satellite constellations, the quality of the models alters. Some incur more systematic errors than others and in some instances, the ground beacons had their own problems contributing similar time-dependent problems in the quality of the solution. These significant analysis details and difficulties cannot be verified using correlation coefficients. Thus, the use of the correlations as stand-alone tool for the TRF quality assessment is not applicable. The correlation coefficients should always be applied simultaneously with other mathematical processes like Helmert transformation parameters, rigorous least adjustment techniques etc. and exclusively as auxiliary tools.

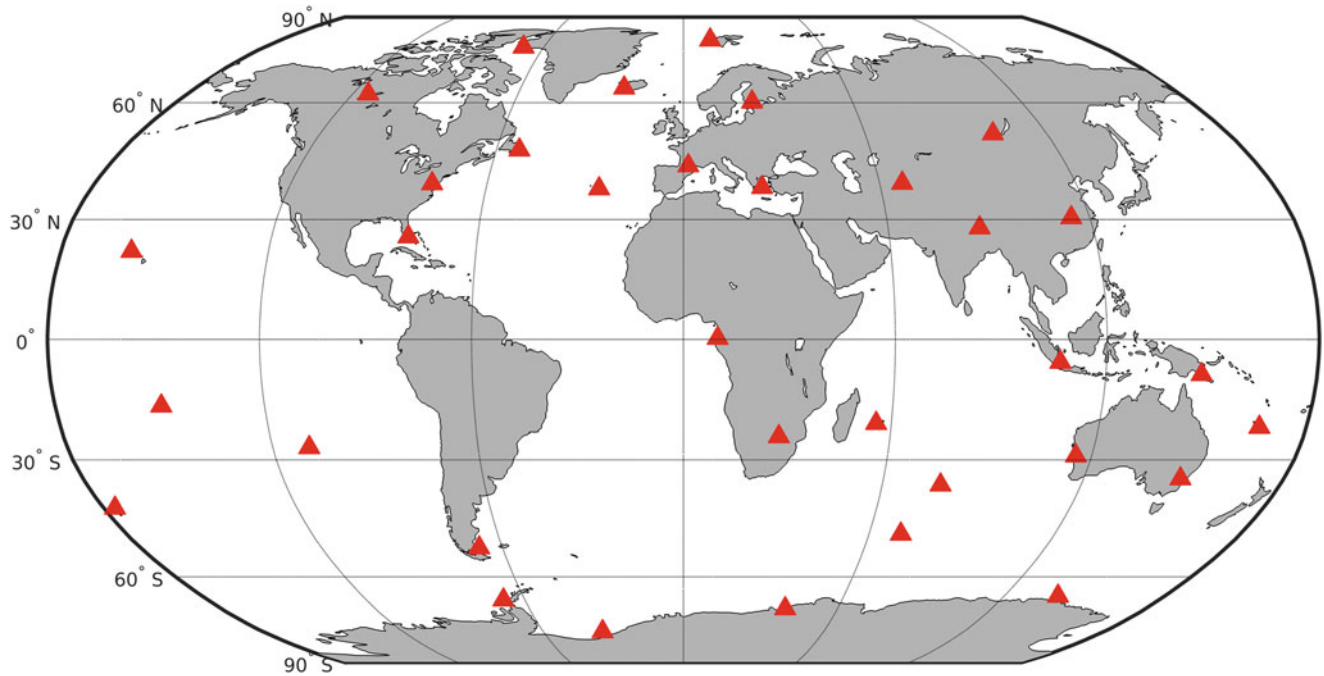


**Fig. 3** The DORIS core stations

**Table 3** The correlations for the IDS solutions and for the ITRF2014

Parameters	IDS-17d1	IDS-19d4	ITRF2014
$t_x, \dot{t}_x$	0.069	-0.663	0.222
$t_y, \dot{t}_y$	0.039	-0.498	0.286
$t_z, \dot{t}_z$	0.034	-0.593	0.255
$D, \dot{D}$	0.009	-0.534	0.255
$t_x, t_y$	-0.024	-0.187	0.046
$t_x, t_z$	-0.003	-0.010	0.032
$t_x, D$	-0.038	-0.144	-0.149
$t_y, t_z$	-0.039	0.081	0.046
$t_y, D$	-0.055	-0.490	0.026
$t_z, D$	-0.106	-0.201	-0.273

## 4 Conclusions

The correlations of the Helmert parameters can stand as an additional diagnostic tool for the TRF assessment. Through the correlations derivation one can check the dependency among the Helmert transformation parameters, thus validating their ability to provide reliable results. We estimate the correlations for the SLR and the VLBI solution and for the DTRF2014. We find that the combinations generally reduce the dependency between the Helmert parameters which indicates of improved network, especially for the VLBI network. The correlation between the scale and its rate for both techniques is low. The SLR correlations among the origin parameters (static and dynamic) are low.

For the IDS and the ITRF2014 (for the DORIS stations), we find interesting results. The IDS17-d1 correlations are low which is also the case for the ITRF2014, although larger than the IDS17-d1 ones. However, for the IDS19-d4 solution the estimated correlations are severely increased. This might be caused from the inclusion of 5 more years of DORIS observations (than the ITRF2014), which probably affects the origin and the scale of the network. It practically means that the origin and the scale of the IDS19-d1 tend to have significant dependencies among each other.

We should underline here that the correlation coefficient between two parameters is very sensitive to the definition of the networks involved (geometry of the network, global distribution of the stations) as well as the data yield and quality contributed by each station and the time span covered by these data. Thus, the correlations could not stand themselves as a unique tool of TRFs quality assessment. Nevertheless, it can be applied in parallel with the Helmert transformation. The correlation can reveal problems regarding the dependency of two parameters and how this kind of dependency is related to intra- and inter-technique combinations, respectively.

**Acknowledgments** Mathis Bloßfeld (DGFI-TUM) is kindly acknowledged for the provision of the SLR-only and VLBI-only TRFs, respectively, of the DTRF2014. The comments and the criticism of the two anonymous reviewers led to significant improvement of the initial manuscript. Therefore, the reviewers are kindly acknowledged.

## References

- Altamimi Z, Sillard P, Boucher C (2002) ITRF2000: A new release of the International Terrestrial Reference Frame for earth science applications. *J Geophys Res* 107(B10):2214. <https://doi.org/10.1029/2001JB000561>
- Altamimi Z, Collilieux X, Legrand J, Garayt B, Boucher C (2007) ITRF2005: A new release of the International Terrestrial Reference Frame based on time series of station positions and Earth Orientation Parameters. *J Geophys Res* 112:B09401. <https://doi.org/10.1029/2007JB004949>
- Altamimi Z, Collilieux X, Boucher C (2008) Accuracy assessment of the ITRF datum definition. [https://doi.org/10.1007/978-3-540-74584-6\\_16](https://doi.org/10.1007/978-3-540-74584-6_16)
- Altamimi Z, Rebischung P, Métivier L, Collilieux X (2016) ITRF2014: A new release of the International Terrestrial Reference Frame modeling nonlinear station motions. *J Geophys Res* 121(B8):6109–6131
- Altamimi Z, Rebischung P, Metivier L, Collilieux X, Chanard K, Teyssendier-de-la-Serve M (2021) Preparatory analysis and development for the ITRF2020. *EGU Abstracts*, EGU21-2056. <https://doi.org/10.5194/egusphere-egu21-2056>
- Angermann D, Drewes H, Krugel M, Meisel B, Gerstl M, Kelm R, Muller H, Seemuller W, Tesmer V (2004) ITRS Combination Center at DGFI: A Terrestrial Reference Frame Realization 2003. *Deutsche Geodätische Kommission, Reihe B, Heft Nr. 313*
- Blewitt G, Heflin MB, Webb FH, Lindqwister UJ, Malla RP (1992) Global coordinates with centimeter accuracy in the International Terrestrial Reference Frame using the Global Positioning System. *Geophys Res Lett* 19:853–856
- Blewitt G, Bock Y, Kouba J (1994) Constraining the IGS polyhedron by distributed processing. In: *Workshop proceedings: densification of ITRF through regional GPS networks*, JPL, Nov 30–Dec 2, pp 21–37
- Collilieux XZ et al (2014) External evaluation of the Terrestrial Reference Frame: report of the task force of the IAG sub-commission 1.2. In: Rizos C, Willis P (eds) *Proceedings of the IAG General Assembly*, Melbourne, Australia, June 28–July 2, 2011. International Association of Geodesy Symposia, vol 139. Springer, Heidelberg, pp 197–202
- DORIS cumulative solutions. [ftp://doris.ensg.ign.fr/pub/doris/products/sinex\\_global/ids/](ftp://doris.ensg.ign.fr/pub/doris/products/sinex_global/ids/)
- Frost J (2020) *Introduction to statistics: an intuitive guide for analyzing data and unlocking discoveries*. Statistics by Jim Publishing, ISBN: 9781735431109
- Kelm R (2003) Rank defect analysis and variance component estimation for inter-technique combination. In: Richter B, Schwegmann W, Dick WR (eds) *Proceedings of the IERS workshop on combination research and global geophysical fluids*, IERS technical note no. 30. Verlag des Bundesamts fuer Kartographie und Geodäsie, Frankfurt am Main, pp 112–114
- Kotsakis C (2013) Generalized inner constraints for geodetic network densification problems. *J Geod* 87(7):661–673
- Liu J, Chen J, Liu P, Tan W, Dong D, Qu W (2021) Comparison and assessment of three ITRS realizations. *Remote Sens* 13:2304. <https://doi.org/10.3390/rs13122304>
- Moreaux G et al (2016) Horizontal and vertical velocities derived from the IDS contribution to ITRF2014, and comparisons with geophysical models. *Geophys J Int* 207(1):209–227. <https://doi.org/10.1093/gji/ggw265>
- Rebischung P (2014) *Can GNSS contribute to improving the ITRF definition?* PhD thesis, Paris, Institut National de l'Information Géographique et Forestière (IGN/LAREG)
- Seitz M, Bloßfeld M, Angermann D, Schmid R, Gerstl M, Seitz F (2016) The new DGFI-TUM realization of the ITRS: DTRF2014 (data). *Deutsches Geodätisches Forschungsinstitut*, Munich. <https://doi.org/10.1594/PANGAEA.864046>
- Sillard P, Boucher C (2001) Review of algebraic constraints in terrestrial reference frame datum definition. *J Geod* 75:63–73

**Open Access** This chapter is licensed under the terms of the Creative Commons Attribution 4.0 International License (<http://creativecommons.org/licenses/by/4.0/>), which permits use, sharing, adaptation, distribution and reproduction in any medium or format, as long as you give appropriate credit to the original author(s) and the source, provide a link to the Creative Commons license and indicate if changes were made.

The images or other third party material in this chapter are included in the chapter's Creative Commons license, unless indicated otherwise in a credit line to the material. If material is not included in the chapter's Creative Commons license and your intended use is not permitted by statutory regulation or exceeds the permitted use, you will need to obtain permission directly from the copyright holder.





# Shimosato Co-Location of the SLR and GNSS Stations

Yuto Nakamura, Shun-ichi Watanabe, Yusuke Yokota, Akira Suzuki, Haruka Ueshiba, and Noritsune Seo

## Abstract

The Japan Coast Guard (JCG) operates Satellite Laser Ranging (SLR) and Global Navigation Satellite System (GNSS) instruments at the Shimosato Hydrographic Observatory (SHO) in Wakayama Prefecture located at the southernmost area of the main island of Japan. SHO is a co-location site where SLR and GNSS can be linked by precisely measuring the local tie vector (relative position) between these two space geodetic techniques. In November 2020, JCG collaborated with the Geospatial Information Authority of Japan (GSI) and performed a local tie survey to precisely determine the local tie vector between the stone marker of the GNSS station and the invariant point (IVP) of the SLR telescope. The IVP of the SLR telescope was determined by an indirect method, in which the reflector targets mounted on the SLR telescope were precisely observed from the surrounding temporary marks. The SLR telescope was rotated at a constant interval during the survey so that the observed target positions form arcs, from which we determined the azimuth and elevation axes; the orthogonal projection of the elevation axis onto the azimuth axis was determined as the IVP. The resulting local tie vector and its variance-covariance information were submitted for the development of the upcoming International Terrestrial Reference Frame 2020 (ITRF2020).

## Keywords

Co-location · GNSS · ITRF · Local tie survey · SLR

**Electronic Supplementary Material** The online version of this article ([https://doi.org/10.1007/1345\\_2022\\_156](https://doi.org/10.1007/1345_2022_156)) contains supplementary material, which is available to authorized users.

Y. Nakamura (✉) · S. Watanabe  
Hydrographic and Oceanographic Department, Japan Coast Guard,  
Tokyo, Japan

Y. Yokota  
Institute of Industrial Science, University of Tokyo, Tokyo, Japan

A. Suzuki · H. Ueshiba  
Geospatial Information Authority of Japan, Tsukuba, Japan

N. Seo  
Shimosato Hydrographic Observatory, Japan Coast Guard,  
Nachikatsuura, Japan

© The Author(s) 2022

J. T. Freymueller, L. Sánchez (eds.), *Geodesy for a Sustainable Earth*,  
International Association of Geodesy Symposia 154, [https://doi.org/10.1007/1345\\_2022\\_156](https://doi.org/10.1007/1345_2022_156)

## 1 Introduction

### 1.1 International Terrestrial Reference Frame and Co-Location

Recent advances in space geodetic techniques such as the Global Navigation Satellite System (GNSS) have enabled us to precisely determine a position on the Earth's surface. The International Terrestrial Reference Frame (ITRF) provided by the International Earth Rotation and Reference System Service (IERS) is one of the realizations of the global geodetic reference frames used to represent three dimensional coordinates on the Earth's surface.

The ITRF is produced using data obtained from GNSS, Satellite Laser Ranging (SLR), Very Long Baseline Inter-



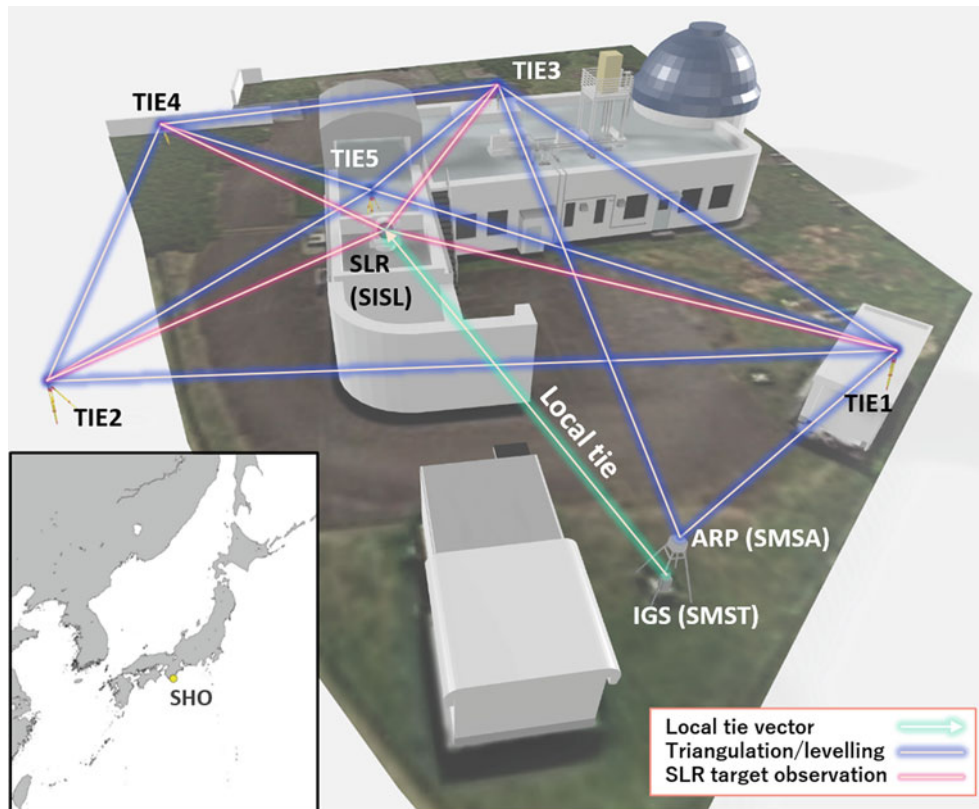


**Fig. 1** Overview of the geodetic stations and the temporary marks in SHO. Green arrow indicates the local tie between the IGS station “SMST” and the SLR invariant point “SISL”. The terrestrial survey network for determining the positions of the temporary marks and the

antenna reference point (ARP) of the GNSS station is shown in blue lines. Pink lines indicate the indirect observations of the targets on the SLR telescope. The location of SHO is indicated in the figure on bottom left

ferometry (VLBI), and Doppler Orbitography and Radiopositioning Integrated by Satellite (DORIS) observations that are conducted at geodetic stations around the globe. To produce the ITRF, it is necessary to merge the reference frames obtained individually from these four space geodetic techniques. The different space geodetic techniques can be linked together by using the local tie vectors (relative positions) of the space geodetic techniques at co-location sites, where multiple space geodetic techniques are operated closely together (Ray and Altamimi 2005). The quantity and accuracy of the local tie vectors are significant factors that affect the quality of ITRF. Thus, to improve the quality of the ITRF, it is important for the observing agencies to precisely measure the local tie vectors at their co-location sites by conducting local tie surveys.

## 1.2 The Shimosato Hydrographic Observatory

The Hydrographic and Oceanographic Department of the Japan Coast Guard (JCG) is responsible for producing nautical charts of the oceans surrounding the Japanese

archipelago. To link these nautical charts to the global geodetic reference frame, JCG has been conducting SLR observation since 1982 at the Shimosato Hydrographic Observatory (SHO), located in Wakayama Prefecture, Japan (Fig. 1). The SLR observation data collected at SHO are regularly submitted to the International Laser Ranging Service (ILRS) to contribute to the realization of the ITRF.

A permanent GNSS antenna was installed above the stone marker representing the origin of the nautical chart, located in SHO. The stone marker “SMST” has been registered to the International GNSS Service (IGS), and the daily RINEX files are submitted regularly. SHO, conducting SLR and GNSS observations simultaneously, functions as a co-location site where these two space geodetic techniques can be linked together.

To contribute to the realization of the upcoming ITRF2020, JCG collaborated with the Geospatial Information Authority of Japan (GSI), which has a prolonged experience in co-locating their VLBI and GNSS stations, to perform a local tie survey at SHO in November 2020. The product of the survey has been submitted to the IERS, and is expected to be used for the construction of the ITRF2020. In this paper, we present the survey and analysis methods of

our local tie survey at the SHO, and evaluate the validity of the resulting local tie vector.

## 2 Survey Instrumentation and Methodology

### 2.1 Local Survey of the Network

In our survey, we constructed a terrestrial survey network consisting of five temporary marks (TIE1, TIE2, TIE3, TIE4, TIE5) in SHO as shown in Fig. 1. A local coordinate system with the origin at temporary mark TIE3 and an x-axis passing through TIE1 has been defined for our local survey network. We measured the azimuth and elevation angles, and distances between the temporary marks using total stations (SOKKIA NET05, TOPCON GTS-700) and survey targets. We have also set up temporary mark HRMD at the Hiramidai viewpoint, which is located approximately 1.3 km east of SHO. An azimuth marker was set at HRMD, which we observed from TIE3 and TIE5 to determine the orientation of the local coordinate system of the survey network.

A terrestrial survey was also conducted between the antenna reference point (ARP) of the GNSS station “SMSA” and the marks visible from the GNSS station (TIE1 and TIE3). We indirectly observed SMSA using total stations, by measuring the angles of the edges of the antenna base and the distance to the reflective tape placed on the edge of the antenna.

GNSS observations were conducted at marks TIE1, TIE3, TIE5, and HRMD to determine geocentric coordinates, which we used to align the survey network to ITRF2014. We conducted static GNSS observations at least 12 hours at these marks using Trimble Zephyr Geodetic antennas and Trimble NetR9 receivers.

Levelling was conducted between the five temporary marks and the ARP of the GNSS station “SMSA”, to determine the precise relative heights between our marks. For the levelling, we used Zeiss DiNi12 and WILD N3 levelling instruments. The levelling data was integrated in the network adjustment to improve the accuracy of the vertical component of the local tie vector.

### 2.2 Indirect Observation of the SLR Telescope IVP

The invariant point (IVP) of the SLR telescope, named “SISL”, is defined as the orthogonal projection of the elevation axis onto the azimuth axis. Since the IVP is inside the SLR telescope and is not visible from outside, we have taken an indirect approach to observe the IVP (Woods 2008). In our indirect observation, we mounted a total of four reflector

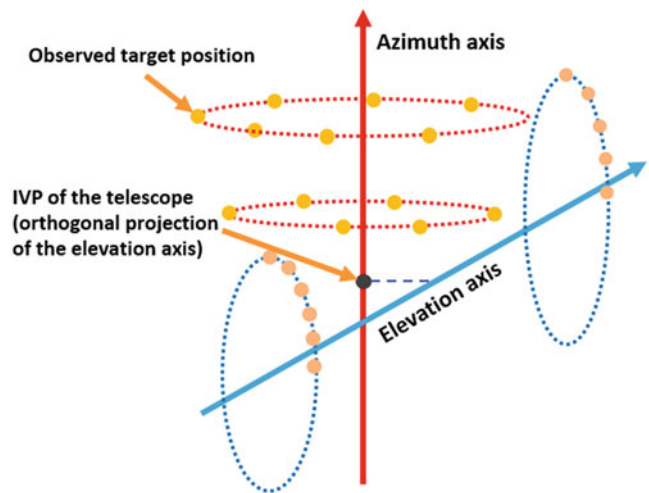


**Fig. 2** Schematic diagram of the indirect observation of the SLR telescope IVP. The target positions form arcs around the azimuth and elevation axes, from which we determine the axes and the IVP

targets (one  $\phi 75$  mm Leica Cateye Reflector and three  $1.5''$  Leica Red Ring Reflectors) on the body of the SLR telescope, and observed these targets from total stations mounted at the surrounding temporary marks TIE1, TIE2, TIE3, and TIE4. Like the terrestrial survey of the network, measurements of the angles and the distance between the temporary marks and the reflector targets were performed using total stations. Note that TIE5 was not used for the indirect observation; this mark was only used for reinforcing our local survey network. During the observation, the SLR telescope was rotated at constant intervals of  $30^\circ$  around the azimuth axis and  $15^\circ$  around the elevation axes, and we observed the targets at the visible marks. There were no limitations to the rotations of the SLR telescope around the azimuth axis, while the rotations of the telescope around the elevation axes were limited between  $0-90^\circ$ .

The target positions observed at different angles scribe arcs around the axes. A vector normal to the planes of the arcs that passes through the center of the arcs can be determined as the axis of rotation. By performing this observation for both the azimuth and elevation axes, the IVP of the SLR telescope (orthogonal projection of the elevation axis on the azimuth axis) can be determined, as depicted in Fig. 2.

## 3 Data Analysis

### 3.1 GNSS Data Processing

Before calculating the local tie vector, it is necessary to process the GNSS data to determine the geocentric coordinates of the marks aligned to ITRF2014, for transforming the local terrestrial survey network. We processed the

GNSS observation data collected during our survey using the online GNSS processing facility AUSPOS (Jia et al. 2014), provided by Geoscience Australia. The geocentric coordinates of the temporary marks where we conducted GNSS observations (TIE1, TIE3, TIE5, HRMD) are shown in Table 1. The obtained geocentric coordinates were aligned to ITRF2014 at the epoch date during the time of the survey.

### 3.2 Calculation of the Vertical Deflection

Terrestrial survey and levelling data are aligned with respect to the true vertical, which is normal to the geoid. To precisely determine the survey network, it is necessary to align the data with respect to the reference ellipsoid by correcting the data using the vertical deflection (VD). For our survey, we calculated the VD at TIE3 using GSIGEO2011 Ver.2 (Koitabashi et al. 2018), a local geoid model for Japan. The calculated VD was used to correct the data of positions in the observatory and HRMD.

### 3.3 Data Analysis for the Local Survey

For the analysis of our survey data and the generation of the local tie Solution Independent Exchange Format (SINEX) file, we used the pyaxis program (<https://github.com/linz/python-linz-pyaxis>) provided by Land Information New Zealand (LINZ). In pyaxis, the total station measurements (TIE1–TIE5 and HRMD), SLR target observation data, levelling data (TIE1–TIE5 and SMSA) were used to estimate the SLR telescope’s IVP. GNSS data at TIE1, TIE3, TIE5, and HRMD were integrated to align the survey results to ITRF2014, and the vertical deflection at TIE3 was used in the analysis to correct the survey and levelling data.

The analysis consists of three phases; first, the positions of the temporary marks (TIE1–TIE5) and the observed SLR target positions are calculated using an unconstrained least squares adjustment. Then, the azimuth and elevation axes of the SLR telescope are estimated by calculating arcs from the unconstrained SLR target positions that are determined in the first step. Using the solutions calculated from unconstrained adjustment, a constrained least squared adjustment is conducted to determine the final solution of the mark

**Table 1** Geocentric coordinates of the temporary marks (TIE1, TIE3, TIE5, HRMD) aligned to ITRF2014, processed using AUSPOS

Mark	X [m]	Y [m]	Z [m]
TIE1	−3822369.6860	3699371.0640	3507581.9565
TIE3	−3822388.5867	3699375.8831	3507558.8488
TIE5	−3822389.0558	3699363.8346	3507570.0013
HRMD	−3823269.3171	3698357.6466	3507628.8106

positions, target positions, and the IVP of the SLR telescope. The GNSS-derived geocentric coordinates are integrated in the analysis to generate geocentric coordinates of the local survey network in SHO aligned to ITRF2014.

## 4 Results and Discussions

The geocentric coordinates of the SLR telescope IVP “SISL”, GNSS antenna ARP “SMSA”, and the temporary marks (TIE1–TIE5) calculated by pyaxis are listed in Table 2.

The local tie vector between the GNSS station’s stone marker “SMST” and the IVP of SLR telescope “SISL”, in topocentric coordinates with the origin at SMSA, was calculated as follows by adding a vertical offset of −1.995 m between SMSA and SMST:

$$(\Delta E, \Delta N, \Delta U) = (7.7680 \text{ m}, -17.9484 \text{ m}, 4.0695 \text{ m}). \quad (1)$$

The standard deviations for each component of the topocentric coordinates of the local tie vector were calculated as follows:

$$(\sigma_E, \sigma_N, \sigma_U) = (0.0028 \text{ m}, 0.0020 \text{ m}, 0.0070 \text{ m}). \quad (2)$$

The offset of the elevation axis from the azimuth axis was  $0.0012 \pm 0.0046$  m, and the non-orthogonality was  $-4.37 \pm 10.36''$ .

To visualize the geometry of the covariance of the local tie vector, we calculated the covariance ellipsoid using the computed variance-covariance matrix. Figure 3 indicates the covariance ellipsoid of the local tie vector, in topocentric coordinates. The covariance ellipsoid is stretched in the vertical direction, with a major axis almost parallel to the local vertical axis.

The coherence between the GNSS observations and the final results of the adjustment of pyaxis was checked by using the geocentric coordinates of marks where GNSS observations were conducted (TIE1, TIE3, and TIE5). We used the geocentric coordinates of these marks obtained from GNSS analysis using AUSPOS and the network adjustment results

**Table 2** Geocentric coordinates of SISL, SMSA, and temporary marks (TIE1–TIE5) obtained by network adjustment using pyaxis

Mark	X [m]	Y [m]	Z [m]
SISL	−3822388.2931	3699363.6397	3507573.0334
SMSA	−3822374.4918	3699361.0929	3507586.8174
TIE1	−3822369.6858	3699371.0590	3507581.9553
TIE2	−3822393.2280	3699348.0481	3507574.9100
TIE3	−3822388.5926	3699375.8844	3507558.8546
TIE4	−3822405.5805	3699359.7255	3507549.9721
TIE5	−3822389.0531	3699363.8451	3507570.0113

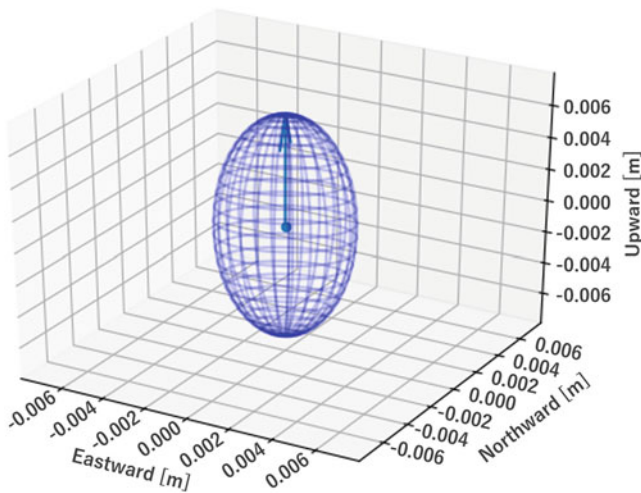


**Fig. 3** Covariance ellipsoid of the local tie vector. The surface of the ellipsoid indicates an error of  $1\sigma$ . The arrow indicates the vector of the major axis

**Table 3** Baseline components between marks TIE1, TIE3, and TIE5 obtained from GNSS observation and network adjustment by pyaxis. Subscript “G” indicates baseline components obtained from the geocentric coordinates in the GNSS SINEX file, and subscript “P” indicates baseline components obtained by using geocentric coordinates in the local tie SINEX file computed by pyaxis

Baseline	$dX_G$ [m]	$dY_G$ [m]	$dZ_G$ [m]
TIE1–TIE3	18.9007	−4.8191	23.1076
TIE1–TIE5	19.3698	7.2294	11.9551
TIE3–TIE5	0.4690	12.0485	−11.1525
Baseline	$dX_P$ [m]	$dY_P$ [m]	$dZ_P$ [m]
TIE1–TIE3	18.9068	−4.8254	23.1007
TIE1–TIE5	19.3673	7.2139	11.9440
TIE3–TIE5	0.4605	12.0393	−11.1567

obtained by pyaxis. To check the coherence, we calculated and compared the baselines between these marks, as indicated in Table 3. The differences of the baselines obtained from the GNSS observations and the network adjustment are within the centimeter level, suggesting that the terrestrial survey results are plausible.

#### 4.1 Comparison with the SLR-GNSS Baseline

To check the plausibility of the obtained local tie vector, we calculated the time series of the baseline between the SLR telescope IVP “SISL” and the GNSS antenna ARP “SMSA”, using the SLR and GNSS observation datasets. We compared the time series of the baseline to the local tie between SMSA to SISL obtained from our local tie survey, in geocentric coordinates:

$$(dX, dY, dZ) = (-13.8013 \text{ m}, 2.5468 \text{ m}, -13.7840 \text{ m}). \quad (3)$$

Figure 4 shows the monthly time series of each component of the vector in geocentric coordinates. The SLR monthly solution was calculated using the ranging data of LAGEOS-1 and LAGEOS-2. The orbits of LAGEOS-1 and LAGEOS-2, the center of the Earth, position of the SLR station (SISL), and the range bias were estimated using the C5++ software (Otsubo et al. 2016). The GNSS monthly time series was calculated by averaging the daily solutions that were obtained from data analysis using RTKLIB 2.4.2 (Takasu 2013). The GNSS data was analyzed in the static precise point positioning (PPP) mode using the IGS final orbits. Note that the position of SISL is aligned to SLRF2014, while the position of SMSA is aligned to IGB14; thus, the baseline is calculated from coordinates in different reference frames. However, both reference frames are based on ITRF2014, so the discrepancy between these reference frames is small enough to be ignored in our plausibility check. Offsets due to the change of the antenna mount in March 2012 (line A in Fig. 5) have been corrected for the data before March 2012. Each component of the local tie obtained from the survey is depicted as a horizontal line in each of the plots of Fig. 4.

The SLR-GNSS baseline between 2012 and 2018 is stable and agrees well with the local tie vector obtained in this survey, suggesting that the result of our local tie survey is reasonable. The global solution implies that the relative position between the SLR and GNSS has not significantly changed during this period. The baseline before 2012 also agrees with the local tie vector, indicating that the local tie has been stable even before the change in the GNSS antenna offset in March 2012. However, after 2018, the discrepancy between the monthly time series of the baseline and the surveyed local tie vector seems to be increasing for all components; the time series indicate a positive trend for  $x$ , and negative trends for  $y$  and  $z$ . This is primarily due to the instability of the SLR time series after 2018, caused by the decrease in observation data for the on-site maintenance of the SLR system after the renewal of our laser oscillator in October 2018 (purple dashed line C in Fig. 4). Overall, we can conclude that our survey results in 2020 does not conflict with the time series of the SLR-GNSS baseline before the renewal of the SLR laser oscillator in 2018, and that the local tie survey does not contain serious errors.

#### 4.2 Possible Error Sources

As indicated in Sect. 4.1, the standard deviations of the local tie vector were 2–3 mm, and 7 mm for the horizontal and vertical components, respectively. The IERS recommends the accuracy of local tie vectors to be at the sub-millimeter level, which we were unable to achieve in this survey.

One of the major potential sources of such large errors may be our procedures when we conducted the indirect

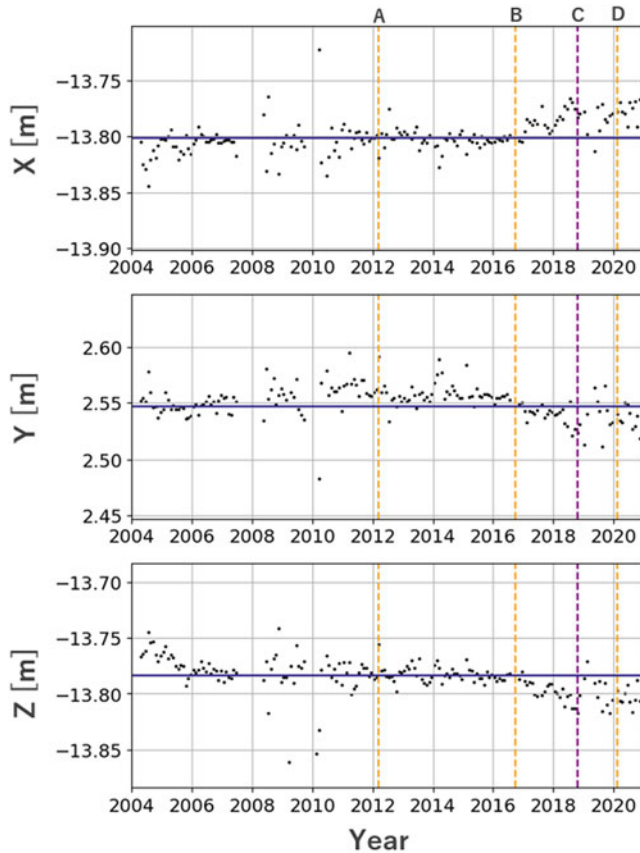


**Fig. 4** Monthly time series of the geocentric coordinates of the baseline between the SLR reference point SISL and the ARP of the GNSS antenna (SMSA) at SHO. Offsets due to the replacement of the GNSS antenna mount in March 2012 have been corrected. Navy solid lines represent the coordinates of the local tie vector between the SLR telescope IVP and the GNSS station ARP obtained from our survey in 2020. Orange dashed lines indicate dates when modifications were made to the GNSS antenna; A (March 2012) is when the antenna mount was changed, B (September 2016) is when the radome and the GNSS antenna were changed, and D (February 2020) is when the radome has been removed. The purple dashed line C (October 2018) is the date of renewal of the SLR laser oscillator

observation of the SLR telescope IVP. During the indirect observation, we observed the target arcs around the elevation axis in between the observation of the target arcs around the azimuth axis, as depicted in Fig. 5, to increase the time efficiency of the indirect observation. As shown in Fig. 5, we interrupted the target observations around the azimuth axis at a certain azimuth angle, and performed the observation of target arcs around the elevation axis. After we finished the observation around the elevation axis, we restored the elevation angle during the azimuth axis observation, and resumed the target observations around the azimuth axis.

Since we had to shut down the mechanics of the SLR telescope during the survey, we have rotated the SLR telescope by hand; for this reason, there is a possibility of large pointing error of the elevation angle every time we restored

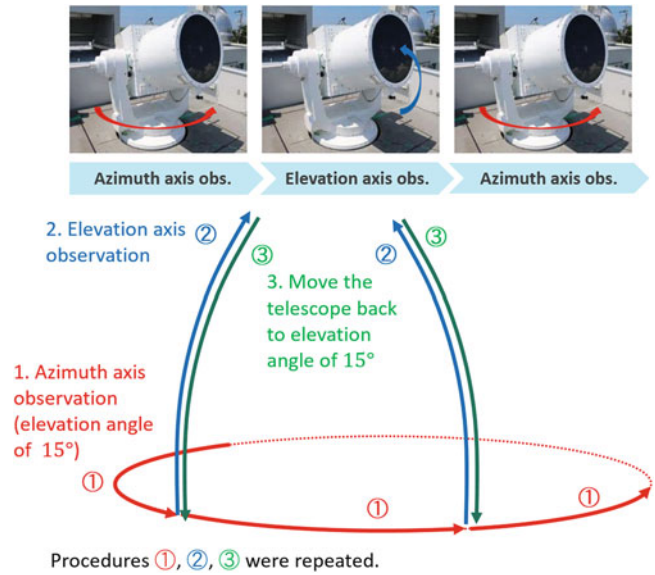


**Fig. 5** Schematic diagram of our indirect observation of the SLR telescope IVP SISL. Target observations for determining the elevation axis were conducted in between the observations for determining the azimuth axis, which is a possible major source of our observational errors

the elevation angle back to  $15^\circ$  for target observation around the azimuth axis. Such procedures would lead to an increase in the variation of the elevation angles of the target positions observed around the azimuth axis, since it is impossible to perfectly restore the elevation angle during the target observation of the azimuth axis. Variation of the elevation angles during the azimuth axis observation would increase the circle fitting residuals of the target positions around the azimuth axis, which would result in errors of the position of the IVP, especially in the vertical component.

## 5 Conclusion

JCG and GSI have conducted a local tie survey at SHO to determine the local tie vector between the SLR telescope IVP and the GNSS station marker. The local tie vector determined in this survey agrees well with the time series of the baseline between the SLR and GNSS. The standard deviations of the local tie vector were approximately 2–3 mm for the horizontal components and 7 mm for the vertical component, in topocentric coordinates. Such large standard deviations may be due to our observation procedures, in which we rotated the SLR telescope around the elevation axes in between the observation of the targets around the azimuth axes during the indirect observation of the IVP. Since the telescope was rotated by hand, there is a possibility of large pointing errors in the elevation angle.

The result of our local tie survey has been submitted to the IERS, for the construction of the upcoming ITRF2020. Despite the difficulties in conducting local tie survey only by the JCG (i.e., maintenance of survey equipment and technical training of staffs), we are expecting to regularly conduct local tie surveys at SHO, to contribute to the future versions of the ITRF and to the global geodesy community.

**Acknowledgements** We thank the surveyors of the Geospatial Information Authority of Japan and the Kinki Regional Survey Department for their devoted work to this local tie survey, and for providing necessary survey instruments. We also thank the staffs of the Geospatial Information Authority of Japan for providing an opportunity for technical training on the analysis of the survey data using pyaxis. We would also like to thank Dr. Toshimichi Otsubo for providing the C5++ software and for giving us comments to improve our manuscript. Finally, we thank the on-site staffs of the Shimosato Hydrographic Observatory for on-site coordination and for their devoted work to this survey and regular SLR observations.

---

## Conflict of Interest

The authors declare that they have no conflict of interest.

## References

- Jia M, Dawson J, Moore M (2014) AUSPOS: Geoscience Australia's on-line GPS positioning service. In: Proceedings of 27th international technical meeting of the satellite division of the institute of navigation, 315–320
- Koitabashi M, Kojima H, Nemoto S, Miyahara B, Hiraoka Y, Yahagi T (2018) Establishment of New Geoid Model for islands in Japan “GSIGEO2011 (Ver.2)” [in Japanese]. *J Geospat Inf Auth Jpn* 130:1–7
- Otsubo T, Matsuo K, Aoyama Y, Yamamoto K, Hobiger T, Kubo-oka T, Sekido M (2016) Effective expansion of satellite laser ranging network to improve global geodetic parameters. *Earth Planets Space* 68:65. <https://doi.org/10.1186/s40623-016-0447-8>
- Ray J, Altamimi Z (2005) Evaluation of co-location ties relating the VLBI and GPS reference frames. *J Geod* 79(4):189–195. <https://doi.org/10.1007/s00190-005-0456-z>
- Takasu T (2013) RTKLIB ver. 2.4.2: An open source program package for GNSS positioning. <http://www.rtklib.com>
- Woods AR (2008) Indirect determination of the invariant reference point (IVP) of SLR and VLBI observing systems. In: Proceedings of the joint symposia: 13th FIG symposium on deformation measurement and analysis & 4th IAG symposium on geodesy for geotechnical and structural engineering

**Open Access** This chapter is licensed under the terms of the Creative Commons Attribution 4.0 International License (<http://creativecommons.org/licenses/by/4.0/>), which permits use, sharing, adaptation, distribution and reproduction in any medium or format, as long as you give appropriate credit to the original author(s) and the source, provide a link to the Creative Commons license and indicate if changes were made.

The images or other third party material in this chapter are included in the chapter's Creative Commons license, unless indicated otherwise in a credit line to the material. If material is not included in the chapter's Creative Commons license and your intended use is not permitted by statutory regulation or exceeds the permitted use, you will need to obtain permission directly from the copyright holder.





# Local Ties at SLR Station Riga

Kalvis Salmins , Viesturs Sprogis, Imants Biļinskis, and Jorge del Pino

## Abstract

The SLR station Riga operates a SLR system within ILRS (Riga 18844401, DOMES number 12302S002) and a collocated GNSS system (RIGA00LVA, DOMES number 12302M002) within IGS and EUREF networks. The reference geodetic mark (DOMES number 12302M001) was used for the mobile SLR system MTLRS operation in 1991. Domes 12302M002 is situated on top of an historical time service building which sits directly on the bedrock. Both other points are placed on concrete foundations built more than 50 years ago. All these points are included in the ITRF database. The first full local ties set was determined in 1995 using a 6 h GPS session run using three GPS receivers. In 2018 three geodetic pillars were installed to improve the local geodetic network at the site. In January 2021, a multitechnique survey campaign produced a new set of local ties and reported to the ITRF and related services. The obtained results show that the local tie stability is at the subcentimeter level over a 25 years period. The true stability may be better, taking into account the measurement technology used in the first survey 25 years ago. But to verify it we need to do more surveys.

## Keywords

GNSS · ITRF · Local ties · Local ties stability · SLR

## 1 Introduction

The SLR station Riga is situated on the grounds of the University of Latvia Botanical Garden. The site started operation before 1957 as part of the University of Latvia Astronomical Observatory. At that time it included the astronomical time service and later a visual satellite tracking observation program (Sputnik 1 October 9, 1957). During the 1960s and 1970s it was an integration and testing place for satellite photographic systems and first generation SLR

systems developed in the frame of the Interkosmos space programs.

The SLR station, Riga 18844401 (DOMES number 12302S002), is a member of the International Laser Ranging Service and has been in operation since 1987. The mobile SLR system MTLRS was positioned during a 1991 SLR collocation campaign over the geodetic mark with DOMES number 12302M001. Both points were first linked in 1992 to the Latvian national geodetic network (Bikše et al. 1992). A permanent GNSS receiver, RIGA00LVA (DOMES number 12302M002) has been working since December 1995. RIGA00LVA is part of the International GNSS Service (IGS) and EUREF. All three points are listed in the ITRF and related services. The three DOMES points are installed on concrete foundations built more than 50 years ago. The GNSS building foundation sits directly on the bedrock. Regular ground water level monitoring is carried out to support the gravimetric measurements done at the Observatory by the Latvian Geospatial Information Agency

K. Salmins (✉) · J. del Pino  
University of Latvia, Institute of Astronomy, Riga, Latvia  
e-mail: [kalvis.salmins@lu.lv](mailto:kalvis.salmins@lu.lv); [jorge.delpino@lu.lv](mailto:jorge.delpino@lu.lv)

V. Sprogis · I. Biļinskis  
Latvian Geospatial Information Agency, Riga, Latvia  
e-mail: [viesturs.sprogis@lgia.gov.lv](mailto:viesturs.sprogis@lgia.gov.lv); [imants.bilinskis@lgia.gov.lv](mailto:imants.bilinskis@lgia.gov.lv)



**Fig. 1** Local Ties panoramic view 2021

**Table 1** Slope distances  $D$  between DOMES pairs, 1995 and 2021 Solutions

DOMES numbers Pairs	$D(m)$ , 1995	$D(m)$ , 2021
12302M001–12302M002	20.908	20.906
12302M002–12302S002	20.206	20.214
12302S002–12302M001	30.542	30.554

(LGIA). The point 12302M001 served as an origin point of the Latvian National Geodetic coordinate system LKS-92. Since April 2018 the SLR station Riga has been a member of GGOS (Global Geodetic Observation System).

The first geodetic ties determination between the DOMES 12302S002 and 12302M002 was done in 1992. They were linked to the national Latvian geodetic network using a combination of triangulation and levelling (Bikše et al. 1992) and transformed to the WGS-84 system. In 1995 the first three DOMES points local ties determination was done using a six-hour GPS session, (Lapuška 1996). These ties were reported to the ITRF in 1996 as the official local tie's solution and were replaced only in 2021. Four partial surveys for monitoring, testing, student's training or diploma work were done in 2004, 2012, 2019 and 2020.

In 2013 an old transit instrument dome was removed, allowing the direct line of sight between the points 12302M002 and 12302M001. In 2018, three additional geodetic pillars (G4100, G4200, G4300) were installed by the Latvian Geospatial Information Agency (LGIA) improving the local geodetic network configuration (Fig. 1). The pillars G4200 and G4300 were installed on old 1970s optical instruments concrete bases, reducing possible settling effects. The pillar G4100 was installed on the same

building as the GNSS receiver. In 2021 a new local ties survey was done by LGIA, and the results were reported as the new official Riga local ties values (Tables 1 and 2).

## 2 Local Tie Determination

In 1995 the local ties determination (Lapuška 1996), was done using three Trimble SSE 4000 GPS receivers in a six-hour session. The SLR telescope invariant point determination was done by placing a GPS antenna directly on the telescope using an attached mounting platform. The GPS antenna phase center was positioned on the telescope's vertical rotational axis. The distance from the antenna phase center to the telescope's horizontal axis was calculated using direct measurements and values taken from telescope drawings. The local ties values given were in the ITRF 92 reference frame. We do not have information on the antenna model and the phase center position value used. We estimate that the antenna displacement from the vertical axis was within 3 mm and error in distance measurement to the horizontal axis also is no worse than 2 mm. We have only the 1995 local ties  $dX$ ,  $dY$ ,  $dZ$  values available (Lapuška 1996) (Table 3). We have not found a full internal report and, as the author died in 2013, the chances of retrieving the original complete information are very low. There is no information on the use of the L1 and L2 signals and meteorological data corrections during processing. The reported standard deviation mean value for a single slope distance component is  $0.5 \pm 0.2$  mm with a range 0.3 to 0.8 mm. In our opinion the reported errors from this survey are underestimated.



**Table 2** Geocentric coordinates X, Y, Z for the 2021 Solution

DOMES	X[m]	Y[m]	Z[m]	$\sigma X$ [mm]	$\sigma Y$ [mm]	$\sigma Z$ [mm]
12302M001	3183914.346	1421473.506	5322796.699	0.0	0.0	0.0
12302M002	3183899.513	1421478.333	5322810.618	1.3	0.9	2.1
12302S002	3183896.103	1421497.005	5322803.666	0.6	1.1	1.6
G4100	3183900.715	1421481.774	5322808.928	1.1	0.7	1.9
G4200	3183891.315	1421467.001	5322815.189	1.2	0.8	2.0
G4300	3183887.008	1421493.091	5322812.652	1.2	0.9	2.1

**Table 3** dX, dY, dZ values for the 1995 and 2021 Solutions

Ties	dX	dY	dZ
Solution 2021 ITRF 2014			
12302M002–12302S002	−3.410	18.672	−6.952
12302M002–12302M001	14.833	−4.827	−13.920
12302M001–12302S002	−18.243	23.499	6.968
Solution 1995 ITRF 1992			
12302M002–12302S002	−3.401	18.661	−6.963
12302M002–12302M001	14.834	−4.832	−13.919
12302M001–12302S002	−18.236	23.493	6.956

In January 2021, LGIA carried out a multisession local ties survey for the new 2018 local configuration using tachymetry and GNSS. Five GNSS receivers Leica Viva GS10 (3 mm + 0.1 ppm/V 3.5 mm + 0.4 ppm accuracy in Static (phase) with long observations mode) and Leica AR20 antennas were used. Two to six hours GNSS sessions were carried out during 5 observing days. Four days were dedicated to the tachymetric measurements for all the points using the Trimble S9 0.5" Robotic, DR Plus Total Station (1 mm + 2 ppm (0.9 mm + 2 ppm) in Prism mode Standard (ISO)) and Leica circular prisms GPHIP, tribrach GZR3 and other additional components. In 2 of the 4 days the SLR telescope invariant point coordinates were determined by simultaneous tachymetric measurements from the pillars G4100 and G4300. In this case the prism GPHIP and tribrach GZR3 were installed on the SLR telescope GNSS antenna mount. A Bohnenstingl monitoring prism was installed at the telescope using a magnetic mount.

The data obtained had a total of 144 measured points; 96 for the azimuth and 48 for the elevation. The azimuth was rotated in 45 degree steps for a 360 degree range, and the elevation step was 10 degrees from 0 to 90 degrees elevation range. The telescope positioning was done using optical limbs. Processing was done using the Trimble Business Center v.5.32, TopoNet v.6.3 and proprietary software for the invariant point calculation. The calculated SLR telescope invariant point coordinates has a total RMS of 2.0 mm (1.1 mm, 1.1 mm and 1.3 mm in the local N, E, h coordinates). The 12302M001, 12302M002 and 12302S002 geocentric coordinates have a single component mean error of  $0.7 \pm 0.8$  mm and  $1.3 \pm 0.5$  mm for the new pillars. The current local ties configuration geometry is shown on Fig.

2. The slopes between the DOMES points are shown with thicker lines. The new DOMES local ties values obtained were submitted to the ITRF and related databases. The survey methods, instrumentation and procedures used were similar to local ties surveys done at other SLR stations (Donal 2013).

### 3 Comparison Between 1995 and 2021 Solutions

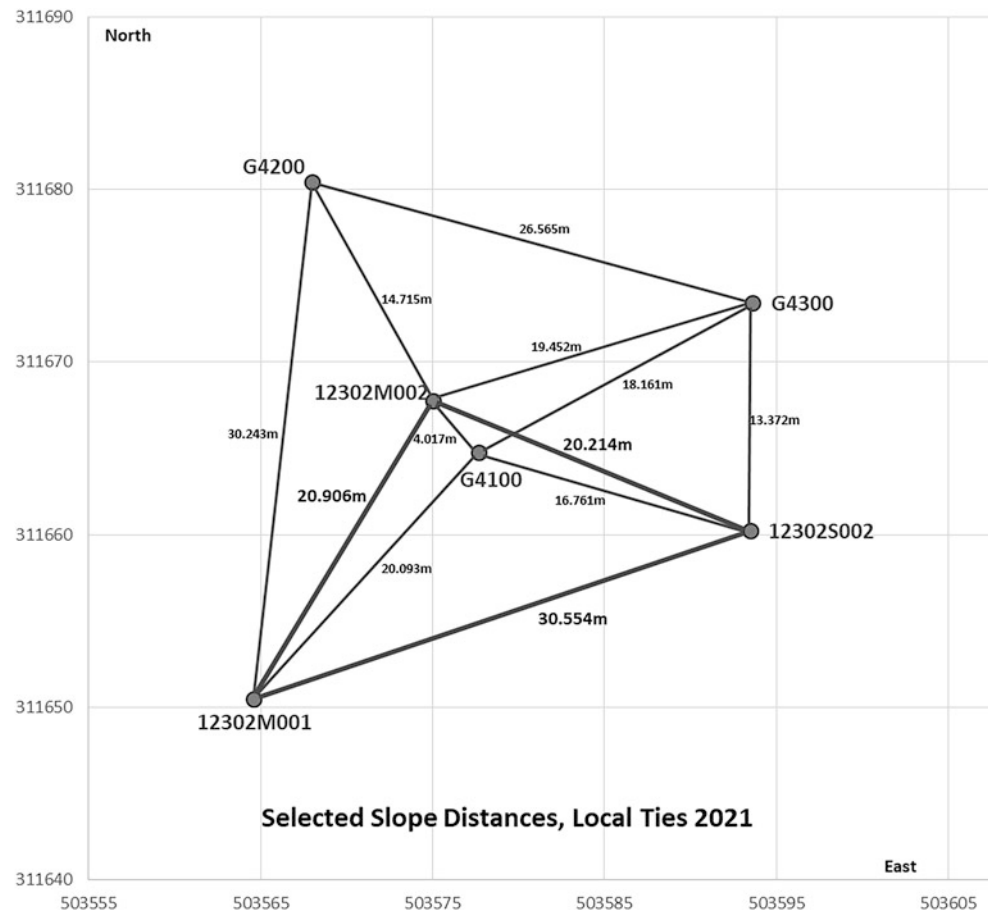
The straightforward way of comparing the two solutions is by direct comparison of the slope distances values connecting the three DOMES points (Table 1). This is because of the available 1995 values. For the same reason, it is not possible to transform the 1995 and 2021 solutions to a common reference frame for a more precise analysis.

The slope distance values changes are on the order of 1 cm or less in a time frame of 25 years. The 2021 slope distances internal errors range from 4.6 mm (12302M001–12302M002) to 2.0 mm (12302S002–12302M001). The 1995–2021 slope differences, calculated from Table 1 are: 12302M001–12302M002  $2.0 \pm 4.6$  mm, 12302M002–12302S002  $8.0 \pm 2.6$  mm and 12302S002–12302M001  $12 \pm 2.0$  mm. The errors shown are the slope distance errors from the 2021 solution. The 12302M001–12302M002 slope change is within the 2021 slope error. The slope change values related to the DOMES 12302S002 are in the 1 cm range but bigger than the corresponding 2021 slope distance errors. We do not take into account the reported 1995 errors, as we assume are not realistic. Assuming that the 1995 errors were similar to the 2021 solution, the 12302S002-related slope changes would be still bigger than the solution errors.

The most probable source for the SLR DOMES point slope values changes shown are the different methods used in 1995 and 2021 for determining the telescope invariant point coordinates. In particular the possible additional error introduced in 1995 on the calculation of the GPS antenna phase center-telescope invariant point distance.

The possibility of a SLR telescope base settling during the 1995–2021 period is very low, given the telescope base age and weight. As the SLR building is isolated from the concrete base, any telescope settling would have been noticed as a

**Fig. 2** Site schematics using the LKS-92 TM geodetic coordinate system, for the local ties 2021 configuration. Abscissa towards North, ordinate towards East, both in meters



vertical change on the precise optical alignment between the outgoing laser beam and the telescope.

#### 4 Monitoring, Testing and Training Surveys in 2004, 2012, 2019 and 2020

These surveys were never considered, for different reasons, reliable enough to replace the 1995 local ties values.

The December 20, 2004 survey used the Sokkia Total Station SET4220 working from an auxiliary point close to the GNSS pillar. The reported direction and distance errors were 10" and 5 mm, respectively. The total number of measurements was only 27. The telescope invariant point determination method was not described. Given the incomplete information, the sparse number of measurements and the reported errors, the results were considered not reliable enough to replace the 1995 values.

The 2012 survey was the J. Šarkovskis' Riga Technical University BSc diploma work (Šarkovskis 2012). Šarkovskis used a combination of GNSS and levelling measurements,

using GNSS and levelling reference points from the national Latvian geodetic network to determine the DOMES coordinates. Šarkovskis did the first attempt to figure out the LS-105 telescope invariant point local coordinates using tachymetry from a single auxiliary observation point while rotating the telescope on azimuth and elevation axis.

However, he used only twenty tachymetric data points, in small azimuth and elevation arcs (90° and 120°). Also, he mentions a possible elevation dependent deformation effect on the data cloud. As a result, the invariant point coordinates could not be derived directly from the cloud data only and had to include the determination of the distance between the telescope's GNSS platform basis and the horizontal axis (with a possible maximum 1.5 mm error).

Both the 2004 and 2012 surveys had to use an additional single intermediate reference point from where the three DOMES points could be visible. This is because of the transit instrument dome blocking the direct view between 12302M001 and 12302M002. The SLR telescope invariant point determination was done only from the additional point, in each case a different one, and with a limited visibility.

The 2019 experimental survey served as a part of the student training process at the Riga Technical University (Kaminskis et al. 2020). Values from a 2011 levelling exercise were used for the processing. The results are not good enough to substitute the 1995 values.

The July 2020 two days GNSS-only survey was done with the goal of using the pillars G4100 and G4300 as new SLR external calibration targets. The DOMES points 12302M001 and 12302M002 and the G4200 pillar were not included in this survey. The new pillars coordinates and the SLR telescope invariant point coordinate determination was done on an eight hours GNSS session using four external GNSS reference points from the LatPos GNSS base station system. Each GNSS set of points were measured during a 1.5 h session. A second SLR telescope GNSS invariant point determination session was done on a different day, during two half hour sessions for each configuration, using the same four GNSS LatPos reference points. As in other GNSS-only surveys the position of the telescope invariant point had to be calculated using a distance correction.

Unfortunately, the 1995 and 2004 surveys documentation are incomplete, and the 2004, 2012, 2019 results can be used only for reference and not for reliable comparison purposes.

As example: the calculated maximum slope differences using all the surveys are for the slope 12302S002–12302M001 (solutions 2021–2004)  $-27.5$  mm and 12302M001–12302M002 (solutions 2004–1995)  $+23.2$  mm. The smallest absolute difference is for the slope 12302S002–12302M002 (solutions 2012–1995)  $3.0$  mm.

For the partial 2020 and 2021 surveys, we have three slopes differences to compare: G4300–G4100 ( $2.9$  mm), G4100–12302S002 ( $2.9$  mm) and G4200–12302S002 ( $5.4$  mm). The first two slope differences are smaller than the mean 2021 slope distance errors of  $4.2$  mm for the three slopes. But still there are differences between the GNSS-only and the 2021 solution for slopes related to 12302S002. The 2021 slope distance values are now used for external calibration purposes.

## 5 Conclusions

To verify the accuracy and stability of the upgraded local ties configuration, the multitechnique survey must be repeated regularly. And to use the same techniques and instrument types as the 2021 session. To improve the accuracy of deter-

mination of the telescope invariant point we must redesign the telescope platform for mounting the GNSS antenna and reflectors. To exclude temperature effects on the invariant point position, the next survey should be done at a similar ambient temperature as the 2021 survey.

We can conclude that, taking into the account the reported possible measurement uncertainties, the incomplete data available from the 1995 survey, and the different measurement techniques used in the 1995 and 2021 solutions, the local ties have been stable, at the one-centimeter level, for more than 25 years. The 1995 measurements formal precision reported was probably too low taking into account that the 1995 geodetic GPS technology applications were just starting.

The 1995 SLR telescope invariant point GPS-only position solution could have contributed to the local ties differences reported here, as it involved an additional independent height component measurement. The fact that the 12302M001–12302M002 slope change, is less than the 2021 slope value error, hints that the other 1995–2021 slope changes reported here are influenced by the 1995 telescope invariant point determination. Hence, we have a reason to assume that the actual stability is better than reported here, and approaching the millimeter levels. Only after the next survey is done this will be fully confirmed

**Acknowledgments** This work was supported by the European Regional Development Fund (Grant No.1.1.1.5/19/A/003).

## References

- Bikše J, Lapuška K, Lazdāns J (1992) Latvijas trigonometriskā tīkla piesaiste pasaules geodēziskajai sistēmai. Riga Technical University Geomatics Institute, Latvia, Riga
- Donal T (2013) Arequipa ITRF co-location survey. IGN, Service de Géodésie et Nivellement, France
- Kaminskis J, Šujakova L, Salmins K, Kaulins J, Goldbergs L (2020) SLR and GNSS test field for global geodetic network assessment in Riga. In: 11th International Conference “Environmental Engineering”, Vilnius Gediminas Technical University, Lithuania, pp 1–6, 21–22 May 2020
- Lapuška K (1996) University of Latvia astronomical observatory space geodesy and geodynamics laboratory activities into the year 1995. In: First Workshop of the IAG Subcommission 8.1 Studies of the Baltic Sea, Latvia, Riga, March 28–29, 1996
- Šarkovskis J (2012) Local Ties at the Astrogeodynamical Station in Riga (In Latvian). BSc Diploma Work, Riga Technical University. <https://nda.rtu.lv/lv/view/3878>

**Open Access** This chapter is licensed under the terms of the Creative Commons Attribution 4.0 International License (<http://creativecommons.org/licenses/by/4.0/>), which permits use, sharing, adaptation, distribution and reproduction in any medium or format, as long as you give appropriate credit to the original author(s) and the source, provide a link to the Creative Commons license and indicate if changes were made.

The images or other third party material in this chapter are included in the chapter's Creative Commons license, unless indicated otherwise in a credit line to the material. If material is not included in the chapter's Creative Commons license and your intended use is not permitted by statutory regulation or exceeds the permitted use, you will need to obtain permission directly from the copyright holder.





# Datum Problem Handling in Local Tie Surveys at Wettzell and Metsähovi

Ulla Kallio, Thomas Klügel, Simo Marila, Swetlana Mähler, Markku Poutanen, Timo Saari, Torben Schüler, and Heli Suurmäki

## Abstract

The datum problem is a fundamental issue in the network adjustment when connecting a local measurement network to an external reference frame. Datum elements in 3D networks are scale, translation, and orientation. We consider here the local tie network at geodetic core stations, where the external reference frame is the latest ITRF realization, ITRF2014, in the mean epoch of terrestrial observations.

Accurate distance measurements are used for the determination of the network scale. Thus the improvement of its accuracy and the inclusion of weather measurements to account for refraction errors are essential. For rotation and translation of the network, we need external information. Angle observations are related to the coordinate system of the instrument (e.g. a tachymeter) which is usually aligned to the plumb line. Instruments have different vertical orientation at every station point and the direction of the plumb line does not coincide with the normal vector of the reference ellipsoid. Horizontally the observed set of angles are oriented in arbitrary or approximately oriented directions.

External information which is needed for solving the absolute orientation are datum points, providing the link to the global coordinate system, and correction terms for the vertical orientation (deflection of the vertical), which can be derived from combined terrestrial/GNSS observations, from a gravity based geoid model, or from astronomical observations.

In this article, we present the solutions/options for the datum problem in the framework of the EMPIR GeoMetre project using the example of the ITRF core stations Metsähovi and Wettzell using transformation-free approaches. The inclusion of distant targets is promising, since in small networks even a millimeter change in the coordinates of a datum point can significantly affect a local tie vector. It is shown that at both stations the determination of the deflection of the vertical using different techniques yield the same results within the measurement error.

## Keywords

Datum problem · Local ties · Network adjustment · Orientation · Scale

The 18SIB01 GeoMetre project has received funding from the EMPIR programme co-financed by the Participating States and from the European Union's Horizon 2020 research and innovation programme.

U. Kallio (✉) · S. Marila · M. Poutanen · T. Saari · H. Suurmäki  
FGI, National Land Survey of Finland, Espoo, Finland

T. Klügel · S. Mähler · T. Schüler  
BKG, Geodetic Observatory Wettzell, Bad Kötzing, Germany

© The Author(s) 2022

J. T. Freymueller, L. Sánchez (eds.), *Geodesy for a Sustainable Earth*, International Association of Geodesy Symposia 154, [https://doi.org/10.1007/1345\\_2022\\_155](https://doi.org/10.1007/1345_2022_155)

## 1 Introduction

The local ties are currently used for the combination of the different space geodetic techniques: Global Navigation Satellite Systems (GNSS), Satellite Laser Ranging (SLR), Very Long Baseline Interferometry (VLBI), and Doppler Orbitography and Radiopositioning Integrated by Satellite (DORIS) system, to realize the International Terrestrial Reference System (ITRS). The local ties include the vectors connecting the reference points of space geodetic instruments. The tie vectors, in most cases with the full covariance matrices, in Solution Independent EXchange format (SINEX) are handled in combination as a fifth technique (Boucher et al. (2015)). The local ties allow in the combination the datum transfer among the techniques. That underlines the importance of accurate local ties. IAG working group WG 1.2.1 “Methodology for surveying geodetic instrument reference points” launched the Local Survey metadata project. The SINEX files of local ties are now collected with metadata about the site surveys (IERS 2021; ITRF 2021).

The reference points of VLBI and SLR telescopes are determined indirectly by monitoring measurements. Points rotating around the axes of the telescopes in several angle positions are monitored and included in the network. The reference points are then estimated in the reference frame of the local survey network using mathematical models (e.g. Harvey (1991), Sarti et al. (2004), Dawson et al. (2007), Lösler (2009), Kallio and Poutanen (2012), Lösler et al. (2021)). GNSS observations refer to the ARP (Antenna Reference Point) at least theoretically with certain uncertainty when antenna calibration tables with Phase Center Offset and Phase Center Variation are used. In tachymeter measurements, a common reference point can be achieved almost directly with the seamless network set up where special accurate adapters connect GNSS antennas and prisms. The small vertical offset can accurately be determined by leveling. The older permanent mast points like METS at Metsähovi on the top of the 20m mast are exceptions. As there is no seamless adapter, the ARP must be measured using the geometry of the antenna: vertically the bottom of the antenna and horizontally the left and right side of the antenna – as proposed in “IERS Technical Note No39” (Poyard 2017).

While the vectors between reference points form the local tie network, the local survey network, including pillar points and permanent GNSS points, connects the monitoring measurements to the same local frame (see Fig. 1). The more instruments the local tie network has, the more monitoring networks must be connected. Metsähovi is an example of a rather compact solution of a local survey network (Fig. 1).

In Wettzell there are more instruments and the local survey network is more complicated (Fig. 2).

Because the local ties should be given in ITRF, the local survey network should be transformed to ITRF. Thus the datum definition of the local survey network plays a key role. For horizontal orientation, there is no other relevant option than the local GNSS/GPS network. For vertical orientation, the known Deflection of Vertical (DoV) as external information can be used. The geo-referencing methods at different co-location sites varies. There is a data field for referencing method in the above-mentioned metadata CSV-file (ITRF 2021). The short look inside the available files shows that without reading the more detailed reports it is almost impossible to say anything about the quality of the orientation or scale: how the GNSS points were situated in the area, were they permanent or temporary GNSS points, what was the session lengths of GNSS observations, or what is the quality of DoVs. The way how the coordinates of GNSS are constrained may influence the results too, and that depends on the software.

There are no limit values available for uncertainties of orientation angles or scale for local ties. The required accuracy of GGOS local ties is set to 1mm and the measurement accuracy 0.1mm (Gross et al. 2009). With these values, the local ties at co-location sites could be equated to the space geodetic techniques. If the distance between space geodetic instruments is 100m the 0.1mm measurement accuracy means  $1 \mu\text{rad}$  ( $0.2''$ ) for angles. The requirement of scale accuracy, 1 ppb (Gross et al. 2009) for GGOS, is hardly applicable to short distances in a local tie network.

The reference point estimation gives the uncertainty of the monitoring part but not the uncertainty of the datum definition part of the local survey network. It has been proved that reference point coordinates can be determined within 0.01mm precision using close-range photogrammetry (Lösler et al. 2021). Thus a small monitoring network, spanning a couple of meters, can be internally extremely accurate. However, the datum noise of the external reference frame, the uncertainty of realization of the local frame in ITRF, is not included in these measures. The influence of orientation and the scale uncertainty of the network must be included in the total uncertainty of local tie vectors.

One task of our work in the GeoMetre project is to mitigate the uncertainties of the orientation and scale of the local frame. The realization of the local frame in ITRF needs external information. Although the local survey network is accurate internally, the quality and handling of the external information influence the final alignment in ITRF. The details of the solutions at Wettzell and Metsähovi are presented separately: at first the Sects. 2 and 3 introduce the co-location sites. In Sects. 2.1 and 3.1 the local survey

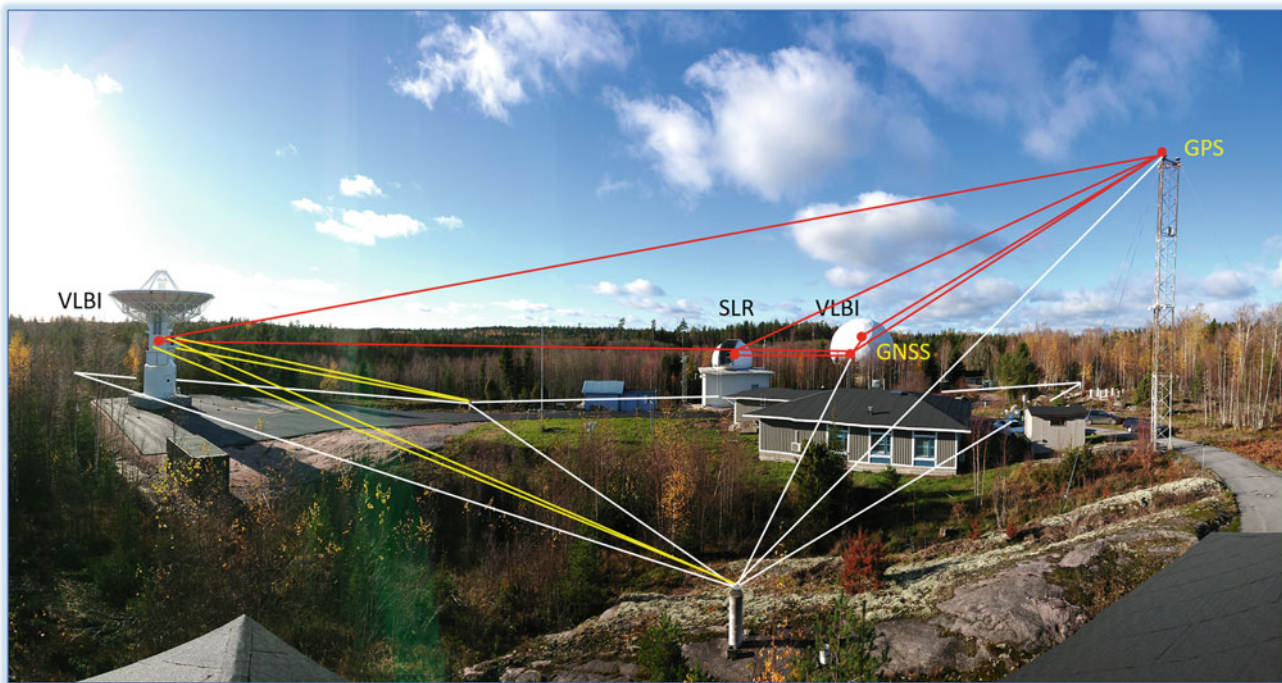


**Fig. 1** The local tie network (red), part of the local survey network (white), and part of the monitoring network (yellow)

networks at the co-location sites are introduced and the subsequent sections describe solutions for the alignment problem datum element by datum element. Although the focus is on the datum problem, the results, the end product of the work, and the local tie vectors are presented at the end of the sections.

## 2 Wettzell

### 2.1 Local Network

The local survey network of the Geodetic Observatory Wettzell (GOW) consists of 30 deeply founded, shielded concrete pillars spread over the entire observatory. They tie the reference points of the space geodetic techniques together to provide local tie vectors for the mutual control and the combination of the different techniques (Fig. 2). Reference points of 3 VLBI antennas, 2 laser-ranging telescopes, 5 GNSS antennas, and 1 DORIS antenna must be measured and tied together. Fixed antennas as used for GNSS and DORIS can be surveyed more or less directly, either by temporarily removing the antenna or using permanent prism mounts for a seamless connection as proposed above. The permanent prism mounts are preferable, because it is not recommended to remove the antennas. The reference points of moving telescopes, however, have to be constructed as described above. This subset of points including the referencing pillars (monitoring setup) of all telescopes must

be included in the network to obtain tie vectors between all space technique reference points. Only the 20-m radio telescope (RTW) has a physical representation of the axis intersection (i.e. the reference point), which can be surveyed directly from outside.

The survey of the most recent solution, which was submitted to the ITRF2020, was done in 2018. In addition to the local network, 3 pillars outside the observatory at distances between 300 and 1200 m were observed in terms of terrestrial survey and GNSS measurements. This setup was established to reduce the problem of orientation uncertainties on short GNSS baselines.

### 2.2 Transformation-Free Approach

Another step to overcome the datum problem is the transformation-free approach, which was optimized in the framework of the GeoMetre project. Usually selected pillars being part of the local survey network are temporally observed by GNSS measurements. The geocentric GNSS coordinates at these so-called pass points are used to perform a Helmert transformation of the local network to convert the local coordinates into the geocentric frame. In the transformation-free approach, no local coordinate system is required. The GNSS coordinates are introduced as datum points in the adjustment procedure, and all measured angles which refer to the local plumb line are used after correction of the local deflection of the vertical (DoV). The distances, which define

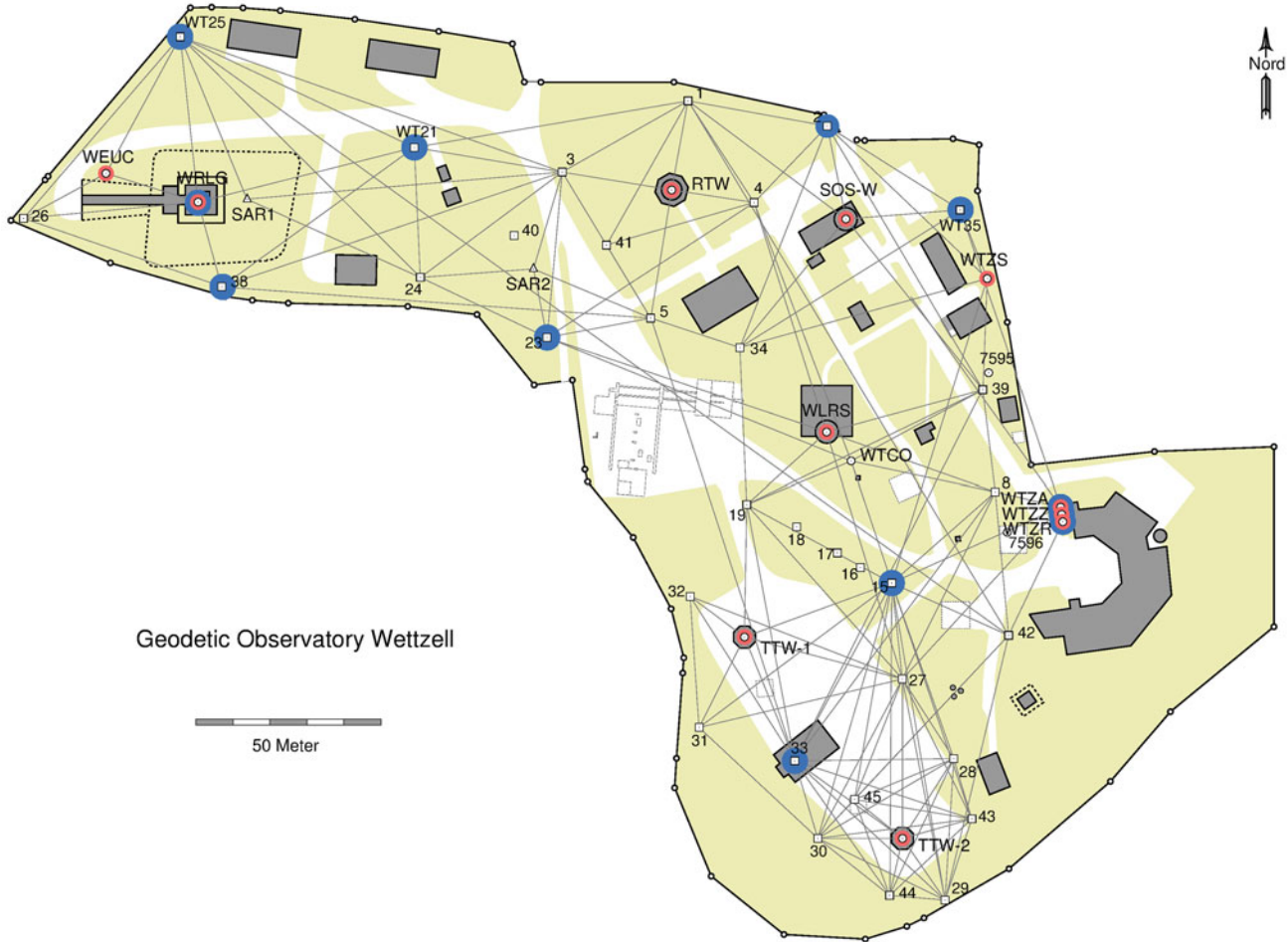


**Fig. 2** Local terrestrial network at Wettzell with the reference points of the space geodetic techniques in red and the used datum points in blue. Reference point labels are explained in Table 1

the network scale as described above, were measured in a classical way, i.e. using a tachymeter and locally measured meteorological quantities to account for refraction.

### 2.3 Deflection of the Vertical

The vertical deflection describes the angular deviation between the direction of the gravity vector and the normal of the ellipsoid surface at a point on the Earth's surface. It can be represented by its North-South component  $\xi$  (positive northward) and East-West component  $\eta$  (positive eastward). There are different techniques to determine the DoV: the astrogeodetic technique, being also known as Helmert DoV, the GNSS-leveling technique, and the gravimetric technique yielding the Molodensky DoV.

In the astrogeodetic technique, the physical (or astronomical) latitude ( $\Phi$ ) and longitude ( $\Lambda$ ) are directly determined by the positions of stars relative to the local plumb line. On the other hand, the geometric (or geodetic) latitude ( $\varphi$ )

and longitude ( $\lambda$ ) are taken from GNSS measurements. The astronomic DoV components are simply calculated by the following relationships (e.g. Heiskanen and Moritz (1984)):

$$\xi = \Phi - \varphi. \quad (1)$$

$$\eta = (\Lambda - \lambda) \cos(\varphi). \quad (2)$$

The astrogeodetic observations were done in August 2018 at GOW using the QDaedalus system mounted on two different tachymeters (Albayrak et al. 2021). On four different pillars on the observatory, seven sessions were performed at each pillar using 250–300 stars per session. The standard deviations are about  $1 \mu\text{rad}$  ( $0.2''$ ) for the TCRM1101 and  $0.5 \mu\text{rad}$  ( $0.1''$ ) for the TDA5005 instrument. Except for pillar WT03, the maximum differences between all sessions at one pillar are below  $1.45 \mu\text{rad}$  ( $0.3''$ ). Although there seems to be a slight gradient between the results at the four locations, an average value of  $-10.57 \mu\text{rad}$  ( $-2.18''$ ) for  $\xi$  and  $-28.36 \mu\text{rad}$  ( $-5.85''$ ) for  $\eta$  was used for the



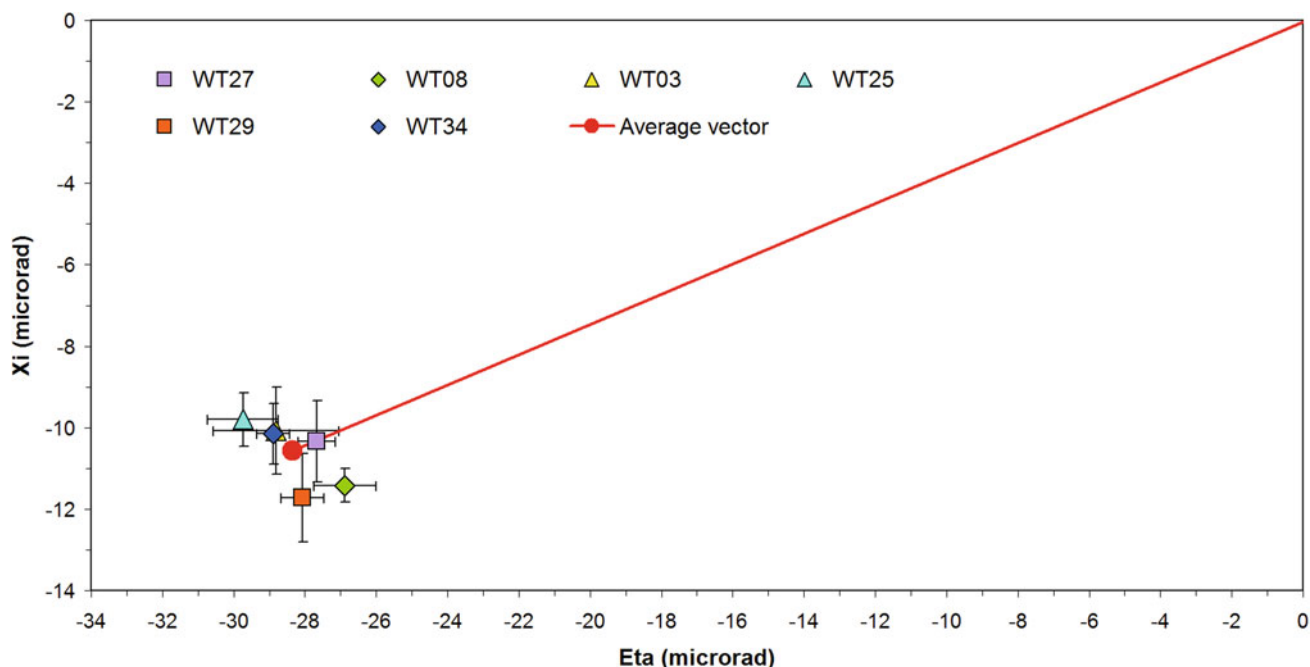


**Fig. 3** Astrogeodetic deflections of the vertical measured at different points at the observatory site, expressed as components  $\xi$  and  $\eta$ . The average vector (red line) is  $30.25 \mu\text{rad}$  ( $6.24''$ ) towards an azimuth of  $249.6^\circ$

entire observatory. This is equivalent to an inclination of  $30.25 \mu\text{rad}$  ( $6.24''$ ) towards WSW (azimuth  $249.6^\circ$ ) (Fig. 3).

The GNSS-leveling technique uses the differences between orthometric heights as determined by leveling and ellipsoidal heights as determined by GNSS. In small networks as considered here, these height differences form a plane that defines the orientation of the equipotential surface at ground level and the ellipsoid surface. It can either be calculated along GNSS baselines (Vittuari et al. 2016) or in a planar constellation by a least-square fit of a plane. Since the uncertainties of the GNSS analyses of a few millimeters in height are large as compared to the baseline length (300m maximum), this technique was not applied in our case.

The gravimetric technique is usually used to determine the the geoid or – in our case – the quasigeoid and thus represents the DoV at the Earth’s surface. The regional quasigeoid like BKG’s GCG2016 model usually reflects large-scale gravimetric structures. To account for small-scale structures, a local fine structure quasigeoid of 10 km radius around the GOW was calculated based on data from a densified gravity network, an improved topographic model, and regional GNSS/leveling co-location points as pass points (Schwabe 2019). First, a pure gravimetric model was computed. In a second step, the solution was fitted to regional pass points by introducing a plane to obtain a model being consistent with the national reference frame. This step is justified since only the deviations from the CGC2016 are considered in this context.

As compared to the GCG2016, the local model exhibits fine structures up to 11 mm over a 4 km distance (Fig. 4). In terms of short-wavelength geoid undulations, these errors account for trends up to 3 mm/km. However, these differences do not apply to the GOW. Hence, the quasigeoid surface at the GOW is well represented by the regional quasigeoid, the differences do not exceed 0.2 mm. Thus the dip of the quasigeoid surface at the observatory site is about 30 mm/km ( $30 \mu\text{rad}$ ,  $6.2''$ ) towards an azimuth of  $250^\circ$  (Fig. 4), which is equivalent to  $-10.26 \mu\text{rad}$  ( $2.12''$ ) and  $-28.19 \mu\text{rad}$  ( $-5.81''$ ) or  $\xi$  and  $\eta$ , respectively. Within the measurement uncertainties, the astrogeodetic and the gravimetric technique yield the same results.

The astrogeodetic DoV components  $\xi$  and  $\eta$  were directly included in the used adjustment software PANDA. GNSS coordinates from selected points indicated in (Fig. 2) were used as datum point coordinates. The results, given as differences with respect to WTZR, are shown in (Table 1).

### 3 Metsähovi

The Metsähovi Geodetic Research Station has been upgraded during last years. It will be one of the northernmost Global Geodetic Observing System (GGOS) Core stations when the renewal process is completed. At Metsähovi there are two VLBI telescopes, the older telescope of Aalto University, and the new VLBI Global Observing System (VGOS) telescope

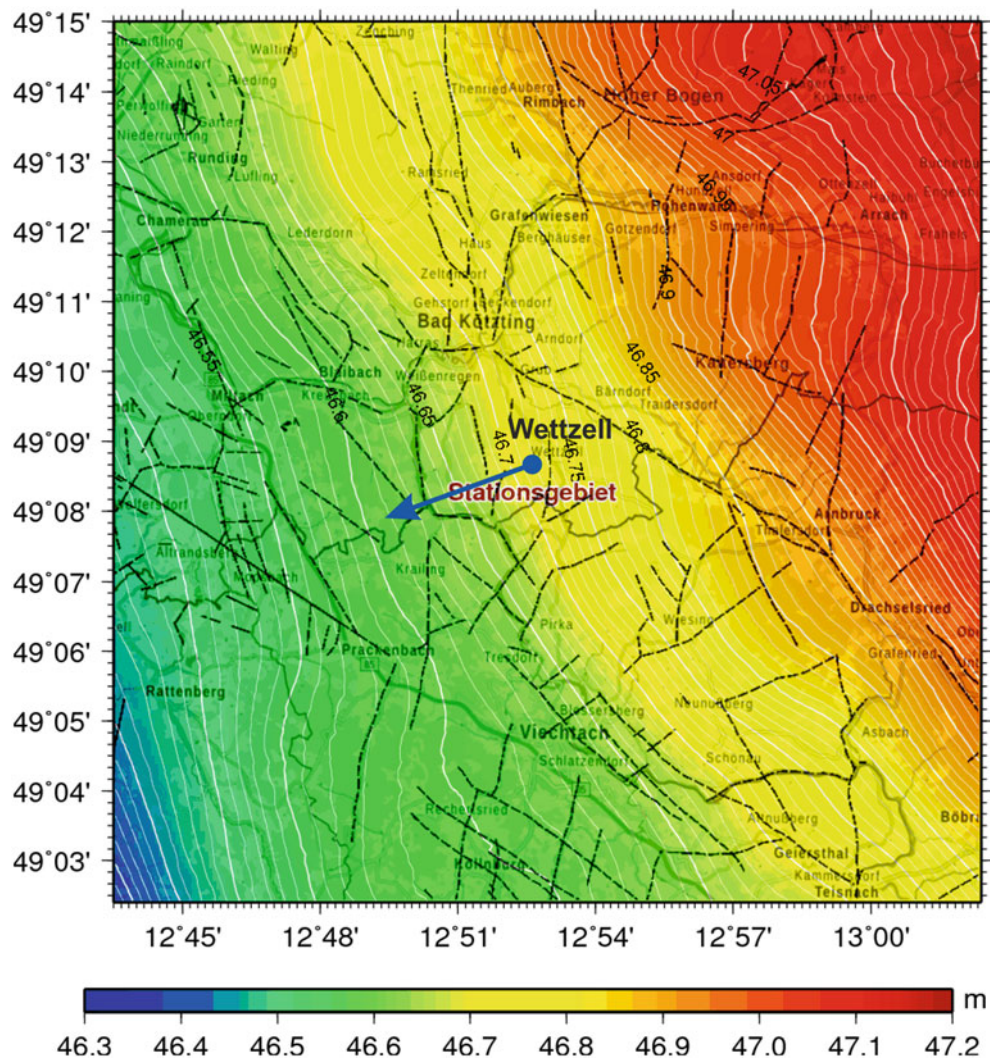


**Fig. 4** The surface of the fine-structure quasigeoid dips  $30 \mu\text{rad}$  ( $6.18''$ ) towards WSW in the Wettzell area

**Table 1** Local ties between the reference points of all space geodetic techniques in Wettzell w.r.t. WTZR and their standard deviations

Station	Technique	Site ID	Domes No.	DX [m]	DY [m]	DZ [m]	rms DX [m]	rms DY [m]	rms DZ [m]
WTZR	GNSS	1202	14201M010	0.00000	0.00000	0.00000	0.00061	0.00026	0.00058
WTZA	GNSS	1204	14201M013	-2.18965	-1.00173	1.89096	0.00062	0.00030	0.00059
WTZZ	GNSS	1205	14201M014	-1.12239	-0.68639	0.90670	0.00060	0.00024	0.00058
WRLG	GNSS	1220	14201M024	-15.58126	-243.24712	52.52927	0.00070	0.00030	0.00133
WTZS	GNSS	1208	14201M015	-45.36698	-31.46797	40.87921	0.00058	0.00059	0.00074
WEUC	DORIS	223	14201S046	-20.86947	-273.46404	53.49741	0.00091	0.00043	0.00148
RTW	VLBI	7224	14201S004	-40.79935	-118.39787	61.31629	0.00021	0.00043	0.00086
SOSW	SLR	7827	14201S045	-49.47589	-71.95635	51.81447	0.00025	0.00042	0.00071
WLRS	SLR	8834	14201S018	-3.82402	-68.20428	15.51548	0.00031	0.00028	0.00074
TTW1	VLBI	7387	14201S043	47.23547	-79.66738	-15.84895	0.00026	0.00047	0.00079
TTW2	VLBI	7388	14201S044	78.54239	-29.16116	-51.98213	0.00052	0.00075	0.00067

owned by National Land Survey of Finland (NLS), a new SLR telescope, and two permanent GNSS antennas – all of them are part of the local tie network. In addition, there is a DORIS beacon, owned by the French government space agency, the Centre National d'Études Spatiales (CNES), about three kilometers away from Metsähovi (NLS 2022).

### 3.1 Local Network

The local survey network at Metsähovi consists of pillar points, mast points, temporary station points, and one ground marker on the floor under the radome of the SLR telescope, including a permanent GNSS point and a permanent Global Positioning System (GPS) point. Besides permanent stations, there were seven semi-permanent GPS points equipped with choke ring antennas on seamless network adapters. Most of the semi-permanent points were occupied for three months (8.–10.2020) during the network measurements. The terrestrial observations, local network, and monitoring network together (Fig. 5), consists of 2624 point-to-point measurements, most of them include two angles and slope distance, and 37 levelled height differences.

### 3.2 Scale

The network data include the scale information from tachymeter distance measurements. Terrestrial observations lack only orientation and translation.

Also, GPS vectors include a scale. However the scale of GPS vectors is not directly traceable to the definition of the meter in the metrological sense but the distance measurements of calibrated tachymeters with accurate refraction index derived from reliable air pressure, temperature, and humidity measurements provide the traceability.

One option in the adjustment is to use GPS vectors as observations. In that case, the GPS scale interfere with the scale coming from tachymeter distances and traceability is compromised. The other option, which we use, is not to use GPS vectors as observations at all. The GPS network was processed separately and the daily solutions with covariance matrices are combined into one solution, which is used as a datum. The inner constraints are formed for rotations and translation, thus the scale results from tachymeter distance observations.

The scale of the tachymeter, traceable to the definition of meter, is transferred from Nummela Standard Baseline (Jokela 2014). The application of the new technology from the Physikalisch-Technische Bundesanstalt (PTB) and CNAM (Conservatoire National des Arts et Métiers) yielding

more accurate distances is planned, in the framework of GeoMetre project, for some of the baselines in the network with simultaneous spectroscopic temperature measurements by Technical Research Centre of Finland (VTT). We plan to adjust the network with some more accurate baselines measured with the new technique. Tachymeter distances can then be weighted appropriately or the scale parameter can be added to observation equations of tachymeter distances. One option is to determine the scale difference between the new instrument and tachymeter and if appropriate, to correct the tachymeter distances.

### 3.3 Translation and Orientation, Seamless Network

The orientation of the local survey network is basically coming from GPS. Permanent and semi-permanent GPS stations provide the datum of the network. The GPS daily solutions were processed with Bernese 5.2 (Dach et al. 2015) and combined with CATREF software (Altamimi et al. 2018). The coordinates and covariance matrix of the combined solution are used as a datum in inner constraint equations. Observation equations for angles and distances in the global Cartesian coordinate system form the observation part of the 3D-network adjustment. With the datum information in inner constraint equations, no further transformations after adjustment are needed. The new seamless adapters (Fig. 6) enable tachymeter measurements simultaneously with GPS. Individually calibrated GPS antennas with the seamless connection of the prisms mitigate the centring errors to less than 0.2mm.

We used two methods for handling the DoV. In the first method the angle observations are corrected to refer to the normal of the ellipsoid using the geoid model and the combined solution of the GPS-network is used for horizontal orientation only. In the second method we did not correct the DoV but solve for the instrument 3D-orientation at each set up.

#### 3.3.1 Using Geoid Model for Vertical Orientation

In the first method the Metsähovi local network station points are oriented vertically using the new local geoid model, FIN\_Geoid\_Geo-Metre\_MH2000. It is an updated version of the high-resolution Finnish geoid model, FIN\_EIGEN-6C4 (Saari and Bilker-Koivula 2018), with the inclusion of Metsähovi gravity data measured by Hannu Ruotsalainen and Selen Dayioglu in 2006 using a Scintrex CG-5 relative gravimeter (Ruotsalainen and Dayioglu 2006). The gravity data contain 122 points covering an area of 1 km × 1 km, with an average point distance of around 100 m. To match the

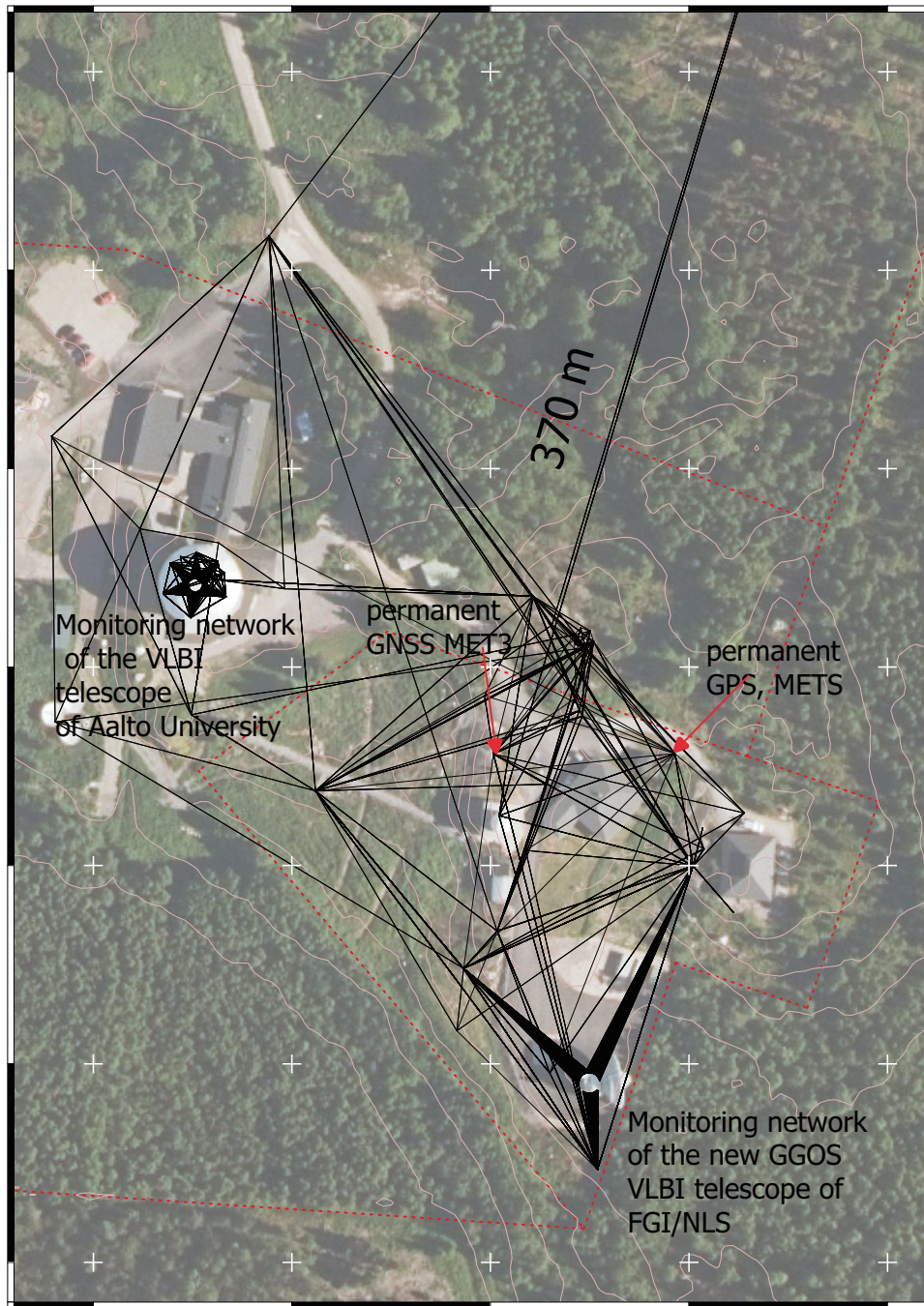


**Fig. 5** Local terrestrial network at Metsähovi

main gravity data, the Metsähovi data has been transformed from the original epoch 1963.0 to 2000.0 and the tide system changed from mean-tide to zero-tide. The whole gravity dataset used in FIN\_EIGEN-6C4 covers Finland and surrounding countries between  $56.8^\circ$  and  $72.2^\circ$  latitude and  $15^\circ$  and  $36^\circ$  longitude. The DoV,  $\xi = -22.32 \mu\text{rad}$  ( $-4.60''$ ) and  $\eta = 33.92 \mu\text{rad}$  ( $7.00''$ ), from the earlier used national geoid

model, FIN2005N00 (Bilker-Koivula and Ollikainen 2009), differ slightly from the new ones but the difference means only 0.2mm in 100m. The components  $\xi = -22.44 \mu\text{rad}$  ( $-4.63''$ ) and  $\eta = 36.08 \mu\text{rad}$  ( $7.44''$ ) of the new geoid agree well with the astronomical ones measured in 1976–1980 (Ollikainen 1987):  $\xi = -22.49 \mu\text{rad}$  ( $-4.64''$ ) and  $\eta = 35.39 \mu\text{rad}$  ( $7.30''$ ). The geodetic coordinates of those



**Fig. 6** The seamless adapter for GNSS antenna and prisms at a pillar point

from the adjustment of Jorma Jokela (Jokela et al. 2016) were firstly defined in the ED87 frame and later transformed to ETRF89 by Matti Ollikainen.

The angle observations refer to the plumb line and are corrected to refer to the ellipsoidal normal at the corresponding point. When we correct the angle observations due to the deflection of vertical, we fix the vertical direction of the instrument in each station point. The observation equations of sets of horizontal angles include orientation unknowns – one for each setup. The inner constraint matrix then includes four rows, one for horizontal orientation of the network and three for translation. The conversion of the geoid based deflections to the level of the earth’s surface can be neglected, since at Metsähovi its vertical distance to the geoid surface is less than 100m.

### 3.3.2 Estimating the 3D Orientation of Instrument

In the second method the 3D orientation angles of each tachymeter set up were estimated, as unknown parameters in a network adjustment, without correcting angle observations using the geoid model. This kind of approach is usually applied in cases where the instrument alignment is not collinear with the plumb line or can not be controlled with

compensators which is the case in some industrial or aboard a ship measurements. However, in the local survey networks at co-location sites, we level the instruments carefully and use compensators for controlling the alignment with the plumb line. Thus, with the assumptions that the instrument is aligned with the plumb line and our datum point coordinates are aligned with ITRF, we can solve for the deflection of vertical for each station point by estimating 3D-rotations for each instrument setup. The datum defect of the normal matrix in the network adjustment, in this case, is six. This approach is quite promising at least in small networks like at Metsähovi. However even 1 mm errors in coordinates of the datum points may cause a significant tilt to the network. At least the individual calibrations for antennas are needed. The seamless setup mitigates the centring errors.

### 3.3.3 Results of Adjustments

The preliminary network adjustments have been performed using the in-house software with two different methods. In both cases, the resulting coordinates of the moving points in the telescope structure were used to estimate the local tie vector from MET3 GNSS ARP to the reference point of the VLBI antenna. There was about 1.5mm difference in height. Horizontally there is no significant discrepancy. The difference in the results of the two cases is due to the orientation of the network. The deflections of vertical components from the geoid model differ from estimated station point deflections  $\xi$  and  $\eta$ ,  $-11.6 \mu\text{rad}$  ( $-2.39''$ ) and  $21.8 \mu\text{rad}$  ( $4.50''$ ), respectively, which explain the difference in the vertical component. The reason for the disagreement of estimated DoVs and DoVs interpolated from the new geoid model is the uncertainty in the GPS coordinates in the vertical direction and the small size of the network.

The network measured in 2014–2015, and the new, measured in 2020–2021 were combined and adjusted. The reference points of METSA13 (the new VLBI telescope) and METSAHOV (the old VLBI telescope) were estimated using the adjusted coordinates of the points rotating around the axes of the telescopes. The local tie vectors from terrestrial measurements are presented in Table 2 relative to the point MET3. The standard deviations of VLBI reference points include the noise of the monitoring. The noise of the datum (orientation) must be included to the total uncertainty. At Metsähovi the reference point of the new SLR telescope will be measured in near future.

**Table 2** Local ties between the reference points of space geodetic techniques in Metsähovi w.r.t. MET3 and their standard deviations

Station	Technique	Site ID	Domes No.	DX [m]	DY [m]	DZ [m]	rms DX [m]	rms DY [m]	rms DZ [m]
MET3	GNSS	MET3	10503M010	0.00000	0.00000	0.00000	0.00000	0.00000	0.00000
METS	GPS	METS	10503S011	-13.39901	44.04350	14.37157	0.00018	0.00018	0.00027
METSA13M	VLBI	7398	10503S017	53.64093	54.40054	-40.21132	0.00003	0.00002	0.00005
METSAHOV	VLBI	7385	10503S002	0.80218	-83.91571	20.33662	0.00004	0.00002	0.00007

## 4 Discussion

In this work two similar strategies to improve the handling of the datum problem at geodetic co-location stations are presented. At the GOW the transformation-free approach has successfully been tested. The required angles of vertical deflection were obtained with an accuracy of about  $1 \mu\text{rad}$  ( $0.2''$ ) by using the astrogeodetic technique and were confirmed by the dip of fine structure quasigeoid surface in the vicinity of the observatory. The network orientation is realized by independent solutions from GNSS observations, which were introduced in the adjustment as datum points. Distant targets improve the accuracy of the horizontal orientation of the network.

At Metsähovi the functional model has been extended to solve for the instrument orientation at each station point. Using the GPS and terrestrial data set measured in 2020 and 2021, it is obvious that the orientation is not satisfyingly solved due to the uncertainties of GPS coordinates in the vertical direction influencing a small tilt to the whole survey network. The horizontal orientation is less sensitive to the tilt.

The other approach where the adjustment is done directly in the global frame without further transformation is suitable. The angle observations were corrected according to the DoV of the new Finnish geoid model. In preliminary adjustments of the Metsähovi network, all the permanent and semi-permanent GPS points were included in the datum in the inner constraint equations.

At both sites the poorly constrained vertical orientation from GNSS observations was significantly improved by the introduction of DoV data in the adjustment of terrestrial observations. Typical GNSS uncertainties of 2 mm in height over a baseline of 100 m result in an orientation error of  $20 \mu\text{rad}$  ( $5''$ ), while the determination of the local DoV using either the astrogeodetic or gravimetric technique can be done with an accuracy of  $1 \mu\text{rad}$  ( $0.2''$ ).

This approach can easily be adopted by other geodetic observatories. If a sufficiently accurate geoid or quasigeoid model is available, the local DoV can be taken from the normal of the (quasi-)geoid surface. But also the use of the astrogeodetic technique is a viable path. Modern instruments like the QDaedalus system allow for quick and accurate

DoV measurements. As the datum problem seems to be the limiting factor in local tie determinations, a consequent integration of DoV observations in local tie solutions could help to further improve and harmonize ITRF solutions, in particular at GGOS core sites. The standard deviations of RP coordinates are a consequence of variance propagation in RP-estimation as an influence of the geometry, the number of VLBI antenna positions, and precision of measured target coordinates. The uncertainties of local tie vector components should also include the uncertainties of orientation and scale of the local survey network.

While the solution of these surveys, which were submitted to the ITRF2020, is based on classical tachymeter measurements, the next ITRF will contain data of the newly developed refraction-compensated distance meters being developed in the framework of the GeoMetre project to further improve the scale of the local ties and the traceability to SI units.

**Acknowledgements** The very productive support of Cornelia Eschelbach and Michael Lösler is gratefully acknowledged. The FGI team thanks Jyri Näränen, Joonas Eskelinen and Arttu Raja-Halli for their help at Metsähovi station during preparations and measurements.

## References

- Albayrak M, Hirt C, Guillaume S, Klügel T (2021) Testing two different qdaedalus systems under similar conditions at geodetic observatory Wettzell and Technical University of Munich. In: Proceedings surveying, geology and mining, ecology and management (SGEM) 2021, section geodesy and mine surveying, Book 2. <https://doi.org/10.5593/sgem2021/2.1/s09.55>
- Altamimi Z, Boucher C, Sillard P, Collilieux X, Paul R (2018) CATREF Software, combination and analysis of terrestrial reference frames. IGN, CATREF training course 19.4.2018 in Paris
- Bilker-Koivula M, Ollikainen M (2009) Suomen geoidmallit ja niiden käyttäminen korkeuden muunnoksissa. Research notes of the Finnish Geodetic Institute (29):48
- Boucher C, Pearlman M, Sarti P (2015) Global geodetic observatories. *Adv Space Res* 55(1):24–39. <https://doi.org/10.1016/j.asr.2014.10.011>
- Dach R, Lutz S, Walser P, Fridez P (2015) Bernese GNSS software version 5.2. User manual. Astronomical Institute, University of Bern, Bern. <https://doi.org/10.7892/boris.72297>, Open Publishing
- Dawson J, Sarti P, Johnston GM, Vittuari L (2007) Indirect approach to invariant point determination for SLR and VLBI systems: an assessment. *J Geodesy* 81(6-8):433–441

- Gross R, Beutler G, Plag HP (2009) Integrated scientific and societal user requirements and functional specifications for the GGOS. Springer, Berlin, Heidelberg, pp 209–224. [https://doi.org/10.1007/978-3-642-02687-4\\_7](https://doi.org/10.1007/978-3-642-02687-4_7)
- Harvey B (1991) Telescope axis surveys. *Aust J Geodesy Photogramm Surv* 1991(54):1–18
- Heiskanen W, Moritz H (1984) Physical geodesy. Technical University Graz, Austria
- IERS (2021) Local Survey metadata project, IERS Message No. 439
- ITRF (2021) Local Survey metadata project. [https://itrf.ign.fr/local\\_survey\\_metadata.php](https://itrf.ign.fr/local_survey_metadata.php)
- Jokela J (2014) Length in geodesy – On metrological traceability of a geospatial measurand. Doctoral thesis, Aalto University. School of Engineering. <http://urn.fi/URN:ISBN:978-951-711-310-6>
- Jokela J, Kallio U, Koivula H, Lahtinen S, Poutanen M (2016) FGI's contribution in the JRP SIB60 "metrology for long distance surveying". In: Proceedings of the 3rd joint international symposium on deformation monitoring (JISDM). [https://doi.org/10.1007/978-3-642-20338-1\\_8](https://doi.org/10.1007/978-3-642-20338-1_8)
- Kallio U, Poutanen M (2012) Can we really promise a mm-accuracy for the local ties on a Geo-VLBI antenna. In: *Geodesy for planet earth*. Springer Science Business Media, pp 35–42. <https://doi.org/10.1007/978-3-642-20338-1-5>
- Lösler M (2009) New mathematical model for reference point determination of an azimuth-elevation type radio telescope. *J Surv Eng* 135(4):131–135. [https://doi.org/10.1061/\(asce\)su.1943-5428.0000010](https://doi.org/10.1061/(asce)su.1943-5428.0000010)
- Lösler M, Eschelbach C, Klügel T, Riepl S (2021) ILRS reference point determination using close range photogrammetry. *Appl Sci* 11(6). <https://doi.org/10.3390/app11062785>
- NLS (2022) <https://www.maanmittauslaitos.fi/en/research/research/metsahovi-geodetic-research-station>
- Ollikainen M (1987) Astro-geodetic deflections of the vertical at first-order triangulation stations. *Resreport 87:4*. Finnish Geodetic Institute
- Poyard JC (2017) IGN best practice for surveying instrument reference points at ITRF co-location sites. Tech. rep., BKG
- Ruotsalainen H, Dayioglu S (2006) Gravity data set, personal communication 2019
- Saari T, Bilker-Koivula M (2018) Applying the GOCE-based GGMs for the quasi-geoid modelling of Finland. *J Appl Geodesy* 12(1):15–27. <https://doi.org/10.1515/jag-2017-0020>
- Sarti P, Sillard P, Vittuari L (2004) Surveying co-located space-geodetic instruments for ITRF computation. *J Geodesy* 78(3):210–222. <https://doi.org/10.1007/s00190-004-0387-0>
- Schwabe J (2019) Feinstrukturgeoid für die Wettzell-Region, Internal Report, BKG, Leipzig
- Vittuari L, Tini MA, Sarti P, Serantoni E, Borghi A, Negusini M, Guillaume S (2016) A comparative study of the applied methods for estimating deflection of the vertical in terrestrial geodetic measurements. *Sensors* 16(4). <https://doi.org/10.3390/s16040565>

**Open Access** This chapter is licensed under the terms of the Creative Commons Attribution 4.0 International License (<http://creativecommons.org/licenses/by/4.0/>), which permits use, sharing, adaptation, distribution and reproduction in any medium or format, as long as you give appropriate credit to the original author(s) and the source, provide a link to the Creative Commons license and indicate if changes were made.

The images or other third party material in this chapter are included in the chapter's Creative Commons license, unless indicated otherwise in a credit line to the material. If material is not included in the chapter's Creative Commons license and your intended use is not permitted by statutory regulation or exceeds the permitted use, you will need to obtain permission directly from the copyright holder.





# Close Range Photogrammetry for High-Precision Reference Point Determination

A Proof of Concept at Satellite Observing System Wettzell

Michael Lösler , Cornelia Eschelbach , and Thomas Klügel

## Abstract

Local tie vectors are a crucial component within the combination of several space geodetic techniques. The vectors define the geometric relations between the space geodetic techniques, referring to the invariant reference points of such techniques. The Global Geodetic Observing System aims for an accuracy of 1 mm in the position on a global scale. In ITRF2014, about 50 % of the used local ties show discrepancies of more than 5 mm w.r.t. the global solution. In the framework of the IAG/IERS Working Group on Site Survey and Co-location or joint research projects like the international GeoMetre project strategies to improve the reference point determination and the local ties are developed. Strategies mainly comprise the development or the recommendation for surveying instruments, developing approaches for transforming local measurements to the global frame, and deriving innovative analysis procedures to derive the reference point of space geodetic techniques.

In this contribution, we focus on the reference point determination. At the Geodetic Observatory Wettzell, a measurement campaign was carried out in September 2020 to evaluate the benefit of close range photogrammetry in the framework of reference point determination. For this purpose, the invariant reference point of a Satellite Laser Ranging telescope was derived several times using various configurations. The estimated reference point and the axis offset vary in a range of  $\pm 0.1$  mm and  $\pm 0.02$  mm, respectively. The resulting standard deviations of the coordinate components of the combined solution are less than 0.1 mm and impressively demonstrate the potential of the presented method.

## Keywords

Bundle adjustment · Close range photogrammetry · GeoMetre · Reference point determination · Satellite laser ranging

## 1 Introduction

A global geodetic reference frame such as the International Terrestrial Reference Frame (ITRF) results from the solu-

M. Lösler (✉) · C. Eschelbach  
Frankfurt University of Applied Sciences; Faculty 1: Architecture -  
Civil Engineering - Geomatics, Laboratory of Industrial Metrology,  
Frankfurt am Main, Germany

T. Klügel  
Federal Agency for Cartography and Geodesy, Geodetic Observatory  
Wettzell, Bad Kötzing, Germany

tion of several space geodetic techniques. A very robust realisation is obtained by a combination of the different techniques. Due to the weak physical connections between these techniques, further information are needed to obtain a reliable frame. One of the most crucial components within the combination are so-called local ties. Local ties are vectors that define the geometric relation between the space geodetic techniques, referring to the invariant reference point (IRP) of each technique. The Global Geodetic Observing System (GGOS) aims for an accuracy of 1 mm in the position on a global scale (Gross et al 2009). Hence, local ties must



be known with sub-millimetre accuracy. However, local ties are identified as a critical component because about 50% of the used local ties in ITRF2014 show discrepancies of more than 5 mm w.r.t. the global solution (Altamimi et al 2017).

The achievable accuracy depends on various factors, namely the procedure of reference point determination, the connection of different IRP over long distances in a common local frame, and the transformation of the vector into a global frame. Strategies to improve the reference point determination and the local ties are developed, within the framework of the IAG/IERS Working Group on Site Survey and Co-location or joint research projects like the international GeoMetre project (Pollinger et al 2022). In this investigation, the benefit of close range photogrammetry is evaluated for reference point determination of a laser telescope used for Satellite Laser Ranging (SLR). For this purpose, a measurement campaign was carried out at the Geodetic Observatory Wettzell (GOW) in September 2020. The IRP of the modern two-colour SLR telescope, the Satellite Observing System Wettzell (SOS-W), was derived seven times using three different measurement configurations. In total, more than 500,000 observations and about 3,000 marker positions at the telescope are recorded. In addition to the individual analysis of the experiments, combination strategies are investigated to derive a common solution of the IRP.

Section 2 deals with the data analysis. The bundle adjustment is the first analysis step to process the image data and is introduced in Sect. 2.1. According to Poyard (2017), the IRP of an SLR telescope is usually derived by indirect methods. In this investigation the modified transformation approach is applied (Lösler et al 2018), which is briefly described in Sect. 2.2. Section 3 summarises the measurement campaign at GOW. The analysis strategy and the obtained results are presented in Sect. 4. Combination approaches to process the results obtained by several experiments are discussed in Sect. 5. Section 6 concludes this investigation.

## 2 Data Analysis

### 2.1 Bundle Adjustment

The collinearity equation maps the observed planar image coordinates  $(x'_i \ y'_i)^T$  of the point  $\mathbf{P}_i$  to the related spatial object coordinates  $(X_i \ Y_i \ Z_i)^T$  via

$$\begin{pmatrix} x'_i \\ y'_i \end{pmatrix}_j = \begin{pmatrix} x'_0 \\ y'_0 \end{pmatrix} + \begin{pmatrix} x_i^* \\ y_i^* \end{pmatrix}_j + \begin{pmatrix} \Delta x'_i \\ \Delta y'_i \end{pmatrix}_j, \quad (1)$$

where

$$x_i^* = -c \frac{r_{11}(X_i - X'_0) + r_{21}(Y_i - Y'_0) + r_{31}(Z_i - Z'_0)}{r_{13}(X_i - X'_0) + r_{23}(Y_i - Y'_0) + r_{33}(Z_i - Z'_0)},$$

$$y_i^* = -c \frac{r_{12}(X_i - X'_0) + r_{22}(Y_i - Y'_0) + r_{32}(Z_i - Z'_0)}{r_{13}(X_i - X'_0) + r_{23}(Y_i - Y'_0) + r_{33}(Z_i - Z'_0)}.$$

Here, the interior orientation parameters consist of the principal distance  $c$ , the coordinates  $(x'_0 \ y'_0)^T$  of the principal point, and

$$\Delta x' = \Delta x'_{\text{sym}} + \Delta x'_{\text{asy}} + \Delta x'_{\text{aff}},$$

$$\Delta y' = \Delta y'_{\text{sym}} + \Delta y'_{\text{asy}} + \Delta y'_{\text{aff}},$$

compensate for radial-symmetric lens distortion, decentring distortion, and affinity and shear effects of the sensor. The radial-symmetric lens distortion is parametrized by a polynomial function and is proportionally applied to the coordinate components, i.e.,

$$\Delta x'_{\text{sym},i} = x_i^* \frac{\Delta r'_{\text{sym},i}}{r'_i}, \quad (2a)$$

$$\Delta y'_{\text{sym},i} = y_i^* \frac{\Delta r'_{\text{sym},i}}{r'_i}, \quad (2b)$$

where  $\Delta r'_{\text{sym},i} = A_1 r_i'^3 + A_2 r_i'^5 + A_3 r_i'^7$  is the polynomial having coefficients  $A_1, A_2, A_3$ , and  $r'_i = \sqrt{x_i^{*2} + y_i^{*2}}$  is the  $i$ -th radial distance (Brown 1971). The decentring distortion with parameters  $B_1, B_2$  reads (Brown 1966, 1971)

$$\Delta x'_{\text{asy},i} = B_1 (r_i'^2 + 2x_i^{*2}) + 2B_2 x_i^* y_i^*, \quad (3a)$$

$$\Delta y'_{\text{asy},i} = B_2 (r_i'^2 + 2y_i^{*2}) + 2B_1 x_i^* y_i^*. \quad (3b)$$

Furthermore, affinity and shear deviations  $C_1, C_2$  of the image plane can be considered by (Luhmann et al 2019, p. 179f)

$$\Delta x'_{\text{aff},i} = C_1 x_i^* + C_2 y_i^*, \quad (4a)$$

$$\Delta y'_{\text{aff},i} = 0. \quad (4b)$$

The  $j$ -th spatial position  $(X'_0 \ Y'_0 \ Z'_0)^T_j$  and orientation  $\mathbf{R}_j$  of the camera are known as exterior orientation parameters, where matrix  $\mathbf{R}_j$  is an orthogonal rotation matrix having elements (Förstner and Wrobel 2016, p. 470)

$$\mathbf{R} = \begin{pmatrix} r_{11} & r_{21} & r_{31} \\ r_{12} & r_{22} & r_{32} \\ r_{13} & r_{23} & r_{33} \end{pmatrix}.$$

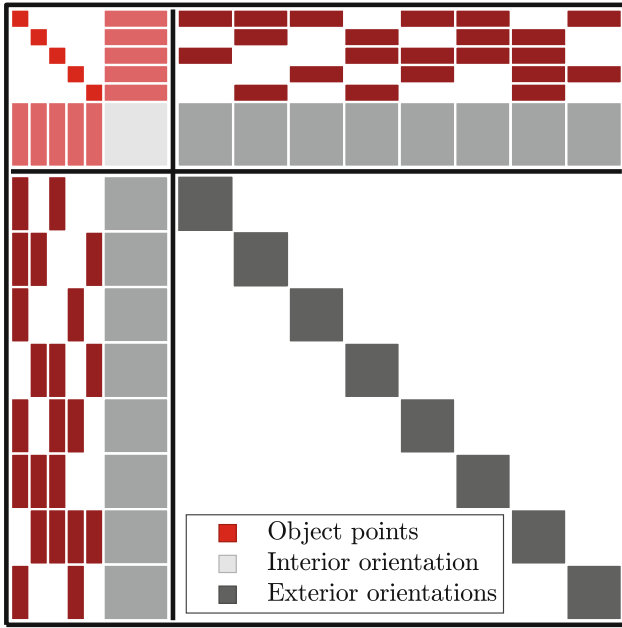


**Fig. 1** Schematic representation of the normal equation matrix of the bundle adjustment

The parameters to be estimated, i.e., the interior and exterior orientation parameters as well as the spatial coordinates of the object points, are iteratively derived using the nonlinear Gauss-Markov model, and leads to the self-calibration approach (Förstner and Wrobel 2016, p. 104f). Figure 1 depicts a schematic representation of the normal equation matrix of the bundle adjustment. The symmetric block matrices at the main diagonal represent the object points (red), the interior orientation (light-grey), and the exterior orientation (dark-grey). Off-diagonal block matrices symbolise functional dependencies and are depicted in corresponding mixed colours, for instance, the correlations between the object points (red) and the exterior orientation (dark-grey) are depicted in dark-red. Obviously, the matrix is sparse, indicated by the white parts. Moreover, the dimension mainly depends on the number of object points but also on the number of taken images, because each image increases the number of parameters to be estimated by further six exterior orientation parameters. Since the estimates of the orientation parameters are unimportant in most applications, pre-elimination strategies are recommended to obtain a compact but complete algebraically equivalent system of equations.

To reduce the normal equation system  $\mathbf{N}\mathbf{x} = \mathbf{n}$ , the matrix is partitioned into sub-matrices (Förstner and Wrobel 2016, p. 94f), i.e.,

$$\begin{bmatrix} \mathbf{N}_{11} & \mathbf{N}_{12} \\ \mathbf{N}_{12}^T & \mathbf{N}_{22} \end{bmatrix} \begin{bmatrix} \mathbf{x}_1 \\ \mathbf{x}_2 \end{bmatrix} = \begin{bmatrix} \mathbf{n}_1 \\ \mathbf{n}_2 \end{bmatrix}, \quad (5)$$

where  $\mathbf{x}_2$  corresponds to the parameters to be eliminated. Let  $\mathbf{N}_{22}$  be invertible, the second line of Eq. (5) yields

$$\mathbf{x}_2 = \mathbf{N}_{22}^{-1} \mathbf{n}_2 - \mathbf{N}_{22}^{-1} \mathbf{N}_{21} \mathbf{x}_1. \quad (6)$$

Substituting Eq. (6) into the first line of Eq. (5) yields the reduced normal equation system  $\bar{\mathbf{N}}\mathbf{x}_1 = \bar{\mathbf{n}}$ , i.e.,

$$(\mathbf{N}_{11} - \mathbf{N}_{12} \mathbf{N}_{22}^{-1} \mathbf{N}_{21}) \mathbf{x}_1 = \mathbf{n}_1 - \mathbf{N}_{12} \mathbf{N}_{22}^{-1} \mathbf{n}_2. \quad (7)$$

As shown in Fig. 1, the exterior orientation parameters of each image yield a symmetric  $6 \times 6$  block matrix. This simple structure motivates a recursive use of Eq. (7), until the exterior orientation parameters are eliminated.

## 2.2 Reference Point Determination

The reference point of an SLR telescope is defined as the orthogonal projection of the elevation axis onto the azimuth axis. This point is independent of the telescope orientation and, thus, often referred to as invariant reference point (IRP). Usually, the IRP cannot be observed by direct measurements, and indirect approaches are needed (Poyard 2017, p. 12f).

Within the GeoMetre project (Pollinger et al 2022), a modified transformation approach is developed. The basic equation reads

$$\mathbf{P}_{i,k} = \mathbf{P}_{\text{IRP}} + \quad (8)$$

$$\mathbf{R}_x(\beta) \mathbf{R}_y(\alpha) \mathbf{R}_z^T(\kappa_k) \mathbf{R}_y(\gamma) (\mathbf{E}_{\text{AO}} + \mathbf{R}_x(\omega_k) \mathbf{p}_i),$$

and describes a transformation between the point  $\mathbf{p}_i$  in the telescope-fixed frame and the corresponding position  $\mathbf{P}_{i,k}$  in an Earth-fixed reference frame (Lösler et al 2021). The index  $k$  denotes a specific telescope orientation defined by the telescope azimuth and elevation angle  $\omega_k$  and  $\kappa_k$ , respectively. The angles  $\alpha$ ,  $\beta$  compensate for the tilt of the telescope azimuth axis w.r.t. the  $Z$ -axis of the reference frame. The non-orthogonality of the telescope axes is modelled by  $\gamma$ .  $\mathbf{R}$  are orthogonal matrices and denote basic rotations about the sub-indexed axis of the (co-rotated) frame.  $\mathbf{E}_{\text{AO}}^T = (0 \ e_{\text{AO}} \ 0)$  represents the axis-offset, and  $\mathbf{P}_{\text{IRP}}$  is the position of the IRP. Figure 2 schematically depicts the transformation approach used to determine the IRP.

In contrast to alternative approaches, Eq. (8) is not restricted to a specific telescope type or does not require predefined telescope orientations. The model is suitable for automated and continues reference point determination during the regular operation process of the telescope (Lösler 2021, p. 72f).

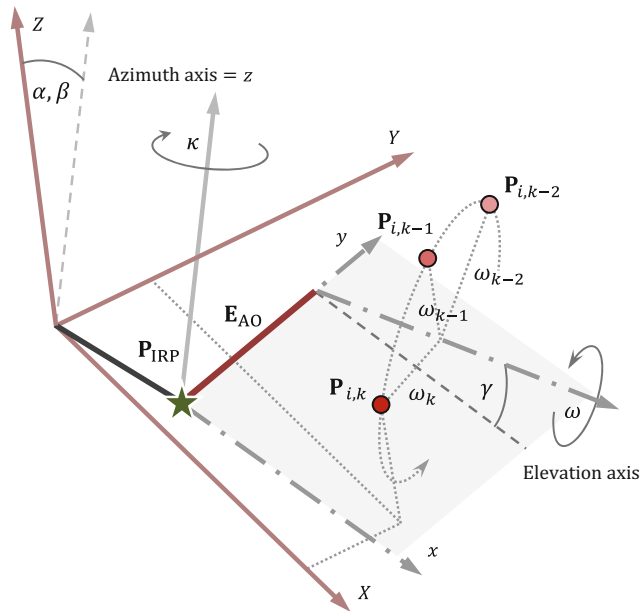


**Fig. 2** Schematic representation of the relations between the telescope-fixed frame and the Earth-fixed reference frame within the determination model of the invariant reference point

### 3 Satellite Observing System Wettzell

In September 2020 a measurement campaign was carried out at GOW and the IRP of the SLR telescope, the Satellite Observing System Wettzell (Riepl et al 2019), was derived using close range photogrammetry for the first time. For data acquisition and analysis Hexagon's Aicon DPA Industrial measurement system was chosen. The maximum permissible error (MPE) specified by the manufacture is  $15 \mu\text{m} + 15 \mu\text{m}/\text{m}$ ; typical standard deviations of a measurement position obtained by a bundle adjustment is stated by  $2 \mu\text{m} + 5 \mu\text{m}/\text{m}$  (Hexagon 2019).

Three different measurement configurations were realised (cf. Fig. 4) and each configuration was carried out at least twice. In total, the campaign comprised of seven experiments. The SOS-W was equipped with uncoded circular black-and-white markers, cf. Fig. 3. Whereas  $M = 12$  markers were used for the first six experiments, the seventh experiment consisted of  $M = 14$  markers. Further 225 coded 14-bit black-and-white markers were mounted at the surrounding of the SOS-W to establish the photogrammetric reference frame. Moreover, nine interoperable 1.5" drift nests were mounted at the dome wall to define the local datum and to ensure data integration. As photogrammetry is a scaleless measurement system, three certified scale bars were established to define the network scale and to trace the measurement to the SI metre. Figure 3 depicts the prepared



**Fig. 3** Prepared telescope and photogrammetric reference frame with scale bar at the dome wall

telescope and the photogrammetric reference frame at the dome wall.

To reduce configuration related dependencies and effects induced by variations in the environmental temperature, the initial azimuth position  $\omega_0$  and the azimuth step-wise  $\Delta\omega$  of the telescope were changed for each repetition of an experiment. Moreover, each experiment configuration (EC) consisted of a specific elevation range. The ranges in elevation  $r$  ( $\Delta\kappa$ ) are given by  $r(30^\circ) = [5^\circ, 30^\circ, 60^\circ, 90^\circ, 120^\circ, 150^\circ, 175^\circ]$  and  $r(40^\circ) = [5^\circ, 40^\circ, 80^\circ, 100^\circ, 140^\circ, 175^\circ]$ , respectively. All experiments were carried out by two different operators (OP). Table 1 summarises the basic design parameters, the experiment temperature  $T$  and the number of mounted markers  $M$  at the telescope.

The camera of the DPA is covered by a robust and heavy-walled IP51-rated camera case to protect the camera against variation in temperature and to ensure the geometric stability of the measuring system. However, as shown by Ma et al (2012), self-heating of the camera induces systematic errors. For that reason, a warming up period of the DPA was considered at the beginning of each experiment.

**Table 1** Design parameters of the experiment configurations w.r.t. the day of year (DOY) in 2020

DOY	EC	OP	$M$	$T$	$\omega_0$	$\Delta\omega$	$r$ ( $\Delta\kappa$ )
255	i	A	12	21.7 °C	0°	60°	30°
256	i	B	12	22.9 °C	30°	60°	30°
257	ii	A	12	24.8 °C	30°	60°	40°
258	ii	B	12	25.5 °C	0°	60°	40°
259	iii	A	12	25.1 °C	22.5°	90°	40°
260	iii	B	12	25.3 °C	67.5°	90°	40°
264	i	A/B	14	17.0 °C	0°	60°	30°

## 4 Analysis and Results

The experiments are preanalysed using the proprietary software package Aicon 3D studio. Since Aicon 3D studio does not provide the fully populated dispersion of the adjusted object points, the in-house software package JAIcOv (2021) is used to perform the final bundle adjustment as described in Sect. 2.1, using the reduced normal equation system in Eq. (7). To obtain comparable and combinable results, the point sets of each experiment are scaled uniformly to the reference temperature  $T_0 = 20^\circ\text{C}$  during the bundle adjustment.

Figure 4 depicts section views of the realised measurement configurations, cf. Table 1. The top views (Fig. 4, left) show symmetrically distributed marker positions surrounding the IRP. This is a reasonable distribution because systematic effects are reduced (Lösler 2021, p. 86ff). Whereas the horizontal position of the IRP is close to the centre, the vertical component lies below the centre as shown in the side views (Fig. 4, right). This kind of distribution is unbalanced. It is restricted by the position of the mounted markers at the telescope and by the elevation working range of the SOS-W.

According to Eq. (1), all experiments are individually analysed using a bundle adjustment with self-calibration approach, as described in Sect. 2.1. Table 2 summarises the number of observations  $n$  and the number of parameters  $u$  to be estimated for each performed bundle adjustment. The number of observed marker positions at the telescope is denoted by  $p$  and strongly depends on the performed experiment configuration, cf. Table 1. The standard deviation of unit weight  $\sigma$  is almost close to its expected value  $E\{\sigma^2\} = 1$  and confirms the mathematical model of the bundle adjustment. The mean standard deviation

$$\sigma_{3D} = \sqrt{\sigma_X^2 + \sigma_Y^2 + \sigma_Z^2} \quad (9)$$

of the observed marker positions does not exceed 0.1 mm, and impressively demonstrates the high measurement accuracy of the DPA system.

The IRP is experiment-wise estimated using Eq. (8) treating the marker positions and the fully populated dispersion matrix of the bundle adjustment as incoming quantities. The marker positions are highly correlated and are a crucial part of IRP determination. If such correlations are neglected, the dispersion of the IRP is significantly overestimated, as recently shown by Lösler et al (2021).

All configurations under consideration yield comparable results, as indicated in Fig. 5. The resulting coordinates of the IRP vary in a range of about  $\pm 0.1$  mm and the standard deviations do not exceed 0.1 mm. Moreover, the axis offset of the SOS-W is not zero but close to zero and insignificant. The variations are in a range of about  $\pm 0.02$  mm, and confirm prior investigations (Lösler et al 2018).

## 5 Combination Approaches

GGOS aims for continues and almost automated reference point determinations. If the IRP is frequently observed, reliable and economic combination strategies are required. The most rigorous approach combines the data on the observation level, i.e., during the bundle adjustment. Depending on the number of observations  $n$  and the number of parameters  $u$  to be estimated, this approach may be time-consuming. In Table 2, basic information about the bundle adjustment of the combined approach (combi) is summarised in the last row. All  $m$  experiments are treated as one common experiment yielding the combined reference point  $\hat{\mathbf{x}}_{\text{IRP}}$  and the corresponding dispersion matrix  $\hat{\Sigma}_{\text{IRP}}$  by

$$\mathbf{x}_{\text{combi}}, \Sigma_{\text{combi}} \Rightarrow \hat{\mathbf{x}}_{\text{IRP}}, \hat{\Sigma}_{\text{IRP}}, \quad (10)$$

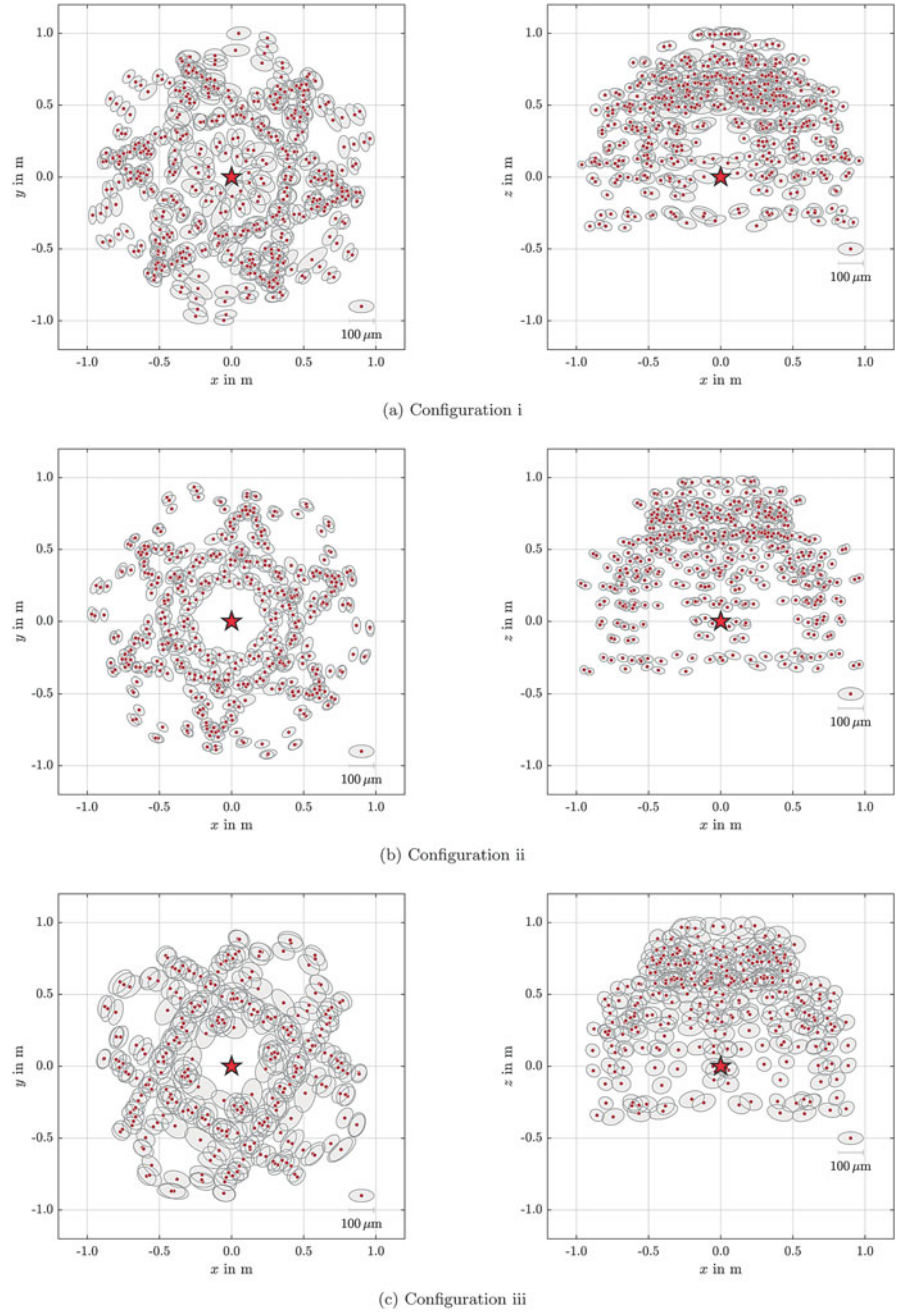
where  $\mathbf{x}_{\text{combi}}$  and  $\Sigma_{\text{combi}}$  denote the estimated positions at the telescope and the related fully populated dispersion matrix obtained from the combined bundle adjustment, respectively.

The experiment-wise approach determines the reference point from  $m$  individually performed bundle adjustments. Correlations within an experiment are taken into account but correlations between the experiments are neglected. The experiment-wise approach reads

$$\left. \begin{array}{l} \mathbf{x}_{\text{exp}}^1, \Sigma_{\text{exp}}^1 \\ \mathbf{x}_{\text{exp}}^2, \Sigma_{\text{exp}}^2 \\ \vdots \\ \mathbf{x}_{\text{exp}}^m, \Sigma_{\text{exp}}^m \end{array} \right\} \Rightarrow \hat{\mathbf{x}}_{\text{IRP}}, \hat{\Sigma}_{\text{IRP}}, \quad (11)$$

where  $\mathbf{x}_{\text{exp}}^i$  and  $\Sigma_{\text{exp}}^i$  denote the estimated positions at the telescope and the related fully populated dispersion matrix

**Fig. 4** Top views (left) and side views (right) of the realised measurement configurations having: (a) six azimuths, seven elevations; (b) six azimuths, six elevations; and (c) four azimuths, six elevations. The observed marker positions and the related confidences are depicted by red dots and grey ellipses, respectively. A red star symbolises the IRP



obtained from the bundle adjustment of the  $i$ -th experiment, respectively. The combination is still based on the original observations. This approach is economic because the number of observations in a single experiment is comparatively small w.r.t. the combined solution. Moreover, the stochastic model used during the IRP determination becomes a manageable block-diagonal structure.

The most simplified approach by far performs the combination on the parameter level, using a weighted sum of individual obtained reference points  $\mathbf{x}_{\text{IRP}}^i$ ,  $\Sigma_{\text{IRP}}^i$  of each experiment  $\mathbf{x}_{\text{exp}}^i$ ,  $\Sigma_{\text{exp}}^i$ . This approach is equivalent to a

recursive filter and is expressed by (Lösler et al 2013, 2016)

$$\left. \begin{array}{l} \mathbf{x}_{\text{exp}}^1, \Sigma_{\text{exp}}^1 \rightarrow \mathbf{x}_{\text{IRP}}^1, \Sigma_{\text{IRP}}^1 \\ \mathbf{x}_{\text{exp}}^2, \Sigma_{\text{exp}}^2 \rightarrow \mathbf{x}_{\text{IRP}}^2, \Sigma_{\text{IRP}}^2 \\ \vdots \\ \mathbf{x}_{\text{exp}}^m, \Sigma_{\text{exp}}^m \rightarrow \mathbf{x}_{\text{IRP}}^m, \Sigma_{\text{IRP}}^m \end{array} \right\} \Rightarrow \hat{\mathbf{x}}_{\text{IRP}}, \hat{\Sigma}_{\text{IRP}}. \quad (12)$$

A comparison of the resulting IRP of the three combination approaches are given in Table 3. Even if correlations between the experiments are neglected, the

**Table 2** Basic information about the bundle adjustment of the individually analysed experiments w.r.t. the day of year (DOY) as well as the combined solution (combi)

DOY	$n$	$u$	$p$	$\sigma_{3D}$	$\sigma$
255	64,367	10,015	478	0.05	0.89
256	82,905	13,003	485	0.05	0.92
257	91,437	12,139	431	0.04	0.95
258	92,817	12,130	432	0.04	0.94
259	62,549	8,383	286	0.07	1.67
260	75,731	9,277	284	0.03	0.92
264	120,005	13,663	588	0.03	0.84
Combi	589,811	75,994	2,984	0.04	1.02

result of the experiment-wise approach is most similar to that of the combination approach on the observation level. The deviations for the parameters are about  $1 \mu\text{m}$ , and the standard deviations of the coordinates differ in a range of  $\ll 0.1 \text{ mm}$ .

Figure 6 depicts the correlations  $\rho$  of the Z-component of an arbitrary position observed at DOY 256. The correlations are derived by the fully populated dispersion  $\Sigma_{\text{combi}}$  of the combined bundle adjustment (Fig. 6, left), and the fully populated dispersion  $\Sigma_{\text{exp}}^2$  of the individually adjusted experiment (Fig. 6, right). The elements in  $\Sigma_{\text{combi}}$  are experiment-wise sorted, and different colours indicate the parameter range of each experiment within the combined solution. Obviously, the structure of the correlations depend on the measurement configuration. The large dependencies of the marker positions observed in a dedicated telescope orientation  $k$  are conspicuous,

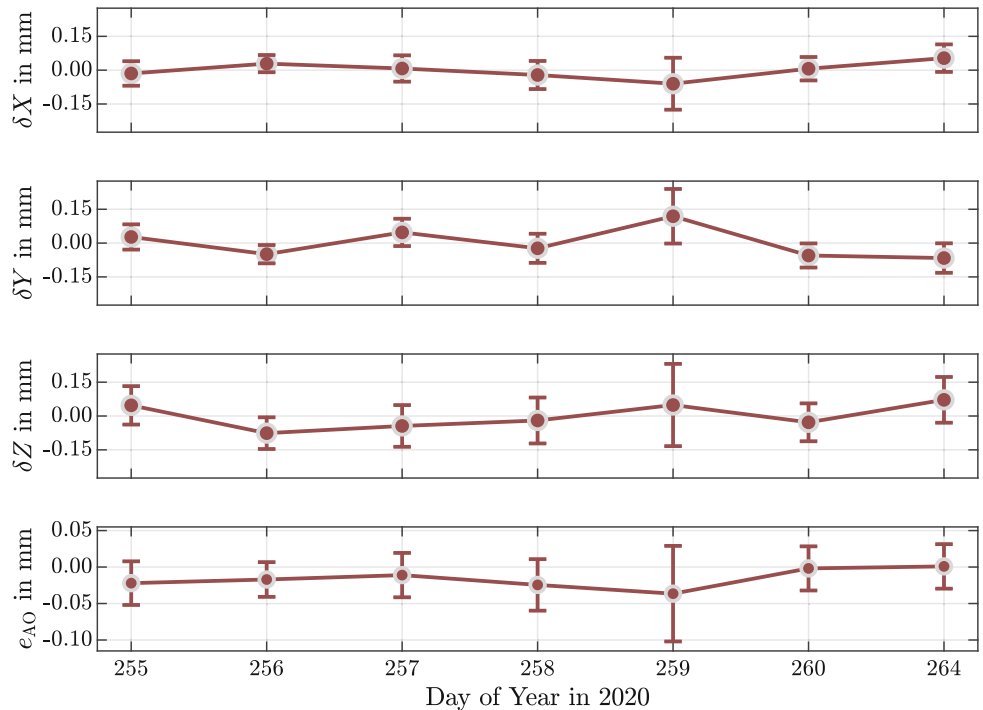
**Table 3** Comparison of the resulting IRP of different combination approaches. The IRP coordinates are reduced w.r.t. the result of the combination on the observation level. All quantities are given in  $\mu\text{m}$ 

Combination	$\delta X$	$\delta Y$	$\delta Z$	$\sigma_X$	$\sigma_Y$	$\sigma_Z$
Observation	–	–	–	7	8	12
Experiment	–1	1	–1	8	8	12
Parameter	6	–9	–18	11	11	18

but also azimuth-dependent correlations are visible within the spectrum. The size of the correlations varies strongly.

Correlations larger than 60 % can be found for simultaneously observed positions in a dedicated telescope orientation, because these positions are mainly observed by identical images. For these positions, the correlations are comparable for  $\Sigma_{\text{combi}}$  and  $\Sigma_{\text{exp}}^i$ .

In contrast, the dependencies between positions observed in various telescope orientations differ clearly. Whereas  $\rho$  is about 30 % for the individually adjusted experiment (Fig. 6, right), the correlations are less than 10 % for the combined solution (Fig. 6, left). Combining several experiments by a common adjustment leads to a decorrelation of the estimated parameters. This reduction in correlations can be traced back to the self-calibration approach of the bundle adjustment described in Sect. 2.1, where individual camera calibration models were introduced per experiment. The remaining correlations are quite small and have only a minor effect on the estimated reference point position  $\hat{\mathbf{x}}_{\text{IRP}}$ . Therefore, the

**Fig. 5** Variations of the estimated IRP coordinates and the axis offset, derived by the individually analysed experiments. Error bars indicate the  $3\sigma$  confidences

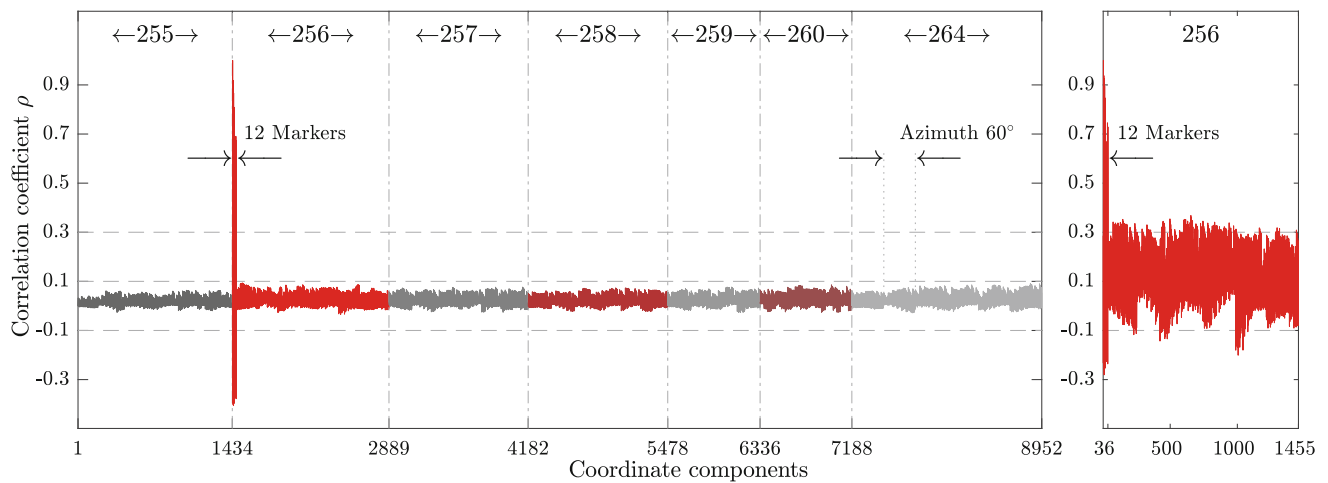


**Fig. 6** Correlations between the Z-component of an arbitrary position and the remaining positions at the telescope structure derived by the fully populated dispersion obtained by the bundle adjustment: Resulting

correlations of the combined solution (left), and resulting correlations of an individual adjusted experiment (right), exemplified depicted for DOY 256

experiment-wise combination yields equivalent results w.r.t. the combination on the observation level even if correlations are neglected.

The mean value obtained by averaged groups is usually unequal to the mean value of the original set. Hence, the combination on the parameter level deviates from the combination on the observation level, cf. Table 3. However, the spatial deviation is less than  $25\ \mu\text{m}$  and is fully covered by the obtained standard deviation. As shown by Lösler et al (2013, 2016), the combination at the parameter level allows the use of a simple and economic recursive filter for processing successively obtained  $\mathbf{x}_{\text{IRP}}^i$ . All investigated combination approaches yield standard deviations  $\ll 0.1\ \text{mm}$  and are suitable to derive a common position of the IRP from the photogrammetric data taken at SOS-W.

derived seven times in a local frame. The variations are in a range of  $\pm 0.1\ \text{mm}$ , and impressively demonstrate the benefit of a photogrammetric based approach. To obtain a common IRP from the photogrammetric data, three combination approaches are evaluated: the combination on the observation level, the experiment-wise combination, and the combination on the parameter level. All combination procedures under consideration yield comparable results. Whereas the combination on the observation level is the most rigorous but also the most time-consuming approach, the combination on the parameter level is the most simplified and economic alternative. The spatial deviation between these approaches is less than  $25\ \mu\text{m}$ , and all combination strategies are suitable to derive a common position of the IRP.

**Acknowledgements** We thank Svetlane Mähler and Stefan Riepl from the Geodetic Observatory Wettzell for their support during the fieldwork.

## 6 Conclusion

Local tie vectors are a crucial component within the combination process for deriving a global geodetic reference frame, because these vectors overcome the weak physical connection between space geodetic techniques. However, inaccurate and outdated vectors bias the global results.

GGOS aims for an accuracy of 1 mm in the position on a global scale, and call for novel strategies to improve the vectors, because about 50% of the present local ties show discrepancies of more than 5 mm w.r.t. the global solution. Within the GeoMetre project, close range photogrammetry is applied for the first time to obtain the IRP of an SLR telescope at GOW. Using three configurations, the IRP was

## Funding

This project 18SIB01 GeoMetre (2020) has received funding from the EMPIR programme co-financed by the Participating States and from the European Union's Horizon 2020 research and innovation programme.

## Availability of Data and Material

All data used in this investigation are available online at <https://www.mdpi.com/2076-3417/11/6/2785/s1>.

## Conflict of Interest

The authors declare that they have no conflict of interest.

## References

- Altamimi Z, Rebischung P, Métivier L, Collilieux X (2017) Analysis and results of ITRF2014. IERS technical note 38, international earth rotation and reference systems service. <http://www.iers.org/TN38>
- Brown DC (1966) Decentering distortion of lenses. *Photogramm Eng* 32(3):444–462
- Brown DC (1971) Close-range camera calibration. *Photogramm Eng* 37(8):855–866
- Förstner W, Wrobel BP (2016) *Photogrammetric computer vision – Statistics, geometry, orientation and reconstruction*. Springer, Cham. <https://doi.org/10.1007/978-3-319-11550-4>
- GeoMetre (2020) Large-scale dimensional measurements for Geodesy – A joint research project within the european metrology research programme EMPIR, Grant Number: 18SIB01. <https://doi.org/10.13039/100014132>
- Gross R, Beutler G, Plag HP (2009) Integrated scientific and societal user requirements and functional specifications for the GGOS. In: Plag HP, Pearlman M (eds) *Global geodetic observing system – Meeting the requirements of a global society on a changing planet in 2020*. Springer, Berlin, pp 209–224. [https://doi.org/10.1007/978-3-642-02687-4\\_7](https://doi.org/10.1007/978-3-642-02687-4_7)
- Hexagon (2019) AICON DPA series – Unrivalled high-end photogrammetry systems, datasheet
- JAIcOv (2021) Java Aicon covariance matrix – Bundle adjustment for close-range photogrammetry. <https://github.com/applied-geodesy/bundle-adjustment>
- Lösler M (2021) *Modellbildungen zur Signalweg- und in-situ Referenzpunktbestimmung von VLBI-Radioteleskopen*. Ph.D. thesis, Technische Universität Berlin, Institute of Geodesy and Geoinformation Science, Geodesy and Adjustment Theory, Berlin. <https://doi.org/10.14279/depositonce-11364>
- Lösler M, Haas R, Eschelbach C (2013) Automated and continual determination of radio telescope reference points with sub-mm accuracy: results from a campaign at the Onsala Space Observatory. *J Geod* 87(8):791–804. <https://doi.org/10.1007/s00190-013-0647-y>
- Lösler M, Haas R, Eschelbach C (2016) Terrestrial monitoring of a radio telescope reference point using comprehensive uncertainty budgeting. *J Geod* 90(5):467–486. <https://doi.org/10.1007/s00190-016-0887-8>
- Lösler M, Eschelbach C, Riepl S (2018) A modified approach for automated reference point determination of SLR and VLBI telescopes. *Tech Mess* 85(10):616–626. <https://doi.org/10.1515/teme-2018-0053>
- Lösler M, Eschelbach C, Klügel T, Riepl S (2021) ILRS reference point determination using close range photogrammetry. *Appl Sci* 11(6):2785. <https://doi.org/10.3390/app11062785>
- Luhmann T, Robson S, Kyle S, Boehm J (2019) *Close-range photogrammetry and 3D imaging*, 3rd edn. Walter de Gruyter GmbH, Berlin. <https://doi.org/10.1515/9783110607253>
- Ma S, Pang J, Ma Q (2012) The systematic error in digital image correlation induced by self-heating of a digital camera. *Meas Sci Technol* 23(2):025403. <https://doi.org/10.1088/0957-0233/23/2/025403>
- Pollinger F, Courde C, Eschelbach C, García-Asenjo LV, Guillory J, Hedekvist PO, Kallio U, Klügel T, Neyezhnikov P, Pesce D, Pisani M, Seppä J, Underwood R, Wezka K, Wiśniewski M (2022) Large-scale dimensional metrology for geodesy - first results from the European GeoMetre project. In: Freymueller JT, Sánchez L (eds) *Geodesy for a sustainable earth, proceedings of the 2021 IAG symposium, International Association of Geodesy Symposia*. Springer, Beijing, China
- Poyard JC (2017) IGN best practice for surveying instrument reference points at ITRF co-location sites. IERS technical note 39, international earth rotation and reference systems service. <http://www.iers.org/TN39>
- Riepl S, Müller H, Mähler S, Eckl J, Klügel T, Schreiber U, Schüler T (2019) Operating two SLR systems at the Geodetic Observatory Wettzell – From local survey to space ties. *J Geod* 8(93):2379–2387. <https://doi.org/10.1007/s00190-019-01243-z>

**Open Access** This chapter is licensed under the terms of the Creative Commons Attribution 4.0 International License (<http://creativecommons.org/licenses/by/4.0/>), which permits use, sharing, adaptation, distribution and reproduction in any medium or format, as long as you give appropriate credit to the original author(s) and the source, provide a link to the Creative Commons license and indicate if changes were made.

The images or other third party material in this chapter are included in the chapter's Creative Commons license, unless indicated otherwise in a credit line to the material. If material is not included in the chapter's Creative Commons license and your intended use is not permitted by statutory regulation or exceeds the permitted use, you will need to obtain permission directly from the copyright holder.







# Frame Accuracy of Combined EPN Weekly Coordinate Solutions

Christopher Kotsakis and Miltiadis Chatzinikos

## Abstract

The scope of this paper is to perform an internal quality assessment, at frame parameter level, on the combined EPN weekly coordinate solutions. Specifically, the weekly SINEX solution files from the EPN Analysis Combination Centre are analyzed in order to infer the internal accuracy of the origin, orientation and scale of the respective epoch solutions. Our investigation covers almost the entire operational period of EPN starting from 1999 up to present time, and it uses both the routine and re-processed (repro2) series of combined weekly solutions. Through the results of this study we are able to assess the impact of various changes or updates that have been applied into the routine GNSS data processing and combination strategies on the quality of the estimated EPN weekly frames.

## Keywords

Combined weekly coordinate solutions · Covariance projection · EPN-repro2 · EUREF permanent network · Frame parameter accuracy

## 1 Introduction

The EUREF Permanent Network (EPN) is a tracking network of more than 350 continuously operating GNSS stations that provides fundamental geodetic measurements and products for Earth science applications in Europe. EPN analysis centers routinely analyze the data from this network and deliver their results to the Analysis Combination Center (ACC) which generates daily and weekly coordinate solutions for all EPN stations in successive realizations of the International Terrestrial Reference System. The latter forms the basis for the European Terrestrial Reference System (ETRS89) which is the backbone for all geodetic and mapping works on the European territory, both on national and international level (Bruyninx 2004; Bruyninx et al. 2009; Ihde et al. 2014).

The ACC weekly estimates for the EPN station coordinates have special importance as they are used by EUREF to maintain the ETRS89 on a continuous basis, in tandem with the formal transformation procedure described in Altamimi (2018). These epoch-tagged solutions offer access to “instantaneous” positions in successive ITRF releases (currently ITRF2014/IGb14), and they complement the long-term secular solution (positions+velocities) which is regularly computed at 15-week intervals via multi-year stacking of position time series at the EPN stations (Bruyninx et al. 2012; Legrand 2017). More details about these solutions can be found in the EUREF/EPN website ([www.epncb.oma.be](http://www.epncb.oma.be)) and the relevant documentation given therein.

Since the EPN constitutes the European densification of the International GNSS Service (IGS) network, all its operational products strive for complete consistency with the IGS standards and models. To comply with this requirement, several changes and updates have been occasionally applied into the EPN’s routine data processing and combination strategies, as noted in various EUREF technical reports and related publications (e.g. Bruyninx et al. 2020; Kenyeres and Bruyninx 2004; Habrich 2011; Bruyninx et al. 2012). These actions theoretically improve all EPN products, yet

C. Kotsakis (✉) · M. Chatzinikos  
Department of Geodesy and Surveying, Aristotle University of  
Thessaloniki, Thessaloniki, Greece  
e-mail: [kotsaki@topo.auth.gr](mailto:kotsaki@topo.auth.gr); [mchatzin@topo.auth.gr](mailto:mchatzin@topo.auth.gr)

no systematic assessment has been pursued to unveil their impact on the estimated weekly frames in the EPN network. Hence the aim of this paper is to investigate the accuracy of the combined EPN weekly coordinate solutions at frame parameter level, and to identify the major sources that have caused noticeable accuracy upgrades throughout the EPN lifetime. A similar assessment is also performed on the latest re-processed series of EPN weekly coordinate solutions (repro2) with the intention to quantify the anticipated improvement with respect to the older routine solutions.

The structure of the paper is organized as follows: the rationale and the mathematical framework of the present study are outlined in Sect. 2; the accuracy evaluation of frame elements in the routine and repro2 combined EPN weekly solutions is presented in Sects. 3 and 4, respectively; finally a few concluding remarks are given in the last section of the paper.

## 2 Theoretical Setting

Starting with a regional network solution that is constrained to a particular global frame (e.g. ITRFxx), the main problem considered herein is to identify the accuracy of individual frame elements that emerge from this solution. The latter is given in terms of a vector of estimated coordinates  $\mathbf{X}$  with a known covariance (CV) matrix  $\Sigma_{\mathbf{X}}$  that depicts their estimation accuracy in the adopted global frame and their intra/inter-station correlations resulting from the network adjustment process. The solution to the aforesaid problem requires an appropriate mapping  $\Sigma_{\mathbf{X}} \mapsto \Sigma_{\theta}$  to transform the network solution accuracy from the station coordinate level to the frame parameter level through a covariance projection based on the Helmert transformation model. Since we consider epoch-only (weekly) solutions in this study, the matrix  $\Sigma_{\theta}$  has dimensions 7 by 7 and its role is to infer the accuracy of the realized origin, orientation and scale in the respective weekly solution.

The inference of frame parameter accuracy in regional or global network solutions is not a straightforward problem with a unique answer. Its treatment is linked to the decomposition of a coordinate CV matrix into a frame-related part (reflecting what may be loosely termed as *datum noise* in the estimated coordinates) and a second part pertaining to *internal or figure noise* which relates to the accuracy of shape characteristics that are reproduced by the estimated coordinates. This problem has its roots in Meissl's inner error theory for geodetic networks and it was investigated during the early seventies in the context of minimally constrained network solutions (Pope 1973) or even in more general settings (Ebner 1974); see also Meissl (1965, 1969). Later on the same problem was revisited by Sillard and Boucher

(2001) for assessing the uncertainty of the origin, orientation and scale of terrestrial frames derived from space geodetic techniques (the so-called *reference system effect* in the terminology of their paper). Additional information on this topic can be found in Blewitt (1998), particularly for the reverse problem of removing frame-related dependencies from coordinate CV matrices in order to exploit them optimally in other combination solutions. A relevant analysis has been also presented in Rebischung (2014, ch. 3) for the purpose of estimating implicit datum-related parameters and their accuracy level from the results of space geodetic solutions.

Without going into mathematical details, let us mention the two alternative equations that have appeared in the geodetic literature for extracting the frame parameter accuracy from a coordinate CV matrix

$$\Sigma_{\theta} = (\mathbf{E}\mathbf{E}^T)^{-1}\mathbf{E}\Sigma_{\mathbf{X}}\mathbf{E}^T(\mathbf{E}\mathbf{E}^T)^{-1} \quad (1)$$

or

$$\Sigma_{\theta} = (\mathbf{E}\Sigma_{\mathbf{X}}^{-1}\mathbf{E}^T)^{-1} \quad (2)$$

where  $\mathbf{E}$  is the Jacobian matrix of Helmert transformation in the underlying network. A theoretical justification for using Eq. (1) instead of Eq. (2) is given in Rebischung (2014), although a more comprehensive analysis for the ‘‘right’’ choice of such covariance mappings is currently missing in the geodetic literature. It is worth noting that, with the exception of a few special (and without practical interest) cases, the first equation shall give larger error variances for the frame parameters, at least in average sense, i.e. the trace of  $\Sigma_{\theta}$  is smaller if it is computed from Eq. (2).

The present study relies exclusively on Eq. (1) and its implementation on the combined weekly solutions in the EPN network. This allows us to capture in a computationally simple way the evolution of frame parameter accuracy in the epoch solutions for the EPN station coordinates. The diagonal elements of  $\Sigma_{\theta}$  reflect a mixture of factors that are embedded into the coordinate CV matrices  $\Sigma_{\mathbf{X}}$  (and the respective Helmert matrices  $\mathbf{E}$ ) and they influence the estimated weekly frames in the EPN network. These factors include the network geometry and its evolution in time (due to the growing number of EPN stations), the type of constraints for the alignment to a global reference frame, the fiducial stations that participate in the applied constraints, other relevant factors which contribute to the enforced orientation and scale of the weekly EPN solutions (satellite orbits, satellite/receiver antenna PCOs, absolute/relative antenna calibration models), as well as additional influences originating from the distributed processing of different subnetworks by the EPN Analysis Centers (AC) and their merging into a

unified weekly solution. Any changes or updates in models and data reduction schemes used in the EPN/AC solutions (and their combination) may cause a noticeable effect on the estimated weekly frames by showing up in the behaviour of  $\Sigma_{\theta}$ .

To recapitulate, the role of Eq. (1) is to describe in a statistical sense the *common-mode errors* (of translation, rotation and scaling type) that occur in constrained or unconstrained network solutions—the same also holds for Eq. (2). Such correlated errors are always present in estimated network coordinates, and they reflect the internal accuracy at which the principal components of the coordinate system (origin, orientation, scale) are realized by the considered solution. Their magnitude is affected by all contributing sources of datum related information and also by their joint interaction due to geometrical network effects. It is emphasized that the weighting level of additive datum constraints affects the matrix  $\Sigma_{\theta}$ , but it is not exactly reproduced in the achievable accuracy of the respective frame parameters (this technical issue requires more involved analysis that is beyond the scope of the present paper).

### 3 Routinely Combined EPN Weekly Coordinate Solutions

#### 3.1 General Information

The operational products for the EPN station positions are created on a routine basis via daily solutions from 16 EPN ACs. Each of these centers regularly processes GNSS data from an assigned subnetwork of EPN stations and generates daily coordinate solutions in SINEX format. These solutions are then analyzed by the EPN/ACC to obtain daily/weekly coordinates and their covariance information for all EPN stations using the Bernese GNSS software (Dach et al. 2015). The combined solutions are tied to the latest realization of the International Terrestrial Reference System, mostly in accordance with IGS reference frame updates (Bruyninx et al. 2012). Their alignment method has evolved since the start of EPN and it is currently based on the use of no-net-translation (NNT) conditions over a fiducial set of 49 IGS stations, in conjunction with fixed satellite orbits in the underlying IGS frame. A complete overview of the successive global frames, the alignment method and the associated fiducial stations that have been used in the combined EPN solutions can be found here: [https://www.epncb.oma.be/\\_productsservices/analysiscentres/combsolframe.php](https://www.epncb.oma.be/_productsservices/analysiscentres/combsolframe.php). A detailed description of GNSS data processing and validation tasks in the EPN is given in Bruyninx et al. (2019).

#### 3.2 Combination Process

The computation of the combined EPN weekly coordinates consists of several steps and layers of quality testing. The main stages of the combination procedure are listed below (see also the relevant information in the EPN ACC website <http://www.epnacc.wat.edu.pl/epnacc/>):

- Daily AC solutions in SINEX format are checked for metadata consistency with station log files and IGS/EPN antenna calibration values. The external constraints in these solutions are removed and normal equations (NEQ) are created.
- The daily AC solutions are iteratively combined into a single solution which is aligned to IGS14 using NNT minimal constraints.
- Each AC solution is compared with the combined daily solution. Also, each combined daily solution is checked against previous weekly solutions.
- Daily combined solutions are stacked into a weekly solution which is compared with previous weekly solutions.

The routine checking of the EPN weekly coordinates at fiducial stations involves their comparison with the official IGS coordinates propagated to the epoch of the respective solution. Stations with coordinate differences exceeding 8 mm in horizontal components, or 15 mm in the vertical component are not used for the alignment to the global IGS frame. The SINEX files of the combined EPN weekly solutions and their summary reports are freely available from several data centers, namely BKG, CDDIS and EPN.

#### 3.3 Accuracy Assessment of EPN Weekly Frames

The following results refer to the combined EPN weekly solutions covering the period from GPS week 1000 (March 1999) to GPS week 2154 (April 2021). After extracting the solution coordinate CV matrices from all SINEX files, the frame-related CV matrices  $\Sigma_{\theta}$  were computed by Eq. (1) for each considered week. As discussed in Sect. 2, the square roots of the diagonal elements of those matrices quantify the internal accuracy of the weekly-realized origin, orientation and scale, in tandem with a global frame to which the EPN weekly solution is aligned to. Their values are depicted in Fig. 1 along with the successive reference frame for each segment of weekly solutions. To allow easier interpretation of the results, the orientation and scale uncertainty has been expressed in mm by multiplying the standard deviations of the respective frame parameters with the mean Earth radius.

The chronological pattern in Fig. 1 reveals the gradual improvement in the internal accuracy of the EPN weekly

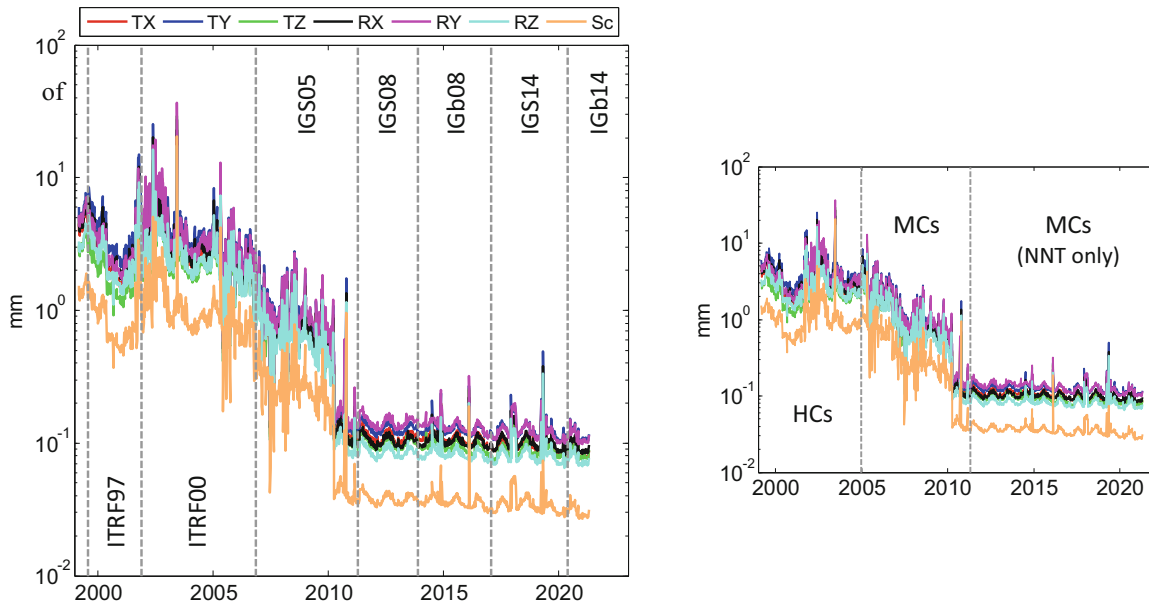


**Fig. 1** Internal accuracy of frame parameters in the combined EPN weekly solutions. The successive reference frames and the type of alignment constraints (HCs: heavy constraints, MCs: minimal constraints) in each segment of weekly solutions are indicated in the plots

frames. At present time (May 2021) their origin and orientation are fixed to ITRF at the level of 0.1 mm ( $1\sigma$ ) per translation/rotation component, whereas their scale shows even higher consistency by a factor of 3. This represents an accuracy upgrade of more than one order of magnitude compared to the EPN weekly solutions in the pre-2005 era. The most drastic improvement occurs in the period 2005–2010, after which the weekly frames are stabilized to the aforesaid accuracy level with small fluctuations that conform to the behavior of the a-posteriori variance factors of the combined solutions. These factors are extracted from the EPN’s weekly combination SINEX files and shown in Fig. 2 for the period 2005–2021. A clear periodic signature exists in their values after 2010, which likely stems from the seasonal performance of ambiguity resolution during the GNSS data processing. The estimated variance factors before 2010 show more erratic behavior with large variations, ranging from 0.005 (GPS week 1433) up to 3.625 (GPS week 1346). It remains unclear the reason causing the stabilization of the variance factors after 2010, which is partly mirrored in the frame accuracy plots of Fig. 1 (a plausible explanation is given at the end of Sect. 3.4).

The scale is the best determined parameter in the EPN weekly frames since it exhibits smaller uncertainty than all other frame parameters throughout the EPN lifetime (see Fig. 1). This is actually reproduced under all ITRF-alignment strategies that have been used in the routine analysis of the EPN network (heavy constraints on fiducial stations, minimal constraints for all frame parameters on fiducial stations, NNT-only constraints on fiducial stations). The enhanced internal accuracy of scale should be largely attributed to the

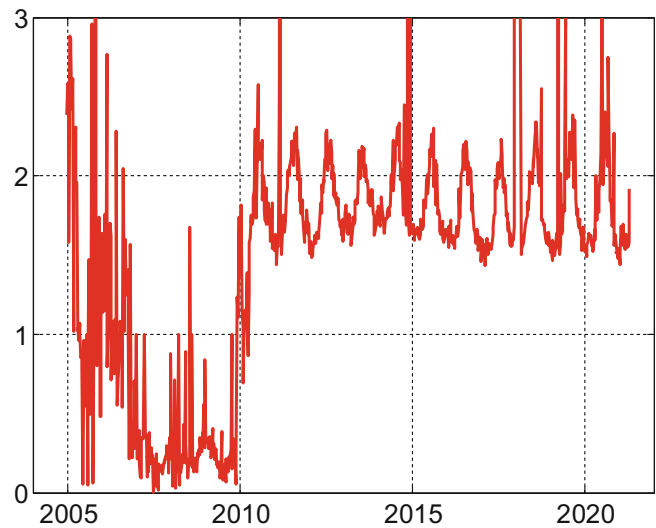


**Fig. 2** A-posteriori variance factors of the combined EPN weekly solutions for the period 12/2004-05/2021

regional character of EPN and its stronger influence on the origin and orientation alignment of the weekly solutions to a global frame.

Despite the multiple layers of quality checking in the EPN products, there exist a few scattered weekly solutions that exhibit sizeable jumps in their frame accuracy level. These sporadic cases do not necessarily coincide with intermittent jumps in the a-posteriori variance factors of Fig. 2, and they are related to overall lower accuracy in the estimated EPN coordinates in the respective solutions.

### 3.4 Changes that Affected the Accuracy of EPN Weekly Frames

The internal accuracy improvement in the EPN weekly frames during the period 2005–2010 is partly related to the change of datum constraints for the combined weekly solutions. After GPS week 1303 (December 2004) the EPN ACC switched its alignment strategy to the ITRF from heavy constraints to minimal constraints, a fact that is closely synchronized with the increase of frame parameter accuracy shown in Fig. 1. An analogous pattern exists in the estimated variance factors of the combined EPN weekly solutions which appear to be systematically reduced over the period 2005–2010, see Fig. 2. Later on (GPS week 1632) the type of datum constraints was changed once more to NNT-only minimal conditions, without causing though any significant variation on the weekly frame accuracy or the estimated variance factors—yet it produces a noticeable effect on frame parameter correlations (see next section).

The enhancement of internal accuracy in the EPN weekly frames (after 2005) should be also attributed to the transition from ITRF2000 to ITRF2005/IGS05 and the concurrent change from relative to absolute model corrections for the GNSS antenna phase center variations. Since GPS week 1400 (November 2006) the IGS adopted absolute PCVs for its routine generation of precise satellite orbits and station coordinates, while the EPN ACs made a similar switch to be fully consistent with the IGS products provided in the IGS05 frame. Additional changes that were enforced at that time in the EPN routine processing include: the mandatory use of the FES2004 model for tidal displacements, the estimation of tropospheric gradient parameters, and the recommended inclusion of GLONASS observations. The switch to IGS05 along with the above changes caused a considerable strengthening to the scale of the EPN weekly frames by improving its accuracy from 1–2 mm to 0.2–0.3 mm as seen in Fig. 3.

Another aspect to be mentioned here is the sudden drop of the sigma values obtained by Eq. (1) for all frame parameters in early 2010 (GPS weeks 1576–1578). This reflects an abrupt improvement in the internal accuracy of the EPN weekly frames by a factor between 3 and 4, which is clearly depicted in Fig. 1. A similar drastic improvement occurs in the formal accuracy of the estimated EPN coordinates extracted from the SINEX files of the combined weekly solutions. The aforesaid behavior is due to the change in the reconstruction of normal equations for the submitted sub-network solutions by the EPN ACs. Specifically, since GPS week 1578 the EPN/ACC started to reconstruct constraint-free NEQs from the contributing weekly AC solutions using complete statistical information that is provided in the SOLUTION/STATISTICS block

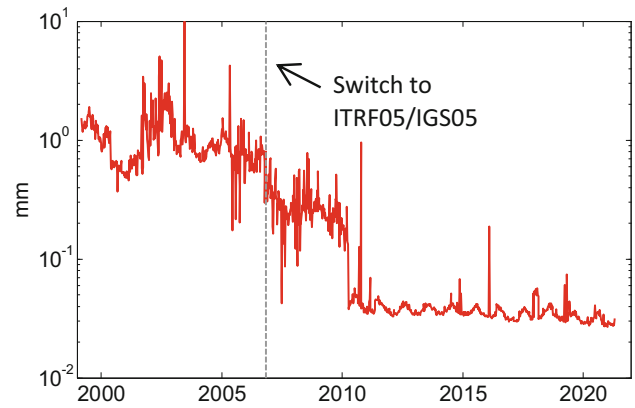


Fig. 3 Scale accuracy in the combined EPN weekly solutions before/after the adoption of absolute PCV models

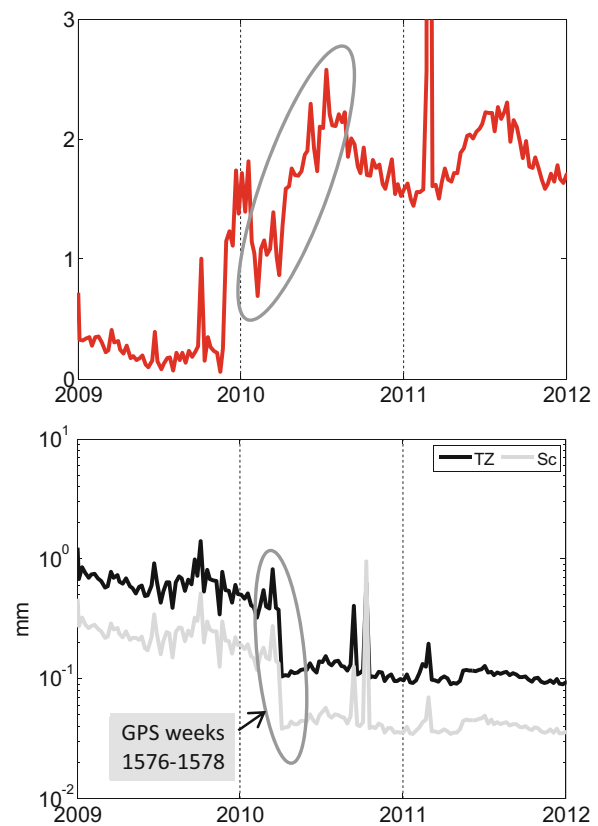


Fig. 4 Contrast of rapid changes in the a-posteriori variance factors (upper plot) and the standard deviations of frame parameters (bottom plot) in combined EPN weekly solutions

of their corresponding SINEX files (Habrich 2011). It remains puzzling, though, the fact that the estimated variance factors of the combined EPN weekly solutions exhibit an increasing trend after GPS week 1577 (March 2010), whereas the weekly frame parameters concurrently experience a rapid decrease in their sigma values, see Fig. 4.

### 3.5 Correlations in EPN Weekly Frame Parameters

The frame parameters of the combined weekly solutions are expected to have strong correlations due to the regional character of the EPN network. Its barycenter is located far away from the geocenter at a distance of more than 6,200 km and almost 4,700 km above the Earth's equatorial plane. This situation inevitably creates artificial dependencies among the inherited origin, orientation and scale of the weekly estimated ITRF coordinates at the EPN stations.

The correlation coefficients of weekly frame parameters were computed from the elements of the CV matrices  $\Sigma_\theta$  and they are shown in Fig. 5 over the entire period 1999–2021. This representation includes in total 21 correlation coefficients among the seven frame parameters of each weekly solution. As seen in these plots, there exist several parameter combinations which sustain high correlations throughout the life span of EPN. Those combinations

refer mostly to pairings between translation and rotation parameters, that is  $T_x/R_y$ ,  $T_y/R_z$ ,  $T_y/R_x$ ,  $T_z/R_y$  (and also  $R_x/R_z$ ), whose correlation level reaches 85–90%, or even higher, in all combined weekly solutions; see Fig. 5b. The downside of this behavior is that the definition of the origin and orientation cannot be sufficiently separated in each weekly solution (i.e. NNT constraints affect also the orientation of the EPN weekly frames with respect to ITRF, which is theoretically defined by the fixed satellite orbits). Another problematic pair is  $T_x/T_z$  which seems to be more sensitive to changes in the combination strategy, such as the switch from heavy to minimal constraints (12/2004) and the reference frame transitions from IGS05 to IGS08 (04/2011) and from IGS08 to IGB08 (01/2014), see the magenta line in Fig. 5b.

The rest of frame parameter pairs shown in Fig. 5 exhibit a mixture of correlation patterns which are largely influenced by the growing number of EPN stations at an annual rate of 13 new entries per year (see Fig. 6). Note that many pairs of

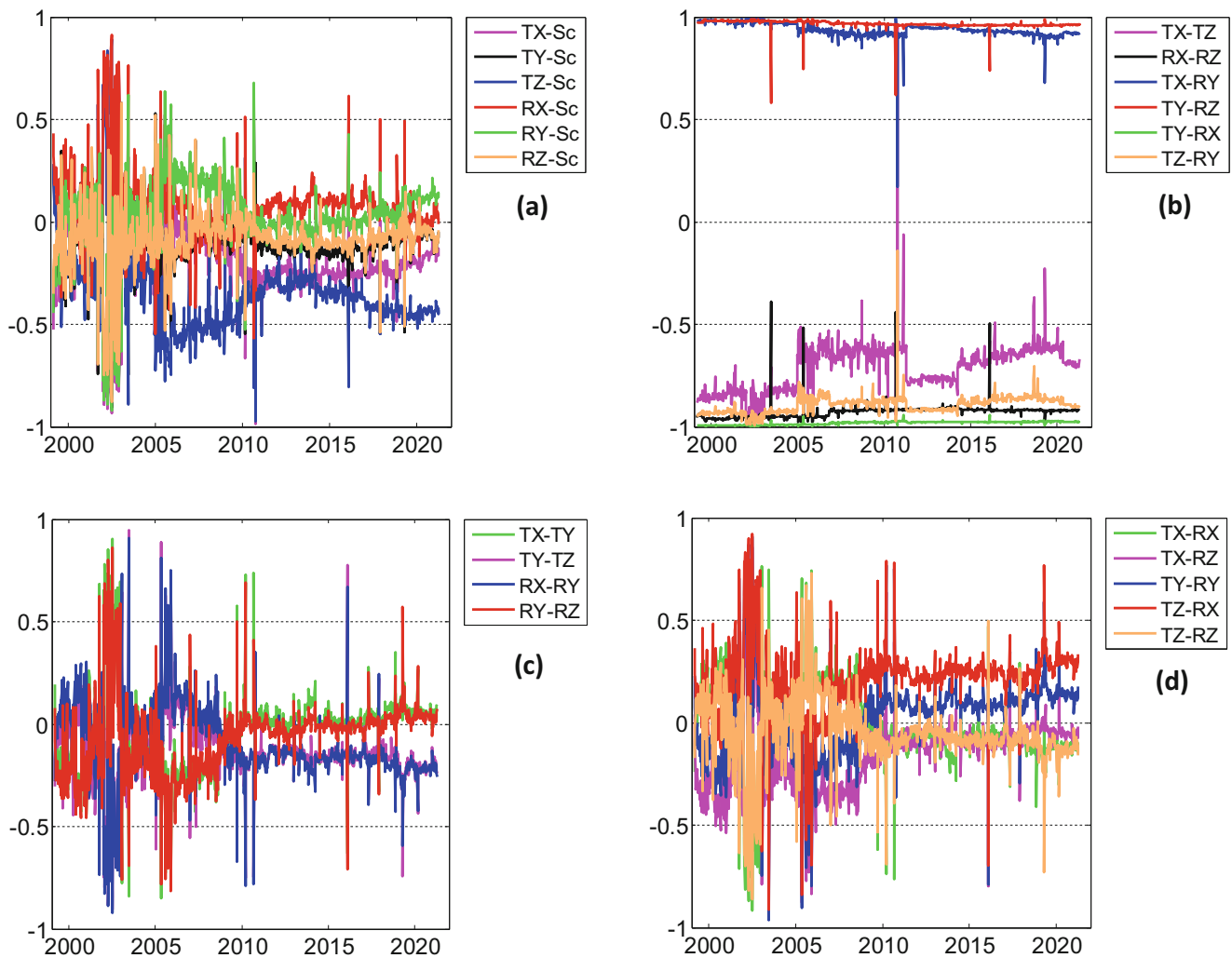


**Fig. 5** Correlation coefficients of frame parameters in combined EPN weekly solutions

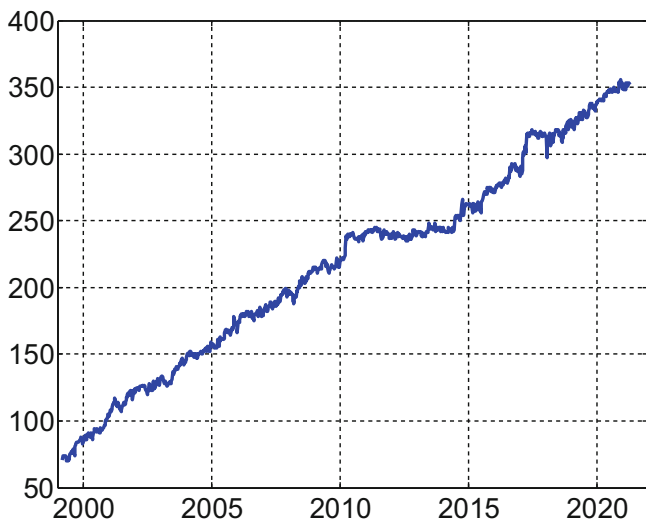


**Fig. 6** Number of stations in combined EPN weekly solutions

frame parameters have larger variability in their correlation coefficients during the period 1999–2009 compared to recent years. This probably occurs due to the successive addition of new stations which is more influential in the early years of EPN. After the last quarter of 2009 the correlation coefficients lower their variability and they do not generally exceed the 20% level. The only exception is the pair  $Tz/Sc$  which exhibits a negative correlation of 40–45% in all combined solutions since 2016. The switching to different reference frames, different alignment strategies and different sets of fiducial stations has also affected in a systematic way several pairs of frame parameters, some of which even reverse the sign of their correlation coefficient throughout the life span of EPN (e.g.  $Tz/Sc$ ,  $Rx/Ry$ ,  $Ty/Ry$ ,  $Ty/Tz$ ).

Lastly, let us point out that the weekly correlations in most pairs of frame parameters retain their tendency before

and after GPS week 1578. This confirms that the abrupt improvement in the internal accuracy of frame parameters in early 2010 (see Fig. 4) is linked to a revised re-scaling for the weekly coordinate CV matrices of the EPN combined solutions, see also Habrich (2011).

#### 4 Re-Processed Combined EPN Weekly Coordinate Solutions

The combined weekly solutions from the routine EPN analysis are affected by reference frame changes, data modeling upgrades and software revisions. Consequently, consistent results over time can only be generated by re-analyzing the historical GNSS observations using a unique set of processing options and a common combination strategy. Thus far two re-processing campaigns have been performed in the EPN network (*repro1* released in 2012, *repro2* released in 2016) resulting in a series of re-estimated combination products (daily/weekly coordinates, troposphere parameters) that are accessible from the EUREF/EPN webpage.

In this study the re-processed weekly coordinate solutions are tested in terms of frame parameter accuracy, in a similar way as the routine solutions of the previous section. Due to space limitations only the results from the EPN-repro2 campaign are given here by pointing out their most distinctive features. It is noted that the repro2 solutions are aligned to the IGB08 frame using NNT-only minimal constraints on selected reference stations, and they extend from the EPN launch until the end of 2014. However the results shown here cover a slightly smaller period between 1999 and 2014 (GPS weeks 1000–1824).

The internal accuracy of the EPN weekly frames from the repro2 solutions has been computed by Eq. (1) and the respective results are shown in Fig. 7. Its chronolog-

**Fig. 7** Internal accuracy of frame parameters in the EPN-repro2 combined weekly solutions

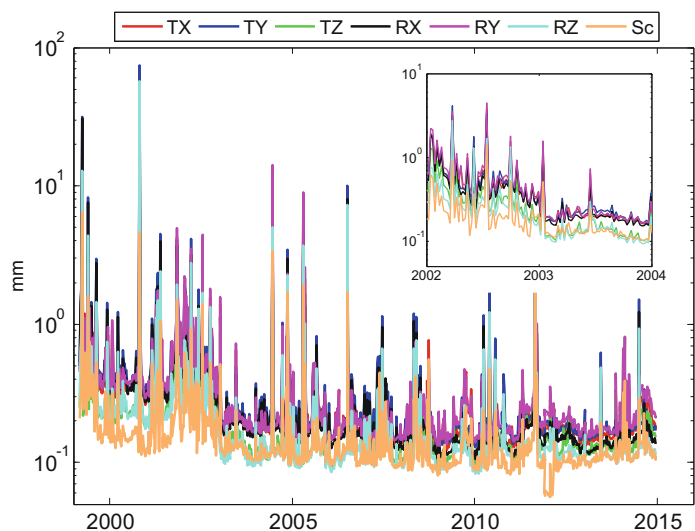
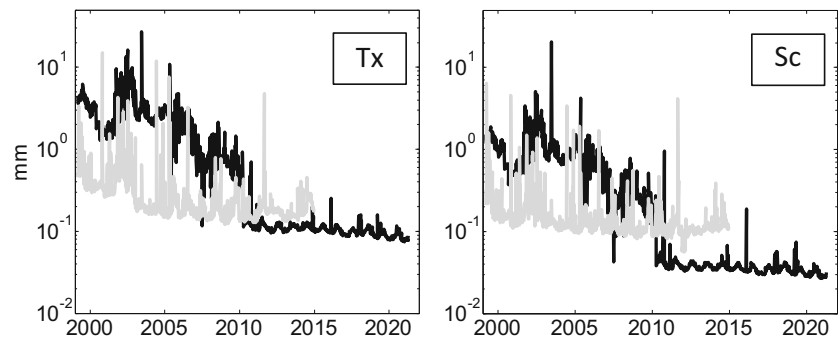


**Fig. 8** Comparison of internal accuracy at frame parameter level between the *routine* (black) and the *repro2* (gray) combined EPN weekly solutions



ical evolution is rather balanced without experiencing the systematic change that appears in the routine EPN weekly frames during the period 2005–2010 (see Fig. 1). After 2003 the sigmas of all frame parameters lie mostly in the range of 0.1–0.3 mm, although there exist several scattered “bad” weeks where the frame accuracy is significantly lower and even exceeds 2–3 mm (this mainly applies to  $T_x$  and the rotational parameters). A gradual improvement from mm to sub-mm level is also visible in the period 2002–2003 for all frame parameters (see Fig. 7). Note that the scale is again the frame parameter with the best internal accuracy in the EPN network, but to a lesser extent compared to the routine solutions.

Overall, the *repro2* weekly frames outperform the routine weekly frames in the EPN network throughout the period 1999–2010. As an example, the estimated standard deviations of  $T_x$  and  $S_c$  from each series of combined weekly solutions are compared in Fig. 8 (similar behavior is also obtained for the rest of frame parameters). The improvement is more profound during the first part of the considered period, and it amounts to several mm for each frame parameter. This part covers the period *before* introducing the absolute PCV corrections and the use of minimal constraints in the routine EPN analysis. After 2006 the gap in frame accuracy between *repro2* and routine weekly solutions diminishes, thus confirming the positive influence of the adopted changes in the GNSS data processing at the EPN stations.

The abrupt improvement in the internal accuracy of the routine weekly frames at GPS week 1578 affects the relative performance between the *repro2* and the routine weekly solutions in the EPN network. As seen in Fig. 8, after the beginning of 2010 the *repro2* solutions show slightly worse accuracy, at frame parameter level, than the routine solutions (especially for the scale parameter).

## 5 Summary

The results of this study revealed the internal accuracy of the frame elements in the combined EPN weekly solutions after their alignment to successive realizations of the International

Terrestrial Reference System. It is verified that a systematic improvement at frame parameter level has occurred in the routine series of such solutions, which reaches almost two orders of magnitude when comparing the recent EPN weekly solutions with the ones obtained in the pre-2005 period. The factors that have mostly contributed to this improvement are: (a) the change of datum constraints for the alignment to ITRF (heavy constraints  $\rightarrow$  minimal constraints), (b) the switch to improved global frame releases, particularly the transition from ITRF2000 to IGS05 in conjunction with the adoption of absolute models for GNSS antenna calibrations, and (c) the change in the reconstruction of constraint-free NEQs from the contributing weekly AC solutions before their combination with the Bernese software (see Sect. 3.4).

Presently, the internal accuracy of the origin and orientation in the routine EPN weekly frames lies at the level of 0.1–0.2 mm, whereas the scale accuracy is even better by a factor of 3. In fact, this performance has remained almost invariable since 2010 (with the presence of small but clear annual fluctuations), and even surpasses the performance of the *repro-2* EPN weekly coordinate solutions. The latter, however, have shown a definite improvement in all frame parameters compared to the routine EPN weekly solutions throughout the period 1999–2010.

## References

- Altamimi Z (2018) Relationship and transformation between the International and the European Terrestrial Reference Systems. EUREF Technical Note 1 (<http://etrs89.ensg.ign.fr/pub/EUREF-TN-1.pdf>)
- Blewitt G (1998) GPS data processing methodology: from theory to applications. In: GPS for Geodesy. Springer, pp 231–270
- Bruyninx C (2004) The EUREF permanent network: a multidisciplinary network serving surveyors as well as scientists. *Geoinformatics* 7:32–35
- Bruyninx C, Altamimi Z, Boucher C, Brockmann E, Caporali A, Gurtner W, Habrich H, Hornik H, Ihde J, Kenyeres A, Mäkinen J, Stangl G, van der Marel H, Simek J, Söhne W, Torres JA, Weber G (2009) The European reference frame: maintenance and products. IAG Symposia Series, vol 134. Springer, pp 131–136
- Bruyninx C, Habrich H, Söhne W, Kenyeres A, Stangl G, Völkens C (2012) Enhancement of the EUREF permanent network services and products. IAG Symposia Series, vol 136. Springer, pp 27–35



- Bruyninx C, Legrand J, Fabian A, Pottiaux E (2019) GNSS metadata and data validation in the EUREF permanent network. *GPS Sol* 23:106
- Bruyninx C, Brockmann E, Kenyeres A, Legrand J, Liwosz T, Pacione R, Söhne W, Völksen C (2020) EPN Regional Network Associate Analysis Center Technical Report, International GNSS Service Technical Report 2018, IGS Central Bureau and University of Bern; Bern Open Publishing, pp 111–124
- Dach R, Lutz S, Walser P, Fridez P (eds) (2015) *Bernese GNSS Software Ver. 5.2. User manual*, Astronomical Institute, University of Bern, Bern Open Publishing, ISBN: 978-3-906813-05-9
- Ebner H (1974) Eine Theorie zur Analyse von Kovarianzmatrizen. *Zeitschrift für Vermessungswesen*:453–461
- Habrich H (2011) EPN analysis Coordinator Report. Presented at the EUREF Symposium 2011, May 25–28, Chisinau, Moldavia
- Ihde J, Habrich H, Sacher M, Söhne W, Altamimi Z, Brockmann E, Bruyninx C, Caporali A, Dousa J, Fernandes R, Hornik H, Kenyeres A, Lidberg M, Mäkinen J, Poutanen M, Stangl G, Torres JA, Völksen C (2014) EUREF's Contribution to National, European and Global Geodetic Infrastructures. IAG Symposia Series, vol 139. Springer, pp 189–196
- Kenyeres A, Bruyninx C (2004) Monitoring of the EPN coordinate time series for improved reference frame maintenance. *GPS Sol* 8(4):200–209
- Legrand J (2017) New EPN multi-year solution expressed in IGS14. Presented at the EUREF LAC Workshop, Brussels, October 25–26, 2017
- Meissl P (1965) Über die innere Genauigkeit dreidimensionaler Punkthaufens. *Zeitschrift für Vermessungswesen* 90:109–118
- Meissl P (1969) *Zusammenfassung und Ausbau der inneren Fehlertheorie eines Punkthaufens*. Deutsche Geodätische Kommission, Reihe A 61:8–21
- Pope AJ (1973) The use of the “solution space” in the analysis of geodetic network adjustments. Presented at the IAG Symposium on Computational Methods in Geometric Geodesy, Oxford, September 2–8, 1973
- Rebischung P (2014) Can GNSS contribute to improving the ITRF definition? PhD Thesis. Institut National de l'Information Géographique et Forestière, IGN/LAREG, Paris, France
- Sillard P, Boucher C (2001) A review of algebraic constraints in terrestrial reference frame datum definition. *J Geod* 75:63–73

**Open Access** This chapter is licensed under the terms of the Creative Commons Attribution 4.0 International License (<http://creativecommons.org/licenses/by/4.0/>), which permits use, sharing, adaptation, distribution and reproduction in any medium or format, as long as you give appropriate credit to the original author(s) and the source, provide a link to the Creative Commons license and indicate if changes were made.

The images or other third party material in this chapter are included in the chapter's Creative Commons license, unless indicated otherwise in a credit line to the material. If material is not included in the chapter's Creative Commons license and your intended use is not permitted by statutory regulation or exceeds the permitted use, you will need to obtain permission directly from the copyright holder.





# The Atlantic Network of Geodynamic and Space Stations (RAEGE)

## A Spanish-Portuguese Infrastructure of Geodetic Stations

José A. López-Pérez, João S. Ferreira, Javier González-García, Francisco J. Beltrán-Martínez, Carlos Albo-Castaño, Beatriz Vaquero-Jiménez, Abel García-Castellano, Javier López-Ramasco, Esther Azcue-Infanzón, Pablo de Vicente-Abad, José A. López-Fernández, Francisco M. Wallenstein, Luís R. Santos, and Sara Pavão

### Abstract

This paper shows the current status of the *Red Atlántica de Estaciones Geodinámicas y Espaciales* (RAEGE), a joint Spanish-Portuguese infrastructure of geodetic stations. When complete, it will be composed of four VGOS (VLBI Global Observing System) radio-telescopes, two in Spain (Yebes and Gran Canaria) and two in Portugal (Santa María and Flores islands, Açores archipelago). The Yebes VGOS radio-telescope is fully operational and integrated in the VGOS core network since 2016. The Santa María VGOS radio-telescope has undergone major maintenance operations and has resume regular IVS observations with its tri-band S/X/Ka receiver since end of May 2021, until it becomes a VGOS station by the second half of 2022. Additionally, each station will include GNSS receivers, gravimeters and a local-tie network. In particular, the RAEGE-Yebes station will have a Satellite Laser Ranging (SLR) system, which is under construction. It can be said that RAEGE is the Spanish-Portuguese response to UN resolution 69/266 and GGOS (Global Geodetic Observing System). The current status of all the four RAEGE stations will be shown.

### Keywords

Geodesy · GGOS · Radiotelescope · Receivers and GNSS · SLR · VGOS · VLBI

J. A. López-Pérez (✉) · J. González-García · F. J. Beltrán-Martínez · C. Albo-Castaño · B. Vaquero-Jiménez · A. García-Castellano · J. López-Ramasco · P. de Vicente-Abad  
Yebes Observatory, Instituto Geográfico Nacional (IGN), Yebes, España

J. S. Ferreira  
Associação RAEGE Açores, Estação RAEGE de Santa María, Vila do Porto, Portugal

E. Azcue-Infanzón · J. A. López-Fernández  
Instituto Geográfico Nacional (IGN), Madrid, España

F. M. Wallenstein · L. R. Santos · S. Pavão  
Estrutura de Missão dos Açores para o Espaço, Ponta Delgada, Portugal

## 1 Introduction: RAEGE Overview

RAEGE is the Spanish and Portuguese acronym for Atlantic Network of Geodynamic and Space Stations. It is a joint infrastructure of geodetic stations created by the Spanish National Geographic Institute (IGN) and the Regional Government of Azores (GRA). As shown in Fig. 1, the network will have four stations: Yebes, Santa María, Flores and Gran Canaria, each one on a different tectonic plate, except Santa María and Gran Canaria, which are both in the African plate. The approximate baseline lengths of this array are given in Table 1.

Every station will host a 13.2 m VGOS radiotelescope, GNSS receivers, gravimeters and a network of concrete

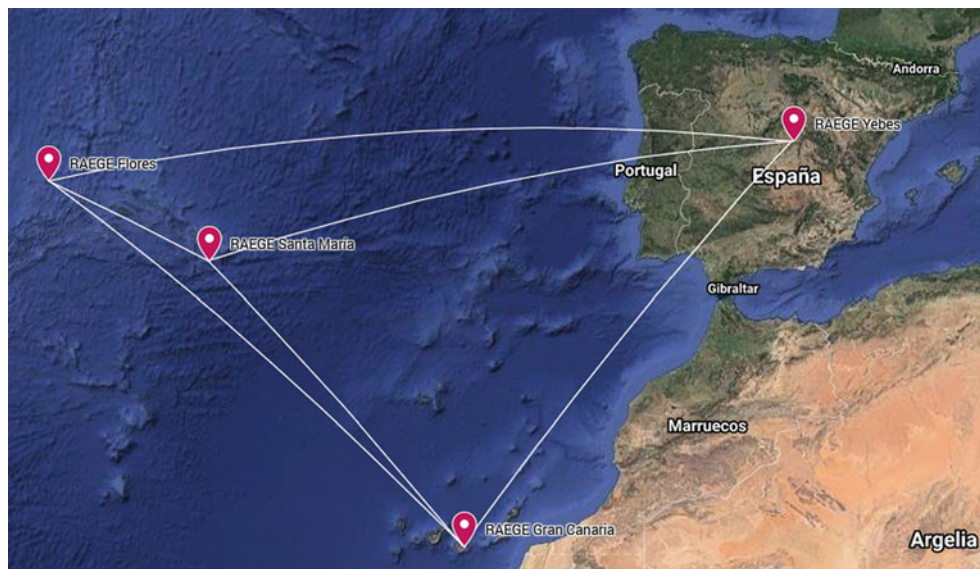


**Fig. 1** Map of RAEGE stations

**Table 1** Approximate baseline lengths for RAEGE stations

Baseline	Length (Km)
Yebes–Gran Canaria	1,800
Yebes–Santa María	2,000
Yebes–Flores	2,400
Gran Canaria–Flores	2,000
Santa María–Flores	540

pillars for the local-tie. Additionally, Yebes station will have a Satellite Laser Ranging system which is under construction. As a result, Yebes Observatory will become the first Spanish GGOS core site. In this way, RAEGE will contribute to achieving the goal of GGOS for a better and accurate understanding of our planet through different space geodesy techniques. More details can be found in <https://www.raege.eu>.

Similar projects were started in Australia (Lovell et al. 2013) and are planned for the Indian subcontinent (Dhar et al. 2021), for instance.

## 2 RAEGE Yebes Station

The first RAEGE station was built in Yebes Observatory, which is a Technological Development Center (TDC) of the International VLBI Service for Geodesy and Astrometry (IVS) since 2015.

The VGOS radiotelescope (see Fig. 2) is performing regular VGOS and EU-VGOS observations.

Its broad band receiver is under upgrade at Yebes Observatory laboratories. Meanwhile, it is observing with the broad band receiver developed for Santa María VGOS



**Fig. 2** Yebes VGOS radiotelescope (foreground) and 40-m radiotelescope (background)

radiotelescope, whose VGOS backends are not available yet. This receiver is the most sensitive one developed so far in Yebes Observatory, as shown in Fig. 3. For frequencies above 6 GHz, the receiver noise is lower than 20 K for each linear polarization. The ripple at frequencies lower than 6 GHz is under investigation, but it seems to be related with mismatching between the Quad-Ridged Flared Horn (QRFH) and the low-noise amplifiers.

It has to be mentioned that Yebes Observatory will be responsible for the construction of the broad band receivers for the VGOS radiotelescopes in HartRAO (South Africa) and Matera (Italy).

Yebes RAEGE has two GNSS permanent stations, YEBE and YEB1. One of them (YEBE) is part of the International

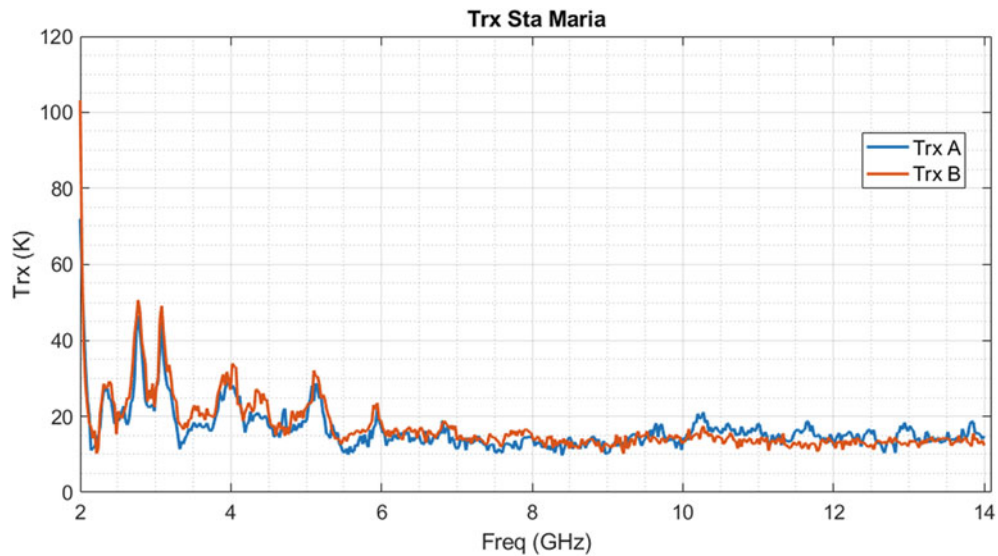


**Fig. 3** Santa María VGOS receiver noise temperature for each linear polarization channel



**Fig. 4** Artist impression of YLARA

GNSS Service (IGS) and EUREF networks, but both of them participate in the EUREF densification project. Additionally, Yebes RAEGE has a network of about twenty four concrete pillars to perform the local-tie and connect the results of each space geodesy technique.

Concerning gravimetry activities, Yebes RAEGE has a laboratory which hosts absolute FG5 and A10 gravimeters, together with a GWR-OSC superconducting one, a seismograph and a SILEX accelerometer. The data of the

gravimeters is submitted to the International Geodynamics and Earth Tide Service (IGETS).

Finally, the Yebes Laser Ranging System (YLARA) is under construction (see Fig. 4). It will have a 70-cm telescope and flexibility for two laser transmitter configurations: piggy-back and Coudé path. This project is already recognized by the International Laser Ranging Service (ILRS) with station name YEBL, SOD number 78176201 and DOMES number 13420S021. It is expected to start operations in early 2023.

After this, Yebes Observatory will become a GGOS core site, the first one in Spain.

### 3 RAEGE Santa María Station

Santa María was the second RAEGE station to be built (see Fig. 5). Currently, the radiotelescope is equipped with a tri-band receiver (S/X/Ka) and a dBBC2 backend, for VLBI. A complete description of this receiver can be seen in López-Pérez et al. (2021).

After one year of heavy maintenance and reparation works in the station, the radiotelescope resumed legacy S/X VLBI observations on May 25th, 2021 in tag-along mode. After one month of operation in this mode, it joined the IVS as a regular station.

It must be mentioned that, in November 2020, this radiotelescope performed joint observations of Bepi-Colombo probe in X and Ka bands together with DSN-JLP antennas. The purpose was a proof-of-concept test to verify whether Doppler shift measurement accuracy can be improved by use of corrections from smaller and stiffer antennas, like RAEGE ones. The results of this test will be shown in Zubair et al. (2021).

The backends for VGOS operation are under procurement and the VGOS receiver is already built and working in Yebes VGOS radiotelescope, while the Yebes receiver is under upgrade in the laboratories. It is planned to install the VGOS receiver and the backend in the second half of 2022, so Santa María will become a VGOS station by the end of 2022.

The station has two GNSS receivers and a GRAVITON gravimeter, but a superconducting one is under procurement, and it is expected to be installed by mid 2022. The measurements they produce are sent to the respective international services. It has a Centaur seismograph and SILEX accelerograph, too.



**Fig. 5** RAEGE Santa María VGOS radiotelescope

Concerning the local-tie, a network of about nine concrete pillars will be built by the end of 2021.

### 4 RAEGE Flores Station

After selecting the site based on the results of RFI measurements, the land was purchased for this station. Then, a topographic survey was performed and later a weather station and a GNSS receiver were installed. This GNSS receiver is registered at IGS, as well.

Currently, the contract for the radiotelescope design and construction is in preparation. The design has to be customized to withstand the usual high wind speeds in this island.

### 5 RAEGE Gran Canaria Station

A site called Artenara was initially identified for this station, but the surrounding area was declared World Heritage by UNESCO in July 2020. Then, IGN decided to look for another site, in order to avoid the loss of such declaration, which is very important for the island.

Several sites were explored from July–November 2020, and one was identified as suitable for the station. Currently, the island authorities are in negotiations for the purchase of the land, which will be granted to IGN. Meanwhile, IGN is preparing the contracts to update the station design for the new site.

## 6 Conclusions and Future Work

Despite the coronavirus crisis, a lot of works have been performed in the stations. In the next few months, for Yebes station, it is planned to:

- Continue with VGOS and EU-VGOS observations
- Finish the upgrade of Yebes VGOS receiver (end of 2021)
- Participate in 1GHz BW tests in 2nd half of 2021 with Yebes antenna equipped with Santa María receiver
- Continue with SLR station construction, to be ready by early 2023

Regarding Santa María station, it is planned to:

- Continue with IVS S/X observations until mid 2022
- Join VGOS network by second half of 2022
- Receive the procurement of Mark6 and dBBC3
- Build local-tie network of concrete pillars

Concerning RAEGE Flores station, it is planned to publish the contract for detailed radiotelescope design and construction.

Finally, for RAEGE Gran Canaria station, IGN has to update projects of civil works for the new site, once the land is purchased and granted.

As a result of all the work presented here, it can be said that RAEGE is the joint Spanish-Portuguese response to UN resolution 69/266 for “A global geodetic reference frame for sustainable development”, and a commitment with GGOS.

**Acknowledgements** The authors want to give special thanks to all the Spanish and Portuguese staff that supports RAEGE activities and goals.

## References

- Dhar S, Tiwari A, Balasubramanian N, Devaraju B, Dikshit O, Prakash J, Mishra P, Agarwal D, Sharma V, Varade D, Laha A, Kumar A, Singh S, Bihari Narayan Singh A, Goyal R, Kumar V (2021) Establishment of state-of-the-art geodesy village in India: Current status and Outlook, EGU general assembly 2021, Online, 19–30 Apr 2021, EGU21-16068. <https://doi.org/10.5194/egusphere-egu21-16068>
- López-Pérez JA, Tercero-Martínez F, Serna-Puente JM, Vaquero-Jiménez B, Patino-Esteban M, García-Carreño P, González-García J, García-Pérez Ó, Beltrán-Martínez FJ, Albo-Castaño C, Gallego-Puyol JD, López-Fernández I, Díez-González C, Malo-Gómez I, Barbas-Calvo L, de Vicente-Abad P, López-Fernández JA (2021) A tri-band cooled receiver for geodetic VLBI. *Sensors* 21:2662. <https://doi.org/10.3390/s21082662>
- Lovell JEJ, McCallum JN, Reid PB, McCulloch PM, Baynes BE, Dickey JM, Shabala SS, Watson CS, Titov O, Ruddick R, Twilley R, Reynolds C, Tingay SJ, Shield P, Adada R, Ellingsen SP, Morgan JS, Bignall HE (2013) The AuScope geodetic VLBI array. *J Geodesy* 87:527–538. <https://doi.org/10.1007/s00190-013-0626-3>
- Zubair A, Christopher V, Sami A, Andre J, Lisa MM, Meegyeong P, José AL-P, João F, Francisco B, Javier G, Carlos A, Paolo C (2021) Advancing solar system dynamics investigations with calibrated precision doppler tracking. Accepted for presentation in AGU Fall meeting, 13–17 Sept. 2021

**Open Access** This chapter is licensed under the terms of the Creative Commons Attribution 4.0 International License (<http://creativecommons.org/licenses/by/4.0/>), which permits use, sharing, adaptation, distribution and reproduction in any medium or format, as long as you give appropriate credit to the original author(s) and the source, provide a link to the Creative Commons license and indicate if changes were made.

The images or other third party material in this chapter are included in the chapter’s Creative Commons license, unless indicated otherwise in a credit line to the material. If material is not included in the chapter’s Creative Commons license and your intended use is not permitted by statutory regulation or exceeds the permitted use, you will need to obtain permission directly from the copyright holder.





# ITRF Densification in Cyprus

Chris Danezis, Miltiadis Chatzinikos, and Christopher Kotsakis

## Abstract

The aim of this paper is to present the results from the GNSS-based densification of the International Terrestrial Reference Frame (ITRF) in the region of Cyprus. The regional network used for this task consists of nine permanent GNSS Cypriot stations (eight stations of the existing CYPOS network plus the NICO station which belongs to the global IGS network) and 34 additional stations of the EUREF Permanent GNSS Network (EPN) which are mostly located in the continental part of Europe. The data used in this densification project include daily GNSS observations at the above stations within a period of 62 months (30/11/2011–28/01/2017). The present study was carried out using the resources of the CyCLOPS strategic research infrastructure unit. A robust procedure was designed for the daily data processing using the Bernese GNSS software v5.2 installed in the CyCLOPS operating center. The multi-year solution is computed by combining the constraint-free daily solutions using the normal equations stacking strategy. The reference frame of the multi-year solution is IGB08 and it was enforced through a no-net-translation condition on the positions and velocities of 24 EPN (Class A) stations. The quality of the computed solution is verified by comparing the estimated velocities with their official EPN\_A\_IGb08\_C1934 values, and reveals minimal differences ( $<1$  mm/year) in all EPN stations for both horizontal and up components.

## Keywords

CYPOS · EUREF/EPN · GNSS data processing · ITRF · Regional network densification

---

C. Danezis  
Department of Civil Engineering and Geomatics, Cyprus University of  
Technology, Limassol, Cyprus

M. Chatzinikos  
Department of Civil Engineering and Geomatics, Cyprus University of  
Technology, Limassol, Cyprus

Department of Geodesy and Surveying, Aristotle University of  
Thessaloniki, Thessaloniki, Greece

C. Kotsakis (✉)  
Department of Geodesy and Surveying, Aristotle University of  
Thessaloniki, Thessaloniki, Greece  
e-mail: [kotsaki@topo.auth.gr](mailto:kotsaki@topo.auth.gr)

## 1 Introduction

Since 2008, a geodetic network of seven permanent GNSS stations is operating in Cyprus to support its national positioning system (CYPOS) under the auspices of the Department of Lands and Surveys (DLS). The network covers the government-controlled areas with inter-station distances of about 60 km (see Fig. 1) and it serves the needs of cadastral, surveying and geodetic applications in Cyprus by means of single-base, network RTK and post-processing positioning services. The monumentation of the CYPOS stations is comprised of stable stainless-steel structures (polar masts) located at specific locations at the rooftop of DLS buildings to achieve unobstructed satellite visibility. In addition to these stations, another permanent GNSS station of the

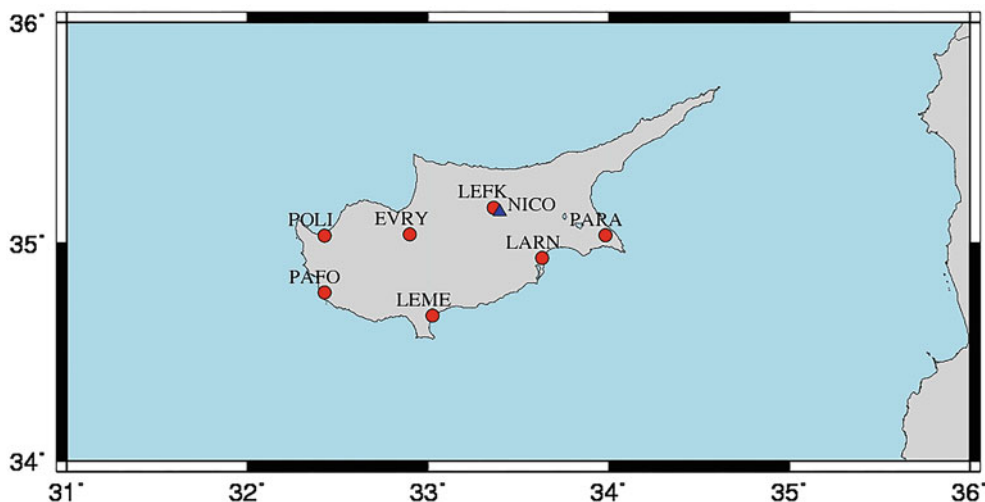


**Fig. 1** The network of permanent GNSS stations in Cyprus. Red circles correspond to CYPOS stations and the blue triangle indicates the NICO station

European Permanent Network (EPN) is located in Nicosia (NICO) and it is operated by the German Federal Agency for Cartography and Geodesy (BKG). NICO is a Tier-1 station that belongs also to the IGS (International GNSS Service) global network (Dow et al. 2009), and it has been continuously delivering GNSS observations in Cyprus since mid-1997. The aforesaid stations comprise the regional network which is used in this study to deliver a GNSS-based densification of the International Terrestrial Reference Frame (ITRF) in the region of Cyprus.

The aim of the present paper is to give an overview of the GNSS data analysis that was performed in the aforementioned network using daily observations within a period of 62 months (30/11/2011–28/01/2017). Our objective is to obtain a multi-year solution (positions + velocities) of the CYPOS network in the most recent ITRF/IGS realization, which could be later exploited for the modernization of the national geodetic reference system in Cyprus. Note that the GNSS processing performed in this study has been done using the newly-founded operation center of the Cyprus Continuously Operating Natural Hazards Monitoring and Prevention System (CyCLOPS). The latter is a strategic research infrastructure unit which has been launched in the Cyprus University of Technology and funded by the European Union Regional Development Fund and the Republic of Cyprus, with utmost objective the establishment of a national network of Tier-1/2 GNSS continuously operating reference stations (CORS) and the respective IT infrastructure to carry out high-performance computation of Earth deformation products. The presented results complement the initial work of Danezis et al. (2020) and they are supplemented by extensive reporting of quality metrics obtained from the GNSS daily data processing and the alignment of the CYPOS

network to the IGB08 reference frame (Rebischung et al. 2012). Unfortunately, at the time of preparing this paper (June 2021) the official IGS products (satellite orbits, Earth rotation parameters, satellite clocks) for the time span of the available data were not released in the latest IGS14 frame (Rebischung and Schmid 2016). Hence, the presented solution needs to be updated to IGS14 in the near future by exploiting additional segments of daily observations (after 2017) at the CYPOS stations that have been omitted from the present study.

The structure of the paper is organized as follows: in Sect. 2 the configuration of the extended GNSS regional network, the main processing options and the results obtained by the analysis of the daily GNSS data are discussed in detail; Sect. 3 describes the computation of the multi-year solution which was obtained by the Bernese software in IGB08, along with its validation against the official positions and velocities of the EPN stations that were included in the stacking adjustment of the daily GNSS observations; finally some conclusions and a brief summary of the overall results are given in Sect. 4.

## 2 GNSS Data Processing

The daily GNSS data processing was performed with the help of the Bernese GNSS software 5.2 (Dach et al. 2015) using a modified version of the RNX2SNX script for the daily network solutions in full compliance with the EUREF guidelines (Legrand et al. 2021). Details of the GNSS processing options are given in Table 1.

The daily GNSS data processing consists of three main parts, the pre-processing of raw data, the baseline processing



**Table 1** Selected options for the daily GNSS data processing

Basic observable	GNSS carrier phase. Code only for receiver clock sync and ambiguity resolution. Melbourne-Wubbenawidelane method
Elevation cut-off angle	10 deg., elevation-dependent weighting (cosz)
Data sampling	30 s and 180 s in final solution
Modeled observable	Ionosphere-free linear combination of double-difference carrier phase
Ground/satellite APC calibration	Absolute antenna phase centre corrections (igs08.atx)
Tidal displacements	IERS 2010 conventions (solid earth tides)FES 2004 (ocean loading corrections)No atmospheric loading corrections
Satellite/receiver clock	Satellite clock biases eliminated by double-differencesReceiver clock corrections estimated in pre-processing using code observations
Orbits and ERPs	IGS final GPS/GLONASS orbits & ERPs
Ionosphere	First-order ionosphere delays eliminated by forming ionosphere-free L1/L2 linear combinationHigher-order ionosphere corrections are appliedRegional ionosphere maps used to increase the number of resolved ambiguities in the QIF, L5/L3 and L1/L2 ambiguity resolution
Ambiguity resolution	Ambiguities are resolved in baseline-by-baseline mode:Melbourne-Wubbenawidelane/narrowlane method (<6,000 km)Quasi-Ionosphere-Free (QIF) (<2000 km)Phase-based widelane/narrowlane method (<200 km)Direct L1/L2 method, also for GLONASS (<20 km)GLONASS is considered for ambiguity resolution (<2000 km)
Troposphere	Dry GMF (prior model), estimation of hourly zenith delay corrections for each station using wet GMFHorizontal gradient parameter estimated/day/station (Chen-Herring)
Reference frame	IGb08, no-net translation conditions on 24 EPN reference stations(EPN_A_IGb08_C1934.snx)

and the final network adjustment. In addition, each part is also divided into a number of steps making the daily GNSS network solutions a complex and demanding procedure. In order to monitor and assess the products derived from each step, a number of auxiliary scripts described in Chatzinikos et al. (2017a, b) were also implemented into our analysis. The goal of these scripts is twofold, firstly to analyze the most important quality metrics obtained from each step of the daily GNSS data processing strategy by the Bernese software and secondly, using these metrics to assess the quality and the performance of the Cypriot GNSS stations with respect to the EUREF Permanent GNSS Network (EPN) stations. More details on those metrics will be given in the following sections.

## 2.1 Network Configuration

The CYPOS GNSS stations are equipped with different receiver/antenna types: the stations EVRY and POLI are equipped with a Leica GMX902GG receiver and a LEIAT504GG + LEIS antenna, whereas the rest five stations (LARN, LEFK, LEME, PAFO, PARA) employ a Leica GRX1200 + GNSS receiver and a LEIR25 + LEIT antenna. The hardware configuration of the NICO station is a Leica GR50 multi-GNSS receiver and a Leica AR25 choke-ring antenna. All stations routinely track GPS and GLONASS satellite signals, while NICO supports also the tracking of Galileo and Beidou signals.

The eight Cypriot stations shown in Fig. 1 are supplemented by 34 stations of the EPN (Bruyninx et al. 2019), thus forming the final configuration of the regional network

to be processed for the purpose of this paper (see Fig. 2). The selected EPN stations are well distributed over the largest part of the European plate, and most of them belong also to the IGS global network. The daily GNSS data that have been used in the present study cover the period from 30/11/2011 up to 28/01/2017 which marks the switch of the official IGS products from the IGb08 to IGS14 reference frame.

## 2.2 Assessment of Daily GNSS Data

The objective of this section is, firstly, to analyze and present the quality of the GNSS raw daily data in the regional network and, secondly, to assess the performance of the Cypriot GNSS stations with respect to the EPN stations. The term “quality” in this context refers to the following characteristics: the daily number of observations and satellites tracked by each station, the number of arcs for the daily observations at each station from each satellite, and the daily precision of the code measurements. The statistical analysis of these characteristics unveils the quality of the GNSS signal tracking performance at each station. For this purpose, four different metrics are employed and presented in this paper, which were derived during the initial step of the Bernese GNSS data processing procedure.

Instead of analyzing the total number of daily observations tracked by each station, we prefer to compute the first metric as the daily mean number of observations per satellite for each frequency and measurement type (code or phase). In this way we can overcome any signal tracking inconsistencies among the station receivers, since some of

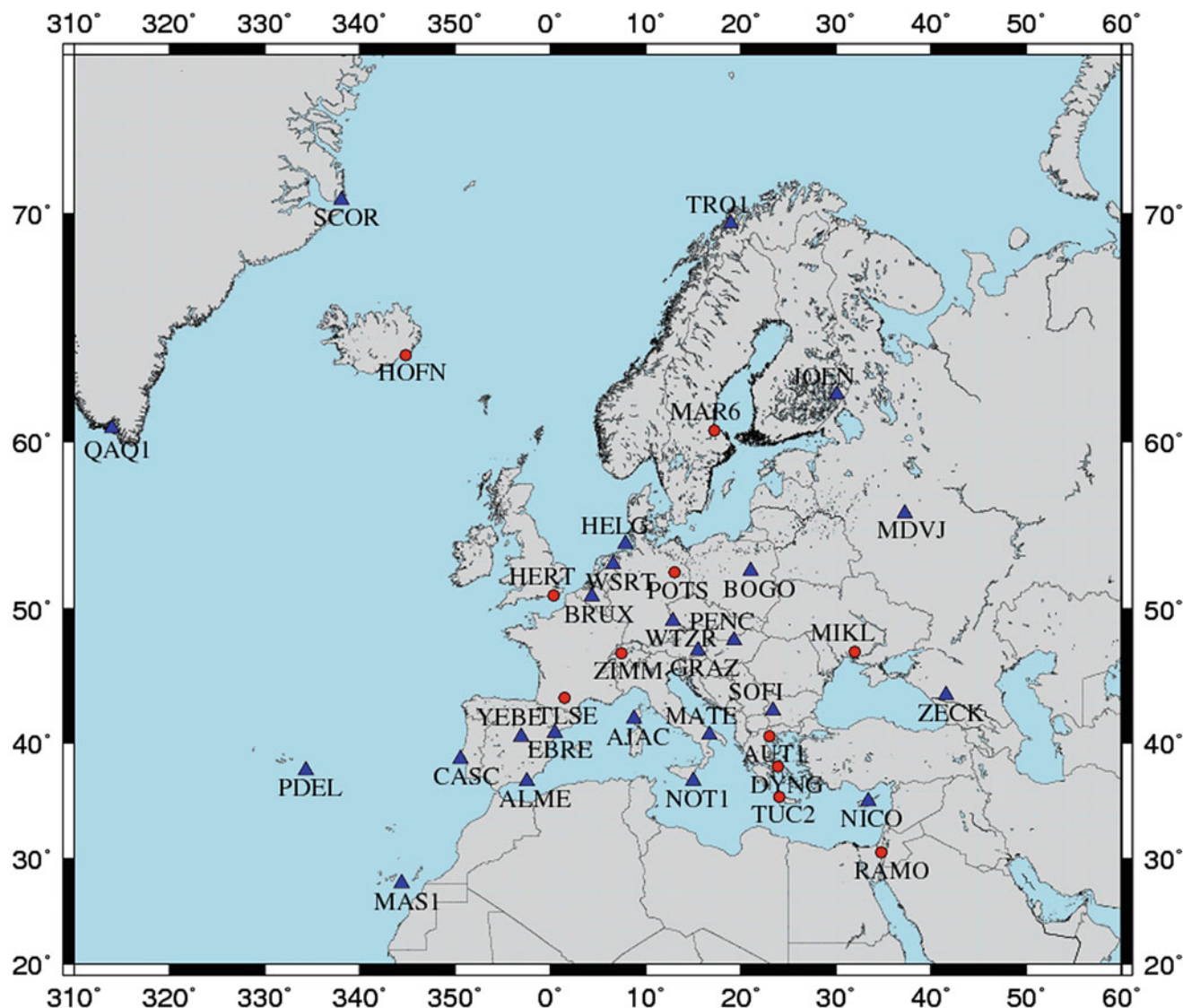


**Fig. 2** Map of EPN stations used in the GNSS data processing. Blue triangles indicate the selected reference stations for the datum definition, while red circles correspond to auxiliary stations which bridge the distant gaps among the network stations

them are tracking signals by both GPS and GLONASS, and some others only from GPS. The second metric refers to the daily mean number of the satellites per epoch tracked by each station. In contrast to the first metric, this one depends on the GNSS constellations tracked by the stations, but it remains independent of the duration of the session data (i.e., the number of epochs constituting the daily GNSS data file). These two metrics constitute a robust tool for assessing the signal tracking performance of each station. In addition, they are totally correlated with the precision of the estimated final daily products, like the network station coordinates and the tropospheric parameters.

The third metric corresponds to the daily number of observed arcs per satellite tracked by each station, and its role is to reveal the stability of the GNSS signal tracking

performance over the regional network. Considering that for almost every point on the Earth the GNSS satellites are visible two times per day (due to their orbital period), the expected number of the arcs-per-satellite for 24-h data sessions is 2. The closer this metric is to that value, the more compact and without signal tracking breaks are the analyzed GNSS daily data. Conversely, if the value of this metric becomes larger than 2, more ambiguities are required to be resolved in the next part of the GNSS processing procedure. The last analyzed metric is the daily root mean square (RMS) of the single point positioning (SPP) technique. With the help of this metric, we can check the precision of the code measurements of each station and, at the same time, the quality performance of each station receiver.

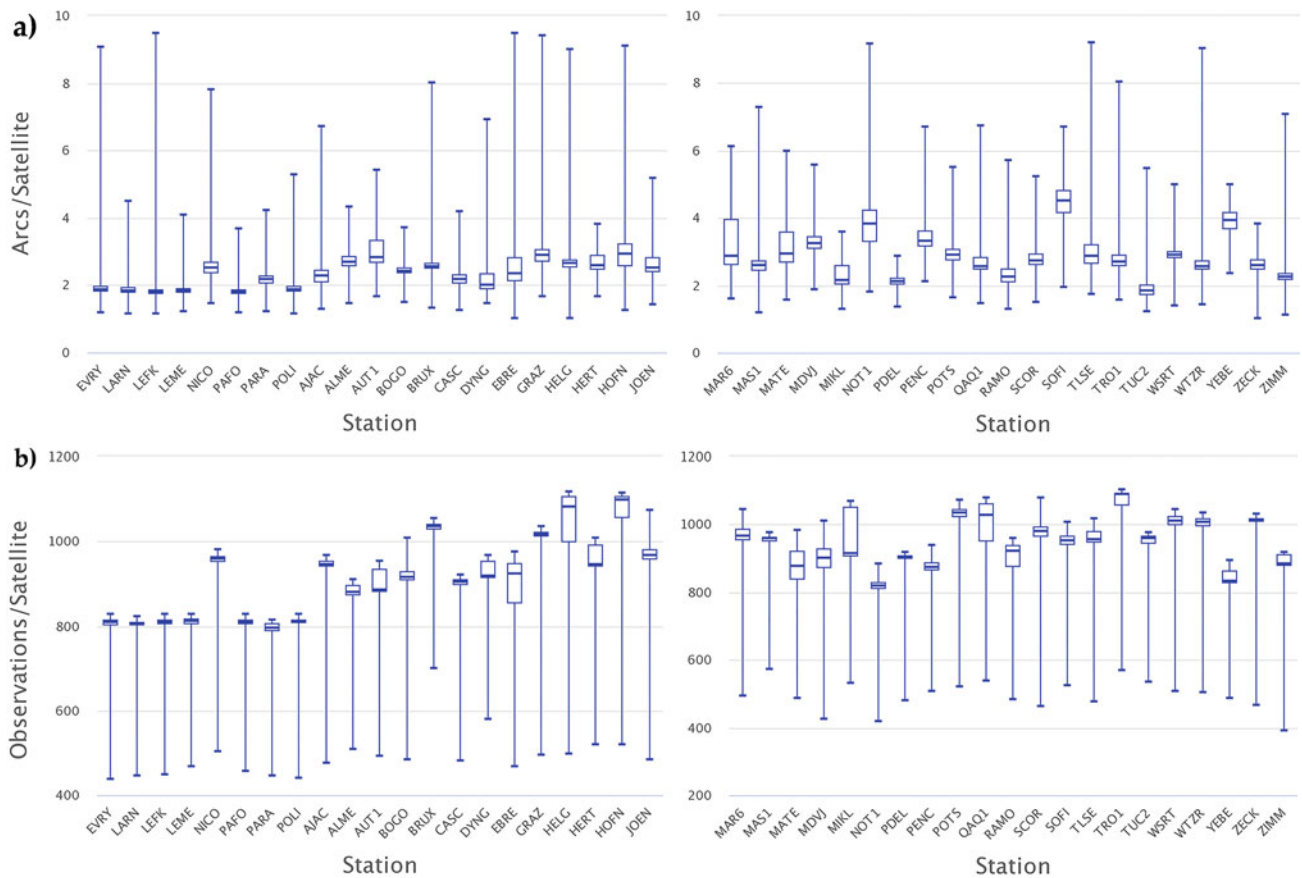


**Fig. 3** Box-plot analysis of the temporal behavior for data-related daily metrics in the regional GNSS network: (a) number of observed arcs per satellite, (b) mean number of observations per satellite

The station-wise behavior of the aforesaid quality metrics is shown in Figs. 3 and 4 with the help of box-plots which constitute a smart and comprehensive tool for the statistical presentation of GNSS signal tracking performance in regional networks. The temporal analysis of all quality metrics was performed separately for each station and it refers to the whole time period of the collected data. Each box in Figs. 3 and 4 corresponds to a particular station and its height represents the interquartile range (IQR) derived from the temporal analysis of each quality metric. The three horizontal lines of the boxes represent different quartile levels (lower-25%, median, upper-75%) and they depict the dispersion of the daily values for each considered metric. The upper and lower lines in Figs. 3 and 4 refer to the maximum and minimum daily values of each metric that were identified from the whole time period of the analyzed data.

The median values of the first two metrics (daily mean number of observations per satellite shown in Fig. 3b, daily mean number of satellites per epoch shown in Fig. 4a) over the whole time period of the analyzed data are 933 and 17, respectively. These could be considered as global values for the current network and they can be used as a reference to compare the respective values derived separately

for each station. The stations HOFN (Iceland) and TRO1 (Norway) exhibit the best performance of GNSS signal tracking, in contrast to the Cypriot stations which show the lowest median values for these two metrics (800 and 15 respectively). On the other hand, the Cypriot stations show the smallest IQR values which reveals the stable tracking performance of their equipment from one day to another. The large IQR values emerged for the stations QAQ1 (Greenland), MIKL (Ukraine) and EBRE (Spain) in Fig. 4a are artificial since the receivers of these stations were upgraded within the considered time period of the analyzed data by adding observations from the GLONASS constellation. If we consider that the median of the IQR values for the entire network are 0.5 for the first metric and 25 for the second one, it is evident that the most unstable tracking performance was presented by the station HELG (Germany). This station presents the highest IQR on the daily mean number of satellites per epoch (1.9) and observations per satellite (107).

The third analyzed metric is the daily number of arcs per satellite and it is depicted in Fig. 3a for all network stations. Its global median value over the entire network is 2.6 arcs per satellite. For the Cypriot stations the median values of this metric vary from 1.8 to 2.1, and they are

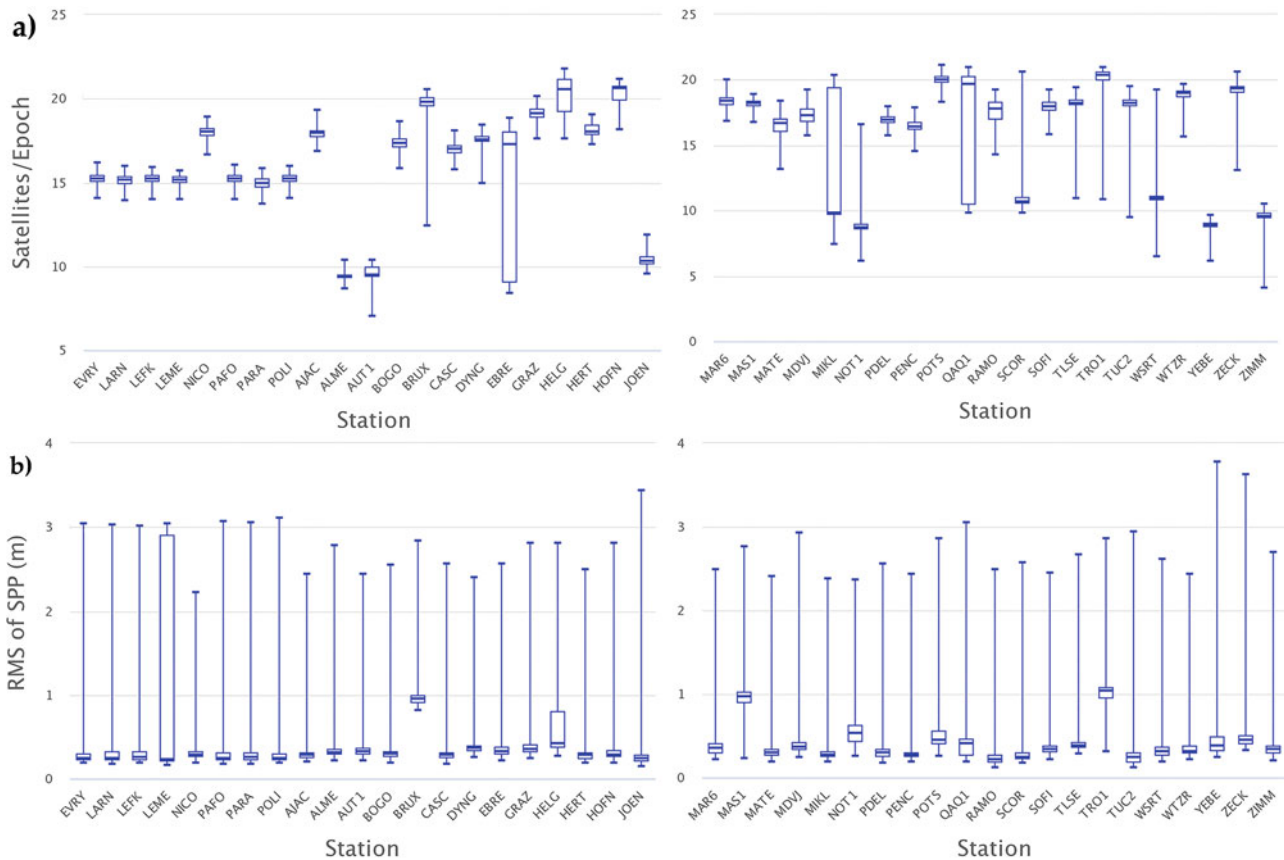


**Fig. 4** Box-plot analysis of the temporal behavior for data-related daily metrics in the regional GNSS network: (a) mean number of observed satellites per epoch, (b) RMS of Single Point Positioning

accompanied by IQR values smaller than 0.2. These results corroborate the stable signal tracking performance at the Cypriot GNSS stations, which was already revealed by the first two metrics. The worst performance is presented by the station SOFI (Bulgaria) which seems to suffer from signal tracking problems as it exhibits a median value of 4.5 arcs per satellite, and also by the station MAR6 (Sweden) which has the highest IQR value ( 1.3) for this particular metric.

The last quality metric to be presented from the pre-processing part of the daily GNSS data is the RMS of the SPP approach, and it is depicted in Fig. 4b for all network stations. This metric represents the precision of the code measurements collected at each station, and its global median value over the entire network is 34 cm. The best performance is reached at the station RAMO (Israel) which shows a daily RMS of about 22 cm, whereas the worst performance occurs at the stations TRO1 (Norway), BRUX (Belgium) and MAS1 (Spain) with daily RMS values to be close to 100 cm (or larger). All other stations seem to have similar precision level for their code measurements, with median values ranging between 22 cm and 45 cm. A special mention needs to be made for the station LEME (Cyprus) which shows a significant variability on the daily precision of its

code measurements (IQR value is about 270 cm), yet the median the daily precision is only 23 cm.

## 2.3 Assessment of Baseline Processing

The next part of the GNSS data processing refers to the analysis of network baselines. This part consists of three individual sub-steps: the formation of the independent baselines which will enter into the last stage of the GNSS data processing procedure (i.e., daily network adjustment), the identification and correction of cycle slips that exist in the baseline data, and the estimation of the baseline integer ambiguities. It should be noted that among these steps the Bernese software performs a number of different strategies for cleaning the baseline data, but we will not refer to these procedures herein and we focus only to the three aforementioned sub-steps.

Applying the OBSMAX strategy (Dach et al. 2015) a number of network baselines were formed for each daily data session. This number varies from 26 to 41 within the entire time period of the GNSS data (see Fig. 5a). The baseline lengths vary from 4 km to 3,222 km, whereas the median

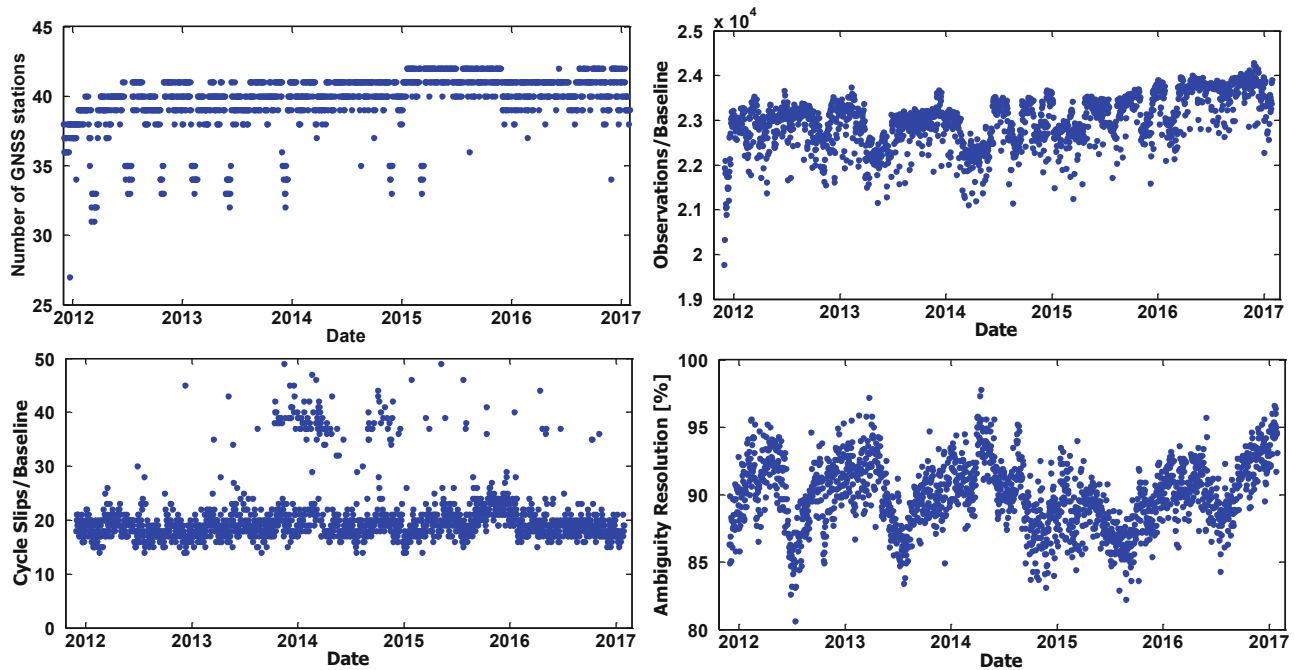


**Fig. 5** Diagnostics from the daily processing in the regional GNSS network: (a) number of stations, (b) number of double difference observations per baseline, (c) normalized number of cycle slips, and (d) percentage of ambiguity resolution

baseline length in the daily networks is 735 km. During the cycle slip correction step, 75 out of 75,062 baselines were rejected due to large RMS values ( $>2$  cm) in their estimated components. In order to reject these baselines and send the Bernese engine back to the single difference formation step, the responsible stations for unaccepted RMS values were identified with the help of auxiliary scripts that were internally applied into the processing procedure. The median of the RMS values of the rest baselines is 11 mm. Figure 5c depicts the daily normalized number of cycle slips per baseline.

Depending on the baseline length, three different ambiguity resolution strategies were applied in the analyzed network (see Table 1). The average ambiguity resolution percentage of the whole processing is 91% and the maximum and minimum values are 80% and 98% respectively. The ambiguity resolution percentage exhibits an intensive annual periodicity with maximum values occurring during the winter and minimum values in the summer period (see Fig. 5d).

## 2.4 Daily Network Solutions

The last part of the daily GNSS data processing is the network adjustment based on the double-difference observational model (e.g., Leick 1995; Hofmann-Wellenhof et al. 2001). This strategy employs the observations of all stations simultaneously by taking into account the generated

mathematical correlations among the input observables. The double-differenced observations were adjusted two times, the first one performed before the ambiguity resolution (free network solution) and the second one after treating the resolved ambiguities as known fixed parameters (fix network solution). The median of the daily RMS values of the estimated coordinates for the whole time period is 1.6 mm in the free network solution. In contrast to the free solution, the addition of the resolved ambiguities improved the precision in all components of the daily estimated coordinates. Specifically, the median of the daily RMS values is 0.8 mm for the X and Z components and 0.4 mm for the Y component. Moreover, the variability of the daily RMS values for the estimated coordinates of all stations decreased with respect to the free daily solutions. The Cypriot stations have the lowest precision of daily estimated coordinates in the Y component, which is almost two times worse than the median value over the entire network.

## 3 Multi-Year Adjustment and Estimation of Station Velocities

The multi-year solution in the regional network of Fig. 2 was computed by combining, at the parameter level, the results obtained from the daily GNSS data processing. Specifically, the station positions and velocities were estimated with the Bernese software v5.2 on the basis of 1878 constraint-free daily solutions using the normal equations

(NEQ) stacking strategy. The reference frame of the multi-year solution is IGb08 (Rebischung et al. 2012) and it was enforced through a no-net-translation (NNT) condition on the positions and velocities of 24 EPN (Class A) selected reference stations shown in Fig. 2. The reference epoch for the estimated positions was set to 2,005.0, in accordance with the reference epoch of the official IGb08 frame.

The daily NEQ stacking and the multi-year network adjustment was performed iteratively in order to identify station position discontinuities and outliers in the available data. Tight relative constraints ( $<0.01$  mm/year) were applied to the estimated station velocities before and after the detected position discontinuities. At each iteration step the post-fit residuals were analyzed separately for each station using the FODITS module which is included in the Bernese software. Two iteration cycles were enough for detecting a total of 11 discontinuities and 16 outliers in the analyzed data. To ensure full compliance of the final multi-year solution with the IGb08 frame, six additional discontinuities at EPN

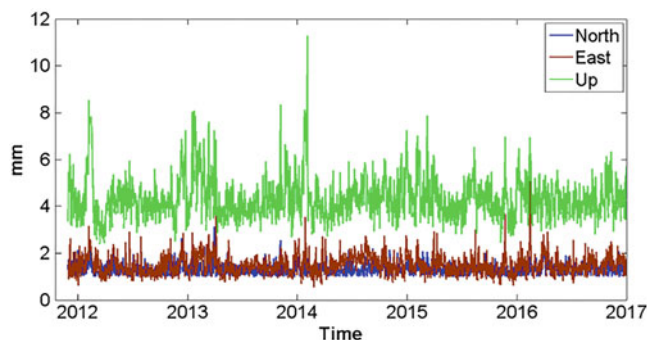


**Fig. 6** RMS of daily post-fit residuals in the multi-year solution

stations were incorporated from the official EUREF solution. It is noted that 15 out of the total 17 discontinuities were caused by equipment changes at EPN stations. The other two position discontinuities occurred at CYPOS stations (LEFK, PAFO) for unknown reasons, yet none of these stations showed evidence of suspected discontinuity on their associated velocity vectors. The RMS values of the post-fit daily residuals in the multi-year solution are shown in Fig. 6 separately for each topocentric component. The respective RMS values for the horizontal components (north/east) of the daily residuals range from 1 mm to 2 mm, whereas the up component does not exceed the level of 5–6 mm. The time series of the estimated Helmert parameters between the multi-year solution and the daily solutions (after their NNT constraining to IGb08 using the official coordinates at the 24 selected EPN reference stations) are shown in Fig. 7.

The estimated position and velocities of the CYPOS stations with respect to IGb08 are given in Table 2. These values have been also transformed to the European Terrestrial Reference System (ETRF2000 realization) using the official transformation tool from the EUREF website (see also Altamimi 2018) and the results are shown in Table 3. Figure 8a, b depict the horizontal velocities of all Cypriot stations in the IGb08 and ETRF2000 frames, respectively. The vertical velocities are not plotted here as their values are rather negligible, with the exception of stations LARN and PAFO. The first one shows a significant vertical motion with downward trend of about 5 mm/year (the nature of this localized vertical motion is currently under investigation) while the second exhibits a considerable uplift at a rate of 1.7 mm/year.

For the purpose of verifying the accuracy of the final multi-year solution, the estimated velocities at the

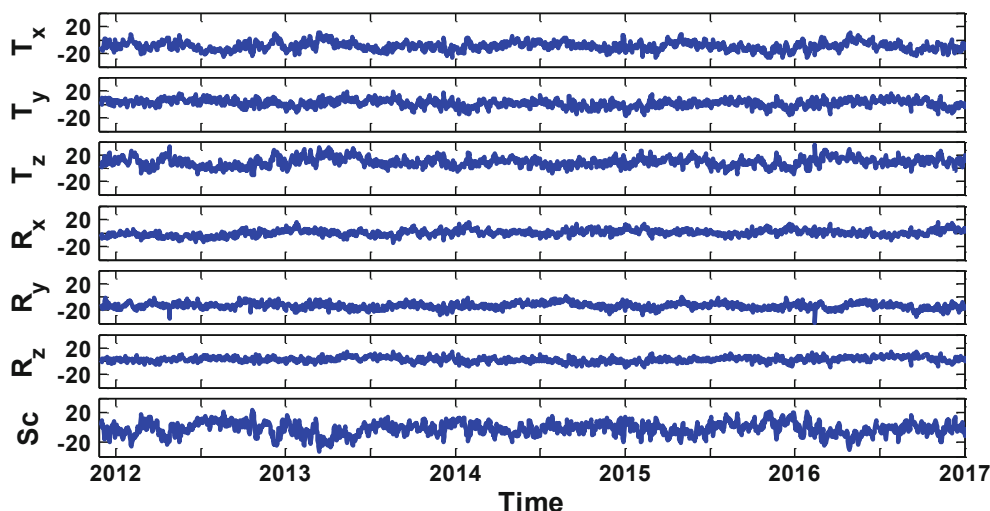


**Fig. 7** Estimated Helmert parameters between the multi-year solution and the NNT-constrained daily solutions in the IGb08 frame. Rotation and scale parameters are expressed in mm after multiplying with the average Earth radius

**Table 2** Estimated positions at epoch  $t_0 = 2005.0$  and geocentric/topocentric velocities of the Cypriot GNSS stations in IGB08. The following time periods apply to these results: (A) 30/11/2011–28/01/2017, (B) 30/11/2011–21/3/2013, (C) 22/3/2013–28/1/2017, (D) 30/11/2011–9/3/2016, (E) 10/3/2016–28/1/2017

	Time period	X ( $t_0$ )(m)	Y ( $t_0$ )(m)	Z ( $t_0$ )(m)	V <sub>X</sub> (mm/year)	V <sub>Y</sub> (mm/year)	V <sub>Z</sub> (mm/year)	V <sub>NORTH</sub> (mm/year)	V <sub>EAST</sub> (mm/year)	V <sub>Up</sub> (mm/year)
EVERY	A	4,389,846.035	2,839,909.319	3,641,645.008	-17.5	11.9	12.2	14.7	19.5	0.2
LARN	A	4,358,623.310	2,899,369.048	3,631,599.949	-21.0	10.3	8.4	13.6	20.2	-4.9
LEFK	B	4,360,035.737	2,870,860.968	3,652,605.816	-18.3	11.0	13.4	16.3	19.3	0.1
	C	4,360,035.736	2,870,860.987	3,652,605.816	-18.4	11.0	13.5	16.4	19.3	0.2
LEME	A	4,403,058.471	2,862,122.638	3,607,630.266	-18.3	12.3	13.0	15.6	20.3	0.3
NICO	A	4,359,415.715	2,874,117.069	3,650,777.829	-18.1	10.7	12.7	15.7	18.9	-0.3
PAFO	D	4,427,028.128	2,812,497.092	3,617,359.846	-17.1	12.3	14.2	16.1	19.6	1.7
	E	4,427,028.124	2,812,497.091	3,617,359.841	-17.1	12.4	14.0	15.9	19.7	1.6
PARA	A	4,335,378.631	2,922,300.281	3,641,064.127	-18.3	10.4	14.4	17.2	18.9	0.6
POLI	A	4,413,130.062	2,803,627.159	3,640,911.041	-17.4	11.5	11.4	14.2	19.1	-0.4

**Table 3** Estimated positions at epoch  $t_0 = 2005.0$  and geocentric/topocentric velocities of the Cypriot GNSS stations in ETRF2000. The following time periods apply to these results: (A) 30/11/2011–28/01/2017, (B) 30/11/2011–21/3/2013, (C) 22/3/2013–28/11/2017, (D) 30/11/2011–9/3/2016, (E) 10/3/2016–28/11/2017

	Time period	X ( $t_0$ )(m)	Y ( $t_0$ )(m)	Z ( $t_0$ )(m)	V <sub>X</sub> (mm/year)	V <sub>Y</sub> (mm/year)	V <sub>Z</sub> (mm/year)	V <sub>NORTH</sub> (mm/year)	V <sub>EAST</sub> (mm/year)	V <sub>Up</sub> (mm/year)
EVERY	A	4,389,846.408	2,839,909.081	3,641,644.798	2.5	-6.0	1.4	1.8	-6.4	-0.2
LARN	A	4,358,623.686	2,899,368.813	3,631,599.741	-0.8	-7.6	-2.4	0.8	-5.9	-5.3
LEFK	B	4,360,036.112	2,870,860.732	3,652,605.607	1.8	-6.8	2.6	3.5	-6.7	-0.3
	C	4,360,036.111	2,870,860.751	3,652,605.607	1.7	-6.8	2.8	3.6	-6.6	-0.3
LEME	A	4,403,058.844	2,862,122.399	3,607,630.055	1.7	-5.7	2.1	2.7	-5.7	-0.2
NICO	A	4,359,416.090	2,874,116.833	3,650,777.620	2.0	-7.2	2.0	2.9	-7.1	-0.7
PAFO	D	4,427,028.499	2,812,496.852	3,617,359.634	2.8	-5.8	3.3	3.2	-6.3	1.2
	E	4,427,028.495	2,812,496.852	3,617,359.630	2.8	-5.7	3.1	3.0	-6.2	1.2
PARA	A	4,335,379.009	2,922,300.047	3,641,063.919	2.0	-7.3	3.8	4.5	-7.1	0.1
POLI	A	4,413,130.433	2,803,626.919	3,640,910.830	2.5	-6.5	0.5	1.3	-6.8	-0.9



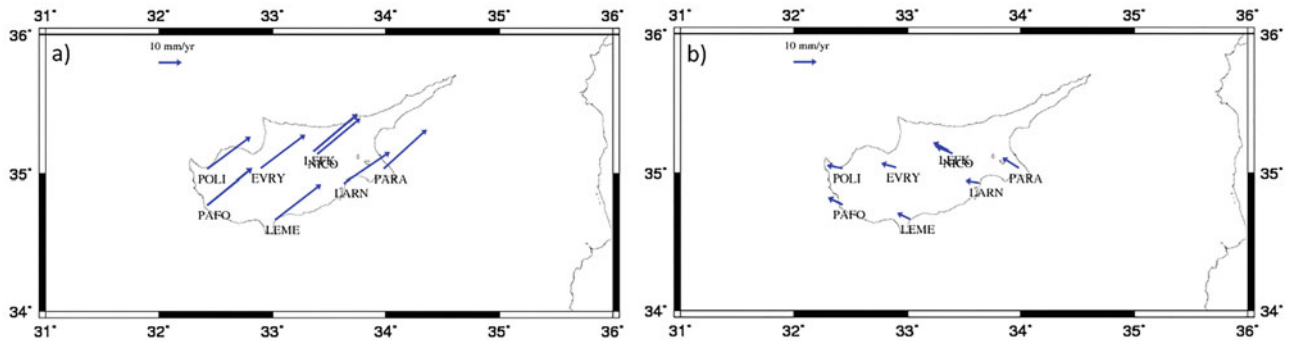


**Fig. 8** Estimated horizontal velocities at the Cypriot GNSS stations in the IGb08 frame (left) and the ETRF2000 frame (right)

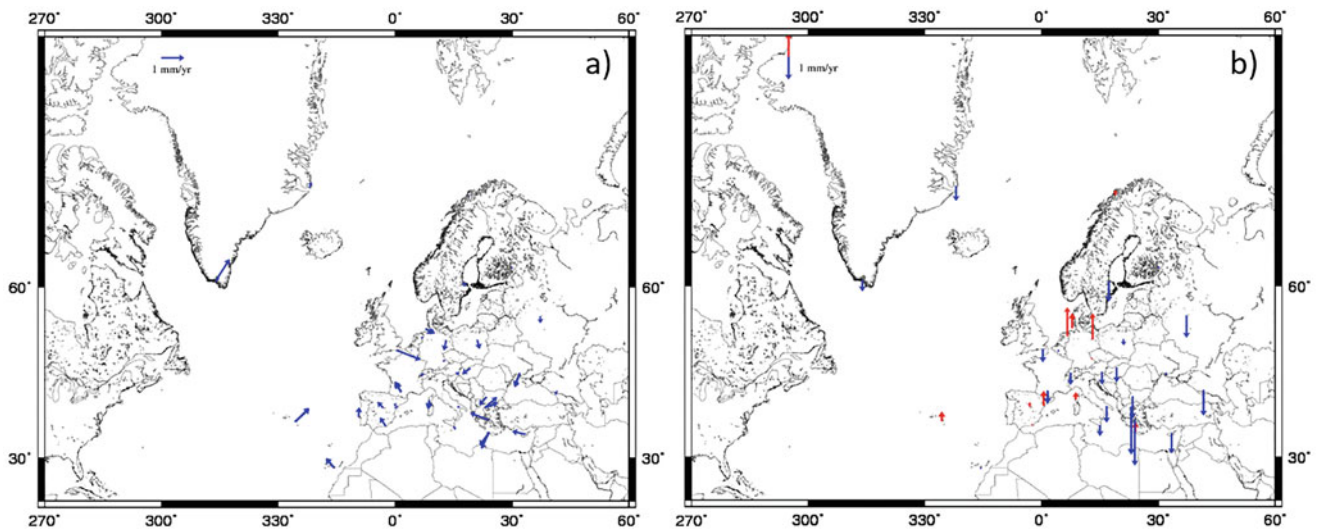


**Fig. 9** The velocity differences at 35 EPN stations (NICO included) in the IGb08 frame at the (a) horizontal and (b) vertical level. The differences are taken between the official values provided by EUREF (EPN\_A\_IGb08\_C1934) and the estimated values from our multi-year solution

35 EPN stations have been compared with the official velocity values provided by EUREF in the IGb08 frame (EPN\_A\_IGb08\_C1934). Figure 9 shows the velocity differences at 35 EPN stations (NICO included) in the IGb08 frame at the horizontal (Fig. 9a) and the vertical level (Fig. 9b), while Fig. 10 depicts the histograms of these velocity differences for the north, east and up components. Their average value is close to zero ( $<0.1$  mm/year) for all three components, whereas their dispersion for the north, east and up components is 0.6 mm/year, 0.4 mm/year and 0.5 mm/year, respectively. Based on these values, it can be inferred that the multi-year solution exhibits a very good agreement with the official EUREF velocities. The existing differences are mainly due to the different time spans of the used daily observations (62 months in our case vs. 25 years in the case of EUREF's multi-year solution), the different computational strategies (NEQ stacking in our case vs. time-series stacking in the case of EUREF's multi-year solution), and the different sets of reference stations that were used for datum definition in the respective solutions.

## 4 Summary

The daily GNSS data of the CYPOS network were processed for a total of 1,878 days within the period 2011–2017, jointly with a subset of 34 stations of the EUREF Permanent GNSS network. Overall, all Cypriot stations provided high quality data with excellent signal tracking performance, observing on average 15 satellites per day and 2 arcs per day for each satellite. The mean ambiguity resolution percentage in the daily solutions of the above network is 91%, whereas the average precision of the daily estimated coordinates is 0.8 mm for the X and Z components and 0.4 mm for the Y component. The constraint-free daily solutions have been subsequently used to compute a multi-year secular solution in the IGb08 frame through the NEQ stacking strategy by applying the NNT condition on the coordinates (positions + velocities) of 24 EPN Class-A reference stations. The resulting solution delivered a high-quality densification of the International Terrestrial Reference Frame in the region

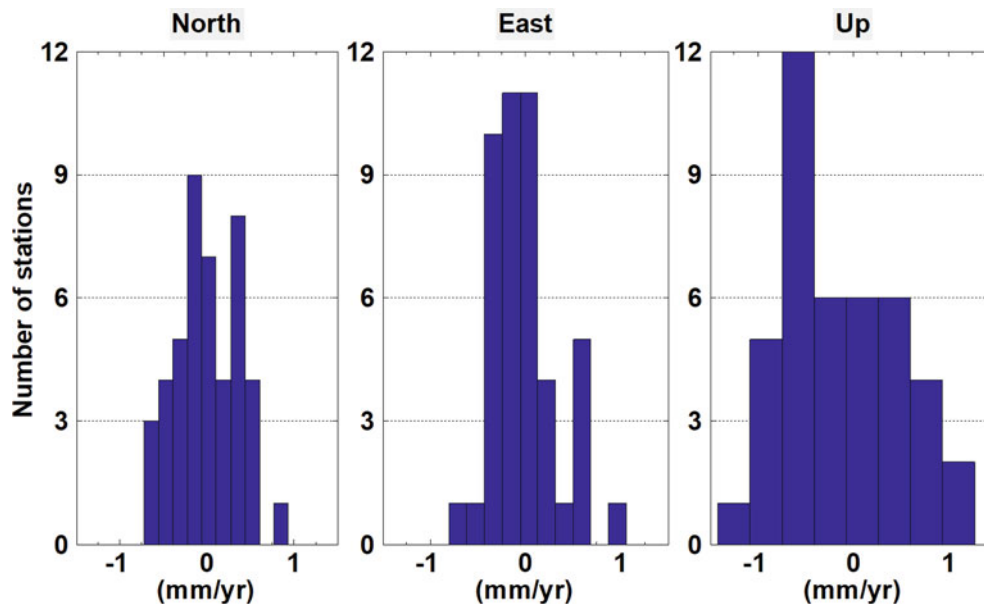


**Fig. 10** Histograms of the velocity differences at 35 EPN stations (NICO included) in the IGB08 frame. The differences are taken between the official values provided by EUREF (EPN\_A\_IGB08\_C1934) and the estimated values from our multi-year solution

of Cyprus, and gave a reliable estimate of the velocity field at the CYPOS stations. The analysis presented in this study will be further continued with the assimilation of additional daily data from the CYPOS stations (after 2017) and the re-computation of a new multi-year solution in the IGS14 reference frame.

**Acknowledgements** This study has been performed in the context of the CyCLOPS project (INFRASTRUCTURES/1216/005) which is co-funded by the European Union Regional Development Fund and the Republic of Cyprus through the Research and Innovation Foundation.

## References

- Altamimi Z (2018) Relationship and transformation between the international and the European terrestrial reference systems. EUREF Technical Note 1. <http://etrs89.ensg.ign.fr/pub/EUREF-TN-1.pdf>
- Bruyninx C, Legrand J, Fabian A, Pottiaux E (2019) GNSS metadata and data validation in the EUREF Permanent Network. *GPS Solutions* 23:106. <https://doi.org/10.1007/s10291-019-0880-9>
- Chatzinikos M, Pottiaux E, Bruyninx C, Legrand J (2017a) Enhancing the reliability of GNSS network solutions: key performance indicators and decision models in the new tool “ROBER”. IGS Workshop, Paris, 3–7 July 2017
- Chatzinikos M, Pottiaux E, Bruyninx C, Legrand J (2017b) ROBER: a new tool for step-wise analysis of the quality of GNSS network-based processing. EUREF Annual Symposium, Wroclaw, 17–19 May 2017
- Dach R, Lutz S, Walser P, Fridez P (2015) Bernese GNSS Software Version 5.2. User manual, Astronomical Institute, University of Bern, Bern Open Publishing. <https://doi.org/10.7892/boris.72297>. ISBN: 978-3-906813-05-9
- Danezis C, Chatzinikos M, Kotsakis C (2020) Linear and nonlinear deformation effects in the permanent GNSS Network of Cyprus. *Sensors* 20(6):1768. <https://doi.org/10.3390/s20061768>
- Dow JM, Neilan RE, Rizos C (2009) The international GNSS service in a changing landscape of global navigation satellite systems. *J Geod* 83:191–198
- Hofmann-Wellenof B, Lichtenegger H, Collins J (2001) *GPS theory and practice*, 5th rev edn. Springer, Wien
- Legrand J, Bruyninx C, Altamimi Z, Caporali Z, Kenyeres A, Lidberg M (2021) Guidelines for EUREF densifications. <https://doi.org/10.24414/ROB-EUREF-Guidelines-DENS>
- Leick A (1995) *GPS satellite surveying*. Wiley, ISBN 0-471-30626-6
- Rebischung P, Schmid R (2016) IGS14/igs14.atx: a new framework for the IGS products. Poster presentation at AGU Fall Meeting, San Francisco, 12–16 December 2016
- Rebischung P, Griffiths J, Ray J, Schmid R, Collilieux X, Garayt B (2012) IGS08: the IGS realization of ITRF2008. *GPS Solutions* 16:483–494

**Open Access** This chapter is licensed under the terms of the Creative Commons Attribution 4.0 International License (<http://creativecommons.org/licenses/by/4.0/>), which permits use, sharing, adaptation, distribution and reproduction in any medium or format, as long as you give appropriate credit to the original author(s) and the source, provide a link to the Creative Commons license and indicate if changes were made.

The images or other third party material in this chapter are included in the chapter’s Creative Commons license, unless indicated otherwise in a credit line to the material. If material is not included in the chapter’s Creative Commons license and your intended use is not permitted by statutory regulation or exceeds the permitted use, you will need to obtain permission directly from the copyright holder.





# Geodetic Analyses at the National Geographic Institute of Spain

José C. Rodríguez, Esther Azcue, Víctor Puente, José A. López-F., José A. López-P., Elena Martínez, José A. Sánchez Sobrino, Marcelino Valdés, Beatriz Vaquero, and Pablo de Vicente

## Abstract

The National Geographic Institute of Spain (IGN Spain) develops, operates, and exploits the Spanish national geodetic networks and their associated infrastructure. This includes the permanent networks of reference GNSS (Global Navigation Satellite System) receivers, VLBI (Very Long Baseline Interferometry) telescopes, and a new SLR (Satellite Laser Ranging) station under construction at the Yebes Observatory. In order to fully exploit the opportunities offered by the availability of these space geodetic techniques, IGN has been operating Analysis Centres of GNSS and VLBI for a number of years, with the recent addition of an Associated Analysis Centre of the International Laser Ranging Service.

IGN Spain is a EUREF Analysis Centre since 2001, contributing with their weekly and daily coordinate solutions to the realisation of the European Terrestrial Reference System. The activities of the AC include projects such as IBERRED, for geodynamic purposes, and the participation in the European E-GVAP programme for meteorological applications. Over the last years, IGN Spain has expanded its contribution to geodetic VLBI analysis, starting in 2019 the operational analysis of VLBI sessions and the submission of the respective solutions (containing consistently estimated Earth Orientation Parameters, station coordinates and source positions) to the International VLBI Service for Geodesy and Astrometry (IVS). Additionally, the reprocessing of the historical VLBI data since 1979 is ongoing, which is the basis for future contributions to the IVS combination series that will be provided for future realisations of the international terrestrial reference frame (ITRF). The latest addition to IGN Spain analysis capabilities is the IGN-Yebes Associated Analysis Centre. Highlights of its activities are the participation in the ITRF2020 reprocessing in collaboration with the Analysis Centre NSGF in the UK, and the computation of SLR centre-of-mass corrections for spherical geodetic satellites.

IGN strives to further exploit the synergies between these groups and work towards the combined analysis of the data. A description of the analysis activities of IGN Spain, along with its future prospects, is presented.

## Keywords

GNSS · IGN · SLR · VLBI

---

J. C. Rodríguez (✉)  
SLR AC, Yebes Observatory (IGN), Yebes, Guadalajara, Spain  
e-mail: [jc.rodriguez@oan.es](mailto:jc.rodriguez@oan.es)

E. Azcue  
GNSS AC, Instituto Geográfico Nacional, Madrid, Spain  
e-mail: [eazcue@mitma.es](mailto:eazcue@mitma.es)

---

V. Puente  
VLBI AC, Instituto Geográfico Nacional, Madrid, Spain  
e-mail: [vpuente@mitma.es](mailto:vpuente@mitma.es)

J. A. López-F. · J. A. Sánchez Sobrino · M. Valdés  
Instituto Geográfico Nacional, Madrid, Spain



**Fig. 1** Aerial view of the Observatory of Yebes, with the 40 m VLBI telescope in the foreground and the VGOS antenna to the right hand side (H.M. Pérez Martínez)

## 1 Introduction

The geodetic infrastructure required to meet the present and future challenges of this discipline range from affordable GNSS receivers deployed in the field to full-blown observatories with a host of complex instruments. Permanent geodetic networks of observing stations and tide gauges; technique-specific instrumentation and ancillary equipment; satellite constellations; computing resources and analysis centres; and data archival and distribution systems, among a multitude of others, are all part of this complex infrastructure (National Research Council 2010). The construction, maintenance and operation of the hardware and facilities involved is a costly endeavour, taken up by a large number of national public agencies and organisations. The societal benefits arising from this effort are manifold and go beyond the contribution to geoscientific research for which precise geodesy provides a basis (National Research Council 2010).

The National Geographic Institute of Spain (IGN Spain, *Instituto Geográfico Nacional*) is the Spanish agency responsible for the design, maintenance and running of the national geodetic networks. This currently includes a network of permanent GNSS stations, tide gauges, legacy and new generation VLBI telescopes, and in the near future a modern, new SLR station. The Observatory of Yebes (Guadalajara), Fig. 1, with a long history of astronomical VLBI research

activities, has contributed geodetic VLBI observations since 1995. In 2014 a new VGOS (VLBI Global Observing System) radiotelescope was installed. This was the first of the four antennas planned within the RAEIGE project (Atlantic Network of Geodynamical Fundamental Stations<sup>1</sup>), which entails the construction of VGOS radiotelescopes in Spanish and Portuguese territories in the North Atlantic region (López-Pérez 2021). With the addition of the SLR system under construction, expected in 2023, Yebes Observatory will become a core site of the Global Geodetic Observing System.

Beyond the most conspicuous physical facilities and instrumentation, the material and human resources required for the processing and analysis of global geodetic data is an integral part of the precise global geodetic infrastructure, resulting in primary and derived products that ultimately enable the exploitation of the observations for scientific and practical use. In parallel with the development of the ground observation networks for various techniques, IGN Spain has devoted ample resources to boost and consolidate its expertise in the area of the analysis of global geodetic data. In this paper we describe recent, and planned activities of the existing IGN analysis centres. These include the analysis of the techniques GNSS, VLBI, and SLR, which IGN currently (or in the immediate future) operates, contributing with its observations to the products operationally generated by the respective services of the International Association of Geodesy.



**Fig. 2** Spanish National GNSS Permanent Network (ERGNSS). Blue triangles are IGN stations; Green triangles are stations in a joint-ownership

## 2 GNSS

The GNSS Analysis Centre (AC) of IGN Spain has a long history and broad experience in GNSS data processing. The activities of this AC started in 1998, for the processing of the Spanish National GNSS Permanent Station Network (ERGNSS). Since then, it has been involved in many national and international projects for both scientific research and civil purposes. In the following, we detail some of the current projects and lines of work of the analysis centre.

### 2.1 The Spanish National GNSS Permanent Network and Real Time Positioning Service

The Spanish permanent GNSS network, ERGNSS, is currently composed of 118 GNSS permanent stations homogeneously distributed throughout the national territory. Some of these stations are in a joint ownership with institutions that manage regional GNSS networks. Four stations are integrated in the International GNSS Service (IGS) network and 25 of them in the EUREF Permanent GNSS Network

(EPN). The location of the stations of the ERGNSS network is shown in Fig. 2.

This network has two fundamental objectives. Firstly, the maintenance of the geodetic frame through the publication of RINEX<sup>2</sup> data and support for postprocessing. Secondly, together with all the GNSS stations operated by regional institutions, the dissemination in real-time of the geodetic frame through the Real Time Positioning Service (SPTR, *Servicio de Posicionamiento en Tiempo Real*<sup>3</sup>). SPTR is an accurate (cm level) real time and freely accessible GNSS positioning service offered by IGN using GNSMART software (GEO++<sup>4</sup>). SPTR is in operation since 2016 and generates GNSS differential network corrections for GPS and GLONASS. The new service including also the GALILEO and BEIDOU constellations became operational in January 2022. This service offers network-based solutions, communicating in real time to a server centre which sends to users modelled corrections for the entire coverage area. Single stations solutions are offered as well. This system finds ap-

<sup>2</sup>Receiver Independent Exchange Format, standard format used to interchange satellite navigation system data.

<sup>3</sup><https://www.ign.es/web/ign/portal/gds-gnss-tiempo-real>.

<sup>4</sup><https://www.geopp.de/gnsmart/>.

lications in the fields of surveying, cartography, agriculture, and civil engineering among others.

## 2.2 EUREF Permanent GNSS Network Analysis Centre

IGN is Analysis Centre of EUREF since 2001, processing solutions for a subnetwork of GNSS permanent stations covering mainly western Europe (Spain, Portugal, France, Italy, Great Britain, Ireland...). The primary purpose is to provide access to the European Terrestrial Reference System 89 (ETRS89), making available GNSS tracking data as well as the time series of precise positions, velocities and tropospheric parameters. The AC computes daily and weekly station positions along with station tropospheric parameters (zenith total delays and gradients). The so-called *rapid* products are available with a latency of one day and are computed using rapid orbits and clocks provided by the Center for Orbit Determination in Europe, (Dach et al. 2020). The *final* products are available with a latency of three weeks and a combined weekly solution is obtained. The software currently used by the AC is Bernese GNSS Software Version 5.2 (Dach et al. 2018), for the processing of GPS, GLONASS and GALILEO observables .

In addition to the routine processing activities, the IGN AC participates in EUREF reprocessing efforts and its densification projects. *Repro* campaigns consist in the reprocessing of historical data employing strategies agreed by the analysis community for the removal of the influence of reference frame changes, including upgrades of modelling standards and software implementations. The EPN densification (Kenyeres et al. 2019) aims to realise a homogeneous, high quality position and velocity product in a well defined reference frame. IGN contributes to the EPN densification project with the regular submission of the IBERRED data analysis results, detailed in the next section.

## 2.3 IBERRED

Apart from the more than 100 GNSS permanent stations of the ERGNSS network, there are several public GNSS permanent stations installed in the Iberian Peninsula and its surroundings, owned by a number of different institutions from Spain and Portugal. IGN processes continuously the majority of these stations (480 stations approximately) in a project called IBERRED (Valdés et al. 2012a). The main objective of IBERRED is the densification of the ERGNSS, getting precise coordinate estimates for other projects, monitoring the behavior of the different stations for geodynamic purposes, and obtaining their position time series and velocity estimation (e.g. Fig. 3). The solutions are submitted to the EUREF

Dense Velocities Project, whose objective is the realisation of a continental-scale, homogeneous, high quality position and velocity product in Europe.<sup>5</sup> Weekly and daily processing is carried out with precise and rapid orbits, respectively. The coordinates from a subnetwork of IBERRED, in combination with solutions from other regional GNSS analysis centres, are used to obtain the official coordinates of the Spanish GNSS stations every year.

## 2.4 GNSS Tropospheric Products for Meteorology

At the request of the Meteorological State Agency of Spain (AEMET), IGN participates since 2008 in the E-GVAP project<sup>6</sup> as an expert GNSS processing institution. The goal of E-GVAP is the application of GNSS data in the field of meteorology, as a near real-time input to the operational numerical weather prediction models. Provided that station coordinates are precisely known, the delay caused by the troposphere in the GNSS signals can be estimated accurately. This parameter, the Zenith Total Delay (ZTD), is determined through the set of slant path delays from each station to all visible satellites, and it is closely related to the content of water vapor in the atmosphere. Assimilating the estimated ZTD into numerical weather prediction models can significantly improve them. As part of its contribution, the IGN AC processes more than 300 GNSS stations every hour in the target geographic area (Valdés et al. 2012b). All the observations from the previous hour are processed, and ZTDs estimated at time steps of 15 min. These are then immediately distributed to the meteorological agencies.

## 2.5 Other Analysis and Research Activities

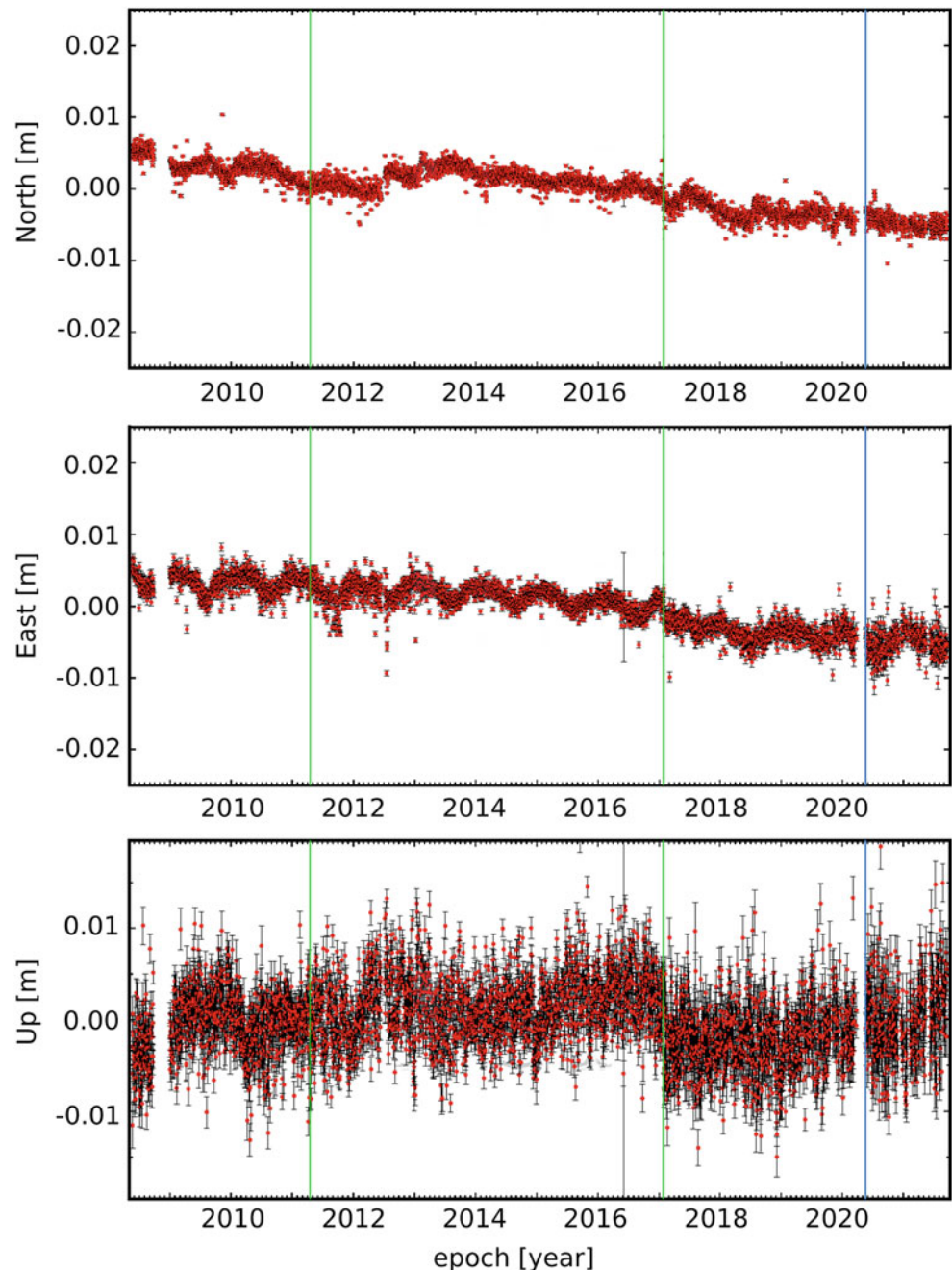
Other research activities in the field of the GNSS in which IGN is involved include the following:

- Volcano monitoring system. IGN develops, operates, and exploits the Spanish national geodetic networks and their associated infrastructure. This includes GNSS networks designed for the monitoring of volcanic activity and the assessment of the associated risks. In the Canary Islands, a regional GNSS network is specially designed and processed to monitor local deformations.
- Tsunami warning system. GNSS data are used to study the ionospheric electron density by analyzing the effect of free electrons on the propagation of dual-frequency GNSS signals. Earthquakes and tsunamis generate many different waves in the atmosphere that can perturb the electronic

<sup>5</sup><https://epnd.sgo-penc.hu/>.

<sup>6</sup><http://egvap.dmi.dk>.

**Fig. 3** Position time series, relative to their mean values, of IGNE GNSS station in Madrid (Spain) w.r.t. ETRS89 (top: North; middle: East; bottom: Up component). The green vertical lines show changes in the reference frame, and the blue lines receiver changes



density in the ionosphere. The propagation through the ionosphere of the perturbations generated by these waves originates the Travelling Ionospheric Disturbances (TID) that can be remotely detected by GNSS. Based on this, the IGN is investigating the integration of GNSS data into the Spanish National Tsunami Warning System for the verification of the occurrence of a tsunami before it arrives at the Spanish coast (Cantavella et al. 2021).

- GNSS reflectometry (GNSS-R) is a technique used for the study of variations in the height of sea level and inland waters, as well as for the study of soil moisture, that

is based on the comparison of the direct and reflected noise signal on GNSS stations. The main advantage of this method is that allows the connection between sea level measurements and the global terrestrial reference frame. With this objective, IGN has conducted a study to compare the sea level time series determined by means of GNSS-R with tide gauge measurements in Spanish stations (Puente et al. 2019). A historical reprocessing of the observations of GNSS receivers co-located with tide gauges is planned to expand the reflectometry time series and perform long-term comparisons.

### 3 VLBI

IGN has a strong background concerning the technical aspects of geodetic VLBI, and hosts VLBI infrastructure: a 40-meter diameter radio telescope located in Yebes (Guadalajara) that participates in VLBI geodetic observation campaigns since 2008, and the VGOS radio telescopes of the RAEGE project (López-Pérez 2021). In order to expand its contribution to geodetic VLBI analysis, IGN set up an analysis team in 2018. As result of this effort, IGN is an official Analysis Centre of the International VLBI Service for Geodesy and Astrometry (IVS) (Nothnagel et al. 2017) since March 2020. The activities of this AC are summarized in the lines of work detailed below.

#### 3.1 Contribution to the IVS

The IVS is in charge of providing VLBI data and products for the scientific community. Among others, IVS products consist of terrestrial and celestial reference frames and Earth Orientation Parameters (EOPs). Solutions in SINEX format<sup>7</sup> estimated by individual Analysis Centres are combined by the IVS Combination Centre.

After test period, IGN started to provide operational solutions for 24 h IVS R1 and R4 sessions in March 2020. Since then, around 150 solutions have been submitted to the IVS Combination Centre. The products should be uploaded in less than 24 h since the data is available. These solutions include estimates of the full set of Earth Orientation Parameters, as well as station and source coordinates. The processing is fully automatized except for the manual interaction usually needed in VLBI analysis in order to identify outliers and clock breaks in the residuals. For the analysis of the VLBI sessions, the software package Where (Kirkvik et al. 2017) is used.

The efforts of the analysis team are now focused on the reprocessing of historical VLBI data since 1979, in order to be ready to contribute to future realisations of the International Terrestrial Reference System within the IVS solution. In addition, it is also foreseen to participate in the future in the operational analysis of VLBI intensives sessions, for the rapid determination of UT1.

#### 3.2 Research Activities

The activity of the AC is not limited to the computation of IVS routine products, but it strives to pursue its own lines of research. The team has conducted studies on the

topic of geodetic VLBI analysis that have already led to publications in the scientific literature. These contributions are summarised below.

A first study (Puente 2021) was focused on the influence of a priori Zenith Wet Delays (ZWD) in the analysis of VLBI CONT sessions. The aim of this paper was to study impact of including external GNSS estimates to model a priori ZWD in VLBI analysis, as well as other models of a priori ZWD. It should be noted that troposphere delay is one of the major sources of error in VLBI analysis. As result of this work, it was found that modelling a priori ZWD has no significant impact either on the VLBI baseline length and coordinates repeatabilities. Nevertheless, using a model for a priori ZWD can modify the magnitude of the estimated coordinates a few millimeters in the up component with respect to the non-modelling approach. Additionally, it was found that modelling a priori ZWD has a small but significant impact on EOPs and troposphere estimates.

A second work (Puente et al. 2021) was devoted to the comparison of common VLBI and GNSS estimates in CONT17 campaign (Behrend et al. 2020). The aim of CONT campaigns is to acquire VLBI data during 15 days of continuous sessions to serve a variety of scientific and technical purposes. In the referred work, VLBI estimates of EOPs, station coordinates and troposphere – Zenith Total Delays (ZTD) and gradients – were compared to those estimated through GNSS observations. Solutions from different AC were considered in the comparison analysis, including all the available IVS and IGS solutions and two VLBI series obtained by IGN, using Where and VieVS (Böhm et al. 2018) software packages. This extensive analysis provides a representative view of the inter-technique differences under the same observation conditions.

Finally, there is also an ongoing activity related to the assessment of the performance of VGOS sessions. This activity is mainly focused on the sessions in which RAEGE antennas are involved, so that appropriate feedback can be provided to the station managers.

### 4 SLR

IGN started its involvement with the International Laser Ranging Service (ILRS) (Pearlman et al. 2019) during the design stages of the new Satellite Laser Ranging station at the Observatory of Yebes. Concurrently with the construction phase of the system, the first activities in the area of data analysis have emerged. Since September 2020, IGN-Yebes is a new Associate Analysis Centre (AAC) of the ILRS. The activities of this AAC since its creation have focused on tasks related to the ILRS contribution to the forthcoming release of the International Terrestrial Reference Frame (ITRF), in the shape of two different efforts detailed below.

<sup>7</sup>Solution INdependent EXchange data format, used in the geodetic community to store and transfer the solutions derived in various types of analysis: <https://www.iers.org/IIERS/EN/Organization/AnalysisCoordinator/SinexFormat/sinex.html>.



#### 4.1 SLR Reprocessing for ITRF

A close collaboration between the ILRS Analysis Centre NSGF (NERC Space Geodesy Facility, UK<sup>8</sup>) and IGN-Yebes AAC was established for the SLR data reprocessing for ITRF2020. The collaboration enabled the timely delivery of the reanalysis, by distributing the burden of assorted issues that arise in the production of these kinds of products, such as software development tasks, implementation of new or updated models, new output formatting requirements, and numerous data quality checks.

Preparations for the reprocessing efforts began within the ILRS Analysis Standing Committee (ASC) in 2020. A number of updates were introduced in the processing strategy. Among these, a major highlight is the new handling of systematic errors in SLR data (Pavlis et al. 2021). The impact of the presence of errors in some critical SLR-derived products was put into sharp relief (Appleby et al. 2016) by the time of publication of ITRF2014. Numerous investigations on this topic followed within the ILRS ASC (Luceri et al. 2019), eventually leading to the adoption of a new analysis strategy to handle range biases, and to a major update of the so-called centre of mass corrections to the spherical geodetic satellites employed by the ILRS in the generation of its official products (Rodríguez et al. 2019). Another significant update in the ILRS reprocessing is the inclusion of new blocks in the SINEX solutions to detail all the corrections applied to the observations. These comprise the set of corrections derived from the combination of the range biases estimated by all ACs in an ILRS ASC pilot project (Pavlis et al. 2021); the new target signature offset values (centre of mass corrections) (Rodríguez et al. 2019); time corrections, mainly from results obtained by the T2L2 experiment on the Jason-2 satellite (Exertier et al. 2017); and known offsets arising from engineering issues communicated by the stations. The breakdown of all the corrections serve the double purpose of i) enabling a strict quality control of the solutions; ii) providing end users with all the quantities that, together with the raw observations, led to the final results obtained. Other new items include the implementation of the recommended model of the high-frequency Earth orientation parameters, the adoption of the IERS secular linear pole model, and the use of gravity models based on the latest GRACE release with associated dealiasing product AOAD (Dobslaw et al. 2017). The specific gravity model employed for the reanalysis in the NSGF/IGN-Yebes solutions was EIGEN-GRGS.RL04.MEAN-FIELD (Lemoine et al. 2019).

NSGF and IGN-Yebes implemented the required changes in the software package SATAN (Sinclair and Appleby 1988), which currently is co-developed by the two centres. The reprocessing comprised almost 40 years of observations

(1983–2020). The solutions are split in two parts, with a first period of 15-day solutions based only on LAGEOS-1 observations, 1983–1993. Here station coordinates are estimated once for the whole arc, and EOPs every three days due to the inherent weakness of the solutions with a single satellite available. This is followed from 1993 onward by 7-day arc combined solutions from LAGEOS-1 and LAGEOS-2, plus Etalon-1 and Etalon-2 observations when these are available in sufficient volumes (since 1995 approximately). For the almost last 30 years of data, daily EOPs (polar motion and LOD) are estimated in the combined solutions, and station coordinates are estimated at the mid-point of the arc, along with the state vectors and other dynamical parameters.

The use of more satellite targets, plus the combination of many cumulative instrumental and modelling improvements achieved throughout the period of analysis, results in improvements of the post-fit RMS of the LAGEOS-1 observations from almost 4 cm in the 1983–1993 period to less than 8 mm in the last decade. For the best stations of the network these figures are in the order of less than 3 cm for the old, single satellite data, and the less than 7 mm obtained with modern data with our setup.

#### 4.2 Target Signature Modelling

IGN-Yebes AAC has provided the latest updates to the set of target signature offset values adopted by the ILRS ASC for all its products (including the ITRF2020 reprocessing). These are fundamental corrections required in the geodetic analysis of SLR data relating the time of flight observations to the centre of mass of the spacecraft, i.e. the actual points whose motions are computed in the orbital analysis. The centre of mass offsets account for the spread and therefore additional delay that the laser pulses experience when reflected off several cube corners arranged over an spherical surface. The calculation of the average optical reflection points and the timing delays caused by the detection equipment requires the use of satellite- and system-specific information, resulting in a set of values that represent the average corrections to apply per normal point<sup>9</sup> (NP).

The modelling upgrade upon which the currently adopted set of values is based on is that given in Rodríguez et al. (2019), where the more detailed approach relative to previous efforts for the computation of these offsets is discussed. Several minor updates to the values of several stations have been produced since the first release, thanks to the input of several users who noticed a few discrepancies in the correction tables. The latest update was originated by the need to reprocess the so-called historical SLR data from

<sup>8</sup><http://sgf.rgo.ac.uk/analysis>.

<sup>9</sup>SLR observations compressed to single values at fixed intervals following certain algorithm; the most common data format for geodetic analysis.

the 1980s. Although correction values for many of these stations had been computed and made available in the original release of the tables, these had not been tested “in the field”. In the reanalysis campaign it was quickly realised that several prominent stations with a strong data contribution in this period were missing, due to inconsistencies between the records and logs available for the pre-ILRS network. Fortunately, most of those stations were part of the first generation of NASA MOBLAS systems, for which several values had already been computed. The pragmatic solution proposed by IGN-Yebes and accepted by the ILRS ASC consisted in computing the average values of all the systems with identical hardware, according to the records, to fill the missing values. At this point, it must be stressed that the precision levels attained by the SLR network in the 1980s were much poorer than current ILRS standards. Those systems were two hardware generations behind the state of the art; lasers, detectors and timers were plagued by a multitude of instrumental limitations; and the standardisation, guidelines and quality control procedures observed today were lacking. Furthermore, detailed information on the hardware configuration and operation of those stations is not always available. As a result, striving to model the behaviour of the pre-ILRS systems with the level of detail possible for the current stations is of limited practical use. At any rate, a strong motivation for providing the missing values on the basis of the same modelling standards is consistency, and with it the possibility to perform meaningful comparisons between data from different stations.

The combined effect of the newly adopted set of centre of mass corrections and the new handling of systematic errors in the solutions results in a scale change of the SLR-specific frame of up to 1 ppb. Of this, the centre of mass corrections alone are responsible for about 0.65 ppb (Rodríguez et al. 2019). Although it must be noted that the co-estimation of range biases with station coordinates absorbs errors in the centre of mass values and are therefore not additive, the overall scale change that can be attributed to the upgraded centre of mass corrections is nevertheless evidence of smaller remaining errors in the technique and its analysis. While previously the scale difference between SLR and VLBI was quantified as  $1.37 \pm 0.10$  ppb in ITRF2014 (Altamimi et al. 2017), the SLR solutions provided for ITRF2020 (both NSGF/IGN-Yebes as well as those from other ACs) result in a much closer agreement between the two techniques, down to approximately 0.3 ppb (Pavlis et al. 2021).

The target signature offsets employed in the ITRF2020 ILRS reprocessing, and subsequent updates including the missing values for core stations operating in the 1983-1993 period, as well as supporting material, can be retrieved from the Yebes Observatory website.<sup>10</sup>

## 5 Conclusions

Geodetic science and its results underpin most research of the Earth system. A number of scientific areas depend directly on the availability of a geodetic infrastructure that provides observations and products with as complete a global coverage as possible. These include sea-level change, terrestrial water cycle, geological hazards, weather and climate, and geodynamics. Additionally, geodetic products enable many practical applications of enormous societal benefits such as early warning systems for natural hazards, road and sea autonomous navigation, precision agriculture, and the precise navigation and orbit determination of Earth-orbiting spacecraft. The availability of geodetic products, their timely delivery, quality and constant improvement is the responsibility of technique-specific analysis centres, funded and run by many different institutions internationally.

The National Geographic Institute of Spain currently counts with analysis centres in GNSS, VLBI, and SLR. In this paper we have reviewed their most salient contributions and recent activities. IGN GNSS AC is fully operational and trained in processing a vast network of stations. The AC is prepared to process solutions with the latest developments in the area of GNSS (e.g. GALILEO observables, regional and global networks). Its current lines of work are aimed at expanding its research activities and reach, open to new projects and both national and international collaborations. Regarding VLBI analysis, IGN has managed to become an official IVS Analysis Centre and to develop its own research. The goal is now set on extending both activities, by increasing its contribution to IVS products and by working on new research lines. Regarding SLR, the recently created ILRS Associate Analysis Centre IGN-Yebes is actively involved with the ILRS Analysis Standing Committee and other ACs for the production of global solutions, including the contribution to ITRF2020 through a collaboration with NSGF AC (UK), and working towards improving some aspects of the data analysis.

An advantage that stems from having analysis capabilities as well as operational responsibilities within the same institute is that the communication between analysts, engineers and operators, can improve. This is particularly important for techniques such as VLBI and SLR, both with a significant amount of manual intervention and much greater complexity in the preparation and running of the observations, compared to a system such as GNSS. Technical issues such as e.g. system calibrations, observational policy, scheduling, or which metadata is provided with the observations, among others, all have a potential impact on their quality and/or their correct interpretation by analysts. Conversely, timely and readily accessible feedback from the latter can help with the adoption of adequate decisions by the operators, and guide engineers towards issues that may need their attention.

<sup>10</sup><https://icts-yebes.oan.es/slr>.

From the point of view of the analysis of geodetic data, it is certainly not a requirement to count with expertise in every technique in the same institution. On the other hand, where this is available, the existence of significant overlap in many areas between the different techniques can lead to increased opportunities for collaboration. Beyond their individual activities, the current plan at IGN is to boost the internal collaboration between the existing analysis centres, towards the production of combined results for the determination of global geodetic parameters. This is an active research area in the geodetic community, always pursuing new strategies to unleash the greatest possible accuracy.

**Acknowledgements** The authors wish to acknowledge the services of the IAG responsible for running the geodetic observational networks and satellite constellations that are the backbone of space geodesy. We also wish to thank the anonymous reviewers who provided very helpful suggestions to improve this manuscript.

## References

- Altamimi Z, Rebischung P, Métivier L, Collilieux X (2017) ITRF2014: a new release of the International Terrestrial Reference Frame modeling nonlinear station motions. *J Geophys Res Solid Earth* 121:6109–6131
- Appleby GM, Rodríguez J, Altamimi Z (2016) Assessment of the accuracy of global geodetic satellite laser ranging observations and estimated impact on ITRF scale: estimation of systematic errors in LAGEOS observations 1993–2014. *J Geod* 90(12):1371–1388
- Behrend D, Thomas C, Gipson J, Himwich E, Le Bail K (2020) On the organization of CONT17. *J Geod* 94. <https://doi.org/10.1007/s00190-020-01436-x>. <https://rdcu.be/b8q0I>
- Böhm J, Böhm S, Boisits J, Girdiuk A, Gruber J, Hellerschmied A, Krásná H, Landskron D, Madzak M, Mayer D, McCallum J, McCallum L, Scharntner M, Teke K (2018) Vienna VLBI and Satellite Software (VieVS) for geodesy and astrometry. *Publ Astronom Soc Pacific* 130(986):044503. <https://doi.org/10.1088/1538-3873/aaa22b>
- Cantavella JV, Herraiz M, Puente V, Gonzalez-Lopez A, Gaité B, Azcue E, Gonzalez C (2022) Tsunami ionospheric disturbances detected by GNSS derived data. Prototype implementation in the Spanish National Tsunami Warning System (In preparation)
- Dach R et al (2018) Bernese GNSS Software Version 5.2
- Dach R, Schaer S, Arnold D, Kalarus M S, Prange L, Stebler P, Villiger A, Jäggi A (2020) CODE final product series for the IGS. Astronomical Institute, University of Bern. <https://doi.org/10.7892/boris.75876.4>. <http://www.aiub.unibe.ch/download/CODE>
- Dobslaw H, Bergmann-Wolf I, Dill R, Poropat L, Thomas M, Dahle C, Esselborn S, König R, Flechtner F (2017) A new high-resolution model of non-tidal atmosphere and ocean mass variability for de-aliasing of satellite gravity observations: AOD1B RL06. *Geophys J Int* 211(1):263–269
- Exertier P, Belli A, Lemoine JM (2017) Time biases in laser ranging observations: a concerning issue of space geodesy. *Adv Space Res* 60(5):948–968
- Kenyeres A, Bellet JG, Bruyninx C, Caporali A, De Doncker F, Drosack B, Duret A, Franke P, Georgiev I, Bingley R, Huisman L, Jivall L, Khoda O, Kollo K, Kurt AI, Lahtinen S, Legrand J, Magyar B, Mesmaker D, Morozova K, Nagl J, Ozdemir S, Papanikolaou X, Parseulinas E, Stangl G, OB Tangen, Valdes M, Ryczywolski M, Zurutuza J, Weber M (2019) Regional integration of long-term national dense GNSS network solutions. *GPS Solutions* 23:122. <https://doi.org/10.1007/s10291-019-0902-7>
- Kirkvik A, Hjelle GA, Dähnn M, Fausk I, Mysen E (2017) Where - A new software for geodetic analysis. 23th EVGA Working Meeting and 18th IVS Analysis Workshop
- Lemoine JM, Biancale R, Reinquin F, Bourgogne S, Gégout P (2019) CNES/GRGS RL04 Earth gravity field models, from GRACE and SLR data. GFZ Data Services. <https://doi.org/10.5880/ICGEM.2019.010>
- López-Pérez JA (2021) RAEGE: a Spanish-Portuguese infrastructure of geodetic stations. Scientific Assembly of the IAG, Beijing
- Luceri V, Pirri M, Rodríguez J, Appleby G, Pavlis EC, Müller H (2019) Systematic errors in SLR data and their impact on the ILRS products. *J Geod* 93:2357–2366
- National Research Council (2010) Precise geodetic infrastructure: national requirements for a shared resource. The National Academies Press, Washington, DC
- Nothnagel A, Artz T, Behrend D, Malkin Z (2017) International VLBI service for geodesy and astrometry - delivering high-quality products and embarking on observations of the next generation. *J Geod* 91:711–721. <https://doi.org/10.1007/s00190-016-0950-5>
- Pavlis E, Luceri C, Basoni A, Sarrocco D, Kuzmich-Cieslak M, Evans K, Bianco G (2021) The International Laser Ranging Service (ILRS) contribution to the development of the ITRF2020. Scientific Assembly of the IAG, Beijing
- Pearlman MR, Noll CE, Pavlis EC, Lemoine FG, Combrink L, Degnan JJ, Kirchner G, Schreiber U (2019) The ILRS: approaching 20 years and planning for the future. *J Geod* 93:2161–2180. <https://doi.org/10.1007/s00190-019-01241-1>
- Puente V (2021) A priori zenith wet delays in the analysis of VLBI CONT sessions. *Adv Space Res* 67:2359–2367. <https://doi.org/10.1016/j.asr.2021.01.027>
- Puente V, Valdés M (2019) Sea level determination in the Spanish coast using GNSS-R. *Proceedings* 19(1):11. II Congreso en Ingeniería y Geomática. <https://doi.org/10.3390/proceedings2019019011>
- Puente V, Azcue E, Gomez-Espada Y, Garcia-Espada S (2021) Comparison of common VLBI and GNSS estimates in CONT17 campaign. *J Geod* 95:120. <https://doi.org/10.1007/s00190-021-01565-x>
- Rodríguez J, Appleby G, Otsubo T (2019) Upgraded modelling for the determination of centre of mass corrections of geodetic SLR satellites: impact on key parameters of the terrestrial reference frame. *J Geod* 93:2553–2568
- Sinclair AT, Appleby GM (1988) SATAN: programs for determination and analysis of satellite orbits from SLR data. SLR Technical Note 8. Greenwich Observatory, Cambridge
- Valdés M, Cano MA, Pascual M, García-Cañada L (2012) Analysis of GNSS permanent stations in Iberian Peninsula, IBERRED Project. 7th Spanish-Portuguese Assembly of Geodesy and Geophysics
- Valdés M, Cano MA, Sánchez-Sobrino JA, Gonzalo P (2012) Determination of the tropospheric delay with near real-time GNSS by the IGN in the European project E-GVAP. 7th Spanish-Portuguese Assembly of Geodesy and Geophysics

**Open Access** This chapter is licensed under the terms of the Creative Commons Attribution 4.0 International License (<http://creativecommons.org/licenses/by/4.0/>), which permits use, sharing, adaptation, distribution and reproduction in any medium or format, as long as you give appropriate credit to the original author(s) and the source, provide a link to the Creative Commons license and indicate if changes were made.

The images or other third party material in this chapter are included in the chapter's Creative Commons license, unless indicated otherwise in a credit line to the material. If material is not included in the chapter's Creative Commons license and your intended use is not permitted by statutory regulation or exceeds the permitted use, you will need to obtain permission directly from the copyright holder.





# Large-Scale Dimensional Metrology for Geodesy—First Results from the European GeoMetre Project

Florian Pollinger, Clément Courde, Cornelia Eschelbach, Luis García-Asenjo, Joffray Guillory, Per Olof Hedekvist, Ulla Kallio, Thomas Klügel, Pavel Neyezhnikov, Damien Pesce, Marco Pisani, Jeremias Seppä, Robin Underwood, Kinga Wezka, and Mariusz Wiśniewski

## Abstract

In a joint effort, experts from measurement science and space-geodesy develop instrumentation and methods to further strengthen traceability to the SI definition of the metre for geodetic reference frames (GRF). GRFs are based on space-geodetic observations. Local tie surveys at co-location sites play an important role for their computation. Novel tools are hence developed for reference point monitoring, but also for local tie vector determination and ground truth provision. This contribution reports on the instrumental approaches and achievements after 24 months project duration and discusses the remaining work in the project.

## Keywords

Novel distance sensor systems · Multilateration systems · SI traceability · GNSS-EDM comparison · Local tie metrology · Air refractivity compensation

**PACS** Metrology, 06.20-f · Length measurement, 06.30.Bp · Geodetic reference systems, 91.10.Ws

---

This project 18SIB01 GeoMetre has received funding from the EMPIR programme co-financed by the Participating States and from the European Union's Horizon 2020 research and innovation programme.

---

F. Pollinger (✉)  
Physikalisch-Technische Bundesanstalt (PTB), Braunschweig,  
Germany  
e-mail: [florian.pollinger@ptb.de](mailto:florian.pollinger@ptb.de)  
<https://www.ptb.de/empir2018/geometre/home/>

C. Courde  
CNRS, Observatoire de la Côte d'Azur, IRD, Géoazur, Université Côte d'Azur, Caussols, France

C. Eschelbach  
Laboratory for Industrial Metrology, Faculty of Architecture, Civil Engineering and Geomatics, Frankfurt University of Applied Sciences, Frankfurt am Main, Germany

L. García-Asenjo  
Departamento de Ingeniería Cartográfica, Geodesia y Fotogrametría, Universitat Politècnica de València, Valencia, Spain

---

J. Guillory  
Conservatoire National des Arts et Métiers (Cnam), Laboratoire commun de métrologie LNE–Cnam, Paris, France

P. O. Hedekvist  
RISE Research Institutes of Sweden, Borås, Sweden

U. Kallio  
Finnish Geospatial Research Institute, National Land Survey of Finland, Masala, Finland

T. Klügel  
Geodetic Observatory Wettzell, Federal Agency for Cartography and Geodesy, Bad Kötzing, Germany

P. Neyezhnikov  
National Scientific Center “Institute of Metrology”, Kharkiv, Ukraine

D. Pesce  
Institut national de l'information géographique et forestière (IGN), Saint-Mandé, France

M. Pisani  
Istituto Nazionale di Ricerca Metrologica (INRIM), Torino, Italy

## 1 Introduction

Geodetic reference frames (GRF) are essential for all georeferencing services. Geoscientists observe global phenomena over decades often by monitoring tiny annual changes. Sea levels, e.g., develop in the order of one millimetre per year. GRF coordinates are the result of multiple sources of input from measurements performed all over the world. The traceability chain to the SI definition of the metre is therefore highly complex. First, each traceability step to the SI needs to be assured for each of the space-geodetic methods themselves. Comparison against SI-traceable reference distances on ground is a very direct way to do this. But this approach requires distances over several kilometres allowing methods like Satellite-Laser-Ranging a satisfactory measurement resolution by their time-of-flight measurement principle. The uncertainty of these long distances should not exceed 1 mm over 5 km. For the joint analysis, traceability must be ensured by the local tie vectors that manifest the geometrical link between the contributing observations. In order to improve the uncertainty and long-term stability of GRF coordinates further, space-geodetic instrumentation and local tie metrology need to be advanced (Gross et al. 2009).

One key challenge to provide low-uncertainty SI-traceability for terrestrial long-range 1D measurements is the fact that the air refractive index needs to be known to a level considerably better than  $10^{-6}$ . This corresponds to an uncertainty of the temperature to better than 1 K or of the ambient pressure to better than 3 mbar along the whole beam path. The standard approach uses a sensor network ideally distributed along the whole distance. Their observations are averaged and set into the compensation formulas by Ciddor (1996) or Bönsch and Potulski (1998), for example. But for outdoor measurements, the local temperature depends on multiple factors, like shadowing, cloud density, ground material, or the current wind speed, which limits the practically achievable uncertainty. During the last decade, European length metrologists have developed novel instrumentation for surveying applications with low uncertainty (Pollinger et al. 2016). The European GeoMetre project intends to develop instrumentation for terrestrial SI-traceable distance measurements further and to find sensible ways for their

contribution to an improved SI traceability of GRFs. In this contribution, we present a survey on the results achieved so far in the project. For a deeper discussion, including a more thorough literature review for each topic, we would like to refer the reader to the respective original publications.

## 2 Instrumentation Development

In order to achieve the targeted low uncertainty of refractivity compensation using environmental sensors, we have systematically investigated several interpolation schemes, proposing an optimized sensor distribution and numerical interpolation scheme (Neyezhnikov et al. 2020a,b). During our work, we also noted a subtle but fatal sign error in the IAG-recommended publication for the group index of refraction by Ciddor and Hill from 1999, leading to a deviation of more than 2 ppm for typical electro-optical distance meter (Pollinger 2020). But beyond networks of point sensors, sensors probing the whole beam path seem preferable: the probing sensor does not affect the temperature distribution along the beam path, and the beam can trespass the probed volume directly. This can be achieved, e.g., by measurement of the speed of sound in the air traversed by the measurement beam. The Cramer equation (1993) connects this quantity to the thermodynamic air properties, in particular the temperature. Indoors, Korpelainen and Lassila demonstrated an acoustic temperature measurement over several meters (2004). Under well-defined geometries, uncertainties of 0.1 K have been achieved (Underwood et al. 2015). Recently, we performed demonstration measurements outdoors up to 200 m (Pisani et al. 2018). To lower the uncertainty limit for the long-range outdoor measurements, we thoroughly revised the experimental set-up and studied the uncertainty and validity of the Cramer equation for typical outdoor conditions. The results of these verification measurements, making use of a spherical resonator originally designed for the refinement of the Boltzmann constant (Gavioso et al. 2011), will be available soon. A major challenge for this method are sound reflections from the ground or other scatterers in the emission cone of the microphones. Optical beams are easier to confine. We pursue spectroscopic thermometry as alternative technology for this reason. This method probes the population of different oxygen molecule excitation states to derive the thermodynamic temperature. This principle has been demonstrated over 860 m (Tomberg et al. 2017). We are now developing this method towards larger flexibility, targeting a setup with emitter and detector at the same measurement end. For both methods, an overall uncertainty of the measured effective temperature of approx. 0.3 K is targeted.

As an alternative to the explicit measurement of the environmental parameters by additional equipment, an in-situ integration of the refractivity compensation to the length

---

J. Seppä  
VTT Technical Research Centre of Finland Ltd, Centre for Metrology  
MIKES, Espoo, Finland

R. Underwood  
National Physical Laboratory, Teddington, UK

K. Wezka  
Faculty of Geodesy and Cartography, Warsaw University of  
Technology, Warsaw, Poland

M. Wiśniewski  
Central Office of Measures, Warszawa, Poland

measurement seems appealing. Since the late 1960s, it is known that the geometric path length can be derived from an optical path measurement with two different optical wavelengths. From early on, instrumentation has been built to exploit this measurement principle for geodetic applications (Earnshaw and Hernandez 1972, e.g.), leading to the commercial terrameter instrument in the early 1980s (Huggett 1981). The method seems straightforward, however, suffers from the highly unfavorable uncertainty scaling. The key to a compensated range measurement using low uncertainty remains a low uncertainty distance measurement of the uncompensated optical path lengths. Advance in radio frequency modulation technique has enabled a distance meter based on intensity modulation with an operation frequency of up to 6 GHz (Guillory et al. 2016), leading to a nominal uncertainty of  $4 \mu\text{m}$  for a ranging beam working at 1550 nm up to 100 m if the refractive index is neglected (Guillory et al. 2019). This so-called ‘Arpent’ system has already demonstrated a measurement capability of more than 5 km. In the GeoMetre project, we include a second working carrier wavelength at 780 nm targeting the two-color dispersive compensation using this robust ranging technology. The good performance of the telemetric system, both in range accuracy and principle robustness against unfavorable environmental conditions in comparison to interferometric approaches, motivated us to use this system as core for a multilateration system for large volume metrology, i.e. in a volume of several tens of metres. We use the single wavelength telemetric unit to feed four rotatable measurement heads. A rotatable reflector which can be oriented towards the measurements heads serves as target. The mechanical design of the measurement head and the target adds to the uncertainty only  $4 \mu\text{m}$  and  $9 \mu\text{m}$ , respectively (Guillory et al. 2020a,b).

As possibly more accurate alternative to modulation-based ranging, we investigate absolute interferometry to realize satisfactory two-color measurements. For the long range measurement, we use the TeleYAG system developed for 1 km range as basis (Meiners-Hagen et al. 2015). This system successfully demonstrated absolute interferometry with two-color refractivity compensation up to 860 m (Meiners-Hagen et al. 2017), but suffered from smaller technical issues. For the upgrade, we developed a fiber-moderated superposition scheme for the measurement beams at 532 and 1064 nm wavelengths (Liu et al. 2020). Moreover, we use a custom-designed achromatic lens system enabling long-range measurements with a beam diameter of up to 120 mm for the 1064 nm measurement beam. The heterodyne interferometer design allows a flexible measurement range and a lock-in based colour separation. We designed an invar-based mounting system, carefully optimized for mechanical and thermal stability (Pilarski et al. 2021). The system components are now complete and verification experiments are in preparation

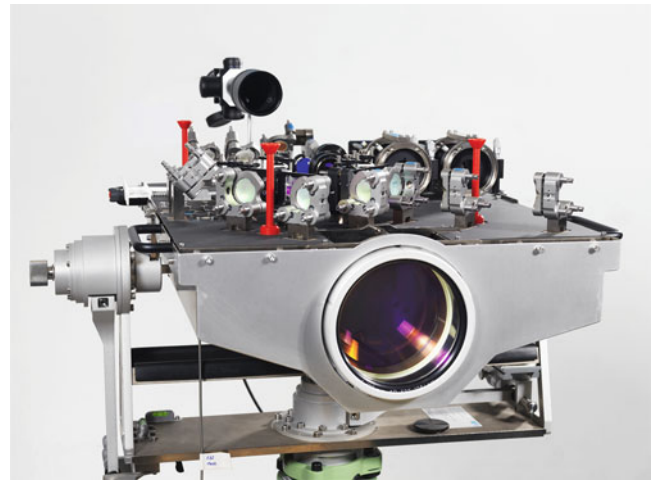


**Fig. 1** Long-range capable two-color interferometer head TeleYAG-II developed by the GeoMetre project

(cf. Fig. 1). Moreover, we use absolute interferometry also for a two-color capable multilateration system. For distances of 10 to 50 m,  $2f/3f$  modulation interferometry allows a compact optical design, while keeping the multi-wavelength measurement approach feasible (Röse et al. 2020).

Besides changing the scale, gradients in the index of refraction are also well known to induce beam bending. We investigate if the non-contact methods can help mitigating this effect. Using the two-color method, it is possible to derive the effective temperature in the beam from the optical path by an auxiliary measurement of the ambient pressure (Meiners-Hagen and Abou-Zeid 2008). The highly unfavorable uncertainty scaling, however, makes this measurement extremely challenging (Röse et al. 2021). As a more robust approach, we also work on a vertical grid of low-cost microphones and sound detectors to use as an ultrasound-based gradient thermometer. So far, a temperature resolution better than 10 mK was demonstrated in the laboratory.

### 3 Reference Baselines

All instrumental developments need to be characterized and compared against each other. For this, we established two novel baselines in Poland: a 252 m reference baseline at the Warsaw University of Technology and the novel European reference network ‘EURO5000’ in the Pieniny Kippen Belt in Poland. The first baseline has seven pillars distributed according to ISO 17123-4 (2012) and is also suitable to compare the project’s different temperature-sensing technologies. EURO5000 consists of five baselines between 1 and 5 km. The novel terrestrial long range reference standards will be studied and verified there. We will also compare these measurements against global navigation satellite sys-

tems (GNSS)-based distance measurements. We will apply a new functional model for GNSS-based length determination (García-Asenjo et al. 2021), modified for the inclusion of tropospheric delays for the kilometric baselines (Baselga et al. 2022). These measurements will be used to establish reference baseline lengths traceable to the SI definition of the metre with an uncertainty considerably below 1 mm. Further field campaigns are planned at the renowned baselines at Nummela and CERN. Thus validated, we will use the Arpent system as reference for a comparison with an SLR distance measurement at the space-geodetic co-location site of Grasse, France.

## 4 Local Tie Metrology

A primary motivation of the GeoMetre project is a substantial contribution to an improvement of local tie metrology. We try a holistic approach, working on improved surveillance network solutions, dynamic reference point monitoring and improved transformation parameters between terrestrial and GNSS observations. We perform our investigations at the space-geodetic co-location sites of Metsähovi, Finland, and Wettzell, Germany. The local networks for the local tie monitoring were refurbished at both sites to reduce the uncertainty of the scale of the local tie vector solutions. Longer baselines were established to improve the orientation solution of the terrestrial network observations. Arpent and TeleYAG-II will be deployed for network campaigns in the next months there. Critical is also the transformation between terrestrial (local) reference system and GNSS (global) reference system. At Metsähovi, adapters for seamless GNSS-terrestrial observations were systematically implemented to the network. We also implemented observations of the local gravity field to the overall network analysis in our effort to reduce the datum problem in terrestrial local ties (Kallio et al. 2022).

A second challenge for local tie metrology is the determination of the reference point of the space-geodetic instrumentation. We propose a laser tracker based approach for an antenna phase center calibration on site without the need to remove the antennas from their permanent installations (Bergstrand et al. 2020). We also investigated gravitational deformation of modern VGOS twin telescopes at Onsala using close-range photogrammetry and deriving a deformation model (Lösler et al. 2019b; Eschelbach et al. 2019). The VLBI antenna deformation at the co-location site of Ny-Ålesund, Norway, was monitored by a combination of terrestrial laser scanning and ranging. For the first time, we also applied close range photogrammetry for the determination of the SLR telescope reference point at Wettzell (Schüler et al. 2019; Lösler et al. 2021) (see Fig. 2). Furthermore, we



**Fig. 2** Close range photogrammetry for SLR reference point determination

developed a new algorithm which considerably eases the synchronization requirements for telescope and measurement system. It allows for an in-process measurement. It has been successfully implemented and validated at Wettzell (Lösler et al. 2019a). In the upcoming final year, we will apply the novel instrumentation to determine the reference baseline networks at Metsähovi and Wettzell and to perform multi-lateration experiments with the novel 3D instrumentation at the Wettzell VLBI telescope.

## 5 Conclusions

In conclusion, half-way through the GeoMetre project lifetime, we can report on considerable progress in surveying instrumentation development. We have made significant steps towards field-capability of many measurement technologies developed in the last decade. We have also established novel reference baselines in Poland which will be available to the geodetic community for instrumentation verification in future. Finally, we upgraded the local tie networks at Wettzell and Metsähovi and demonstrated and implemented new methods for reference monitoring. Some of them have already contributed to the respective vectors of the upcoming ITRF 2020 solution. In the next months, we will verify the novel instrumentation at the new reference baselines and will then deploy them to Metsähovi and Wettzell for local tie measurements. Finally, we will evaluate the individual impact of all approaches to an improvement of the local tie vector uncertainty.

## Conflict of Interest

The authors declare that they have no conflict of interest.



## References

- Baselga S, García-Asenjo L, Garrigues P, Luján R (2022) GBDM+: An improved methodology for a GNSS-based distance meter. *Measur Sci Technol* 33(8):085620
- Bergstrand S, Jarlemark P, Herbertsson M (2020) Quantifying errors in GNSS antenna calibrations. *J Geodesy* 94(10):105
- Bönsch G, Potulski E (1998) Measurement of the refractive index of air and comparison with modified Edlén's formulae. *Metrologia* 35(2):133–139
- Ciddor PE (1996) Refractive index of air: new equations for the visible and near infrared. *Appl Opt* 35(9):1566–1573
- Ciddor PE, Hill RJ (1999) Refractive index of air. 2. Group index. *Appl Opt* 38(9):1663–1667
- Cramer O (1993) The variation of the specific heat ratio and the speed of sound in air with temperature, pressure, humidity, and CO<sub>2</sub> concentration. *J Acoust Soc Am* 93(5):2510–2516
- Earnshaw KB, Hernandez EN (1972) Two-laser optical distance-measuring instrument that corrects for the atmospheric index of refraction. *Appl Opt* 11(4):749–754
- Eschelbach C, Loesler M, Haas R, Greiwe A (2019) Measuring focal length variations of VGOS telescopes using unmanned aerial systems. In: Haas R, García-Espada S, Lopez Fernández JA, (eds) Proceedings of the 24th European VLBI group for geodesy and astrometry working meeting, vol 24, pp 172–176, Madrid, 11 2019. Centro Nacional de Información Geográfica (CNIG)
- García-Asenjo L, Baselga S, Atkins C, Garrigues P (2021) Development of a submillimetric GNSS-based distance meter for length metrology. *Sensors* 21(4):1145
- Gavioso RM, Benedetto G, Madonna Ripa D, Giuliano Albo PA, Guianvarc'h C, Merlone A, Pitre L, Truong D, Moro F, Cuccaro R (2011) Progress in INRiM experiment for the determination of the Boltzmann constant with a quasi-spherical resonator. *Int J Thermophys* 32(7):1339
- Gross R, Beutler G, Plag H (2009) Integrated scientific and societal user requirements and functional specifications for the GGOS. In: Plag H, Pearlman M (eds) Global geodetic observing system meeting the requirements of a global society on a changing planet in 2020, pp 209–224. Springer, Berlin, Heidelberg
- Guillory J, Šmid R, Garcia-Marquez J, Truong D, Alexandre C, Wallerand J-P (2016) High resolution kilometric range optical telemetry in air by radio frequency phase measurement. *Rev Sci Instrum* 87(7):075105
- Guillory J, Teyssendier de la Serve M, Truong D, Alexandre C, Wallerand J-P (2019) Uncertainty assessment of optical distance measurements at micrometer level accuracy for long-range applications. *IEEE Trans Instrum Measur* 68(6):2260–2267
- Guillory J, Truong D, Wallerand J-P (2020a) Uncertainty assessment of a prototype of multilateration coordinate measurement system. *Precision Engineering* 66:496–506
- Guillory J, Truong D, Wallerand J-P (2020b) Assessment of the mechanical errors of a prototype of an optical multilateration system. *Rev Sci Instrum* 91(2):025004
- Huggett G (1981) Two-color terrameter. *Tectonophysics* 71(1):29–39
- ISO (2012) ISO 17123-4:2012 Optics and optical instruments – Field procedures for testing geodetic and surveying instruments – Part 4: Electro-optical distance meters (EDM measurements to reflectors)
- Kallio U, Klügel T, Marila S, Mähler S, Poutanen M, Saari T, Schüler T, Suurmäki H (2022) Datum problem handling in local tie surveys at wettzell and metsähovi. In: International association of geodesy symposia. Springer, Berlin, Heidelberg. [https://doi.org/10.1007/1345\\_2022\\_155](https://doi.org/10.1007/1345_2022_155)
- Korpelainen V, Lassila A (2004) Acoustic method for determination of the effective temperature and refractive index of air in accurate length interferometry. *Optical Engineering* 43(10):2400–2409
- Liu Y, Röse A, Prellinger G, Köchert P, Zhu J, Pollinger F (2020) Combining harmonic laser beams by fiber components for refractivity-compensating two-color interferometry. *J Lightwave Technol* 38(7):1945–1952
- Lösler M, Eschelbach C, Riepl S, Schüler T (2019a) A modified approach for process-integrated reference point determination. In: Haas R, García-Espada S, Lopez Fernández JA (eds) Proceedings of the 24th European VLBI group for geodesy and astrometry working meeting, vol 24, pp 17–21, Madrid, 11 2019. Centro Nacional de Información Geográfica (CNIG). ISBN 978-84-416-5634-5
- Lösler M, Haas R, Eschelbach C, Greiwe A (2019b) Gravitational deformation of ring-focus antennas for VGOS: first investigations at the Onsala twin telescopes project. *J Geodesy* 93:1–19
- Lösler M, Eschelbach C, Klügel T, Riepl S (2021) ILRS reference point determination using close range photogrammetry. *Applied Sciences* 11(6):2785
- Meiners-Hagen K, Abou-Zeid A (2008) Refractive index determination in length measurement by two-colour interferometry. *Measur Sci Technol* 19:084004
- Meiners-Hagen K, Bosnjakovic A, Köchert P, Pollinger F (2015) Air index compensated interferometer as a prospective novel primary standard for baseline calibrations. *Measur Sci Technol* 26(8):084002
- Meiners-Hagen K, Meyer T, Mildner J, Pollinger F (2017) Si-traceable absolute distance measurement over more than 800 meters with sub-nanometer interferometry by two-color inline refractivity compensation. *Appl Phys Lett* 111(19):191104
- Neyezhmakov P, Kupko V, Panasenko T, Prokopov A, Skliarov V, Shloma A (2020a) Analysis of accuracy requirements to the meteorological sensors used to compensate for the influence of the Earth's atmosphere in high precision length measurement. In: SMSI 2020 - Measurement science
- Neyezhmakov P, Prokopov O, Panasenko T, Trevoho I, Shloma A (2020b) Comparative analysis of quadrature formulas for the mean integral refractive index of air in high-precision ranging. *Modern Achiev Geodesic Sci Ind* 1(39):69–73
- Pilarski F, Schmaljohann F, Weinrich S, Huisman J, Truong D, Meyer T, Köchert P, Schödel R, Pollinger F (2021) Design and manufacture of a reference interferometer for long-range distance metrology. In: Conference proceedings - euspen's 21st international conference & exhibition, Copenhagen, DK, June 2021, pp 511–512
- Pisani M, Astrua M, Zucco M (2018) An acoustic thermometer for air refractive index estimation in long distance interferometric measurements. *Metrologia* 55(1):67
- Pollinger F (2020) Refractive index of air. 2. Group index: comment. *Appl Opt* 59(31):9771–9772
- Pollinger F, Bauch A, Meiners-Hagen K, Astrua M, Zucco M, Bergstrand S, Görres B, Kuhlmann H, Jokela J, Kallio U, Koivula H, Poutanen M, Neyezhmakov P, Kupko V, Merimaa M, Niemeier W, Saraiva F, Schön S, van den Berg SA, Wallerand J-P (2016) Metrology for long distance surveying: A joint attempt to improve traceability of long distance measurements. In: Rizos C, Willis P (eds) IAG 150 years, pp 651–656. Springer International Publishing, Cham
- Röse A, Liu Y, Köchert P, Prellinger G, Manske E, Pollinger F (2020) Modulation-based long-range interferometry as basis for an optical two-color temperature sensor. In: Conference proceedings - euspen's 20th international conference & exhibition, Geneva, CH, June 2020
- Röse A, Köchert P, Prellinger G, Manske E, Pollinger F (2021) Monte-Carlo analysis of challenges and limitations of dispersion-based optical thermometry. In: SMSI 2021 - Sensors and instrumentation, pp 203–204
- Schüler T, Riepl S, Eschelbach C, Lösler M (2019) Zur Bestimmung des ILRS-Referenzpunktes am Satellite Observing System Wettzell. In: Luhmann T, Schumacher C (eds) Photogrammetrie - laserscanning - Optische 3D-Messtechnik: Beiträge der 18. Oldenburger 3D-Tage

- 2019, vol 2019, pp 162–175. Wichmann Verlag. ISBN 978-3-87907-660-4
- Tomberg T, Fordell T, Jokela J, Merimaa M, Hieta T (2017) Spectroscopic thermometry for long-distance surveying. *Appl Opt* 56(2):239–246
- Underwood R, Gardiner T, Finlayson A, Few J, Wilkinson J, Bell S, Merrison J, Iverson JJ, de Podesta M (2015) A combined non-contact acoustic thermometer and infrared hygrometer for atmospheric measurements. *Meteorological Applications* 22(S1):830–835

**Open Access** This chapter is licensed under the terms of the Creative Commons Attribution 4.0 International License (<http://creativecommons.org/licenses/by/4.0/>), which permits use, sharing, adaptation, distribution and reproduction in any medium or format, as long as you give appropriate credit to the original author(s) and the source, provide a link to the Creative Commons license and indicate if changes were made.

The images or other third party material in this chapter are included in the chapter's Creative Commons license, unless indicated otherwise in a credit line to the material. If material is not included in the chapter's Creative Commons license and your intended use is not permitted by statutory regulation or exceeds the permitted use, you will need to obtain permission directly from the copyright holder.





# GGOS Bureau of Products and Standards: Description and Promotion of Geodetic Products

D. Angermann, T. Gruber, M. Gerstl, R. Heinkelmann, U. Hugentobler,  
L. Sánchez, P. Steigenberger, R. Gross, K. Heki, U. Marti, H. Schuh, M. Sehnal,  
and M. Thomas

## Abstract

The Bureau of Products and Standards (BPS) is a key component of the Global Geodetic Observing System (GGOS) of the International Association of Geodesy (IAG). It supports GGOS in its goal to provide consistent geodetic products needed to monitor, map, and understand changes in the Earth's shape, rotation, and gravity field. In its present structure, the two Committees "Earth System Modeling" and "Essential Geodetic Variables" as well as the Working Group "Towards a consistent set of parameters for the definition of a new Geodetic Reference System (GRS)" are associated to the BPS. This paper presents the structure and role of the BPS and it highlights some of the recent activities. A major focus is on the classification and description of geodetic products and their representation at the renewed GGOS website ([www.ggos.org](http://www.ggos.org)). This website serves as an "entrance door" to geodetic products to satisfy different user needs and communities (e.g., geodesists, geophysicists, other geosciences and further customers) in order to make geodesy more visible to other disciplines and to society.

## Keywords

BPS inventory · Bureau of Products and Standards (BPS) · Geodesy · Geodetic products · GGOS · GGOS website · Standards and conventions

D. Angermann (✉) · T. Gruber · M. Gerstl · U. Hugentobler ·  
L. Sánchez  
Technical University of Munich (TUM), Munich, Germany  
e-mail: [detlef.angermann@tum.de](mailto:detlef.angermann@tum.de)

R. Heinkelmann · H. Schuh · M. Thomas  
Helmholtz Centre Potsdam, German Research Centre for Geosciences  
(GFZ), Potsdam, Germany

P. Steigenberger  
Deutsches Zentrum für Luft- und Raumfahrt (DLR), Cologne,  
Germany

R. Gross  
Jet Propulsion Laboratory, California Institute of Technology,  
Pasadena, CA, USA

K. Heki  
Hokkaido University, Sapporo, Japan

U. Marti  
Bundesamt für Landestopographie, Swisstopo, Bern, Switzerland

## 1 Introduction

The GGOS Bureau of Products and Standards (BPS), formerly known as Bureau for Standards and Conventions (BSC), was established as a component of the Global Geodetic Observing System (GGOS) of the International Association of Geodesy (IAG) in 2009. The organizational structure of GGOS and a description of its components is given in Miyahara et al. (2020), published in the Geodesist's Handbook 2020 (Poutanen and Rozsa 2020).

The BPS is chaired by the Technical University of Munich (TUM) within the Research Group Satellite Geodesy (Forschungsgruppe Satellitengeodäsie, FGS). Further

M. Sehnal  
Bundesamt für Eich- und Vermessungswesen (BEV), Vienna, Austria

involved partners are GFZ (Helmholtz Centre Potsdam, German Research Centre for Geosciences, Potsdam) and DLR (German Aerospace Centre, Oberpfaffenhofen). The organizational structure and further information about the BPS can be found in Angermann et al. (2018, 2020), and at the GGOS website ([www.ggos.org](http://www.ggos.org)).

The work of the BPS is fundamentally built on the IAG Scientific Services and the products they derive on an operational basis for Earth monitoring making use of various space geodetic observation techniques such as Very Long Baseline Interferometry (VLBI), Satellite and Lunar Laser Ranging (SLR/LLR), Global Navigation Satellite Systems (GNSS), Doppler Orbitography and Radiopositioning Integrated on Satellite (DORIS), satellite altimetry, gravity satellite missions, gravimetry, etc.

With the ongoing technological improvements of the Earth observing systems, geodesy provides the potential to determine unambiguously and with utmost precision the geometric shape of land, ice and ocean surfaces as well as the rotation and gravity field of the Earth as global functions of space and time. Thus, geodesy provides the metrological basis for Earth system research and for reliably monitoring climate change phenomena (e.g., sea level variations, melting of ice sheets, continental water storage). To ensure consistent results and to fully benefit from the technological improvements and high accuracy of the geodetic observations, reliable reference frames as well as common standards, conventions and models are essential for the data analysis and product generation.

A key objective of the BPS is to keep track and to foster homogenization of adopted geodetic standards and conventions across all components of the IAG as a fundamental basis for the generation of consistent geometric and gravimetric products. Towards reaching these goals, the BPS has compiled an inventory of standards and conventions used for the generation of IAG products (Angermann et al. 2016 and 2020), published in the Geodesist's Handbook 2016 and 2020 (Drewes et al. 2016; Poutanen and Rozsa 2020). This inventory presents the current status, identifies gaps and inconsistencies as well as interactions between different products. It also provides open issues and recommendations regarding standards and conventions used for the generation of IAG products. In this way, the BPS supports IAG in its goal to obtain geodetic products of highest accuracy and consistency. Moreover, the Bureau contributes to the development of new geodetic products, needed for Earth sciences and society. In the framework of the renewing of the GGOS website, the BPS closely interacts with the GGOS Coordinating Office regarding the representation of geodetic products. In cooperation with the IAG Services, other data providers and the GGOS Science Panel members, user-friendly product descriptions have been generated and implemented at the GGOS website.

The scope of this paper is summarized as follows: Sect. 2 presents the objectives and tasks of the BPS as given in the BPS Implementation Plan 2020–2022, including its associated GGOS components. The main focus is on the recent BPS activities related to the representation of geodetic products at the renewed GGOS website, which is presented in Sect. 3. Finally, conclusions are provided in Sect. 4.

---

## 2 Objectives and Tasks of the BPS

The BPS supports GGOS in its goal to obtain geodetic products of highest accuracy and consistency. Thereby, the focus is on the evaluation of adopted geodetic standards and conventions across all IAG components to further improve the consistency of products describing the geometry, rotation and gravity field of the Earth. The work is primarily built on the IAG Service activities in the field of data analysis, combination and product generation. The BPS acts as contact and coordinating point regarding homogenization of standards and IAG products.

Figure 1 represents an overview and schedule of the BPS tasks as specified in the latest BPS Implementation Plan 2020–2022. The activities of the BPS are divided into three main categories: Coordination activities, specific tasks of the BPS, and outreach activities.

The first category comprises GGOS Consortium meetings (annually), GGOS Coordinating Board meetings (twice per year) and monthly telecons of the GGOS Executive Committee to ensure a regular exchange of information among the GGOS components and to manage the strategic planning and day-to-day activities. Furthermore, external and internal BPS meetings are regularly scheduled to coordinate and perform the operational Bureau work.

Among the specific tasks of the BPS, a recent key activity was the updating of the BPS inventory of standards and conventions used for the generation of IAG products (Angermann et al. 2020). The tasks also comprise the interaction with IAG and other entities in the field of standards and conventions such as the contribution to the rewriting/revising of the IERS Conventions, mainly in the function as Chapter Expert for Chapter 1 “General definitions and numerical standards”. Moreover, the BPS director acts as representative to ISO/TC 211 and to the UN-GGIM Subcommittee on Geodesy (SCoG) Working Group “Data Sharing and Development of Geodetic Standards”. The BPS also cooperates with the newly established Global Geodetic Centre of Excellence (GGCE) of the UN and the International Astronomical Union (IAU).

The third category includes various outreach activities, such as supporting the GGOS Coordinating Office concerning the renewing of the GGOS website, in particular regarding the description and representation of geodetic products

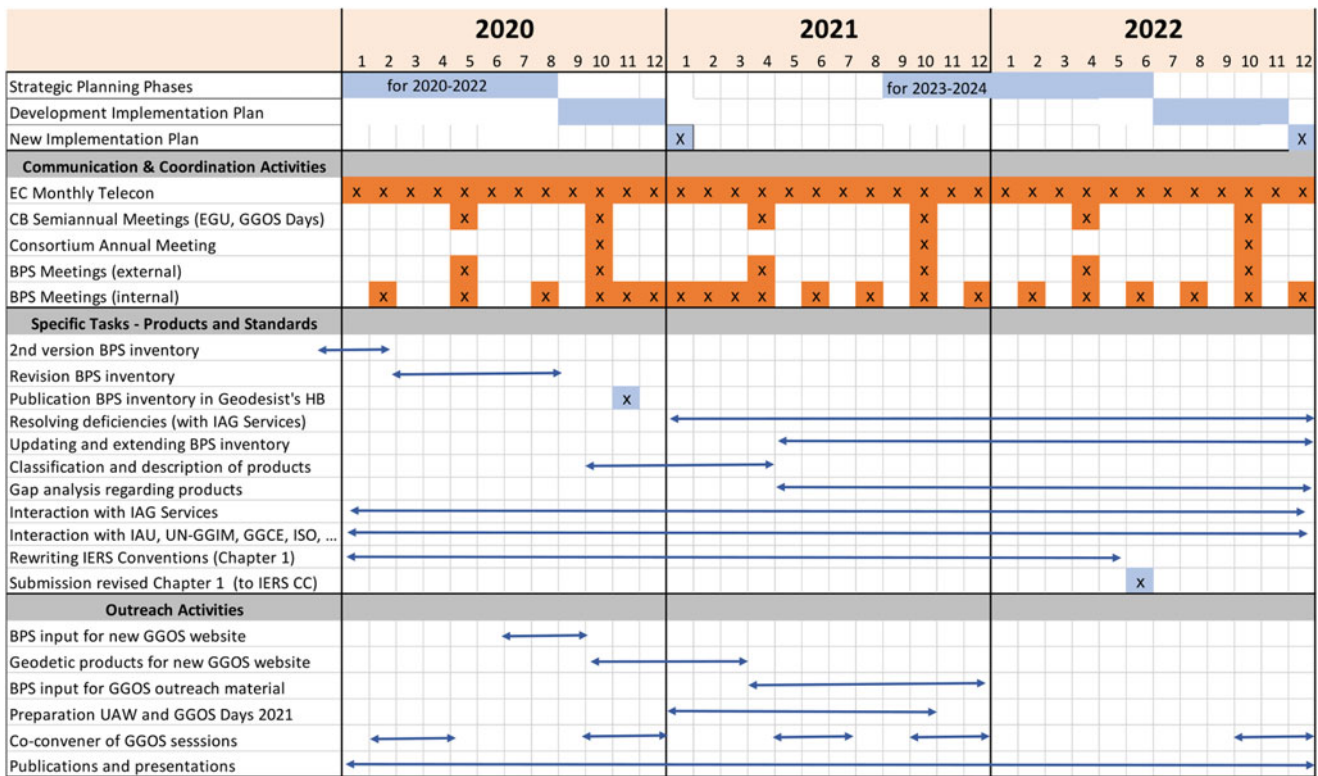


Fig. 1 Overview and schedule of BPS activities

(see Sect. 3) as well as the presentation of BPS activities and results at workshops, conferences, and to publish them in scientific journals.

In its current structure, the following GGOS components are associated to the BPS:

- Committee “Contributions to Earth System Modeling” (see Sect. 2.1)
- Committee “Definition of Essential Geodetic Variables” (see Sect. 2.2)
- Working Group “Towards a consistent set of parameters for the definition of a new GRS” (see Sect. 2.3)

### 2.1 Committee “Contributions to Earth System Modeling”

The major goal of this committee is the preparation of a physically consistent numerical Earth system model for near-surface dynamics. Such a modular model approach is expected to allow for homogeneous processing, interpretation, and prediction of geodetic parameters, i.e., Earth rotation, gravity field and surface deformation, and thus, to finally contribute to a better understanding of dynamical processes in the Earth system reflected in geodetic observables.

Traditionally, various independent models tailored to specific spatial and temporal scales and to specific dynamical processes in individual sub-systems of the Earth are applied in order to estimate particular contributions to observed variations of geodetic parameters. Although it is well known that the individual sub-systems are coupled via fluxes of mass, energy and momentum, these interactions are generally not adequately considered or even neglected, and the total amount of geophysical excitation is mostly described by a simple linear addition of the individual contributions. Another deficiency results from the fact that the various estimates are based on different standards and parameters and use diverse analysis strategies and formats.

Thus, in order to ensure physical consistency, such as mass conservation, and to consider feedbacks, a modular model approach with individual elements representing sub-systems or components interacting through boundary conditions is mandatory. The envisaged system model approach has to be designed in such a way that it (i) ensures consistent interactions and physical fluxes among sub-systems, (ii) is applicable to all geodetic quantities, (iii) allows self-consistent predictions of geodetic parameters, and (iv) can be used for interpretation, cross-validation and integration of different observational data sets.

## 2.2 Committee “Definition of Essential Geodetic Variables”

The Committee on the Definition of Essential Geodetic Variables (EGVs) was formed with the objective of compiling a list of observed variables that describe the essential geodetic properties of the Earth. Since geodesy encompasses the rotation, gravity, and shape of the Earth, the list of EGVs should include Earth orientation parameters, gravity harmonics, positions of reference objects (ground stations, radio sources) and surface topography coefficients amongst others. Besides the primary variables needed to characterize the geodetic properties of the Earth, a hierarchy of other variables associated with or derived from the primary variables could also be compiled.

For example, the time rate-of-change of polar motion could be considered sub-variables of polar motion; the period and Q of the Chandler wobble could be considered supporting variables of polar motion; and the polar motion excitation functions could be considered variables derived from polar motion, its sub-variables of polar motion rate, and its supporting variables of the Chandler period and Q. Along with the hierarchical list of EGVs, information about the variables could also be given such as how they are observed, the accuracy and resolution with which they are observed, who is responsible for observing them, and where numerical values of them can be obtained.

## 2.3 Working Group “Towards a Consistent Set of Parameters for the Definition of a New GRS”

The main task of this WG is to define a consistent set of parameters and formulas for the definition of a new conventional Geodetic Reference System (GRS). This includes the geometry (size and shape of a reference ellipsoid), the gravity field (normal gravity field of this ellipsoid), terrestrial time and Earth rotation. More background information is provided in, e.g., Angermann et al. (2020), Ihde et al. (2017), Sánchez et al. (2021).

This new definition becomes necessary because, since the introduction of the GRS80 (Moritz 2000), the knowledge in geodesy has improved a lot (e.g. GNSS, gravity space missions) and the use of the parameters became inaccurate and inconsistent over time. The problem of the permanent Earth tide was not yet a topic at the epoch of the definition of GRS80. The acceptance of the IAG Resolution No. 1 released at the IUGG 2015 General Assembly (Drewes et al. 2016), which defines the potential at sea level ( $W_0$ ) even increases the inconsistency in the geodetic parameters of the conventional GRS in use.

The new set of parameters is based on the four fundamental parameters:  $W_0$  (potential at reference level),  $J_2$  (dynamic form factor, “flattening”), GM (geocentric gravitational constant) and  $\omega$  (angular velocity of the Earth). All these quantities are well observed and monitored by various geodetic space techniques. Most of the defining parameters change with time. This includes seasonal variations and long-term trends. Nevertheless, in order to keep things simple for the user, this time variability will not be treated in the published definition of a new GRS.

Besides the calculation of a new set of parameters, the main task will be to convince the users to adopt such a system as a new global reference. Since many users just consider GRS80 as a conventional model for the conversion of geocentric coordinates or for the calculation of gravity anomalies, such a replacement of the geodetic reference system needs to be further discussed within the community.

## 3 Description and Representation of Geodetic Products at the GGOS Website

In the last two years, the GGOS Coordinating Office worked intensively together with all GGOS components and other experts of the geodetic community to launch a new GGOS website ([www.ggos.org](http://www.ggos.org)). This new site now emphasizes more on the “Observing System” than on the “GGOS organization” itself. Therefore, the website was enhanced to provide an extensive information platform to bring the IAG observations, products and services into the focus, and to provide a unique information platform as a central access point. In this way, the new GGOS website serves now as an “entrance door” to make geodesy more visible to other disciplines and to society. Illustrative graphics guide the users to easily understandable descriptions about geodetic observations and products. For users who want to get more detailed information, links to the websites and data repositories of the IAG Services and other sources are provided.

In the framework of the renewing of the GGOS website, the BPS supports the GGOS Coordinating Office regarding the representation of geodetic products. With the success and engagement of the IAG Services and their contributing analysis and combination centers an extensive portfolio of geodetic products is routinely provided. This forms the basis to improve the understanding of our dynamic planet and to monitor global change phenomena as well as for a broad spectrum of various applications (e.g., satellite navigation, surveying, mapping, engineering, geo-information systems).

Two classifications for the geodetic products have been implemented at the GGOS website:

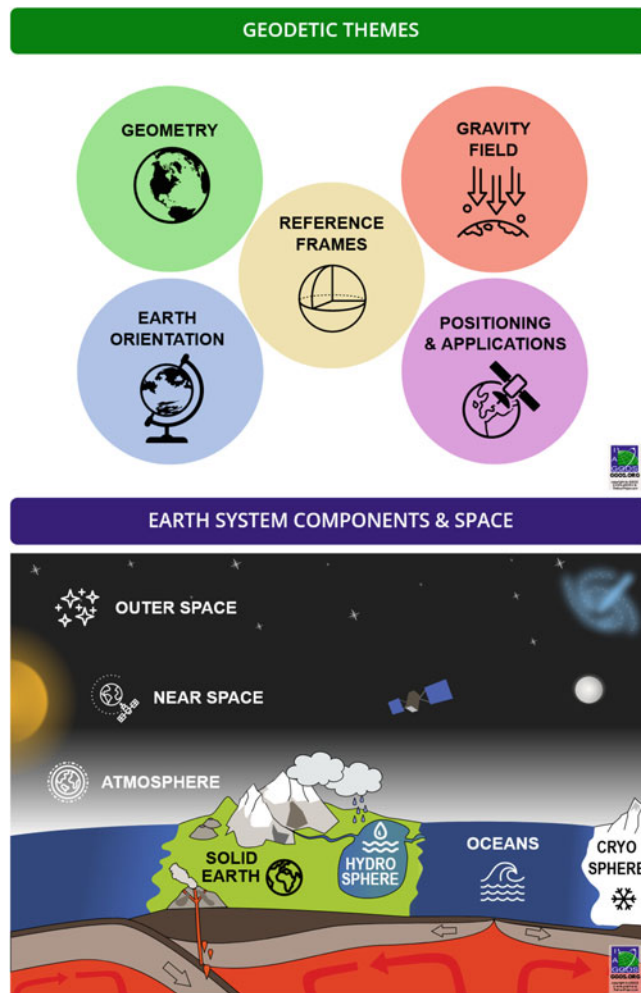


**Fig. 2** Screenshot of the GGOS website for the two classifications of geodetic products ([www.ggos.org](http://www.ggos.org), screenshot taken on 2021-09-22)

- **Geodetic themes:** Reference frames, geometry, Earth orientation, gravity field, positioning and applications.
- **Earth system components and space:** Outer and near space, atmosphere, hydrosphere, oceans, cryosphere, solid Earth.

Option 1 provides the classical geodetic view, whereas users from other disciplines may prefer the second classification to discover the product descriptions. A screenshot of the GGOS website illustrates these two classifications of the geodetic products (see Fig. 2). With these visualization tools, users can navigate to a specific product description either via the geodetic themes or Earth system components. As an example, Fig. 3 shows a screenshot of the description for the terrestrial reference frame.

All geodetic product descriptions are structured in a similar way. At the top level, a typical symbol for a particular product is displayed (left), its name is highlighted in a green box (middle) and the label (right) indicates if it's an official IAG product. Directly under the product's name, a so-called "appetizing question" is displayed to attract users to visit the GGOS website. As a next item, the descriptions comprise an easily understandable introduction with some general information and typical applications for the particular product, followed by an illustrative graphic. The "Read More ..." button provides the option to get further information for those users, who want to learn more about the geodetic product. And for those who would like to use this particular product for their studies, web links to the IAG Services and other data providers, as well as the respective data and product sources are displayed. Moreover, related references are provided to give more background information.

Until now, about 23 product descriptions have been prepared by the BPS members in cooperation with representatives of the IAG Services, other data providers and various experts in the field. The descriptions have been reviewed by the members of the GGOS Science Panel coordinated by its chair Kosuke Heki, and then implemented at the GGOS website by Martin Sehnal, the director of the GGOS Coordinating Office. Figure 4 provides a list of the currently available product descriptions, along with the so-called "appetizing question" for each particular product. With such an information portal, GGOS is contributing to advertise geodetic products also to other disciplines and to make geodesy more visible in the geoscientific community and beyond.

In addition to the product description of the terrestrial reference frame, we provide some further examples for geodetic products displayed at the GGOS website, representing geometry, gravity field and atmosphere.

Geodetic core products are station positions and their temporal variations at the Earth's surface. These products form the basis for many activities, ranging from classical geodetic tasks, disaster prevention and mitigation to the monitoring of geodynamic effects and climate change phenomena. In addition to official IAG products (e.g., ITRF station positions and velocities), the GGOS website also displays data products provided by other institutions such as the Nevada Geodetic Laboratory (NGL). Figure 5 shows a global GPS network of over 19,000 geodetic stations which are routinely processed to derive a variety of geodetic products (e.g., station positions and velocities, atmospheric water vapor). These products are openly available at NGL's comprehensive GPS products portal (<http://geodesy.unr.edu/>, Blewitt et al. 2018).

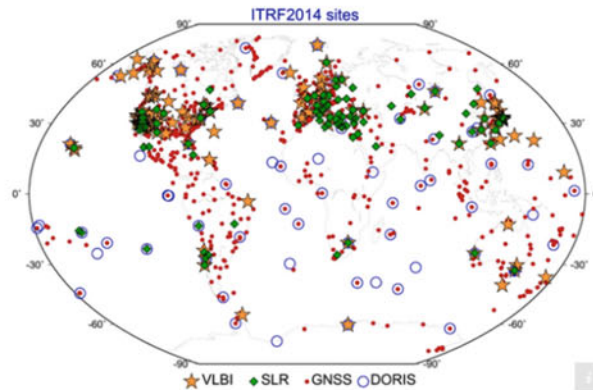


## Terrestrial Reference Frame



How can we provide a stable reference for measuring changes of our planet?

The [International Association of Geodesy \(IAG\)](#) recommends the International Terrestrial Reference Frame (ITRF) as the **standard terrestrial reference frame** for **positioning, satellite navigation and Earth science applications**, as well as for the definition and alignment of national and regional reference frames (see IAG Resolution No. 1, 2019). The importance of geodetic reference frames has been recognized by the United Nations, too. In February 2015, the [UN General Assembly](#) adopted its first geospatial resolution "[A Global Geodetic Reference Frame for Sustainable Development](#)".



ITRF station distribution [Source: Altamimi et al., 2016]

[Read More ...](#)

## Data Sources



### ITRS CENTRE

The [ITRS Centre](#) is responsible for the maintenance of the [International Terrestrial Reference System \(ITRS\)](#) and the [International Terrestrial Reference Frame \(ITRF\)](#). It is maintained by the [IGN](#) in France.



### IERS

[International Earth Rotation and Reference Systems Service](#)

## Further Information



Altamimi Z., P. Rebischung, L. Métivier, X. Collilieux. ITRF2014: A new release of the International Terrestrial Reference Frame modeling nonlinear station motions. *Journal of Geophysical Research: Solid Earth* 121.8, pp. 6109-6131, DOI: 10.1002/2016JB013098, 2016.

**Fig. 3** Screenshot from the GGOS website for the product description of the terrestrial reference frame ([www.ggos.org](http://www.ggos.org), screenshot taken on 2021-11-24)



<b>Reference Frames</b>		
	Terrestrial reference frame	How can we provide a stable reference for measuring changes of our planet?
	Celestial reference frame	How can we link Earth and space?
	Gravity reference frame	How to refer gravity measurements at the Earth surface to a uniform reference?
	Height reference frame	What is a height above sea level?
<b>Geometry</b>		
Land surface	Station positions & variations	Why do we need precise positioning and navigation on Earth and in space?
	Digital elevation model	How can the Earth's surface be represented?
	Surface deformation models	Why is the Earth's surface in constant change?
Ocean surface and lakes	Sea surface heights	How can the height of oceans be observed?
	Ocean topography models	What are dynamic ocean topography models and why are they needed?
	Sea level change	How fast is the sea level rising?
	Tide gauge records	What is the best sea level reference along the coasts?
Ice surface	Ice sheets and glaciers - variations	How fast is the ice being lost in Greenland and Antarctica?
<b>Gravity field</b>		
	Global gravity field models	How and why does the Earth's gravity change with location?
	Gravity field temporal variations	Why is the gravity field variable?
	Regional / local geoid models	What is a geoid and why is it needed?
	Terrestrial gravity data	What is the purpose of measuring gravity on the Earth's surface?
	Ice sheets and glaciers - variations	How fast is the ice being lost in Greenland and Antarctica?
	Height systems	Why are height systems so important?
<b>Earth Orientation</b>		
	Earth orientation parameters	Why are days getting longer and Earth is wobbling?
<b>Positioning and Applications</b>		
Atmosphere	Atmospheric products	How can space geodetic techniques observe the atmosphere?
	Lower neutral atmosphere	How can geodesy contribute to weather prediction?
	Ionosphere	How does electron density affect positioning and navigation?
	Thermosphere	How does the atmosphere influence low-flying satellites?
GNSS products	GNSS satellite orbits and clocks	How positioning benefits from precise satellite orbits and clocks?

**Fig. 4** List of product descriptions that are currently displayed at the GGOS website, including an “appetizing question” for each particular product, status: 2021-11-15

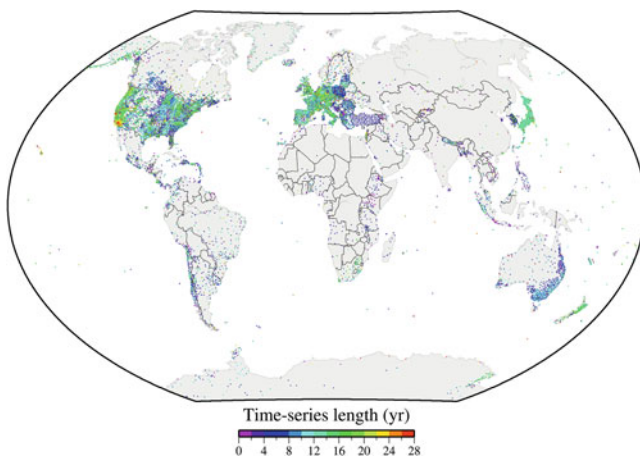


**Fig. 5** Global network of over 19,000 geodetic GPS stations processed by the Nevada Geodetic Laboratory (NGL) in USA (Source: Blewitt et al. 2018)

Also global gravity field models are fundamental geodetic products (see Fig. 6). These products provide information about the physical Earth's shape, its interior and fluid envelope. They are essential for many Earth system research areas such as quantifying mass distribution and mass transport, monitoring oceanic transport, continental hydrology, ice mass balance and sea level, and dynamics of mantle and crust. The GGOS website gives an overview about static and time-variable gravity field models and provides a link to the respective IAG Services, the International Centre for Global Earth Models (ICGEM, Ince et al. 2019), coordinated by the International Gravity Field Service (IGFS), as well as the International Combination Service for Time-VARIABLE Gravity Fields (COST-G, Jäggi et al. 2020), which is the Product Centre of the IGFS for time-variable gravity fields. In addition to these official IAG Service products, the GGOS website also displays high-level products such as temporal

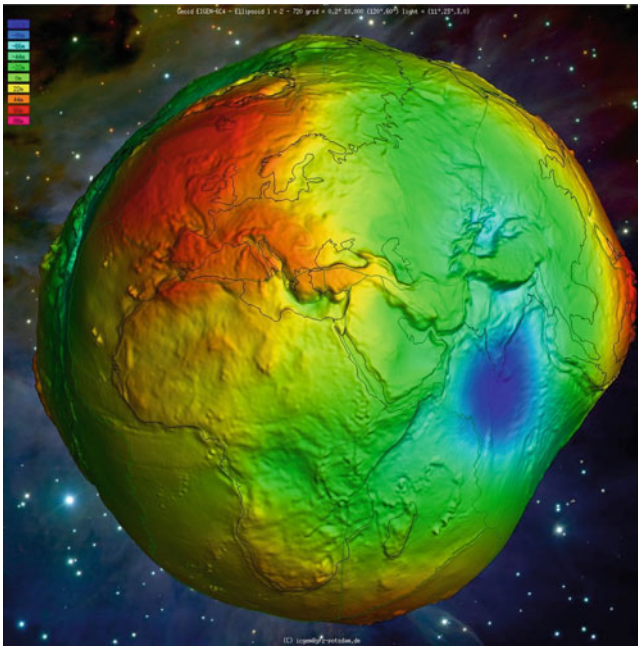


**Fig. 6** Geoid from combined global gravity field model EIGEN-6C4 (Source: Ince et al. 2019)

variations of ice sheets in Greenland and Antarctica (<https://ggos.org/item/ice-sheets-glaciers/>), including a link to the providers. These derived products are highly relevant to society, since phenomena such as the global sea level rise are largely driven by accelerated melting of the Greenland and Antarctica ice sheets and glaciers, and could be catastrophic for millions of people in the future.

A further example from the GGOS products pages is provided in Fig. 7. It shows the impact of the 2017 typhoon Noru on the distribution of atmospheric delay gradients and zenith wet delays (ZWD) in central Japan. The method for the calculation of the ZWD is described in Arief and Heki (2020). Routinely generated are such troposphere products by the International GNSS Service (IGS) and the International VLBI Service for Geodesy and Astrometry (IVS). Furthermore, the GGOS website provides a link to troposphere products at the regional level such as EUREF, the Regional Reference Frame for Europe, and SIRGAS, the Geocentric Reference Frame for the Americas. The ZWDs derived from space geodetic techniques provide important atmospheric information for weather models.

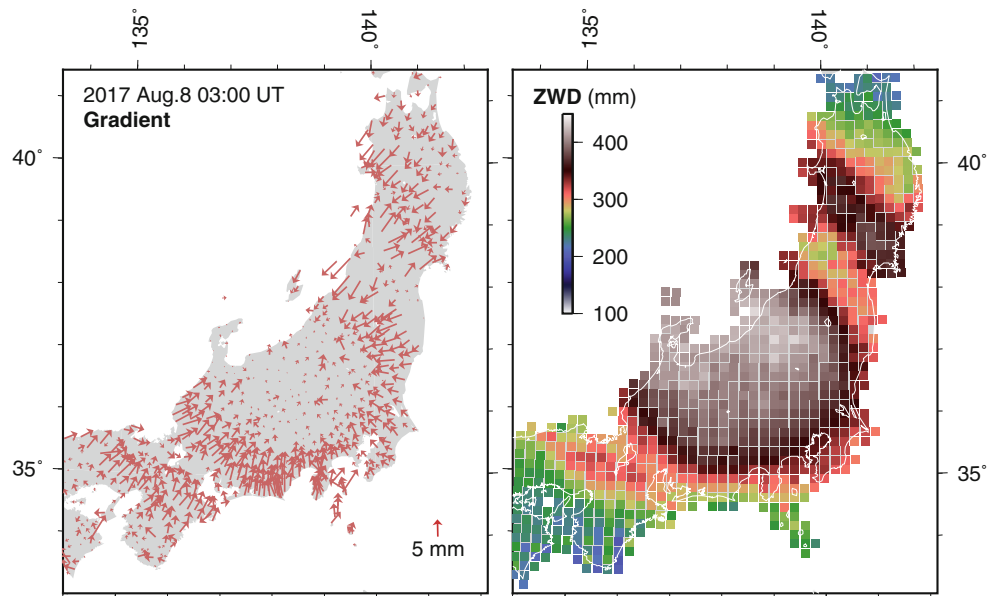


**Fig. 7** Distribution of atmospheric delay gradients (left) and wet delays (right) when the 2017 typhoon Noru made landfall in central Japan (for more details see Arief and Heki 2020)

## 4 Conclusions

The IAG strives to provide geodetic results at the highest level of precision and consistency, which fundamentally requires that the processing and combination of the contributing geometric and gravimetric observations are based on unified standards and conventions. In cooperation with the IAG Services and other entities involved, the BPS contributes to this goal by evaluating the adopted standards and conventions across all IAG components and by regularly updating the BPS inventory.

The recent BPS activities focused on the classification of geodetic products and on the generation of user-friendly descriptions, which have been implemented at the renewed GGOS website. With this, GGOS provides a unique information platform and a central access point for geodetic data and products, which should help to make them easier findable and which should also contribute to make other disciplines and society aware of geodesy and its beneficial products.

**Acknowledgements** GGOS is built upon the foundation provided by the IAG Services, Commissions, and Inter-Commission Committees. The support and efforts of the IAG components is gratefully acknowledged. Furthermore, the authors thank the IAG Services, the other providers and contributing experts, as well as the members of the GGOS Science Panel for their support. The work of Richard Gross described in this paper was carried out at the Jet Propulsion Laboratory, California Institute of Technology, under contract with the National Aeronautics and Space Administration.

## References

- Altamimi Z, Rebischung P, Métivier L, Collilieux X (2016) ITRF2014: A new release of the International Terrestrial Reference Frame modeling nonlinear station motions. *J Geophys Res Solid Earth* 121(8):6109–6131. <https://doi.org/10.1002/2016JB013098>
- Angermann D, Gruber T, Gerstl M, Heinkelmann R, Hugentobler U, Sánchez L, Steigenberger P (2016) GGOS Bureau of Products and Standards: Inventory of standards and conventions used for the generation of IAG products. In: Drewes H, Kuglitsch F, Adám J, Rozsa S (eds) *The geodesist's handbook 2016*. *J Geod* 90(10):1095–1156. <https://doi.org/10.1007/s00190-016-0948-z>
- Angermann D, Gruber T, Gerstl M, Heinkelmann R, Hugentobler U, Sánchez L, Steigenberger P (2018) GGOS Bureau of Products and Standards: Recent activities and future plans. In: Freymueller J, Sánchez L (eds) *International association of geodesy symposia*, vol 149. Springer, pp 153–159. [https://doi.org/10.1007/1345\\_2018\\_28](https://doi.org/10.1007/1345_2018_28)
- Angermann D, Gruber T, Gerstl M, Heinkelmann R, Hugentobler U, Sánchez L, Steigenberger P (2020) GGOS Bureau of Products and Standards: Inventory of standards and conventions used for the generation of IAG products. In: Poutanen, Rozsa S (eds) *The geodesist's handbook 2020*. *J Geod* 94(11):221–292. <https://doi.org/10.1007/s00190-020-01434-z>
- Arief S, Heki K (2020) GNSS meteorology for disastrous rainfalls in 2017–2019 summer in SW Japan: A new approach utilizing atmospheric delay gradients. *Front Earth Sci* 8:182. <https://doi.org/10.3389/feart.2020.00182>
- Blewitt G, Hammond W, and Kreemer C (2018) Harnessing the GPS data explosion for interdisciplinary science. *Eos* 99. <https://doi.org/10.1029/2018EO104623>
- Drewes H, Kuglitsch F, Adám J, Rozsa S (eds) (2016) *The geodesist's handbook 2016*. *J Geod* 90(10):1095–1156. <https://doi.org/10.1007/s00190-016-0948-z>
- Ihde J, Sánchez L, Barzaghi R, Drewes H, Förste C, Gruber T, Liebsch G, Marti U, Pail R, Sideris M (2017) Definition and proposed realization of the International Height Reference System (IHRs). *Surv Geophys* 38(3):549–570. <https://doi.org/10.1007/s10712-017-9409-3>
- Ince ES, Barthelmes F, Reißland S, Elger K, Förste C, Flechtner F, Schuh H (2019) ICGEM – 15 years of successful collection and distribution of global gravitational models, associated services and future plans. *Earth Syst Sci Data* 11:647–674. <https://doi.org/10.5194/essd-11-647-2019>
- Jäggi A, Meyer U, Lasser M, et al. (2020) International Combination Service for Time-Varying Gravity Fields (COST-G). In: *International Association of Geodesy Symposia*. Springer, Berlin, Heidelberg. [https://doi.org/10.1007/1345\\_2020\\_109](https://doi.org/10.1007/1345_2020_109)
- Miyahara B, Sánchez L, Sehnal M (2020) Global Geodetic Observing System (GGOS). In: Poutanen M, Rozsa S (eds) *The geodesist's handbook 2020*. *J Geod* 94(11):197–220. <https://doi.org/10.1007/s00190-020-01434-z>
- Moritz H (2000) Geodetic reference system 1980. *J Geod* 74(1):128–162. <https://doi.org/10.1007/s001900050278>
- Poutanen M, Rozsa S (eds) *The geodesist's handbook 2020*. *J Geod* 94(11). <https://doi.org/10.1007/s00190-020-01434-z>
- Sánchez L, Agren J, Huang J, Wang YM, Mäkinen J, Pail R, Riccardo R, Vergos G, Ahlgren K, Liu Q (2021) Strategy for the realisation of the International Height Reference System (IHRs). *J Geod* 95(3). <https://doi.org/10.1007/s00190-021-01481-0>

**Open Access** This chapter is licensed under the terms of the Creative Commons Attribution 4.0 International License (<http://creativecommons.org/licenses/by/4.0/>), which permits use, sharing, adaptation, distribution and reproduction in any medium or format, as long as you give appropriate credit to the original author(s) and the source, provide a link to the Creative Commons license and indicate if changes were made.

The images or other third party material in this chapter are included in the chapter's Creative Commons license, unless indicated otherwise in a credit line to the material. If material is not included in the chapter's Creative Commons license and your intended use is not permitted by statutory regulation or exceeds the permitted use, you will need to obtain permission directly from the copyright holder.



---

## Part II

# Physical Height Systems



# Can an Earth Gravitational Model Augmented by a Topographic Gravity Field Model Realize the International Height Reference System Accurately?

Jianliang Huang, Marc Véronneau, John W. Crowley, Bianca D'Aoust, and Goran Pavlic

## Abstract

In this study, we evaluate the suitability of recent Earth Gravitational Models (EGMs) for the realization of the International Height Reference System (IHR) in Canada. Topographic gravity field models have been used to augment EGMs to spatial resolution reaching 2' (about 4 km), which is comparable to regional geoid models. The advantages of using an EGM over a regional approach for the IHR are its uniform representation of the Earth's gravity field and its conformance to international standards and conventions. The main challenge is access to, and best use of knowledge of the regional gravity and topographic data. On the one hand, we determine that two recent hybrid models (EIGEN-6C4 and XGM2019) augmented by topographic signals give geopotential values ( $W_p$ ) with accuracy of  $0.3 \text{ m}^2 \text{ s}^{-2}$ , which is close to those estimated by the Canadian regional geoid models at the 11 International Height Reference Frame sites in Canada. On the other hand, two recent augmented satellite-only models (DIR-R6 and GOCO06s) give  $W_p$  with accuracies between  $1.5$  and  $1.7 \text{ m}^2 \text{ s}^{-2}$  in Canada.

## Keywords

International Height Reference System (IHR) · Geopotential · Earth Gravitational Model (EGM) · Topographic Gravity Field Model (TGFM)

## 1 Introduction

The spatial resolution of Earth Gravitational Models (EGMs) has improved drastically over the last two decades. This presents a possible opportunity for a more standardized approach to the realization of the International Height Reference System (IHR). There are generally three types of EGMs: (1) satellite-only such as DIR-R6 (Förste et al. 2019) and GOCO06s (Kvas et al. 2019); (2) hybrid such as EGM2008 (Pavlis et al. 2012) and EIGEN-6C4 (Förste

et al. 2014); and (3) topographically-augmented such as XGM2019e (Zingerle et al. 2020). Type 3 combines either Type 1 or Type 2 with a Topographic Gravity Field Model (TGFM), such as Earth2014 (Rexer et al. 2017) and ROLI (Ince et al. 2020). The high spatial resolution of digital elevation models (DEMs) and the recent development of TGFMs allow EGMs to reach a spatial resolution of 2' (about 4 km), which is comparable to regional (quasi-) geoid models. In this paper, we add the postfix 'e' to represent an EGM that is augmented by a TGFM like XGM2019e (e.g., EGMe, EIGEN-6C4e, DIR-R6e, etc.).

In principle, either an EGMe or a regional (quasi-) geoid model can realize the IHR (Sánchez et al. 2021). Either approach has its advantages and disadvantages. On the one hand, the former can ensure a consistent realization of the IHR by a homogeneous mathematical representation, but may be subject to larger commission and omission errors than the latter, due primarily to the lack of gravity data in some regions and a limited gravity field spectrum. This is less

Her Majesty the Queen in Right of Canada, as represented by the Minister of Natural Resources.

J. Huang (✉) · M. Véronneau · J.W. Crowley · B. D'Aoust · G. Pavlic  
Canadian Geodetic Survey, Surveyor General Branch, Natural Resources Canada, Ottawa, ON, Canada  
e-mail: [jianliang.huang@nrcan-rncan.gc.ca](mailto:jianliang.huang@nrcan-rncan.gc.ca)

the case for Canada as the gravity data is publically available for the development of EGMs (see e.g. Pavlis et al. 2012). On the other hand, experts at national geodetic agencies and universities can develop regional geoid models by having access to the best gravity data available and DEMs in their regions, but the methodologies employed among distinct regional geoid models may still generate an uncertainty of several centimetres (see e.g. Wang et al. 2021a).

In this study, we evaluate the suitability of the hybrid EGMs augmented by TGFMs, and the accuracy of the augmented satellite-only EGMs for the realization of the IHRS in Canada. Section 2 describes the method for computing the geopotential ( $W_p$ ) at a site. Section 3 highlights features of the EGMs to be evaluated and describes three regional geoid models selected for comparison. Section 4 estimates the errors of EGMs for the realization of the IHRS. Finally, Sect. 5 summarizes this study and presents an outlook on advancements in the future.

## 2 Methods for Computing $W_p$

The geopotential  $W_p$  at the Earth's surface in the mean tide system (MT) is calculated from a geoid model as follows (Véronneau 2021):

$$W_p = W_{0(\text{CGG2013a})} - H^{\text{MT}} \bar{g} \quad (1)$$

$$H^{\text{MT}} = (h - N) + dH^{\text{MT}} \quad (2)$$

$$dH^{\text{MT}} = -0.68 * (9.9 - 26.6 \sin^2 \varphi) * 0.01 \quad (3)$$

$$\bar{g} = g_p + 0.0424 \times 10^{-5} H^{\text{MT}} + TC \quad (4)$$

where  $W_{0(\text{CGG2013a})} = 62,636,856.0 \text{ m}^2 \text{ s}^{-2}$  (adopted  $W_0$  for North America, Véronneau and Huang 2016),  $H$ ,  $h$  and  $N$  are orthometric, ellipsoidal and geoid heights (m),  $g_p$  and  $\bar{g}$  are gravity ( $\text{m s}^{-2}$ ) at the topographical surface and mean gravity along the plumb line, and  $TC$  ( $\text{m s}^{-2}$ ) is a terrain correction to refine the classical Helmert reduction (0.0424).  $TC$  is calculated at regular interval between the geoid ( $i = 0$ ) and the topographical surface ( $i = n$ ). It can be expressed as:

$$TC = \sum_{i=0}^n MS_n^i + MD_n^i - MS_i + MD_i \quad (5)$$

where  $MS_n^i$  and  $MD_n^i$  are the attraction of the mass surplus and mass deficiency calculated at the topographical surface ( $n$ ) as for the classical terrain correction. However, the calculation of  $MD_n^i$  is not lower than height  $i$ .  $MS_i$  and  $MD_i$  are the attraction of the same masses, but calculated at height  $i$ .

## 3 Geoid Models Computed from EGMs and Regional Geoid Models

We include the four latest EGMs augmented by TGFMs, having spatial resolutions of 2' to 3', which are close to those of regional geoid models in Canada. They are briefly described below. More details can be found in the corresponding references cited.

- **EIGEN-6C4e** (degree and order (d/o) 3660) combines EIGEN-6C4 (Förste et al. 2014) and the ROLI topographic gravity field model (Ince et al. 2020). The transition band merging the two models is between spherical harmonic degrees 2000 and 2100. EIGEN-6C4 makes use of the EGM2008 gravity grid with a spatial resolution of 5' over land and DTU10 over the oceans (Andersen 2010). The low-degree components are determined using the GOCE satellite data, identical to DIR-R5 (Bruinsma et al. 2014).
- **XGM2019e** (d/o 5540; Zingerle et al. 2020) combines the GOCO06s satellite-only model (Kvas et al. 2019), a 15' global gravity grid of the landmass provided by the National Geospatial-Intelligence Agency (NGA), the DTU13 marine gravity grid (Andersen et al. 2013), and the Earth2014 topographic gravity field model (Rexer et al. 2016, 2017).
- **DIR-R6e** (d/o 3660) combines the DIR-R6 satellite-only model (Förste et al. 2019) and ROLI. The transition band is between spherical harmonic degrees 220 and 250 (Ince et al. 2020).
- **SATOP2** (d/o 5540) is an updated model of SATOP1, which is based on GOCO05s (Mayer-Gürr 2015), and augmented using Earth2014 (Zingerle et al. 2019). GOCO06s replaces GOCO05s in SATOP2 (Pail per. comm. 2021; Zingerle 2022). Following the naming convention in this study, it can be considered as GOCO06se.

The geoid models for the four EGMs are calculated as the sum of the height anomaly synthesized on the GRS80 reference ellipsoid (Moritz 1980) and the negative topographic bias (Eq. 25, Sjöberg 2007; Eq. 2.5, Huang and Véronneau 2015):

$$N_{n_{\text{max}}}(\Omega) = N_0(\Omega) + N_1(\Omega) + N_{2 \sim n_{\text{max}}}(\Omega) + C_T(\Omega) \quad (6)$$

$\Omega$  is the geocentric angle denoting the pair ( $\theta$ ,  $\lambda$ ), the spherical co-latitude and longitude. The first and second terms on the right side of Eq. (6) are the components for degrees 0 and 1 (Huang and Véronneau 2013). The third term represents the sum of the spherical harmonic components of the height anomaly or biased geoid height on the reference ellipsoid from degrees 2 to  $n_{\text{max}}$  synthesized from the EGMs.

It is subject to the analytical downward continuation (ADC) error, which is defined as the result of both analytical continuation of the potential inside the topographic masses and the truncation of the harmonic series by Sjöberg (2011). The fourth term is the negative topographic bias to correct for the ADC error, and can be written as:

$$C_T(\Omega) = -\frac{2\pi G\rho H^2}{\gamma_E} \left(1 + \frac{2H}{3R}\right) \quad (7)$$

where  $G$  is the gravitational constant,  $\rho = 2.67\text{g/cm}^3$  is the mean topographic mass density,  $\gamma_E$  is the normal gravity on the reference ellipsoid,  $R$  is the mean radius of the Earth. Sjöberg (2007, 2009) proved that Eq. (7) is exact. Sjöberg (2011) found that the ADC error agrees well with the topographic bias in most cases except in high mountains in the case study of EGM2008. This reflects the state of the art of this method. It is an open question on how well the topographic bias corrects for the ADC error for EGMe with the maximum degree higher than EGM2008. The comparison between the geopotential values estimated from the regional geoid model in Canada and the EGMe helps answer this question partially. Further studies are required on the ADC error for the EGMe, but this topic is well beyond the scope of this study. Readers of interest can find more discussion on this topic by Jekeli (1981), Wang (1997) and Ågren (2004) etc. Program GrafLab v.2.1.4 implements the extended-range arithmetic algorithm for the spherical harmonic synthesis (Bucha and Janák 2013). It is used for the spherical harmonic synthesis up to  $d/o$  5540 for this study. The topographic bias is calculated using a DEM, which combines DEMs from Natural Resources Canada (NRCan), the National Oceanic and Atmospheric Administration (NOAA) and STRM4.1 (see Huang and Véronneau 2013).

It should be noted that the geopotential values from EGMes can also be synthesized directly from their spherical harmonic coefficients at a site on the Earth's surface. However, it is questionable in theory if the spherical harmonic representation of topographical potential by the external type of TGFM on the Earth's surface is convergent at the site (see e.g. Moritz 2015). Even though the truncated TGFM series is finite, the resulting topographic potential value is theoretically invalid at a surface site below the bounding sphere encompassing the entire earth masses (Brillouin sphere). One may argue that this type of potential value is approximate enough over flat regions and oceans.

Three regional geoid models developed at the Canadian Geodetic Survey (CGS), NRCan, are selected for this study:

- **CGG2013a** is the official geoid model ( $2' \times 2'$ ) realizing the Canadian Geodetic Vertical Datum of 2013 (CGVD2013) (Véronneau and Huang 2016). It is determined using the Stokes-Helmert method with a

degree-banded Stokes kernel modification (Huang and Véronneau 2013). The reference EGM is EIGEN-6C3stat (Förste et al. 2013). The modified Stokes kernel has a transition band between degrees 120 and 180 (about 200 km wavelength). The gravity data include 2.2 million measurements distributed across North America that were collected over land, oceans, lake surfaces and ice caps by ground, shipboard and airborne surveys. DTU10 is used to fill up most of the oceans. CGG2013a comes with a standard deviation model, which is estimated from the calibrated standard deviations of EIGEN-6C3stat and the standard deviation grid of gravity data. This error model is realistic over flat areas, but tends to be pessimistic over mountainous areas.

- **PCGG18-055** is an experimental geoid model to improve upon CGG2013a. This model differs from CGG2013a by the reference EGM and the Stokes kernel modification. EIGEN-6C4 is used for the reference model, and the modified Stokes kernel has a transition band between degrees 150 and 210, increasing the satellite contribution with respect to CGG2013a.
- **PCGG20-21A** is an experimental geoid model developed towards the North American-Pacific Geopotential Datum of 2022. The reference EGM is xG20refA (Wang et al. 2021b), which is a combination of EGM2008 and GOCO06s by the National Geodetic Survey (NGS), NOAA. The modified Stokes kernel has a transition band between degrees 150 and 220. The terrestrial gravity grid is a composite of land gravity data, DTU15 marine gravity data (Andersen et al. 2016), ArcGP v2020 for Greenland (Beale per. comm. 2020), and EGM2008 for data gaps over land outside North America. This model reflects recent progress in geoid development at CGS.

The selection of the three geoid models above allows us to examine dependence of their evaluation results. CGG2013a and PCGG18-055 use the same gravity data and DEM, but two different EGMs and Stokes kernel modifications. They can demonstrate the dependence on the combination of EGM. PCGG20-21A uses a different EGM, gravity dataset and DEM from the former two models representing a state of the art geoid model developed at CGS. It can manifest the dependence on the evolution of geoid development.

#### 4 Geopotential Values at the IHRF Sites in Canada

There are eleven International Height Reference Frame (IHRF) sites in Canada (see Fig. 1). The geopotential  $W_p$  is calculated for the four EGMes and the three regional geoid models using Eq. (1). The geometric reference frame and epoch of the ellipsoidal heights are ITRF2014 (Altamimi et al. 2016) and January 15, 2021, respectively. Table 1

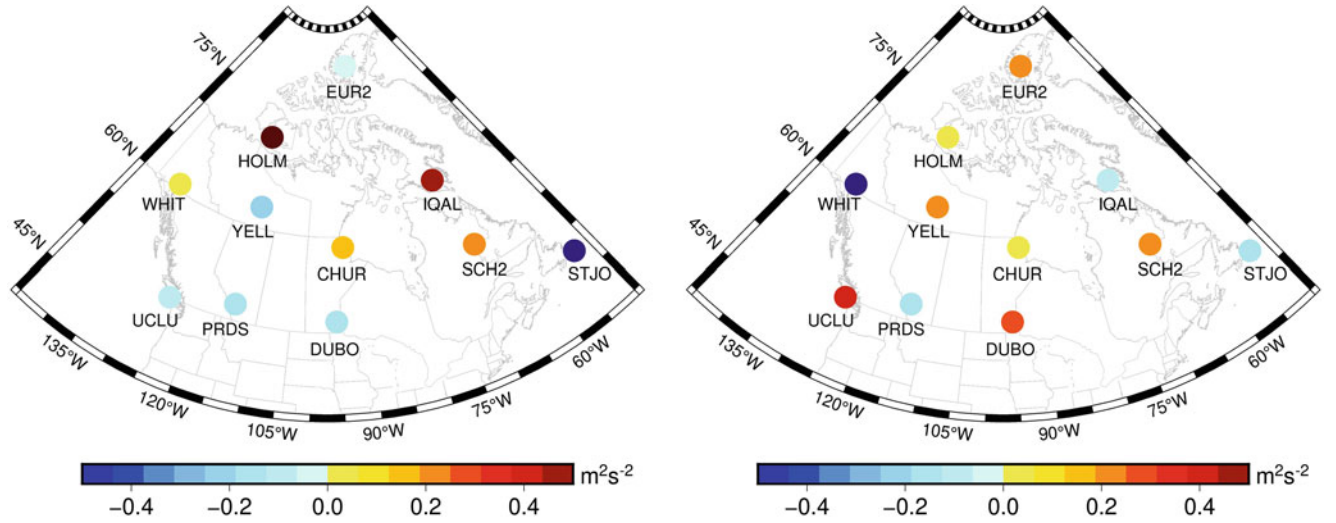


**Fig. 1** Differences between  $W_p$  estimates from EIGEN-6C4e (d/o 3660) and CGG2013a (left panel); and from XGM2019e (d/o 5540) and PCGG20-21A (right panel) at the 11 IHRF sites in Canada

**Table 1** Geopotential  $W_p$  at the 11 IHRF sites in Canada.  $W_p$  is computed in the mean-tide system (Units:  $\text{m}^2 \text{s}^{-2}$ )

Station ID	$W_p^a$	$W_p(\text{Model}) - W_p(\text{CGG2013a})$					
	CGG2013a	PCGG18-055	PCGG20-21A	EIGEN-6C4e	XGM2019e	DIR-R6e	SATOP2
CHUR	36570.46	0.13	0.08	0.15	0.08	0.51	-0.41
DUBO	34157.73	-0.08	0.00	-0.17	0.30	1.41	2.19
EUR2	36634.13	0.32	0.04	-0.04	0.29	0.56	1.54
HOLM	36689.62	0.05	0.05	0.51	0.06	-1.70	-1.90
IQAL	35851.45	0.12	-0.03	0.49	-0.10	1.40	1.78
PRDS	24459.14	-0.14	0.09	-0.13	-0.08	2.34	1.91
SCH2	31765.84	0.17	0.26	0.24	0.48	1.95	0.83
STJO	35452.02	-0.19	0.08	-0.50	-0.05	2.40	1.46
UCLU	36573.31	0.00	-0.02	-0.11	0.38	-2.68	-1.33
WHIT	22919.47	0.02	-0.10	0.06	-0.83	-1.11	-1.28
YELL	34814.95	0.08	0.03	-0.21	0.24	0.05	0.37
Mean		0.04	0.05	0.03	0.07	0.47	0.47
Range (max.-min.)		0.51	0.36	1.01	1.31	5.08	4.09
RMS		0.15	0.10	0.29	0.35	1.68	1.48

<sup>a</sup> Geopotential is subtracted by a common reference value of  $62,600,000 \text{ m}^2 \text{ s}^{-2}$

gives the geopotential at each site for CGG2013a, and the deviations with respect to CGG2013a for the other six models.

The geopotential results and their statistics in Table 1 show that the regional geoid models, augmented hybrid models and satellite-only models are distinctly different. The two regional geoid models agree well with the reference model CGG2013a. The augmented hybrid models have comparable statistics with respect to CGG2013a, but a bit larger than the regional models. We have discussed the ADC error in Sect. 3. The RMS differences of  $0.29$  and  $0.35 \text{ m}^2 \text{ s}^{-2}$  for EIGEN-6C4e and XGM2019e in Table 1 also contain the ADC error, thus give the upper bounds of ADC error numerically at the 11 IHRF sites. As the ADC error depends on topography at an IHRF site, these upper bounds are not

applicable for other regions. Finally, the augmented satellite-only models show by far the largest differences from the reference model due to the absence of the mid-wavelength components of the gravity field.

To answer the question in the title of paper, we estimate the standard deviations of the augmented EGM models by the following equation:

$$\sigma_{\text{EGMe}} = \sqrt{RMS^2 - \sigma_{\text{CGG2013a}}^2} \quad (8)$$

where the Root Mean Square (RMS) is from Table 1.  $\sigma_{\text{CGG2013}}$  is the mean standard deviation calculated from the standard deviations of CGG2013a at the 11 IHRF sites. It is about  $0.2 \text{ m}^2 \text{ s}^{-2}$  for both arithmetic mean and RMS of the CGG2013a standard deviations at the 11



sites. Statistically speaking, the RMS estimate tends to be more meaningful. Eq. (8) is approximate because errors of CGG2013a and EGMs are correlated due to the use of GOCE models and/or Canadian terrestrial gravity data. The standard deviation estimates of the  $W_p$  values from EIGEN-6C4e and XGM2019e are 0.2 and 0.3  $\text{m}^2 \text{s}^{-2}$ , respectively, while the corresponding estimates for DIR-R6e and SATOP2 are 1.7 and 1.5  $\text{m}^2 \text{s}^{-2}$ , respectively. The 11 IHRF sites cover various and vast landscapes in Canada. Thus, the level of errors for the satellite-only EGMs is indicative globally. However, there are regions worldwide with stronger topography gradients than the ones in Canada and the accuracy of the topographic models is not homogenous. Additionally, the synthetic gravity signals inferred from the topography models are based on a constant crustal mass density value (2.67  $\text{g/cm}^3$ ) over land (except for oceans, Greenland and Antarctica), for which it does not necessarily represent the true mass density. Considering these factors, standard deviations for DIR-R6e and SATOP2 in certain regions could be larger than the estimates in Canada. Geopotential values  $W_p$  computed from the augmented hybrid and satellite-only models are also compared with the recent PCGG20-21A, and the statistics are shown in Table 2. As expected, they are largely similar to the statistics in Table 1. This suggests that the evaluation results do not depend on the selected regional model. Nevertheless, it is meaningful to eliminate the impact of using different reference EGMs for the regional model. CGG2013a used EIGEN-6C3stat—an earlier release of EIGEN-6C4, while both XGM2019e and PCGG20-21A are based on GOCO06s. Therefore, a comparison between each pair of them better indicates errors in the  $W_p$  estimates from EIGEN-6C4e and XGM2019e. The agreement between EIGEN-6C4e and CGG2013a is similar to the agreement between XGM2019e and PCGG20-21A, but shows distinct patterns (see Fig. 1). Assuming the equal errors between each pair, the  $W_p$  estimates for EIGEN-6C4e and XGM2019e would have an RMS error of 0.2  $\text{m}^2 \text{s}^{-2}$ , which is equal to the mean standard deviation of CGG2013a at the 11 IHRF sites. The comparison between XGM2019e and EIGEN-6C4e indicates that their RMS errors for  $W_p$  are about 0.3  $\text{m}^2 \text{s}^{-2}$ , again assuming equal errors between them.

**Table 2** Statistics of differences for the  $W_p$  values estimated from the regional geoid models and EGMs at the 11 IHRF sites in Canada. Units:  $\text{m}^2 \text{s}^{-2}$

Models	Min.	Max.	Mean	Range	RMS
EIGEN-6C4e – PCGG20-21A	−0.58	0.52	−0.02	1.10	0.30
XGM2019e – PCGG20-21A	−0.73	0.39	0.02	1.12	0.30
DIR-R6e – PCGG20-21A	−2.66	2.33	0.42	4.99	1.62
SATOP2 – PCGG20-21A	−1.95	2.19	0.42	4.14	1.45
XGM2019e – EIGEN-6C4e	−0.89	0.48	0.04	1.37	0.46

The standard deviation model for CGG2013a is also representative for PCGG18-055 because it uses the same modelling method and terrestrial gravity data. The use of different EGMs in CGG2013a and PCGG18-055 generates only a minor effect on the accuracy. The mean standard deviations in CGG2013a for the Canadian Rockies, the Maritimes and the Great Lakes region are 6.6 cm, 1.6 cm and 1.5 cm, respectively. The GPS-Levelling validation shows that PCGG18-055 performs better than the two hybrid-augmented EGMs by a few centimetres over the Canadian Rockies, but the three models are comparable over the two other regions. It indicates that the difference between hybrid-augmented EGMs (i.e., EIGEN-6C4e, XGM2019e) and regional models becomes marginal outside regions with rough topography.

In addition, we estimated the standard deviations of the two satellite-only EGMs from the standard deviation model of CGG2013a and the RMS differences between the EGMs and PCGG18-055 for the same three regions using Eq. (8). The estimates for DIR-R6e become 16.1 cm, 16.9 cm and 23.7 cm over the Canadian Rockies, the Maritimes and the Great Lakes regions, respectively. The corresponding estimates for SATOP2 are 10.8 cm, 14.5 cm and 20.3 cm, respectively. These estimates are largely consistent with the standard deviation estimates of  $W_p$  at the 11 IHRF sites for DIR-R6e and SATOP2.

## 5 Conclusions and Outlook

The answer to the question in the title is: not yet. The RMS difference between the  $W_p$  values at the eleven IHRF sites calculated from the two TGFm-augmented hybrid models, i.e., EIGEN-6C4e and XGM2019e, is 0.5  $\text{m}^2 \text{s}^{-2}$ . Furthermore, these  $W_p$  values differ from those determined from the two experimental regional geoid models by an RMS of 0.3  $\text{m}^2 \text{s}^{-2}$ . For the two hybrid models, the RMS error of  $W_p$  is 0.3  $\text{m}^2 \text{s}^{-2}$  assuming the equal error between them. This is three times the magnitude of the targeted accuracy of 0.1  $\text{m}^2 \text{s}^{-2}$  stated for the IHRF (Sánchez et al. 2021). We should point out that the study region (Canada) has a good distribution of quality surface gravity data and these data are included in the two hybrid EGMs. Therefore, the error estimates are only applicable for regions with a similar gravity data coverage. As for the satellite-only models DIR-R6 and GOCO06s that are augmented by the topographic gravity field models, they provide  $W_p$  values with standard deviations between 1.5 and 1.7  $\text{m}^2 \text{s}^{-2}$  at the eleven Canadian IHRF sites. These values are significantly larger than the error estimates for the two hybrid EGMs. This suggests that the surface gravity data is still essential to generate EGMs with high accuracy.

Overall, the usage of TGFM-augmented EGMs looks promising in the future. On the one hand, digital elevation models have improved with the use of airborne and space mapping technologies. On the other hand, the set of global gravity data will continue to improve with the development of national (quasi-) geoid-based vertical datums and the IHRF. In the meantime, the topographic gravity field forward modelling is a scientific effort that will push the spatial resolution of TGFM to new levels. However, they should be used with caution in any geophysical applications as they do not represent the actual gravitational field of topographic (or any other modelled) masses. Another issue is the use of these external type of harmonic series inside the domain of their convergence.

**Acknowledgements** We would like to acknowledge Dr. Juraj Janák from Slovak University of Technology for providing GrafLab and examples; Dr. Elmas Sinem Ince from GFZ, Germany for providing EIGEN-6C4e and DIR-R6e, and Dr. Roland Pail from Technical University of Munich for providing SATOP2 for this study. The constructive comments by the two anonymous reviewers and the associate editor are highly appreciated. This is NRCan contribution number 2022101.

## References

- Ågren J (2004) The analytical continuation bias in geoid determination using potential coefficients and terrestrial gravity data. *J Geod* 78:314–332. <https://doi.org/10.1007/s00190-004-0395-0>
- Altamimi Z, Rebischung P, Metivier L, Collilieux X (2016) ITRF2014: a new release of the International Terrestrial Reference Frame modeling nonlinear station motions. *J Geophys Res Solid Earth* 121. <https://doi.org/10.1002/2016JB013098>
- Andersen OB (2010) The DTU10 gravity field and mean sea surface. Second international symposium of the gravity field of the Earth (IGFS2), Fairbanks, Alaska, USA
- Andersen OB, Knudsen P, Kenyon S, Factor J, Holmes S (2013) The DTU13 global marine gravity field—first evaluation. Ocean Surf Topogr Sci Team Meet, Boulder, Colorado
- Andersen OB, Stenseng L, Piccioni G, Knudsen P (2016) The DTU15 MSS (Mean Sea Surface) and DTU15LAT (Lowest Astronomical Tide) reference surface. Abstract from ESA Living Planet Symposium 2016, Prague, Czech Republic. [http://lps16.esa.int/page\\_session189.php#1579p](http://lps16.esa.int/page_session189.php#1579p)
- Bruinsma SL, Förste C, Abrikosov O, Lemoine J-M, Marty J-C, Mulet S, Rio M-H, Bonvalot S (2014) ESA's satellite-only gravity field model via the direct approach based on all GOCE data. *Geophys Res Lett* 41:7508–7514. <https://doi.org/10.1002/2014GL062045>
- Bucha B, Janák J (2013) A MATLAB-based graphical user interface program for computing functionals of the geopotential up to ultra-high degrees and orders. *Comput Geosci* 56:186–196. <https://doi.org/10.1016/j.cageo.2013.03.012>
- Förste C, Bruinsma S, Marty JC, Flechtner F, Abrikosov O, Dahle C, Lemoine JM, Neumayer KH, Biancale R, Barthelmes F, König R (2013) EIGEN-6C3—the newest high resolution global combined gravity field model based on the 4th release of the GOCE direct approach. International Association of Geodesy Scientific Assembly, Sept. 1–6, 2013, Potsdam, Germany
- Förste C, Bruinsma S, Abrikosov O, Lemoine JM, Marty J, Flechtner F, Balmino G, Barthelmes F, Biancale R (2014) EIGEN-6C4 the latest combined global gravity field model including GOCE data up to degree and order 2190 of GFZ Potsdam and GRGS Toulouse. GFZ Data Serv. <https://doi.org/10.5880/icgem.2015.1>
- Förste C, Abrikosov O, Bruinsma S, Dahle C, König R, Lemoine JM (2019) ESA's Release 6 GOCE gravity field model by means of the direct approach based on improved filtering of the reprocessed gradients of the entire mission (GO\_CONS\_GCF\_2\_DIR\_R6). GFZ Data Serv. <https://doi.org/10.5880/ICGEM.2019.004>
- Huang J, Véronneau M (2013) Canadian gravimetric geoid model 2010. *J Geod* 87:771–790. <https://doi.org/10.1007/s00190-013-0645-0>
- Huang J, Véronneau M (2015) Assessments of recent GRACE and GOCE Release 5 global geopotential models in Canada. *Newton's Bulletin*, N. 5, pp 127–148
- Ince ES, Abrykosov O, Förste C et al (2020) Forward gravity modelling to augment high-resolution combined gravity field models. *Surv Geophys* 41:767–804. <https://doi.org/10.1007/s10712-020-09590-9>
- Jekeli C (1981) The downward continuation to the Earth's surface of the truncated spherical and ellipsoidal harmonic series of gravity and height anomalies. Rep no. 323, Department of Geodetic Science and Surveying, The Ohio State University, Columbus, Ohio
- Kvas A, Mayer-Gürr T, Krauss S, Brockmann JM, Schubert T, Schuh W-D, Pail R, Gruber T, Jäggi A, Meyer U (2019) The satellite-only gravity field model GOCO06s. GFZ Data Serv. <https://doi.org/10.5880/ICGEM.2019.002>
- Mayer-Gürr T (2015) The combined satellite gravity field model GOCO05s, EGU General Assembly Conference Abstracts, 17, p 12364
- Moritz H (1980) Geodetic Reference System 1980. *Bull Geod* 62(2):187–192
- Moritz H (2015) Classical physical geodesy. In: Freedon W, Nashed M, Sonar T (eds) Handbook of geomathematics. Springer, Berlin, Heidelberg. [https://doi.org/10.1007/978-3-642-54551-1\\_6](https://doi.org/10.1007/978-3-642-54551-1_6)
- Pavlis NK, Holmes SA, Kenyon SC, Factor JK (2012) The development and evaluation of the Earth Gravitational Model 2008 (EGM2008). *J Geophys Res* 117:B04406. <https://doi.org/10.1029/2011JB008916>
- Rexer M, Hirt C, Claessens S, Tenzer R (2016) Layer-based modelling of the Earth's gravitational potential up to 10-km scale in spherical harmonics in spherical and ellipsoidal approximation. *Surv Geophys* 37(6):1035–1074. <https://doi.org/10.1007/s10712-016-9382-2>
- Rexer M, Hirt C, Pail R (2017) High-resolution global forward modelling: a degree-5480 global ellipsoidal topographic potential model. In: EGU general assembly conference abstracts, 19, p 7725. <https://ui.adsabs.harvard.edu/abs/2017EGUGA..19.7725R>
- Sánchez L, Ågren J, Huang J et al (2021) Strategy for the realisation of the International Height Reference System (IHRs). *J Geod* 95:33. <https://doi.org/10.1007/s00190-021-01481-0>
- Sjöberg LE (2007) The topographic bias by analytical continuation in physical geodesy. *J Geod* 81:345–350. <https://doi.org/10.1007/s00190-006-0112-2>
- Sjöberg LE (2009) On the topographic bias in geoid determination by the external gravity field. *J Geod* 83:967–972. <https://doi.org/10.1007/s00190-009-0314-5>
- Sjöberg LE (2011) A numerical study of the analytical downward continuation error in geoid computation by EGM08. *J Geod Sci* 1(1):2–8. <https://doi.org/10.2478/v10156-010-0001-8>
- Véronneau M (2021) Technical Report – Mean Gravity along the Plumb line and Separation between Geoid to Quasi-geoid, Canadian Geodetic Survey, Natural Resources Canada
- Véronneau M, Huang J (2016) The Canadian geodetic vertical datum of 2013 (CGVD2013). *Geomatica* 70(1):9–19

- Wang YM (1997) On the error of analytical downward continuation of the Earth's external gravitational potential on and inside the Earth's surface. *J Geod* 71:70–82
- Wang YM, Sánchez L, Ágren J et al (2021a) Colorado geoid computation experiment: overview and summary. *J Geod* 95:127. <https://doi.org/10.1007/s00190-021-01567-9>
- Wang et al (2021b) Technical details of xGEOID2020, National Geodetic Survey, NOAA
- Zingerle P (2022) Advanced methodologies for large-scale gravity field modelling. PhD thesis, 2022. ISBN 978-3-7696-5300-7. <https://nbn-resolving.org/urn/resolver.pl?urn:nbn:de:bvb:91-diss-20220204-1627470-1-6>
- Zingerle P, Pail R, Scheinert M, Schaller T (2019) Evaluation of terrestrial and airborne gravity data over Antarctica: a generic approach. *J Geod Sci* 9:29–40. <https://doi.org/10.1515/jogs-2019-0004>
- Zingerle P, Pail R, Gruber T et al (2020) The combined global gravity field model XGM2019e. *J Geod* 94:66. <https://doi.org/10.1007/s00190-020-01398-0>

**Open Access** This chapter is licensed under the terms of the Creative Commons Attribution 4.0 International License (<http://creativecommons.org/licenses/by/4.0/>), which permits use, sharing, adaptation, distribution and reproduction in any medium or format, as long as you give appropriate credit to the original author(s) and the source, provide a link to the Creative Commons license and indicate if changes were made.

The images or other third party material in this chapter are included in the chapter's Creative Commons license, unless indicated otherwise in a credit line to the material. If material is not included in the chapter's Creative Commons license and your intended use is not permitted by statutory regulation or exceeds the permitted use, you will need to obtain permission directly from the copyright holder.





# Assessing Molodensky's Heights: A Rebuttal

R. Kingdon, P. Vaníček, M. Santos, Z. Martinec, and I. Foroughi

## Abstract

This paper is written as a progression of the ongoing discussion in geodesy about the merits of the Molodensky height system versus the classical height system. It is a rebuttal of a publication in the *Proceedings of the IX Hotine-Marussi Symposium on Mathematical Geodesy* by Victor Popadyev titled “On the Advantage of Normal Heights: Once More on the Shape of Quasigeoid.” Even though Popadyev’s paper was not presented at the symposium it was published in the proceedings regardless. It purports to address a presentation from the symposium titled “The shape of the quasigeoid”, that applied a set of criteria to judge the suitability of the quasigeoid as a vertical reference surface, ultimately finding it inferior due to its edges and folds. The proceedings paper acknowledges these irregularities in the quasigeoid, but instead argues that the Molodensky system, apart from any vertical reference surface, should be evaluated on two different and more favorable criteria, and finds it superior on that basis. Herein, we continue the ongoing discussion by clarifying some of the misunderstandings in the Popadyev paper and explaining that even on the favourable criteria proposed the Molodensky system holds no advantages over the classical system.

## Keywords

Classical heights · Molodensky heights · Normal heights · Orthometric heights · Quasigeoid

## 1 Introduction

An unfortunate circumstance forces us to write this contribution to the discussion between the classical and Molodensky’s normal height systems in the form of a rebuttal rather than in the form of a standard scientific paper. An article with Victor Popadyev as the first author (Popadyev 2019) appears in the *Proceedings of the IX Hotine-Marussi*

*Symposium on Mathematical Geodesy*, staged in Rome on June 18 to 22, 2018, titled “On the Advantage of Normal Heights: Once More on the Shape of Quasigeoid”, The paper appears to have undergone little peer review, and was accepted and published in these Proceedings despite not having been presented at the symposium.

A paper by the first 3 authors, entitled “The shape of the quasigeoid”, was presented and discussed during the Hotine – Marussi Symposium but not submitted for publication in the Proceedings. It examined the behavior of the quasigeoid in a differential sense, demonstrating that it is a surface with folds and edges—sometimes substantial ones—and questioning whether it is suitable for use as a reference surface in a modern height system. Popadyev’s paper was written with the aim of “analyzing the arguments in [our presentation],” and begins by affirming our central thesis

R. Kingdon · P. Vaníček · M. Santos (✉) · I. Foroughi  
Department of Geodesy and Geomatics Engineering, University of  
New Brunswick, Fredericton, NB, Canada  
e-mail: [robert.kingdon@unb.ca](mailto:robert.kingdon@unb.ca); [msantos@unb.ca](mailto:msantos@unb.ca)

Z. Martinec  
School of Cosmic Physics, Geophysics Section, Dublin Institute for  
Advanced Studies, Dublin 2, Ireland

that the quasigeoid has the same irregularities in shape as the topographical surface does but goes on to argue along some different lines that the Molodensky system of heights is still superior. Although Popadyev does not address our thesis beyond this affirmation, and has not provided a substantial counter to it, a reader having only Popadyev's account of our presentation might be misled to think his paper is a definitive rebuttal of our work. This contribution is meant to address some of Popadyev's arguments and to situate his paper in the context of an ongoing discussion about the relative merits of the Molodensky height system and the classical height system.

To be clear about our terminology, by the term *height system* we understand the combination of a height reference surface and a defined height metric prescribing the distance from a point to that surface. In a classical height system, the orthometric height is the shortest (space geodesic) distance from a point to the geoid in a Riemannian physical space. In a geodetic height system, the geodetic height is the shortest distance from a point to a reference ellipsoid in a Euclidian geometrical space. Such definitions may be complemented by a practical realization of the height system either via a set of benchmarks with known heights, via a reference surface model that provides the location of the surface for each horizontal position, or via a combination of both.

## 2 Auxiliary Arguments

Many of the arguments that Popadyev recounts for the Molodensky system and against the classical system, such as the requirement in the classical system of knowing the topographical density, are not new. Popadyev acknowledges and embraces the historical nature of such debates. These debates, while important, are not closely related to our thesis, so we will not refute them in detail. However, we do take issue with Popadyev reiterating the historical arguments for the Molodensky system while he, and any reviewers of his paper, have ignored the massive body of work showing that they are no longer valid (Vaníček and Martinec 1994; Martinec and Vaníček 1994; Martinec and Vaníček 1996; Vaníček et al. 1999; Huang et al. 2001; Janák and Vaníček 2001; Tenzer et al. 2003; Tenzer and Vaníček 2003; Tenzer et al. 2005; Kingdon et al. 2005; Santos et al. 2006; Ellmann and Vaníček 2007; Ellmann et al. 2007; Cheraghi et al. 2007; Kingdon et al. 2009; Kingdon et al. 2012; Foroughi and Tenzer 2017; Foroughi et al. 2017a, b; Janák et al. 2017; Goli et al. 2018; Foroughi 2018; Foroughi et al. 2019; Sheng et al. 2019; Vaníček and Santos 2019; Goli et al. 2019a, b)—the references indicated come mostly from geodesists who follow the “University of New Brunswick’s (UNB) line of thought” (as this is a rebuttal paper) but it is by no means complete, as many other colleagues dedicated to

the classical theory validate our assumptions. Among other things, this substantial list of references shows that several quantities Popadyev claims are “unknown” or “unknowable” can be determined with sufficient accuracy. The issue is prominent in Popadyev's variant of the Molodensky thought experiment, where he purports that the geoid cannot be uniquely determined from gravity measured on Earth's surface because two mass-density distributions within Earth may produce the same external gravity measurements but produce different geoids. Molodensky's original argument was quite simple: “neither the geoid, nor the orthometric height can be ever known with sufficient accuracy because one would need to know the topographical mass density to a level that, can never be achieved”. There are two problems with this argument. The first is that the topo-mass non-homogeneity affects the accuracy of the classically computed geoid less than Molodensky would expect. The rule of thumb is that the error from this source is about 10% of the error one would commit by neglecting the effect of topography of constant density, i.e., a few decimetres at the most. The second problem is that the topo-mass distribution was known very poorly or not at all in the mid-twentieth century. This is not the case anymore and the lateral topographical non-homogeneity is now known, probably better than to 10%, over large parts of the globe. In Molodensky's original thought experiment, two masses entirely within the geoid were invoked; in Popadyev's version the masses are partly within the topography as well. In fact, only the part of the mass-density distribution that is within the topography (i.e., outside the geoid) is required to uniquely determine the shape of the geoid from surface measurements, and it does not need to be known all that well. In most situations, modeling topographical density as a constant average density value provides centimetre-level accuracy, while in more complex areas a simple laterally varying density model is usually sufficient (Vaníček et al. 2012).

While some of Popadyev's claims would be reasonable were they not already addressed well in existing literature, others are simply untrue. One example is the statement that “the solution of the boundary value problems of the Newton potential in all cases requires that the earth's surface should be smoothed out to the Lyapunov's conditions.” This is a requirement in the Molodensky theory, but not in the classical theory, and in any case does not have bearing on the actual shape of the reference surfaces but only on how they are determined. It is a strange point for Popadyev to broach, because this difficulty is one of the main failings of the Molodensky theory as it pertains to determination of the quasigeoid. Over half a century of work has failed to produce an exact solution to the Molodensky Boundary Value Problem for the actual, irregular topographical surface, hence the requirement that the surface be regularized, or that some alternative approach be applied. The discretization

of topography for solving the downward continuation of gravity from the Earth's surface to the Bjerhammar sphere regularises the instabilities hidden in the downward continuation. For instance, the spatial discretization of topographical heights by  $5 \text{ arcmin} \times 5 \text{ arcmin}$  in the rough terrain of the Rocky Mountains regularises the DWC very efficiently (Martinec et al. 1996). However, making the discretization of topo heights finer, there is a limit, below which the DWC is numerically unstable. For example, for the Irish topography, this limit is a grid step of about 400 m size (Sajjadi et al. 2021).

Likewise, Sect. 2 of Popadyev's paper was mostly devoted to demonstrating issues with figures that, while the corrections are appreciated, have no bearing on the validity of our conclusions. The discussion of the "auxiliary" terminology in Sect. 3 and the dated listing of advantages of normal heights there also do not strongly bear on our thesis, and indeed many of the listed advantages are now shared by both the classical and Molodensky height systems.

These tangential issues do form part of the larger debate on height systems, but we did not really discuss them in our presentation, so we will not discuss them further here.

### 3 Main Arguments

At the beginning of his paper, Popadyev affirms our thesis that "The main disadvantage of the quasi-geoid boils down to the well-known fact that near the singular points of the earth's surface (conical cusps and faces) . . . the surface of the quasigeoid heights . . . also has the peculiarity." Having accepted our thesis, he advances two arguments for why these "peculiarities" of the quasigeoid's shape should not matter, those being:

1. Normal heights when practically determined are referenced to a single point at a tide gauge rather than to a surface, and the heights are a quantity associated with the measurement points themselves rather than with an abstract surface, so the question of the shape of their reference surface is moot; and
2. The main criteria for evaluating a height system should be how well the system reflects the gravity field at the observation point and how well it minimizes the corrections that must be applied to levelling observations, and the Molodensky system remains superior in these two criteria.

One problem with these arguments is that instead of addressing properties of a height system, they refer to only a single mode of positioning—differential levelling—that is becoming less and less common, especially over large distances where orthometric or normal corrections are likely to be applied. Geoid and quasigeoid models in many parts of the world reach centimetre precision or better (e.g., Foroughi et

al. 2019, Van Westrum et al. 2021). This contrasts with height systems realized through differential levelling between benchmarks, which suffer from systematic errors associated with leveling measurements. In many areas, geoid quality is good enough that GNSS heighting can provide better accuracy than differential levelling (e.g., Brown et al. 2018), and often more economically over large distances, relegating differential levelling to more local applications. A growing list of countries have replaced levelling-based vertical datums—i.e., datums established by levelling to benchmarks, corrected for the influence of gravity—entirely by geoid-based datums that are realized entirely by the production of a geoid model (e.g., New Zealand Amos 2010; Canada Véronneau and Huang 2016, and the United States of America Smith 2021). Unlike levelling-based datums, geoid-based datums do not suffer from the systematic errors, maintenance requirements, and restrictions on benchmark accessibility that exist in levelling-based datums. In other words, it is simply becoming less correct to say that heights are measured relative to a tide gauge by levelling. While some situations, such as underground surveying over long distances, still require levelling corrections, these situations are becoming fewer.

Popadyev's first objection also begs discussion on a theoretical level, as he refers to an unorthodox conception of a height system whereby heights are defined only as differences in vertical position relative to a tide gauge, representing a point on the datum, according to some metric. Included in this discussion is the questionable statement that "a quasigeoid is not a 'vertical reference surface'," which defies the common conception and application of the quasigeoid. A more complete and orthodox definition, as already mentioned, defines heights by prescribing a reference surface (e.g., a geoid, a quasigeoid, or an ellipsoid) and defining some metric for the vertical distance to a point above the reference surface. This type of definition does not refer, as Popadyev's does, to a specific method of realizing a height system at certain points. It can be realized in different ways. It also defines heights everywhere, and not just at benchmarks. Consider, for example, an aircraft positioned using GNSS. Its elevation cannot be defined in Popadyev's system, where heights are defined only at a set of benchmarks. By contrast, the aircraft's elevation in a complete height system is defined in a straightforward way as the distance to the aircraft from a reference surface according to a prescribed metric. It is difficult to see a reason to ignore the reference surface in defining a height system, except if one wished to avoid invoking a reference surface with some indefensible characteristics, like the quasigeoid.

Let us add a small detour here to address an objection raised by few that the appropriate comparison involving geodetic height, geoidal height and orthometric height is not accurate enough to assess the accuracy of a geoid model under the assumption that since geoidal height and ortho-

metric height are a function of density, density would be eliminated from the assessment as they would be the same with opposite sign. We disagree with this reasoning both from a theoretical as well as from a practical perspective. From a theoretical perspective, the impact of topographical density in the computation of orthometric height and of a geoidal model are different as they are used differently through each process, and that can be shown mathematically by laying down all terms of the equations. From a practical perspective, it suffices to evaluate two geoidal heights varying only density values. Their resulting geoidal heights will be distinct, which would render different comparisons against the orthometric height. We are currently working on a paper to address this issue. End of detour.

We turn to the second point we have extracted from Popadyev's work, that we are not proposing the right criteria for choosing a height system. To reiterate, the criteria we proposed, which were criteria for a vertical reference surface rather than a whole height system, were:

1. The surface should be a horizontal surface, i.e., the natural "up" and "down" directions should be perpendicular to it,
2. For any horizontal position, there should be only one point with height equal to 0; i.e., the surface should not be folded,
3. The surface should at least be differentiable so that it can be used for slopes, i.e., each point on the surface should have only one first derivative in any,
4. The surface should change gradually and predictably over time,
5. It should be possible with adequate data and available methodology to determine the location of the surface,
6. The determination of the surface should be possible to an adequate accuracy and precision for vertical positioning applications.

These are not necessary and sufficient criteria for a height system, as they were not intended to be. Heights in a system should also be holonomic, for example, which has to do with the chosen metric as well as the reference surface. A list of criteria for choosing a height system have been presented in Berlin by Vaníček (2018).

Instead of addressing the criteria actually proposed, in Sect. 4 Popadyev says we should not use "how easy or intuitively clear" a reference surface is as a criterion. We did not use that as a criterion, but it may be a good addition to our list. From a practical standpoint, users are far more likely adopt a system and to use it correctly if they can understand it. After dismissing one criterion we did not propose, Popadyev goes on to propose two criteria of his own:

1. "how the heights under consideration characterize the level surfaces at the place where the geodetic work is carried out (for geodesy, it is not those level surfaces passing inside the Earth that are important, but those

that cross the earth's surface of a given spot, the local horizons)," and

2. "how large are the gravimetric corrections required in case[s] when the measured elevations are converted into the height differences in the adopted system."

These criteria seem cherry-picked in an attempt to support Popadyev's arguments, but we will still treat them both in turn.

The first of Popadyev's criteria needs further treatment. Let us temporarily humor Mr. Popadyev and deal only with heights at benchmarks, determined using differential levelling. In this case, the orthometric height  $H^O$  at a point is defined as (Heiskanen and Moritz 1967, eq. 4-21):

$$H^O(r_t, \Omega) = \frac{C(r_t, \Omega)}{\bar{g}(r_t, \Omega)}, \quad (1)$$

where the position of the point is given by natural coordinates, comprising radial coordinate  $r_t$  and horizontal coordinates  $\Omega$ . In the formula,  $C$  is the geopotential number at the point, while  $\bar{g}$  is the mean value of gravity along the plumbline extending below the point to the geoid. This formula in the completely defined orthometric height system prescribes the metric mentioned above for measuring height of the point above the geoid. In Popadyev's conception, it would instead represent the height difference to the point from a benchmark, which should have an equivalent value if the benchmark falls on the geoid.

The normal height,  $H^N$ , of the same point is defined as (Heiskanen and Moritz 1967, eq. 4-43):

$$H^N(r_t, \Omega) = \frac{C(r_t, \Omega)}{\bar{\gamma}(r_t, \Omega)}, \quad (2)$$

where the only difference is that now the mean gravity between the point and the geoid is replaced by  $\bar{\gamma}$ , representing the mean normal gravity along the normal plumbline from a point on the telluroid having the same horizontal position as the surface point, to the reference ellipsoid.

As is evident from Eqs. 1 and 2, the metrics for orthometric and normal height both have just as much to do with gravity at a measurement point on the surface of the topography, via the geopotential number  $C$ . The only difference is that the metric used for orthometric heights involves the actual gravity field, while the metric for normal heights involves the normal approximation to the actual gravity field.

Claims that the normal height system has more to do with the gravity field at Earth's surface often arise not from a treatment of heights like Popadyev's, but from the way reference surfaces are calculated in the more orthodox definition, relative to a reference surface. As we have in

the past, we will consider the height anomaly,  $\zeta$ , defined as 3-dimensionally varying quantity that is a function of disturbing potential,  $T$ , at a point of interest (Vaníček et al. 2004, Eq. 6):

$$\zeta(r, \Omega) = \frac{T(r, \Omega)}{\gamma(r - \zeta[r, \Omega], \Omega)}, \quad (3)$$

where  $\gamma$  is the normal gravity and  $r$  is the radial natural coordinate of the point of interest. Defined in this way, the height anomaly is a scalar field having a defined value for every point on Earth. When evaluated on any equipotential surface with constant potential  $W_s$ , the height anomalies describe the location of that surface relative to the corresponding reference ellipsoid, where the “corresponding reference ellipsoid” is the contour of the normal potential field having potential  $U_s = W_s$ . The geoid ellipsoid separation,  $N$ , is then simply the values of the height anomaly field on the equipotential surface where  $W_s = W_o$ . Thus:

$$N(\Omega) = \zeta(r_g, \Omega), \quad (4)$$

where  $r_g$  is the radial natural coordinate of the geoid's surface. The quasigeoid-ellipsoid separation,  $\zeta_{qg}$ , is given by the values the height anomaly takes on the *topographical surface* instead of the values on the geoid surface, or on any equipotential surface, and can be expressed as:

$$\zeta_{qg}(\Omega) = \zeta(r_t, \Omega), \quad (5)$$

where  $r_t$  is the radial natural coordinate of the topographical surface. For a point P at the topographical surface, there is a sense in which the value of the quasigeoid-ellipsoid separation at P has something more to do with the gravity field at P than the geoid-ellipsoid separation does, but the quasigeoid surface as a whole does not characterize the gravity field at P. The slope of the quasigeoid at P, for example, is not the slope of an equipotential surface of Earth's gravity field there. Even in the unlikely scenario that topography is perfectly level with constant geopotential  $W_t$ , the quasigeoid's surface would have a north-south slope due to north-south variations in the value of normal gravity.

We have shown that the claim that normal heights have more to do with gravity at a point of interest is true only in a very limited sense, and it is certainly not true at all that normal heights characterize the “level surfaces . . . that cross the earth's surface [at] a given spot,” because normal heights are not heights relative to level surfaces. There is also a sense in which orthometric heights have more to do with a point of observation: They are actually the distance to that point from the geoid. Normal heights, strictly defined, are the height of a point on the telluroid—not of the observation point—

relative to a reference ellipsoid (e.g., Featherstone and Kuhn 2006). If heights that “characterize the level surfaces” at the observation point are really desired, dynamic heights fit the requirement best.

In the second of Popadyev's criteria, he suggests we should use a height system that minimizes gravimetric corrections to levelling. This concern is overblown. Despite Popadyev's implications to the contrary, gravimetric corrections are almost never required in practical levelling work unless it is being done for very specific purposes such as water drainage—in which case only the dynamic correction should be used anyway—or if the levelling is being done over a very long distance such that typical measures to counteract the effect of Earth's curvature do not adequately account for gravity field variations. In these rare situations, gravimetric corrections would be avoided not because of the complexity of the orthometric vs. normal corrections: Nowadays, both may be computed to a sufficient accuracy for most purposes using available elevation and density data sets (e.g., Hwang and Hsiao 2003). Rather, gravimetric corrections are undesirable because they require additional specialized measurements to determine gravity values along the levelling line. These additional measurements are needed even if only the dynamic correction will be applied, so they must be made regardless of whether orthometric or normal corrections will also be applied thereafter.

As to whether the overall orthometric or normal corrections will be larger, this depends on the nature of the gravity field in a given area, and the extent to which its variations do or do not counteract the dynamic correction. The orthometric correction,  $c^O$ , to a height difference between points A and B, may be written (Heiskanen and Moritz 1967, eqs. 4-32 and 4-33):

$$c_{AB}^O = c_{AB}^D + \frac{\bar{g}_A - g_{ref}}{g_{ref}} H_A^O - \frac{\bar{g}_B - g_{ref}}{g_{ref}} H_B^O, \quad (6)$$

where  $c^D$  is the dynamic correction;  $\bar{g}_A$  and  $\bar{g}_B$  represent the mean gravity along the plumb lines below points A and B;  $g_{ref}$  is the arbitrary reference gravity value used for dynamic heights; and  $H_A^O$  and  $H_B^O$  are the orthometric heights of points A and B. For a line of constant orthometric height  $H^O_{AB}$ , the correction reduces to:

$$C_{AB}^O = C_{AB}^D + H_{AB}^O \left( \frac{\bar{g}_A - \bar{g}_B}{g_{ref}} \right). \quad (7)$$

It is apparent that the sign of the correction will fluctuate depending on which end of the leveling line has the larger mean gravity. There will be even more fluctuation for a line that does not have a constant height. Sometimes the orthometric correction will be larger than the dynamic correction, and sometimes smaller, but on the whole the value



will fluctuate around that of the dynamic correction. The same is true for normal heights. Of the main height systems, the dynamic heights actually fit Popadyev's second criterion just as well as orthometric or normal heights. Indeed, taking his two criteria together, we should always choose dynamic heights over normal or orthometric heights—but, since we know dynamic heights are rarely the best choice of height system, Popadyev's two criteria must be inadequate.

Finally, we will turn to the numerical example Popadyev (2019) provides in Sect. 4.2 of his paper. He intends with this example to substantiate the success of normal heights in meeting his two criteria. The stated purpose of this model is to “estimate the convenience of using normal or orthometric heights.” In the example, he considers a spherical “Earth” with a spherical “massif” of a different density embedded in it, and examines the behavior of the normal and orthometric heights relative to the dynamic heights along a horizontal tunnel through the massif. This is a very simple and unrealistic model, but simplified models are often used to explore gravitational effects, so it can't be dismissed on that basis alone. The problem is that Popadyev's model has been simplified in ways that make it unsuitable for analyzing the problem it is meant to analyze, because it is constructed in a way that minimizes any differences between dynamic and normal heights, while allowing differences between dynamic and orthometric heights. Popadyev notes this about his model, saying that “In this particular case, the normal heights give a result equivalent to that of dynamic heights.”

In particular, because Popadyev's Earth is a spherically symmetric body, it also has a spherically symmetric normal gravity field, such that at any constant “geodetic” height above the sphere, the value of normal gravity will also be constant. This is in contrast to the real oblate spheroidal Earth, where north-south variations in normal gravity are the largest variations in Earth's gravity field. Furthermore, Popadyev chooses to deal with heights along a line of constant height. In doing so, he guarantees a constant normal gravity value, making the normal correction and the dynamic correction equivalent.

Since the numerical test is carefully tuned to yield the result Popadyev desires, and to exclude real-world effects that might refute his claims, it has little value as evidence.

## 4 Conclusions

While his paper is presented as a response to our critique of the quasigeoid, and quasigeoids are indeed important for GNSS heighting in a Molodensky system, Popadyev does not mount a substantial defense of the quasigeoid as a reference surface. He acknowledges the quasigeoid's irregular shape, and advances only arguments for it that have been refuted many times before. He then turns instead to

arguments in favour of the Molodensky height system apart from the quasigeoid, mainly in the context of differential levelling. While this was not the topic of the presentation he is responding to, he brings up some points that are worth addressing.

Popadyev argues that the merits of a height system should be judged only on two rather specific criteria, which he appears to have chosen to give the Molodensky system an advantage. He suggests that:

1. A height system should characterize the level surfaces passing through points at Earth's surface where observations are made, and
2. Corrections to differential levelling observations to transform them into the chosen height system should be as small as possible, so that they are usually negligible.

Other important criteria we suggested in our presentation, and summarized in this paper, are ignored without comment, and even where Popadyev's criteria are applied the Molodensky system does not have a clear advantage.

Popadyev's first criterion is vaguely expressed, and it is not clear why it is required so long as observations can be related to heights in the system. In any case, upon analysis we see that neither Molodensky nor classical heights have an advantage in meeting the criterion; certainly not in comparison to dynamic heights which are most strongly related to the level surfaces of Earth's gravity field.

The second criterion refers to a practical consideration about how a height system is implemented. This should be secondary to ensuring that the height system has essential properties, such as holonomy. As with the first criterion we have still applied it, and found no advantage of Molodensky heights over other systems. Normal corrections are not always smaller than the orthometric corrections, and most common applications of heights take place over such small areas and have such large error allowances that both corrections are approximately equal to 0. Popadyev uses a hypothetical model designed so that the normal corrections will be small in an attempt to prove that they are smaller than the orthometric corrections, but because the model is tuned to produce his desired result it has little persuasive value.

In summary, Popadyev's paper has not refuted the points made in our presentation. In many cases, it has not attempted to. It has voiced some rarely heard arguments for the Molodensky system, but these arguments are not very strong. Had Popadyev made his comments during the conference we would have had the opportunity to clarify them on spot.

**Acknowledgment** Ismael Foroughi was supported by Mitacs Application No. IT25135.

**Authors' Contributions** R.K. and P.V. developed the main arguments and collaboratively wrote the paper; M.S., Z.M., and I.F. contributed substantially to the development of the ideas; all edited drafts of the paper.

**Data Availability Statement** Data sharing is not applicable to this article as no datasets were generated or analysed during the current study.

## References

- Amos M (2010) New Zealand Vertical Datum 2009. New Zealand Surveyor, No. 300
- Brown N, McCubbine J, Featherston W, Gowans N, Woods A, Baran I (2018) AUSGeoid2020 combined gravimetric–geometric model: location-specific uncertainties and baseline-length-dependent error decorrelation. *J Geodesy* 92(12):1457–1465. <https://doi.org/10.1007/s00190-018-1202-7>
- Cheraghi H, Hatam Y, Vaníček P, Najafi Alamdari M, Djamour Y, Qarakhani J, Saadat R (2007) Effect of lateral topographical density variations on the geoid in Iran. In: Poster presentation at General Assembly of European Geosciences Union, Vienna, April 15–20
- Ellmann A, Vaníček P (2007) UNB application of Stokes-Helmert's approach to geoid computation. *J Geodyn* 43(2):200–213. <https://doi.org/10.1016/j.jog.2006.09.019>
- Ellmann A, Vaníček P, Santos M, Kingdon R (2007) Interrelation between the geoid and orthometric heights, First International Symposium of The International Gravity Field Service (IGFS), oral presentation, August 28 - September 1, 2006, Istanbul, Turkey. Forsberg R, Kilicoglu A (eds) Proceedings of the 1st International Symposium of the International Gravity Field Service “Gravity Field of the Earth”. General Command of Mapping, Ankara, Turkey, pp 130–135
- Featherstone W, Kuhn M (2006) Height systems and vertical datums: a review in the Australian context. *Spatial Sci* 51(1) <https://doi.org/10.1080/14498596.2006.9635062>
- Foroughi I (2018) Accuracy of the classical height system. Doctoral dissertation, University of New Brunswick
- Foroughi I, Tenzer R (2017) Comparison of different methods for estimating the geoid-to-quasi-geoid separation. *Geophys J Int* 210(2):1001–1020. <https://doi.org/10.1093/gji/ggx221>
- Foroughi I, Vaníček P, Novák P, Kingdon RW, Sheng M, Santos MC (2017a) Optimal combination of satellite and terrestrial gravity data for regional geoid determination using Stokes-Helmert's method, the Auvergne test case. In: International Symposium on Gravity, Geoid and Height Systems 2016. Springer, Cham, pp 37–43
- Foroughi I, Vaníček P, Sheng M, Kingdon R, Santos M (2017b) In defense of the classical height system. *Geophys J Int* 211(2):1154–1161. <https://doi.org/10.1093/gji/ggx366>
- Foroughi I, Vaníček P, Kingdon R, Goli M, Sheng M, Afrasteh Y, Novák P, Santos M (2019) Sub-centimetre geoid. *J Geodesy* 93(6):849–868. <https://doi.org/10.1007/s00190-019-01257-7>
- Goli M, Foroughi I, Novák P (2018) On estimation of stopping criteria for iterative solutions of gravity downward continuation. *Canadian J Earth Sci* 55(4). <https://doi.org/10.1139/cjes-2017-0208>
- Goli M, Foroughi I, Novák P (2019a) Application of the one-step integration method for determination of the regional gravimetric geoid. *J Geodesy* 93:1631–1644. <https://doi.org/10.1007/s00190-019-01272-8>
- Goli M, Foroughi I, Novák P (2019b) The effect of the noise, spatial distribution, and interpolation of ground gravity data on uncertainties of estimated geoidal heights. *Stud Geophys Geod* 63:35–54. <https://doi.org/10.1007/s11200-018-1013-6>
- Heiskanen WA, Moritz H (1967) Physical geodesy. Freeman and Co., San Francisco
- Huang J, Vaníček P, Pagiatakis S, Brink W (2001) Effect of topographical mass density variation on gravity and the geoid in the Canadian Rocky Mountains. *J Geodesy* 74(11–12):805–815
- Hwang C, Hsiao Y-S (2003) Orthometric corrections from leveling, gravity, density and elevation data: a case study in Taiwan. *J Geodesy* 77(5):279–291
- Janák J, Vaníček P (2001) Improvement of the University of New Brunswick's gravimetric geoid model for Canada, poster presentation at IAG General Assembly, Budapest, Sept. 3 to 7
- Janák J, Vaníček P, Foroughi I, Kingdon R, Sheng M, Santos MC (2017) Computation of precise geoid model of Auvergne using current UNB Stokes-Helmert's approach. *Contrib Geophys Geodesy* 47(3):201–229. <https://doi.org/10.1515/congeo-2017-001>
- Kingdon R, Vaníček P, Santos M (2009) Modeling topographical density for geoid determination. *Can J Earth Sci* 46(8):571–585
- Kingdon R, Vaníček P, Santos M (2012) Effects of hypothetical complex mass density distributions on geoidal height. *Geodesy for Planet Earth* In: Kenyon S, Pacino M, Marti U (eds) International Association of Geodesy IAG2009 “Geodesy for Planet Earth” Scientific Assembly, Buenos Aires, Argentina, 31 August–4 September, 2009. International Association of Geodesy Symposia, Vol. 135. Springer, New York
- Kingdon RW, Vaníček P, Santos M, Ellmann A, Tenzer R (2005) Toward an improved height system for Canada. *Geomatica* 59(3):241–249
- Martinec Z, Vaníček P (1994) The indirect effect of Stokes-Helmert's technique for a spherical approximation of the geoid. *Manuscripta Geodaetica* 19(2):213–219
- Martinec Z, Vaníček P (1996) Formulation of the boundary-value problem for geoid determination with a higher-order reference field. *Geophys J Int* 126:219–228
- Martinec Z, Vaníček P, Mainville A, Véronneau M (1996) Evaluation of topographical effects in precise geoid determination from densely sampled heights. *J Geodesy* 70(11):746–754
- Popadyev V (2019) On the advantage of normal heights: once more on the shape of Quasigeoid. In: Novák P, Crespi M, Sneeuw N, Sansò F (eds) IX Hotine-Marussi Symposium on Mathematical Geodesy: Proceedings of the Symposium in Rome, June 18–22, 2018. International Association of Geodesy Symposia 151:25–31. <https://doi.org/10.1007/978-3-030-54267-2>
- Sajjadi S, Martinec Z, Prendergast P, Hagedoorn J, Šachl L (2021) The stability criterion for downward continuation of surface gravity data with various spatial resolutions over Ireland. *Studia Geophysica et Geodaetica* 65:219–234. <https://doi.org/10.1007/s11200-020-0769-7>
- Santos M, Vaníček P, Featherstone WE, Kingdon R, Martin B-A, Kuhn M, Tenzer R (2006) Relation between the rigorous and Helmert's definitions of orthometric heights. *J Geodesy* 80:691–704
- Sheng MB, Shaw C, Vaníček P, Kingdon RW, Santos M, Foroughi I (2019) Formulation and validation of a global laterally varying topographical density model. *Tectonophysics* 762:45–60. <https://doi.org/10.1016/j.tecto.2019.04.005>
- Smith D (2021) National Spatial Reference System (NSRS) Modernization Overview. Presented at the 2021 National Geodetic Survey Geospatial Summit, Tuesday, 4 May
- Tenzer R, Vaníček P (2003) The correction to Helmert's orthometric height due to actual lateral variation of topographical density. *Revista Brasileira de Cartografia* 55(2):44–47
- Tenzer R, Vaníček P, Novák P (2003) Far-zone contribution to the topographical effects in the Stokes-Helmert method of geoid determination. *Studia Geophysica et Geodaetica* 47:467–480
- Tenzer R, Vaníček P, Santos M, Featherstone WE, Kuhn M (2005) Rigorous orthometric heights. *J Geodesy* 79:1432–1394. <https://doi.org/10.1007/s001-005-0445-2>
- Van Westrum D, Ahlgren K, Hirt C, Guillame S (2021) A Geoid Slope Validation Survey (2017) in the rugged terrain of Colorado, USA. *J Geodesy* 95(9):online, 19 pp. <https://doi.org/10.1007/s00190-020-01463-8>

- Vaniček P (2018) Selection of an appropriate height system for geomatics. GIS Congress 2018, 27–28 September
- Vaniček P, Martinec Z (1994) Stokes-Helmert scheme for the evaluation of a precise geoid. *Manuscripta Geodaetica* 19:119–128
- Vaniček P, Santos M (2019) What height system should be used in geomatics. *Int J Earth Environ Sci* 4:160. <https://doi.org/10.15344/2456-351X/2019/160>
- Vaniček P, Huang J, Novák P, Véronneau M, Pagiatakis S, Martinec Z, Featherstone WE (1999) Determination of boundary values for the Stokes-Helmert problem. *J Geodesy* 73:180–192
- Vaniček P, Tenzer R, Sjöberg LE, Martinec Z, Featherstone WE (2004) New views of the spherical Bouguer gravity anomaly. *J Geophys Int* 159(2):460–472
- Vaniček P, Kingdon R, Santos M (2012) Geoid versus quasi-geoid: a case of physics versus geometry. *Contrib Geophys Geodesy* 42(1):101–119
- Véronneau M, Huang J (2016) The Canadian Geodetic Vertical Datum of 2013 (CGVD2013). *Geomatica* 70(1):9–19. <https://doi.org/10.5623/cig2016-101>





**Open Access** This chapter is licensed under the terms of the Creative Commons Attribution 4.0 International License (<http://creativecommons.org/licenses/by/4.0/>), which permits use, sharing, adaptation, distribution and reproduction in any medium or format, as long as you give appropriate credit to the original author(s) and the source, provide a link to the Creative Commons license and indicate if changes were made.

The images or other third party material in this chapter are included in the chapter's Creative Commons license, unless indicated otherwise in a credit line to the material. If material is not included in the chapter's Creative Commons license and your intended use is not permitted by statutory regulation or exceeds the permitted use, you will need to obtain permission directly from the copyright holder.





# On the Accuracy of Geoid Heights Derived from Discrete GNSS/Levelling Data Using Kriging Interpolation

Emanuele Alcaras , Pier Paolo Amoroso , Ugo Falchi ,  
and Claudio Parente 

## Abstract

Local geoid models presenting higher resolution than global ones are generally derived by a combination of different datasets, integrating individual pure astrogeodetic, gravimetric and GNSS/levelling solutions. To define local geoid, different interpolators may be applied starting from dataset of geoid height values. It is well known that the accuracy of the resulting models depends not only by interpolation method, but also by points numerosity and distribution. This article aims to analyse the performance of Kriging approaches in dependence of the density of the dataset. The experiments are carried out on geoid heights extracted in random way from an already existing local geoid model: different subsets are organized containing an increasing number of points in the same area and each of them is submitted to Kriging interpolations (Universal Kriging and Ordinary Kriging). The resulting models are compared with the original one and residuals are calculated to evaluate the accuracy in dependence of point density. The results demonstrate the efficiency of the Kriging methods, highlighting the possibility to achieve higher accuracy (a few centimetres) using a point density of 1 point/100 sqkm, in absence of gravity anomalies. Ordinary Kriging provides better results than Universal Kriging but the undulations between the resulting models are minimal (a few millimetres) when a high number of points is involved. Furthermore, the results highlight the limit of the leave one out Cross validation since it supplies higher residuals than direct comparison for both Universal Kriging and Ordinary Kriging, when few points are used.

## Keywords

Accuracy · Geoid height · Interpolation · Kriging · Local geoid

E. Alcaras · P.P. Amoroso  
International PhD Programme “Environment, Resources and Sustainable Development”, Department of Science and Technology, Parthenope University of Naples, Naples, Italy  
e-mail: [emanuele.alcaras@studenti.uniparthenope.it](mailto:emanuele.alcaras@studenti.uniparthenope.it); [pierpaolo.amoroso@studenti.uniparthenope.it](mailto:pierpaolo.amoroso@studenti.uniparthenope.it)

U. Falchi · C. Parente (✉)  
Department of Science and Technology, Parthenope University of Naples, Naples, Italy  
e-mail: [ugo.falchi@uniparthenope.it](mailto:ugo.falchi@uniparthenope.it); [claudio.parente@uniparthenope.it](mailto:claudio.parente@uniparthenope.it)

## 1 Introduction

The determination of the geoid, the equipotential surface of the earth's gravitational field that is closest to an average ocean surface (Barzaghi et al. 2002), is essential to measure the heights above the sea level. In fact, it represents the reference surface for orthometric heights, i.e., levelled heights corrected for gravity effects. It is known that the orthometric height of a point is nothing more than the distance from the point to the geoid, measured along a plumb line. The information on the geoid height (or geoid undulation), approximately defined as difference between the orthometric altitude and the ellipsoidal altitude, is fundamental in many

application fields, e.g., for geophysical studies relating to crustal structures (Rapp 1974) and oceanographic studies relating to the topography of the sea surface (Blinken and Koch 1999). Different techniques can be adopted for geoid modelling and detailed descriptions of them are available in literature (Erol and Çelik 2004a; Eteje and Oduyebo 2018). We can distinguish at least five different approaches: the GNSS/levelling technique, the Gravimetric technique, the Astrogeodetic technique, the Satellite technique, the hybrid approach (including and integrating two or more techniques). Those approaches differ for used data; particularly the satellite technique incorporates orbit perturbations (ranging to satellites), gradiometry, satellite-to-satellite tracking, etc.

There are global geoid models (GGMs) such as EGM 1996 (Smith and Milbert 1997) and EGM 2008 (Pavlis et al. 2008; Barzaghi et al. 2016; Maglione et al. 2018): they represent correctly only the external gravity potential. The geoid must be derived by considering topography and its mass density variations. A GGM supports the conversion of ellipsoidal heights to orthometric heights with accuracies varying between few centimetres to even a metre (Denker et al. 2009; Pavlis et al. 2012; Alcaras et al. 2022). There are also local geoid models that present higher level of accuracy: they are generally developed using local (surface or aerial) gravity data compared with the GNSS/levelling measurements (Sideris and She 1995; Huang et al. 2007). In fact, to determine an accurate local geoid, it is necessary to take full advantage of all types of data/information in an integrated solution (Chen and Luo 2004). In other terms, the accuracy of a local geoid model can be improved by integrating an existing gravimetric geoid model with the ellipsoidal height and orthometric height derived from GNSS/levelling (You 2006).

Geoid height values (GHVs) already known in specific points (Geoid Height Points, GHPs) can be interpolated to define a local Geoid model (GM) (Erol and Çelik 2004b; Das et al. 2018; Falchi et al. 2018). Since different interpolation methods can be adopted (Erol and Erol 2021; Erol and Erol 2013), different results are expected (Ferrara and Parente 2021): there is no absolutely best interpolation method but only the optimal choice under certain circumstance (Yang et al. 2004). Nevertheless, some studies show the high level of performance of Kriging interpolators (Erol and Çelik 2004b; Falchi et al. 2018). For consequence, we decide to consider these algorithms for our study.

This article aims to analyse the relationship between the density of GHPs and the accuracy of each local geoid derived from those points using Universal (UK) and Ordinary Kriging (OK) interpolators. Since the spatial complexity of the function to be interpolated, the results are related to the roughness of the considered surface. To have a valid reference for calculating the accuracy of the resulting models, an already existing local geoid model concerning Corsica

Isle (France) is chosen and assumed as source for extracting different subsets containing different number of points in the same area.

The article is organised as follows. Section 2 describes the materials and methods: 12 different datasets are selected including an increasing number of GHPs from 24 to 960; OK and UK interpolators are applied to each dataset. Section 3 presents and discusses the results comparing the levels of accuracy of 24 GMs, 12 for each interpolation algorithm in dependence of the number of the GHPs including in each dataset; particularly the accuracy is tested using the starting GM as reference. Section 4 draws out our conclusions.

## 2 Data and Methods

The experiments are carried out on geoid heights extracted in random way from an already existing local geoid model concerning Corsica Isle (France) and covering an area located between the following ellipsoidal WGS84 coordinates: lon min =  $8^{\circ} 24' 00''$ , lon max =  $9^{\circ} 44' 00''$ , lat min =  $41^{\circ} 11' 15''$ , lat max =  $43^{\circ} 12' 45''$ . The Geoid model includes 81 rows  $\times$  40 columns, presents a grid spacing of 1.5' in latitude and 2' in longitude and covers an area of about 24,767.74 sqkm (Institut Géographique National - IGN 2010). It is an adaptation of the QGC02 model, the gravimetric quasi-geoid model for the Corsica region (Duquenne et al. 2004), to 60 GNSS/levelling points: it has been assessed by using 15 independent GNSS/levelling points, showing differences with a RMSE of 3.4 cm (L'Ecu 2009). The geoid heights range between 44.947 m and 50.592 m; roughness, i.e. the degree of the surface irregularity that is calculated by the largest inter-cell difference of a central pixel and its surrounding cell, ranges between 0.007 m and 1.302 m. Figures 1 and 2 show respectively: the study area with the geolocalization of the dataset and the 3D visualization of the geoid model.

The Geoid model is converted in grid vector points and 12 different subsets are extracted in random way from them including an increasing number of elements in the study area from 24 to 960. Each extracted point coincides with the respective grid node: no interpolation algorithm is applied in this phase and the value provided by the initial grid is preserved in any case. In order to ensure a sufficiently homogeneous distribution of the points over the whole considered area, a grid presenting cell size  $19.9995'$  (long.)  $\times$   $20.25'$  (lat.) is introduced. For consequence the geoid area is subdivided in 24 cells (mean area: 1031.99 sqkm) and an equal number of GHPs (minimum 1, maximum 40) is maintained in each cell for each subset. Figure 3 shows two subsets including respectively 240 GHPs (0.010 point/sqkm) and 960 GHPs (0.039 point/sqkm).

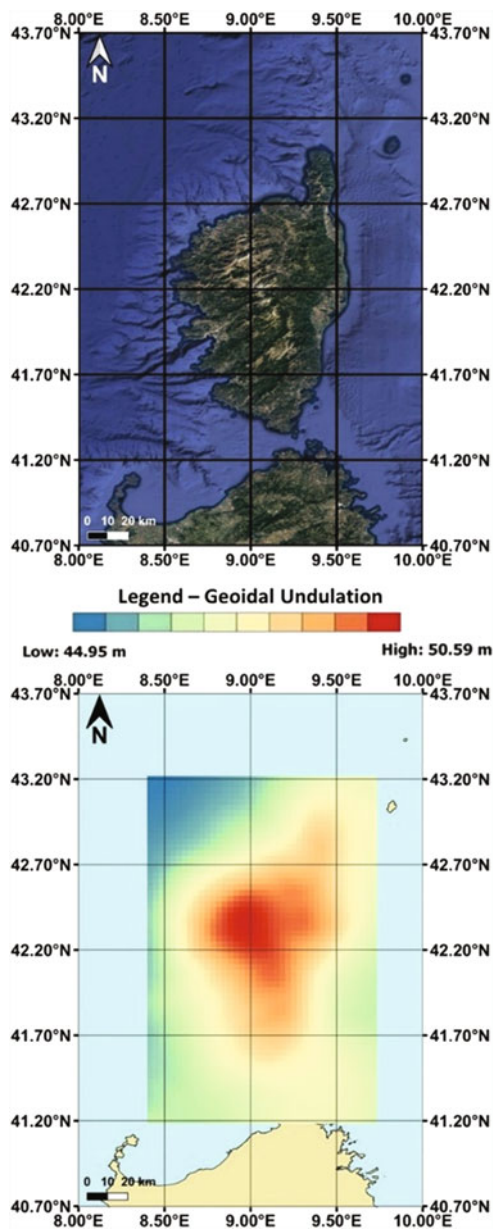


**Fig. 1** The study area referred to WGS84 ellipsoidal coordinates: territorial framework of Corsica edited from Google Earth data (Upper); Initial dataset: geoid of Corsica (grid spacing: 1.5' in latitude and 2' in longitude) (Lower)

Each subset is submitted to Kriging interpolators, namely OK and UK, both based on the geo-statistical model which uses the spatial correlation between sampled points to estimate the value at an unknown point (Krivoruchko 2012).

Kriging interpolation methods assume that the spatial variation of any continuous attribute is often too irregular to be modelled by a simple mathematical function, so a stochastic surface is more suitable to represent it (Oliver and Webster 1990).

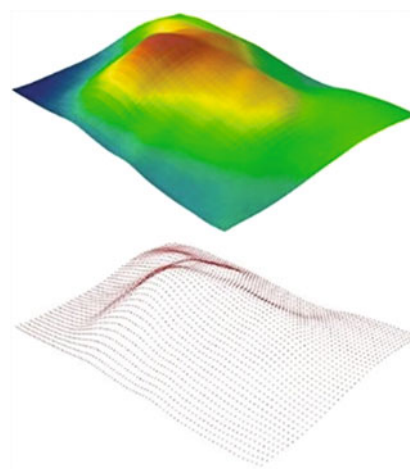


**Fig. 2** Initial geoid model in 3D visualization as continuous surface (upper) and as grid points (lower)

For consequence Kriging methods can supply models that better represent and describe the geoid heights since it allows a more consistent prediction of the values in the non-sampled points. To understand the difference between the OK and the UK, a very wide range of sources is available in the literature and can be consulted (Martin and Simpson 2003; Kiš 2016).

OK assumes the model:

$$z(x_0) = \sum_{i=1}^n \lambda_i z(x_i) \tag{1}$$

where  $\lambda_i$  are the kriging weights. The function  $z(x_i)$  is composed of a deterministic component  $\mu$  and a random function  $\varepsilon(x_i)$  (ESRI 2016).

$$z(x_i) = \mu + \varepsilon(x_i) \tag{2}$$

The deterministic component is a constant value for each  $x_i$  location in each area.

UK assumes the model (ESRI 2016):

$$z(x_i) = \mu(x_i) + \varepsilon(x_i) \tag{3}$$

where,  $z(x_i)$  is the variable of interest,  $\mu(x_i)$  is some deterministic function and  $\varepsilon(x_i)$  is random variation (Gundogdu and Guney 2007).

Unlike OK, where the mean  $\mu$  is assumed constant over the entire region of study, UK assumes that the mean  $\mu(x_i)$  is dependent on the spatial location (Mesić Kiš 2016).

Both OK and UK analyse the variability of the points with increasing distances (variance) and adopt a mathematical model to describe it. Usually, a software for Kriging method application provides the user with different types of

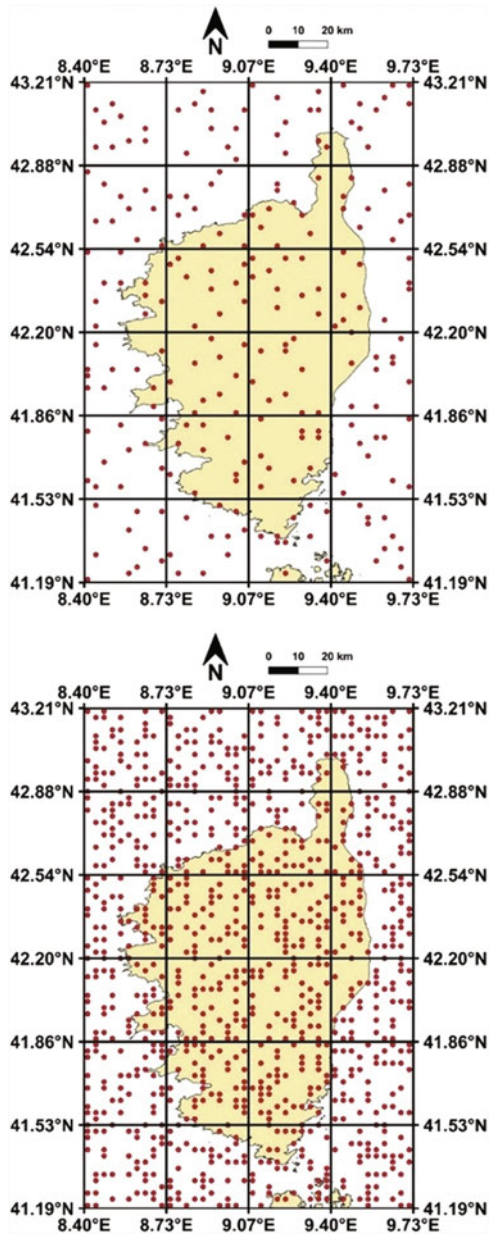


**Fig. 3** Examples of subsets extracted from the initial models: the subset including 240 points (upper) and the subset including 960 points (lower) used for Kriging interpolations

semi-variogram, the mathematical function that graphically represents the spatial correlation between the input point values (Jian et al. 1996). In this study the choice of the mathematical model to fit the experimental data is carried out using the best performing one that results Stable model (ESRI 2016). We fix Lag = 12; Minimum neighbours = 2; Maximum neighbours = 5; 4 sectors with 45° offset. We also apply the optimization option supplied by the software that allows to increase the result accuracy. For consequence specific parameters are automatically determined, e.g. lag size and research radius.

The resulting GMs are tested by means of leave one out cross validation (Fasshauer and Zhang 2007) as well as using direct comparison with the original geoid. The subsequent residuals between initial undulation values and corresponding interpolated values are used to analyse and evaluate the accuracy in dependence of point density.

### 3 Results and Discussion

Significant statistical parameters (minimum, maximum and root mean square error) of all residuals for each dataset are shown in Table 1 for OK applications analysed by Cross validation, and in Table 2 for the same applications analysed by direct comparison.

In a similar way, significant statistical parameters of all residuals for each dataset are shown in Table 3 for UK applications analysed by Cross validation, and in Table 4 for the same applications analysed by direct comparison.

**Table 1** Statistics of the residuals produced by cross validation for the Ordinary Kriging

Count	Min (m)	Max (m)	Mean (m)	RMSE (m)
24	-0.65	1.66	0.237	0.609
48	-0.41	0.45	0.024	0.192
72	-0.41	0.48	0.004	0.142
96	-0.30	0.23	0.007	0.104
120	-0.20	0.26	0.003	0.085
144	-0.19	0.21	0.000	0.069
168	-0.15	0.18	0.000	0.058
192	-0.17	0.21	0.005	0.049
216	-0.11	0.16	0.004	0.041
240	-0.10	0.15	0.003	0.039
480	-0.13	0.09	0.001	0.022
960	-0.09	0.07	0.000	0.012

**Table 2** Statistics of residuals produced by direct comparison for Ordinary Kriging

Count	Min (m)	Max (m)	Mean (m)	RMSE (m)
24	-0.57	1.45	0.041	0.281
48	-0.54	0.42	-0.027	0.130
72	-0.43	0.27	-0.008	0.089
96	-0.28	0.40	-0.003	0.075
120	-0.25	0.22	-0.005	0.057
144	-0.30	0.23	-0.011	0.055
168	-0.26	0.21	-0.010	0.049
192	-0.24	0.24	-0.008	0.048
216	-0.24	0.15	-0.008	0.045
240	-0.24	0.16	-0.007	0.045
480	-0.13	0.12	-0.005	0.034
960	-0.14	0.09	-0.006	0.032

**Table 3** Statistics of the residuals produced by cross validation for the Universal Kriging

Count	Min (m)	Max (m)	Mean (m)	RMSE (m)
24	-4.48	2.21	-0.124	1.402
48	-0.78	1.07	0.056	0.371
72	-0.60	0.64	0.059	0.227
96	-0.50	0.47	0.024	0.168
120	-0.42	0.53	0.006	0.151
144	-0.42	0.41	-0.003	0.129
168	-0.28	0.30	0.005	0.105
192	-0.28	0.26	0.007	0.090
216	-0.26	0.25	0.008	0.080
240	-0.19	0.26	0.005	0.069
480	-0.15	0.12	0.001	0.032
960	-0.11	0.09	0.001	0.018

**Table 4** Statistics of residuals produced by direct comparison for Universal Kriging

Count	Min (m)	Max (m)	Mean (m)	RMSE (m)
24	-1.51	1.45	0.162	0.475
48	-1.16	0.77	-0.002	0.270
72	-0.75	0.72	0.008	0.198
96	-0.70	0.64	0.006	0.154
120	-0.56	0.51	0.000	0.123
144	-0.42	0.49	-0.003	0.106
168	-0.34	0.38	-0.004	0.090
192	-0.28	0.35	-0.004	0.078
216	-0.25	0.35	-0.001	0.069
240	-0.25	0.32	-0.003	0.064
480	-0.18	0.15	-0.006	0.039
960	-0.16	0.11	-0.005	0.034

The results demonstrate the efficiency of the Kriging methods, highlighting the possibility to achieve higher accuracy in dependence of an adequate density of GHPs. For OK the RMSE value rapidly decreases from the first to the fifth subset (from 0.609 m to 0.085 m using Cross validation, from 0.281 m to 0.057 m using direct comparison), while the variation slows down in subsequent groups. The trend of RMSE values for UK from the first to the fifth subset is similar, even if higher values are found (from 1.402 m to 0.151 m using Cross validation, from 0.475 m to 0.123 m using direct comparison).

The trend is clearly shown in Fig. 4 which plots the value of the RMSE in the case of OK and UK products directly compared with the initial geoid model.

Both methods of cross validation and direct comparison show a better performance of OK compared to UK. In

consideration of the formulas (2) and (3), this seems to remark that it is correct to consider the deterministic component constant over the entire region of study rather than dependent on the spatial location. However, in the presence of a high number of points (480 or 960), the differences between the results of the two interpolators tend to become minimal (e.g. 0.006 m for 960 GHPs using Cross validation, 0.002 m for the same subset using direct comparison). In other terms, the higher number of points reduces the differences because it allows to better define the deterministic component assumed as dependent on the spatial location. Furthermore, the results highlight the limit of the leave one out Cross validation since it supplies higher residuals than direct comparison for both UK and OK, when a few points are used.

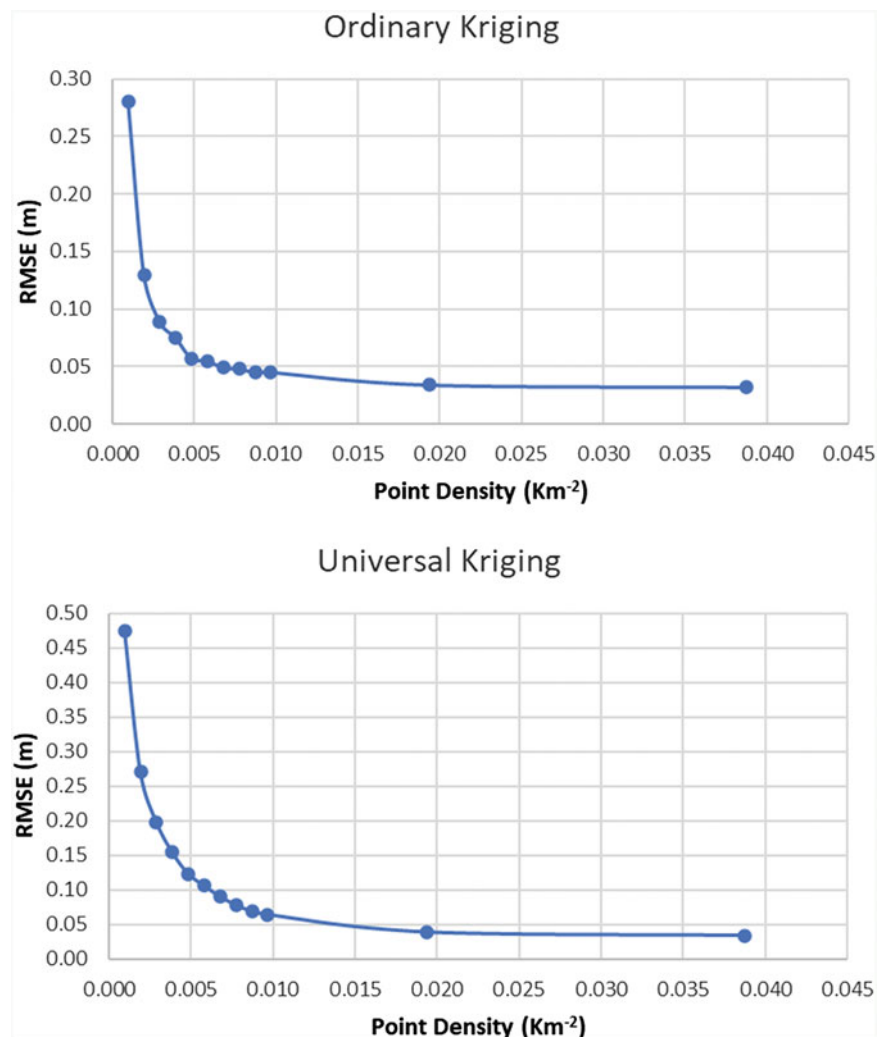
For example, Erol and Çelik (2004b) achieved an accuracy of about 0.03 m using UK as an interpolation method, and 1 GHP/3 km. Abdulrahman (2021) achieved an accuracy of about 0.243 m using OK and 1 GHP/0.350 km, but in this case measurements are carried out by means Total Station (Trigonometric Levelling).

## 4 Conclusion

The study demonstrates the efficiency of the Kriging methods for local Geoid determination, highlighting the relationship between the density of GHPs and the accuracy of the resulting model. OK provides better results than UK but the undulations between the resulting models are minimal (a few millimetres) when a high number of GHPs is involved. In fact, the limited extension of the considered area advises to take the deterministic component as a constant (OK): vice versa, if considered variable (UK), a higher number of points is necessary to determine its value more accurately. Using a few points, leave one out cross validation supplies higher residuals than direct comparison for both UK and OK, remarking the opportunity to consider this effect when testing GMs. For the analysed study area, using a density of 1 point/100 sqkm, direct comparison highlights that RMSE is less than 5 cm for OK application and less than 7 cm for UK. The current experiments testify that both the interpolation algorithms can be applied to determine accurate local geoid using 3.9 points/100 sqkm. The influence of the analysed region topography on the accuracy results needs further investigation.



**Fig. 4** Ordinary Kriging RMSE and Universal Kriging RMSE values (in meters) plotting for direct comparison



## References

- Abdulrahman FH (2021) Determination of the local geoid model in Duhok Region, University of Duhok Campus as a Case study. *Ain Shams Eng J* 12(2):1293–1304
- Alcaras E, Amoroso PP, Parente C (2022) The influence of interpolated point location and density on 3D bathymetric models generated by Kriging methods: an application on the Giglio Island Seabed (Italy). *Geosciences* 12(2):62
- Barzaghi R, Betti B, Borghi A, Sona G, Tornatore V (2002) The Italian quasi-geoid ITALGEO99. *Bollettino di geodesia e scienze affini* 61(1):33–51
- Barzaghi R, Carrion D, Pepe M, Prezioso G (2016) Computing the deflection of the vertical for improving aerial surveys: a comparison between EGM2008 and ITALGEO05 estimates. *Sensors* 16(8):1168
- Blinken R, Koch KR (1999) Estimation of geoid and sea surface topography from satellite altimetry by the adjoint method. *Bollettino di Geofisica Teorica ed Applicata* 40(3–4):347–352
- Chen YQ, Luo Z (2004) A hybrid method to determine a local geoid model-case study. *Earth Planets Space* 56(4):419–427
- Das RK, Samanta S, Jana SK, Rosa R (2018) Polynomial interpolation methods in development of local geoid model. *Egypt J Remote Sens Space Sci* 21(3):265–271
- Denker H, Barriot JP, Barzaghi R, Fairhead D, Forsberg R, Ihde J et al (2009) The development of the European gravimetric geoid model EGG07. In: *Observing our changing earth*. Springer, Berlin, Heidelberg, pp 177–185
- Duquenne H, Olesen AV, Forsberg R, Gidskehaug A (2004) Amelioration du champ de pesanteur et du geoïde autour de la Corse par gravimétrie aéroportée. *Revue XYZ* 101:67–74
- Erol B, Çelik RN (2004a, May) Precise local geoid determination to make GPS technique more effective in practical applications of geodesy. In: *FIG working week*, vol 17(3), pp 22–27
- Erol B, Çelik RN (2004b, July) Modelling local GPS/levelling geoid with the assessment of inverse distance weighting and geostatistical Kriging methods. In: *XXth ISPRS Congress*, Istanbul, Turkey
- Erol B, Erol S (2013) Learning-based computing techniques in geoid modeling for precise height transformation. *Comput Geosci* 52:95–107
- Erol S, Erol B (2021) A comparative assessment of different interpolation algorithms for prediction of GNSS/levelling geoid surface using scattered control data. *Measurement* 173:108623
- ESRI (2016) *Using ArcGIS geostatistical analyst*. Redlands, CA, USA
- Eteje SO, Oduyebo OF (2018) Procedure for the determination of local gravimetric-geometric geoid model. *Int J Adv Sci Res Eng* 4(8):206–214
- Falchi U, Parente C, Prezioso G (2018) Global geoid adjustment on local area for GIS applications using GNSS permanent station coordinates. *Geodesy Cartography* 44(3):80–88

- Fasshauer GE, Zhang JG (2007) On choosing “optimal” shape parameters for RBF approximation. *Numer Algorithms* 45(1–4):345–368
- Ferrara G, Parente C (2021) Adaptation of the Global Geoid Model EGM2008 on Campania Region (Italy) based on geodetic network points. *ISPRS-Int Arch Photogramm Remote Sens Spatial Inf Sci* 46:145–150
- Gundogdu KS, Guney I (2007) Spatial analyses of groundwater levels using universal kriging. *J Earth Syst Sci* 116(1):49–55
- Huang J, Fotopoulos G, Cheng MK, Véronneau M, Sideris MG (2007) On the estimation of the regional geoid error in Canada. In: *Dynamic planet*. Springer, Berlin, Heidelberg, pp 272–279
- Institut Géographique National - IGN (2010) Descriptifs quasi-geoides et grilles de conversion altimétrique sur la France métropolitaine. Laboratoire de Recherche en Géodesie, Service de Géodesie et Nivellement
- Jian X, Olea RA, Yu YS (1996) Semivariogram modeling by weighted least squares. *Comput Geosci* 22(4):387–397
- Kiš IM (2016) Comparison of Ordinary and Universal Kriging interpolation techniques on a depth variable (a case of linear spatial trend), case study of the Šandrovac Field. *Rudarsko-geološko-naftni zbornik (The Mining-Geological-Petroleum Bulletin)* 31(2):41–58
- Krivoruchko K (2012) Empirical bayesian Kriging. *ArcUser Fall* 6(10)
- L’Ecu F (2009) Corse: rapport de constitution de la grille de conversion altimétrique RAC09, IGN/SGN RT/G 81
- Maglione P, Parente C, Vallario A (2018) Accuracy of global geoid height models in local area: tests on Campania region (Italy). *Int J Civ Eng Technol* 9(3):1049–1057
- Martin JD, Simpson TW (2003, January) A study on the use of Kriging models to approximate deterministic computer models. In: *International design engineering technical conferences and computers and information in engineering conference*, 37009, pp 567–576
- Mesić Kiš I (2016) Comparison of Ordinary and Universal Kriging interpolation techniques on a depth variable (a case of linear spatial trend), case study of the Šandrovac Field. *Rudarsko-geološko-naftni zbornik* 31(2):41–58
- Oliver MA, Webster R (1990) Kriging: a method of interpolation for geographical information systems. *Int J Geogr Inf Syst* 4(3):313–332
- Pavlis N, Kenyon S, Factor J, Holmes S (2008) Earth gravitational model 2008. In: *SEG Technical Program Expanded Abstracts 2008*, Society of Exploration Geophysicists, pp 761–763
- Pavlis NK, Holmes SA, Kenyon SC, Factor JK (2012) The development and evaluation of the Earth Gravitational Model 2008 (EGM2008). *J Geophys Res: Solid Earth* 117(B4)
- Rapp RH (1974) The geoid: definition and determination. *Eos Trans Am Geophys Union* 55(3):118–126
- Sideris MG, She BB (1995) A new, high-resolution geoid for Canada and part of the US by the 1D-FFT method. *Bulletin Géodésique* 69(2):92–108
- Smith DA, Milbert DG (1997) Evaluation of the EGM96 model of the geopotential in the United States. *Bulletin of the International Geoid Service*
- Yang CS, Kao SP, Lee FB, Hung PS (2004) Twelve different interpolation methods: a case study of Surfer 8.0. In: *Proceedings of the XXth ISPRS Congress*, vol 35, pp 778–785
- You RJ (2006) Local geoid improvement using GPS and leveling data: case study. *J Surv Eng* 132(3):101–107

**Open Access** This chapter is licensed under the terms of the Creative Commons Attribution 4.0 International License (<http://creativecommons.org/licenses/by/4.0/>), which permits use, sharing, adaptation, distribution and reproduction in any medium or format, as long as you give appropriate credit to the original author(s) and the source, provide a link to the Creative Commons license and indicate if changes were made.

The images or other third party material in this chapter are included in the chapter’s Creative Commons license, unless indicated otherwise in a credit line to the material. If material is not included in the chapter’s Creative Commons license and your intended use is not permitted by statutory regulation or exceeds the permitted use, you will need to obtain permission directly from the copyright holder.





# Gravimetric Geoid Modeling by Stokes and Second Helmert's Condensation Method in Yogyakarta, Indonesia

Brian Bramanto, Kosasih Prijatna, Muhammad Syahrullah Fathulhuda, and Arisauna Maulidyan Pahlevi

## Abstract

Since the last decade, Indonesia has continuously improved the accuracy of the national geoid model by conducting rapid gravity acquisition using airborne and terrestrial gravimetry. As gravity data have been collected thoroughly in all regions, the time has come to carry out Indonesia's geoid modeling. We started our study by employing the Stokes and Second Helmert's condensation method to our terrestrial gravity data in Yogyakarta, Indonesia, with a target area of  $1^\circ \times 1^\circ$ . The computation was based on the commonly applied remove-compute-restore process. We used a satellite-only geopotential model of GO\_CONS\_GCF\_2\_TIM\_R6 up to degree 300 to remove and restore the long-wavelength part of the gravity field within the modeling process. Numerical results show that few cm of geoid model accuracy was achieved when we compared it to the validation points. Also, our best performance geoid is estimated to be better than the Earth Gravitational Model 2008 (EGM2008) geoid model by up to 2.8 cm in terms of standard deviation.

## Keywords

Geoid modeling · Helmert's second condensation · Stokes

## 1 Introduction

Historically, the Indonesian Geoid Model 1981 was the first geoid model of Indonesia. It was developed by combining a global geoid model with an altimetry-derived geoid. However, the accuracy is considered poor. It was estimated to approximately 5 m (Kahar et al. 1997). A decade later, an effort was made to create a better, unified, and single geoid model of Indonesia. Under the official name of the Indonesian Geoid Model 1996 (INDGED96), it was constructed by tailoring different sources of gravity measurements (Kahar et al. 1997). The dataset consisted of more than 200,000

terrestrial gravity points and 150,000 marine gravity points (Kasenda et al. 2000). Despite the huge number of gravity data used from the dataset for geoid modeling, limitations still could not be avoided, i.e., the uneven distribution of gravity measurements. As a result, INDGED96 showed a relatively poor geoid model accuracy at one region compared with other regions. For example, the difference between gravimetric and geometric geoid (height difference between geodetic height obtained from Global Navigation Satellite System (GNSS) and orthometric height observed from leveling) in Java Island was ranging from 0.2 to 1.0 m, while in Sumatra island was ranging from 0.5 to 1.5 m (Kahar et al. 1997; Kasenda et al. 2000).

The development of more precise global geoid models using global observations gives another alternative geoid solution for Indonesia. For example, Earth Gravitational Model (EGM) 2008 by Pavlis et al. (2012) is commonly used for geoid model in many countries, including Indonesia. According to the information released by International Center for Global Earth Models (ICGEM), the overall accuracy

B. Bramanto (✉) · K. Prijatna · M.S. Fathulhuda  
Geodesy Research Group, Faculty of Earth Sciences and Technology,  
Institut Teknologi Bandung, Bandung, Indonesia  
e-mail: [brian.bramanto@itb.ac.id](mailto:brian.bramanto@itb.ac.id)

A. M. Pahlevi  
Geospatial Information Agency of Indonesia, Bogor, Indonesia

of EGM2008 was estimated to 18.7 cm from the comparison between geoid height and seven GNSS/leveling datasets. An effort to assess the accuracy of EGM2008 in Indonesia had also been made. The mean difference obtained from validation points was calculated to 0.596 m (Heliani 2016).

Notably, the reported accuracy of the mentioned geoid models is still low for the Indonesia region. To improve the quality of the geoid model, the Geospatial Agency of Indonesia (BIG) began to measure a completely new gravity dataset through terrestrial gravity measurements with a sampling interval of every 5 km in several major cities (Syafarianty et al. 2021). In addition, BIG also deployed several airborne gravity measurements (Pahlevi et al. 2015, 2019; Bramanto et al. 2021) since the last decade. As a result, the new gravity dataset covers all primary islands in Indonesia, and the time has come to determine the Indonesia geoid model. The generated geoid model, with a reliable accuracy, is expected to accelerate the provision of large-scale maps in Indonesia. Additionally, a precise geoid model is useful for various applications, e.g., datum unification (Pan and Sjöberg 1998), mapping the crustal and lithosphere thickness (Fullea et al. 2007), and deriving the ocean circulation together with altimetry observations (Jayne 2006).

Several methods to calculate gravimetric geoid have been proposed by many studies. One may use the remove-compute-restore (RCR; Schwarz et al. 1990) method under the Stokes (Stokes 1849) and second Helmert's condensation scheme (Ellmann and Vaníček 2007) (to simplify, we call this as Stokes-Helmert). This study attempts to test the Stokes-Helmert scheme to our terrestrial gravity data in a relatively small area of Yogyakarta, Indonesia, with a target area of  $1^\circ$  by  $1^\circ$ . This article is organized as follows: Sect. 2 outlines the data and basic methodology used for geoid modeling, Sect. 3 displays results, and finally Sect. 4 summarizes this study.

## 2 Data and Method

### 2.1 Data Used

The geoid model is constructed and modeled by using several gravity datasets. First, we used terrestrial gravity measurements as the primary dataset. The BIG conducted these measurements using a relative gravimeter of Scintrex CG-5 with a total of 129 measurement points. Measurements were carried out with an interval of approximately 5 km. Second, as the computation of the geoid model requires integration of gravity data to some extent, we used the Global Geopotential Model (GGM) of EGM2008 to complete missing gravity data that was not covered by gravity measurements. It was extended to  $1.5^\circ$  from the outermost point of the terrestrial gravity data. The fill-in data was calculated every 5 km at topographic elevation following the characteristic of terres-

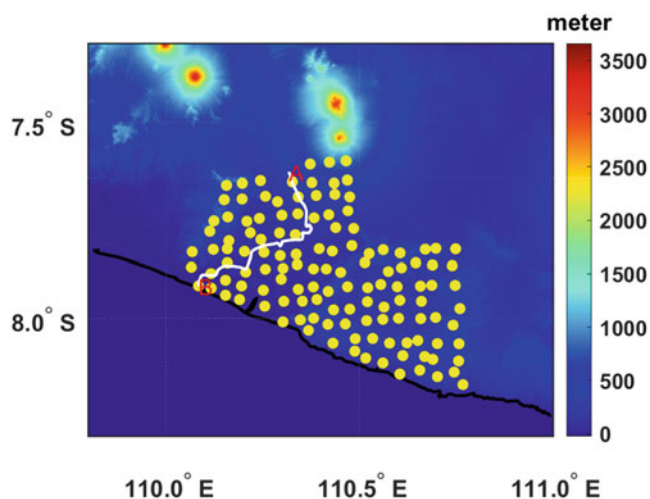


**Fig. 1** Distribution of terrestrial gravity data (yellow dots) and GNSS/leveling line A–B (white line) used for this study. Land topography is also plotted in the background using the 3 arc-second grid of SRTM (Farr et al. 2007) data. The black line indicates the coastlines

trial gravity data. These fill-in data were treated similar to the observed gravity and included later for grid interpolation using Least Square Collocation (LSC; Tscherning 2015). Third, we used the GGM of GO\_CONS\_GCF\_2\_TIM\_R6 up to degree 300 (Brockmann et al. 2021) as the chosen reference GGM in the remove-restore method. In addition, a Digital Elevation Model (DEM) is needed for correcting terrain effects on gravity measurements. The 3 arc-second grid of Shuttle Radar Topography Mission (SRTM; Farr et al. 2007) data was used in this study. Gravity data, including fill-in gravity data, were provided in a 4-by-4 degree region. At the same time, the DEM data stretched  $1^\circ$  beyond the gravity data outer boundary.

Additionally, we used the geometric geoid heights from GNSS/leveling observations to assess the performance of the generated geoid model. The expected accuracy of the GNSS/leveling is within cm level as we treated our validation points to be equivalent to the national vertical geodetic network. This is sufficient to assess cm-level geoid height model accuracy.

Figure 1 shows the distribution of terrestrial gravity data and the GNSS/leveling line used in this study.

### 2.2 RCR Under Stokes-Helmert Scheme

We began our computation by firstly reducing our gravity data from the Earth's surface to the geoid and constructing the free-air gravity anomalies. This indicates that all topographic masses above geoid are condensed to the geoid according to Helmert's second method of condensation. The observed gravity is reduced to the geoid surface using the free-air gravity gradient, obtaining the free-air gravity

anomaly. Mathematically, the free-air gravity anomalies can be described as follows (Featherstone and Dentith 1998):

$$\Delta g_{FA} = g - \gamma_Q + \delta g_{FC} + \delta g_{ATM} \quad (1)$$

where  $g$  is the gravity observation,  $\gamma$  is the normal gravity on the chosen reference ellipsoid,  $\delta g_{FC}$  is the free-air gravity correction, and  $\delta g_{ATM}$  is the atmospheric correction that arises due to additional systematic error when determining the ellipsoidal parameters, e.g., the Geodetic Reference System 1980 (GRS80). The parameters that define ellipsoid parameters were mostly estimated from satellite geodetic data. Eventually, the estimated normal gravity includes the atmospheric mass effects. On the contrary, the terrestrial gravity data does not include these effects (Featherstone and Dentith 1998; Yang 2013).

From the free-air gravity anomalies, we further computed the residual Faye anomalies  $\Delta g_{Faye}^{res}$  as follows:

$$\Delta g_{Faye}^{res} = \Delta g_{FA} + \delta g_{TC} - \delta g_{SITE} - \Delta g_{GGM} \quad (2)$$

where  $\delta g_{TC}$  is the terrain correction which is determined from the irregular terrain after removing the planar Bouguer gravity effects,  $\delta g_{SITE}$  is the secondary gravity indirect effect due to the removal of Helmert's topographic masses, and  $\Delta g_{GGM}$  is the reference gravity effects from the chosen GGM. In this study, we followed the International Association of Geodesy (IAG) resolution 2015 for the geopotential value ( $W_0$ ) of 62,636,853.4 m<sup>2</sup>/s<sup>2</sup>. Further details to calculate these terms can be seen in many references (e.g., Omang and Forsberg (2000); Smith and Roman (2001)).

Notice that the application of Helmert's second condensation produces a slightly different potential from the actual potential. Eventually, the resulting (co)geoid does not coincide with the actual geoid in reality. The corresponding gravity indirect effect and secondary indirect effects to geoid height should be introduced to compensate for this systematic error.

Many publications provide a full description of the RCR method for computing the geoid model, e.g., Omang and Forsberg (2000). In principle, the geoid height  $N$  is calculated as a sum of reference and residual components of the geoid model and can be expressed as follows:

$$N = N_{GGM} + N_{res} + \delta N_1 + \delta N_2 \quad (3)$$

where  $N_{GGM}$  is the reference geoid height from the chosen GGM,  $N_{res}$  is the residual geoid height,  $\delta N_1$ , and  $\delta N_2$  are the respective first and secondary indirect effects to geoid height. Detailed explanation related to the calculation of the reference geoid height and indirect effects to geoid height can be seen in Omang and Forsberg (2000), Smith and Roman (2001).

Next, the residual geoid height component can be calculated using a classical Stokes formula as follows:

$$N_{res} = \frac{R}{4\pi\gamma} \iint_{\sigma} \Delta g_{Faye}^{res} S(\psi) d\sigma \quad (4)$$

where  $R$  is the mean radius of the Earth,  $\gamma$  is the normal gravity,  $S(\psi)$  is the Stokes's kernel with  $\psi$  as the angular distance between the computation and running point, and  $d\sigma$  is the surface element.

In the present study, Stokes integral was evaluated using the Fast Fourier Transform (FFT) method and under different integration radii. This was done to assess the effect of different integration radii. The following are the practical application of RCR under Stokes-Helmert scheme to compute the residual geoid height in this study:

1. Reduce the free-air gravity anomalies by removing the corresponding planar Bouguer effects and adding the respective terrain corrections.
2. Remove the long-wavelength gravity component using the chosen reference gravity effects.
3. Eliminate the indirect gravity effect from the data.
4. Grid the resulting anomalies from step 1–3 using LSC.
5. Restore the Bouguer plate anomaly to the corresponding grid sampling obtaining residual gridded Faye anomalies as given by Eq. 2.
6. Compute the residual geoid height from the gridded Faye gravity anomalies by using the FFT approach.

### 3 Results and Discussions

As described in Sect. 2.2, we computed several 1 arc-minute bins of gravimetric geoid models with different integration radii (i.e., 0.5°, 1.0°, and 1.5° of integration radius) for the residual components. Afterward, the final geoid model for each integration radius was finalized by adding the reference geoid height obtained from the chosen GGM and indirect geoid height effects. Figure 2 displays the geoid height models for each integration radius. In general, the computed geoid height models, including the ocean area of the surrounding study area, ranges between 18 to 27.5 m. They have a positive gradient towards to north-east direction and perpendicular to the coastline. The significant discrepancy between the geoid model with 0.5° integration radius and other geoid models occurs at the mountainous area in the northern part of the study area and at the sea area in the other direction.

We compared our geoid height models with GNSS/leveling data to assess the performance of our computed geoid height models. Table 1 lists the statistics of the discrepancy between our geoid height models and geometric geoid height from GNSS/leveling data. The third

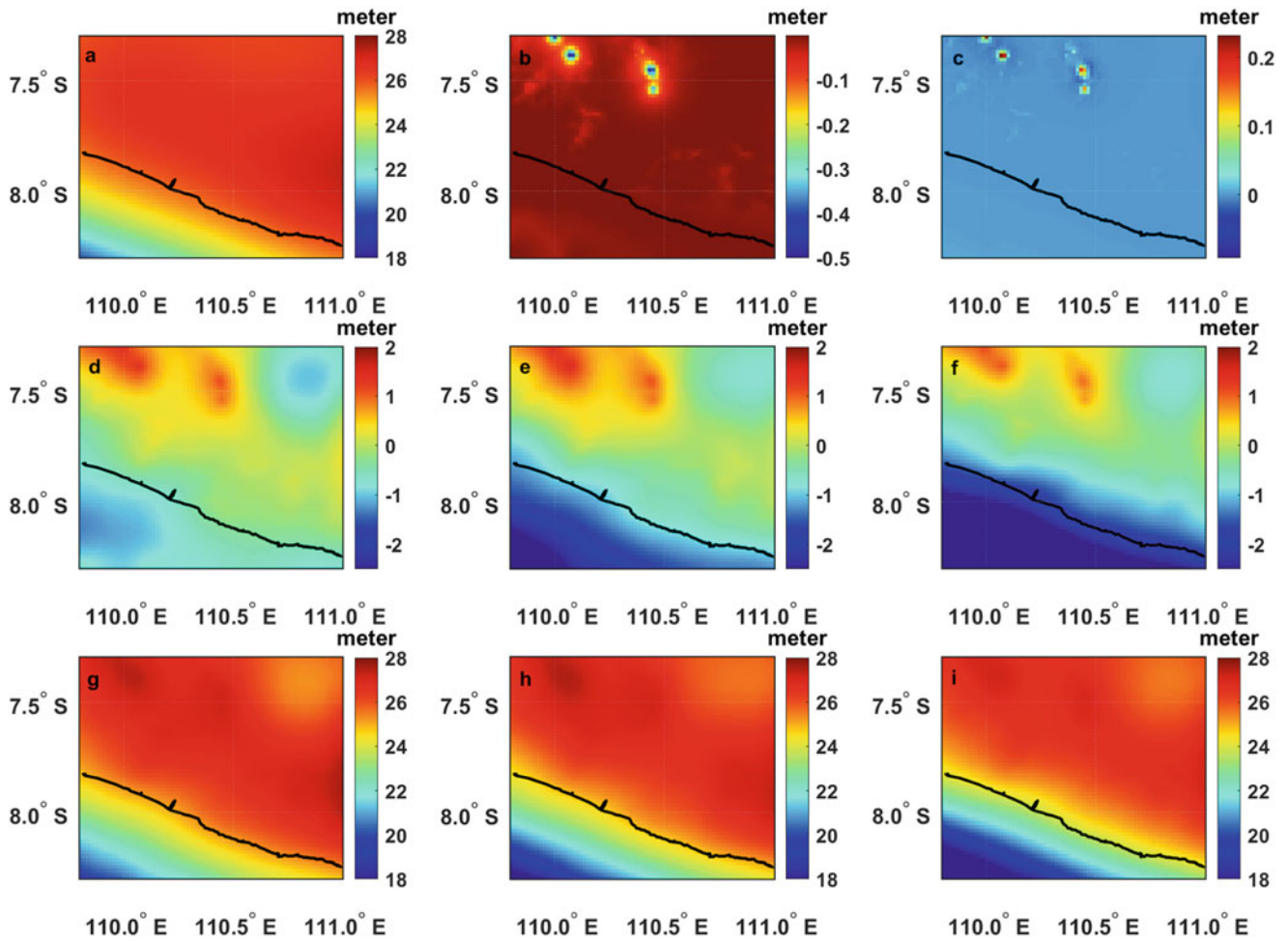


**Fig. 2** Computed models for (a) reference geoid height, (b) first indirect, and (c) secondary indirect effect to geoid height. The terms (d), (e), and (f) stands for the residual geoid models with 0.5°, 1.0°, and

1.5° integration radius, respectively. The terms (g), (h), and (i) displays the corresponding total geoid height models for 0.5°, 1.0°, and 1.5° integration radius

**Table 1** Estimated standard deviation (SD) and mean of geoid difference for each generated geoid height models and EGM2008 geoid height model (unit in cm)

	0.5°	1.0°	1.5°	EGM2008
SD	8.2	5.1	15.2	7.9
Mean	54.3	33.8	-10.1	51.2

geoid height model (1.5° of integration radius) gives the smallest absolute mean bias (-10.1 cm) compared to the GNSS/leveling data. However, it appears to have the most significant standard deviation value of 15.2 cm. Take a closer look at the comparison between gravimetric and geometric geoid height at validation points (Fig. 3), the third geoid height model seems to has a larger gradient/trend of geoid height, resulting in a poor geoid model accuracy. This and together with the estimated standard deviation values in Table 1 imply that increase in radius integration does not improve the accuracy of geoid model. Our results show that

the best geoid height model was the one computed using 1° with integration radius, shown by the low standard deviation of 5.1 cm.

We further assess whether the inclusion of the recent terrestrial gravity observations will improve the geoid model’s performance or not, e.g., by also evaluating the global geoid model at the GNSS leveling points. Therefore, we computed the geoid height based on the commonly used GGM of EGM2008 at the GNSS/leveling points. As shown in Table 1, the standard deviation of geoid difference between EGM2008 and GNSS/leveling is estimated to be 7.9 cm. At the same time, the corresponding mean bias is calculated to be 51.2 cm. This standard deviation indicates that our computed geoid height is better than EGM2008, with improvement of 2.8 cm or 35.4%. It makes us confident to choose the computed geoid with radius integration of 1° for further implementations and applications.

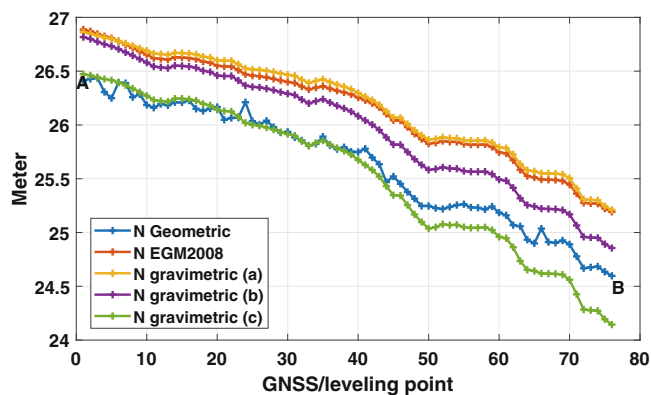


**Fig. 3** Comparison between geometric and gravimetric geoid models. The terms (a), (b), and (c) represent the correspond gravimetric geoid models with  $0.5^\circ$ ,  $1.0^\circ$ , and  $1.5^\circ$  of integration radius

It should be noted that bias still exists in the computed geoid model. Therefore, it is essential to correct it before using it for real-world applications, e.g., survey and mapping applications. One can model the differences between gravimetric and geometric geoid using a lower degree of polynomial surface, representing the overall trend in the observations (Kiliçoğlu et al. 2011). However, we consider only using the estimated mean bias listed in Table 1 to correct our geoid model as we only have a limited and relatively south-north direction of the GNSS/leveling line.

Recalling the need for fast and accurate large-scale maps (1:1,000 scale), advanced mapping and surveying technologies, such as GNSS and airborne LiDAR (Light Detection and Ranging) mapping, can be used to produce such maps. GNSS and airborne LiDAR mapping can provide fast and accurate points (Bramanto et al. 2019; Gumilar et al. 2019; Mahdianpari et al. 2021). However, one main drawback of the GNSS and airborne LiDAR mapping is the reported height referenced to the ellipsoid. Eventually, we need an accurate geoid model to transform it into orthometric heights. Recalling the accuracy of the computed geoid model (5.1 cm) and airborne LiDAR mapping (vertical accuracy of 15 cm Andersen et al. (2005)), the error propagation of the produced map is expected to be 15.8 cm. It becomes smaller when we consider using GNSS, with vertical accuracy of approximately 10 cm (Bramanto et al. 2019), to produce such a map. We estimate the error propagation of the produced map to 11.2 cm when using the GNSS method. These values are considerably small compared to the expected vertical height accuracy from a 1:1,000 scale map of 20 cm by the Indonesian map accuracy standard.

Despite our promising results of the geoid height model, we also highlight some limitations in the present study that can enhance the geoid height model shortly. First, we only used terrestrial gravity data in our analysis. In a rough terrain condition (e.g., in the mountainous area), terrestrial gravity

data acquisition can be challenging. Therefore, an airborne gravimeter can complement the need for gravity data in such areas. A work reported that the combination between terrestrial and airborne-based gravimetry could improve the geoid height model accuracy by up to 12% in the mountainous area (Jiang et al. 2020). In addition, altimetry-based gravity data can also be used to complete the gravity data acquisition over the ocean areas.

Second, the accuracy of the DEM used in this study remains unclear. DEM is used to correct topographical-related gravity and geoid height in geoid modeling. Hence, additional investigation regarding the accuracy of DEM used should be carried out. Also, comparison with the national DEM of the DEMNAS (The official Indonesian DEM provided by the BIG) is another interesting topic to explore. Related to the topographical geoid effects, the use of lateral density variation also contributes significant effects to the geoid height up to 10 cm (Huang et al. 2001).

Finally, the evaluation points were still limited to one line and did not cover the entire area. Matsuo and Kuroishi (2020) also mentioned that there would be errors during the leveling acquisitions. Eventually, such errors would accumulate and propagate to the respective orthometric heights. Furthermore, no orthometric correction was applied to the data. Hwang and Hsiao (2003) reported that a significant orthometric correction was observed when the leveling was done near and in the mountainous area. Therefore, adding more GNSS/leveling evaluation points and implementing the additional orthometric correction to leveling observations is advisable.

#### 4 Final Remarks

We have computed the local geoid height models using the combination of Stokes formula and second Helmert's condensation method in Yogyakarta, Indonesia. The result shows a good agreement with the GNSS/leveling data, with the standard deviation is estimated to 5.1 cm for the best performance geoid height model. The computed geoid shows a promising result and can be used for various mapping applications and align with the Indonesian standard of map accuracy. We will continue our study by combining the terrestrial gravity data with the airborne and altimetry-based gravity data in Indonesia to develop the geoid model for a larger area.

**Acknowledgements** We thank to the support from the Institute for Research and Community Services-Institut Teknologi Bandung (LPPM-ITB) through the 'Riset Peningkatan Kapasitas Dosen Muda 2021' program under contract number FITB.PN-6-01-2021 and the Center for Geodesy Control Network and Geodynamics-Geospatial Information Agency of Indonesia (PJKGG-BIG).

## Conflict of Interest

The authors declare that they have no conflict of interest.

## References

- Andersen HE, Reutebuch SE, Mc Gaughey RJ (2005) Accuracy of an IFSAR-derived digital terrain model under a conifer forest canopy. *Can J Remote Sensing* 31(4):283–288. <https://doi.org/10.5589/m05-016>
- Bramanto B, Gumilar I, Taufik M, Hermawan IMDA (2019) Long-range single baseline RTK GNSS positioning for land cadastral survey mapping. *E3S Web of Conference* 94(01022)
- Bramanto B, Prijatna K, Pahlevi AM, Sarsito DA, Dahrin D, Variandy ED, Munthaha RIS (2021) Determination of gravity anomalies in Java, Indonesia, from airborne gravity survey. *Terr Atmospheric Ocean Sci* 32(5). <https://doi.org/10.3319/TAO.2021.06.04.01>
- Brockmann JM, Schubert T, Schuh WD (2021) An improved model of the Earth's static gravity field solely derived from reprocessed GOCE data, vol 42(2). Springer Netherlands. <https://doi.org/10.1007/s10712-020-09626-0>
- Ellmann A, Vaníček P (2007) UNB application of Stokes-Helmert's approach to geoid computation. *J Geodynam* 43(2):200–213. <https://doi.org/10.1016/j.jog.2006.09.019>
- Farr TG, Rosen PA, Caro E, Crippen R, Duren R, Hensley S, Kobrick M, Paller M, Rodriguez E, Roth L, Seal D, Shaffer S, Shimada J, Umland J, Werner M, Oskin M, Burbank D, Alsdorf D (2007) The shuttle radar topography mission. *Rev Geophys* 45(RG2004). <https://doi.org/10.1029/2005RG000183>
- Featherstone WE, Dentith MC (1998) A geodetic approach to gravity data reduction for geophysics. *Comput Geosci* 23(10):1063–1070
- Fuller J, Fernández M, Zeyen H, Vergés J (2007) A rapid method to map the crustal and lithospheric thickness using elevation, geoid anomaly and thermal analysis. Application to the Gibraltar Arc System, Atlas Mountains and adjacent zones. *Tectonophysics* 430(1-4):97–117. <https://doi.org/10.1016/j.tecto.2006.11.003>
- Gumilar I, Bramanto B, Rahman FF, Hermawan IMD (2019) Variability and performance of short to long-range single baseline RTK GNSS positioning in Indonesia. *E3S Web of Conferences* 94(01012)
- Heliani LS (2016) Evaluation of global geopotential model and its application on local geoid modelling of Java Island, Indonesia. In: *AIP Conference Proceedings*, vol 1755(100005). <https://doi.org/10.1063/1.4958534>
- Huang J, Vaníček P, Pagiatakis S, Brink W (2001) Effect of topographical density on geoid in the Canadian Rocky Mountains. *J Geod* 74:805–815
- Hwang C, Hsiao Y (2003) Orthometric corrections from leveling, gravity, density and elevation data: A case study in Taiwan. *J Geod* 77:279–291. <https://doi.org/10.1007/s00190-003-0325-6>
- Jayne SR (2006) Circulation of the North Atlantic Ocean from altimetry and the gravity recovery and climate experiment geoid. *J Geophys Res Oceans* 111(3):1–17. <https://doi.org/10.1029/2005JC003128>
- Jiang T, Dang Y, Zhang C (2020) Gravimetric geoid modeling from the combination of satellite gravity model, terrestrial and airborne gravity data: A case study in the mountainous area, Colorado. *Earth Planets Space* 72(189). <https://doi.org/10.1186/s40623-020-01287-y>
- Kahar J, Kasenda A, Prijatna K (1997) The Indonesian geoid model 1996. In: Segawa J, Fujimoto H, Okubo S (eds) *Gravity, geoid and marine geodesy*. International Association of Geodesy Symposia, vol. 117. Springer, Berlin, Heidelberg
- Kasenda A, Komara AM, Sutisna S (2000) The Indonesian gravity field and the geoid model. In: Rummel R, Drewes H, Bosch W, Hornik H (eds) *Towards an integrated global geodetic observing system (IGGOS)*. International Association of Geodesy Symposia, vol 120. Springer, Berlin, Heidelberg, pp 245–247. [https://doi.org/10.1007/978-3-642-59745-9\\_51](https://doi.org/10.1007/978-3-642-59745-9_51)
- Kiliçoğlu A, Direnç A, Yıldız H, Bölme M, Aktuğ B, Simav M, Lenk O (2011) Regional gravimetric quasi-geoid model and transformation surface to national height system for Turkey (THG-09). *Studia Geophys et Geod* 55(4):557–578. <https://doi.org/10.1007/s11200-010-9023-z>
- Mahdianpari M, Elizabeth J, Mohammadimanesh F, Warren S, Puestow T, Salehi B, Brisco B (2021) Smart solutions for smart cities: Urban wetland mapping using very-high resolution satellite imagery and airborne LiDAR data in the City of St. John's. NL, Canada. *J Environ Manage* 280(111676). <https://doi.org/10.1016/j.jenvman.2020.111676>
- Matsuo K, Kuroishi Y (2020) Refinement of a gravimetric geoid model for Japan using GOCE and an updated regional gravity field model. *Earth Planets Space* 72(33). <https://doi.org/10.1186/s40623-020-01158-6>
- Omang OC, Forsberg R (2000) How to handle topography in practical geoid determination: Three examples. *J Geod* 74(6):458–466. <https://doi.org/10.1007/s001900000107>
- Pahlevi A, Pangastuti D, Sofia N, Kasenda A (2015) Determination of gravimetric geoid model in Sulawesi - Indonesia. In: *FIG working week 2015*, Sofia, Bulgaria
- Pahlevi A, Bramanto B, Triarahmadhana B, Huda S, Pangastuti D, Nur A, Wijaya D, Prijatna K, Julianto M, Wijanarto A (2019) Airborne gravity survey, towards a precise Indonesian geoid model (Case study : Sumatera Island). *IOP Conf Ser: Earth Environ Sci* 389(012050). <https://doi.org/10.1088/1755-1315/389/1/012050>
- Pan M, Sjöberg LE (1998) Unification of vertical datums by GPS and gravimetric geoid models with application to Fennoscandia. *J Geod* 72(2):64–70. <https://doi.org/10.1007/s0019000050149>
- Pavlis NK, Holmes SA, Kenyon SC, Factor JK (2012) The development and evaluation of the Earth gravitational model 2008 (EGM2008). *J Geophys Res* 117(B04406):1–38. <https://doi.org/10.1029/2011JB008916>
- Schwarz K, Sideris M, Forsberg R (1990) The use of FFT techniques in physical geodesy. *Geophys J Int* 100:485–514
- Smith DA, Roman DR (2001) GEOID99 and G99SSS: 1-arc-minute geoid models for the United States. *J Geod* 75(9-10):469–490. <https://doi.org/10.1007/s001900100200>
- Stokes G (1849) On the variation of gravity at the surface of the Earth. *Trans Camb phil Soc Math Phys Sci* 8(5):672–695



- Syafarianty AN, Pahlevi AM, Suyatno ER, Oktavia SN, Pramono GH (2021) The grid optimization of the terrestrial gravity survey (Case study: Central Part of Java Island). IOP Conf Ser: Earth Environ Sci 731(012010). <https://doi.org/10.1088/1755-1315/731/1/012010>
- Tscherning CC (2015) Least-squares collocation. In: Grafarend E (ed) Encyclopedia of geodesy. Springer, Cham. <https://doi.org/10.1007/978-3-319-02370-0>
- Yang HJ (2013) Geoid determination based on a combination of terrestrial and airborne gravity data in South Korea. Tech. rep., The Ohio State University, Ohio

**Open Access** This chapter is licensed under the terms of the Creative Commons Attribution 4.0 International License (<http://creativecommons.org/licenses/by/4.0/>), which permits use, sharing, adaptation, distribution and reproduction in any medium or format, as long as you give appropriate credit to the original author(s) and the source, provide a link to the Creative Commons license and indicate if changes were made.

The images or other third party material in this chapter are included in the chapter's Creative Commons license, unless indicated otherwise in a credit line to the material. If material is not included in the chapter's Creative Commons license and your intended use is not permitted by statutory regulation or exceeds the permitted use, you will need to obtain permission directly from the copyright holder.





# A Geodetic Determination of the Gravitational Potential Difference Toward a 100-km-Scale Clock Frequency Comparison in a Plate Subduction Zone

Yoshiyuki Tanaka and Yosuke Aoki

## Abstract

Recent advances in the developments of optical atomic clocks have enabled  $10^{-18}$ -level frequency comparisons between fibre-linked clocks. Therefore, chronometric leveling with an uncertainty on the order of 1 cm has become possible, based on the general theory of relativity. Since measurement uncertainty does not deteriorate with increasing fibre length, applications of chronometric leveling in geodesy, particularly unification of height reference systems, have been actively studied. In Japan, a frequency comparison is under experimentation using a fibre link connecting two optical lattice clocks approximately 100 km apart. This study estimates both the potential difference between these two clock sites with a geodetic method and its uncertainty to verify the results of chronometric leveling, which will be obtained in the near future. We use orthometric heights derived from leveling surveys repeated for monitoring crustal deformation. When discussing an uncertainty at the 1-cm level in height, the effects of temporal variations in the gravitational potential on the height measurement need to be considered due to various geophysical phenomena, including tides. Our results show that the uncertainty in the height measurements by geodetic leveling is the largest and that tidal potential changes during the height measurements can cause systematic errors of a few mm. The effects due to variations in the nontidal ocean bottom pressure and atmospheric pressure are more than an order of magnitude smaller than the tidal effects at this spatial scale. An upper limit of groundwater effects is also estimated. In a future comparison with clocks with an uncertainty on the order of  $10^{-19}$ , tidal potential changes and groundwater effects must be more rigorously evaluated.

## Keywords

Chronometric leveling · Crustal deformation · Gravitational potential · Optical lattice clock · Relativistic geodesy · Tides

---

Y. Tanaka (✉)  
Department of Earth and Planetary Science, Graduate School of  
Science, The University of Tokyo, Tokyo, Japan  
e-mail: [y-tanaka@eps.s.u-tokyo.ac.jp](mailto:y-tanaka@eps.s.u-tokyo.ac.jp)

Y. Aoki  
Earthquake Research Institute, The University of Tokyo, Tokyo, Japan  
e-mail: [yaoki@eri.u-tokyo.ac.jp](mailto:yaoki@eri.u-tokyo.ac.jp)

---

## 1 Introduction

The general theory of relativity predicts that a clock put at a higher position by 1 cm near the Earth's surface ticks faster by approximately  $10^{-18}$  than another clock at a lower position (Müller et al. 2018). Using this nature, one can measure the height difference between two fibre-linked optical clocks by comparing their frequencies (Denker et al. 2017; Delva et al. 2019). Modern optical clocks allow decimetre- to centimetre-level chronometric leveling (e.g., Lisdat et

al. 2016; Koller et al. 2017; Grotti et al. 2018; McGrew et al. 2018; Oelker et al. 2019). Chronometric leveling requires a measurement time of only several hours or less to achieve such uncertainty. Furthermore, the uncertainty does not increase with the fibre length. These facts contrast with the time-consuming geodetic leveling in which measurement errors accumulate with increasing distance. The use of fibre-linked optical clocks has therefore been actively studied to unify height reference systems across European countries (Wu and Müller 2020).

Uncertainties in optical lattice clocks (OLCs) have improved year by year, including in Japan (Ushijima et al. 2015; Katori et al. 2015; Takano et al. 2016; Ushijima et al. 2018; Takamoto et al. 2020; Katori 2021). Detection of the gravitational red shift using transportable OLCs was recently demonstrated at the Tokyo Skytree by a team led by RIKEN and the University of Tokyo (Takamoto et al. 2020). A clock on the ground and another clock at the observatory 450 m above the ground were vertically fibre-linked, and the observed potential difference agreed with geodetic survey results at 1–5 cm in terms of height. For the next step, the team is planning to carry out a frequency comparison experiment using a 100-km-scale fibre network around Tokyo (Akatsuka et al. 2020). The use of state-of-the-art optical lattice clocks with fractional uncertainties on the order of  $10^{-19}$  has been proposed for the purpose of improving crustal deformation monitoring (Tanaka and Katori 2021).

The purpose of the current study is to confirm the results of clock frequency comparison experiments which will be carried out with the above 100-km scale network, using a geodetic method. Determining the difference in the gravity potential [or equivalently the orthometric height (Hofmann-Wellenhof and Moritz 2006)] between two sites 100 km apart with an uncertainty of 1 cm or below would be a geodetically interesting topic, when considering the following three aspects. (1) The accuracy of traditional leveling can be better than that of the so-called GNSS-geoid method to determine the height difference for such a distance (Sect. 4.3). (2) Deflection of the vertical due to tides that occurs during each measurement in the leveling survey accumulates along the route, which could cause a bias in the height difference (Kuroishi 2010). This effect may be observable for a 100-km scale leveling network. (3) Local potential changes that cannot be observed with satellite gravity missions such as GRACE and GRACE-FO (<https://gracefo.jpl.nasa.gov/>) must be evaluated in some way. In addition to these three aspects, plate subduction causes temporal variations in height.

Several examples that estimate the potential differences between clock sites with geodetic methods have been reported. Denker et al. (2017) described European geodetic leveling campaigns to confirm chronometric leveling in the context of the ITOC (International Timescales with Optical

Clocks, <http://projects.npl.co.uk/itoc/project>). Comparisons between chronometric leveling with the GNSS-geoid method and traditional leveling have been documented in Takano et al. (2016), Lisdat et al. (2016), Grotti et al. (2018), Delva et al. (2019), Riedel et al. (2020) and Takamoto et al. (2020). However, examples that estimate the potential difference for a 100-km scale, which are dedicated to confirming chronometric leveling, are still limited. Therefore, it is worth presenting the methodology and the result for the geodetic determination of the gravitational potential difference for the current case.

The remainder of this paper is structured as follows. In Sect. 2, we describe the methods and data used to determine the gravitational potential difference. A method to quantify the tidal effects on the leveling survey is also presented. In Sect. 3, we show the obtained potential difference and estimate its uncertainty. In Sect. 4, we discuss uncertainties due to geophysical phenomena other than tides. Finally, we summarize a budget for the uncertainty in Sect. 5.

## 2 Methods and Data

### 2.1 The Study Area and the Height Reference System

Figure 1a, b show the study area. The Philippine Sea Plate and the Pacific Plate subduct toward the northwest beneath the continental plate. The clock sites C1 at NTT BRL (Basic Research Laboratories) and C2 at RIKEN are located west and northwest of Tokyo Bay. The leveling route connecting these sites is approximately 100 km long (Fig. 1b). In Japan, the orthometric height is adopted as the national height system. Hereafter, we represent orthometric height simply as height. Figure 1b, e show that the heights along the leveling route are relatively low except for the rapid increase near the site C1. Below we explain the methods used to determine the static potential difference between C1 and C2 and its uncertainty.

### 2.2 Repeated Leveling Surveys

In the study area, more than 500 benchmarks (BMs) are deployed for monitoring groundwater pumping and tectonic effects. The local governments and the Geospatial Information Authority of Japan (GSI) have conducted the first-order leveling every 1–3 years at these BMs. The blue curve in Fig. 1e shows the height profile along the route connecting the nearest BM to the NTT BRL (A27) and that to the RIKEN (01–02). Surface gravity values to calculate heights are provided by the GSI. The results of the leveling surveys are compiled, to which a network adjustment with 13 fixed

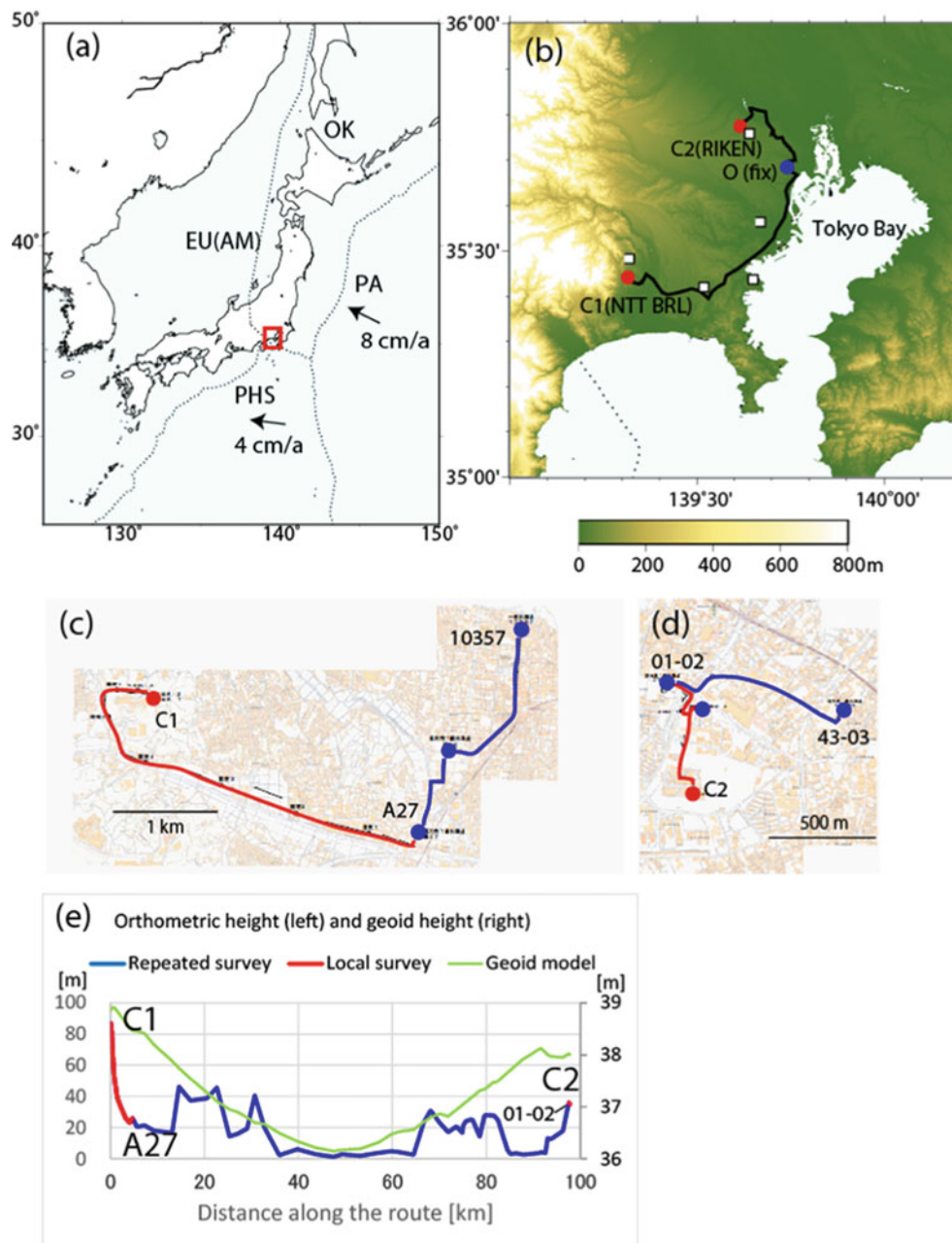


**Fig. 1** The study area and the leveling route. (a) The area marked by the red box is magnified in (b). (b) The black curve is the leveling route connecting the clock sites marked by the red circles. The blue circle is the origin of the height system. (c, d) Survey routes near the clock sites. Height on the BMs on the blue lines headed to the fixed origin in (b)

have been repeatedly observed whereas the gravity and the height along the red lines were measured in this study. The distance is 5 km from C1 to A27 and 1 km from C2 to 01-02. (e) Profiles of the orthometric height at epoch 2020.0 and the national geoid model (GSIGEO2011) along the route

sites (the origin O in Fig. 1b and the 12 BMs. Most are located in the inland stable areas) is applied. The resulting heights have been published annually.

To confirm the quality of the height data, Fig. 2a shows the error of closure for each loop in the leveling survey network. Assuming that the error of closure has the same dependency on a survey distance as the prescribed limit ( $2.0 \text{ [mm]} \sqrt{S \text{ [km]}}$ , Imakiire and Hakiwa (2004)), we inferred

an average behavior of the loop closure error. The average error and the standard deviation around this average were approximately 1/4 and 1/5 of the limit, respectively. The expected error for the height difference over a distance of 100 km was  $\pm 13 \text{ mm}$  for the 95% confidence level.

In addition to the above error depending on distances, differences between the nominal height at a reference BM and the actual mean sea level could cause a systematic

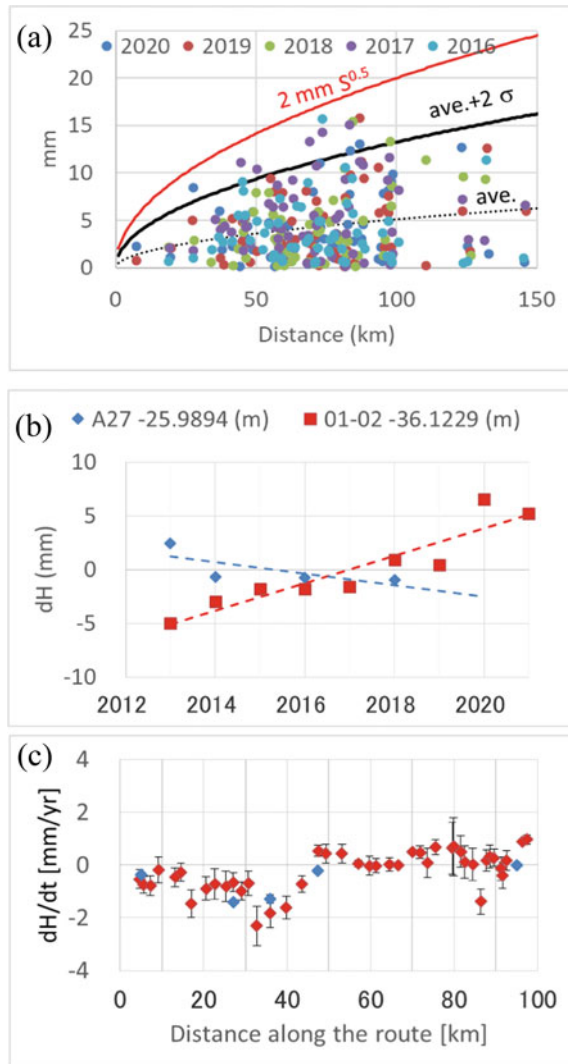


**Fig. 2** Results of the repeated surveys. (a) Error of loop closure observed for recent 5 years in the study area. The horizontal axis represents the length of each loop. The red curve denotes the allowable error and the black curve represents a 2-sigma error, obtained by assuming that the error of closure is proportional to the square root of the distance. (b) Height changes at the two BMs closest to the clock sites. The height at epoch 2020.0 and the linear trend during 2013–2018 were inferred by the least-squares method. (c) Vertical velocities at the BMs along the survey route shown in Fig. 1b. The blue marks show velocities at the GNSS stations shown in Fig. 1b

error (e.g., Kelsey and Gray 1972; Reibischung et al. 2008; Featherstone and Filmer 2012). In our case, the orthometric heights were based on the origin O in Fig. 1b, and its bias vanishes when calculating the height difference between the two clock sites.

Secular height changes have also been observed at these BMs as we will see later in Sect. 3.1. To improve the reliability for the determination of the height difference between A27 and 01-02, we applied a least-squares method to the multiyear height data and inferred a linear trend and

the height at the epoch of Jan. 1, 2020, assuming white noise.

### 2.3 Leveling Survey Near the Clock Sites

Figure 1c, d show the routes for the local leveling survey near the clock sites. First-order leveling was carried out by Showa Holdings Co., Ltd., in January and February 2020. In the laboratories, the height at a specific point on the vacuum chamber of the OLC was determined. The vertical distance from this point to the location of the atoms is mechanically constant and will be measured in late 2022 with an uncertainty below 1 mm by first-order leveling. The uncertainties were evaluated using the round-trip error.

Surface gravity along the short routes shown in Fig. 1c, d was measured by the authors, using a Lacoste-Romberg G-type relative gravimeter (S/N 705) on February 18, 2020. The survey started from the basement room of the Earthquake Research Institute, the University of Tokyo, where the absolute gravity value was determined with an FG5 (S/N 109). The difference of a round-trip survey after removing the solid-Earth tides and a linear drift was  $<10 \mu\text{Gal}$ , and this error was negligible in the height determination.

### 2.4 Tidal Effects on the Leveling

In the presence of body tides, the individual relative heights observed in the leveling survey increase by  $(1 + k - h)\Delta\phi/g$ , where  $\Delta\phi$  denotes the tidal potential difference between two measurement sites,  $g$  is the average surface gravity and  $k$  and  $h$  are the tidal Love numbers. Similarly, the effect of ocean tides can be estimated with the load Love numbers. These effects are not corrected for in the above first-order leveling data. This implies that a survey result obtained in an observation period differs from that obtained in another observation period, even if the measurement error is zero. Kuroishi (2010) estimated the tidal effects for major routes of the first-order leveling survey in northern and southwestern Japan (Hokkaido, Sanyo and Kyushu). He reported that the RMS of the effects per division (2 km) was 0.1 mm for body tides and 0.15 mm for ocean tides and that the effects of body tides were larger in the latitudinal direction. This result means that the effects could be several mm if accumulated over 100 km. Also in chronometric leveling, tidal effects with a similar amount occur (Fig. 3a). However, the effects appear in a simpler manner than in geodetic leveling, since the effects do not accumulate along the route.

In this paper, we estimated the tidal effects on leveling in a similar manner to Kuroishi (2010). The survey route and time of individual measurements were simplified as follows. The route shown in Fig. 1b was divided into 2-

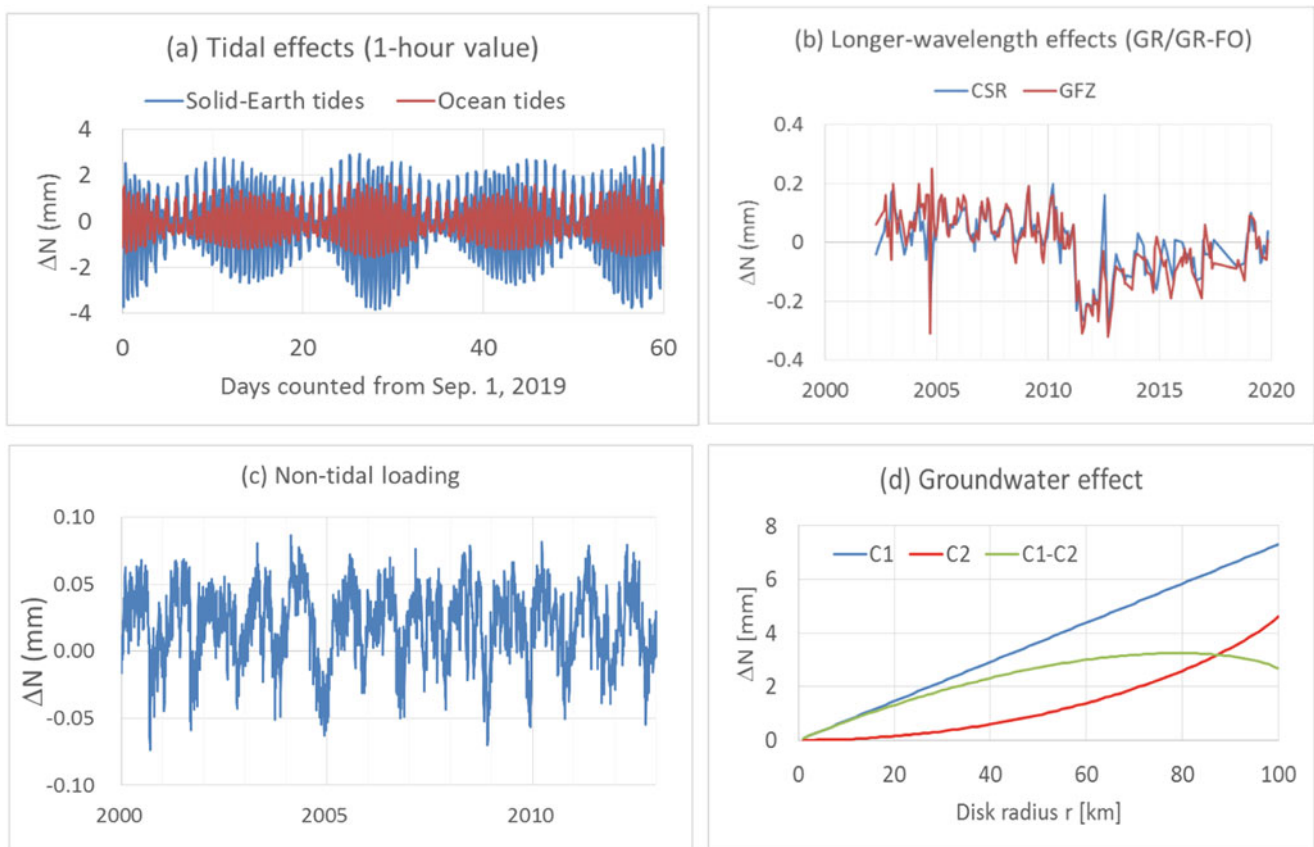


**Fig. 3** Potential differences from clock sites C1 to C2 in terms of geoid height caused by various geophysical phenomena. (a) Solid-Earth (body) and ocean tides. (b) Longer wavelength changes observed with GRACE and GRACE-FO satellites (monthly value). CSR and GFZ denote data analysis centers. (c) A nontidal effect estimated with an

ocean model (daily value). (d) The potential change at C1 and C2 for an extreme case, caused by a disk with a thickness of 1.7 m and a radius  $r$ , filled with water. The centre of the disk is put 1 m below C1. C1 and C2 are located at  $r = 0$  and 100 km, respectively. The green curve represents the potential difference between C1 and C2

km segments. Furthermore, each segment was separated into three intervals of equal length. A round-trip survey was performed for each interval with a time of 5 min for an individual height measurement. The measurements were performed from 9 am to 6 pm, thus, a 2-km segment was surveyed each day. The complete survey took 50 days. The potential difference during an individual measurement along the route was computed, using the software tide4n based on Tamura’s potential (Tamura 1987) for the body tides and GOTIC2 (Matsumoto et al. 2001) for the ocean tides. The relative height changes due to these tidal effects accumulated along the whole route.

### 3 Results

#### 3.1 Leveling

Figure 2b shows the heights from 2013 to 2021 at A27 and 01–02 obtained in the repeated surveys. Table 1 shows the result of the least-squares estimate for the velocity and

**Table 1** The inferred velocity ( $V$ ) and height ( $H$ ) at the nearest BMs to the clocks

BM	$V$ (mm/year)	$H$ ( $t = 2020.0$ ) (m)
A27	$-0.5 \pm 0.3$	$25.9868 \pm 0.0014$
01-02	$1.3 \pm 0.2$	$36.1267 \pm 0.0015$

The uncertainties for  $1\sigma$  are shown

height. Because the average error of loop closure varied little from year to year, we assumed that the multiyear height data had the same uncertainty. Then, the uncertainty ( $2\sigma$ ) of the linear regression model for the height difference from A27 to 01–02 at epoch 2020.0 was estimated as 4.1 ( $= 2\sqrt{1.4^2 + 1.5^2}$ ) mm. The uncertainty of 4 mm was approximately 1/3 of the  $2\sigma$  error of loop closure for the distance of 100 km (13 mm, Sect. 2.2). The fact that the former uncertainty was smaller was reasonable because the model used multiyear data to obtain the height difference at an epoch.

We estimated velocities at BMs along the route shown in Fig. 1b in the same manner. Figure 2c shows the result. The vertical velocities at the nearest continuous GNSS stations

(white squares in Fig. 1b), inferred from the daily coordinates during the 2015–2020 period, are also superimposed (Tsuji and Hatanaka 2018). We see that both velocities agree within 1 mm/year. Larger subsidence rates at distances of approximately 30 km were also observed in past leveling surveys, which could be explained by interplate coupling (Nishimura et al. 2007). The good agreement between the GNSS and the leveling results also implies that the choice of the fixed sites in the network adjustment is correct.

Adding the above height difference between A27 and 01–02 to the result of the local survey (Sect. 2.2), the height difference from C1 to C2 was  $-63.3014$  ( $=35.9554-99.2568$ ) m. The sum of the round-trip errors for the two local survey routes was 2.3 mm for  $1\sigma$ . Adding this error, the uncertainty for the height difference between C1 and C2 became  $\pm 6.2$  ( $=\sqrt{4.1^2 + 4.6^2}$ ) mm for the 95% confidence level.

### 3.2 Tidal Effects

Most of the repeated surveys were carried out in autumn. Therefore, we investigated the tidal effects in this season. As an example, Fig. 3a shows the geoid height difference caused by tides between C1 and C2 during 2 months starting from Sep. 1, 2019. We see that amplitudes for the body and ocean tides are within 4 mm and 2 mm, respectively.

Table 2 shows the tidal effects when changing the starting day of the 50-day survey from Sep. 1 to Oct. 1 in 2018 and 2019. From the left two columns for the body tides, we see that all the effects are negative, ranging from  $-2.5$  to  $-1$  mm. Furthermore, we note that the amount of the effect changes approximately every 2 weeks in both years, which is considered a reflection of spring and neap tides. For comparison, the right column for the body tides shows cases when the whole route was split into seven sections and the surveys for these sections were simultaneously initiated. Also in these cases, the effects were all negative. The average of the body tides from 9 am to 6 pm in Fig. 3a was  $-1.2$  mm, which was consistent with the negative sign of the above effects. We confirmed that the effects of the body tides on the height difference became positive when the survey is done during the night, indicating that measurement time (day/night) could systematically change the observed height difference by a few mm.

The effects of the ocean tides were smaller than those of the body tides, which was reasonable, considering the smaller amplitude of the ocean tides (Fig. 3a). As in the case of the body tides, the effects of the ocean tides were also negative or zero in both 2018 and 2019. The average of the ocean tides from 9 am to 6 pm in Fig. 3a was  $-0.2$  mm. However, when the survey was done simultaneously for the seven sections, the effects were positive in most cases (right column for the ocean tides). This indicates that when a bias

**Table 2** Effects of the temporal variations in the tidal potential on the leveling when the survey is initiated on different days (simulation) (Unit: mm)

Start	Body tides			Ocean tides		
	2019	2018	2019 <sup>a</sup>	2019	2018	2019 <sup>a</sup>
Sep 1	-1.0	-2.1	-1.9	-0.3	0.0	0.8
Sep 5	-2.4	-2.4	-1.2	-0.1	-0.7	0.1
Sep 8	-2.5	-1.4	-0.7	-0.6	-0.9	0.2
Sep 11	-1.9	-1.1	-1.3	-1.0	-0.5	0.4
Sep 15	-1.1	-2.1	-1.7	-0.6	-0.2	0.5
Sep 22	-2.5	-1.8	-1.6	-0.6	-1.0	-0.1
Oct 1	-1.2	-2.2	-1.9	-0.5	-0.5	0.0

The height at C2 relative to C1 is shown

<sup>a</sup>Cases when the surveys on the seven sections start simultaneously at the dates shown

in the tides is smaller ( $-0.2$  mm in the current case), the sign of the effects on the height difference could change. To reveal this mechanism, a detailed study associated with observation time and directions of the sections is necessary.

The sum of the effects due to the body and ocean tides on the height difference ranged from  $-3.5$  to  $-0.2$  mm, which could amount to a half of the measurement uncertainty estimated in Sect. 3.1. The error of closure shown in Fig. 2a could include the tidal effects to some extent.

## 4 Discussion

### 4.1 Treatment of Tides for Comparison with Chronometric Leveling

To compare a potential difference obtained by chronometric leveling with that obtained by geodetic leveling, an appropriate reduction for tides must be applied. Chronometric leveling measures an instantaneous potential difference between two clocks caused by all geophysical phenomena, including tides. In the above first-order leveling, no tidal effects are removed (Kuroishi 2003). Therefore, the leveling data include the permanent tide and the temporally varying tidal effects as considered in Sects. 2.4 and 3.2.

A natural choice to compare the two potential differences is to adopt the mean tidal system, where only the temporarily varying tidal components are removed (Ekman 1989; Mäkinen 2021). In the reduction for chronometric data, tidal models (excluding the permanent tide) can be used. On the other hand, the tidal effects on the leveling due to the temporally varying components were estimated as a few mm (Sect. 3.2). The amount of a few mm might be minor if we compare the geodetic result with chronometric leveling with an uncertainty of several cm or larger. However, when the uncertainty of chronometric leveling reaches 1 cm or below, a rigorous reduction of the leveling data should be considered,

in which tidal models are applied to individual relative height measurements.

## 4.2 Other Effects

Thus far, we have considered uncertainties due to tides, which are relatively accurately evaluated. Below, we discuss other effects that cause temporal potential changes (e.g., Voigt et al. 2016; Leßmann and Müller 2018; Schröder et al. 2021), assuming that a chronometric measurement and a leveling survey are performed in different observation periods.

### 4.2.1 Long Wavelength Changes

Long-wavelength potential differences between the two clock sites can be estimated using satellite gravity data. Figure 3b shows the difference in the monthly geoid height changes from 2002 to 2020 observed with GRACE and GRACE-FO satellite missions (<http://thegraceplotter.com/>). The spatial resolution is  $> 200$  km. We see that annual variations are within  $\pm 0.1$  mm with a rapid decrease in Mar. 2011 of 0.3 mm and a subsequent slow increase of 0.025 mm/year, reflecting the coseismic and postseismic deformation due to the 2011 M9 Tohoku earthquake.

### 4.2.2 Nontidal Loading

Next, we consider shorter-wavelength potential differences. We estimated the potential difference caused by nontidal ocean bottom pressure (OBP) changes, using a data assimilation model of the Meteorological Research Institute of Japan (Usui et al. 2006). The model input data included wind stress, rainfall and thermal fluxes; temperature and salinity profiles and sea surface height based on in situ and satellite observations were assimilated. The spatial resolution of the OBP was  $0.1^\circ \times 0.1^\circ$ . Annual changes in the OBP in Tokyo Bay and south of C1 (Fig. 1b) were  $\pm 1.5$  hPa or less. Longer-term OBP changes were insignificant. Figure 3c shows the estimated difference in the geoid height change between C1 and C2. We see that the nontidal effect is within  $\pm 0.1$  mm, which is an order of magnitude smaller than the effects of ocean tides (Fig. 3a).

### 4.2.3 Groundwater

The groundwater levels observed in the study area, published by the local governments, were dominated by seasonal changes with different amplitudes and phases. It is difficult to identify the spatial extents of the groundwater movements since groundwater levels are observed at points. When modeling groundwater movements, local heterogeneities in the soil characteristics must also be considered. In this study, we simply estimated an upper limit of the groundwater contribution to the potential difference between C1 and C2, considering an extreme case, using precipitation data only.

The average annual precipitation during 1981–2010, observed at the Japan Meteorological Agency (JMA) AMeDAS stations in the study area, were 1,500–1,700 mm. We suppose that the centre of a disk with a radius of  $r$  [km] and a thickness of  $w = 1,700$  [mm], filled with water, is located 1 m below the site C1. Figure 3d shows the geoid height change at C1 and C2, caused by the disk mass for different values of  $r$ . We see that the maximum difference between the clock sites is 3.3 mm for  $r \sim 80$  km. This case would give an upper limit because i) run off to the ocean is neglected (i.e.,  $w$  is overestimated) and ii) the mass anomaly is “coherent” for  $0 \leq r \leq 80$  km. In actuality, changes in the groundwater levels are more heterogeneous and phases of the annual variations are different from one location to another. Therefore, the sum of the effects on the individual relative height measurements in a more realistic case should become smaller than in the coherent case assumed in this model. When the disk is located below C2 instead of C1, the sign reverses. Consequently, the range can be estimated as  $\pm 3.3$  mm.

### 4.2.4 Atmospheric Loading

Finally, we estimated the effects of atmospheric loading. We investigated the difference in the atmospheric pressure during 1981–2010 between the AMeDAS stations Yokohama (closest to C1) and Tokyo (closest to C2). Annual changes in the difference were within 0.15 hPa, which was an order of magnitude smaller than the non-tidal effects. The effect estimated with a disk model of a radius of 100 km was smaller than 0.1 mm on the geoid height difference.

## 4.3 The GNSS-Geoid Method

An alternative method to determine the height at a location is to subtract the geoid height from the ellipsoidal height. The standard deviation of the Japanese geoid model is approximately 2 cm (Miyahara et al. 2014). Adding an uncertainty by a GNSS observation for the ellipsoidal height, the uncertainty for the (orthometric) height is expected to be 3 cm, which is larger than the uncertainty estimated in this study. To verify our results, we will perform this GNSS-geoid approach in the near future.

## 5 Summary

We have determined a potential difference with geodetic leveling and discussed its uncertainty, in order to verify a potential difference that will be observed by a 100-km scale chronometric leveling. Table 3 summarizes the uncertainties considered in this study. The largest uncertainty comes from



**Table 3** The uncertainties in the height difference between clock sites C1 and C2 determined by the leveling-gravity method (Unit: mm)

	Kind	Uncertainty (mm)	Remarks
A	Measurement err.	$\pm 6.2$ (95%)	Including linear regression err.
B	Body tides	-2.5/-1.0	Tamura's potential
C	Ocean tides	-1.0/0.8	GOTIC2
D	Long wavelength	-0.1/0.1	Annual change by GRACE (-FO)
E	Non-tidal loading	-0.1/0.1	Ocean model (JMA)
F	Atmospheric loading	0.0/0.0	Pressure data (JMA), $r = 100$ km
G	Groundwater	-3.3/3.3	An extreme case, $r = 80$ km
H	Total	-13.2/9.5	Sum of A-G

The numeral values before and after the slashes denote the minimum and maximum values

the accumulation of individual measurement errors of leveling. The second largest uncertainty arises from tides, which could cause a bias rather than a random error. The effects of nontidal OBPs, longer wavelengths and atmospheric pressure changes are smaller than 1 mm. These uncertainties are more than an order of magnitude smaller than those of the potential differences between NPL (National Physical Laboratory, United Kingdom) and PTB (Physikalisch-Technische Bundesanstalt, Germany) estimated by Voigt et al. (2016). This is reasonable considering that the distance of 100 km between our sites is shorter than the distance between NPL and PTB. The upper limit of the effect of groundwater, estimated for an extreme case, does not exceed  $\pm 4$  mm. The amount of 4 mm is comparable with continental water effects estimated by Voigt et al. (2016), who stated that local hydrological effects are negligible. The total uncertainty for the height difference between RIKEN and NTT BRL in our study is estimated to be smaller than  $\pm 1.5$  cm. In a future comparison of clocks with uncertainties of the order of  $10^{-19}$ , tidal potential changes and groundwater effects need to be more rigorously evaluated.

**Acknowledgements** We are grateful to the two anonymous reviewers who gave us valuable comments to improve the manuscript. We acknowledge the GSI, the Tokyo metropolitan government, the Saitama and the Kanagawa prefectural governments for providing the geodetic and groundwater data. We also acknowledge the JMA for providing weather data and the ocean model. The satellite gravity data were made with [thegraceplotter.com](http://thegraceplotter.com), courtesy of CNES/GRGS. This work was supported by JST Grant Number JPMJMI18A1 and JSPS KAKENHI Grant Number 21H05204. Some figures were created using the Generic Mapping Tools (Wessel and Smith 1991).

**Author Contributions** Y.T. designed the research and performed the data analysis. Y.T. and Y.A. performed gravity observation.

**Data Availability** All data generated during the current study are available on reasonable request.

## References

- Akatsuka T et al (2020) Optical frequency distribution using laser repeater stations with planar lightwave circuits. *Opt Express* 28(7):9186–9197. <https://doi.org/10.1364/OE.383526>
- Delva P, Denker H, Lion G (2019) Chronometric geodesy: methods and applications. In: Pützfeld D, Lämmerzahl C (eds) *Relativistic geodesy, foundations and applications*. Springer, Berlin, pp 25–85. <https://doi.org/10.1007/978-3-030-11500-5>
- Denker H, Timmen L, Voigt C, Weyers S, Peik E, Margolis HS, Delva P, Wolf P, Petit G (2017) Geodetic methods to determine the relativistic redshift at the level of 10–18 in the context of international timescales—a review and practical results. *J Geod* 92:487–516
- Ekman M (1989) Impacts on geodynamic phenomena on systems for height and gravity. *Bull Geodes* 63:281–296
- Featherstone WE, Filmer MS (2012) The north-south tilt in the Australian Height Datum is explained by the ocean's mean dynamic topography. *J Geophys Res* 117:C08035. <https://doi.org/10.1029/2012JC007974>
- Grotti J, Koller S, Vogt S et al (2018) Geodesy and metrology with a transportable optical clock. *Nat Phys* 14:437–441. <https://doi.org/10.1038/s41567-017-0042-3>
- Hofmann-Wellenhof B, Moritz H (2006) *Physical geodesy*, 2nd edn. Springer, Wien, p 403. <https://doi.org/10.1007/978-3-211-33545-1>
- Imakiire T, Hakoïwa E (2004) JGD2000 (vertical) -The New Height System of Japan. *Bulletin of Geospatial Information Authority of Japan* 61:31–51
- Katori H (2021) Longitudinal Ramsey spectroscopy of atoms for continuous operation of optical clocks. *Appl Phys Exp* 14:072006
- Katori H, Ovsiannikov VD, Marmo SI, Palchikov VG (2015) Strategies for reducing the light shift in atomic clocks. *Phys Rev A* 91:052503
- Kelsey J, Gray DA (1972) Geodetic aspects concerning possible subsidence in southeastern England. *Philos Trans R Soc Lond A* 272(1221):141–149
- Koller SB, Grotti J, Vogt S, Al-Masoudi A, Dörscher S, Häfner S, Sterr U, Lisdat C (2017) Transportable optical lattice clock with  $7 \times 10^{-17}$  uncertainty. *Phys Rev Lett* 118(7):073601
- Kuroishi Y (2003) Reference frames in space geodesy era-part 1: gravity and height. *Bull Geospat Inf Authority Jpn* 102:21–32. (in Japanese)
- Kuroishi Y (2010) Effects of astronomic tides and ocean tidal loading on leveling—partly estimation for the first-order leveling in Japan. *J Geodetic Soc Japan* 56:59–72. (in Japanese with an English abstract)
- Leßmann and Müller (2018) Analysis of non-tidal ocean loading for gravitational potential observations in northern Europe. *J Geodyn* 119:23–28. <https://doi.org/10.1016/j.jog.2018.05.008>
- Lisdat C, Grosche G, Quintin N et al (2016) A clock network for geodesy and fundamental science. *Nat Commun* 7:12443. <https://doi.org/10.1038/ncomms12443>
- Mäkinen J (2021) The permanent tide and the International Height Reference Frame IHRF. *J Geod* 95:106. <https://doi.org/10.1007/s00190-021-01541-5>
- Matsumoto K, Sato T, Takanezawa T, Ooe M (2001) GOTIC2: a program for computation of oceanic tidal loading effect. *J Geodetic Soc Japan* 47:243–248
- McGrew WF, Zhang X, Fasano RJ, Schäffer SA, Beloy K, Nicolodi D, Brown RC, Hinkley N, Milani G, Schioppo M, Yoon TH, Ludlow AD (2018) Atomic clock performance enabling geodesy below the centimetre level. *Nature* 564(7734):87–90. <https://doi.org/10.1038/s41586-018-0738-2>
- Miyahara B, Kodama T, Kuroishi Y (2014) Development of new hybrid geoid model for Japan, “GSIGEO 2011”. *Bull Geospat Inf Authority Jpn* 62:11–20

- Müller J et al (2018) High performance clocks and gravity field determination. *Space Sci Rev* 214:5. <https://doi.org/10.1007/s11214-017-0431-z>
- Nishimura T, Sagiya T, Stein RS (2007) Crustal block kinematics and seismic potential of the northernmost Philippine Sea plate and Izu microplate, central Japan, inferred from GPS and leveling data. *J Geophys Res* 112:B05414. <https://doi.org/10.1029/2005JB004102>
- Oelker E, Hutson RB, Kennedy CJ et al (2019) Demonstration of  $4.8 \times 10^{-17}$  stability at 1 s for two independent optical clocks. *Nat Photonics* 13:714–719. <https://doi.org/10.1038/s41566-019-0493-4>
- Reibischung P, Duquenne H, Duquenne F (2008) The new French zero-order levelling network – first global results and possible consequences for UELN, EUREF Symposium, Brussels, 18–21 June 2008
- Riedel F et al (2020) Direct comparisons of European primary and secondary frequency standards via satellite techniques. *Metrologia* 57:045005. <https://doi.org/10.1088/1681-7575/ab6745>
- Schröder S, Stellmer S, Kusche J (2021) Potential and scientific requirements of optical clock networks for validating satellite-derived time-variable gravity data. *Geophys J Int* 226:764–779. <https://doi.org/10.1093/gji/ggab132>
- Takamoto M, Ushijima I, Ohmae N, Yahagi T, Kokado K, Shinkai H, Katori H (2020) Test of general relativity by a pair of transportable optical lattice clocks. *Nat Photon* 14(7):411–415. <https://doi.org/10.1038/s41566-020-0619-8>
- Takano T, Takamoto M, Ushijima I, Ohmae N, Akatsuka T, Yamaguchi A, Kuroishi Y, Munekane H, Miyahara B, Katori H (2016) Geopotential measurements with synchronously linked optical lattice clocks. *Nat Photon* 10(10):662–666. <https://doi.org/10.1038/nphoton.2016.159>
- Tamura Y (1987) A harmonic development of the tide-generating potential. *Marees Terrestres Bulletin d'Informations* 99:6813–6855
- Tanaka Y, Katori H (2021) Exploring potential applications of optical lattice clocks in a plate subduction zone. *J Geod.* <https://doi.org/10.1007/s00190-021-01548-y>
- Tsuji H, Hatanaka Y (2018) GEONET as infrastructure for disaster mitigation. *J Disaster Res* 13:424–432. <https://doi.org/10.20965/jdr.2018.p0424>
- Ushijima I, Takamoto M, Das M, Ohkubo T, Katori H (2015) Cryogenic optical lattice clocks. *Nat Photon* 9:185–189. <https://doi.org/10.1038/nphoton.2015.5>
- Ushijima I, Takamoto M, Katori H (2018) Operational magic intensity for Sr optical lattice clocks. *Phys Rev Lett* 121:263202. <https://doi.org/10.1103/PhysRevLett.121.263202>
- Usui N, Ishizaki S, Fujii Y, Tsujino H, Yasuda T, Kamachi M (2006) Meteorological Research Institute multivariate ocean variational estimation (MOVE) system: some early results. *Adv Space Res* 37:806–822. <https://doi.org/10.1016/j.asr.2005.09.022>
- Voigt C, Denker H, Timmen L (2016) Time-variable gravity potential components for optical clock comparisons and the definition of international time scales. *Metrologia* 53:1365–1383. <https://doi.org/10.1088/0026-1394/53/6/1365>
- Wessel P, Smith WHF (1991) Free software helps map and display data. *Eos Trans AGU* 72(441):445–446
- Wu H, Müller J (2020) Towards an international height reference frame using clock networks. In: *International association of geodesy symposia*. Springer, Berlin. [https://doi.org/10.1007/1345\\_2020\\_97](https://doi.org/10.1007/1345_2020_97)

**Open Access** This chapter is licensed under the terms of the Creative Commons Attribution 4.0 International License (<http://creativecommons.org/licenses/by/4.0/>), which permits use, sharing, adaptation, distribution and reproduction in any medium or format, as long as you give appropriate credit to the original author(s) and the source, provide a link to the Creative Commons license and indicate if changes were made.

The images or other third party material in this chapter are included in the chapter's Creative Commons license, unless indicated otherwise in a credit line to the material. If material is not included in the chapter's Creative Commons license and your intended use is not permitted by statutory regulation or exceeds the permitted use, you will need to obtain permission directly from the copyright holder.





# Validation of the Hellenic Gravity Network in the Frame of the ModernGravNet Project

Vassilios N. Grigoriadis, Vassilios D. Andritsanos, and Dimitrios Natsiopoulos

## Abstract

In the frame of the “Modernization of the Hellenic Gravity Network - ModernGravNet” project, relative and absolute gravity measurements were carried out at selected 1st and 2nd order benchmarks of the Hellenic gravity network. These measurements are used first for the evaluation of the network. Then, as the official network gravity values are referenced to the Potsdam gravity system, transformation parameters are determined for converting official values to the new gravity system as it is defined by the absolute gravity measurements. A northeast to southwest trend is revealed from corrections computed from the parametric modeling. Moreover, global geopotential models are assessed at the network benchmarks as a first step towards the development of a new geoid model for Greece and successively the establishment of a national geoid-based vertical datum.

## Keywords

Gravity network · Greece

## 1 Introduction

One of the fundamental geodetic and geophysical infrastructure of a country is the gravity network. The traditional gravity network includes all the benchmarks (BMs) whose value was measured using absolute or relative gravimeters and that was finally obtained after performing network adjustment. The backbone of the network are the first order BMs that in turn are used for its densification and consequently the development of the second, third, etc. order BMs. The Hellenic gravity network comprises of 143 1st and 2nd order BMs located both on land and on islands and is maintained by the Hellenic Military Geographical Service (HMGS). The

first gravity measurements were carried out in the 1950s, whereas the gravity network started to be established in 1960s (Melissinos 2021). The network was measured using relative gravimeters with the reference BM located in Athens at the HGMS headquarters. The latter was connected to a reference station located at the entrance of Facoltà di Ingegneria Civile e Industriale (former Facoltà di Ingegneria) of the Sapienza Università di Roma (Bureau Gravimétrique International station no. 001294). As the reference value referred to the Potsdam gravity system (Torge 1989, p. 314), the values of the Hellenic network were considered initially in 1970 to be larger by 13.8 mGal, while in 1989 by 14.89 mGal (Melissinos 2021), although HGMS still provides gravity values in the Potsdam gravity system. It should be noted that there is no official documentation (technical report or publication) describing the Hellenic gravity network (as of September 2021). This lack of documentation makes difficult any attempt to assess the gravity network as there is no available information regarding its accuracy and computational details (e.g., corrections used, tidal system). Especially for the tidal system, this is even more complicated as the reference value of the Potsdam system could be considered as mean-tide but the ties made to other national

V. N. Grigoriadis (✉) · D. Natsiopoulos  
Laboratory of Gravity Field Research and Applications, Department of Geodesy and Surveying, Aristotle University of Thessaloniki, Thessaloniki, Greece  
e-mail: [nezos@topo.auth.gr](mailto:nezos@topo.auth.gr)

V. D. Andritsanos  
Geospatial Technologies Lab, Department of Surveying and Geoinformatics Engineering, University of West Attica, Athens, Greece

reference points after 1950s–1960s were made using modern relative gravimeters and therefore tidal corrections (either for a tide-free or zero-tide system) should have been applied. Moreover, these problems propagate to any other measured gravity point values. Consequently, the development of a gravity database for the Hellenic region, see, for example, Grigoriadis (2009), becomes a non-trivial procedure, where one has to deal with inconsistencies among different datasets measured at different time periods.

As most gravity networks worldwide were established in the previous century, efforts are made in different countries for their modernization (e.g. Krynski et al. 2013). Modernization implies the move from a traditional gravity network to a gravity infrastructure that consists of reference BMs measured with absolute gravimeters similarly to the establishment of the International Gravity Reference System (Wziontek et al. 2021). In this frame and in 2020, the “Modernization of the Hellenic Gravity Network - Modern-GravNet” project started with the aim to initially assess the status and evaluate the current gravity network in Greece and propose the means and methods for establishing a new modern gravity infrastructure. For the assessment, a total of 25 BMs (24 on land and 1 on an island) were measured using absolute and relative gravimeters out of the 143 BMs that comprise the first and second order network, i.e., approx. 18% of the total BMs or 21% when excluding BMs on islands. The present study describes the measurements and comparisons that were carried out for the evaluation of the Hellenic gravity network as well as the determination of a parametric model for transforming old gravity values to the current newly measured gravity field as it is defined by the recent absolute measurements. Additionally, the new measured values are used for assessing the reduced field obtained after subtracting the contribution of Global Geopotential Models (GGMs) and the remove of the Residual Terrain Modeling (RTM) effect (Forsberg 1984).

## 2 Measurements and Comparisons

A Micro-g LaCoste A10 absolute gravimeter with serial number 027 (A10-#027) was used for establishing a new reference station in the Laboratory of Gravity Field Research and Applications (GravLab) in Thessaloniki, northern Greece. Before performing the measurements, the A10-#027 was calibrated (laser beam wavelengths:  $\lambda_{red} = 632.9912464$  nm,  $\lambda_{blue} = 632.9902813$  nm) by Micro-g LaCoste and was compared against the company’s FG5-265 and FG5-302, showing an acceptable difference in measured value equal to about 1  $\mu$ Gal. Although the initial plan was to measure all the Hellenic gravity

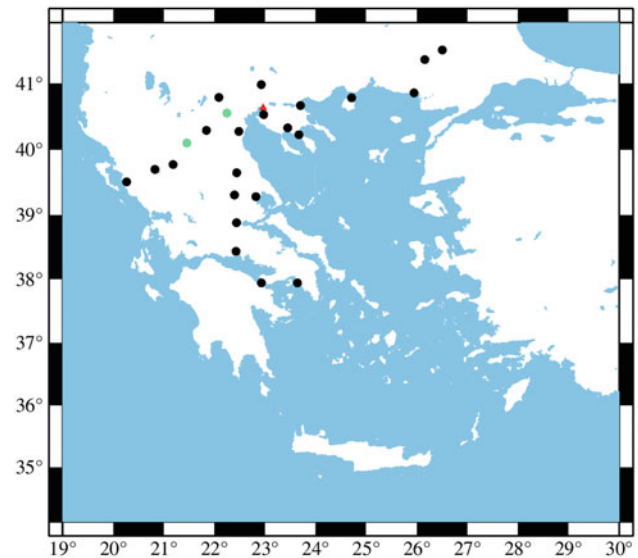


**Fig. 1** Measured BMs (black: with CG5/CG6, green: with A10) and the GravLab-B reference station (red: with A10)

network benchmarks with the absolute gravimeter, only two benchmarks were measured due to a short-circuit in one of the instrument’s electronic boards. Therefore, the rest of the network benchmarks were measured using two Scintrex CG5 relative gravimeters with the GravLab gravity station as reference. Each relative measurement lasted 5 min and each absolute 30 min. The mean uncertainty was 15  $\mu$ Gal and 11  $\mu$ Gal for the relative and absolute measurements respectively and varied based on the measurement site conditions. The precise location of each benchmark was obtained using GNSS receivers following the Network Real-Time Kinematic method (NRTK) but this was not always possible as it will be described next. The location of the measured benchmarks classified by measuring method used are shown in Fig. 1.

For each benchmark, additional measurements were carried out using the relative gravimeters for determining the local vertical gravity gradient. Measurements were obtained at two different height levels, one on the benchmark and the other at about 60 cm above by placing the instrument on a tripod and using a plumb bob for centering. The determined vertical gravity gradient was used for referring the measured gravity value at the gravity sensor on the benchmark.

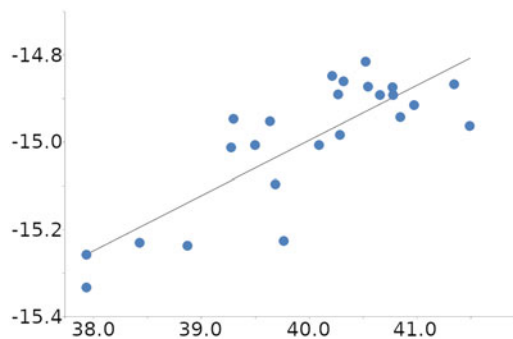
The measured gravity was also corrected for tides and polar motion. Earth tides and ocean loading were computed following Spiridonov et al. (2018) using the FES2012 model (Carrère et al. 2012) and the ATLANTIDA software. Polar motion was taken into account using the International Earth Rotation and Reference System Service (IERS) bulletins A by applying (Eq. 4) in Wahr (1985).

**Table 1** Differences between measured and official values [mGal]

	Mean	Stdev	Min	Max
$g_{\text{obs}} - g_{\text{official}}$	-15.00	0.15	-15.34	-14.82

Apart from the calibration of the relative gravimeters by Scintrex and prior to the start of the campaign, their long-term drift correction was determined using the CG5's software-based automated method and their tilt sensors offsets were adjusted. For the short-term (residual) drift and as the measurements each day started and ended at the GravLab station, this was considered linear with respect to time and therefore linearly apportioned to each measured benchmark based on the time of each measurement. It should be noted that each benchmark was measured only one time and therefore no network was formed/adjusted.

The statistics of the differences between the measured and the official values are given in Table 1 for a total of 24 points out of the 25. The excluded point was measured unsuccessfully three times in different months but the measurement error was too high (see Discussion). Although the mean value of statistics of the differences equal to  $-15.00$  mGal is very close to the value of  $-14.89$  mGal found in 1989 by HGMS (see Introduction) and could be justified by a small variation in the gravity field, the standard deviation and range of the differences were further investigated as they were deemed significant. Therefore, it was decided to first examine any possible correlation between the differences with the station coordinates. Indeed, it was discovered that the differences are correlated to the geodetic latitude of the BMs (see Fig. 2) but not to their geodetic longitude and geometric height. As stated before, due to lack of documentation any effort to justify these differences is not safe as there could be many reasons for this, like, for example, inconsistent tidal corrections or per area network adjustments—starting from southern Greece (national reference point) and continuing to northern Greece. This latitude dependence though cannot be attributed

**Fig. 2** BM gravity differences versus BM latitude (x-axis: geodetic latitude [deg], y-axis: differences [mGal])

to the tidal system of the measurements. The authors performed the comparisons and the computations described in the next section using all tidal systems without noticing significant differences (some  $\mu\text{Gals}$ ), which is expected since Greece is a small country. As this latitude dependent correlation affects not only the BMs but also any measurement referenced to them and by taking into account that the majority of the available gravity values in Greece refer to the national network, it was decided to determine a parametric model. This parametric model would absorb these differences and allow the conversion of existing values to the current gravity field as it was obtained from the absolute gravity measurements. Moreover, it would better depict the variation of differences, as it will be shown in the next section.

From the measured gravity values, surface gravity anomalies were obtained and reduced gravity anomaly fields were computed by subtracting the contribution of GGMs. The selected GGMs are: (a) EIGEN-6C4 (Förste et al. 2014) with a maximum degree/order (d/o) 2190, (b) EGM2008 (Pavlis et al. 2012) with a maximum d/o 2190 and (c) the family of XGM2019 models that includes XGM2019 (max d/o 760)/XGM2019e (max d/o 5540)/XGM2019e\_2159 (max d/o 2190) (Zingerle et al. 2020). The selection includes models that have commonly been used in geoid modeling (EIGEN-6C4 and EGM2008) as well as the latest XGM2019 family of models based on the latest reprocessing of GOCE satellite data that incorporate also other improvements from its predecessors. The reduced field statistics were computed for d/o 760, 2190 and 5540 are shown in Table 2. It should be mentioned that XGM2019e includes also topographically derived gravity. For d/o 760 the models perform equally well with similar statistical results, while for d/o 2190 the XGM2019 models present a larger standard deviation than EGM2008 and EIGEN-6C4. Similar conclusions may be drawn from Table 3 that provides the statistics of the residual gravity anomaly field after removing the RTM effect precomputed up to d/o 2160 from the Earth2014 model (Rexer et

**Table 2** Reduced gravity anomaly field for the BMs after subtracting the contribution of GGMs [mGal]

GGM	d/o	Mean	Stdev	Min	Max
Unreduced field	–	11.37	37.21	-75.80	105.69
EIGEN-6C4	760	-21.09	20.66	-59.38	27.45
EGM2008		-21.02	20.96	-58.80	26.63
XGM2019		-22.71	21.09	-56.97	35.75
XGM2019e_2159 / XGM2019e		-20.70	21.03	-58.41	29.98
EIGEN-6C4	2190	-8.55	12.82	-38.94	15.20
EGM2008		-8.48	12.96	-38.07	18.17
XGM2019		-8.63	18.34	-41.72	28.05
XGM2019e		-9.18	18.25	-41.37	30.01
XGM2019e	5540	-4.51	14.39	-23.86	31.80

**Table 3** Residual gravity anomaly field for the BMs after subtracting the contribution of GGMs and topography (A: Earth2014, B: ERTM) [mGal]

GGM	d/o	Topo	Mean	Stdev	Min	Max
Unreduced field	–	–	11.37	37.21	–75.80	105.69
EIGEN-6C4	760	A&B	–2.91	9.96	–17.47	25.19
EGM2008			–2.84	10.20	–17.73	24.37
XGM2019			–4.52	13.00	–23.00	33.49
XGM2019e_2159 / XGM2019e			–2.52	11.17	–20.11	27.72
EIGEN-6C4	2190	B	–2.26	4.05	–10.79	4.14
EGM2008			–2.20	4.28	–9.12	6.54
XGM2019e_2159			–2.35	11.17	–20.35	26.84
XGM2019e			–2.90	11.04	–19.01	28.80

al. 2016) and from d/o 2160/2190 up to about 80,000 from the ERTM model (Hirt et al. 2014). It should be pointed out that the number of BMs is limited. But, the statistics imply that even older models should be examined along with the new ones in the investigations for producing residual gravity fields for geoid modeling. The latter being the next step towards the modernization of the Hellenic vertical datum. Furthermore, the majority of the models shown in Table 3 present a consistent residual field in terms of mean value (about 2–3 mGal). By considering the results of Table 2, where models used with the same d/o of expansion present a similar mean value in the statistics of the reduced field, it may be deduced that the 2–3 mGal mean value is partly attributed to the zero-degree term of the geopotential models and partly to the RTM reductions inability to fully model the remaining gravity field.

### 3 Parametric Modeling

Six different parametric models were utilized to identify possible biases and tilts between the new measurements and the official values at the benchmarks. The differences  $g$  are modelled by

$$g = g_{obs} - g_{official} = a^T x + v \quad (1)$$

where  $g_{obs}$  and  $g_{official}$  are the matrices of the observed and official gravity values respectively,  $\alpha$  the design matrix,  $x$  the matrix of unknown model parameters to be determined and  $v$  the errors matrix. The six parametric models are:

**Model A**, a 4-parameter datum shift model (Heiskanen and Moritz 1967, Ch. 5; Fotopoulos 2003, eq. 3.31):

$$g = a + b \cos \varphi_i \cos \lambda_i + c \cos \varphi_i \sin \lambda_i + d \sin \varphi_i + v_i \quad (2)$$

**Model B**, a 5-parameter datum shift model (Heiskanen and Moritz 1967, Ch. 5; Fotopoulos 2003, eq. 3.33):

$$g = a + b \cos \varphi_i \cos \lambda_i + c \cos \varphi_i \sin \lambda_i + d \sin \varphi_i + e \sin^2 \varphi_i + v_i \quad (3)$$

**Model C**, a simple linear model (translation/bias and scale) (Torge 1989, eq. 9.1):

$$g = a + b (g_{i\ official} - \bar{g}) + v_i \quad (4)$$

**Model D**, an extended model based on Model C:

$$g = a + b (g_{i\ official} - \bar{g}) + c (\varphi_i - \bar{\varphi}) + d (\lambda_i - \bar{\lambda}) \cos \varphi_i + v_i \quad (5)$$

**Models E and F**, mixed linear with polynomial models of first ( $m_{max} = n_{max} = 1$ ) and second order respectively ( $m_{max} = n_{max} = 2$ ) taking into account the measured gravity field:

$$g = b (g_{i\ official} - \bar{g}) + \sum_{m=0}^{m_{max}} \sum_{n=0}^{n_{max}} x_k c (\varphi_i - \bar{\varphi})^n (\lambda_i - \bar{\lambda})^m \cos^m \varphi_i + v_i \quad (6)$$

where  $a, b, c, d, e$  and  $x_k$  are the model parameters,  $k$  is equal to  $(3m + n)$ ,  $\bar{g}$  is the mean value of the measured gravity,  $\varphi$  and  $\lambda$  are the geodetic latitude and longitude of each BM and  $\bar{\varphi}$  and  $\bar{\lambda}$  are the mean geodetic latitude and longitude respectively. It should be noticed that for Eq. (6),  $x_0$  is same as the bias (translation) found in Eqs. (2) to (5), i.e., parameter  $a$ . It is to be noted that models D, E and F are based on A, B and C and are proposed in the frame of the present study.

The validation of the models was carried out similarly to Fotopoulos (2003) but for the mathematical model of gravity differences (see Eq. 1). Therefore, all models were assessed by examining the statistics of the differences before and after fitting the differences to the models, estimating the goodness of fit and evaluating the significance of the model parameters. Moreover, data snooping was used for determining points that did not adjust well to the determined parametric models. The goodness of fit is given by the measure of fit  $R^2$  or the adjusted measure of fit  $R_a^2$  (Sen and Srivastava 1990, Eq. 2.37). The testing of significance of the model parameters was carried out following the backward elimination approach (see Fotopoulos 2003, section 3.5.4).

**Table 4** Parametric modeling statistics using a VCE-based weighting [mGal]

	Mean	Stdev	Min	Max	$R_a^2$
Before	-15.00	0.15	-15.34	-14.82	-
Model A	0.00	0.07	-0.18	0.14	0.83
Model B	0.00	0.07	-0.19	0.14	0.84
Model C	0.00	0.10	-0.22	0.10	0.62
Model D	0.00	0.06	-0.10	0.13	0.88
Model E	0.00	0.06	-0.08	0.14	0.89
Model F	0.00	0.04	-0.13	0.06	0.96

An important factor in the computation process is the weighting of the input differences. Three different scenarios were examined: (A) All observations have the same weight and the weight matrix was selected to be equal to the identity matrix. (B) By applying the law of error propagation, the error of each difference  $\sigma_g$  is obtained by:

$$\sigma_g^2 = \sigma_{g_{obs}}^2 + \sigma_{g_{official}}^2 \quad (7)$$

where  $\sigma_{g_{obs}}$  is the measurement error. The  $\sigma_{g_{official}}$  is the official error for each BM which is unknown and was set equal to 0.02 mGal by taking into account the published values in the Bureau Gravimetric International (BGI) database. Therefore, the weight of each observation is equal to  $1/\sigma_g^2$ . (C) Variance Component Estimation (VCE) was used for determining the weight matrix similarly to Kotsakis and Sideris (1999) but for the gravity model of Eq. (1).

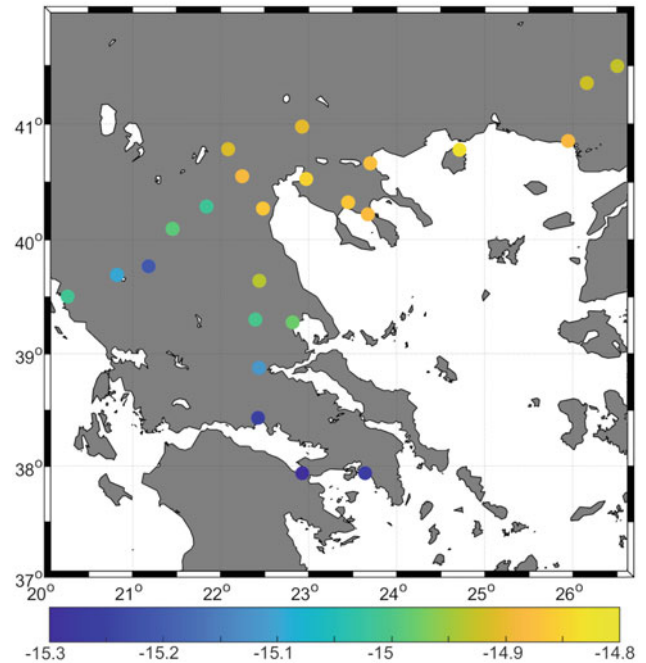
Out of the three aforementioned weighting scenarios the most stable and robust solutions were obtained by the third one. The statistical results before and after fit for the six models determined using the VCE-based weighting are provided in Table 4. It should be noticed that all model parameters passed the parameter significance test. From Table 4, it may be deduced that model F provides the best results. The determined model parameters for models E and F are provided in Table 5 with  $\bar{g}$ ,  $\bar{\varphi}$  and  $\bar{\lambda}$  equal to 980142.596 mGal,  $39^\circ.98184489$  and  $22^\circ.97894569$  respectively. In Fig. 3 are presented the corrections applied by Model F where a southwest (SW) to northeast (NE) trend is revealed. Regarding the parameters of model F, it should be noticed that the standard deviation of parameters  $x_2$  and  $x_3$  is larger than their value, i.e. these parameters have a high estimation uncertainty. This does not occur for the rest of the models. Given though the results of Table 4, it is suggested to use model E or F.

## 4 Discussion

Apart from the conclusions drawn from the statistical results presented previously, a few additional remarks should be made regarding the Hellenic gravity network design and its BMs. The gravity network was designed as an independent

**Table 5** Parameters of model E and F using a VCE-based weighting scheme [mGal]

Parameter	Value	Stdev	Parameter	Value	Stdev
<i>model E</i>					
$b$	0.0007	0.0002	$x_0$	-14.9925	0.0153
$x_1$	-0.0339	0.0180	$x_2$	0.0893	0.0188
$x_3$	-0.0213	0.0144			
<i>model F</i>					
$b$	0.0010	0.0002	$x_0$	-14.9429	0.0479
$x_1$	-0.0658	0.0193	$x_2$	-0.0131	0.0255
$x_3$	0.0054	0.0484	$x_4$	0.0576	0.0160
$x_5$	0.0283	0.0183	$x_6$	-0.0544	0.0420
$x_7$	0.0752	0.0278	$x_8$	-0.0488	0.0278

**Fig. 3** Corrections from parametric model F at the gravity network BMs [mGal]

network, i.e., a network with its own BMs that has no connection to the vertical or trigonometric network apart from some few BMs that are common. At the time the network was established in the 1960s, Global Navigation Satellite Systems (GNSS) technology was unknown and measurements were difficult to perform. Moreover, some BMs are located next to buildings while other at airports, where the selection was mostly based on keeping the BM safe, while the size of the BM was sometimes not adequate for placing an absolute gravimeter. Additionally, although some BMs have a concrete body with a steal plate on top, others have nothing specific on the ground and the instrument must be placed according to photographs or approximately close to a point described in the BM identification documents. Last, a problem that was also met during the measurements, although some BMs have a concrete body that could be

considered a stable basis, this did not occur for a BM that was excluded from the computations. As the measurement noise was very high, it was concluded that the concrete body does not guarantee that the area is noise-free. Therefore, it is suggested that measurements should be made before establishing a BM, while a geotechnical soil study could improve the site selection.

Considering the present, where the main aim is the establishment of a modern geoid-based vertical datum, and taking into account the experience accumulated from the measurements, the authors propose that the next generation of gravity BMs should be common with the ones of the vertical datum and should be in a clear-view area where GNSS measurements can be easily obtained. This would improve not only the evaluation/computation of geoid models but also the monitoring for changes over time.

Different GGMs were used to produce a reduced gravity and a residual gravity field, after removing the RTM effect, from the measured gravity at the BMs. The reduction statistics showed that older models still provide good reduction results and should be included in any investigation carried out for producing a residual field for geoid modeling.

Last, some remarks are made regarding the clear SW to NE trend that exists in the Hellenic gravity network and was revealed by the parametric modeling. First, this trend indicates the necessity to correct all previous available gravity values. The mixed linear/first and second degree polynomial models performed better than the other models and therefore their parameters are suggested to be used for correcting the old Potsdam values. A similar SW to NE trend though was found also in a previous study by Andritsanos et al. (2017), where they compared GNSS/leveling derived geoid heights at trigonometric BMs versus GOCE-based GGMs derived geoid heights. It is known that corrections have been made to the heights of the GNSS/leveling BMs for the Earth's gravity field but these would not justify the observed trend. Therefore, further investigations are required to connect their results with the present study.

**Acknowledgement** This work, part of the ModernGravNet research project, was supported by the Hellenic Foundation for Research and Innovation (H.F.R.I.) under the “1st Call for H.F.R.I. Research Projects to support Faculty Members & Researchers and the Procurement of High-and the procurement of high-cost research equipment grant” (Project Number: 1550). The authors thank also the Hellenic Military Geographical Service for kindly providing the official network gravity values.

## References

- Andritsanos VD, Grigoriadis VN, Natsiopoulos DA, Vergos GS, Gruber T, Fecher T (2017) GOCE variance and covariance contribution to height system unification. In: International association of geodesy symposia. Springer, Berlin. [https://doi.org/10.1007/1345\\_2017\\_12](https://doi.org/10.1007/1345_2017_12)
- Carrère L, Lyard F, Cancet M, Guillot A, Roblou L (2012) FES2012: a new global tidal model taking advantage of nearly 20 years of altimetry. In: Proceedings of meeting “20 Years of Altimetry”, Venice 2012
- Forsberg R (1984) A study of terrain reductions, density anomalies and geophysical inversion methods in gravity field modelling, Technical Report, OSU Report No 355. Department of Geodetic Science, The Ohio State University, Ohio, USA
- Förste C et al (2014) EIGEN-6C4 The latest combined global gravity field model including GOCE data up to degree and order 2190 of GFZ Potsdam and GRGS Toulouse. Presented at the 5th GOCE User Workshop, Paris, France, 25–28 November
- Fotopoulos G (2003) An analysis on the optimal combination of geoid, orthometric and ellipsoidal height data. UCGE Report no 20185. Department of Geomatics Engineering, University of Calgary, Alberta, Canada. <https://doi.org/10.11575/PRISM/10883>
- Grigoriadis VN (2009) Geodetic and geophysical approach of the Earth's gravity field and applications in the Hellenic area. PhD Dissertation, Department of Geodesy & Surveying, School of Rural and Surveying Engineering, Aristotle University of Thessaloniki. (In Greek) <https://doi.org/10.12681/eadd/30653>
- Heiskanen WA, Moritz H (1967) Physical geodesy. WH Freeman and Co, San Francisco
- Hirt C, Kuhn M, Claessens S, Pail R, Seitz K, Gruber T (2014) Study of the Earth's short scale gravity field using the ERTM2160 gravity model. *Comput Geosci* 73:71–80. <https://doi.org/10.1016/j.cageo.2014.09.001>
- Kotsakis C, Sideris MG (1999) On the adjustment of combined GPS/levelling/geoid networks. *J Geodesy* 73:412–421. <https://doi.org/10.1007/s001900050261>
- Kryniski J, Olszak T, Barlik M, Dykowski P (2013) New gravity control in Poland – needs, the concept and the design. *Geodesy Cartogr* 62(1):3–21. <https://doi.org/10.2478/geocart-2013-0001>
- Melissinos P (2021) Private communication.
- Pavlis NK, Holmes SA, Kenyon SC, Factor JK (2012) The development and evaluation of the Earth Gravitational Model 2008 (EGM2008). *J Geophys Res Solid Earth* 117(B4). <https://doi.org/10.1029/2011JB008916>
- Rexer M, Hirt C, Claessens S, Tenzer R (2016) Layer-based modelling of the Earth's gravitational potential up to 10-km Scale in spherical harmonics in spherical and ellipsoidal approximation. *Surv Geophys* 37:1035–1074. <https://doi.org/10.1007/s10712-016-9382-2>
- Sen A, Srivastava M (1990) Regression analysis. Springer, New York. <https://doi.org/10.1007/978-1-4612-4470-7>
- Spiridonov EA, Yushkin VD, Vinogradova O. Yu., Afanasyeva LV (2018) The Atlantida 3.1\_2014 program for earth tide prediction: new version. *Seismic Instrum*, 54(6): 650–661. doi:<https://doi.org/10.3103/S0747923918060129>
- Torge W (1989) Gravimetry. de Gruyter, Berlin
- Wahr JM (1985) Deformation induced by polar motion. *J Geophys Res Solid Earth* 90(B11):9363–9368. <https://doi.org/10.1029/JB090iB11p09363>



- Wziontek H, Bonvalot S, Falk R, Gabalda G, Mäkinen J, Pálinkáš V, Rülke A, Vitushkin L (2021) Status of the international gravity reference system and frame. *J Geodesy*. <https://doi.org/10.1007/s00190-020-01438-9>
- Zingerle P, Pail R, Gruber T, Oikonomidou X (2020) The combined global gravity field model XGM2019e. *J Geodesy* 94:64. <https://doi.org/10.1007/s00190-020-01398-0>

**Open Access** This chapter is licensed under the terms of the Creative Commons Attribution 4.0 International License (<http://creativecommons.org/licenses/by/4.0/>), which permits use, sharing, adaptation, distribution and reproduction in any medium or format, as long as you give appropriate credit to the original author(s) and the source, provide a link to the Creative Commons license and indicate if changes were made.

The images or other third party material in this chapter are included in the chapter's Creative Commons license, unless indicated otherwise in a credit line to the material. If material is not included in the chapter's Creative Commons license and your intended use is not permitted by statutory regulation or exceeds the permitted use, you will need to obtain permission directly from the copyright holder.



---

**Part III**

**Global Gravity Field Modeling**



# Combined Gravity Solution from SLR and GRACE/GRACE-FO

Zhigui Kang, John Ries, Srinivas Bettadpur, Himanshu Save, and Byron Tapley

## Abstract

The recovery of Earth's time variable gravity field from satellite data relied heavily on Satellite Laser Ranging (SLR) before the recent GRACE and GRACE Follow-On satellite gravity missions. Currently, the monthly gravity solutions from GRACE/GRACE-FO provide important global information about the temporal variations of gravity field. However, there are a few low-degree coefficients derived from GRACE/GRACE-FO that are not well determined, because of the satellite gravity mission configuration and issues with the accelerometer data. These low-degree coefficients can be determined reasonably well using SLR data from the dedicated SLR satellite configuration and can be used to replace the less well-determined values from GRACE/GRACE-FO. A more rigorous and consistent approach is to directly combine SLR and GRACE/GRACE-FO gravity solutions in a simultaneous solution. This paper presents a combination strategy for gravity field recovery from combined SLR and GRACE/GRACE-FO mission data. To correctly account for all correlations, the combination is performed at the information (normal) equation level. The coefficients  $C_{20}$  and  $C_{30}$  are determined mainly from SLR by renaming  $C_{20}$  and  $C_{30}$  parameters in GRACE/GRACE-FO information equations. The results show that the combined products are improved in comparison with the nominal GRACE/GRACE-FO gravity solutions. The gravity field products are evaluated by comparing different gravity solutions through coefficient-wise comparison, equivalent water height variations and mass changes over selected areas.

## Keywords

GRACE · GRACE-FO · Satellite gravimetry · SLR

## 1 Introduction

The temporal variations of the Earth's gravity field provide important information related to the mass transport within the complete Earth system. Before satellite gravity missions like the Gravity Recovery and Climate Experiment (GRACE) and GRACE Follow-On (FO), studying the low-degree gravity field variations relied heavily on Satellite Laser Ranging (SLR) (Cheng and Tapley 1999;

Bloßfeld et al. 2015; Sośnica et al. 2015). GRACE/GRACE-FO are dedicated satellite gravity missions for observing temporal variations of the gravity field with higher spatial resolution than that possible with just SLR ranging (Tapley et al. 2004; Flechtner et al. 2015; Landerer et al. 2019).

GRACE is a joint project between the National Aeronautics and Space Administration (NASA) and the Deutsches Zentrum für Luft- und Raumfahrt (DLR). The primary objective of the GRACE mission is to map, with unprecedented accuracy, the long- to medium-wavelength spherical harmonic coefficients of the Earth's gravity field and to observe its temporal variations. The twin GRACE satellites were launched on March 17, 2002 into near-polar orbits with

Z. Kang (✉) · J. Ries · S. Bettadpur · H. Save · B. Tapley  
Center for Space Research, Austin, TX, USA  
e-mail: kang@csr.utexas.edu

an initial altitude of approximately 500 km. The mission ended in October 2017. GRACE-FO is the successor of the GRACE mission with the same objective. The primary object is to continue the 15.5 year GRACE record. The twin GRACE-FO satellites were launched on May 22, 2018 into near-polar and near 500 km altitude orbits. In addition to GRACE-comparable scientific instruments, GRACE-FO also carries a Laser Ranging Interferometer (LRI) for making high accuracy relative motion measurements, as a technology demonstration experiment in support of future gravity mapping missions.

SLR contributes most to the determination of low-degree gravity field. Due to an inhomogeneous and sparse SLR network, the SLR-derived middle and high-degree coefficients of the gravity field are not well determined. Therefore, the SLR gravity solutions can be only used for observing the temporal variations of lowest degree and order terms.

Currently, GRACE/GRACE-FO-derived monthly gravity solutions provide important information about the temporal variations of the Earth's gravity field. However, there are a few low-degree coefficients that are not well determined in the GRACE and GRACE-FO monthly solutions due to the satellite gravity mission configuration and issues with the accelerometer data. These low-degree coefficients, on the other hand, can be reasonably well determined from SLR data. Therefore, for the released gravity field solutions, the coefficient  $C_{20}$  from the GRACE monthly gravity solutions as well as coefficients  $C_{20}$  and  $C_{30}$  from the GRACE-FO monthly gravity solutions are replaced by SLR-based estimates. In addition, the GRACE/GRACE-FO missions are not implemented with repeating ground tracks; the altitude decays throughout the mission due to the effects of atmospheric drag. The change in altitude leads to periods during which the monthly gravity solutions are determined in the presence of deep resonances. The resonance effects during these periods lead to a degraded gravity solution quality when compared to the non-resonant periods.

Based on the background described above, we study the combined gravity solution from SLR and GRACE/GRACE-FO. The main purpose of this study is to demonstrate that a solution can be obtained that does not require any coefficient replacements. The study also considers whether the combined solutions are better than the solutions with  $C_{20}$  and  $C_{30}$  replaced. This paper presents combination strategies. The coefficients  $C_{20}$  and  $C_{30}$  are determined mainly from SLR by renaming  $C_{20}$  and  $C_{30}$  parameters in GRACE/GRACE-FO information equations. The main challenges are how to weight the different data types and at what level to make the combination.

## 2 GRACE and GRACE-FO Gravity Recovery

For GRACE and GRACE-FO gravity recovery, we use the dynamic gravity recovery method that is based on the dynamic orbit determination. The dynamic method is the so-called variational method (Reigber 1989; Yuan 1991), which uses a conventional least squares adjustment. For GRACE and GRACE-FO, a month of data is typically processed to produce a monthly gravity field (Tapley et al. 2005; Kang et al. 2020).

The GRACE/GRACE-FO gravity recovery is performed in several steps. The edited GPS and KBR observations are created in the first step during GRACE/GRACE-FO precise orbit determination (POD). Then, the reference orbits are generated by using edited GPS data and accelerometer measurements, which replace the non-gravitational force models. However, the accelerometer data for GRACE-D (one of the GRACE-FO satellites) are the transplanted accelerometer data products generated by JPL (McCullough et al. 2019) to account for a failure of the GRACE-D accelerometer. With the improved reference orbit, the partial derivatives for all the estimated parameters are computed for each arc and each observation type (GPS and KBR). In the final step, the gravity field coefficients, along with other dynamical, measurement and orbital parameters, are estimated in a combination of all available information for the month using an optimal weighting method (Yuan 1991; Kang et al. 2020) for each arc and KBR observation type. By this process, we obtain not only the monthly gravity solution from GRACE/GRACE-FO only but also the degree and order 60 information equations for later combination with SLR.

## 3 SLR Gravity Recovery

For SLR gravity recovery, we use the same method as that used for the GRACE/GRACE-FO data. The SLR gravity solutions and information equations presented here are derived from a combination of seven SLR satellites (LAGEOS-1/2, Ajisai, Starlette, Stella, LARES and Larets). Prior to the availability of LARES, the  $C_{30}$  and  $C_{50}$  coefficients could not be accurately recovered, but when the LARES data is included, a complete  $5 \times 5$  plus  $C_{6,1}$  and  $S_{6,1}$  are reasonably well determined from the seven SLR satellites (Bloßfeld et al. 2015; Sośnica et al. 2015). The processing arc length for the higher altitude satellites (LAGEOS-1/2) is 6-days; 3-days is used for the remaining lower altitude satellites. These relatively short arc lengths are required to keep the non-conservative force model errors from building up too much.

The SLR gravity recovery is performed in several steps. The edited SLR observations are created in the first step during SLR POD to edit out observation outliers. Then, the reference orbits are generated using the edited SLR data. Next, the partial derivatives for all the estimated parameters (SLR satellite initial state, drag coefficients, empirical along-track accelerations and gravity field coefficients) for each arc of each satellite are computed. In the next step, the sub-monthly information is combined into monthly information equations for each satellite, which are then combined using optimal weighting into the information equations for SLR. The optimal weighting occurs at the satellite level rather than the original arc level. This provides a more reliable estimate of the contribution from each satellite to the SLR combination. From this, we determine the monthly SLR gravity solution up to degree and order 5 plus  $C_{61}$  and  $S_{61}$  as well as the  $60 \times 60$  information equations required for the combination. In this final combination, the average weight factors for LAGEOS-1/2, LARES, Starlette, Stella, Ajisai and Larets were 15, 15, 16, 8, 10, 5, and 2, respectively. The high weight factor for LARES indicates its importance for gravity recovery, while the Larets contribution is relatively low. The SLR data for all satellites had an *a priori* sigma of 4 cm; consequently the *a posteriori* sigmas for LAGEOS-1/2 and LARES can be deduced to be approximately 1 cm, and 1.3, 1.4, 1.8 and 2.8 cm for Stella, Starlette, Ajisai and Larets, respectively.

#### 4 Combined Gravity Solution

The approach used here was the optimally weighted combination of the information equations for SLR and GRACE/GRACE-FO. The GRACE/GRACE-FO-only solution is available to compare to the combination to evaluate the contribution of SLR. After the  $60 \times 60$  information equations are generated for each, solving for the following equation obtains the combined solution:

$$(F_{GRA}N_{GRA} + F_{SLR}N_{SLR})X = F_{GRA}B_{GRA} + F_{SLR}B_{SLR} \quad (1)$$

where  $F_{GRA}$  and  $F_{SLR}$  are weight factors for GRACE/GRACE-FO and SLR,  $N_{GRA}$  and  $N_{SLR}$  are the global information equation matrices of GRACE/GRACE-FO and SLR,  $X$  is the vector of unknown gravity field coefficients, and  $B_{GRA}$  and  $B_{SLR}$  are the right-hand side vectors of the information equation. The reduced global information equations are generated by pre-eliminating all non-gravity field parameters.

#### 5 Test Case and Combination Strategies

The data span is from 2013 to 2021, which includes both nominal and non-nominal operation periods for GRACE/GRACE-FO as well as the availability of the LARES SLR data. A reliable  $C_{30}$  coefficient can be well determined from a combination of LARES and other SLR satellite data.

There are four cases which can be used for comparisons and discussions: (1) GRACE/GRACE-FO only; (2) SLR only; (3) Combined solutions; (4) GRACE/GRACE-FO with SLR  $C_{20}$  and  $C_{30}$  replacements.

One important impact on gravity field recovery is the density and uniformity of the data coverage of the Earth. During nominal mission operations periods, GRACE/GRACE-FO KBR data generally have good coverage. For SLR, data coverage is not uniform, and there are many gaps due to an inhomogeneous and sparse SLR tracking network. SLR data can be only used for determining a complete low degree/order gravity field because of the data coverage limitation. However, SLR is also sensitive to some middle and high degree coefficients, primarily terms at or near the resonant orders. The determination of these terms is likely improved in the combined solutions.

One of the issues for the combined solutions is to determine what level of observation information is to be used. We have decided the best approach is to perform the combined solution at the information equation level (Haberkorn et al. 2015). This allows for a clear evaluation of the contribution of SLR to the combination solution. Another issue is related to the relative weights of the GRACE/GRACE-FO and SLR information equations. For GRACE/GRACE-FO, the information equations have been carefully weighted by down-weighting the GPS data and optimally weighting the KBR data (Kang et al. 2020). For SLR, optimal weighting for each SLR satellite for each month was applied.

The  $C_{20}$  coefficient from GRACE and GRACE-FO and  $C_{30}$  coefficient from GRACE-FO are not accurately determined. To ensure the estimates for  $C_{20}$  and  $C_{30}$  derived from SLR are not adversely affected, the variable names for  $C_{20}$  and  $C_{30}$  from GRACE/GRACE-FO information equations are renamed. In this way, the negative effects of  $C_{20}$  and  $C_{30}$  from GRACE/GRACE-FO are eliminated, and the  $C_{20}$  and  $C_{30}$  coefficients are determined from the SLR data alone.

#### 6 Results and Discussion

The monthly combined solutions were determined using the approach described above. The SLR and GRACE/GRACE-FO contributions were individually combined into their

**Fig. 1** Weight factors for combined monthly gravity solutions (GRACE/GRACE-FO: red; SLR: green)

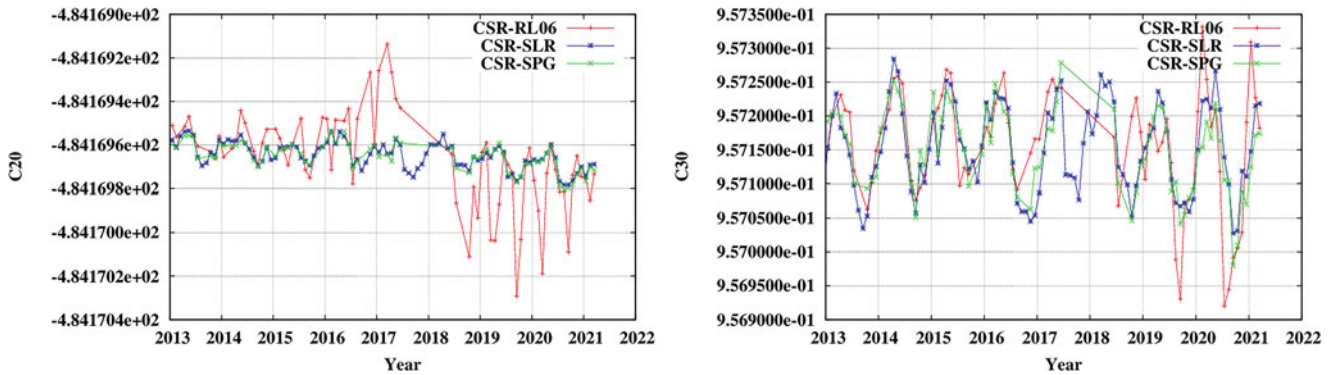
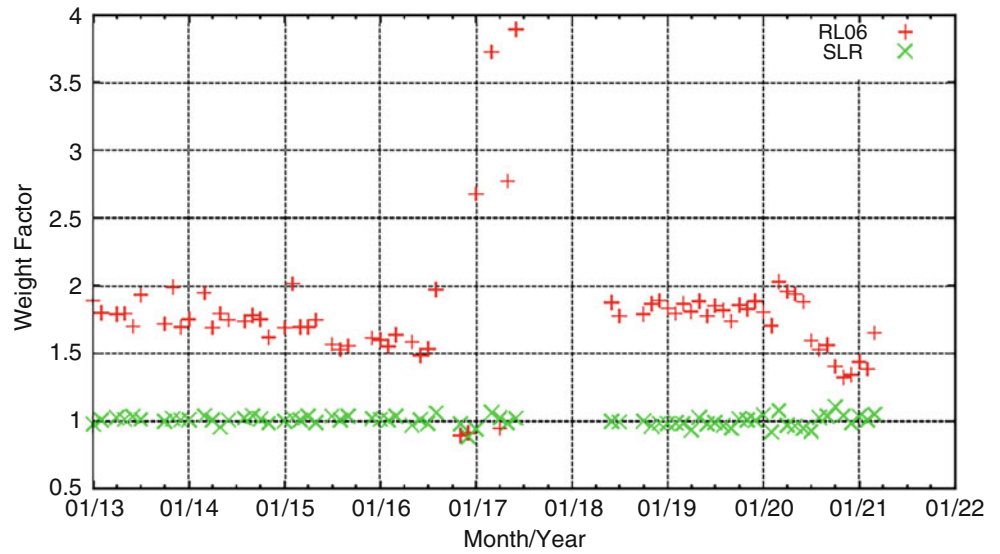


**Fig. 2**  $C_{20}$  and  $C_{30}$  coefficient time series from GRACE/GRACE-FO RL06 (red), SLR (blue) and combined solutions SPG (green)

respective information equations using optimal weighting. The apriori weights for SLR are determined based on the RMS of SLR solution post-fits (1–3 cm). The apriori GPS weight is derived from the fixed RMS (2.12 cm). The apriori KBR weights are determined based on the RMS of the post-fits (about  $0.22 \mu\text{m/s}$  for GRACE and  $0.08 \mu\text{m/s}$  for GRACE-FO). Since the original observations were optimally weighted in their respective accumulation, their weight factors should not significantly change at the combination level (Fig. 1). The SLR weight factors stay around 1 and the GRACE/GRACE-FO weight factors rose slightly to the range of 1.5–2, with a few higher weight factors during late 2016 and early 2017 (when the accelerometers were particularly unreliable). The factors for GRACE/GRACE-FO not being close to one are probably due to the down-weighted GPS data in the GRACE/GRACE-FO solutions and/or to the larger contribution from GRACE/GRACE-FO for the combined solution in comparison to SLR, particularly for the middle and high-degree terms. The final weights for the combined solutions are computed based on the SLR and GRACE/GRACE-FO apriori weights times estimated

SLR and GRACE/GRACE-FO scale factors, respectively. The average RMS's for final weights are 1–3 cm for SLR; 1.58 cm for GPS;  $0.16 \mu\text{m/s}$  for GRACE KBR and  $0.06 \mu\text{m/s}$  for GRACE-FO KBR, respectively.

One of the solution requirements is the  $C_{20}$  and  $C_{30}$  coefficients from combined solutions should be not significantly different from the SLR-derived values. Figure 2 shows the comparisons of  $C_{20}$  and  $C_{30}$  coefficient time series for GRACE/GRACE-FO RL06 (red), SLR (blue) and combined solutions SPG (SLR Plus GRACE/GRACE-FO) (green). The GRACE/GRACE-FO-derived  $C_{20}$  and GRACE-FO-derived  $C_{30}$  estimates have periods with unrealistic variations. The differences between the SLR and SPG solutions for  $C_{20}$  and  $C_{30}$  are not particularly significant.

To study the effects of the solution approach on the other terms in a  $60 \times 60$  combined solution for two mission modes, Fig. 3 shows the spherical harmonic coefficient differences between GRACE RL06 and the combined solution SPG for a nominal operation month (May 2013) and for a deep resonance period month (February 2015). For the nominal month, there are a few coefficient differences, particularly

**Fig. 3** Spherical harmonic coefficient differences between GRACE RL06 and combined solution SPG (left) for a nominal operation month (May 2013) and for a deep resonance month (February 2015) (right)

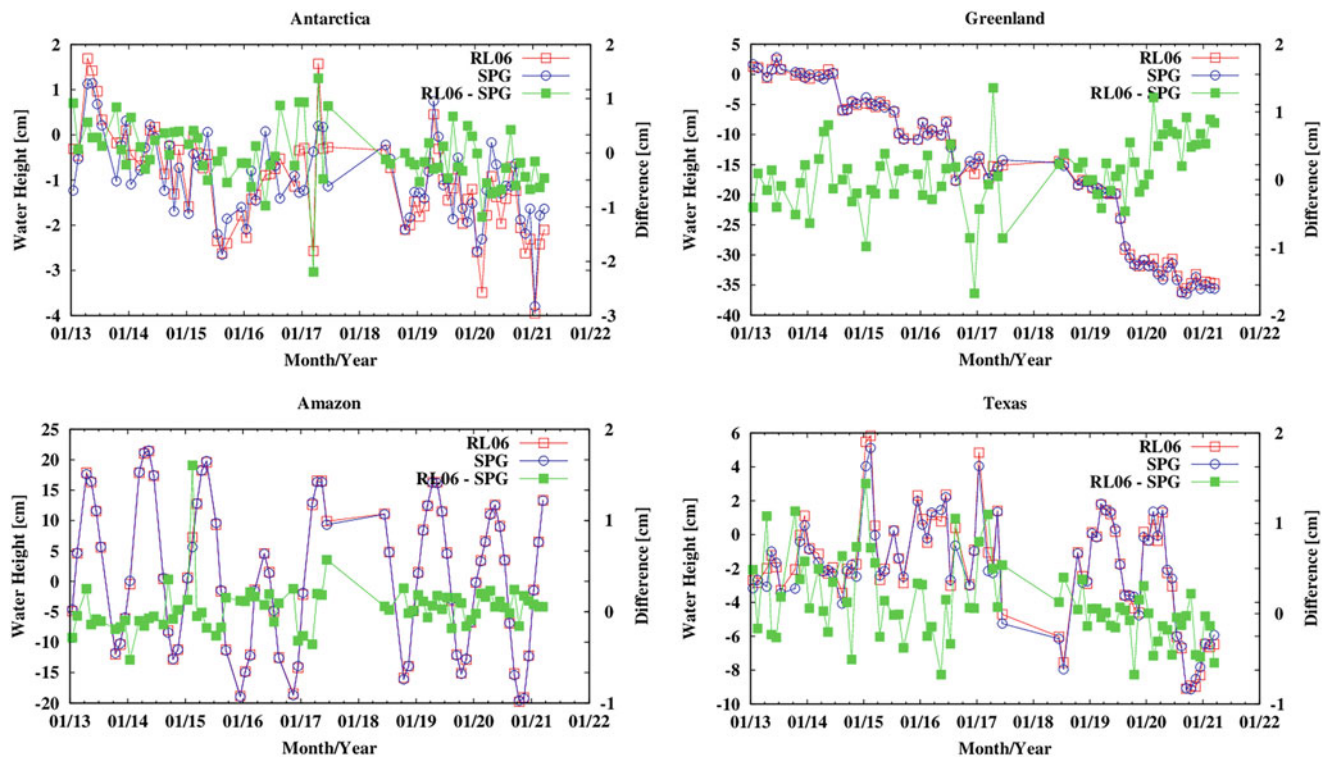
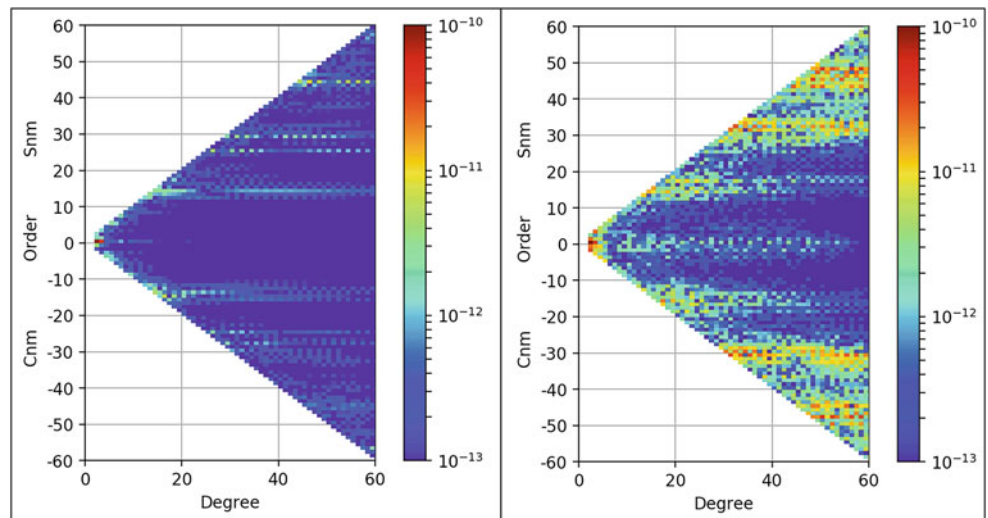


**Fig. 4** Equivalent water height (EWH) variations for Antarctica (top left), Greenland (top right), Amazon (bottom left) and Texas (bottom right) for GRACE/GRACE-FO RL06 (red) and combined solutions

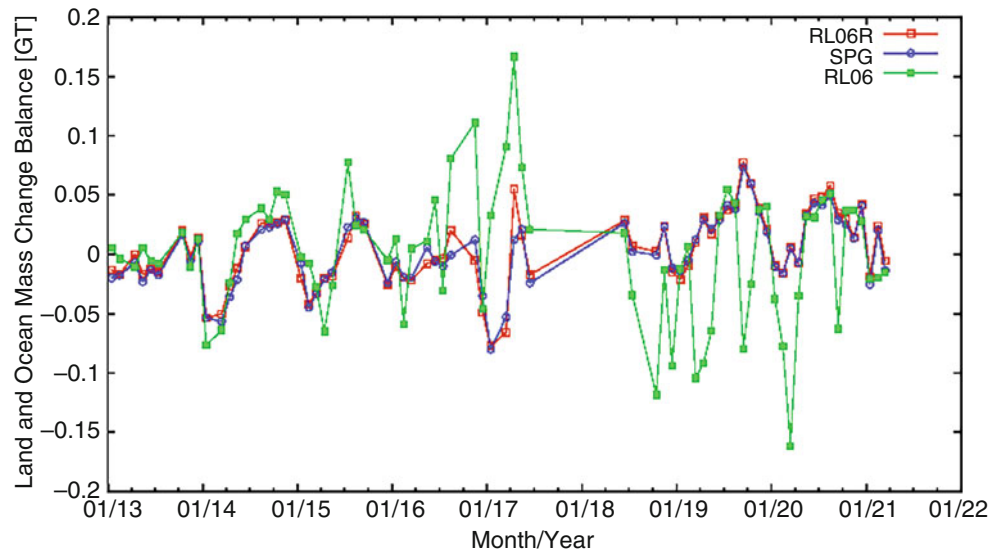
SPG (blue), EWH difference between GRACE/GRACE-FO and combined solutions (green). Note that the full signal scale is shown on the left with the difference scale on the right

at resonance orders (15, 25, 28 ...). However, for a deep resonance month, there are a number of large coefficient differences, which demonstrates the impact of SLR on the combined solutions.

To validate the combined solutions, the equivalent water height (EWH) variations for selected areas are computed. Figure 4 shows the EWH variations for Antarctica, Greenland, Amazon and Texas areas for GRACE/GRACE-FO RL06 (red), combined solutions SPG (blue) and

differences between RL06 and SPG (green). The EWH is smoothed by a Gaussian filter with 350 km radius (Swenson and Wahr 2002). Generally, there are no significant differences considering the current accuracy limitation of about 1 cm water height. However, the differences for some months (GRACE/GRACE-FO non-nominal months i.e., deep resonance and/or single accelerometer) are more than 1 cm. The combined solutions show reasonable variation patterns.

**Fig. 5** Difference between land and ocean mass change for GRACE/GRACE-FO RL06R (red) with  $C_{20}$  and  $C_{30}$  replacement, combined solutions SPG (blue) and GRACE/GRACE-FO RL06 (green) without  $C_{20}$  and  $C_{30}$  replacement



By comparing different gravity solutions through coefficient-wise comparison, and EWH variations, we compare the relative differences for the different solutions and evaluate the solutions based on the resulting variation patterns. To absolutely validate the gravity solutions, differences between land and ocean mass change for different gravity solutions (Fig. 5) are compared. If the gravity solutions were perfect, the difference between land and ocean mass change would be zero. To get the results, the monthly mass changes for land and ocean are first computed. Then, the changes are differenced. The differences for GRACE/GRACE-FO RL06 (green) without  $C_{20}$  and  $C_{30}$  replacements are clearly sometimes far away from zero. Therefore, the replacements are necessary. Generally, there are no significant differences between the GRACE/GRACE-FO RL06R (red) with  $C_{20}$  and  $C_{30}$  replacements and the combined solutions SPG (blue) under the current solution accuracy. However, the mass change balances around 2017 show that the combined solutions are likely better than GRACE/GRACE-FO gravity solutions. This indicates that the SLR data are having some influence on other coefficients that is more beneficial when the GRACE data are affected by issues with the accelerometers.

## 7 Conclusions

The combined gravity solutions from GRACE/GRACE-FO and SLR were performed based on our approach and combination strategies. The following conclusions can be drawn.

Combined gravity solutions from GRACE/GRACE-FO and SLR can be directly used by GRACE/GRACE-FO users without any coefficient replacements. There are no significant differences in the  $C_{20}$  and  $C_{30}$  coefficients for the

combined and SLR gravity solutions. The SLR data have a positive impact on  $C_{20}$  and  $C_{30}$  coefficients but also provides improved estimates for the other coefficients, particularly for the resonance coefficients. The SLR data has more impact on the combined solutions when the GRACE data has problems (such as deep resonance in Jan/Feb 2015 and single accelerometer in Nov/Dec 2016 and 2017). These results show that the combined products are improved in comparison with the nominal GRACE/GRACE-FO gravity solutions and are evaluated by the comparison of the coefficients, equivalent water height changes as well as land and ocean mass change balance.

**Acknowledgements** The authors would like to thank the International Global Navigation Satellite System (GNSS) Service (IGS) for providing the GPS ground station data and GPS satellite orbit products and the International Laser Range Service (ILRS) for the SLR data. The Texas Advanced Computing Center (TACC) at the University of Texas at Austin provided high performance computing resources. This research was supported by JPL contract 1604489.

## References

- Bloßfeld M, Müller H, Gerstl M, Štefka V, Bouman J, Göttl F, Horwath M (2015) Second-degree Stokes coefficients from multi-satellite SLR. *J Geod* 89(9):857–871
- Cheng M, Tapley B (1999) Seasonal variations in low degree zonal harmonics of the Earth's gravity field from satellite laser ranging observations. *J Geophys Res* 104:2667–2681
- Flechtner F, Morton P, Watkins M, Webb F (2015) Status of the GRACE following-on mission. In: Proceedings of the international association of geodesy symposia gravity, geoid and height system (2012, Venice), IAGS-D-12-00141
- Haberkorn C, Blossfeld M, Bouman J, Fuchs M, Schmidt M (2015) Towards a consistent estimation of the Earth's gravity field by combining normal equation matrices from GRACE and SLR. In: IAG 150 years, vol 143, pp 375–381



- Kang Z, Bettadpur S, Nagel P, Save H, Poole S, Pie N (2020) GRACE-FO precise orbit determination and gravity recovery. *J Geod* 94:85. <https://doi.org/10.1007/s00190-020-01414-3>
- Landerer F, Flechtner F, Webb F, Watkins M, Save H, Bettadpur S, Gaston R (2019) GRACE following-on: mission status and first mass change observations. IUGG, 8–18 July 2019, Montreal
- McCullough C, Harvey N, Save H (2019) Description of calibrated GRACE-FO accelerometer data products. JPL D-103863. [https://podaac-tools.jpl.nasa.gov/drive/files/allData/gracefo/docs/GFO\\_ACT.JPL-D-103863.20190520.pdf](https://podaac-tools.jpl.nasa.gov/drive/files/allData/gracefo/docs/GFO_ACT.JPL-D-103863.20190520.pdf)
- Reigber C (1989) In: Theory of satellite geodesy and gravity field determination, Lecture Notes in Earth Sciences, vol 25. Springer, Berlin. <https://doi.org/10.1007/BFb0010546>
- Sośnica K, Jäggi A, Meyer U, Thaller D, Beutler G, Arnold D, Dach R (2015) Time variable Earth's gravity field from SLR satellites. *J Geod* 89(10):945–960
- Swenson S, Wahr J (2002) Methods for interring regional surface-mass anomalies from Gravity Recovery and Climate Experiment (GRACE) measurements of time-variable gravity. *J Geophys Res* 107:2193
- Tapley B, Bettadpur S, Watkins M, Reigber C (2004) The gravity recovery and climate experiment: mission overview and early results. *Geophys Res Lett* 31(9):L09607. <https://doi.org/10.1029/2004GL019920>
- Tapley B, Ries J, Bettadpur S, Chambers D, Cheng M, Condi F, Gunter B, Kang Z, Nagel P, Pastor R, Pekker T, Poole S, Wang F (2005) GGM02 – an improved Earth gravity field model from GRACE. *J Geod* 79:467–478
- Yuan D (1991) The determination and error assessment of the Earth's gravity field model. Center for Space Research Report CSR-91-01, The University of Texas at Austin

**Open Access** This chapter is licensed under the terms of the Creative Commons Attribution 4.0 International License (<http://creativecommons.org/licenses/by/4.0/>), which permits use, sharing, adaptation, distribution and reproduction in any medium or format, as long as you give appropriate credit to the original author(s) and the source, provide a link to the Creative Commons license and indicate if changes were made.

The images or other third party material in this chapter are included in the chapter's Creative Commons license, unless indicated otherwise in a credit line to the material. If material is not included in the chapter's Creative Commons license and your intended use is not permitted by statutory regulation or exceeds the permitted use, you will need to obtain permission directly from the copyright holder.





# Contribution of LARES SLR Data to Co-estimated Earth Geopotential Coefficients

Linda Geisser, Ulrich Meyer, Daniel Arnold, and Adrian Jäggi

## Abstract

The Satellite Laser Ranging (SLR) processing at the Astronomical Institute of the University of Bern (AIUB) is currently extended from the geodetic satellites LAGEOS-1/2 and Etalon-1/2 to also include LARES. The orbits are determined in 7-day arcs together with station coordinates, low-degree spherical harmonic (SH) coefficients of the Earth's gravity field, Earth Rotation Parameters (ERP), geocenter variations and range biases for selected stations. Due to the lower orbital altitude, LARES experiences a more variable environment such that the orbit parametrization has to be adapted. In this paper, we present SLR solutions for 5 years with different orbit parametrizations for LARES, i.e., LARES 7-day arcs are either determined from one set of orbit parameters and stochastic pulses at fixed time-intervals, or by stacking of seven daily arcs with continuity conditions at the day boundaries, so-called long-arcs. Including LARES does slightly improve the ERP and does not degrade the quality of the estimated SH coefficients and station coordinates. Additionally, it allows co-estimating the SH coefficient  $C_{30}$  and further low-degree SH coefficients.

## Keywords

Earth rotation parameters · Gravity field coefficients · LAGEOS · LARES · Long-arc computation · SLR

## 1 Introduction

The Astronomical Institute of the University of Bern (AIUB) is an associated analysis center of the International Laser Ranging Service (ILRS, Pearlman et al. 2019) and collaborates with the analysis center at the Federal Agency for Cartography and Geodesy (BKG) in Germany to generate products for the ILRS from measurements to the geodetic SLR satellites (Pearlman et al. 2019) in the frame of the analysis center activities at BKG. The existing SLR processing at AIUB is based on the geodetic, i.e., spherical SLR satellites LAGEOS-1/2 and Etalon-1/2. According to the ILRS the orbits of these SLR satellites are determined in 7-day

arcs. Additionally, station coordinates, low-degree spherical harmonic (SH) coefficients of the Earth's gravity field, Earth Rotation Parameters (ERP), geocenter variations and range biases for selected stations are co-estimated. Initially, it was planned that the ILRS contribution to ITRF2020 (Altamimi et al. 2018) should be based on LAGEOS-1/2, Etalon-1/2 and additionally on LARES (LAsER Relativity Satellite). This motivated to extend the SLR processing at AIUB to also include LARES. With a mean semi-major axis of only 7820 km LARES is a low Earth orbiting (LEO) satellite and therefore experiences a more variable orbit environment, i.e., Earth's time-variable gravity field and upper atmosphere density variations, which has to be taken into account in the orbit parametrization. But the higher sensitivity on the SH coefficients of the Earth's gravity field from LARES also allows co-estimating SH coefficients up to degree 6 (e.g., Bloßfeld et al. 2018; Bloßfeld et al. 2019). Even if nowadays the determination of the Earth's time-variable gravity field is

L. Geisser (✉) · U. Meyer · D. Arnold · A. Jäggi  
Astronomical Institute of the University of Bern, Bern, Switzerland  
e-mail: [linda.geisser@unibe.ch](mailto:linda.geisser@unibe.ch)

mostly based on dedicated gravimetry satellite missions, i.e., the Gravity Recovery And Climate Experiment (GRACE) (Tapley 2004) and GRACE Follow-on (Landerer et al. 2020), the geodetic technique of SLR is best suited to determine some low-degree gravity field coefficients, especially the zonal SH coefficients  $C_{20}$  and  $C_{30}$  (e.g., Bianco et al. 1998, Maier et al. 2012, Loomis et al. 2020). In this paper, we study the optimal orbit parametrization for LARES by either using 7-day true-arcs, or by so-called long-arcs (Beutler et al. 1996), which are created by stacking daily normal equations with continuity conditions for the orbit parameters at the day boundaries. The long-arc computation is already regularly and successfully used in the GNSS processing (Lutz et al. 2016) at the Center for Orbit Determination in Europe (CODE, Dach et al. 2009). The quality of the combined SLR solution is validated by comparing all parameters with internal and external quality metrics.

## 2 SLR Processing at AIUB

The SLR data provided by the ILRS used for this study are processed with the Bernese GNSS Software (BSW, Dach et al. 2015). In a first step each satellite group (i.e. A: LAGEOS-1/2, B: Etalon-1/2, C: LARES), is individually analyzed using the same background models (see Table 1). In addition, the corresponding Normal Equation Systems (NEQs) are set up. The satellite orbits are generally characterized in the BSW by six osculating orbital elements referring to the beginning of the arc and up to nine dynamical parameters (Beutler et al. 1994). Section 2.1 describes the different orbit modeling approaches for the satellite groups. Finally, the satellite-group-specific NEQs are combined for generating the multi-satellite solution (Sect. 2.2). The satellite orbits are determined together with station coordinates, range biases for selected stations as recommended by the ILRS, and the global geodetic parameters of interest, i.e., ERP, geocenter variations and SH coefficients of the Earth's gravity field.

### 2.1 Orbit Modeling

For LAGEOS and Etalon 7-day “true”-arcs are generated, which are represented by the six initial osculating orbital elements and three dynamical orbit parameters, i.e., a constant acceleration  $S_0$  and once-per-revolution (OPR) sine and cosine accelerations ( $S_S$  resp.  $S_C$ ) in along-track as a function of the satellites' argument of latitude. OPR accelerations in cross-track ( $W$ ) are avoided, because of the strong correlation between the OPR sine acceleration in  $W$  and the zonal SH coefficient  $C_{20}$ , e.g., Jäggi et al. (2012) and Bloßfeld et al. (2014). Due to the more variable orbit envi-

ronment at the low altitude of LARES, a more sophisticated orbit parametrization is needed than for the higher orbiting LAGEOS and Etalon satellites. Air drag is modeled using the model NRLMSISE-00 (Picone et al. 2002).

In this study, two different approaches are investigated. On the one hand, the orbit of LARES is parametrized in analogy to the orbit parametrization used for LAGEOS. On the other hand, daily LARES arcs are generated in a first step according to the orbit parametrization of LAGEOS. This means that daily normal equations with one set of osculating and dynamical orbit parameters are set up. Then the long-arc computation allows combining the daily arcs into a 7-day arc by transforming the initial osculating elements of the daily NEQs into one set of osculating elements referring to the beginning of the 7-day arc (Beutler et al. 1996). The dynamic orbit parameters may be kept in the NEQ as daily parameters or, alternatively, be stacked to one parameter for the entire arc. The former strategy provides more flexibility to account for modeling deficiencies. The long-arc computation realizes a continuous arc over several days by stacking daily arcs with continuity conditions at the day boundaries.

Additionally, daily pseudo-stochastic pulses in along-track ( $S$ ) can partially absorb possible air drag mismodeling. Table 1 lists the background models used for the SLR data processing. All SLR solutions are based on the static Earth gravity field GGM05S (Ries et al. 2018).

In addition to the above mentioned orbit parameters also the geodetic and instrument parameters listed in Table 2 are

**Table 1** A priori background models for SLR data processing

Models	Description
Reference frame	SLRF2014 <sup>1</sup>
ERP	IERS-14-C04 <sup>2</sup>
Nutation model	IAU2000 (Mathews et al. 2002)
Subdaily pole model	DESAI: IERS conventions 2010 (Petit and Luzum 2010)
Ocean tide model	FES2014b: d/o 30 (Lyard et al. 2021) + admittances
Earth Tides	Solid earth tides, Pole tides and Ocean pole tides: IERS 2010 (Petit and Luzum 2010)
Loading corrections	Ocean tidal loading: FES2014 Atmospheric tidal loading: Ray and Ponte (Ray and Ponte 2003)
De-aliasing products	Atmosphere + Ocean RL06: d/o 30 incl. S1- and S2-atmosphere tides (Dobslaw et al. 2017)
Earth gravity field	GGM05S: d/o 90 (Ries et al. 2018)

<sup>1</sup>[https://cddis.nasa.gov/archive/slr/products/resource/SLRF2014\\_POS+VEL\\_2030.0\\_200325.snx](https://cddis.nasa.gov/archive/slr/products/resource/SLRF2014_POS+VEL_2030.0_200325.snx).

<sup>2</sup><https://hpiers.obspm.fr/eoppc/eopc04/>.

**Table 2** Estimated parameters

Parameters	LAGEOS/Etalon	LARES
Osculating elements	1 set per 7 days	
Dynamical parameters	1 set per 7 days	1 set per 7 days (7d true-arc)
		1 set per day (7d long-arc)
Stochastic pulses	None	None
		Twice per day: along-track ( $S$ ) cross-track ( $W$ )
Station coordinates	1 set per 7 days	
	NNR/NNT minimal constraint	
Geocenter coordinates	1 set per 7 days	
Range biases	1 set per 7 days	
	Selected stations	All stations
ERP	Daily	
	Piecewise linear	
SH coefficients	1 set per 7 days	
	Up to degree and order ( $d/o$ ) 4	

simultaneously estimated. In the special case of the long-arc computation for LARES, daily station coordinates, geocenter coordinates, range biases and SH coefficients are combined into a weekly solution. Hence, these solutions cover all ‘three pillars’ of geodesy, i.e., geokinematics, Earth rotation and the Earth’s gravity field (Rummel et al. 2005), and ensure a highest possible level of consistency. The datum is defined by the no-net-rotation (NNR) and no-net-translation (NNT) minimum constraint conditions for the verified ILRS core stations,<sup>3</sup> which have more than 30 observations available per week. A station contributes to the weekly solution if it provides more than 9 normal points to both LAGEOS satellites or more than 2 normal points to LARES. Etalon observations are only included if the station also observed one of the LAGEOS satellites during the week. The ERP are estimated based on a daily piecewise linear model, where the 4th offset of UT1-UTC is fixed to the a priori series and the length of day is constrained with 2 ms/day. The pole coordinates are constrained with 30 mas, which corresponds to the 1 m constraint recommended by the ILRS. Since the geocenter is estimated as a geometric offset, only the SH coefficients from  $d/o$  2 up to  $d/o$  4 are co-estimated.

## 2.2 Combination

In the SLR solution, the combination of different satellites reduces the correlation between orbit parameters, geodetic parameters, and SH coefficients (e.g. Sośnica et al. 2014; Bloßfeld et al. 2019). The lower altitude and therefore the

higher sensitivity of LARES on the Earth’s gravity field also allows it to co-estimate SH coefficients up to degree 4.

The NEQs are set up satellite-specific and contain all relevant parameters. These NEQs are then combined, where common parameters are stacked. The Etalon data are rescaled with a variance factor of  $3^{-2}$ , which corresponds to the standard value within the ILRS Analysis Standing Committee. The variance factor of LARES data is currently set to  $1.5^{-2}$  and was determined empirically by checking the quality of the geodetic parameters.

## 3 Validation of the SLR Solutions

The quality of the generated SLR solutions are validated by comparing the estimated geodetic parameters, i.e.,

- Gravity field coefficients with the external model CSR\_Monthly\_5x5\_Gravity\_Harmonics<sup>4</sup> (Cheng et al. 2011) labelled as CSR, which is comparable with the Technical Note 14 (Loomis et al. 2020),
- ERP with IERS-14-C04<sup>2</sup> (Bizouard et al. 2019) at 12-h epochs,
- Station coordinates through the RMS of the Helmert transformations w.r.t. SLRF2014.

Figure 1 (top) shows the time series of weekly co-estimated SH coefficients  $C_{20}$  for five years covering 2015–2019. The LAGEOS-only solution, where only  $C_{20}$  is co-estimated, is capable to estimate a reliable  $C_{20}$ . This is expected, Sosnica (2014) already pointed out the high sensitivity of combined LAGEOS solutions to  $C_{20}$ . If LARES is included the gravity field parameters have to be co-estimated up to  $d/o$  4, to properly account for the additional sensitivity gained from the significantly lower LARES orbit. Both for including LARES as 7d true-arc or as a 7d-arc based on the long-arc computation, the time series of  $C_{20}$  is very similar to the LAGEOS-only solution. All solutions show a semi-annual and annual signal (Fig. 1, bottom). Nevertheless, all solutions have a small offset  $1.1 \cdot 10^{-10}$  (resp.  $0.85 \cdot 10^{-10}$  with LARES) with respect to the reference series of CSR (see Table 3). The variability of the gravity field coefficients is described by the RMS of the weekly SLR solutions w.r.t. the corresponding 4-weeks solutions, which are generated by stacking 4 weekly multi-satellite SLR solutions with pre-eliminating all parameters besides the gravity field coefficients. The lower LARES orbit altitude and consequently higher sensitivity to the Earth’s gravity field, together with the orbit inclination different to the LAGEOS satellites, allow it to estimate  $C_{30}$ . Due to the strong correlation between the OPR accelerations in along-track and  $C_{30}$  (Bloßfeld et al. 2018), a meaningful

<sup>3</sup>[https://ilrs.dgfi.tum.de/fileadmin/data\\_handling/](https://ilrs.dgfi.tum.de/fileadmin/data_handling/).

<sup>4</sup>[https://download.csr.utexas.edu/pub/slr/degree\\_5/](https://download.csr.utexas.edu/pub/slr/degree_5/).

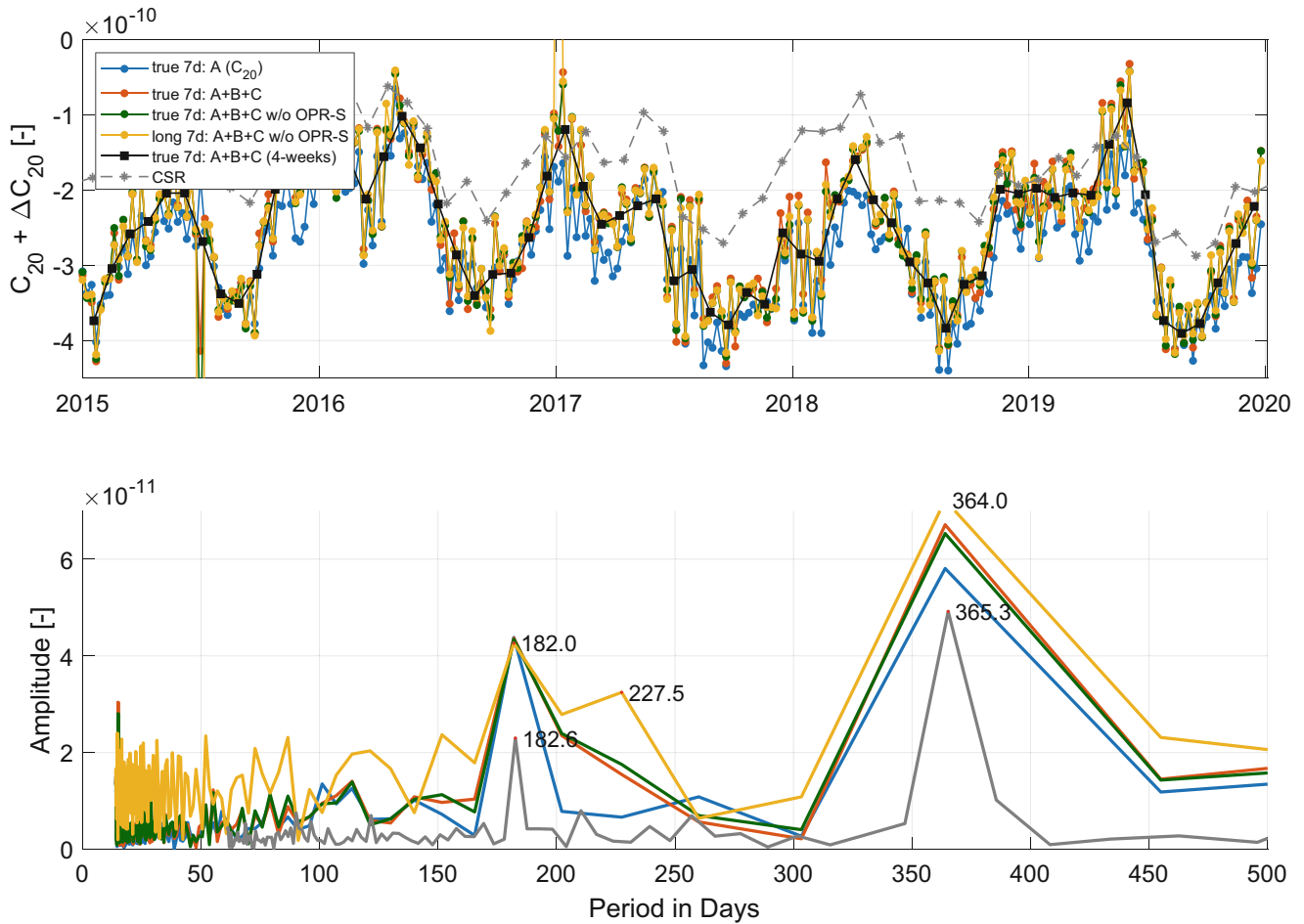


**Fig. 1** Time series of weekly resp. monthly co-estimated gravity field coefficients  $C_{20}$  (with  $\Delta C_{20} = 0.48416945732 \cdot 10^{-3}$ ) (top) and the spectral analysis (bottom) for different SLR solutions

estimation of  $C_{30}$  is only possible if the OPR accelerations in along-track are not set up (Fig. 2). The  $C_{30}$  series shows again an offset with respect to the reference series of CSR. In addition the annual and semi-annual signals are noticeably larger than for the reference series. The RMS of  $C_{30}$  can be slightly reduced by estimating additional stochastic pulses in along-track and cross-track.

The comparison of the estimated ERP, i.e., polar motion (x-pole and y-pole) and UT1-UTC shows that including LARES as a 7d true-arc without estimating stochastic pulses increases the WRMS of the polar motion by 24% in x-direction resp. 19% in y-direction (see Table 4). However, if the orbit parametrization of LARES is extended with additional parameters, i.e., twice per day stochastic pulses in cross-track and along-track, the WRMS and the mean biases can again be significantly reduced.

The quality of the station coordinates is validated by comparing the RMS of the Helmert transformation w.r.t. SLRF2014 (see Fig. 3). Only stations that were used for the datum definition were considered in this analysis. Including

**Table 3** Offset to CSR solution and RMS of Earth’s gravity field coefficients  $C_{20}$  and  $C_{30}$  w.r.t. 4-weeks gravity field solutions

Solutions		$C_{20}$		$C_{30}$	
		Offset [10 <sup>-10</sup> ]	RMS [10 <sup>-11</sup> ]	Offset [10 <sup>-10</sup> ]	RMS [10 <sup>-11</sup> ]
7d true-arc	A	1.10	3.26	-	-
	A+B+C	0.82	4.27	-2.02	96.41
	A+B+C: a	0.82	4.11	-1.06	4.15
	A+B+C: a + b	0.82	4.04	-1.06	3.91
7d long-arc	A+B+C	0.81	4.04	-0.31	41.97
	A+B+C: a	0.81	4.20	-1.03	4.04
	A+B+C: a + b	0.85	4.59	-1.06	3.86

A: LAGEOS-1/2  
 B: Etalon-1/2  
 C: LARES  
 a: w/o OPR-S for C  
 b: w/ stoch. pl. in S and W for C

LARES with OPR accelerations in along-track increases the RMS by around 18% in North, 26% in East and 4% in Up compared with the LAGEOS-only solution. If for

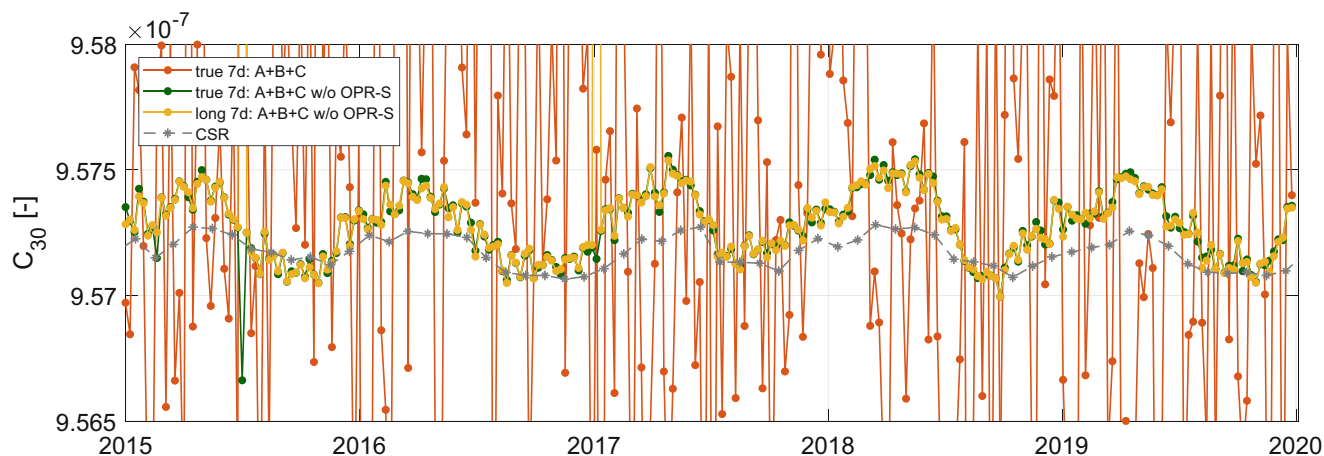


**Fig. 2** Time series of weekly co-estimated gravity field coefficients  $C_{30}$  for different SLR solutions

**Table 4** Comparison of ERP for different SLR solutions

Solutions		Mean bias			WRMS		
		x-pole [ $\mu$ as]	y-pole [ $\mu$ as]	UT1-UTC [ $\mu$ s]	x-pole [ $\mu$ as]	y-pole [ $\mu$ as]	UT1-UTC [ $\mu$ s]
7d true-arc	A	89.2	24.8	-0.6	161.1	135.1	23.1
	A+B+C	70.2	9.6	1.1	199.7	161.3	25.9
	A+B+C: <i>a</i>	70.5	12.7	0.3	209.4	167.5	25.0
	A+B+C: <i>a + b</i>	55.9	20.5	0.6	136.3	125.1	23.1
7d long-arc	A+B+C	69.1	18.8	1.6	189.5	161.4	24.2
	A+B+C: <i>a</i>	70.7	13.8	1.1	202.6	164.6	23.5
	A+B+C: <i>a + b</i>	56.3	18.6	0.1	144.3	132.1	23.5

A: LAGEOS-1/2

B: Etalon-1/2

C: LARES

*a*: w/o OPR-S for C

*b*: w/ stoch. pl. in S and W for C

both orbit parametrizations, i.e., 7d true-arc and 7d long-arc of LARES, stochastic pulses in along-track and cross-track are set up, the RMS of the Helmert transformation can be reduced. In the case of the 7d true-arc, it is even possible to get smaller RMS than for the LAGEOS-only solution.

The geocenter coordinates are very similar for all the discussed solutions and therefore they are not shown in this paper.

## 4 Conclusions

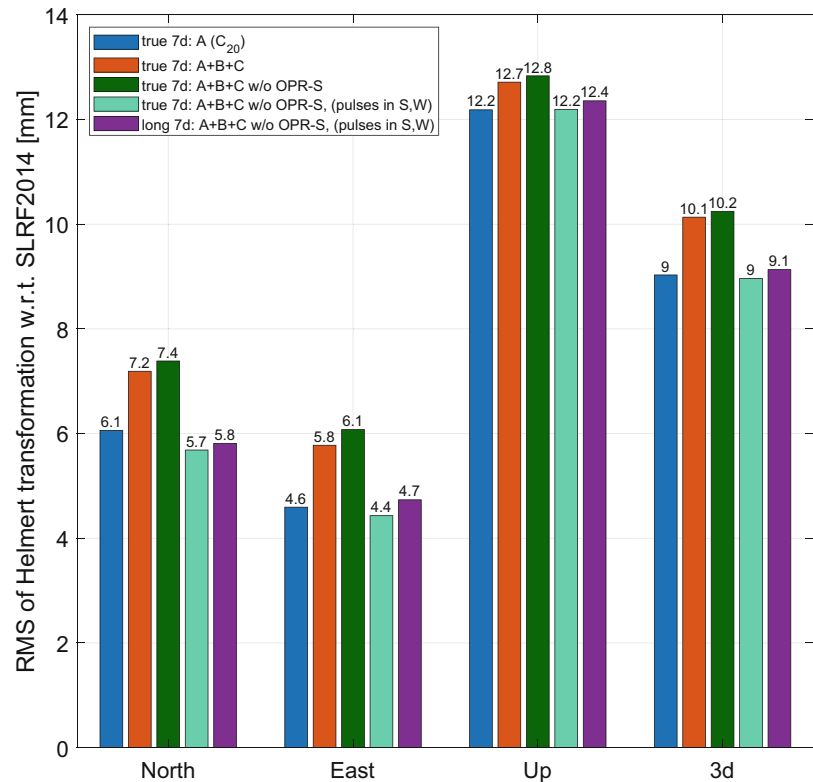
We extended our SLR processing based on LAGEOS-1/2 and Etalon-1/2 to also use normal points from the LEO satellite LARES. Due to its lower altitude, the orbit environment is more variable and the orbit modeling becomes more challenging. Therefore, we investigated two different orbit modeling approaches for LARES:

- 7d true-arc: one set of initial osculating orbital elements and one set of dynamical orbit parameters estimated for 7 days,
- 7d long-arc: one set of initial osculating orbital elements and daily dynamical orbit parameters estimated for 7 days.

The results showed that including LARES does not degrade the already well defined SH coefficient of Earth's gravity field  $C_{20}$  w.r.t. the LAGEOS-only solution. In addition it allows to precisely estimating  $C_{30}$ , if the OPR accelerations in along-track are not set up for LARES. Nevertheless, the larger amplitude of  $C_{30}$  requires further investigations.

The analysis of the ERP showed that including LARES without any additional stochastic pulses in along-track and cross-track, the WRMS of the polar motion increases significantly compared with the LAGEOS-only solution. In addition, the comparison of the RMS of the Helmert transformation w.r.t. SLRF2014 results in the same conclusion that additional stochastic pulses improve the quality of the station coordinates. This indicates that orbit modeling defi-

**Fig. 3** RMS of the Helmert transformation w.r.t. SLRF2014 in North, East, Up and in 3D for different SLR solutions



ciencies for LARES can be reduced by setting up stochastic pulses in along-track and cross-track, without harming  $C_{20}$ .

Furthermore, the comparison of the ERP and the RMS of the Helmert transformation shows that the 7d true-arc is slightly better than the 7d long-arc for LARES, if the orbit parametrization of LARES is added with stochastic pulses. This research can now be used at AIUB as a basis for generating a multi-satellite SLR solution with, e.g., Starlette and Stella, where due to the low altitudes we expect to use the long-arc computation. As for example Bloßfeld et al. (2018) demonstrated, with a multi-satellite solution, we should be able to also co-estimate higher degrees of the gravity field than  $C_{30}$ . Since in combined solutions the relative weighting is very important, further studies, e.g. variance component estimation, to find the optimal variance factors to increase the quality of the SLR solution should be performed.

**Acknowledgements** This research was supported by the European Research Council under the grant agreement no. 817919 (project SPACE TIE). All views expressed are those of the authors and not of the European Research Council. Calculations were performed on UBELIX (<http://www.id.unibe.ch/hpc>), the HPC cluster at the University of Bern.

We thank the two anonymous reviewers for their helpful remarks.

## References

- Altamimi Z, Rebischung P, Collilieux X, Metivier L, Chanard K (2018) Roadmap toward ITRF2020. In: AGU fall meeting abstracts, vol 2018, pp G42A–08
- Beutler G, Brockmann E, Gurtner W, Hugentobler U, Mervart L, Rothacher M, Verdun A (1994) Extended orbit modeling techniques at the CODE processing center of the international GPS service for geodynamics (IGS): theory and initial results. *Manuscr Geod* 19(6):367–386
- Beutler G, Brockmann E, Hugentobler U, Mervart L, Rothacher M, Weber R (1996) Combining consecutive short arcs into long arcs for precise and efficient GPS orbit determination. *J Geod* 70(5):287–299. <https://doi.org/10.1007/BF00867349>
- Bianco G, Devoti R, Fermi M, Luceri V, Rutigliano P, Sciarretta C (1998) Estimation of low degree geopotential coefficients using SLR data. *Planet Space Sci* 46(11–12):1633–1638. [https://doi.org/10.1016/S0032-0633\(97\)00215-8](https://doi.org/10.1016/S0032-0633(97)00215-8)
- Bizouard C, Lambert S, Gattano C, Becker O, Richard JY (2019) The IERS EOP 14C04 solution for Earth orientation parameters consistent with ITRF 2014. *J Geod* 93(5):621–633. <https://doi.org/10.1007/s00190-018-1186-3>
- Bloßfeld M, Gerstl M, Hugentobler U, Angermann D, Müller H (2014) Systematic effects in LOD from SLR observations. *Adv Space Res* 54(6):1049–1063. <https://doi.org/10.1016/j.asr.2014.06.009>
- Bloßfeld M, Rudenko S, Kehm A, Panafidina N, Müller H, Angermann D, Hugentobler U, Seitz M (2018) Consistent estimation of geodetic parameters from SLR satellite constellation measurements. *J Geod* 92(9):1003–1021. <https://doi.org/10.1007/s00190-018-1166-7>

- Bloßfeld M, Müller H, Gerstl M, Štefka V, Bouman J, Göttl F, Horwath M (2019) Second-degree Stokes coefficients from multi-satellite SLR. *J Geod* 89(9):857–871. <https://doi.org/10.1007/s00190-015-0819-z>
- Cheng M, Ries JC, Tapley BD (2011) Variations of the Earth's figure axis from satellite laser ranging and GRACE. *J Geophys Res* 116(B1):B01409. <https://doi.org/10.1029/2010JB000850>
- Dach R, Brockmann E, Schaer S, Beutler G, Meindl M, Prange L, Bock H, Jäggi A, Ostini L (2009) GNSS processing at CODE: Status report. *J Geod* 83(3-4):353–365. <https://doi.org/10.1007/s00190-008-0281-2>
- Dach R, Lutz S, Walser P, Fridez P (2015) Bernese GNSS software version 5.2. user manual. <https://doi.org/10.7892/BORIS.72297>
- Dobslaw H, Bergmann-Wolf I, Dill R, Poropat L, Thomas M, Dahle C, Esselborn S, König R, Flechtner F (2017) A new high-resolution model of non-tidal atmosphere and ocean mass variability for de-aliasing of satellite gravity observations: AOD1B RL06. *Geophys J Int* 211(1):263–269. <https://doi.org/10.1093/gji/ggx302>
- Jäggi A, Sošnica K, Thaller D, Beutler G (2012) Validation and estimation of low-degree gravity field coefficients using LAGEOS. *Mitteilungen des Bundesamtes fuer Kartographie und Geodäsie Band 48*, "Proceedings of the 17th International Workshop on Laser Ranging, Extending the Range", May 16–20, 2011 Bad Koetzing, Germany 48:302–304
- Landerer FW, Flechtner FM, Save H, Webb FH, Bandikova T, Bertiger WI, Bettadpur SV, Byun SH, Dahle C, Dobslaw H, Fahnestock E, Harvey N, Kang Z, Kruizinga GLH, Loomis BD, McCullough C, Murböck M, Nagel P, Paik M, Pie N, Poole S, Strelakov D, Tamisiea ME, Wang F, Watkins MM, Wen HY, Wiese DN, Yuan DN (2020) Extending the global mass change data record: Grace follow-on instrument and science data performance. *Geophys Res Lett* 47(12):e2020GL088306. <https://doi.org/10.1029/2020GL088306>
- Loomis BD, Rachlin KE, Wiese DN, Landerer FW, Luthcke SB (2020) Replacing grace/grace-fo with satellite laser ranging: Impacts on antarctic ice sheet mass change. *Geophys Res Lett* 47(3):e2019GL085488. <https://doi.org/10.1029/2019GL085488>
- Lutz S, Meindl M, Steigenberger P, Beutler G, Sošnica K, Schaer S, Dach R, Arnold D, Thaller D, Jäggi A (2016) Impact of the arc length on GNSS analysis results. *J Geod* 90(4):365–378. <https://doi.org/10.1007/s00190-015-0878-1>
- Lyard FH, Allain DJ, Cancet M, Carrère L, Picot N (2021) FES2014 global ocean tide atlas: Design and performance. *Ocean Sci* 17(3):615–649. <https://doi.org/10.5194/os-17-615-2021>
- Maier A, Krauss S, Hausleitner W, Baur O (2012) Contribution of satellite laser ranging to combined gravity field models. *Adv Space Res* 49(3):556–565. <https://doi.org/10.1016/j.asr.2011.10.026>
- Mathews PM, Herring TA, Buffett BA (2002) Modeling of nutation and precession: New nutation series for nonrigid Earth and insights into the Earth's interior: New nutation series and the Earth's interior. *J Geophys Res* 107(B4):ETG 3–1–ETG 3–26. <https://doi.org/10.1029/2001JB000390>
- Pearlman MR, Noll CE, Pavlis EC, Lemoine FG, Combrink L, Degnan JJ, Kirchner G, Schreiber U (2019) The ILRS: Approaching 20 years and planning for the future. *J Geod* 93(11):2161–2180. <https://doi.org/10.1007/s00190-019-01241-1>
- Petit G, Luzum B (2010) IERS Technical Note; No. 36. Frankfurt am Main: Verlag des Bundesamts für Kartographie und Geodäsie (36):179 p
- Picone JM, Hedin AE, Drob DP, Aikin AC (2002) Nrlmsise-00 empirical model of the atmosphere: Statistical comparisons and scientific issues. *J Geophys Res Space Phys* 107(A12):SIA 15–1–SIA 15–16. <https://doi.org/10.1029/2002JA009430>
- Ray RD, Ponte RM (2003) Barometric tides from ecmwf operational analyses. *Annales Geophysicae* 21(8):1897–1910. <https://doi.org/10.5194/angeo-21-1897-2003>
- Ries J, Bettadpur S, Eanes R, Kang Z, Ko U, McCullough C, Nagel P, Pie N, Poole S, Richter T, Save H, Tapley B (2018) Development and evaluation of the global gravity model GGM05. CSR-16-02, Center of Space Research, The University of Texas at Austin
- Rummel R, Rothacher M, Beutler G (2005) Integrated global geodetic observing system (IGGOS)—science rationale. *J Geodyn* 40(4):357–362. <https://doi.org/10.1016/j.jog.2005.06.003>
- Sošnica K, Jäggi A, Thaller D, Beutler G, Dach R (2014) Contribution of Starlette, Stella, and AJISAI to the SLR-derived global reference frame. *J Geod* 88(8):789–804. <https://doi.org/10.1007/s00190-014-0722-z>
- Sosnica KJ (2014) Determination of precise satellite orbits and geodetic parameters using satellite laser ranging. <https://doi.org/10.7892/BORIS.53915>
- Tapley BD (2004) GRACE measurements of mass variability in the Earth system. *Science* 305(5683):503–505. <https://doi.org/10.1126/science.1099192>

**Open Access** This chapter is licensed under the terms of the Creative Commons Attribution 4.0 International License (<http://creativecommons.org/licenses/by/4.0/>), which permits use, sharing, adaptation, distribution and reproduction in any medium or format, as long as you give appropriate credit to the original author(s) and the source, provide a link to the Creative Commons license and indicate if changes were made.

The images or other third party material in this chapter are included in the chapter's Creative Commons license, unless indicated otherwise in a credit line to the material. If material is not included in the chapter's Creative Commons license and your intended use is not permitted by statutory regulation or exceeds the permitted use, you will need to obtain permission directly from the copyright holder.







# Determination and Combination of Monthly Gravity Field Time Series from Kinematic Orbits of GRACE, GRACE-FO and Swarm

Thomas Grombein, Martin Lasser, Daniel Arnold, Ulrich Meyer, and Adrian Jäggi

## Abstract

Dedicated gravity field missions like GRACE and GRACE-FO use ultra-precise inter-satellite ranging observations to derive time series of monthly gravity field solutions. In addition, any (non-dedicated) Low Earth Orbiting (LEO) satellite with a dual-frequency GNSS receiver may also serve as a gravity field sensor. To this end, GPS-derived kinematic LEO orbit positions are used as pseudo-observations for gravity field recovery. Although less sensitive, this technique can provide valuable information for the monitoring of large-scale time-variable gravity signals, particularly for those months where no inter-satellite ranging measurements are available. Due to a growing number of LEO satellites that collect continuous and mostly uninterrupted GPS data, the value of a combined multi-LEO gravity field time series is likely to increase in the near future.

In this paper, we present monthly gravity field time series derived from GPS-based kinematic orbit positions of the GRACE, GRACE-FO and Swarm missions. We analyze their individual contribution as well as the additional benefit of their combination. For this purpose, two combination strategies at solution level are studied that are based on (i) least-squares variance component estimation, and (ii) stochastic properties of the gravity field solutions. By evaluating mass variations in Greenland and the Amazon river basin, the resulting gravity field time series are assessed with respect to superior solutions based on inter-satellite ranging.

## Keywords

GPS-based gravity field recovery · GRACE · GRACE-FO · Gravity field combination · Kinematic orbits · LEO satellites · Swarm · Time-variable gravity

## 1 Introduction

The Earth's gravity field and its temporal variations provide an important source of information for the monitoring of mass transport and mass distribution in the Earth's system. Dedicated satellite missions like the Gravity Recovery And Climate Experiment (GRACE, Tapley et al.

2004) and its successor GRACE Follow-On (GRACE-FO, Landerer et al. 2020) allow to resolve the Earth's time-variable gravity field on a monthly basis using ultra-precise inter-satellite ranging derived from K-band or laser ranging data.

Alternative gravity field information can be obtained from Low Earth Orbiting (LEO) satellites that are equipped with a high-quality (geodetic) GNSS receiver. For this purpose, GPS tracking data may be used to derive precise kinematic orbits (Švehla and Rothacher 2005). As kinematic orbit positions are purely geometrically determined and independent of the LEO orbital dynamics, they are well suited for

T. Grombein (✉) · M. Lasser · D. Arnold · U. Meyer · A. Jäggi  
Astronomical Institute, University of Bern, Bern, Switzerland  
e-mail: [thomas.grombein@aiub.unibe.ch](mailto:thomas.grombein@aiub.unibe.ch)

gravity field recovery. Several methods have been proposed to derive gravity field information from kinematic LEO orbit positions, see, e.g., Baur et al. (2014) for a detailed overview.

Many studies have demonstrated that it is feasible to recover large-scale time-variable gravity field signals from kinematic LEO orbits, see, e.g., Weigelt et al. (2013), Guo et al. (2020) and Grombein et al. (2021) for studies related to the dedicated gravity field missions CHAMP, GRACE and GOCE, respectively. In recent years, time-variable gravity information derived from GPS tracking data of the (non-dedicated) magnetic field mission Swarm (Friis-Christensen et al. 2008) moved into focus to bridge the gap between the GRACE and GRACE-FO missions, see, e.g., Richter et al. (2021). Moreover, monthly gravity field solutions from Swarm kinematic orbits are computed by different institutes and operationally combined (Teixeira da Encarnação et al. 2020) in the frame of the International Combination Service for Time-variable Gravity Fields (COST-G, Jäggi et al. 2020).

Beside such a single-mission combination, the increasing number of operational scientific LEO satellites and commercial satellite constellations makes it attractive to strive for a combined GPS-based gravity field time series derived from multiple LEO satellites. Such a combination will take advantage of (i) a large number of mostly uninterrupted observations, and (ii) the variety of complementary orbital configurations that can improve the spatio-temporal resolution. Moreover, such a multi-LEO combination might play an important role for a continuation of gravity field time series when no dedicated mission is in orbit, e.g., due to a potential failure of GRACE-FO or a large gap until the next generation gravity field mission (NGGM) is launched.

At the Astronomical Institute of the University of Bern (AIUB), GPS-based precise orbit determination (POD) is routinely performed for a variety of LEO satellite using the POD strategy described in Jäggi et al. (2006) that is implemented in the Bernese GNSS Software (Dach et al. 2015). Kinematic orbits are processed in 24 h orbital arcs in a batch least-squares adjustment using the ionosphere-free linear combination of the undifferenced GPS carrier phase observations. For this purpose, the final CODE GNSS orbits (Dach et al. 2009) and 5 s satellite clock corrections (Bock et al. 2009) are used. Furthermore, for each LEO GPS receiver antenna, in-flight calibrated phase center variation maps are generated by a residual stacking approach (Jäggi et al. 2009). Beside conventional ambiguity-float orbits, also ambiguity-fixed orbits are recently being computed based on new phase bias and clock products (Schaer et al. 2021). Kinematic orbits have been generated for various LEO satellites like CHAMP, GRACE and GOCE or are routinely processed for a growing number of operational missions like GRACE-FO and Swarm or the fleet of Sentinel satellites. This offers the opportunity to explore the contribution of these kinematic orbits to the recovery of the Earth's time-variable gravity field.

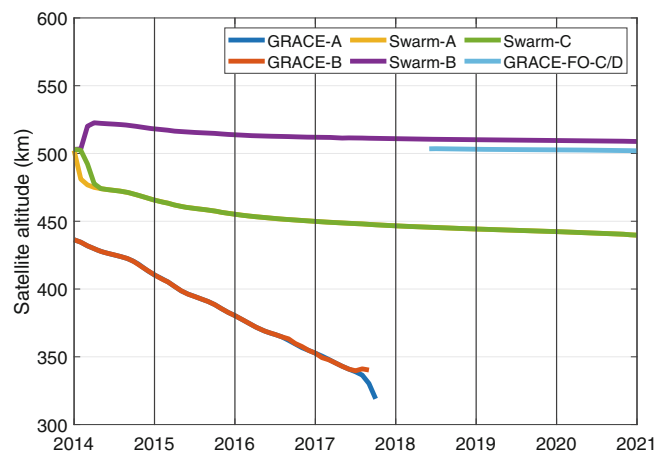


**Fig. 1** Orbital altitudes of the GRACE, GRACE-FO and Swarm satellites derived from their kinematic orbit positions (monthly mean values)

In the present study, we use the kinematic LEO orbit positions from the dedicated satellite missions GRACE and GRACE-FO as well as from the non-dedicated Swarm constellation in order to determine and combine monthly gravity field time series covering about seven years between Jan 2014 and Feb 2021. As illustrated in Fig. 1, the orbital altitudes of these LEO satellites are quite different. This certainly represents a major difference to the setting of combinations performed within COST-G. Therefore, it needs to be analyzed if classical combination schemes based on variance component estimation (VCE) as applied by COST-G can be adapted for this scenario.

The paper is organized as follows: in Sect. 2 details about the input data and gravity field recovery are provided. While the quality of the derived gravity field time series is analyzed in Sect. 3, two strategies for a combination at solution level are introduced and applied in Sect. 4. By evaluating time-variable gravity field signals in Greenland and the Amazon river basin, Sect. 5 studies the individual contribution of the time series and the additional value of their combination. Finally, Sect. 6 concludes with a summary and an outlook.

## 2 Gravity Field Recovery

The monthly GPS-based LEO gravity field time series presented in this study are generated with the Celestial Mechanics Approach (CMA, Beutler et al. 2010) as it is implemented in a development version of the Bernese GNSS Software. Following the procedure described in Jäggi et al. (2016), the GPS-derived kinematic LEO orbit positions and their epoch-wise covariance information are used as pseudo-observations to perform gravity field recovery in a generalized orbit determination problem, where arc-specific orbit and gravity field

**Table 1** Overview and processing details of GPS-based gravity field time series for different LEO satellites

LEO satellites	GRACE-A/B	GRACE-FO-C/D	Swarm-A/B/C
Processing period	Jan 2014 – Oct 2017	Jun 2018 – Feb 2021	Jan 2014 – Feb 2021
Kinematic orbit type	Ambiguity-float	Ambiguity-fixed	Ambiguity-float/-fixed <sup>a</sup>
Data sampling	10 s	10 s	10 s / 5 s <sup>b</sup>
Accelerometer data	Used	Used	Not used
Initial conditions	6 orbital elements (daily)		6 orbital elements (daily)
Empirical parameters	—		Constant accelerations (daily)
Stochastic parameters	PCA <sup>c</sup> (15 min, 10 nm s <sup>-2</sup> constr.)		PCA <sup>c</sup> (15 min, 10 / 7.07 nm s <sup>-2</sup> constr. <sup>b</sup> )
Accelerometer parameters	Bias + scaling factors (daily)		—
Gravity field coefficients	Degree and order 90 (monthly)		Degree and order 70 (monthly)
Reference	This paper		Dahle et al. (2017)

<sup>a</sup>Since 2020-01-26 <sup>b</sup> Since 2014-07-15 <sup>c</sup> PCA: Piecewise constant accelerations

parameters are estimated simultaneously. Non-gravitational forces are not explicitly modeled but considered by measured accelerometer data and/or absorbed by arc-specific empirical acceleration (e.g., constant, once- or twice-per-revolution). Remaining deficiencies are compensated by constrained stochastic parameters (e.g., pulses or piecewise constant accelerations), see Jäggi et al. (2006). Daily normal equations (NEQs) are set up and orbit parameters are pre-eliminated. These NEQs are then stacked month-wise and inverted to solve for monthly gravity field coefficients.

Table 1 provides details on the input data and the conducted gravity field processing for the different LEO satellites. We make use of our in-house generated GPS-based kinematic orbit products for GRACE-A/B (Arnold and Jäggi 2020a), GRACE-FO-C/D (Arnold and Jäggi 2020b), and Swarm-A/B/C (Arnold and Jäggi 2021) that are publicly available.<sup>1</sup> The GRACE/-FO kinematic orbit positions have a data sampling rate of 10 s. While this is also the case for the first months of Swarm, orbits starting from Jul 2014 feature an increased sampling rate of 1 s. For gravity field recovery, a downsampling to 5 s is used as a compromise of runtime reduction and required accuracy (comparisons show that differences are mainly restricted to the high frequency noise). Moreover, the kinematic Swarm positions are based on screened GPS measurements to mitigate ionosphere-induced disturbances affecting the orbit and gravity field quality (e.g., Dahle et al. 2017).

For gravity field recovery, the following parameters are used: beside the six daily orbital elements, stochastic parameters in terms of piecewise constant accelerations (PCA) are estimated in radial, along-track and cross-track direction at intervals of 15 min, using constraints as specified in Table 1 (intervals and constraints are empirically determined and found to be suitable in many studies with the CMA). To maintain an equal influence of the PCAs, the constraints for Swarm need to be reduced by a factor of  $\sqrt{2}$  in Jul

2014 to account for the doubling of the sampling rate. In the GRACE/-FO processing, accelerometer measurements are taken into account whenever available, by co-estimating additional accelerometer bias and scaling factors. Moreover, in the case of the Swarm gravity field recovery, daily constant accelerations are estimated, which is implicitly also the case for GRACE/-FO due to the used accelerometer biases. Finally, gravity field parameters in terms of spherical harmonic (SH) coefficients up to degree and order (d/o) 90 (GRACE/-FO) and 70 (Swarm) are determined without applying any regularization.

It should be noted that the used maximum degree is far above the expected signal content and sensitivity of the GPS observations. However, this choice is motivated to (i) prevent that an omission error propagates into the low-degree coefficients (Guo et al. 2020), and to (ii) guarantee that the estimated SH coefficients are not biased towards the used a priori gravity field model due to an inconsistent maximum degree (Meyer et al. 2015).

While the gravity field recovery for GRACE/-FO has been conducted within this study, the monthly Swarm gravity fields are the operational AIUB solutions (Dahle et al. 2017) that contribute to the Swarm COST-G combination. In the considered time period between Jan 2014 and Feb 2021, the gravity field time series recovered from the kinematic orbits of GRACE, GRACE-FO and Swarm consist of 46, 33 and 86 monthly solutions, respectively. For each mission, combined as well as individual satellite time series have been generated. All monthly solutions are independent from each other as no temporal filtering is applied as, e.g., done in Weigelt et al. (2013) and Zhong et al. (2021).

### 3 Characteristics of Gravity Field Time Series

In order to analyze the quality of the GPS-based LEO gravity field time series, Fig. 2 shows difference degree amplitudes in terms of geoid heights with respect to the monthly ITSG-

<sup>1</sup>[http://www.aiub.unibe.ch/download/LEO\\_ORBITS](http://www.aiub.unibe.ch/download/LEO_ORBITS)

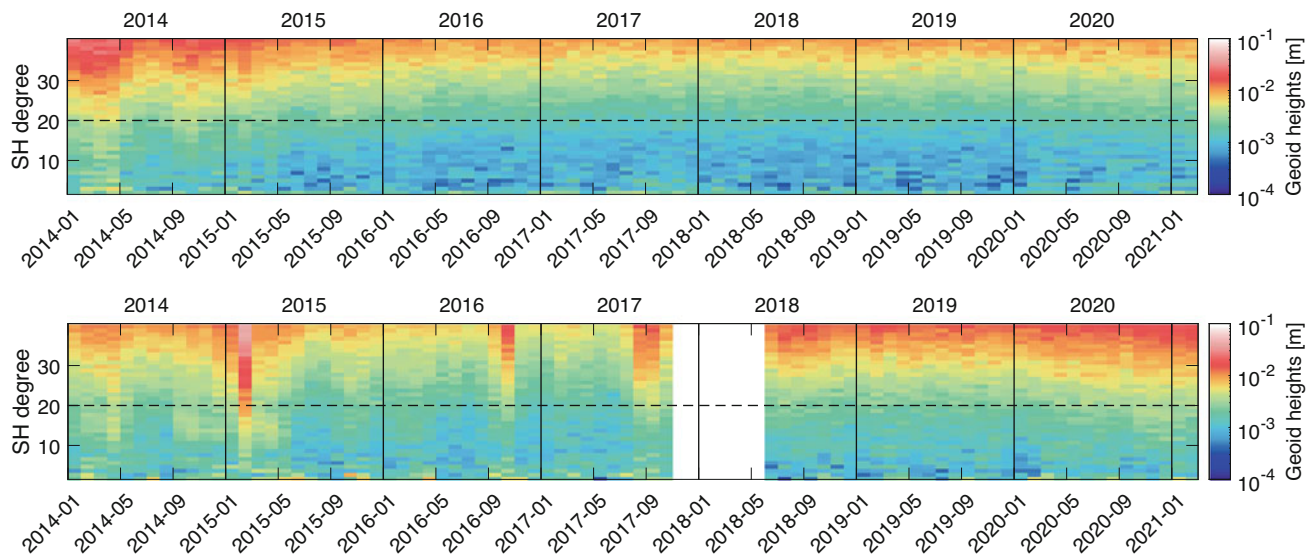


**Fig. 2** Difference degree amplitudes (degree 2 to 40) in terms of geoid heights with respect to monthly ITSG-Grace2018 solutions for the GPS-based gravity field time series of GRACE (*top left*), GRACE-FO (*top*

*right*), and Swarm (*bottom*) in the time span Jan 2014 – Feb 2021. Note that gaps in the monthly ITSG-Grace2018 solutions are filled by interpolation

Grace2018 solutions based on superior GRACE/-FO K-band data (Kvas et al. 2019). For the analysis in this section, gaps in the ITSG-Grace2018 time series are filled using interpolation at the epochs of the GPS-based solutions. Difference degree amplitudes shown in Fig. 2 are confined to degrees up to 40 in order to focus on the relevant signal content of the GPS-based gravity field solutions.

In the case of GRACE (Fig. 2, top left), the difference degree amplitudes generally exhibit values at the mm-level. However, the time series is apparently affected by several disturbances. For the lower degrees, seasonal variations in the difference degree amplitudes are visible, particularly in the years 2014 and 2015. Here, the GRACE solutions in spring and autumn systematically show larger differences for degrees up to 20–30. This systemic behavior can be associated with the ionospheric activity. As described in Sect. 2, a ionospheric-induced degradation of GPS-based gravity fields has been reported for Swarm (Dahle et al. 2017) and GOCE (Jäggi et al. 2015), but can also be observed for GRACE in this study. This is confirmed by Fig. 3, where geoid height differences for the GPS-based GRACE gravity fields of Aug 2014 and Apr 2015 are plotted in the space domain. In contrast to the unaffected month Aug 2014, the solution for Apr 2015 reveals typical signatures of ionospheric-induced artifacts in two bands along the geomagnetic equator. Starting from mid-2015, the quality of the GRACE monthly gravity field solutions gradually improved due to (i) a period of lower ionospheric activity, and (ii) the rapidly decreasing orbital altitudes of the GRACE satellites (cf. Fig. 1).

Besides seasonal disturbances, prominent discrepancies in the GRACE time series can be detected for Feb 2015 and Oct 2016. In both cases, the degradation of the monthly

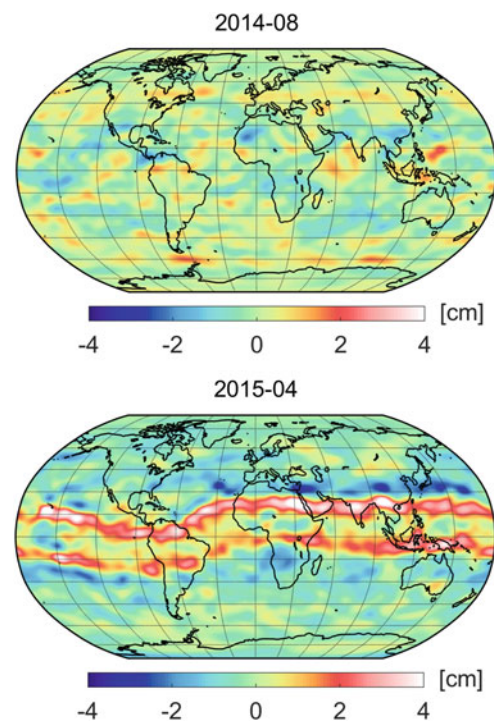


**Fig. 3** Geoid height differences with respect to ITSG-Grace2018 of the GRACE GPS-based gravity field solutions for Aug 2014 (*top*) and Apr 2015 (*bottom*). Gaussian smoothing with a 500 km radius is applied

solutions can be explained by a sparse ground track coverage due to periods of near repeat orbits. Although it might be expected that only higher degrees suffer from spatial coverage problems, difference degree amplitudes for Feb 2015, as show in Fig. 4 (top), illustrate that the impact strongly depends on the maximum degree used for the gravity field

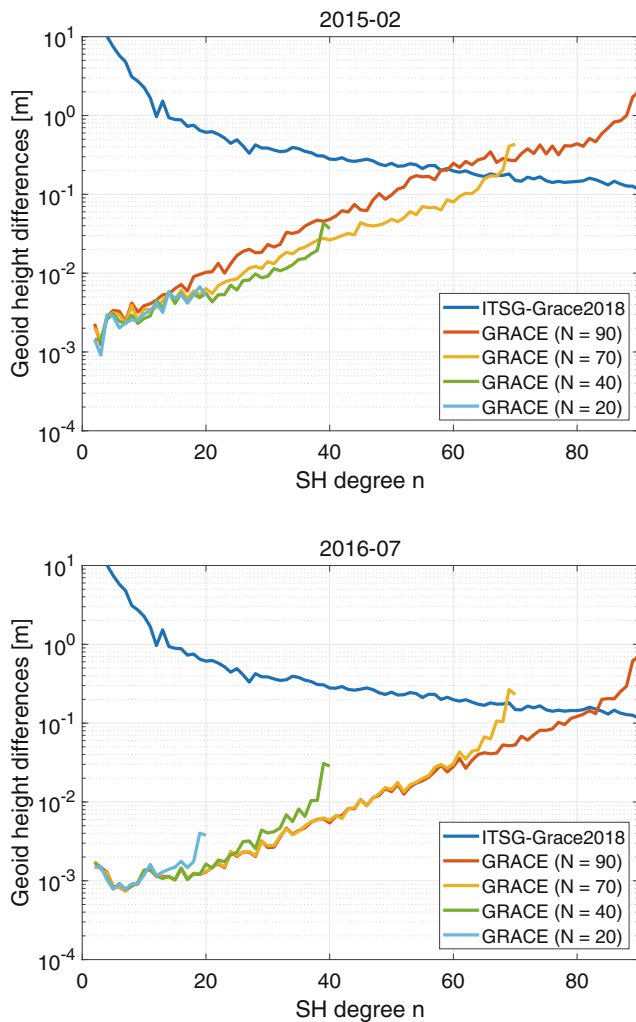


**Fig. 4** Difference degree amplitudes in terms of geoid heights with respect to ITSG-Grace2018 for GRACE GPS-based gravity field solutions with different values for the maximum degree  $N \in \{90, 70, 40, 20\}$  in the case of Feb 2015 (*top*) and Jul 2016 (*bottom*)

estimation. With an increasing maximum degree, the quality of the solutions decreases, demonstrating a high correlation between higher and lower degree coefficients. However, as shown in Fig. 4 (bottom), solutions with a lower maximum degree reveal large omission errors in the case of a nominal month like Jul 2016. Moreover, it should be noted that the plotted solutions with a lower maximum degree (e.g., 20 or 40) still require the use of a higher degree a priori gravity field to obtain a sufficiently accurate initial orbit determination. This inconsistency in the maximum degree might introduce a priori knowledge to the estimation (as mentioned in Sect. 1).

Similar to GRACE, the difference degree amplitudes of the Swarm time series shown in Fig. 2 (bottom) also reveal a limited performance in the early mission phase, mainly related to non-optimal settings of the GPS receivers (cf. van den IJssel et al. 2016). Starting in May 2015, the

quality of the Swarm time series substantially improves when several modifications of the GPS tracking loop bandwidths have been performed (Dahle et al. 2017). The benefit is most impressively visible for the relevant degrees below 20.

In comparison to the GRACE-FO time series (Fig. 2, top right), the Swarm solutions are of superior quality, which is also reflected when plotting the ratio of both time series (not shown). This again is consistent with differences in the satellites' altitudes (cf. Fig. 1). Beginning in Feb 2020, a degradation can be identified in both GPS-based gravity field time series. While for Swarm it is only slightly visible in the lower degrees, this behavior is more pronounced in the case of GRACE-FO, where apparently all degrees are affected. The appearance of this effect coincides with the activation of a new flex power mode for various GPS satellites in Feb 2020 that allows to redistribute the transmit power between different signal components (cf. Steigenberger et al. 2019). As also reported by Huang et al. (2022), this causes problems with some LEO GPS receivers (e.g., GRACE-FO), resulting in a slightly degraded quality of the orbit and gravity field solutions in this study.

#### 4 Combination of Gravity Field Time Series

In the framework of COST-G, monthly gravity field time series are operationally combined to provide consolidated and improved products (Jäggi et al. 2020). Solutions from different institutes (analysis centers) are combined based on data of a single LEO mission, e.g., solutions based on K-band data from GRACE/-FO or GPS data from Swarm. The gravity field combination can either be done at solution or NEQ level, where the latter case benefits from taking into account the full correlations between the estimated parameter. However, as outlined in Teixeira da Encarnação and Visser (2019), a robust NEQ level combination is based on the assumption of equivalent information content of all NEQs. In the above described combination scenario (single LEO mission, multi-institutional approach), heterogeneous processing and error modeling strategies make it necessary to introduce empirical factors to balance the impact of the individual NEQs (cf. Meyer et al. 2019). But even following such a procedure, Teixeira da Encarnação et al. (2020) reported that a combination of Swarm GPS-based gravity field models at solution level provides a better agreement to GRACE K-band data than a combination at NEQ level.

In the scenario of this study (multi-LEO mission, single approach), we are confronted with similar issues, as the individual gravity field solutions differ in their signal content and sensitivity, e.g., due to differences in the orbital altitude or the sampling rate of the kinematic positions. Thus, to simplify the analysis in a first step, the focus of this paper

is confined to the combination of gravity field time series at solution level. In the following, the performance of two combination strategies is studied: (i) a VCE approach using monthly relative field-wise weights, and (ii) a “stochastic” combination that takes into account the standard deviations (formal errors) of the SH coefficients. Both combination strategies are briefly introduced in the following and applied to the individual satellite solutions.

#### 4.1 VCE Combination

Based on iterative least-squares VCE (Teunissen and Amiri-Simkooei 2008) as frequently used for stacking of NEQs, Jean et al. (2018) introduced a VCE approach at solution level that is applied for the COST-G combination. Following Meyer et al. (2019), the gravity field coefficients of the individual solutions are used as pseudo-observations (i.e., the design, weight and normal matrix all become identity matrices) to iteratively derive monthly field-wise weights.

Assuming there are  $N$  solutions with their SH coefficients  $x_{nm}^i \in \{C_{nm}^i, S_{nm}^i\}, i = 1, \dots, N$ , where  $n$  and  $m$  are the SH degree and order, the weighted combination in an iteration step  $k$  is defined by

$$\hat{x}_{nm}^{(k)} = \frac{1}{\sum_{i=1}^N w^{i,k}} \sum_{i=1}^N w^{i,k} x_{nm}^i, \quad (1)$$

where  $w^{i,k}$  denotes the weight of solution  $i$  in iteration step  $k$ . Starting with equal weights  $w^{i,0} = 1/N$  for each solution, the weights in iteration  $k$  are given by

$$w^{i,k} = \left(1 - \frac{w^{i,k-1}}{\sum_{i=1}^N w^{i,k-1}}\right) \left[ \text{RMS} \left( x_{nm}^i - \hat{x}_{nm}^{(k-1)} \right) \right]^{-2}, \quad (2)$$

where RMS is the root-mean-square value.

For the estimation of VCE weights, we analyzed to which maximum degree the SH coefficients should be introduced to Eq. (2), e.g., degree 70, 40, or 20. Similar to findings in Teixeira da Encarnação et al. (2020), it turned out that the used maximum degree needs to be restricted to prevent that VCE weights are strongly dominated by the noise of the higher degrees. A comparison of VCE combinations based on weights derived from SH coefficients up to degree 20 and 40 reveals a slightly better performance for degree 40 in terms of estimated mass trends and variations (Sect. 5).

For the case where SH coefficients up to degree 40 are taken into account, Fig. 5 presents the resulting monthly VCE weights after four iteration steps, where a sufficient convergence level is reached (cf. Meyer et al. 2019). The overall differences reflected in the weights are clearly correlated with the different orbital altitudes of the LEO satellites

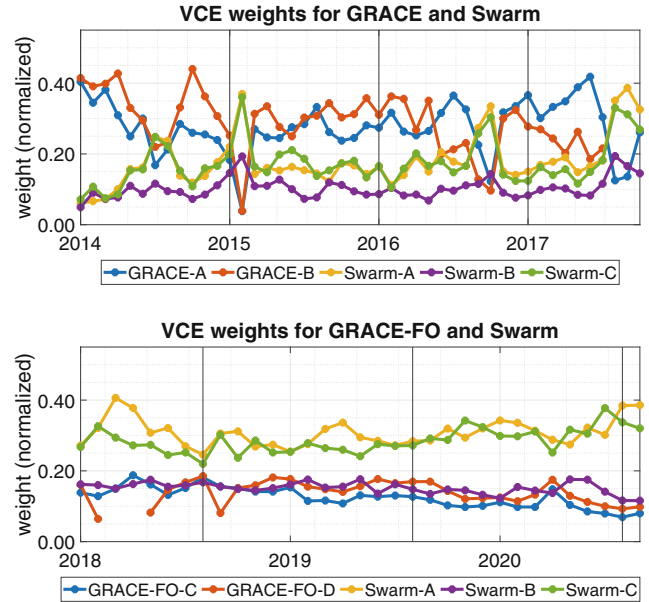


**Fig. 5** Monthly field-wise weights derived from VCE (four iterations) based on the SH coefficients up to  $d/o$  40 of the GPS-based gravity field solutions for the LEO satellites of the GRACE and Swarm missions between Jan 2014 and Oct 2017 (top), as well as the GRACE-FO and Swarm missions between Jun 2018 and Feb 2021 (bottom)

as plotted in Fig. 1. This might be explained as follows: satellites at lower altitudes obtain higher weights as they have a higher sensitivity to the Earth’s gravity field with a lower noise level. However, satellites at lower altitudes are generally more affected by ionospheric disturbances that influence the quality of the gravity field recovery, see, e.g., Fig. 2 in the case of GRACE. In this regard, the VCE weights seems to be less sensitive as only in a few months, where the GRACE solution suffers from severe problems like the near repeat orbits in Feb 2015 and Oct 2016, the sequence significantly changes.

#### 4.2 Stochastic Combination

In the case of the stochastic combination, the SH coefficients  $x_{nm}^i$  of the individual solutions are combined based on their respective standard deviations  $\sigma_{x_{nm}^i}$  obtained from the least-squares adjustment. Generalized from the formulas presented in Huang and Véronneau (2013), monthly coefficient-wise weights are determined by

$$w_{nm}^i = \frac{1}{\sum_{i=1}^N (\sigma_{x_{nm}^i})^2} \sum_{\substack{j=1, \dots, N \\ j \neq i}} (\sigma_{x_{nm}^j})^2. \quad (3)$$

As the standard deviations  $\sigma_{x_{nm}^i}$  depend on the number of observations, differences in the sampling rates of the kinematic positions (see Table 1) need to be compensated. To this end, the increased sampling rate of the Swarm kinematic

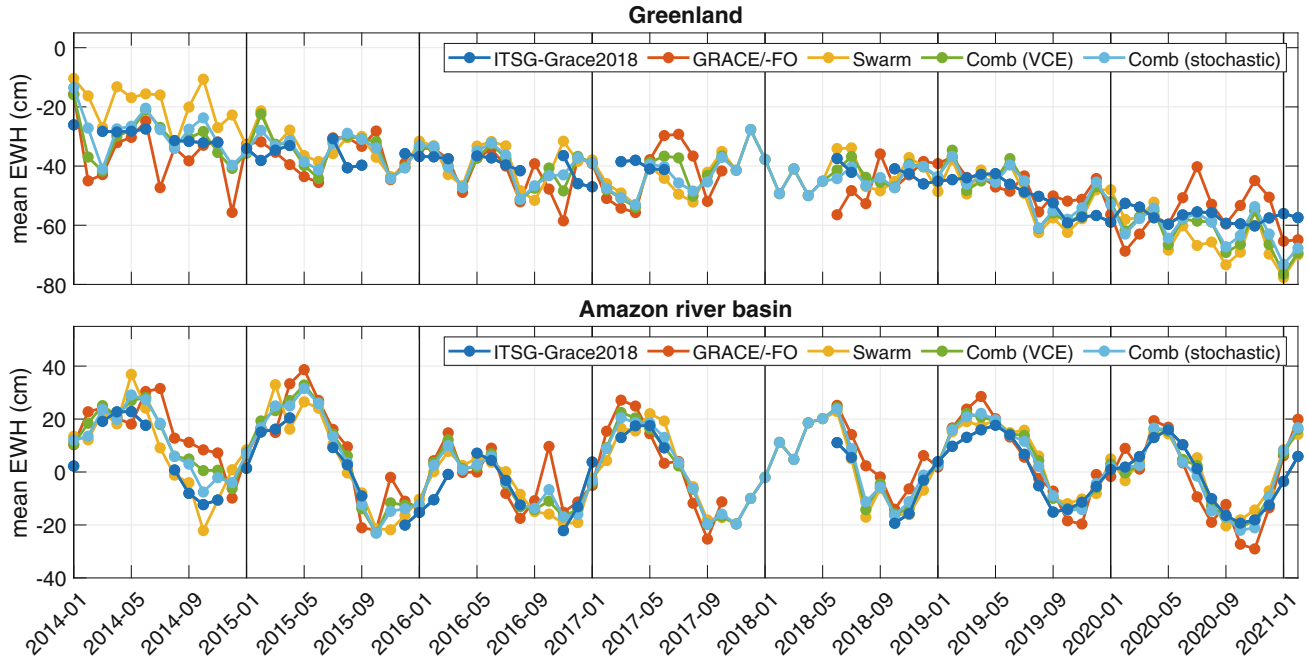


**Fig. 6** Time-variable gravity field signal (up to d/o 20) of the Greenland ice sheet (*top*) and the Amazon river basin (*bottom*) recovered from GRACE, GRACE-FO and Swarm kinematic positions and combina-

tions thereof in comparison to ITSG-Grace2018. Gaussian smoothing with a 500 km radius is applied

positions from 10 to 5 s is considered by applying a factor of  $\sqrt{2}$  to the standard deviations of the Swarm solutions starting from Jul 2014. The weighted combination is then defined by

$$\hat{x}_{nm} = \frac{1}{\sum_{i=1}^N w_{nm}^i} \sum_{i=1}^N w_{nm}^i x_{nm}^i. \quad (4)$$

## 5 Evaluation of Mass Trends and Variations

In this section, we use the monthly GPS-based gravity field solutions and their combinations to recover time-variable mass trends and variations. For this purpose, we analyze time series of mean equivalent water height (EWH) values over the Greenland ice sheet (area:  $\sim 2.07 \times 10^6 \text{ km}^2$ ) and the Amazon river basin (area:  $\sim 6.21 \times 10^6 \text{ km}^2$ ), regions with strong ice mass loss or high hydrology-induced seasonal variations. For assessment, a time series derived from monthly ITSG-Grace2018 solutions will serve as a superior reference.

The time series are derived as follows: (i) monthly SH coefficients are transformed to EWH (Wahr et al. 1998), subtracted by the signal of GOCO06s (Kvas et al. 2021) to remove the static gravity field part, and smoothed by a 500 km Gaussian filter, (ii) for each month, these SH coefficients are evaluated up to d/o 20 to compute EWH values on a regular  $0.5^\circ \times 0.5^\circ$  grid covering the selected regions, (iii) values are averaged over these regions to derive

**Table 2** RMS differences (cm) of GPS-based gravity field time series and their combinations with respect to ITSG-Grace2018 for Greenland and the Amazon river basin for Jan 2014 – Jun 2017 ( $T_1$ ) and Jun 2018 – Feb 2021 ( $T_2$ ). For comparison, values are also shown for a combination using the arithmetic average of the SH coefficients

	Greenland		Amazon	
	$T_1$	$T_2$	$T_1$	$T_2$
GRACE/-FO	8.23	8.07	9.95	7.70
Swarm	9.23	8.35	6.61	5.26
Comb (VCE)	7.40	7.18	7.14	5.11
Comb (stochastic)	7.06	6.43	6.15	5.23
Comb (average)	7.15	6.17	6.29	5.37

monthly area-weighted mean EWH estimates (i.e., weighted by the cosine of the latitude of the grid cells).

In Fig. 6, the time series of mean EWH values derived from the LEO gravity field solutions and combinations thereof are displayed and compared to ITSG-Grace2018. Results are shown for the Greenland ice sheet and the Amazon river basin at the top and bottom of Fig. 6, respectively. To quantify the performance of the time series, Table 2 provides RMS differences of their mean EWH values with respect to ITSG-Grace2018. For this purpose, the time series is split into two time spans,  $T_1$  (Jan 2014–Jun 2017) and  $T_2$  (Jun 2018–Feb 2021), representing the GRACE and GRACE-FO mission periods, respectively. Note that values in Table 2 are based solely on months with available ITSG-Grace2018 solutions, i.e., 31 months in each time span.

In the case of Greenland (Fig. 6, top), the mass loss represented by the ITSG-Grace2018 time series (blue curve) decreases from about  $-20$  to  $-60$  cm between 2014 and 2021, showing some smaller seasonal variations. Although the GPS-derived time series of GRACE/-FO (red curve) and Swarm (yellow curve) have a larger scatter, they provide a remarkably good long-term agreement with the K-band solution. At the beginning of the time span, the GRACE and Swarm solutions exhibit some larger discrepancies. The mean EWH values derived from Swarm are systematically larger than those of ITSG-Grace2018, which can be attributed to the problems in the early mission phase pointed out in Sect. 3. In contrast, the GRACE time series tends to produce smaller values than ITSG-Grace2018 in this period. Here, larger amplitudes follow a certain periodicity that is related to the 161-day cycle when the  $\beta$  angle of the GRACE orbit is crossing zero ( $\beta$ : angle between the orbital plane and the Earth-Sun direction). For these periods (e.g., in Feb, Jul, Dec in the case of 2014), it is known that the recovery of the  $C_{20}$  coefficient is affected in GRACE GPS and K-band solutions (Cheng and Ries 2017). However, in contrast to gaps in the K-band time series (mainly due to instrument shut-downs in these periods), the derived GRACE GPS-only time series is uninterrupted.

The benefit of a continuous time series can also be highlighted for the gap between GRACE and GRACE-FO, where GRACE GPS data can provide four additional monthly solutions at the end of the mission. This can be of particular interest as during the GRACE/-FO gap in 2017 and 2018, the ice mass loss trend in Greenland is significantly attenuated (cf. Sasgen et al. 2020). This temporary phenomenon is reflected by a roughly constant mean EWH value in the GPS-based time series of GRACE, and particularly Swarm.

While the RMS differences in Table 2 demonstrate that the GRACE time series is more consistent to the ITSG-Grace2018 signal in the time period  $T_1$  (8.23 cm compared to 9.23 cm for Swarm), the GPS-based GRACE-FO and Swarm time series achieve comparable results in period  $T_2$ , both obtaining RMS differences at a lower 8 cm-level. Here it is noticeable that starting with 2020 (when GPS flex power was activated), the scatter in the GRACE-FO time series significantly increases and the Swarm time series tends to gradually drift away from the ITSG-Grace2018 signal.

For the Amazon river basin (Fig. 6, bottom), the time-variable gravity signal of ITSG-Grace2018 shows strong seasonal variations between  $\pm 20$  cm, where maximum and minimum values are reached in spring and autumn, respectively. Compared to Greenland, the GPS-based LEO time series for the Amazon river basin are generally more consistent to ITSG-Grace2018, particularly in the case of Swarm, where RMS differences are significantly smaller (up to 37% in time period  $T_2$ , see Table 2). This can certainly be explained by the approximately three times larger area compared to

Greenland, where potential discrepancies in the EWH values average out to a larger extent. The only exception is the performance of the GRACE time series in  $T_1$ , attaining a large RMS difference of  $\sim 10$  cm.

Mostly at the beginning of the time span  $T_1$ , the Swarm and particularly the GRACE time series tend to over- or underestimate the peaks of the seasonal variations. Moreover, two prominent outliers are visible in the GRACE time series, in Nov 2015 and Oct 2016, where in the latter case the gravity field signal is impaired due to coverage problems in this month. During the first months of the GRACE/-FO data gap, when K-band data was unavailable but GPS data was still being collected, both LEO time series match quite well and produce a reasonable signal. While the GRACE-FO time series shows slightly larger amplitudes in the seasonal peaks, the Swarm time series is remarkably consistent to the ITSG-Grace2018 signal for the time period  $T_2$ , which is also indicated by the small RMS difference of 5.26 cm in Table 2.

The combined LEO gravity field time series are plotted by the green and light-blue curves in Fig. 6. Generally, it can be seen that both combinations are able to reduce the scatter around the ITSG-Grace2018 signal (e.g., in 2014 for Greenland) and effectively compensate for outliers of the individual solutions (e.g., in Oct 2016 for the Amazon river basin). The improved performance is also reflected by reduced RMS values in Table 2. In the case of Greenland, a decrease in the RMS differences of up to 11% and 20% can be detected for the VCE and stochastic combination, respectively, relative to the best individual time series. Due to the generally good performance of the Swarm time series in the case of the Amazon river basin, the additional value for a combination with the GRACE and GRACE-FO solutions is limited. Therefore, as visible from Table 2, improvements in the RMS differences with respect to the Swarm time series are confined to a maximum reduction of 3% and 7% for the VCE and stochastic combination, respectively.

In total, both combination strategies achieve comparable results with a preference for the stochastic combination that provides smaller residuals to ITSG-Grace2018 in 52% (Greenland) and 58% (Amazon river basin) of the months and outperforms the VCE combination in terms of RMS differences (except for  $T_2$  in the latter case). For comparison, Table 2 also provides RMS differences for a combination based on the arithmetic average of the SH coefficients. In the time span  $T_1$  its performance is in between the analyzed combinations, while in  $T_2$  the RMS difference is about 4% smaller (Greenland) or 2% larger (Amazon river basin) compared to the stochastic combination.

One of the most noticeable differences between the time series of the VCE and stochastic combinations can be seen for the Amazon river basin in Oct 2014. For this month, Fig. 7 shows the gridded EWH residuals of the different solutions



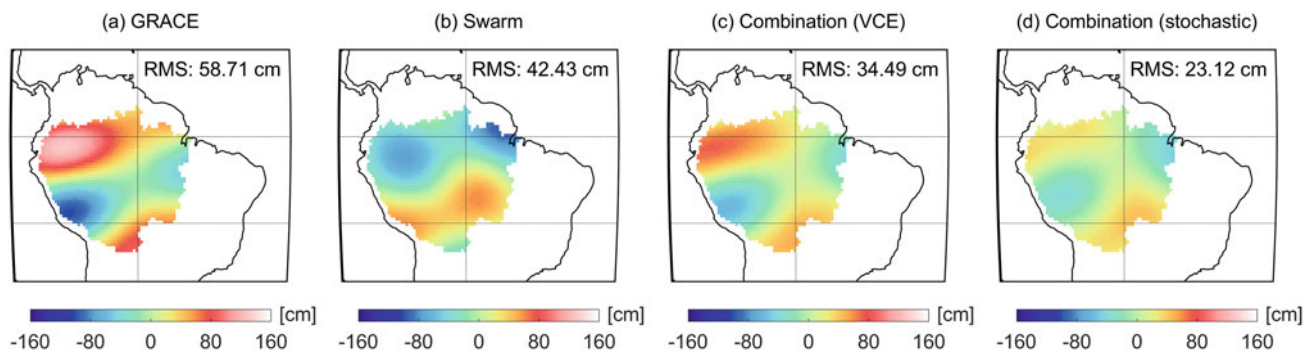


**Fig. 7** Equivalent water height differences (up to d/o 20) with respect to ITSG-Grace2018 of (a) GRACE and (b) Swarm GPS-based gravity field solution as well as their (c) VCE and (d) stochastic combination for Oct 2014 in the Amazon river basin. Gaussian smoothing with a 500 km

radius is applied. Additionally, for each solution the area-weighted RMS of the differences is specified, i.e., weighted by the cosine of the latitude

with respect to ITSG-Grace2018. Here, the GRACE-derived values reveal strong positive anomalies in the northern and southern part of the Amazon river basin, resulting in the high mean EWH value displayed in Fig. 6. Both of these anomalies are related to ionospheric-induced artifacts along the geomagnetic equator (cf. Fig. 3). In contrast, the Swarm solution is far less affected by the ionosphere, but also shows stronger positive and negative differences in the south and north of the Amazon river basin, respectively.

Concerning the combinations, it can be seen that they are both able to reduce the disturbances of the individual solutions. However, the VCE combination is apparently more driven by the GRACE solution as can be seen by the considerably large remaining residuals in the north of the Amazon river basin. This dominance of the GRACE solution can be seen as a consequence of the strong impact of the orbital altitudes on the VCE weights as shown in Fig. 5. Thus, this example illustrates the disadvantage of the VCE combination approach when using inhomogeneous data from different LEO satellites. In contrast, the stochastic combination is capable to strongly attenuate the anomalies originating from the GRACE and Swarm solutions. In terms of weighted RMS values with respect to ITSG-Grace2018, the stochastic combination provides a 30 % smaller value, underlining that this procedure is more robust against outliers.

(d/o 20). Moreover, it was demonstrated that a combination of the time series provides a further improved estimation of time-variable signals, indicated by a reduction of RMS differences by ~10 % to 20 % with respect to a inter-satellite ranging solution. Here, it can be pointed out that the VCE combination at solution level as applied for COST-G is of limited use for a multi-mission scenario, as derived weights are mainly driven by the different altitudes of the LEOs. This might be related to the used simple case where the normal matrix is equal to the identity matrix, which cannot properly reflect differences in the geometry of LEO missions. In comparison, a combination that takes into account the standard deviations (formal errors) of the gravity field coefficients, turned out to cope better with this setting and underlines the importance of a degree-dependent weighting.

As a next step, we aim to extend our monthly GRACE/-FO time series and include gravity field information derived from additional LEO satellites, e.g., from the Sentinel constellation. Further improvements of the current GRACE time series can be expected by a refinement of the used kinematic orbits, e.g., considering measures to mitigate the influence of ionospheric disturbances would be beneficial for the years 2014 and 2015. Beside a classical screening as currently done for the operational Swarm orbits, advanced weighting techniques might also be considered (cf. Schreiter et al. 2019) that have demonstrated their advantage, e.g., in the GOCE GPS-based gravity field recovery (Grombein et al. 2019). Finally, we will focus on the combination of the GPS-based gravity field time series at normal equation level.

## 6 Conclusions and Outlook

In this paper, we use GPS-based kinematic LEO orbit positions of the GRACE, GRACE-FO and Swarm missions to recover time-variable gravity field signals. By studying mass variations in Greenland and the Amazon river basin, the GPS-based gravity field time series are in good agreement with those derived from inter-satellite ranging and are able to fill gaps reasonably at spatial scales of about 1000 km

**Acknowledgements** The authors would like acknowledge two anonymous reviewers for their comments, which helped to improve the manuscript. This research was supported by the European Research Council under the grant agreement no. 817919 (project SPACE TIE). All views expressed are those of the authors and not of the European Research Council. Calculations in this study were performed on UBELIX, the HPC cluster at the University of Bern.

## References

- Arnold D, Jäggi A (2020a) AIUB GRACE kinematic orbits, release 01. Astronomical Institute, University of Bern. <https://doi.org/10.48350/158372>
- Arnold D, Jäggi A (2020b) AIUB GRACE-FO kinematic orbits, release 01. Astronomical Institute, University of Bern. <https://doi.org/10.7892/boris.147231>
- Arnold D, Jäggi A (2021) AIUB Swarm kinematic orbits, release 03. Astronomical Institute, University of Bern. <https://doi.org/10.48350/158373>
- Baur O, et al. (2014) Comparison of GOCE-GPS gravity fields derived by different approaches. *J Geod* 88(10):959–973. <https://doi.org/10.1007/s00190-014-0736-6>
- Beutler G, Jäggi A, Mervart L, Meyer U (2010) The celestial mechanics approach: theoretical foundations. *J Geod* 84(10):605–624. <https://doi.org/10.1007/s00190-010-0401-7>
- Bock H, Dach R, Jäggi A, Beutler G (2009) High-rate GPS clock corrections from CODE: support of 1 Hz applications. *J Geod* 83(11):1083–1094. <https://doi.org/10.1007/s00190-009-0326-1>
- Cheng M, Ries J (2017) The unexpected signal in GRACE estimates of  $C_{20}$ . *J Geod* 91(8):897–914. <https://doi.org/10.1007/s00190-016-0995-5>
- Dach R, et al. (2009) GNSS processing at CODE: status report. *J Geod* 83(3–4):353–365. <https://doi.org/10.1007/s00190-008-0281-2>
- Dach R, Lutz S, Walser P, Fridez P (eds) (2015) Bernese GNSS Software Version 5.2, Documentation. Astronomical Institute, University of Bern. <https://doi.org/10.7892/boris.72297>
- Dahle C, Arnold D, Jäggi A (2017) Impact of tracking loop settings of the Swarm GPS receiver on gravity field recovery. *Adv Space Res* 59(12):2843–2854. <https://doi.org/10.1016/j.asr.2017.03.003>
- Friis-Christensen E, Lühr H, Knudsen D, Haagmans R (2008) Swarm – an Earth observation mission investigating geospace. *Adv Space Res* 41(1):210–216. <https://doi.org/10.1016/j.asr.2006.10.008>
- Grombein T, Arnold D, Jäggi A (2019) GPS-based gravity field recovery from reprocessed GOCE precise science orbits. In: *Geophys Res Abstr vol 21, EGU 2019, Vienna*. <https://doi.org/10.7892/boris.143198>
- Grombein T, Arnold D, Jäggi A (2021) Time-variable gravity field recovery from reprocessed GOCE precise science orbits. 43rd COSPAR SA, Sydney. <https://doi.org/10.48350/152967>
- Guo X, Ditmar P, Zhao Q, Xiao Y (2020) Improved recovery of temporal variations of the Earth's gravity field from satellite kinematic orbits using an epoch-difference scheme. *J Geod* 94(8):69. <https://doi.org/10.1007/s00190-020-01392-6>
- Huang J, Véronneau M (2013) Canadian gravimetric geoid model 2010. *J Geod* 87(8):771–790. <https://doi.org/10.1007/s00190-013-0645-0>
- Huang W, et al. (2022) Estimation of GPS transmitter antenna phase center offsets by integrating space-based GPS observations. *Adv Space Res* 69(7):2682–2696. <https://doi.org/10.1016/j.asr.2022.01.004>
- Jäggi A, Hugentobler U, Beutler G (2006) Pseudo-stochastic orbit modeling techniques for low-Earth orbiters. *J Geod* 80(1):47–60. <https://doi.org/10.1007/s00190-006-0029-9>
- Jäggi A, et al. (2009) Phase center modeling for LEO GPS receiver antennas and its impact on precise orbit determination. *J Geod* 83(12):1145–1162. <https://doi.org/10.1007/s00190-009-0333-2>
- Jäggi A, Bock H, Meyer U, Beutler G, van den IJssel J (2015) GOCE: assessment of GPS-only gravity field determination. *J Geod* 89(1):33–48. <https://doi.org/10.1007/s00190-014-0759-z>
- Jäggi A, et al. (2016) Swarm kinematic orbits and gravity fields from 18 months of GPS data. *Adv Space Res* 57(1):218–233. <https://doi.org/10.1016/j.asr.2015.10.035>
- Jäggi A, et al. (2020) International combination service for time-variable gravity fields – Start of operational phase and future perspectives. In: *IAG Symp*. [https://doi.org/10.1007/1345\\_2020\\_109](https://doi.org/10.1007/1345_2020_109)
- Jean Y, Meyer U, Jäggi A (2018) Combination of GRACE monthly gravity field solutions from different processing strategies. *J Geod* 92(11):1313–1328. <https://doi.org/10.1007/s00190-018-1123-5>
- Kvas A, et al. (2019) ITSG-Grace2018: overview and evaluation of a new GRACE-only gravity field time series. *J Geophys Res* 124(8):9332–9344. <https://doi.org/10.1029/2019JB017415>
- Kvas A, et al. (2021) GOCO06s – a satellite-only global gravity field model. *Earth Syst Sci Data* 13(1):99–118. <https://doi.org/10.5194/essd-13-99-2021>
- Landerer FW, et al. (2020) Extending the global mass change data record: GRACE Follow-On instrument and science data performance. *Geophys Res Lett* 47(12):e2020GL088306. <https://doi.org/10.1029/2020GL088306>
- Meyer U, Jäggi A, Beutler G, Bock H (2015) The impact of common versus separate estimation of orbit parameters on GRACE gravity field. *J Geod* 89(7):685–696. <https://doi.org/10.1007/s00190-015-0807-3>
- Meyer U, et al. (2019) Combination of GRACE monthly gravity fields on the normal equation level. *J Geod* 93(9):1645–1658. <https://doi.org/10.1007/s00190-019-01274-6>
- Richter H, et al. (2021) Reconstructing GRACE-type time-variable gravity from the Swarm satellites. *Sci Rep* 11(2):1117. <https://doi.org/10.1038/s41598-020-80752-w>
- Sasgen I, et al. (2020) Return to rapid ice loss in Greenland and record loss in 2019 detected by the GRACE-FO satellites. *Commun Earth Environ* 1(8). <https://doi.org/10.1038/s43247-020-0010-1>
- Schaer S, et al. (2021) The CODE ambiguity-fixed clock and phase bias analysis products: generation, properties, and performance. *J Geod* 95(7):81. <https://doi.org/10.1007/s00190-021-01521-9>
- Schreiter L, Arnold D, Sterken V, Jäggi A (2019) Mitigation of ionospheric signatures in Swarm GPS gravity field estimation using weighting strategies. *Ann Geophys* 37(1):111–127. <https://doi.org/10.5194/angeo-37-111-2019>
- Steigenberger P, Thörlert S, Montenbruck O (2019) Flex power on GPS Block IIR-M and IIF. *GPS Solut* 23(1):8. <https://doi.org/10.1007/s10291-018-0797-8>
- Švehla D, Rothacher M (2005) Kinematic precise orbit determination for gravity field determination. In: *IAG Symp 128*, pp 181–188. [https://doi.org/10.1007/3-540-27432-4\\_32](https://doi.org/10.1007/3-540-27432-4_32)
- Tapley BD, Bettadpur S, Watkins M, Reigber C (2004) The gravity recovery and climate experiment: Mission overview and early results. *Geophys Res Lett* 31(9):L09607. <https://doi.org/10.1029/2004GL019920>
- Teixeira da Encarnação J, Visser P (2019) TN-03: Swarm models validation. <https://doi.org/10.13140/RG.2.2.33313.76640>
- Teixeira da Encarnação J, et al. (2020) Description of the multi-approach gravity field models from Swarm GPS data. *Earth Syst Sci Data* 12(2):1385–1417. <https://doi.org/10.5194/essd-12-1385-2020>
- Teunissen PJ, Amiri-Simkooei A (2008) Least-squares variance component estimation. *J Geod* 82(2):65–82. <https://doi.org/10.1007/s00190-007-0157-x>
- van den IJssel J, Forte B, Montenbruck O (2016) Impact of Swarm GPS receiver updates on POD performance. *Earth Planets Space* 68(1):85. <https://doi.org/10.1186/s40623-016-0459-4>
- Wahr J, Molenaar M, Bryan F (1998) Time variability of the Earth's gravity field: hydrological and oceanic effects and their possible detection using GRACE. *J Geophys Res* 103(B12):30205–30229. <https://doi.org/10.1029/98JB02844>
- Weigelt M, et al. (2013) Time-variable gravity signal in Greenland revealed by high-low satellite-to-satellite tracking. *J Geophys Res* 118(7):3848–3859. <https://doi.org/10.1002/jgrb.50283>
- Zhong L, Sósnička K, Weigelt M, Liu B, Zou X (2021) Time-variable gravity field from the combination of HLSST and SLR. *Remote Sens* 13(17):3491. <https://doi.org/10.3390/rs13173491>

**Open Access** This chapter is licensed under the terms of the Creative Commons Attribution 4.0 International License (<http://creativecommons.org/licenses/by/4.0/>), which permits use, sharing, adaptation, distribution and reproduction in any medium or format, as long as you give appropriate credit to the original author(s) and the source, provide a link to the Creative Commons license and indicate if changes were made.

The images or other third party material in this chapter are included in the chapter's Creative Commons license, unless indicated otherwise in a credit line to the material. If material is not included in the chapter's Creative Commons license and your intended use is not permitted by statutory regulation or exceeds the permitted use, you will need to obtain permission directly from the copyright holder.





# Topographic Gravity Field Modelling for Improving High-Resolution Global Gravity Field Models

E. Sinem Ince, Christoph Förste, Oleh Abrykosov, and Frank Flechtner

## Abstract

The global gravitational potential generated by the attraction of the Earth's topographic masses has been computed in spectral domain. The mass-source information is provided by the 1 arcmin resolution Earth2014 relief model and four averaged density values for rock, ocean, lake, and ice areas. The topography and bathymetry are split into confocal ellipsoidal shells of a defined thickness. Based on the provided mass-source information, the gravitational potential is expanded for each shell and then summed up to represent the complete gravitational potential of the topography (and bathymetry). In this contribution, we present the impact of different shell thicknesses to the model accuracy and computation time. Moreover, we expanded our topographic gravity field model up to spherical harmonic degree and order 5,494. Such short scale mass information represented by the topography can be used to complement high-resolution combined static gravity field models for the very high-frequency components of the gravity field. As an example, we enhanced (augmented) EIGEN-6C4 model with the high frequency components retrieved from the topographic model. The deflections of vertical values computed from the augmented model are compared w.r.t. ground truth observations in Germany, Southern Colorado and Iowa (USA) which suggest as expected a considerable improvement over rugged mountainous regions and comparable residuals in areas of moderate topography.

## Keywords

Enhanced (augmented) gravity field models · High resolution global gravity field modelling · Topographic gravity field

## 1 Introduction

High-resolution global gravity field models (GGMs) retrieved from combination of satellite-derived observations and terrestrial gravity measurements represent the finest details of the gravitational field. Spatial resolution of such models reaches up to 9 km in EGM2008 (Pavlis et al. 2012) and EIGEN-6C4 (Förste et al. 2014) which are prominent examples of high-resolution combined global

gravity field models. Combined global gravity field models can be enhanced by modelling the omitted part of the signal (or the very high frequency components of the gravity field) via (gravity) forward modelling techniques. For example, a recently published model XGM2019e delivers an enhanced spatial resolution of about 3.6 km based on gravity information derived from topography (Zingerle et al. 2020). Forward modelling has been commonly used in geophysics (Götze and Lahmeyer 1988; Shin et al. 2006) and planetary science (Wieczorek and Simons 2005; Wieczorek 2007). Recently, the technique is used in geodesy as well not only to retrieve high frequency components of the gravity field and to enhance global gravity field models up to very high degree and order (d/o) expansions (Hirt et al. 2016),

E.S. Ince (✉) · C. Förste · O. Abrykosov · F. Flechtner  
Helmholtz Centre Potsdam German Research Centre for Geosciences,  
GFZ Potsdam, Potsdam, Germany  
e-mail: [elmas.sinem.ince@gfz-potsdam.de](mailto:elmas.sinem.ince@gfz-potsdam.de)

but also to approximate the gravity field in areas with no or limited gravity measurements.

The calculation of forward models can be performed in spatial or spectral domain which have different pros and cons. The reader is referred to literature for different state-of-the-art examples (e.g., Grombein et al. 2016; Rexer et al. 2016; Root et al. 2016; Tenzer et al. 2016). Topographic gravity field models are used: (a) to enhance the representation of the high frequency components of the gravity field (reducing omission error), (b) to compute the topographic attraction which is then removed from gravity measurements helping to investigate the residual signal, and (c) to interpolate and predict gravity values in regions that have sparse or no gravity measurements. Moreover, topographic gravity field models contribute to enhance the figure of the Earth and provide insight to subsurface mass-density distribution when used together with actual gravity measurements and other datasets (e.g., seismic measurements).

In recent geodetic applications, the application of a topographic gravity field is particularly important for the definition and determination of a worldwide unified height system. This application area is one of the focus topics of the Global Geodetic Observing System (GGOS, <https://ggos.org>) of the International Association of Geodesy (IAG) which is on the unification of height systems and realization of the International Height Reference System (IHRs). Such a reference system can only be achieved via the contribution of high-resolution topographic gravity field models especially over the areas that are lacking gravity observations (Sánchez et al. 2021).

In this contribution, we use a multi-layer approach and consider different average density values for different layers. Starting from the lowermost ellipsoid up to the bounding ellipsoid, the calculations are defined for subsequent shells whose thickness has an important effect on the final product. Our primary focus is to advance our preliminary work (Ince et al. 2020) on the reduction of the omission error and increase the resolution of the most recent high-resolution combined static global gravity field models via enhancing the spatial and spectral content of the topographic model. We also investigate the impact of the shell thickness in the computed products and determine an optimum thickness interval for the computations. Based on our previous study (Ince et al. 2020), comparisons of an augmented (enhanced) version of EIGEN-6C4 w.r.t. external ground-truth datasets clearly indicate the improvements that are due to the contribution of the topographic model. The ground-truth data include GNSS/levelling-derived geoid undulations, terrestrial gravity data, and deflections of the vertical (DoV) measurements. The results indicated improvement in terms of root mean square (RMS) and mean values of up to 30% which supports the contribution of the forward model in the medium and high-frequency interval that are applicable to small spatial

scale gravity features. In this paper, we present the analysis of the impact of different shell thicknesses and the expansion of the topographic gravity field model from spherical harmonic degree 3,660 up to 5,494. Corresponding evaluation results are provided based on high-quality deflections of vertical data available in Germany and recently published datasets from southern Colorado and Iowa, USA.

## 2 Methodology

In order to compute topographic potentials, we formulate an ellipsoidal approximation in spectral domain in which we can introduce different mass layers as input. In the current study, we use rock, ocean, lake and ice layers as provided by the shape files of Earth2014 (Hirt and Rexer 2015). Moreover, we subdivide the topography and bathymetry into shells and compute the potential of each shell on the bounding ellipsoid that is defined outside of all the masses. Once the density is known (estimated from the combination of four layers mentioned above) for each grid point within each shell, especially over the regions of land-coast transition, ellipsoidal surface harmonic analysis of the laterally varying density values can be performed. The details of the methodology and formulae used in this paper are given in Ince et al. (2020).

The topographic potential is at first represented in terms of ellipsoidal harmonic coefficients and then transformed into spherical harmonic coefficients. For this purpose, the ellipsoidal harmonic coefficients are represented in terms of density integrals which can be derived once the series expansion of the reciprocal distance is formulated (Hobson 1931; Ince et al. 2020). These coefficients are computed by integrating lateral density variations derived from the four averaged density values within a sequence of thin volumetric shells bounded by confocal ellipsoids for lower and upper bounds of the shells. Within each shell, the density is assumed to vary only in the lateral direction. That means, from cell to cell of a corresponding grid the density value can change. For each shell, the density can then be expanded into series of surface harmonics.

In the final stage, the ellipsoidal harmonic coefficients of the potential are computed, which are sums of the coefficients of each individual shell. In our analysis, the computations are performed to degree and order 10,800 that corresponds to the resolution of grids of the input data Earth2014 (1 arcmin). To avoid spectral leakage and aliasing problems, the computed ellipsoidal potential coefficients have been set to zero above degree 3,600 and 5,400, respectively. Finally, Jekeli's transformation is applied to retrieve the spherical harmonic coefficients below or equal to 3,660 and 5,494, respectively from the ellipsoidal harmonic coefficients of these example models.

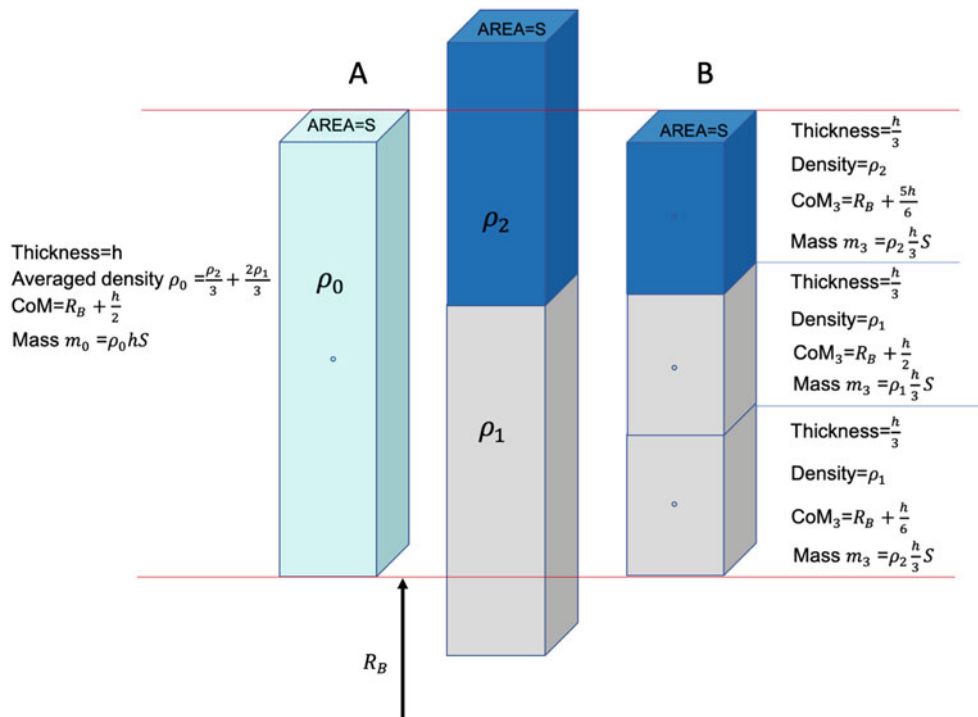


**Fig. 1** Representation of different density and thickness mass sources in a simplified form. Note that the middle compartment represents the vertical density distribution of the original mass source, the left compartment represented as A is the (assumed) condensed density

distribution with shell thickness  $h$ , and the right compartment(s) represented as B is the density distribution with three shells of thickness  $h/3$ . Note that CoM refers to center of mass of the respective compartment, and  $h$  and  $h/3$  are selected arbitrary for the example

The thickness of the shells mentioned above play a role in the computation efficiency and accuracy of the outcomes. Therefore, different shell thicknesses have been tested whose results are presented in the following section. For visual simplification purposes, the confocal ellipsoidal shells (see Fig. 2 in Ince et al. 2020) that have been used in our calculations are represented as compartment blocks with different thickness and density values assigned (see Fig. 1). The calculation of the topographic potential between the lower and upper bounding surfaces (red lines) of the compartment can be performed by applying two scenarios using ellipsoidal confocals: A) An averaged condensed density value assigned to the entire compartment of interest (single layer approach), or B) Different density and height (shape) information assigned to the same compartment defined in A) (multi-layer approach). The topographic potentials computed from different shell thicknesses and respective density values assigned are not equal for A and B. Such differences, based on the approach applied, must be investigated and considered in the calculations. The current study presents the result obtained from multi-layer approach and thinner shell thickness (method B) which are derived from the provided four averaged densities. It should be noted that future studies should preferably aim to include high spatial resolution laterally and radially varying density models and

corresponding elevation information than using just average four density values.

In summary, the results retrieved from using one condensed density value and one thick shell for the entire compartment (A) are different and underpowered (as explained later) than the results that are retrieved by using different density values (averaged values in our case) and smaller shell thicknesses (B). How small the shell thicknesses need to be is investigated in the current study by using respective density values under consideration of the knowledge of the type of the shell (e.g., rock or ice) that are retrieved from the Earth2014 shape files. The current study uses Method B since it is more realistic as shown in the following section.

### 3 Analysis

The analyses performed in this section are twofold. The first one is the investigation of the reduction of the omission error in the combined GGM based on the further expansion of the topographic gravity field models in terms of spectral and spatial resolution. More precisely, using the forward modelling technique explained above we increased the spectral and spatial content of our preliminary topographic gravity field model ROLI (Rock, Ocean, Lake, Ice) from spherical

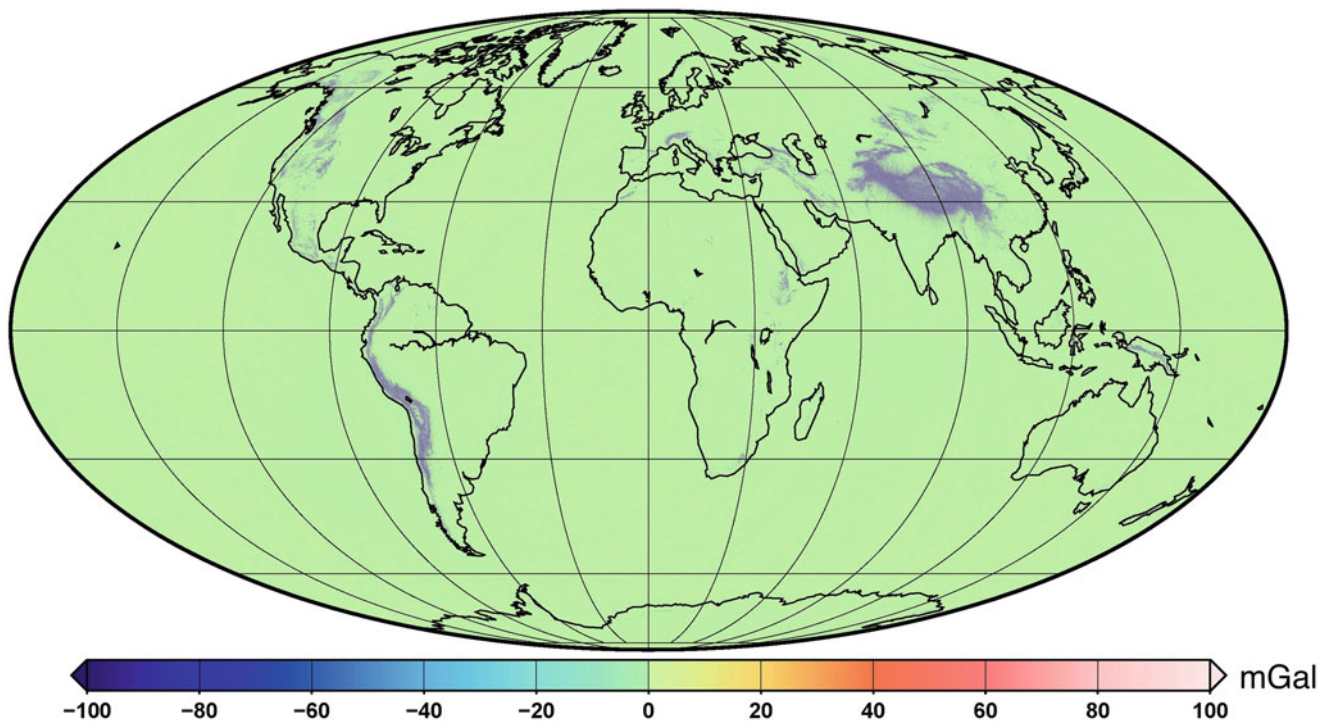


**Fig. 2** The differences between the enhanced models of maximum degree 3,660 and 5,494 in terms of gravity disturbance (in mGal) computed on the Earth's surface [mean value: 30.37 mGal]

harmonic degree 3,660 up to 5,494 that corresponds to about 5.4 km and 3.6 km spatial resolution, respectively. The contribution is presented in Fig. 2. It is clearly visible that high mountainous areas suffer from the omitted signal content. Currently available state-of-the-art GGMs in these areas can be improved via high resolution topographic gravity field models. However, the visible leakage problem needs to be investigated in more detail. The true gravity field of the topography can be approximated better with a higher degree expansion model that requires high-resolution density and elevation content. Himalayas, Andes, Mexico, North and East Anatolia, and Canadian and American Rockies are prominent examples that will benefit from the extension from degree 3,660 to degree 5,494.

The second investigation performed is on the impact of the shell thickness in the calculation procedure. Calculation from an “optimum” thickness should deliver precise results and be affordable by the available computing sources. In our analyses, we tested 5 m, 10 m, 15 m, 20 m, 30 m, 60 m, and 120 m shell thickness and present the results in terms of degree variances in Fig. 3. The computation times of the calculations using 5 m and 30 m thick shells are about 38 and 7 h, respectively. These computations were done in a parallelized way using 256 Cores on a Linux compute node cluster consisting of 2.10 GHz Intel Xeon Gold 6230 CPUs.

The example shows that the power of the signal decreases as the shell thicknesses increase which was already proven by the simplified example presented in Fig. 1. Ellipsoidal harmonic coefficients of the potential of each shell (see Ince et al. 2020) can be treated as a result of vertical numerical integration between corresponding lower and upper boundaries (confocal ellipsoids) of the shell using the trapezoidal rule. Thus, generally, the smaller the integration interval (thickness of shells) the smaller the integration error. This consideration can serve as a crude explanation of the above mentioned decrease of the power of the signal when the shell thickness increases. Therefore, “thin enough” shell thickness needs to be selected for the calculations followed in our algorithm for a realistic and more accurate representation of the potential.

Based on the comparisons in terms of geoid undulation, results computed from 5 m and 10 m thickness mass sources coincide with the reference EIGEN-6C4 spectrum in Fig. 3. A reliable topographic model is expected to provide similar signal content with EIGEN-6C4 in the medium to high frequency bandwidth interval. The results of the other thicknesses included in our analyses are underpowered and shifted away from the expected results. The differences between the 5 m and 10 m shell thicknesses are presented in Fig. 4. These differences are very small in terms of geoid undulation and may not be meaningful considering the current developments

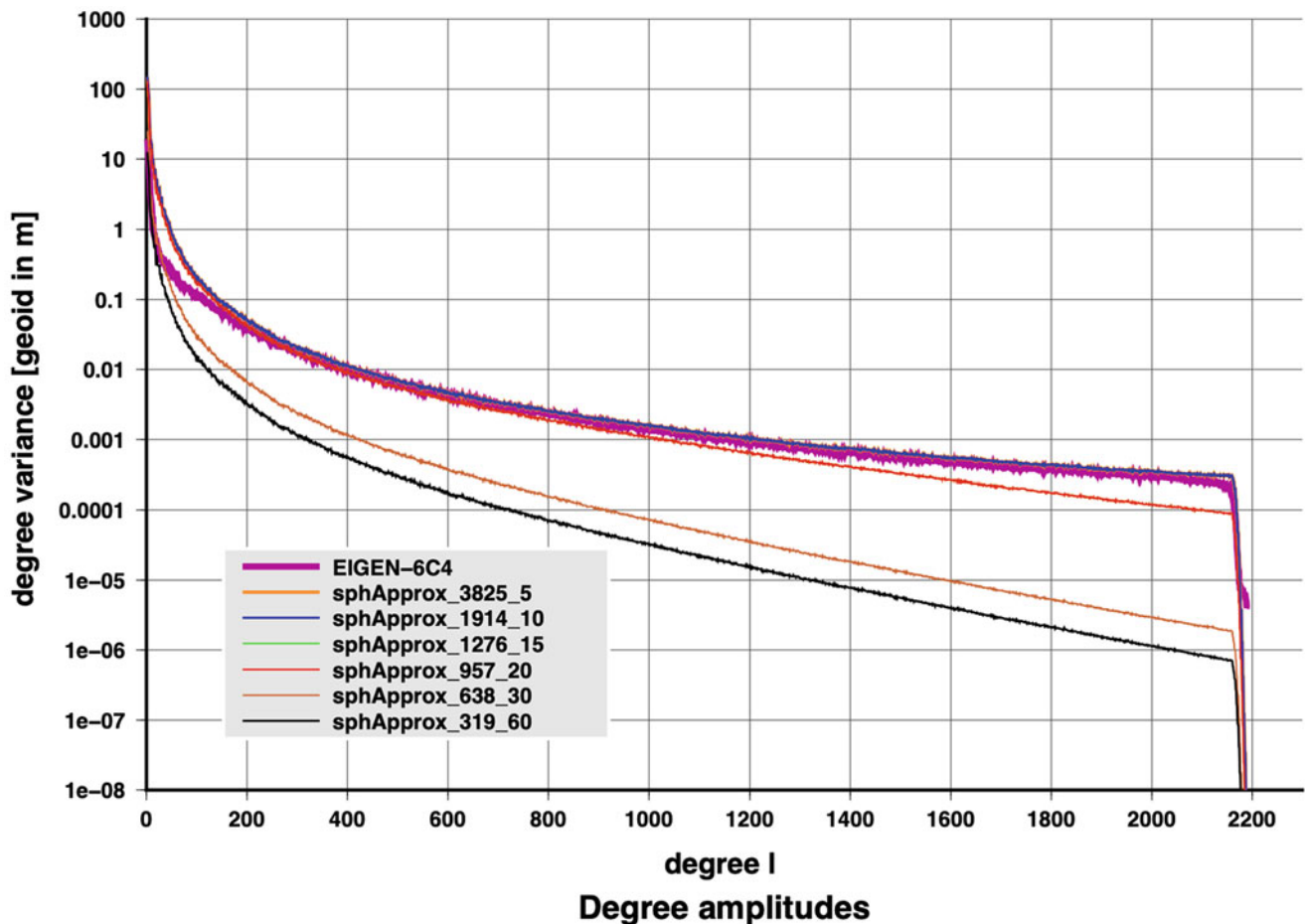


**Fig. 3** Degree variance results of different shell thicknesses (5, 10, 15, 20, 30 and 60 m), and respective number of shells (3,825, 1,914, 1,276, 957, 638, 319) are represented in terms of geoid undulation. Note that the thicker shell thicknesses result in underpowered signal

in the field of height systems. However, gravity anomalies of the same representation might be meaningful in regional to local studies. Therefore, we used 5 m shell thickness in our calculations.

#### 4 Evaluation of the Enhanced Model w.r.t. Ground Data

Our preliminary model (Abrykosov et al. 2019) was evaluated against different sets of ground truth data and global models. Terrestrial gravity measurements, GNSS/Levelling-derived geoid undulations and deflections of the vertical were among the ground truth data included. In this study, we evaluate the new enhanced model using deflections of the vertical only since (a) astrogeodetic vertical deflections retrieved from astronomical observations are assumed to contain the full signal spectrum (Torge 2001) and (b) it is a type of dataset that is very sensitive to the high frequency components of the gravity field. Therefore, provided that they fulfill the requirements in terms accuracy and spatial

extent such datasets are very reliable to quantify the enhancement in the augmented models and the reduction of the signal omission error in the combined high-resolution GGMs.

The deflections of the vertical data from Germany used in this study are provided by Voigt (2013) and are the same used in Ince et al. (2020). In addition, we included the deflections of vertical measured in the rugged terrain of Colorado during the Geoid Slope Validation Survey in 2017 (GSVS17) published by van Westrum et al. (2021) and in the moderate topography of Iowa during the GSVS14 (Wang et al. 2017). The German measurements were taken along two profiles of different topographic features of the North-South and East-West Germany with a spacing of 3–4 km. As shown in Fig. 5a, North-South profile consists of 216 measurement points, whereas the East-West profile consists of 154 measurement points. The Colorado data shown in Fig. 5b. on the other hand include 222 observation points and are sampled at about 1.6 km interval. The measurement points over Iowa region are mainly located along a highway and consist of 204 survey benchmarks. The observations in Germany which have an accuracy level of about 0.1'' fulfill



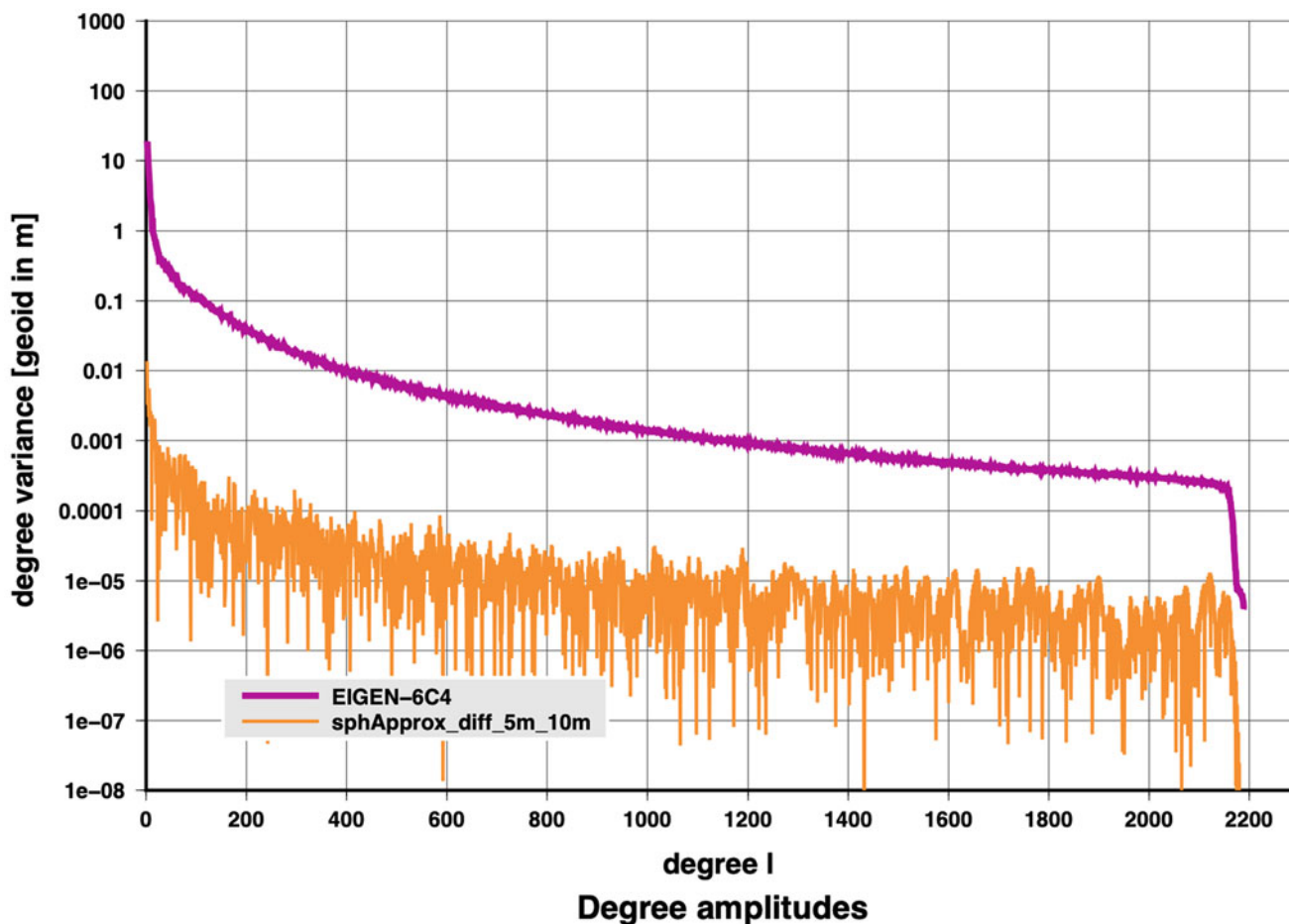


**Fig. 4** Degree variance differences of 5 m and 10 m shell thickness in terms of geoid undulation

the requirements of our evaluation purpose (Voigt 2013). The newly measured DoVs in the Colorado region have an observational accuracy of  $0.04''$  and are one of the best high-quality ground truth data that can be used to validate our enhanced and topographic gravity field models. Also, these three test areas have different topographical characteristics which help to evaluate our enhanced models consistently.

The comparisons are performed for EIGEN-6C4, and two enhanced EIGEN-6C4 models up to degree 3,660 and 5,494, respectively. High-frequency components of the Earth's gravity field that are smaller than 5 arcmin are not represented in the EIGEN-6C4 due to the truncation of the model at degree 2,190. Since the topography generates a considerable part of the deflection of vertical signal (Forsberg and Tscherning 1981), the omitted signal components are retrieved from topographic gravity field models and used in the enhancement of EIGEN-6C4. According to Torge (1981), such omission errors can reach up to a few arc seconds in the case DoVs.

Based on our comparisons w.r.t. DoV measurements in Germany and the USA, significant improvement is expected in mountainous regions. The differences between the model

derived DoVs are compared with the ground truth observations in the three areas of different topographic characteristics. The distribution of the residuals derived from EIGEN-6C4 and two enhanced models with respect to the elevation of the measurement points are represented for the east-west ( $\eta$ ) and north-south ( $\xi$ ) components of the deflection of verticals for Germany, Colorado, and Iowa in Figs. 6, 7 and 8, respectively. As expected, the residuals increase with increasing elevation which reach 8 arcsec in mountainous Colorado, for example.

The RMS values for the three regions are summarised in Tables 1, 2, and 3. The residuals computed w.r.t EIGEN-6C4 reflect the signal omission and commission error in the global gravity field models as well the uncertainty of the ground truth vertical deflections. The residuals are smaller for the enhanced models since the omission error due to the high frequency signals is reduced by augmenting topographical gravity field information. The residual RMS values are reduced for the expanded models by up to 40% in the  $\xi$  component of the North-South Profile in Germany (see Table 1) and over 30% for the  $\eta$  component in Colorado (see Table 2) which is a clear indication that the high frequencies

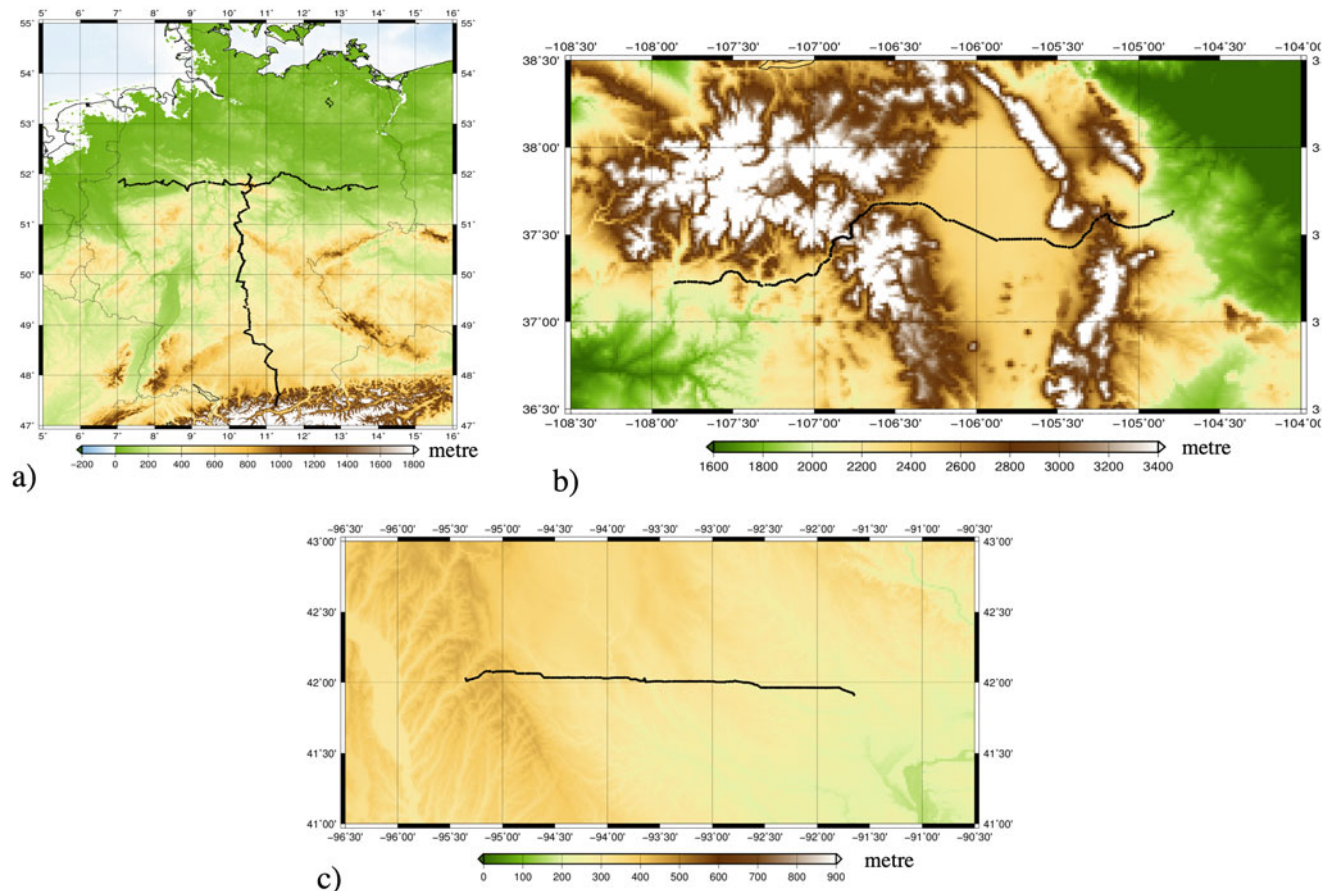


**Fig. 5** The distribution of the measurement points in (a) Germany (East-West and North-South profiles), (b) Colorado region and (c) Iowa, in the USA. Note the differences in the elevation characteristics from flat-moderate to rugged

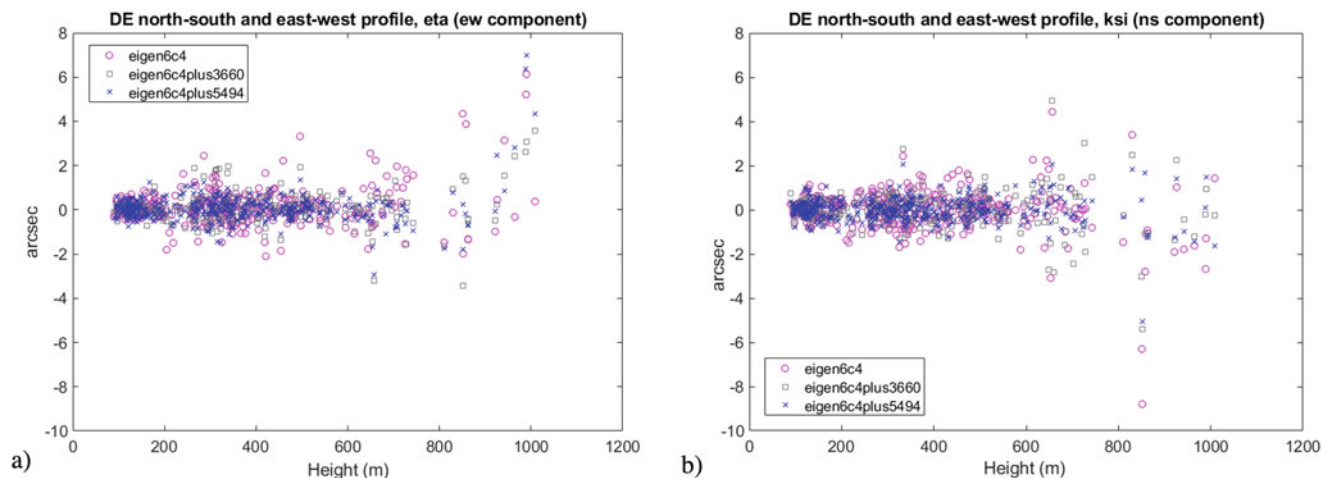


**Fig. 6** The distribution of the residuals between the ground truth astronomical DoVs and the DoVs computed from EIGEN-6C4, and the two enhanced models in Germany for (a)  $\eta$  (b)  $\xi$

of global gravity field models such as EIGEN-6C4 can be significantly improved using forward modelled topographic gravity field models. Further improvement is visible in Germany between the augmented models up to degree 3,660

and 5,494, respectively but it also points to inconsistencies especially in  $\eta$ . For the flat and moderate topography, the topographic gravity field models are not expected to improve the GGM representation drastically. Therefore, the residuals

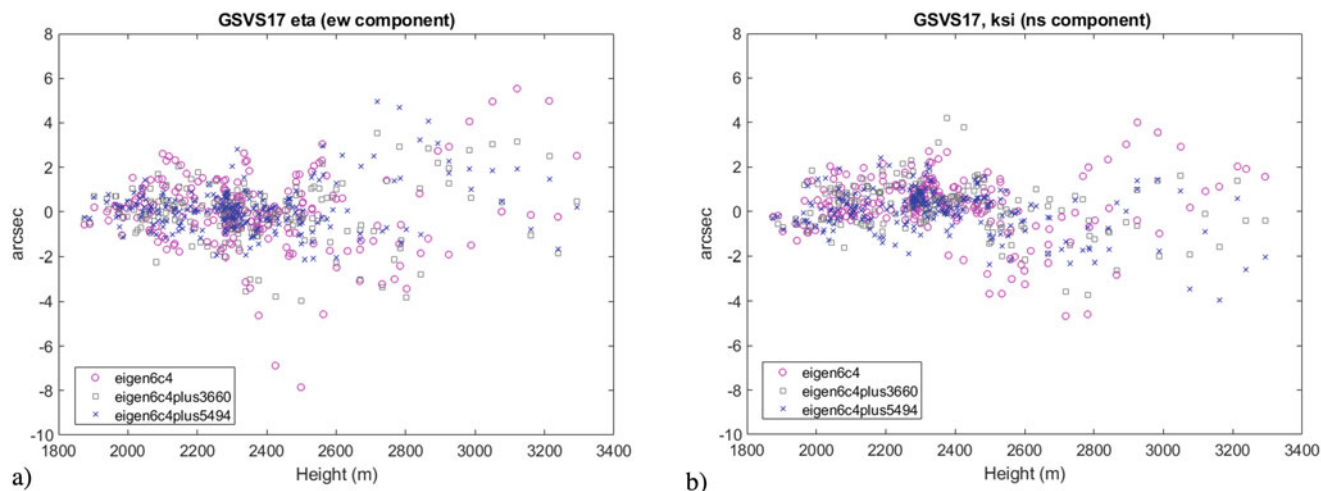


**Fig. 7** The distribution of the residuals between the ground truth astronomical DoVs and the DoVs computed from EIGEN-6C4, and the two enhanced models in Colorado region for (a)  $\eta$  (b)  $\xi$

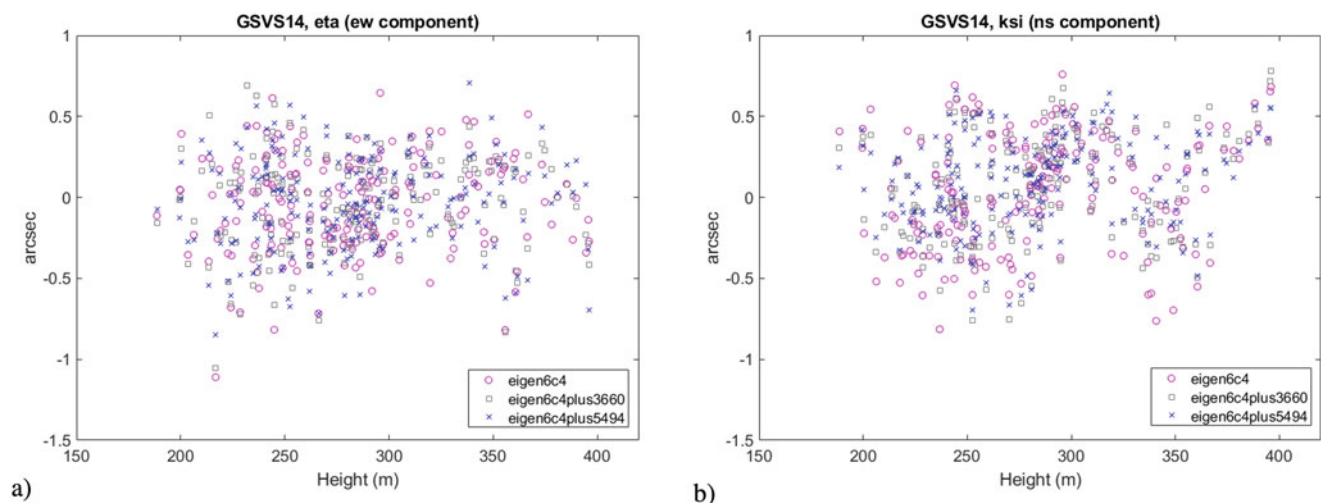


**Fig. 8** The distribution of the residuals between the ground truth astronomical DoVs and the DoVs computed from EIGEN-6C4, and the two enhanced models in Iowa for (a)  $\eta$  (b)  $\xi$

**Table 1** The RMS values of the residual deflections of vertical between EIGEN-6C4, the expanded model EIGEN-6C4.2000.2100.exp.3660, EIGEN-6C4.2000.2100.exp.5494, and the terrestrial astrogeodetic measurements in Germany (Voigt 2013).

The corresponding numbers of the measurement points are given in brackets. The reader is advised to use the recomputed RMS values presented in this paper instead of those in Ince et al. (2020) which are subject to an error in the east-west component

Deflection of the vertical (arcsec)	Profile	North-South Profile (216 pt)		East-West Profile (154 pt)	
		$\xi$	$\eta$	$\xi$	$\eta$
	max d/o	rms	rms	rms	rms
EIGEN-6C4	2,190	1.09	0.99	0.71	0.55
EIGEN-6C4.2000.2100.exp.3660	3,660	<b>0.92</b>	<b>0.78</b>	<b>0.51</b>	<b>0.38</b>
EIGEN-6C4.2000.2100.exp.5494	<b>5,494</b>	<b>0.66</b>	<b>0.92</b>	<b>0.46</b>	<b>0.40</b>

are not reduced for enhanced models (eigen6c4plus3660 and eigen6c4plus5494) as summarised in Table 3.

Our results in Germany are consistent with the findings of Voigt (2013), Voigt and Denker (2018) and Hirt (2010) where the authors added the effect of the RTM (Residual Terrain Model) to the deflection of vertical values computed

from the EGM2008. Introducing realistic density values for instance via laterally (and radially) varying density models (e.g., UNB\_TopoDensT\_2v01, Sheng et al. 2019) instead of the averaged density values, the calculation of topographic gravity field can improve the agreement between the computed model and ground truth values.

**Table 2** The RMS values of the residual deflections of vertical between EIGEN-6C4, the expanded model EIGEN-6C4.2000.2100.exp.3660, EIGEN-6C4.2000.2100.exp.5494, and the terrestrial astrogeodetic measurements in GSVS17 Colorado, USA (van Westrum et al. 2021). The corresponding number of the measurement points is given in brackets

Deflection of the vertical (arcsec)	max d/o	Colorado DoV data (222 pt)	
		$\xi$	$\eta$
EIGEN-6C4	2,190	1.26	1.62
EIGEN-6C4.2000.2100.exp.3660	3,660	<b>1.02</b>	<b>1.18</b>
EIGEN-6C4.2000.2100.exp.5494	<b>5,494</b>	<b>0.97</b>	<b>1.07</b>

**Table 3** The RMS values of the residual deflections of vertical between EIGEN-6C4, the expanded model EIGEN-6C4.2000.2100.exp.3660, EIGEN-6C4.2000.2100.exp.5494, and the terrestrial astrogeodetic measurements in GSVS14 Iowa, USA (Wang et al. 2017). The corresponding number of the measurement points is given in brackets

Deflection of the vertical (arcsec)	max d/o	Iowa DoV data (204 pt)	
		$\xi$	$\eta$
EIGEN-6C4	2,190	0.34	0.29
EIGEN-6C4.2000.2100.exp.3660	3,660	<b>0.31</b>	<b>0.28</b>
EIGEN-6C4.2000.2100.exp.5494	<b>5,494</b>	<b>0.28</b>	<b>0.29</b>

## 5 Conclusion and Future Work

We forward modelled a topographic gravity field based on ellipsoidal approximation in spectral domain using multi-layer density information together with globally distributed elevation data retrieved from Earth2014. The algorithm used expresses the gravity field of the subsequent shells in terms of ellipsoidal harmonic coefficients which are then transformed into spherical harmonic coefficients. In this study, we investigated the impact of the shell thickness of the confocal ellipsoids that is fundamental in the algorithm applied. It is shown that thinner shell thicknesses provide more accurate results, but the computational burden has to be tackled.

We use the developed topographic gravity field model to enhance high resolution combined global gravity field models. The existing combined global gravity field model example EIGEN-6C4 is augmented with the topographic gravity field model that is forward modelled using the high-resolution digital elevation model and average density estimations for different layers of the Earth's upper crust. The high frequency components of the gravity field are assumed to be mainly due to the topography. Therefore, topographic gravity field models

are complementary to the existing models as well as to fill areas that lack actual gravity data. In the current study, we presented two enhanced combined global gravity field models up to degree 3,660 and 5,494, respectively and demonstrated the further contribution of the very high degree components above degree 3,660. The results are evaluated w.r.t ground truth data, namely deflections of vertical observations in Germany and in Colorado and Iowa regions, USA. The results indicate that the omission error in mountainous areas can be reduced significantly using topographic gravity field model augmented combined models.

It is known that the reliability of the topographic gravity field models is determined by the included input data and the applied algorithms. The resolution of the input data, the uncertainties and validity of the elevation and density values, and the algorithm followed are important parameters. In this study, we modelled the topographic gravity field using average topographic, seawater, freshwater, and glacial densities. Further improvement is possible by introducing more realistic topographic density models as an input to our method.

The ROLI\_EllApprox\_SphN\_3660\_plusGRS80 (Abrykosov et al. 2019) is available on the ICGEM Service ([http://icgem.gfz-potsdam.de/tom\\_reltopo](http://icgem.gfz-potsdam.de/tom_reltopo), Ince et al. 2019) and can be accessed and downloaded freely also from <https://doi.org/10.5880/ICGEM.2019.011>. The newly developed model ROLI\_EllApprox\_SphN\_5494\_plusGRS80 and augmented (enhanced) models are available upon request from the authors.

**Acknowledgements** We would like to thank Dr. Blazej Bucha and an anonymous reviewer for their thorough review and constructive feedback which improved the content of the paper.

## References

- Abrykosov O, Ince ES, Förste C, Flechtner F (2019) Rock-Ocean-Lake-Ice topographic gravity field model (ROLI model) expanded up to degree 3660. GFZ Data Serv. <https://doi.org/10.5880/ICGEM.2019.011>
- Forsberg R, Tscherning CC (1981) The use of height data in gravity field approximation by collocation. J Geophys Res 86(B9):7843–7854
- Förste C, Bruinsma S, Abrykosov O, Lemoine JM, Marty JC, Flechtner F, Balmino G, Barthelmes F, Biancale R (2014) EIGEN-6C4 The latest combined global gravity field model including GOCE data up to degree and order 2190 of GFZ Potsdam and GRGS Toulouse. GFZ Data Serv. <https://doi.org/10.5880/icgem.2015.1>
- Götze HJ, Lahmeyer B (1988) Application of three-dimensional interactive modeling in gravity and magnetics. Geophysics 53(8):1096–1108
- Grombein T, Seitz K, Heck B (2016) The Rock–Water–Ice topographic gravity field model RWI\_TOPO\_2015 and its comparison to a conventional Rock-Equivalent version. Surv Geophys 37(5):937–976. <https://doi.org/10.1007/s10712-016-9376-0>

- Hirt C (2010) Prediction of vertical deflections from high-degree spherical harmonic synthesis and residual terrain model data. *J Geod* 84(3):179–190. <https://doi.org/10.1007/s00190-009-0354-x>
- Hirt C, Rexer M (2015) Earth2014 1 arc-min shape, topography, bedrock and ice-sheet models – available as gridded data and degree-10,800 spherical harmonics. *Int J Appl Earth Obs Geoinf* 39:103–112. <https://doi.org/10.1016/j.jag.2015.03.001>
- Hirt C, Reußner E, Rexer M, Kuhn M (2016) Topographic gravity modelling for global Bouguer maps to degree 2,160: Validation of spectral and spatial domain forward modelling techniques at the 10 microGal level. *J Geophys Res Solid Earth* 121:B51763. <https://doi.org/10.1002/2016JB013249>
- Hobson EW (1931) *The theory of spherical and ellipsoidal harmonics*. Cambridge University Press, Cambridge
- Ince ES, Barthelmes F, Reißland S, Elger K, Förste C, Flechtner F, Schuh H (2019) ICGEM – 15 years of successful collection and distribution of global gravitational models, associated services and future plans. *Earth Syst Sci Data* 11:647–674. <https://doi.org/10.5194/essd-11-647-2019>
- Ince ES, Abyrkosov O, Förste C, Flechtner F (2020) Forward gravity modelling to augment high-resolution combined gravity field models. *Surv Geophys* 41:767–804. <https://doi.org/10.1007/s10712-020-09590-9>
- Pavlis NK, Holmes SA, Kenyon SC, Factor JK (2012) The development and evaluation of the Earth Gravitational Model 2008 (EGM2008). *J Geophys Res Solid Earth* 117(B4). <https://doi.org/10.1029/2011JB008916>
- Rexer M, Hirt C, Claessens S, Tenzer R (2016) Layer-based modelling of the Earth’s gravitational potential up to 10-km scale in spherical harmonics in spherical and ellipsoidal approximation. *Surv Geophys* 37(6):1035–1074. <https://doi.org/10.1007/s10712-016-9382-2>
- Root BC, Novák P, Dirks D, Kaban M, van der Wal W, Vermeersen LLA (2016) On a spectral method for forward gravity field modelling. *J Geodyn* 97:22–30. <https://doi.org/10.1016/j.jog.2016.02.008>
- Sánchez L, Ågren J, Huang J et al (2021) Strategy for the realisation of the International Height Reference System (IHRs). *J Geod* 95:33. <https://doi.org/10.1007/s00190-021-01481-0>
- Sheng M, Shaw C, Vanicek P, Kingdon R, Santos M, Foroughi I (2019) Formulation and validation of a global laterally varying topographical density model. *Tectonophysics* 762:45–60
- Shin YH, Choi KS, Xu H (2006) Three-dimensional forward and inverse models for gravity fields based on the Fast Fourier Transform. *Comput Geosci* 32(6):727–738
- Tenzer R, Hirt C, Novák P, Pitoňák M, Šprlák M (2016) Contribution of mass density heterogeneities to the quasigeoid-to-geoid separation. *J Geod* 90(1):65–80
- Torge W (1981) *Resultate und Probleme der Geoidbestimmung*. Wiss. Arb. der Fachr. Vermessungswesen der Univ. Hannover Nr. 100
- Torge W (2001) *Geodesy*, 3rd edn. de Gruyter, Berlin
- van Westrum D, Ahlgren K, Hirt C, Guillaume S (2021) A Geoid Slope Validation Survey (2017) in the rugged terrain of Colorado, USA. *J Geod* 95(9). <https://doi.org/10.1007/s00190-020-01463-8>
- Voigt C (2013) *Astrogeodätische Lotabweichungen zur Validierung von Schwerefeldmodellen*, PhD Thesis, (Wissenschaftliche Arbeiten der Fachrichtung Geodäsie und Geoinformatik der Leibniz-Universität Hannover; Nr. 305), Hannover: Fachrichtung Geodäsie und Geoinformatik der Leibniz-Univ., X, 188 S. p
- Voigt C, Denker H (2018) Dataset: astrogeodetic vertical deflections along two profiles in Germany for the validation of gravity field models. <https://doi.org/10.25835/0092586>
- Wang YM, Becker C, Mader G et al (2017) The Geoid Slope Validation Survey 2014 and GRAV-D airborne gravity enhanced geoid comparison results in Iowa. *J Geod* 91:1261–1276. <https://doi.org/10.1007/s00190-017-1022-1>
- Wieczorek MA (2007) Gravity and topography of the terrestrial planets. *Treatise Geophy* 10:165–206
- Wieczorek MA, Simons FJ (2005) Localized spectral analysis on the sphere. *Geophys J Int* 162(3):655–675
- Zingerle P, Pail R, Gruber T et al (2020) The combined global gravity field model XGM2019e. *J Geod* 94(66). <https://doi.org/10.1007/s00190-020-01398-0>








**Open Access** This chapter is licensed under the terms of the Creative Commons Attribution 4.0 International License (<http://creativecommons.org/licenses/by/4.0/>), which permits use, sharing, adaptation, distribution and reproduction in any medium or format, as long as you give appropriate credit to the original author(s) and the source, provide a link to the Creative Commons license and indicate if changes were made.

The images or other third party material in this chapter are included in the chapter’s Creative Commons license, unless indicated otherwise in a credit line to the material. If material is not included in the chapter’s Creative Commons license and your intended use is not permitted by statutory regulation or exceeds the permitted use, you will need to obtain permission directly from the copyright holder.





# The Benefit of Accelerometers Based on Cold Atom Interferometry for Future Satellite Gravity Missions

Annikе Knabe , Manuel Schilling , Hu Wu , Alireza HosseiniArani ,  
Jürgen Müller , Quentin Beaufils , and Franck Pereira dos Santos 

## Abstract

Satellite gravity missions, like GRACE and GRACE Follow-On, successfully map the Earth's gravity field and its change over time. With the addition of the laser ranging interferometer (LRI) to GRACE-FO, a significant improvement over GRACE for inter-satellite ranging was achieved. One of the limiting factors is the accelerometer for measuring the non-gravitational forces acting on the satellite. The classical electrostatic accelerometers are affected by a drift at low frequencies. This drawback can be counterbalanced by adding an accelerometer based on cold atom interferometry (CAI) due to its high long-term stability. The CAI concept has already been successfully demonstrated in ground experiments and is expected to show an even higher sensitivity in space.

In order to investigate the potential of the CAI concept for future satellite gravity missions, a closed-loop simulation is performed in the context of GRACE-FO like missions. The sensitivity of the CAI accelerometer is estimated based on state-of-the-art ground sensors and predictions for space applications. The sensor performance is tested for different scenarios and the benefits to the gravity field solutions are quantitatively evaluated. It is shown that a classical accelerometer aided by CAI technology improves the results of the gravity field recovery especially in reducing the striping effects. The non-gravitational accelerations are modelled using a detailed surface model of a GRACE-like satellite body. This is required for a realistic determination of the variations of the non-gravitational accelerations during one interferometer cycle. It is demonstrated that the estimated error due to this variation is significant. We consider different orbit altitudes and also analyze the effect of drag compensation.

## Keywords

Closed-loop simulation · Cold atom interferometer accelerometry · Future satellite gravity missions

A. Knabe (✉) · H. Wu · A. HosseiniArani · J. Müller  
Institut für Erdmessung, Leibniz Universität Hannover, Hannover,  
Germany  
e-mail: [knabe@ife.uni-hannover.de](mailto:knabe@ife.uni-hannover.de)

M. Schilling  
Institut für Satellitengeodäsie und Inertialsensorik, Deutsches Zentrum  
für Luft- und Raumfahrt e.V. (DLR), Hannover, Germany

Q. Beaufils · F. Pereira dos Santos  
LNE-SYRTE, Observatoire de Paris-PSL Université, CNRS, Sorbonne  
Université, Paris, France

## 1 Introduction

The Earth's gravity field and its variation are of great interest for several disciplines (Pail et al. 2015). The measurement of the time-variable gravity field, i.e. monitoring of mass variations, was successfully realized by the satellite mission GRACE (Tapley et al. 2019) and is now continued by GRACE Follow-On (Landerer et al. 2020). The limiting factor on the instrument level is the accelerometer.

It is needed to measure the non-gravitational accelerations acting on the satellite which are subtracted in the post-processing to retrieve the Earth's gravity field information. In the current satellite missions, electrostatic accelerometers are used. These sensors are characterized by their low noise at the high frequencies. The main drawbacks of electrostatic accelerometers are the drift at the low frequencies and the difficulty in the estimation of biases and scale factors.

The technology of Cold Atom Interferometry (CAI) could solve these challenges. A cloud of independent cold atoms constitute the test mass in an atom interferometer. The benefit of atom interferometry accelerometers is their high long-term stability and good knowledge of the scale factor which is based on the frequency stability of the laser system. Simulation studies like Abrykosov et al. (2019) and Müller and Wu (2020) show promising improvements by CAI for the gravity field recovery. In Fig. 1, the noise behaviour of the accelerometer types are displayed in terms of Amplitude Spectral Density (ASD), which is defined as the square root of the Power Spectral Density (PSD). The hybrid sensor is a combination of an atomic interferometer and an electrostatic accelerometer. The performances for CAI are based on the anticipation of a large interrogation time in microgravity. In this contribution, a closed-loop simulation is performed to study the benefit of CAI accelerometry. The sensitivity of the measurements increases with higher interaction time. As the satellite is moving during the measurements, the non-gravitational acceleration varies in one interferometer cycle. In this study we use a cycle time (duration of one CAI measurement) of 12 s and evaluate the variation of the acceleration using the transfer function of an atomic interferometer.

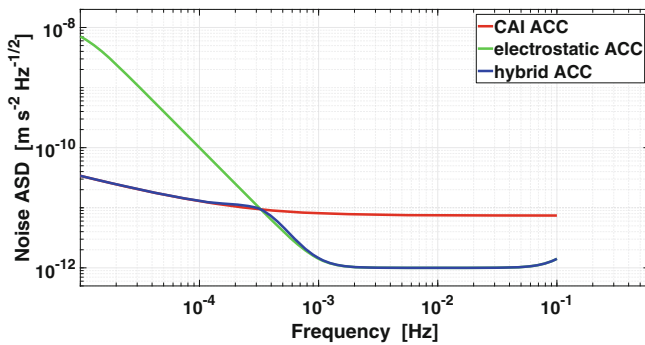


**Fig. 1** Anticipated ASD of a space accelerometer noise: CAI accelerometer, electrostatic accelerometer and hybrid accelerometer

## 2 Performance of an Atom Interferometry Accelerometer

In an atom interferometer, cold atoms are in free fall and operate as test mass. Laser pulses in a time interval  $T$  are used to split and recombine the atomic wave functions into different momentum states according to the superposition principle (Pereira dos Santos and Landragin 2007; Schilling et al. 2012). The output phase  $\Phi$  can be obtained by measuring the relative atomic populations in the output states after recombination. The acceleration  $a_k$  during cycle  $k$  is obtained from the measured phase  $\Phi_k$  with the evolution time  $T$ :

$$a_k = \frac{\Phi_k}{k_{eff} T^2}, \quad (1)$$

where  $k_{eff} = |\mathbf{k}_{eff}|$  is the norm of the effective wave vector of the laser light used to transfer momentum to the atoms (Kasevich and Chu 1991). In this study, the duration of one interferometer measurement cycle  $T_c$  is 12 s. It consists of the preparation time  $T_p$ , the interferometer duration  $2T$  and the detection time  $T_d$ :

$$T_c = T_p + 2T + T_d. \quad (2)$$

As the sensitivity of the accelerometer to the acceleration varies during one measurement cycle, the transfer function must be taken into account. The phase of the interferometer  $\Phi_k$  at the  $k$ -th cycle is given by

$$\Phi_k = k_{eff} \int_{kT_c}^{(k+1)T_c} g_{a,k}(t) a(t) dt. \quad (3)$$

The response function  $g_{a,k}$  (see Fig. 2) is given by

$$\begin{aligned} g_{a,k}(t) &= 0 && \text{for } kT_c < t < kT_c + T_p, \\ g_{a,k}(t) &= t - (kT_c + T_p) && \text{for } kT_c + T_p < t < kT_c + T_p + T, \\ g_{a,k}(t) &= kT_c + T_p + 2T - t && \text{for } kT_c + T_p + T < t < kT_c + T_p + 2T, \\ g_{a,k}(t) &= 0 && \text{for } kT_c + T_p + 2T < t < (k+1)T_c. \end{aligned}$$

To estimate the performance, we used parameters based on state of the art accelerometers on ground. The number of interfering atoms is  $N = 10^6$  and the contrast is  $C = 0.8$ . The momentum transfer, depending on laser wavelength  $\lambda$ ,

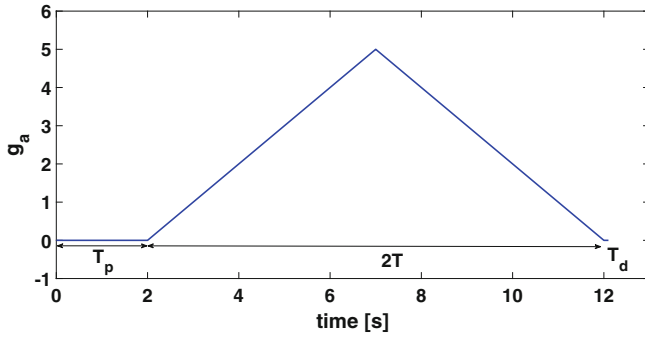


**Fig. 2** Response in the time domain of the transfer function for the conversion of the phase shift to acceleration

is  $k_{eff} = 4\pi\lambda \approx 1.6 \times 10^7/\text{m}$  for a two photon Raman transition using rubidium atoms. Microgravity in space is expected to allow for a dramatic increase of the free fall interferometer interrogation time  $T$ , which would greatly improve the performances of a CAI. For the following calculations we consider a measurement time of  $T = 5$  s and a preparation time of 2 s. The detection time is neglected as it is only a few tens of ms.

The quantum projection limited phase noise is given by

$$\sigma_\phi = \sqrt{\frac{T_c}{C^2 N}} = 4.2 \text{ mrad}/\sqrt{\text{Hz}}. \quad (4)$$

The sensitivity function of a 3 pulse atom interferometer is

$$H(f) = 16 \frac{(2k_{eff})^2}{(2\pi f)^4} \sin^4(2\pi f T/2). \quad (5)$$

In order to take into account fluctuations of systematic effects, we impose a  $1/f$  flicker floor noise of  $\sigma_f = 0.1$  mrad. The acceleration PSD can then be expressed as (see Fig. 3)

$$S_a^2(f) = (2\sigma_\phi^2 + 2 \ln(2)\sigma_f^2/f)/H(f). \quad (6)$$

We use this model in the following to estimate the performances of a CAI accelerometer in a satellite.

### 3 Variation of Non-Gravitational Accelerations Within One Interferometer Cycle

Time series of the non-gravitational accelerations are simulated with the Extended High Performance Satellite Dynamics Simulator (XHPS) Software (Wöske et al. 2016) developed by ZARM/DLR. Models for atmospheric drag and solar radiation pressure, Earth albedo, thermal radiation pressure and infrared are included in the simulations. In

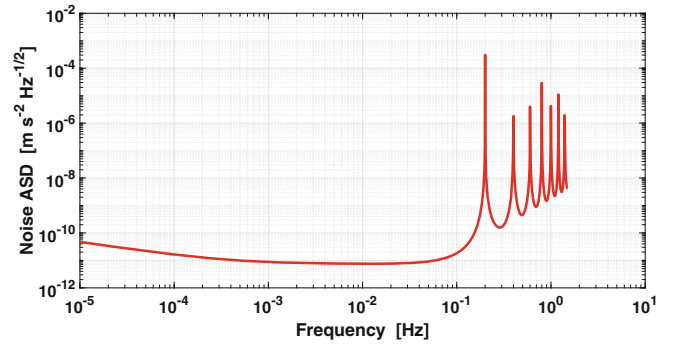


**Fig. 3** Anticipated ASD of a space CAI accelerometer noise

this study, only accelerations in the along-track direction are included, because in this direction the magnitude of the non-gravitational accelerations is the biggest and consequently the biggest effect is expected here. In this section, only a single satellite is investigated. An attitude control system with a nadir pointing mode is included in the calculation of the non-gravitational accelerations. Misalignment errors and errors due to the non-orthogonality of the accelerometer frame axes are not considered in this study. Degradation induced by the cross-track and nadir axes would appear when the true alignment differs from the target alignment. Two simulations are investigated with satellite altitudes of 467 km and 303 km. The satellite's mass is assumed to be equal to 600.98 kg. A detailed surface model of a GRACE-like satellite body is used. The mass and shape of the satellite and the altitude of 467 km are the parameters of the GRACE-FO mission, allowing a realistic comparison to the results of the mission. In addition, a lower altitude of 303 km is chosen, which would lead to a higher sensitivity to the gravity field signal at the cost of higher non-gravitational accelerations and is thus interesting for future gravity missions. In order to get a continuous signal for the computation of  $\phi_k$  in Eq. (3), the acceleration time series is approximated with an interpolation polynomial. The Newton polynomial interpolation is applied for each cycle separately. The best agreement is achieved with a quadratic polynomial. The variation between the minimum acceleration and the maximum acceleration within one cycle is calculated for the two satellite orbits (Fig. 4). The variation in 12 s is of the order of  $10^{-9} \text{ m/s}^2$  for an altitude of 467 km and  $10^{-8} \text{ m/s}^2$  for an altitude of 303 km. This variation is higher than the accelerometer noise itself (Fig. 1).

The transfer function of an atomic interferometer is used to investigate the effect of this variation in one cycle. The output of the atom interferometer is compared to the true acceleration value at  $t = 7$  s of each cycle, i.e. the middle time of the interferometer. In Fig. 5 the ASD of this difference and the ASD of the variation in one cycle are shown. The estimated error of the acceleration measurements is at the level of



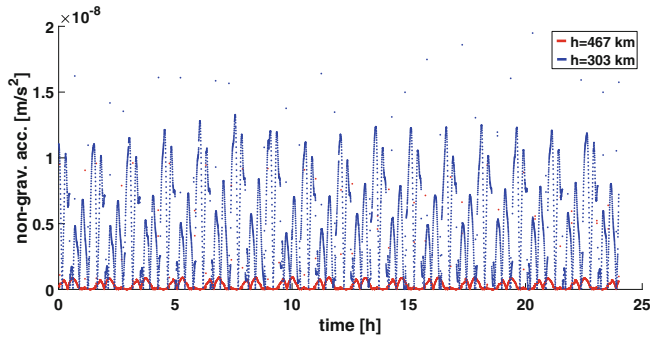


**Fig. 4** Variation of non-gravitational accelerations within one interferometer cycle for two different altitudes: 467 km (red) and 303 km (blue)

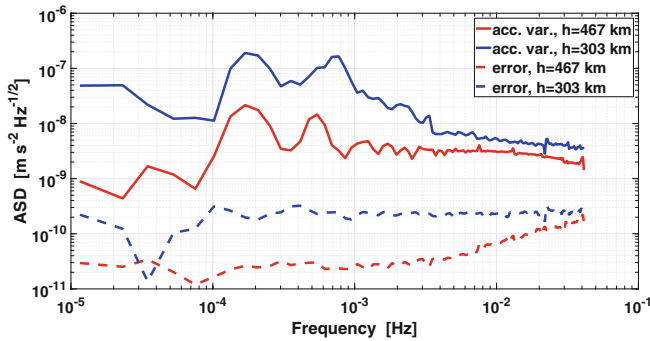


**Fig. 5** ASD of variation of non-gravitational accelerations within one interferometer cycle (acc. var.) and corresponding error contribution to the CAI measurements (error) for two different altitudes: 467 km and 303 km

$3 \times 10^{-11} \text{ m/s}^2$  for an altitude of 467 km and  $2 \times 10^{-10} \text{ m/s}^2$  for an altitude of 303 km. In comparison to the acceleration noise this error contribution is significant, which shows that one needs to take into account the temporal filtering of non-inertial accelerations due to the interferometer response function.

Furthermore, the impact of using a drag compensation system is studied. The thruster is modelled with parameters of the GOCE mission. The thruster noise is simulated using a PSD model (Canuto et al. 2010):

$$S_{thr}^2(f) = \left( \left( \frac{0.005}{f} \right)^2 + 1 \right) (10^{-6})^2 \text{ N}^2/\text{Hz}. \quad (7)$$

For the thruster system a maximum thrust level of 21 mN, a minimum thrust level of 0.6 mN and a possible rate of change of 2.5 mN/s are considered. As it is impossible to find a good fitting polynomial for the time series including thruster noise, a filter is first applied. A second order Butterworth filter with cutoff frequencies of  $1 \times 10^{-6} \text{ Hz}$  and  $5 \times 10^{-3} \text{ Hz}$  is used. The variation of accelerations within one interferometer cycle is shown in Fig. 6 and its ASD in Fig. 7. The estimated error contribution due to the residual variation of

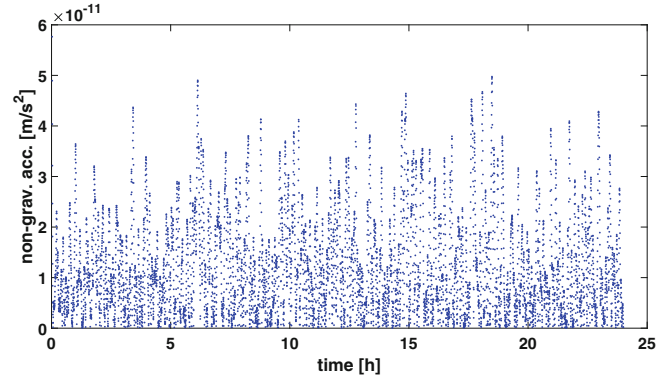


**Fig. 6** Residual variation of non-gravitational accelerations within one interferometer cycle under drag free control

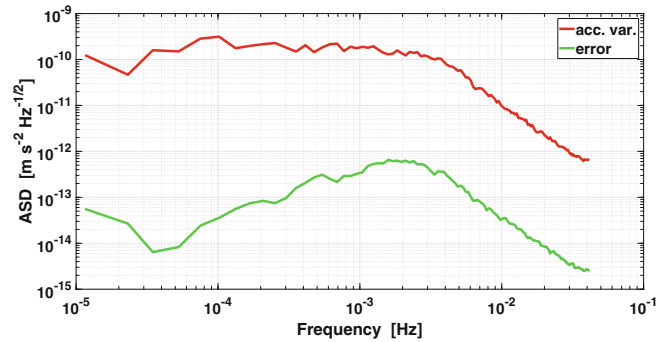


**Fig. 7** ASD of residual variation of non-gravitational accelerations within one interferometer cycle and corresponding error contribution under drag free control

non-gravitational accelerations is now below the noise of an atomic interferometer and hence acceptable (Fig. 7). In summary, the acceleration variation in one interferometer cycle has to be taken into account because it can have a critical impact on the performance of the CAI accelerometer. A balance between the cycle time length and sensitivity has to be found. Drag compensation is a good option to reduce the impact of this acceleration variation.

## 4 Closed-Loop Simulation

### 4.1 Simulation Procedure

A closed-loop simulation of a GRACE-FO like mission is performed to investigate the potential of the combination of an electrostatic and a CAI accelerometer. Figure 8 shows the flowchart of the simulation procedure. It consists of the synthesis of range accelerations based on the input satellite orbit and the gravity field model, addition of instrument noise and model errors and the gravity field recovery. The reference gravity field model is only a static model which means no temporal gravity field signals are included, since

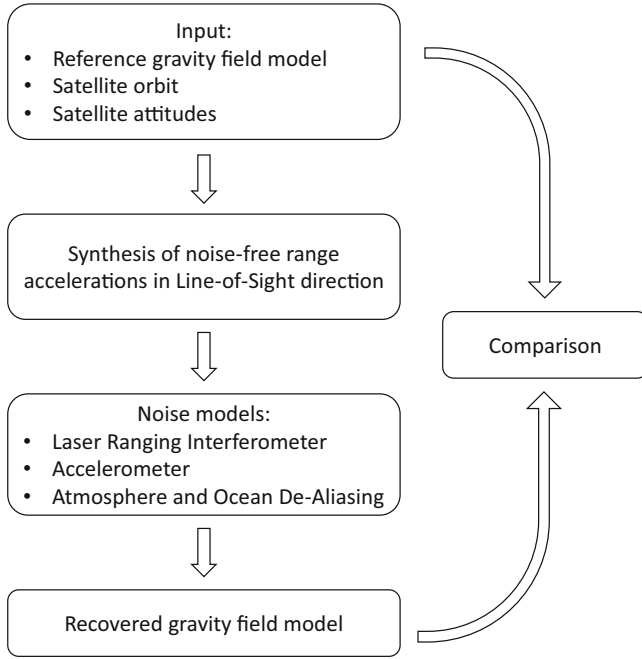


**Fig. 8** Flowchart of the closed-loop simulation

the main purpose of this study is to evaluate the contributions of CAI accelerometer w.r.t. the electrostatic one. In order to recover the temporal gravity fields, in a future study we will use a sequence of monthly simulated data which includes not only the static model but also the temporal signals. Ocean tide errors and non-tidal gravity field signals are not included, but an error due to Atmosphere and Ocean Aliasing is considered. We know that some ocean tide components might cause aliasing effects on recovered solutions. But as a preliminary study, we suppose that the ocean tides and direct tides can be precisely modelled and reduced from the observations. The range accelerations in Line-of-Sight direction  $\ddot{\rho}$ , measured by the Laser Ranging Interferometer (LRI), are synthesized with:

$$\ddot{\rho} = \ddot{\mathbf{r}}_{AB} \mathbf{e}_{AB} + \dot{\mathbf{r}}_{AB} \dot{\mathbf{e}}_{AB}, \quad (8)$$

where  $\ddot{\mathbf{r}}_{AB} = \ddot{\mathbf{r}}_B - \ddot{\mathbf{r}}_A$  is the difference of the gradient of the Earth's gravitational potential at the positions of the two satellites A and B,  $\mathbf{e}_{AB}$  is the unit vector of the Line-of-Sight and  $\dot{\mathbf{e}}_{AB}$  is its derivative,  $\dot{\mathbf{r}}_{AB} = \dot{\mathbf{r}}_B - \dot{\mathbf{r}}_A$  is the velocity difference between satellites A and B. The second term  $\dot{\mathbf{r}}_{AB} \dot{\mathbf{e}}_{AB}$  is neglected in this study because no acceleration measurements for its estimation are needed and the focus is put on the benefit of novel accelerometers. The magnitude of this term is estimated to be lower than  $4.3 \times 10^{-9} \text{ m/s}^2$  for a GRACE-like mission scenario. In the next step, noise models for different error sources are added: LRI measurement noise, accelerometer noise and Atmospheric and Ocean

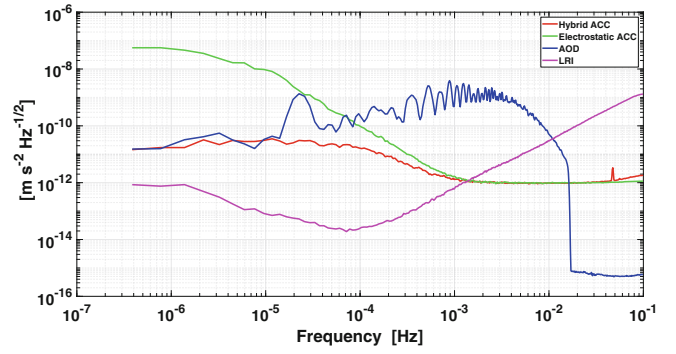


**Fig. 9** ASD of the different noise sources

De-Aliasing noise (AOD). The LRI noise is modelled according to Abich et al. (2019). The Atmospheric and Ocean De-Aliasing models errors are assumed as 10% of AOD1B RL6 (Dobslaw et al. 2017). The ASD of these noise contributions is shown in Fig. 9. The spherical harmonic coefficients  $S_{nm}$  and  $C_{nm}$  are estimated with a least-squares adjustment. The observation equation of the adjustment is linear as the range accelerations provide a direct link to the gravity field coefficients. The gravity field model is solved up to degree and order 90. The reference gravity field model is Eigen-6c4 (Foerste et al. 2014) and the GRACE orbit from April 2006 is used. A perfect alignment of each satellite is assumed so that the non-gravitational accelerations can be measured with accuracy by the 1-axis hybrid accelerometer in this study. The variance-covariance matrix, which is assembled from the post-fit residuals, is used for the stochastic modelling.

## 4.2 Simulation Results

For the evaluation the differences between the input reference gravity field model and the recovered gravity field model are calculated. The coefficient differences of gravity fields recovered applying different types of accelerometers are then compared. The evaluation is carried out in the spectral and the space domain. The equivalent water height (EWH) is calculated to validate the results in the space domain using the following equation (Schrama et al. 2007; Wahr et al. 1998):

$$\Delta EWH = \frac{R \rho_e}{3\rho_w} \sum_{n=0}^N \frac{2n+1}{1+k_n} \sum_{m=0}^n (\Delta C_{nm} \cos(m\lambda) + \Delta S_{nm} \sin(m\lambda)) P_{nm}(\cos(\Theta)), \quad (9)$$

where  $R$  is the radius of the Earth,  $\rho_e$  is the average density of the Earth,  $\rho_w$  is the density of water,  $k_n$  is Love number of degree  $n$ ,  $\lambda$  is the longitude and  $\Theta$  the polar distance.

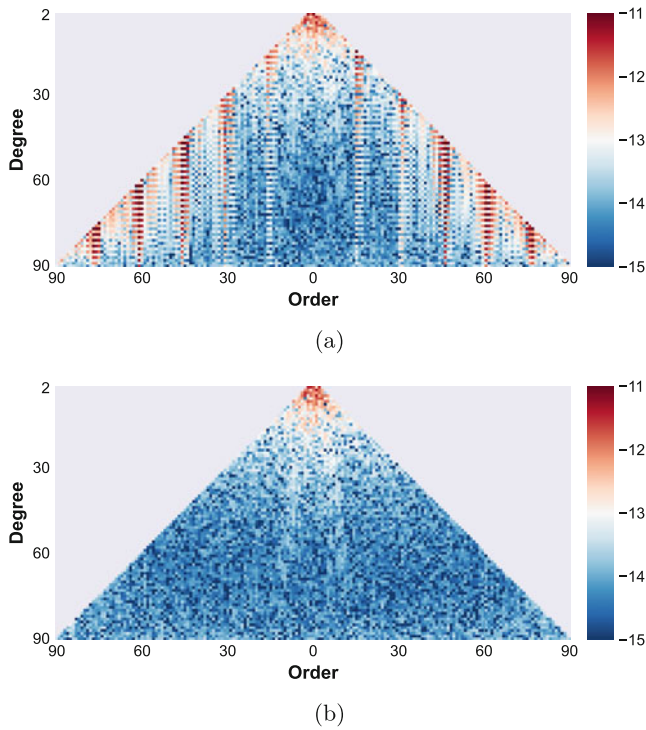


**Fig. 10** Coefficient differences between recovered and reference gravity field using in the closed-loop simulation the noise model of (a) an electrostatic accelerometer and (b) a hybrid accelerometer

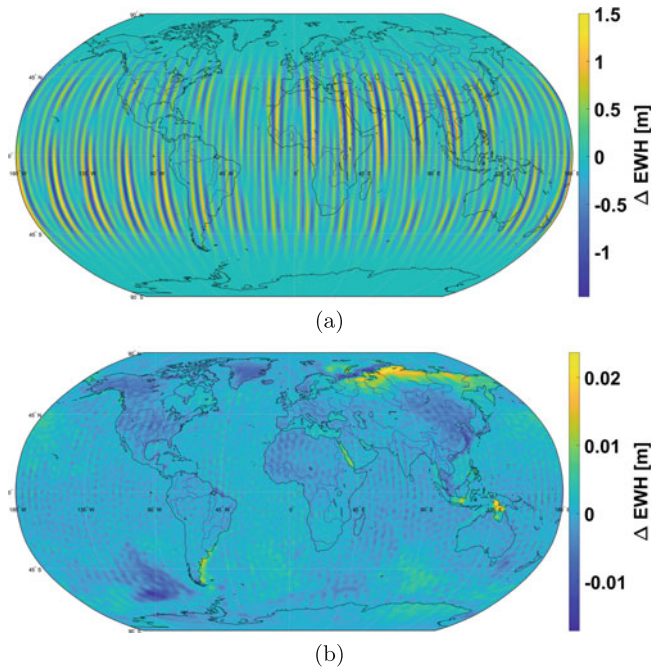


**Fig. 11** Coefficient differences between recovered and reference gravity field expressed in terms of equivalent water height using in the closed-loop simulation the noise model of (a) an electrostatic accelerometer and (b) a hybrid accelerometer

$\Delta C_{nm}$  and  $\Delta S_{nm}$  are the coefficient differences and  $P_{nm}$  are the Legendre functions.

In Fig. 10, the true errors are represented as two-dimensional spectrum. The result with the electrostatic accelerometer shows large striping effects at orders  $m = 16 \times k, k \in \mathbb{N}$ . These specific orders correspond to the orbit frequency and multiples of it. This reveals, that the CAI accelerometer counteracts the problem with orbit resonances and striping effects owing to its low noise in the low frequencies. It can be concluded that the bias drift of the electrostatic accelerometer in the low frequencies causes degradation in the orbital resonance order 16 and integer multiples of it. However, this problem can also be solved by filtering because the frequencies below  $1.8 \times 10^{-4}$  Hz imply no gravity field signal. In McGirr et al. (2022), an improvement of the GRACE gravity solutions is achieved by applying a high-pass filter to the accelerometer data and removing the low-frequency components below  $4.5 \times 10^{-5}$  Hz.

The evaluation of the true errors in the spatial domain confirms a great improvement of the recovered gravity field for the simulation with a hybrid accelerometer. The striping effects using an electrostatic accelerometer are also visible in the space domain (Fig. 11). The striping effects in North-South direction are caused by the sampling and flight direction of the in-line pair. These systematic effects are characteristic for the GRACE solution. That is why, typically a filter is applied to the solutions. The stripes in the space domain are largely reduced by the combination with the CAI accelerometer. The errors expressed as EWH are two orders of magnitude lower when using the hybrid sensor. In Fig. 11b, the dominant factor is the AOD error. This can be observed by comparing the coefficient differences to the input AOD noise. The solution using an electrostatic accelerometer is also degraded by the AOD noise.

According to Abrykov et al. (2019) the accelerometer noise is not the limiting factor when considering all non-tidal temporal signals. It must be noted that several assumptions are applied in our study. Some contributors to the error budget due to temporal variations are not considered. One example is the ocean tide aliasing which is one of the limiting factors. For a more realistic investigation, further signals and errors have to be included in upcoming studies.

## 5 Conclusions

The performance of an atom interferometry accelerometer is estimated based on state of the art atomic accelerometers on ground and various predicted space scenarios. The decisive advantage of the CAI sensor is its high long-term stability.

The variation of accelerations within one interferometer cycle is analysed using the transfer function of an atomic interferometer. For both simulations with altitudes of 303 km and 467 km the corresponding error is bigger

than the anticipated CAI noise. It means, this aspect is significant and must be considered for future gravity field missions. Consequently, a possible reduction of this effect when using a drag compensation system is studied. The simulation including drag compensation shows a reduced error contribution which is below the anticipated noise level of the atom interferometer.

A closed-loop simulation is performed to investigate the benefit of the CAI sensor for the recovered gravity field. The gravity field solution shows an improvement by a factor of two when using a hybridization of a CAI accelerometer and a classical electrostatic accelerometer. In the space domain, the striping effect is largely reduced. Accordingly, frequencies below  $1 \times 10^{-4}$  Hz have an influence on the gravity solutions, which can be justified by the bias drift of the accelerometer. Nevertheless, the signal below this frequency could also be removed by filtering without affecting the gravity field solution. The coefficient differences between recovered and reference gravity field indicate the input AOD error. This is especially visible when using a hybrid accelerometer and shows that the aliasing effects are the limiting factor. However, it has to be noted that not all temporal signals are included in our simulation and their effect to the gravity field solution might be even bigger.

**Acknowledgements** The results presented here were partially carried out on the cluster system at the Leibniz University of Hannover, Germany. We acknowledge the support by the Deutsche Forschungsgemeinschaft (DFG, German Research Foundation) – Project-ID 434617780 – SFB 1464. A.H. acknowledges the support by the DLR-Institute for Satellite Geodesy and Inertial Sensing. A.K. acknowledges its initial funding by the Ministry of Science and Culture of the German State of Lower Saxony from “Niedersächsisches Vorab”. H.W. acknowledges the funding by the German Research Foundation (DFG) under Germany’s Excellence Strategy – EXC-2123 QuantumFrontiers – 390837967. F.P.d.S. and Q.B. thank CNES for support (QUANTA project).

## Conflict of Interest

The authors declare that they have no conflict of interest.

**Author Contributions** Q.B. and F.P.d.S. provided input for the performance of the atom interferometer. H.W., M.S. and A.K. developed the software. A.K. performed the computations and wrote the first draft of the manuscript. All authors provided critical input to the manuscript and approved the final version.

**Data Availability Statement** Datasets generated in this study are available from the corresponding author on reasonable request.

## References

Abich K, Abramovici A, Ampanan B, Baatzsch A, Okihiro BB, Barr DC, Bize MP, Bogan C, Braxmaier C, Burke MJ, Clark KC, Dahl C,

- Dahl K, Danzmann K, Davis MA, de Vine G, Dickson JA, Dubovitsky S, Eckardt A, Ester T, Barranco GF, Flatscher R, Flechtner F, Folkner WM, Francis S, Gilbert MS, Gilles F, Gohlke M, Grossard N, Guenther B, Hager P, Hauden J, Heine F, Heinzl G, Herding M, Hinz M, Howell J, Katsumura M, Kaufer M, Klipstein W, Koch A, Kruger M, Larsen K, Lebeda A, Lebeda A, Leikert T, Liebe CC, Liu J, Lobmeyer L, Mahrtdt C, Mangoldt T, McKenzie K, Misfeldt M, Morton PR, Müller V, Murray AT, Nguyen DJ, Nicklaus K, Pierce R, Ravich JA, Reavis G, Reiche J, Sanjuan J, Schütze D, Seiter C, Shaddock D, Sheard B, Sileo M, Spero R, Spiers G, Stede G, Stephens M, Sutton A, Trinh J, Voss K, Wang D, Wang RT, Ware B, Wegener H, Windisch S, Woodruff C, Zender B, Zimmermann M (2019) In-orbit performance of the GRACE follow-on laser ranging interferometer. *Phy Rev Lett* 123(3):031101. <https://doi.org/10.1103/PhysRevLett.123.031101>
- Abrykosov P, Pail R, Gruber T, Zahzam N, Bresson A, Hardy E, Christophe B, Bidel Y, Carraz O, Siemes C (2019) Impact of a novel hybrid accelerometer on satellite gravimetry performance. *Adv Space Res* 63(10):3235–3248. <https://doi.org/10.1016/j.asr.2019.01.034>
- Canuto E, Molano A, Massotti L (2010) Drag-free control of the GOCE satellite: Noise and observer design. *IEEE T Contr Syst T* 18(2):501–509. <https://doi.org/10.1109/TCST.2009.2020169>
- Dobslaw H, Bergmann-Wolf I, Dill R, Poropat L, Thomas M, Dahle C, Esselborn S, König R, Flechtner F (2017) A new high-resolution model of non-tidal atmosphere and ocean mass variability for de-aliasing of satellite gravity observations: AOD1B RL06. *Geophys J Int* 211(1):263–269. <https://doi.org/10.1093/gji/ggx302>
- Foerste C, Bruinsma S, Abrykosov O, Lemoine JM, Marty JC, Flechtner F, Balmino F, Gand Barthelmes, Biancale R (2014) EIGEN-6C4 The latest combined global gravity field model including GOCE data up to degree and order 2190 of GFZ Potsdam and GRGS Toulouse. *GFZ data services* 10. <https://doi.org/10.5880/icgem.2015.1>
- Kasevich M, Chu S (1991) Atomic interferometry using stimulated Raman transitions. *Phy Rev Lett* 67(2):181–184. <https://doi.org/10.1103/PhysRevLett.67.181>
- Landerer FW, Flechtner FM, Save H, Webb FH, Bandikova T, Bertiger WI, Bettadpur SV, Byun SH, Dahle C, Dobslaw H, Fahnstock E, Harvey N, Kang Z, Kruizinga GLH, Loomis BD, McCullough C, Murböck M, Nagel P, Paik M, Pie N, Poole S, Strelakov D, Tamisiea ME, Wang F, Watkins MM, Wen HY, Wiese DN, Yuan DN (2020) Extending the global mass change data record: GRACE Follow-On instrument and science data performance. *Geophys Res Lett* 47(12):e88306. <https://doi.org/10.1029/2020GL088306>
- McGirr R, Tregoning P, Allgeyer S, McQueen H, Purcell A (2022) Mitigation of thermal noise in GRACE accelerometer observations. *Adv Space Res* 69(1):386–401. <https://doi.org/10.1016/j.asr.2021.10.055>
- Müller J, Wu H (2020) Using quantum optical sensors for determining the Earth’s gravity field from space. *J Geod* 94(8):1–14. <https://doi.org/10.1007/s00190-020-01401-8>
- Pail R, Bingham R, Braitenberg C, Dobslaw H, Eicker A, Güntner A, Horwath M, Ivins E, Longuevergne L, Panet I, et al. (2015) Science and user needs for observing global mass transport to understand global change and to benefit society. *Surv Geophys* 36(6):743–772. <https://doi.org/10.1007/s10712-015-9348-9>
- Pereira dos Santos F, Landragin A (2007) Getting the measure of atom interferometry. *Phys World* 20(11):32–37. <https://doi.org/10.1088/2058-7058/20/11/38>
- Schilling M, Timmen L, Müller J (2012) Einsatz der Atominterferometrie in der Geodäsie. *zfv* 137(3/2012):185–194. <https://doi.org/10.15488/3097>
- Schrama EJO, Wouters B, Lavallée DA (2007) Signal and noise in Gravity Recovery And Climate Experiment (GRACE) observed surface mass variations. *J Geophys Res* 112(B08407). <https://doi.org/10.1029/2006JB004882>

- Tapley BD, Watkins MM, Flechtner F, Reigber C, Bettadpur S, Rodell M, Sasgen I, Famiglietti JS, Landerer FW, Chambers DP, Reager JT, Gardner AS, Save H, Ivins ER, Swenson SC, Boening C, Dahle C, Wiese DN, Dobslaw H, Tamisiea ME, Velicogna I (2019) Contributions of GRACE to understanding climate change. *Nat Clim Change* 9:358–369. <https://doi.org/10.1038/s41558-019-0456-2>
- Wahr J, Molenaar M, Bryan F (1998) Time variability of the Earth's gravity field: Hydrological and oceanic effects and their possible detection using GRACE. *J Geophys Res* 103(B12):30205–30229. <https://doi.org/10.1029/98JB02844>
- Wöske F, Kato T, List M, Rievers B (2016) Development of a high precision simulation tool for gravity recovery missions like GRACE. In: Zanetti R, Russel RP, Ozimek MT, Bowes AL (eds) *Proceedings of the 26th AAS/AIAA space flight mechanics meeting held February 14–18, 2016*. *Advances in the Astronautical Sciences*, vol 158, pp 2445–2457

**Open Access** This chapter is licensed under the terms of the Creative Commons Attribution 4.0 International License (<http://creativecommons.org/licenses/by/4.0/>), which permits use, sharing, adaptation, distribution and reproduction in any medium or format, as long as you give appropriate credit to the original author(s) and the source, provide a link to the Creative Commons license and indicate if changes were made.

The images or other third party material in this chapter are included in the chapter's Creative Commons license, unless indicated otherwise in a credit line to the material. If material is not included in the chapter's Creative Commons license and your intended use is not permitted by statutory regulation or exceeds the permitted use, you will need to obtain permission directly from the copyright holder.





# Kalman-Filter Based Hybridization of Classic and Cold Atom Interferometry Accelerometers for Future Satellite Gravity Missions

Alireza HosseiniArani , Benjamin Tennstedt , Manuel Schilling ,  
Annike Knabe , Hu Wu , Steffen Schön , and Jürgen Müller 

## Abstract

Proof-of-principle demonstrations have been made for cold atom interferometer (CAI) sensors. Using CAI-based accelerometers in the next generation of satellite gravimetry missions can provide long-term stability and precise measurements of the non-gravitational forces acting on the satellites. This would allow a better understanding of climate change processes and geophysical phenomena which require long-term monitoring of mass variations with sufficient spatial and temporal resolution. The proposed accuracy and long-term stability of CAI-based accelerometers appear promising, while there are some major drawbacks in the long dead times and the comparatively small dynamic range of the sensors. One interesting way to handle these limitations is to use a hybridization with a conventional navigation sensor. This study discusses one possible solution to employ measurements of a CAI accelerometer together with a conventional Inertial Measurement Unit (IMU) using a Kalman filter framework.

A hybrid navigation solution of these two sensors for applications on ground has already been demonstrated in simulations. Here, we adapt this method to a space-based GRACE-like gravimetry mission. A simulation is performed, where the sensitivity of the CAI accelerometer is estimated based on state-of-the-art ground sensors and further published space scenarios. Our results show that the Kalman filter framework can be used to combine the measurements of conventional inertial measurement units with the CAI accelerometers measurements in a way to benefit from the high accuracy of the conventional IMU measurements in higher frequencies together with the high stability of CAI measurements in lower frequencies. We will discuss the challenges, potential solutions, and the possible performance limits of the proposed hybrid accelerometry scenario.

## Keywords

Atom interferometry · Hybrid accelerometer · Quantum sensor · Satellite gravimetry

A. HosseiniArani (✉)

Leibniz University Hannover, Institute of Geodesy, Hannover,  
Germany

German Aerospace Center, Institute for Satellite Geodesy and Inertial  
Sensing, Hannover, Germany

e-mail: [hosseiniarani@ife.uni-hannover.de](mailto:hosseiniarani@ife.uni-hannover.de)

B. Tennstedt · A. Knabe · S. Schön · J. Müller

Leibniz University Hannover, Institute of Geodesy, Hannover,  
Germany

M. Schilling

German Aerospace Center, Institute for Satellite Geodesy and Inertial  
Sensing, Hannover, Germany

## 1 Introduction

The satellite gravimetry missions GRACE and GRACE-FO have enabled the monitoring of the global time variable gravity field. The results contributed to quantifying mass changes related to climate change (Tapley et al. 2019) and new insights into processes of the Earth's interior (Mandea et al. 2020). The gravity field solutions are limited in the very low degrees at  $C_{20}$  and, for times with only one operational accelerometer on two satellites, even at  $C_{30}$  (Loomis et al. 2020). These coefficients are typically replaced with satellite laser ranging solutions. The spatial resolution is limited at a few hundred kilometers for the typical monthly gravity field solutions. For future missions a resolution at the order of 100 km or below is needed to address the requirements of the scientific community (Pail et al. 2015). This would allow, amongst others, to monitor the mass balance of smaller glaciers or contribute to the water management as well as drought or flood predictions on a regional scale.

The GRACE-FO mission added a laser ranging interferometer (LRI) as a major innovation compared to the K-band ranging system (KBR) on the GRACE mission. Currently the LRI is a technical demonstrator for inter-satellite ranging and GRACE-FO still employs KBR as the main instrument. Future missions will probably rely on a LRI system (see e.g. Haagmans et al. 2020) because the current LRI performance already exceeds the mission requirements of  $80 \text{ nm}/\sqrt{\text{Hz}}$  (Abich et al. 2019) and the GRACE KBR noise of  $1 \mu\text{m}/\sqrt{\text{Hz}}$ . The performance of the electrostatic accelerometer (ACC) for GRACE-FO, however, has not changed significantly from the GRACE mission (Christophe et al. 2015).

Figure 1 shows the ACC and ranging system error models of GRACE and GRACE-FO as amplitude spectral densities in range accelerations. The potential improvement of the gravity field solutions is in the frequency range above  $10^{-3} \text{ Hz}$ . One of the main deficiencies of GRACE gravity field solutions, the so called striping effect, is not improved in GRACE-FO solutions. This effect, which manifests itself as low frequency stripes in the spatial domain, is caused by the predominantly North–South direction of the observations, unmodelled temporal variations of atmosphere and ocean, but also a drift of the ACC in frequencies below  $10^{-3} \text{ Hz}$ . The stripes are typically reduced by signal processing, e.g. a 300 km Gaussian filter, which, however, also affects the gravity signal.

The development of electrostatic ACC for future missions (e.g. Christophe et al. 2018) shows an improvement in instrumental noise by more than one order of magnitude for frequencies above  $10^{-3} \text{ Hz}$  while keeping an approximately  $1/\sqrt{f}$  low frequency drift. Cold Atom Interferometry (CAI;

see Sect. 2) is one potential technology to overcome the limitation of the electrostatic ACCs in lower frequencies. Additionally, the CAI measurement enables the calibration of the electrostatic accelerometer by a second bias and drift free in-situ measurement of the non gravitational accelerations. Currently, this type of calibration step uses modelled non-gravitational accelerations (see e.g. Klinger and Mayer-Gürr 2016; Wöske et al. 2019).

The proposed accuracy and long-term stability of CAI-based accelerometers appear promising, while there are some major drawbacks in the long dead times and the comparatively small dynamic range of the sensor. One promising way to handle the drawbacks of atom interferometry is to use it in hybrid combination together with conventional navigation sensors. The CAI measurement then has to be combined with the electrostatic ACC, for which we present a Kalman filter based approach (Sect. 3) to create a hybrid one-axis accelerometer (Sect. 4) oriented in the along-track direction.

## 2 Orbit and Accelerometer Modelling

### 2.1 Cold Atom Interferometer Accelerometry

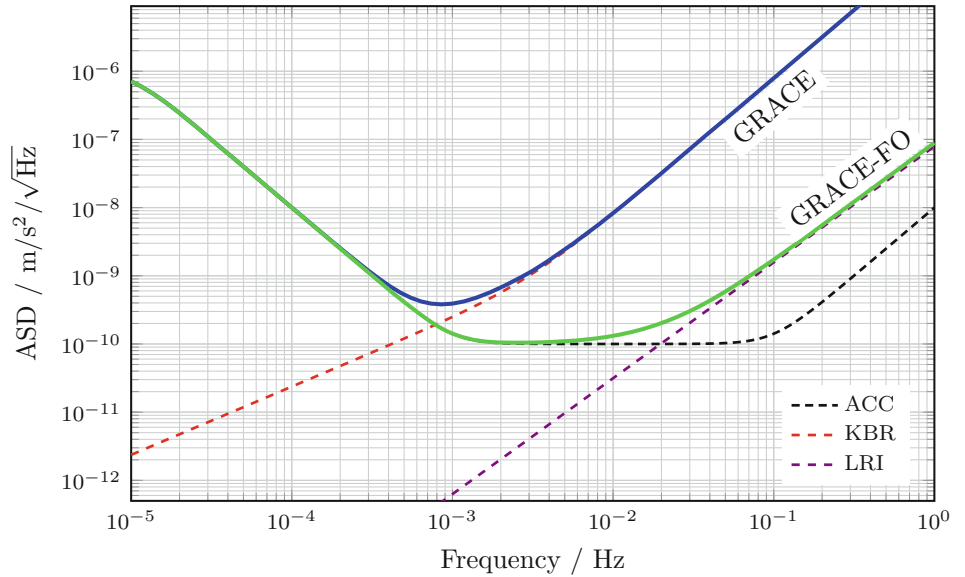
Cold Atom Interferometry utilises atoms as test masses in an interferometer realised by a sequence of specific laser pulses. A light pulse atom interferometer can be implemented in different ways. See Abend et al. (2020) for an overview. Only a brief introduction based on Kasevich and Chu (1991) is given here. The atom interferometer consists of three laser pulses acting as either beam splitter or mirror. The frequencies of two parallel counter-propagating lasers beams are chosen to be in resonance with a two-photon Raman transition. The first light pulse creates a beam splitter, putting about 50 % of the atoms in a superposition of the initial state with an excited state (having absorbed energy and momentum of two photons). After a time interval  $T$  a second light pulse initiates a transition of all atoms from excited back to initial state or vice versa. After a second time interval  $T$  a second beam splitter closes the interferometer. The leading order atom interferometer phase  $\Delta\Phi$  is described by

$$\Delta\Phi = (\mathbf{k}_{\text{eff}} \cdot \mathbf{a} - \alpha)T^2 + \Phi_L \quad (1)$$

with the acceleration  $\mathbf{a}$  acting on the atoms and the effective optical wave vector of the laser light  $\mathbf{k}_{\text{eff}}$ , which describes the photon momentum exchange.<sup>1</sup> The Raman laser phase  $\Phi_L$  is added to the last light pulse to operate the interfer-

<sup>1</sup>The momentum transferred is  $\hbar\mathbf{k}_{\text{eff}}$  where  $\hbar$  is the reduced Planck constant.

**Fig. 1** Amplitude spectral densities in range accelerations in the along-track direction of dominant noise sources for GRACE(-FO) satellite missions with electrostatic accelerometer (ACC; Flury et al. 2008; Christophe et al. 2015) and microwave- or laser-ranging system (KBR,LRI; Thomas 1999; Abich et al. 2019). ACC performance includes an estimate for temperature dependent bias variations in low frequencies (Christophe et al. 2018)



ometer, e.g., mid-fringe (cf. Sect. 3.2). The linear frequency ramp  $\alpha$  is added to compensate for the acceleration of the atoms. The acceleration in direction of  $\mathbf{k}_{\text{eff}}$  is canceled out if  $\alpha = |\mathbf{k}_{\text{eff}} \cdot \mathbf{a}|$ . This way, all measurements of a CAI can be traced back to (laser) frequencies. More specifically,  $\Delta\Phi$  measures the projection of the acceleration  $\mathbf{a}$  along  $\mathbf{k}_{\text{eff}}$ , e.g. in terrestrial applications  $\mathbf{k}_{\text{eff}}$  is aligned in parallel to  $\mathbf{g}$  to create a gravimeter. In a satellite setting,  $\mathbf{a}$  are the non-gravitational accelerations acting on the satellite. Assuming the CAI is in the center of mass and  $\mathbf{k}_{\text{eff}}$  is aligned in the along-track direction,  $\Delta\Phi$  would be a measure of the non-gravitational accelerations in the along-track direction.

According to Eq. (1) the sensitivity of the CAI can be increased by either applying methods with a higher photon momentum transfer (e.g. multiphoton Bragg diffraction) or increasing the pulse separation time  $T$ . For terrestrial applications  $T$  is limited by the length of the free fall distance of the atoms, e.g. up to 300 ms for a transportable (Freier et al. 2016) and 1.2 s for a stationary instrument (Schilling et al. 2020). As atoms and satellites in space are in free fall, these restrictions do not apply and longer times  $T$  are possible. Limiting factors are, for example, the thermal expansion of the atomic cloud.

The technical realisation of the CAI is of lesser importance at this stage. Considering the intended duration of a single interferometer sequence, using Bose-Einstein Condensates might also be the preferred choice (Becker et al. 2018). In this study, individual measurements of the CAI-ACC have a certain duration and its time series have certain spectral properties while the measurements are also affected by external effects like rotations.

## 2.2 In-Orbit Simulation of Electrostatic and CAI Accelerometers

In this study we consider a GRACE-like satellite pair in a circular polar orbit around the Earth with an altitude of 480 km. The simulation is implemented in the MATLAB/Simulink based eXtended High Performance satellite dynamics Simulator (XHPS; Wöske et al. 2019) developed by ZARM/DLR. XHPS calculates the orbits of a GRACE-FO mission scenario under consideration of the Earth's gravity field 'EGM2008' (up to d/o 90), non-gravitational forces (atmospheric drag, solar radiation pressure, Earth albedo and thermal radiation pressure) and the GRACE satellite geometry. To consider the effect of non-gravitational forces on the spacecraft, we use a detailed surface model of the satellite body included in XHPS.

The IMU measures the linear accelerations and angular rates acting on the satellite. In this study, we consider a simplified case, where we assume to have a perfect knowledge of the angular velocities and therefore, only the measurements of linear accelerations by an electrostatic accelerometer (E-ACC) are considered as the measurements of conventional IMU.

The E-ACC measures the sum of non-gravitational accelerations acting on the satellite in three orthogonal directions (along-track, cross-track and radial). The sensor model of an E-ACC, based on the GRACE ACC sensitive axis with a noise level of  $10^{-10} \text{ m/s}^2/\sqrt{\text{Hz}}$  in frequencies above  $10^{-3} \text{ Hz}$ , is implemented in XHPS. The sampling rate of the E-ACC is 10 Hz.

Later during this study, we also use a more accurate model of E-ACC with a noise level of  $10^{-11} \text{ m/s}^2/\sqrt{\text{Hz}}$  in



frequencies above  $10^{-3}$  Hz and test the performance of its hybridization with the CAI-ACC model.

The functionality of the algorithm also depends on the accelerometer noise in timescales of the CAI measurement duration. Although better performing E-ACC have already been flown in space (e.g. GOCE; Marque et al. 2010) or are published as recent developments (Christophe et al. 2018), the GRACE-FO type accelerometer was chosen to later compare with GRACE-FO gravity field solutions. This scenario is also a worst case scenario, i.e. if our method works successfully for this accelerometer, an accelerometer with a lower noise is not a priority to enable a hybrid accelerometer. A conventional E-ACC usually has its best performance in higher frequencies, while at lower frequencies the measurements suffer from a large noise. The low frequency noise shows its impact on the measured accelerations as a bias (see Fig. 4). The accelerometer measurements therefore can be written as:

$$A_{ACC} = B + S \cdot A_{non-grav.} + N, \quad (2)$$

where  $B$  is the accelerometer bias,  $S$  is the accelerometer scaling factor and  $N$  stands for the random noise. In this study, we ignore the scaling factor and focus on the determination of the E-ACC bias.

For the CAI-ACC a white noise at the level of  $10^{-10}$  m/s<sup>2</sup>/√Hz is assumed. The assumption is based on the results of terrestrial applications (e.g. Freier et al. 2016) and the fact that the CAI measurement is directly related to the frequency stability of the laser system (see also Eq. (1) and Abich et al. 2019; Sanjuan et al. 2021). As shown by Abrykosov et al. (2019), a CAI-ACC with a higher noise level will not improve the gravity field solution. Therefore, it is also unlikely that a gravity field mission will be launched with a CAI-ACC performing not at least at this level (Alonso et al. 2022).

The signal of the CAI accelerometer is modelled based on Eq. (1). However, because of the change of the non-gravitational acceleration during the CAI interrogation time, we integrate this equation by considering the sensitivity function of CAI as described in Knabe et al. (2022).

For the noise modelling, we use a band-limited white noise in the frequency range of  $10^{-5}$  Hz to  $10^{-1}$  Hz from which we produce a noise time series. Then, we add this noise to the acceleration signal and calculate the measured phase of the cold atom interferometry accelerometer.

### 3 Extended Kalman Filter

The benefit of the hybridization of cold atom and electrostatic accelerometers for gravity field missions under certain circumstances has already been shown (e.g. Abrykosov

et al. 2019). These studies typically generate noise-only time series for the two accelerometers and combine them, e.g., by filtering. The hybrid accelerometer noise, converted to ranging accelerations, is then added to the ranging observations prior to gravity field recovery. Our method aims at combining the (noisy) measurements of the two accelerometers while simultaneously using the measurements of the electrostatic accelerometer to solve phase ambiguities of the cold atom interferometer. The method introduced here can potentially be used in real time for data generated by future hybrid sensors and has already been demonstrated by experiment for application in inertial navigation (Weddig et al. 2021).

The measurements of the CAI and the electrostatic ACC have different sampling rates, e.g. 0.1 Hz and 10 Hz, which have to be combined to create a hybrid accelerometer. In this study, we adapt an extended Kalman filter (EKF) based approach used for inertial navigation (Tennstedt and Schön 2021). This filter system uses the E-ACC data as input to the dynamic model in order to predict the phase shift and the expected observation of the atom interferometer, effectively solving the fringe ambiguity. The CAI data is then used as actual observation in return to estimate the bias of the E-ACC. The equations are stated for a system oriented in the along-track direction. This can be realized by a single CAI sensor with its sensitive axis oriented along the respective spatial axis of the body-frame of the vehicle.

The functionality of the algorithm depends on the amplitude of the input signal (non-gravitational accelerations) as well as the change in a given time interval and these are largest in the along-track direction for our scenario. The amplitude and change of signal for the cross-track and radial axis are smaller and require less accuracy from the electrostatic accelerometer to solve the phase ambiguity of a single measurement.

#### 3.1 Dynamic System and Phase Prediction

The measurement of CAI and IMU is combined in the body-frame (b-frame), which is aligned with the CAI sensor. In order to predict the phase shift which is based on the position of the atoms in the laser field during the interrogation pulses, cf. Tennstedt and Schön (2021) and Antoine and Borde (2003), the motion equations of the atoms in the body-frame are utilized. The state vector reads

$$\mathbf{x} = [q^b, v^b, b_a]^T, \quad (3)$$

with  $v^b$  as atom velocity and  $q^b$  as atom position in the along-track direction in the body-frame affected by the accelerations and acceleration bias  $b_a$  of the electrostatic IMU.

The evolution of the kinematic state can be described by the following system of ordinary differential equations (ODE).

$$\dot{q}^b = v^b, \quad (4)$$

$$\dot{v}^b = f^b + b_a, \quad (5)$$

$$\dot{b}_a = 0, \quad (6)$$

where  $f^b$  are specific forces affecting the system, i.e. non-gravitational accelerations. It is assumed that the platform is stabilized and thus no Coriolis term due to the rotation occurs.

For the prediction step of the filter, this system is numerically solved by trapezoid integration. The predicted phase shift of the interferometer is given by (Tennstedt and Schön 2021):

$$\Phi_{pred} = k_{\text{eff}} \left( q^b(T_f) - 2q^b\left(\frac{1}{2}T_f\right) \right), \quad (7)$$

where the total filter step time  $T_f$  equals twice the interrogation time  $T_f = 2T$ . The two atom positions at  $T$  and  $2T$  are gained from the numerical integration.

For the covariance propagation, the transition matrix  $\mathbf{F}_k$  is needed. The systems solution after discretisation yields:

$$\mathbf{x}_{k+1} = \mathbf{F}_k \mathbf{x}_k + \mathbf{B}_k \mathbf{u}_k + \mathbf{w}_k. \quad (8)$$

The homogeneous part of the solution is characterized by the wanted transition matrix  $\mathbf{F}_k$ :

$$\mathbf{F}_k = \begin{pmatrix} 1 & \Delta t & 0 \\ 0 & 1 & \Delta t \\ 0 & 0 & 1 \end{pmatrix}, \quad (9)$$

where  $\Delta t$  is the filter time constant.

The particular solution with the input matrix  $\mathbf{B}_k = [\frac{1}{2}\Delta t^2, \Delta t, 1]^T$  denotes any perturbations that affect the system, here mainly resembled by accelerations  $\mathbf{u}_k = f^b$ , as well as another additive noise component  $\mathbf{w}_k$  to allow the adaption of the filter.

The system noise  $\mathbf{Q}_k$  can be approximated:

$$\mathbf{Q}_k = (\mathbf{B}_k E[\mathbf{u}_k \mathbf{u}_k^T] \mathbf{B}_k^T + E[\mathbf{w}_k \mathbf{w}_k^T]) \Delta t. \quad (10)$$

The formal variance  $E[\mathbf{u}_k \mathbf{u}_k^T]$  is used to include the E-ACC data uncertainty.

### 3.2 CAI Observation Equation

The CAI observation equation is based on the transition probability  $p$  that follows the sinusoidal fringe pattern:

$$p = A \cos(\Phi_L + \Phi_{pred} + \delta\Phi) + p_0. \quad (11)$$

The fringe amplitude  $A$  and zero offset  $p_0$  are regarded as known constants over the time of the experiments. The laser phase  $\Phi_L$  is assumed to be regulated by the controller so that the sum of  $\Phi_L + \Phi_{pred}$  is always at the operating point  $\pi/2$  (*mid-fringe*).

The error phase shift  $\delta\Phi$  is the part that results from any errors of the accelerations measured by the conventional IMU, here biases. It couples the observation equation with the state parameters.

In order to enable a connection between this phase shift and the system model, Eq. (5) is utilized again. This time the equation is solved analytically under the assumption of a time-constant system during the measuring interval, making it easier to derive the matrix  $\mathbf{H}$ .

Since the filter is only active during the measurement cycle of the CAI,  $T_f$  essentially equals the filter time constant  $\Delta t$  that was introduced before.

The integrated acceleration bias leads to the following velocity increment:

$$\delta v = b_a T_f. \quad (12)$$

The equation for  $\delta\Phi$  is then

$$\delta\Phi = \frac{1}{4} k_{\text{eff}} b_a T_f^2, \quad (13)$$

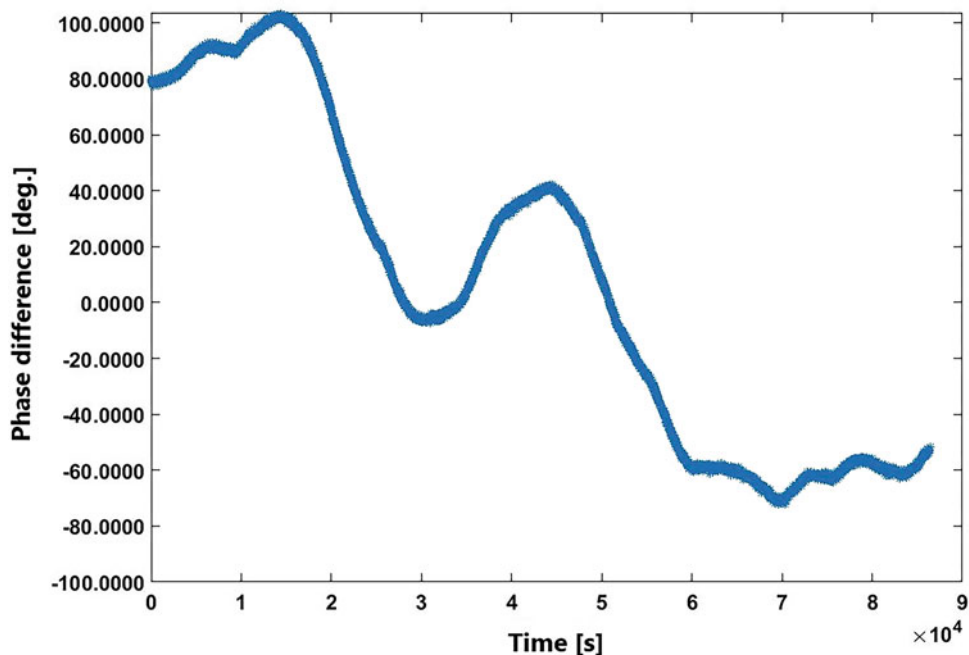
which is similar to the more familiar expression  $\delta\Phi = k_{\text{eff}} a T^2$  from the first section. All discussed values plugged into Eq. (11) result in:

$$p = A \cos\left(\frac{\pi}{2} + \frac{1}{4} k_{\text{eff}} b_a T_f^2\right) + p_0. \quad (14)$$

The final observation matrix  $\mathbf{H} = \frac{\partial p}{\partial \mathbf{x}}$  reads:

$$\mathbf{H}^T = \begin{pmatrix} 0 \\ 0 \\ -\frac{1}{4} A \cdot k_{\text{eff}} T_f^2 \end{pmatrix}. \quad (15)$$

**Fig. 2** The difference between the true CAI phase and the determined phase based on the E-ACC measurements in one day of the mission



Note that the constant system assumption is only necessary for the calculation of the measurement sensitivities in matrix **H**. The calculation of the innovation follows the original non-linear equations described before.

The observation uncertainty of the atom interferometer measurement is expressed in  $R = \sigma_p^2$ .

## 4 Results and Discussion

### 4.1 Solving for the Phase Ambiguity

The CAI sensor has a phase ambiguity which has to be solved for. Our approach here is to use the phase shift equivalent to the acceleration measured by E-ACC to determine the target part of the cosine interval. This only works if the bias and the integrated noise of the IMU in the respective measurement cycle is smaller than half of the cosine flank  $\pi/2$ .

In the case that the phase difference between the CAI and the predicted phase is higher than  $\pi/2$ , but lower than  $\pi$ , the filter will not be able to directly estimate the phase ambiguity. However, it will likely converge to the right direction and in the next iteration there is a good chance that the phase difference is further reduced. Therefore, after a few iterations, the CAI phase ambiguity will be estimated correctly.

Monte Carlo simulations of in-flight CAI-ACC and E-ACC are performed to study the phase differences and to verify whether or not this approach can be used for the case of satellite gravimetry. Those simulations show that in most of the cases (>95%) the phase difference  $\phi_{IMU} - \phi_{CAI}$

stays below the limit of  $\pi$  (see Fig. 2). The assumptions here are the satellite altitude of 480 km, the CAI interferometer duration of 10 s and assumed E-ACC noise as shown in Fig. 1.

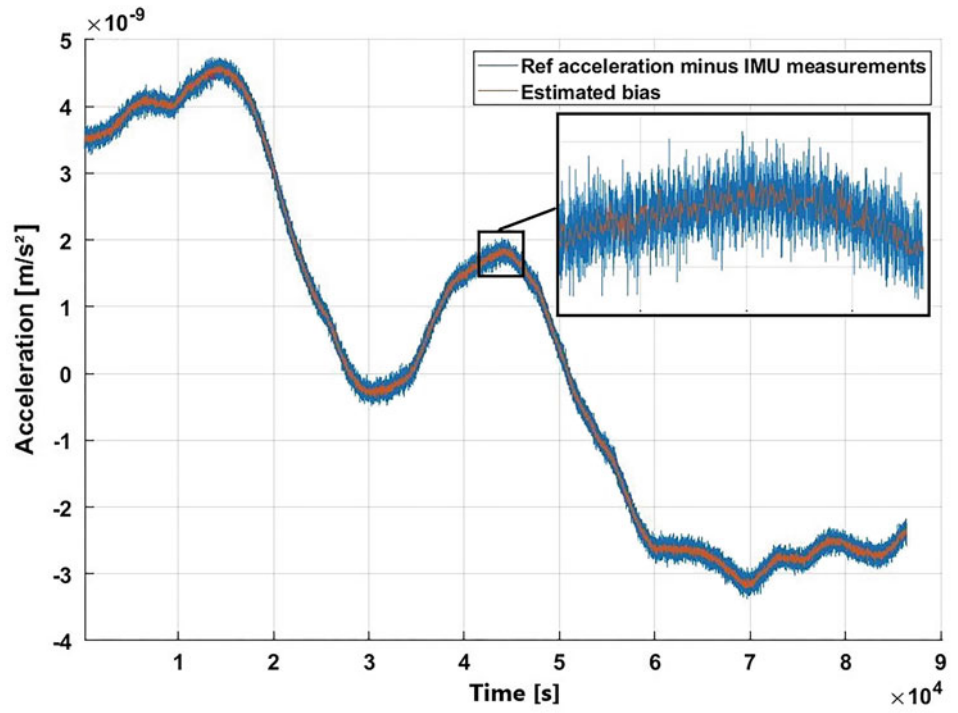
Our investigation shows that in the few cases where the CAI and IMU phase difference temporarily go beyond the  $\pi$  limit, the difference between the CAI and predicted phase (IMU phase plus the estimated error model) is still below the limit and the filter is able to recover the bias. Therefore, the final estimation of bias and acceleration is not considerably affected by it.

### 4.2 Hybridization of CAI-ACC with the GRACE-FO E-ACC

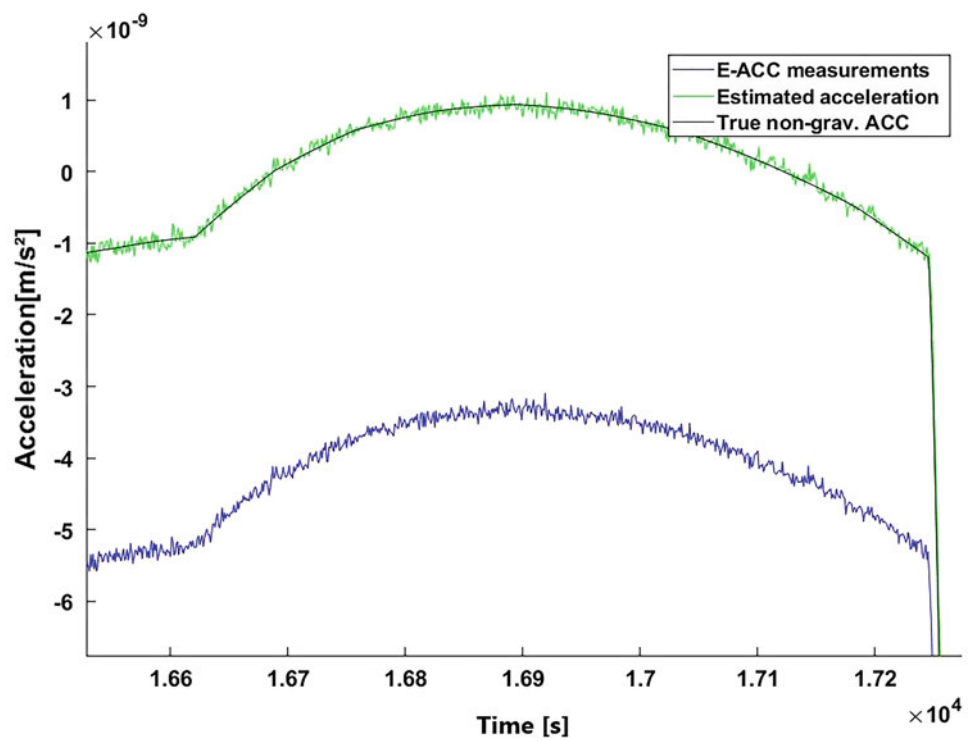
For the first test scenario, we consider an electrostatic accelerometer with the same performance as the GRACE-FO accelerometer as discussed in Sect. 2.2. Figure 3 shows the estimated bias as an output of the EKF compared to the true E-ACC bias (non-gravitational signal minus E-ACC measurements). Figure 4 compares the filtered accelerations to the model of non-gravitational accelerations and the measurements of the E-ACC. One can notice the improvements that are achieved in the measured accelerations by using a CAI accelerometer. The Kalman filter also recognises the steep decline in non-gravitational accelerations due to the entry of the satellite into the Earth's penumbra.

To truly compare the output of the filter to the original, one must look at the noise in the frequency domain.

**Fig. 3** Blue: The difference between non-gravitational accelerations and the measurements of E-ACC; Magenta: Estimated ACC bias using extended Kalman filtering



**Fig. 4** Short segment of non-gravitational accelerations with measurements of E-ACC (blue), estimated accelerations using the Kalman filter (green) and true non-gravitational accelerations (black) as modelled in XHPS; the steep decline is due to the entry of the satellite into the Earth's penumbra



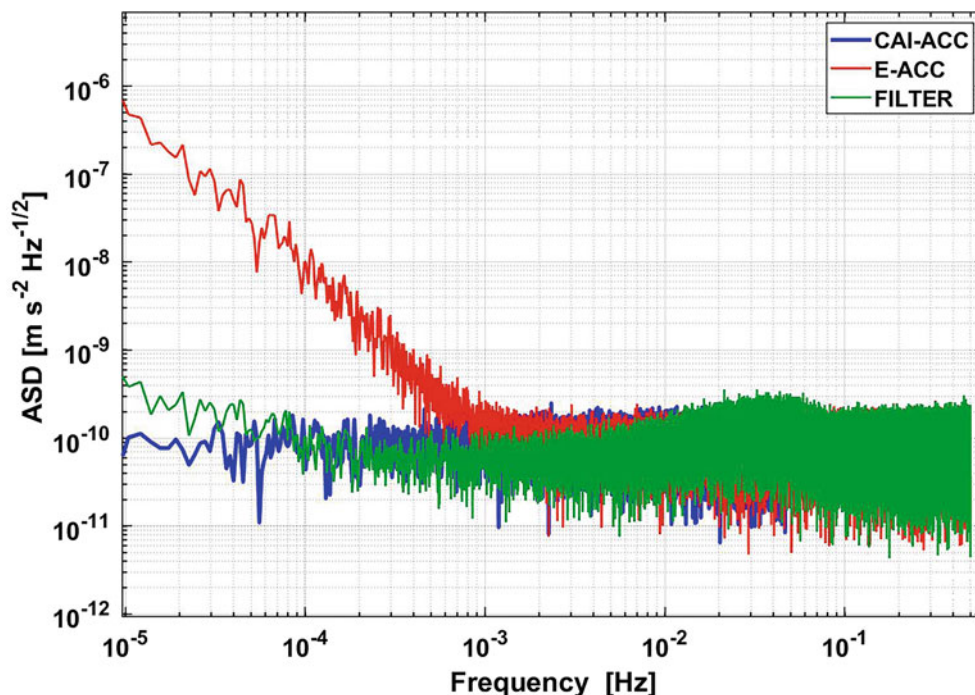


**Fig. 5** Hybridization of CAI-ACC with the GRACE-FO E-ACC; spectral representation of the solutions in terms of amplitude spectral density for CAI-ACC (blue) and E-ACC measurements (red), and the Kalman filter (green)

Figure 5 shows the amplitude spectral densities of the CAI and electrostatic accelerometer together with the filter solution, with the modelled non-gravitational accelerations removed. The filter output has gained the accuracy of CAI-ACC measurements at lower frequencies as well as benefiting from the accuracy of E-ACC at higher frequencies.

### 4.3 Hybridization of CAI-ACC with an Improved E-ACC

In the second test scenario, we assume an E-ACC with a noise level of  $10^{-11} \text{ m/s}^2/\sqrt{\text{Hz}}$  in frequencies above  $10^{-3} \text{ Hz}$  and test the performance of its hybridization with the CAI-ACC model. In this case, because of the higher accuracy of E-ACC, the phase difference between the IMU measurements and the CAI measurements are considerably lower and in most of the cases ( $>98\%$ ) remain below  $\pi/2$  which then leads to a better estimation of the CAI ambiguity.

Figure 6 compares the amplitude spectral densities of the CAI, electrostatic accelerometer together with the filter solution, with the modelled non-gravitational accelerations removed. The filter output has reached the good accuracy of E-ACC measurements at higher frequencies as well as benefiting from the stability of CAI-ACC measurements at lower frequencies. These results, suggest that the described filter is perfectly able to be adopted to different electrostatic

and CAI accelerometer accuracies and find the optimal solution in different scenarios.

However, to fully benefit from the instrumental improvements of the quantum accelerometers as well as the LRI, progress to reduce temporal aliasing is also necessary. This is achieved by improved background modelling, e.g., the next generation of AOD products, and deploying multiple satellite pairs. The application of our method in such mission scenarios is part of the ongoing work on this topic.

### 4.4 Discussion on the Impact of Rotational Accelerations and Gravity Gradient on the Measurements

The effect of rotational accelerations and gravity gradients are not considered in this study. However, here we discuss certain properties which are relevant for CAI measurements. The main rotation, which affects a CAI accelerometer in the along-track direction of a satellite, is the rotation about the cross-track axis due to the orbital frequency. The biggest contribution of this rotation on the atom interferometer phase shift comes from the Coriolis acceleration (Sagnac effect) induced by the atomic velocity in the radial direction (Lévêque et al. 2021).

In addition to the Coriolis acceleration, we have the Euler acceleration and the centrifugal acceleration. However, depending on position and orientation of CAI-ACC in the

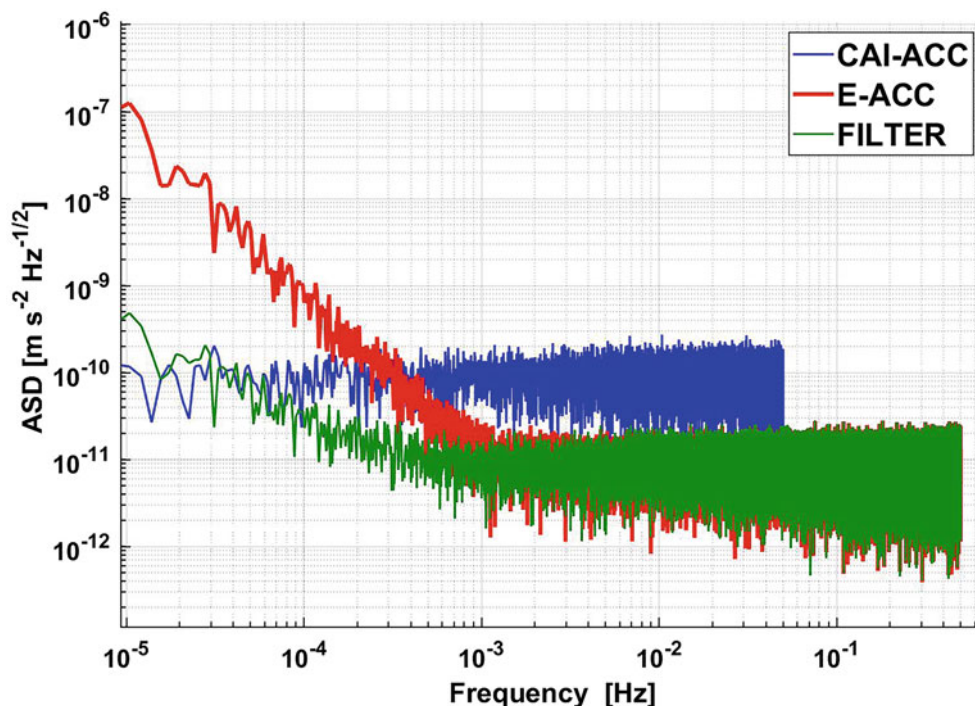


**Fig. 6** Hybridization of CAI-ACC with an improved E-ACC; spectral representation of the solutions in terms of amplitude spectral density for CAI-ACC (blue) and E-ACC measurements (red), and the Kalman filter (green)

satellite frame, the CAI-ACC might not see parts of these effects. For example, if the CAI-ACC is placed on top of the E-ACC on the  $z$  axis (nadir direction), the centrifugal acceleration would be perpendicular to the CAI-ACC sensitivity axis in along-track direction and therefore, it would not be seen by the instrument. In addition to the rotational accelerations, higher order contributions couple these inertial forces, in particular with gravity gradients. This additional phase shift induces a bias on the measurement of the instrument (Lévêque et al. 2021). The effect of rotational accelerations during one CAI cycle is either physically compensated or the CAI phase shift is calculated and corrected this way. The latter method, however, does not restore the contrast loss due to the Coriolis effect. Therefore, a technical solution would be advantageous.

The impact of the main rotation due to the orbital frequency, can be passively compensated by counter rotating the Raman wave vector, e.g., by designing the laser beam path of the atom interferometer accordingly (see e.g. Migliaccio et al. 2019; Trimeche et al. 2019, for a nadir pointing gradiometer). For the remaining small residual rotation errors, a high performance gyroscope can be used in order to measure the rotation and mathematically cancel its contribution on the output phase shift (Lévêque et al. 2021). The residual rotation errors can also be compensated by active tip-tilt actuation of the retro-reflection mirror (Lan et al. 2012; Migliaccio et al. 2019), preferably mounted directly to the E-ACC housing. Alternatively, the design described by

Christophe et al. (2018) for a hybrid accelerometer uses the electrostatic accelerometer proof mass as reference mirror in the Raman interferometer, effectively linking both measurements.

When the E-ACC test mass is in the center of mass of the satellite, the atomic test mass cannot be in the center of mass at the same time. The initial position of the atoms will have an offset with respect to the center of mass after the cooling step of the atom interferometer sequence resulting in a gravity gradient and a gravitational pull of the satellites mass on the atoms. Based on this initial position, which is identical for each atom interferometer sequence, and the mass distribution of the satellite a systematic bias can be calculated and corrected in the atom interferometer phase. The impact of rotational accelerations and positioning of CAI-ACC and E-ACC inside the satellite will be considered in an upcoming study.

Goswami et al. (2021) have shown that the GRACE-FO attitude and orbit control system is capable of controlling the satellites attitude within  $\pm 100 \mu\text{rad}$ , which is the mission requirement for the pointing accuracy of the LRI (Abich et al. 2019). The beam steering mechanism of the LRI has demonstrated a pointing error below  $10 \mu\text{rad}$  in the lab (Schütze et al. 2014). Investigations of LRI data estimate the noise of the beam steering to be below  $2 \mu\text{rad}/\sqrt{\text{Hz}}$ . The combination of the LRI differential wavefront sensing and beam steering with the star camera and IMU is proposed to increase the overall accuracy of the attitude determination

and therefore, it can be used to further reduce the effect of the satellite rotation on the phase shift (Goswami et al. 2021).

## 5 Conclusions

Satellite gravity missions successfully map the Earth's gravity field and its change over time. Accelerometers determine the non-gravitational accelerations acting on the satellite. One limiting factor in the gravimetry missions is the accelerometer performance especially in lower frequencies. Using CAI-based accelerometers in the next generation of satellite gravimetry missions can provide long-term stability and precise measurements of the non-gravitational forces acting on the satellites. This would allow a better monitoring of several geophysical phenomena.

We study the hybridization of CAI and electrostatic accelerometers by applying an extended Kalman filter to the measurements. In this approach the classic IMU resolves the high-frequency non-gravitational accelerations while the precision of the calculated hybrid solution benefits from the superior long-term CAI accuracy. Our results show that the EKF can be used to combine the measurements of conventional inertial measurement units with the CAI accelerometers measurements in a way to benefit from both measurements.

For the next generation of satellite gravimetry missions, using a lower altitude and also CAI accelerometers with longer interrogation times will be beneficial. We will study those cases in the future. One major challenge would be that with longer interrogation time, the sensitivity of CAI would be higher and as a result, the dynamical range of the CAI sensor would be smaller. Therefore, one might not be able to determine the CAI ambiguity directly with the measurements of the E-ACC. Drag compensation which would decrease the amplitude of the input accelerations closer to the dynamical range of the CAI-ACC could be a solution here.

In the future, we will also study more complex cases where the impact of rotational rates and gravity gradients are also considered on the CAI measurements and we will compare the achievable accuracy of the recovery of the gravity field with the data from current gravimetry missions. We will also run a number of simulations where we use hybrid accelerometers with different configurations and on different satellite constellations, e.g. on low-altitude drag-free satellites. We will then compare the results to find the optimal scenarios for using hybrid accelerometers in future satellite gravimetry.

**Acknowledgements** This work is supported by the Deutsche Forschungsgemeinschaft (DFG, German Research Foundation) Collaborative Research Center 1464 “TerraQ” – 434617780 and Germany's Excellence Strategy – EXC-2123 “QuantumFrontiers” – 390837967.

B.T. acknowledges support from the Federal Ministry for Economic Affairs and Energy (BMWi), Project 50RK1957. A.K. acknowledges support from “Niedersächsisches Vorab” through initial funding of research in the DLR-SI institute.

**Author Contributions** A.H., B.T. designed and performed the main studies. A.H. modelled the electrostatic and CAI accelerometers. B.T. adapted EKF. A.H., B.T., M.S. wrote first draft. A.K. created initial GRACE simulation scenario. All authors provided critical input to the final version.

**Data Availability Statement** Datasets generated in this study are available from the corresponding author on reasonable request.

## References

- Abend S, Gersemann M, Schubert C, Schlipfert D, Rasel EM, Zimmermann M, Efremov MA, Roura A, Narducci FA, Schleich WP (2020) Atom interferometry and its applications. In: Rasel EM, Schleich W, Wölk S (eds) Proceedings of the international school of physics, vol 197, pp 345–392. <https://doi.org/10.3254/978-1-61499-937-9-345>
- Abich K, Abramovici A, Amparan B, Baatzsch A, Okihiro BB, Barr DC, et al. (2019) In-orbit performance of the GRACE follow-on laser ranging interferometer. *Phys Rev Lett* 123(3):031101. <https://doi.org/10.1103/PhysRevLett.123.031101>
- Abrykosov P, Pail R, Gruber T, Zahzam N, Bresson A, Hardy E, Christophe B, Bidet Y, Carraz O, Siemes C (2019) Impact of a novel hybrid accelerometer on satellite gravimetry performance. *Adv Space Res* 63(10):3235–3248. <https://doi.org/10.1016/j.asr.2019.01.034>
- Alonso I, Alpigiani C, Altschul B, Araujo H, Arduini G, Arlt J, Badurina L, Balaz A, Bandarupally S, et al. (2022) Cold atoms in space: Community workshop summary and proposed road-map. <https://arxiv.org/abs/2201.07789>
- Antoine C, Borde CJ (2003) Quantum theory of atomic clocks and gravito-inertial sensors: an update. *J Opt B Quantum Semiclass Opt* 5(2):S199–S207. <https://doi.org/10.1088/1464-4266/5/2/380>
- Becker D, Lachmann MD, Seidel ST, Ahlers H, Dinkelaker AN, Grosse J, et al. (2018) Space-borne Bose–Einstein condensation for precision interferometry. *Nature* 562(7727):391–395. <https://doi.org/10.1038/s41586-018-0605-1>
- Christophe B, Boulanger D, Foulon B, Huynh PA, Lebat V, Liorzou F, Perrot E (2015) A new generation of ultra-sensitive electrostatic accelerometers for GRACE Follow-On and towards the next generation gravity missions. *Acta Astronaut* 117:1–7. <https://doi.org/10.1016/j.actaastro.2015.06.021>
- Christophe B, Foulon B, Liorzou F, Lebat V, Boulanger D, Huynh PA, Zahzam N, Bidet Y, Bresson A (2018) Status of development of the future accelerometers for next generation gravity missions. In: Freymueller JT, Sánchez L (eds) International symposium on advancing geodesy in a changing world, vol 149. Springer International Publishing, Cham, International Association of Geodesy Symposia, pp 85–89. [https://doi.org/10.1007/1345\\_2018\\_42](https://doi.org/10.1007/1345_2018_42)
- Flury J, Bettadpur S, Tapley BD (2008) Precise accelerometry onboard the GRACE gravity field satellite mission. *Adv Space Res* 42(8):1414–1423. <https://doi.org/10.1016/j.asr.2008.05.004>
- Freier C, Hauth M, Schkolnik V, Leykauf B, Schilling M, Wziontek H, Scherneck HG, Müller J, Peters A (2016) Mobile quantum gravity sensor with unprecedented stability. *J Phys Conf Ser* 723:012050. <https://doi.org/10.1088/1742-6596/723/1/012050>

- Goswami S, Francis SP, Bandikova T, Spero RE (2021) Analysis of GRACE Follow-On laser ranging interferometer derived intersatellite pointing angles. *IEEE Sens J* 21(17):19209–19221. <https://doi.org/10.1109/JSEN.2021.3090790>
- Haagmans R, Siemes C, Massotti L, Carraz O, Silvestrin P (2020) ESA's next-generation gravity mission concepts. *Rend Lincei-Sci Fis* 31:15–25. <https://doi.org/10.1007/s12210-020-00875-0>
- Kasevich M, Chu S (1991) Atomic interferometry using stimulated Raman transitions. *Phys Rev Lett* 67(2):181–184. <https://doi.org/10.1103/PhysRevLett.67.181>
- Klinger B, Mayer-Gürr T (2016) The role of accelerometer data calibration within GRACE gravity field recovery: Results from ITSG-Grace2016. *Adv Space Res* 58(9):1597–1609. <https://doi.org/10.1016/j.asr.2016.08.007>
- Knabe A, Schilling M, Wu H, HosseiniArani A, Müller J, Beaufile Q, Pereira dos Santos F (2022) The benefit of accelerometers based on cold atom interferometry for future satellite gravity missions. In: Freymueller J, Sánchez L (eds) *Proceedings of the international association of geodesy symposia*, Beijing, China, June 28–July 2 2021. [https://doi.org/10.1007/1345\\_2022\\_151](https://doi.org/10.1007/1345_2022_151)
- Lan SY, Kuan PC, Estey B, Haslinger P, Müller H (2012) Influence of the coriolis force in atom interferometry. *Phys Rev Lett* 108(9):090402. <https://doi.org/10.1103/PhysRevLett.108.090402>
- Loomis BD, Rachlin KE, Wiese DN, Landerer FW, Luthcke SB (2020) Replacing GRACE/GRACE-FO with satellite laser ranging: Impacts on Antarctic ice sheet mass change. *Geophys Res Lett* 47(3):e2019GL085488. <https://doi.org/10.1029/2019GL085488>
- Lévesque T, Fallet C, Manda M, Biancale R, Lemoine JM, Tardivel S, Delavault S, Piquereau A, Bourgogne S, Pereira Dos Santos F, Battelier B, Bouyer P (2021) Gravity field mapping using laser coupled quantum accelerometers in space. *J Geod* 95(15). <https://doi.org/10.1007/s00190-020-01462-9>
- Manda M, Dehant V, Cazenave A (2020) GRACE—gravity data for understanding the deep Earth's interior. *Remote Sens* 12(24):4186. <https://doi.org/10.3390/rs12244186>
- Marque JP, Christophe B, Foulon B (2010) Accelerometers of the GOCE mission: return of experience from one year of in-orbit. In: *ESA living planet symposium*, vol 686, 28.06.–02.07.2010, Bergen, Norway, p 57
- Migliaccio F, Reguzzoni M, Batsukh K, Tino GM, Rosi G, Sorrentino F, Braitenberg C, Pivetta T, Barbolla DF, Zoffoli S (2019) MOCASS: A satellite mission concept using cold atom interferometry for measuring the Earth gravity field. *Surv Geophys* 40(5):1029–1053. <https://doi.org/10.1007/s10712-019-09566-4>
- Pail R, Bingham R, Braitenberg C, Dobslaw H, Eicker A, Güntner A, Horwath M, Ivins E, Longuevergne L, Panet I, Wouters B, IUGG Expert Panel (2015) Science and user needs for observing global mass transport to understand global change and to benefit society. *Surv Geophys* 36(6):743–772. <https://doi.org/10.1007/s10712-015-9348-9>
- Sanjuan J, Abich K, Blümel L, Gohlke M, Gualani V, Oswald M, Wegehaupt T, Schuldt T, Braxmaier C (2021) Simultaneous laser frequency stabilization to an optical cavity and an iodine frequency reference. *Opt Lett* 46(2):360–363. <https://doi.org/10.1364/OL.413419>
- Schilling M, Wodey E, Timmen L, Tell D, Zipfel KH, Schlippert D, Schubert C, Rasel EM, Müller J (2020) Gravity field modelling for the Hannover 10 m atom interferometer. *J Geod* 94(12):122. <https://doi.org/10.1007/s00190-020-01451-y>
- Schütze D, Stede G, Müller V, Gerberding O, Bandikova T, Sheard BS, Heinzel G, Danzmann K (2014) Laser beam steering for GRACE Follow-On intersatellite interferometry. *Opt Express* 22(20):24117–24132. <https://doi.org/10.1364/OE.22.024117>
- Tapley BD, Watkins MM, Flechtner F, Reigber C, Bettadpur S, Rodell M, et al. (2019) Contributions of GRACE to understanding climate change. *Nat Clim Change* 9(5):358–369. <https://doi.org/10.1038/s41558-019-0456-2>
- Tennstedt B, Schön S (2021) Integration of atom interferometers and inertial measurement units to improve navigation performance. In: *28th Saint Petersburg International Conference on Integrated Navigation Systems (ICINS)*, 31.05.–02.06.2021, St. Petersburg, Russia, IEEE, Piscataway, NJ. <https://doi.org/10.23919/ICINS43216.2021.9470809>
- Thomas JB (1999) An analysis of gravity-field estimation based on intersatellite dual-1-way biased ranging. *Tech. Rep. JPL Publication 98-15*, Jet Propulsion Laboratory, Pasadena, California
- Trimeche A, Battelier B, Becker D, Bertoldi A, Bouyer P, Braxmaier C, Charron E, Corgier R, Cornelius M, Douch K, Gaaloul N, Herrmann S, Müller J, Rasel E, Schubert C, Wu H, Pereira Dos Santos F (2019) Concept study and preliminary design of a cold atom interferometer for space gravity gradiometry. *Classical Quant Grav* 36(21):215004. <https://doi.org/10.1088/1361-6382/ab4548>
- Weddig NB, Tennstedt B, Schön S (2021) Performance evaluation of a three-dimensional cold atom interferometer based inertial navigation system. In: Hecker P (ed) *2021 DGON Inertial Sensors and Systems (ISS)*, 29.–30.09.2021 IEEE, Braunschweig, Germany, pp 1–20
- Wöske F, Kato T, Rievers B, List M (2019) GRACE accelerometer calibration by high precision non-gravitational force modeling. *Adv Space Res* 63(3):1318–1335. <https://doi.org/10.1016/j.asr.2018.10.025>

**Open Access** This chapter is licensed under the terms of the Creative Commons Attribution 4.0 International License (<http://creativecommons.org/licenses/by/4.0/>), which permits use, sharing, adaptation, distribution and reproduction in any medium or format, as long as you give appropriate credit to the original author(s) and the source, provide a link to the Creative Commons license and indicate if changes were made.

The images or other third party material in this chapter are included in the chapter's Creative Commons license, unless indicated otherwise in a credit line to the material. If material is not included in the chapter's Creative Commons license and your intended use is not permitted by statutory regulation or exceeds the permitted use, you will need to obtain permission directly from the copyright holder.







# Gravimetry by Nanoscale Parametric Amplifiers Driven by Radiation-Induced Dispersion Force Modulation

Fabrizio Pinto

## Abstract

Here we present early results from lumped-element numerical simulations of a novel class of nano electromechanical systems (NEMS) presently being considered for ground-based gravimetry and future micro accelerometry applications in GPS-denied environments, including spacecraft. The strategy we discuss is based on measuring the effects of non-inertial or gravitational forces on the dynamics of a standard oscillator driven at its resonance frequency by a time-dependent electrostatic potential. In order to substantially enhance the sensitivity of the instrument, the oscillating mass is made to simultaneously interact with a nearby boundary so as to be affected by quantum electrodynamic Casimir forces. Furthermore, unlike previously published proposals, in the design presented herein the Casimir boundary does not oscillate but it is a fixed semiconducting layer. As already demonstrated experimentally, this arrangement enables Casimir force time-modulation by semiconductor back-illumination. Such a design strategy, first suggested by this author as a promising approach to gravitational wave detection in different nano-sensors, allows for the realization of a Casimir force-pumped mechanical parametric amplifier. Such devices can, in principle, yield gains of several orders of magnitude in the mechanical response amplitude over the response from standard unpumped oscillators. The numerical proof-of-concept first presented herein points to a potentially new class of gravimetry products based on exploiting appropriately engineered dispersion forces as an emerging enabling general purpose technology on the nanoscale.

## Keywords

Dispersion force engineering · Nanodevices and spacecraft systems · Novel accelerometers · Quantum technology for geodesy

## 1 Introduction

The existence of interatomic forces between two neutral, spherically symmetrical atoms in the unretarded regime was first considered by means of the tools of the new quantum mechanics by Wang (1927), and the problem was success-

fully solved by Von Eiseschitz and London (1930). London coined the term “dispersion effect” to describe such forces because of their dependence upon atomic polarizability. A few years later, in order to explain mounting discrepancies between experimental data about particle interactions in lyophobic colloids (Verwey and Overbeek 1946; Verwey 1947) and theoretical predictions from the London theory, Casimir and Polder, following an early intuition by Overbeek, developed the first theory of van der Waals forces within the retarded regime based on quantum electrodynamics (QED) (Casimir and Polder 1948). Shortly thereafter, inspired by a remark by Niels Bohr during a conversation in

F. Pinto (✉)

EKOSPACE and Department of Aerospace Engineering, Faculty of Engineering, Izmir University of Economics, Balçova/Izmir, Türkiye  
e-mail: [fabrizio.pinto@ieu.edu.tr](mailto:fabrizio.pinto@ieu.edu.tr)

© The Author(s) 2022

J. T. Freymueller, L. Sánchez (eds.), *Geodesy for a Sustainable Earth*, International Association of Geodesy Symposia 154, [https://doi.org/10.1007/1345\\_2022\\_179](https://doi.org/10.1007/1345_2022_179)

233

Copenhagen (Pinto 2019), Casimir published his celebrated calculation of the attractive force between two perfectly conducting plates in terms of the zero-point-energy of the electromagnetic field (Casimir 1948), an approach that many years later he referred to as “Poor Man’s Q.E.D.” (Casimir 1987) (for an introductory discussion of such issues see the treatment of dispersion forces by the author at Pinto (2018)).

Circumventing the negative effects of adhesion (Buks and Roukes 2001), such as *stiction*, to avoid the destruction of nanodevices (Beeby et al. 2004; Corigliano et al. 2018) is but one example of “dispersion force engineering” (Pinto 2008, 2019), that is, “manipulating dispersion forces to achieve a causally quantifiable success” (Pinto 2019). This activity, first discussed in detail by the present author (Pinto 2008, 2019), recognizes the role played by harnessing dispersion forces in device design as meeting the general requirements (Rotolo et al. 2015; Wang 2017) of an “emerging enabling general-purpose technology” (EEGPT) (Pinto 2019). The evolution of dispersion forces from a physical phenomenon to be studied in the laboratory and to be theoretically understood (Pinto 2019) to a technological tool to be exploited is occurring by the development of techniques to manipulate such interactions in space and to modulate them in time.

A remarkable recent example of the successful manipulation of dispersion forces (Pinto 2019) is ‘gecko glue,’ defined as a class of synthetic adhesives that “recapitulate,” (Mahdavi et al. 2008) in the biotechnological sense (Mendes 2013), key features of gecko feet, including both chemically glueless adhesion in a dry environment and the dense fibrillary arrays of hairlike setae found in the pads of gecko toes (Autumn et al. 2002). These nanomaterials have quickly moved from a theoretical concept to applications in robotics (Henrey et al. 2013), including recently in the International Space Station (Cauligi et al. 2020), and to enabling otherwise impossible human climbing of vertical glass walls (Hawkes et al. 2015). Another example of novel applications wholly enabled by dispersion force engineering is the revolutionary nanotube-based nonvolatile random access memory (NRAM) made by Nantero and tested in the Space Shuttle Atlantis during STS-125 (Nelson 2009). Finally, this author has discussed in detail (Pinto 2019) what can be considered as the archetype of inventions entirely enabled by dispersion force engineering, that is, the now lesser known Johansson blocks. These amazingly accurate mechanical gauges, developed decades before quantum mechanics was introduced, are highly polished to dramatically enhance the effect of van der Waals forces. Indeed, Johansson blocks were mentioned by Feynman in his memorable speech, “There’s Plenty of Room at the Bottom” (Feynman 1992), and, in his *Lectures*, they are presented as “exemplifying the direct attraction between the atoms on one block for the atoms on the other block” (Feynman et al. 1963, Sec. 12-3).

This paper is yet another step forward in the unfolding of dispersion force engineering within the specific context of a novel accelerometer featuring design innovations based on technologies derived from quantum field theory. Past studies explored the impact of Casimir forces on the performance of traditional NEMS proposed for use in space applications (Bilhaut and Duraffourg 2009), specifically including possible negative effects in accelerometers (Andreucci et al. 2006). However, most previous investigations considered strategies to avoid nonlinearities, pull-in, and stiction rather than to enable novel performance. In important studies in which the Casimir force was considered as a possible enabling factor, this was typically restricted to the static Casimir force (Serry et al. 1995). In experiments reporting use of the Casimir force as an actuation mechanism, modulation was successfully achieved mechanically, by varying the width of the gap between the two interacting boundaries (Chan et al. 2001a,b).

Two previous contributions to this subfield by the present author will be crucial in what follows (Sect. 2). The former was the observation that, in analogy to the vibration of a condenser microphone membrane, experimentally demonstrated dispersion force modulation based on semiconductor back-illumination enables oscillator actuation by a Casimir boundary at rest (Pinto 1999, 2014a). The latter contribution was that, by an appropriate choice of the dispersion force modulation frequency, a Casimir oscillator can serve as a mechanical parametric amplifier, thus leading to dramatic sensitivity enhancement (Pinto 2014b, 2017). This suggestion was applied to gravitational wave detection by a different NEMS but the unique advantages of Casimir force parametric amplification persist in the present system. Although, presently, “there is no experimental observation of parametrically amplified Casimir coupling” (Javor et al. 2021), the parametric amplification approach resulting from the former strategy above presents several performance and nanofabrication advantages over that obtained from a standard mechanical pump (Imboden et al. 2014; Stange et al. 2019; Javor et al. 2021; Gong et al. 2021; Stange et al. 2021). Furthermore, although one specific proposal exists to apply the well-developed analytical theory of Casimir force mechanical parametric amplification (Imboden et al. 2014) to magnetic gradiometry, also featuring numerical simulations (Javor et al. 2021), the present paper may be the only reported application of such design concepts to micro-g accelerometry and gravimetry. Finally, although important experimental and computational reports about combined electrostatic forced and parametric oscillators do exist (Rugar and Grutter 1991; Zhang and Meng 2005; Rhoads et al. 2008; Moran et al. 2013), the results reported herein, to the best of this author’s knowledge, may be the only numerical simulations of Casimir force parametric oscillators carried out without approximating the dynamics of a system employed in accelerometry.

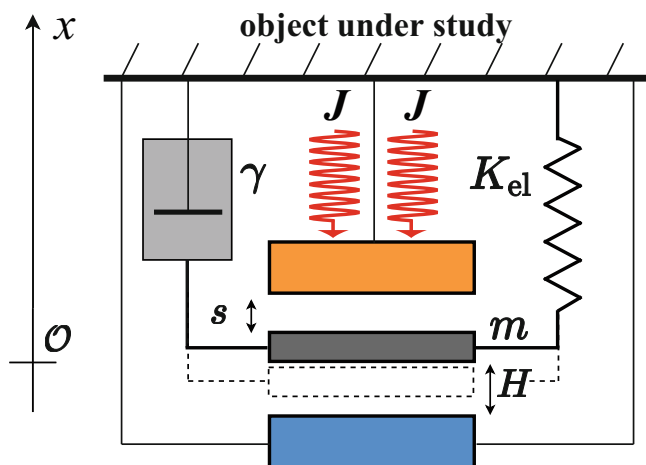


**Fig. 1** Nano-oscillator of proof mass  $m$  under the action of a linear restoring force of elastic constant,  $K_{el}$ , and combined electrostatic and Casimir forces. The friction force is described as  $F_{\text{fric}} = -\gamma\dot{x}$ . The radiation ( $J$ ) back-illuminating the semiconducting layer (orange) is indicated in red. The distance  $s$  is the gap width between the top face of the proof mass and the bottom face of the semiconducting layer when the center of mass of the oscillator is at  $x = 0$ , and similarly for the distance to the electrode (blue),  $H$  (see also Fig. 2)

Although limited by the brevity needed for this report, in the following Section (Sect. 2), we summarize the basic concepts and tools to manipulate dispersion forces in semiconductors by illumination. In Sect. 3, in order to validate our lumped-element oscillator model, we connect the results from our numerical simulations to well-known published experimental and theoretical results. In order of increasing sophistication, starting from a harmonic oscillator (Sect. 3.1), we very briefly discuss electrostatically driven oscillators (Sect. 3.2), static Casimir force perturbations (Sect. 3.3), and parametric amplifiers pumped by a back-illuminated, *fixed*, semiconducting boundary (Sect. 3.4). In Sect. 4, we present the effect of acceleration on the response of the parametric amplifier of Sect. 3.4. The paper closes with Summary and Conclusions, followed by a brief Appendix containing essential information about the numerical approach executed within the Mathematica language (Fig. 1).

## 2 Casimir Force Manipulation

One of the key design innovations introduced in this paper is the implementation of a parametric amplification pump by time-manipulation of the Casimir force between a *fixed* semiconducting boundary and the oscillating proof mass. A treatment of the dependency of dispersion forces in semiconductors on illumination is beyond the scope of this short paper. However, for the purpose of providing an intuitive argument, we recall that the Casimir force (properly,

a pressure) between two imperfect conductors of plasma frequency  $\omega_p$ , for which the dielectric function can be written as  $\epsilon(\omega) \simeq 1 - \omega_p^2/\omega^2$ , is approximately given by  $P(\omega_p, s) = P_{\text{Cas}}(1 - \frac{16}{3}c/\omega_p s)$ , where  $P_{\text{Cas}} = -\pi^2\hbar c/(240s^4)$  is the ideal Casimir force,  $s$  is the gap between the two boundaries, and  $c$  is the speed of light (Lifshitz 1956 and Milonni 1994, p. 229). This result predicts that the magnitude and analytical behavior of the pressure can be altered, for instance, by back-illuminating the boundaries so as to increase the plasma frequency, resulting in a pressure increase. This extremely important effect was first reported in 1979 by Arnold et al. (1979), who employed a novel dynamical detection technique based on a modified condenser microphone placed in a moderate vacuum (Hunklinger et al. 1972). Although the result played an important part in the history of Casimir force experimentation, its technological implications were not noticed until the present author reported the possibility to implement thermodynamical engines on the nanoscale by means of this process (Pinto 1999, 2014a). More recently, new results, acquired with a modified atomic force microscope (AFM), have appeared, confirming the possibility to control dispersion forces by illumination on the nanoscale (Chen et al. 2007a,b).

The computation of the dielectric function to be used in the Lifshitz theory double integral (Lifshitz 1956; Dzyaloshinskii et al. 1961) is not trivial, requiring care about the numerical data involved, appropriate modeling of the irradiation process (Inui 2007), and consideration of subtle thermodynamical issues that have been the subject of intense debate (Klimchitskaya et al. 2009). The present author has reported results from a parametric description of the silicon dielectric function, particularly appropriate for industrial applications (Pinto 2017, Sec. 4).

In this paper, for the purpose of providing a rapid proof-of-concept, it is simply assumed that the back-illumination intensity as a function of time can be programmed so as to yield a Casimir force varying as  $P(s_{\text{eff}}; t) = P_{\text{Cas}}[1 + \epsilon_{\text{Cas}} \cos(2\omega_{es, \text{Cas}}t + \phi)]$ , where  $s_{\text{eff}} < s$  is an effective distance smaller than the actual distance (to satisfy the strict constraint that no Casimir pressure can be larger than the ideal value),  $\epsilon_{\text{Cas}}$  is a parameter connected to the typical description of parametric resonance via the Mathieu equation (Kittel et al. 1965; Landau and Lifshitz 1976; Rhoads et al. 2010) and  $\phi$  is the phase difference between the pump and the electrostatic actuator signals (Fig. 2).

## 3 Nanomechanical Oscillators

The dynamical evolution of NEMS is intrinsically non-linear due to the non-linearity in the coupling between the driving forces and the device structures (Frangi et al. 2008,

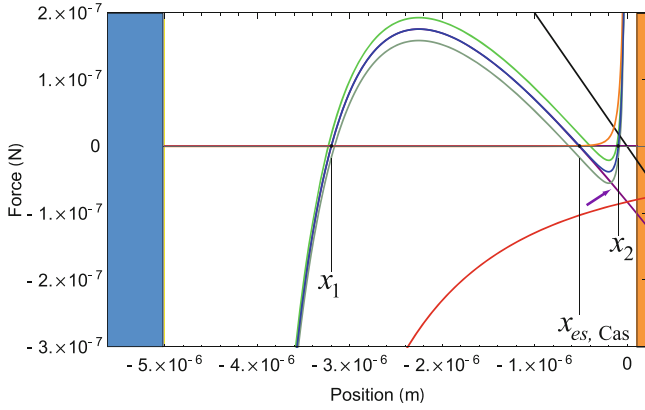


**Fig. 2** Forces acting on the lumped mass, as a function of interboundary distance. On the left (blue,  $x = -5 \mu\text{m}$ ) is the electrode; on the right (orange,  $x = 0.5 \mu\text{m}$ ) is the semiconducting surface. Forces: elastic force (black); Casimir force (orange); electrostatic force (red); total force in the inertial case and in the absence of the Casimir force (purple, shown by the purple arrow at far right); total force in the inertial case in the presence of the Casimir force (blue); total force when the device experiences an acceleration  $a_{DUT} = 1g$  (light green), total force when the device experiences an acceleration  $a_{DUT} = -1g$  (dark green). If the Casimir force is absent, there exist two positions of equilibrium; if the Casimir force is present, there exist three (black dots), of which two ( $x_{1,2}$ ) are unstable and one ( $x_{es,Cas}$ ), whose coordinate is given in Table 1, is stable. For convenience, the proof mass is an infinitely thin layer located at its center of mass. In a physically correct representation retaining the assigned interboundary distances, the right face of the electrode and the left face of the Casimir boundary should be moved by  $\delta_{PM}/2 = 5 \mu\text{m}$  to the left and to the right of their positions in this figure, respectively (see also Fig. 1)

Ch. 7). Consequently, a first approach to the study of the behavior of these systems is often based on linearized, or at least highly simplified, analytical treatments. Despite the obviously important guiding role played by such idealized results, the need for – and the attendant challenges of – realistic numerical simulations to guide the research and development process was recognized long ago (Senturia et al. 1997).

In what follows, we present numerical experiments carried out without any approximations in the treatment of force non-linearities and by integrating the equation of motion numerically to relatively long final times  $t_{fin} \gtrsim 10^3 T_0$ , where  $T_0$  is the natural period of oscillation. In order to insure full reproducibility, in the Appendix we provide basic input information needed to implement these calculations within the Wolfram Mathematica system (v. 11.3.0.0). The results presented in Secs. 3.1, 3.2, 3.3, and 3.4 provide validation of the algorithms by establishing connections to fundamental mechanics as well as to published theoretical and experimental studies in progressively more complex regimes. The numerical experiments about Casimir force-driven parametric amplifiers presented herein complement published analytical results about electrostatic and Casimir force driven systems (Rugar and Grutter 1991; Pinto 2014b;

Imboden et al. 2014; Pinto 2017). The first numerical simulations of a Casimir force parametric amplifier, employed as a magnetic gradiometer in a very different configuration than we consider here, have appeared only very recently (Javor et al. 2021).

### 3.1 Free and Dampened Harmonic Oscillators

As a first test to establish the parameters needed to achieve reliable long term numerical integration (see Appendix for further details), the elementary case of free and dampened harmonic oscillators are first tested. With reference to the numerical adopted parameters shown in Table 1, the relative numerical position error between the analytical solution,  $x_{an}$ , and the numerical solution,  $x_{num}$ , at a final integration time  $t_{fin} = 1 \text{ s}$  ( $\simeq 1,703$  oscillation cycles), is found to be  $[x_{an}(t_{fin}) - x_{num}(t_{fin})]/x_{an}(t_{fin}) \sim 10^{-7}$  and  $3 \times 10^{-6}$  for the free and dampened oscillator, respectively. In absolute terms, these errors are completely negligible since the proof mass is at a distance  $H \sim 1 \mu\text{m}$  from the electrode and  $s \sim 0.3 \mu\text{m}$  from the Casimir boundary (Fig. 1). Even assuming larger integration errors in the more complex systems we analyze below, this limitation does not affect the conclusions drawn from our analysis.

### 3.2 Electrostatically Driven Oscillators

Let us now consider motion driven by the electrostatic force due to a facing electrode (Beeby et al. 2004) biased at a voltage  $V_{tot}(t) = V_{bias} + V_{AC}(t)$ , placed at  $x = -H$  below the position of the lower face of the proof mass when  $V_{tot} = 0 \text{ V}$ , chosen as the origin of the  $x$ -axis (Fig. 1). With this geometry and choice of axis orientation, the net force acting on the proof mass is:

$$F_{net}(t) = -K_{el}x(t) - \frac{1}{2}\epsilon_0 \frac{W_{PM}L_{PM}V_{bias}^2(t)}{(x(t) - H)^2}. \quad (1)$$

A numerical solution algorithm yields the coordinates of the unstable and stable positions of equilibrium,  $x_1$  and  $x_{es}$ , respectively, for the bias voltage,  $V_{bias}$ , given in Table 1; oscillatory motion is only possible in the neighborhood of the stable position of equilibrium at  $x_{es}$ , whereas motion with  $x(t) < x_1$  immediately leads to electrostatic pull-in to the electrode.

As is well known (Chan and Stambaugh 2009), the gradient of the interaction – in this case, the second derivative of the capacitance – causes a significant shift of the resonant frequency,  $\omega_0 \rightarrow \omega_{0,es}$ . This effect can be immediately derived by expanding Eq. (1) to first order in  $\xi(t) =$

**Table 1** Casimir force parametric amplification accelerometer parameters

Fundamental constants	Symbol	Recommended value <sup>a</sup>	
Vacuum electric permittivity	$\epsilon_0$	$8.854187812810^{-12} \text{ F}\cdot\text{m}^{-1}$	
Speed of light in vacuum	$c$	$2.9979245810^8 \text{ m/s}$	
Reduced Planck constant	$\hbar$	$1.05457181710^{-34} \text{ J}\cdot\text{s}$	
Standard gravity	$g_0$	$9.80665 \text{ m/s}^2$	
<i>Material properties</i>	<i>Symbol</i>	<i>Tabulated value</i>	
Silicon density	$\rho_{\text{Si}}$	$2.33 \times 10^3 \text{ kg/m}^3$	
<i>Lumped parameter model inputs</i>	<i>Symbol</i>	<i>Nominal value</i>	
Proof mass width	$W_{\text{PM}}$	$150 \text{ }\mu\text{m}$	
Proof mass length	$L_{\text{PM}}$	$500 \text{ }\mu\text{m}$	
Proof mass thickness	$\delta_{\text{PM}}$	$10 \text{ }\mu\text{m}$	
Elastic constant	$K_{\text{el}}$	$0.2 \text{ N}\cdot\text{m}$	
Quality factor	$Q$	$10^3$	
Electrode-proof mass gap ( $V_{\text{bias}} = 0 \text{ V}$ )	$H$	$5.0 \text{ }\mu\text{m}$	
Bias voltage	$V_{\text{bias}}$	$2.5 \text{ V}$	
<i>Computed model parameters</i>	<i>Symbol/Equation</i>	<i>Theoretical value</i>	<i>Estimated value<sup>b</sup></i>
Capacitance	$C = \epsilon_0 L_{\text{PM}} W_{\text{PM}} / H$	$0.132813 \text{ pF}$	
Electrostatic sensitivity	$S_{\text{es}} =  dC/dH $	$26.5626 \text{ aF/nm}$	
Proof mass	$m = W_{\text{PM}} L_{\text{PM}} \delta_{\text{PM}} \rho_{\text{Si}}$	$1.7475 \times 10^{-11} \text{ kg}$	
Free angular frequency	$\omega_0 = \sqrt{K_{\text{el}}/m}$	$10.698094 \times 10^3 \text{ s}^{-1}$	
Electrostatically shifted frequency	$\omega_{\text{es}}$	$9.386385 \times 10^3 \text{ s}^{-1}$	$(9.38638498 \pm 0.00009482) \times 10^3 \text{ s}^{-1}$
Electrostatically-Casimir shifted frequency	$\omega_{\text{es,Cas}} (s = 0.1 \text{ }\mu\text{m})$	$9.2506487 \times 10^3 \text{ s}^{-1}$	$(9.2493 \pm 0.0005) \times 10^3 \text{ s}^{-1}$
Electrostatically-Casimir shifted frequency	$\omega_{\text{es,Cas}} (s = 0.2 \text{ }\mu\text{m})$	$9.3242324 \times 10^3 \text{ s}^{-1}$	$(9.3240 \pm 0.0003) \times 10^3 \text{ s}^{-1}$
Acceleration-shifted frequency ( $a_{\text{DUT}} = 1g$ )	$\omega_{\text{es,Cas}} (s = 0.1 \text{ }\mu\text{m})$	$9.0916483 \times 10^3 \text{ s}^{-1}$	
Stable equilibrium (no Casimir force)	$x_{\text{es}}$	$-0.51607580 \text{ }\mu\text{m}$	
Stable equilibrium (Casimir force, inertial)	$x_{\text{es,Cas}} (s = 0.1 \text{ }\mu\text{m})$	$-0.51154986 \text{ }\mu\text{m}$	
Stable equilibrium (Casimir force, inertial)	$x_{\text{es,Cas}} (s = 0.2 \text{ }\mu\text{m})$	$-0.51363449 \text{ }\mu\text{m}$	
Stable equilibrium (Casimir force, $a_{\text{DUT}} = 1g$ )	$x_{\text{es,Cas}} (s = 0.1 \text{ }\mu\text{m})$	$-0.39567671 \text{ }\mu\text{m}$	
Response (inertial, pump off)	$X_0 (s = 0.1 \text{ }\mu\text{m})$		$45.5281 \text{ nm}$
Response ( $a_{\text{DUT}} = 1 \text{ mg}$ , pump off)	$X_0 (s = 0.1 \text{ }\mu\text{m})$		$45.4679 \text{ nm}$
Mechanical sensitivity (pump off)	$S_{\text{mech}}$		$60.2 \text{ nm/g}$
Response (inertial, $\epsilon_{\text{Cas}} = 0.2$ , $\phi = -162^\circ$ )	$X_0 (s = 0.1 \text{ }\mu\text{m})$		$0.10957 \text{ }\mu\text{m}$
Response ( $a_{\text{DUT}} = 1 \text{ mg}$ , $\epsilon_{\text{Cas}} = 0.2$ )	$X_0 (s = 0.1 \text{ }\mu\text{m})$		$0.10949 \text{ }\mu\text{m}$
Mechanical sensitivity ( $\epsilon_{\text{Cas}} = 0.2$ , $\phi = -162^\circ$ )	$S_{\text{mech}}$		$87.7 \text{ nm/g}$
Overall sensitivity ( $\epsilon_{\text{Cas}} = 0.2$ , $\phi = -162^\circ$ )	$S = S_{\text{es}} \cdot S_{\text{mech}}$		$2.66 \text{ fF/g}$

<sup>a</sup> NIST 2018 CODATA Recommended Values

<sup>b</sup> The resonance frequency was estimated by a non-linear fit to a Lorentzian with the numerical data from Case 1 (Fig. 3)

$|x(t) - x_{\text{es}}| \ll H$  and by collecting the first order term in  $\xi(t)$  with the elastic force, which yields, in our coordinate system:

$$\omega_{0,\text{es}} = \sqrt{\omega_0^2 - \frac{\epsilon_0 W_{\text{PM}} L_{\text{PM}} V_{\text{bias}}^2}{m |x_{\text{es}}|^3}}. \quad (2)$$

In order to validate this expression, this frequency shift is detected by calculating the dynamical amplitude response of the system to a signal obtained by imposing a signal  $V_{\text{AC}}(t) = V_{\text{AC},0} \cos \omega t$ . The resonance frequency is determined by a non-linear best fit of the amplitude data to the standard forced oscillator amplitude response (Feynman et al. 1963, Ch. 23; Kittel et al. 1965, Ch. 7) by means of the Origin package (v. 8.5.1). The results are shown in Fig. 3 and in Table 1.

### 3.3 Oscillators with Static Casimir Force Perturbation

In this Section, we consider the dynamical effects of the Casimir force between the proof mass and a fixed plate placed above the upper boundary of the proof mass across an empty gap of width  $s$  (Fig. 1). As previously discussed (Sect. 2), the attractive Casimir force on the proof mass, assuming perfectly conducting, parallel plane boundaries, neglecting edge effects, is  $F_{\text{Cas}} = (W_{\text{PM}} L_{\text{PM}}) \pi^2 \hbar c / (240 s^4)$  (Table 1) in our reference frame.

The special case including a constant Casimir force (in the sense defined at Sect. 2) but excluding both electrostatic actuation ( $V_{\text{tot}} = 0 \text{ V}$ ) and frictional forces was first treated by Maclay and collaborators (Serry et al. 1995). Although, under those circumstances, the energy of the system is

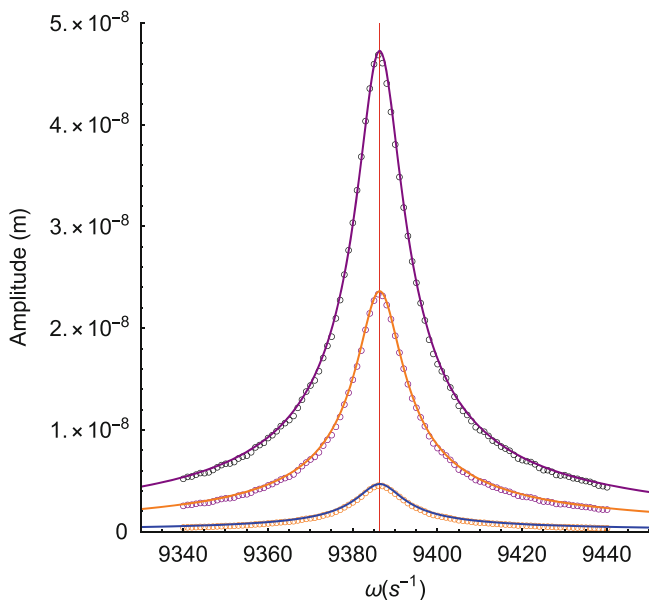


**Fig. 3** Response of the system of Table 1 to electrostatic actuation (no Casimir force), for  $V_{\text{bias}} = 2.5 \text{ V}$  and  $V_{\text{AC}} = 100 \text{ } \mu\text{V}$  (Case 1, top curve),  $V_{\text{AC}} = 50 \text{ } \mu\text{V}$  (Case 2, middle curve) and  $V_{\text{AC}} = 5 \text{ } \mu\text{V}$  (Case 3, bottom curve) (compare to Chan et al. 2001b, Fig. 2)

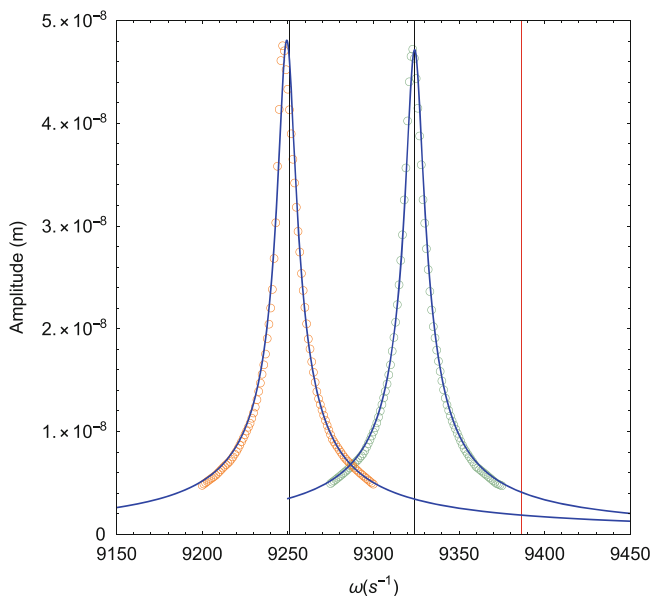


**Fig. 4** Response of the system of Table 1 to electrostatic actuation (with Casimir force), for  $s = 0.1 \text{ } \mu\text{m}$  (left, orange) and  $s = 0.2 \text{ } \mu\text{m}$  (right, green). Also shown are the best fits yielding the estimated resonance frequencies in Table 1 (blue) and the resonant frequency in the absence of the Casimir force (red). The distortion from the Lorentz curve due to Casimir force-induced non-linearities is evident as a peak asymmetry in the curve on the left (compare to Chan et al. 2001b, Fig. 4a)

conserved so that resonances cannot occur, that early attack to the problem highlighted the extreme sensitivity of the dynamical evolution of NEMS to Casimir force magnitude

and geometry. This, in turn, led to the breakthrough conclusion, fully confirmed by the later evolution of this field of studies (Pinto 2019), that “...the attractive force between parallel surfaces may not always have to be dealt with as a nuisance; rather, it may be manipulated to perform useful tasks ...” (Serry et al. 1995).

In analogy to the electrostatic case, the presence of a Casimir interaction gradient causes a resonance frequency shift (Chan et al. 2001b) extremely sensitive to the Casimir gap width (Fig. 4).

### 3.4 Combined Forced and Parametric Oscillators

The combined presence of forced electrostatic oscillations and Casimir force parametric resonance have been the subject of two independent research efforts. In one, the electrostatic pumping by a *fixed* electrode adopted by Rugar and Grutter (1991) was replaced by Casimir force pumping produced by a periodically oscillating mass (Imboden et al. 2014; Stange et al. 2019; Javor et al. 2021). In the other, pursued by this author (Pinto 2014b, 2017), Casimir force pumping is again produced by a *fixed* boundary by means of Casimir force time-manipulation. The results for the gain from our numerical simulations are shown in Fig. 5.

## 4 Accelerometry with Casimir Force Amplifiers

Having validated the approach of this paper, we can proceed to reporting simulations of the proof-of-concept lumped parameter model enabled by Casimir force parametric amplification with back-illumination of a fixed semiconducting boundary operated in open-loop mode and employed as an accelerometer. The frequency shift for an acceleration  $a_{\text{DUT}} = 1g$  is shown in Fig. 6. An instrument monitoring the mechanical response at resonance could detect an acceleration both as a measurable resonance frequency peak shift and as a capacitance change in a non-inertial reference frame. Importantly, in this first report, we show a gain  $\approx 2.4$  at the appropriate phase  $\phi$ . However, the choice of NEMS parameter values made here was quite conservative and only aimed at showing proof of concept. It is well known from the theory of Casimir force parametric resonance that, by decreasing the Casimir force gap,  $s$ , and by appropriately adjusting all design parameters, gains  $\sim 10^3$  are feasible (Imboden et al. 2014). Therefore, the overall sensitivity,  $S$ , given by the product of the electrical and mechanical sensitivities (Frangi et al. 2015) and shown in Table 1, can be expected to rise to  $S \approx 3 \times 10^3 \text{ fF/g}$ . This compares quite favorably with

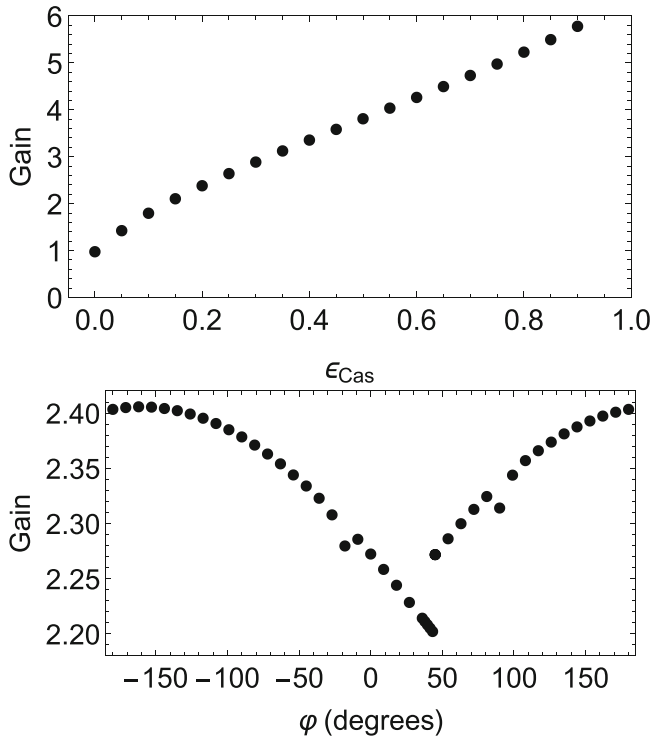


**Fig. 5** The gain, defined as the ratio of the response amplitude with pump-on to the same quantity with pump-off ( $G = X_0(\text{pump-on})/X_0(\text{pump-off})$ ), as a function of the Casimir force modulation parameter,  $\epsilon_{\text{Cas}}$  (top) and the phase between the forcing electrostatic potential and the pump,  $\phi$  (bottom) (compare to Rugar and Grutter 1991, Fig. 2). Although the latter diagram shows a general behavior mindful of that of the corresponding quantity in the electrostatic case, nonlinearities are seen to give rise to additional features. For instance, two smaller dips exist on either side of the main deamplification minimum. Also, the deamplification minimum (amplification maximum) does not take place for  $\phi = 0^\circ$  ( $\phi = \pm 180^\circ$ ) but for  $\phi \simeq 43^\circ$  ( $\phi \simeq -162^\circ$ ) and its minimum is larger than in the electrostatic case

values  $\sim 1 - 10$  fF/g typical of commercial highly sensitive accelerometers (Corigliano et al. 2018).

## 5 Summary and Conclusions

In this paper, we have presented a novel concept for a micro-g accelerometer with features attractive in such applications as geodetic continuous ground-based gravitational field monitoring and in the determination of non-gravitational acceleration in orbiting spacecraft. The architecture of the proposed device is based on a nano-electromechanical system (NEMS) driven by the simultaneous application of forced electrostatic oscillations by a biased electrode, further parametrically amplified by a pump modulating Casimir forces via back-illumination of a semiconducting boundary.

In order to amplify the magnitude of the response of the system, we adopted a strategy first proposed by the author

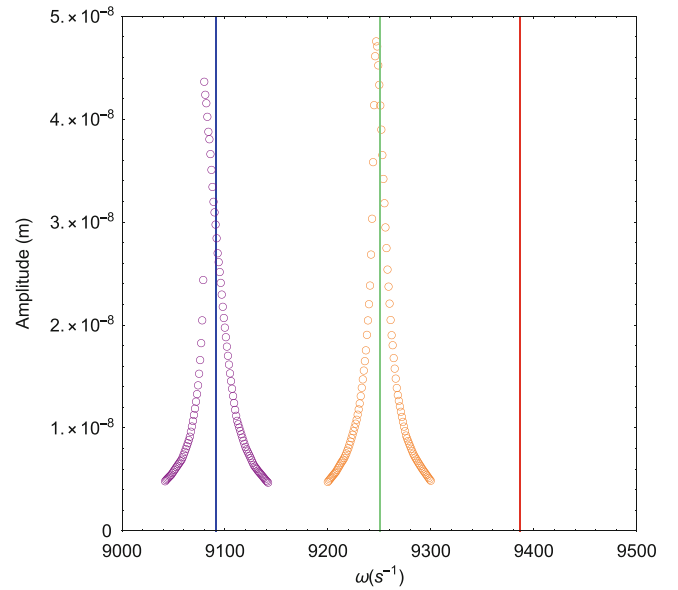


**Fig. 6** Response of the system of Table 1 forced by electrostatic actuation (with Casimir force), for  $s = 0.1 \mu\text{m}$  (right, orange) in an inertial reference frame (same data as in Fig. 4), compared to the same system undergoing an acceleration  $a_{\text{DUT}} = 1g$  (left, purple). The theoretical resonance frequencies without Casimir force (red), with Casimir force in an inertial frame (black), and with Casimir force in a non-inertial frame (blue) are also displayed. The extreme peak asymmetry due to Casimir force-induced non-linearities is further enhanced by the effect of the fictitious force acting on the proof-mass

in the context of table-top gravitational wave detection, that is, parametric amplification achieved by modulation of the Casimir force by illumination. By adopting values of the design parameters typical of Casimir force experimentation with NEMS, we demonstrated by numerical simulations that the pump can yield a moderate amplification factor.

Among the advantages of the design discussed herein is that the Casimir force parametric amplifier is not driven by mechanical oscillations of the Casimir boundary, as in the very few other reports in the literature, but is produced by illumination of fixed boundaries. Also, the inherent tunability of the potential well is extremely promising within the context of possible closed-loop implementations.

For reasons of space, in this short discussion we only aimed at presenting a numerical proof-of-concept of the design. However, existing analytical treatments developed by other authors in different contexts clearly show that the parametric amplification gain can reasonably be expected to actually reach several orders of magnitude.

In addition to exploring the very rich parameter space of the system we discussed, our next steps will include extensive explorations of non-linearities, simulations of the effects of noise, and closed-loop applications.

The results of such follow-up exhaustive analysis will be applied to instrumentation applications typical of geodesy,

particularly connected to such main geodetic goals as gravitational measurements with a relative accuracy of 1 ppb. Furthermore, the novel NEMS technology presented herein, enabled by the existence of modulated quantum electrodynamic forces caused by the uncertainty principle in systems with boundaries, should be considered as yet another research effort in the field of quantum technologies and related instrumentation for geodesy.

## Appendix: Wolfram Mathematica Algorithms

The strategy followed in all cases is the direct numerical integration of the equations of motion by the function `NDSolve` in Wolfram Mathematica (Wolfram Research 2018) (see also Pinto 2018; Dubin 2003). The choice of the `Method` strategy is important to treat the full problem, in which both the electrostatic potential and the Casimir force are time dependent and are turned on and off by Heaviside step functions. The resonance frequency and amplitude of the system response are determined by a Lorentzian best-fit with the `Origin` package. Additional Mathematica testing is done by the discrete Fourier transform of the solution with the `Fourier` function and by means of the `PeakDetect` and `FindPeaks` functions. A similar mathematical approach was pioneered by Maclay and collaborators (Serry et al. 1995), whose numerical findings we confirmed and greatly expanded.

## Conflict of Interest

The authors declare that they have no conflict of interest.

## References

- Andreucci P, Duraffourg L, Ollier E, Nguyen V, Delay MT, Robert P (2006) In: Proceedings of IEEE sensors. IEEE, Daegu, Korea, pp 1057–1060
- Arnold W, Hunklinger S, Dransfeld K (1979) *Phys Rev B* 19(4):6049
- Autumn K, Sitti M, Liang YA, Peattie AM, Hansen WR, Sponberg S, Kenny TW, Fearing RS, Israelachvili JN, Full RJ (2002) *Proc Natl Acad Sci USA* 99(19):12252
- Beeby S, Ensell G, Kraft M, White N (2004) MEMS mechanical sensors. Artech House, Boston
- Bilhaut L, Duraffourg L (2009) *Acta Astronautica* 65(9–10):1272
- Buks E, Roukes ML (2001) *Phys Rev B* 63(3):033402
- Casimir HBG (1948) *Proc Kon Ned Akad Wetenschap* 51:793
- Casimir HBG (1987) In: Greiner W (ed) *Physics of strong fields*. Springer, US, pp 957–964
- Casimir HBG, Polder D (1948) *Phys Rev* 73(4):360
- Cauligi A, Chen TG, Suresh SA, Dille M, Ruiz RG, Vargas AM, Pavone M, Cutkosky MR (2020) In: International symposium on artificial intelligence, robotics and automation in space (i-SAIRAS), Pasadena, California
- Chan HB, Stambaugh C (2009) In: Applications of nonlinear dynamics. Springer, Berlin, Heidelberg, pp 15–24
- Chan HB, Aksyuk VA, Kleiman RN, Bishop DJ, Capasso F (2001a) *Science* 291:1941
- Chan HB, Aksyuk V, Kleiman R, Bishop D, Capasso F (2001b) *Phys Rev Lett* 87(21):21
- Chen F, Klimchitskaya GL, Mostepanenko VM, Mohideen U (2007a) *Phys Rev B* 76:035338
- Chen F, Klimchitskaya GL, Mostepanenko VM, Mohideen U (2007b) *Opt Express* 15(8):4823
- Corigliano A, Ardito R, Comi C, Frangi A, Ghisi A, Mariani S (2018) *Mechanics of microsystems. The Wiley microsystem and nanotechnology series*. Wiley, Hoboken, NJ
- Dubin D (2003) *Numerical and analytical methods for scientists and engineers using mathematica*. Wiley-Interscience, Hoboken, NJ
- Dzyaloshinskii I, Lifshitz EM, Pitaevskii LP (1961) *Adv Phys* 10(38):165
- Feynman RP (1992) *J Microelectromech Syst* 1(1):60
- Feynman RP, Leighton RB, Sands M (1963) *The Feynman's lectures on physics*. Caltech, Pasadena
- Frangi A, Cercignani C, Mukherjee S, Aluru N (eds) (2008) *Advances in multiphysics simulation and experimental testing of MEMS*. Imperial College Press, London
- Frangi A, Laghi G, Langfelder G, Minotti P, Zerbini S (2015) *J Microelectromech Syst* 24(4):1077
- Gong T, Corrado MR, Mahbub AR, Sheldon C, Munday JN (2021) *Nanophotonics* 10(1):523
- Hawkes EW, Eason EV, Christensen DL, Cutkosky MR (2015) *J R Soc Interface* 12(102):20140675
- Henrey M, Krahn J, Ahmed A, Wormnes K, Menon C (2013) In: 12th symposium on advanced space technologies in robotics and automation ASTRA 2013, ESA/ESTEC (May 15–17). Noordwijk, The Netherlands, pp 1–6
- Hunklinger S, Geisselman H, Arnold W (1972) *Rev Sci Instrum* 43(4):584
- Imboden M, Morrison J, Campbell DK, Bishop DJ (2014) *J Appl Phys* 116:134504
- Inui N (2007) *J Phys Conf Ser* 89:012018
- Javor J, Yao Z, Imboden M (2021) *Microsyst Nanoeng* 17:73
- Kittel C, Knight WD, Ruderman MA (1965) *Berkeley physics course, vol 1 (Mechanics)* 1st edn. McGraw Hill Book Company, New York
- Klimchitskaya GL, Mohideen U, Mostepanenko VM (2009) *Rev Mod Phys* 81:1827
- Landau LD, Lifshitz EM, *Mechanics*, 3rd edn. Pergamon Press, Oxford (1976)
- Lifshitz EM (1956) *Sov Phys JETP* 2(1):73
- Mahdavi A, Ferreira L, Sundback C, Nichol JW, Chan EP, Carter DJD, Bettinger CJ, Patanavanich S, Chignozha L, Ben-Joseph E, Galakatos A, Pryor H, Pomerantseva I, Masiakos PT, Faquin W, Zumbuehl A, Hong S, Borenstein J, Vacanti J, Langer R, Karp JM (2008) *Proc Natl Acad Sci USA* 105(7):2307
- Mendes PM (2013) *Che Soc Rev* 42(24):9199
- Milonni PW (1994) *The quantum vacuum*. Academic Press, San Diego
- Moran K, Burgner C, Shaw S, Turner K (2013) In: *Nonlinear theory and its applications, IEICE*, vol 4, pp 198–224
- Nelson B (2009) *Nanotechnology Now*, 9–11
- Pinto F (1999) *Phys Rev B* 60(21):14740
- Pinto F (2008) In: El-Genk MS (ed) *Space technology and applications int. forum (STAIF-2008)* AIP Conf. Proc. 969. AIP, Melville, New York, pp 959–968
- Pinto F (2014a) *Am Sci* 102:280
- Pinto F (2014b) *Int J Mod Phys D* 23(12):1442001
- Pinto F (2017) In: Bianchi M, Jantzen RT, Ruffini R (eds) *Proceedings of the fourteenth marcel grossmann meeting on general relativity, held in Rome, Italy, 12–18 July 2015*. World Scientific, Singapore, pp 3175–3182



- Pinto F (2018) In: Di Bartolo B (ed) Quantum nano-photonics, NATO science for peace and security series B: Physics and biophysics (Erice, Sicily, Italy). Springer Nature B. V., Berlin, pp 149–180
- Pinto F (2019) In: Schulz MJ, Shanov VN, Yin J, Cahay M (eds) Nanotube superfiber materials, science to commercialization, chap 29. Elsevier, Amsterdam, pp 729–794
- Rhoads JF, Miller NJ, Shaw SW, Feeny BF (2008) *J Vibration Acoust* 130:061006. ASME, Las Vegas, NV
- Rhoads JF, Shaw SW, Turner KL (2010) *J Dyn Syst Measur Control* 132(3):034001
- Rotolo D, Hicks D, Martin BR (2015) *Research Policy* 44:1827
- Rugar D, Grutter P (1991) *Phys Rev Lett* 67(6):699
- Senturia S, Azuru N, White J (1997) *IEEE Comput Sci Eng* 4(1):30
- Serry FM, Walliser D, Maclay G (1995) *J Microelectromech Sys* 4(4):193
- Stange A, Imboden M, Javor J (2019) *Microsyst Nanoeng* 5:14
- Stange A, Campbell DK, Bishop DJ (2021) *Phys Today* 74:42
- Verwey EJW (1947) *J Phys Colloid Chem* 51:631
- Verwey EJW, Overbeek JTG (1946) *Trans Faraday Soc* 42(7):B117
- Von Eiseschitz R, London F (1930) *Z Phys* 60:491
- Wang SC (1927) *Phys Z* 28:663
- Wang Q (2017) *J Assoc Inf Sci Tech* 69(2):3631634
- Wolfram Research (2018) *Mathematica* 11.3.0.0. <https://www.wolfram.com/mathematica>
- Zhang W, Meng G (2005) *Sensors Actuat A Phys* 119(2):291

**Open Access** This chapter is licensed under the terms of the Creative Commons Attribution 4.0 International License (<http://creativecommons.org/licenses/by/4.0/>), which permits use, sharing, adaptation, distribution and reproduction in any medium or format, as long as you give appropriate credit to the original author(s) and the source, provide a link to the Creative Commons license and indicate if changes were made.

The images or other third party material in this chapter are included in the chapter's Creative Commons license, unless indicated otherwise in a credit line to the material. If material is not included in the chapter's Creative Commons license and your intended use is not permitted by statutory regulation or exceeds the permitted use, you will need to obtain permission directly from the copyright holder.



---

## Part IV

### Earth Rotation



# On the Improvement of Combined EOP Series by Adding 24-h VLBI Sessions to VLBI Intensives and GNSS Data

Lisa Lengert, Daniela Thaller, Claudia Flohrer, Hendrik Hellmers, and Anastasiia Girdiuk

## Abstract

The publicly available Earth Orientation Parameter (EOP) time series provided by the Earth Orientation Centre of the IERS (e.g., IERS Bulletin A, IERS 14 C04) result from the combination of individual space-geodetic solutions on a daily basis, i.e., a parameter-level combination. Current activities of the Federal Agency for Cartography and Geodesy (BKG) focus on the development of a combination strategy, the main objective of which is to improve the consistency between the space-geodetic techniques through common parameters, i.e., mainly EOP, but also station coordinates and tropospheric parameters using local ties and atmospheric ties, respectively. In this study, we present our combination strategy and the results of the combination of VLBI data available within approximately two weeks (i.e., Intensive and R1/R4 sessions) with data from the global GNSS network. The combination is done at the normal equation (NEQ) level on a daily and multi-day basis. We compare our EOP solutions with the respective daily and multi-day single-technique EOP solutions as well as with the low-latency inter-technique EOP time series (COMBI RAP) examined in previous studies, which is based on the combination of GNSS and VLBI Intensive data only. We found regarding the dUT1 solution, that the addition of the VLBI R1/R4 sessions to the VLBI Intensives and GNSS data has a positive impact on the entire 7-day solution, and especially stabilizes the dUT1 estimates of the boundary days of the multi-day continuous polygon. The dUT1 estimates of the left and right boundary day compared to IERS Bulletin A and COMBI RAP reveal an improvement in terms of WRMS of the residuals by 2.3  $\mu\text{s}$  and 1.4  $\mu\text{s}$ , respectively. For the pole coordinates, the consistency of the estimates with external reference series is almost at the same level as for the COMBI RAP solution.

## Keywords

Combination at the normal equation level · EOP · Global geodetic reference frame · GNSS · Space-geodetic techniques · VLBI intensives · VLBI rapid sessions

## 1 Introduction

The realization of the global geodetic reference systems comprises the Terrestrial Reference Frame (TRF), the Celestial Reference Frame (CRF) as well as the Earth Orientation

Parameters (EOP). The latter allow for the transformation between the TRF and CRF. The EOP are represented by the difference dUT1 between Universal Time UT1 and Coordinated Universal Time UTC, the polar motion components  $x_p$  and  $y_p$ , and the celestial pole offsets  $\delta X$  and  $\delta Y$ . Each of the EOP typically comes along with a drift parameter covering temporal changes. Therein, the Length-of-Day (LOD), which represents the temporal derivative of dUT1, plays a key role in our combination approach (Thaller 2008; Blossfeld 2015).

L. Lengert (✉) · D. Thaller · C. Flohrer · H. Hellmers · A. Girdiuk  
Federal Agency for Cartography and Geodesy, Section G1, Frankfurt  
am Main, Germany  
e-mail: [lisa.lengert@bkg.bund.de](mailto:lisa.lengert@bkg.bund.de)

The realization of the global reference systems is based on the observation data of the four most-important space-geodetic techniques: Very Long Baseline Interferometry (VLBI), Global Navigation Satellite Systems (GNSS), Satellite Laser Ranging (SLR) and Doppler Orbitography and Radiopositioning Integrated by Satellite (DORIS) (Dick and Thaller 2020). Since the space techniques have different strengths and weaknesses, a combination of all techniques is required for best possible estimation of the reference system products.

However, the current combination methods used for the estimation of the official reference system products have some weaknesses and do not ensure full consistency between TRF, CRF, and EOP. Furthermore, in particular for VLBI and SLR, not all of the available observational data is used in the TRF, CRF and EOP estimation so far.

The aim of our study is the development of an improved combination method with the focus on the estimation of a consistent time series of all EOP. For this purpose, we focus in this paper on the combination of all VLBI data available within approx. two weeks (i.e. Intensive and R1-/R4-sessions) with data of the global GNSS network based on the normal equation (NEQ) level. The combination of individual technique contributions at the NEQ level represents the second most rigorous combination method (Thaller 2008; Seitz 2009; Schmid 2009; Blossfeld 2015). For this purpose constraint-free NEQs are stacked to one NEQ system before applying datum constraints and solving for parameters. The resulting parameter solutions, typically including EOP, TRF, CRF and other technique-specific parameters, are more consistent than those from the combination approach performed at the parameter level which is typically applied for the generation of the official IERS EOP products. With the combination at NEQ level the same underlying reference frame can be assured and the correlations between the parameters are considered. If the modelling and parameterization of identical parameters have been handled in the same way for each input NEQ system, the combination on NEQ level can be considered as a good approximation for the combination on observation level, being the most rigorous combination approach.

The dUT1 parameter is the most variable quantity among the EOP with significant unpredictable variations (Dermanis and Mueller 1978; Artz et al. 2014). These can only be measured with the quasi space-fixed technique VLBI (Thaller 2008). The IVS-R1/R4 observation campaigns are conducted every Monday and Thursday. Due to the global IVS network involving up to ten antennas, they are suitable for the determination of all five EOP.

However, these R1/R4 sessions have a rather long latency up to 15 days, from collecting the data until the availability of the SINEX (Solution INdependent EXchange format) files (Nothnagel et al. 2017).

For the daily monitoring of dUT1, VLBI experiments of 1 h duration are organized at least once a day, i.e., the so-called Intensives (INT). These campaigns include two or three antennas whose baselines are characterized by a large east-west extension that is particularly sensitive to dUT1 (Robertson et al. 2008; Leek et al. 2015). Due to the sparse network and short observation time, the INT sessions are not suitable for the determination of other EOP components. The big advantages of these sessions are, however, the latency of two days or even less as well as the scheduling for each day (Nothnagel and Schnell 2008; Nothnagel et al. 2017; Dermanis and Mueller 1978). Figure 1 illustrates the weekly session distribution of the GNSS and both VLBI observation campaigns used for our combination. It becomes obvious from Fig. 1 that a VLBI-only EOP product will not be regularly spaced.

Table 1 summarizes the different abilities to determine EOP using GNSS and both VLBI observation types: the biweekly 24-h *Rapid* (R1/R4) and daily 1-h *Intensive* (INT) sessions. The satellite-based GNSS is primarily sensitive to polar motion and LOD. The latter can be derived from GNSS

**Table 1** Contributions of GNSS, 1-h VLBI INT sessions and 24-h VLBI R1/R4 sessions to the determination of EOP

	GNSS	VLBI INT	VLBI R1/R4
$x_p, y_p$	✓	✗	✓
$\dot{x}_p, \dot{y}_p$	✓	✗	✓
dUT1	✗	✓	✓
LOD	✓	✗	✓
$\delta X, \delta Y$	✗	✗	✓

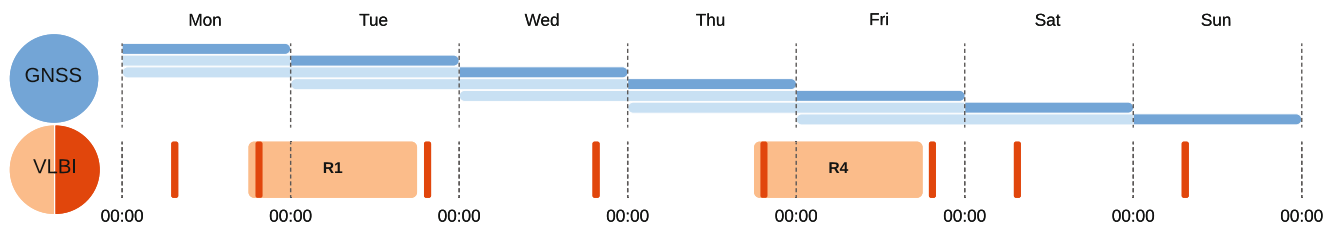


**Fig. 1** Weekly distribution of the GNSS and VLBI observation campaigns used for the combination (GNSS Rapid from CODE AC (dark blue: extracted day; light blue: pre-eliminated days), VLBI Rapid (R1/R4) from BKG AC (light orange), VLBI Intensive from BKG AC (dark orange))

with high internal accuracy but it is systematically biased due to orbit model deficiencies (primarily caused by solar radiation pressure) of the GNSS satellites (Meindl et al. 2014; Thaller et al. 2014; Arnold et al. 2015; Zajdel et al. 2021).

The contributions of GNSS and VLBI INT to the EOP determination are complementary, so that a daily, consistent and regularly spaced low-latency EOP product (except for the celestial pole offsets) can be estimated by combining data of these two observation campaigns (see Table 1). The additional combination with VLBI R1/R4 data further stabilizes all EOP twice per week and enables the estimation of high-precision EOP including the celestial pole offsets with a latency of about two weeks.

In this paper, we focus on the comparison of both combined EOP solutions: the low-latency GNSS and VLBI INT EOP and the extended EOP solution that includes also VLBI R1/R4 data.

## 2 Combination Methodology

In this paper, we present two different combination approaches:

### 1. Combination “rapid” (COMBI RAP):

The multi-day combination of GNSS with VLBI INT only, with a latency of about two days.

### 2. Combination “final” (COMBI FIN):

The multi-day combination of GNSS, VLBI INT and VLBI R1/R4 with a latency of about two weeks.

The combination process is based on a least-squares algorithm using NEQs based on VLBI and GNSS Rapid observation campaigns provided via SINEX files by the BKG IVS Analysis Centre (AC) and CODE<sup>1</sup> (Center for Orbit Determination in Europe) IGS AC, respectively (Engelhardt et al. 2020; Dach et al. 2015). Table 2 summarizes the explicit parameters of the technique-specific NEQs. The VLBI R1/R4 NEQs contain station coordinates (X,Y,Z) and radio source coordinates ( $\alpha$ ,  $\delta$ ) in addition to all five components of the EOP and their temporal derivatives (except for the drift parameter of  $\delta X$  and  $\delta Y$ ). The EOP are parameterized at the middle observation epoch (MOE) of the respective VLBI session (Thorandt et al. 2017). The parameterization of the VLBI INT NEQs is the same, except for the missing celestial pole offsets and source coordinates. The EOP of the GNSS NEQs are parameterized as continuous piecewise linear (pwl) offsets at the day boundaries (0 h, 24 h)

**Table 2** Parameters explicitly contained in the VLBI and GNSS NEQs provided in the SINEX files by the BKG AC and the CODE AC, respectively

	VLBI R1/R4	VLBI INT	GNSS
EOP	dUT1	dUT1	dUT1 (pwl)
	LOD	LOD	–
	$x_p, y_p$	$x_p, y_p$	$x_p, y_p$ (pwl)
	$\dot{x}_p, \dot{y}_p$	$\dot{x}_p, \dot{y}_p$	–
	$\delta X, \delta Y$	–	–
TRF	X,Y,Z	X,Y,Z	X,Y,Z
CRF	$\alpha, \delta$	–	–
GNSS-specific	–	–	Geocenter coordinates
	–	–	Satellite phase center offsets (Z)

including the GNSS observations of three consecutive days. Hence, information about linear temporal changes in EOP are implicitly included (Dach et al. 2015). Additionally to the EOP, the GNSS NEQs include station coordinates, geocenter coordinates (GCC) and satellite phase center offsets (PCO) in Z-direction. All other parameters are pre-eliminated before generating the corresponding SINEX file. Figure 2 summarizes the processing steps and the entire combination procedure. It is an extension of the combination scheme presented in Lengert et al. (2022). It is extended by the multi-day intra-technique VLBI combination (n-VLBI) and the final combination (COMBI FIN) presented hereafter.

For the processing we use the *Combination and Solution* package of the *DGFI Orbit and Geodetic parameter estimation Software* (DOGS-CS), developed at DGFI-TUM (Deutsches Geodätisches Forschungsinstitut, Technische Universität München) (Gerstl et al. 2004).

In order to get a homogenized, datum-free input for the subsequent intra- and inter-technique combination process, each technique-specific NEQ undergoes several transformation procedures. First, the parameterization of the VLBI EOP is adapted to that of the GNSS EOP by converting the offsets and drifts into a continuous pwl polygon with offsets at 0 h and 24 h. In the case of pole coordinates, a linear epoch transformation can be used. The parameters dUT1 and LOD need for the transformation a regularization process using short-term tidal variations accordingly to the IERS Conventions (Petit and Luzum 2010). The advantage of the regularization is, that the reduced parameter  $UT1_R$  and  $LOD_R$  can be approximated by a linear interpolation (Blossfeld 2015). In the case of VLBI R1/R4 NEQs, the observation time window usually includes two standard week-days, i.e., Monday and Tuesday in case of R1 sessions, and Thursday and Friday in case of R4 sessions (see Fig. 1). The current VLBI analysis at the IVS AC provides NEQs in SINEX files that do not allow us to optimally convert the VLBI contribution to a 24-h

<sup>1</sup>CODE is a consortium of the Astronomical Institute of the University of Bern (AIUB, Bern, Switzerland), the Swiss Federal Office of Topography (swisstopo, Wabern, Switzerland), the Federal Agency for Cartography and Geodesy (BKG, Frankfurt a. M., Germany), and the Institut für Astronomische und Physikalische Geodäsie, Technische Universität München (IAPG/TUM, Munich, Germany).

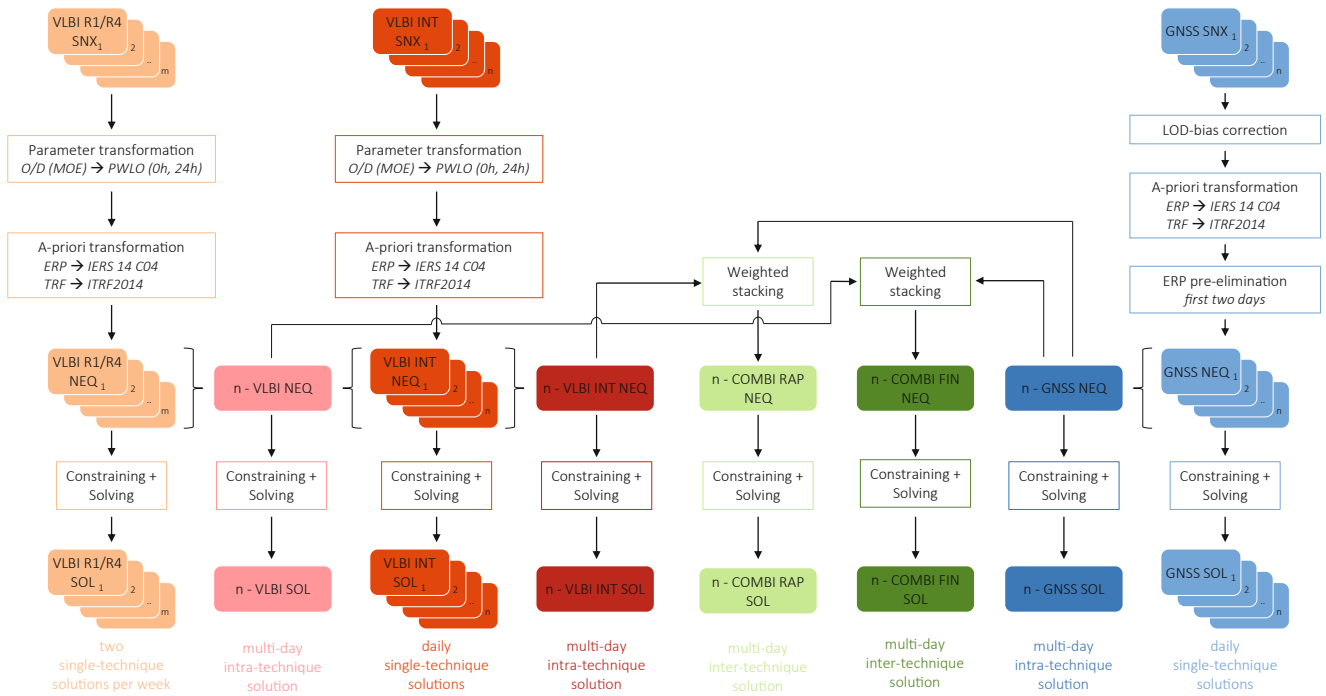


**Fig. 2** Schematic representation of the entire combination strategy and the different solutions. (Extended version of the combination scheme in Lengert et al. (2022))

polygon parameterization of the EOP series. We therefore decided to select the day with the majority of observations (usually Tuesday (R1) and Friday (R4)), and to transform the EOP offset and drift parameters from MOE into two offsets each at 0 h and 24 h of the second day of the respective session (Thaller et al. 2009).

For GNSS, a LOD bias correction must be performed to reduce the drift of the estimated GNSS dUT1 time series due to orbit model deficiencies of the GNSS satellites. Therefore, the dUT1 parameters are corrected using a linear parameter transformation with a time-dependent offset derived from the mean GNSS LOD bias (w.r.t. IERS 14 C04 and IERS Bulletin A) of  $-7.7 \mu\text{s/d}$ . The bias is characterized by a high temporal stability. The mean observation epoch of the 3-day GNSS interval (middle day, 12 h) was chosen as reference point with  $0 \mu\text{s}$  correction. Studies have shown that the selection of the reference point with no correction does not affect the estimated dUT1 values. The addition of Galileo observations into the analysis process has no noticeable effect on the magnitude of the bias (Lengert et al. 2022). Furthermore, the EOP of the last day of each GNSS Rapid are extracted and the EOP offsets of the first two days of the 3-day polygons are pre-eliminated.

In addition, the a priori values of the parameters of all technique-specific NEQs are transformed to a consistent set. For the EOP and station coordinates we chose the *IERS 14 C04* and *ITRF2014* series, respectively (Bizouard et al. 2019; Altamimi et al. 2016). If no ITRF coordinates

are available, the a priori values provided in the SINEX files are retained.

After these transformations, the homogenized NEQs with identical parameterization and a priori values are ready for further combination steps.

In the first combination step, multi-day intra-technique combined NEQs and solutions are generated (see columns 2, 4, 7 in Fig. 2). Therefore, the NEQ systems of consecutive days are accumulated to one NEQ system to obtain a continuous EOP parameterization consisting of a pwl offset polygon up to seven days long. In the case of VLBI, we generated two different multi-day NEQ systems: one containing only the daily 1-h VLBI INT observation campaigns, and a second NEQ series additionally containing the 24-h R1/R4 sessions. The resulting NEQ systems are labeled with “n-VLBI INT”, “n-VLBI”, respectively, with “n” being the total number of combined consecutive days. In case of GNSS, the generation of a multi-day GNSS NEQ (labeled “n-GNSS”) is straight forward.

In the second step, these multi-day single-technique NEQs are combined using a constant technique-specific scaling factor to generate multi-day inter-technique combined NEQ systems. The chosen scaling factor reflects almost the ratio between the technique- or session-specific observation duration. Detailed information on the determination of the appropriate scaling factor can be found in Lengert et al. (2022). For the solution COMBI RAP, the n-GNSS NEQ is combined with the n-VLBI INT NEQ, whereas for COMBI

FIN, the intra-technique combined  $n$ -VLBI NEQ is used instead, i.e. additionally including R1/R4 VLBI sessions (see green parts in Fig. 2). After applying datum conditions and other technique-specific constraints, all these datum-free NEQ systems can be solved for the parameters to be estimated. In summary, eight different solution types are obtained. These are listed in the last row of Fig. 2. Based on these daily and  $n$ -day solutions, time series of EOP are generated for further analysis by using a sliding window approach that is shifted over the daily single-technique NEQs. The NEQs within the window are combined into a multi-day NEQ system. In the next step the window is shifted by one day and the combination is repeated. This procedure is iterated over the whole series of daily NEQs.

### 3 Resulting EOP Series

For the validation of the estimated multi-day EOP, we generate for each time series seven sub-series by extracting EOP of the same day  $d$  from each multi-day pwl offset polygon. The analysis day  $d$  ranges from 0 to  $-6$  and represents the analyzed day within the multi-day polygon, with  $d = 0$  being the rightmost and  $d = -6$  the leftmost day on the time axis. As a result, seven sub-series ( $d = 0, -1, -2, \dots, -6$ ), each with two EOP estimates per day at 0 h and 24 h, can be generated for a weekly combination approach.

To obtain one validation epoch per day, the estimated EOP at 0 h and 24 h are interpolated to a mean epoch, i.e. 12 h.

The problem of validating EOP series is the absence of a known truth. Instead we can compare them against other external EOP products. Hence, we analyse the differences between our estimated EOP series and the *IERS Bulletin A* or *IERS 14 C04* series, interpolated at the very same validation epochs. We study the Weighted Root Mean Square (WRMS) of the time series of EOP residuals. The weighting factors for the WRMS calculation are determined by the reciprocal value of the individual EOP variance.

In the following, we focus on the EOP series estimated from a 7-day solution.

The WRMS values of the dUT1 differences with respect to *IERS Bulletin A* estimated by the COMBI RAP and COMBI FIN approaches are shown in Fig. 3. The comparison epoch is 12 h. The WRMS values of the single-day VLBI INT solution (with fixed LOD a priori values) and the weekly intra-technique combination (7-VLBI INT) are depicted additionally.

Detailed information about the session-wise single-technique solutions (GNSS, VLBI INT, VLBI R1/R4), intra-technique combined solutions ( $n$ -VLBI INT,  $n$ -GNSS) and the rapid combination (COMBI RAP) as well as the session-wise combination of GNSS and VLBI R1/R4 can be found in Lengert et al. (2021).

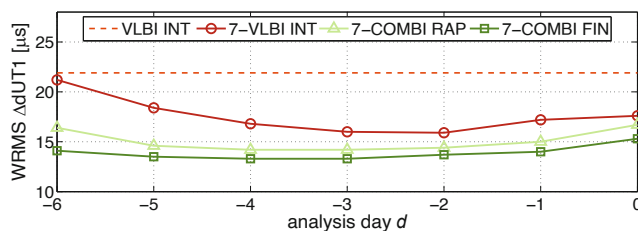


**Fig. 3** WRMS values of dUT1 estimates resulting from different analysis approaches compared to *IERS Bulletin A*. The analysis epoch is 12 h

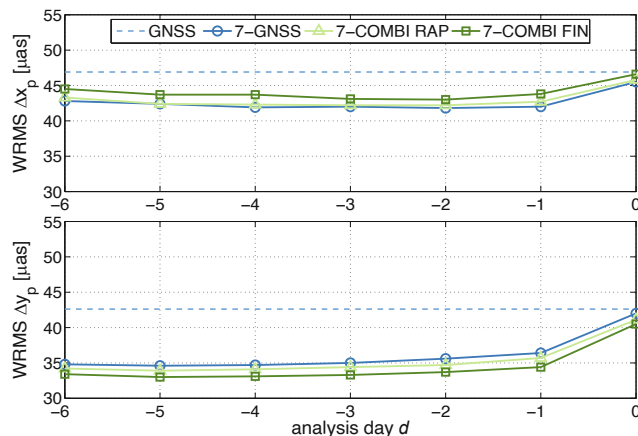


**Fig. 4** WRMS values of the pole coordinate  $x_p$  (top) and  $y_p$  (bottom) estimates resulting from different analysis approaches compared to *IERS 14 C04*. The analysis epoch is 12 h

Figure 3 shows that for the dUT1 parameter an improvement in all WRMS values can be achieved by adding 24 h VLBI data. The biggest reduction in the WRMS values of  $2.3 \mu\text{s}$  and  $1.4 \mu\text{s}$  compared to the COMBI RAP solution is visible for the boundary days  $d = -6$  and  $d = 0$ , respectively. In accordance with expectations, the estimates are stabilized by adding the 24-h VLBI data available twice a week.

Figure 4 shows the WRMS values of the six extracted  $x_p$  (top) and  $y_p$  (bottom) sub-series, resulting from the multi-day  $n$ -GNSS solutions and inter-technique combination solutions 7-COMBI RAP and 7-COMBI FIN w.r.t. *IERS 14 C04* analyzed at 12 h epochs for each analysis day  $d$ . The WRMS values of the single-day GNSS solution (GNSS) is depicted additionally as dashed line.

For the pole coordinate components  $x_p$  and  $y_p$ , a slight decrease in the WRMS values of  $1.4 \mu\text{as}$  and  $0.6 \mu\text{as}$  of the multi-day single-technique solutions (7-GNSS) compared to the session-wise single-technique solutions (GNSS), can be determined by evaluating the results of day  $d = 0$ . A significant improvement of the WRMS values can be observed in particular for the analysis days  $d \leq -2$ . A similar behavior of the WRMS values can be observed for the inter-technique combined solution COMBI RAP and COMBI

**Table 3** Comparison of the different types of dUT1 and pole coordinate solutions with *IERS Bulletin A* and *IERS 14 C04*, respectively. WRMS of the differences computed at 12:00 UTC epochs

	Analysis day $d$	-6	-5	-4	-3	-2	-1	0
dUT1 [ $\mu$ s]	VLBI INT	–	–	–	–	–	–	21.9
	VLBI R1/R4	–	–	–	–	–	–	9.5
	7-VLBI INT	21.2	18.4	16.8	16.0	15.9	17.2	17.6
	7-COMBI RAP	16.4	14.6	14.2	14.2	14.4	15.0	16.7
	7-COMBI FIN	14.1	13.5	13.3	13.3	13.7	14.0	15.3
$x_p$ [ $\mu$ as]	GNSS	–	–	–	–	–	–	46.9
	VLBI R1/R4	–	–	–	–	–	–	123.7
	7-GNSS	42.8	42.4	41.9	42.0	41.8	42.0	45.5
	7-COMBI RAP	43.3	42.4	42.3	42.2	42.2	42.7	45.8
	7-COMBI FIN	44.5	43.7	43.7	43.1	43.0	43.8	46.6
$y_p$ [ $\mu$ as]	GNSS	–	–	–	–	–	–	42.6
	VLBI R1/R4	–	–	–	–	–	–	123.7
	7-GNSS	34.8	34.6	34.7	35.0	35.6	36.4	42.0
	7-COMBI RAP	34.2	33.9	34.1	34.4	34.7	35.7	41.1
	7-COMBI FIN	33.4	33.0	33.1	33.3	33.7	34.4	40.5

FIN. While for the y-component of the pole coordinates the WRMS values improve slightly with increasing number of VLBI data, a slight deterioration is observed for the x-component. Comparing the mean average and the weighted standard deviation (WSTD) of the time series we conclude that this effect is caused by an increasing offset of the whole time series towards zero. The WSTD values, which can be interpreted as a quantification of noise, decrease slightly on average when more VLBI data are added. However, it is not possible to distinguish whether the offset of the time series is caused by an inaccuracy of the estimates or of the reference time series.

Table 3 summarizes all WRMS values of the dUT1 and pole coordinates residuals, corresponding to Figs. 3 and 4.

At first glance, it might surprise that the WRMS values do not show a symmetric behavior reflecting the typical decrease of precision at the boundaries of the combined observation window for a GNSS multi-day solution as well as for the multi-day inter-technique combined solution (which is dominated of GNSS for the pole coordinates solution). The reason can be found in the characteristic of our GNSS input. It should be kept in mind that we process GNSS NEQs with continuous 3-day pwl polygons. Although the EOP parameters of the first two days have been pre-eliminated, these are implicitly contained in the NEQs and stabilize the pole coordinates of the days on the very left side of the time axis.

## 4 Conclusion and Outlook

Our study focuses on the multi-day inter-technique combination of GNSS, VLBI Intensives and VLBI R1/R4 data on the normal equation level. The complementary daily contributions of GNSS and VLBI Intensives data to the EOP estimation together with the contribution of VLBI R1/R4

sessions to all five EOP components twice per week, enables a consistent estimation of a full set of high-precision EOP with daily resolution in one common adjustment. Due to the daily resolution we are also able to accumulate the NEQs of consecutive days in order to stabilize the estimates.

The paper focuses on the comparison of the low-latency EOP resulting from the combination of GNSS and VLBI INT data (COMBI RAP) and the extended EOP solution that includes also VLBI R1/R4 data (COMBI FIN). For the parameter dUT1, we obtained a significant improvement in WRMS values compared to the individual technique-specific EOP (VLBI, n-VLBI INT) as well as to the ones resulting from COMBI RAP.

The improvement in WRMS values is largest for days located at the edge of the multi-day polygon ( $d = 0$  and  $d = -(n - 1)$ ). This means that especially the dUT1 parameters, which have a continuity condition only to one side of the polygon, benefit most from the additional information of the VLBI R1/R4 data. Thus, by combining the GNSS and VLBI INT data together with VLBI R1/R4 sessions, an almost constant accuracy level of the dUT1 estimates within the multi-day polygon is achieved.

For the pole coordinates a slight improvement of the WRMS values compared to the multi-day GNSS-only and COMBI RAP EOP can be achieved only for the y-component. For the x-component, no significant improvement of the WRMS values can be observed, but a slight improvement of the WSTD values. The noise of the entire time series decreases slightly, but the offset w.r.t. the zero line increases when more VLBI data are added.

Since the 24-h VLBI R1/R4 sessions are available with about two weeks delay, the pole coordinate estimates of the IERS EOP products (IERS Bulletin A) rely primarily on GNSS and SLR data. It is not surprising, therefore, that the estimates of pole coordinates based purely on GNSS data match the IERS pole coordinate reference products best, and



that those that additionally include VLBI data differ slightly from the IERS estimates.

In summary, a significant improvement can be achieved for the parameter  $dUT1$  by adding VLBI R1/R4 data to the combination of VLBI INT and GNSS data. For the pole coordinates, the accuracy of the estimates is almost at the same level as for the COMBI RAP solution.

Based on the improved combination method, we intent to set up a new operational BKG-EOP product. Once in place, BKG will be the first institution (according to current knowledge) providing a complete and homogeneously combined EOP product with daily resolution and short latency (1–2 days) with open access for the international community.

In the future we plan to extend the combination of GNSS and VLBI data by adding SLR data in order to exploit the benefit of the combination to its maximum extent.

## References

- Altamimi Z, Rebischung P, Métivier L, Collilieux X (2016) ITRF2014: A new release of the international terrestrial reference frame modeling nonlinear station motions. *J Geophys Res Solid Earth* 121:6109–6131. <https://doi.org/10.1002/2016JB013098>
- Arnold D, Meindl M, Beutler G, Dach R, Schaer S, Lutz S, Prange L, Sosnica K, Mervart L, Jäggi A (2015) CODE's new solar radiation pressure model for GNSS orbit determination. *J Geodesy* 89:775–791. <https://doi.org/10.1007/s00190-015-0814-4>
- Artz T, Bernhard L, Nothnagel A, Steigenberger P, Tesmer S (2014) A comment on the article “A collinearity diagnosis of the GNSS geocenter determination” by P. Rebischung, Z. Altamimi, and T. Springer. *J Geodesy* 89:189–194. <https://link.springer.com/article/10.1007/s00190-011-0512-9>
- Bizouard Ch, Lambert S, Gattano C, Becker O, Richard J-Y (2019) The IERS EOP 14C04 solution for Earth orientation parameters consistent with ITRF 2014. *J Geodesy* 93. <https://doi.org/10.1007/s00190-018-1186-3>
- Blossfeld M (2015) The key role of Satellite Laser Ranging towards the integrated estimation of geometry, rotation and gravitational field of the Earth. Dissertation der Ingenieurakademie Bau Geo Umwelt der Technischen Universität München, München, 2015. ISBN 978-3-7696-5157-7
- Dach R, Schaer S, Arnold D, Orliac E, Prange L, Susnik A, Villiger A, Grahl A, Mervart L, Jäggi A, Beutler G, Brockmann E, Ineichen D, Lutz S, Wiget A, Rülke A, Thaller D, Habrich H, Söhne W, Ihde J et al. (2016) CODE Analysis center: Technical Report 2015. In: Jean Y, Dach R (eds) IGS technical report 2015. IGS Central Bureau, Bern, pp 25–43
- Dermanis A, Mueller I (1978) Earth rotation and network geometry optimization for very long baseline interferometers. *J Bull Géod* 52:131–158. <https://doi.org/10.1007/BF02521695>
- Dick WR, Thaller D (eds) (2020) IERS annual report 2018. International Earth rotation and reference systems service, Central Bureau. Verlag des Bundesamts für Kartographie und Geodäsie, Frankfurt am Main, 207 pp. ISBN 978-3-86482-136-3
- Engelhardt G, Thorandt V, Ullrich D, Girdiuk A, Halsig S, Iddink A, Jaron F, Karbon M, Nothnagel A (2020) BKG/IGGB VLBI analysis center. In: Armstrong KL, Baver KD, Behrend D (eds) International VLBI service for geodesy and astrometry 2017+2018 biennial report. NASA/TP-2020-219041; NASA Goddard Space Flight Center, Greenbelt, MD, USA, pp 204–207
- Gerstl M, Kelm R, Müller H, Ehrmsperger W (2004) DOGS-CS: Kombination und Lösung großer Gleichungssysteme. DGFI (Deutsches Geodätisches Forschungsinstitut) MG/01/1995/DGFI
- Leek J, Artz T, Nothnagel A (2015) Optimized scheduling of VLBI UT1 intensive sessions for twin telescopes employing impact factor analysis. *J Geodesy* 89:911–924. <https://doi.org/10.1007/s00190-015-0823-3>
- Lengert L, Thaller D, Flohrer C, Hellmers H, Girdiuk A (2021) Combination of GNSS and VLBI data for consistent estimation of Earth rotation parameters. In: 25th European VLBI group for geodesy and astrometry (EVGA 2021) working meeting. R. Haas und G. Elgered
- Lengert L, Flohrer C, Girdiuk A, Hellmers H, Thaller D (2022) Single- and multi-day combination of VLBI and GNSS data for consistent estimation of low-latency Earth rotation parameters. To be submitted to JoG
- Meindl M, Beutler G, Thaller D, Dach R, Schaer S, Jaeggi A (2014) Methodology for the combination of sub-daily Earth rotation from GPS and VLBI observations. *J Geodesy* 86:221–239. <https://doi.org/10.1007/s00190-014-0765-1>
- Nothnagel A, Schnell D (2008) The impact of errors in polar motion and nutation on UT1 determinations from VLBI Intensive observations. *J Geodesy* 82:863–869. <https://doi.org/10.1007/s00190-008-0212-2>
- Nothnagel A, Artz T, Behrend D, Malkin Z (2017) International VLBI service for geodesy and astrometry: delivering high-quality products and embarking on observations of the next generation. *J Geodesy* 91:711–721. <https://doi.org/10.1007/s00190-016-0950-5>
- Petit G, Luzum B (eds) (2010) IERS technical note, no. 36. In: International Earth rotation and reference systems service, Central Bureau. Verlag des Bundesamts für Kartographie und Geodäsie, Frankfurt am Main. ISBN 3-89888-989-6, ISSN 1019-456
- Robertson DS, Carter WE, Campbell J, Schuh H (2008) Daily Earth rotation determinations from IRIS very long baseline interferometry. *Nature* 316(6027):424–427
- Seitz M (2009) Kombination geodätischer Raumbeobachtungsverfahren zur Realisierung eines terrestrischen Referenzsystems. Dissertation der Fakultät für Forst-, Geo- und Hydrowissenschaften der Technischen Universität Dresden. ISBN 978-3-7696-5042-6
- Schmid R (2009) Zur Kombination von VLBI und GNSS. Dissertation der Fakultät für Bauingenieur- und Vermessungswesen der Technischen Universität München
- Thaller D (2008) Inter-technique combination based on homogeneous normal equation systems including station coordinates, Earth orientation and troposphere parameters. Dissertation, scientific technical report STR 08/15, Deutsches GeoForschungsZentrum. ISSN 1610-0956. <https://doi.org/10.2312/GFZ.b103-08153>
- Thaller D, Rothacher M, Krügel M (2009) Combining one year of homogeneously processed GPS, VLBI and SLR data. In: Drewes H (eds) Geodetic reference frames, IAG Symposia, vol 134. Springer, pp 17–22. <https://doi.org/10.1007/978-3-642-00860-3-45>
- Thaller D, Sosnica K, Dach R, Jaeggi A, Beutler G, Maraynen M, Richter B (2014) Geocenter coordinates from GNSS and combined GNSS-SLR solutions using satellite co-locations. *Earth on the edge: Science for a sustainable planet*, vol 139. International Association of Geodesy Symposia, pp 129–134. <https://doi.org/10.1007/978-3-642-37222-3-16>
- Thorandt V, Engelhardt G, Ullrich D, Arzt T, Halsig S, Holst C, Iddink A, Jaron F, Nothnagel A (2017) BKG/IGGB VLBI analysis center. In: Baver KD, Behrend D, Armstrong KL (eds) International VLBI service for geodesy and astrometry 2015+2016 biennial report, NASA/TP-2017-219021
- Zajdel R, Sosnica K, Bury G, Dach R, Prange L, Kazmierski K (2021) Sub-daily polar motion from GPS, GLONASS, and Galileo. *J Geodesy* 95:3. <https://doi.org/10.1007/s00190-020-01453-w>

**Open Access** This chapter is licensed under the terms of the Creative Commons Attribution 4.0 International License (<http://creativecommons.org/licenses/by/4.0/>), which permits use, sharing, adaptation, distribution and reproduction in any medium or format, as long as you give appropriate credit to the original author(s) and the source, provide a link to the Creative Commons license and indicate if changes were made.

The images or other third party material in this chapter are included in the chapter's Creative Commons license, unless indicated otherwise in a credit line to the material. If material is not included in the chapter's Creative Commons license and your intended use is not permitted by statutory regulation or exceeds the permitted use, you will need to obtain permission directly from the copyright holder.





# Investigating the Relationship Between Length of Day and El-Niño Using Wavelet Coherence Method

Shrishail Raut, Sadegh Modiri, Robert Heinkelmann, Kyriakos Balidakis, Santiago Belda, Chaiyaporn Kitpracha, and Harald Schuh

## Abstract

The relationship between the length of day (LOD) and El-Niño Southern Oscillation (ENSO) has been well studied since the 1980s. LOD is the negative time-derivative of UT1-UTC, which is directly proportional to Earth Rotation Angle (ERA), one of the Earth Orientation Parameters (EOP). The EOP can be determined using Very Long Baseline Interferometry (VLBI), which is a space geodetic technique. In addition, satellite techniques such as the Global Navigation Satellite System (GNSS), Satellite Laser Ranging (SLR), Doppler Orbitography and Radiopositioning Integrated by Satellite (DORIS) can provide Earth Rotation Parameters, i.e., polar motion and LOD. ENSO is a climate phenomenon occurring over the tropical eastern Pacific Ocean that mainly affects the tropics and the subtropics. Extreme ENSO events can cause extreme weather like flooding and droughts in many parts of the world. In this work, we investigated the effect of ENSO on the LOD from January 1979 to April 2022 using the wavelet coherence method. This method computes the coherence between the two non-stationary time-series in the time-frequency domain using the real-valued Morlet wavelet. We used the Multivariate ENSO index version 2 (MEI v.2) which is the most robust series as the climate index for the ENSO, and LOD time-series from IERS (EOP 14 C04 (IAU2000A)). We also used Oceanic Niño and Southern Oscillation index in this study for comparison. The results show strong coherence of 0.7 to 0.9 at major ENSO events for the periods 2–4 years between LOD and MEI.v2.

## Keywords

Climate · El-Niño · Geodesy · Length of day

S. Raut (✉) · C. Kitpracha · H. Schuh  
GFZ German Research Centre for Geosciences, Space Geodetic  
Techniques, Potsdam, Germany

Technische Universität Berlin, Chair Satellite Geodesy, Berlin,  
Germany  
e-mail: [raut@gfz-potsdam.de](mailto:raut@gfz-potsdam.de)

S. Modiri  
Federal Agency for Cartography and Geodesy (BKG), Frankfurt,  
Germany

R. Heinkelmann  
GFZ German Research Centre for Geosciences, Space Geodetic  
Techniques, Potsdam, Germany

## 1 Introduction

This paper discusses the impact of the major El-Niño Southern Oscillation (ENSO) events on the length of day (LOD). The relationship between ENSO and LOD is well known in the scientific community since the 1980s. Gipson (2016) suggested that the major ENSO events

K. Balidakis  
GFZ German Research Centre for Geosciences, Earth System  
Modelling, Potsdam, Germany

S. Belda  
Applied Mathematics Dept., UAVAC, University of Alicante, Alicante,  
Spain

of 1997–98 and 2016 caused a change of  $750 \mu\text{s d}^{-1}$  in LOD. Also, Le Bail et al. (2014) found that there is a significant correlation between Multivariate ENSO Index (MEI) and various components of LOD. In this study, we mainly focused on the relationship between LOD and ENSO index such as Multivariate ENSO Index version 2 (MEI.v2), which is the most robust index as compared to the other indices. We also investigated the relationship between LOD and other ENSO indices, such as Southern Oscillation Index (SOI) and Oceanic Niño Index (ONI) as well, for comparison.

There are various methods which can be used to understand the relationship between LOD and ENSO. For example, previous studies have used the Singular Spectrum Analysis (SSA) method (Gross et al. 1996; Dickey et al. 2011), plain decomposition (Chao 1984, 1989), or de-trended fluctuation analysis (Alvarez-Ramirez et al. 2010). For this study, we used the wavelet coherence analysis method with several geophysical time series applications (Grinsted et al. 2004; Modiri et al. 2021; Modiri 2021). The wavelet coherence analysis technique effectively recognizes regions of high co-motion in the time-frequency domain, which helps us understand the amount of coherence at various periods between LOD and ENSO during major ENSO events. Kumar and Foufoula-Georgiou (1997) describes the wavelet analysis for geophysical applications.

## 2 Data

### 2.1 Length of Day (LOD)

The LOD is a part of the Earth Orientation Parameters (EOP) and is the negative time derivative of UT1-UTC. It is the difference between the duration of the day measured by space geodetic techniques such as Very Long Baseline Interferometry (VLBI), Global Navigation Satellite System (GNSS), and the nominal day with a duration of 86 400 TAI-compatible seconds. For this study, we use the LOD time-series, obtained from the IERS EOP 14 C04 combined solution (Bizouard et al. 2019), having a daily temporal resolution (see Fig. 1) and epoch at midnight UTC. The LOD time series used in this study spans from January 1st 1979 to April 1st 2022.

### 2.2 El-Niño Southern Oscillation (ENSO)

El-Niño southern oscillation (ENSO) is a coupled oceanic-atmospheric extreme weather event occurring in the eastern

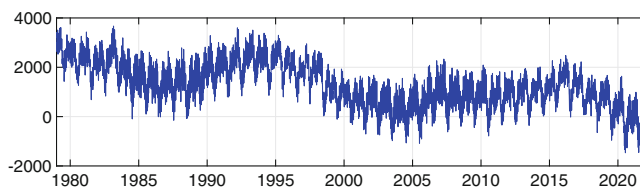


**Fig. 1** LOD time-series from 1st January 1979 to 1st April 2022 (IERS EOP 14 C04), daily resolution. (LOD values are in  $\mu\text{s d}^{-1}$ )

equatorial region of the Pacific ocean. It can be characterized by variations in the Sea Surface Temperature (SST) and the trade winds. The oscillations with different periods are irregular. The ENSO typically consists of three phases lasting between 2–7 years: the warming phase which is also known as El-Niño, the neutral phase, and the cooling phase, which is also known as La-Niña. The El-Niño can be divided into several categories based on where the highest tropical Pacific SST anomalies occur.

The standard El-Niño can also be categorized as the Eastern Pacific El-Niño, having the Pacific SST anomaly in the Eastern Pacific regions (near the coasts of Southern America). In the case of the other type of El-Niño, known as the Central Pacific (CP) El-Niño, the Pacific SST anomaly occurs in the Central Pacific region (near the International dateline).

There are several indices available to quantify the ENSO activity. These include Multivariate ENSO Index (MEI.v2), Southern Oscillation Index (SOI), Oceanic Niño Index (ONI), etc. The Multi-Variate ENSO Index version 2 (MEI.v2) is the most robust index and is computed using five different parameters, namely, sea level pressure (SLP), sea surface temperature (SST), surface zonal winds (U), surface meridional winds (V), and outgoing longwave radiation (OLR) over the tropical Pacific basin ( $30^{\circ}\text{S}$ – $30^{\circ}\text{N}$  and  $100^{\circ}\text{E}$ – $70^{\circ}\text{W}$ ). The MEI.v2 values are provided as two-month seasons, i.e., December-January, January-February, etc. The Southern Oscillation Index (SOI) is the atmospheric component of the ENSO and is computed by the sea level pressure difference between stations in Tahiti and Darwin.<sup>1</sup> This index is, however noisier in comparison to the MEI.v2 index. The Oceanic Niño Index (ONI) is computed by taking a three-month running mean of SST of the equatorial region ( $5^{\circ}\text{N}$ – $5^{\circ}\text{S}$ ,  $170^{\circ}\text{W}$ – $120^{\circ}\text{W}$ ).<sup>2</sup> However, in this paper, we focused on the MEI.v2 index as it is a suitable index for global parameters such as LOD. The MEI.v2 time-series

<sup>1</sup><https://psl.noaa.gov/data/correlation/soi.data>.

<sup>2</sup><https://psl.noaa.gov/data/correlation/oni.data>.

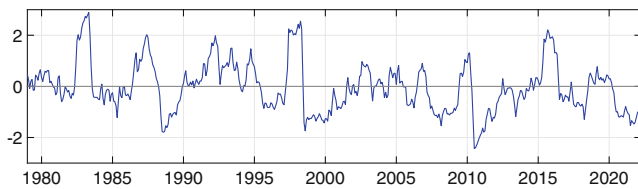


**Fig. 2** MEI.v2 time-series from 1st January 1979 to 1st April 2022, monthly values (*The values are dimensionless*)

plot is illustrated in Fig. 2 using datasets<sup>3</sup> from Physical Sciences Laboratory (PSL).<sup>4</sup> The period of MEI.v2 datasets is January 1st 1979 to April 1st 2022 in the study. We focus on the three major El-Niño events that last from January 1982 to December 1983, January 1997 to December 1998, and January 2015 to December 2016. These three events had MEI.v2 indices above 2.0, which characterizes them as very strong El-Niño events.

### 3 Methodology

We performed a wavelet coherence analysis (WCA) between LOD and MEI.v2. The temporal resolution of the LOD time series is daily in contrast to the monthly values of the MEI.v2 index. Consequently, we re-sampled the monthly ENSO index to a daily resolution by linear interpolation to synchronize the data sets. As the original sampling of the MEI.v2 index is monthly (30 days), the Nyquist period would be equal to twice the original sampling period, i.e., two months (60 days). Therefore, we did not consider the coherence of the periods less than the Nyquist period, i.e., 60 days. Besides, we also employed WCA between LOD with SOI and ONI to see how other ENSO indices perform in contrast to MEI.v2. However, we will only discuss the important points.

#### 3.1 Wavelet Coherence (WC) Method

This method computes the magnitude-squared wavelet coherence, i.e., the coherence between two non-stationary time series in the time-frequency plane. The WCA is grounded in the continuous wavelet transform (CWT) contrary to discrete wavelet transform (DWT). The CWT can be defined as (Torrence and Webster 1999):

$$W^X(n, s) = \sqrt{\frac{\Delta t}{s}} \sum_{n=1}^N x(n) \psi_0^*[\hat{n} - n] \left( \frac{\Delta t}{t} \right) \quad (1)$$

where,  $W$  denotes the CWT of a time series  $x(n)$ ,  $n$  the time index,  $s$  the wavelet scale,  $N$  the length of the time series,  $\Delta t$  the time step,  $\psi_0$  the mother wavelet function, and  $*$  indicates the complex conjugate. The wavelet cross-spectrum is defined as a measure of the distribution of power of two signals and can be expressed as:

$$W^{XY}(n, s) = W^X(n, s) W^{Y*}(n, s) \quad (2)$$

where the  $W^{XY}(n, s)$  is the joint power between the two time-series  $x(n)$  and  $y(n)$ . We computed the squared cross-wavelet coherence function  $R^2$ , which tells us the amount of how coherent the cross-wavelet transform is in the time-frequency domain. The  $R^2$  can be expressed through the following equation:

$$R^2(n, s) = \frac{|S(s^{-1} W^{XY}(n, s))|^2}{S(s^{-1} |W^X(n, s)|^2) \times S(s^{-1} |W^Y(n, s)|^2)} \quad (3)$$

where  $S$  is a smoothing operator, which can be described as:

$$S(W) = S_{scale}(S_{time}(W_n(s))) \quad (4)$$

where  $S_{scale}$  is the smoothing along the scale axis of a wavelet and  $S_{time}$  the smoothing time. It is interesting to note that Eq. 1 is similar to the standard correlation coefficient equation. The wavelet coherence can be considered as a localized correlation coefficient in the time-frequency domain.

There are mainly three types of wavelets, namely, Generalised Morse, Analytical Morlet, and Bump wavelet. We chose a real-valued Morlet wavelet as it is recommended for feature extraction from geophysical signals (Grinsted et al. 2004) and for retaining phase information in the wavelet spectrum (Chao et al. 2014). Phase arrows indicate the relative phase relationship between these two series. If the phase arrows are pointing right, the two series are in phase, and if the phase arrows point towards the left, it means they are in anti-phase. In the case the phase arrows face downwards, LOD series leads the MEI.v2 index. Mathematically, a real-valued Morlet wavelet is represented as:

$$\psi(x) = C \exp(-x^2) \cos(5x) \quad (5)$$

where,  $C$  is the normalization constant.

It is important to discuss the coherence values in terms of their significance level w.r.t. the confidence level and degree of freedom (Chao and Chung 2019). We determined the statistical significance of the wavelet coherence using the Monte Carlo method. This is performed only for the values outside the cone of influence. We carried out this analysis using the MATLAB® (MathWorks®) toolbox for

<sup>3</sup><https://psl.noaa.gov/enso/mei/data/meiv2.data>.

<sup>4</sup><https://psl.noaa.gov/>.

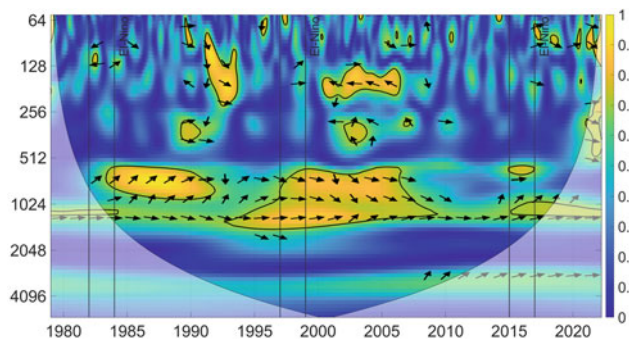


**Fig. 3** Wavelet Coherence between LOD and MEI.v2. Plot description: The left y-axis is the period (in days) and the color bar corresponds to Magnitude-Squared Coherence. The vertical solid lines represent the three major ENSO events of El-Niño. The line that separates the white-faded portion and the remaining plot represents the Cone of Influence. The enclosed region by contour lines indicate the statistically significant regions (5% significance level against red noise). The arrows represent the phase information

performing cross wavelet and wavelet coherence analysis<sup>5</sup> provided by Grinsted et al. (2004).

## 4 Result and Discussion

This section discusses the coherence of MEI.v2 index and LOD for the periods ranging from around 600 (1.6 years) to 1500 days (4 years) as these periods show high coherence. The coherence between LOD and MEI.v2 index is illustrated in Fig. 3. We will only discuss the regions that are statistically significant (surrounded by black contour lines). The coherence between LOD with SOI and ONI is also discussed briefly.

### 4.1 El-Niño Event of 1982–83

In this case, the ENSO event lasted for approximately nine months ( $MEI.v2 > 2$ ). From the Fig. 3, we can observe a strong coherence between LOD and ENSO starting from the middle of the event interval. Table 1 indicates a strong coherence of more than 0.75, for the periods from approximately 593 to 792 days. An interesting fact to note is that we also observe a continual strong coherence up to the year 1992 for the periods from 593 to 792 days. The occurrence of medium to strong ENSO events in 1987–88 and 1991–92 could be a reason. In addition, looking at the phase information, the ENSO seems to lead the LOD by  $45^\circ$ . We also observe a strong coherence of 0.76 at the shorter periods of 111 to 124 days shortly before the ENSO reaches its peak. The phase

<sup>5</sup><https://noc.ac.uk/business/marine-data-products/cross-wavelet-wavelet-coherence-toolbox-matlab>.

**Table 1** Coherence between LOD and MEI.v2 for ENSO event of 1982–83

Period (in days)	Coherence
111	0.76
117	0.77
124	0.75
628	0.75
666	0.77
706	0.77

information indicates that LOD and ENSO have an anti-phase during these periods.

For LOD and ONI, we observed periods and phase information similar to LOD and MEI.v2. However, in the case of LOD and SOI, we observed high coherence for the periods of around one year, and the phase information is opposite as compared to LOD and MEI.v2.

### 4.2 El-Niño Event of 1997–98

This El-Niño event is widely considered as one of the most powerful El-Niño recorded in history. The MEI.v2 index remains above 2 for 12 months. We can see from the Fig. 3 that there is a strong coherence between LOD and MEI.v2 mainly at longer periods. As from Table 2, we observe coherence between 0.75 and 0.85 for the periods from 706 to 1120 days. A much higher coherence of more than 0.85 is seen for periods 1187 to 1332 days. Besides, LOD and ENSO are almost in phase for periods from 706 to 1332 days. For the period of 62 days, the coherence is approximately 0.80. This coherence occurred shortly before the ENSO reached its maximum. We do not find any reliable phase information for these periods. An interesting fact to be noted is that the coherence between ENSO and LOD continues until the year 2009, even though there were no more strong El-Niños during these years.

In the case of LOD and ONI, we observed strong coherency and the phase information at similar periods as in LOD and MEI.v2. For LOD and SOI, we noticed strong coherency at periods of approximately two to four years. However, both the parameters are anti-phase.

**Table 2** Coherence between LOD and MEI.v2 for ENSO event of 1997–98

Period (in days)	Coherence	Period (in days)	Coherence
62	0.79	998	0.75
666	0.74	1057	0.77
706	0.77	1120	0.81
748	0.78	1187	0.86
792	0.78	1280	0.87
839	0.77	1332	0.85

**Table 3** Coherence between LOD and MEI.v2 for ENSO event of 2015–16

Period (in days)	Coherence
593	0.77
628	0.76

### 4.3 El-Niño Event of 2015–16

In this case, the MEI.v2 index is above 2 only for two months (September to October 2015). We observe a strong coherence between LOD and MEI.v2 of approximately 0.77 for the periods of 593 to 628 days (Table 3). The phase information is insufficient for drawing conclusions. We do not observe any coherence between LOD and ENSO after the ENSO event dissipated unlike to the previous two ENSO events. The reason could be the relatively smaller intensity and duration of ENSO.

We can see strong coherency between LOD and ONI at around two years, and the phase information is insufficient to derive any conclusions. In the case of LOD and SOI, we cannot observe any strong coherency, and subsequently, no phase information is available.

## 5 Conclusions

Although the relationship between LOD and ENSO has been studied extensively in the past, using the wavelet coherence method reveals a complex interaction between these two data sets (Fig. 3; Tables 1, 2, 3). The ENSO events of 1982–83 and 1997–98 show a strong coherence with LOD. In contrast, the ENSO event of 2015–16 does not show strong coherence with LOD despite having only slightly less strength as the previous two ENSO events. This indicates that the strength of an ENSO event is not the only factor affecting LOD, and the duration of the ENSO might be an important factor as well.

In the 1982–83 ENSO event, we saw a strong coherence of more than 0.75 for periods 593 to 792 days and coherence of 0.76 for periods 111 to 124 days between LOD and MEI.v2. Concerning the phase information, we observed ENSO leading LOD by  $45^\circ$  for a longer period and anti-phase between them for shorter periods. Another important observation is that the strong coherence between LOD and ENSO continued until 1992. The main reason could be the longer duration of the ENSO event and the ENSO events of 1987–88 and 1991–92.

During the 1997–98 ENSO event, we saw a strong coherence between LOD and MEI.v2 from 0.75 to 0.85 for periods 706 to 1120 days. For periods 1187 to 1332 days, we observed stronger coherence above 0.85. The LOD and ENSO were in phase for these long periods. The coherence

for period of 62 days was around 0.80. However, we did not find definitive phase information for these shorter periods.

For the recent 2015–16 ENSO event, we observed the coherence between LOD and MEI.v2 of 0.77 and 0.80 for periods 593 to 628 days and 41 to 52 days, respectively. We cannot conclude regarding the phase due to insufficient information.

We also performed WCA between LOD with ONI and SOI for comparison. ONI can be used as an alternative ENSO index to MEI.v2 for performing WCA with LOD. We do not recommend using SOI for WCA with LOD, as it did not show any coherency during the 2015–16 ENSO event. SOI could be only sensitive to extreme ENSO conditions that last for a longer duration.

Figure 3 shows good inter-annual coherence not only during the three significant El-Niño occurrences but also throughout the entire period, including the La-Niñas and the El-Niño off-shoots. As a result, it is evident that ENSO has a positive and negative impact on LOD, which is consistent with physics. When we look at these three ENSO events, we observe a strong coherence between LOD and ENSO at periods less than a year shortly before the ENSO reached its maximum intensity. This occurrence is common for all three ENSO events. When comparing the three ENSO events, we observe that they affected LOD at different periods despite having similar strengths. This additionally suggests that every ENSO event interacts differently with LOD. The complex behavior of coherence phasing during the different El-Niños is presumably because the three El-Niños are of different types: East-Pacific and Central-Pacific. Thus, it might be possible to understand different types of ENSO in greater depth by using its complex interaction with LOD in the future. This study could be beneficial to getting more reliable LOD models/predictions needed to meet the existing accuracy goals of global geodesy (Plag et al. 2009).

**Acknowledgements** We obtained the various ENSO indices from National Oceanic and Atmospheric Administration (NOAA), Physical Sciences Laboratory, USA. The LOD time-series was provided by the International Earth Rotation and Reference System Service (IERS). Kyriakos Balidakis is funded by the Deutsche Forschungsgemeinschaft (DFG, German Research Foundation)—Project-ID 434617780—SFB 1464 (TerraQ). Santiago Belda was partially supported by Generalitat Valenciana (SEJIGENT/2021/001), the European Union—NextGenerationEU (ZAMBRANO 21-04) and Ministerio de Ciencia e Innovación (Spanish Project PID2020-119383GB-I00). Chaiyaporn Kitpracha acknowledges funding from Deutscher Akademischer Austauschdienst (DAAD) under grant number 91650950.

### Conflict of Interest

The authors declare that they have no conflict of interest.

## References

- Alvarez-Ramirez J, Dagdug L, Rojas G (2010) Cycles in the scaling properties of length-of-day variations. *J Geodynam* 49(2):105–110. <https://doi.org/10.1016/j.jog.2009.10.008>
- Bizouard C, Lambert S, Gattano C, Becker O, Richard JY (2019) The IERS EOP 14C04 solution for Earth orientation parameters consistent with ITRF 2014. *J Geodesy* 93(5):621–633. <https://doi.org/10.1007/s00190-018-1186-3>
- Chao B (1984) Interannual length-of-day variation with relation to the southern oscillation/El Nino. *Geophys Res Lett* 11(5):541–544. <https://doi.org/10.1029/GL011i005p00541>
- Chao BF (1989) Length-of-day variations caused by El Nino-Southern Oscillation and quasi-biennial oscillation. *Science* 243(4893):923–925. <https://doi.org/10.1126/science.243.4893.923>
- Chao B, Chung C (2019) On estimating the cross correlation and least squares fit of one data set to another with time shift. *Earth Space Sci* 6(8):1409–1415
- Chao BF, Chung W, Shih Z, Hsieh Y (2014) Earth's rotation variations: a wavelet analysis. *Terra Nova* 26(4):260–264
- Dickey JO, Marcus SL, de Viron O (2011) Air temperature and anthropogenic forcing: Insights from the solid Earth. *J Climate* 24(2):569–574. <https://doi.org/10.1175/2010JCLI3500.1>
- Gipson J (2016) El Nino and VLBI Measured Length of Day. In: Behrend D, Baver KD, Armstrong KL (eds) *IVS 2016 general meeting proceedings: New Horizons with VGOS*, p 336
- Grinsted A, Moore JC, Jevrejeva S (2004) Application of the cross wavelet transform and wavelet coherence to geophysical time series. *Nonlinear Process Geophys* 11(5/6):561–566. <https://doi.org/10.5194/npg-11-561-2004>
- Gross RS, Marcus SL, Eubanks TM, Dickey JO, Keppenne CL (1996) Detection of an ENSO signal in seasonal length-of-day variations. *Geophys Res Lett* 23(23):3373–3376. <https://doi.org/10.1029/96GL03260>
- Kumar P, Foufoula-Georgiou E (1997) Wavelet analysis for geophysical applications. *Rev Geophys* 35(4):385–412. <https://doi.org/10.1029/97RG00427>
- Le Bail K, Gipson JM, MacMillan DS (2014) Quantifying the correlation between the MEI and LOD variations by decomposing LOD with singular spectrum analysis. In: *Earth on the edge: Science for a sustainable planet*. Springer, pp 473–477. [https://doi.org/10.1007/978-3-642-37222-3\\_63](https://doi.org/10.1007/978-3-642-37222-3_63)
- Modiri S (2021) On the improvement of earth orientation parameters estimation : using modern space geodetic techniques. Doctoral thesis, Technische Universität Berlin, Berlin. <https://doi.org/10.14279/depositonce-11975>
- Modiri S, Heinkelmann R, Belda S, Malkin Z, Hoseini M, Korte M, Ferrándiz JM, Schuh H (2021) Towards understanding the interconnection between celestial pole motion and Earth's magnetic field using space geodetic techniques. *Sensors* 21(22):7555
- Plag HP, Rothacher M, Pearlman M, Neilan R, Ma C (2009) The global geodetic observing system. In: *Advances in geosciences: Volume 13: Solid Earth (SE)*. World Scientific, pp 105–127
- Torrence C, Webster PJ (1999) Interdecadal changes in the ENSO-monsoon system. *J Climate* 12(8):2679–2690

**Open Access** This chapter is licensed under the terms of the Creative Commons Attribution 4.0 International License (<http://creativecommons.org/licenses/by/4.0/>), which permits use, sharing, adaptation, distribution and reproduction in any medium or format, as long as you give appropriate credit to the original author(s) and the source, provide a link to the Creative Commons license and indicate if changes were made.

The images or other third party material in this chapter are included in the chapter's Creative Commons license, unless indicated otherwise in a credit line to the material. If material is not included in the chapter's Creative Commons license and your intended use is not permitted by statutory regulation or exceeds the permitted use, you will need to obtain permission directly from the copyright holder.







# Estimation of Earth Rotation Parameter UT1 from Lunar Laser Ranging Observations

Liliane Biskupek, Vishwa Vijay Singh, and Jürgen Müller

## Abstract

Since 1969 Lunar Laser Ranging (LLR) data have been collected by different observatories and analysed by various analysis groups. LLR is providing the longest time series of any space geodetic technique for studying the Earth-Moon dynamics. In recent years, observations have been carried out with larger telescopes and at infra-red (IR) wavelength, resulting in a better distribution of precise LLR data over the lunar orbit and the observed retro-reflectors on the Moon. The increased number of high-accuracy observations allows for more accurate determination of Earth Orientation Parameters (EOPs) from LLR data compared to previous years. In this study we focus on  $\Delta$ UT1 results from different constellations and compare our LLR solution to the IERS EOP C04 series.

## Keywords

Earth rotation parameters · Earth rotation phase · Lunar laser ranging

## 1 Introduction

With the landing of Apollo 11 astronauts on the Moon in July 1969 the first LLR retro-reflector was deployed on the lunar surface. Until 1973, four additional retro-reflectors had been installed on the Moon: two reflectors by the astronauts of the Apollo 14 and 15 missions, and two reflectors mounted on the unmanned Soviet Lunokhod rovers. Measurements from the Earth to the retro-reflectors have primarily been carried out from six observatories that were or are capable to range to the Moon: the McDonald Laser Ranging Station, USA (MLRS), the Lure Observatory on Maui/Hawaii, USA (LURE), the Côte d'Azur Observatory, France (OCA), the

Apache Point Observatory Lunar Laser ranging Operation, USA (APOLLO), the Matera Laser Ranging Observatory, Italy (MLRO) and the Geodetic Observatory Wettzell, Germany (WLRS). For more than 52 years now, there are LLR measurements of the round-trip travel time of laser pulses between observatories on the Earth and retro-reflectors on the Moon. The measurement of round trip travel times with short laser pulses is challenging. The average number of returning photons is less than one per laser pulse (Chabé et al. 2020; Murphy 2013), mainly because of the beam divergence of the laser pulses due to the atmospheric turbulence and diffraction effects of the retro-reflectors (Murphy et al. 2010). Further signal loss occurs in the paths of the transmitting and detection optics, in the atmosphere and due to the reflectivity of the retro-reflectors (Müller et al. 2019). A series of single measurements over 5 min to 15 min is used to calculate a so-called normal point (NP) (Michelsen 2010) which is the observable in the LLR analysis. Analysing the data, various research questions related to the Earth-Moon system are investigated. Today, LLR is one of the major tools to test General Relativity in the solar system, e.g. testing the equivalence principle, temporal variation of the gravitational constant  $G$ , Yukawa term, metric parameters, and geodetic

L. Biskupek (✉) · J. Müller  
Institute of Geodesy (IfE), Leibniz University Hannover, Hannover,  
Germany  
e-mail: [biskupek@ife.uni-hannover.de](mailto:biskupek@ife.uni-hannover.de)

V.V. Singh  
Institute of Geodesy (IfE), Leibniz University Hannover, Hannover,  
Germany

Institute for Satellite Geodesy and Inertial Sensing, German Aerospace  
Center (DLR), Hannover, Germany

precession (Biskupek et al. 2021; Zhang et al. 2020; Hofmann and Müller 2018; Viswanathan et al. 2018; Williams et al. 2012). Furthermore, LLR can also be used to determine parameters of the Earth-Moon system like its mass, the lunar orbit and libration (Pavlov et al. 2016; Williams et al. 2013), terrestrial and celestial reference frames and the coordinates of observatories and retro-reflectors (Hofmann et al. 2018; Müller et al. 2009). In Germany, beginning in the early 1980s, the software package LUNAR (LUNAr laser ranging Analysis softwaRE) was developed to study the Earth-Moon system and to determine the various related model parameters. In this study we focus on the determination of the Earth rotation parameter  $\Delta\text{UT1}$ .  $\Delta\text{UT0}$  is a special case of Universal Time (UT) at a certain location. It can only be measured by LLR as well as Very Long Baseline Interferometry (VLBI).

## 2 Analysis and Observations

Currently, the analysis of LLR data includes 28,093 NPs for the time span April 1970–April 2021. The temporal distribution of the measured NPs over the last 52 years is given in Fig. 1. One can see in the legend that more than 60% of the NPs were observed by OCA, 40% with green and 21% with IR laser wavelength (measurements with laser wavelength of  $\lambda = 693.8\text{ nm}$  and  $\lambda = 532\text{ nm}$  are listed in the figure as OCA green). In the last years, only OCA and APOLLO provided regular NPs, some NPs also came from MLRO and WLRS. As of 2015, many NPs were measured with laser pulses at IR wavelength, enabling distance measurements near new and full Moon (Chabé et al. 2020) for OCA and WLRS. This leads to a better coverage of the lunar orbit over the synodic month, i.e. the time span in which the Sun, the Earth, and the Moon return to a similar constellation again. With a better coverage of the lunar orbit, it is possible to

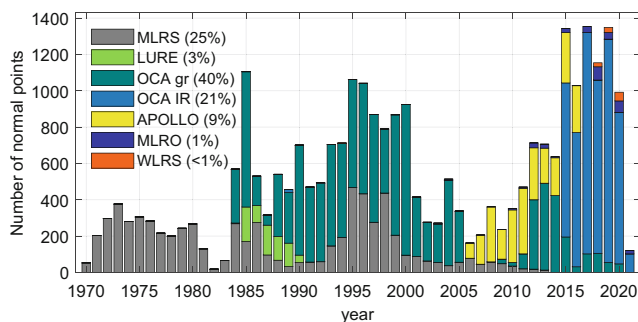


**Fig. 1** Distribution of the 28,093 NPs over the time span April 1970–April 2021. The legend gives the percentages of the contribution of the respective observatories. The three observatories McDonald, MLRS1 and MLRS2 are linked in the analysis and listed here as MLRS. OCA measurements with laser wavelength of  $\lambda = 693.8\text{ nm}$  and  $\lambda = 532\text{ nm}$  are indicated as OCA gr

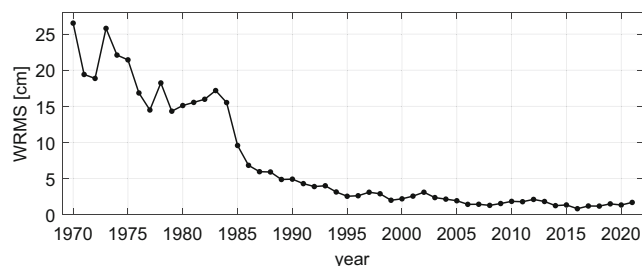


**Fig. 2** Annual weighted RMS (WRMS) of the one-way post-fit residuals for 28,093 NPs for the time span April 1970–April 2021

perform a more uniform estimation of various parameters of the Earth-Moon system. Nevertheless the distribution of the NPs has a big impact on the determination of the parameters. Furthermore, non-uniform data distribution is one reason for correlations between solution parameters (Williams et al. 2009). The measured NPs serve as observations in the analysis. They are treated as uncorrelated for the stochastic model of the least-squares adjustment and are weighted according to their accuracies.

In the LLR analysis, the parameters of the LLR model are determined by fitting them to the LLR observations using the least-squares adjustment. The ephemeris of the solar system bodies are integrated simultaneously with the rotation of the Moon. For the rotation of the Earth two series of EOPs are used: until 01.01.1983, the Kalman Earth Orientation Filter (KEOF) series COMB2019 (Ratcliff and Gross 2020) and from 02.01.1983 the IERS EOP C04 series (Bizouard et al. 2019). The difference between the two EOP series is the input data, as only the COMB series includes LLR NPs. Therefore, this series fits the LLR analysis better in the initial phase of the observations. After 01.01.1983, the differences between the two EOP series are small (only a few mas and ms), so that the IERS series is used for timeliness reasons. The coordinates and velocities of the LLR observatories are determined in the International Terrestrial Reference System (ITRS). The weighted RMS of the one-way post-fit residuals of the LLR analysis is better than 1.5 cm for the last years, see Fig. 2.

## 3 $\Delta\text{UT1}$ from LLR

The terrestrial pole coordinates  $x_p$  and  $y_p$ , describe the change of the rotation axis in relation to the Earth's surface. The rotational motion of the Earth is given by the Earth rotation phase  $\Delta\text{UT1}$  and the Length-of-Day LOD. All these parameters are summarised as Earth Rotation Parameters (ERPs). Together with the celestial pole offsets  $\delta X$  and  $\delta Y$ , as corrections to the conventional precession-nutation model, they define the Earth Orientation Parameter (EOP).

As shown by Dickey et al. (1985), Müller (1991) and Pavlov (2019), it is possible to determine the ERPs from the post-fit residuals of the least-squares adjustment of LLR data. In this way the variation of longitude  $\Delta UT0$  can be determined by

$$\Delta UT0 = \Delta UT1 + \frac{(x_p \sin(\lambda) + y_p \cos(\lambda)) \tan(\phi)}{15 \times 1.002737909}, \quad (1)$$

as combination of  $\Delta UT1$  and the terrestrial pole coordinates  $x_p, y_p$ , with the observatories longitude  $\lambda$  and latitude  $\phi$  (Chapront-Touzé et al. 2000). The variation of latitude VOL is given by

$$VOL = x_p \cos \lambda - y_p \sin \lambda. \quad (2)$$

The disadvantage of this approach is that the correlations between the ERPs and the other parameters of the Earth-Moon system can not be investigated. Biskupek (2015) changed the analysis strategy. In the rotation matrix between the Earth-fixed ITRS and the space-fixed Geocentric Celestial Reference System (GCRS) the ERPs are used in the LLR analysis, thus they can be determined in the least-squares adjustment along with other parameters of the Earth-Moon system. The correlations with these parameters are also obtained and can be investigated directly. Biskupek (2015) gave the equations for the partial derivatives of ERPs and discussed the results of the different possible methods to obtain ERPs from LLR, such as selecting certain time spans of data or specific nights for which a minimum number of NPs is available. The main result of this research was that the determination for specific nights with a minimum of 5 NPs is a better method than the ERP determination for longer time spans. From the analysis of 20,047 NPs (1970–2013), the uncertainty in  $\Delta UT1$  was about 400  $\mu$ s. Hofmann et al. (2018) discussed the results of estimating the Earth rotation phase for a time span with 23,261 NPs (1970–2016). They achieved an uncertainty of 89  $\mu$ s when estimating  $\Delta UT1$  from all observatories and of 44  $\mu$ s when estimating  $\Delta UT1$  from only OCA and APOLLO. The IR measurements from OCA with better coverage of the lunar orbit and more NPs that are available per night lead to an improved situation for the LLR observables. This enables a better and more stable estimation of ERPs from LLR, which achieve lower uncertainties compared to previous results. A further study concerning ERP determination from LLR data with more details is published by Singh et al. (2022).

For ERP determination in the LLR analysis, the whole data set of NPs is pre-analysed, where different configurations can be taken into account. Thus, it is possible to estimate ERPs from the data of all observatories or only for a single observatory. It is also possible to vary the number of NPs per night or to choose specific wavelengths. In the

current study we focused on the determination of the Earth rotation phase  $\Delta UT1$ . Several studies with different characteristics were performed, like different numbers of NPs per night from different observatories and different combination of the wavelength of the measured NPs. Two studies with the best results are with data from OCA and are discussed in the following.

The main characteristics of the two studies were the same. The  $\Delta UT1$  values were determined from the LLR data for specific nights. The minimum number of NPs for one night to be considered in the  $\Delta UT1$  determination was set to 10, i.e. nights with fewer NPs were not considered in the fit. Simultaneously, the coordinates of the observatories were determined for one epoch, namely J2000 (01.01.2000, 0:00 UTC), of the whole LLR data set. Theoretically, it is also possible to determine velocities of the observatories from the whole LLR data set. Since there are correlations between  $\Delta UT1$ , coordinates and velocities on the one hand, as well as large deviations of station coordinates to the ITRF2014 on the other hand, the velocities were fixed to their ITRF2014 values. However, as the APOLLO observatory is not included in the ITRF2014 solution, we used the velocity of the White Sands GNSS observatory instead. The a-priori EOP values were used from COMB2019/IERS C04 series and fixed for those nights that were not considered in the fit. For a complete list of parameters determined together with the  $\Delta UT1$  values (e.g. station coordinates and range biases), except the station velocities, see Singh et al. (2021). The difference in the two study cases was the wavelength of the used laser and the resulting different number of nights for the  $\Delta UT1$  determination. In study 1 there were 714 nights for the time span April 1984–March 2021 in which NPs were measured with green or IR laser wavelength. For study 2 there were 259 nights for the time span March 2015–March 2021 in which NPs were measured with IR laser wavelength only.

Figure 3 shows the results for the two studies where the deviations from the IERS C04 series and their uncertainties are given. A previous study has shown that the uncertainties of the estimated parameters from our LLR analysis were too small (Hofmann et al. 2018), as some small random and systematic errors remained in the LLR analysis. Systematic errors include the uneven distribution of NPs during the synodic month, and the constellation of Earth and Moon when observing an LLR NP, because of the inaccuracy of atmospheric delay models for low altitude observations. A further error source is the imperfection of lunar ephemeris, e.g. because of simplified modelling of the asteroids. These errors are different for each observation. Random errors result from the general measurement accuracy of LLR, are different for each night, and depend on the observatory measuring the NPs. Furthermore, the  $\Delta UT1$  determination is constrained by the a priori EOP series for nights when

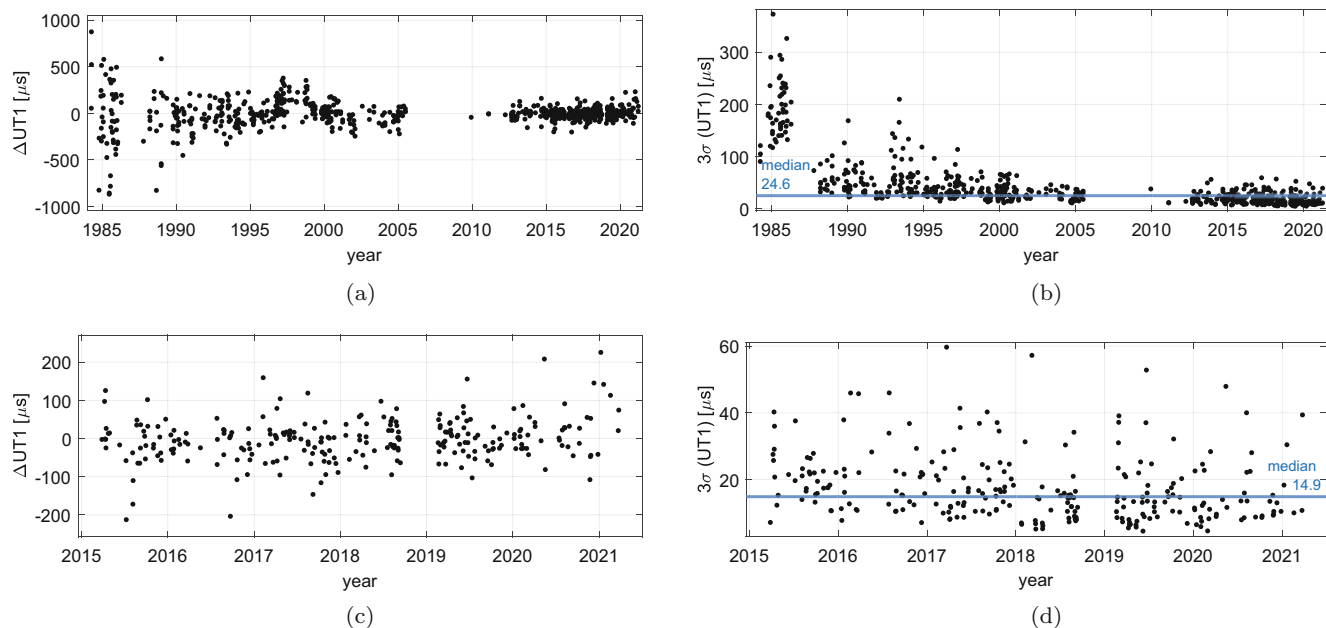


**Fig. 3** Results of studies 1 and 2 on the determination of  $\Delta UT1$  from LLR data in different configurations. (a)  $\Delta UT1$  deviations from the IERS C04 series as determined in study 1 from green and IR NPs. (b) Uncertainty of the  $\Delta UT1$  values of study 1 for the individual nights

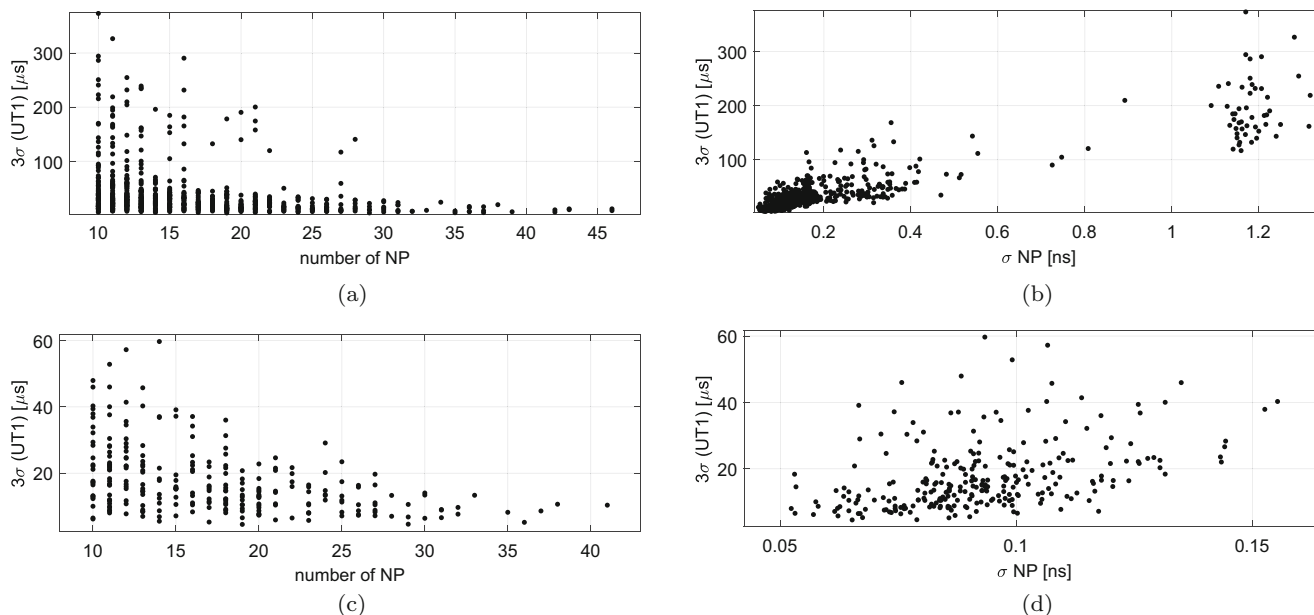
no values are estimated. Additionally, according to Eq. (1) the pole coordinates also affect  $\Delta UT1$ . In our case we fixed the pole coordinates to the IERS C04 series and assumed them to be error-free, which is not the case. The following uncertainties are given as 3 times the formal errors from the least-squares adjustment.

Figure 3a gives the fitted  $\Delta UT1$  deviations to the IERS C04 series as determined in study 1, where NPs measured with green or IR laser wavelength were used. The values vary between  $\pm 200 \mu s$  with a mean of  $4.3 \mu s$  and some higher values before the year 2000 due to the poorer measurement accuracy of this period. The RMS is  $149.2 \mu s$ . The uncertainties of the  $\Delta UT1$  deviations are in the range of  $4.5 \mu s$  to  $373.1 \mu s$  with a median of  $24.6 \mu s$ , shown in Fig. 3b. For study 2 using only IR data the fitted  $\Delta UT1$  deviations to the IERS C04 series are given in Fig. 3c. The values vary between  $\pm 100 \mu s$  with a mean of  $2.7 \mu s$  and some higher values. The RMS is  $56.4 \mu s$ . Figure 3d gives the corresponding uncertainties, which range between  $4.5 \mu s$  to  $60.0 \mu s$  with a median of  $14.89 \mu s$ . In previous studies (Hofmann et al. 2018), a higher uncertainty of  $32 \mu s$  was achieved, although in these studies the minimum number of NPs per night was 14 and thus higher than now. Since the time span of used NPs was only until 2016, the very accurate and well distributed OCA NPs measured in IR were not part of that analysis. The advantage of the IR OCA data seems obvious here. They improve the overall uncertainty of the least-squares adjustment and allow

and the median of all nights. (c)  $\Delta UT1$  deviations from the IERS C04 series as determined in study 2 from IR NPs only. (d) Uncertainty of the  $\Delta UT1$  values of study 2 for the individual nights and the median of all nights

fitting  $\Delta UT1$  values with lower uncertainty from less NPs per night.

The influence of the number and accuracy of the NPs on the determination of  $\Delta UT1$  is analysed in more detail in Fig. 4 where scatter plots show the relationship between the number or accuracy of the NPs and the uncertainty of  $\Delta UT1$ . Correlation coefficients were determined from each combination of data sets that are given in the plots. The accuracies of the input NPs were averaged for each night considered and plotted on the horizontal axis of Fig. 4b and d. In study 1 with NPs measured with green or IR laser wavelength, the number of NPs does not have a very large effect on the uncertainty of  $\Delta UT1$  (see Fig. 4a), the correlation coefficient is only  $-0.27$ . The accuracy of NPs is more important in this study (see Fig. 4b), as reflected by a correlation coefficient of  $0.91$  with the uncertainty of  $\Delta UT1$ . In study 2, using only IR NPs with a more homogeneous accuracy between each NP, the correlation coefficient between the accuracy of NPs and the uncertainty of  $\Delta UT1$  with  $0.41$  is lower than in study 1 (see Fig. 4d). Here, the number of NPs has a larger effect compared with study 1 (see Fig. 4c) and the correlation coefficient is  $-0.43$ . This means that for the determination of  $\Delta UT1$  a high accuracy of the NPs is beneficial for data sets with inhomogeneous input data accuracy, but also a high number of NPs per night is important in the analysis. Both criteria of the input data play a role in the determination of  $\Delta UT1$ .



**Fig. 4** Different scatter plot for studies 1 and 2 between the LLR NPs and the determined uncertainty of  $\Delta UT1$ . **(a)** Study 1 (green and IR NPs): Scatter plot of the number of NPs and the estimated uncertainty of  $\Delta UT1$ . The correlation coefficient is  $-0.27$ . **(b)** Study 1 (green and IR NPs): Scatter plot of the measured accuracy of NPs and the estimated

uncertainty of  $\Delta UT1$ . The correlation coefficient is  $0.91$ . **(c)** Study 2 (IR NPs only): Scatter plot of the number of NPs and the estimated uncertainty of  $\Delta UT1$ . The correlation coefficient is  $-0.43$ . **(d)** Study 2 (IR NPs only): Scatter plot of the measured accuracy of NPs and the estimated uncertainty of  $\Delta UT1$ . The correlation coefficient is  $0.41$

In both studies, no significant correlations of  $\Delta UT1$  values and other parameters of the Earth-Moon system were found in the least-squares adjustment. Comparable results for  $\Delta UT1$  with an uncertainty of  $15 \mu s$  are obtained from VLBI data (Gambis and Luzum 2011).

## 4 Conclusions

As described above ERPs can be determined from LLR data analysis. The best LLR result is obtained from the high-accurate IR OCA data with 10 NPs per night with a median uncertainty of  $14.89 \mu s$ . The high-accurate IR data from OCA are very beneficial for the  $\Delta UT1$  determination, because of their distribution over the reflectors and synodic month as well as the higher number of NPs for one night. The data reduce the overall uncertainty of the least-squares adjustment and allow fitting  $\Delta UT1$  values with lower uncertainty from fewer NPs per night compared to previous studies.

Deviations from the IERS C04 series are in the range of  $\pm 100 \mu s$  at best, with a mean of  $2.7 \mu s$  and an RMS of  $56.4 \mu s$ . The mean uncertainty is  $14.89 \mu s$ . These LLR results are in a range of uncertainty which is comparable to daily  $\Delta UT1$  values determined from VLBI with  $15 \mu s$  (Gambis and Luzum 2011). Nevertheless the LLR uncertainties seem to be too optimistic. Therefore as next step,  $\Delta UT1$  and also values for pole coordinates from all LLR stations will be determined together and analysed to find the best strategy

for ERP determination from LLR data. It will also be further investigated, which parameters of the Earth-Moon system should be determined together with the ERPs. This will lead to a more realistic estimation of their uncertainties.

With more IR data from the observatories OCA and WLRS, it is expected that the parameters of the least-squares adjustment can be further decorrelated and then station velocities might be determined along with ERPs and station coordinates. Additionally an optimised strategy regarding the number and accuracy of NPs per night is investigated (Singh et al. 2022).

**Acknowledgements** We acknowledge with gratitude, that more than 52 years of processed LLR data have been obtained under the efforts of the personnel at McDonald Laser Ranging Station, USA, Côte d’Azur Observatory, France, Lure Observatory on Maui/Hawaii, USA, Apache Point Observatory Lunar Laser ranging Operation, USA, Matera Laser Ranging Observatory, Italy and Geodetic Observatory Wettzell, Germany. We also acknowledge with thanks the funding by the Deutsche Forschungsgemeinschaft (DFG, German Research Foundation) under Germany’s Excellence Strategy (EXC-2123 QuantumFrontiers—Project-ID 390837967).

**Funding** This research was funded by the Deutsche Forschungsgemeinschaft (DFG, German Research Foundation) under Germany’s Excellence Strategy (EXC-2123 QuantumFrontiers—Project-ID 390837967), and Deutsches Zentrum für Luft- und Raumfahrt (DLR).

**Conflict of Interest** The authors declare that they have no conflict of interest.

**Data Availability** LLR data is collected, archived, and distributed under the auspices of the International Laser Ranging Service (ILRS)

(Pearlman et al. 2019). All LLR NPs used for these studies are available from the Crustal Dynamics Data Information System (CDDIS) at NASA's Archive for Space Geodesy Data, USA, (Noll 2010) at the website.<sup>1</sup> The KEOF COMB2019 EOP time series is available at the website<sup>2</sup> and the IERS C04 EOP time series is available at the website.<sup>3</sup>

**Code Availability** All calculations were done by unpublished custom code.

**Authors' Contributions** All authors contributed to the development of these studies and provided ideas to its content. Data collection and analysis were performed by VVS and LB. The first draft of the manuscript was written by LB, and all authors commented on previous versions of the manuscript. All authors read and approved the final manuscript.

## References

- Biskupek L (2015) Bestimmung der Erdorientierung mit Lunar Laser Ranging. PhD thesis, Leibniz Universität Hannover. <https://doi.org/10.15488/4721>, Deutsche Geodätische Kommission bei der Bayerischen Akademie der Wissenschaften, Reihe C, Nr. 742
- Biskupek L, Müller J, Torre JM (2021) Benefit of new high-precision LLR data for the determination of relativistic parameters. *Universe* 7(2). <https://doi.org/10.3390/universe7020034>
- Bizouard C, Lambert S, Gattano C, Becker O, Richard JY (2019) The IERS EOP 14C04 solution for Earth orientation parameters consistent with ITRF 2014. *J Geodesy* 93(5):621–633. <https://doi.org/10.1007/s00190-018-1186-3>
- Chabé J, Courde C, Torre JM, Bouquillon S, Bourgoïn A, Aimar M, Albanése D, Chauvineau B, Maríey H, Martinot-Lagarde G, Maurice N, Phung DH, Samain E, Viot H (2020) Recent progress in Lunar Laser Ranging at Grasse Laser Ranging Station. *Earth Space Sci* 7(3):e2019EA000785. <https://doi.org/10.1029/2019EA000785>
- Chapront-Touzé M, Chapront J, Francou G (2000) Determination of UT0 with LLR observations. In: *Proceedings of the Journées 1999 "Motion of Celestial Bodies, Astrometry and Astronomical Reference Frames"*, pp 217–220
- Dickey JO, Newhall XX, Williams JG (1985) Earth orientation from Lunar Laser Ranging and an error analysis of Polar motion services. *J Geophys Res* 90(B11):9353–9362
- Gambis D, Luzum B (2011) Earth rotation monitoring, UT1 determination and prediction. *Metrologia* 48(4):S165–S170
- Hofmann F, Müller J (2018) Relativistic tests with Lunar Laser Ranging. *Classical Quantum Gravity* 35(3):035015. <https://doi.org/10.1088/1361-6382/aa8f7a>
- Hofmann F, Biskupek L, Müller J (2018) Contributions to reference systems from Lunar Laser Ranging using the IfE analysis model. *J Geodesy* 92(9):975–987. <https://doi.org/10.1007/s00190-018-1109-3>
- Michelsen EL (2010) Normal point generation and first photon bias correction in APOLLO Lunar Laser Ranging. PhD thesis, University of California, San Diego
- Müller J (1991) Analyse von Lasermessungen zum Mond im Rahmen einer post-Newton'schen Theorie. PhD thesis, Technische Universität München, Deutsche Geodätische Kommission bei der Bayerischen Akademie der Wissenschaften, Reihe C, Nr. 383
- Müller J, Biskupek L, Oberst J, Schreiber U (2009) Contribution of Lunar Laser Ranging to realise geodetic reference systems. In: Drewes H (ed) *Geodetic reference frames*. International Association of Geodesy Symposia, vol 134. Springer, Berlin, Heidelberg, pp 55–59. <https://doi.org/10.1007/978-3-642-00860-3>
- Müller J, Murphy TW, Schreiber U, Shelus PJ, Torre JM, Williams JG, Boggs DH, Bouquillon S, Bourgoïn A, Hofmann F (2019) Lunar Laser Ranging: a tool for general relativity, lunar geophysics and Earth science. *J Geodesy* 93(11):2195–2210. <https://doi.org/10.1007/s00190-019-01296-0>
- Murphy TW (2013) Lunar Laser Ranging: the millimeter challenge. *Rep Progress Phys* 76(7):076901
- Murphy TW, Adelberger EG, Battat JBR, Hoyle CD, McMillan RJ, Michelsen EL, Samad RL, Stubbs CW, Swanson HE (2010) Long-term degradation of optical devices on the Moon. *Icarus* 208(1):31–35. <https://doi.org/10.1016/j.icarus.2010.02.015>
- Noll CE (2010) The crustal dynamics data information system: A resource to support scientific analysis using space geodesy. *Adv Space Res* 45(12):1421–1440. <https://doi.org/10.1016/j.asr.2010.01.018>
- Pavlov DA (2019) Role of Lunar Laser Ranging in realization of terrestrial, lunar, and ephemeris reference frames. *J Geodesy* 94(1):5. <https://doi.org/10.1007/s00190-019-01333-y>
- Pavlov DA, Williams JG, Suvorkin VV (2016) Determining parameters of Moon's orbital and rotational motion from LLR observations using GRAIL and IERS-recommended models. *Celest Mech Dyn Astron* 126(1):61–88. <https://doi.org/10.1007/s10569-016-9712-1>
- Pearlman MR, Noll CE, Pavlis EC, Lemoine FG, Combrink L, Degnan JJ, Kirchner G, Schreiber U (2019) The ILRS: approaching 20 years and planning for the future. *J Geodesy* 93(11):2161–2180. <https://doi.org/10.1007/s00190-019-01241-1>
- Ratcliff JT, Gross RS (2020) Combinations of Earth Orientation Measurements: SPACE2019, COMB2019, and POLE2019. Tech. Rep. JPL Publication 20-3, Jet Propulsion Laboratory
- Singh VV, Biskupek L, Müller J, Zhang M (2021) Impact of non-tidal station loading in LLR. *Adv Space Res* 67(12):3925–3941. <https://doi.org/10.1016/j.asr.2021.03.018>
- Singh VV, Biskupek L, Müller J, Zhang M (2022) Earth rotation parameter estimation from LLR. *Adv Space Res*. <https://doi.org/10.1016/j.asr.2022.07.038>
- Viswanathan V, Fienga A, Minazzoli O, Bernus L, Laskar J, Gastineau M (2018) The new lunar ephemeris INPOP17a and its application to fundamental physics. *Mon Not R Astron Soc* 476(2):1877–1888. <https://doi.org/10.1093/mnras/sty096>
- Williams JG, Turyshev SG, Boggs DH (2009) Lunar Laser Ranging tests of the equivalence principle with the Earth and Moon. *Int J Modern Phys D* 18(7):1129–1175. <https://doi.org/10.1142/S021827180901500X>
- Williams JG, Turyshev SG, Boggs DH (2012) Lunar Laser Ranging tests of the equivalence principle. *Classical Quantum Gravity* 29(18):184004
- Williams JG, Boggs DH, Folkner WM (2013) DE430 Lunar orbit, physical librations, and surface coordinates. JPL Interoffice Memorandum IOM 335-JW,DB,Wf-20080314-001, Jet Propulsion Laboratory, California Institute of Technology, Pasadena, California
- Zhang M, Müller J, Biskupek L (2020) Test of the equivalence principle for galaxy's dark matter by Lunar Laser Ranging. *Celest Mech Dyn Astron* 132(4):25. <https://doi.org/10.1007/s10569-020-09964-6>

<sup>1</sup>[https://cddis.nasa.gov/Data\\_and\\_Derived\\_Products/SLR/Lunar\\_laser\\_ranging\\_data.html](https://cddis.nasa.gov/Data_and_Derived_Products/SLR/Lunar_laser_ranging_data.html).

<sup>2</sup><https://keof.jpl.nasa.gov/combinations/latest/>.

<sup>3</sup><https://www.iers.org/IERS/EN/DataProducts/EarthOrientationData/eop.html>.

**Open Access** This chapter is licensed under the terms of the Creative Commons Attribution 4.0 International License (<http://creativecommons.org/licenses/by/4.0/>), which permits use, sharing, adaptation, distribution and reproduction in any medium or format, as long as you give appropriate credit to the original author(s) and the source, provide a link to the Creative Commons license and indicate if changes were made.

The images or other third party material in this chapter are included in the chapter's Creative Commons license, unless indicated otherwise in a credit line to the material. If material is not included in the chapter's Creative Commons license and your intended use is not permitted by statutory regulation or exceeds the permitted use, you will need to obtain permission directly from the copyright holder.



---

**Part V**

**Surface Deformation Monitoring**





# Determination of a GNSS-Based Velocity Field of the African Continent

Saturday E. Usifoh, Benjamin Männel, Pierre Sakic, Joseph D. Dodo, and Harald Schuh

## Abstract

GNSS-based velocity fields are a key tool to assess the boundaries around major deforming areas, to explain the main patterns of surface motion and deformation, to analytically review existing kinematics models and finally, to study the underlying tectonic activities. Determination of a velocity field for Africa is of great importance in the determination of the African Reference Frame; this is essential for better understanding the African plate tectonics. Therefore, this study focusses on the determination of the African velocity fields using continuously operated GNSS stations. We processed and analyzed 11 years of data obtained from a total number of 145 GNSS site using GFZ's EPOS.P8 software. The result shows that Africa moves in the North-East direction. The station coordinates derived with PPP show averaged RMS values of 2.9 mm, 9.9 mm and 8.5 mm for the north, east and up components with respect to the estimated trajectory models. Horizontal velocities at sites located on stable Nubia plate fit a single plate model with residual motion below 1 mm/year of RMS. We confirm significant southeast motion in Morocco and Zambia with residual velocities of 1.4 mm/year and 0.9 mm/year, respectively. We estimate the Euler Poles for Nubia and Somalia with  $48.59^{\circ}\text{N}$ ,  $-78.64^{\circ}\text{E}$ ,  $0.264^{\circ}/\text{Myr}$  and  $60.38^{\circ}\text{N}$ ,  $-83.33^{\circ}\text{E}$ ,  $0.272^{\circ}/\text{Myr}$ , respectively. Vertical velocities range from  $-2$  to  $+2$  mm/year, close to their uncertainties, with no distinct geographic pattern. The study also provides continental-wide position and velocity field solution for Africa, and can also be considered as a contribution to the upcoming AFREF, the African Geodetic Reference Frame.

## Keywords

GNSS · Plate tectonics · Precise Point Positioning (PPP) · Velocity field

S. E. Usifoh (✉)

GFZ German Research Centre for Geosciences, Potsdam, Germany

Institut für Geodäsie und Geoinformationstechnik Technische Universität, Berlin, Germany

Centre for Geodesy and Geodynamics, Toro, Bauchi State, Nigeria  
e-mail: [parker@gfz-potsdam.de](mailto:parker@gfz-potsdam.de)

B. Männel · P. Sakic

GFZ German Research Centre for Geosciences, Potsdam, Germany

J. D. Dodo

Centre for Geodesy and Geodynamics, Toro, Bauchi State, Nigeria

H. Schuh

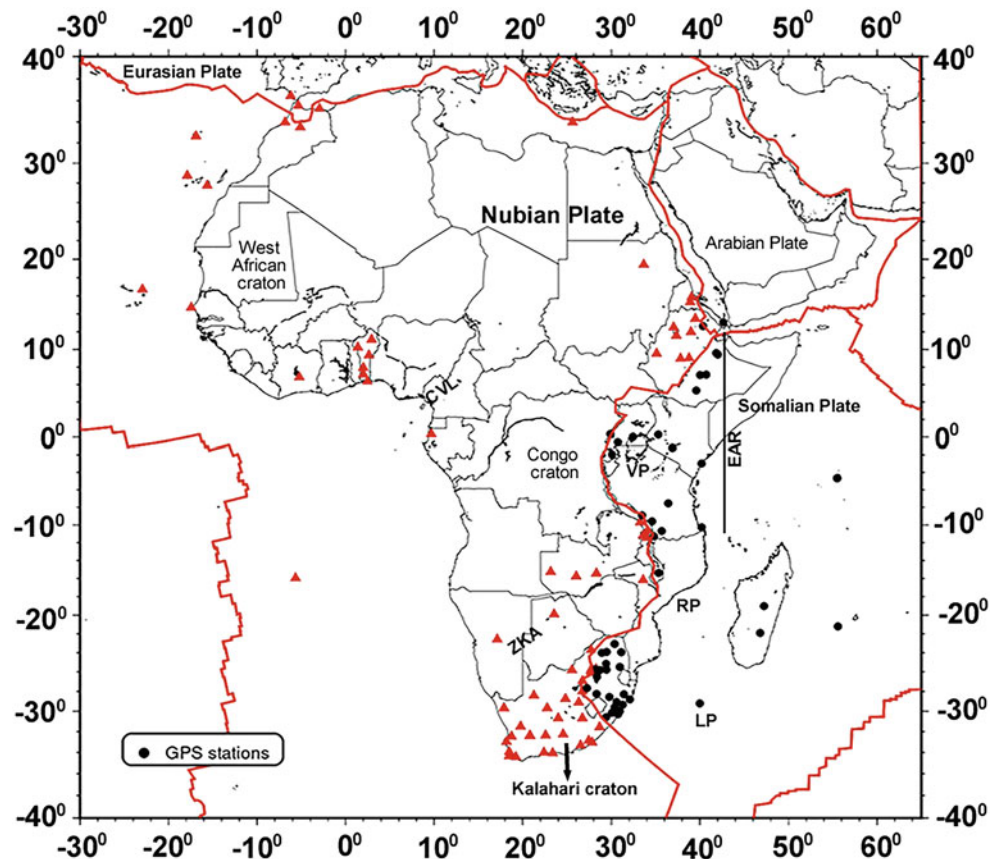
GFZ German Research Centre for Geosciences, Potsdam, Germany

Institut für Geodäsie und Geoinformationstechnik Technische Universität, Berlin, Germany

## 1 Introduction

The African Continent comprises of several cratons, stable blocks of old crust with deep roots in the subcontinental lithospheric mantle, and less stable terranes, which converged together to form the African Plate during the assembly of the supercontinent Pangea about 250 million years ago (Begg et al. 2009). The cratons include the Kalahari Craton, Congo Craton, Tanzania Craton, and West African Craton (see Fig. 1). The cratons were widely separated in the past, but brought together during the Pan-African orogeny and stayed together when Gondwana split up. The cratons are joined by orogeny belts, regions of highly deformed rock where the tectonic plates have engaged (Saria et al.

**Fig. 1** Map showing the major tectonic setting of Africa, the Craton and the GNSS stations used in this study. VP Victoria Plate, LP Lwandle Plate, RP Rovuma Plate, ZKA Zimbabwe-Kalahari Axis, CVL Cameroon Volcanic Line. Red triangle (GPS stations used to compute Euler vector in Nubian Plate), black dots (GPS stations used to compute Euler vector in Somalian Plate), and solid red line shows the major plate boundaries as given in the PB2002 model (Bird et al. 2002)

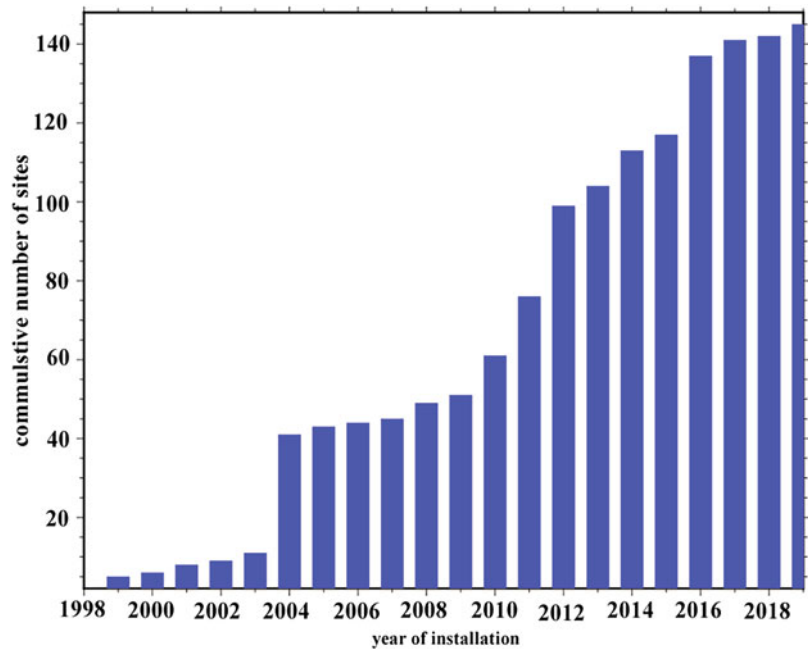


2013). The African plate that moved relatively slowly for the last 150 Ma (Lithgow-Bertelloni and Silveri 1998; Torsvik et al. 2010) is an interesting plate for studying intraplate magmatism. It contains various intraplate volcanic segments that are remote from the African plate boundaries. Such segment is the NE-SW oriented Cameroon Volcanic Line which bisects the angle where the coast of Africa makes a  $90^\circ$  bend from the western coast along the south of the West African craton and the southern coast along west of the Congo craton (see Fig. 1). It is characterized by moderate magnitude earthquakes and active volcanism (Aka et al. 2004; Milelli et al. 2012). Moreso, the East African Rift System (EARS), is a place where the Earth's tectonic forces create new plates by splitting apart old ones. In other words, it is a fracture in the Earth's surface that widens over time. The Nubian Plate makes up most of Africa, while the smaller plate that is pulling away is named Somalian Plate. These two plates are moving away from each other and also away from the Arabian plate to the north (Chu and Gordon 1999). The point where these three plates meet is the triple-junction at the Afar region of Ethiopia. However, all the rifting in East Africa is not confined to the Horn of Africa; it further extends to south into Kenya, Tanzania and Great Lakes region of Africa. The East African Rift system reaching from the Afar

in the northern Ethiopia to Mozambique in the south shows spreading rates of up to 5 mm/year (Saria et al. 2013).

The dynamics of the tectonic plate activities of the Earth are the major causes for ground motion. Beginning from the mid-1980s, the Global Navigation Satellite Systems (GNSS) have been effectively used in determining plate tectonic movement and other geodynamic phenomena. Over the last years, the monitoring of station coordinates located on the Earth's surface has become a great interest. Determination of velocity fields produces the means of analysing intra- and inter-plate geodynamic interactivities and other crustal disturbances (Holden et al. 2017; Kierulf et al. 2021). Saria et al. (2013) carried out some geodynamic studies for Africa from the combined GPS and DORIS space geodetic solutions, and observed that the velocity on the stable Nubia fits to a single rigid plate model with a WRMS of 0.6 mm/year, that is consistent with the current uncertainty of geodetic measurements in the region. Investigation of GNSS-based monitoring of continental-wide variations in Africa (Nubia) and Arabia plate shows that there is little variation in rates of motion along the boundary, ranging from  $5.4 \pm 1$  mm/year in the eastern Mediterranean to  $4.5 \pm 1$  mm/year near Gibraltar (McClusky et al. 2003), hence, this study tends to focus on the determination of velocity field for Africa.

**Fig. 2** Bar chart showing the cumulative number of continuous GNSS stations in Africa from 1998 to 2019. There was a speedy increase from 2004 to 2019



This introduction is followed by Sect. 2 the methodology and processing strategies. Section 3 presents the results, and Sect. 4 conclusions and recommendations.

## 2 Input Data

### 2.1 GNSS Data Collection and Processing

The GNSS data set used in this study includes 11 years of observations (2009–2019) from GNSS sites where data are openly available (see Fig. 1). A total number of 145 GNSS sites were used and the data were obtained from TrigNet<sup>1</sup> a network of continuously operating system base stations that are located in South Africa, from the UNAVCO archive<sup>2</sup> and the AFREF archive.<sup>3</sup> There are other GNSS network stations in Africa that are operating but unfortunately, could not be included due to data restriction. All openly available GNSS data used in this paper were processed; stations less than 3 years of observations were skipped. This is slightly above 2.5 years which is the minimum amount of time required to average out seasonal signals unrelated to the long term motions of interest in order to obtain a good velocity estimate (Blewitt and Lavallée 2002). There has been a rapid increase of GNSS stations in the years from 2004 to 2019 (see Fig. 2).

We analyse the GNSS data in PPP mode using the GFZ's EPOS.P8 software, based on GFZ repro3 solution (Männel et al. 2020). Precise point positioning (PPP) method is a robust method that focused on the processing of measurements from stand-alone GNSS receivers to compute high accurate positions (Zumberge et al. 1997), and has become cost effective in achieving centimeter-level accuracy. GNSS orbit modelling, satellite clocks and Earth Rotation Parameters (ERP) from GFZ repro3 were introduced apriori (Männel et al. 2021). We processed zero-differenced GPS observations using ionosphere-free linear combination with a 5 min sampling rate, to estimate daily station coordinates and tropospheric delays with 1 h ZTD and 24 h troposphere gradients. Phase ambiguities were not re-solved but estimated. We applied models following the IERS 2010 Conventions (Petit and Luzum 2010) and repro3 setup.<sup>4</sup> As the orbit products are provided in the repro3-specific reference frame, our coordinates are determined in this IGSR3 frame (Rebischung 2021). To ensure consistency, GNSS phase center corrections given in igsR3\_2077.atx were applied.

These daily solutions were used to generate position time series, which we closely inspected to identify outliers, offsets, or discontinuities. Coordinate and data conversion were done based on the GeodeZYX toolbox (Sakic et al. 2019). Subsequently, we used the Sari software (Santamaría-Góm 2019), to model site positions as the sum of (1) linear term representing secular displacement (2) offsets caused by

<sup>1</sup> <http://data.unavco.org/archive/gnss/rinex/obs>: Date access 9th June, 2020.

<sup>2</sup> <http://afredata.org>: Date access 25th August, 2020.

<sup>3</sup> <ftp://ftp.trigent.co.za>: Date access 13th September, 2020.

<sup>4</sup> [acc.igs.org/repro3/repro3.html](http://acc.igs.org/repro3/repro3.html): Date access: 15th January, 2021.

earthquakes, and other effects, mostly equipment changes and (3) periodic components. The model equation for each of the component (east, north, up) is given below

$$y = a + bt + \sum_{i=1}^N ciGi(t) + d \sin(2\pi t) + e \cos(2\pi t) \quad (1)$$

where  $a$  is the coordinate (initial position at reference epoch),  $b$  is the linear velocity (trend),  $c$  are the discontinuities,  $d$  and  $e$  are the annual amplitudes,  $t$  is the time epoch,  $G_i$  is the binary operator equal to zero, if  $t$  is less than zero or equal to 1, if  $t$  is greater or equal to zero, respectively. Sites, especially those with frequent offsets, including, PRE1, PRE2, HRAO (all in South Africa), NAZR, DAFT (all in Ethiopia) showed too many outliers and offsets and were therefore excluded from the final solution.

### 3 Results and Discussion

#### 3.1 Raw Time Series, FUNC (Madeira Island, Portugal) and LSMH (Ladysmith, South African)

From the raw coordinate time series, in the north and east components of the two stations, a linear trend is observed with a pronounced positive slope which shows north-east motion of  $27 \pm 0.3$  mm/year. Moreover, it can be observed that the height (up) component is quite noisier than the horizontal components which are due to observation geometry. In order to model the station trajectories, we used Eq. (1) to estimate the linear trend, annual signals and discontinuities. The estimated linear trend and the residual coordinates are shown in Fig. 3 and Table 1.

As shown in Fig. 3, FUNC and LSMH move with 17–18 mm/year towards north. The east component shows a similar trend for both stations with a velocity of 15–17 mm/year. We compared the velocity results computed using PPP solutions with the velocity results computed using UNAVCO plate motion calculator with respect to GSRM2.1 (Kreemer et al. 2014) (see Table 2), though there is a difference of 1.0–1.6 mm/year and 0.9–1.3 mm/year in the north and east direction, respectively, their difference is insignificant. For the vertical component their velocities are  $0.6 \pm 0.2$  mm/year and  $0.4 \pm 0.2$  mm/year, respectively. This slight motion could be from vertical uplift movements caused by atmospheric pressure variation and mass loading redistribution of non-tidal ocean loading and soil moisture (El-Fiky et al. 1997). The up component shows yearly variations with deterministic model (shown in red) containing harmonics, based on the least-squares approach. We notice in the up components, periodic surface deformations of about 25 mm, which are not apparent in the north and east components. These surface deformations are believed to be due to a large influence of non-tidal loading especially hydrological loading (Männel et al. 2019; Liu et al. 2017). We compared our velocity estimates against the ITRF2014 and found only minor discrepancies of 1–0 mm/year and 0 to –0.1 mm/year in the North and the East direction, respectively.

Figure 4 shows detrended data of the two selected stations FUNC and LSMH. The Root Mean Squares (RMS) of the residuals, i.e. the observed minus the computed, are 4.4 mm, 8.1 mm, 8.6 mm and 2.2 mm, 6.7 mm, 7.4 mm for the north, east and up components, respectively. We observe in Table 1 that the RMS in the north component is smaller than that of the east components in both stations, and highest in the up components. This is related to (1) observation geometry and (2) that the ambiguities are not fixed (float solution), which

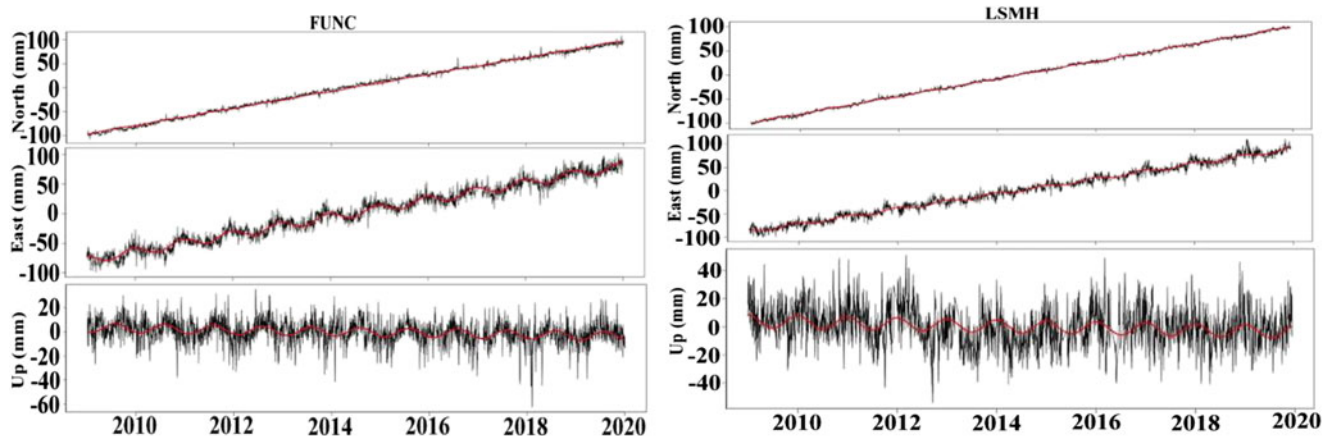


**Fig. 3** Time series of the GNSS stations FUNC (Madeira Island, Portugal) and LSMH (Ladysmith, South African) using combined function of linear and sinusoidal approach

**Table 1** Time series characteristics (velocities, root mean squares, and annual amplitudes for north, east and up components) for stations FUNC and LSMH

Station	Velocities (mm/year)			RMS (mm)			Annual ampl. (mm)		
	North	East	Up	North	East	Up	North	East	Up
FUNC	17 ± 0.1	15 ± 0.1	0.6 ± 0.2	3.4	8.1	8.6	0.9 ± 0.1	7.1 ± 0.2	3.7 ± 0.2
LSMH	18 ± 0.0	17 ± 0.1	0.4 ± 0.2	2.2	6.7	7.4	1.2 ± 0.2	3.5 ± 0.1	2.5 ± 0.2

**Table 2** Comparison of horizontal velocities computed with UNAVCO plate motion calculator

Station	Velocities (mm/year) computed with model GSRM2.1 (2014)		Velocities (mm/year), GNSS (this study)		Difference (mm/year)	
	North	East	North	East	North	East
FUNC	18.0	15.1	17.0	15.0	1.0	0.1
LSMH	19.6	18.3	18.0	17.0	1.6	1.3

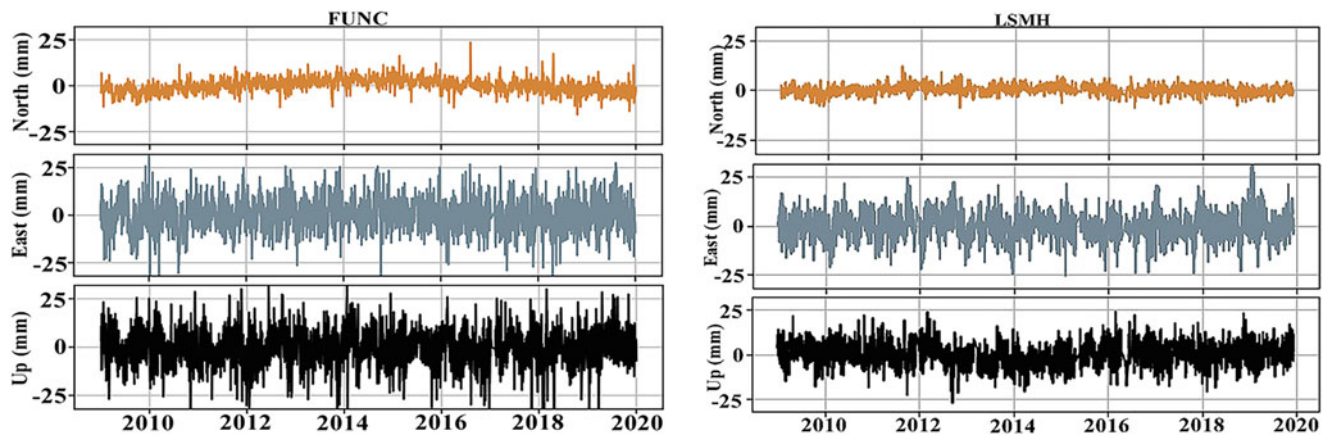


**Fig. 4** Detrended linear characteristics in time series of the GNSS stations FUNC (Madeira Island, Portugal) and LSMH (Ladysmith, South African)

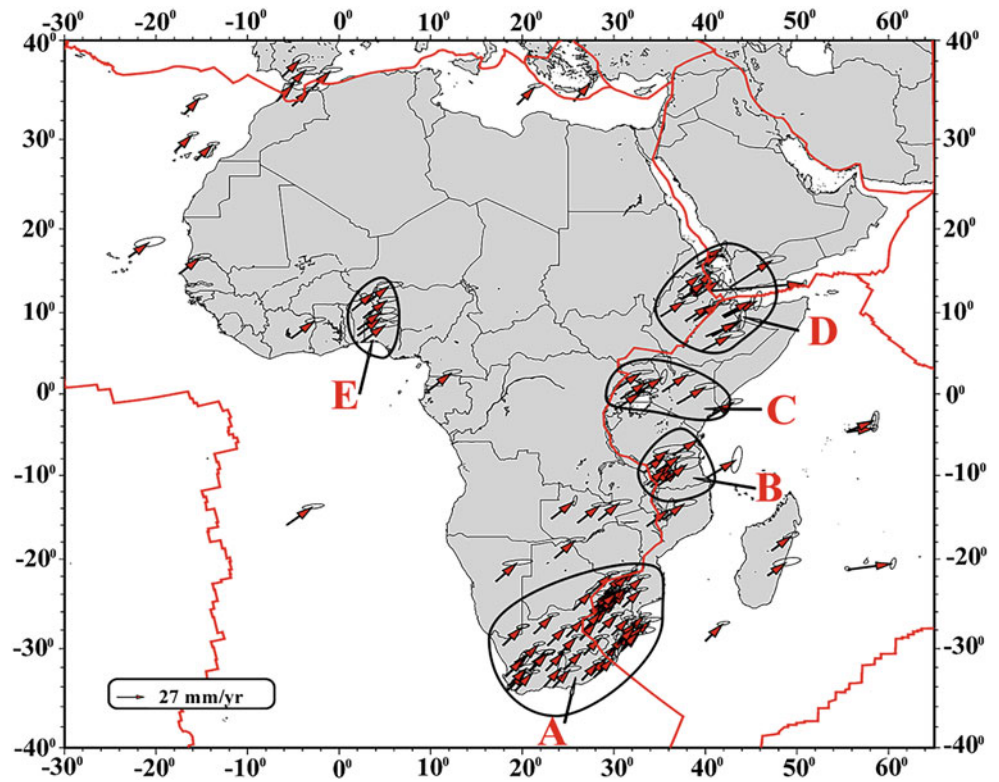
is causing a larger RMS in the east component. In addition, considering both stations, we observed that the RMS of station FUNC is higher in all the components than that of station LSMH, which shows that station LSMH is more stable to that of the station FUNC. This is most probably related to the station monuments as FUNC is located at the terrace of an old building whereas station LSMH is located on a concrete block.

Figure 5 shows the horizontal velocity fields for the whole Africa. We grouped the horizontal and vertical velocity field estimates into different groups A, B, C, D and E as indicated in Figs. 5 and 6, according to their velocity pattern. From our observations, the estimated horizontal geodetic velocities show completely the same pattern, thus indicating that African plate moves as rigid plate in north east direction with respect to the IGSR3 reference frame with velocity field of each group and their corresponding root mean square given Table 3.

The mean horizontal velocity for the overall block in north east direction is  $27 \pm 0.3$  mm/year with average root mean square residuals for north, east and up components of 2.9 mm, 9.9 mm and 8.5 mm respectively. Looking at B (Tanzania) and E (Benin Republic), we observe that

their horizontal velocities are the same which shows that the two blocks are moving in north east direction at the same rate. In addition, for group C (Kenya, Rwanda and Uganda) and group D (Ethiopia), their velocities stand out with a slight local velocity difference with respect to IGSR3 due to their location on the great valley rift (stratovolcano), as previous studies have shown that the African continent is undergoing continuous rifting along the East African Rift System (Ring 2014; Gaina et al. 2013). Considering group A (South Africa), stations KOKS (Kokstad), DRBN (Durban), STAN (Stanger) and GREY (Greytown), located in the Kwa-Zulu Natal province exhibit different but significant vertical displacement of velocity values of  $+1.5 \pm 0.2$  mm/year,  $+1.7 \pm 0.3$  mm/year,  $+1.8 \pm 0.3$  mm/year and  $-1.6 \pm 0.3$  mm/year, respectively. Stations KOKS, DRBN and STAN all in Kwa-Zulu Natal show uplift, which could be due to seismically active zones (one lesser, one greater in linear extent) across the continent ocean boundary at high angle (Hartnady 1990). In group B (Tanzania), we observed a significant change which probably indicates an uplift vertical displacement of velocity field approximately ranging from  $-2$  to  $+2$  mm/year; in agreement with Saria et al. (2013). As

**Fig. 5** Horizontal velocity with respect to IGSR3 and error ellipses of 95% confidence level



**Fig. 6** Vertical velocities with respect to IGSR3 derived from this study

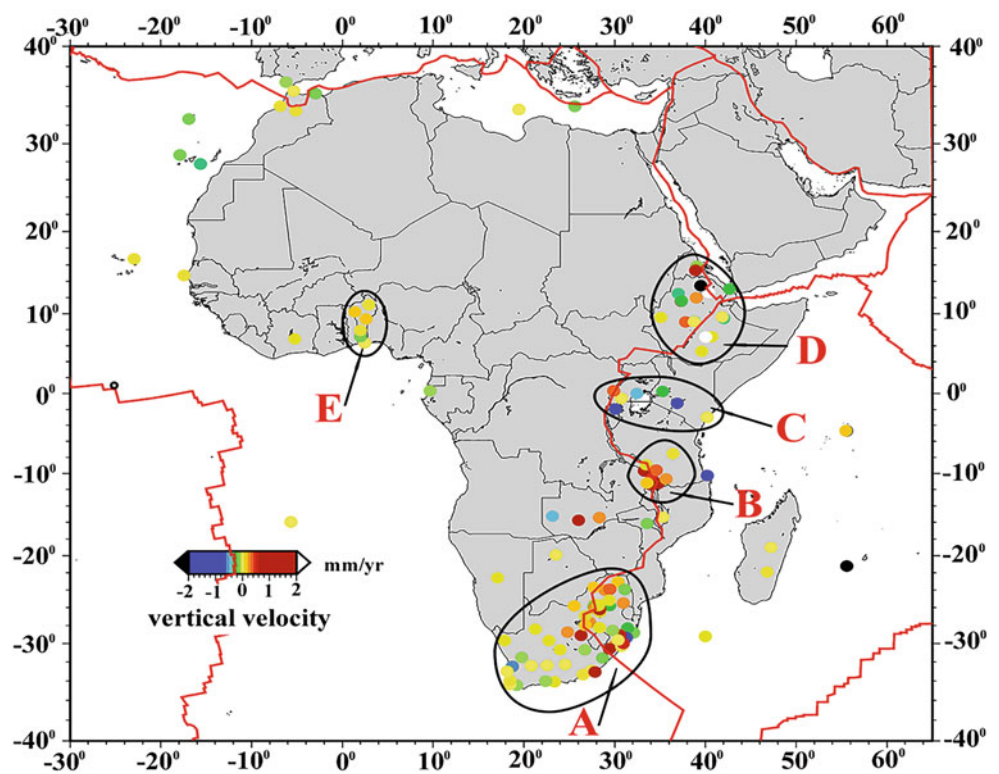


**Table 3** Horizontal and vertical velocity and the root mean square of each group according to their patterns

	Group A (South Africa)	Group B (Tanzania)	Group C (Kenya/Rwanda/Uganda)	Group D (Ethiopia)	Group E (Benin Rep.)
Horizontal velo. (mm/year)	25 ± 0.1	29 ± 0.1	31 ± 0.1	32 ± 0.2	29 ± 0.1
Vertical velo. (mm/year)	1.3 ± 0.1	1.9 ± 0.2	1.5 ± 0.2	5.2 ± 0.2	0.4 ± 0.2
RMS (mm)	4.9	5.8	5.3	5.9	7.2
Ampl. (mm)	2.6 ± 0.2	2.4 ± 0.3	2.1 ± 0.2	2.8 ± 0.5	3.2 ± 0.5

anticipated, uncertainties expeditiously decrease with time series length.

### 3.2 Euler Pole Parameter Estimation

We generated a rigid plate model by estimating plate rotations (Euler poles). Hence, we group the stations according to their location (Fig. 5), while testing the rigid plate assumption. We estimate the rotation rate vector for the Nubian and the Somalian plate and tested the significance relative to the IGSR3 interpretation using sites outside the deformation zones along the plate boundaries, and by excluding nearby redundant sites (Fig. 7). Stations NAZR, DABT and HERM were removed after outlier detection. Previous reports of Nubian and Somalian plate uses fewer sites, so we define a new subset of sites with a larger and better geographic distribution (Saria et al. 2013). The angular velocity of the Nubian plate with respect to IGSR3 (Table 4 and Fig. 7)

is close to the recent estimate of Altamimi et al. (2017). The uncertainty associated with this new angular rotation of Nubia with respect to IGSR3 so far is the smallest, most likely because the solution presented in this study is based on a larger number of GNSS sites and longer observation time span.

Nevertheless, a significant limitation is the lack of dense, homogeneous continuous GNSS network over most of the Africa. With respect to stable part of Nubia, the residual velocities as given in Fig. 7, shows regions with significant deformation. It is expected that in the eastern part of the East African Rift, larger residuals are observed as this region contains various microplates (Wedmore et al. 2021). We also observed a deviation from the plate rigidity in stations RABT, IFR1, TETN in Morocco and MONG in Zambia with their residual velocities tended towards SSE at average velocities 1.4 mm/year and 0.9 mm/year respectively.

For the Somalian plate, we selected 55 GNSS stations to estimate site velocities as shown in (Fig. 1). We observed

**Fig. 7** Residuals of the observed plate-fixed velocities relative to the modelled using the estimated Euler Pole with respect to Nubia and Somalian plate

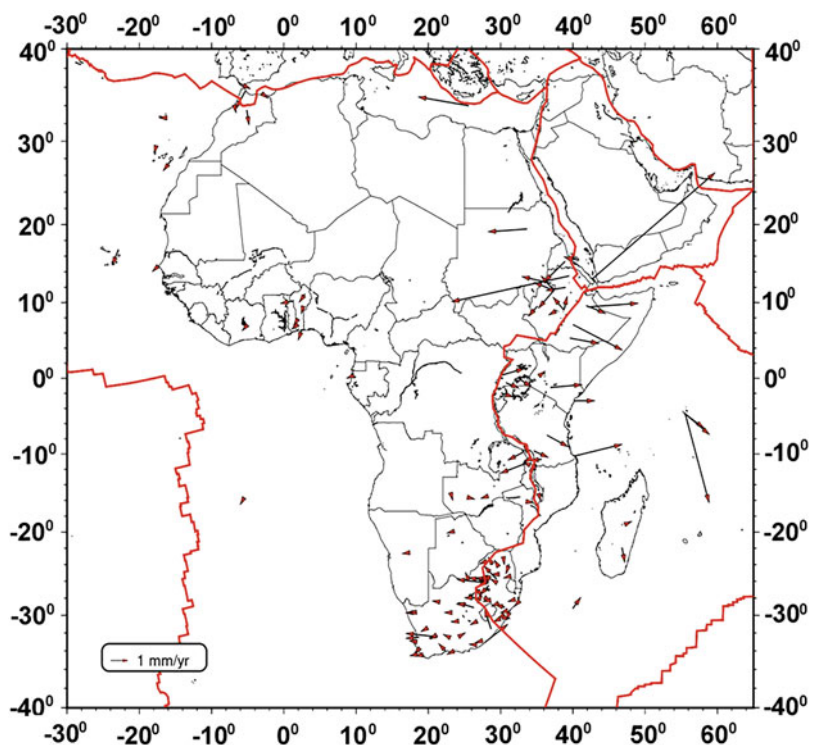


**Table 4** Estimated plate kinematic parameters

Plate (IGSR3)	Num. of sites	Lat (deg)	Long (deg)	$\omega_x$ (mas/year)	$\omega_y$ (mas/year)	$\omega_z$ (mas/year)	Angular velocity ( $^{\circ}$ /Myr)	WRMS			
								E (mm/year)	N (mm/year)		
Nubian	79	48.59	-78.64	0.035	-0.174	0.201	$0.264 \pm 0.000$	0.12	0.17		
±		0.265	0.611	0.002	0.000	0.001					
Somalian	55	60.38	-83.33	0.016	-0.134	0.237	$0.272 \pm 0.017$	0.21	0.17		
±		0.238	0.407	0.009	0.006	0.020					
ITRF2014				Altamimi et al. (2017)							
Nubian	24	48.79	-80.33	0.099	-0.614	0.733	$0.267 \pm 0.001$	0.28	0.36		
±		0.290	0.110	0.004	0.003	0.001					
Somalian	3	49.24	-94.15	-0.121	-0.794	0.332	$0.332 \pm 0.882$	0.32	0.30		
±		0.260	0.720	0.035	0.034	0.008					



that stations in the volcanically active island Reunion (Fig. 7) have velocities that are agreeing with the rigid Somalian and could therefore be used to define its kinematics. Stations NEGE and ROBE (Ethiopia), located 15 km from the rift, and MTDK (Tanzania), located 100 km from the Tanzania Rift, are also agreeing with rigid Somalian.

## 4 Conclusions

In this study, we processed data of 145 stations from 2009 to 2019 with GFZ EPOS.P8 solution in PPP mode. These data sets were taken from a geodetic network precisely designed and surveyed to measure tectonic motion through the South African network, UNAVCO and AFREF. The resulting coordinates were used to determine the horizontal and vertical velocity fields with respect to IGSR3. The linear trends in the coordinate time series were estimated by fitting a trend to the data and estimate its velocity coefficients using the least-squares principle. We observed that Africa is moving in north-east motion with respect to IGSR3 with the overall horizontal average velocity field of  $27 \pm 0.3$  mm/year and with vertical uplift in Tanzania with velocity field ranging from  $-2$  to  $+2$  mm/year; other regions show no significant changes. Moreover, the present availability of geodetic sites in Africa is not even and the intra-plate deformation at regional or local scales with the current networks may not be detectable.

This study provides for the entire continent of Africa the position/velocity solution precisely expressed with reference frame IGSR3, and hence it will serve as a base in the contribution to the computation of the velocity field of Africa in the determination of the upcoming African Reference Frame AFREF and also gives a better understanding of the African plate tectonics, that appears to be lacking in earlier studies of the AFREF reports. Though much effort has been made on GNSS site distribution in Africa, most part of the African continent still remains undersampled. Effort to augment the geodetic infrastructure is under way, through link academic research projects, AFREF or in the level of surveying applications. Hence, the objective of this new data will help in the establishment and maintenance of a unified geodetic reference network for Africa which will serve as a fundamental basis for national reference networks that will fully be consistent and homogeneous with the global reference frame of the International Reference Frame (ITRF).

**Acknowledgements** The authors would like to thank and express their gratitude to the South African Network (TrigNet), UNAVCO, AFREF, and IGS (Johnson et al. 2017) for making their GNSS data available.

**Availability of Data and Materials** The data used to support the findings of this study are available on their website cited as footnote.

**Conflict of Interest** The authors declare that they have no conflicts of interest.

**Authors' Contributions** Saturday Ehisemhen Usifoh downloaded the data, processed, analysed and wrote the manuscript. BM, PS, DJ, and HS verified the feasibility of the method, checked the processing, the analysis, the interpretation, and the discussion of the results. All authors joined in revising the manuscript and figures modification.

**Code Availability** Not applicable.

**Ethics Approval and Consent to Participate** Not applicable.

**Consent for Publication** Not applicable.

**Funding** Not applicable.

## References

- Aka FT, Keisuke N, Minoru K, Hirochika S, Greg T, Bekoa A, Joseph H (2004) Symmetrical Helium isotope distribution on the Cameroon Volcanic Lines, West Africa. *Chem Geol* 203(3–4):205–223. <https://doi.org/10.1016/j.chemgeo.2003.10.003>
- Altamimi Z, Métivier L, Rebischung P, Rouby H, Collilieux X (2017) ITRF2014 plate motion model. *Geophys J Int* 209:1906–1912. <https://doi.org/10.1093/gji/ggx136>
- Begg GC, Griffin WL, Napapov LM, O'Reilly SY, Grand SP, O'Neill CJ, Hronsky JMA, Poudjom Djomani Y, Swan CJ, Deen T, Bowden P (2009) The lithospheric architecture of Africa: seismic tomography, mantle petrology and tectonic evolution. *Geosphere* 5:23–50. <https://doi.org/10.1130/GES00179.1>
- Bird P, Kagan YY, Jackson DD (2002) Plate tectonics and earthquake potential of spreading ridges and oceanic transform faults. In: Stein S, Freymueller JT (eds) Plate boundary zones, Geophysical monograph series, vol 30. AGU, Washington DC, pp 203–218. <https://doi.org/10.1029/GD030p0203>
- Blewitt G, Lavallée D (2002) Effect of annual signals on geodetic velocity. *J Geophys Res* 107(B7):2145. <https://doi.org/10.1029/2001JB000570>
- Chu D, Gordon RG (1999) Evidence for motion between Nubia and Somalian along the southwest Indian. *Nature* 398:64–67. <https://doi.org/10.1038/18014>
- El-Fiky GS, Teruyuki K, Yoichiro F (1997) Distribution of vertical crustal movement rates in the Tohoku district, Japan, predicted by least squares collocation. *J Geod* 71:432–442. <https://doi.org/10.1007/s001900050111>
- Gaina C, Torsvik TH, van Hinsbergen DJJ, Medvedev S, Werner SC, Labails C (2013) The African plate: a history of oceanic crust accretion and subduction since the Jurassic. *Tectonophysics* 604:4–25. <https://doi.org/10.1016/j.tecto.2013.05.037>
- Hartnady CJH (1990) Seismicity and plate boundary evolution in southeastern Africa. *S Afr J Geol* 93(3):473–484. [https://hdl.handle.net/10520/AJA10120750\\_853](https://hdl.handle.net/10520/AJA10120750_853)
- Holden L, Silcock D, Choy S, Cas R, Ailleres L, Fourniers N (2017) Evaluating a campaign GNSS velocity field derived from an online precise point positioning service. *Geophys J Int* 208:246–256. <https://doi.org/10.1093/gji/ggw372>
- Johnson G, Riddell A, Housler G (2017) The International GNSS service. Springer, Cham, pp 967–982. <https://doi.org/10.1007/978-3-319-42928-1>
- Kierulf HP, Steffen H, Barletta VR, Lidberg M, Johansson J, Kristiansen O, Tarasov L (2021) A GNSS velocity field for geophysical applications in Fennoscandia. *J Geodyn* 146:101845. <https://doi.org/10.1016/j.jog.2021.10184>

- Kreemer C, Blewitt G, Klein EC (2014) A geodetic plate motion and Global Strain Rate Model. *Geochem Geophys Geosyst* 15:3849–3889. <https://doi.org/10.1002/2014GC005407>
- Lithgow-Bertelloni C, Silveri PG (1998) Dynamics topography, plate driving forces and the Africa superwell. *Nature* 395:269–272. <https://doi.org/10.1038/26212>
- Liu L, Khan SA, van Dam T, Ma JHY, Bevis M (2017) Annual variations in GPS-measured vertical displacements near Upernavik Isstrøm (Greenland) and contributions from surface mass loading. *J Geophys Res Solid Earth* 122:677–691. <https://doi.org/10.1002/2016JB013494>
- Männel B, Dobsław H, Dill R, Glaser S, Balidakis K, Thomas M, Schuh H (2019) Correcting surface loading at the observation level: impact on global GNSS and VLBI station networks. *J Geod* 93:2003–2017. <https://doi.org/10.1007/s00190-019-01298>
- Männel B, Brandt A, Bradke M, Sakic P, Brack A, Nischan T (2020) Status of IGS reprocessing activities at GFZ. In: *International Association of Geodesy Symposia*. Springer, Heidelberg. [https://doi.org/10.1007/1345\\_2020\\_98](https://doi.org/10.1007/1345_2020_98)
- Männel B, Brandt A, Bradke M, Sakic P, Brack A, Nischan T (2021) GFZ repro3 product series for the international GNSS service (IGS). GFZ Data Services. <https://doi.org/10.5880/GFZ.1.1.2021.001>
- McClusky S, Reilinger R, Mahmoud S, Ben D, Tealeb A (2003) GPS constraints on Africa (Nubia) and Arabian plate motions. *Geophys J Int* 155:126–138. <https://doi.org/10.1046/j.1365-246X.2003.02023>
- Milelli L, Fourel L, Jaupart C (2012) Lithospheric instability origin for the Cameroon Volcanic Line. *Earth Planet Sci Lett* 335–336:80–87. <https://doi.org/10.1016/j.epsl.2012.04.028>
- Petit G, Luzum B (2010) IERS conventions. IERS technical note 36. Verlag des Bundesamts für Kartographie und Geodäsie, Frankfurt am Main. ISBN: 3–89888–989-6
- Rebuschung P (2021) IGS3\_2077.atx. <https://doi.org/10.5190/egusphere-egu21-2144>
- Ring U (2014) The East African rift system. *Aust J Earth Sci* 107:132–146
- Sakic P, Ballu V, Mansur G (2019) The GeodeZYX toolbox: a versatile python 3 toolbox for geodetic-oriented purposes. V. 4.0 GFZ Data services. <https://doi.org/10.5880/GFZ.1.1.2019.002>
- Santamaría-Góm A (2019) Sari: interactive GNSS position time series analysis, vol (0123456789). Part of Springer Nature (2019, online). <https://doi.org/10.1007/s10291-0846-y>
- Saria E, Calais E, Altamimi Z, Willis P, Farak H (2013) A new velocity field for Africa from combined GPS and DORIS space geodetic solutions: contribution to the definition of the African reference frame (AFREF). *J Geophys Res Solid Earth* 118:1677–1697. <https://doi.org/10.1002/jgrb.50137>
- Torsvik TH, Steinberger B, Gurnis M, Gaina C (2010) Plate tectonic and net lithosphere rotation over the past 150 My. *Earth Planet Sci Lett* 291:106–112. <https://doi.org/10.1016/j.epsl.2009.12.055>
- Wedmore LNJ, Biggs J, Floyd M, Fagereng Å, Mdala H, Chindandali P et al (2021) Geodetic constraints on cratonic microplates and broad strain during rifting of thick Southern African lithosphere. *Geophys Res Lett* 48:e2021GL093785. <https://doi.org/10.1029/2021GL093785>
- Zumberge JF, Heflin MB, Jefferson DC, Watkins MM, Webb FH (1997) Precise point positioning for the efficient and robust analysis of GPS data from large networks. *J Geophys Res* 102(B3):5005–5017. <https://doi.org/10.1029/96JB03860>

**Open Access** This chapter is licensed under the terms of the Creative Commons Attribution 4.0 International License (<http://creativecommons.org/licenses/by/4.0/>), which permits use, sharing, adaptation, distribution and reproduction in any medium or format, as long as you give appropriate credit to the original author(s) and the source, provide a link to the Creative Commons license and indicate if changes were made.

The images or other third party material in this chapter are included in the chapter's Creative Commons license, unless indicated otherwise in a credit line to the material. If material is not included in the chapter's Creative Commons license and your intended use is not permitted by statutory regulation or exceeds the permitted use, you will need to obtain permission directly from the copyright holder.





# Vertical Land Motion at Tide Gauges Observed by GNSS: A New GFZ-TIGA Solution

Benjamin Männel, Tilo Schöne, Markus Bradke, and Harald Schuh

## Abstract

Long-term tide gauge records provide valuable insights to sea level variations but interpretation requires an accurate determination of associated vertical land motion. Within the Tide Gauge Benchmark Monitoring Pilot Project of the International GNSS Service dedicated reprocessing campaigns are performed for GNSS stations co-located with tide gauges. Based on 341 stations the GFZ contribution to the third TIGA reprocessing provides vertical land motion rates for 230 stations at or close to recently active tide gauges. GNSS station coordinate time series determined by using a network approach and a conventional time series analysis show mean repeatabilities of 2.9, 3.3, and 5.6 mm for north, east, and up coordinates. The derived vertical velocity pattern is analyzed but also compared to the ALTIGAPS and the ULR6a solutions showing mean differences of  $0.04 \text{ mm yr}^{-1}$  and  $-0.1 \text{ mm yr}^{-1}$ , respectively. By correcting tide gauge records available via PSMSL for the individual vertical station velocity including eventually velocity changes geocentric sea level changes are determined. Compared to AVISO's multi-mission altimetric trend map a difference of  $-0.7 \text{ mm yr}^{-1}$  is determined.

## Keywords

GNSS · Sea level · Tide gauge · TIGA · Vertical land motion

## 1 Introduction

Sea level change is a major threat for the coastal communities and one of the prominent signs of global change. Thanks to long-term tide gauge records and supported by several space-borne altimeters since 1991, sea level changes can be observed with high accuracy. For the past century, Church and White (2011) estimated an absolute sea level trend from tide gauges of  $1.7 \pm 0.2 \text{ mm yr}^{-1}$  which was later revised to  $1.56 \pm 0.33 \text{ mm yr}^{-1}$  (Frederikse et al. 2020). In

recent years, the global sea level change rate increased. For example, AVISO (2021) reports a trend of  $3.4 \text{ mm yr}^{-1}$  based on radar altimeter data between 1993 and 2020. However, especially for coastal regions the relative local sea level trend may differ significantly but is an important key indicator to determine the impact on coastal regions. The differences between geocentric and relative trends are caused by specific environmental conditions, like differences in water temperature, salinity stratification or coastal ocean currents and surge but also strongly on the vertical land motion (i.e., coastal uplift and subsidence). An extensive review on sea level variability in coastal regions is provided in Woodworth et al. (2019). Knowing the vertical land motion is essential to project the local and regional sea level trends and to support societal decision-making and effective coastal protection mechanisms (Siriwardane-Zoysa et al. 2021; Bott et al. 2021). According to Wöppelmann and Marcos (2016) the required accuracy for ver-

B. Männel (✉) · T. Schöne · M. Bradke · H. Schuh  
Deutsches GeoForschungsZentrum GFZ, Telegrafenberg, Potsdam,  
Germany

H. Schuh  
Institute of Geodesy and Geoinformation Science, Technische  
Universität Berlin, Berlin, Germany

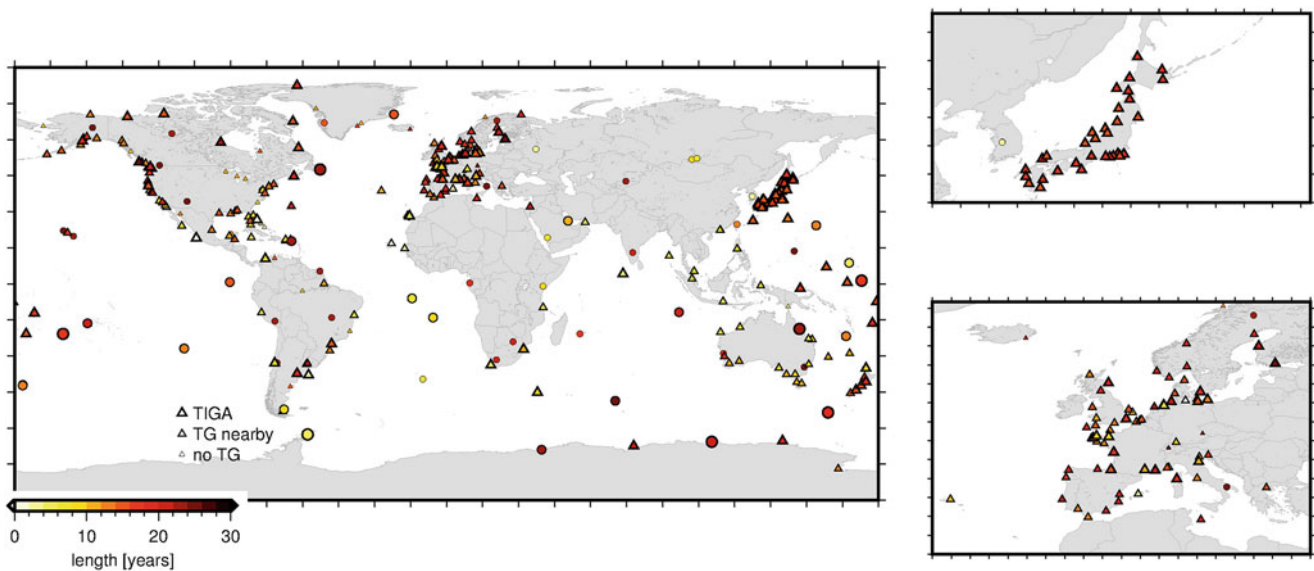


**Fig. 1** Station selection: IGS14 core stations used to define the geodetic datum (*circle*) and freely estimated stations (*triangle*); symbol size identifies TIGA stations, stations with closely tide gauges and

stations without tide gauge connection; the color-coding represents the time series length. Regions with dense stations networks are plotted additionally: Japan (*top, right*), Europe (*right, bottom*)

tical station velocities at tide gauges is at the level of  $0.5 \text{ mm yr}^{-1}$ .

To support the estimation of accurate vertical land motion, the International GNSS Service (IGS, Johnston et al. 2017) initiated the IGS Tide Gauge Benchmark Monitoring Pilot Project (TIGA) in 2001 (Schöne et al. 2009). The main objective, to derive vertical land motion in a well-defined global reference frame, also includes the support of installing and maintaining the global network of GNSS at tide gauges and the collection of GNSS data of stations at or close to tide gauges as well as data processing, time series analysis, and distribution of results. Over the past 20 years, the institutes supporting TIGA performed regularly extensive reprocessing campaigns to derive the best possible and most consistent time series solutions. Previous TIGA solutions were presented for example by Rudenko et al. (2010, 2013), Deng et al. (2016), Santamaría-Gómez et al. (2012). Within the IGS third reprocessing campaign (repro3) a new TIGA reprocessing effort was undertaken and supported by GFZ and University of La Rochelle (ULR). The main motivation of the current TIGA reprocessing was to keep the consistency with the updated IGS reprocessing setup especially regarding the satellite modeling as well as to extend the individual coordinate time series to ensure up-to-date vertical land motion estimates.

In this publication we present the GFZ TIGA contribution computed within the repro3 framework. Following this introduction, the station selection and the applied processing strategy is described in Sect. 2. Section 3 discusses the derive time series and the estimated vertical velocities whereas comparisons with sea level records and altimetric data sets

are presented in Sect. 4. Within Sect. 4 we assess also the quality of sea level records corrected by the GNSS-based trends. The paper closes with a brief summary and some conclusions in Sect. 5.

## 2 Station Selection and Data Processing

Compared to the previous GFZ TIGA contribution (Deng et al. 2016) with in total 794 stations a smaller station set was defined for the GFZ contribution to the TIGA reprocessing associated with the IGS third reprocessing campaign. In total 341 stations were selected containing 101 TIGA stations and 153 stations co-located to tide gauges. The geographical distribution of these stations is shown in Fig. 1. Due to the overall distribution of GNSS stations linked to tide gauges station clusters are visible along the European, Japanese, and partly the North American coastlines. To ensure a reliable definition of the geodetic datum the 66 GNSS stations defined as simplified IGS14 core network in the repro3 station priority list<sup>1</sup> were selected additionally (indicated by circles in Fig. 1). Obviously, 36 of these core stations are without connection to tide gauges and mostly located far from coastlines. However, eight datum stations are also TIGA stations and additional 21 are co-located with a tide gauge. Moreover, 30 additional stations without connection to tide gauges were processed, most of them located close to shorelines. Exceptions are NAUS (Manaus, Brazil) which

<sup>1</sup>[http://acc.igs.org/repro3/repro3\\_station\\_priority\\_list\\_060819.pdf](http://acc.igs.org/repro3/repro3_station_priority_list_060819.pdf), accessed August 2021.

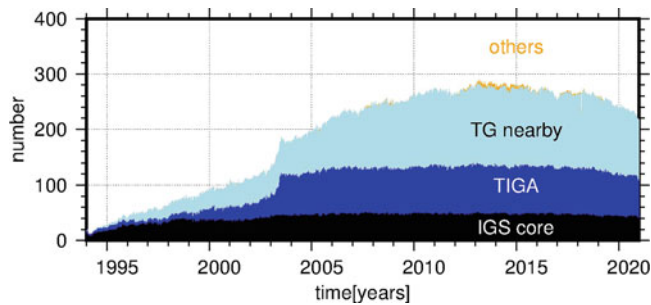


**Fig. 2** Number of stations contained in each daily solution, stations are grouped accordingly; *IGS core* refers to the simplified IGS14 core network defined in repro3

was selected for further investigations regarding loading effects as well as WTZR (Wetzell, Germany) and ZIMM (Zimmerwald, Switzerland), which were added for quality control. Three other stations are located close to the Great Lakes in North America (SAG1, STB1, WIS1). The associated station meta-data are taken from the GFZ Sensor Meta Information SYStem (semisys, Bradke 2020).

The number of stations processed for each day between 1994 and 2020 are presented in Fig. 2. While less than 100 stations were available for the years before 2000, this number increased especially in 2003 with the addition of TIGA stations from Japan. The decrease visible for the recent years is mostly associated to the decommissioned stations previously co-located to tide gauges and similarly visible in the repro3 submissions (Rebischung 2021). A rather stable number of 70–80 and 40–50 stations were processed from 2003 onwards for the TIGA and IGS core stations, respectively.

For the processing, a network approach was chosen with ambiguity fixing according to Ge et al. (2005) but without orbit determination. Therefore, we introduced the orbit and clock products provided in the GFZ repro3 solution (Männel et al. 2021). The main reason for this strategy (compared for example to the GFZ TIGA solution GT2 described in Deng et al. 2016) was to reduce the computational and personnel work load. To ensure consistency, the TIGA processing strategy followed the IGS repro3 settings<sup>2</sup> and is described in detail in Table 1. This is especially true for the antenna corrections where the igsR3\_2135.atx file was used with GPS transmitter offsets adjusted to the pre-launch calibrated Galileo PCOs provided by EUSPA. The derived coordinates are thus given in the consistently derived IGSR3 reference frame whose terrestrial scale differs from the ITRF2014 scale by around 1.2 ppb at epoch 2010.0 plus a drift of 0.03 ppb yr<sup>-1</sup>, which corresponds roughly to 0.2 mm yr<sup>-1</sup> as

**Table 1** Summary of estimation and processing strategy; time span 1994–2020; GFZ software EPOS.P8 was used to process the GNSS data

Modeling and a-priori information	
Observations	Ionosphere-linear combination formed by undifferenced GPS observations
A priori products	Orbits, clock corrections, Earth rotation parameters from GFZ repro3 solution (Männel et al. 2020; Männel et al. 2021)
Tropospheric correction	Troposphere delays computed with Saastamoinen, mapped with VMF (Böhm et al. 2006)
Ionospheric correction	1st order effect considered with ionosphere-free linear combination, 2nd order correction applied
GNSS phase center	Corrections from dedicated repro3 ANTEX applied (igsR3_2135.atx, <a href="http://ftp.aiub.unibe.ch/users/villiger/igsR3_2135.atx">http://ftp.aiub.unibe.ch/users/villiger/igsR3_2135.atx</a> )
Gravity potential	GOCO6s up to degree and order 12 (Kvas et al. 2019)
Solid Earth tides	According to IERS 2010 Conventions (Petit and Luzum 2010)
Permanent tide	Conventional tide free
Ocean tide model	FES2014b (Lyard et al. 2006)
Ocean loading	Tidal: FES2014b (Lyard et al. 2006)
Atmospheric loading	Tidal: $S_1$ and $S_2$ corrections (Ray and Ponte 2003)
High-frequent EOP model	Desai-Sibois model (Desai and Sibois 2016)
Mean pole tide	Linear mean pole as adopted by the IERS in 2018
Parametrization	
Station coordinates	NNT & NNR constraints applied to 66 datum stations (reference frame IGSR3 as described in IGS-mail 8026 ( <a href="https://lists.igs.org/pipermail/igsmail/2021/008022.html">https://lists.igs.org/pipermail/igsmail/2021/008022.html</a> ))
Troposphere	25 zenith delays; VMF; two gradient pairs per station and day
Receiver clock	Pre-eliminated every epoch
GNSS ambiguities	Ambiguity fixing according to Ge et al. (2005)
Products	
Station coordinates	Provided in daily SINEX files
Troposphere	ZTD and gradients are provided in daily TROP SINEX files (version 2.00)

described in IGS-mail 8026.<sup>3</sup> In addition, only GPS was processed compared to the three-constellation-solution of the GFZ repro3 solution.

To describe the processed TIGA solution some relevant indicators are discussed in the following. Figure 3 presents the number of daily processed phase observations in the com-

<sup>2</sup><https://www.igs.org/acc/reprocessing/>, last accessed August 2021.

<sup>3</sup><https://lists.igs.org/pipermail/igsmail/2021/008022.html>, assessed August 2021. Comparing our results given here to solutions given in ITRF2014 includes therefore a scale difference.

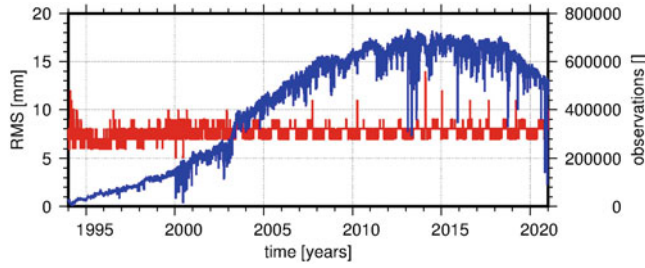


**Fig. 3** RMS of residuals averaged over all stations and satellites (*red*) and number of processed observations per day (*blue*)

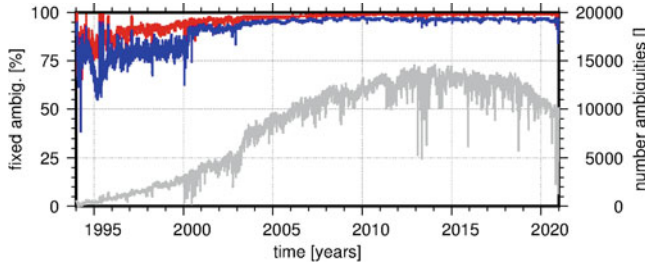


**Fig. 4** Number of ambiguities per day (*grey*) and ratio of fixed narrow (*blue*) and widelane (*red*) ambiguities

monly used ionosphere-free linear combination. Between 2008 and 2020 more than 600,000 observations were processed daily while their overall distribution follows naturally the characteristics of Fig. 2. For a few days the number of observations dropped due to a rather rigorous outlier exclusion. Additionally, the residual statistics are provided in Fig. 3. Residuals are defined here as the difference between GNSS observations and adjusted values in the GNSS processing. Except for the first years the RMS computed over all residuals within one day ranges between 7 and 9 mm. The associated number of ambiguities, given in Fig. 4, follows the distribution of the observations. Except for a lower fixing rate before 2000, mostly 99% of the ambiguities are successfully fixed during the processing. Exceptional high resolution rates in the early years for example in 1995 are related to periods when anti-spoofing was switched off (Steigenberger 2009). The derived daily solutions are stored in conventional SINEX files for a later combination. They are available for further investigation via Männel et al. (2022).

### 3 Time Series Analysis

After converting the derived cartesian station coordinates (X,Y,Z) into topocentric coordinates (north, east, up) the time series analysis was performed using the Bernese GNSS Software FODITS programme (Ostini 2012; Dach et al. 2015). The fully functional model was set up including initial coordinates  $\mathbf{d}_0$  and velocities  $\mathbf{v}_0$ , discontinuities  $\mathbf{d}_k$ ,

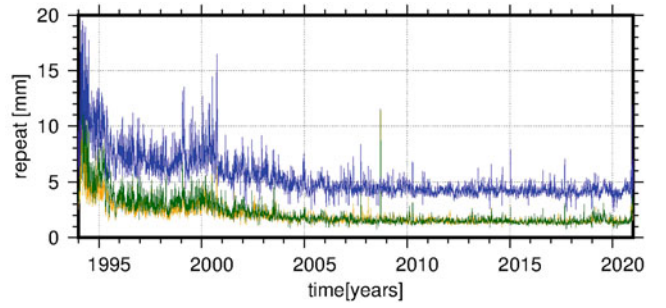


**Fig. 5** RMS between coordinates and trajectory model (repeatabilities) averaged daily in north (*orange*), east (*green*), and up (*blue*) direction

outliers  $\mathbf{s}_k$ , velocity changes  $\mathbf{v}_k$ , and components of periodic functions  $\mathbf{p}_{a,k}$ ,  $\mathbf{p}_{b,k}$  (Dach et al. 2015):

$$\begin{aligned}
 f(t_i) &= \mathbf{d}_0(t_0) + \mathbf{v}_0(t_i - T_0) \\
 &+ \sum_{k=1}^{n_d} \mathbf{d}_k \eta_{d,k}(t_i) + \sum_{k=1}^{n_s} \mathbf{s}_k \eta_{s,k}(t_i) + \sum_{k=1}^{n_v} \mathbf{v}_k \eta_{d,k}(t_i) \\
 &+ \sum_{k=1}^{n_p} [\mathbf{p}_{a,k} \cos(\omega_k(t_i - t_0)) + \mathbf{p}_{b,k} \sin(\omega_k(t_i - t_0))] \eta_{p,k}(t_i).
 \end{aligned} \quad (1)$$

Indicator functions  $\eta_x$  describe the validity of the corresponding components. Overall, 332 vertical time series were reliably assessed, whereas nine stations with less than 1000 daily coordinate estimates were excluded from the further investigations. The averaged time series length amounts to 5314 coordinate sets which corresponds to around 14 years. Overall 2327 coordinate discontinuities (i.e., on average seven per station) were found, they are mostly caused by hardware replacements and earthquakes. More important to vertical land motion, 275 velocity changes are identified mostly associated with earthquakes while 145 stations show constant linear trends. Annual and semi-annual signals were found for nearly all stations with globally averaged amplitudes of 3.9 and 1.1 mm, respectively. However, these amplitudes vary significantly as they depend strongly on station specific environmental conditions especially on non-tidal loading. As shown, for example in Männel et al. (2019) especially continental hydrology has a strong annual (i.e., periodic) component which needs to be estimated in the time series analysis if corresponding loading corrections are not considered. The remaining residuals, i.e., the difference between coordinate and trajectory model, is summarized in Fig. 5 averaged over all stations. While the corresponding RMS values (also known as repeatabilities) are higher in the earlier years, a stable behavior with 1–2 mm for the horizontal and 4–5 mm for the vertical component can be noticed from 2005 onwards. The mean values averaged over all stations per coordinate direction are 2.9, 3.3, and 5.6 mm for north, east, and up.

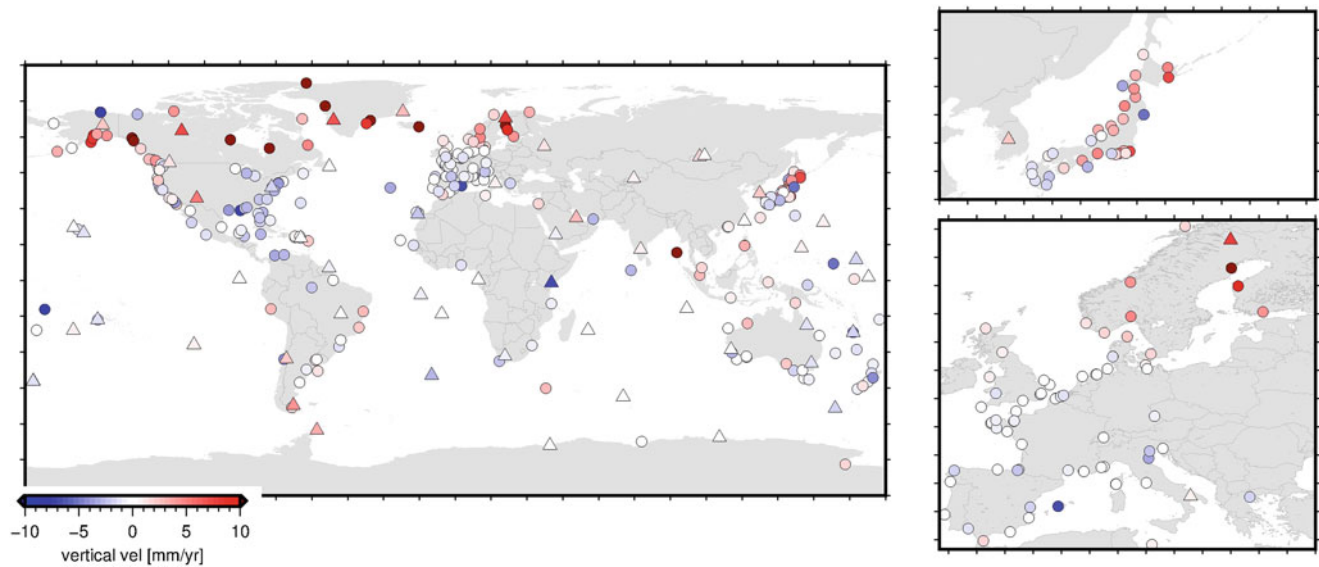


**Fig. 6** Vertical velocity rates for all datum (triangle) and freely estimated stations (circle), velocity rates determined for periods shorter than 2.5 yrs are not plotted. If velocity change were estimated the

velocity with the longest interval is given. Regions with dense stations networks are plotted additionally: Japan (*top, right*), Europe (*right, bottom*)

Figure 6 shows the vertical land motion rates estimated for the remaining 323 stations, i.e., after removing the nine stations with only short time series. Overall dedicated velocity patterns are visible. The formal errors are derived based on a white and power-law noise model. Driven by glacial isostatic adjustment (GIA) large uplift rates are visible for many stations above  $45^{\circ}\text{N}$ . In Fennoscandia associated uplift rates of up to  $8.2 \pm 0.4 \text{ mm yr}^{-1}$  (VAAS, Finland) and  $10.5 \pm 0.2 \text{ mm yr}^{-1}$  (SKE0, Sweden) are determined. For stations in Iceland and Greenland strong uplift is visible as well reaching for example  $12.9 \pm 0.4 \text{ mm yr}^{-1}$  (KSNB, East Greenland),  $15.0 \pm 0.4 \text{ mm yr}^{-1}$  (SRMP, West Greenland), and  $13.7 \pm 0.2 \text{ mm yr}^{-1}$  (HOFN, Iceland). Similar values were reported in dedicated studies by Bevis et al. (2019), Wake et al. (2016), Ludwigsen et al. (2020) and others. Especially, in Greenland the GIA-driven viscoelastic uplift is superimposed by a significant elastic response on the negative mass balance of the Greenland Ice Sheet since 1992 (IMBIE Team 2020). This is visible for the long time series of KELY (West Greenland) where we determine a subsidence of  $-1.6 \pm 0.8 \text{ mm yr}^{-1}$  before 2005 (in line with Dietrich et al. 2005) and a significant uplift of  $6.6 \pm 0.3 \text{ mm yr}^{-1}$  afterwards. A similar increase is found at KULU (East Greenland) where the uplift increased from  $3.7 \pm 0.6 \text{ mm yr}^{-1}$  to  $10.0 \pm 0.3 \text{ mm yr}^{-1}$  in 2005. While stations in Canada and Alaska are also subject to GIA overlaying effect dominate the vertical land motion locally. For example, stations DSL1 ( $-3.3 \pm 0.2 \text{ mm yr}^{-1}$ ) and PBOC ( $-7.3 \pm 0.3 \text{ mm yr}^{-1}$ ) located at Prudhoe Bay show strong subsidence related to local oil production (Ludwigsen et al. 2020). The region around the Kenai

Fjords with stations SELD ( $8.4 \pm 0.3 \text{ mm yr}^{-1}$ ) and AC67 ( $8.3 \pm 0.2 \text{ mm yr}^{-1}$ ) are subject to strong postseismic uplift caused by the Prince William Sound earthquake in 1964 (Huang et al. 2020). Strong uplift rates are present also for southeast Alaska (AB44 with  $16.6 \pm 0.4 \text{ mm yr}^{-1}$  and AB50 with  $17.5 \pm 0.4 \text{ mm yr}^{-1}$ ) caused by rapid viscoelastic relaxation following the retreat of Little Ice Age glaciers (Larsen et al. 2005). Significant subsidence rates occur along the US coastlines of the Atlantic Ocean and Gulf of Mexico related mostly to ground water depletion and sediment compaction (Karegar et al. 2015, 2016). Largest values are visible for the Mississippi delta (GRIS,  $-7.2 \pm 0.1 \text{ mm yr}^{-1}$ ) and the New York Bay area (SHK5,  $-3.6 \pm 0.2 \text{ mm yr}^{-1}$ ). For Japan plotted velocity rates indicate land uplift for the northern part including Honshu while stations at Kyushu and Shikoku show mostly subsidence. Interesting to note is also the significant uplift signal of  $24.3 \pm 0.4 \text{ mm yr}^{-1}$  for PBRI (Andaman islands) which is related to postseismic signal following the Sumatra earthquake 2004 (Paul et al. 2012).

To assess the derived vertical land motion, we computed the differences between our solution and the rates provided in the ALTIGAPS solution (Pfeffer and Allemand 2016) based on the ULR5 solution. Overall, no offset ( $0.04 \pm 0.1 \text{ mm yr}^{-1}$ ) could be detected, however, the RMS of all possible 137 differences reaches still  $1.7 \text{ mm yr}^{-1}$ . This is mostly caused by the different handling of velocity changes in the ALTIGAPS dataset. Compared to the newer ULR6a solution (Santamaría-Gómez et al. 2016) a difference of  $-0.1 \pm 0.1 \text{ mm yr}^{-1}$  (RMS  $1.7 \text{ mm yr}^{-1}$ ) was determined. For the previous GT2 solution (Deng et al. 2016) available

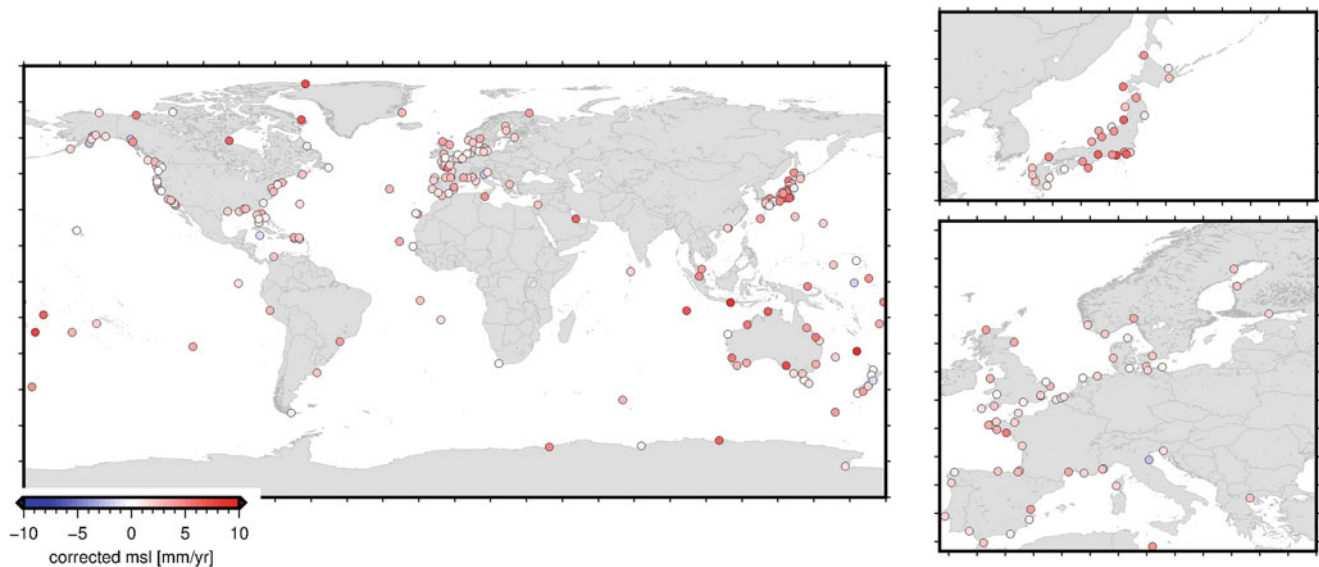


**Fig. 7** Mean sea level trend for all tide gauges corrected for the estimated vertical land motion. Regions with dense stations networks are plotted additionally: Japan (*top, right*), Europe (*right, bottom*)

at SONEL<sup>4</sup> we found an underestimation with respect to ALTIGAPS (mean difference  $-0.3 \pm 0.1 \text{ mm yr}^{-1}$ ) and ULR6a ( $-0.4 \pm 0.1 \text{ mm yr}^{-1}$ ).

#### 4 Tide Gauge Records

An assessment of the new TIGA repro3 solution on sea level estimates was performed based on selected tide gauges. Overall, a distance shorter than 10 m between the tide gauges and the GNSS stations was found for 62 stations, while distances of larger than 1 km were found for 140 stations. A largest distance allowed is 31 km for the tide gauge at Helsinki (Finland, PSMSL ID 14) and the IGS station at Metsahovi (METS) both located at a stable craton. Revised Local Reference (RLR) monthly data<sup>5</sup> provided by the Permanent Service for Mean Sea Level (PSMSL, Holgate et al. 2013) were used to derive the local sea level trends. In summary, 258 tide gauge records were available on PSMSL for the co-located tide gauges, with 241 records being in the RLR format (93%). For tide gauges without RLR data, metric data (i.e., records not adjusted to a local reference) were applied after a careful manual screening (17 records). After excluding 28 records where measurements ended before 1990, 230 records have been used in this investigation. Relative sea level changes were computed using a basic linear regression. A comparison between the derived sea

level trends and values reported by NOAA<sup>6</sup> reveals a good consistency with an average difference of  $0.1 \text{ mm yr}^{-1}$  and an RMS of  $0.8 \text{ mm yr}^{-1}$ . Overall 76 tide gauges available in both solutions were considered in this assessment. In general, strong relative sea level trends are visible especially for tide gauges in the Baltic Sea (around  $-7 \text{ mm yr}^{-1}$ ), along Alaska's Pacific coast (up to  $-18 \text{ mm yr}^{-1}$ ), at the Gulf of Mexico (up to  $+9 \text{ mm yr}^{-1}$ ).

After correcting the monthly tide gauge records for the GNSS-based vertical land motion the associated sea level changes were computed similar to the relative trends, i.e., by using a basic linear regression. While changes in the vertical land motion were considered as recommended by Klos et al. (2019) the GNSS-based velocities were extrapolated back in time for correcting the full tide gauge record. This strategy is discussed in more detail in Wöppelmann et al. (2007). In addition, for a few tide gauge records discontinuities had to be introduced. As pointed out by Rudenko et al. (2013) trend changes for January 1998 and 2009 had to be considered for the tide gauge at Churchill (Canada, PSMSL 447) to account for increase discharge into Hudson Bay. Related to groundwater removal a velocity change was set up for February 2003 for the tide gauge Hillarys (Australia, PSMSL 1761). For Aomori (PSMSL 1092) and Ogi (PSMSL 1344), both located in Japan, discontinuities related to the Tohoku earthquake (March 2011) were set up. Figure 7 shows the derived geocentric mean sea level trends for all considered tide gauges. For most of the tide gauges positive trends, i.e., increasing geocentric sea level can be noticed. The spatial

<sup>4</sup>[https://www.sonel.org/IMG/txt/vertical\\_velocities\\_table\\_gt2.txt](https://www.sonel.org/IMG/txt/vertical_velocities_table_gt2.txt).

<sup>5</sup>Records in RLR format are reduced to a local reference.

<sup>6</sup><https://tidesandcurrents.noaa.gov/sltrends/mslGlobalTrendsTable.html>, accessed August 19, 2021.



variability between the trends of individual stations in terms of RMS is  $2.0 \text{ mm yr}^{-1}$  (which is significantly smaller than for the relative sea level with a variability  $3.3 \text{ mm yr}^{-1}$ ). Negative trends at some stations are caused by local effects. For example at Porto Garibaldi a relative sea level trend of  $+1.0 \text{ mm yr}^{-1}$  is determined from the RLR data. However, after considering the local subsidence rate of  $-3.2 \text{ mm yr}^{-1}$  the geocentric sea level trend results to  $-2.2 \text{ mm yr}^{-1}$  which agrees to the finding of Meli et al. (2021).

Based on AVISO's multi-mission altimetric trend map (AVISO 2021) the derived tide gauge trends were compared to the closest grid point. Overall, a difference of  $-0.7 \text{ mm yr}^{-1}$  shows systematic smaller trends observed by the tide gauges which could be related to the different time periods as the altimetry covers only the time between 1993 and 2020. For this period AVISO reports a global trend of  $3.4 \text{ mm yr}^{-1}$  compared to  $2.3 \pm 0.1 \text{ mm yr}^{-1}$  averaged from the 230 tide gauges considered in this study. The global trend derived from tide gauges increases to  $3.0 \pm 0.2 \text{ mm yr}^{-1}$  if considering only data records between 1993 and 2020. Correspondingly, the difference to the AVISO map decreases to  $0.2 \pm 0.2 \text{ mm yr}^{-1}$ . The individual differences have an RMS of  $2.5 \text{ mm yr}^{-1}$  showing the discrepancy between local tide gauge observations and multi-mission altimetry. Comparing our solution with the previous GT2 solution (Deng et al. 2016), we found a comparable difference to AVISO of  $-0.6 \text{ mm yr}^{-1}$ , but with GT2 having a larger RMS of  $3.2 \text{ mm yr}^{-1}$ .

## 5 Summary and Conclusions

Estimating vertical land motion is important to transfer relative sea level measurements at tide gauges into geocentric sea level trends. With the IGS TIGA project vertical land motion patterns are determined based on co-located GNSS stations. In the framework of the third IGS reprocessing campaign we processed long-term observations for 341 GNSS stations globally distributed and mostly located at or close to tide gauges. Based on a network approach and subsequent time series analysis vertical velocities were estimated for 230 recently active tide gauges. The repeatabilities of the GNSS time series are 1–2 mm for the horizontal components and 4–5 mm for the vertical. After assessing the GNSS-based vertical land motion estimates they were used to compute geocentric sea level trends. Comparing the derived sea level trends to AVISO's multi-mission altimetric trend map reveals an overall difference of  $-0.7 \text{ mm yr}^{-1}$  ( $0.2 \text{ mm yr}^{-1}$  for tide gauge data to 1993–2020).

**Acknowledgements** The authors want to thank IGS, SONEL and PSMSL for making the GNSS data and the tide gauge records publicly available. We would also like to thank two anonymous reviewers for

their assistance in evaluating this paper and their helpful recommendations.

**Author Contributions** B.M. and T.S. defined the study. M. B. and B.M. prepared and processed the GNSS data including all relevant metadata. All authors contributed to the analysis, interpretation, and discussion of the results. B.M. prepared the manuscript with major contributions from T.S. and H.S. All authors read and approved the final manuscript.

**Data Availability Statement** All GNSS data are available at IGS and TIGA data centers, respectively. The tide gauge data records are available at PSMSL. The GFZ repro3 and TIGA products are available via Männel et al. (2021) and Männel et al. (2022), respectively.

## References

- AVISO (2021) Mean sea level rise. <https://www.aviso.altimetry.fr/en/data/products/ocean-indicators-products/mean-sea-level.html>, online; accessed 15-August-2021
- Bevis M, Harig C, Khan SA, Brown A, Simons FJ, Willis M, Fettweis X, van den Broeke MR, Madsen FB, Kendrick E, Caccamise DJ, van Dam T, Knudsen P, Nylen T (2019) Accelerating changes in ice mass within Greenland, and the ice sheet's sensitivity to atmospheric forcing. *Proc Natl Acad Sci* 116(6):1934–1939. <https://doi.org/10.1073/pnas.1806562116>
- Böhm J, Werl B, Schuh H (2006) Troposphere mapping functions for GPS and VLBI from European Centre for medium-range weather forecasts operational analysis data. *J Geophys Res* 111(B2):B02406. <https://doi.org/10.1029/2005JB003629>
- Bott LM, Schöne T, Illigner J, Haghshenas Haghghi M, Gisevius K, Braun B (2021) Land subsidence in Jakarta and Semarang Bay – The relationship between physical processes, risk perception, and household adaptation. *Ocean Coastal Manag* 211:105775. <https://doi.org/10.1016/j.ocecoaman.2021.105775>
- Bradke M (2020) SEMISYS - Sensor Meta Information System V. 4.1. GFZ data services <https://doi.org/10.5880/GFZ.1.1.2020.005>
- Church J, White N (2011) Sea-level rise from the late 19th to the early 21st century. *Surv Geophys* 32:585–602. <https://doi.org/10.1007/s10712-011-9119-1>
- Dach R, Lutz S, Walser P, Fridez P (2015) Bernese GNSS Software Version 5.2. Bern. <https://doi.org/10.7892/boris.72297>
- Deng Z, Gendt G, Schöne T (2016) Status of the IGS-TIGA tide gauge data reprocessing at GFZ. In: Rizos C, Willis P (eds) IAG 150 years. Springer International Publishing, pp 33–40. [https://doi.org/10.1007/1345\\_2015\\_156](https://doi.org/10.1007/1345_2015_156)
- Desai SD, Sibois AE (2016) Evaluating predicted diurnal and semidiurnal tidal variations in polar motion with gps-based observations. *J Geophys Res Solid Earth* 121(7):5237–5256. <https://doi.org/10.1002/2016JB013125>
- Dietrich R, Rülke A, Scheinert M (2005) Present-day vertical crustal deformations in West Greenland from repeated GPS observations. *Geophys J Int* 163:865–874. <https://doi.org/10.1111/j.1365-246X.2005.02766.x>
- Frederikse T, Landerer F, Caron L, Adhikari S, Parkes D, Humphrey VW, Dangendorf S, Hogarth P, Zanna L, Cheng L, Wu YH (2020) The causes of sea-level rise since 1900. *Nature* 584:393–397. <https://doi.org/10.1038/s41586-020-2591-3>
- Ge M, Gendt G, Dick G, Zhang FP, Reigber C (2005) Impact of GPS satellite antenna offsets on scale changes in global network solutions. *Geophys Res Lett* 32(6):L06310. <https://doi.org/10.1029/2004GL022224>
- Holgate SJ, Matthews A, Woodworth PL, Rickards LJ, Tamisieva ME, Bradshaw E, Foden PR, Gordon KM, Jevrejeva S, Pugh J (2013)

- New data systems and products at the permanent service for mean sea level. *J Coastal Res* 29(3):493–504. <https://doi.org/10.2112/JCOASTRES-D-12-00175.1>
- Huang K, Hu Y, Freymueller JT (2020) Decadal viscoelastic post-seismic deformation of the 1964 Mw9.2 Alaska earthquake. *J Geophys Res Solid Earth* 125(9):e2020JB019649. <https://doi.org/10.1029/2020JB019649>. e2020JB019649 2020JB019649
- IMBIE Team (2020) Mass balance of the Greenland Ice Sheet from 1992 to 2018. *Nature* 579:233–239. <https://doi.org/10.1038/s41586-019-1855-2>
- Johnston G, Riddell A, Hausler G (2017) The International GNSS service. Springer International Publishing, Cham, Switzerland, pp 967–982. <https://doi.org/10.1007/978-3-319-42928-1>
- Karegar MA, Dixon TH, Malservici R (2015) A three-dimensional surface velocity field for the Mississippi Delta: Implications for coastal restoration and flood potential. *Geology* 43(6):519–522. <https://doi.org/10.1130/G36598.1>
- Karegar MA, Dixon TH, Engelhart SE (2016) Subsidence along the Atlantic Coast of North America: Insights from GPS and late Holocene relative sea level data. *Geophys Res Lett* 43(7):3126–3133. <https://doi.org/10.1002/2016GL068015>
- Klos A, Kusche J, Fenoglio-Marc MS, Luciana Bos, Bogusz J (2019) Introducing a vertical land motion model for improving estimates of sea level rates derived from tide gauge records affected by earthquakes. *GPS Solut* 23(102). <https://doi.org/10.1007/s10291-019-0896-1>
- Kvas A, Mayer-Gürr T, Krauss S, Brockmann JM, Schubert T, Schuh WD, Pail R, Gruber T, Jäggi A, Meyer U (2019) The satellite-only gravity field model goco06s. <https://doi.org/10.5880/ICGEM.2019.002>. <http://dataservices.gfz-potsdam.de/icgem/showshort.php?id=escidoc:4081892>
- Larsen CF, Motyka RJ, Freymueller JT, Echelmeyer KA, Ivins ER (2005) Rapid viscoelastic uplift in southeast Alaska caused by post-Little Ice Age glacial retreat. *EPSL* 237(3):548–560. <https://doi.org/10.1016/j.epsl.2005.06.032>
- Ludwigsen CA, Khan SA, Andersen OB, Marzeion B (2020) Vertical land motion from present-day deglaciation in the wider Arctic. *Geophys Res Lett* 47(19). <https://doi.org/10.1029/2020GL088144>
- Lyard F, Lefevre F, Letellier T, Francis O (2006) Modelling the global ocean tides: modern insights from FES2004. *Ocean Dynamics* 56(5–6):394–415. <https://doi.org/10.1007/s10236-006-0086-x>
- Männel B, Dobsław H, Dill R, Glaser S, Balidakis K, Thomas M, Schuh H (2019) Correcting surface loading at the observation level: impact on global GNSS and VLBI station networks. *J Geod* 93:2003–2017. <https://doi.org/10.1007/s00190-019-01298-y>
- Männel B, Brandt A, Bradke M, Sakic P, Brack A, Nischan T (2020) Status of IGS reprocessing activities at GFZ. Springer Berlin Heidelberg, Berlin, Heidelberg, pp 1–7. [https://doi.org/10.1007/1345\\_2020\\_98](https://doi.org/10.1007/1345_2020_98)
- Männel B, Brandt A, Bradke M, Sakic P, Brack A, Nischan T (2021) GFZ repro3 product series for the International GNSS Service (IGS). GFZ data services. <https://doi.org/10.5880/GFZ.1.1.2021.001>
- Männel B, Schöne T, Bradke M (2022) GFZ reprocessing product series for the IGS Tide Gauge Benchmark Monitoring. GFZ data services. <https://doi.org/10.5880/GFZ.1.1.2022.001>
- Meli M, Olivieri M, Romagnoli C (2021) Sea-level change along the emilia-romagna coast from tide gauge and satellite altimetry. *Remote Sensing* 13(1). <https://doi.org/10.3390/rs13010097>
- Ostini C (2012) Analysis and Quality Assessment of GNSS-Derived Parameter Time Series. PhD thesis, Philosophisch-naturwissenschaftlichen Fakultät of the University of Bern
- Paul J, Rajendran CP, Lowry AR, Andrade V, Rajendran K (2012) Andaman postseismic deformation observations: Still slipping after all these years? *Bull Seismol Soc Am* 102(1):343–351. <https://doi.org/10.1785/0120110074>
- Petit G, Luzum B (2010) IERS Conventions (2010). IERS Technical Note 36. Verlag des Bundesamts für Kartographie und Geodäsie, Frankfurt am Main, ISBN 3-89888-989-6
- Pfeffer J, Allemann P (2016) The key role of vertical land motions in coastal sea level variations: A global synthesis of multisatellite altimetry, tide gauge data and gps measurements. *Earth Planet Sci Lett* 439:39–47. <https://doi.org/10.1016/j.epsl.2016.01.027>
- Ray R, Ponte R (2003) Barometric tides from ECMWF operational analyses. *Ann Geophys* 21(8):1897–1910
- Rebischung P (2021) Terrestrial frame solutions from the third igs reprocessing: the igs contribution to itrf2020. In: Tour de IGS. <https://www.igs.org/tour-de-igs-repro3/>
- Rudenko S, Thaller D, Gendt G, Dähnn M, Schöne T (2010) Reanalysis of GPS data at tide gauges and the combination for the IGS TIGA pilot project. Springer, Berlin, Heidelberg, pp 335–340. [https://doi.org/10.1007/978-3-642-10228-8\\_27](https://doi.org/10.1007/978-3-642-10228-8_27)
- Rudenko S, Schön N, Uhlemann M, Gendt G (2013) Reprocessed height time series for gps stations. *Solid Earth* 4(1):23–41. <https://doi.org/10.5194/se-4-23-2013>
- Santamaría-Gómez A, Gravelle M, Collilieux X, Guichard M, Miguez BM, Tiphaneau P, Wöppelmann G (2012) Mitigating the effects of vertical land motion in tide gauge records using a state-of-the-art GPS velocity field. *Global Planet Change* 98–99:6–17. <https://doi.org/10.1016/j.gloplacha.2012.07.007>
- Santamaría-Gómez A, Gravelle M, Wöppelmann G (2016) GPS solution ULR6. SONEL data center. [https://doi.org/10.26166/sonel\\_ulr6a](https://doi.org/10.26166/sonel_ulr6a)
- Schöne T, Schön N, Thaller D (2009) IGS tide gauge benchmark monitoring pilot project (TIGA): Scientific benefits. *J Geod* 83:249–261. <https://doi.org/10.1007/s00190-008-0269-y>
- Siriwardane-de Zoysa R, Schöne T, Herbeck J, Illigner J, Haghghi M, Simarmata H (2021) The ‘wickedness’ of governing land subsidence: Policy perspectives from urban Southeast Asia. *PLoS ONE* 16(6):e0250208. <https://doi.org/10.1371/journal.pone.0250208>
- Steigenberger P (2009) Reprocessing of a global GPS network. PhD thesis, Technische Universität München
- Wake LM, Lecavalier BS, Bevis M (2016) Glacial isostatic adjustment (GIA) in Greenland: A review. *Current Climate Change Rep* 2(3):101–111. <https://doi.org/10.1007/s40641-016-0040-z>
- Woodworth PL, Melet A, Marcos M, Ray RD, Wöppelmann G, Sasaki YN, Cirano M, Hibbert A, Huthnance JM, Monserrat S, Merrifield MA (2019) Forcing factors affecting sea level changes at the coast. *Surv Geophys* 40(6):1351–1397. <https://doi.org/10.1007/s10712-019-09531-1>
- Wöppelmann G, Marcos M (2016) Vertical land motion as a key to understanding sea level change and variability. *Rev Geophys* 54(1):64–92. <https://doi.org/10.1002/2015RG000502>
- Wöppelmann G, Martín Míguez B, Bouin MN, Altamimi Z (2007) Geocentric sea-level trend estimates from GPS analyses at relevant tide gauges world-wide. *Global Planet Change* 57(3):396–406. <https://doi.org/10.1016/j.gloplacha.2007.02.002>

**Open Access** This chapter is licensed under the terms of the Creative Commons Attribution 4.0 International License (<http://creativecommons.org/licenses/by/4.0/>), which permits use, sharing, adaptation, distribution and reproduction in any medium or format, as long as you give appropriate credit to the original author(s) and the source, provide a link to the Creative Commons license and indicate if changes were made.

The images or other third party material in this chapter are included in the chapter's Creative Commons license, unless indicated otherwise in a credit line to the material. If material is not included in the chapter's Creative Commons license and your intended use is not permitted by statutory regulation or exceeds the permitted use, you will need to obtain permission directly from the copyright holder.





# CyCLOPS: A National Integrated GNSS/InSAR Strategic Research Infrastructure for Monitoring Geohazards and Forming the Next Generation Datum of the Republic of Cyprus

Chris Danezis, Dimitris Kakoullis, Kyriaki Fotiou, Marina Pekri, Miltiadis Chatzinikos, Christopher Kotsakis, Ramon Brcic, Michael Eineder, Marios Nikolaidis, Georgios Ioannou, Andreas Christofe, Nicholas Kyriakides, George Melillos, Michalakis Christoforou, Marios Tzouvaras, Sylvana Pilidou, Kyriacos Themistocleous, and Diofantos Hadjimitsis

## Abstract

The objective of this paper is to introduce CyCLOPS, a novel strategic research infrastructure unit, and present its current progress of implementation, and integration in the National geodetic, geophysical and geotechnical infrastructure of the government-controlled areas of the Republic of Cyprus. CyCLOPS is co-funded by the European Regional Development Fund and the Republic of Cyprus through the Research and Innovation Foundation under the grant agreement RIF/INFRASTRUCTURES/1216/0050. CyCLOPS is developed via the collaboration of the Cyprus University of Technology (CUT) and the German Aerospace Center (DLR), and supported by the Cyprus Geological Survey Department and the Department of Lands and Surveys. The main objective of CyCLOPS is to establish an integrated infrastructure for space-based monitoring of geohazards using the most prominent earth observation technologies (EO), such as GNSS and InSAR. Furthermore, the infrastructure will densify and form the backbone for the definition of the next generation national datum of the Republic of Cyprus. Eleven Tier-1/2 state-of-the-art GNSS CORS, precise weather stations, tiltmeters and specifically designed InSAR triangular trihedral corner reflectors will be deployed, in a collocated fashion, at selected locations throughout the government-controlled areas of Cyprus. The collocated configuration will be established and installed to be compliant with the most stringent CORS monumentation specifications, support all current GNSS constellations and SAR missions. Finally, one of CyCLOPS' fundamental aims is to actively contribute to the on-going efforts and growing demand for more precise positioning services and high-quality modern reference frames, in conformity with the recommendations of the UN-GGIM (and its Subcommittee of Geodesy) to establish and enhance national geodetic infrastructures to support the sustainable management of geospatial information on the changing Earth.

## Keywords

Corner reflectors · CORS · Cyprus · GNSS · SAR

C. Danezis (✉) · D. Kakoullis · K. Fotiou · M. Pekri · M. Chatzinikos · M. Nikolaidis · G. Ioannou · A. Christofe · N. Kyriakides · G. Melillos · M. Christoforou · M. Tzouvaras · K. Themistocleous · D. Hadjimitsis

Cyprus University of Technology, Department of Civil Engineering and Geomatics, Limassol, Cyprus

ERATOSTHENES Centre of Excellence, Limassol, Cyprus  
e-mail: [chris.danezis@cut.ac.cy](mailto:chris.danezis@cut.ac.cy)

## 1 Introduction

Ground deformation may occur for natural or anthropogenic reasons and results in coordinate shifts that impact geodetic infrastructure. Tectonic plate motion is concerned primarily with horizontal surface movements, although local deformation may result in considerable vertical movements that impact the vertical datum (Fuhrmann et al. 2018).

Various approaches, such as space-based, airborne, terrestrial geodetic, and geotechnical techniques, can be used to analyze ground deformation and surface displacement in cases of landslides and ground subsidence. The assessment of landslide monitoring methods indicates that only space-based technologies (i.e., GPS/GNSS, InSAR) achieve high accuracy and precise 3D displacement determination with increased spatial resolution when used in an integrated approach (Kakoullis and Danezis 2020).

GNSS enable mm-level absolute accuracy deformation determination of a single point on the physical surface (Staudacher and Peltier 2016). On the other hand, InSAR provides mm- to cm- level relative accuracy deformation products (i.e. displacement and velocity), with respect to a reference point that is considered to be fixed, covering wide areas and not single points on the surface of the Earth (Balss et al. 2018; Zhao et al. 2019). Nevertheless, since the actual behavior of the reference point is unknown, the persistent scatterers' geolocation typically only reaches a sub-metre level of precision, frequently missing a connection to physical objects on the Earth's surface (Czikhardt et al. 2021).

InSAR calculates the rate of change in the slanted line of sight (LoS) of the satellite at regional level with spatial resolution up to 10 m. Due to the generally steep incidence angle of the SAR satellite sensor, the LoS is particularly sensitive to vertical land displacement; it also incorporates any displacement in the east-west direction as a result of the near-polar orbital plane of SAR satellites. GNSS is more sensitive to detecting horizontal displacements at both the east-west and north-south directions (Parker et al. 2017a) and estimates vertical land displacement in terms of ellipsoidal heights at discrete positions.

Precise deformation monitoring applications using SAR acquisitions require data calibration, which is divided to internal and external calibration. The internal calibration revolves the assessment of radar performance using internally generated calibrated signal sources, which may be derived from pre-flight tests (Freeman 1992). The external calibration uses ground targets of known backscatter coefficient (e.g. Corner Reflectors) to ensure an end-to-end SAR system calibration. External calibration aims to convert the pixel intensity of a feature in an image to a physical quantity such as the Radar Cross Section (RCS). This is achieved through the calculation of a calibration coefficient by the radiometric measurements obtained from Corner Reflectors (CRs). Evidently, when CRs collocate with a CORS, the calibration process will lead to more effective estimation of interferometric phases, and thus more reliable deformation products (Garthwaite et al. 2015).

InSAR deformation trends are two-dimensional, while GNSS provide displacement trends in 3D. However, a GNSS-estimated displacement refers to a single point on the physical surface, whereas InSAR offers deformation products of superior spatial resolution (Del Soldato et al. 2021). Hence, GNSS and InSAR can be combined and complement each other by designating a known deformation rate computed by means of GNSS to an InSAR 2D image pixel value and, therefore, assign both products to the same reference. Furthermore, InSAR can only measure surface deformation, whereas GNSS displacement trends are mainly estimated using monuments with very stringent stability specifications, anchored in stable geological background (e.g. bedrock) i.e., below the surface of the Earth.

Many governments and organizations have established space-based deformation monitoring systems, such as CORS networks. However, only a few organizations (e.g., AGOS) have established integrated CORS and CR arrays, which geospatial and geophysical institutions widely regard as the most effective approach of monitoring solid earth processes and natural hazards. The Cyprus Continuously Operating Natural Hazards Monitoring and Prevention System, abbreviated CyCLOPS, is developed in Cyprus from the CUT Laboratory of Geodesy in collaboration with German Aerospace Center (DLR) and is supported by the Cyprus Geological Survey Department, the Department of Lands and Surveys, the Ministry of Defence, the Electricity Authority of Cyprus, the Association of Rural and Surveying Engineers, and the European Plate Observing Systems (EPOS). It is noted that the infrastructure is co-funded by the European Union Regional Development Fund and the Republic of Cyprus via the national Research and Innovation Foundation.

CyCLOPS was established under a twofold perspective: (a) to become the first dedicated strategic research infras-

---

C. Kotsakis  
Cyprus University of Technology, Department of Civil Engineering  
and Geomatics, Limassol, Cyprus

Aristotle University of Thessaloniki, Faculty of Engineering, School of  
Rural and Surveying Engineering, Thessaloniki, Greece

R. Brcic · M. Eineder  
German Aerospace Center, SAR Signal Processing Department,  
Wessling, Germany

S. Pilidou  
Cyprus Geological Survey Department, Lefkosia, Cyprus

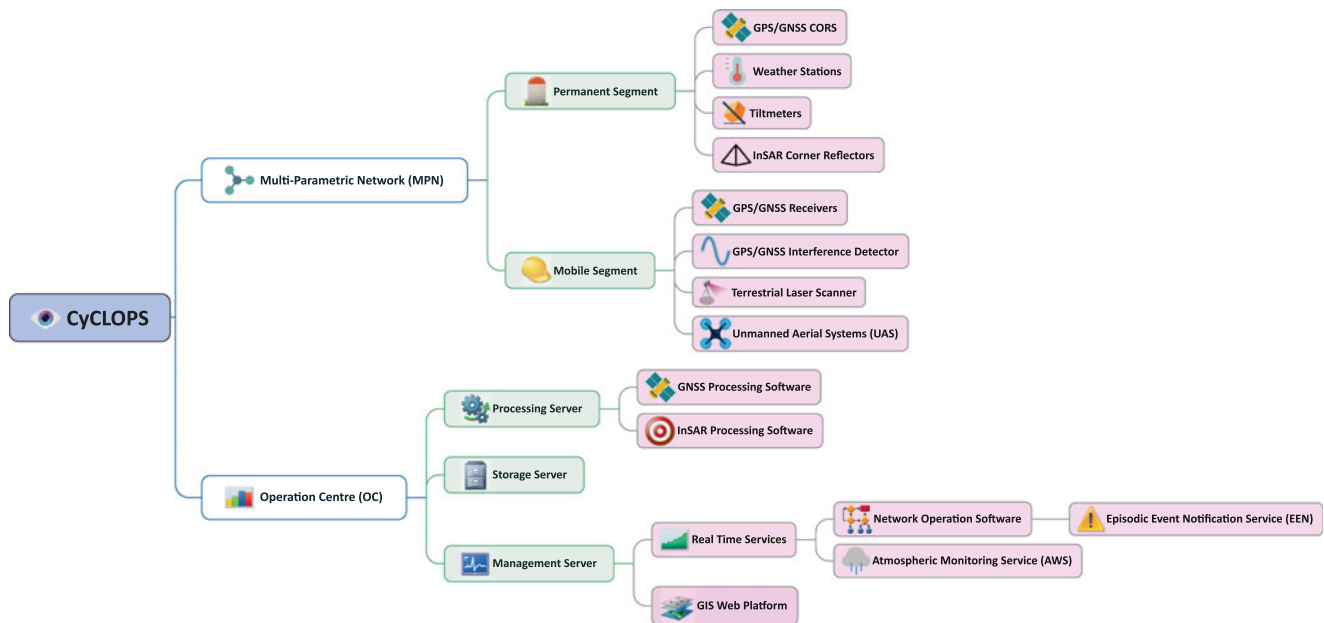


**Fig. 1** The components of CyCLOPS (Danezis et al. 2019)

structure for monitoring geohazards in Cyprus utilizing an integrated GNSS + InSAR approach, and (b) to form the backbone of the national geodetic infrastructure. Regarding the latter, its Tier-1/2 GNSS CORS will be the ones that will tie the new datum to the international and regional frames, yielding a new modern and kinematic national coordinate reference frame. Evidently, the utmost objective of this unit is to promote the recommendations of the UN-GGIM on the establishment and modernization of national geodetic infrastructures towards a changing Earth.

## 2 The Architecture of CyCLOPS

CyCLOPS comprises two components (Danezis et al. 2019), the architecture of which is illustrated in Fig. 1:

1. The multi-parametric network (MPN), which contains all the heterogeneous sensors, and
2. The Operations Centre (OC), which is responsible for managing, storing, and processing all the incoming information.

The MPN consists of the Permanent Segment (PS) and the Mobile Segment (MS). The PS includes permanent sites with a collocated configuration of one Tier-1/2 specifications GNSS CORS and two CRs in opposite facing configuration to account for both the ascending and descending passess of SAR satellite constellations per site. To date, a total number of six (6) permanent sites have been established throughout the government controlled areas of the Republic of Cyprus (see Fig. 2).

The MS is consisted of five (5) GNSS mobile stations deployed in areas of interest (AOI), which have already suffered the impact of natural and anthropogenic hazards.

### 2.1 The Permanent Segment (PS)

Among of the most apparent CORS applications is the monitoring of crustal motion, which necessitates a high level of accuracy and precision on a continuous basis. To reduce GNSS signal distortion and increase the quality of calculating positions, IGS, EPN, and UNAVCO have implemented strict instrumentation and monumentation requirements (IGS 2007; NGS 2018; EUREF Permanent GNSS Network Central Bureau 2022). The exact locations of the six (6) permanent sites were carefully chosen via a semi-automatic multi-criteria GIS-based methodology developed by the CUT Laboratory of Geodesy. Note that all sites were in close proximity with stations of the national seismological network to (a) ensure the existence of the required geological background (i.e. bedrock) and (b) augment the existing network of seismographs with GNSS and CRs and, hence, form supersites for monitoring solid earth processes.

#### 2.1.1 GNSS Station Monumentation

Two types were adopted for the monumentation of GNSS CORS; the shallow drilled braced monument type (SDBM) and a specifically designed stainless-steel truss, which provides sub-millimetric vibration at extreme environmental conditions. The SDBM is categorized by UNAVCO as one of the two monument types (along with the deep drilled

**Fig. 2** Site Locations of the Permanent Segment. Green triangles indicate the reference stations (Kakoullis et al. 2022)

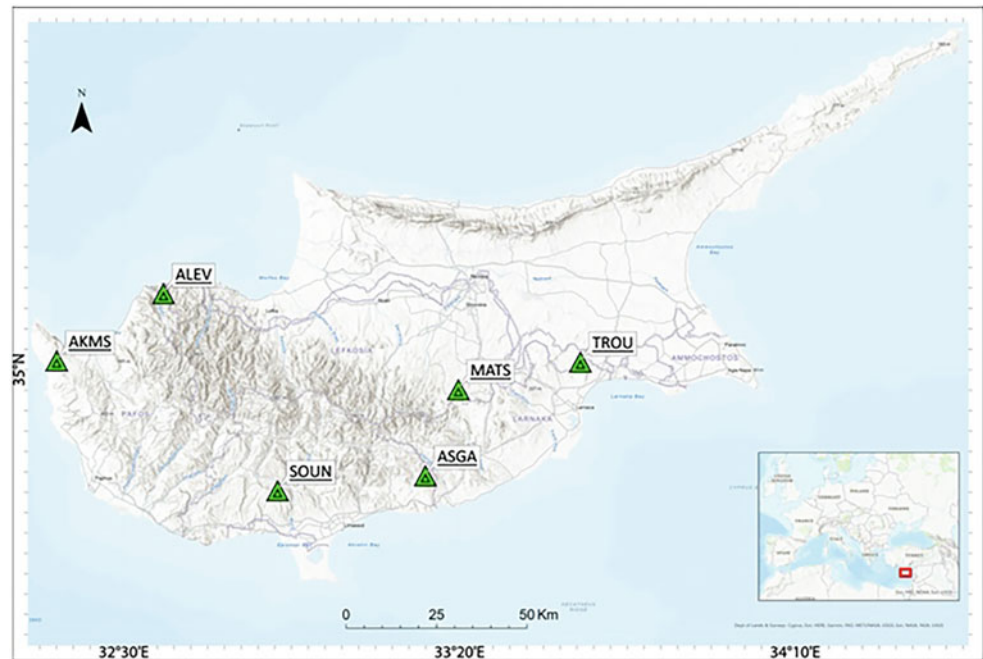


**Fig. 3** The shallow drilled braced monument type used in the CyCLOPS PS

braced monument type for looser soils) with the highest degree of stability compared to traditional approaches (e.g. concrete pillars). In our case the SDBM (UNAVCO 2010) was implemented using four solid stainless-steel rods (304) to form a quadpod (see Fig. 3). Each rod was anchored at a drilling depth of 2 m using one of the highest-quality epoxy resins currently available in the market. The SDBM monument type was chosen at locations where bedrock lies on the surface or at depths up to 0.5 m below, taking all precautions to mitigate thermal effects. Towards this direction, all rods have been electrostatically painted using special paint for stainless-steel structures.

In cases where solid bedrock was located at a greater depth (1 m), a different approach was chosen; a reinforced concrete foundation was installed between the monument and the bedrock. First, the foundation was anchored on the bedrock. Consequently, a specifically designed 3 m-tall metallic truss was anchored in the foundation (see Fig. 4). Again, all parts of the metallic truss were made of stainless-steel (304), and they were also coated with electrostatic paint. The structural design of the truss enables sub-millimetric vibration at extreme wind conditions, such as wind speeds of 140 km/h.

In all cases, GNSS antennas were mounted on SCIGN mounts, which represent the highest standard for the installation of GNSS antennas on permanent monumentation (UNAVCO 2014).

It is noted that the GNSS CORS infrastructure is hosted in secured sites in government-controlled areas of Cyprus. In all cases, appropriate fencing is installed to prevent unauthorized access to the equipment and minimize station disturbance upon installation.

### 2.1.2 CR Monumentation

Apart from the GNSS CORS, each site of the permanent segment features two (2) corner reflectors. Specifically, our six sites were equipped with two triangular trihedral CRs, with a side length of 1.5 m, in an opposite-facing configuration for ascending and descending mode, respectively. The CRs were sought to be located in areas of low backscatter coefficient ( $\sigma_0$  – *sigma nought*), at a distance greater than 30 m away from the GNSS antenna, with no



**Fig. 4** The stainless steel truss monument type specifically designed for the stability requirements of the CyCLOPS permanent segment

inter-visibility to mitigate unwanted multipath effects in GNSS observations (Parker et al. 2017b).

The base of each CR was positioned on top of a thin layer of reinforced concrete, which was founded over bedrock. The CR anchoring was carried out using three tall anchors to ensure bedrock penetration and their fastening was done using the same quality epoxy resin as in the case of GNSS CORS monumentation. Furthermore, appropriate wood fencing was installed to minimize CR disturbance from animals (see Fig. 5).

### 2.1.3 MPN Instrumentation

As shown in Table 1, each station of the MPN includes state-of-the-art geodetic-grade GNSS antennas and receivers, collocated with precise meteorological instrumentation (weather station) and very sensitive tiltmeters. The configuration is powered by solar panels, gel batteries and charging balancers to provide sufficient power supply, even during periods of sunlight absence, and enable seamless operation of all sensors.



**Fig. 5** The installation of a permanent CR

**Table 1** Instrumentation of the CyCLOPS MPN

Equipment	Model
GNSS Antenna:	Trimble <sup>®</sup> GNSS-Ti v2 Choke ring (individually calibrated by Geo++)
GNSS Receiver:	Trimble <sup>®</sup> Alloy GNSS receiver
Weather Station:	VAISALA PTU307
Tiltmeter:	Jewell D711-A-S

The GNSS receiver model that powers both the PS and MS is the Trimble<sup>®</sup> Alloy. The latter supports high-rate signal tracking, at 100 Hz to monitor high-frequency ground motion signals and support real-time formats for observable output (i.e., CMR, CMRPlus, CMR X, GAGAN, RTX, RTCM 2.x, RTCM 3.x SDCM). Moreover, the specific receiver features an on-board absolute precise point positioning (PPP) capability, which can estimate its absolute position with centimeter-level accuracy in real-time (Trimble 2020).

The GNSS antenna, which powers both the PS and the MS is the Trimble GNSS Ti-v2 choke ring geodetic grade antenna. The latter includes elements with very stable phase centers and appropriate technology to achieve effective multipath rejection, ensure seamless data acquisition, and enable displacement monitoring at the millimeter-level. The antenna is protected by a suitable radome, which covers both the element and the ground plane. The radome used in both the PS and the MS antennas is the SCIGN short radome type. Note that each antenna has been individually calibrated by Geo++ (supporting all GNSS) for the most accurate determination of its phase center and to be aligned with the IGS specifications for Tier-1 permanent stations (IGS 2015). Similarly to the Alloy receiver, the antenna design is future-proof by supporting all available and planned GNSS signals (Trimble 2017).

The weather station used in CyCLOPS is the Vaisala PTU307 integrated transmitter, which can record temperature with an accuracy of  $\pm 0.2$  °C, barometric pressure at an accuracy of  $\pm 0.10$  hPa, and relative humidity with accuracy  $\pm 1\%$ . Furthermore, all sensor probes are housed in a specifically designed solar radiation shield to minimize temperature effects on pressure measurements. The specific configuration is the apparent choice for outdoor and demand-



ing environments. Note that all sensors are fully compliant with the EPN guideline (EUREF Permanent GNSS Network Central Bureau 2022; Vaisala 2019). The position of the meteorological station with respect to the GNSS antenna has been determined using precise digital leveling. Finally, the weather station is connected to the station's communication infrastructure to relay information to the OC at regular intervals. In total, eleven (11) weather station unit support CyCLOPS.

The great sensitivity of electronic tiltmeters enables the detection of micro-displacements that would otherwise be undetected by other monitoring sensors, such as GNSS or InSAR. In any case, tiltmeters should be an integral component of a geodetic monitoring system because of their low cost and great sensitivity (Battaglia et al. 2021). Each CyCLOPS site is augmented by one (1) high-precision tiltmeter (Jewell D711-A-S), which has been clamped on the center pole of the monumentation to record even the smallest tilt deflection and check the stability of the reference station monumentation. Again, the tiltmeter is connected to the station's communication infrastructure to transmit information to the OC for further processing.

The station telemetry is established via appropriate wireless communication infrastructure of high bandwidth (Air2Fiber) to transmit sensor information to the OC in real-time.

The receivers, loggers and routers are housed in a specifically designed highly-durable IP65 enclosure made of stainless steel 1.4301 (ANSI 304) to withstand extreme weather conditions (both heat and cold). The enclosure design is intended to support both permanent and mobile configurations. The internal design features an integrated air ventilation system comprised of fans, temperature sensors and air holes to maintain internal temperature at low levels, especially during summer.

The power supply of the entire configuration is based on a solar power integrated solution. This was deemed necessary since most sites are located in remote areas without the possibility of direct AC power supply. Thus, the enclosure supports a solar panel and accommodates six large 110 Ah GEL batteries to enable at least 5 days of power supply in the absence of sunlight. The solar panels are mounted on the enclosure via removable level arms and offer 360 W/24 V capable of charging the aforementioned batteries (see Fig. 6). Furthermore, the power supply system is empowered by a power telemetry system and a charging balancer to prolong battery life. The energy telemetry system offers real-time information on solar panel performance and can provide on-time notifications in case of panel malfunction or theft. Moreover, the system enables a remote power-down capability to deal with potential equipment reboot issues, avoid unnecessary on-site presence of technical personnel, especially in cases of remote sites.



**Fig. 6** The integrated enclosure—solar panel configuration used in CyCLOPS permanent and mobile stations



**Fig. 7** The triangular trihedral Corner Reflector (CR) type deployed at the CyCLOPS permanent sites

#### 2.1.4 Corner Reflectors

The triangular trihedral corner reflectors that were installed in the PS were constructed in collaboration with the German Aerospace Center (DLR) in order to be used in monitoring and calibration operations. The design of the CRs offers orientation flexibility of  $0^{\circ}$ – $360^{\circ}$  in azimuth and  $-10^{\circ}$  to  $45^{\circ}$  in terms of elevation. Consequently, they support every available space-based SAR constellation from Sentinel-1 to CosmoSkymed and TerraSAR-X. The CRs are made of high-grade aluminum coated with special paint to maximize radar backscatter (see Fig. 7). Furthermore, each plane has been precisely levelled with a tolerance of less than  $\pm 2$  mm, which has been verified with laser tracker measurements to enable maximum phase center stability.

Note that each CR was levelled and oriented using a Brunton<sup>®</sup> Axis Transit precise compass ( $\pm 0.5^{\circ}$ ) to achieve the highest degree of visibility and radar cross-section (RCS)

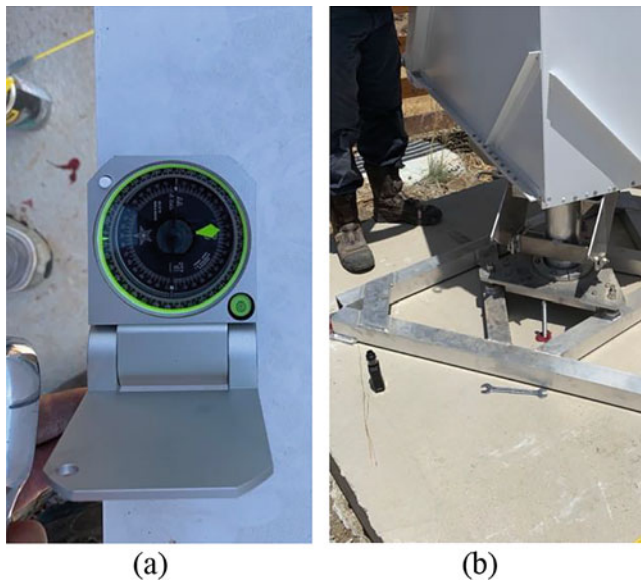


**Fig. 8** (a) The levelling and orientation of CRs and (b) the anchoring of the CR permanent marker i.e., its reference point

values from SAR satellites according to pass direction (ascending or descending). The CRs are currently oriented towards Sentinel-1 satellites. Furthermore, at each CR, a permanent marker, also anchored into bedrock, was established for the precise determination of the position of its reference point and the estimation of local ties thereafter (see Fig. 8). Special attention was given so that the marker enables the conduct of terrestrial geodetic measurements using high accuracy prisms.

### 2.1.5 Collocation of GNSS and Corner Reflectors

The collocation of GNSS antennas and CRs promotes SAR performance by providing it with useful geodynamic and atmospheric corrections and enables the application of additional techniques in monitoring and calibration activities.

The collocation GNSS and InSAR CRs is mandatory to perform an accurate datum connection. Hence, installing artificial persistent scatterers—such as corner reflectors—next to the GNSS antennas and calculating the persistent scatterers' phase center ensures that the relative displacement is negligible (Mahapatra et al. 2017).

CRs can be identified in image pixels and are mostly used as permanent ground control points for InSAR, with phase and amplitude stability, in the time domain (Ferretti et al. 2001; Fotiou and Danezis 2020). Therefore, the CRs can be used as benchmarks in the frame of a geodetic network based on the geodetic datum's dynamic behavior (Garthwaite 2017).

As mentioned earlier, in the case of CyCLOPS, two CRs were installed per PS site. The collocation was carried out



**Fig. 9** The collocation of a GNSS CORS and a corner reflector (descending mode) in the ALEV site

taking into account various parameters affecting both SAR and GNSS, such as sky visibility, GNSS/CR line of sight, the value of backscattering coefficient ( $\sigma_0$ ), terrain slope, aspect and many more. All these parameters were processed in the framework of a semi-automated multi-criteria GIS-based methodology to derive the most suitable and efficient locations for both GNSS antennas and CRs. An example of the collocation can be seen in Fig. 9.

## 2.2 The Mobile Segment (MS)

The MS monumentation is designed with utmost objective to be easily deployed in areas of interest (AoI). Consequently, the GNSS antenna is mounted on a specifically designed stainless circular hollow section (CHS) pole, which is anchored into the ground (see Fig. 10). The pole is mounted vertically and bolted with six screw-pins, which are installed in drilled holes and epoxied to a depth up to 20 cm. This design enables quick levelling of the pole, similarly to a tribrach approach. The pole's diameter is 15 cm and its height is 2 m. Additionally, two inlets have been fabricated on the CHS; one at the upper level and the other at the bottom. These inlets allow the pole to be internally filled with oil, which minimizes thermal expansion effects. Furthermore, the pole features a custom base for the accommodation of the digital tiltmeter, which monitors the stability of the mobile configuration. Finally, at the top of the pole, a specific hydraulic bolt has been welded to enable the installation of the SCIGN mount and, hence, the GNSS antenna.

In all cases, cables are protected via a pliable conduit ideal for outdoor exposed installations due to its resistance to UV radiation, extreme weather conditions and rodents resistance. Note, that the same type of conduit is used in every exposed cable for all sensors of the MPN. The design of the mobile stations has been carried out and fine-tuned in collaboration with JGC Geinformation Systems SA. Furthermore, each MS station is equipped with the same weather station and tiltmeter as in the case of the PS sites.

Apart from the GNSS mobile stations, the MS is augmented by a tactical-grade Unmanned Airborne System

**Fig. 10** The mobile segment of CyCLOPS



(UAS), the SenseFly eBee X RTK, for mapping large areas, and derive precise digital terrain models, which are used in various phases of the processing chain. Finally, the MS includes a precise laser scanner, the Leica C10, to precisely model areas of interest.

### 2.3 The Operation Center (OC)

The operation center (OC) is comprised of the necessary IT infrastructure to achieve increased computing performance, adequate storage and system redundancy (availability). Therefore, a virtualized and highly compartmentalized IT architecture was chosen. The basic system includes two identical physical machines (hosts), which offer in total 768 GB of RAM and 128-vcors. The hosts are connected to a Storage Area Network (SAN), with dual RAID controllers for system redundancy. Furthermore, the OC features a secondary backup layer i.e., a Network Attached Storage (NAS) device with redundant power supply to enable storage redundancy via enterprise-grade backup software. The IT infrastructure is installed in a dedicated cabinet at the Cyprus University of Technology Data Center (Fig. 11).

The overall system is highly compartmentalized and designed with utmost objective the uninterrupted operation of all modules without internal interference

or interdependence. Therefore, each operation (module) is assigned to dedicated virtual machines (VMs) or dockers. The software that handles the operation of the GNSS stations, the storage of the incoming information (GNSS, meteo and tiltmeter observations) is Trimble® Pivot Platform (TPP). Through TPP, CyCLOPS provides single-base and network RTK services, and will augment and improve the accuracy and reliability of the national GNSS infrastructure.

The OC features a dedicated atmospheric monitoring service, which provides temporal information on critical measures, such as the Integrated Precipitable Water Vapor (IPWV) and Total Electron Content (TEC), the I95 index and the predicted ionospheric and geometric errors (see Fig. 12).

GNSS post-processing operations are carried out in a separate VM, where AIUB Bernese GNSS and NASA's GipsyX coexist to handle various scenarios, such as network adjustment and estimation of deformation products. Similarly, SAR, UAV, LAS processing and GIS operations are assigned to separate VMs. Finally, the OC features a GIS web server to visualize and disseminate services regarding the deformation results, and hazards risk maps along with a in-house developed crowdsourcing app focused on disaster risk reduction. All elements, communicate with a database server, which stores and populates the processing results and the relevant geospatial information.

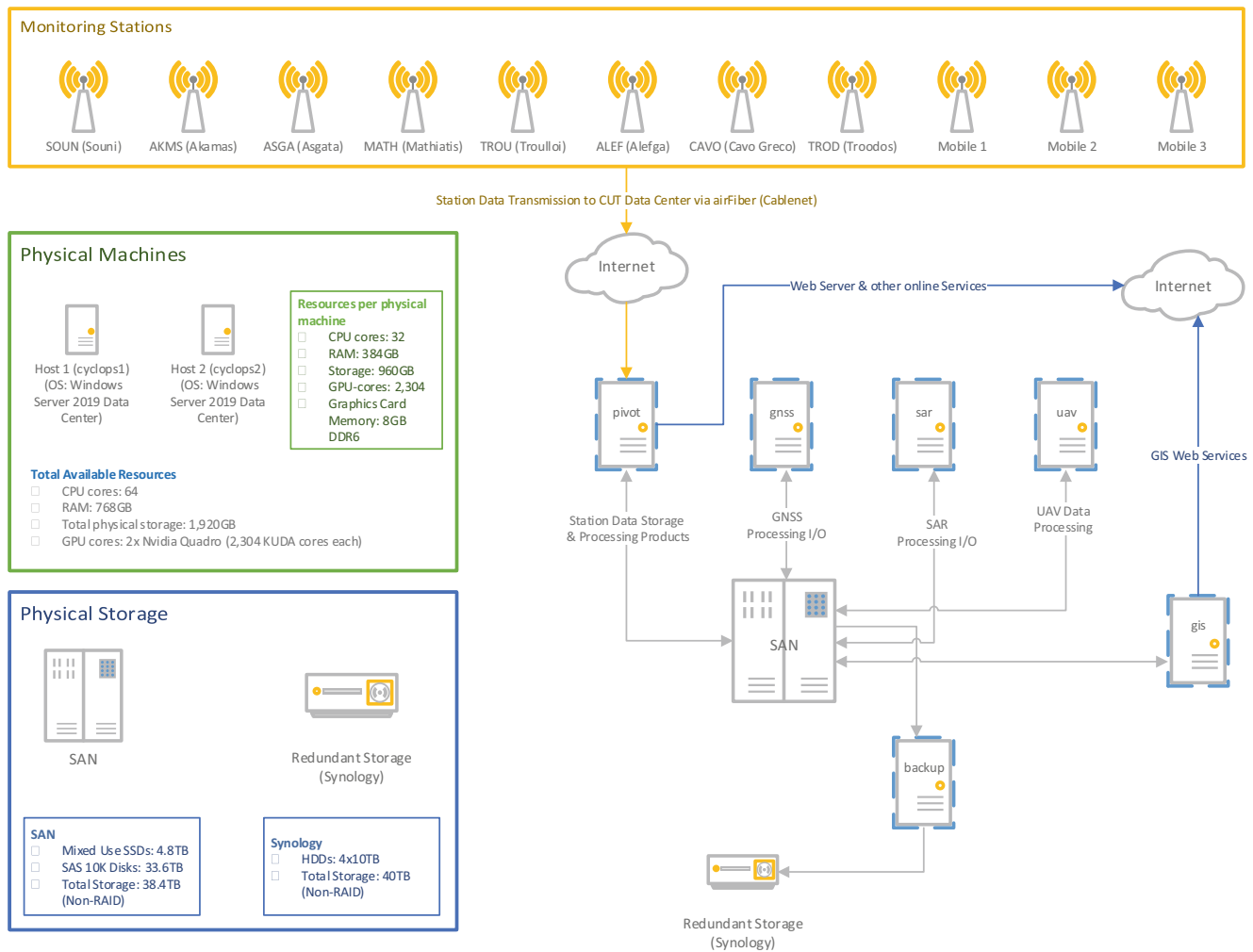


**Fig. 11** The diagram of the OC’s internal architecture

### 3 Initial Processing Results

The preanalysis and initial processing of the CyCLOPS CORS were carried out along with 19 GNSS reference stations from the EUREF Permanent GNSS Network (EUREF Permanent GNSS Network Central Bureau 2022). Note that most of these stations also belong to the International GNSS Service network (Dow et al. 2009). The double-difference strategy (e.g. (Hofmann-Wellenhof et al. 2012; Teunissen and Kleusberg 2012) was then applied for the daily GNSS data processing via the Bernese GNSS software 5.2 (Dach et al. 2015). The processing strategy was performed following the EUREF guidelines (Legrand et al. 2021) and running a modified version of the RNX2SNX script. Details of the GNSS processing options are given in Table 2.

Some preliminary results on the precision of the daily solutions are presented for a time span of 18 days (15/09/2021–02/10/2021), firstly, via the RMS of the Helmert transformation residuals applied between the estimated stations coordinates and those provided by the IGB14 solution (see Fig. 13) and, secondly, with the help of the a-posteriori variance factor obtained by each daily network adjustment (see Fig. 14).

Some preliminary results regarding the preprocessing of the GNSS stations are shown with the help of boxplots in Figs. 15 and 16. The RMS of the Single Point Positioning (SPP) solution for each CyCLOPS CORS is illustrated in Fig. 15, whilst in Fig. 16 the number of tracked satellites (GPS + GLN) per day for the same stations is presented. These indicators were estimated from the same time span of data (15/09/2021–02/10/2021).

**Fig. 12** A snapshot of the CyCLOPS' dedicated atmospheric service (Date: 07.05.2021 – 10:00)

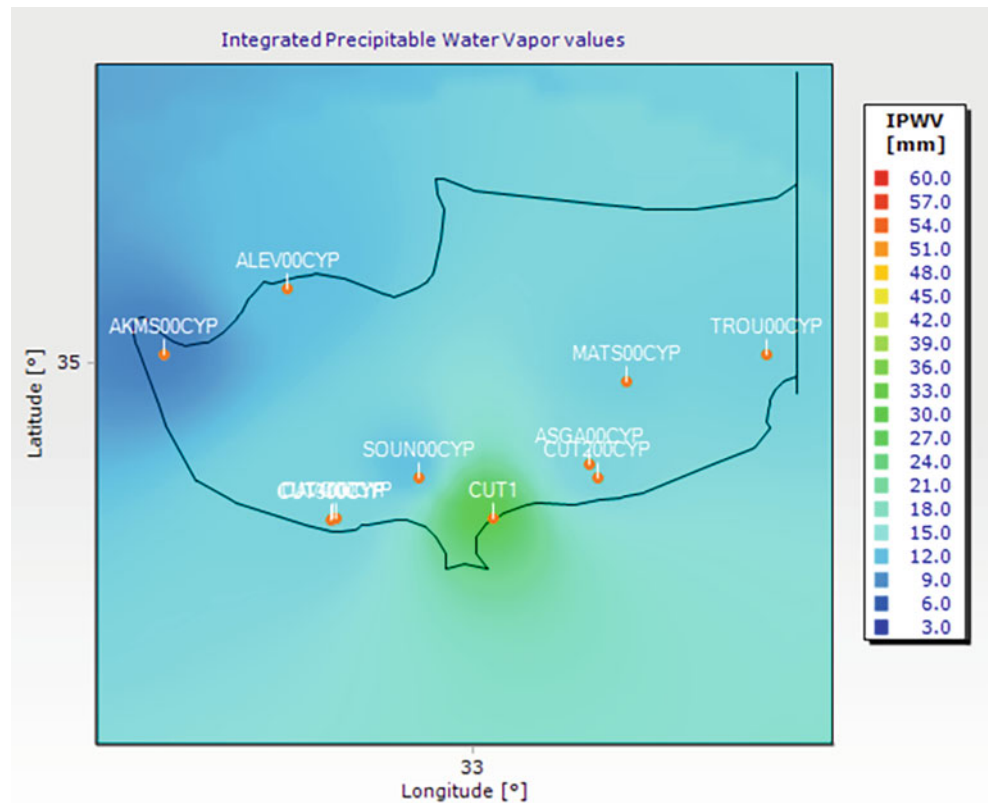


**Table 2** GNSS Data Processing options

Basic observable	GNSS carrier phase. Code only for receiver clock sync and ambiguity resolution. Melbourne-Wubbenawidelane method.
Elevation cut-off angle	3 deg., elevation-dependent weighting (cosz).
Data sampling	30 s and 180 s in final solution.
Modeled observable	Ionosphere-free linear combination of double-difference carrier phase.
Ground/satellite APC calibration	Absolute antenna phase Centre corrections (igs14.atx).
Tidal displacements	IERS 2010 conventions (solid earth tides).FES 2004 (ocean loading corrections).No atmospheric loading corrections.
Satellite/receiver clock	Satellite clock biases eliminated by double-differences.Receiver clock corrections estimated in pre-processing using code observations.
Orbits and ERPs	IGS final GPS/GLONASS orbits & ERPs.
Ionosphere	First-order ionosphere delays eliminated by forming ionosphere-free L1/L2 linear combination.Higher-order ionosphere corrections are applied.Regional ionosphere maps were used to increase the number of resolved ambiguities in the QIF, L5/L3 and L1/L2 ambiguity resolution.
Ambiguity resolution	Ambiguities are resolved in baseline-by-baseline mode:Melbourne-Wubbenawidelane approach (< 6,000 km)Quasi-ionosphere-free (QIF) approach (<2,000 km)Phase-based widelane/narrowlane method (<200 km)Direct L1/L2 method, also for GLONASS (<20 km)GLONASS is considered for ambiguity resolution (<2,000 km).
Troposphere	Dry GMF (prior model), estimation of hourly zenith delay corrections for each station using wet GMF.Horizontal gradient parameter estimated/day/station (Chen-Herring).
Reference frame	IGb14, no-net translation conditions on ref. station coordinates (IGb14.snx)

**Fig. 13** The a-posteriori variance factor of the daily GNSS network adjustments

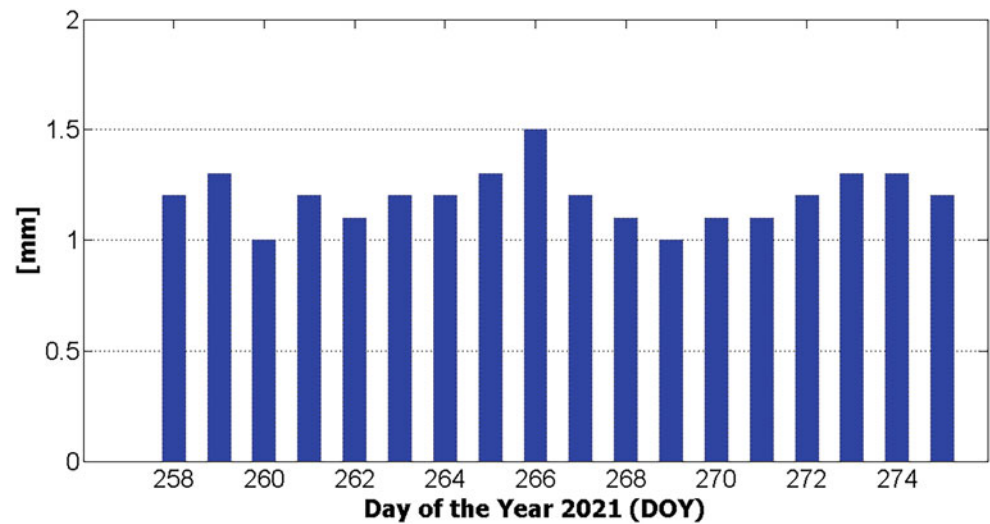
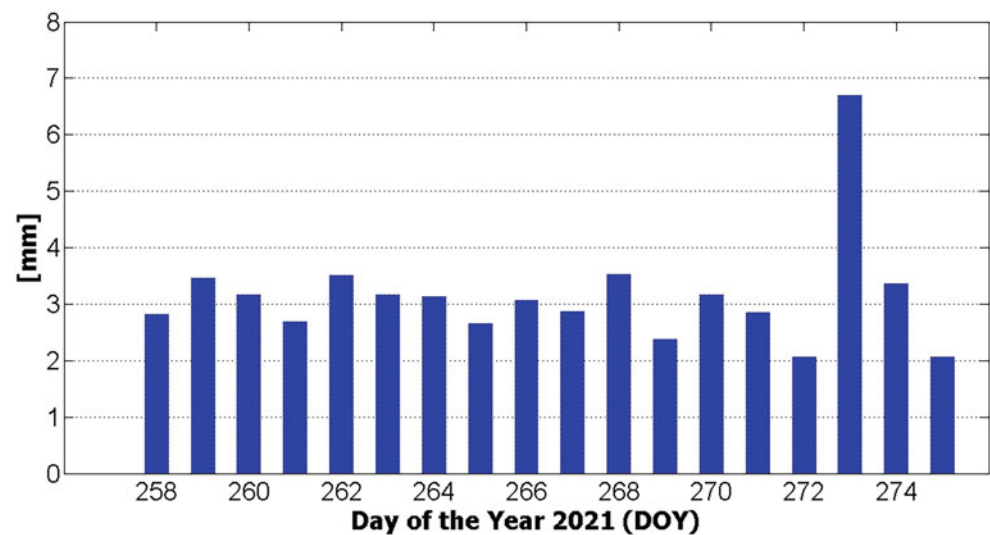


**Fig. 14** RMS of the Helmert transformation residuals between the estimated coordinates of the network and those derived from the IGB14 solution



## 4 Summary

This paper summarizes the current status in the implementation of CyCLOPS, a national strategic research infrastructure unit established by the Cyprus University of Technology department of Civil Engineering and Geomatics. CyCLOPS is the first strategic infrastructure in the region, which combines permanent GNSS stations with SAR Corner Reflectors with a national coverage. All GNSS permanent stations have been installed and instrumented by embracing

requirements for Tier-1/2 stations as set by IGS, UNAVCO and EPN. The corner reflectors have been designed and installed based on equally strict criteria in collaboration with the German Aerospace Center (DLR). Finally, the unit is powered by an IT infrastructure that handles processing of the incoming information and dissemination of the results via suitable web services. CyCLOPS will augment the national geodetic infrastructure by providing accurate and reliable positioning services and form the backbone for the next generation datum of the Republic of Cyprus.

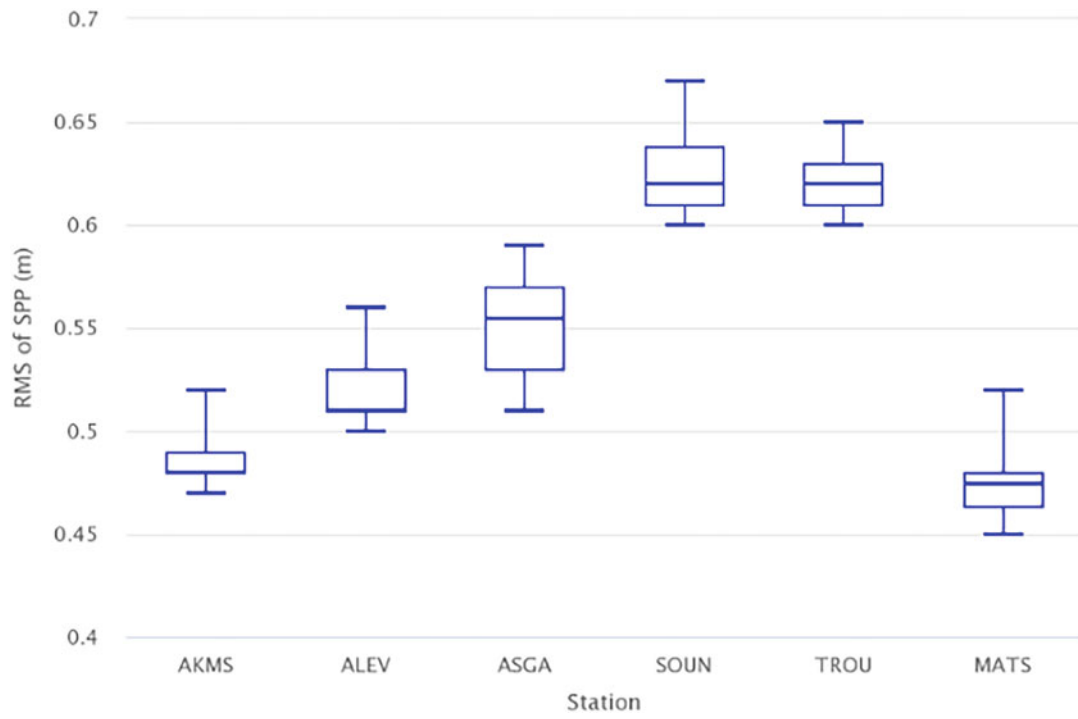
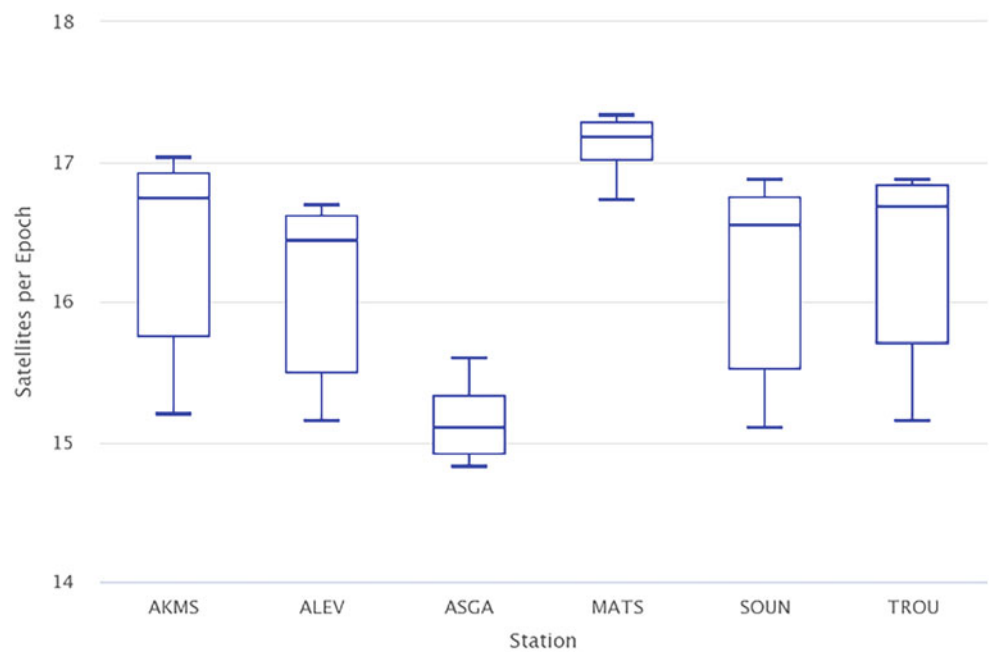


**Fig. 15** RMS of the Single Point Positioning solutions

**Fig. 16** Number of tracked satellites (GPS + GLN) per day



**Acknowledgements** The CyCLOPS project (INFRASTRUCTURES/1216/0050) is co-funded by the European Union Regional Development Fund and the Republic of Cyprus through the Research and Innovation Foundation (RIF).

## References

- Balls U, Gisinger C, Eineder M (2018) Measurements on the absolute 2-D and 3-D localization accuracy of TerraSAR-X. *Remote Sens* 10(4):656. <https://doi.org/10.3390/rs10040656>
- Battaglia M et al (2021) Monitoring volcanic deformation. In: Alderton D, Elias SA (eds) *Encyclopedia of geology*, 2nd edn. Academic, Oxford, pp 774–804. <https://doi.org/10.1016/B978-0-08-102908-4.00132-6>
- Czikhardt R, van der Marel H, Papco J (2021) GECORIS: an open-source toolbox for analyzing time series of corner reflectors in InSAR geodesy. *Remote Sens* 13(5):926. <https://doi.org/10.3390/rs13050926>
- Dach R et al (2015) Bernese GNSS software version 5.2. University of Bern, Bern Open Publishing. Available at: <http://boris.unibe.ch/72297/1/DOCU52.pdf>. Accessed: 31 Mar 2017
- Danezis C et al (2019) CyCLOPS: A Novel Strategic Research Infrastructure Unit for Continuous Integrated Spaced-based Monitoring of Geohazards. In: *Monitoring of geohazards*. 4th Joint International Symposium on Deformation Monitoring (JISDM), 15–17 May 2019. JISDM, Athens, Greece, p 9
- Del Soldato M et al (2021) Review of works combining GNSS and InSAR in Europe. *Remote Sens* 13(9):1684. <https://doi.org/10.3390/rs13091684>
- Dow JM, Neilan RE, Rizos C (2009) The international GNSS service in a changing landscape of global navigation satellite systems. *J Geod* 83(3):191–198
- EUREF Permanent GNSS Network Central Bureau (2022) Guidelines for EPN Stations and Operational Centres. <https://doi.org/10.24414/ROB-EUREF-GUIDELINES-STATION>
- Ferretti A, Prati C, Rocca F (2001) Permanent scatterers in SAR interferometry. *IEEE Trans Geosci Remote Sens* 39(1):8–20. <https://doi.org/10.1109/36.898661>
- Fotiou K, Danezis C (2020) An overview of electronic corner reflectors and their use in ground deformation monitoring applications. In: *Eighth international conference on remote sensing and geoinformation of the environment (RSCy2020)*. Eighth international conference on remote sensing and geoinformation of the environment (RSCy2020). SPIE, pp 216–224. <https://doi.org/10.1117/12.2571886>
- Freeman A (1992) SAR calibration: an overview. *IEEE Trans Geosci Remote Sens* 30(6):1107–1121. <https://doi.org/10.1109/36.193786>
- Fuhrmann T et al (2018) Combination of GNSS and InSAR for Future Australian Datums. In: *Proceedings of the International Global Navigation Satellite Systems Association IGSS Symposium*. IGSS 2018, Colombo Theatres, Kensington Campus, UNSW, pp 1–13
- Garthwaite MC (2017) On the design of radar corner reflectors for deformation monitoring in multi-frequency InSAR. *Remote Sens* 9(7):648. <https://doi.org/10.3390/rs9070648>
- Garthwaite MC et al (2015) The Design of Radar Corner Reflectors for the Australian geophysical observing system: a single design suitable for InSAR deformation monitoring and SAR calibration at multiple microwave frequency bands. *Geoscience Australia*, Canberra, Australia. <https://doi.org/10.11636/Record.2015.003>
- Hofmann-Wellenhof B, Lichtenegger H, Collins J (2012) *Global positioning system: theory and practice*. Springer Science & Business Media
- IGS (2007) *IGS Site Guidelines*. Infrastructure Committee, Central Bureau, Pasadena, p 15. Available at: <https://kb.igs.org/hc/en-us/articles/201142366-IGS-FAQ-May-2007>. Accessed 28 Jan 2020
- IGS (2015) *IGS site guidelines*. Infrastructure Committee, Central Bureau, Pasadena. Available at: <https://igs.org/documents/guidelines>. Accessed 31 Jan 2020
- Kakoullis D, Danezis C (2020) Permanent infrastructures for continuous space-based monitoring of natural hazards. In: *Eighth International Conference on Remote Sensing and Geoinformation of the Environment (RSCy2020)*. Eighth International Conference on Remote Sensing and Geoinformation of the Environment (RSCy2020). International Society for Optics and Photonics, Paphos, Cyprus, p 115241F. <https://doi.org/10.1117/12.2571201>
- Kakoullis D et al (2022) Considerations and multi-criteria decision analysis for the installation of collocated permanent GNSS and SAR infrastructures for continuous space-based monitoring of natural hazards. *Remote Sens* 14(4):1020. <https://doi.org/10.3390/rs14041020>
- Legrand J et al (2021) Guidelines for EUREF Densifications. EPN [Preprint]. <https://doi.org/10.24414/ROB-EUREF-Guidelines-DENS>
- Mahapatra P et al (2017) InSAR datum connection using GNSS-augmented radar transponders. *J Geod* 92:21–32. <https://doi.org/10.1007/s00190-017-1041-y>
- NGS (2018) *Guidelines for new and existing continuously operating reference stations (CORS)*. NOAA, Silver Spring, p 21. Available at: [https://www.ngs.noaa.gov/PUBS\\_LIB/CORS\\_guidelines.pdf](https://www.ngs.noaa.gov/PUBS_LIB/CORS_guidelines.pdf). Accessed: 28 Jan 2020
- Parker AL et al (2017a) Practical considerations before installing ground-based geodetic infrastructure for integrated InSAR and cGNSS monitoring of vertical land motion. *Sensors* 17(8):1753. <https://doi.org/10.3390/s17081753>
- Parker AL et al (2017b) Practical considerations before installing ground-based geodetic infrastructure for integrated InSAR and cGNSS monitoring of vertical land motion. *Sensors (Basel, Switzerland)* 17(8). <https://doi.org/10.3390/s17081753>
- Staudacher T, Peltier A (2016) Ground deformation at piton de la Fournaise, a review from 20 years of GNSS monitoring. In: Bachelery P et al (eds) *Active volcanoes of the Southwest Indian Ocean: piton de la Fournaise and Karthala*. Springer (Active Volcanoes of the World), Berlin, Heidelberg, pp 251–269. [https://doi.org/10.1007/978-3-642-31395-0\\_15](https://doi.org/10.1007/978-3-642-31395-0_15)
- Teunissen PJG, Kleusberg A (2012) *GPS for geodesy*. Springer Science & Business Media
- Trimble (2017) *Trimble GNSS Geodetic Antennas*. Trimble. Available at: [https://trl.trimble.com/docushare/dsweb/Get/Document-410894/022543-429G\\_Antenna\\_BRO\\_USL\\_0817\\_LR.pdf](https://trl.trimble.com/docushare/dsweb/Get/Document-410894/022543-429G_Antenna_BRO_USL_0817_LR.pdf)
- Trimble (2020) *Trimble Alloy GNSS Reference Receiver User Guide*. Trimble. Available at: [https://trl.trimble.com/docushare/dsweb/Get/Document-880342/Alloy\\_User\\_guide.pdf](https://trl.trimble.com/docushare/dsweb/Get/Document-880342/Alloy_User_guide.pdf)
- UNAVCO (2010) *Shallow Drilled Braced Monument*. Available at: <https://kb.unavco.org/kb/article.php?id=301>. Accessed 27 Nov 2019
- UNAVCO (2014) *GNSS Antenna Mounts*. Available at: <https://kb.unavco.org/kb/article.php?id=394>. Accessed 16 Nov 2021
- Vaisala (2019) *Vaisala Combined Pressure, Humidity, and Temperature Transmitter PTU300*. Vaisala. Available at: <https://www.vaisala.com/sites/default/files/documents/PTU300-Users-Guide-in-English-M210796EN-J.pdf>
- Zhao Q et al (2019) Generation of long-term InSAR ground displacement time-series through a novel multi-sensor data merging technique: the case study of the Shanghai coastal area. *ISPRS J Photogramm Remote Sens* 154:10–27. <https://doi.org/10.1016/j.isprsjprs.2019.05.005>



**Open Access** This chapter is licensed under the terms of the Creative Commons Attribution 4.0 International License (<http://creativecommons.org/licenses/by/4.0/>), which permits use, sharing, adaptation, distribution and reproduction in any medium or format, as long as you give appropriate credit to the original author(s) and the source, provide a link to the Creative Commons license and indicate if changes were made.

The images or other third party material in this chapter are included in the chapter's Creative Commons license, unless indicated otherwise in a credit line to the material. If material is not included in the chapter's Creative Commons license and your intended use is not permitted by statutory regulation or exceeds the permitted use, you will need to obtain permission directly from the copyright holder.



---

**Part VI**

**GNSS Positioning**



# Dilution of Precision (DOP) Factors for Evaluating Observations to Galileo Satellites with VLBI

Helene Wolf, Johannes Böhm, Matthias Schartner, Urs Hugentobler, Benedikt Soja, and Axel Nothnagel

## Abstract

Installing a VLBI transmitter on Galileo satellites will allow observing satellites in parallel to quasars with Very Long Baseline Interferometry (VLBI) telescopes. This offers a variety of new applications such as the direct determination of the absolute orientation of the satellite constellation with respect to the International Celestial Reference Frame (ICRF) and the improvement of the Terrestrial Reference Frame (TRF) exploiting the possibilities of direct high precision tying of the different space geodetic equipment. In preparation of these observations by enhancing the capabilities of the VLBI scheduling program VieSched++, we perform an evaluation study of observations of a Galileo satellite employing Dilution of Precision (DOP) factors. The idea is to introduce DOP factors in the decision process of VieSched++ after a thorough assessment of DOP factors for individual parameters. In our study, we choose an existing network of VLBI Global Observing System (VGOS) type telescopes for observing Galileo satellite GSAT0212 within a 24 h arbitrary session. Preparing the DOP factor analysis, we first carry out a theoretical study to investigate the VLBI sensitivity to satellite orbit displacements in the local orbital frame with normal (radial), tangential and cross-track direction. This analysis shows that the highest sensitivity of a satellite observation is that of the tangential component if the direction of the satellite track is parallel to the direction of the observing baseline. A satellite observation is most sensitive towards the cross-track component if these two directions are orthogonal to each other. The DOP factor analysis itself is performed separating the satellite position again into its three components and adding a separate DOP factor for the UT1-UTC (dUT1) parameter. The periods, where satellite observations are possible, were determined using VieSched++. At a later stage, these DOP factors will be used as an optimization criterion for the scheduling process. The DOP factors of potential observations from the chosen VGOS network to GSAT0212 reach minimum DOP values of 27.13 in normal, 1.49 in tangential, and 1.67 in cross-track direction and 0.45 for determining dUT1. With these results, which have confirmed intuitive considerations on the relative magnitudes, we have laid the groundwork for using DOP factors as driving criteria in the scheduling process of Galileo satellites embedded in regular VLBI observations of quasars.

The original version of this chapter was revised. Missing double vertical lines for  $L_2$  in Eq. 2 had been added. A correction to this chapter can be found at [https://doi.org/10.1007/1345\\_2022\\_187](https://doi.org/10.1007/1345_2022_187).

H. Wolf (✉) · J. Böhm · A. Nothnagel  
Department of Geodesy and Geoinformation, TU Wien, Wien, Austria  
e-mail: [helene.wolf@tuwien.ac.at](mailto:helene.wolf@tuwien.ac.at)

M. Schartner · B. Soja  
Institute of Geodesy and Photogrammetry, ETH Zürich, Zürich,  
Switzerland

U. Hugentobler  
Institute for Astronomical and Physical Geodesy, TU München,  
München, Germany

© The Author(s) 2022

J. T. Freymueller, L. Sánchez (eds.), *Geodesy for a Sustainable Earth*,  
International Association of Geodesy Symposia 154, [https://doi.org/10.1007/1345\\_2022\\_165](https://doi.org/10.1007/1345_2022_165)

### Keywords

Dilution of Precision (DOP) factors · Galileo · VGOS · VieSched++ · VLBI

## 1 Introduction

Very Long Baseline Interferometry (VLBI) is a space geodetic technique which is contributing in the determination of the International Terrestrial Reference Frame (ITRF) (Altamimi et al. 2016) and is determining the International Celestial Reference Frame (ICRF; Charlot et al. 2020) and is uniquely able to provide the full set of Earth Orientation Parameters (EOP; Petit and Luzum 2010) by observing very distant radio sources. The mounting of a VLBI transmitter on board of Galileo satellites would allow to observe both, quasars and satellites, with VLBI telescopes in parallel (Fig. 1). This will bring new opportunities for improvements in the above products along with some challenges in the overall realization. To observe geodetic satellites with radio telescopes employed for routine geodetic VLBI observations, it is necessary that the satellites transmit signals that mimic the emission of quasars and other compact extra-galactic radio sources. This raises questions about technical aspects of generating and emitting an artificial signal on Galileo satellites for VLBI observations and the successful observation and correlation, as already discussed in McCallum et al. (2016) and Jaradat et al. (2021).

Observations to satellites with VLBI antennas bring a variety of new opportunities as they enable the connection of the satellite positions with the celestial reference frame. This allows the determination of the absolute orientation of the satellite constellation with respect to the ICRF and the comparison of the satellite's position with the position obtained by using other space geodetic techniques.

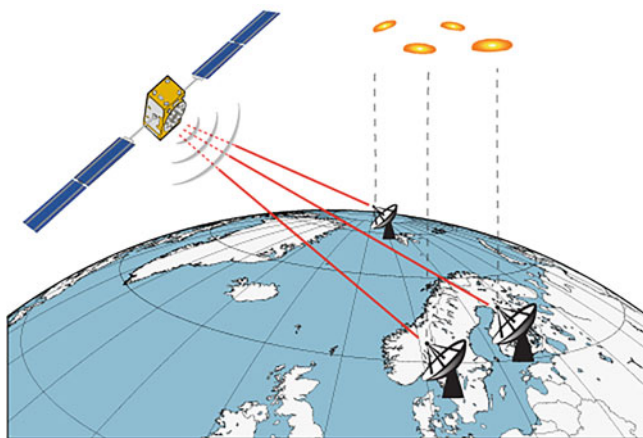


**Fig. 1** Illustration of observations to satellites and quasars with VLBI telescopes

Connecting the geodetic techniques on satellites via space-ties enables an improved determination of the Terrestrial Reference Frame (ITRF), provided the tie vectors on the satellites are measured and known with utmost accuracy.

So far only few experiments have been conducted tracking a satellite with VLBI by either directly observing Global Navigation Satellite System (GNSS) signals (Plank et al. 2017; Tornatore et al. 2014) or signals of a dedicated VLBI transmitter (Hellerschmied et al. 2018; Hellerschmied 2018). However, several simulation studies were carried out with regard to satellite tracking for the realization of inter-technique frame ties (Plank 2013; Plank et al. 2016) and for incorporating and improving co-location in space (Anderson et al. 2018; Herrera Pinzn and Rothacher 2020). The already existing laser reflector arrays on Galileo satellites allow the observation of the satellites with Satellite Laser Ranging (SLR). Therefore, Galileo satellites integrate both GNSS and SLR techniques, which formed the basis for different studies on the combination of these observations (Thaller et al. 2011), using the satellite co-locations for determining precise Galileo orbits (Bury et al. 2021a) and realizing the geodetic datum (Bury et al. 2021b).

Further, combining VLBI observations of quasars and satellites in parallel allows Precise Orbit Determination (POD) of these Earth satellites for which the feasibility and potential of geodetic VLBI was examined before (Kłopotek et al. 2020; Mammadaliyev et al. 2021). In the course of a new project at TU Wien called VLBI2Galileo funded by the Austrian Science Fund (FWF), VLBI observations to Galileo satellites will be investigated in detail. The objectives of the project are the optimisation of the satellite scheduling process using Dilution of Precision (DOP) factors (Swanson 1978) as well as the implementation of orbit estimation from VLBI observations in the Vienna VLBI and Satellite Software (VieVS; Böhm et al. 2018).

## 2 Satellite Scheduling in VieSched++

Recently, the scheduling software VieSched++ (Schartner and Böhm 2019) has been extended by a satellite scheduling module (Wolf 2021) which allows the inclusion of satellite observations in a schedule among observations to quasars in a manual or automatic fashion. Depending on the satellite orbit and the chosen VLBI network, different observation periods are available during which a satellite is visible from more than two stations. Theoretically, potential observing times during these periods could be evaluated using DOP

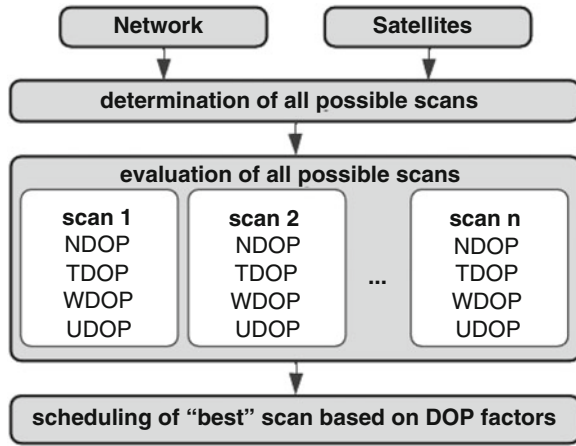


**Fig. 2** Flowchart of using different DOP factors, i.e. normal DOP (NDOP), tangential DOP (TDOP), cross-track DOP (WDOP) and UT1-UTC DOP (UDOP), as weight factors during the scheduling of satellite scans

factors indicating the sensitivity of the VLBI observation towards specific parameters. In future this could be realized in VieSched++ by providing the values of the DOP factors to the scheduler as indicators and support in deciding which scan to schedule in case the satellite scans are scheduled manually. If the satellite scans are scheduled automatically, the DOP factors represent an opportunity to be used as an optimization criterion during the scheduling process of a satellite scan. A possible implementation would be to determine all possible scans to the selected satellites from a chosen network and further evaluate those by the different DOP factors in order to finally select and schedule the best possible scan based on these indicators (Fig. 2).

### 3 Dilution of Precision Factors

Dilution of Precision factors indicate the change of the observable by a change of a specific parameter and therefore represent the sensitivity of the VLBI observation towards this parameter. The UT1-UTC Dilution of Precision (UDOP) factor is introduced by Belli (2020) and indicates the sensitivity of VLBI observations to satellites to UT1-UTC (dUT1). For the purpose of evaluating a satellite observation in the scheduling process with regard to its sensitivity to the position of the satellite, we introduce three further DOP factors. In the following, these DOP factors depicting the sensitivity of an observation towards the components of the satellite position in the local orbital frame with normal (N), tangential (T), and cross-track (W) direction (NTW-frame) are described. This orbital frame is aligned with the unit vectors

$$\mathbf{e}_N = \mathbf{e}_T \times \mathbf{e}_W, \quad \mathbf{e}_T = \frac{\dot{\mathbf{r}}}{\|\dot{\mathbf{r}}\|}, \quad \mathbf{e}_W = \frac{\mathbf{r} \times \dot{\mathbf{r}}}{\|\mathbf{r} \times \dot{\mathbf{r}}\|}, \quad (1)$$

which are defined by the Earth Centered Inertial (ECI) position  $\mathbf{r}$  and velocity  $\dot{\mathbf{r}}$  vectors of the satellite. The unit vector  $\mathbf{e}_T$  is along the orbital velocity vector (tangential),  $\mathbf{e}_W$  along the orbital angular momentum vector (cross-track) and  $\mathbf{e}_N$  is completing the right handed system.

The DOP factors correspond to the partial derivatives of a simplified model of an observation equation of the time delay in the Geocentric Celestial Reference System (GCRS; see Hellerschmied (2018) and the formalism described by Klioner (1991)) with respect to the satellite position in the GCRS which are formulated as

$$\begin{pmatrix} \frac{\partial \Delta\tau}{\partial x} \\ \frac{\partial \Delta\tau}{\partial y} \\ \frac{\partial \Delta\tau}{\partial z} \end{pmatrix} = \frac{1}{c} \left[ \frac{\mathbf{L}_2}{\|\mathbf{L}_2\|} - \frac{\mathbf{L}_1}{\|\mathbf{L}_1\|} \right] - \frac{1}{c^2} \left[ \dot{\omega}_2 - \frac{\mathbf{L}_1}{\|\mathbf{L}_1\| \|\mathbf{L}_2\|} (\mathbf{L}_2 \cdot \dot{\omega}_2) \right. \\ \left. + \|\mathbf{L}_1\| \frac{\mathbf{L}_2}{\|\mathbf{L}_2\|^3} (\mathbf{L}_2 \cdot \dot{\omega}_2) - \frac{\|\mathbf{L}_1\|}{\|\mathbf{L}_2\|} \dot{\omega}_2 \right], \quad (2)$$

where  $c$  denotes the speed of light,  $\mathbf{L}_1$  and  $\mathbf{L}_2$  the GCRS vectors between the satellite and the first and second VLBI station and  $\dot{\omega}_2$  represents the GCRS velocity vector of the second station. The scaling factor  $(1 - L_G)$ , where  $L_G = 6.969290134 \times 10^{-10}$  is a defining constant (Petit and Luzum 2010), to transform the time delay from the Geocentric Coordinate Time (TCG) to the Terrestrial Time (TT) was neglected due to its rather small influence. Further, these partial derivatives are multiplied with the speed of light in order to transform their unit from time per length to dimensionless and a subsequent rotation into the orbit fixed satellite system (NTW-frame) is applied.

The partial derivatives of the time delay with respect to the satellite position in the orbital frame are determined for each baseline and represent the entries in the Jacobian matrix  $A$ . In this approach the matrix  $A$  is formed for each component separately, as it is shown for the normal component in Eq. 3.

The normal equation matrix  $N$  is calculated with  $A^T P A$ , where  $A^T$  denotes the transposed Jacobian matrix and  $P$  the weight matrix, which is in this work assumed as the unit matrix (Eq. 4). The cofactor matrix  $Q_{xx}$  is the inverse of  $N$ . Finally, the NDOP factor is calculated from the square root of  $Q_{xx}$  (Eq. 6) and therefore indicates the uncertainty in the normal component based on the geometrical configuration.

The approach outlined for the determination of the NDOP (Eqs. 3–5) is also applied to calculate the TDOP (Eq. 7) and WDOP (Eq. 8) using the partial derivatives of the time delay with respect to the tangential and cross-track component. The UDOP factor is determined in the same way as the other DOP factors but taking the sensitivity of the different VLBI satellite observations towards UT1-UTC into account. The mathematical derivation on how to determine the sensitivity towards UT1-UTC and further the UDOP can be found in Belli (2020).

These DOP factors represent the orbital error in the respective component per VLBI measurement error, both in units of length. For example, the normal DOP refers to the normal orbital error.

$$A = \begin{pmatrix} \frac{\delta \Delta \tau_1}{\delta n} \\ \frac{\delta \Delta \tau_2}{\delta n} \\ \vdots \\ \frac{\delta \Delta \tau_n}{\delta n} \end{pmatrix} \quad (3)$$

$$N = A^T P A = \begin{pmatrix} \frac{\delta \Delta \tau_1}{\delta n} & \frac{\delta \Delta \tau_2}{\delta n} & \dots & \frac{\delta \Delta \tau_n}{\delta n} \end{pmatrix} \cdot \begin{pmatrix} \frac{\delta \Delta \tau_1}{\delta n} \\ \frac{\delta \Delta \tau_2}{\delta n} \\ \vdots \\ \frac{\delta \Delta \tau_n}{\delta n} \end{pmatrix} = \quad (4)$$

$$\left( \frac{\delta \Delta \tau_1}{\delta n} \right)^2 + \left( \frac{\delta \Delta \tau_2}{\delta n} \right)^2 + \dots + \left( \frac{\delta \Delta \tau_n}{\delta n} \right)^2 \quad (5)$$

$$Q_{xx} = N^{-1} = \frac{1}{\left( \frac{\delta \Delta \tau_1}{\delta n} \right)^2 + \left( \frac{\delta \Delta \tau_2}{\delta n} \right)^2 + \dots + \left( \frac{\delta \Delta \tau_n}{\delta n} \right)^2} \quad (5)$$

$$NDOP = \sqrt{\frac{1}{\left( \frac{\delta \Delta \tau_1}{\delta n} \right)^2 + \left( \frac{\delta \Delta \tau_2}{\delta n} \right)^2 + \dots + \left( \frac{\delta \Delta \tau_n}{\delta n} \right)^2}} \quad (6)$$

$$TDOP = \sqrt{\frac{1}{\left( \frac{\delta \Delta \tau_1}{\delta t} \right)^2 + \left( \frac{\delta \Delta \tau_2}{\delta t} \right)^2 + \dots + \left( \frac{\delta \Delta \tau_n}{\delta t} \right)^2}} \quad (7)$$

$$WDOP = \sqrt{\frac{1}{\left( \frac{\delta \Delta \tau_1}{\delta w} \right)^2 + \left( \frac{\delta \Delta \tau_2}{\delta w} \right)^2 + \dots + \left( \frac{\delta \Delta \tau_n}{\delta w} \right)^2}} \quad (8)$$

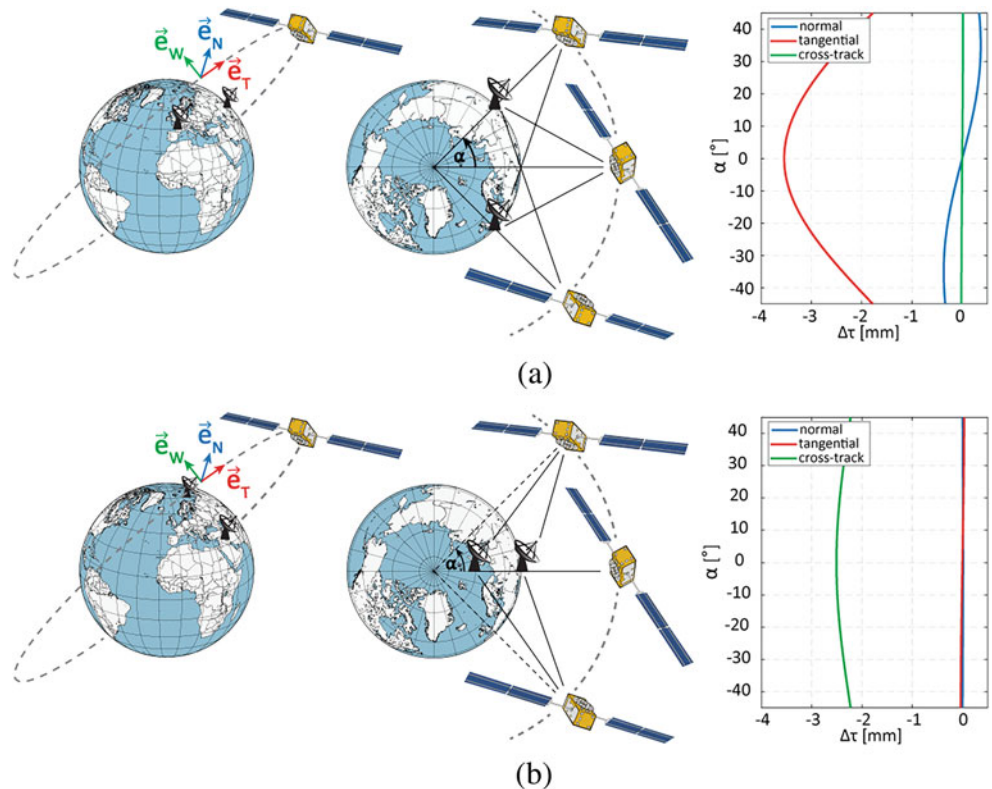
The smaller the value of the respective DOP, the higher the sensitivity of the observation towards the corresponding component and the better the geometric configuration of the satellite position with respect to the observing stations for determining this component.

#### 4 Sensitivity of Satellite Observations

Different geometric constellations of satellites with respect to baselines produce different impacts of the VLBI observations on the satellite position parameters. To prepare for the DOP investigations (Sect. 5), we examine the sensitivity of satellite observations with VLBI to satellite orbit displacements. Here, the impact  $\Delta\tau$  of a satellite orbit displacement by one centimeter in the normal, tangential and cross-track component on  $\tau$ , the difference in arrival time of the radio signal between pairs of radio telescopes, is determined and depicted in Fig. 3.

Scenario (a) analyses the impact for observations of two stations at  $45^\circ$  latitude with a difference of  $90^\circ$  in longitude forming an east-west baseline. For this observation geometry, the VLBI observable is almost insensitive for the cross-track component (green) and hardly sensitive for the normal com-

**Fig. 3** Illustration of two scenarios of two VLBI stations observing a satellite between  $-45^\circ$  and  $45^\circ$  for the satellite position angle  $\alpha$  defined in the illustration in the middle. The left plots illustrate the observing scenario. The right plots depict the impact  $\Delta\tau$  of a 1 cm orbit displacement in normal (blue), tangential (red) and cross-track (green) direction on the observable  $\tau$ . (a) Observations to a satellite from two VLBI stations forming an east-west baseline. (b) Observations to a satellite from two VLBI stations forming a north-south baseline



ponent (blue), especially if the satellite is exactly between the two stations, the impact of a change in normal direction becomes zero. The shift of the satellite in tangential direction (red) has a greater impact on the observable which can be as large as 3.5 mm.

Scenario (b) depicts two VLBI stations located at the same longitude being  $40^\circ$  apart in terms of latitude forming a north-south baseline. The impact on the observable for this constellation is insignificant if the satellite is shifted in the normal or tangential direction. However, this observation geometry is suitable to determine the cross-track component as the impact on the observable by a shift in this direction is greater than 2 mm.

This theoretical analysis shows that a satellite observation is most sensitive towards the tangential component if the direction of the satellite track is parallel to the observing baseline. The highest sensitivity towards the cross-track component arises if the direction of the satellite track is orthogonal to the observing baseline. The impact on the VLBI observable by a change in the normal component was significantly smaller for both observation setups, which therefore represents the component which is worse determinable as expected for a pseudorange measurement system.

## 5 Results

As a representative example, our investigations concentrate on one day of observations of the Galileo satellite GSAT0212 with a currently operational network of five VLBI Global Observing System (VGOS; Petrachenko et al. 2012) type stations (Fig. 4). For this network, we determined the DOP factors described in Sect. 3, i.e., normal DOP (NDOP), tangential DOP (TDOP), and cross-track DOP (WDOP), as well as the UT1-UTC DOP (UDOP). The analysis is carried out for 24 h starting on June 7, 2021 00:00:00 UTC (Fig. 5). Table 1 shows the minimum values of the determined DOP factors for this analysis.

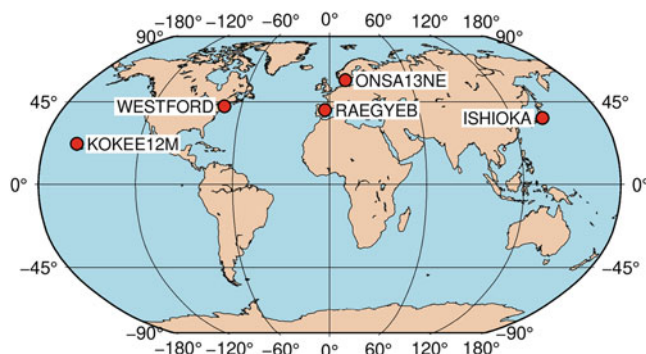


Fig. 4 VGOS stations considered in this study

**Table 1** Minimum values of the DOP factors for the performed analysis

	NDOP	TDOP	WDOP	UDOP
GSAT0212 (E03)	27.13	1.49	1.67	0.45

### 5.1 Normal DOP Factor

The normal DOP factor indicates the sensitivity of a satellite observation to the normal (radial) component of the satellite position in the NTW-frame. It is evident that the values of the NDOP are in general higher compared to values of other DOP factors (Fig. 5b). By relating the values of the NDOP with the number of stations, for which the satellite is visible simultaneously, it can be stated that the values of the NDOP are lower if the satellite is visible from more stations at the same time. For example, the NDOP is below 60, when the satellite's trajectory is above North America and the satellite is visible for about 4.5 h from all five stations. When the satellite travels southwards and is only visible from two stations, the NDOP jumps to a value greater than 60. The same can be observed when the satellite is orbiting over Europe where it is visible for four stations simultaneously for 25 min (Fig. 5a). This position results in an NDOP value of 27.13, which is the minimum value for this study and therefore represents the best suitable satellite position for determining the normal component.

### 5.2 Tangential DOP Factor

The sensitivity of a satellite observation to the tangential component of the satellite position is represented by the TDOP factor. As it was described in Sect. 4, the values of the TDOP are lower if the direction of the satellite track is parallel to the observing baseline which represents an appropriate observation geometry for determining the tangential component (Fig. 5c). This can be recognized when the satellite is orbiting above Europe being visible for four stations simultaneously for 25 min (Fig. 5a). For this and the further positions the TDOP value drops from more than five to a value below four as the satellite becomes visible for the station ISHIOKA and the direction of the baseline between ONSA13NE and ISHIOKA is similar to the direction of the satellite track. For the performed analysis the best observation geometry for determining the tangential component reaches a value of 1.49 for the TDOP factor.

### 5.3 Cross-Track DOP Factor

The cross-track DOP factor indicates the sensitivity of a satellite observation with VLBI to the cross-track component

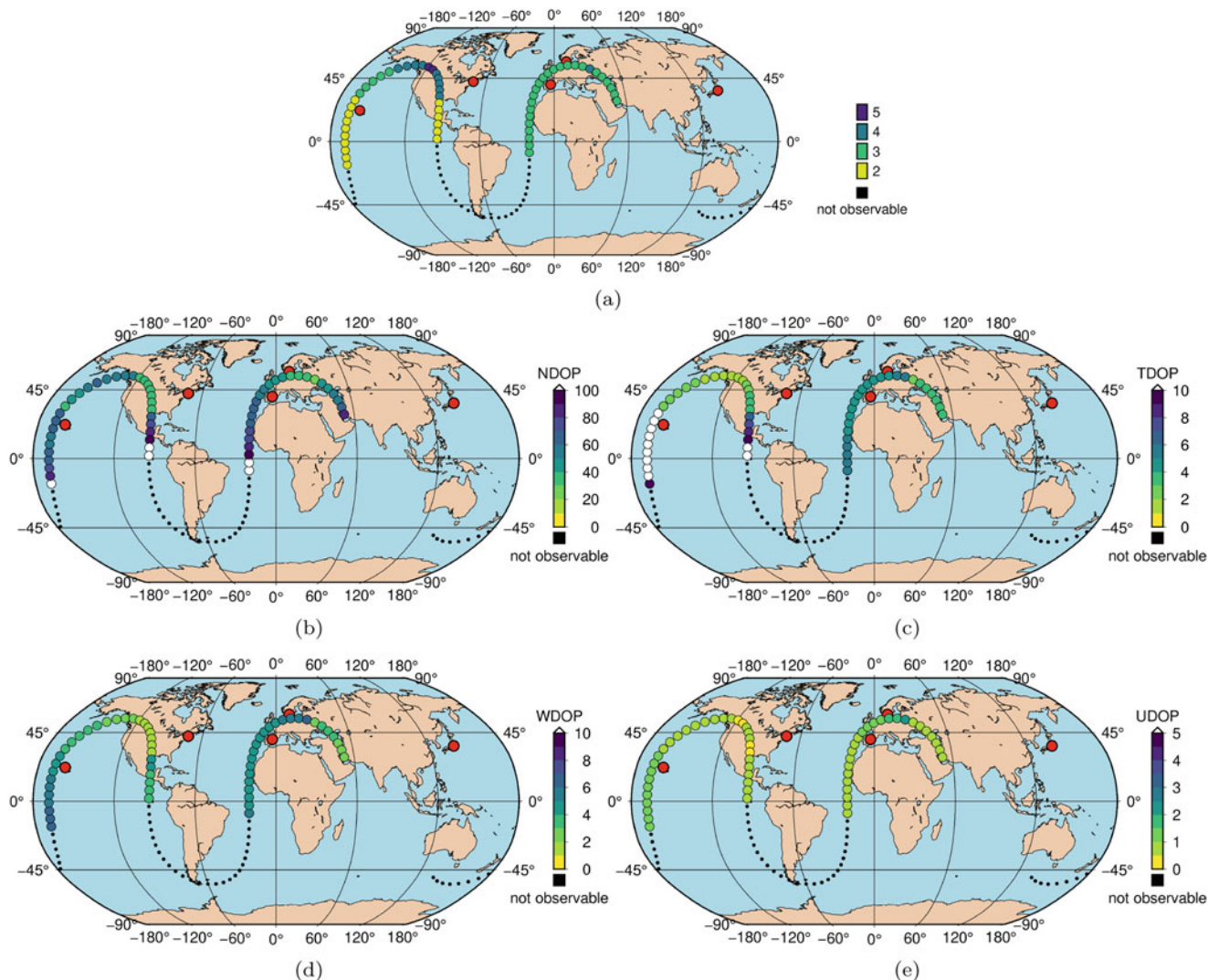


**Fig. 5** Ground track of the satellite GSAT0212 (E03) during 24 h starting on June 7, 2021 00:00:00 UTC. The dots represent the position of the satellite over Earth in a 15 min interval color-coded by (a) number of stations from which the satellite is visible and by the values of the (b)

NDOP, (c) TDOP, (d) WDOP and (e) UDOP factor. The smaller black dots represent positions where the satellite is not visible from at least two stations and the white circles represent positions with DOP values exceeding the scale

of the satellite position in the local orbital frame. The results in Fig. 5d confirm the outcomes of the theoretical study described in Sect. 4 as the values of WDOP are lower and an observation is therefore more sensitive towards the cross-track component if the direction of the satellite track is orthogonal to the observing baseline and the satellite passes through the observing stations. This is clearly visible when the satellite travels over North America where the WDOP value is below two and the satellite is visible for four or five stations simultaneously. Within these positions a minimum value of 1.67 is reached. When the satellite is travelling further southwards and is not visible anymore for the two stations in Europe the WDOP reaches values above three as the direction of the remaining baseline between KOKEE12M and WESTFORD and the direction of the

satellite track for these positions are not close to orthogonal anymore.

#### 5.4 UT1-UTC DOP Factor

The UDOP factor represents the sensitivity of satellite observations to UT1-UTC. More precisely, it constitutes the UT1-UTC error on the Earth equator per VLBI measurement error, both in units of length and is therefore dimensionless. The results depict that the UDOP factor reaches the smallest values compared to the other DOP factors (Fig. 5e). The best observation geometry for determining dUT1 occurs when the satellite passes through stations forming baselines with a long east-west extension which results in a minimum value of



0.45 for this study. A visibility from stations forming north-south baselines correspond to a less sensitive observation geometry for dUT1. The minimum value is reached when the satellite is visible for three stations simultaneously and it is passing between these stations, namely KOKEE12M, WESTFORD and RAEGYEB. The impact of the observation geometry between the satellite and the observing stations on the UDOP factor can also be recognized when the satellite passes over Europe. Before the satellite becomes visible for four stations for a short period, becoming observable for the station ISHIOKA, the value of the UDOP factor is greater than one. Even though the satellite is visible for an east-west baseline for these positions it is not passing between these two stations. As soon as the satellite becomes visible for the station ISHIOKA the UDOP value drops below one as the satellite is now orbiting through stations forming a baseline with a long east-west extension.

## 6 Conclusion

In this study, all potential observation periods on June 7, 2021 to the Galileo satellite GSAT0212 from a network including five VGOS type stations were determined and investigated in terms of the Dilution of Precision (DOP) factors regarding the satellite position in the NTW-frame, namely normal DOP, tangential DOP and cross-track DOP, as well as the UT1-UTC DOP. The performed analysis has confirmed the well-known fact that the normal component is significantly worse determinable compared to the tangential and cross-track component. In order to investigate different approaches for precise orbit determination in future, the normal component may have to be constrained in the analysis stage by either using the ranging information of SLR observations or constraining it to the a-priori orbit information. A suitable observation geometry for determining the tangential component arises if the satellite track direction is parallel to the baseline between the observing stations. This reflects that the highest sensitivity is obtained in the tangential direction in a plane containing the baseline. In contrast, the cross-track component can be well determined if the direction of the satellite track is orthogonal to the observing baseline. A highly sensitive observation geometry with respect to dUT1 is constituted if the satellite passes between two stations forming a baseline with a long east-west extension. With these investigations, we have demonstrated that the DOP factors introduced here are suitable quantities for the evaluation and preferential selection of satellite observing geometries. As a consequence, we will use them for optimising the scheduling of satellite observations in VieSched++. The findings of this study are also applicable to legacy S/X and combinations of VGOS and legacy S/X VLBI systems, as well as to other satellite systems. Finally,

DOP factors are not only suitable for individual observations but could possibly also be introduced as a factor for characterizing the quality of the whole observing schedule for the determination of the absolute orientation of a satellite constellation.

**Acknowledgements** The authors thank the Austrian Science Fund (FWF) for supporting this work within project VLBI2Galileo (P 33925N).

## References

- Altamimi Z, Rebischung P, Métivier L, Collilieux X (2016) ITRF2014: A new release of the International Terrestrial Reference Frame modeling non-linear station motions: ITRF2014. *J Geophys Res Solid Earth* 121. <https://doi.org/10.1002/2016JB013098>
- Anderson J, Beyerle G, Glaser S, Liu L, Männel B, Nilsson T, Heinkelmann R, Schuh H (2018) Simulations of VLBI observations of a geodetic satellite providing co-location in space. *J Geodesy* 92. <https://doi.org/10.1007/s00190-018-1115-5>
- Belli F (2020) Transfer of absolute orientation to Galileo orbits with VLBI. Master thesis, Technical University of Munich
- Bury G, Sošnica K, Zajdel R, Strugarek D, Hugentobler U (2021a) Determination of precise Galileo orbits using combined GNSS and SLR observations. *GPS Solutions* 1:11. <https://doi.org/10.1007/s10291-020-01045-3>
- Bury G, Sošnica K, Zajdel R, Strugarek D, Hugentobler U (2021b) Geodetic datum realization using SLR-GNSS co-location onboard Galileo and GLONASS. *J Geophys Res (Solid Earth)* 126(10):e22211. <https://doi.org/10.1029/2021JB022211>
- Böhm J, Böhm S, Boisits J, Girdiuk A, Gruber J, Hellerschmied A, Krasna H, Landskron D, Madzak M, Mayer D, McCallum J, McCallum L, Schartner M, Teke K (2018) Vienna VLBI and Satellite Software (VieVS) for geodesy and astrometry. *Publications of the Astronomical Society of the Pacific*, vol 130, p 044503. <https://doi.org/10.1088/1538-3873/aaa22b>
- Charlot P, Jacobs CS, Gordon D, Lambert S, de Witt A, Böhm J, Fey AL, Heinkelmann R, Skurikhina E, Titov O, Arias EF, Bolotin S, Bourda G, Ma C, Malkin Z, Nothnagel A, Mayer D, MacMillan DS, Nilsson T, Gaume R (2020) The third realization of the international celestial reference frame by very long baseline interferometry. *A&A* 644:A159. <https://doi.org/10.1051/0004-6361/202038368>
- Hellerschmied A (2018) Satellite Observation with VLBI. Doctoral thesis, Technical University of Vienna. <http://repositum.tuwien.ac.at/urn:nbn:at:at-ubtuw:1-118370>
- Hellerschmied A, McCallum L, McCallum J, Sun J, Böhm J, Cao J (2018) Observing APOD with the AuScope VLBI array. *Sensors* 18(5). <https://doi.org/10.3390/s18051587>. <https://www.mdpi.com/1424-8220/18/5/1587>
- Herrera Pinzón I, Rothacher M (2020) Co-location of space geodetic techniques: Studies on intra-technique short baselines. In: *International association of geodesy symposia*. Springer, Berlin, Heidelberg. [https://doi.org/10.1007/1345\\_2020\\_95](https://doi.org/10.1007/1345_2020_95)
- Jaradat A, Jaron F, Gruber J, Nothnagel A (2021) Considerations of VLBI transmitters on Galileo satellites. *Adv Space Res* 68(3):1281–1300. <https://doi.org/10.1016/j.asr.2021.04.048>
- Klioner S (1991) General relativistic model of VLBI observables. In: *Proceedings of AGU chapman conference on geodetic VLBI: Monitoring Global Change*
- Klopotek G, Hobiger T, Haas R, Otsubo T (2020) Geodetic VLBI for precise orbit determination of Earth satellites: a simulation study. *J Geodesy* 94:56. <https://doi.org/10.1007/s00190-020-01381-9>

- Mammadaliyev N, Schreiner P, Glaser S, Neumayer KH, Koenig R, Heinkelmann R, Schuh H (2021) Potential of VLBI observations to satellites for precise orbit determination. In: EGU general assembly conference abstracts, pp EGU21–12458
- McCallum J, Plank L, Hellerschmied A, Böhm J, Lovell J (2016) Technical challenges in VLBI observations of GNSS sources. In: Proceedings of the first international workshop on VLBI observations of near-field targets, pp 1864–1113
- Petit G, Luzum B (2010) IERS conventions 2010. IERS Technical Note 36:180
- Petrachenko WT, Niell AE, Corey BE, Behrend D, Schuh H, Wresnik J (2012) VLBI2010: Next Generation VLBI System for Geodesy and Astrometry. In: Kenyon S, Pacino MC, Marti U (eds) Geodesy for planet earth. Springer, Berlin, Heidelberg, pp 999–1005
- Plank L (2013) VLBI satellite tracking for the realization of frame ties. <http://www.ub.tuwien.ac.at/diss/AC11121594.pdf>
- Plank L, Böhm J, Schuh H (2016) Simulated VLBI Satellite Tracking of the GNSS Constellation: Observing Strategies. In: Rizos C, Willis P (eds) IAG 150 Years. Springer International Publishing, Cham, pp 85–90
- Plank L, Hellerschmied A, McCallum J, Böhm J, Lovell J (2017) VLBI observations of GNSS-satellites: from scheduling to analysis. *J Geodesy* 91:867–880
- Schartner M, Böhm J (2019) VieSched++: A new VLBI scheduling software for geodesy and astrometry. *Publications of the Astronomical Society of the Pacific*, vol 131, p 084501. <https://doi.org/10.1088/1538-3873/ab1820>
- Swanson ER (1978) Geometric dilution of precision. *Annu Navigat* 25:425–429. <https://doi.org/10.1002/j.2161-4296.1978.tb01345.x>
- Thaller D, Dach R, Seitz M, Beutler G, Mareyen M, Richter B (2011) Combination of GNSS and SLR observations using satellite collocations. *J Geodesy* 85:257–272. <https://doi.org/10.1007/s00190-010-0433-z>
- Tornatore V, Haas R, Casey S, Duev D, Pogrebenko S, Calvés G (2014) Direct VLBI observations of global navigation satellite system signals, vol 139, pp 247–252. [https://doi.org/10.1007/978-3-642-37222-3\\_32](https://doi.org/10.1007/978-3-642-37222-3_32)
- Wolf H (2021) Satellite scheduling with VieSched++. Master thesis, Technical University of Vienna. <https://doi.org/10.34726/hss.2021.87526>

**Open Access** This chapter is licensed under the terms of the Creative Commons Attribution 4.0 International License (<http://creativecommons.org/licenses/by/4.0/>), which permits use, sharing, adaptation, distribution and reproduction in any medium or format, as long as you give appropriate credit to the original author(s) and the source, provide a link to the Creative Commons license and indicate if changes were made.

The images or other third party material in this chapter are included in the chapter's Creative Commons license, unless indicated otherwise in a credit line to the material. If material is not included in the chapter's Creative Commons license and your intended use is not permitted by statutory regulation or exceeds the permitted use, you will need to obtain permission directly from the copyright holder.





# On the Limits of State-of-the-Art GNSS Receivers in Frequency Transfer

Thomas Krawinkel and Steffen Schön

## Abstract

GNSS frequency transfer (FT) based on precise point positioning delivers instability values down to sub- $10^{-16}$  between two modern receivers. In the present study we investigate the technical limits such receivers impose on FT by means of a dedicated experiment at Germany's national metrology institute (PTB). For this purpose, four geodetic receivers, two of the same type each, were all connected to one single antenna and fed by the highly stable UTC (PTB) frequency signal. Since all error sources affecting the satellite signals are the same for all receivers, they cancel out when forming receiver-to-receiver single differences (SDs). Due to the fact that the remaining SD carrier phase ambiguities can be easily fixed to integer values, only the relative receiver clock error remains in the SDs. We assess the instability of three different receiver combinations, two with the same receiver type (intra-receiver) and one with different types (inter-receiver). The intra-receiver pairs reach lower instability values faster than the inter-receiver combination, which is in part caused by the different signal tracking modes of the receivers. To be specific, the  $10^{-18}$  instability range was only reached by the intra-receiver pairs, whereas the inter-receiver combination already hits its noise floor at about  $1.5 \cdot 10^{-17}$ . In addition, our analysis of using different observation type combinations only shows small differences regarding the link instability.

## Keywords

Allan deviation · Frequency transfer · GNSS

## 1 Introduction

Today, frequency transfer (FT) based on Global Navigation Satellite System (GNSS) measurements is used as a standard technique (Defraigne 2017). To this end, GNSS receivers are

connected to frequency standards or atomic clocks whose frequency is to be compared. Typically, the recorded GNSS data are analyzed using the precise point positioning (PPP) method (Zumberge et al. 1997). The obtained receiver clock error time series of different stations serve as a starting quantity for frequency transfer. Currently, on the analysis side, GNSS FT achieves sub- $10^{-16}$  instability values by means of integer PPP (Petit 2021). On the side of the receivers, the stability of the internal hardware delays is most important for the achievable FT instability. This includes delay variations in each receiver itself as well as different behaviors of these variations between the receivers involved. In theory, if all error sources were eliminated or well controlled, the instability of GNSS-based FT should be dominated by white frequency noise at the level of the noise of the GNSS

This research was funded by the Deutsche Forschungsgemeinschaft (DFG, German Research Foundation) – project number 434617780 – SFB 1464.

T. Krawinkel (✉) · S. Schön  
Leibniz University Hannover, Institut für Erdmessung, Hannover,  
Germany  
e-mail: [krawinkel@ife.uni-hannover.de](mailto:krawinkel@ife.uni-hannover.de)

observation type in use. When using modern, state-of-the-art GNSS receivers, this limit would be in the range of a few millimeters. According to manufacturer's data, for example JAVAD GNSS (2021), carrier phase precision – in zenith direction – amounts to 1 mm. In order to also take into account noisier GNSS observations in low elevation angles, we assess the range limit to 1–3 mm.

On our way to pushing the limits of GNSS FT to the instability range of  $10^{-17}$  within the framework of the Collaborative Research Centre *TerraQ (Relativistic and Quantum-based Geodesy)*, in a first step, we want to assess the minimum achievable frequency instability between two GNSS receivers. The metrological foundation for our investigations is a dedicated experiment we carried out at the Physikalisch-Technische Bundesanstalt (PTB), Germany's national metrology institute, where we have the possibility to set up the receivers in a controlled environment. This means that all receivers were connected to the same antenna as well as the same frequency signal of the locally generated approximation of Coordinated Universal Time (UTC), referred to as UTC(PTB) (Bauch et al. 2012). We analyze the recorded GPS and Galileo carrier phase observations based on between-receiver single differences (SDs) with our in-house GNSS software, and examine the instability of each receiver link by means of the modified Allan deviation (Allan 1987; Allan and Barnes 1981). The remainder of the paper is structured as follows. In Sect. 2 the experimental set up is described. Next, Sect. 3 details the data analysis, and the obtained results are presented and discussed in Sect. 4.

## 2 Experiment

The entire GNSS measurement campaign was carried out from April 20 to May 10, 2021 in and on top of the Meitner building at PTB. Here, the receivers were installed in a laboratory where temperature and humidity were controlled by an air conditioning system. The relative humidity was steered around a value of 50% with a  $1\sigma$  of 4%, and the temperature was stabilized at about 22.9 °C with a  $1\sigma$  of 0.1 °C.

The main measurement equipment consisted of four modern geodetic GNSS receivers, namely two JAVAD OMEGA (serial no.: 0046, 0047) and two Septentrio PolaRx5TR (serial no.: 1345, 1372). In the first part of the experiment, which lasted for ten days (April 20–29, 2021) and which we will discuss in this article, all of these receivers were connected to one single antenna, a Leica AR20 with radome, via an active signal splitter. Furthermore, all receivers were driven by the same 10 MHz UTC(PTB) signal. Such a measurement configuration is usually referred to as a zero baseline (ZB), common clock (CC) configuration. Photographs of the installations and a schematic depiction of the measurement configuration are shown in Figs. 1 and 2.

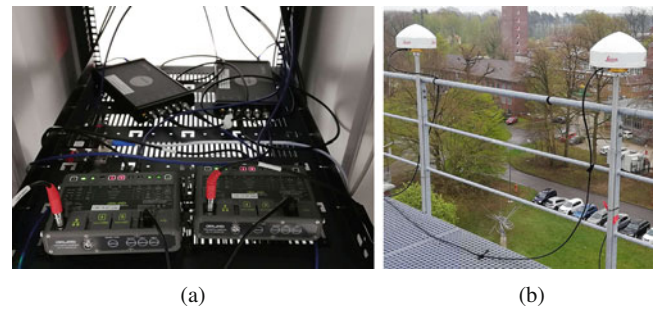


**Fig. 1** GNSS equipment used during the experiment. Note that in the first part of the measurement campaign, the receivers were only connected to the left antenna. (a) Receivers. (b) Antennas

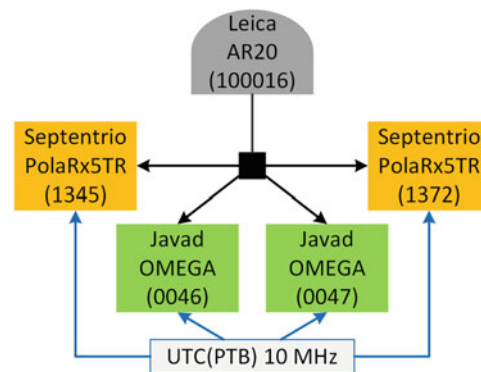


**Fig. 2** Schematic depiction of the zero-baseline, common-clock measurement configuration during the experiment

The signal paths from the antenna to each receiver were identical to ensure identical delays. In addition to GPS and Galileo, the receivers track also GLONASS and BeiDou signals with a data rate of 1 Hz. A more detailed description of the experiment can be found in Krawinkel et al. (2021).

## 3 Data Analysis

We investigate the current technical limits of GNSS FT by means of the continuous ZB-CC measurements which lasted for ten full days as discussed in Sect. 2. To be more specific, we use our in-house MATLAB-based GNSS toolbox to analyze the GPS and Galileo carrier phase observations with a sampling interval of 30 s. In order to be able to use GPS and Galileo observations in a consistent way, we apply final satellite orbit and clock products computed within the frame of the Multi-GNSS Experiment (MGEX) project by the Centre National d'Etudes Spatiales, Collecte Localisation Satellites (CNES/CLS) (Montenbruck et al. 2017; Loyer et al. 2012; Katsigianni et al. 2019).

When forming carrier phase single differences  $\Delta L$  of any signal frequency ( $L_1$ ,  $L_2$ , etc.) in a ZB-CC measurement configuration between two receivers  $A$ ,  $B$  and satellite  $j$ ,

distance-dependent signal errors like atmospheric propagation delays, site-specific errors such as multipath or antenna-related cancel out. Consequently, they are not modeled or corrected in our analysis. The relative geometry can be computed from very accurate a-priori satellite and receiver coordinates. Thus, only the carrier phase ambiguity  $\Delta N$  of each satellite and the relative clock offset  $\Delta\delta t_{A,B}$  between the receivers remain as unknowns:

$$\Delta L_{A,B}^j = c \cdot \Delta\delta t_{A,B} + \lambda \cdot \Delta N_{A,B}^j + \Delta\epsilon_{A,B} \quad (1)$$

with the speed of light  $c$ , carrier phase wavelength  $\lambda$ , and carrier phase observation noise  $\Delta\epsilon_{A,B}$ . Due to the fact that the observation geometries for both receivers are virtually the same, ambiguity resolution is a relatively simple task and can be achieved by means of rounding to the nearest integer value. In our case, all ambiguities could be successfully fixed to integer cycles given that the initial real-valued ambiguities were close to integer cycles by 1.5% or less.

From the ambiguity-fixed original single-frequency SD observations, we compute dual-frequency ionosphere-free (IF) observables for each receiver. Although they are noisier by a factor of three compared to single-frequency observables, we use IF observables since that is the primary observation type used in practical GNSS FT (Defraigne 2017; Weinbach 2013). Thus, we can derive more consistent and meaningful conclusions from the results – computed with IF observables – because they represent a typical GNSS FT use case.

Averaging the resulting IF SD observables of all satellites then yields one estimate for the relative receiver clock error at each measurement epoch (Weinbach et al. 2009). Finally, we do not apply any elevation-dependent weighting scheme since this slightly increases the noise of the resulting clock error time series. This behavior is visible in the two mean SD time series of the JAVAD receiver pair on the first day of the experiment shown in Fig. 3. One time series is computed with an identity weighting and the other with a cosine weighting based on the satellite elevation angle. In the end, the results when using either one of the two weighting schemes are only marginally different. Potentially erroneous observations at low elevations are eliminated by applying an elevation cutoff angle of 15°.

From the total of four receivers, we compute the results for different receiver pairs. We will discuss those of the following combinations:

1. Both JAVAD receivers
  2. Both Septentrio receivers
  3. One JAVAD (0046), one Septentrio (1345) receiver
- Since the first two combinations use identical receivers of the same manufacturer, we refer to them as *intra-receiver* combinations, whereas the third pair is designated as an *inter-receiver* combination.

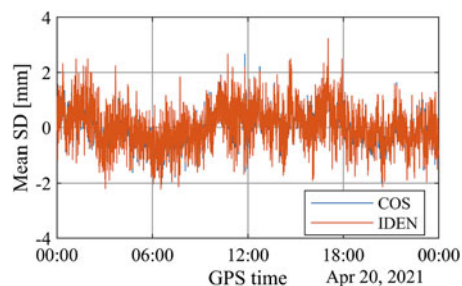


**Fig. 3** Mean single differences (SDs) between the two JAVAD receivers (0046, 0047) with identity (IDEN) and cosine elevation (COS) weighting for ionosphere-free linear combination GL1C-GL2W (cf. Table 1)

## 4 Results

The relative receiver clock errors are represented by the mean SD of all satellites, thus we refer to the time series shown in Figs. 4, 5, 6 as such. They are computed for five different IF linear combinations based on these original observation types:

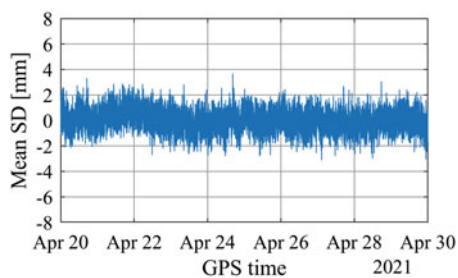
- GPS
  - L1 C/A, L2W
  - L1 C/A, L2C
  - L1 C/A, L5
- Galileo
  - E1, E5a
  - E1, E5 (AltBOC)

Because JAVAD and Septentrio receivers track GPS L2C, L5 as well as Galileo E5 signals in different ways, the designation of their respective IF combinations becomes a bit cumbersome. A description of the corresponding abbreviations used in the figures in this section can be found in Table 1.

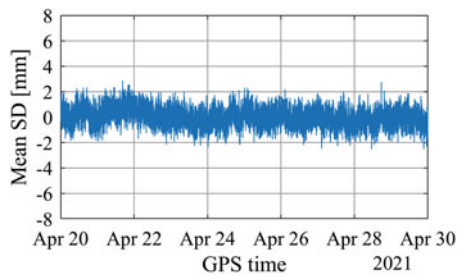
The mean SDs for the two intra-receiver combinations and the inter-receiver pair are shown in Figs. 4, 5, 6, respectively. Since the noise of GNSS carrier phase observations is typically specified in millimeters, we choose this unit for these figures. All depicted time series are each reduced by an offset. Due to the fact that the receivers are not calibrated for any signal delays, these offsets basically represent arbitrary

**Table 1** Carrier phase observation types used for ionosphere-free linear combinations in data analysis according to Romero (2020)

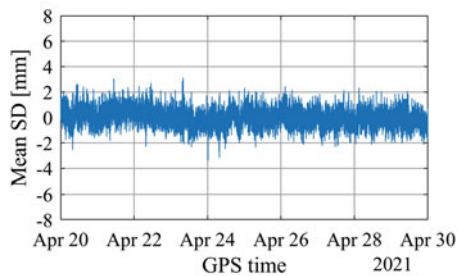
Abbreviation	System	Frequency (channel)
GL1C	GPS	L1 (C/A)
GL2W	GPS	L2 (Z-tracking and similar)
GL2X, GL2L	GPS	L2C (M+L), L2C (L)
GL5X, GL5Q	GPS	L5 (I+Q), L5 (Q)
EL1X, EL1C	Galileo	E1 (OS data+pilot), E1 (OS pilot)
EL5X, EL5Q	Galileo	E5a (I+Q), E5a (Q)
EL8X, EL8Q	Galileo	E5 (I+Q), E5 (Q)



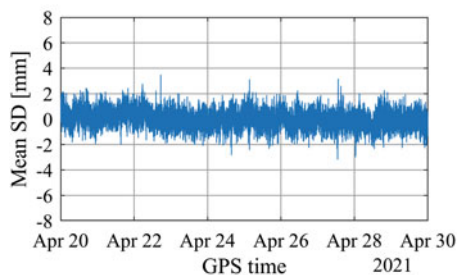
(a)



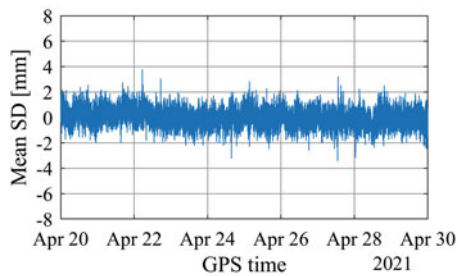
(b)



(c)

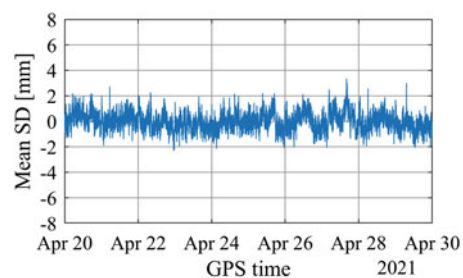


(d)

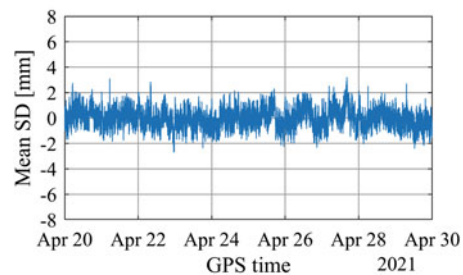


(e)

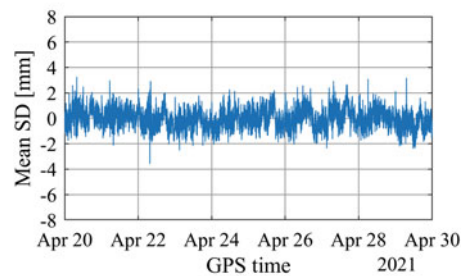
**Fig. 4** Mean single differences (SDs) between the two JAVAD receivers (0046, 0047) for ionosphere-free linear combinations of various observation types. The abbreviations of the latter are explained in Table 1. (a) GL1C-GL2X. (b) GL1C-GL5X. (c) EL1X-EL5X. (d) EL1X-EL8X. (e) EL1X-EL8X



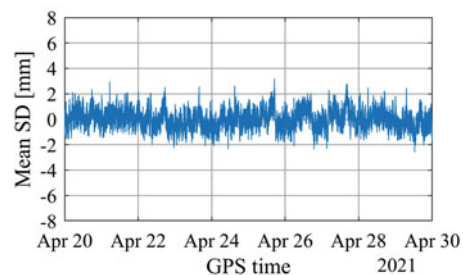
(a)



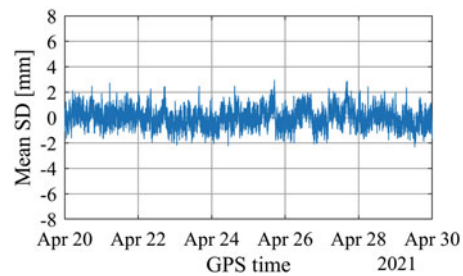
(b)



(c)



(d)



(e)

**Fig. 5** Mean single differences (SDs) between the two Septentrio receivers (1345, 1372) for ionosphere-free linear combinations of various observation types. The abbreviations of the latter are explained in Table 1. (a) GL1C-GL2W. (b) GL1C-GL2L. (c) GL1C-GL5Q. (d) EL1C-EL5Q. (e) EL1C-EL8Q

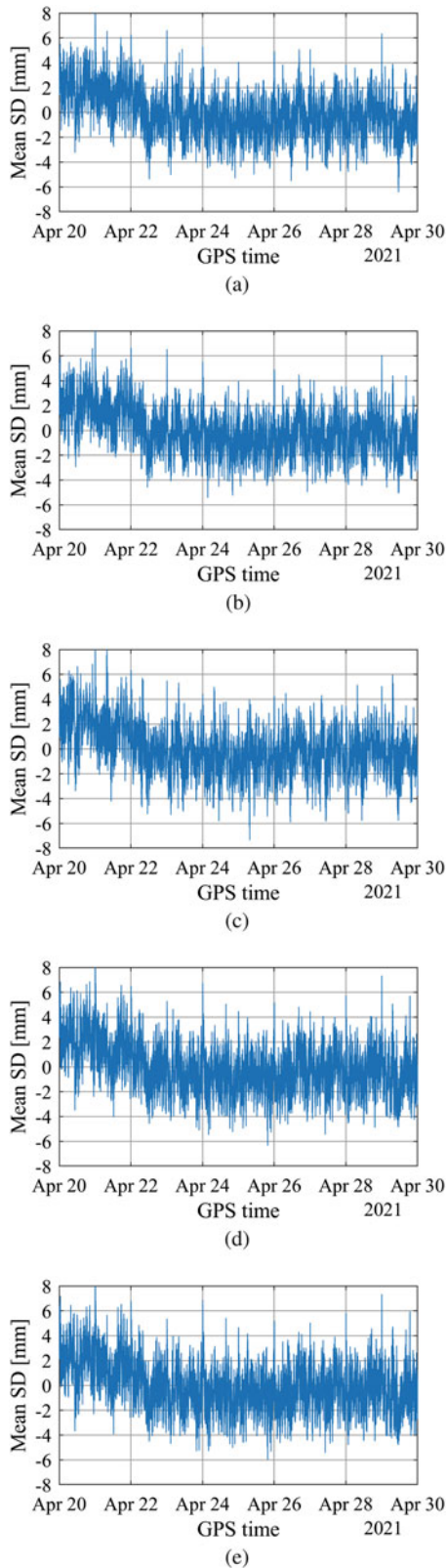


**Fig. 6** Mean single differences (SDs) between the first JAVAD receiver (0046) and the first Septentrio receiver (1345) for ionosphere-free linear combinations of various observation types. The abbreviations of the latter are explained in Table 1. (a) GL1C-GL2W. (b) GL1C-GL2(X/L). (c) GL1C-GL5(X/Q). (d) EL1(X/C)-EL8(X/Q). (e) EL1(X/C)-EL8(X/Q)

observation-specific hardware delays between the involved receivers.

In an ideal case, the remaining time series should resemble a white noise process. From our results, the JAVAD receiver pair gets the closest to that expected behavior (Fig. 4). The time series of the Septentrio receiver combination look similar (Fig. 5). Although being less noisy in comparison, they reveal certain systematic effects. Overall, the two intra-receiver pairs have  $1\sigma$ -precision levels of 0.7 mm, whereas the inter-receiver combination (Fig. 6) shows a more than two times higher value of 1.8 mm.

Furthermore, these time series also exhibit a running-in effect over the course of the first two days of the measurement campaign. Nevertheless, all these noise levels are well in the range of the assumed precision of IF carrier phase observations from a geodetic receiver of about 1–3 mm. A summary of the time series statistics, i.e. their mean values and standard deviations, is given in Table 2. Regarding the different observation types for each receiver combination, only small differences are visible.

From the mean SD results, we can derive the frequency instability of each receiver link as shown in Fig. 7 in terms of modified Allan deviations:

$$\sigma_y^2(\tau) = \frac{1}{2m^2\tau^2(N-3m+1)} \sum_{j=1}^{N-3m+1} \left( \sum_{i=j}^{j+m-1} (x_{i+2m} - 2x_{i+m} + x_i) \right)^2 \quad (2)$$

with time error measurement  $x_i$ , averaging time  $\tau = m\tau_0$  consisting of averaging factor  $m$  and basic sampling interval  $\tau_0$  of a finite data set of length  $N$ .

**Table 2** Mean value and standard deviation (STD) of various mean ionosphere-free single difference time series. The observation types are explained in Table 1

Receiver pair	Observation types	Mean (mm)	STD (mm)
2 JAVAD (0046, 0047)	GL1C-GL2W	56.8	0.8
	GL1C-GL2X	56.3	0.7
	GL1C-GL5X	-91.6	0.7
	EL1X-EL5X	-92.1	0.6
	EL1X-EL8X	83.9	0.7
2 Septentrio (1345, 1372)	GL1C-GL2W	245.6	0.7
	GL1C-GL2L	245.7	0.7
	GL1C-GL5Q	-15.7	0.7
	EL1C-EL5Q	-15.4	0.7
	EL1C-EL8Q	-0.7	0.7
1 JAVAD (0046), 1 Septentrio (1345)	GL1C-GL2W	-224.0	1.7
	GL1C-GL2(X/L)	-222.9	1.7
	GL1C-GL5(X/Q)	-126.5	1.8
	EL1(X/C)-EL5(X/Q)	-128.0	1.8
	EL1(X/C)-EL8(X/Q)	-174.2	1.8

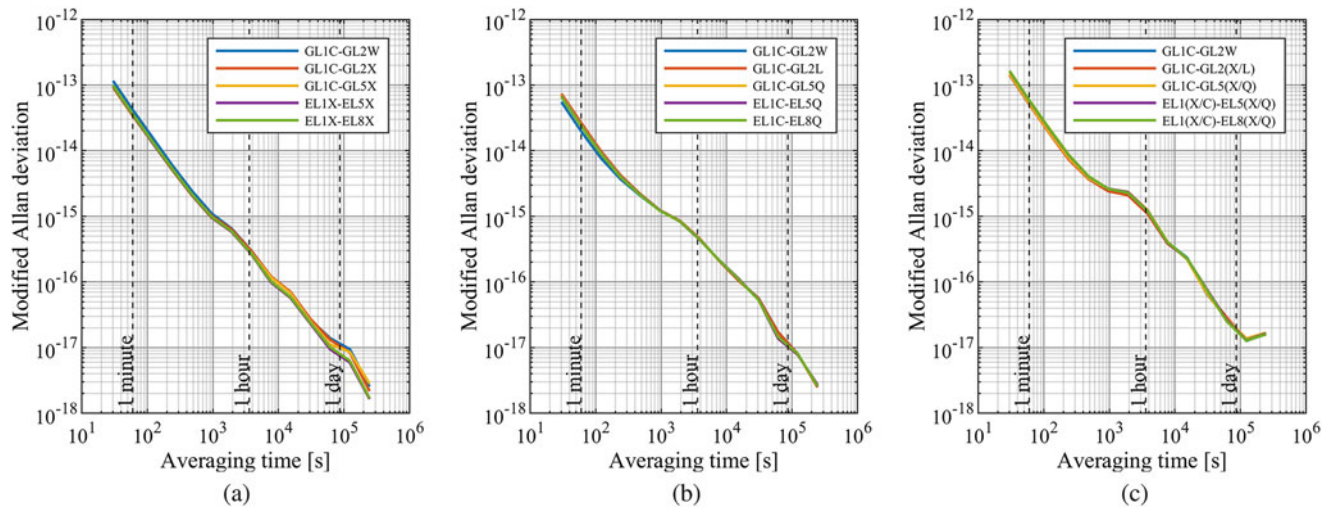


**Fig. 7** Frequency instability of 10-day continuous GNSS measurements in terms of modified Allan deviations for all three receiver links for ionosphere-free linear combinations of various observation

types. The abbreviations of the latter are explained in Table 1. (a) JAVAD (0046, 0047). (b) Septentrio (1345, 1372). (c) JAVAD (0046), Septentrio (1345)

The intra-receiver combinations provide a better overall performance than the inter-receiver pair, where the latter seems to reach its flicker floor before getting to the  $10^{-18}$  instability range. One reason for this behavior could be that the JAVAD and Septentrio receivers use different tracking modes for modern GNSS signals. The JAVAD receiver combination reaches a frequency instability of  $1 \cdot 10^{-17}$  after an averaging time of approximately 5900 s using Galileo E1-E5a (EL1X-EL5X) signals. The use of modern GPS L2C (GL2X/L) and L5 (GL5X/Q) signals results in smaller instability values as compared to legacy L1 (GL1C) and L2 (GL2W) signals. For both intra-receiver pairs, the noise floor is not yet visible in this 10-day data set.

## 5 Conclusions

In this contribution, we presented the results of the first part of a dedicated GNSS measurement campaign that lasted for ten days and was carried out at Germany's national metrology institute (PTB) in the spring of 2021. Four geodetic receivers, namely two JAVAD OMEGA, and two Septentrio PolaRx5TR, were connected to a single geodetic GNSS antenna and driven by an external UTC(PTB) frequency

signal. The main goal of our investigations was to explore the current technical limits of GNSS frequency transfer with state-of-the-art GNSS equipment. For this, we analyzed the recorded carrier phase observations with our in-house GNSS software in a single-difference approach between two receivers each. In this very specific zero-baseline, common-clock measurement configuration, after fixing the phase ambiguities to integer values, the remaining signal theoretically only contains the relative hardware delays between the receivers. Averaging these single differences (SDs) across all satellites yields a time series that represents exactly that. This method was applied to three different GPS and two different ionosphere-free observation type combinations. The instability of each receiver link was assessed by means of Allan deviations derived from averaged SDs. The results show that links consisting of two receivers of the same type reach lower instability ranges faster than the combination of two different receiver types. One reason for this are the different tracking modes used by JAVAD and Septentrio receivers. In summary, the  $10^{-18}$  instability range was only reached by the intra-receiver pairs, whereas the inter-receiver combination already hits its noise floor at  $1.5 \cdot 10^{-17}$ . Furthermore, the use of different observation type combinations only leads to small differences regarding the link instability.



**Acknowledgements** The authors would also like to thank Dr. Andreas Bauch and his team at PTB for their assistance and support in preparing, conducting and analyzing the experiment.

## Conflict of Interest

The authors declare that they have no conflict of interest and that they do not attempt to recommend any of the instruments under test. It is noted that the performance of the equipment presented in this paper depends on the particular environment and the individual instruments in use. Other instruments of the same type or the same manufacturer may show different behavior. The readers are, however, encouraged to test their own equipment to identify the system performance with respect to a particular application.

## References

- Allan DW (1987) Time and frequency (time-domain) characterization, estimation, and prediction of precision clocks and oscillators. *IEEE Trans Ultrason Ferroelectr Freq Control* 34(6):647–654
- Allan DW, Barnes JA (1981) A modified “Allan Variance” with increased oscillator characterization ability. In: *Proceedings of the 35th annual frequency control symposium*, Philadelphia, PA, USA, pp 470–475. <https://doi.org/10.1109/FREQ.1981.200514>
- Bauch A, Weyers S, Piester D, Staliuniene E, Yang W (2012) Generation of UTC(PTB) as a fountain-clock based time scale. *Metrologia* 49(3):180–188. <https://doi.org/10.1088/0026-1394/49/3/180>
- Defraigne P (2017) GNSS Time and frequency transfer. In: Teunissen PJG, Montenbruck O (eds) *Springer handbook of global navigation satellite systems*. Springer International Publishing, pp 1187–1206
- JAVAD GNSS (2021) GNSS receiver TRIUMPH-OMEGA datasheet. [https://download.javad.com/sheets/OMEGA\\_Datasheet.pdf](https://download.javad.com/sheets/OMEGA_Datasheet.pdf)
- Katsigianni G, Loyer S, Perosanz F, Mercier F, Zajdel R, Sošnica K (2019) Improving Galileo orbit determination using zero-difference ambiguity fixing in a Multi-GNSS processing. *Adv Space Res* 63(9):2952–2963. <https://doi.org/10.1016/j.asr.2018.08.035>
- Krawinkel T, Schön S, Bauch A (2021) Recent and future activities at Leibniz University Hannover in GNSS frequency transfer. In: 2021 joint conference of the European frequency and time forum and the IEEE international frequency control symposium
- Loyer S, Perosanz F, Mercier F, Capdeville H, Marty JC (2012) Zero-difference GPS ambiguity resolution at CNES-CLS IGS Analysis Center. *J Geodesy* 86(11):991–1003. <https://doi.org/10.1007/s00190-012-0559-2>
- Montenbruck O, Steigenberger P, Prange L, Deng Z, Zhao Q, Perosanz F, Romero I, Noll C, Stürze A, Weber G, Schmid R, MacLeod K, Schaer S (2017) The Multi-GNSS Experiment (MGEX) of the International GNSS Service (IGS) – Achievements, prospects and challenges. *Adv Space Res* 59(7):1671–1697. <https://doi.org/10.1016/j.asr.2017.01.011>
- Petit G (2021) Sub- $10^{-16}$  accuracy GNSS frequency transfer with IPPP. *GPS Solutions* 25(1). <https://doi.org/10.1007/s10291-020-01062-2>
- Romero I (2020) RINEX: The Receiver Independent Exchange Format Version 3.05. <https://files.igs.org/pub/data/format/rinex305.pdf>
- Weinbach U (2013) Feasibility and impact of receiver clock modeling in precise GPS data analysis: Dissertation. Veröffentlichungen der DGK Reihe C, Dissertationen, München: Verlag der Bayerischen Akademie der Wissenschaften. [http://www.dgk.badw.de/fileadmin/user\\_upload/Files/DGK/docs/c-692.pdf](http://www.dgk.badw.de/fileadmin/user_upload/Files/DGK/docs/c-692.pdf)
- Weinbach U, Schön S, Feldmann T (2009) Evaluation of state-of-the-art geodetic GPS receivers for frequency comparisons. In: 2009 joint conference of the European frequency and time forum and the IEEE international frequency control symposium, pp 263–268. <https://doi.org/10.1109/FREQ.2009.5168182>
- Zumberge JF, Heflin MB, Jefferson DC, Watkins MM, Webb FH (1997) Precise point positioning for the efficient and robust analysis of GPS data from large networks. *J Geophys Res Solid Earth* 102(B3):5005–5017. <https://doi.org/10.1029/96JB03860>

**Open Access** This chapter is licensed under the terms of the Creative Commons Attribution 4.0 International License (<http://creativecommons.org/licenses/by/4.0/>), which permits use, sharing, adaptation, distribution and reproduction in any medium or format, as long as you give appropriate credit to the original author(s) and the source, provide a link to the Creative Commons license and indicate if changes were made.

The images or other third party material in this chapter are included in the chapter’s Creative Commons license, unless indicated otherwise in a credit line to the material. If material is not included in the chapter’s Creative Commons license and your intended use is not permitted by statutory regulation or exceeds the permitted use, you will need to obtain permission directly from the copyright holder.





# On the Effect of Antenna Calibration Errors on Geodetic Estimates

## Investigation on Zero and Double Difference Approaches

Tobias Kersten, Grzegorz Krzan, Karol Dawidowicz, and Steffen Schön

### Abstract

This paper addresses an approach to assess the impact of phase centre correction errors of selected receiving antennas in the Polish ASG-Eupos network using GNSS processing strategies such as zero differencing and double differencing. The objective is to characterise the nature of the error patterns of GNSS receiver antennas and to understand their impact on GNSS derived integrated water vapour and geodetic estimates. A semi-analytical approach for characterising variants of error patterns is applied. Differences of up to +12 mm between type-mean and individual receiver antenna calibrations of current antenna models on the ionosphere-free linear combination are identified for repeatable pattern deformations. The analyses show that repeatable effects on tropospheric estimates of up to 8 mm – which corresponds to approx.  $1.2 \text{ kg/m}^2$  – occur even though only 5 mm variations were applied to the pattern. The results of our analysis show a strong correlation with the type of error patterns that affect the estimates differently. Due to the complex relationship between datum settings, processing strategy, baseline orientation and satellite sky distribution, artefacts in GNSS processing models and their effects must to be modelled in order to achieve a better understanding in the context of GNSS networks and GNSS meteorology.

### Keywords

Coordinates · Double difference (DD) · Generic patterns · Phase centre corrections (PCC) · Zenith tropospheric delays (ZTD) · Zero difference (ZD)

## 1 Introduction

Meteorology and climate monitoring are crucial to both tracking and monitoring extreme weather phenomena and understanding of climate change and its impact. The Global Navigation Satellite System (GNSS) – starting with GPS (Tralli et al. 1992) – serves since the early 1990s as one of several observation techniques to derive a vertical profile of water vapour content and its composition in the lower atmo-

sphere (troposphere). This provides important information about the structure of the monitoring of our most important greenhouse gas.

Several GNSS networks provide atmospheric products for global weather forecasting or monitoring of humidity in the lower atmosphere as an absolute measure, e.g. the International GNSS Service (IGS), the European Permanent Network (EPN) or the Global Climate upper air reference network (GRUAN, Vaquero-Martinez et al. 2019).

Bock and Parracho (2019) found biases in the time series of integrated water vapor (IWV) between  $1\text{--}4 \text{ kg/m}^2$  with a standard deviation of below  $2 \text{ kg/m}^2$  and also showed a strong relation between geographical, topographical and climatic features and demonstrated persistence of small-scale variability despite a reanalysis.

T. Kersten (✉) · S. Schön  
Leibniz University Hannover, Institut für Erdmessung (IfE), Hannover, Germany

G. Krzan · K. Dawidowicz  
University of Warmia and Mazury (UWM), Olsztyn, Poland

Ning et al. (2016) pointed out the challenge of deriving GNSS troposphere estimates that satisfy the demands of climate research. It is worth noting that data processing artefacts and imperfect models are easily introduced into the tropospheric estimates leading, e.g. to artificial trends of up to  $0.15 \text{ kg}/(\text{m}^2 \text{ year})$ . Nguyen et al. (2021) show the effect of different *a priori* models for the hydrostatic zenith delay that are as critical as the quality of the antenna/radome calibrations and applied mapping functions.

There are two techniques to achieve receiver antenna corrections. The first is a calibration in an anechoic chamber (Zeimetz and Kuhlmann 2008) using synthetic signals and the second is a robot arm that uses in-situ available GNSS radio signals (Menge et al. 1998). In general, good comparability below 1–2 mm phase differences was found between both techniques and selected antennas. But also higher differences of 4–6 mm are reported among the methods (Krzan et al. 2020). This magnitude occur also between type mean and individual calibrations. Systematic deviations that occur significantly reduce the achievable quality as a result of the very complex interactions of GNSS antennas with their entire environment and location. The impact of PCCs inaccuracies on geodetic and meteorological estimates strongly relies on: (1) the concept and philosophy of implemented processing approach, (2) the types of applied observations or linear combinations used, (3) the number and type of parameters estimated, (4) the mapping function chosen, and (5) the local satellite coverage, i.e the geographic location. Santerre et al. (2017) emphasised the impact of the local sky distribution. Douša et al. (2016) stressed the need of consistent and accurate GNSS carrier phase centre corrections (PCCs) for satellite and receiver antennas to monitor severe weather events and climate. Vey et al. (2009) reported magnitudes of up to  $\pm 1 \text{ kg}/\text{m}^2$  due to antenna and radome changes in GPS IWV time series, which is related to approx.  $\pm 7 \text{ mm}$  variation in the zenith total delay (ZTD).

The complex interaction of PCCs and the troposphere underlines the need to assess the quality and reliability of PCC sets for receiving antennas on both frequently used GNSS processing strategies, the zero difference (ZD, Zumberge et al. 1997) approach and the double difference (DD, Odijk and Wanninger 2017) approach.

Since neither the cause of the error effect of the receiver patterns nor their influence on the estimates are sufficiently well known, this paper sheds light on the complex interaction with tropospheric parameters in order to better answer the important question of the required accuracy and the impact of the receiver antennas on the absolute GNSS IWV estimates.

## 2 Troposphere and Antenna Phase Centre Calibrations

### 2.1 Troposphere Estimates

GNSS radio signal refraction in the troposphere is frequency independent and subsequently has to be modelled and estimated in terms of signal delay. According to Davis et al. (1985), two parts are combined to the ZTD, the hydrostatic delay ( $ZTD_h$ ) and the moisture (wet) delay ( $ZTD_w$ ) such as

$$ZTD = ZTD_h \cdot f_h(e) + ZTD_w \cdot f_w(e) \quad (1)$$

where  $ZTD_h$  is the *a priori* model for hydrostatic part,  $f_h(e)$  and  $f_w(e)$  reflect the mapping function for the dry and wet part, respectively, and  $e$  denotes the elevation angle. The ZTDs are linked to the Integrated Water Vapour (IWV, in  $\text{kg}/\text{m}^2$ ) or the Predictable Water Vapour (PWV, in mm) by transformation with additional measures, i.e. temperature and atmospheric pressure, taking into account uncertainty measures (Bevis et al. 1992). In addition, Beutler et al. (1988) explored how ZTDs correlate with station height by a factor of 1:–3, meaning that 1 mm error in the troposphere modelling results in a –3 mm offset in station height. These relations negatively affect the accuracy, precision, and homogeneity of GNSS ZTD and PWV/IWV time series.

### 2.2 Antenna Phase Centre Calibrations

The antenna PCCs are essential for high accuracy processing since the calibration values define the location of the GNSS antenna phase centre. This is not a common fixed location but rather a surface that varies with the properties of the antenna, the entire surrounding. The PCCs are defined as a function of local azimuth  $\phi$  and elevation  $\theta$  angle, frequency  $f$ , GNSS system  $s$ . They are separated into a mean phase centre offset (PCO) and phase centre variations (PCVs)

$$PCC_{s,f}(\phi, \theta) = -\mathbf{e}^T \mathbf{PCO}_{s,f} + PCV_{s,f}(\phi, \theta) + r_{s,f} \quad (2)$$

with the unit line-of-sight vector  $\mathbf{e}$  to the satellite and  $r_{s,f}$  expressing the one degree of freedom (Rothacher et al. 1995).

The results of calibration methods – whether in anechoic chambers or on robotic arms – are sets of gridded correction values presented in ANTEX format (Rothacher and Schmid 2010). While the effect of type mean or individual calibration on station coordinates is discussed on global and regional scales (Araszkiewicz and Völksen 2016; Villiger et al. 2020; Krzan et al. 2020), there is a need to assess the impact of

the accuracy of PCC patterns on meteorological parameters in order to provide uncertainty bounds for e.g. ZTDs and understand sources of bias in IWV time series.

### 2.3 Issues of Receiver Antenna Patterns

To illustrate the current challenges, our study analysis a set of representative receiving antennas from a regional network (Polish ASG-EUPOS), which are summarised in Table 1 and depicted in Fig. 1. The individual PCCs are retrieved from the network operator’s website (ASG EUPOS 2021), while the corresponding type means origin from IGS (IGS CB 2021)

Differences of type means and individual antenna calibrations can easily reach levels of more than  $\pm 1$  mm on each frequency, which is an international accepted consensus (so called *rule-of-thumb*). By applying the ionosphere-free (LO) linear combination as needed for regional and global GNSS processing, these differences increase rapidly.

The analysis of elevation-only dependent  $\Delta$ PCCs can mislead the comparison as examples in Fig. 2 indicate. There, different pattern structures are identified with systematic repetitions. Figure 2a shows deviations below 4 mm except a wobble at 135° azimuth. The  $\Delta$ PCC pattern also shows a repeated ring structure with magnitudes of +3 mm. Regard-

**Table 1** Stations of AGS-EUPOS network and related receive antenna equipment used in this setup

Station	Antenna	Dome	Serial No.	Cal.-Date
BYDG	TRM59900.00	SCIS	5347361485	2014-06-12
CHHN	TRM55971.00	TZGD	36334	2007-10-31
DAZI	TRM59900.00	SCIS	5317361068	2014-09-23
GNIÉ	LEIAR20	LEIM	17098001	2015-09-30
GRUD	TRM55971.00	TZGD	77056	2007-11-13
ILAW	TRM55971.00	TZGD	36524	2007-10-26
KONI	LEIAR20	LEIM	18208017	2015-10-02
KUTN	TRM59900.00	SCIS	5316361054	2014-09-19
SOCH	TRM55971.00	TZGD	36130	2010-02-18
WLOC	TRM55971.00	TZGD	1440929151	2010-02-17

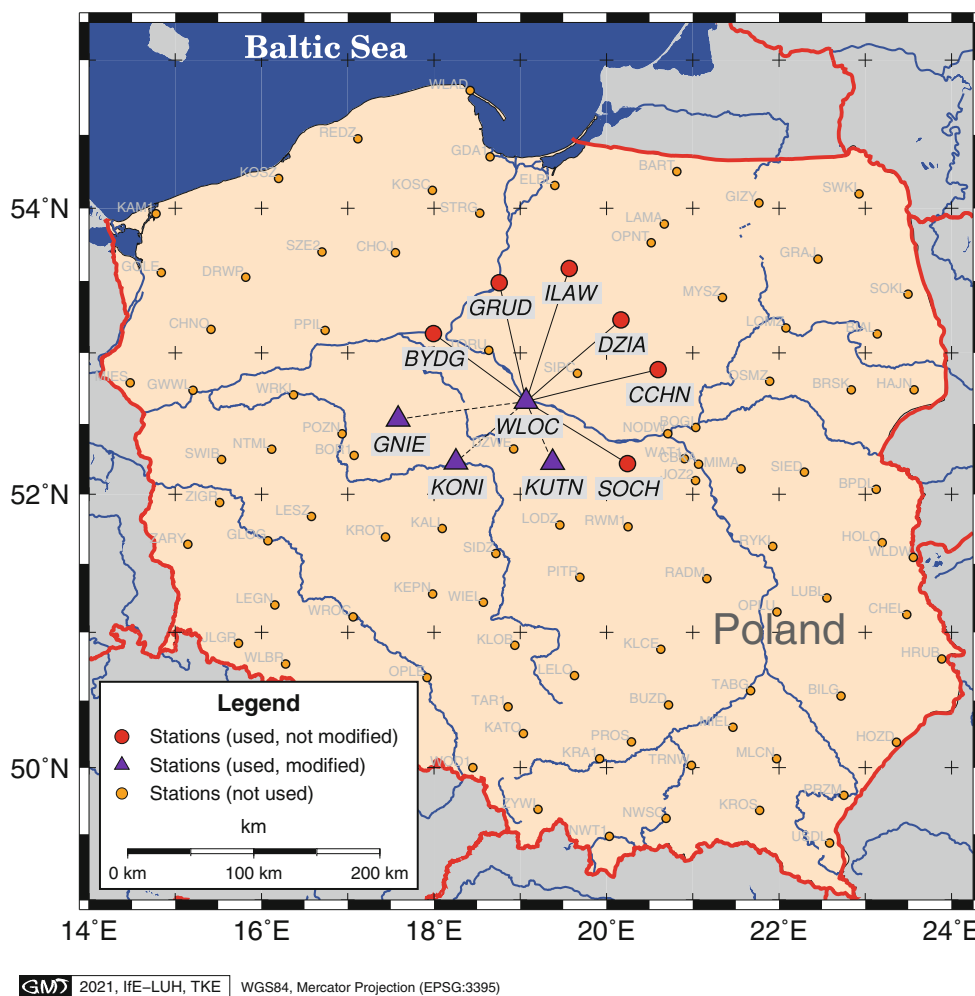
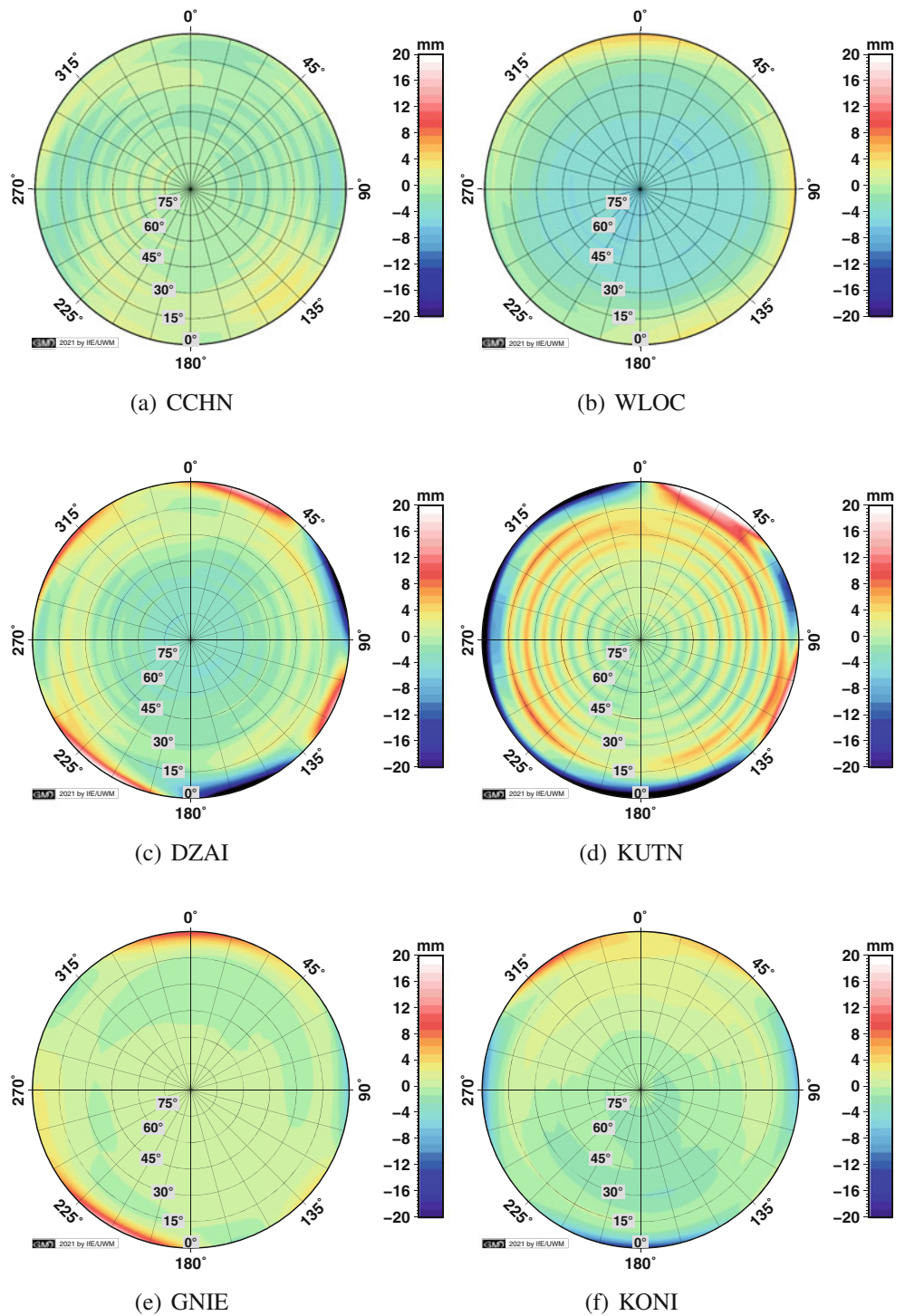


**Fig. 1** Network to assess deviations between PCC models on a minimum constraint network

**Fig. 2** Differential PCC ( $\Delta PCC$ ) pattern for ionosphere-free linear-combination between type-mean and individual calibrations for different receiver antennas, (a,b) TRM55971.00 TZGD, (c,d) TRM59900.00 SCIS and (e,f) LEIAR20 LEIM



ing Fig. 2d, such structure appears again for approx. every 15° elevation angle with magnitudes of +8 mm that occur – despite higher deviations below 5° elevation – also at mid-elevation.

Smaller but systematic deviations between 4–6 mm are detected for the other groups of GNSS antennas with not symmetrically distributed deviations. This indicates that for different geographic locations those pattern topologies (cf.

Fig. 2) will have non-negligible effect above 5° elevation angle.

Mean L0 biases for  $\Delta PCC$  (type mean vs. individual calibrations) vary in our study per group (i.e. antenna model) and overall between -3.6 mm and +2.0 mm for individual antennas (cf. Table 2).

An alternative metric for the comparison of two patterns is the range  $\Delta_{min}^{max}\{PCC\}$  of the differences that considers the

variation with the azimuth and elevation angle (cf. Table 2). In the case of individual  $\Delta PCC$ s, ranges at L0 with magnitudes of 8 mm up to 22.5 mm are detected.

Those variations are projected through zero difference (ZD) processing, e.g. in Precise Point Positioning (PPP, Zumberge et al. 1997), onto the estimated parameters.

In the case of differential GNSS data processing, such as double difference (DD), a different scenario results, as  $\Delta PCC$ s from two independent antennas  $i$  and  $j$  are now combined to form a new set, such as

$$\delta\Delta PCC = \Delta PCC_i - \Delta PCC_j, \quad (3)$$

**Table 2** Summary of mean L0  $\Delta PCC$  pattern for both individual antenna patterns and difference patterns on selected baselines w.r.t WLOC

Station	Mean L0 bias		L0 Range	
	$\Delta PCC$ [mm]	$\delta\Delta PCC_{WLOC}^i$ [mm]	$\Delta PCC$ [mm]	$\delta\Delta PCC_{WLOC}^i$ [mm]
BYDG	-2.4	-3.9	8.5	10.5
CHHN	1.1	-0.4	8.0	8.8
DAZI	-1.8	-3.1	13.3	15.9
GNIE	0.2	-1.5	5.4	12.3
GRUD	0.6	-0.8	9.9	9.9
ILAW	1.1	-0.4	10.5	9.2
KONI	-1.2	-2.8	11.8	16.9
KUTN	-3.6	-5.0	22.5	21.5
SOCH	2.0	0.5	10.4	8.9
WLOC	1.4	-	7.9	-

where the resulting effect can be understood as a baseline-specific antenna. Figure 3 shows this relation for the case of pure elevation dependent differences  $\delta\Delta PCC$ s for several baselines with respect to station WLOC (cf. Fig. 1 and Table 1). For some baselines, the  $\delta\Delta PCC$ s do not exceed three millimetres. However, at elevation angles of 15° significant deviations of up to -10 mm occur if only the elevation dependent  $\delta\Delta PCC$  are considered, or up to -12 mm if the ranges of azimuthal deviations are also considered. By correlating the mean number of available observations with the distribution of realistic satellite constellation for mid latitude located ground stations (cf. Fig. 3), the largest deviation of the  $\delta\Delta PCC$  pattern on L0 occurs at elevation angles with the highest number of expected observations (5500-4000 at 15-30° elevation range), considering an elevation dependent weighting. Menge et al. (1998) describe the effect of an erroneous pattern in terms of geographical location and baseline length.

It is worth noting that the analysis of elevation dependent PCCs can lead to significant misinterpretations of the pattern deviations. Hence, they only can serve as an initial indicator (cf. Table 2). They do not provide reliable benchmarks for comprehensive quality assessment.

Examining the range metric for L0 in Table 2, the smallest deviations result from the fact that the same antenna type (TRM55971.00 TZGD) is combined when forming the baseline (mean L0 bias of -0.8 mm to +0.5 mm with a corresponding range of 9-10 mm). Larger

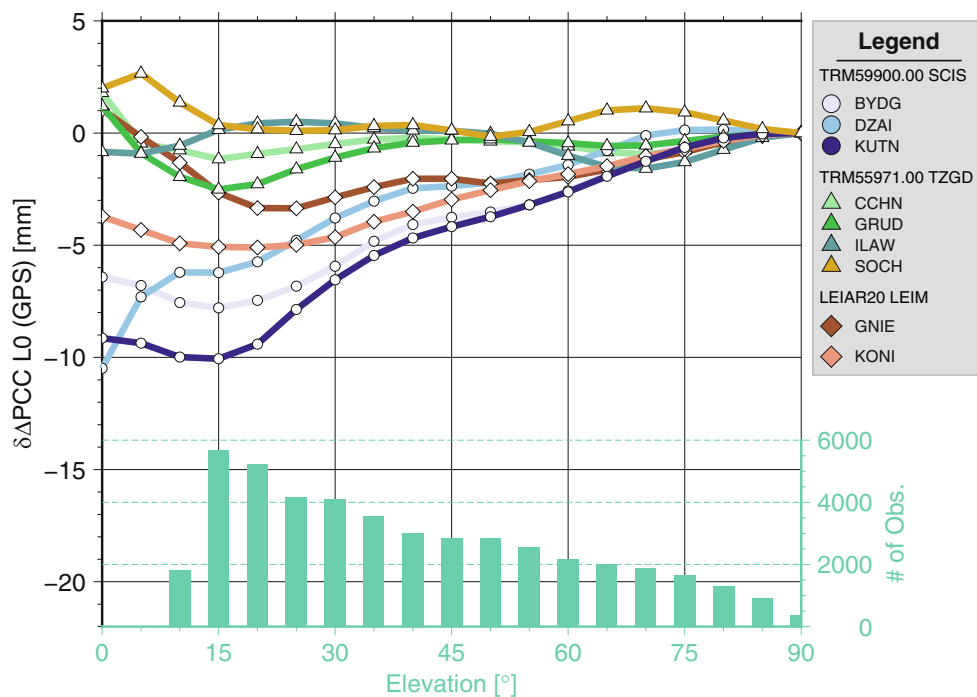
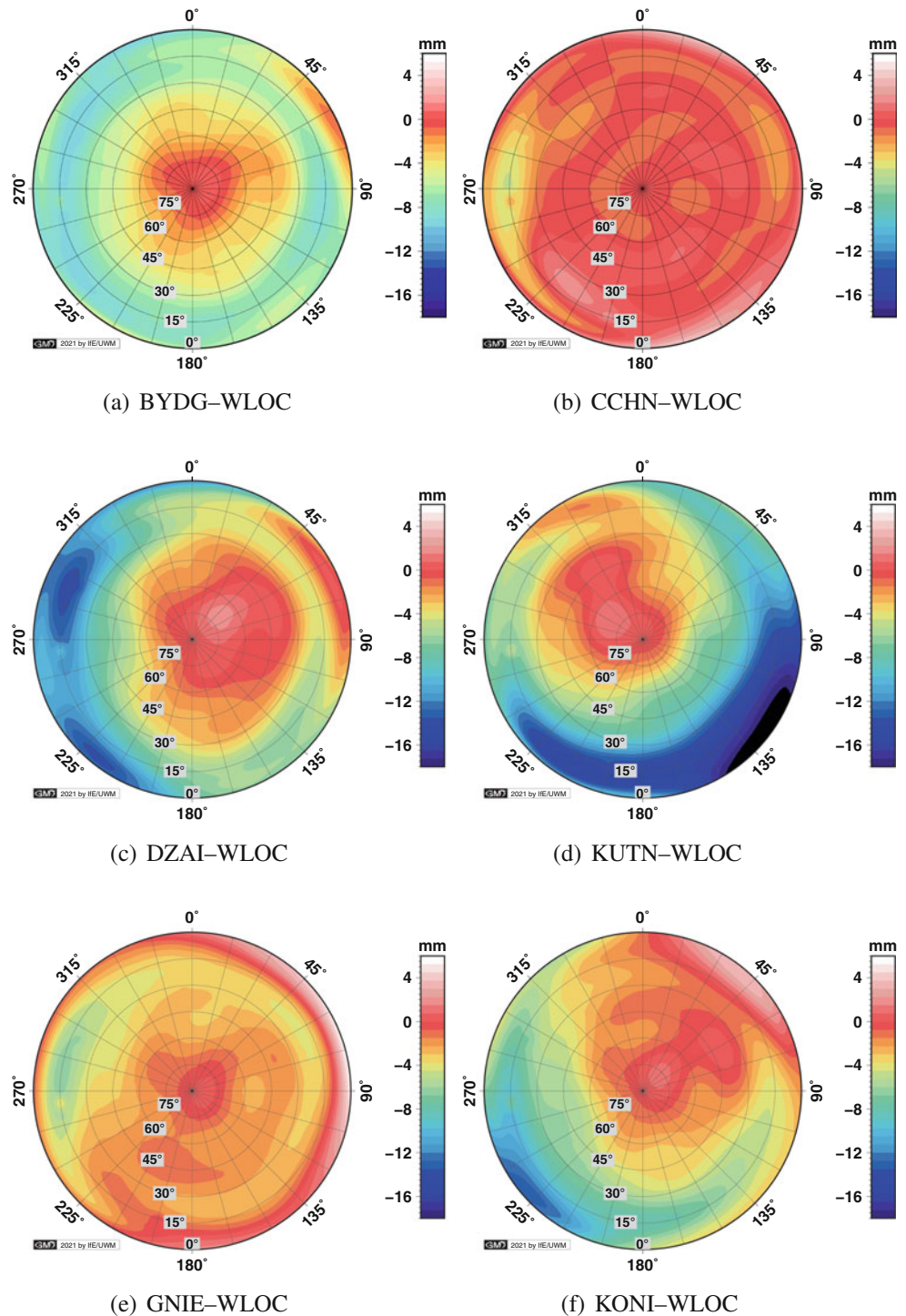


**Fig. 3** Individual derivations of elevation dependent  $\Delta PCC$ s for analysed baselines and their mean distribution of maximal number of observations per elevation bin

**Fig. 4** Different receiver antennas baseline specific  $\delta\Delta\text{PCC}$  for ionosphere-free (L0) linear combination for type mean and individual calibrations with respect to WLOC, (a,b) TRM55971.00 TZGD, (c,d) TRM59900.00 SCIS and (e,f) LEIAR20 LEIM



deviations are caused by different antenna models (cf. Table 2).

Azimuth and elevation angle dependent  $\delta\Delta\text{PCC}$ s are provided in Fig. 4, highlighting that deviations for CCHN can vary from  $-4\text{ mm}$  to  $+4\text{ mm}$  in the best case. Larger deviations are also reported, which results in systematic effects. This is shown, for example, in a  $\Delta h \sin \theta$  effect, with  $\Delta h = -8\text{ mm}$  at the station BYDG.

For the stations DZAI, KUTN and KONI a shift of the pattern from  $0\text{ mm}$  to  $-12\text{ mm}$  is found as well. On the contrary, a twist is present at GNIE (cf. Fig. 4). These features occur regularly, suggesting that modelling of these components by measures of the generic pattern (Geiger 1988; Kersten and Schön 2016) is beneficial to assess the appropriate type and characteristics of the resulting impact.

### 3 Modelling and Assessing GNSS Antenna Variability

#### 3.1 Generic Patterns

Two approaches are possible to assess the effect of different PCC patterns: (1) applying the two patterns (individual and type mean PCCs) in the processing and analysing the effect on the parameters, or (2) modelling the  $\Delta$ PCC and  $\delta\Delta$ PCC for the corresponding processing strategy, such as ZD and DD, and achieve a numerical model for typical characteristics. In this paper, we apply the second approach for a case study – following a semi-analytical approach.

Analytical formulations of generic patterns are introduced by Geiger (1988). They are parameterised by continuous integral functions with parameters for the local azimuth  $\lambda$  and elevation angle  $\theta$  that results in a range error  $\delta\delta r(\lambda, \theta)$ . Considering the findings from Sect. 2.3, we validate selected generic patterns (cf. Table 3). Characteristics and magnitudes of pattern variability are resulting from previous section (cf. Table 2).

*One and four-wire* model applies to study asymmetrical structures as

$$\delta\delta r(\theta, \lambda) = A \sin \theta + D \cdot \sin \theta \cos (N\lambda + (p4W\theta - Na_0)) \tag{4}$$

with amplitudes  $A$  and  $D$ , the number of wires  $N$ , the polarisation  $p$  of the antenna (corresponding to  $p = -1$  for right hand circular polarised) and the number of windings  $W \equiv 1$ , and the initial azimuth  $a_0 = 0$ . The parameter  $N$  applies for the one/four-wire model ( $N = 1/4$ ).

*Chess board* is a regular pattern in  $\lambda$  with factors for cosine and sine functions  $cl, sl$  and in  $\theta$  with factors  $ct, st$  that are applied in

$$\delta\delta r(\theta, \lambda) = A (\cos ct\theta) \sin (st\theta) \cos(cl\lambda) \cos (sl\lambda) \tag{5}$$

to interpret and model the variability of PCC patterns.

#### 3.2 Methodology and Evaluation

The original PCC patterns are applied as regular using the ANTEX format. The modified patterns  $PCC^*$  are applied

**Table 3** Model parameters for generic patterns in the analysis study

No	Model	A [mm]	N	D [mm]	Chess board		
					ct	cl	st = sl
1	One-wire helix	5	1	5	–	–	–
2	Four-wire helix	5	1	5	–	–	–
3	Four-wire helix	20	1	5	–	–	–
4	Chess board	5	–	–	7	3	1

by considering the range errors  $\delta\delta r(\theta, \lambda)$  on the individual patterns using Eq. (2) for selected station  $i$  like

$$\{PCC_{s,f}^*\}_i = \{PCC_{s,f}\}_i + \delta\delta r, \tag{6}$$

which are shown in Fig. 1. These  $\{PCC_{s,f}^*\}_i$  are also formulated in ANTEX format and are applied accordingly in the GNSS processing. As a result, this study seeks to answer the question of whether the semi-analytical method provides enough information to analyse the effects of the antennas with sufficient accuracy to justify continuing towards a purely analytical approach in future.

Following the requirements of a realistic scenario, selected sites (approx. 35%) in a network of at least ten GNSS stations (cf. Fig. 1) are modified. The stations are selected to be at similar altitude, circularly distributed, and having similar baseline lengths relative to the centre station Włocławec (WLOC). The network is adjusted using minimum constraint datum.

The GNSS data processing for ten consecutive days applies for both, ZD (estimation strategy) using the NAPEOS GNSS Software (Springer and Dow 2009), and DD (elimination strategy) using Bernese GNSS Software (Dach et al. 2015). Close similar configurations are used in the processing of the data in a normal equation batch strategy. In NAPEOS, the ZTDs are modelled with Saastamoinen (Saastamoinen 1972) and Global Pressure and Temperature (GPT) model and as mapping function the corresponding global mapping function (GMF). In Bernese, we apply the dry Vienna Mapping Function (VMF, Boehm et al. 2006) as the ZTD model and for the wet part the corresponding VMF wet mapping function. In both cases the resolution of the ZTDs is one hour with loose absolute and relative constraints. The impact of antenna variability was analysed by comparing the modified network solution against a reference solution, derived by applying individual PCC corrections for all ten days.

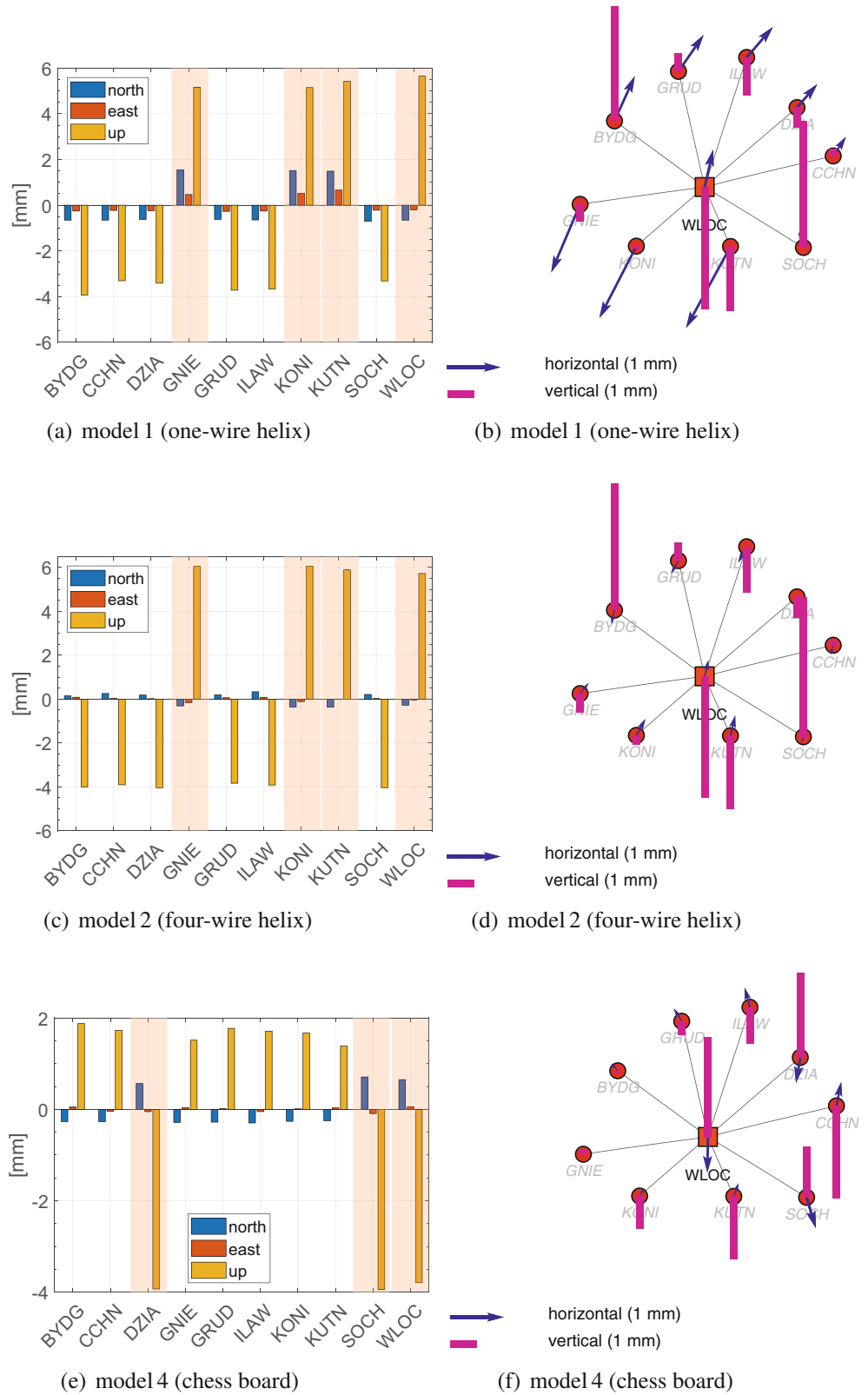
## 4 Results

### 4.1 Position Domain

The variability of the receiver antenna PCCs are analysed for both ZD and DD processing approach and result in similar solutions. The applied error pattern introduce affine distortions to the processed network for all studied cases through the chosen datum setting (minimum constraint). This is illustrated in Fig. 5 by the combined ten days solution on the coordinate domain. While the asymmetrical case of one-wire helix (model 1, cf. Fig. 5a) leads to deviation in the topocentric North, East and Up component, this is not the case for the symmetrical patterns (cf. Fig. 5c) as the



**Fig. 5** Results of combined network solution for individual models and modified PCCs for positions (a, c, e) and network distortion as residuals after a 3d Helmert transformation (b, d, f). Shaded backgrounds in (a, c, e) indicate the stations that were modified with pre-defined generic patterns



effect is projected in majority to the Up component. This relationship became apparent through the effects on the overall geometry of the network, as shown in Figs. 5b, d

and f for the residuals of a 3d Helmert transformation with respect to the reference solution. Because of the minimum constraint datum, the effects of the modified stations in the

network will be absorbed by all the non-modified stations. This leads to the effect that all unmodified stations will show a negative offset that is the result of the sum of all effected stations divided by the number of all unaffected stations. Example: in Fig. 5c an impact on the Up component of +6 mm is introduced, leading to a magnitude of 24 mm which is distributed by all 6 unmodified stations that result to an offset of -4 mm in the Up component. Those findings are close similar to achieve for the other studied models, but the effect in the Up component varies slightly due to additional effects on the horizontal components.

The characteristic of the deformed pattern also leads to a deformation of the overall network geometry, as shown in Fig. 5b. There, the network enlarges towards the northeast and southwest, resulting in a scaling effect that has its origin in the centre of the network. However, the scaling has more effect on the position estimates and less on the ZTDs, as the impact on the Up component is different. Nevertheless, the spatial distribution of the effects in the Up component of the network is important to know, as it will affect the spatial distribution of the ZTDs and thus the PWV/IWV derivatives.

## 4.2 Troposphere Parameters

The effects on the tropospheric parameters are in close relation to the network geometry and thus the effects of the Up component. An explanation gives Fig. 6 for statistical metrics, such as cumulative histogram and quantile graphs. The asymmetrical case of one-wire helix (model 1) affects all position components (height and horizontal), leading into variations below 4 mm for approx. 95% of ZTDs (cf. Fig. 6a). Assuming a symmetrical pattern with exactly the same magnitude of distortion leads to higher deviations, so that only 80% of all ZTDs of less than 4 mm are affected, but higher values of up to 8 mm definitely appear (cf. Fig. 6b). Assuming a gross error in the patterns (amplitude of 20 mm, model 3) results again to the fact that 95% of ZTD biases are below 4 mm for the non-affected stations (cf. Fig. 6c), but now the impact of affected antennas on the network is separated. The smallest impact is detected for model 4 – a asymmetrical variation with regular variations along azimuth and elevation angles – that results to variation of ZTDs of below 3 mm in 95% of all ZTDs.

The effect that is introduced by modified PCCs seems to be normal distributed in a first approximation at least between  $\pm 1.5$  mm (cf. Figs. 6e–h). However, in the case of model 2 (cf. Fig. 6f) and model 4 (cf. Fig. 6h) not only an offset was detected but also a systematic variation. The offsets found in the quantile graphs are in correspondence to the magnitudes listed in Table 4. The RMS values of model 1 are quite small with 2.2 mm and show only marginal differences for the affected stations (cf. Table 4). It is worth

**Table 4** Summary of results for the ZTD time series estimates versus the reference solution for the models 1–3; the asterisk mark correspond to those stations where modified PCC patterns were applied

	Model 1		Model 2		Model 3	
	Bias [mm]	RMS [mm]	Bias [mm]	RMS [mm]	Bias [mm]	RMS [mm]
BYDG	0.2	2.2	-0.4	3.7	-2.0	3.2
CCHN	0.4	2.2	-0.5	3.7	-1.8	3.2
DZAI	0.3	2.1	-0.5	3.7	-2.0	3.3
GNIE*	1.1	2.6	0.9	3.7	2.2	3.9
GRUD	0.3	2.1	-0.4	3.7	-2.0	3.2
ILAW	0.2	2.1	-0.4	3.7	-1.9	3.2
KONI*	1.2	2.5	0.8	3.7	2.0	3.5
KUTN*	1.2	2.5	0.9	3.7	2.2	3.7
SOCH	0.4	2.1	-0.5	3.7	-1.9	3.2
WLOC*	1.5	2.5	0.8	3.7	1.7	3.5

noting that the noise of the ZTDs gets also affected by the kind of applied generic pattern, which indicates a close relation between the characteristic of error contribution on the pattern and effect on the estimated ZTDs.

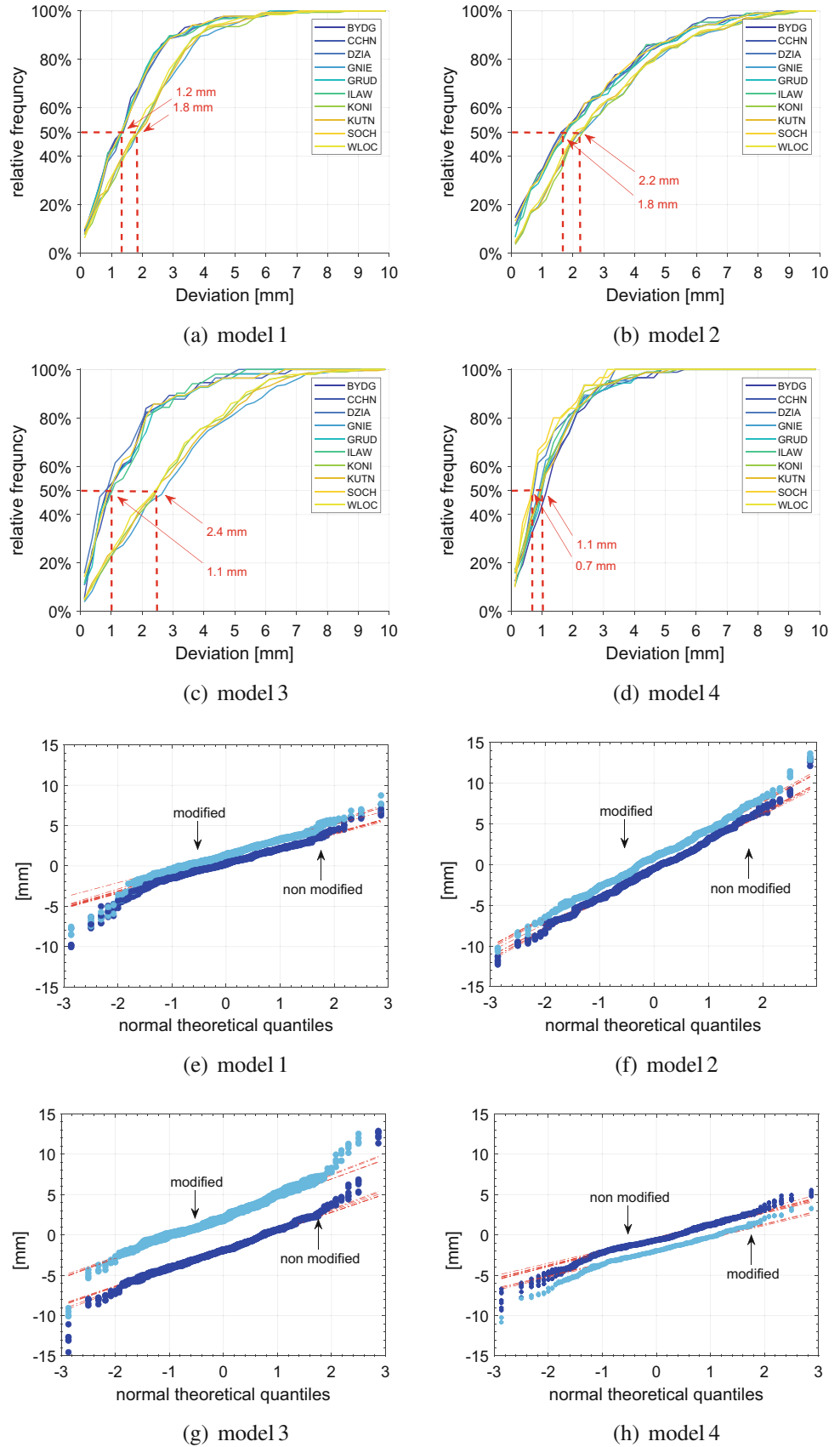
## 5 Conclusions

In this contribution, we have shown that deviations and defects in the PCC patterns are likely to have significant effects on the position level and on estimated ZTDs. With this study, there is a contribution to trace the error on the pattern and assign the impact in order to gain more understanding on the current shortcomings of GNSS water vapour time series – i.e. to gather information on the cause and effect. Currently, such variations are found, for example, between type mean and individual calibrations, which have different magnitudes and pattern characteristics. For instance, we have shown that frequency dependent deviations are significantly amplified with the L0 linear combination, so that the effects on the PCC patterns easily reach up to 12 mm. Likewise, we have been able to assign repeatable pattern variations. Our work has also shown that a pure elevation dependent representation is neither adequate nor beneficial to qualitatively describe the variability of the variations.

The structure of PCC patterns are the key to applying analytical functions for describing these variations. To learn how each PCC topology behaves in GNSS data processing – taking into account the satellite geometry – we processed the patterns in ZD and DD and compared the results with respect to the ZTDs.

Because of high correlation of the Up component and ZTDs, similarities are found. Depending on the patterns, non-normally distributed deviations have been identified on the ZTDs, which are related to the type of introduced distortion and show deviations of up to 8 mm. The effect on the

**Fig. 6** Variations of ZTDs by cumulative histograms (a–d) and quantile representation (e–h) considering a minimum constraint datum



ZTDs is also strongly depending on the selected datum and varies accordingly.

Consequently, future models need to take into account the datum setting in addition to the analytical description of the antenna deviation and the underlying satellite geometry.

**Acknowledgements** The authors gratefully acknowledge the Polish ASG-EUPOS network providers for the ANTEX antenna and RINEX observation files from their network. We also thank the Centre of Orbit Determination in Europe (CODE) and the European Space Operations Centre (ESOC) at ESA, which provide high accurate GNSS products.

## References

- Araszkiewicz A, Völksen C (2016) The impact of the antenna phase center models on the coordinates in the EUREF permanent network. *GPS Solut* 21(2):747–757. <https://doi.org/10.1007/s10291-016-0564-7>
- ASG EUPOS (2021) <https://www.asgeupos.pl>
- Beutler G, Bauersima I, Gurtner W, Rothacher M, Schildknecht T, Geiger A (1988) Atmospheric effects on geodetic space measurements, chap Atmospheric refraction and other important biases in GPS carrier phase observations, pp 15–43
- Bevis M, Businger S, Herring T, Rocken C, Anthes R, Ware R (1992) GPS meteorology: Remote sensing of atmospheric water vapor using the Global Positioning System. *J Geophys Res* 97:15787–15801
- Bock O, Parracho AC (2019) Consistency and representativeness of integrated water vapour from ground-based GPS observations and ERA-interim reanalysis. *ACP* 19(14):9453–9468. <https://doi.org/10.5194/acp-19-9453-2019>
- Boehm J, Werl B, Schuh H (2006) Troposphere mapping functions for GPS and very long baseline interferometry from European Centre for Medium-Range Weather Forecasts Operational Analysis Data. *J Geophys Res* 111(B2):B02406. <https://doi.org/10.1029/2005JB003629>
- Dach R, Lutz S, Walser P, Fridez P (eds) (2015) Bernese GNSS software version 5.2. University of Bern, Bern Open Publishing. <https://doi.org/10.7892/boris.72297>
- Davis JL, Herring TA, Shapiro II, Rogers AEE, Elgered G (1985) Geodesy by radio interferometry: Effects of atmospheric modeling errors on estimates of baseline length. *Radio Sci* 20(6):1593–1607. <https://doi.org/10.1029/rs020i006p01593>
- Douša J, Dick G, Kačmařík M, Brožková R, Zus F, Brenot H, Stoycheva A, Möller G, Kaplon J (2016) Benchmark campaign and case study episode in central Europe for development and assessment of advanced GNSS tropospheric models and products. *Atmos Meas Tech* 9(7):2989–3008. <https://doi.org/10.5194/amt-9-2989-2016>
- Geiger A (1988) Modeling of phase centre variation and its influence on GPS-positioning. In: *GPS-techniques applied to geodesy and surveying*. Lecture Notes in Earth Sciences, vol 19. Springer, pp 210–222. <https://doi.org/10.1007/BFb0011339>
- IGS CB (2021) <https://igs.org/>
- Kersten T, Schön S (2016) Receiver antenna phase center models and their impact on geodetic parameters. In: *IAG Symposia*, vol 147. Springer, Cham, pp 253–259. [https://doi.org/10.1007/1345\\_2016\\_233](https://doi.org/10.1007/1345_2016_233)
- Krzan G, Dawidowicz K, Wielgosz P (2020) Antenna phase center correction differences from robot and chamber calibrations: The case study LEIAR25. *GPS Solutions* 24(2). <https://doi.org/10.1007/s10291-020-0957-5>
- Menge F, Seeber G, Völksen C, Wübbena G, Schmitz M (1998) Results of the absolute field calibration of GPS antenna PCV. In: *ION GPS 1998*, Sept. 15–18, Nashville, TN, USA, pp 31–38
- Nguyen KN, Quarello A, Bock O, Lebarbier E (2021) Sensitivity of change-point detection and trend estimates to GNSS IWV time series properties. *Atm* 12(9):1102. <https://doi.org/10.3390/atmos12091102>
- Ning T, Wickert J, Deng Z, Heise S, Dick G, Vey S, Schöne T (2016) Homogenized time series of the atmospheric water vapor content obtained from the GNSS reprocessed data. *J Clim* 29(7):2443–2456. <https://doi.org/10.1175/JCLI-D-15-0158.1>
- Odijk D, Wanninger L (2017) Differential positioning. In: *Springer Handbook of global navigation satellite systems*. Springer, pp 753–780. [https://doi.org/10.1007/978-3-319-42928-1\\_26](https://doi.org/10.1007/978-3-319-42928-1_26)
- Rothacher M, Schmid R (2010) ANTEX: The antenna exchange format, Version 1.4. <https://files.igs.org/pub/data/format/antex14.txt>
- Rothacher M, Schaer S, Mervat L, Beutler G (1995) Determination of antenna phase center variations using GPS data. In: *IGS workshop*, 15–18 May, Potsdam, Germany
- Saastamoinen J (1972) Contributions to the theory of atmospheric refraction. *Bull géodésique* 105(1):279–298. <https://doi.org/10.1007/BF02521844>
- Santerre R, Geiger A, Banville S (2017) Geometry of GPS dilution of precision: revisited. *GPS Solut* 21(4):1747–1763. <https://doi.org/10.1007/s10291-017-0649-y>
- Springer T, Dow JM (2009) NAPEOS—mathematical models and algorithms. Tech. rep., European Space Agency (ESA/ESOC, Darmstadt)
- Tralli DM, Lichten SM, Herring TA (1992) Comparison of Kalman filter estimates of zenith atmospheric path delays using the Global Positioning System and very long baseline interferometry. *Radio Sci* 27(6):999–1007. <https://doi.org/10.1029/92rs01779>
- Vaquero-Martinez J, Antón M, de Galisteo JPO, Román R, Cachorro VE, Mateos D (2019) Comparison of integrated water vapor from GNSS and radiosounding at four GRUAN stations. *Sci Total Environ* 648:1639–1648. <https://doi.org/10.1016/j.scitotenv.2018.08.192>
- Vey S, Dietrich R, Fritsche M, Rülke A, Steigenberger P, Rothacher M (2009) On the homogeneity and interpretation of precipitable water time series derived from global GPS observations. *J Geophys Res* 114(D10). <https://doi.org/10.1029/2008JD010415>
- Villiger A, Dach R, Schaer S, Prange L, Zimmermann F, Kuhlmann H, Wübbena G, Schmitz M, Beutler G, Jäggi A (2020) GNSS scale determination using calibrated receiver and Galileo satellite antenna patterns. *J Geod* 94(9). <https://doi.org/10.1007/s00190-020-01417-0>
- Zeimet P, Kuhlmann H (2008) On the accuracy of absolute GNSS antenna calibration and the conception of a New Anechoic chamber. In: *FIG working week 2008 - Integrating generations*, June 14–19, Stockholm, Sweden, p 16
- Zumberge JF, Heflin MB, Jefferson DC, Watkins MM, Webb FH (1997) Precise point positioning for the efficient and robust analysis of GPS data from large networks. *J Geophys Res* 102(B3):5005–5017. <https://doi.org/10.1029/96JB03860>

**Open Access** This chapter is licensed under the terms of the Creative Commons Attribution 4.0 International License (<http://creativecommons.org/licenses/by/4.0/>), which permits use, sharing, adaptation, distribution and reproduction in any medium or format, as long as you give appropriate credit to the original author(s) and the source, provide a link to the Creative Commons license and indicate if changes were made.

The images or other third party material in this chapter are included in the chapter's Creative Commons license, unless indicated otherwise in a credit line to the material. If material is not included in the chapter's Creative Commons license and your intended use is not permitted by statutory regulation or exceeds the permitted use, you will need to obtain permission directly from the copyright holder.





# Estimation and Validation of Codephase Center Correction Using the Empirical Mode Decomposition

Yannick Brev a , Johannes Kröger , Tobias Kersten , and Steffen Schön

## Abstract

In high precision Global Navigation Satellite Systems (GNSS) applications, it is necessary to take phase center corrections (PCC) into account. Beside these corrections for carrier phase measurements, also corrections for the codephase are necessary, so called codephase center corrections (CPC). The CPC, also known as group delay variations, are antenna dependent delays of the received codephase, which are varying with azimuth and elevation of the incoming GNSS signal. A concept for estimating absolute CPC and PCC for multi GNSS signals has been established by the Institut für Erdmessung.

In this paper, the standard calibration approach with a sampling rate of 1 Hz is briefly described, which works well for PCC estimation. The main challenge of this approach for estimating repeatable CPC patterns is the significantly higher noise to pattern ratio in the observations compared to PCC determination. Therefore, an alternative processing strategy is presented in this contribution. By increasing the sampling rate to 10 Hz, the empirical mode decomposition can be used to reduce the noise of the input observations by maintaining all pattern information. With this method, the calibration repeatability is improved by 46% to 60% for GPS and Galileo C1C signals for a geodetic antenna. Moreover, the estimated pattern is validated in the positioning domain with a single point positioning approach. By considering the estimated CPC the accuracy of the height component can be improved.

## Keywords

Absolute antenna calibration · Codephase center corrections · Empirical mode decomposition · Group delay variations

## 1 Introduction

To ensure accurate positioning with Global Navigation Satellite Systems (GNSS), like precise point positioning (PPP), all error sources should be taken into account. One of them are phase center corrections (PCC), which can be divided into a constant part, the mean phase center offset (PCO),

and direction-dependent part, so called phase center variations (PCV, Rothacher et al. (1995)). Absolute PCC can be estimated by using synthetic GNSS carrier frequencies in an anechoic chamber (Görres et al. 2006) or by using real GNSS observations in the field and a robot to rotate and tilt the antenna under test. Since the PCC estimation is independent from the PCC of a reference antenna, this approach is referred to as an *absolute calibration*.

A concept for determining absolute PCC for GPS and GLONASS L1 and L2 signals with a robot was developed at the Institut für Erdmessung (IfE) in close cooperation with GEO++ (Menge et al. 1998; Wübbena et al. 2000; Böder et al. 2001). Further improvements at IfE extended the

Y. Brev a (✉) · J. Kröger · T. Kersten · S. Schön  
Leibniz Universität Hannover, Institut für Erdmessung, Hannover,  
Germany  
e-mail: [brev a@ife.uni-hannover.de](mailto:brev a@ife.uni-hannover.de)

approach to estimated PCC also for new multi-GNSS signals like GPS L5, Galileo or Beidou (Kröger et al. 2019, 2021).

Beside the well known PCC, also antenna related code delays (CPC)—also known as group delay variations (GDV)—become more important nowadays, e.g. for navigation or ambiguity resolution. In code-carrier linear combinations (LC), like Melbourne-Wübbena, the CPC can have an impact on the ambiguity resolution, when the magnitude of the respective antenna CPC is in the range of the LC wavelength. Kersten and Schön (2017) demonstrated, that jumps and drifts in the L1 carrier phase solution can be avoided by applying the CPC. In principle, the algorithm for absolute PCC estimation can also be used to estimate CPC. Kersten and Schön (2017) showed the estimated CPC pattern for different low cost and geodetic antennas for GPS C1C signal, Brevia et al. (2019) estimated multi-GNSS CPC. Only a few other groups published their work on CPC/GDV. Wübbena et al. (2008) estimated CPC with their robot in a real-time process in a Kalman filter based on undifferentiated observations. The group from TU Dresden determined satellite and receiver antenna GDV together in a network approach by using code-minus-carrier linear combinations (CMC, Wanninger et al. (2017), Beer et al. (2019)). In 2019, Geo++ published absolute GDV for a set of 36 antennas (Wübbena et al. 2019); based on these values Beer et al. (2021) were able to estimate absolute GDV for GNSS-satellite antennas with their CMC approach. However, one of the main challenges of CPC estimation compared to PCC, is the low pattern to noise ratio.

In this paper, an improved strategy to estimate absolute CPC is presented that aims to reduce the observation noise without deforming the CPC pattern. Section 2 briefly describes the current standard algorithm with 1 Hz sampling rate for estimating absolute CPC at IfE and illustrates challenges for achieving calibrations with a high repeatability. Section 3 describes the (ensemble) empirical mode decomposition (EEMD), which was introduced by Huang et al. (1998), where Sect. 4 shows the benefits of this method in antenna calibration and the necessity of a higher sampling rate. Calibration results of a geodetic antenna for GPS and Galileo C1C signal with the EEMD approach are shown in Sect. 5. A validation with a single point positioning (SPP) approach is reported in Sect. 6. Section 7 closes this paper with a conclusion.

## 2 Antenna Calibration at IfE

### 2.1 Definition of Codephase Center Correction

CPC are antenna dependent delays of the received codephase, which vary with azimuth ( $\alpha$ ) and elevation ( $el$ ) of

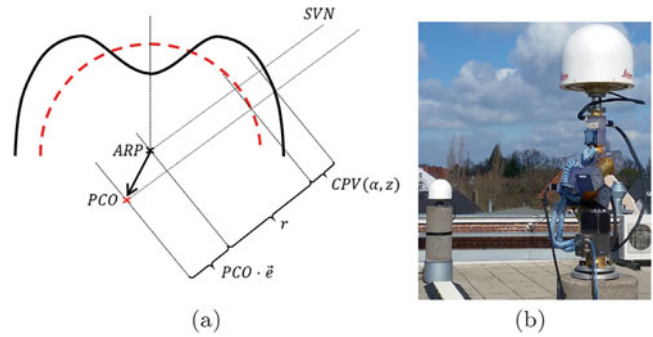


**Fig. 1** Basic definitions (a) Definition of CPC (b) and calibration setup at IfE

the incoming signal. The CPC are divided into a codephase center offset (PCO), which is projected onto the line-of-sight unit vector  $e$  towards the satellite  $k$  and codephase center variation (CPV). They can be calculated by

$$CPC(\alpha^k, el^k) = -PCO \cdot e(\alpha^k, el^k) + CPV(\alpha^k, el^k) + r. \quad (1)$$

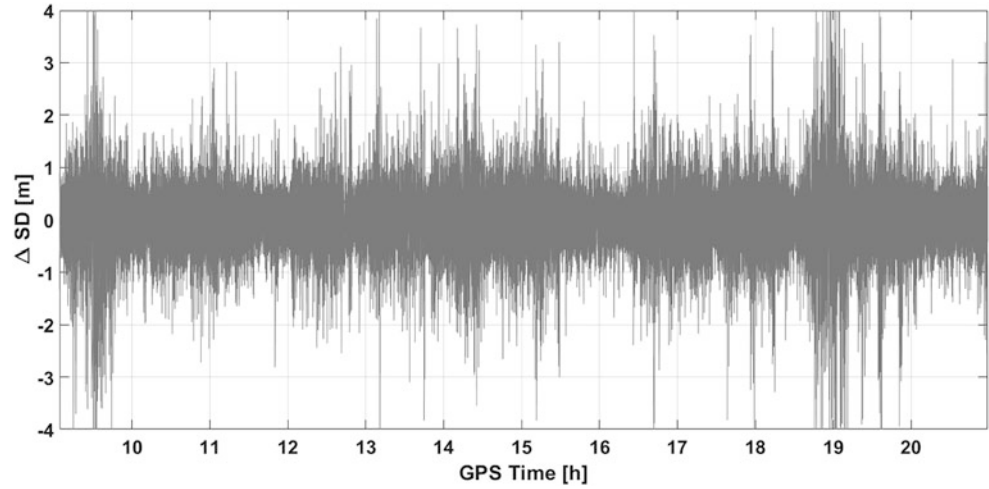
The parameter  $r$  is a constant part, which cannot be estimated without additional information. To remove the rank deficit, a datum has to be defined.

Figure 1a shows a sketch of the geometrical interpretation of the CPC. The dashed red line indicates the theoretical omnidirectional radiation pattern. The CPV are defined by the difference between the actual and the ideal codephase front in direction of the incoming GNSS signal. The PCO is defined by the difference between the antenna reference point (ARP) and the mean codephase center. IfE developed an algorithm to estimate CPC and PCC, which is described in the next following Sects. 2.2 and 2.3.

### 2.2 Data Acquisition

IfE is a calibration facility accepted by the IGS. For the estimation of phase and codephase center corrections a robot tilts and rotates the antenna under test (AUT) around a specific point in space. In the foreground of Fig. 1b the robot can be seen with an AUT. The geodetic antenna in the background is used as a reference. Both forming a short baseline of about 8 m. Each antenna is connected to a Septentrio PolaRx5TR receiver which are synchronised by an external frequency standard (Stanford Rubidium FS725). This setup allows forming time-differenced single differences  $\Delta SD$  with a sampling rate of 1 Hz. The benefit of this approach is, that almost all errors sources are cancelled out or are reduced to a negligible magnitude. This holds true for atmospheric refraction, multipath effects due to the environment, satellite dependent errors, CPC of the reference

**Fig. 2** Time differenced single differences with a sampling interval of 1 Hz for a Novatel703GGG.R2



antenna, etc:

$$\Delta SD^k(t_i) = \Delta CPC_{AUT}^k(t_i, t_{i+1}) + \epsilon \quad (2)$$

with  $\Delta CPC$  the CPC pattern difference of the antenna under test between two robot poses and noise  $\epsilon$ .

Figure 2 shows exemplary the  $\Delta SD$  from a calibration of a Novatel703GGG.R2 (S/N: 12420018) for the GPS C1C signal.

### 2.3 Estimation Approach

The CPC are in general parameterised as spherical harmonics:

$$CPC(a^k, z^k) = \sum_{m=1}^{m_{max}} \sum_{n=0}^m \tilde{P}_{mn}(\cos z^k) \cdot (a_{mn} \cos(n\alpha^k) + b_{mn} \sin(n\alpha^k)) \quad (3)$$

with degree  $m = 8$  and order  $n = 8$ , the fully normalised Legendre function  $\tilde{P}$ , azimuth  $\alpha$  and zenith angle  $z$ . First, the unknowns  $a_{mn}$  and  $b_{mn}$  are estimated with the input observations  $\Delta SD$  in a least-squares adjustment. Afterwards, the estimated coefficients are inserted again in Eq. 3 to estimate a grid with a width of typically 5 degree. From this grid, the unknown PCO of the AUT is estimated in a least-squares adjustment, where the residuals indicate the CPV. A detail description of the estimation process can be found in Kersten and Schön (2017) and Kröger et al. (2021).

### 2.4 Challenges for Determining Codephase Center Correction

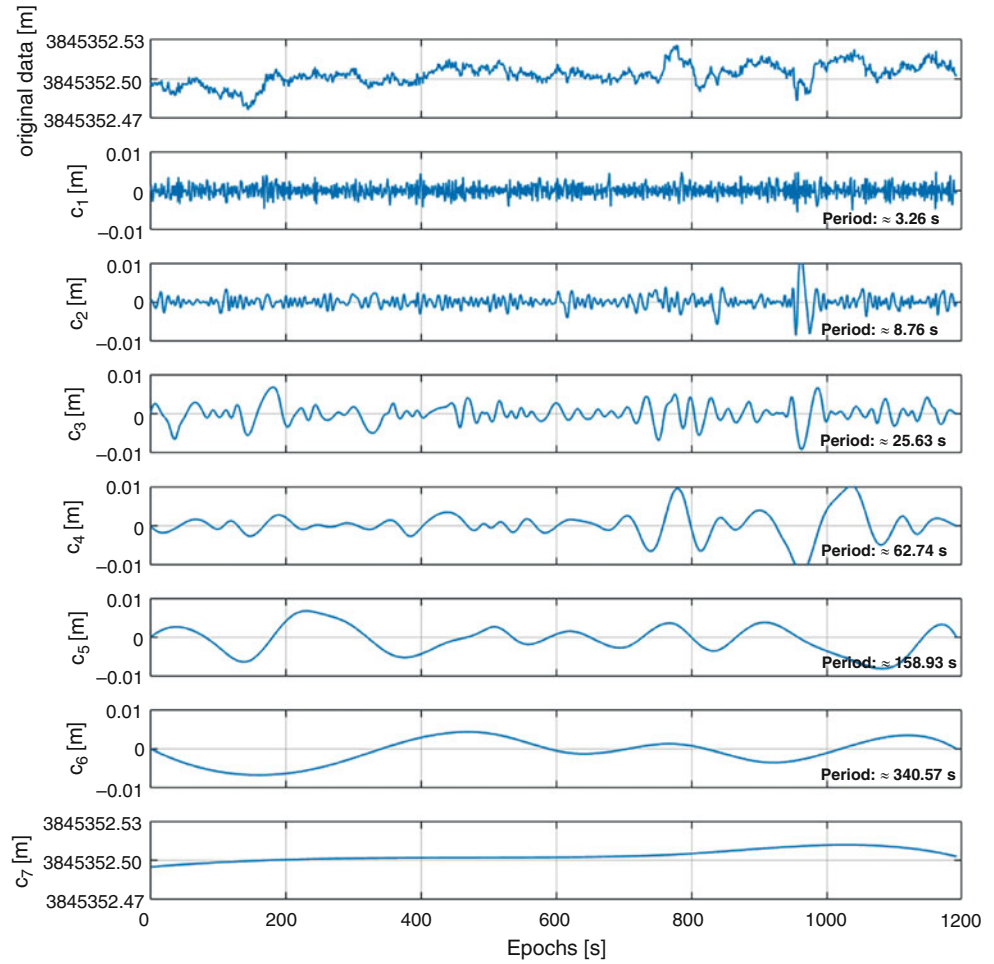
The estimation of PCC works well with the described approach. The repeatability of the estimated patterns for several GNSS signals are below 1 mm RMS (Kröger et al. 2020). This is possible, because the magnitude of the  $\Delta SD$  correlates with the PCC pattern. In other words, the noise is not dominating the signal, which leads to a very good pattern to noise ratio. However, for codephase signals, the ratio between pattern and noise is less favourable, up to a factor of 100. To improve the repeatability of the codephase pattern, the noise needs to be reduced to increase the pattern to noise ratio without losing important pattern information. Here, the applicability of the empirical mode decomposition is tested for this task.

### 3 (Ensemble) Empirical Mode Decomposition

In order to reduce the noise of the input  $\Delta SD$  and simultaneously maintaining all pattern information, the empirical mode decomposition (EMD) is introduced here. This time frequency data analysis method, developed by Huang et al. (1998), allows to decompose any complex dataset (non-linear, non-stationary, ...) into finite number of intrinsic mode functions (IMF). An IMF has to fulfil two conditions: (i) number of extrema and zero crossings must be equal or differ at most by one and (ii) the mean value of the two envelopes, defined by local maxima and minima, is zero.



**Fig. 3** Example of EMD for a time series measured with RTK shown in the top panel



All depending IMF from a time series  $X(t)$  can be calculated by using the sifting process. To this end, the local maxima and minima of  $X(t)$  have to be identified first. Afterwards, the local extrema are connected by a cubic spline interpolation separately to define an upper and a lower envelope. Next, the epochwise mean value  $m_1$  of the two envelopes is calculated and subtracted from the original time series to get the first component  $h_1$ :

$$h_1 = X(t) - m_1. \quad (4)$$

In general,  $h_1$  does not fulfil the conditions of an IMF, so the sifting process is repeated  $k$  times, until  $h_{1k}$  fulfil the required conditions:

$$h_{1k} = h_{1(k-1)} - m_{1k}. \quad (5)$$

In every iteration step, the envelopes are defined from the previous component  $h_{1(k-1)}$  with their mean  $m_{1k}$ . The last component  $h_{1k}$  is then defined as the first IMF  $c_1$ . The second

IMF can be calculated similarly, where the input time series are now the residuals  $r_1$ ,

$$r_1 = X(t) - c_1. \quad (6)$$

This process is repeated, until all depending IMF from the signal are calculated.

The first IMF shows the highest frequency component of the data, whereas the last one represents the long periodic trend. This is also visible in Fig. 3, where an example of the EMD on a static 1 Hz RTK measurement is shown. Here, the ECEF X coordinate is presented in the top subfigure. The IMF  $c_1$  to  $c_6$  are depicted in the lower subfigures. The last subfigure shows the remaining part  $c_7$  (long periodic trend), which not fulfil the conditions of an IMF. It can be clearly seen, that the minimum period, which can be calculated equals two times the amount of data points from a specific IMF divided by the amount of corresponding zero crossings. It is decreasing with higher IMF. The original signal can be fully rebuilt by summing up all IMF and the remaining part.

An issue of the EMD is the mode mixing problem, which often occur due to signal intermittency (Huang et al. 1999). Usually, every IMF has a physical characteristic scale, which describes a physical phenomenon in the data. When this scale is intermittent, the physical interpretation of the IMF could be wrong. For example, two different physical processes can be represented in one IMF, which is in general not possible. To avoid mode mixing, Wu and Huang (2009) introduced the ensemble empirical mode decomposition, a truly noise-assisted data analysis. The main idea of this method is to repeat the sifting process several times while adding every time different white noise to the original time series. By calculating the (ensemble) mean of each IMF, after the sifting process runs are finished, the added white noise cancels out, but the EEMD components are maintained. This reduces significantly the possibility of mode mixing.

---

## 4 Benefits of EEMD in Antenna Calibration

The main problem to estimate repeatable CPC pattern, as mentioned in Sect. 2.4, is the low pattern to noise ratio. The EEMD can be used to reduce the noise of the  $\Delta$ SD. For this purpose, the standard 1 Hz sampling rate is not high enough, because the EEMD would filter out important pattern information. To maintain this information a higher sampling rate of the observations is necessary.

### 4.1 Movement of Robot and Data Acquisition

To explain the necessity of a higher sampling rate, the robot movement and measurement sequence have to be analysed first. The robot tilts and rotates the AUT around a fixed point in space. To calculate its position accurately, a robot model from a calibration with a laser tracker is used. The robot has five degrees of freedom, which allows to hold the fixed position in static phases. Due to the complex robot dynamics, only the phases when the robot is at rest are used for the calibration to avoid dynamic stress on the receiver tracking loops. Consequently, observations within the movements of typically 1 s between the robot poses are unusable. By forming time-differenced single differences, CPC information are only contained in differences between phases at rest in different robot poses; differences between measurements of the same robot pose contain only noise. This means that the highest frequency of signatures related to CPC pattern is 1 Hz, considering the standard calibration settings (robot rotation and tilting duration of at least one second).

### 4.2 Necessity of a Higher Sample Rate

For the noise reduction of  $\Delta$ SD, the EEMD method is used. The idea is, that the high-frequency noise is gathered in the first IMF of the data. Thereby, this IMF is calculated and subtracted from the original  $\Delta$ SD, which results in a less noisy time series. By using this method on the standard 1 Hz approach, important pattern information would be lost.

Figure 4 demonstrates this issue. Here, a calibration data set (GPS C1C) for a Novatel703GGG.R2 (S/N: 12420018) from 2nd April 2021 with a sampling rate of 1 Hz is shown. The original data from GPS satellite PRN 6 is presented in the top subfigure and the corresponding IMFs are shown below (only three IMFs are shown here for demonstration). By calculating the period and the corresponding frequency of each IMF, it is visible, that the first IMF has a frequency of approximately 0.3 Hz. Consequently, by considering the robot movement (Sect. 4.1), pattern information is contained in the first IMF and would be neglected with the subtraction. When the sampling rate of the observations is increased to 10 Hz, the frequency of the corresponding IMF also increases by a factor of 10. This leads to a frequency of approximately 3 Hz for the first IMF. That means, this IMF contains the high frequency noise of the original  $\Delta$ SD but no CPC pattern information. By subtracting the first IMF from the original  $\Delta$ SD the noise is significantly reduced by maintaining all important pattern information.

Figure 5 shows in grey the original GPS C1C 10 Hz  $\Delta$ SD for a calibration for the Novatel703GGG.R2 antenna. The  $\Delta$ SD by using the EEMD approach is presented in red. It is clearly visible, that the overall noise of the data is significantly reduced. The modified data can be used as input for the estimation process to estimate more repeatable CPC pattern compared to the standard 1 Hz approach.

---

## 5 Calibration Results

Four calibrations were carried out for two antennas. The LEIAR20 LEIM (S/N: 22100016) antenna was calibrated on 3rd, 4th, 8th and 9th of March 2021, which are following named as P<sub>1</sub> to P<sub>4</sub>. Each calibration had a duration of about 12 hours. The estimated mean pattern of the four calibrations are shown in Fig. 6 for the GPS C1C signal ((a) and (b)) and for the Galileo C1C signal ((c) and (d)). The left column demonstrates the pattern estimated with the standard 1 Hz approach and the right column with the 10 Hz EEMD approach.

It is visible, that the pattern show a similar behaviour for the two different satellite systems for both approaches with nearly no azimuthal variations. However, the resulting CPC with the two approaches differs. The standard approach

**Fig. 4** EEMD of time differenced single differences  $\Delta$ SD with a sampling interval of 1 Hz for a Novatel703GGG.R2

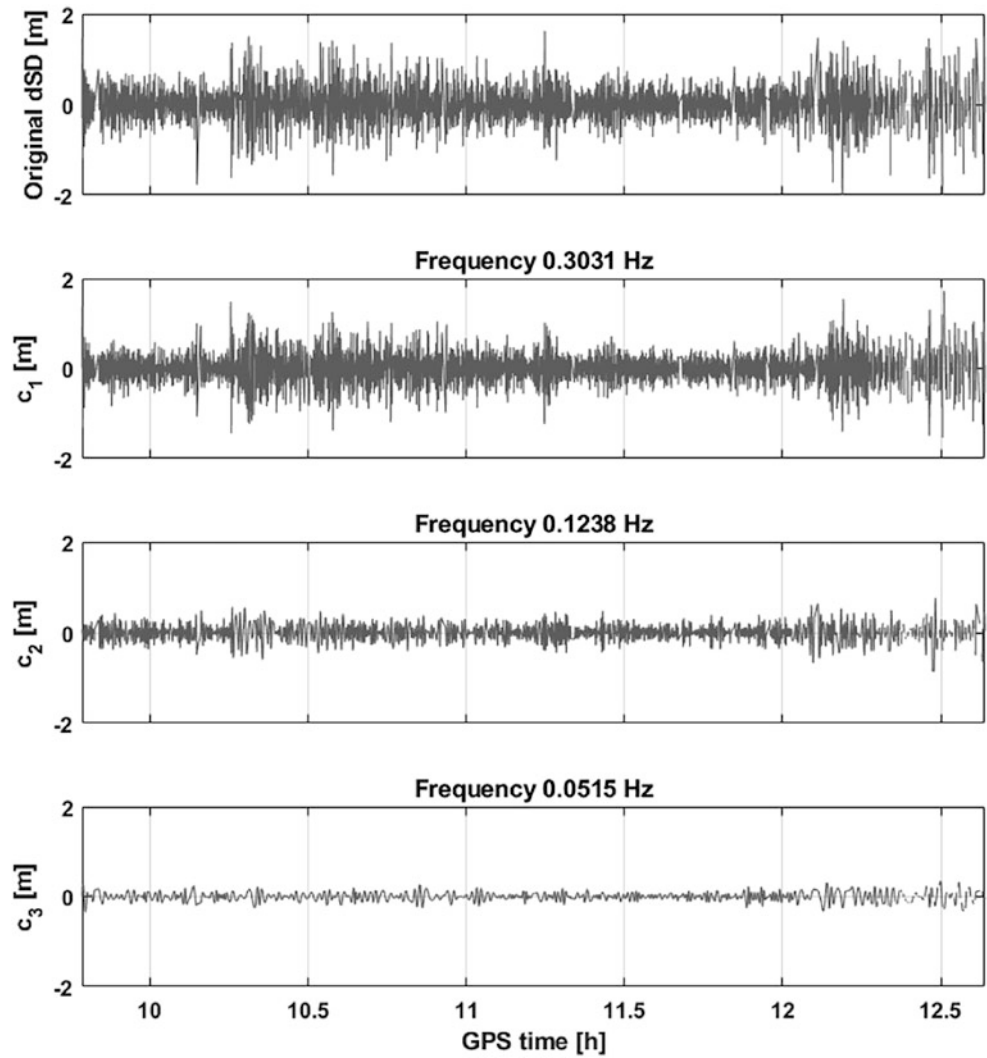


**Fig. 5**  $\Delta$ SD without (grey) and with (red) EEMD approach with a sampling interval of 10 Hz for a Novatel703GGG.R2

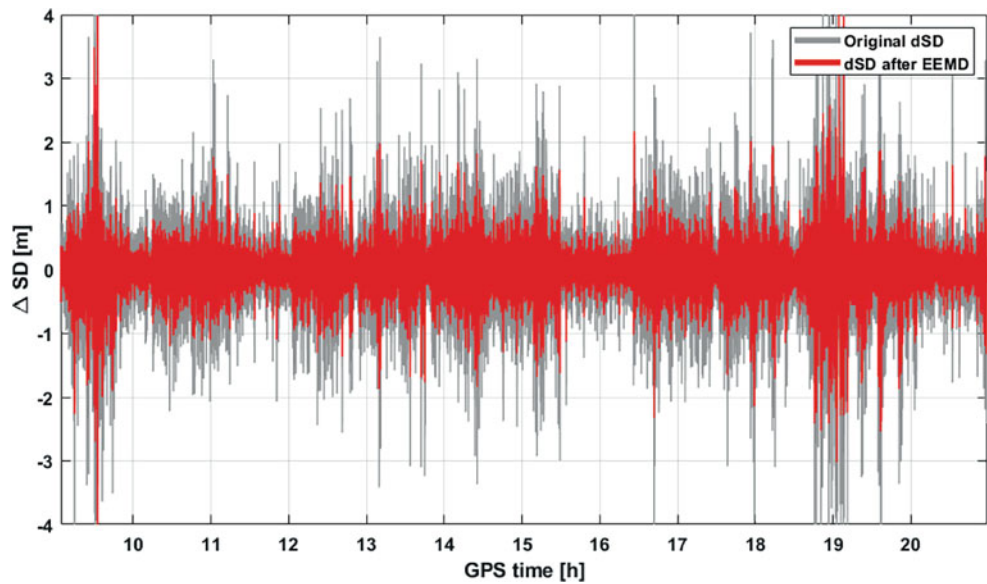


**Fig. 6** Estimated mean CPC pattern for GPS C1C (a,b) and Galileo C1C (c,d) with the standard 1 Hz (left) and the EEMD (right) approach

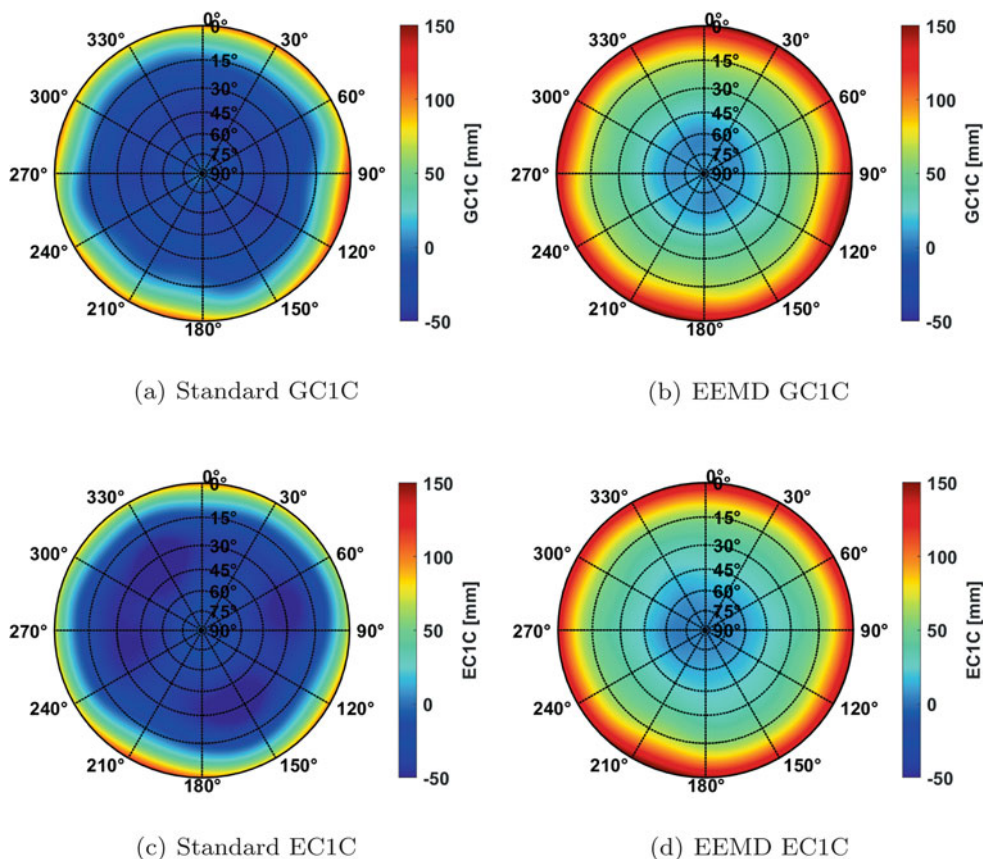


**Table 1** Calibration repeatability of LEIAR20 LEIM (S/N: 22100016) antenna. The listed values demonstrate the absolute difference between two individual calibrations for three cases in [mm]: (1) <68.3%, (2) <95.4% or (3) <99.7% of all differences are below

the value listed. The left part of the table shows the standard 1 Hz approach for GPS and Galileo C1C signal, the right part represents the results with the EEMD approach

Comparison	Standard						EEMD					
	GC1C			EC1C			GC1C			EC1C		
	(1)	(2)	(3)	(1)	(2)	(3)	(1)	(2)	(3)	(1)	(2)	(3)
P <sub>1</sub> P <sub>2</sub>	21.4	62.4	117.6	36.0	67.5	81.6	7.6	34.5	62.6	13.7	26.5	34.2
P <sub>1</sub> P <sub>3</sub>	67.6	138.3	163.7	15.8	74.5	125.6	27.7	41.5	51.8	5.9	24.7	40.4
P <sub>1</sub> P <sub>4</sub>	29.5	49.1	82.1	27.2	74.9	103.9	11.4	34.6	46.6	12.4	54.8	75.1
P <sub>2</sub> P <sub>3</sub>	48.7	96.1	129.7	35.6	73.5	91.5	18.2	30.3	39.6	12.5	25.7	36.3
P <sub>2</sub> P <sub>4</sub>	44.6	86.0	148.8	38.8	93.2	147.5	17.8	61.9	103.0	20.0	67.6	94.2
P <sub>3</sub> P <sub>4</sub>	87.5	115.9	198.4	23.4	134.7	187	36.1	69.3	91.1	13.3	74.9	98.1
Average	49.9	91.3	140.1	29.5	86.4	122.9	19.8	45.4	65.8	13.0	45.7	63.1

shows a smaller magnitude and has negative CPC values, which are not visible with the EEMD approach. For a better comparison of both methods, the repeatability of the individual calibrations is analysed. Therefore, the absolute difference pattern of each possible calibration combination is calculated.

The results are shown in Table 1 and are also depicted in Fig. 7 for GPS C1C and Fig. 8 for Galileo C1C. In the table, three different cases are listed: 68.3% (1), 95.4% (2) or 99.7% (3) of the differences between two calibrations

are below the listed value in [mm]. Considering the average (mean value of all possible pattern combinations) it is clearly visible, that the EEMD approach improves the repeatability compared to the standard 1 Hz approach for both signals. For example, comparing the GPS C1C signal, an improvement from 49.9 mm to 19.9 mm (1), 91.3 mm to 45.4 mm (2) and 140.1 mm to 63.1 mm (3) can be reached, which correspond to 46% to 60% improvement. Similar results can be achieved for the Galileo C1C signal.

**Fig. 7** Calibration repeatability of LEIAR20 LEIM (S/N: 22100016) antenna for GPS C1C signal. The top figures (a,b) show cumulative histograms of the difference CPC pattern for each possible calibration combination. The bottom figures (c,d) show the different CPC pattern w.r.t. a type mean pattern against the elevation. The left row shows the results for the standard 1 Hz approach, the right row for the EEMD approach

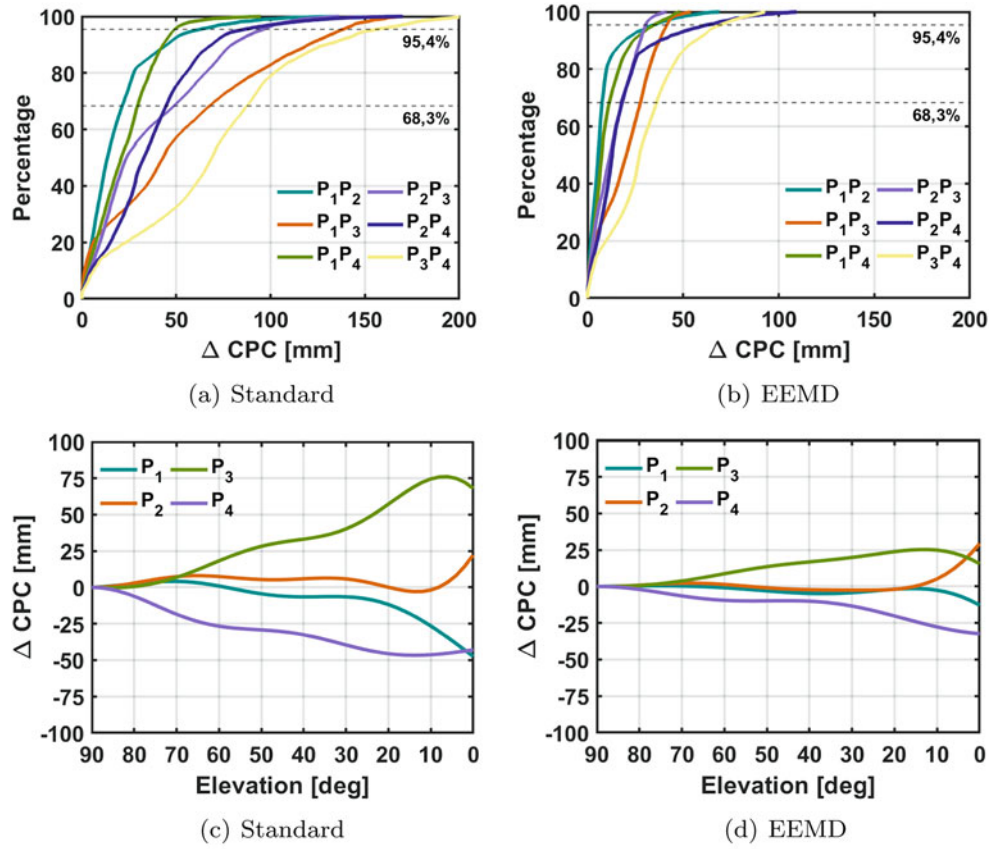
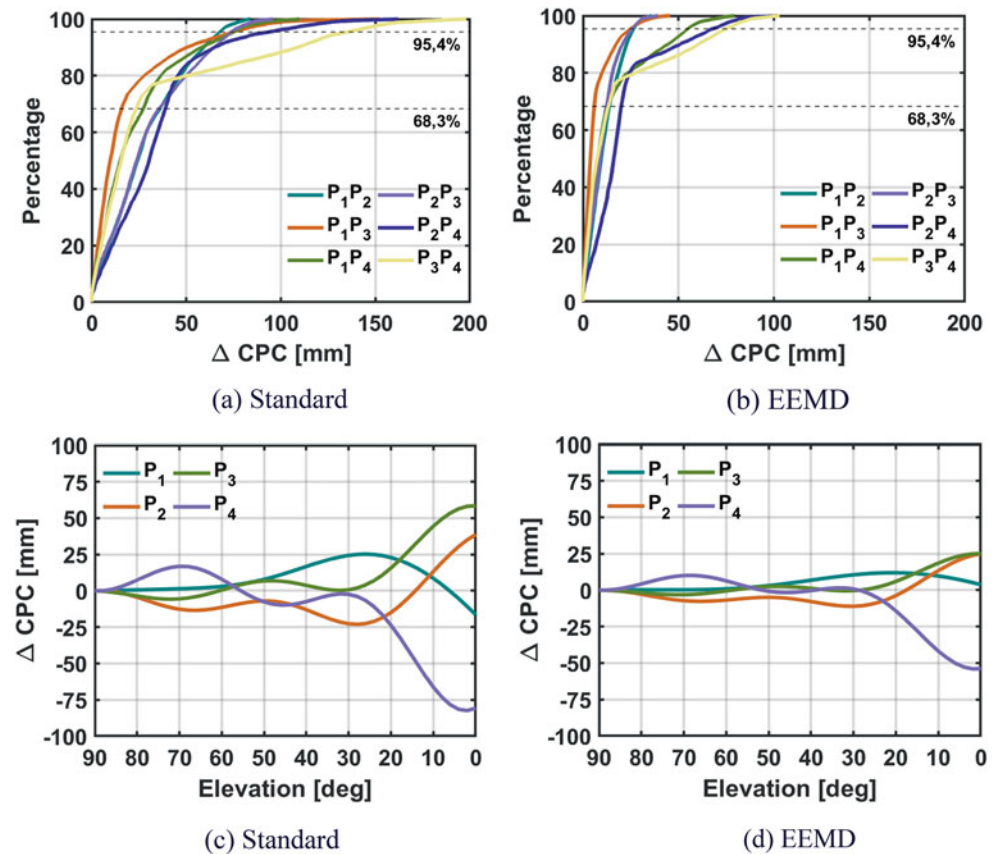


**Fig. 8** Calibration repeatability for the same LEIAR20 LEIM antenna. The figures are in the same order as in Fig. 7, however, the Galileo C1C signal is shown here



This is also visible in Fig. 7a and b, where the absolute differences of the difference pattern are presented in a cumulative histogram with standard (a) and EEMD (b) method. It can be seen, that the three quantiles are faster reached with the EEMD as with the standard approach.

The corresponding NOAZI plots are presented in Fig. 7c and d for both methods. The NOAZI CPC pattern for each calibration are depicted w.r.t. to the mean pattern. The estimated patterns with the standard approach scatter much more ( $-5$  cm to  $7.5$  cm) compared to the EEMD ( $-3$  cm to  $2.5$  cm), especially at low elevation angles. Similar results are achieved for Galileo C1C (Fig. 8), however, with less scattering results for the standard method. Nevertheless, an improvement by using the EEMD method is also visible.

Another four calibrations for a NOV703GGG.R2 NONE (S/N: 1240018) were carried out from April 2nd to 5th, 2021. A similar calibration repeatability for the GPS C1C signal is achievable. An improvement of (1)  $48.5$  mm to  $19.5$  mm, (2)  $106$  mm to  $41.4$  mm and (3)  $167.1$  mm to  $70.1$  mm can be reached, which corresponds to 60%.

## 6 Validation

In order to validate the estimated CPC pattern, a static experiment was carried out in May 2021. Here, the NOV703GGG.R2 NONE (S/N: 1240018) and the LEIAR20 LEIM (S/N: 22100016) were mounted on a pillar at the measurement roof from IfE (Fig. 9). In general, CPC and also PCC pattern can be validated in observation domain by calculating SD in a common clock assembly. This setup cancels out mostly all error sources, except the differential multipath effect, receiver depending errors sources as well as the differential CPC/PCC pattern between the two antennas. By correcting the SD with the antenna pattern, the RMS should be improved (Kröger et al. 2021). In order to see antenna dependent effects in the SD, the patterns of the two antennas must differ. Consequently, this validation approach cannot be used for the CPC of the considered antennas, due to a very similar pattern (Fig. 10). The differential CPC reach up to  $2$ – $3$  cm, which gets lost within the code noise.

Therefore, a validation in positioning domain is performed with a single point positioning approach. Table 2 shows the results of the SPP approach for the LEIAR20 LEIM (S/N: 22100016) (left) and NOV703GGG.R2 NONE (S/N: 1240018) (right) antenna for a static measurement



Fig. 9 Validation setup

from May 17th, 2021. The SPP were calculated epochwise with a cutoff angle of 5 degrees and an elevation dependent weighting. Here, the median of the estimated topocentric coordinates w.r.t. to the reference coordinates, which were estimated in a local GPS/ GLONASS L1 network solution 2018 with sub-millimeter accuracy, are shown. The CPC pattern for the two analysed geodetic antennas in this contribution are very similar to their PCC. One method is to add the PCO for carrier phase to the antenna height, to compensate this lack of. The SPP results, by adding the carrier phase PCO, are listed in the top row (1) of Table 2. The bottom row (2) shows the results by additional considering the differential CPC pattern. As expected, the accuracy increases when taking CPC into account, especially in the Up component. Since the CPV of geodetic antennas are generally small compared to the PCO, the improvement can be achieved mostly in the Up component. The amount of improvement corresponds to the difference between carrier and code PCO. Similar improvement can be reached on the other three days of the experiment.

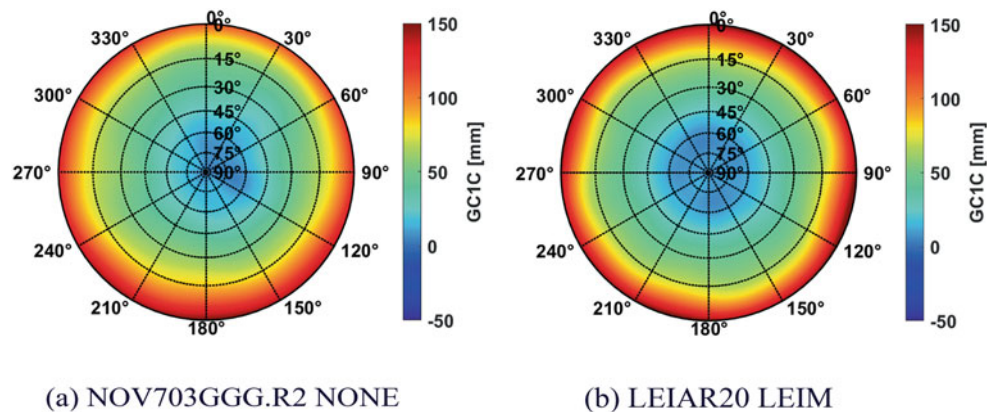


**Fig. 10** Estimated mean GPS CIC CPC

**Table 2** Results of the SPP approach with added carrier phase PCO on the antenna height (1) and with added carrier phase PCO plus differential CPC (2). Here, the median of the topocentric coordinates are shown w.r.t. reference coordinates in [m]

	LEIAR20			NOV703GGG.R2		
	North	East	Up	North	East	Up
(1)	0.634	0.519	−0.203	0.623	0.548	0.034
(2)	0.632	0.521	−0.162	0.614	0.541	0.001

## 7 Conclusion

In this paper, an improved preprocessing for estimating absolute CPC was proposed. The current CPC calibration approach was briefly described. This approach works well for PCC estimation, however, the smaller pattern to noise ratio in the codephase observations results in a worse repeatability of the CPC pattern. Therefore, the EEMD method is used to significantly reduce the noise of the input  $\Delta SD$  by preserving all important pattern information. In order to use the EEMD, the sampling rate of the observations has to be increased to 10 Hz. This leads to a better repeatability of the estimated CPC pattern compared to the standard 1 Hz approach. An average improvement of 46% to 60% for a geodetic LEIAR20 LEIM antenna and 60% for a NOV703GGG.R2 NONE is achievable. To validate the calibration results, a single point positioning approach was used. The SPP shows, that considering CPC pattern can improve the accuracy, especially in the Up component. If no CPC pattern are available, a good alternative is to consider the carrier phase center offset, because the CPC and PCC pattern of the analysed geodetic antennas in this contribution are very similar. For low cost antennas, the CPC and PCC distinguish more, so that a CPC correction should be applied.

**Acknowledgements** Parts of the work were funded by the Deutsche Forschungsgemeinschaft (DFG, German Research Foundation)—Project-ID 434617780—SFB 1464.

## References

- Beer S, Wanninger L, Heßelbarth A (2019) Galileo and GLONASS group delay variations. *GPS Solutions* 24(1). <https://doi.org/10.1007/s10291-019-0939-7>
- Beer S, Wanninger L, Heßelbarth A (2021) Estimation of absolute GNSS satellite antenna group delay variations based on those of absolute receiver antenna group delays. *GPS solutions* 25(110):10. <https://doi.org/10.1007/s10291-021-01137-8>
- Böder V, Menge F, Seeber G, Wübbena G, Schmitz M (2001) How to deal with station dependent errors, new developments of the absolute field calibration of PCV and phase-multipath with a precise robot. In: *ION GPS 2001*, September 11–14, Salt Lake City, UT, USA, pp 2166–2176
- Breva Y, Kröger J, Kersten T, Schön S (2019) Estimation and validation of receiver antenna codephase variations for multi GNSS. In: *7th international colloquium on scientific and fundamental aspects of GNSS*, September 4–6, Zürich, Switzerland
- Görres B, Campbell J, Becker M, Siemes M (2006) Absolute calibration of GPS antennas: laboratory results and comparison with field and robot techniques. *GPS Solutions* 10(2):136–145. <https://doi.org/10.1007/s10291-005-0015-3>
- Huang NE, Shen Z, Long SR, Wu MC, Shih HH, Zheng Q, Yen NC, Tung CC, Liu HH (1998) The empirical mode decomposition and the hilbert spectrum for nonlinear and non-stationary time series analysis. In: *Proceedings of the royal society a mathematical, physical and engineering sciences*. <https://doi.org/10.1098/rspa.1998.0193>
- Huang NE, Shen Z, Long SR (1999) A new view of nonlinear water waves: The hilbert spectrum. *Annu Rev Fluid Mech* 31(1):417–457. <https://doi.org/10.1146/annurev.fluid.31.1.417>
- Kersten T, Schön S (2017) GPS code phase variations (CPV) for GNSS receiver antennas and their effect on geodetic parameters and ambiguity resolution. *J Geodesy* 91:579–596. <https://doi.org/10.1007/s00190-016-0984-8>
- Kröger J, Breva Y, Kersten T, Schön S (2019) Phase center corrections for new GNSS-signals. In: *Geophysical research abstracts* 21, no. 21 in *Geophysical Research Abstracts*. <https://doi.org/10.15488/4682>
- Kröger J, Kersten T, Breva Y, Schön S (2020) Robot-based calibration of Multi-GNSS receiver antennas using real satellite signals. In: *14th European conference on antennas and propagation (EUCAP)*, virtual conference, Copenhagen, Denmark
- Kröger J, Breva Y, Kersten T, Schön S (2021) Multi-frequency multi-GNSS receiver antenna calibration at IfE: concept - calibration results - validation. In: *Advances in space research*. <https://doi.org/10.1016/j.asr.2021.01.029>

- Menge F, Seeber G, Völksen C, Wübbena G, Schmitz M (1998) Results of the absolute field calibration of GPS antenna PCV. In: ION GPS 1998, September 15–18, Nashville, TN, USA, pp 31–38
- Rothacher M, Schaer S, Mervat L, Beutler G (1995) Determination of antenna phase center variations using GPS data. In: Presentation at the IGS workshop - special topics and new directions, May 15–18, Potsdam, Germany, p 16
- Wanninger L, Sumaya H, Beer S (2017) Group delay variations of GPS transmitting and receiving antennas. *J Geodesy* 91(9):1099–1116. <https://doi.org/10.1007/s00190-017-1012-3>
- Wu Z, Huang NE (2009) Ensemble empirical mode decomposition: a noise-assisted data analysis method. *Adv Adaptive Data Anal* 139(1):1–41. <https://doi.org/10.1142/S1793536909000047>
- Wübbena G, Schmitz M, Menge F, Böder V, Seeber G (2000) Automated Absolute Field Calibration of GPS Antennas in Real-Time. In: ION GPS 2000, September 19–22, Salt Lake City, UT, USA, pp 2512–2522
- Wübbena G, Schmitz M, Propp M (2008) Antenna group delay calibration with the geo++ robot-extensions to code observable. In: IGS analysis workshop, poster, June, pp 2–6
- Wübbena G, Schmitz M, Warneke A (2019) GEO++ absolute multi frequency GNSS antenna calibration. In: EUREF analysis center (AC) workshop, October 16–17, Warsaw, Poland. [https://www.geopp.com/pdf/gpp\\_cal125\\_euref19\\_p.pdf](https://www.geopp.com/pdf/gpp_cal125_euref19_p.pdf)

**Open Access** This chapter is licensed under the terms of the Creative Commons Attribution 4.0 International License (<http://creativecommons.org/licenses/by/4.0/>), which permits use, sharing, adaptation, distribution and reproduction in any medium or format, as long as you give appropriate credit to the original author(s) and the source, provide a link to the Creative Commons license and indicate if changes were made.

The images or other third party material in this chapter are included in the chapter's Creative Commons license, unless indicated otherwise in a credit line to the material. If material is not included in the chapter's Creative Commons license and your intended use is not permitted by statutory regulation or exceeds the permitted use, you will need to obtain permission directly from the copyright holder.







# On the Potential of Image Similarity Metrics for Comparing Phase Center Corrections

Johannes Kröger, Tobias Kersten, Yannick Breva, and Steffen Schön

## Abstract

For highly precise and accurate positioning and navigation with Global Navigation Satellite Systems (GNSS), it is mandatory to take phase center corrections (PCC) into account. These corrections are provided by different calibration facilities and methods. Currently, discussions in the framework of the International GNSS Service (IGS) antenna working group (AWG) are ongoing on how to accept new calibration facilities as an official IGS calibration facility.

In this paper, different image similarity measures and their potential for comparing PCC are presented. Currently used comparison strategies are discussed and their performance is illustrated with several geodetic antennas. We show that correlation coefficients are an appropriate measure to compare different sets of PCC since they perform independently of a constant part within the patterns. However, feature detection algorithms like the Speeded-Up Robust Features (SURF) mostly do not find distinctive structures within the PCC differences due to the smooth character of PCC. Therefore, they are inapplicable for comparing PCC. Singular Value Decomposition (SVD) of PCC differences ( $\Delta PCC$ ) can be used to analyse which structures  $\Delta PCC$  are composed of. We show that characteristic structures can be found within  $\Delta PCC$ . Therefore, the SVD is a promising tool to analyse the impact of PCC differences in the coordinate domain.

## Keywords

Image similarity metrics · Multi-GNSS processing · Phase center corrections · Singular value decomposition

## 1 Introduction

In order to obtain highly precise and accurate positioning and navigation solutions with Global Navigation Satellite Systems (GNSS), it is mandatory to take all error sources adequately into account. This includes phase center corrections (PCC) which are composed of a phase center offset (PCO) and azimuth- and zenith-dependent phase center variations (PCV). Due to the relative character of GNSS measurements, i.e. pseudoranges, a constant part  $r$  can additionally be

present. The PCO is projected onto the unit line-of-sight vector  $e$  towards a satellite  $k$  with azimuth angle  $\alpha$  and zenith angle  $z$

$$PCC(\alpha^k, z^k) = -PCO \cdot e(\alpha^k, z^k) + PCV(\alpha^k, z^k) + r. \quad (1)$$

PCC are provided by different facilities and calibration methods. Nowadays, the absolute correction values for receiver antennas are either determined in an anechoic chamber (Görres et al. 2006; Becker et al. 2010; Zeimet 2010; Caizzone et al. 2021) or in the field by use of a robot (Bilich et al. 2018; Willi et al. 2019; Wübbena et al. 2019; Dawidowicz et al. 2021; Kröger et al. 2021; Wanninger et al.

J. Kröger (✉) · T. Kersten · Y. Breva · S. Schön  
Leibniz Universität Hannover, Hannover, Germany

2021) and are published in the Antenna Exchange (ANTEX) file (Rothacher and Schmid 2010).

Since newer GNSS frequencies (e.g. GPS L5) or systems, like Galileo or Beidou, are increasingly used in multi-GNSS processing and therefore added in the ANTEX file, there is the need for appropriate comparison strategies. Additionally, new calibration facilities want to contribute to the International GNSS Service (IGS) antenna working group (AWG). To this end, discussions are currently ongoing on what basis (parameters, thresholds, validation strategies, etc.) new calibration facilities should be accepted. This underlines the need of appropriate PCC comparison strategies.

The paper is structured as follows: Sect. 2 presents the different representation types of PCC and states the feasibility of image similarity metrics for comparing PCC. Section 3 shows the currently used comparison strategies based on different antenna types. In Sect. 4, global image similarity measures and their potential for comparing PCC are introduced. Section 5 deals with feature detection algorithms and their advantages and drawbacks for comparing PCC. Section 6 presents the singular value decomposition and its use in the context of PCC. Finally, Sect. 7 closes the paper with conclusion.

## 2 Representation of PCC

Usually, PCC are parametrized and estimated by use of spherical harmonic (SH) functions. Subsequently, the PCC are mapped on a regular grid with a typical step size of  $5^\circ$  azimuth  $\alpha$  and  $5^\circ$  zenith angle  $z$ .

Figure 1 shows two different representation types of GPS L1 PCC for a geodetic choke ring antenna, widely used at reference stations (LEIAR25.R3 LEIT). The corrections values reach a magnitude of 160 mm. Since the Up-component of the PCO has the biggest impact (158.67 mm), a clearly elevation-dependent behaviour is detectable.

Figure 1a depicts the PCC in a stereographic projection, Fig. 1b on a regular grid. As it can be clearly seen in the latter figure, the PCC can be interpreted as a two-dimensional image. In this case, the actual grey-scale value of a pixel  $x_{ij}$  is equivalent to the metric correction value  $PCC(\alpha, z)$ . Therefore, image similarity metrics can principally be used to compare PCC.

## 3 Current Comparison Strategies

Currently, different sets of PCC ( $PCC_A$ ,  $PCC_B$ ) are mainly compared by computing the differences at the pattern level. In this paper, whenever differences of two PCC sets  $\Delta PCC$  are analysed, the individually estimated PCC between the

calibration method Chamber and ROBOT are studied

$$\begin{aligned} \Delta PCC &= PCC_A - PCC_B \\ &= PCC_{CHAMBER} - PCC_{ROBOT}. \end{aligned} \quad (2)$$

The following analyses are carried out with the individually estimated PCC for different antennas listed in Table 1. All of them are used in the EUREF Permanent GNSS Network (EPN) (Bruyninx and Legrand 2017). Note, that for PCC6 – a TRM15990 SCIS antenna – no individual calibration is available for method ROBOT so that the type mean values are used instead.

Since PCO and PCV cannot be considered separately, it is important to take the full sets of PCC for comparisons into account as they contain all information. Moreover, a constant part  $r$  may be present which results from the PCC datum definition or the strategy applied to estimate PCO and PCV. If only small PCC differences  $PCV_{A,B}$  should be analysed, the different sets can be transformed to a common PCO set (Menge et al. 1998)

$$\begin{aligned} PCV_{A,B}(\alpha, z) &= (PCO_B - PCO_A) \cdot e(\alpha, z) + \\ &PCV_A(\alpha, z) + \Delta r. \end{aligned} \quad (3)$$

If the constant parts  $r_{A,B}$  are not explicitly known,  $\Delta r$  can not be taken separately into account but may be present within  $PCV_{A,B}$ . With Eq. 3 different sets of PCV ( $\Delta PCV$ ) can be compared

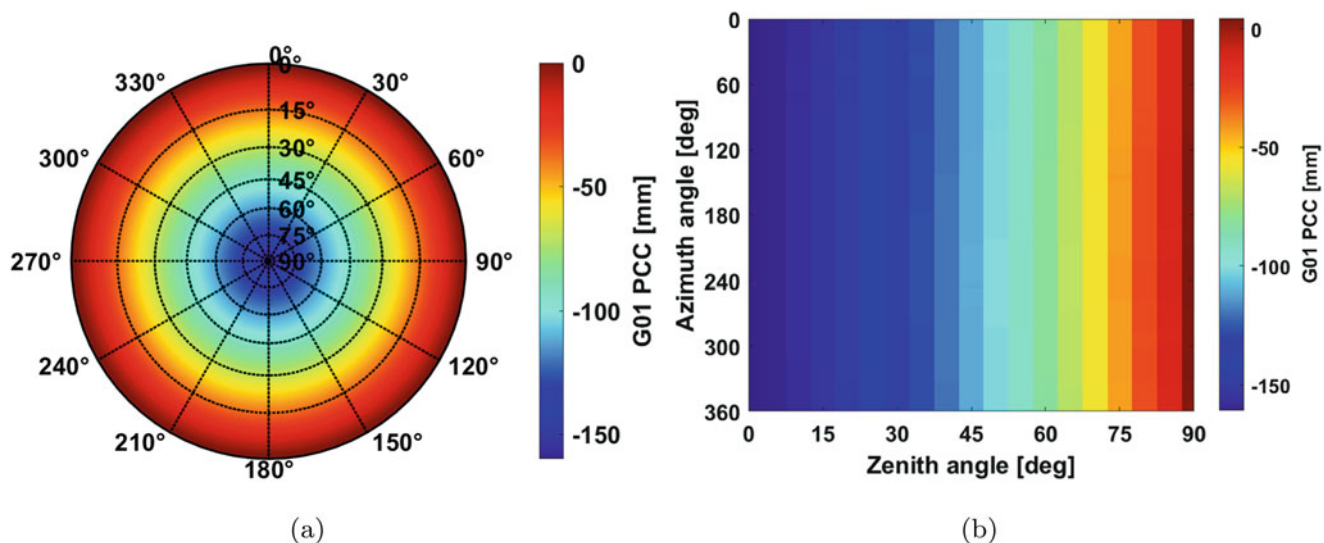
$$\Delta PCV = PCV_{A,B} - PCV_B. \quad (4)$$

Figure 2a shows only elevation-dependent GPS L1 differences by calculating the mean value per  $5^\circ$  azimuth bin. In addition, the minimum and maximum absolute difference per bin are depicted in dashed lines. The differences are shown for two cases: (i) blue-coloured original  $\Delta PCC$  and (ii) red-coloured constrained  $\Delta PCC$ , so that the PCC are zero at zenith ( $z = 0$ ). This is equal to subtracting a constant value from one of the pattern, which is a valid transformation of PCC (Schön and Kersten 2013).

In Fig. 2a it can be clearly seen that the differences are larger for the non-constrained  $\Delta PCC$  at low and middle zenith angles ( $z \leq 80^\circ$ ). Here, the differences are in the range of 0.8 mm to 1.7 mm whereas the differences for the constrained  $\Delta PCC$  are between  $-0.9$  mm and 0.2 mm.

In the past, a rule of thumb was applied by the IGS that deviations between sets of PCC of the same antenna have to be smaller than 1 mm beneath  $80^\circ$  zenith angles of only zenith-dependent pattern. However, for this example the goal is only achieved for the constrained  $\Delta PCC$ .

Figure 2b shows the absolute  $\Delta PCC$  in a cumulative histogram. Here, zenith- and azimuth dependent PCC are



**Fig. 1** Different representations of GPS L1 (G01) PCC of a LEIAR25.R3 LEIT antenna (denoted as PCC1 in Table 1) as (a) stereographic projection and (b) grid view

**Table 1** Individually calibrated antennas (methods CHAMBER & ROBOT) used for PCC comparison analyses

ID	Antenna name	Radom	Serial number
PCC1	LEIAR25.R3	LEIT	09390011
PCC2	LEIAR25.R3	LEIT	09050002
PCC3	LEIAR25.R4	LEIT	08500021
PCC4	LEIAR25.R4	LEIT	725072
PCC5	LEIAR25.R3	NONE	09300021
PCC6	TRM15990	SCIS	5744338072 <sup>a</sup>

<sup>a</sup> Only type mean PCC for method ROBOT

considered. Again, the red-coloured constrained  $\Delta PCC$  show lower deviations compared to the non-constrained blue-coloured  $\Delta PCC$ . While 73 % of the constrained  $\Delta PCC$  are below 1 mm, for the non-constrained  $\Delta PCC$  these are only 33 %. Both representations underline the need of a more detailed guideline of the comparison.

Table 2 shows the characteristic values for the depicted  $\Delta PCC$  of PCC1. The maximum, the Root Mean Square (RMS) and a certain threshold, e.g. stating percentage of  $\Delta PCC < 1$  mm, depend on the constant value  $r$  within the PCC. The standard deviation, range<sup>1</sup> and spread<sup>2</sup>, however, are independent of  $r$ .

Furthermore, the characteristic values shown here give higher numbers when the PCC are not zero-zenith constrained. This underlines the need of taking possible different PCC datum definitions or the strategy how to separate PCO and PCV during the analysis of the calibration adequately into account.

<sup>1</sup>range =  $\max(\Delta PCC) - \min(\Delta PCC)$

<sup>2</sup>spread =  $\text{range}(PCC_A) - \text{range}(PCC_B)$

Although the spread performs independently from a constant part, it should be noted that the measure changes if a transformation as shown in Eq. 3 is performed.

Moreover, a currently used comparison strategy is the investigation of the impact of  $\Delta PCC$  in the coordinate domain as shown in Willi et al. (2019) and Kröger et al. (2021). In this case, the comparisons cannot be immediately interpreted since the achieved results are heavily dependent on the used processing strategy, e.g. cutoff angles, tropospheric models, observations weights, station location, used systems and signals, etc.

## 4 Global Image Similarity Measures

In this section, two global image similarity measures are exemplary analysed w.r.t their applicability to compare different sets of PCC. While the big advantage is that only one metric describes the similarity, the drawback is that the spatial structure of the  $\Delta PCC$  gets lost. However, this is needed if the impact in the coordinate domain should be analysed in detail.

### 4.1 Correlation Coefficients

Correlation coefficients give the similarity between two sequences of numbers and vary typically between  $-1$  and  $+1$ , whereas  $c = +1$  is called *perfect positive correlation* (Goshtasby 2012).

Here, the feasibility of using the Pearson correlation coefficient  $c$  to compare different sets of PCC is exemplarily studied. Since each pattern  $PCC_s$  is normalised with respect

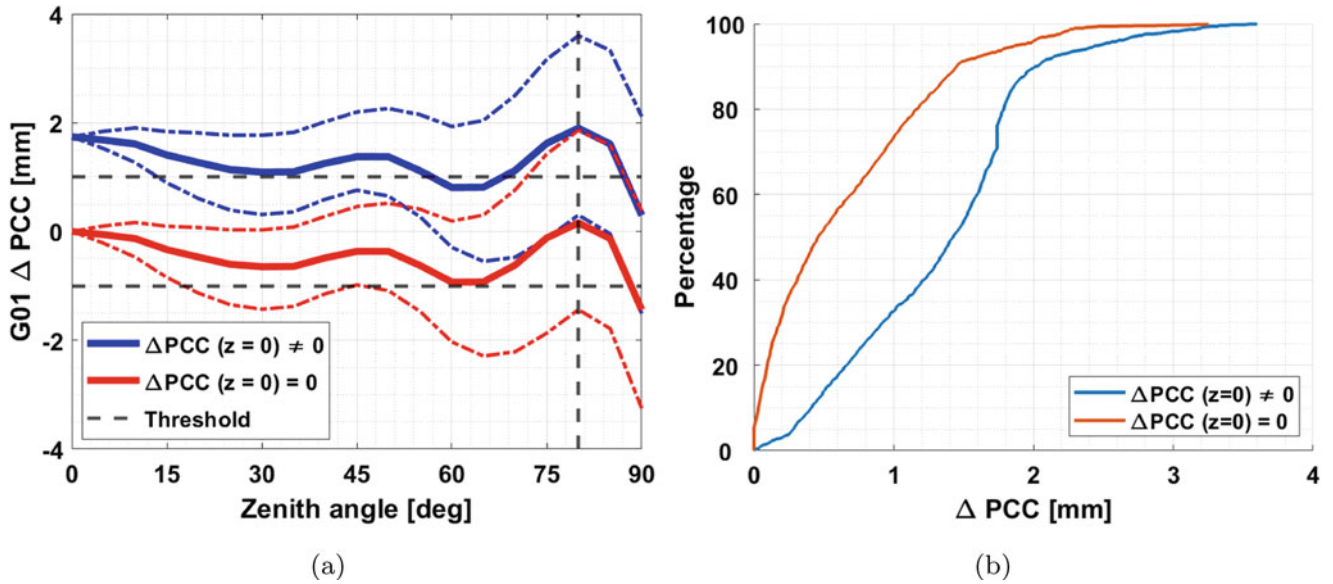


**Fig. 2** Representation of  $\Delta PCC$  (method CHAMBER - ROBOT) of a LEIAR25.R3 LEIT antenna (PCC1 in Table 1) as (a) zenith dependent  $\Delta PCC$  and (b) in a cumulative histogram of absolute  $\Delta PCC$

**Table 2** Characteristic values for  $\Delta PCC$  of PCC1

Characteristic value	Non-constrained	Constrained
Maximum	3.60 mm	3.25 mm
RMS	1.49 mm	0.89 mm
Threshold (<1 mm)	32.59 %	73.40 %
Standard deviation		0.76 mm
Spread		1.78 mm
Range		3.63 mm

to its standard deviation  $\sigma_s$  and mean value  $\overline{PCC_s}$ ,  $c$  performs independently of  $r_s$  (Goshtasby 2012)

$$c = \frac{1}{n} \sum_{i=1}^n \left( \frac{(PCC_A - \overline{PCC_A})}{\sigma_{PCC_A}} \right) \cdot \left( \frac{(PCC_B - \overline{PCC_B})}{\sigma_{PCC_B}} \right). \quad (5)$$

Since the  $PCO_{Up}$  component is the most dominating part in PCC (cf. Fig. 1), PCC sets of the same antenna are quite similar so that the coefficients give usually high correlations.

Therefore, different sets of PCC need to be transformed to a common PCO beforehand, following Eq. 3. Subsequently, Table 3 shows the Pearson correlation coefficients for the original  $\Delta PCC$  and the transformed ones ( $\Delta \widehat{PCCV}$ ). For both differences, height offsets  $\Delta H$  of 5 mm and 10 mm have been additionally added to one of the pattern so that the corresponding change of  $c$  can be seen. While  $c$  gives values close to one for  $\Delta PCC$ , the  $\sin(\Delta H)$  offsets are clearly

**Table 3** Similarity of non-transformed  $\Delta PCC$  and transformed  $\Delta \widehat{PCCV}$  expressed by Pearson correlation coefficient  $c$  for PCC1

Scenario	$\Delta H$ [mm]	$\Delta PCC$	$\Delta \widehat{PCCV}$
Original $\Delta PCC$	0	0.9998923	0.9450931
$PCC_A + \sin \Delta H$	5	0.9998917	0.8592048
$PCC_A + \sin \Delta H$	10	0.9998896	0.7682259

projected into the correlation coefficient for the transformed  $\Delta \widehat{PCCV}$ .

Figure 3a shows the relation between the absolute maximum value of  $\Delta \widehat{PCCV}$  and  $c$ . Here, the numbers are given for  $\Delta \widehat{PCCV}$  constrained to zero in zenith (depicted by squares) and non-constrained  $\Delta \widehat{PCCV}$ , illustrated by circles. Therefore, it can be again clearly seen that the maximum – as a characteristic value for describing the similarity between different sets of PCC – do not perform independently from a constant value  $r$ . Moreover, it gets clear that the  $\Delta \widehat{PCCV}$  can be quite similar by means of  $c$  although the maximum value states a low similarity. As an example serves PCC6. Here, the highest deviation in terms of the maximum value is – as expected – present since an individual calibration is compared with the type mean calibration. On the other hand, the maximum deviation may indicate a high similarity of  $\Delta \widehat{PCCV}$  while the correlation coefficient gives a low similarity, cf. PCC3.

The same conclusions can be drawn from Fig. 3b, where the relation between  $c$  and the RMS of  $\Delta \widehat{PCCV}$  is illustrated. The highest similarity can again be observed for PCC5, the lowest similarity for PCC6.

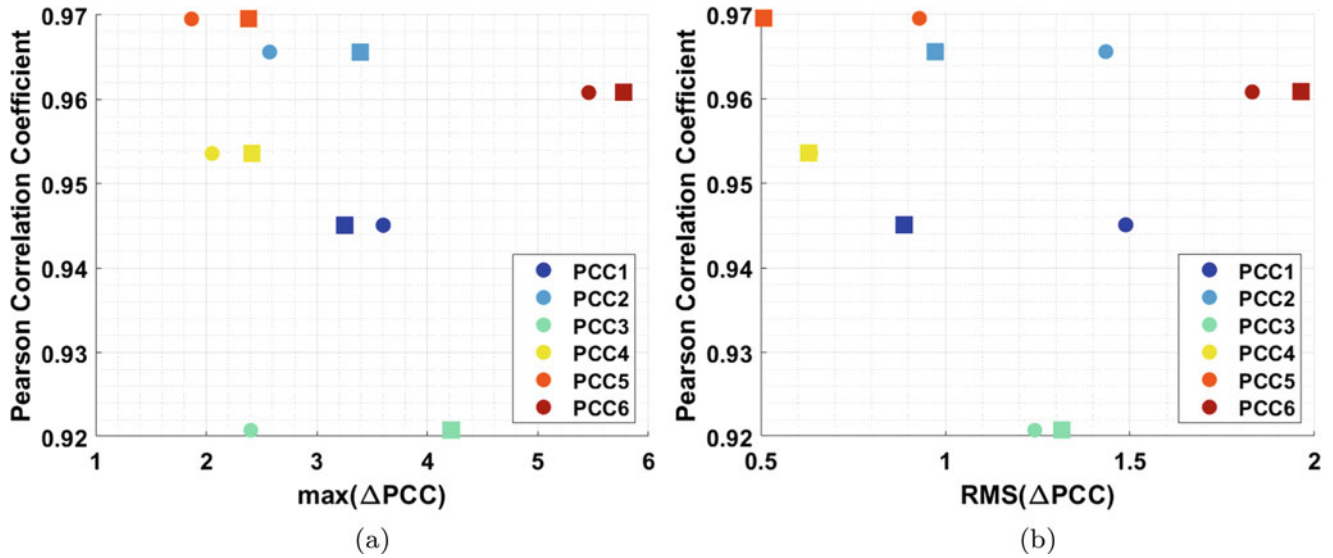


**Fig. 3** Relations between Pearson correlation coefficient  $c$  and (a) maximum differences and (b) RMS of  $\Delta PCV$ . Zero zenith constrained  $\Delta PCV$  are shown by squares, non-constrained  $\Delta PCV$  by circles

### 4.2 Structural Similarity Index

The Structural SIMilarity (SSIM) index introduced by Wang et al. (2004) measures the similarity of an input image w.r.t. a reference image. Since it is not only constrained to image processing but can also used as a similarity measure for comparing any two signals, it can be used to compare different sets of PCC. However, they need to be rescaled beforehand, since the input signals have to be non-negative.

The SSIM is composed of three components so that an overall similarity measure  $S(x,y)$  is achieved

$$S(x, y) = f(l(x, y), c(x, y), s(x, y)) \tag{6}$$

with  $x$  indicating in our case  $PCC_A$  and  $y$  denoting  $PCC_B$ , each pattern rescaled to the interval  $[0\ 1]$ .

The function  $l(x,y)$  compares the luminance by mainly comparing the mean values of the input signals. The term  $c(x,y)$  is a contrast comparison by comparing the standard deviations of each pattern. The function  $s(x,y)$  is a structure comparison which normalises the signals w.r.t their standard deviations. All three terms contain constants ( $C_1, C_2, C_3$ ) to avoid instabilities. Moreover, each function can be weighted to adjust its relative importance.

In accordance with Wang et al. (2004), following constants have been used for the investigations carried out in this contribution:  $C_1 = 1 \cdot 10^{-4}$ ,  $C_2 = 9 \cdot 10^{-4}$ ,  $C_3 = C_2/2$ . The weights have been chosen to 1 so that consequently all terms have the same influence on  $S$ .

Figure 4a shows the relation between  $S$  and the maximum differences of  $\Delta PCV$ . Again, zero zenith constrained  $\Delta PCV$  are shown by squares, non-constrained  $\Delta PCV$  by circles. It can be seen that the SSIM is not affected by a constant value within the PCC and that the index performs overall similar to  $c$  (cf. Fig. 3a). However, especially for PCC6  $S$  states a lower similarity compared to  $c$ . The same conclusions can be drawn from Fig. 4b, where the relation between  $S$  and the RMS of  $\Delta PCV$  is shown.

All in all, the SSIM is a very powerful measure to compare different sets of PCC. However, a change of the parameters ( $C_k$  and weights) and the corresponding impact on  $S$  needs further investigations. Thanks to its ease of application the Pearson correlation coefficient could be used for comparisons of PCC since it gives principally the same conclusions.

## 5 Feature Detection Algorithms

Feature detection algorithms are widely used to find distinctive and corresponding points in two images of the same scene. According to Bay et al. (2008), they can be divided into three main steps: (i) detection of *interest points* like corners or blobs, (ii) representation of the *interest point's* neighbourhood by a feature vector – known as the *descriptor* – and (iii) matching of the *descriptors* between different images.

In the context of comparing PCC, feature detection algorithms could be used to find blobs in  $\Delta PCC$  which would indicate larger PCC differences in a certain area. Figure 5

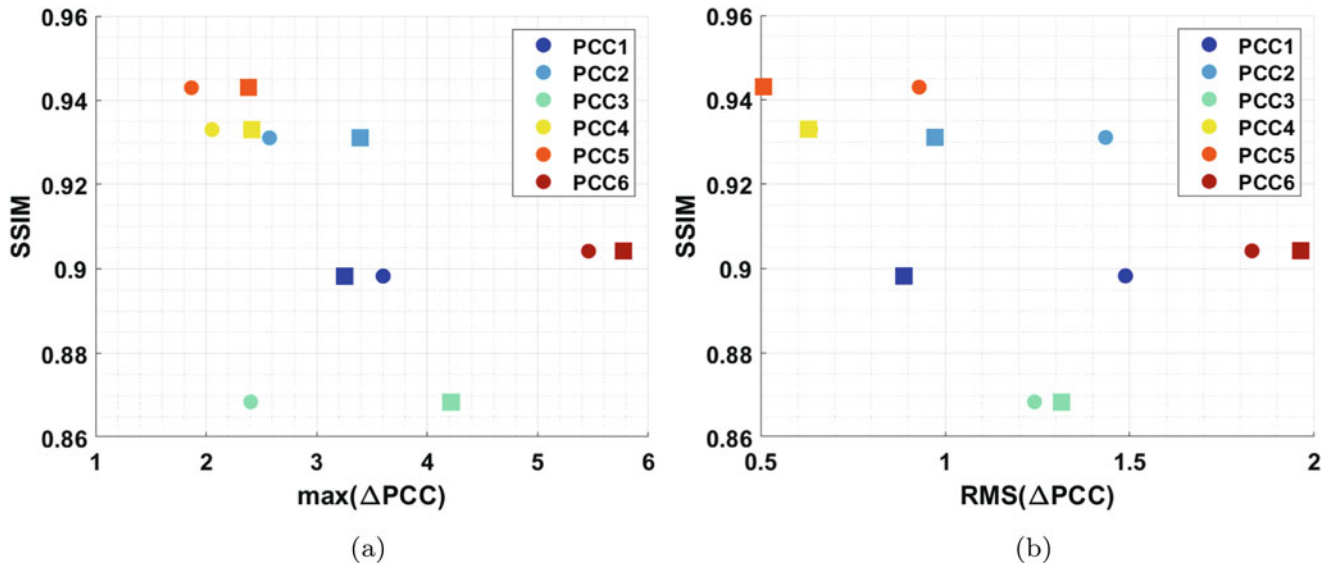


**Fig. 4** Relations between SSIM  $S$  and (a) maximum differences and (b) RMS of  $\Delta\widehat{PCCV}$ . Zero zenith constrained  $\Delta\widehat{PCCV}$  are shown by squares, non-constrained  $\Delta\widehat{PCCV}$  by circles

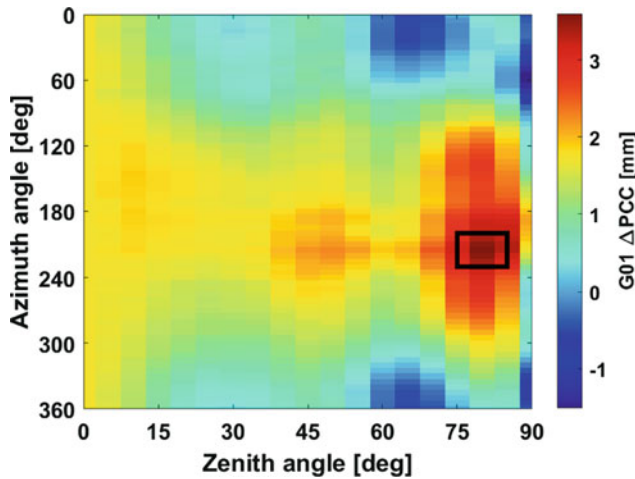


**Fig. 5**  $\Delta PCC1$

shows the  $\Delta PCC$  of PCC1. The black rectangle highlights a local structure which could be detected by a feature detection algorithm.

We used the Speeded-Up Robust Features (SURF) algorithm in order to find blobs in  $\Delta PCC$ . It is a scale- and rotation-invariant detector and descriptor proposed by Bay et al. (2008). Our analyses have shown that the so-called blob features are mainly not detected since PCC are due to estimation by SH quite smooth. Moreover, the PCC resolution of  $5^\circ$  steps makes a detection quite hard because fine structures get lost. Also taking the  $\Delta\widehat{PCCV}$  as the input

image or carrying out a rescaling of the differences to the interval  $[0, 1]$  does not lead to a successful result by use of the SURF algorithm.

## 6 Singular Value Decomposition

The Singular Value Decomposition (SVD) is a widely used tool for e.g. matrix characterisation, data reduction or the solving of nearly singular linear equations (Stewart 1993; Wall et al. 2003). Here, in the context of comparing PCC, SVD can be used to express the  $\Delta PCC$  as the product of the three matrices  $U$ ,  $S$  and  $V$ , whereas the matrix  $S$  contains the singular values  $s_i$  on the main diagonal

$$\Delta PCC = U \cdot S \cdot V^T = \sum_{i=1}^n u_i \cdot s_i \cdot v_i^T = \sum_{i=1}^n M_i \quad (7)$$

The SVD can be used to analyse which structures  $\Delta PCC$  are composed of and to investigate if structures are present within  $\Delta PCC$ , which could be neglected. It is an approximation of the  $\Delta PCC$  data matrix in terms of the Frobenius norm. The rectangular data matrix represents a map of the hemisphere. It should be noted that each grid point contributes equally to the Frobenius norm, although grid points at high zenith angles represents a larger area of the spherical segment. This is a general drawback of the commonly used mapping method for PCC.

Figure 6 shows the differences between the complete  $\Delta PCC1$  and the summation of SVD results of  $\Delta PCC1$  up to  $M_4$  in a cumulative histogram. If the first four SVD structures are summed up, most of the  $\Delta PCC$  information is kept since the differences to the full  $\Delta PCC$  are smaller than 0.2 mm. All other structures can be assumed to be neglectable.

This is also underlined by Fig. 7, which depicts these findings for different antennas. In Fig. 7a, the magnitude of the singular values  $s_i$  are shown. For all samples, the first singular value  $s_1$  contains by far the most information.

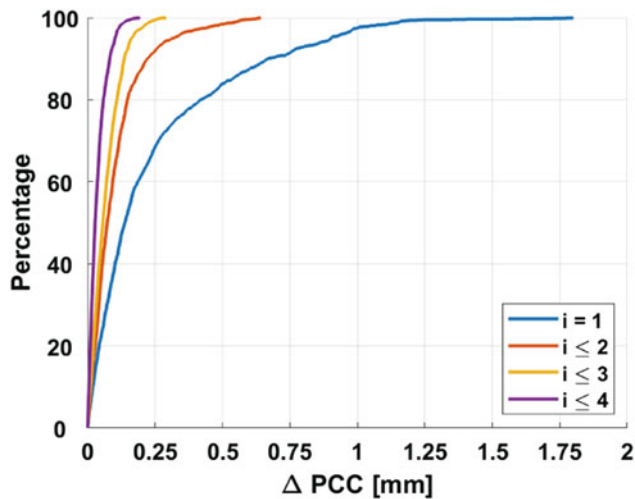


Fig. 6 SVD of  $\Delta PCC1$

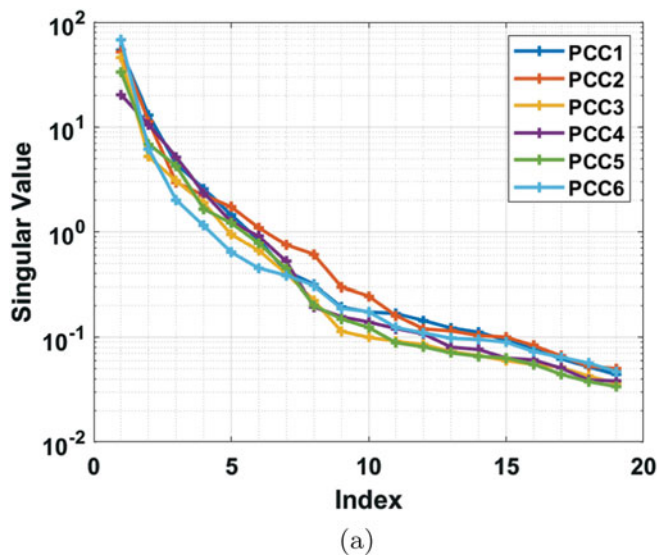


Figure 7b illustrates the differences between the full  $\Delta PCC$  set and the first four structures ( $s < 5$ , cf. Eq. 7) in a cumulative histogram. These structures contain almost all  $\Delta PCC$  information since the differences to the full  $\Delta PCC$  are below 0.25 mm.

Figure 8 shows simulated  $\Delta PCC$  with different introduced offsets for the PCO. In Figs. 8a–c one offset has been introduced: 5 mm for the horizontal components North (N) and East (E), 160 mm for the horizontal Up component (U). In Figs. 8e and f offsets for all three PCO components have been introduced, using the above-mentioned order of magnitudes. While for the first cases all pattern information is contained in  $M_1$ , for the latter case  $M_1$  and  $M_2$  contain these structures.

Clearly visible structures can be found for all cases. They depend on the respective trigonometrical functions for calculating the PCO. Therefore, for example, the negative North offset of 5 mm is present for azimuth angles  $0^\circ$  and  $360^\circ$  and zenith angle  $90^\circ$ , see Fig. 8a. Keep in mind the changed sign of the PCO within the PCC, cf. Eq. 1.

Figures 9, 10, 11, 12 show the SVD of  $\Delta PCC$  up to  $M_4$  for four of the six different antennas introduced in Table 1 (PCC1, PCC2, PCC5, PCC6). For all examples, it can be clearly seen that the order of magnitude decreases with increasing degree of the singular value  $s$ . Please note the different scales for the colour-coded  $\Delta PCC$ . This representation is chosen so that small structures for the different antennas are detectable.

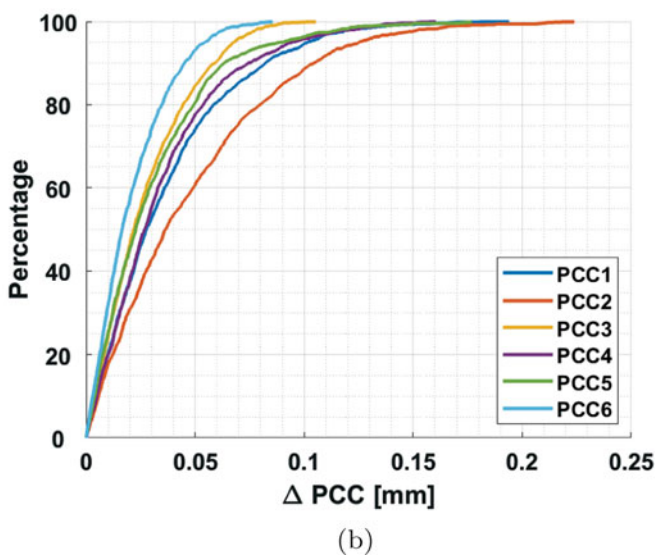
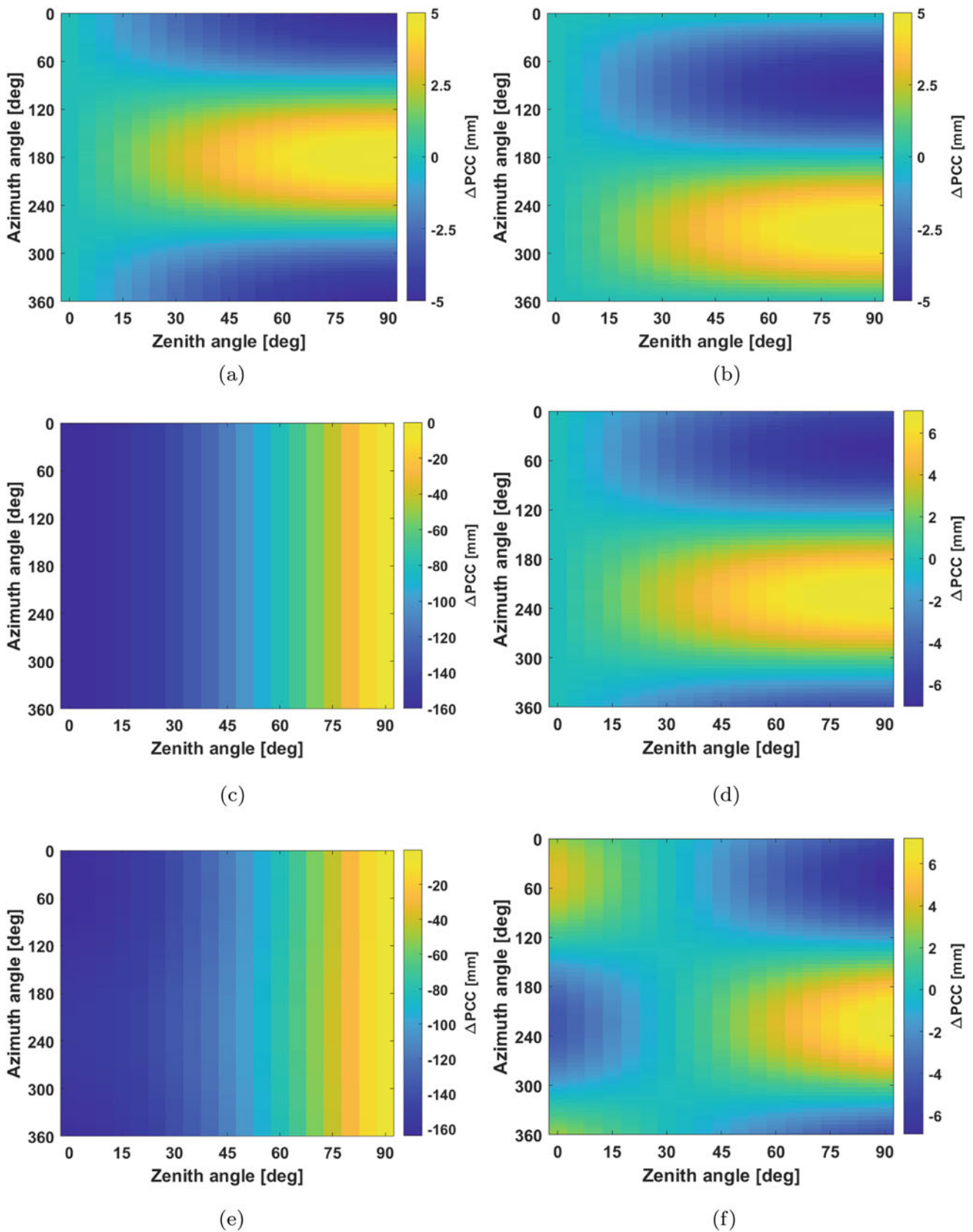
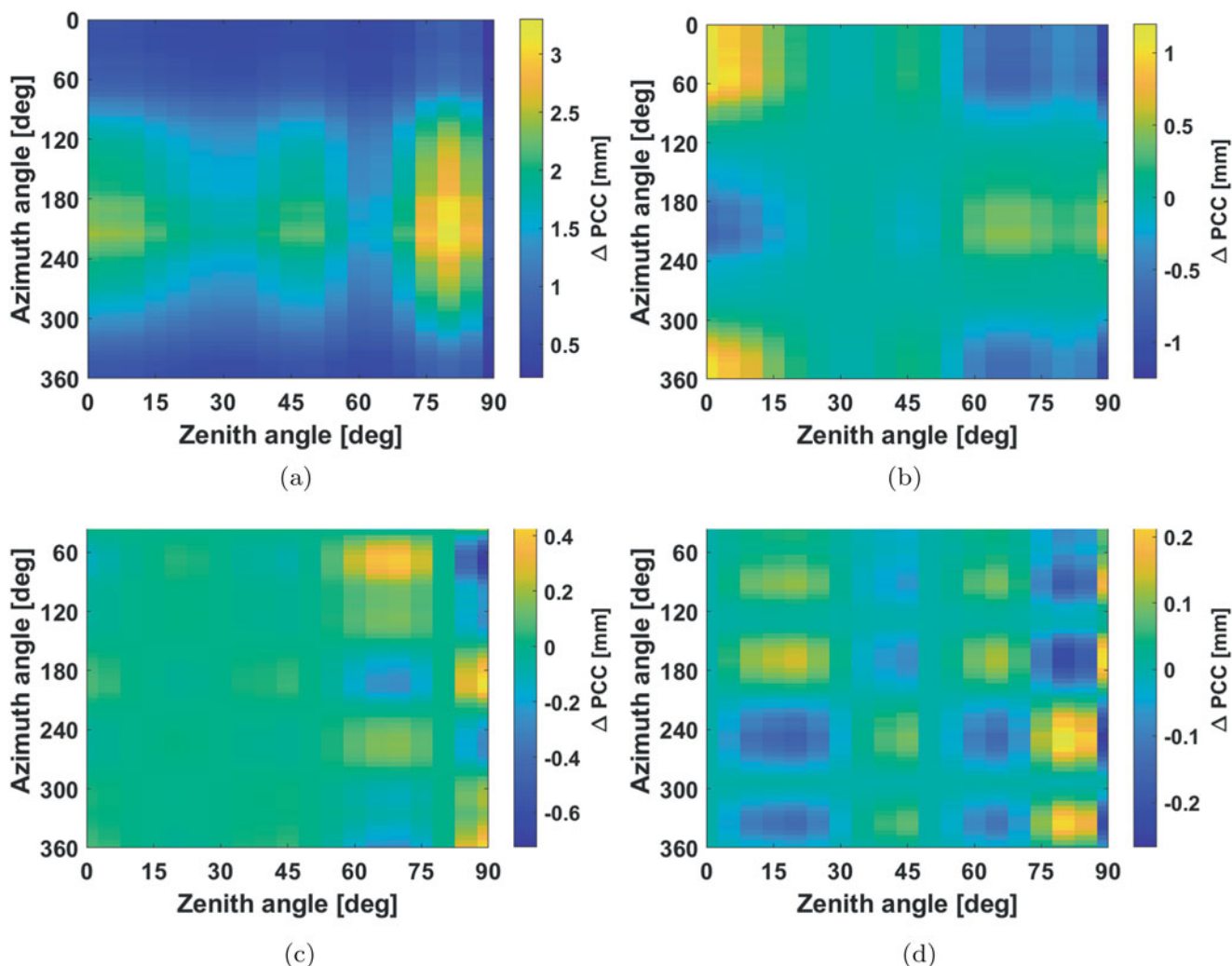


Fig. 7 SVD results for different antenna types showing (a) the magnitude of singular values  $s_i$  and (b) differences between full  $\Delta PCC$  and summation of individual structures up to  $M_4$ , cf. Table 1



**Fig. 8** SVD of simulated PCC with introducing different PCO offsets. (a)  $M_1$ ,  $N = 5$  mm,  $M_1$ ,  $E = 5$  mm. (b)  $M_1$ ,  $U = 160$  mm. (c)  $M_1$ ,  $N = E = 5$  mm. (d)  $M_1$ ,  $N = E = 5$  mm,  $U = 160$  mm. (e)  $M_2$ ,  $N = E = 5$  mm,  $U = 160$  mm





**Fig. 9** SVD of  $\Delta PCC1$  (LEIAR25.R3 LEIT). (a)  $M_1$ . (b)  $M_2$ . (c)  $M_3$ . (d)  $M_4$

A higher similarity between the different antennas is observable with increasing degree  $i$ . For example, a chessboard behaviour is detectable for  $M_4$  for all antennas. This incisive structure can also be found partly in  $M_3$ , e.g. visible in Fig. 9c at high zenith angles, in Fig. 10c or in Fig. 11c. This chessboard structure is to some extent related to the chosen degree and order of the SH expansion. Since the used parameters are usually not reported, a detailed analysis of the relation between number of zero crossings and degree and order of the SH expansion cannot be carried out here, but needs further investigation. It is worth noticing that this structure was also used by Geiger (1988) as a specific antenna type in order to analyse analytically the impact in the position domain. This underlines that the SVD can be a promising tool for error propagation from pattern level to position domain.

If the SVD results of  $PCC1$  in Fig. 9 are compared to the full difference pattern shown in Fig. 5, the main structures are reflected in  $M_1$ . Actually, the advantage of SVD gets clear when having a look on  $M_2$ , since this structure would otherwise not be detectable. By comparing  $M_2$  (Fig. 9b) with  $M_2$  of the simulated  $PCC$  in Fig. 8f, an overall comparable structure is observable. This could indicate, that the  $\Delta PCC$  of  $PCC1$  includes a larger offset in at least one of the horizontal PCO components, i.e. North or East. Although a single comparison of the PCO components without taking the corresponding PCV into account for comparing different sets of  $PCC$  is not fully correct, it can give a first idea of the differences. In this case,  $\Delta N = 1.18$  mm which could explain the structure and order of magnitude of  $M_2$ . However, some parts of this structures could additionally be present in  $M_1$ ,  $M_3$  or  $M_4$ .

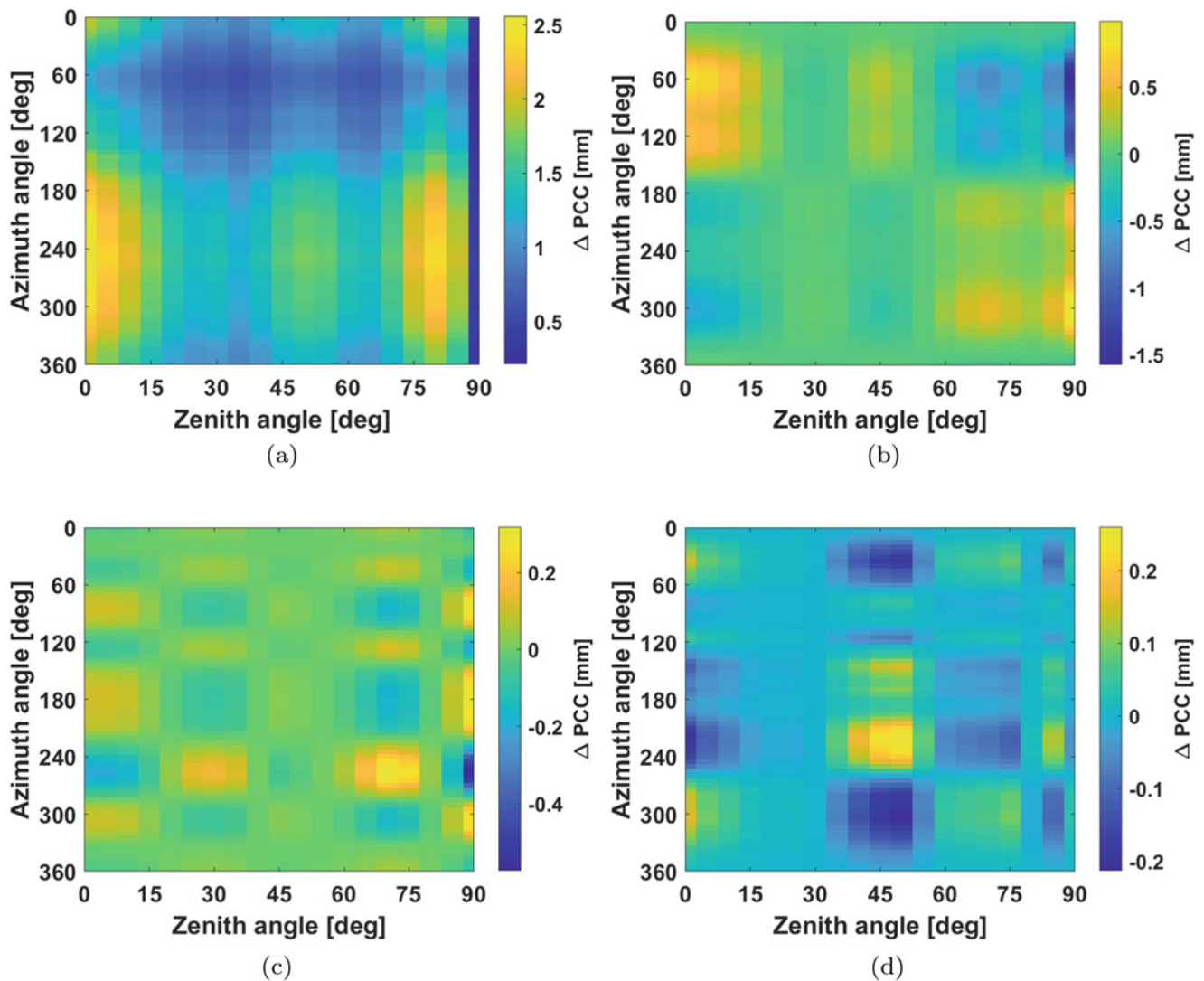


**Fig. 10** SVD of  $\Delta PCC_2$  (LEIAR25.R3 LEIT). (a)  $M_1$ . (b)  $M_2$ . (c)  $M_3$ . (d)  $M_4$

Another behaviour of the simulated PCC can be detected in Fig. 12a for  $M_1$ . In this case, a clear PCO-Up offset can be seen, similar to the one shown in Figs. 8c and e. This is reflected as mainly zenith-dependent differences in  $M_1$ .

## 7 Conclusion

In this paper, we presented the potential of image similarity metrics for comparing PCC. We showed that the Pearson correlation coefficient  $c$  is an appropriate way to

measure the similarity of different PCC sets by a scalar quantity. However, it needs to be transformed beforehand to a common PCO. We demonstrated that  $c$  is independent of a constant part within the pattern and that it is – compared to the powerful SSIM – easy to use. Additionally, the results were compared w.r.t. widely used comparison metrics like the RMS or maximum deviation of  $\Delta PCC$ .

Our analyses of SURF, as an example for a feature detection algorithm, showed that mostly distinctive structures within  $\Delta PCC$  are not found. This is due to the smooth character of the PCC.

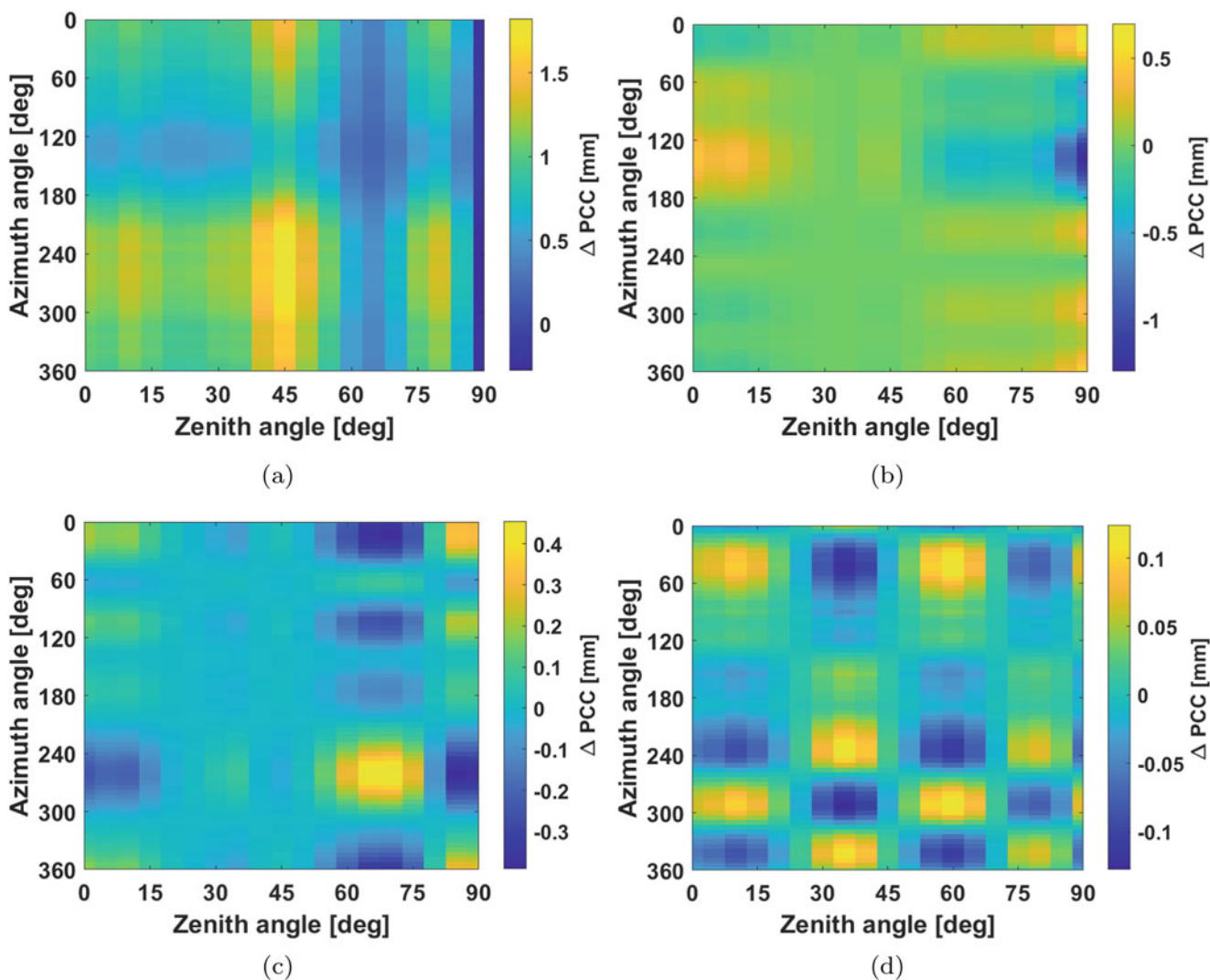


**Fig. 11** SVD of  $\Delta PCC_5$  (LEIAR25.R3 NONE). (a)  $M_1$ . (b)  $M_2$ . (c)  $M_3$ . (d)  $M_4$

On the other hand, SVD of  $\Delta PCC$  can be a promising tool to analyse the impact of PCC differences from the pattern level to the coordinate domain. We illustrated that recurring structures can be found in the differences, i.e. offsets in the horizontal or vertical PCO components. Moreover, a chessboard structure is mostly found within the pattern, which is most probably linked to the used degree and order of the SH synthesis.

In future, a detailed analysis of the relation between the chessboard structures and the SH synthesis need to be carried out. Furthermore, the obtained structures should be used to assess the impact in the coordinate domain. Our findings are a good basis for this, since almost all pattern information ( $\Delta < 0.25$  mm) is contained within the first four degrees of the SVD. Therefore, the complex structures of PCC can be simplified.

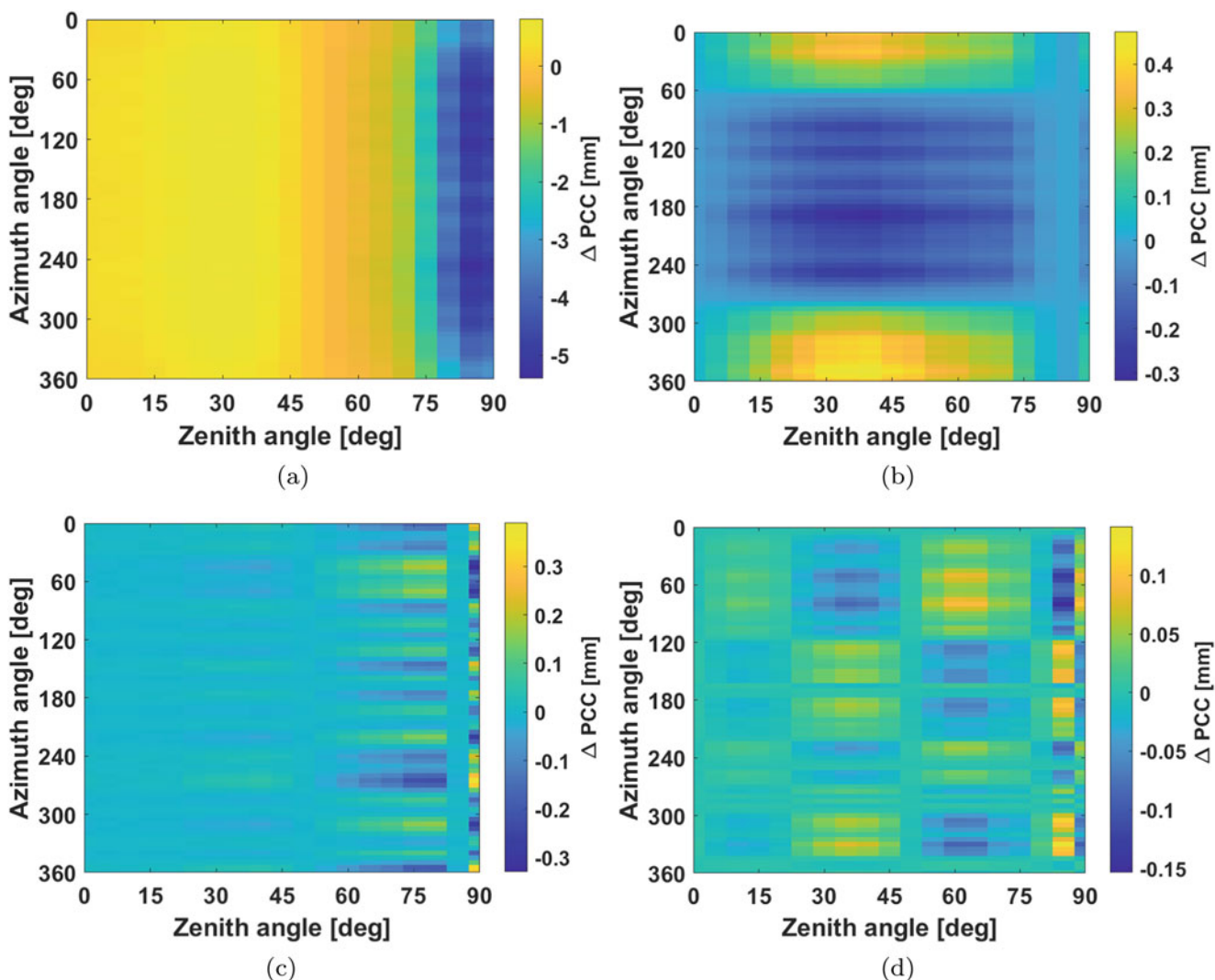


**Fig. 12** SVD of  $\Delta PCC_6$  (TRM15990 SCIS). (a)  $M_1$ . (b)  $M_2$ . (c)  $M_3$ . (d)  $M_4$

**Acknowledgements** The authors would like to thank Franz Rottensteiner from the Institute of Photogrammetry and Geoinformation (IPI) for valuable comments and fruitful discussions on different image similarity metrics.

## References

- Bay H, Ess A, Tuytelaars T, Van Gool L (2008) Speeded-Up Robust Features (SURF). *Comput Vis Image Underst* 110(3):346–359. <https://doi.org/10.1016/j.cviu.2007.09.014>
- Becker M, Zeimet P, Schönemann E (2010) Anechoic Chamber calibrations of phase center variations for new and existing GNSS signals and potential impacts in IGS processing. In: Presentation at the IGS Workshop 2010 and vertical rates symposium, June 28–July 2, Newcastle, United Kingdom of Great Britain
- Bilich A, Mader G, Geoghegan C (2018) 6-axis robot for absolute antenna calibration at the US National Geodetic Survey. In: Presentation at the IGS workshop 2018, October 29–November 2, Wuhan, China, poster
- Bruyninx C, Legrand J (2017) Receiver antenna calibrations available from the EPN CB. In: EUREF AC workshop, October 25–26, Brussels, Belgium
- Caizzone S, Schönfeldt M, Elmarissi W, Ciriuc MS (2021) Antennas as precise sensors for GNSS reference stations and high-performance PNT applications on earth and in space. *Sensors* 21(12). <https://doi.org/10.3390/s21124192>
- Dawidowicz K, Rapiski J, Smieja M, Wielgosz P, Kwasniak D, Jarmolowski W, Grzegory T, Tomaszewski D, Janicka J, Gołaszewski P, Wolak B, Baryla R, Krzan G, Stepniak K, Florin-Catalin G, Brzostowski K (2021) Preliminary results of an Astri/UWM EGNSS receiver antenna calibration facility. *Sensors* 21(14). <https://doi.org/10.3390/s21144639>
- Geiger A (1988) Modeling of phase center variation and its influence on GPS-positioning. In: Groten E, Strauss R (eds) *GPS-techniques applied to geodesy and surveying*, proceedings of the international GPS-workshop Darmstadt, April 10 to 13, 1988, vol 19. Springer, pp 210–222. <https://doi.org/10.1007/bfb0011339>
- Goshtasby AA (2012) *Image registration: Principles, tools and methods*. Springer Science & Business Media. <https://doi.org/10.1007/978-1-4471-2458-0>

- Görres B, Campbell J, Becker M, Siemes M (2006) Absolute calibration of GPS antennas: Laboratory results and comparison with field and robot techniques. *GPS Solutions* 10(2):136–145. <https://doi.org/10.1007/s10291-005-0015-3>
- Kröger J, Kersten T, Breva Y, Schön S (2021) Multi-frequency multi-GNSS receiver antenna calibration at IfE: Concept - calibration results - validation. *Adv Space Res.* <https://doi.org/10.1016/j.asr.2021.01.029>
- Menge F, Seeber G, Völksen C, Wübbena G, Schmitz M (1998) Results of the absolute field calibration of GPS antenna PCV. In: Proceedings of the 11th international technical meeting of the Satellite Division of The Institute of Navigation (ION GPS 1998), September 15–18, Nashville, TN, USA, Institute of Navigation, IEEE, pp 31–38
- Rothacher M, Schmid R (2010) ANTEX: The antenna exchange format, Version 1.4. Tech. rep.
- Schön S, Kersten T (2013) On adequate comparison of Antenna Phase Center variations. In: Presentation at the American Geophysical Union, Annual Fall Meeting 2013, December 09.–13., San Francisco, CA, USA
- Stewart GW (1993) On the early history of the singular value decomposition. *SIAM Review* 35(4):551–566
- Wall ME, Rechtsteiner A, Rocha LM (2003) Singular value decomposition and principal component analysis. In: A practical approach to microarray data analysis. Springer, pp 91–109
- Wang Z, Bovik A, Sheikh H, Simoncelli E (2004) Image quality assessment: from error visibility to structural similarity. *IEEE Trans Image Process* 13(4):600–612. <https://doi.org/10.1109/TIP.2003.819861>
- Wanninger L, Thiemig M, Frevert V (2021) Multi-frequency quadrifilar helix antennas for cm-accurate GNSS positioning. *J Appl Geodesy.* <https://doi.org/10.1515/jag-2021-0042>
- Willi D, Lutz S, Brockmann E, Rothacher M (2019) Absolute field calibration for multi-GNSS receiver antennas at ETH Zurich. *GPS Solutions* 24(1). <https://doi.org/10.1007/s10291-019-0941-0>
- Wübbena G, Schmitz M, Warneke A (2019) Geo++ absolute multi frequency GNSS antenna calibration. In: Presentation at the EUREF Analysis Center (AC) Workshop, October 16–17, Warsaw, Poland
- Zeimetz P (2010) Zur Entwicklung und Bewertung der absoluten GNSS-Antennenkalibrierung im HF-Labor. PhD thesis, Institut für Geodäsie und Geoinformation, Universität Bonn

**Open Access** This chapter is licensed under the terms of the Creative Commons Attribution 4.0 International License (<http://creativecommons.org/licenses/by/4.0/>), which permits use, sharing, adaptation, distribution and reproduction in any medium or format, as long as you give appropriate credit to the original author(s) and the source, provide a link to the Creative Commons license and indicate if changes were made.

The images or other third party material in this chapter are included in the chapter's Creative Commons license, unless indicated otherwise in a credit line to the material. If material is not included in the chapter's Creative Commons license and your intended use is not permitted by statutory regulation or exceeds the permitted use, you will need to obtain permission directly from the copyright holder.





# Multipath Characterization Using Ray-Tracing in Urban Trenches

Lucy Icking, Fabian Ruwisch, and Steffen Schön

## Abstract

Multipath in urban environments still represents a great challenge for Global Navigation Satellite System (GNSS) positioning as it is a degrading factor which limits the attainable accuracy, precision and integrity. In an urban trench, the dense building structures in the vicinity of the antenna cause reflections of the satellite signals resulting in multipath errors. Various work has been presented for simulating reflections for stations under laboratory conditions, yet the simulative analysis of multipath propagation in urban environments is currently developing.

In this contribution, we enhanced an existing Ray-Tracing algorithm which identifies potentially multipath affected satellite signals. So far, it calculates reflection points on a plane ground and estimates the resulting multipath error. We extended it for the urban area case by introducing a 3D city building model with possible reflections on all surfaces of the buildings. Based on the geometry between the antenna position, satellite position and the reflection surface, the extra path delays, the characteristics of the propagation channel and the signal amplitudes are calculated. The resulting multipath errors are then estimated from the discriminator function using state of the art correlator parameters and antenna models.

For a validation, the simulation results are compared with code-minus-carrier combination from a real GNSS experiment in a dense urban area in Hannover. We find that the simulated multipath errors fit the observations in terms of the amplitude, but with uncertainties in the building model, the multipath wave length is too large. The distance to the reflection surface is a key factor which influences the multipath wavelength.

## Keywords

3DMA GNSS · Multipath · Ray-Tracing · Urban GNSS

## 1 Introduction

GNSS positioning in urban areas is still a challenging task due to surrounding buildings causing signal reflection and blockage. These environmental conditions lead to non-line-of-sight (NLOS) and multipath (LOS plus reflection) signal

receptions which is the main error source of GNSS positioning in urban areas (McGraw et al. 2021). In literature, it is usually differentiated between an urban canyon with high rise buildings on both sides of the street (e.g. New York, Hong Kong) and urban trenches with low rise buildings, often found in European cities like Hannover or Toulouse (Betaille et al. 2013). Although there are less satellite blockages in urban trenches than in urban canyons, the buildings still reduce the availability of satellites and increase the probability for multipath errors compared to open sky areas as they present large reflection surfaces (Groves 2013; Hsu 2017). While there are already many approaches developed

L. Icking (✉) · F. Ruwisch · S. Schön  
Leibniz Universität Hannover, Institut für Erdmessung, Hannover,  
Germany  
e-mail: [icking@ife.uni-hannover.de](mailto:icking@ife.uni-hannover.de)

to exclude NLOS signals (Obst et al. 2012; Peyraud et al. 2013) or to correct NLOS signals (Suzuki and Kubo 2013; Hsu et al. 2016), a detailed study to model multipath signals in a realistic urban scenario is still missing. Various work has been presented for simulating reflections under laboratory conditions to evaluate the characteristics and the impact of multipath on GNSS observations. This includes Hannah (2001) and Smyrnaiois et al. (2013), where an antenna is set up on the ground with precisely known height to model and analyze the impact of multipath on the signal strength and carrier phase error. In Smyrnaiois et al. (2012), a precise laser scan building model for ray tracing is applied to show in a simulation that at a typical GNSS reference station, the code error due to multipath for one satellite can reach 0.2 m. Yet, the simulative analysis of multipath propagation in urban environments is currently still under development (cf. van Diggelen (2021); Zhang et al. (2021)) and needs more investigation on the behavior of signal errors and the required accuracy of the building models.

In this work, we use Ray-Tracing to identify epochs in which multipath occurs in a first step and apply multipath modelling in a second step. To this end, we include environmental aspects from a building model and from material properties as well receiver and antenna characteristics for a detailed look on the multipath error. Furthermore, we take a look at the limitations of current building models accuracy on multipath modelling.

The remainder of this paper is structured as follows. In Sect. 2, we give an overview over the methodology of the study, namely the simulation of multipath errors and the setup for the urban experiment. In Sect. 3, we will take a detailed look on the results of the comparison between multipath simulation and measured error. Lastly, Sect. 4 will sum up the findings and give a brief outlook.

## 2 Methodology

### 2.1 Simulation

For the simulation purpose, we need several input parameters as shown in the first row of Fig. 1. To perform the Ray-Tracing algorithm, a building model is applied in level of detail 2, meaning that buildings are represented by a cuboid with a simplified roof on top. The height accuracy of the roofs inside the building model is  $\pm 1$  m (Landeshauptstadt Hannover, FB Planen und Stadtentwicklung, Bereich Geoinformation 2017). Additionally, the values of permittivity and conductivity of the wall's material are taken from International Telecommunication Union Radiocommunication Sector (ITU-R).

As the simulation is performed for the time and place of the experiment later described in this paper, the coordinates

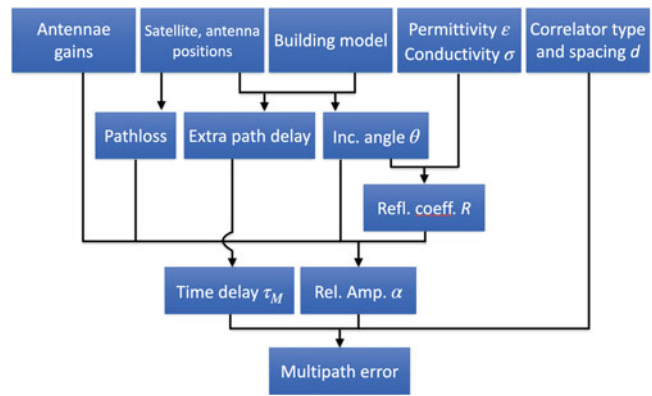


**Fig. 1** General flowchart of the multipath error calculation following (Smyrnaiois et al. 2013)

**Table 1** Signal ray characterization based on LOS and reflection possibility

Class	LOS	Reflection
LOS	Yes	No
Multipath	Yes	Yes
NLOS	No	Yes
Blocked	No	No

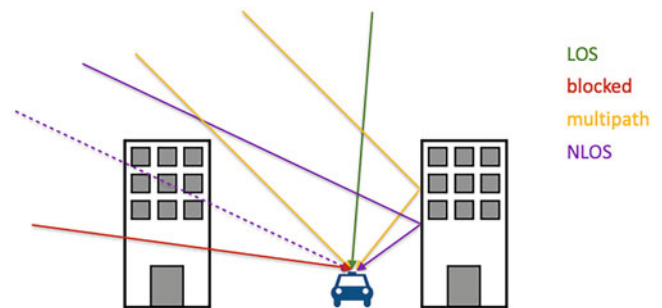


**Fig. 2** Signal ray characterization in urban trench

of the satellites and antenna need to be known for the same time period. While the satellite coordinates are taken from MGEX orbits (Deng et al. 2016), the antenna position from the experiment is calculated through relative positioning with a nearby reference station. The values according to the antenna gain patterns and correlator type and spacing come into account later in the process of receiver delay-lock-loop (DLL) simulation. To begin with the Ray-Tracing as described in Icking et al. (2020), we need to classify the signal rays depending on whether the satellite is within line-of-sight (LOS) and if a reflection on a building model surface is possible. In Table 1, the different ray classes with their respective conditions are listed. A schematic overview is given in Fig. 2, accordingly. In this contribution, we only take the multipath case into account. This condition is reached if the direct line-of-sight (LOS) to the satellite is visible and a reflection on a building surface is possible at the

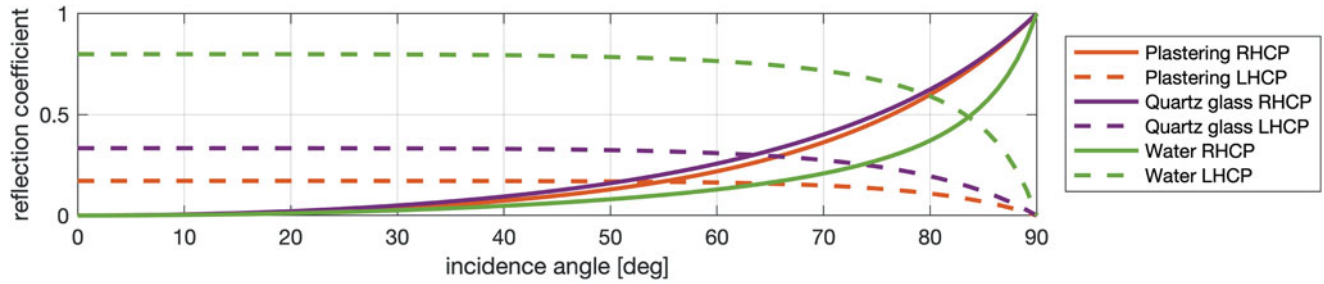


**Fig. 3** Right-Hand-Circular-Polarized (RHCP) and Left-Hand-Circular-Polarized (LHCP) reflection coefficients for selected materials

same time. During the Ray-Tracing process, we are able to calculate the extra path delay  $\delta$  of the reflected signal and the incidence angle  $\theta$  at the reflection surface. In a next step, the reflection coefficient  $R$  is determined following International Telecommunication Union Radiocommunication Sector (ITU-R) and Smyrnaio et al. (2013) as the combination of the perpendicularly polarized component  $R_{\perp}$  and the parallelly polarized component  $R_{\parallel}$ :

$$R_{\perp} = \frac{\cos(\theta) - \sqrt{\varepsilon - \sin^2(\theta)}}{\cos(\theta) + \sqrt{\varepsilon - \sin^2(\theta)}} \quad (1)$$

$$R_{\parallel} = \frac{\varepsilon \cos(\theta) - \sqrt{\varepsilon - \sin^2(\theta)}}{\varepsilon \cos(\theta) + \sqrt{\varepsilon - \sin^2(\theta)}} \quad (2)$$

$$R_{\text{RHCP}} = \frac{R_{\perp} + R_{\parallel}}{2} \quad (3)$$

$$R_{\text{LHCP}} = \frac{R_{\perp} - R_{\parallel}}{2}, \quad (4)$$

where  $\varepsilon$  is the complex dielectric constant

$$\varepsilon = \varepsilon_r - i60\lambda\sigma \quad (5)$$

with  $\lambda$  being the carrier phase wavelength. As input values, the permittivity  $\varepsilon_r$  and conductivity  $\sigma$  of the facade material has been set to  $\varepsilon_r = 2 \frac{F}{m}$  and  $\sigma = 2 \cdot 10^{-5} \frac{S}{m}$ .

The impact of different materials on  $R$  is visible in Fig. 3. The solid line represents the reflection coefficient for the Right-Hand-Circular-Polarized (RHCP), the dashed line for the Left-Hand-Circular-Polarized (LHCP) part of the signal. The chosen material parameters above represent plastering, however it can be noticed that a watery surface would change the coefficients drastically. Quartz glass windows also have a different reflection coefficient, though the difference to plastering is greater for the LHCP part.

The relative amplitude  $\alpha$  between the direct and indirect signal is calculated from  $R$ ,  $\theta$ , the pathloss and the receiver and transmitter antenna gains. The resulting multipath error  $\rho_{\text{MP}}$  at the DLL Discriminator is a function of the correlator

spacing, extra path delay  $\delta$  and  $\alpha$  and can be approximated according to Bilich (2006) by

$$\rho_{\text{MP}} = \frac{\alpha\delta \cos\left(\frac{2\pi\delta}{\lambda}\right)}{1 + \alpha \cos\left(\frac{2\pi\delta}{\lambda}\right)}. \quad (6)$$

The multipath error oscillates, its amplitude is mainly determined by the relative amplitude while the oscillation frequency depends on the extra path delay.

## 2.2 Experiment and Observations

For a validation of the simulation concept, an experiment was conducted in a residential area of Hannover, Germany. A car was parked in a street with a width of approx. 12 m between buildings and a building height of approx. 20 m. Since it is parked at the side of the street, the distance from the antenna to the closest building is 2.6 m. A photo of the antenna mounted on the roof of the car can be seen in Fig. 4. The measurement collection lasted for 7 h at a rate of 1 Hz. The skyplot (cf., Fig. 5) gives an overview of four exemplary GPS satellites which will be analyzed in detail. Additionally, the included obstruction mask shows the harsh challenging location of the experiment. In this work, we focus on the GPS L1 signal. Signals with lower carrier



**Fig. 4** Antenna setup in Hannover residential area with narrow streets



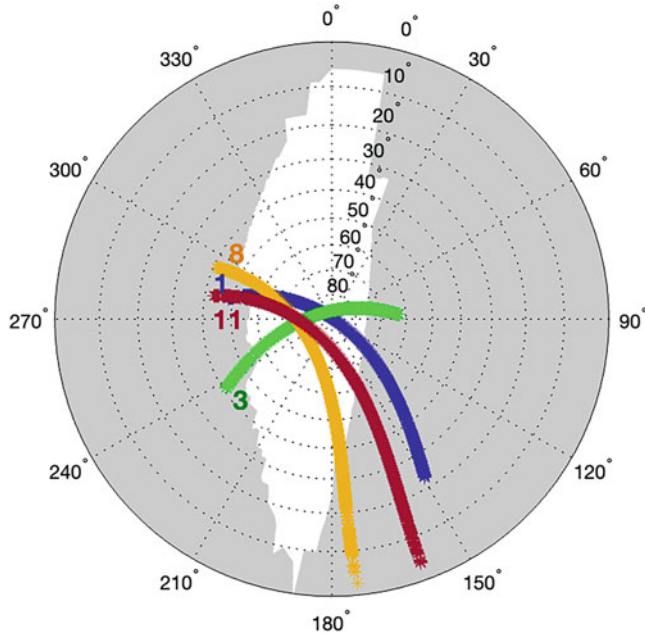


**Fig. 5** Skyplot of selected satellites G01, G03, G08, G11. The obstructed area in the skyplot is represented in gray

frequencies compared to  $L1$ , e.g.  $L2$  and  $L5$ , would have a lower oscillation frequency according to Eq. 6.

To analyze station dependent multipath effects, Code-Minus-Carrier (CMC) values are calculated from the recorded observations (Braasch 2017). To this end, for each arc we perform

$$\begin{aligned} \text{CMC} &= \rho_{L1} - \phi_{L1} \\ &= \text{MP}_{\rho_{L1}} - \text{MP}_{\phi_{L1}} - 2I_{L1} + N\lambda_{L1} + \epsilon_{\rho_{L1}} - \epsilon_{\phi_{L1}} \end{aligned} \quad (7)$$

where  $\rho$  and  $\phi$  represent the code and carrier phase observations taken from the observed minus computed. This way, all the common error effects are already deducted. The CMC consists of the code and carrier phase multipath error (the latter is negligible due to its magnitude), twice the ionospheric delay  $I$ , the carrier phase integer ambiguity  $N$  and the code and carrier phase noise  $\epsilon_{\rho_{L1}}$   $\epsilon_{\phi_{L1}}$ . For the mitigation of the remaining ionospheric effects, the IGS TEC map is applied (Hernández-Pajares et al. 2009). The unknown integer ambiguity is assumed to be constant for each arc. Therefore, we use the simple rounding method

$$N = \text{round} \left( \frac{\text{med}(\text{CMC})}{\lambda_{L1}} \right) \cdot \lambda_{L1} \quad (8)$$

to obtain the respective integer ambiguities, with  $\lambda_{L1}$  being the wavelength of  $L1$  frequency.

### 3 Results

Figure 6 shows the calculated CMC for selected satellites together with the simulated multipath error as a black line. The occurrence of multipath, detected by the Ray-Tracing, is colored in yellow.

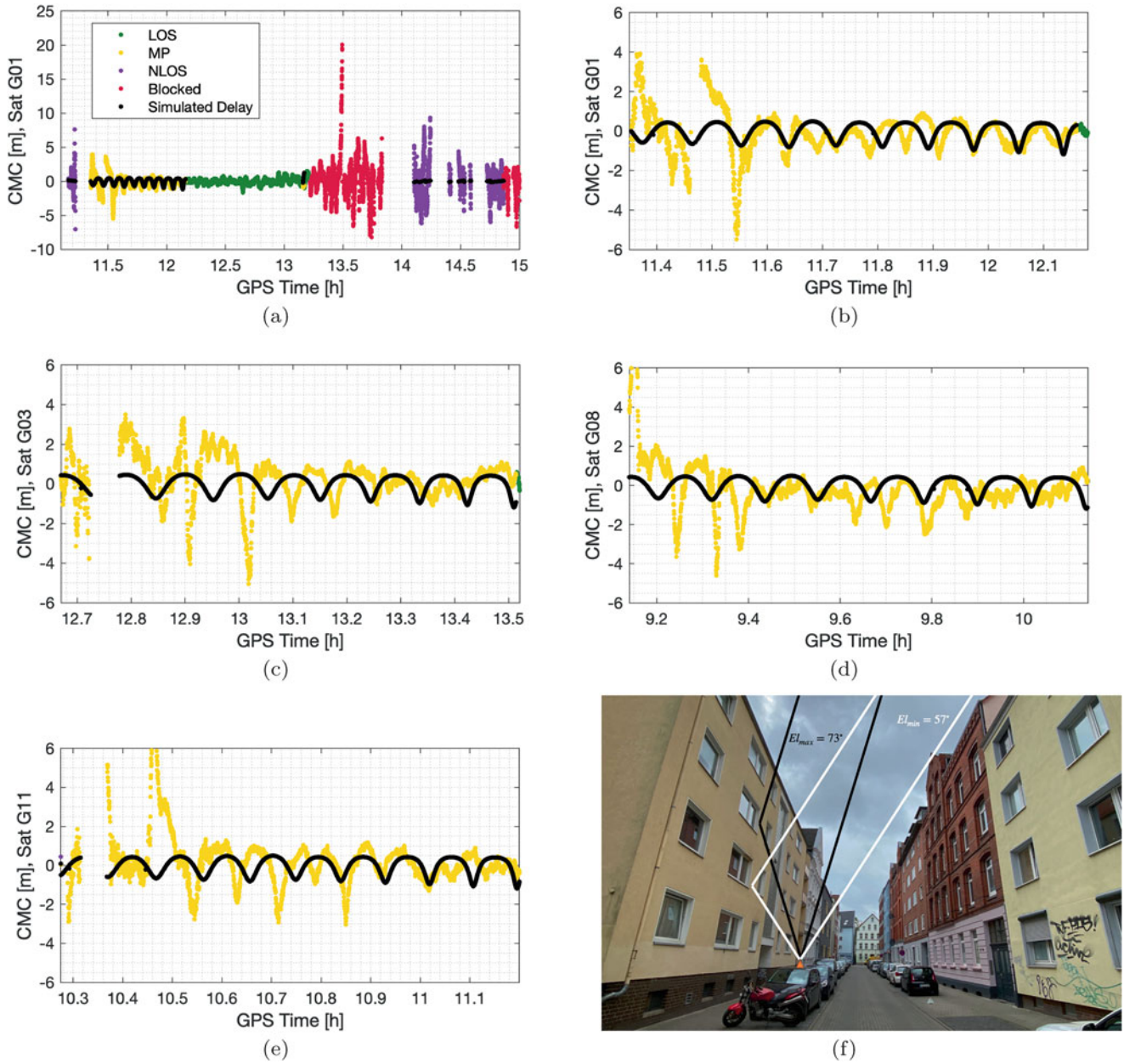
For a first overview, Fig. 6a shows the CMC for satellite G01 over the whole observation period. It is already noticeable that the different classes—LOS, multipath, NLOS and blocked—have a different behavior and error level. During the blocked part, the CMCs reach error levels of up to 20 m and generally vary between  $-8$  m and  $+6$  m, marking the highest error range of the four different zones. Also, the purple coded NLOS has a higher error range of  $-7$  m and  $+10$  m compared to other classes. During green LOS periods, the error is noticeably the lowest with values mostly below 1 m.

Figure 6b now shows a close-up of the multipath section of satellite G01 together with the simulated multipath in black. This multipath section is illustrated in Fig. 6f schematically for the minimum and maximum elevation angle in which a multipath reflection can take place at the experiment site. We can observe the oscillations in the yellow CMC signal, indicating multipath with an amplitude of approx. 1.5 m and a wavelength of approx.  $\lambda = 3$  min 46 sec in the later part. The wavelength is not constant throughout the whole multipath section. At the beginning of the time series, there are large deviations with a structure not similar to the multipath error oscillations in the later time. These are most likely due to other effects occurring during the transition from NLOS to LOS, namely diffraction or multipath of additionally reflected signals.

When comparing the simulated multipath error now with the observed one, we can see that the amplitude of 1.5 m fits well, however the wavelength is not quite met. This is found similarly for satellites G03, G08 and G11 in Figs. 6c–e.

For all satellites, the errors in the beginning of the multipath sections are higher and more irregular, again probably due to additional effects. Satellite G03 shows a higher multipath amplitude than the simulation between 13 and 13.2 h, before transitioning to a noisy state. The wavelength difference between simulations and observations for satellites G08 and G11 is obvious, with the simulations estimating the wavelength too long.

As the wavelength is highly depending on the extra path delay of the reflected signal, the question about the accuracy of the building model rises. The longer the distance between the antenna and the building in the model, the greater the extra path delay, causing a shorter wavelength. As the extra path delay is highest during a perpendicular reflection, a low elevation and an across-street satellite azimuth angle also result in a shorter wavelength.



**Fig. 6** CMC observations color-coded with respect to their respective zones and simulated multipath error for selected satellites in black. (f) schematically shows the minimum and maximum elevation angle for the multipath case at the experiment site

This error factor is tested in Fig. 7. It has to be noted that with the increased reflector distance, the time of the sections for multipath are also shifted. The higher extra path delay causes a higher frequency of the multipath signal, meeting the observations. When subtracting the simulated multipath from the observations in Fig. 7b, we experience an error reduction to less than a meter in the second half of the time series. This method of correction model however is highly dependent on the phase shift of the multipath simulation.

To examine the sensitivity of the reflector distance, we replace the extra path delay  $\delta$  in Eq. 6 with the horizontal, perpendicular distance from the antenna to the reflector  $d_h$ ,

$$\delta = 2 \cdot d_h \cdot \cos(EI_{sat} - EI_n) \cdot \cos(Az_{sat} - Az_n). \quad (9)$$

$EI_{sat}$  and  $Az_{sat}$  denote the elevation and azimuth angle of the satellite,  $EI_n$  and  $Az_n$  those of the reflector normal vector, respectively.

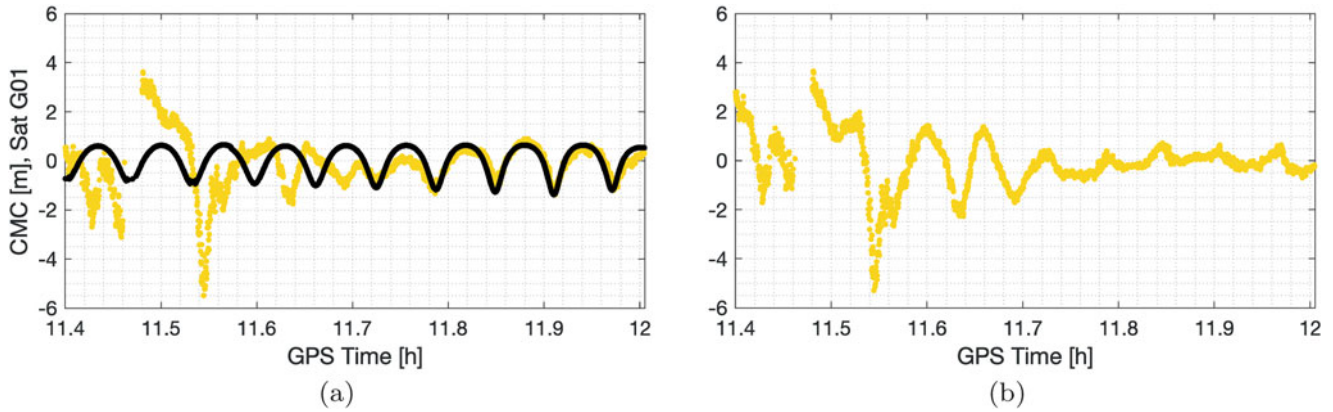


**Fig. 7** CMC of G01 (a) with an increased distance to the reflection surface to fit the MP, (b) corrected by the simulated delay

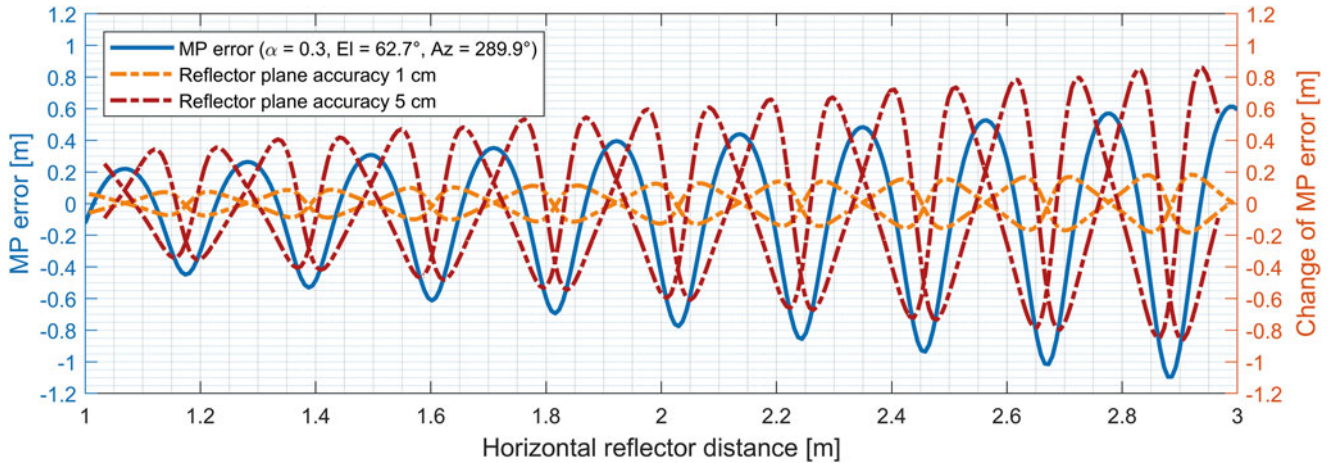


**Fig. 8** Code multipath error for one specific satellite position with changing horizontal reflector distance in blue.  $Az_n = 276.5^\circ$  for the vertical reflection plane. The orange/red curves show the influence of different reflection plane accuracies

Taking the parameters of satellite G01 as in Fig. 7, we can see that the multipath error changes a whole period within a reflector distance of 21 cm (cf. blue line in Fig. 8). If the distance to the reflector is wrongly determined, instead of correcting the multipath error, it can be in fact increased. The dashed lines show the difference of the multipath error calculated at one specific reflector distance to the multipath error obtained at  $d_h \pm 1$  cm and  $d_h \pm 5$  cm, respectively. With an accuracy for the horizontal distance  $d_h$  of 1 cm as in the orange dashed line, the maximum error of determining the multipath error is  $\pm 20$  cm. With a lower accuracy of 5 cm as in the red dashed line, the wrong-determination can go up to  $\pm 80$  cm, which is even higher than the actual error. This concludes that the horizontal distance to the reflector plane is highly sensitive to the cm-level.

## 4 Conclusion and Outlook

In this contribution, we present a method to characterize and classify signal rays as well as an approach to simulate the multipath error using a Ray-Tracing approach, taking environmental information and receiver properties into account. We could observe that the sections classified as multipath indeed contain oscillations highly indicating multipath. However, additional effects like diffraction or multipath of additionally reflected signals will come into place during those sections causing higher errors. The classification needs to include some transition phases as the signal condition does not switch states within one sudden epoch.

Concerning the simulated multipath error, we were able to see that the magnitude of the simulation fits to decimeter

level in epochs with stable and regular multipath oscillations. Nevertheless, the wavelength and the phase of the multipath observations prove to be hard to match. The inaccuracies and generalized characteristics of the building model in use will influence the extra path delay, directly affecting the wavelength of the simulated multipath.

We have shown a sensitivity analysis for the change of the code multipath error with respect to the change of the horizontal distance to the reflector. To precisely match the observed errors with the simulation results, both the antenna and reflector position have to be known in cm-level. On the other hand, this sensitivity may open opportunities to determine the actual distance to the reflector from the observed multipath errors and hence, to improve the lateral positioning in urban trenches.

**Acknowledgements** This work was supported by the German Research Foundation (DFG) as part of the Research Training Group i.c.sens [RTG 2159] as well as by TÜV-Rheinland (PT-TÜV) under the grant 19A20002C funded by the German Federal Ministry for Economic Affairs and Energy (BMWi). Special thanks to Septentrio N.V. for sharing detailed receiver information.

## References

- Betaille D, Peyret F, Ortiz M, Miquel S, Fontenay L (2013) A new modeling based on urban trenches to improve GNSS positioning quality of service in cities. *IEEE Intell Transp Syst Mag* 5(3):59–70. <https://doi.org/10.1109/mits.2013.2263460>
- Bilich AL (2006) Improving the precision and accuracy of geodetic GPS: Applications to multipath and seismology. Ph.D. thesis, University of Colorado
- Braasch MS (2017) Springer handbook of global navigation satellite systems, chap. 15. Multipath, pp 443–468. Springer International Publishing
- Deng Z, Fritsche M, Nischan T, Bradke M (2016) Multi-GNSS ultra rapid orbit-, clock- & EOP-product series. Tech. rep., GFZ data services. <https://doi.org/10.5880/GFZ.1.1.2016.003>
- Groves P (2013) GNSS solutions: Multipath vs. NLOS signals. How does non-line-of-sight reception differ from multipath interference. *Inside GNSS (Mag)* 8:40–42
- Hannah BM (2001) Modelling and simulation of GPS multipath propagation. Ph.D. thesis, Queensland University Of Technology
- Hernández-Pajares M, Juan JM, Sanz J, Orus R, García-Rigo A, Felzens J, Komjathy A, Schaer SC, Krankowski A (2009) The IGS VTEC maps: A reliable source of ionospheric information since 1998. *J Geodesy* 83(3):263–275. <https://doi.org/10.1007/s00190-008-0266-1>
- Hsu LT (2017) Analysis and modeling GPS NLOS effect in highly urbanized area. *GPS Solutions* 22(1):7. <https://doi.org/10.1007/s10291-017-0667-9>
- Hsu LT, Gu Y, Kamijo S (2016) 3D building model-based pedestrian positioning method using GPS/GLONASS/QZSS and its reliability calculation. *GPS Solutions* 20(3):413–428. <https://doi.org/10.1007/s10291-015-0451-7>
- Icking L, Kersten T, Schön S (2020) Evaluating the urban trench model for improved GNSS positioning in urban areas. In: 2020 IEEE/ION position, location and navigation symposium (PLANS). IEEE. <https://doi.org/10.1109/plans46316.2020.9109998>
- International Telecommunication Union Radiocommunication Sector (ITU-R) (2019) Recommendation ITU-R P.527-5 electrical characteristics of the surface of the Earth. Tech. Rep. P.527-5
- Landeshauptstadt Hannover, FB Planen und Stadtentwicklung, Bereich Geoinformation (2017) Produktinformation Digitales 3D-Stadtmodell. Landeshauptstadt Hannover, Rudolf-Hillebrecht-Platz 1, 30159 Hannover, 3rd edn.
- McGraw GA, Groves PD, Ashman BW (2021) Position, navigation, and timing technologies in the 21st century: integrated satellite navigation, sensor systems, and civil applications, chap. 22. Robust Positioning in the Presence of Multipath and NLOS GNSS Signals, pp 551–589. Wiley, Hoboken, New Jersey
- Obst M, Bauer S, Wanielik G (2012) Urban multipath detection and mitigation with dynamic 3D maps for reliable land vehicle localization. In: Proceedings of the 2012 IEEE/ION position, location and navigation symposium, pp 685–691. IEEE. <https://doi.org/10.1109/plans.2012.6236944>
- Peyraud S, Betaille D, Renault S, Ortiz M, Mougél F, Meizel D, Peyret F (2013) About non-line-of-sight satellite detection and exclusion in a 3d map-aided localization algorithm. *Sensors* 13(1):829–847. <https://doi.org/10.3390/s130100829>
- Smyrmaios M, Schön S, Nicolas ML, Kurner T (2012) Ray-tracing approach versus double difference, multipath characterization in a multiple ray scenario. In: 2012 6th ESA workshop on satellite navigation technologies (Navitec 2012) & European workshop on GNSS signals and signal processing. IEEE. <https://doi.org/10.1109/navitec.2012.6423089>
- Smyrmaios M, Schön S, Nicolàs ML (2013) Multipath propagation, characterization and model in GNSS. In: Jin S (ed) Geodetic sciences - observations, modeling and applications, earth and planetary sciences, chap. 2, pp 99–125. InTech, Rijeka, Croatia, License: CC BY 3.0 - open access. <https://doi.org/10.5772/54567>
- Suzuki T, Kubo N (2013) Correcting GNSS multipath errors using a 3D surface model and particle filter. In: Proceedings of the 26th international technical meeting of the satellite division of The Institute of Navigation (ION GNSS+ 2013), pp 1583–1595. Nashville, TN
- van Diggelen F (2021) Google's use of 3D building models to solve urban GNSS. In: ITM/PTTI 2021 keynote
- Zhang G, Xu B, Ng HF, Hsu LT (2021) GNSS RUMS: GNSS realistic urban multiagent simulator for collaborative positioning research. *Remote Sensing* 13(4):544. <https://doi.org/10.3390/rs13040544>

**Open Access** This chapter is licensed under the terms of the Creative Commons Attribution 4.0 International License (<http://creativecommons.org/licenses/by/4.0/>), which permits use, sharing, adaptation, distribution and reproduction in any medium or format, as long as you give appropriate credit to the original author(s) and the source, provide a link to the Creative Commons license and indicate if changes were made.

The images or other third party material in this chapter are included in the chapter's Creative Commons license, unless indicated otherwise in a credit line to the material. If material is not included in the chapter's Creative Commons license and your intended use is not permitted by statutory regulation or exceeds the permitted use, you will need to obtain permission directly from the copyright holder.





# Bounding the Residual Tropospheric Error by Interval Analysis

Jingyao Su and Steffen Schön

## Abstract

GNSS integrity monitoring requires proper bounding to characterize all ranging error sources. Unlike classical approaches based on probabilistic assumptions, our alternative integrity approach depends on deterministic interval bounds as inputs. The intrinsically linear uncertainty propagation with intervals is adequate to describe remaining systematic uncertainty, the so-called imprecision. In this contribution, we make a proposal on how to derive the required intervals in order to quantify and bound the residual error for empirical troposphere models, based on the refined sensitivity analysis via interval arithmetic. We evaluated experimentally the Saastamoinen model with (i) a priori ISO standard atmosphere, and (ii) on-site meteorological measurements from IGS and Deutscher Wetterdienst (DWD) stations as inputs. We obtain consistent and complete enclosure of residual ZPD errors w.r.t IGS ZPD products. Thanks to the DWD dense network, interval maps for meteorological parameters and residual ZPD errors are generated for Germany as by-products. These experimental results and products are finally validated, taking advantage of the high-quality tropospheric delays estimated by the Vienna Ray Tracer. Overall, the results indicate that our strategy based on interval analysis successfully bounds tropospheric model uncertainty. This will contribute to a realistic uncertainty assessment of GNSS-based single point positioning.

## Keywords

Error bounding · Global navigation satellite systems · Integrity · Interval analysis · Residual tropospheric error

## 1 Introduction

Nowadays, GNSS is used for many safety-critical applications, such as aviation and autonomous driving, where the high-integrity performance of the navigation system must be ensured. To assess the integrity, i.e., the trust that we can put into a navigation solution, all contributing observation error sources are to be quantified and propagated to the

position domain. A Protection Level (PL) is calculated as the bound on these propagated errors, including code noise and multipath, clock and orbit errors, residual ionospheric error, and residual tropospheric error (Rife et al. 2006). To avoid any underestimation of the PLs, these separate error sources need to be modeled and bounded properly.

As one of the primary error sources, the tropospheric error is in practice widely corrected by well-developed empirical troposphere models. For example, the Saastamoinen model is applied in a “blind” mode with a priori standard atmosphere, e.g., ISO2533 (ISO et al. 1995) or U.S. standard atmosphere, and the Global Pressure and Temperature model GPT2 (Lagler et al. 2013); the Radio Technical Commission for Aeronautics (RTCA) recommends the model of Askne

J. Su (✉) · S. Schön  
Institut für Erdmessung, Leibniz Universität Hannover, Hannover,  
Germany  
e-mail: [suj@ife.uni-hannover.de](mailto:suj@ife.uni-hannover.de); [schoen@ife.uni-hannover.de](mailto:schoen@ife.uni-hannover.de)

and Nordius (1987) to estimate the wet delay for the minimum operational performance standard (MOPS) (RTCA-DO229 2006); these two models are also adopted in GPT2w (Böhm et al. 2015) and GPT3 (Landskron and Böhm 2018), fed with corresponding empirical meteorological models. The performance of these models must be evaluated, and the residual error must be modeled to ensure high-integrity navigation solutions.

Up until now, the residual tropospheric error is treated stochastically in almost all bounding methods, and subsequently a quadratic error propagation is applied. For example, MOPS indicates a maximum vertical error of 0.12 m in terms of standard deviation globally for its correction model (RTCA-DO229 2006); In aviation, the overbounding method is developed based on conservative approximations of cumulative density function (CDF) (DeCleene 2000; Rife et al. 2006); Rózsa (2018) and Rózsa et al. (2020) introduced the generalized extreme value theory to account for the tails of the distribution and developed residual tropospheric error models; Gallon et al. (2021) investigated time correlation modeling by bounding the autocorrelation function (ACF) and power spectral density (PSD). The resulting bounds on stochastic parameters for residual tropospheric errors are utilized in Kalman filters.

The methods mentioned above are applied almost exclusively in a stochastic manner. However, the exact error distribution is often unknown, and remaining systematic errors may persist so that alternative linear uncertainty propagation should be studied (Schön and Kutterer 2005). Unlike classical approaches based on probabilistic assumptions, the alternative integrity approach depends on deterministic interval bounds as inputs, which are usually defined as the maximum variation of the error in worst cases or with a confidence level under probabilistic assumptions (Dbouk and Schön 2019; Su and Schön 2022). Very few studies have yet focused on the determination of meaningful observation interval bounds in general and on interval bounding for residual tropospheric errors in particular. Schön and Kutterer (2006) introduced the method of sensitivity analysis to GNSS applications but still did not validate with real data.

This contribution, in response, will make a proposal on how to derive the required interval bounds based on interval analysis in order to quantify and bound the residual tropospheric error and validate it, as summarized in Fig. 1.

The remainder is organized as follows: Sect. 2 reviews the sensitivity analysis and refines it in view of interval arithmetic. Section 3 introduced the strategy how we estimate the uncertainty of model influence factors. In Sect. 4, we implement the proposed method with the Saastamoinen model with a priori standard atmosphere (ISO2533). We obtain the uncertainty of meteorological parameters taking advantage of IGS meteorological measurements as well as climate

data from the Deutsche Wetterdienst (DWD). Interval maps for meteorological parameters and residual ZPD errors that assess their uncertainty are generated as by-products over Germany. Finally, we validate the resulting bounds through comparison of tropospheric delay residuals based on empirical cumulative functions in Sect. 5. Concluding remarks and an outlook are given in Sect. 6.

## 2 Methodology: Sensitivity Analysis

This section first summarizes the definitions and basic operations of intervals; next reviews the concept of sensitivity analysis that is applied in previous studies, and reformulate the method in view of interval arithmetic.

### 2.1 Basics of Interval Arithmetic

An interval is defined as  $[x] = [\underline{x}, \bar{x}]$ , with  $\underline{x}$  being the lower bound and  $\bar{x}$  upper bound.

For any bounded, and non-empty interval  $[x]$ , the midpoint  $mid([x]) = x_m$  and radius  $rad([x]) = x_r$  are defined as:

$$mid([x]) = x_m \triangleq \frac{\underline{x} + \bar{x}}{2}, \quad rad([x]) = x_r \triangleq \frac{\bar{x} - \underline{x}}{2} \quad (1)$$

The real-valued arithmetic operations can be mostly extended to intervals, with the same basic operators:  $+$ ,  $-$ ,  $\times$ ,  $\div$ ,  $\sin$ ,  $\tan$ ,  $\exp$  and so on:

$$[x] \diamond [y] = \{x \diamond y \in \mathbb{R} \mid x \in [x], y \in [y]\} \quad (2)$$

where  $[x]$  and  $[y]$  are intervals and  $\diamond$  can be any of the algebraic operations listed above.

Similarly, an interval vector or interval matrix is higher dimensional, which are defined as the Cartesian product of  $n$  and  $m \times n$  interval, separately.

If  $f$  represents a real-valued function of a single real variable  $x$ , the range of values determined by  $f(x)$  as  $x$  varies within a given interval  $[x]$  is the image of set  $\{x \mid x \in [x]\}$  under mapping  $f$ :

$$f([x]) = \{f(x) \mid x \in [x]\} \quad (3)$$

Analogously, if  $f$  is a function of multiple real variable  $\mathbf{x} = [x_1, \dots, x_m]^T$ , the output interval of  $f$  when its  $i$ -th variable  $x_i$  varies in an interval  $[x_i]$  reads:

$$f([x_i] \mid \mathbf{x}^*) = \{f(\mathbf{x}) \mid x_i \in [x_i], \mathbf{x}_{(\dots, i-1, i+1, \dots)} = \mathbf{x}_{(\dots, i-1, i+1, \dots)}^*\}$$

in other words, the set image of  $[x_i]$  under the mapping  $f$ ; all other variables have their values from  $\mathbf{x}^*$ .

Interested readers will find more detailed introduction about interval computations in textbooks, e.g., Jaulin et al. (2001) and Moore et al. (2009).

### 2.2 Sensitivity Analysis in View of Intervals

Sensitivity analysis is a forward modeling approach to assess the uncertainty due to remaining systematic errors (ISO et al. 1995) and can be applied on GNSS observations (Schön and Kutterer 2006). The basic idea behind is as follows: the empirical models are built based on assumptions deviating from reality and approximations with uncertainty. Hence, the constants and parameters used in the models are often only imprecisely known and associated with a given range. Their uncertainties should contribute to a maximum range of variation (interval) for the model’s output. This interval reflects the uncertainty due to remaining systematic errors.

To this end, the approach by Schön and Kutterer (2006) computes sensitivity coefficients through partial differentiation and subsequently computes an interval radius for the final uncertainty budget:

Consider a dedicated model  $f$  with  $m$  influence factors  $\mathbf{x} = \{x_i, i = 1, \dots, m\}$ . For given values of  $\mathbf{x} = \mathbf{x}^*$ , and their uncertainty in terms of interval radii  $\mathbf{x}_r$ , the matrix of sensitivity coefficients  $\mathbf{F}$  and final interval radius  $f_r$  read:

$$\mathbf{F} = \frac{\partial f(\mathbf{x}^*)}{\partial \mathbf{x}_r}, f_r = |\mathbf{F}| \cdot \mathbf{x}_r \tag{4}$$

For this method, the partial differentiability of the dedicated model must be given, and uncertainties of influence factors

are assumed to be small enough, which, however, are sometimes invalid.

To cope with this issue, we propose to implement the sensitivity analysis via interval arithmetic:

The model’s uncertainty budget (interval value  $[f]$ ) is expressed as the sum of all influence factors’ contributions:

$$[f] \triangleq [\underline{f}, \overline{f}] = \sum_i^m [f_i] + f(\mathbf{x}^*) \tag{5}$$

with a lower bound ( $\underline{f}$ ) and an upper bound ( $\overline{f}$ ).

The sensitivity  $f_i$  of  $f$  w.r.t the change of one specific influence factor  $x_i$  in its interval  $[x_i] \triangleq [\underline{\Delta x_i}, \overline{\Delta x_i}] + x_i^* = [\underline{x_i}, \overline{x_i}]$  is determined by:

$$[f_i] \triangleq f([x_i] | \mathbf{x}^*) - f(\mathbf{x}^*) \tag{6}$$

The uncertainty is evaluated via interval arithmetic instead of real-valued operations on interval radii, therefore, the resulting uncertainty intervals are not necessarily symmetric w.r.t  $f(\mathbf{x}^*)$ .

### 3 Estimate the Uncertainty of Model Influence Factors

It can be noticed from Sect. 2 that the key to the proposed interval-based sensitivity analysis is the reliable characterization of model’s influence factors and the assessment of their uncertainties. This is because every single influence factor contributes an uncertainty interval to the overall budget, cf. Eqs. 5, 6.

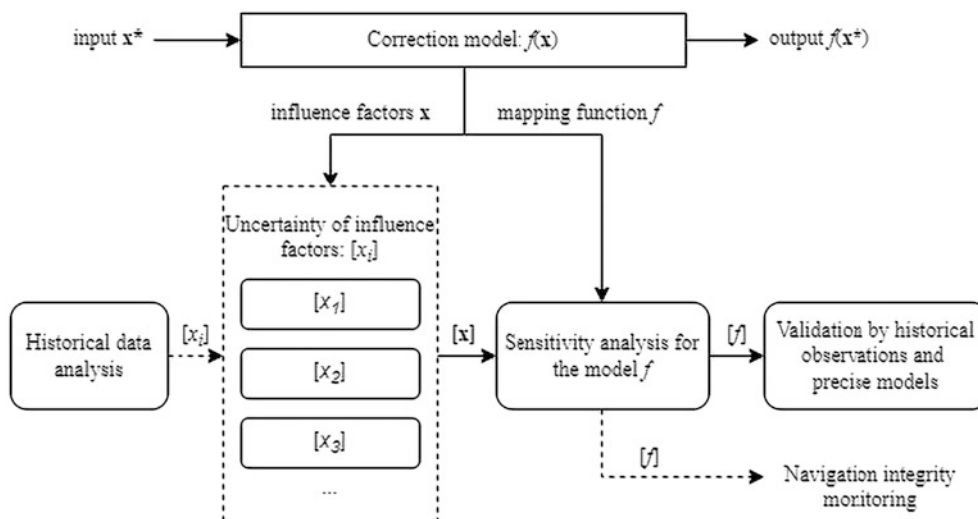


**Fig. 1** Flowchart of the study: for a given correction model  $f(\mathbf{x})$ , we derive its sensitivity w.r.t all influence factors  $[\mathbf{x}]$  mathematically and determine its uncertainty budget  $[f]$  from all contributions. The outputs

are interval bounds under dedicated condition for further integrity applications. They are validated in this study using historical data and precise models

According to JCGM (2008), the uncertainties of model influence factors are evaluated by scientific judgement based on all of the available information:

- uncertainty information indicated in the construction process of the model
- expert knowledge or experience of the behavior and properties of relevant factors
- manufacturer’s specification
- information provided by model’s accuracy evaluations
- uncertainties assigned to reference data taken from handbooks

This paper focuses on the Saastamoinen model (Saastamoinen 1972), which shows that the zenith tropospheric delay (ZPD) can be calculated from surface meteorological parameters as:

$$\Delta L = \beta_1 \frac{(1 + \beta_2 \cos^2(\theta) + \beta_3 H)}{\cos(z)} [p + \beta_4 \frac{T}{e} + \beta_5 e - B \tan^2(z)] + \delta_r \quad (7)$$

where  $\Delta L$  is the range correction,  $p$  is the pressure at the antenna site in  $hPa$ ,  $e$  the partial water vapor pressure in  $hPa$ ,  $T$  the absolute temperature in *Kelvin*,  $B$  and  $\delta_r$  correction terms,  $\beta_1, \beta_2, \dots, \beta_5$  constants, and  $z$  the apparent zenith distance, determined from true zenith distance  $Z$  of the satellite by the formula  $z = Z - \delta z$  with:

$$\delta_z = \frac{\alpha_1}{T} \tan(Z) (p + \frac{\alpha_2}{T} e) - \alpha_3 \tan(Z) (\tan^2(Z) + 1) \frac{p}{1000} \quad (8)$$

where  $\alpha_1, \alpha_2, \alpha_3$  and  $\alpha_4$  are constant coefficients, and  $Z$  can be determined from the station height  $H$  in *meter*, station latitude  $\phi$  in *degree* and satellite elevation  $\theta$  in *radius*. All the primary variables and constants above-mentioned constitute the vector of influence factors  $\mathbf{x}$ , cf. Eqs. 5, 6, for the Saastamoinen model:  $\mathbf{x}_{SAAST} = [T, p, e, \alpha_1, \alpha_2, \alpha_3, \beta_1, \beta_2, \beta_3, \beta_4, \beta_5, H, \phi, \theta]^T$ .

Any physical quantity should only be given with a meaningful number of digits. Half of the last digit of the quantity is often referred to as rounding error. We follow this concept at the first step, assigning an uncertainty due to rounding error to all influence factors of the Saastamoinen model  $\mathbf{x}_{SAAST}$ . This corresponds to the radii of symmetric intervals, cf. Sect. 2.2. For example, Dbouk and Schön (2019) suggests  $Rad([p]) = 0.5 \cdot 10^{-4}$ , when the input value for surface pressure is provided 4-digit.

However, this evaluation of uncertainty may not be realistic, sometimes too optimistic. The actual range of variation for some factors may have a different order of magnitude. In the case of the Saastamoinen model, researchers have studied the uncertainty of a constant coefficient  $\beta_1 = 2.277 \cdot 10^{-3}$ : an error bar of  $0.5 \cdot 10^{-6}$

is given by Davis et al. (1985); Zhang et al. (2016) suggests a value of  $2.2794 \cdot 10^{-3}$ . We adopt a larger value for its interval radius, i.e., the difference of the suggested value to original one plus rounding error,  $Rad([\beta_1]) = (2.4 + 0.5) \cdot 10^{-6}$ , indicating the maximum range of variation of  $\beta_1$ .

Additional care must be paid to the meteorological parameters, because they are inputs of the model and they vary temporally and spatially, having significant influence on the model’s output. According to Feng et al. (2020), the pressure measurements at ground level are less representative of the “true” mean surface pressure than those at a higher level, probably due to turbulence. This will introduce uncertainty to the Saastamoinen model. Therefore, we propose performing long-term statistics against on-site meteorological measurements to estimate their interval bounds. In this contribution, the ISO2533 standard atmosphere is used as the a priori parameters to feed the Saastamoinen model. We define a sliding window of two consecutive months on the time series and from each window, we take all the difference values of the standard atmosphere w.r.t the on-site measurements. The window slides in daily steps. Next, the upper and lower bounds of an interval are derived as a pair of quantiles of data within the sliding window. The quantile pairs should be determined based on the requirement of applications, e.g., [5%, 95%], [0.15%, 99.85%] and minimum/maximum values etc. In this way, daily interval bounds are obtained, i.e.,  $[p]$ ,  $[T]$ , and  $[e]$ .

Figure 2 shows the example results for the IGS stations Potsdam (POTS, a-1, b-1 and c-1) and Oberpfaffenhofen (OBE4, a-2, b-2 and c-2) during the year 2020: residuals of the ISO standard atmosphere (w.r.t on-site measurements, dots in grey) and interval bounds (colored curves) for those parameters, i.e., temperature ( $T$ ), surface pressure ( $p$ ) and water vapor pressure ( $e$ ). The bounds of min/max values are wider, enclosing all the residuals, while the bounds of quantile pairs are relatively narrower, and violated by occasional extreme values.

## 4 Assessment of Residual Tropospheric Error

After having obtained uncertainty intervals of all influence factors  $\mathbf{x}_{SAAST}$ , the sensitivity analysis is implemented for the Saastamoinen model via interval arithmetic based on Eq. 6, resulting in  $S_f(x_{SAAST,i})$ , the sensitivity of the model  $f_{SAAST}$  w.r.t to each of the 14 elements of  $\mathbf{x}_{SAAST}$ . Subsequently,  $[f_{SAAST}]$ , the interval bounds for residual tropospheric errors are computed based on Eq. 5.

To demonstrate results, we compute ZPD residuals, defined as the difference of computed ZPD from the Saastamoinen model w.r.t reference estimates. By definition, the



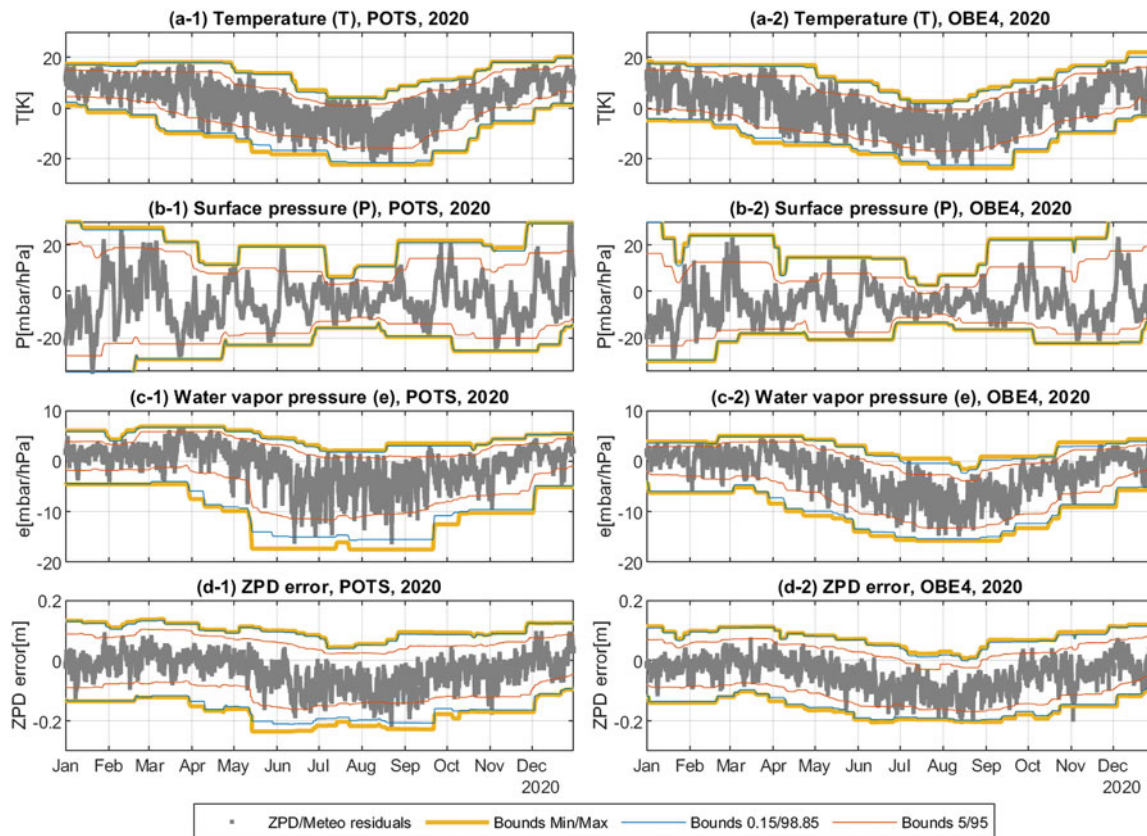


**Fig. 2** Example results of IGS station POTS (left) and OBE4 (right) in 2020: residuals (ISO-to-RNX) and bounds for meteorological parameters (temperature, pressure, partial water vapour) from long-term

statistics. ZPD bounds are computed with these results, and compared to residuals (Saastamoinen with ISO-to-IGS ZPD)

actual “residual ZPD error” is referenced to the truth. For IGS stations POTS and OBE4, we take the IGS ZPD products as reference. In Fig. 2 (d-1, d-2), the residuals are shown as grey dots, compared with the assessed interval bounds (colored curves, obtained with corresponding meteorological interval bounds). We expect complete enclosure of grey dots by colored curves. Obviously, this is the case for the widest interval bounds at POTS station, obtained with min/max meteorological interval bounds. As a comparison, other bounds, computed from quantile pairs, are narrower but may be exceeded by the residuals. For the OBE4 station, an exception can be observed on Nov. 4, 2020, during a short period of which the residuals are not enclosed by any bounds. The cause might be any perturbation occurring in the atmosphere, which cannot be captured by the surface measurements. The uncertainty for meteorological parameters is subsequently underestimated at these epochs, resulting in failures in ZPD bounding. This issue should be resolved in future works by refining the estimation for the uncertainty of relevant influence factors.

In addition, Deutscher Wetterdienst (DWD) operates a dense network of climate sensors over Germany, facilitating the analysis for multiple stations and the estimation for the

geographical distribution of error bounds over the country. We applied a linear interpolation to the scattered dataset and obtained a  $0.25^\circ \times 0.25^\circ$  gridded network. Example results for three meteorological parameters on the day 239 of 2020 are shown in Fig. 3. Using these interval bounds as input to the proposed sensitivity analysis, the interval maps for residual ZPD errors are obtained, cf. Fig. 4. Cross-sections of the interval maps in Fig. 4 along  $9.7^\circ\text{E}$  and  $11.3^\circ\text{E}$  meridians, which cross Hannover and Potsdam, are presented in Fig. 5. From these figures, we are interested in seeking potential dependency of the uncertainty intervals for residual ZPD error on meteorological parameters in terms of their geographical distributions. There are some interesting remarks:

- The “wet” troposphere dominates the overall interval bound, (i) similar pattern of two-dimensional geographical distribution can be found between water vapor pressure (cf. Fig. 3) and residual ZPD error (cf. Fig. 4), (ii) similar tendency of their one-dimensional latitudinal variation can also be observed in Fig. 5.
- Empirical tropospheric correction models may not capture the impact of regional, small-scaled weather events, during which the interval bounds should be expanded

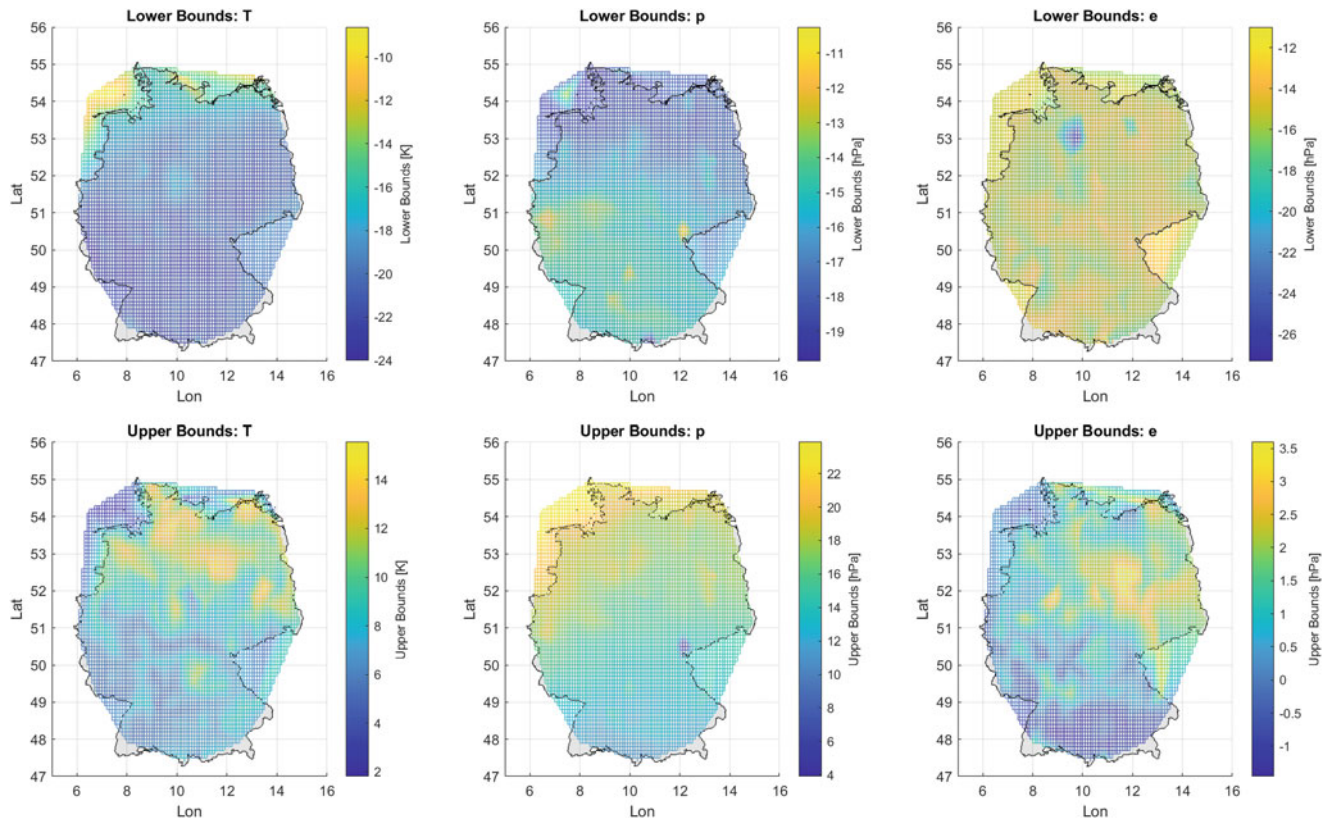


**Fig. 3** Geographical distribution of lower interval bounds (upper column) and upper interval (lower column) bounds (right) for meteorological parameters over Germany on DOY 239 in 2020. The interval bounds are obtained based on statistics for on-site measurements from 215 out of 345 DWD stations

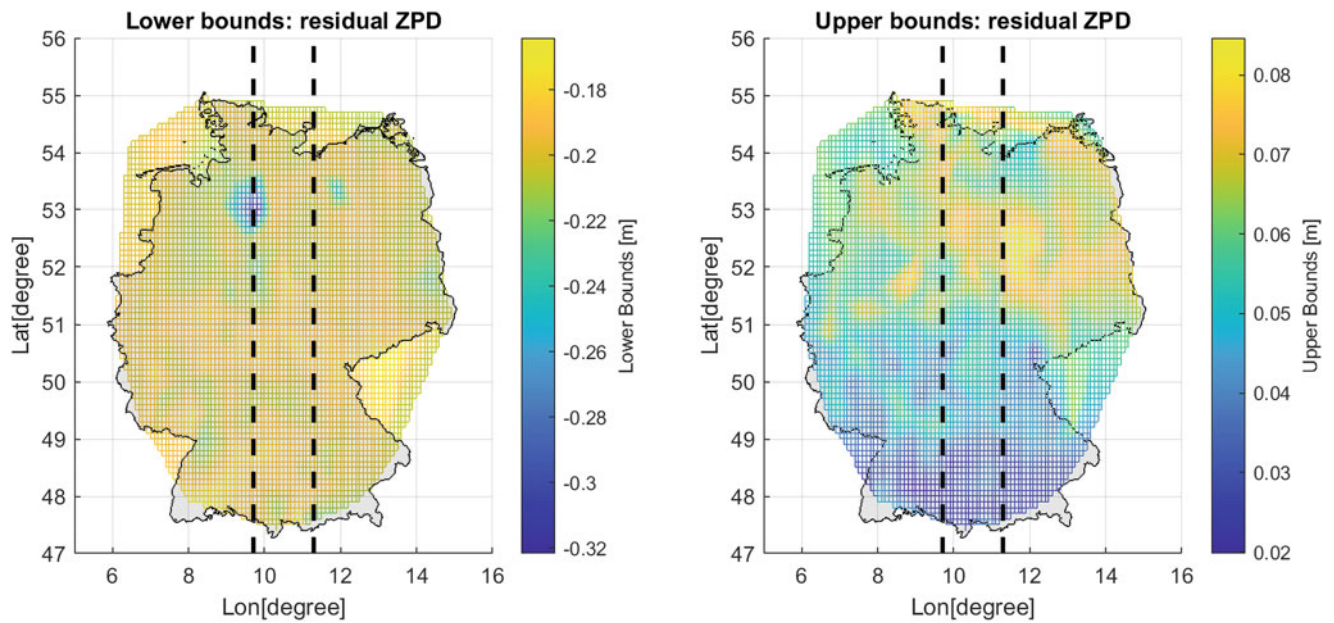


**Fig. 4** Geographical distribution of lower interval bounds (left) and upper interval bounds (right) for bounding the residual ZPD error over Germany on DOY 239 in 2020. The computation is based on the proposed sensitivity analysis of the Saastamoinen model using interval bounds from Fig. 3

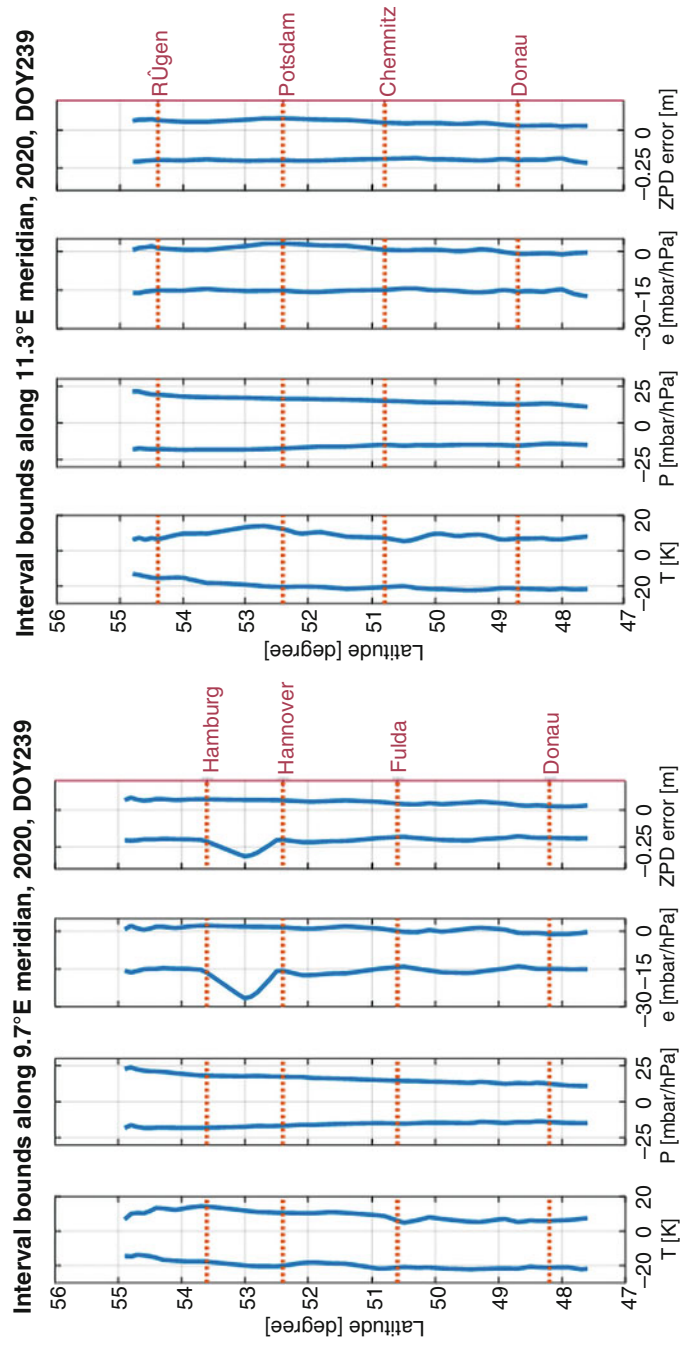


**Fig. 5** Example results: interval bounds for meteorological parameters (from ISO-to-DWD) and ZPD (Saastamoinen with ISO) along the 9.7°E and 11.3°E meridians (denoted in Fig. 4 as black dashed lines) on DOY 239 in 2020. Climate data source: Deutscher Wetterdienst (DWD)

correspondingly. This is visible in Fig. 5: the region between Hamburg and Hannover indicates significant wider intervals for water vapor pressure and residual ZPD error. Counterparts exist in the interval maps in Fig. 4.

- The interval maps for residual ZPD errors show good agreements with the station-wise experimental results. We take POTS station on day 239 of 2020 as an example, which is visible in both of Fig. 2 (d-1, Oct. 26th on  $x$ -axis) and Fig. 5 (right, the fourth sub-figure, 52.379°N on  $y$ -axis): they are assessed based on different uncertainty evaluation for meteorological parameters (Fig. 2 using on-site measurements directly, and Fig. 5 using interpolated values from sensor network), nevertheless, resulting in very close interval values. In fact, we also tested with the other station OBE4 and with more days, showing the difference of ZPD bounds of mm to 10 mm level.

## 5 Validation

In this section, we aim to evaluate how well the bounds enclose potential deviations of the model outputs (e.g., Saastamoinen model with ISO) from reality. Since ground truth for tropospheric delays is difficult to achieve, we take (i) the IGS ZPD products and (ii) estimates from Vienna Ray-Tracer (RT) as reference. The ray-tracing technique directly reconstructs the true signal path and subsequently computes the atmospheric delay along the path based on numerical weather models, hence provides high-quality ZPD and SPD (slant directions) estimation (Hofmeister and Böhm 2017). However, this approach is computational expensive and has a relatively low temporal resolution (6 h), which prevents its usage in real-time applications. We additionally analyze the Saastamoinen model with inputs of on-site meteorological measurements (RNX) for comparison. Intervals for influence

factors and subsequently for residual ZPD errors are determined with same methods, and again referred to IGS ZPD products as well as ray-traced delays.

We define bound-minus-residual (BMR) values, i.e.,  $\underline{\Delta}$ ,  $\overline{\Delta}$ , as the over-bounding indicator:

$$\underline{\Delta} = \underline{f} - (T_M - T_R), \quad \overline{\Delta} = \overline{f} - (T_M - T_R) \quad (9)$$

where  $\underline{f}$  and  $\overline{f}$  are lower and upper bounds of the intervals,  $T_M$  and  $T_R$  denote the modeled troposphere correction and reference delay, respectively. The BMR naturally indicates over-bounding performance for dedicated interval bounds, i.e.,  $\overline{\Delta}$  is supposed to have positive sign and  $\underline{\Delta}$  negative, while both are expected close to zero ideally. Computing a large amount of data, it would be beneficial to observe the statistical parameters, e.g., the empirical cumulative density function (ECDF). Two key aspects regarding ECDF curves are of interest:

1. Success of bounding: whether the bounds sufficiently enclose all residuals, i.e., positive  $\overline{\Delta}$  and negative  $\underline{\Delta}$
2. Conservativity of over-bounding: the width of margin between the bounds and residuals in case of successful bounding, i.e., the deviation of curves from the  $y$ -axis

The ECDF curves for all scenarios for POTS are presented in Fig. 6. We show the values of the 90% percentile and min/max intervals of all ECDF in Table 1. The 90% bound is also indicated as a horizontal dashed red line in Fig. 6. It is worth noting that:

- An input of whether standard atmosphere or on-site meteorological measurements to the Saastamoinen model makes few difference to the uncertainty budget of residual tropospheric errors, no matter in zenith direction, or in slant directions. This is because the inputs to the Saastamoinen model are representative values. Neither of them is advantageous in uncertainty due to the construction process of the model.

**Fig. 6** ECDF of BMR values ( $[\underline{\Delta}, \overline{\Delta}]$ ) for POTS station. The input meteorological data is from either standard atmosphere (ISO) or on-site measurements (RNX); the tropospheric delay residuals are from either zenith delays (ZPD) or slant delays (SPD); the reference data is from either IGS ZPD products (IGS) or Ray-Tracing Technique (RT). 90% of the values are located above the red dashed line

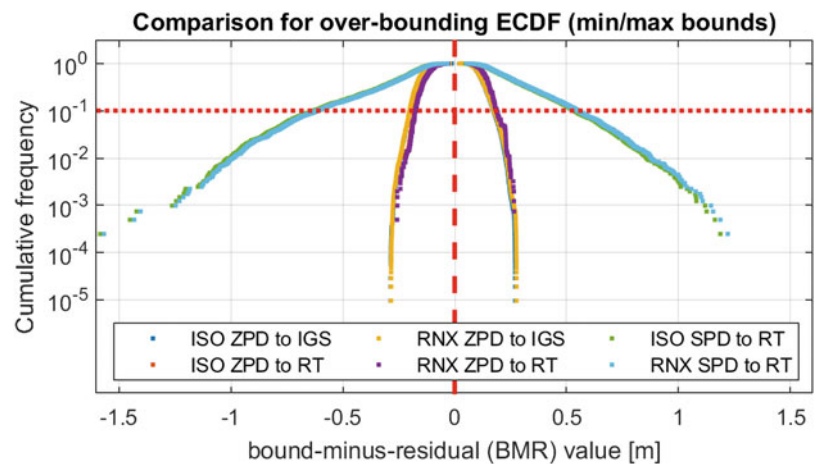


**Table 1** 90% and min/max interval of ECDF for BMR values ( $\underline{\Delta}$ ,  $\overline{\Delta}$ ) for six scenarios as de-

Scenario	90% interval [m]	min/max interval [m]
ISO-ZPD-IGS	[-0.201, 0.174]	[-0.286, 0.271]
ISO-ZPD-RT	[-0.179, 0.182]	[-0.260, 0.260]
RNX-ZPD-IGS	[-0.201, 0.176]	[-0.284, 0.276]
RNX-ZPD-RT	[-0.175, 0.187]	[-0.257, 0.266]
ISO-SPD-RT	[-0.626, 0.537]	[-1.582, 1.322]
RNX-SPD-RT	[-0.613, 0.551]	[-1.566, 1.353]

- Being referred to whether the IGS ZPD products or ray-traced delays, the BMR shows a slight difference in ECDF curves. Both reference data are of high-quality, thus can be cross-checked.
- The ECDF curves are not necessarily symmetric to the  $y$ -axis, because (i) the accuracy of reference is never perfect, and (ii) some influence factors being aligned with symmetric uncertainty intervals may not be adequately assessed. For example, the absolute values  $|\underline{\Delta}|$  are usually greater than  $|\overline{\Delta}|$  in zenith direction for IGS-referenced scenarios (dark blue and yellow). Meanwhile, this is not necessary the case of RT-referenced curves (green, orange, purple and light blue), which are shifted around 2 cm to the right side w.r.t IGS-referenced ones.
- Mapping function: we didn't make an evaluation on the impact of mapping functions in the proposed method but directly inflate the intervals with corresponding mapping factors for slant directions. Therefore, the ECDF curves for SPD (green and light blue) are significantly wider than those for ZPD. Nevertheless, the impact of uncertainty due to mapping functions may be observed from, i.e., the change of asymmetry of ECDF curves from zenith to slant directions: in Table 1, we notice  $|\underline{\Delta}| \leq |\overline{\Delta}|$  for "ISO-ZPD-RT" and "RNX-ZPD-RT" for 90% and min/max intervals, while "ISO-SPD-RT" and "RNX-SPD-RT" are in the opposite situation, i.e.,  $|\underline{\Delta}| > |\overline{\Delta}|$ . This finding suggests the presence of systematic error due to mapping functions, which has to be captured by an additional interval.

## 6 Conclusions and Outlook

Taking the example of the Saastamoinen model, our implementation indicates the feasibility of the proposed method in qualifying and bounding residual tropospheric errors, based on sensitivity analysis via interval arithmetic. To evaluate the bounding performance, we computed bound-minus-residual (BMR) values as over-bounding indicators. Either standard atmosphere or on-site meteorological measurements are input to the Saastamoinen model. Tropospheric delay estimates provided by the IGS and Vienna Ray-Tracer are

taken as reference value. All ZPD and SPD residuals were successfully bounded for test data at POTS station. 90% of the over-bounding BMR values for ZPD are no greater than around 0.2 m.

Uncertainties of the model influence factors must be carefully assessed. The estimation for meteorological parameters is done through long-term statistics against on-site measurements. The usage of on-site measurements facilitates the modeling and bounding of seasonal and geographical dependency. Taking advantage of a dense network of climate sensors such as Deutscher Wetterdienst (DWD), we showed the generation of interval maps to assess the uncertainty for meteorological parameters and residual ZPD errors.

Further work will focus on the potential impact of the mapping functions, as well as the implementation of other empirical tropospheric correction models.

**Acknowledgements** This work was supported by the German Research Foundation (DFG) as part of the Research Training Group i.c.sens [RTG 2159].

The authors gratefully acknowledge Deutscher Wetterdienst (DWD) for providing climate data, Helmholtz-Centre Potsdam GFZ German Research Centre for Geosciences for providing measurement data at POTS and OBE4 stations, International GNSS Service (IGS) for providing GNSS data and products, TU Wien for providing access to the online Ray-Tracer.

## References

- Askne J, Nordius H (1987) Estimation of tropospheric delay for microwaves from surface weather data. *Radio Science* 22(03):379–386. <https://doi.org/10.1029/RS022i003p00379>
- Böhm J, Möller G, Schindelegger M, Pain G, Weber R (2015) Development of an improved empirical model for slant delays in the troposphere (GPT2w). *GPS Solutions* 19(3):433–441. <https://doi.org/10.1007/s10291-014-0403-7>
- Davis JL, Herring TA, Shapiro II, Rogers AEE, Elgered G (1985) Geodesy by radio interferometry: Effects of atmospheric modeling errors on estimates of baseline length. *Radio Science* 20(6):1593–1607. <https://doi.org/10.1029/RS020i006p01593>
- Dbouk H, Schön S (2019) Reliability and integrity measures of GPS positioning via geometrical constraints. In: Proceedings of the 2019 international technical meeting of the institute of navigation, pp 730–743. <https://doi.org/10.33012/2019.16722>
- DeCleene B (2000) Defining pseudorange integrity-overbounding. In: Proceedings of the 13th international technical meeting of the satellite division of the institute of navigation (ION GPS 2000), pp 1916–1924
- Feng P, Li F, Yan J, Zhang F, Barriot JP (2020) Assessment of the accuracy of the Saastamoinen model and VMF1/VMF3 mapping functions with respect to ray-tracing from radiosonde data in the framework of GNSS meteorology. *Remote Sensing* 12(20):3337. <https://doi.org/10.3390/rs12203337>
- Gallon E, Joerg M, Pervan B (2021) Robust modeling of GNSS tropospheric delay dynamics. *IEEE Trans Aerospace Electron Syst* 57(5):2992–3003. <https://doi.org/10.1109/TAES.2021.3068441>

- Hofmeister A, Böhm J (2017) Application of ray-traced tropospheric slant delays to geodetic VLBI analysis. *J Geodesy* 91(8):945–964. <https://doi.org/10.1007/s00190-017-1000-7>
- ISO, IEC, OIML, BIPM (1995) Guide to the expression of uncertainty in measurement. Geneva, Switzerland 122:16–17
- Jaulin L, Kieffer M, Didrit O, Walter E (2001) Applied interval analysis: With examples in parameter and state estimation, robust control and robotics. Springer, London
- JCGM (2008) Evaluation of measurement data - guide to the expression of uncertainty in measurement: JCGM 100:2008 (GUM 1995 with minor corrections)
- Lagler K, Schindelegger M, Böhm J, Krásná H, Nilsson T (2013) GPT2: Empirical slant delay model for radio space geodetic techniques. *Geophys Res Lett* 40(6):1069–1073. <https://doi.org/10.1002/grl.50288>
- Landskron D, Böhm J (2018) VMF3/GPT3: refined discrete and empirical troposphere mapping functions. *J Geodesy* 92(4):349–360. <https://doi.org/10.1007/s00190-017-1066-2>
- Moore RE, Kearfott RB, Cloud MJ (2009) Introduction to interval analysis. SIAM
- Rife J, Pullen S, Enge P, Pervan B (2006) Paired overbounding for nonideal bias and waas error distributions. *IEEE Trans on Aerospace Electronic Syst* 42(4):1386–1395. <https://doi.org/10.1109/taes.2006.314579>
- Rózsa S (2018) A new approach for assessing tropospheric delay model performance for safety-of-life GNSS applications. In: Heck A, Seitz K, Grombein T, Mayer M, Stövchase JM, Sumaya H, Wampach M, Westerhaus M, Dalheimer L, Senger P (eds) (Schw)Ehre, wem (Schw)Ehre gebührt : Festschrift zur Verabschiedung von Prof. Dr.-Ing. Dr. h.c. Bernhard Heck, KIT Scientific Publishing. <https://doi.org/10.5445/IR/1000080241>
- Rózsa S, Ambrus B, Juni I, Ober PB, Mile M (2020) An advanced residual error model for tropospheric delay estimation. *GPS Solutions* 24(4):1–15. <https://doi.org/10.1007/s10291-020-01017-7>
- RTCA-DO229 (2006) Minimum operational performance standards for global positioning system/wide area augmentation system airborne equipment. RTCA
- Saastamoinen J (1972) Contributions to the theory of atmospheric refraction. *Bulletin Géodésique (1946–1975)* 105(1):279–298. <https://doi.org/10.1007/bf02521844>
- Schön S, Kutterer H (2005) Realistic uncertainty measures for GPS observations. In: Sansò F (ed) A window on the future of geodesy, international association of geodesy symposia, vol 128. Springer, Berlin/Heidelberg, pp 54–59. [https://doi.org/10.1007/3-540-27432-4\\_10](https://doi.org/10.1007/3-540-27432-4_10)
- Schön S, Kutterer H (2006) Uncertainty in GPS networks due to remaining systematic errors: The interval approach. *J Geodesy* 80(3):150–162. <https://doi.org/10.1007/s00190-006-0042-z>
- Su J, Schön S (2022) Deterministic approaches for bounding GNSS uncertainty: A comparative analysis. In: 2022 10th workshop on satellite navigation technology (NAVITEC), pp 1–8. <https://doi.org/10.1109/NAVITEC53682.2022.9847545>
- Zhang D, Guo J, Chen M, Shi J, Zhou L (2016) Quantitative assessment of meteorological and tropospheric zenith hydrostatic delay models. *Adv Space Res* 58(6):1033–1043. <https://doi.org/10.1016/j.asr.2016.05.055>

**Open Access** This chapter is licensed under the terms of the Creative Commons Attribution 4.0 International License (<http://creativecommons.org/licenses/by/4.0/>), which permits use, sharing, adaptation, distribution and reproduction in any medium or format, as long as you give appropriate credit to the original author(s) and the source, provide a link to the Creative Commons license and indicate if changes were made.

The images or other third party material in this chapter are included in the chapter's Creative Commons license, unless indicated otherwise in a credit line to the material. If material is not included in the chapter's Creative Commons license and your intended use is not permitted by statutory regulation or exceeds the permitted use, you will need to obtain permission directly from the copyright holder.





# Precise Orbit Determination of CubeSats Using Proposed Observations Weighting Model

Amir Allahviridi-Zadeh , Ahmed El-Mowafy , and Kan Wang

## Abstract

CubeSats can be used for many space missions and Earth science applications if their orbits can be determined precisely. The Precise Orbit Determination (POD) methods are well developed for large LEO satellites during the last two decades. However, CubeSats are built from Commercial Off-The-Shelf (COTS) components and have their own characteristics, which need more investigations. In this paper, precise orbits of 17 3U-CubeSats in the Spire Global constellation are determined using both the reduced-dynamic and the kinematic POD methods. The limitations in using elevation-dependent weighting models for CubeSats POD are also discussed and, as an alternative approach, a weighting model based on the Signal-to-Noise Ratio (SNR) has been proposed. One-month processing of these CubeSats revealed that around 40% of orbits can be determined at the decimeter accuracy, while 50% have accuracy at centimeters. Such precise orbits fulfil most mission requirements that require such POD accuracy. Internal validation methods confirmed the POD procedure and approved the distinction of weighting based on SNR values over the elevation angles.

## Keywords

CubeSats · Precise orbit determination (POD) · Signal-to-noise ratio (SNR) · Weighting model

## 1 Introduction

CubeSats are small low-cost and low-power satellites that can be used for many space missions. Precise Orbit Determination (POD) of CubeSats is essential for some missions such as radio-occultation, Interferometric Synthetic Aperture Radar (InSAR), satellite altimetry, gravity field recovery, and future mega-constellations as an augmentation system for positioning and navigation (Allahviridi-Zadeh and El-

Mowafy 2022). POD of CubeSats using the observations of Global Navigation Satellite Systems (GNSS) can be performed using the reduced-dynamic and the kinematic methods in post-mission or real-time (Allahviridi-Zadeh et al. 2022a). In this study, we analyze the POD of CubeSats from the Spire CubeSat Constellation (Spire Global, Inc.), comparing elevation angle-dependent and Signal-to-Noise ratio (SNR) based weighting models.

The Spire Global constellation of nanosatellites consists of more than 145 3U-CubeSats ( $10 \times 10 \times 30$  cm) that were launched mostly in Sun-synchronous and various other orbits with different altitudes (445–600 km). Most are equipped with the STRATOS GNSS receiver module to receive 1-Hz dual-frequency GPS signals (L1C/A and L2L) using a compatible zenith-mounted GNSS antenna. It also simultaneously collects 50-Hz signals dual-frequency multi-GNSS signals through the high-gain, side-mounted antennas from setting or rising GNSS satellites to perform Radio Occul-

A. Allahviridi-Zadeh (✉) · A. El-Mowafy  
GNSS-SPAN Group, School of Earth and Planetary Sciences, Curtin  
University, Perth, Australia  
e-mail: [amir.allahviridizadeh@curtin.edu.au](mailto:amir.allahviridizadeh@curtin.edu.au)

K. Wang  
National Time Service Center, Chinese Academy of Sciences, Xi'an,  
China

University of Chinese Academy of Sciences, Beijing, China

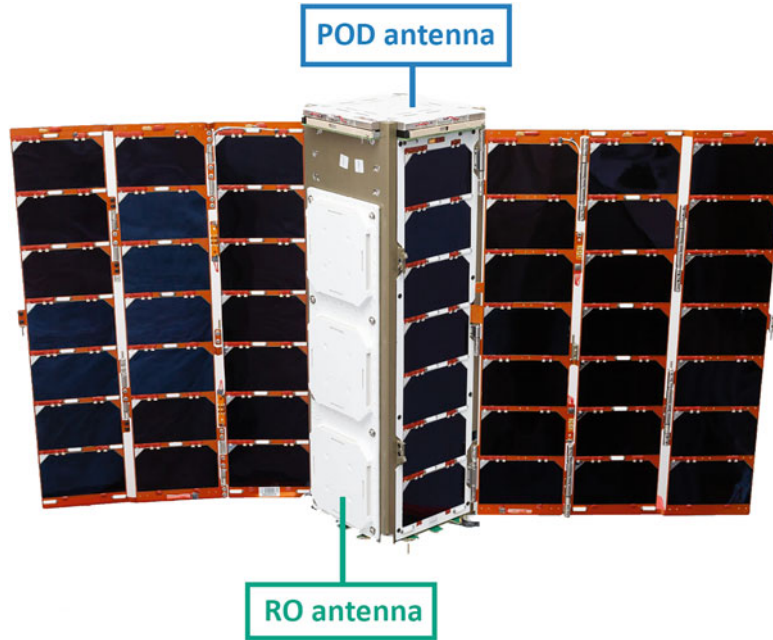


**Fig. 1** Structure of the Spire 3U RO CubeSat (Credit: Spire Global, Inc.)

tation (RO). The location of the POD and RO high-gain antennas on the Spire's CubeSats are depicted in Fig. 1.

## 2 Precise Orbit Determination

The reduced-dynamic POD (RD-POD) is considered the main method in this study. It is based on exploiting available dynamic models as well as GNSS observations to estimate the CubeSat's state vector, which includes position and velocity, clock offsets, float ambiguities, and some piece-wise constant stochastic accelerations to compensate for deficiencies in dynamic models (Allahviridi-Zadeh et al. 2022a). The type of data used, processing information, and models in the RD-POD processing are provided in Table 1.

### 2.1 Weighting Models

Equal weighting of GNSS observations can be considered for the POD of Low Earth Orbit (LEO) satellites. However, this model is not optimal due to factors causing mis-modelled errors, such as higher-order ionosphere scintillation, near field multipath, etc. One may suggest using the elevation-angle dependent (defined here for brevity as elevation-dependent) weighting models such as  $\sin^2\theta$ . The analysis of the observation residuals in the validation step (see Sect. 2.3.3) reveals that this type of models is not optimal for reflecting the actual noise level of the CubeSats observations. This is due to the fact that these models

are developed to account for the effect of the tropospheric delays and multipath, mainly for users on the Earth surface (Hobiger and Jakowski 2017), whereas CubeSats fly above the troposphere layer. Besides, in order to correctly apply the elevation-dependent model, the CubeSat should effectively record the attitude information, such as the quaternions. This, however, may not be available for CubeSats with low-power budget. Hence, we propose to use a direct signal quality indicator, i.e. the SNR, which equals to the ratio of the signal power to the noise power of the modulated signal at the correlator output. The proposed SNR-based model for weighting the observations ( $\Phi_i$ ) can be expressed as:

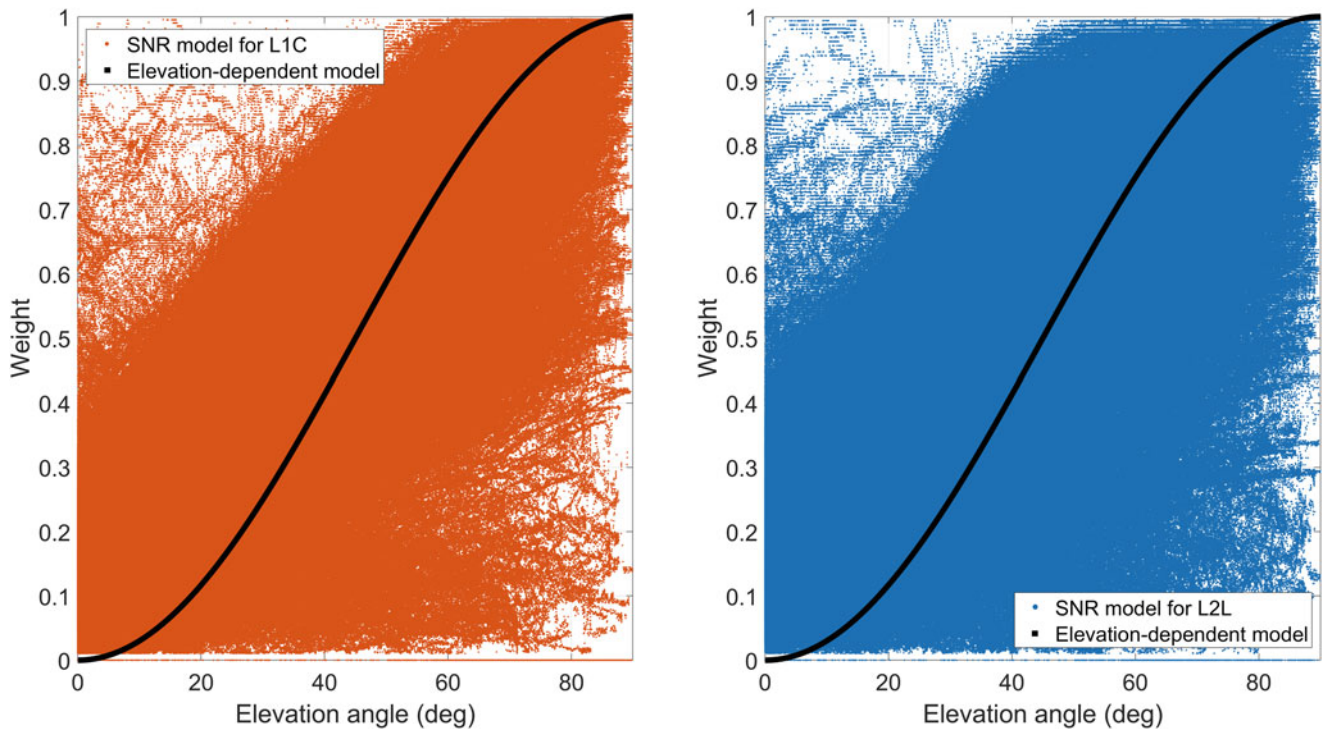
$$W(\Phi_i) = \left( 0.1 + 0.9 * \left( \frac{\Delta SNR_{i,min}}{\Delta SNR_{max,min}} \right) \right)^2 \quad (1)$$

where  $\Delta SNR_{i,min}$  is the difference between the observation SNR value and the minimum SNR of all observations, and  $\Delta SNR_{max,min}$  is the difference between the maximum and minimum SNR values among all observations. The coefficients 0.1 and 0.9 on the right-hand side of Eq. 1 are used to give the maximum weight, i.e., 1, to the observation which has the highest SNR value, and a very low weight, i.e., 0.01, to the observation with the lowest SNR. A similar model has been developed for baseline processing (Luo 2013), however, the way of choosing the maximum and minimum SNR values and applying weights for double differences are different. Figure 2 compares the weights generated from applying the elevation-dependent weighting model ( $\sin^2\theta$ ) and the SNR-based model (Eq. 1) for different elevation angles ( $\theta$ ) for one-month observations of CubeSat PRN099. Two



**Table 1** CubeSats POD processing models and parameters

Item	Description
Gravity field/Earth tide/Relativity/Other planets	EGM 2008 (Pavlis et al. 2008)/FES2004 (Lyard et al. 2006)/IERS 2010 (Petit and Luzum 2010)/DE405 (Standish 1998)
Observation model	1-Hz dual-frequency GPS Ionosphere-Free
A-priori code and phase standard deviation	0.1 m, 1 mm (Zenith, L1)
Empirical acceleration	piece-wise constant accelerations
Attitude information, Quaternions, Antenna phase center offsets (PCO) and variations (PCV)	Provided by Spire Global, Inc. and applied (Allahviridi-Zadeh 2021b)
Weighting model (tested)	Elevation-dependent or SNR-based models
GNSS orbits and clocks	IGS-RTS and CODE final

**Fig. 2** Observation weights from the SNR- and the elevation-dependent weighting models for one month (16/12/2020–15/01/2021) of L1C (left) and L2L (right) signals from all available GPS satellites as observed on CubeSat PRN099

models behave differently in weighting the observations. For example, the SNR-based model gives higher weights to the observations from low elevation angles for both L1C and L2L signals compared with the elevation-dependent model depending on the received signal strength. It can be more realistic for signals in space, since they are not affected by the troposphere, and the amount of near-field multipath is low, mainly due to the CubeSat structure (see Fig. 1). Realistic weighting is crucial in the POD of the low-power CubeSats since they are allowed to record the observations for a limited time based on their power budget and mission requirements (personal communication with the CubeSat developers (Allahviridi-Zadeh 2021a)). Therefore, losing observations due to incorrect weighting may even lead to the unavailability of POD procedure for the Kinematic mode. It does not generally though take place for the satellites that

record GNSS observations continuously, since the RD-POD of these satellites can run even in the presence of duty-cycled GNSS data (i.e., available at certain percentage of the orbit due to the need of the low available onboard power to sensors other than GNSS) (Wang et al. 2020).

## 2.2 POD Results

One month (from 16 December 2020 to 15 January 2021) of all available observations of 17 3U-CubeSats from the Spire Global constellation are processed in this study. A list of these CubeSats and their specifications are given in Allahviridi-Zadeh et al. 2022b. The observations comprise several segments each day. Each segment has around 1.5 h (orbital period) of 1-Hz dual-frequency GPS data. The

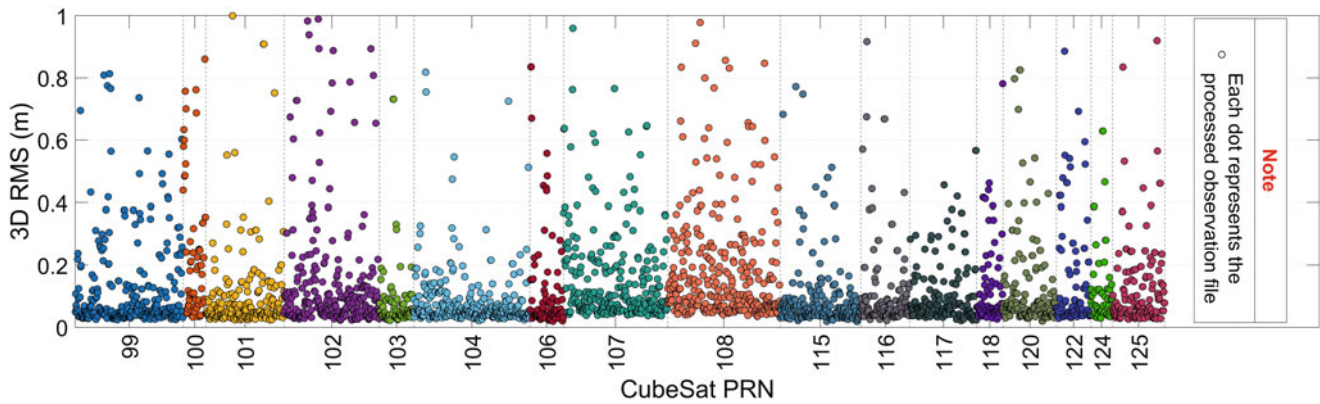


**Fig. 3** 3D-RMS of differences between RD-POD and Kinematic POD (Kin-POD) for all CubeSats. Each segment related to each CubeSat PRN contains all processed file during one month (16/12/2020–15/01/2021)

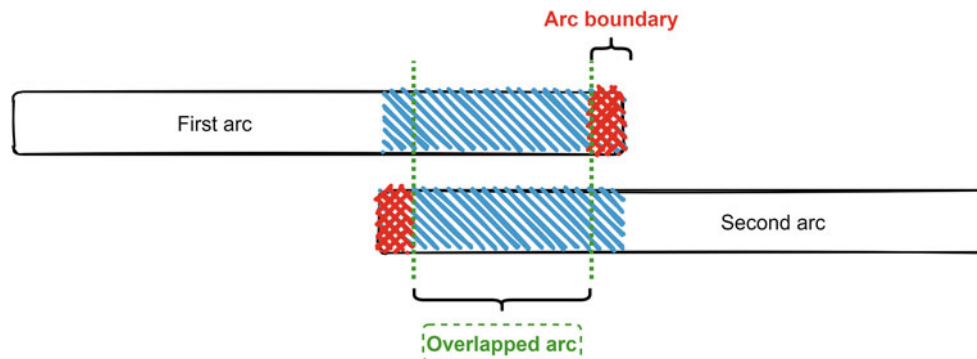


**Fig. 4** Overlapped arc between two consecutive orbits. The red cross hatches indicate the arc boundaries

related observable-specific signal biases for L1C and L2L are synchronized with the applied precise GNSS orbits and clocks (Schaer 2016). A comparison between the reduced-dynamic orbits, as the most precise obtainable orbits in this study, and the kinematic orbits are plotted in Fig. 3 in the radial (R), along-track (S), and cross-track (W) directions. In this comparison, 40% of kinematic orbits have 3D root mean square (3D-RMS) of decimeters, while half of them have accuracies at a few centimeters. Such orbits can fulfil the requirements of different space missions and earth-science applications such as radio occultation, InSAR, the Earth monitoring, etc. (Allahviridi-Zadeh et al. 2021).

### 2.3 POD Validation

The Spire CubeSats are not equipped with Satellite Laser Ranging (SLR) reflectors, and thus, external validation is not possible. Therefore, the internal methods including the overlapping arcs, residuals analysis, and goodness of fit checks are used to validate the POD results. Their results are described in the following sections.

#### 2.3.1 Overlapping Arcs

The overlapping validation is performed by testing two consecutive arcs longer than 24 h (e.g. 30 h) and checking the differences in the overlapped part. The estimated CubeSats orbits are all around 1.5 h arcs due to the length of the observation segments. All possible overlapped arcs between all estimated orbits of each CubeSat, except for the arc boundaries, are considered for this validation method. Figure 4 shows a sample of the overlapped arc between two consecutive orbits.

The RMS of the overlapped differences for RD-POD and Kinematic POD (Kin-POD) in all directions are plotted in Fig. 5. Small RMS values indicate validation of the POD procedure. The overall average reduction in RMS for the Kin-POD, are also observed when using the SNR-based weighting (dark colours) against the elevation-dependent model (light colours). This confirms the benefits of using the SNR-based model for the CubeSat's kinematic POD. The average percentage of the RMS reduction for all CubeSats are provided in Table 2. In the RD-POD, the overlapping results applying both models are similar. This could be

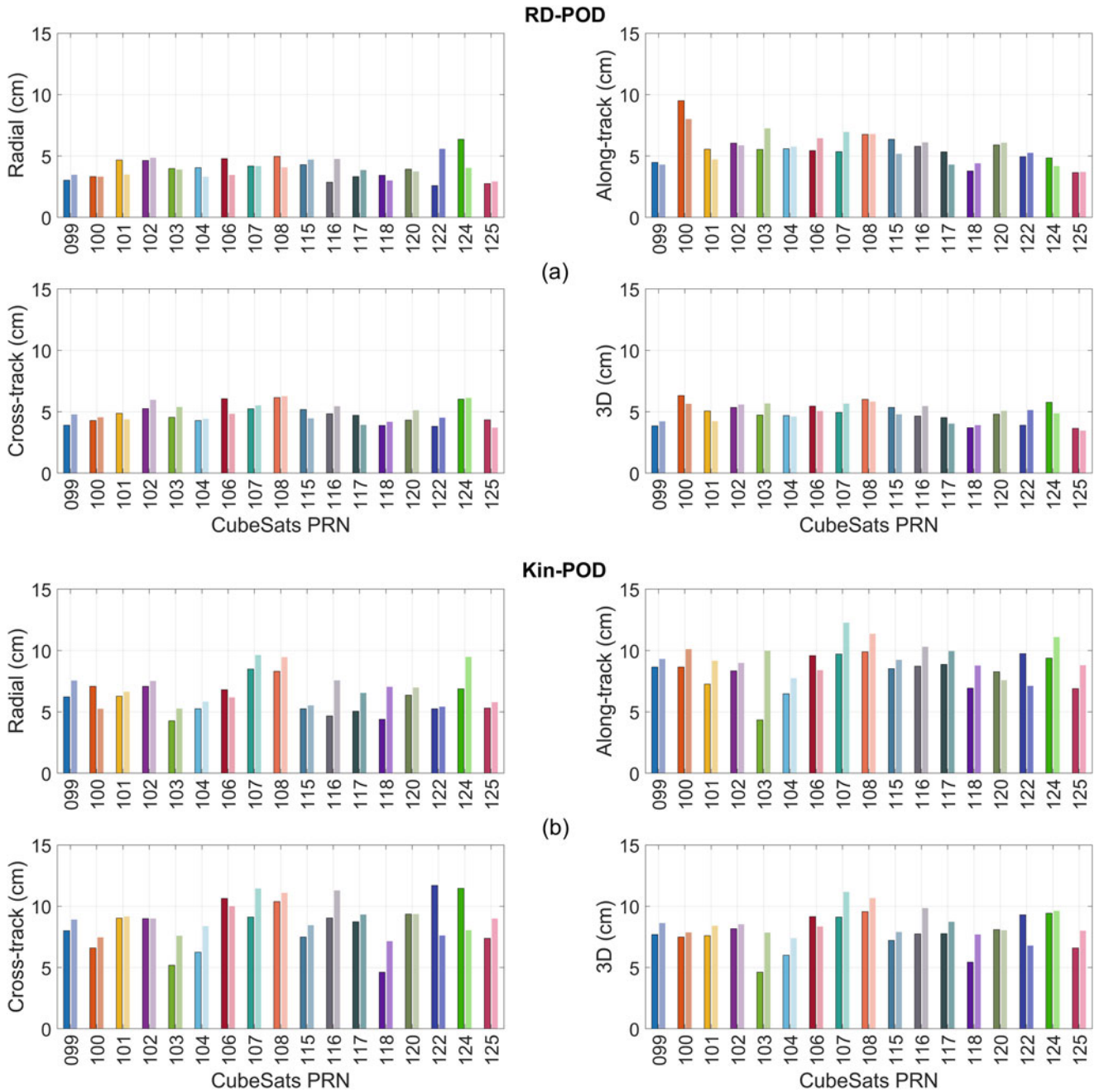


**Fig. 5** RMS of overlapping validation for RD-POD (a) and Kin-POD (b). (Dark colours: using the SNR-based model – Light colours: using the elevation-dependent model)

due to the impact of using similar dynamic models and estimating the piecewise accelerations in the RD-POD using both weighting models.

**2.3.2 Goodness of Fit**

The a-posteriori variance can be expressed as:

$$\hat{\sigma}_0^2 = \frac{\|\hat{e}\|_W^2}{dof}$$

(2) where  $(\|\hat{e}\|_W^2 = \hat{e}^T W \hat{e})$  is the weighted squared norm of the observation residuals ( $\hat{e}$ ) using the observation weight

**Table 2** Mean percentage of the RMS reduction due to the proposed SNR-based model compared to the elevation-dependent model for all CubeSats in all directions

POD	Radial (%)	Along-Track (%)	Cross-Track (%)	3D (%)
RD	<b>0.0</b>	<b>0.1</b>	<b>0.0</b>	<b>0.1</b>
Kin	<b>11.2</b>	<b>11.1</b>	<b>5.7</b>	<b>9.5</b>

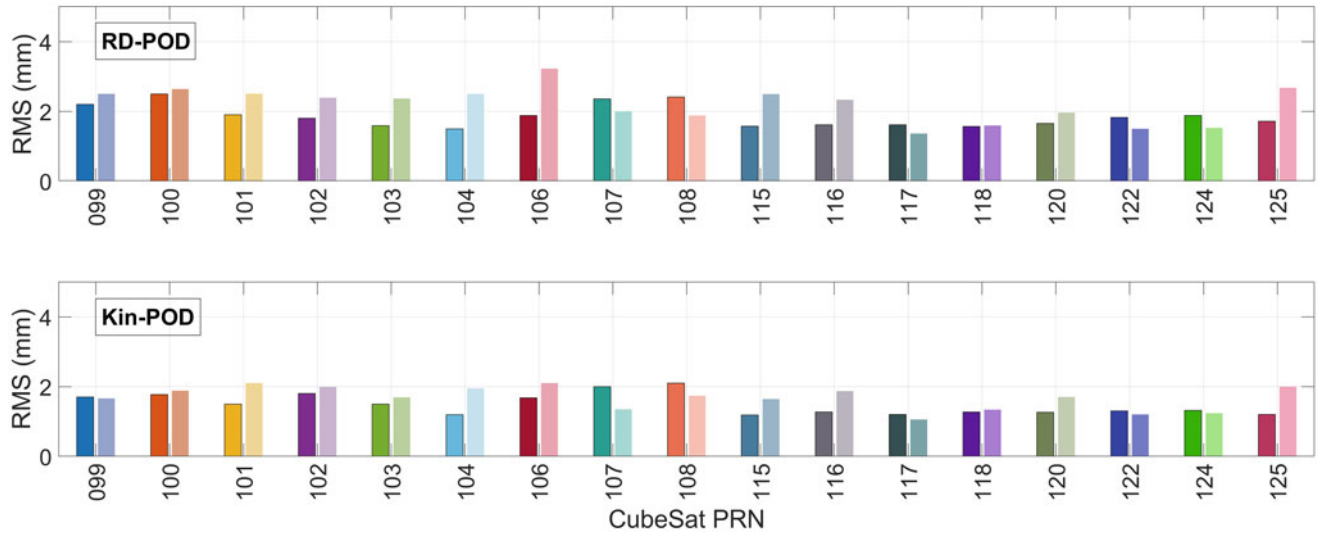


**Fig. 6** RMS of the a-posteriori sigma for all CubeSats for RD-POD (top) and Kin-POD (bottom). (Dark colours: using the SNR-based model—Light colours: using the elevation-dependent model)

**Table 3** Mean value of the a-posteriori STD of all CubeSats from RD-POD and Kin-POD

POD	Mean value of the a-posteriori sigma (mm)	
	SNR-based model	Elevation-dependent model
RD	1.85	2.20
Kin	1.48	1.67

matrix ( $W$ ) and  $dof$  denotes the degrees of freedom. The ratio of a-posteriori variance to the a-priori variance (see Table 1) can be used as a self-consistency check of the goodness of fit using the following chi-squared test with selected confidence region ( $\alpha$ ) (Strang and Borre 1997):

$$\frac{\hat{\sigma}_0^2}{\sigma_0^s} < \frac{\chi_{dof, 1-\alpha}^2}{dof} \quad (3)$$

The a-posteriori standard deviation (STD) values of all CubeSats are plotted in Fig. 6. They are all less than 3 mm which represents an acceptable fitting model to the POD problem. The mean of all a-posteriori STD values for all tested CubeSats are given in Table 3. In total, 16% and 11% reduction in the a-posteriori STD values are observed in the case of POD using SNR-based weighting model for RD-POD and Kin-POD, respectively.

### 2.3.3 Residual Analysis

The final validation check is the observation residual analysis. As a representative example, the GPS ionosphere-free (IF) phase residuals for CubeSat PRN-099 are plotted in Fig. 7. The ambiguities were estimated as float values in our POD processing. The residuals are at sub-centimeter to centimeter

level mainly due to the onboard COTS receiver/antenna, as well as using the IF-LC which increases the noise compared to the use of uncombined signals. However, the reduction of the residuals is obvious for the POD using the SNR-based model. Similar trends are observed for other CubeSats.

The CubeSats cross the eclipse region several times per day. Although the solar radiation pressure is significantly low due to the absence of sunlight, there is a thermal re-radiation as an additional effect of the solar radiation pressure in these regions (Švehla 2018). A cylindrical model proposed by Allahviridi-Zadeh (2013, 2022) and Allahviridi-Zadeh et al. (2016) is used to estimate the eclipse region and analyse the residual behaviours. No significant changes on residuals can be observed for crossing this region. The reason is that such effect has been captured by the estimation of stochastic accelerations in the POD procedure.

## 3 Conclusion

The proposed SNR-based weighting model reduced the IF phase residuals compared to the traditional elevation angle-dependent model. The internal validation including comparing overlapping arcs and the a-posteriori STD confirmed the improved performance of CubeSats' POD using the proposed SNR-based weighting model. The generated CubeSats orbits have a precision that fulfils the requirements of different space and Earth science applications. The impact of using such a weighting model on ambiguity resolution is among our next studies.

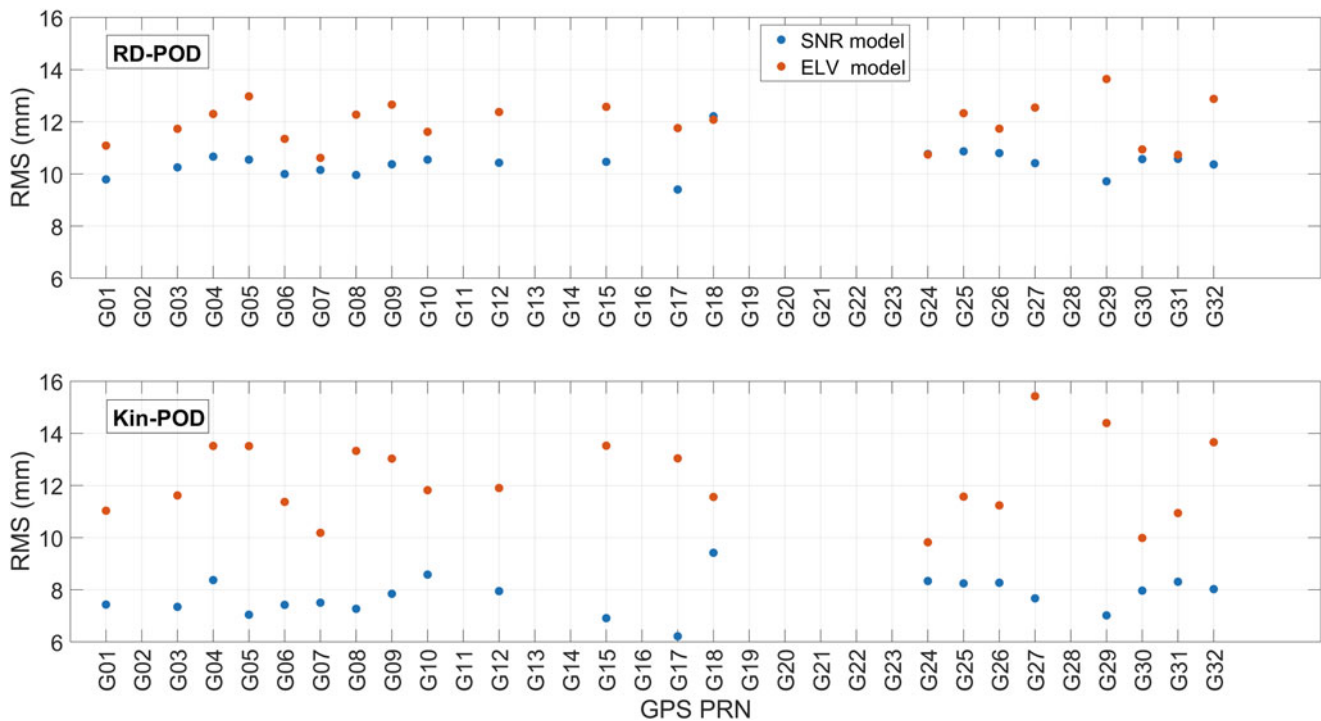


**Fig. 7** The RMS of IF phase residuals from the RD-POD (top) and the Kin-POD (bottom) for CubeSat PRN099. The RMS values are derived from one month of all observations of all GPS satellites

**Acknowledgments** We would like to thank Spire Global, Inc for providing the nanosatellite data for scientific research. Special thanks to Dallas Masters, Ph.D., Director of Earth observations/GNSS and his team for our discussions on the satellite structure and for providing the required information. This work is funded by the Australian Research Council under the discovery project “Tracking Formation-Flying of Nanosatellites Using Inter-Satellite Links” (DP 190102444). Third author receives fund from the Chinese Academy of Science (CAS) “Light of West China” Program (No. XAB2018YDYLO1).

## References

- Allahverdi-Zadeh A, Asgari J, Amiri-Simkooei AR (2016) Investigation of GPS draconitic year effect on GPS time series of eliminated eclipsing GPS satellite data. *J Geod Sci* 6. <https://doi.org/10.1515/jogs-2016-0007>
- Allahverdi-Zadeh A (2013) Evaluation of the GPS observable effects located in the earth shadow on permanent station position time series. MSc thesis, Geomatics Engineering Department, University of Isfahan. <https://doi.org/10.13140/RG.2.2.28151.32167>
- Allahverdi-Zadeh A (2021a) Software Defined Radio (SDR) as a GNSS receiver in future CubeSats. In: Internship with Binar Space Program – Innovation Central Perth. Curtin University, Perth, Western Australia. <https://doi.org/10.13140/RG.2.2.28290.20166>
- Allahverdi-Zadeh A (2021b) Phase centre variation of the GNSS antenna onboard the CubeSats and its impact on precise orbit determination. In: Proceedings of the GSA Earth Sciences Student Symposium, Western Australia (GESSS-WA), Perth, Australia, 25 November 2021. <https://doi.org/10.13140/RG.2.2.10355.45607/1>
- Allahverdi-Zadeh A, Wang K, El-Mowafy A (2021) POD of small LEO satellites based on precise real-time MADOCA and SBAS-aided PPP corrections. *GPS Solut* 25:31. <https://doi.org/10.1007/s10291-020-01078-8>
- Allahverdi-Zadeh A (2022) Shadow toolbox. figshare. Software. <https://doi.org/10.6084/m9.figshare.19085546.v1>
- Allahverdi-Zadeh A, El-Mowafy A (2022) The impact of precise inter-satellite ranges on relative precise orbit determination in a smart CubeSats constellation, EGU General Assembly 2022, Vienna, Austria, 23–27 May 2022, EGU22-2215, <https://doi.org/10.5194/egusphere-egu22-2215>
- Allahverdi-Zadeh A, Wang K, El-Mowafy A (2022a) Precise orbit determination of LEO satellites based on undifferenced GNSS observations. *J Surv Eng* 148:03121001. [https://doi.org/10.1061/\(ASCE\)SU.1943-5428.0000382](https://doi.org/10.1061/(ASCE)SU.1943-5428.0000382)
- Allahverdi-Zadeh A, Awange J, El-Mowafy A, Ding T, Wang K (2022b) Stability of CubeSat clocks and their impacts on GNSS radio occultation. *Remote Sens* 14:362. <https://doi.org/10.3390/rs14020362>
- Hobiger T, Jakowski N (2017) Atmospheric signal propagation. In: Teunissen PJG, Montenbruck O (eds) Springer handbook of global navigation satellite systems. Springer International Publishing, Cham, pp 165–193. [https://doi.org/10.1007/978-3-319-42928-1\\_6](https://doi.org/10.1007/978-3-319-42928-1_6)
- Luo X (2013) Observation weighting using signal quality measures. In: GPS stochastic modelling: signal quality measures and ARMA processes. Springer, Berlin, pp 137–162. [https://doi.org/10.1007/978-3-642-34836-5\\_5](https://doi.org/10.1007/978-3-642-34836-5_5)
- Lyard F, Lefevre F, Letellier T, Francis O (2006) Modelling the global ocean tides: modern insights from FES2004. *Ocean Dyn* 56:394–415. <https://doi.org/10.1007/s10236-006-0086-x>
- Pavlis N, Kenyon S, Factor J, Holmes S (2008) Earth gravitational model 2008. In: SEG technical program expanded abstracts 2008. SEG technical program expanded abstracts. Society of Exploration Geophysicists, pp 761–763. <https://doi.org/10.1190/1.3063757>
- Petit G, Luzum B (2010) IERS conventions. (IERS Technical Note; 36) Frankfurt am Main: Verlag des Bundesamts für Kartographie und Geodäsie, p 179. ISBN 3-89888-989-6
- Schaer S (2016) SINEX BIAS—Solution (Software/technique) Independent Exchange Format for GNSS BIASes Version 1.00. In: IGS

- workshop on GNSS biases, Bern, Switzerland. [http://ftp.aiub.unibe.ch/bcwg/format/sinex\\_bias\\_100.pdf](http://ftp.aiub.unibe.ch/bcwg/format/sinex_bias_100.pdf)
- Spire Global Inc. <https://spire.com/>. Accessed 13 August 2021
- Strang G, Borre K (1997) Linear algebra, geodesy, and GPS. Wellesley-Cambridge Press
- Švehla D (2018) Geometrical theory of satellite orbits and gravity field. Springer, Online. <https://doi.org/10.1007/978-3-319-76873-1>
- Wang K, Allahviridi-Zadeh A, El-Mowafy A, Gross JN (2020) A sensitivity study of POD using dual-frequency GPS for cubesats data limitation and resources. Remote Sens 12(13):2107. <https://doi.org/10.3390/rs12132107>

**Open Access** This chapter is licensed under the terms of the Creative Commons Attribution 4.0 International License (<http://creativecommons.org/licenses/by/4.0/>), which permits use, sharing, adaptation, distribution and reproduction in any medium or format, as long as you give appropriate credit to the original author(s) and the source, provide a link to the Creative Commons license and indicate if changes were made.

The images or other third party material in this chapter are included in the chapter's Creative Commons license, unless indicated otherwise in a credit line to the material. If material is not included in the chapter's Creative Commons license and your intended use is not permitted by statutory regulation or exceeds the permitted use, you will need to obtain permission directly from the copyright holder.



---

**Part VII**

**Geodetic Atmospheric and Remote Sensing**



# Optimal TEC Forecast Models Based on Machine Learning and Time Series Analysis Techniques: A Preliminary Study on the Ring of Fire

Nhung Le , Benjamin Männel , Pierre Sakic , Chinh Thai Nguyen ,  
Hoa Thi Pham, and Harald Schuh

## Abstract

Geomagnetic storms are one of the major factors causing Total Electron Content (TEC) anomalies. Analyses of TEC fluctuations also provide a valuable understanding of the mechanisms of earthquakes and tsunamis. However, there is no clear consistency in investigations of TEC disturbances that should be considered simultaneously in both solar and seismic activities. Therefore, based on Machine Learning (ML) and time series analysis techniques, we build TEC forecast models to study relationships among ionospheric anomalies, geomagnetic storms, and earthquakes. Robust statistical tests are used to select the optimal models and estimate forecast performance. Depending on the quality of input data and sampling rates, the forecast performance can get from 2.0 to 2.5 TECU for 3-day predictions using daily time series and reach up to 1.3 TECU using one-minute time series. These models present significant relationships between the ionosphere, solar activity, and seismic events, which can be applied to hazard warning systems.

## Keywords

GNSS · Machine Learning · Optimal forecast model · Statistical test · TEC forecast

## 1 Introduction

The Ring of Fire, also referred to as the Pacific Rims, is the boundary of continental plates, ocean trenches (Rinard Hinga 2015), the intersection of major ocean currents (“Major Currents | Ocean Tracks.” [Online]. <https://oceantracks.org/library/the-north-pacific-ocean/major-currents>), and is affected by extreme weather events associated with the global climate change over the last decades (Ishii 2018; Eckstein et al. 2021; Cracknell and Varotsos 2021). The Ring of Fire contains approximately 850 to 1,000 volcanoes that have been active during the last 11,700 years (Siebert et al. 2010), with 90% of the Earth’s earthquakes and 81% of the world’s largest earthquakes occurring here (United States Geological Survey 1999). In addition, the place often experiences natural catastrophes such as earthquakes, volcanic eruptions, tsunamis, landslides, sea-level rise, and hurricanes. However, it is just known as a region frequently happening seismic activities rather than other natural events. Hence, we will provide a primary view of the mathematical

N. Le (✉) · B. Männel · P. Sakic · C.T. Nguyen · H. Schuh  
GFZ German Research Centre for Geosciences, Potsdam, Germany

N. Le · H. Schuh  
Institute for Geodesy and Geographic Information Technology, Berlin,  
Germany  
e-mail: [nhung@gfz-potsdam.de](mailto:nhung@gfz-potsdam.de)

N. Le · H.T. Pham  
Hanoi University of Natural Resources and Environment, Hanoi,  
Vietnam  
e-mail: [nhung@gfz-potsdam.de](mailto:nhung@gfz-potsdam.de)

P. Sakic  
Institut de Physique du Globe de Paris, Paris-Cité University, Paris,  
France

C.T. Nguyen  
Hanoi University of Mining and Geology, Hanoi, Vietnam

H.T. Pham  
School of Earth and Planetary Sciences, Spatial Sciences Discipline,  
Curtin University, Perth, WA, Australia



relationships between ionospheric variations, solar activity, and tectonic processes using a combination of geospatial measurements and geomagnetic observations for VTEC (Vertical Total Electron Content) forecasts.

Furthermore, there is a close interaction between solid Earth and the atmosphere, where particles, electrons in the ionosphere, and matter in the oceans act as conductors to propagate acoustic waves generated from the Rayleigh waves of seismic activity (Jin et al. 2019; Tanimoto et al. 2015). Over the last decades, there has been a powerful research stream about ionospheric disturbances associated with earthquakes, tsunamis, and volcanic eruptions (Jin et al. 2019; Tanimoto et al. 2015; Heki 2011). Determination of the disturbances related to seismic activity is possible based on different methods and instruments, e.g., using the French DEMETER<sup>1</sup> satellite (Athanasidou et al. 2011; Zhao et al. 2020), or the continuously GNSS (Global Navigation Satellite Systems) networks like the GEONET<sup>2</sup> in Japan and the SEALION (Southeast Asia Low-latitude Ionospheric Network) including ionosondes, scintillation monitors, and magnetometers (Ishii 2018). However, the Earth's geomagnetic field changes provoked by space weather events also lead to ionospheric disturbances (Blagoveshchensky et al. 2018). Geomagnetic storms are major disturbances of the Earth's magnetosphere as an exchange of energy from the solar wind plasma into the space environment surrounding Earth (Blagoveshchensky et al. 2018; Maurya et al. 2018; "Geomagnetic Storms | NOAA / NWS Space Weather Prediction Center." [Online]. <https://www.swpc.noaa.gov/phenomena/geomagnetic-storms>; Singh et al. 2010); for example, the strongest geomagnetic storm of the 24th solar cycle on St. Patrick's Days 2015 causing significant TEC fluctuations is indicated in a range of studies (Maurya et al. 2018; Yadav et al. 2016; Elvira et al. 2015). Monitoring ionospheric anomalies can thus provide insights into solid Earth processes. Moreover, TEC forecast models can contribute to early warning systems for natural disasters. This will be a potential approach to study an active tectonic region with many extreme weather events like the Ring of Fire.

Machine Learning (ML), its first notion appeared in the 1930s and experienced the two winters of artificial intelligence due to the lack of data sources and computation capacity (Silaparasetty 2020), has been becoming a powerful trend, especially for regression and classification domains. For regression ML, algorithms have been widely applied, ranging from Support Vector Machine (SVM), Ensemble (Naras and Schmidt 2021; Panigrahi et al. 2021; Inyurt et al. 2020) to Neural networks and Fuzzy techniques (Sun et al. 2017; Venkata Ratnam et al. 2017; Lee et al. 2021). Currently, there are three main approaches for building

regression ML models, including (1) gradient descent (e.g., Linear and Gaussian), (2) random forest (e.g., Regression trees and Tree-ensembles), and (3) distance-based algorithms (e.g., Support Vector Machine). Over the literary studies, the Root Mean Square Errors (RMSE) vary mainly from 3 to 5 TECU (Sun et al. 2017; Homam 2015; Zhukov et al. 2018), while some can reach up to 1.5 to 2.2 TECU (Liu et al. 2020). Nevertheless, pushing up the accuracy of forecast models beyond the reliability of input data has no statistical meaning and even can cause virtual prediction performance and misleading results.

In this study, we use robust statistical analysis to identify the optimal forecast models whose forecast accuracy is equivalent to that of the input observations. In this way, besides applying to early warning, these forecast models can replace or adjust missing observations. Moreover, the forecasts match three critical requirements of robust statistics: efficiency for mathematical models, stability for resistance to minor errors, and mutation for acceptable large errors.

## 2 Data and Methods

### 2.1 Data

This study adopts GNSS, earthquake, and geomagnetic storm data in the Ring of Fire region. GNSS data from 2007 to 2019 (the 24th solar cycle) are available at the central data bank for NASA's crustal dynamics project CDDIS.<sup>3</sup> The observation files contain GNSS data (30-second sampling rate) in the receiver independent exchange (RINEX) format from the international GNSS service (IGS) stations. These data are the basis for determining TEC time series using the GPS-TEC analysis software with different sampling rates (daily, hourly, and one-minute) (Seemala 2011). Sixty-four selected IGS stations (Fig. 1) ensure the strict requirements like nearby the epicenters of the investigated earthquakes or capturing the phenomena associated closely with solar activity like geomagnetic storms and auroras.

Data of earthquakes (e.g., location, magnitude, depth) and geomagnetic storms (e.g., Ap, Dst, R-sunspot, solar wind speed, etc.) are taken from the world prediction centers. They are the space weather prediction center NOAA,<sup>4</sup> USA; the world data center for geomagnetism WDC,<sup>5</sup> Tokyo, Japan; the seismic data center GEOFON,<sup>6</sup> GFZ Potsdam, Germany; and Space weather live,<sup>7</sup> Belgium. In addition, remarkable earthquakes with magnitude ( $M_w$ ) from 6.5 to 9.0

<sup>3</sup><https://cddis.nasa.gov/>.

<sup>4</sup><https://www.noaa.gov/>.

<sup>5</sup><https://wdc.kugi.kyoto-u.ac.jp/>.

<sup>6</sup><https://geofon.gfz-potsdam.de/>.

<sup>7</sup><https://www.spaceweatherlive.com/>.

<sup>1</sup><http://demeter.cnrs-orleans.fr/dmt/index.html>.

<sup>2</sup>[https://www.gsi.go.jp/ENGLISH/geonet\\_english.html](https://www.gsi.go.jp/ENGLISH/geonet_english.html).

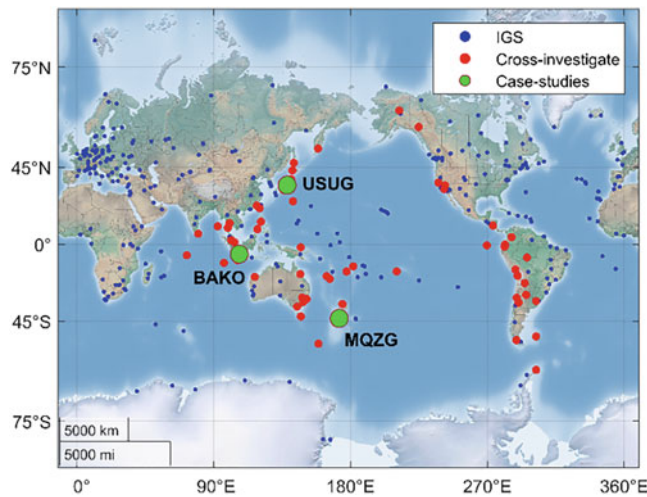


**Fig. 1** Investigation of TEC disturbances at the IGS stations in the Ring of Fire

and the strong geomagnetic storms in the 24th solar cycle are collected to verify TEC disturbances measured on the forecast models.

## 2.2 Methods

Investigations are designed based on a combination of case and cross-sectional studies. Two case studies are the most significant earthquake, Tohoku-Oki 9.0 Mw, in 2011 and the strongest geomagnetic storm 8 Kp in the 24th solar cycle (March 2015). Investigations along the Ring of Fire are also performed to search for TEC disturbances before the noticeable earthquakes. In addition, data of the geomagnetic storms is also the basis for determining quiet days to build the noise-free forecast models.

We carry out two schemes in which the first one investigates 19 mathematical models (Table 1) based on five ML algorithms (Linear, Gaussian, SVM, Ensemble, and Regression Tree) using apps in MATLAB<sup>®</sup>. This scheme is the basis to determine the optimal ML algorithms for TEC forecasts. Furthermore, we compare these algorithms to Neural Networks to assess the shallow ML comprehensively. The second scheme uses these algorithms to build noise-free forecast models applied to warning systems of ionospheric anomalies related to geomagnetic storms and seismic activities. In addition, some techniques are applied to enhance forecast performance, including optimal filters of noise and outliers to clean raw data, interpolation to fill out missing data, and k-fold cross-validation to overcome underfitting and overfitting.

## 3 Results and Discussions

### 3.1 Optimal VTEC Forecast Models

In this study, we experimentalize by building the optimal forecast model of VTEC at the IGS station BAKO (Indonesia) using GNSS data observed from 2007 to 2019.

#### 3.1.1 Raw Data Cleaning and Statistical Analysis

There is no rigid standard of statistical thresholds for all datasets. Instead, the size of the thresholds is determined based on some criteria, such as data characteristics, required accuracy, and processing schemes. When the data are big enough, observations have a Gaussian normal distribution, i.e., the so-called “bell curve”. In this pattern, lower thresholds will remove more observations. Usually, we set a threshold of 95% for high-accuracy tasks to ensure that all input data are as clean as possible. However, in deformation analysis, setting a low threshold for filtering noise and outliers might lose valuable information for anomaly detections. In this study, we thus choose a statistical threshold of 99% for all filters (Fig. 2).

We combine different data sources to train VTEC forecast models that values in time series vary in a vast range. Therefore, determining the suitability of predictors for these models is necessary. Statistical tests ANOVA (Analysis of Variance) select the best-suited variables (predictors) in twelve indices of the solar activity (Table 2). We remove variables with high multicollinearity (Kp and Dst indices) or non-correlation (Magnetic scalar and Magnetic vector). The remaining eight variables meet the requirements of statistical tests for robust mathematical models. Table 2 indicates the selected variables are significant statistics (p-values < 0.05), in which the influence of the Lyman-alpha variable on VTEC reaches the highest ( $B = 0.70$ ).

In the normal distribution test, the mean and standard deviation of VTEC residuals are 0 and 1, respectively (Fig. 3). The adjusted R square value is larger than 0.5, and the F test is in the confidence interval (Table 3). Therefore, the indices of solar activity show statistical relevance to the VTEC time series. These eight predictors can provide robust mathematical models with high performance that are not unduly affected by outliers.

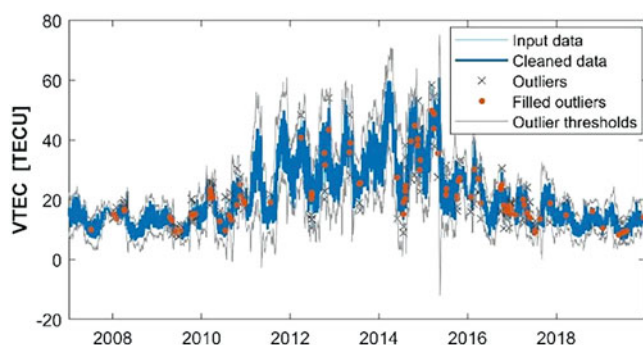
#### 3.1.2 Optimal Forecast Models

Figure 4 presents five forecast models selected from 19 investigated algorithms. These models have the highest accuracy corresponding to the five regression ML methods; further details are shown in (Table 1). The RMSE values are equal

**Table 1** ML models' accuracy for three-day forecasts of VTEC

Regression ML models	RMSE_Regression	MAE_Regression	RMSE_Test	MAE_Test
Linear	4.23	3.04	2.35	1.91
Interaction Linear	4.72	3.12	2.34	1.71
<b>Robust Linear</b>	<b>4.24</b>	<b>3.03</b>	<b>2.36</b>	<b>1.71</b>
Stepwise Linear	4.23	3.03	2.43	1.68
Fine Tree	4.74	3.39	2.98	2.37
<b>Coarse Tree</b>	<b>4.26</b>	<b>3.03</b>	<b>2.48</b>	<b>1.96</b>
Medium Tree	4.36	3.09	2.42	1.91
<b>Booted Tree Ensemble</b>	<b>3.79</b>	<b>2.69</b>	<b>2.03</b>	<b>1.62</b>
Bagged Tree Ensemble	4.09	2.92	2.23	1.80
Linear SVM	4.24	3.03	2.14	1.69
Quadratic SVM	4.72	3.09	2.08	1.64
Cubic SVM	41.78	4.16	2.19	1.71
Fine Gaussian SVM	4.78	3.42	8.80	8.16
Medium Gaussian SVM	4.08	2.92	2.56	2.08
<b>Coarse Gaussian SVM</b>	<b>4.21</b>	<b>3.01</b>	<b>2.15</b>	<b>1.71</b>
Rational Quadratic GPR	3.96	2.81	2.53	2.06
Squared Exponential GPR	4.11	2.96	2.28	1.85
Matern 5/2 GPR	3.90	2.77	2.13	2.62
<b>Exponential GPR</b>	<b>3.82</b>	<b>2.77</b>	<b>2.09</b>	<b>1.72</b>

Note: Unit of error values: TECU; RMSE (Root mean square error); MAE (Mean absolute error)



**Fig. 2** Outlier filtering of the daily VTEC time series at station BAKO using the Moving Median algorithm, with a sliding window of 30 days

to 2.03, 2.09, 2.25, 2.36, and 2.48 TECU, corresponding to the Booted Tree Ensemble, Exponential Gaussian, Coarse Gaussian SVM, Robust Linear, and Coarse Regression Tree. In the criteria of accuracy, the Ensemble and Gaussian algorithms outperform others. However, there are some cut-offs on the Tree-based models (e.g., the Bagged tree ensemble and Coarse tree). Hence, we use Gaussian for building VTEC forecast models at station BAKO.

To evaluate the forecast performance, we compare the Exponential Gaussian models to Narrow Neural Networks (Fig. 5). The finding shows that the forecast performance based on Gaussian is far better than feedforward Neural Networks, with the RMSEs of 2.09 and 2.29 TECU, respectively.

Statistical analyses also further demonstrate the robustness of the VTEC forecast model based on Gaussian. For example, in Table 4, the predictions (outputs) and observations (inputs) have significant statistical equivalence and mathematical correlation (Fisher test  $< F_{\text{critical}}$  and correlation coefficients in Pearson test  $> 0.5$ ).

### 3.2 Noise-Free Forecast Models for VTEC Anomaly Detection

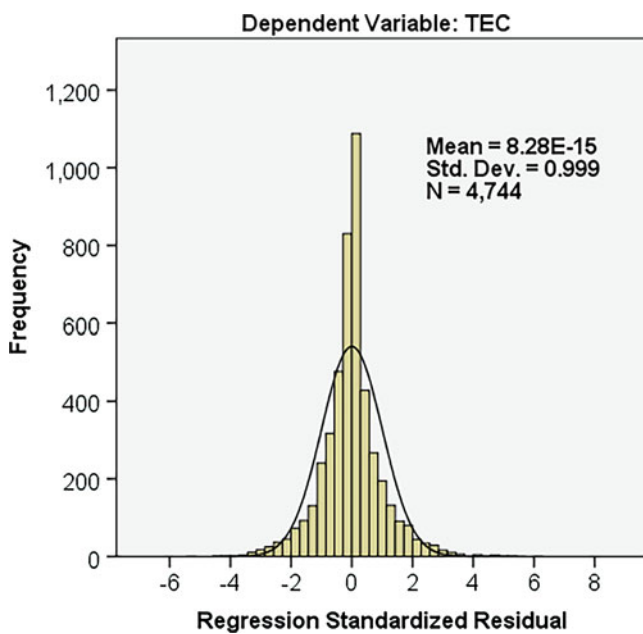
Two noise-free forecast models are built to detect ionospheric anomalies corresponding to two case studies of the strongest earthquake and geomagnetic storm in the 24th solar cycle on the Ring of Fire. We select the IGS stations USUD (Japan) and MQZG (New Zealand) to observe these phenomena.

#### 3.2.1 Noise Filtering for the VTEC Time Series

After cleaning outliers, the VTEC times series are smoothed by the Savitzky–Golay algorithm at a statistical threshold of 99% (Fig. 6). Depending on data characteristics, sampling rates, and the applied ML algorithms, the size of the sliding windows should be tuned via some trials to find the best-suited one. Finally, augmented Dickey-Fuller (ADF) tests the stationarity of the time series (Table 5). The finding shows that the VTEC time series at the IGS stations USUD and MQZG is stationary; the ADF absolute values are 5.164 and 4.140, respectively, which are larger than  $t_{\text{critical}}$  at

**Table 2** Multivariate correlation analysis of the parameters associated with the solar activity in VTEC forecasts at station BAKO

Variables	Unstandardized coefficients		<i>t</i> -test	Sig. levels (p-values)	Collinearity statistics	
	B	Std. error			Tolerance	VIF
YEAR	0.080	0.020	4.16	0.000	0.55	1.82
DOY	0.001	0.001	-2.10	0.036	0.99	1.01
Magnetic_Scalar	0.009	0.102	0.88	0.379	0.18	5.56
Magnetic_Vector	-0.002	0.103	-1.19	0.234	0.19	5.26
Proton_Density	0.005	0.002	-2.09	0.037	0.99	1.01
Plasma_Speed	0.004	0.001	-4.79	0.000	0.69	1.45
Kp_Index	-0.02	0.027	-0.80	0.426	0.12	8.33
R_Sunspot	0.024	0.002	11.33	0.000	0.33	3.03
Dst_Index	-0.007	0.011	-6.86	0.000	0.14	7.14
Ap_Index	0.023	0.009	1.96	0.050	0.68	1.47
F10.7	0.004	0.002	2.06	0.039	0.56	1.79
Lyman_Alpha	0.702	0.045	15.37	0.000	0.23	4.35

**Fig. 3** Normal distribution testing of the VTEC time series at station BAKO with a probability of 95%

statistical levels. Therefore, these VTEC time series meet the requirements of stable forecast models for ionospheric anomaly detection.

### 3.2.2 Detection of VTEC Anomalies Before the Strong Earthquakes

Figure 7 shows the VTEC changes within the 30 days before the investigated earthquakes on the Ring of Fire observed by the IGS stations surrounding the epicenters. There were considerable fluctuations in VTEC before these earthquakes. TEC disturbances related to the stronger earthquakes were seen earlier and longer than the smaller ones.

The TEC variations appeared from a few days (e.g., the 6.5 Mw earthquake in India) to 2 weeks (e.g., the 9.0 Mw

earthquake in Japan) before the mainshock. Therefore, we use the VTEC time series (at a one-minute sampling rate) on quiet days (from 20 to 30 days before the earthquakes) to train noise-free forecast models.

The earthquakes and space weather data show that March 2010 were quiet days. For example, the recorded strongest earthquake in Japan was only 4.6 Mw on the 7th, and the most noticeable geomagnetic storm was 4 Kp on the 11th. Hence, we use VTEC in March 2010 to verify the reliability of the forecast models.

Figure 8a shows the forecasts based on the Exponential Gaussian and Boosted-tree Ensemble, with the RMSEs of 1.30 and 1.44 TECU, respectively. The amplitude of ionospheric fluctuations measured on the Gaussian-based model reached 19.37 TECU on 8th March 2011 (Fig. 8b). These variations exceed the forecast RMSE; thus, we can apply these models to detect TEC anomalies caused by large earthquakes.

### 3.2.3 Detection of VTEC Anomalies on Geomagnetic Storm Days

We use VTEC data from January 2013 to November 2014 (at an hourly sampling rate) at the IGS station MQZG (New Zealand) to train the noise-free forecast models. The 3-month data (from 01st November 2014 to 28th February 2015) are used to test the models. Figure 9 describes VTEC predictions based on the Bagged-tree Ensemble and Exponential Gaussian algorithms, with the RMSE of 2.26 and 2.48 TECU and the correlations (0.748 and 0.719), respectively.

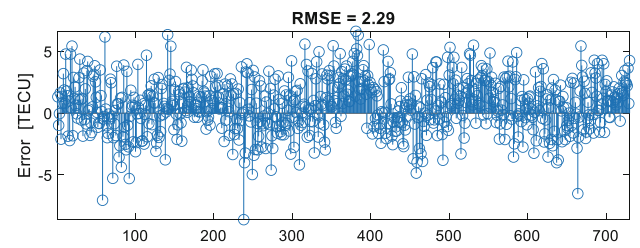
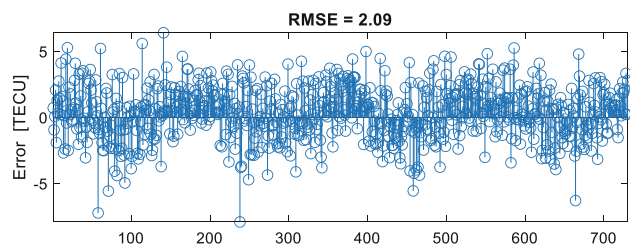
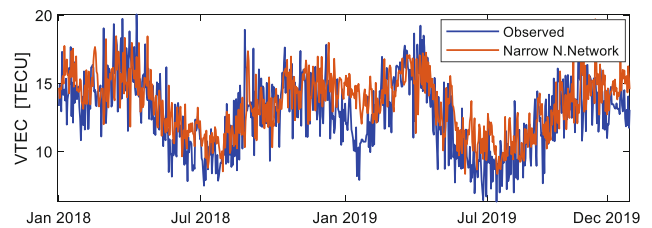
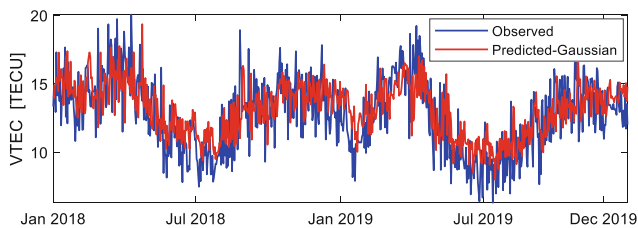
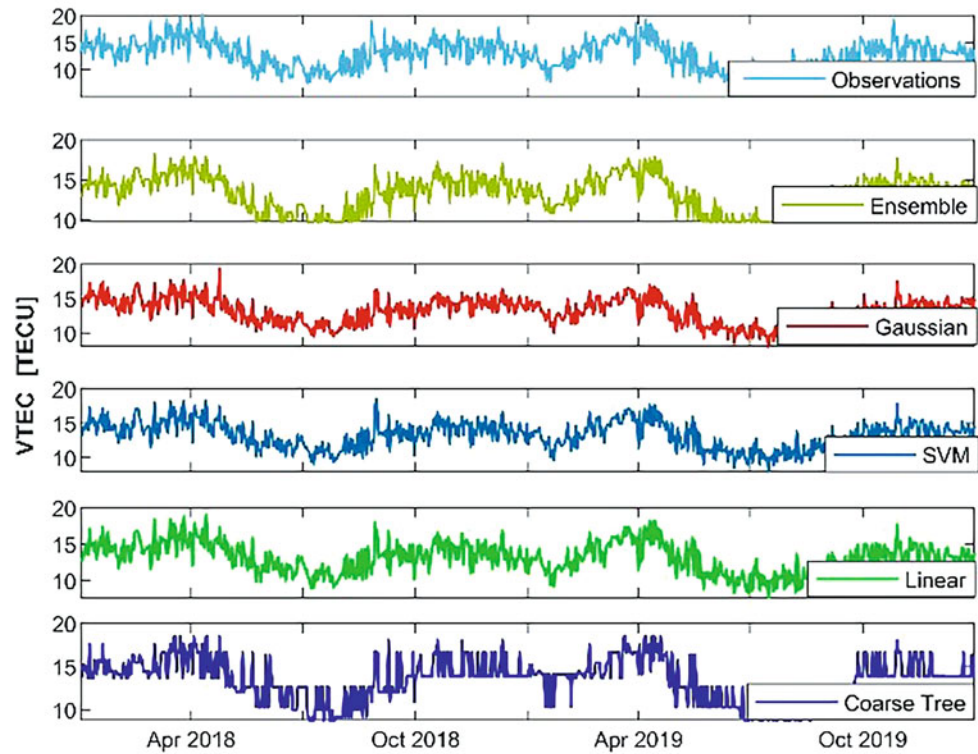
The TEC disturbances caused by the geomagnetic storms in March 2015 are detected in the Ensemble model (Fig. 10). The variation amplitude reaches 13.87 and 12.35 TECU, matching the first and second geomagnetic storms in March 2015 (Table 6), three times greater than other quiet days, and exceeds five times the model errors (RMSE). Therefore, these models can be applied for ionospheric anomaly detection caused by geomagnetic storms and solar activity.

**Table 3** Suitability testing of predictors for VTEC forecast models

R	R squares	Adjusted R squares	Std. errors	Change statistics				
				R squares change	F change	df1	df2	Sig. F change
0.952	0.906	0.906	3.908	0.906	5,090.897	9	4,734	0.000

Predictors: Plasma\_Speed, DOY, Proton\_Density, YEAR, Ap\_Index, F10.7, R\_Sunspot, Lyman\_Alpha  
 Dependent variable: VTEC

**Fig. 4** Three-day forecast of VTEC at station BAKO using five ML algorithms



(a)

(b)

**Fig. 5** Three-day forecasts of VTEC at station BAKO using Exponential Gaussian (a) and Narrow Neural Networks (b)

**Table 4** Statistical testing of the VTEC predictions based on the Exponential Gaussian algorithm

Statistical test	Three-day forecast	Observations
Mean (S)	13.23	12.77
Variance (s)	4.92	6.10
Degrees of freedom (v)	690	690
$F_{test}$	<b>0.707</b>	Fisher test
$F_{critical\ one-tail}$	<b>0.885</b>	
Correlation coefficient (r)	<b>0.78</b>	Pearson test

Unit of Mean and Variance: TECU

**Fig. 6** Smoothing the hourly VTEC time series at station MQZG by the Savitzky–Golay filter at a sliding window of 24 h

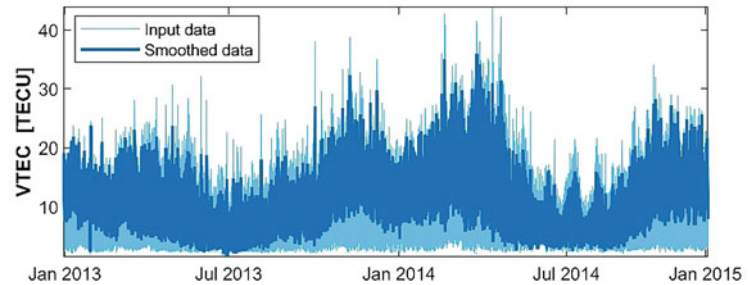
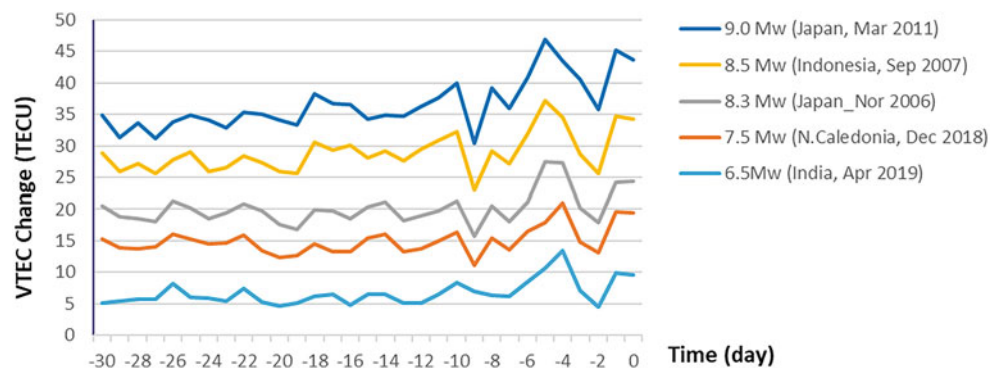


**Table 5** Stationarity testing of the VTEC time series using the Augmented Dickey-Fuller (ADF) algorithm

ADF test	Station USUD		Station MQZG	
	$t$	p-value	$t$	p-value
Levels	<b>-5.164</b>	8.62E-05	<b>-4.140</b>	0.0006
1%	-3.959		-3.959	
5%	-3.410		-3.410	
10%	-3.127		-3.127	

**Fig. 7** VTEC changes at the IGS stations 30 days before (-) the mainshocks of the earthquakes



Generally, in the five investigated shallow ML techniques, the Gaussian and Ensemble models reach the highest accuracy while the Regression Tree model remains the least. The ML-based forecast models can apply to ionospheric anomaly detection with an accuracy of 1.5 to 2.0 TECU. Filtering noise can considerably improve forecast models' accuracy but also reduce the granularity of the predictions. Therefore, applying noise filters is recommended for long-term forecasts or training noise-free forecast models in early warning systems. In this case, there are two options for using filters. The first is to remove the noise for inputs (predictors) and the other for outputs (forecast models). However, the efficiency of noise filtering often varies in different datasets and ML models. Thus, trials should be performed on sample data to determine which option will be applied.

## 4 Conclusions

Combining time series analysis techniques and Machine Learning is an effective solution for building high-performance forecast models. The Ensemble and Gaussian algorithms enable to provide the most robust mathematical models. Applying noise filtering can considerably improve the forecast accuracy for noise-free TEC models. There are mathematical correlations between the TEC disturbances and solar and seismic activities, but no clear relationship between the amplitude of these TEC fluctuations and the magnitude of geomagnetic storms and earthquakes. Therefore, extending investigations should be performed in further research. The research finding will open a promising prospect for

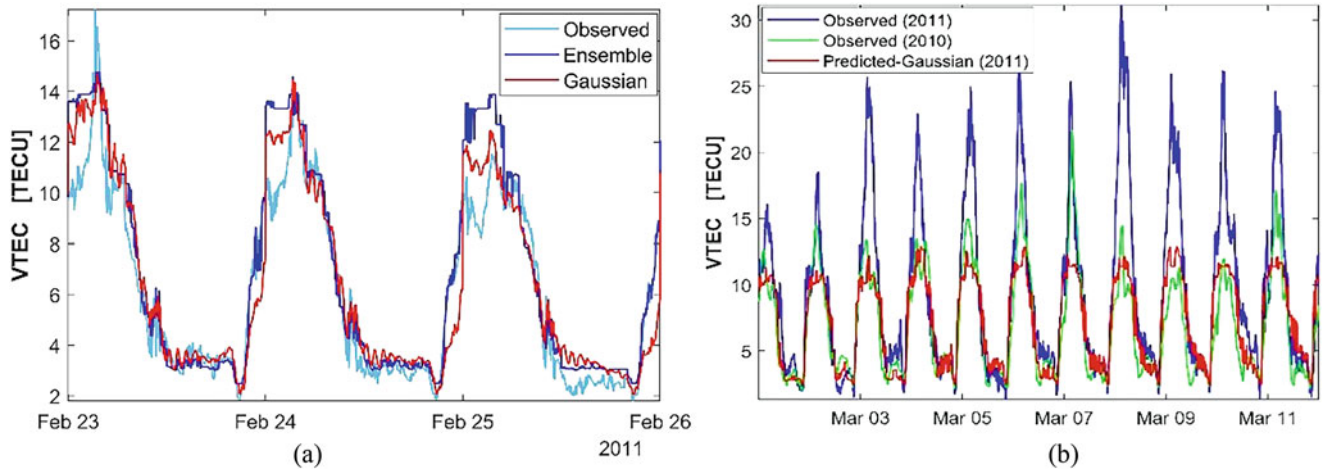


**Fig. 8** Evaluation of the forecast accuracy of the Gaussian and Ensemble models at station USUD in Japan (a) and the 1-day forecasts based on Gaussian to detect VTEC anomalies related to the earthquake Tohoku-Oki (b)

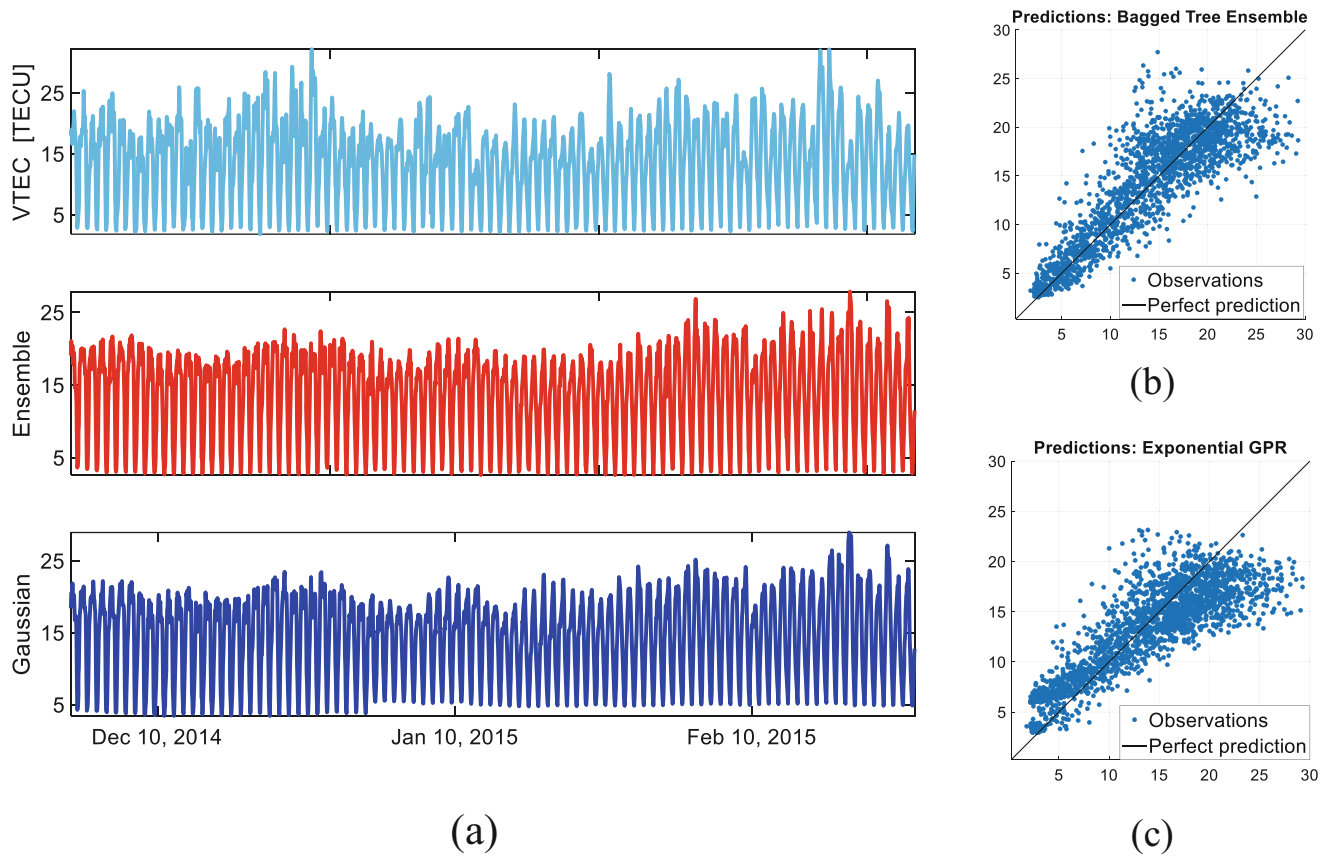


**Fig. 9** Evaluation of the VTEC forecast accuracy at station MQZG (a) and the correlations between predictions and observations, Ensemble = 0.748 (b) and Gaussian = 0.719 (c)

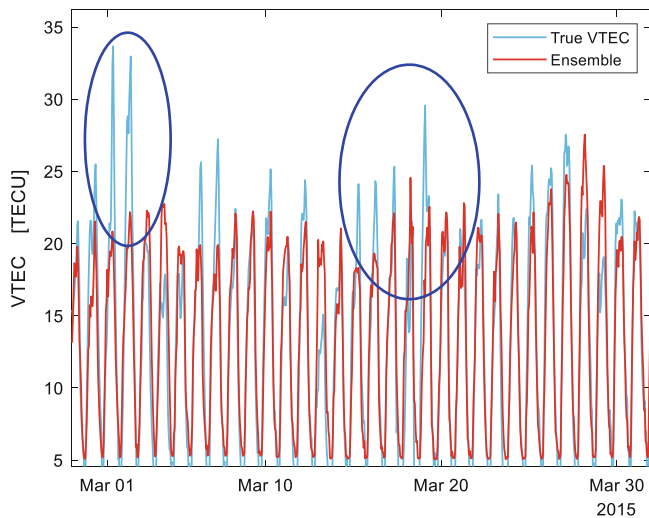


**Fig. 10** VTEC disturbance detection on the geomagnetic storm days using the Ensemble algorithm

**Table 6** Geomagnetic storms in March 2015

Date	Ap	Kp
01/03/2015	26	5+
02/03/2015	28	5+
17/03/2015	108	8–
18/03/2015	47	6
19/03/2015	26	5+
22/03/2015	24	6+

(+) Upper; (–) Under

applying Machine Learning and geophysical-combined geodetic measurements to determine interactions between the major spheres of the Earth's climate system and hazard management.

**Acknowledgments** The authors gratefully acknowledge the International GNSS Service (IGS); the world data center for geomagnetism, Kyoto, Japan; NOAA space weather prediction center, USA; GEO-FON data center, GFZ Potsdam, Germany; and Space weather live, Belgium, for providing GNSS data and information of earthquakes and geomagnetic storms. We have used the Machine Learning toolboxes in MATLAB® to train forecast models and the GPS-TEC analysis software 3.03 provided by Dr. Gopi Krishna Seemala, Indian Institute of Geomagnetism (IIG), Navi Mumbai, India.

#### Conflict of Interests

The authors declare that they have no competing interests.

#### Authors' Contributions

All of the authors have fair contributions.

## References

Athanasiou MA, Anagnostopoulos GC, Iliopoulos AC, Pavlos GP, David CN (2011) Enhanced ULF radiation observed by DEMETER two months around the strong 2010 Haiti earthquake. *Nat Hazards*

- Earth Syst Sci* 11(4):1091–1098. <https://doi.org/10.5194/nhess-11-1091-2011>
- Blagoveshchensky DV, Maltseva OA, Sergeeva MA (2018) Impact of magnetic storms on the global TEC distribution. *Ann Geophys* 36(4):1057–1071. <https://doi.org/10.5194/angeo-36-1057-2018>
- Cracknell AP, Varotsos CA (2021) Understanding global climate change, 2nd edn. Taylor & Francis
- Eckstein D, Künzel V, Schäfer L (2021) Global climate risk index 2021: who suffers most from extreme weather events? Weather-related loss events in 2019 and 2000–2019. Germanwatch e.V
- Elvira A, Irina Z, Matthias F (2015) Ionospheric response to the 2015 St. Patrick's Day storm: a global multi-instrumental overview. *J Geophys Res Space Phys*:9023–9037. <https://doi.org/10.1029/2006JA011892>
- Heki K (2011) Ionospheric electron enhancement preceding the 2011 Tohoku-Oki earthquake. *Geophys Res Lett* 38(17). <https://doi.org/10.1029/2011GL047908>
- Homam MJ (2015) Initial prediction of Total Electron Content (TEC) at a low latitude station using neural network. In: 2014 IEEE Asia-Pacific Conf. Appl. Electromagn. APACE 2014 - Proceeding, no. 2, pp 111–114. <https://doi.org/10.1109/APACE.2014.7043754>
- Inyurt S, Hasanpour M, Alihsan K (2020) Ionospheric TEC forecasting using Gaussian Process Regression (GPR) and Multiple Linear Regression (MLR) in Turkey. *Astrophys Space Sci*. <https://doi.org/10.1007/s10509-020-03817-2>
- Ishii M (2018) Extreme space weather research in Japan, vol 1957. Elsevier Inc.
- Jin S, Jin R, Liu X (2019) GNSS atmospheric seismology. Springer
- Lee S, Ji EY, Moon YJ, Park E (2021) One-day forecasting of global TEC using a novel deep learning model. *Space Weather* 19(1). <https://doi.org/10.1029/2020SW002600>
- Liu L, Zou S, Yao Y, Wang Z (2020) Forecasting global ionospheric TEC Using deep learning approach. *Space Weather* 18(11):1–12. <https://doi.org/10.1029/2020SW002501>
- Maurya AK, Venkatesham K, Kumar S, Singh R, Tiwari P, Singh AK (2018) Effects of St. Patrick's Day Geomagnetic Storm of March 2015 and of June 2015 on Low-Equatorial D Region Ionosphere. *J Geophys Res Space Phys* 123(8):6836–6850. <https://doi.org/10.1029/2018JA025536>
- Natras R, Schmidt M (2021) Ionospheric VTEC forecasting using machine learning. <https://doi.org/10.5194/egusphere-egu21-8907>
- Panigrahi S, Pattanayak RM, Sethy PK, Behera SK (2021) Forecasting of sunspot time series using a hybridization of ARIMA, ETS and SVM methods. *Sol Phys* 296(1). <https://doi.org/10.1007/s11207-020-01757-2>
- Rinard Hinga BD (2015) Ring of fire an encyclopedia of the Pacific Rims earthquakes, tsunamis, and volcanoes. Copyright © 2015 by ABC-CLIO, LLC All
- Seemala GK (2011) GPS-TEC analysis software. [Online]. Copyright © 2011 Gopi Seemala. All rights reserved
- Siebert L, Simkin T, Kimberly P (2010) Volcanoes of the world, 3rd edn. © 2010 by the Smithsonian Institution
- Silaparasetty N (2020) Machine learning concepts with Python and the Jupyter Notebook Environment, 2nd edn. Nikita Silaparasetty, Bangalore
- Singh K, Tripathi R, Mishra AP (2010) Solar and interplanetary disturbances responsible for geomagnetic storms. *J Phys Conf Ser* 208. <https://doi.org/10.1088/1742-6596/208/1/012068>
- Sun W et al (2017) Forecasting of ionospheric vertical total electron content (TEC) using LSTM networks. *Proc. 2017 Int. Conf. Mach. Learn. Cybern. ICMLC 2017*, vol 2, pp 340–344. <https://doi.org/10.1109/ICMLC.2017.8108945>
- Tanimoto T, Heki K, Artru-Lambin J (2015) Treatise on geophysics: interaction of solid earth, atmosphere, and ionosphere, vol 4. Elsevier B.V.



- United States Geological Survey (1999) Ring of fire, this dynamic earth, USGS [Online]. <https://pubs.usgs.gov/gip/dynamic/fire.html>
- Venkata Ratnam D, Vindhya G, Dabbakuti JRKK (2017) Ionospheric forecasting model using fuzzy logic-based gradient descent method. *Geod Geodyn* 8(5):305–310. <https://doi.org/10.1016/j.geog.2017.05.003>
- Yadav S, Sunda S, Sridharan R (2016) The impact of the 17 March 2015 St. Patrick's Day storm on the evolutionary pattern of equatorial ionization anomaly over the Indian longitudes using high-resolution spatiotemporal TEC maps: New insights. *Space Weather* 14(10):786–801. <https://doi.org/10.1002/2016SW001408>
- Zhao S, Shen XH, Zhima Z, Zhou C (2020) The very low-frequency transmitter radio wave anomalies related to the 2010 Ms 7.1 Yushu earthquake observed by the DEMETER satellite and the possible mechanism. *Ann Geophys* 38(5):969–981. <https://doi.org/10.5194/angeo-38-969-2020>
- Zhukov A, Sidorov DN, Mylnikova A, Yasyukevich Y (2018) Machine learning methodology for ionosphere total electron content nowcasting. <https://doi.org/10.13140/rg.2.2.19349.83685>

**Open Access** This chapter is licensed under the terms of the Creative Commons Attribution 4.0 International License (<http://creativecommons.org/licenses/by/4.0/>), which permits use, sharing, adaptation, distribution and reproduction in any medium or format, as long as you give appropriate credit to the original author(s) and the source, provide a link to the Creative Commons license and indicate if changes were made.

The images or other third party material in this chapter are included in the chapter's Creative Commons license, unless indicated otherwise in a credit line to the material. If material is not included in the chapter's Creative Commons license and your intended use is not permitted by statutory regulation or exceeds the permitted use, you will need to obtain permission directly from the copyright holder.





# Sensitivity of Shipborne GNSS Troposphere Retrieval to Processing Parameters

Aurélie Panetier , Pierre Bosser, and Ali Khenchaf

## Abstract

Water vapor is a key variable in meteorology and climate studies. Since the late 90s, Global Navigation Satellite System (GNSS) estimates from ground antennas are commonly used for its description. Indeed, propagation delays are due to the transit of the signal through the atmosphere. The correction of these delays is a crucial step that is needed for the precise GNSS positioning. Integrated Water Vapor (IWV) contents are derived from these delays and are used to describe the distribution of water vapour in the atmosphere.

However, severe meteorological phenomena often originate over the oceans and could strongly affect coastal regions. These phenomena are less well described or forecasted because of the small number of observations available in these regions. In this context, the potential of shipborne GNSS measurements has already been highlighted.

This work aims at investigating the impact of some GNSS processing parameters on IWV retrieval from a shipborne antenna in PPP mode. The studied parameters are cutoff angle, random walk of the estimated delays, and observation weighting. Data were collected for 2 months in 2018 by the GNSS antenna of a vessel operating in the Bay of Brest, France. The impact of the parameters is assessed by comparing the shipborne GNSS-derived IWV to the IWV estimated from a close GNSS ground station, and those computed by the ERA5 reanalysis and operational radiosonde profiles from the nearest Météo-France station. The most satisfying parameterization is shown to have Root Mean Squared (RMS) differences of  $0.5 \text{ kg m}^{-2}$ ,  $0.9 \text{ kg m}^{-2}$ , and  $1.2 \text{ kg m}^{-2}$  compared to GNSS ground station, ERA5, and radiosonde respectively. These conclusive results are also confirmed by comparing the GNSS height estimates to the measurements from the Brest tide gauge, with an RMS difference of 4.9 cm.

## Keywords

Climatology · IWV · Meteorology · PPP · Shipborne GNSS

## 1 Introduction

Severe meteorological phenomena often originate in the ocean and can strongly affect coastal regions. In order to be able to secure the coastal regions, atmospheric monitoring is required in these areas. The role played by water vapor in atmosphere dynamics is crucial (Bengtsson 2010); its observation is essential but difficult to achieve over the oceans. Indeed, water vapor measurements generally consist

A. Panetier (✉) · A. Khenchaf  
Lab-STICC/PIM UMR 6285 CNRS, ENSTA Bretagne, Brest, France  
e-mail: [aurelie.panetier@ensta-bretagne.org](mailto:aurelie.panetier@ensta-bretagne.org)

P. Bosser  
Lab-STICC/M3 UMR 6285 CNRS, ENSTA Bretagne, Brest, France

of surface measurements from ships and buoys (Smith et al. 2019). The water vapor column above the oceans can also be retrieved by satellite radiometers, but this technique provides a low spatial and temporal resolution (Kealy et al. 2012).

Since the late 90s, several studies have highlighted the contribution of GNSS measurements from ground antennas in the retrieval of Integrated Water Vapor (IWV) (Bevis et al. 1992; Haase et al. 2003; Bosser et al. 2010; Bock et al. 2013; Mahfouf et al. 2015). Indeed, the GNSS signal propagation through the troposphere is affected by water vapor. The induced propagation delay is computed in the form of the Zenith Total Delay (ZTD). The ZTD is composed of two parts. First, the Zenith Hydrostatic Delay (ZHD), which can be easily computed from the atmospheric pressure at the antenna height. Secondly, the Zenith Wet Delay (ZWD), which is highly variable and has to be estimated in the GNSS analysis (Boehm and Schuh 2013). Then, the IWV can be derived from the ZWD (Bevis et al. 1992). This kind of IWV retrieval is mainly restricted to land areas with ground GNSS antennas. However, shipborne GNSS IWV retrieval could be of great interest to contribute to water vapor description above the oceans. Some recent studies have already conducted shipborne GNSS IWV retrievals (Wang et al. 2019; Bosser et al. 2021; Mannel et al. 2021). They show an agreement with conventionally measured IWV between 1 and 3  $\text{kg m}^{-2}$  (Bock et al. 2016; Ning et al. 2016). These differences are due to the uncertainties in the GNSS measurement, as well as processing parameters that are chosen into the modelling used for the analysis of the GNSS raw data.

The quality of GNSS IWV retrieval could be affected by multipath, consisting of the reflection of GNSS signal, and the high correlation between the ZWD and the height estimates during the analysis (Elosegui et al. 1995), particularly in kinematic mode where both of them are estimated at every epoch. Some analysis parameters could be tuned in order to mitigate these effects. A high cut-off angle on satellite elevation will reduce the multipath effect; a low value will help to decorrelate ZWD and height estimates. An elevation dependent weighting of observations will also permit to mitigate the multipath. Finally, a suitable choice of the random walk on the ZWD will help the algorithm to decorrelate height and ZWD estimates as well. This study aims at investigating the impact of these GNSS processing parameters on the IWV retrieval from a shipborne GNSS antenna. Here we processed only GPS raw data acquired on the French survey vessel Panopée. It was operating in the Bay of Brest during 49 days between March, 30th and May, 17th of 2018.

The datasets used in this study and the data processing will be detailed in Sect. 2. The Sect. 3 will present the results of the height and IWV retrieval from the shipborne GNSS antenna, and their comparison to other water vapor datasets described in Sect. 2. Finally, Sect. 4 will draw conclusions regarding the identification of a configuration that stands out

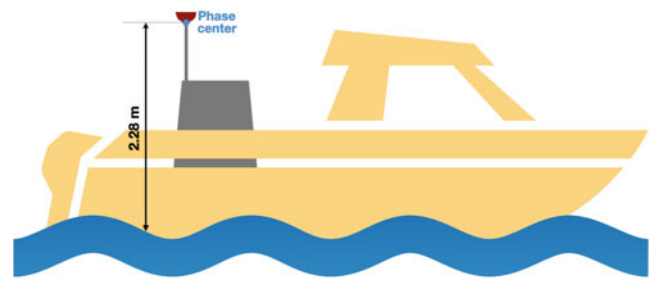


Fig. 1 Panopée antenna

from the rest of the tested parameters, and will highlight the perspectives.

## 2 Data

### 2.1 Shipborne Antenna Dataset

The GNSS antenna PANO is onboard the French survey vessel Panopée operating in the Bay of Brest. The antenna is mounted on a pole located on the echosounder well at the back of the vessel, as illustrated in Fig. 1.

This location was chosen in order to reduce the multipath effects that could affect the antenna, due to the vessel structure. The chosen dataset has a length of 49 days from day 89 to day 137 of year 2018 (March, 30th to May, 17th). During this period, the vessel Panopée was operating in the Brest harbor for hydrographic purposes. It was docked more than 90% of the time, leaving for at most a couple of hours straight.

The Gipsy-Oasis II v. 6.4 software (hereafter GIPSY) developed by the Jet Propulsion Laboratory (JPL) of the National Aeronautics and Spatial Agency (NASA), is used to process the PANO dataset (Zumberge et al. 1997). GNSS constellations other than GPS are not supported by GIPSY for kinematic PPP processing with ambiguity resolution (Bertiger et al. 2010), only the GPS data are studied here. The data are processed with a time resolution of 30 s with high-resolution final clocks and orbit products from JPL. To avoid edge effects, it was processed in a 30 h window centered on each day from which the 00–24 h parameters were extracted. The International Earth Rotation and Reference Systems Service (IERS) conventions for solid Earth tides were applied (Petit and Luzum 2010). The Finite Element Solution tide model FES2004 (Lyard et al. 2006) was also applied for ocean tide loading effects, using the coefficients computed by the ocean tide loading provider.<sup>1</sup> The a priori values for ZHD and ZWD, and the coefficients for the mapping functions were extracted from the Technische Universität Wien (TU Wien) VMF database.<sup>2</sup> Three different values, detailed in

<sup>1</sup>Machiel Simon Bos and Hans-Georg Scherneck, <http://holt.oso.chalmers.se/loading/>, last access: 07/09/2021.

<sup>2</sup><https://vmf.geo.tuwien.ac.at/>, last access: 07/09/2021.

**Table 1** Values used for each of the three tested processing parameters. The  $\sin$  and  $\sqrt{\sin}$  weighting functions of the satellite elevation are applied on the phase observations with a 10 mm uncertainty

Cut-off	Random walk	Weighting
3°	3 mm h <sup>-1/2</sup>	uniform
7°	5 mm h <sup>-1/2</sup>	$\sin$
10°	10 mm h <sup>-1/2</sup>	$\sqrt{\sin}$

Table 1, are tested for each of the three following tested parameters:

- cut-off angle of the satellite elevation, for decreasing the multipath effect and the correlation between ZTD and antenna height estimates;
- random walk on the ZWD modeling, for constraining the ZWD variations to decorrelate ZTD and antenna height estimation;
- satellite elevation weighting on a 10 mm uncertainty for phase observations, for limiting the multipath effect impacting the signal.

The method used to derive the IWV from the ZTD is fully described in Bosser et al. (2021). The IWV is computed from the ZWD with a semi-empirical function using the mean temperature of the air column above the antenna (Bevis et al. 1992). The values for mean temperature were extracted from the TU Wien database.<sup>3</sup> To estimate the wet part, the hydrostatic part must be first computed thanks to the pressure at the antenna height. To that end, the mean sea level pressure retrieved from the European Center for Medium-range Weather Forecasts (ECMWF) fifth ReAnalysis ERA5 is used to compute the ZHD at the mean sea level height according to the Saastamoinen formula (Saastamoinen 1972). The ZHD value is then adjusted with the height difference between the mean sea level and the antenna.

## 2.2 Comparison Datasets

*Reference Ground Based GNSS Antenna* As the vessel Panopée is evolving in the harbor of Brest, it is located close to the Brest ground reference antenna BRST (operated by IGN<sup>4</sup>), with a distance smaller than 10 km. A cut-off angle of 7° with a uniform weighting on phase elevation of 10 mm, and a random walk on the ZWD of 5 kg m<sup>-2</sup> are used to process the BRST data. To stay consistent with the PANO processing, the time resolution is 30 s with high-resolution final satellite products in the GIPSY settings. As BRST is a ground reference station, the data is processed in static PPP mode, in contrast with the kinematic mode used for processing the moving PANO antenna. This processing

strategy has already been applied in many studies (Bock et al. 2016, 2021; Bosser and Bock 2021) and has therefore already been validated.

*Penfeld Tide Gauge* The harbor of Brest houses the Penfeld digital tide gauge operated by the Shom.<sup>5</sup> It provides a reference set of data to qualify the calculation of the PANO antenna height by comparison. It will then be used in order to assess the proper estimation of height and ZTD in the GNSS analysis despite of their strong correlation.

The tide gauge measurement has a 10-min time resolution. Consequently, to compare the PANO height to the tide gauge, we will use the nearest time method. This method consists of taking the PANO height value of the closest time to each tide gauge measurement time.

*ERA5 Reanalysis* The ERA5 reanalysis provided by Copernicus of the ECMWF delivers hourly atmospheric parameters on a 0.25-degree grid all over the Earth (Hersbach et al. 2020). A reanalysis of the water column is directly provided by ERA5 through the so called TCWV product. An extrapolation of the ERA5 value at the location and the height of the PANO antenna is made (Bock et al. 2005) and their IWV are compared by matching the times.

*Radiosonde of Guipavas* Météo-France has a radiosonde station in Brest-Guipavas (less than 20 km from Brest harbor). The sonde data were retrieved from the University of Wyoming sounding archive.<sup>6</sup> The dataset is composed of twice-daily launched sondes measuring the water column in the troposphere.

IWV values are computed by the integration of humidity profiles as proposed in Bock et al. (2021). The radiosonde IWV value is extrapolated to the PANO antenna height as in Bock et al. (2005). Then, the radiosonde IWV is also compared to the PANO IWV by matching the times.

## 3 Qualification of the PANO Results

### 3.1 Antenna Height

First, the PANO height is assessed by comparison to the Brest tide gauge in order to qualify the impact of the choice of the parameterization on the height estimation of the antenna. The vertical lever arm of the shipborne antenna is known with a 1–2 cm accuracy due to the loading of the vessel. The RMS of the difference, varying from 4.9 cm to 6.0 cm depending on the configurations, might be impacted by this uncertainty and should not be used to compare the height

<sup>3</sup><https://vmf.geo.tuwien.ac.at/>, last access: 07/09/2021.

<sup>4</sup><http://rgp.ign.fr/STATIONS/#BRST>, last access : 07/09/2021.

<sup>5</sup><http://dx.doi.org/10.17183/REFMAR>.

<sup>6</sup><http://weather.uwyo.edu/upperair/sounding.html>, last access: 07/09/2021.

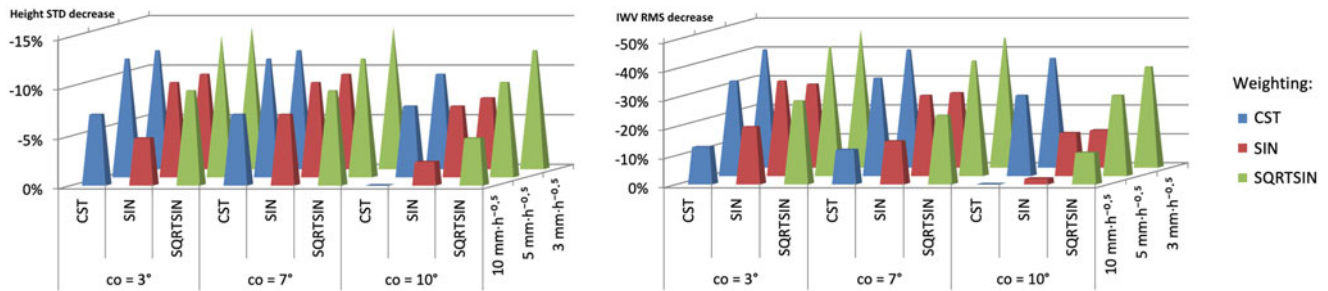


**Fig. 2** Decrease of STD with respect to the worst STD for the PANO height comparison to the Brest tide gauge (left plot) and decrease of RMS with respect to the worst RMS for the PANO IWV comparison to

the ground station BRST IWV (right plot). The highest peaks represent the best configuration as the RMS error or the STD is improved, as the lowest of all the parameterizations

of the PANO antenna with the tide gauge. Therefore, the standard deviations (STD) of the differences are computed for each treatment. The provided STD of the difference in the most unfavorable case is of 4.2 cm. This applies to the configuration of  $10^\circ$  cut-off angle, uniform weighting function of the elevation, and  $10 \text{ mm h}^{-1/2}$  random walk on ZWD. Considering the uncertainty of the vertical lever arm, a STD higher than 4.0 cm is considered to be deteriorating the height estimate. Then, the contribution of each configuration is assessed by computing the decreases of STD with respect to the worst STD value of 4.2 cm. The resulting percentages are shown in Fig. 2 (left).

One can observe here that when parameterizing the PPP processing of the PANO antenna with the sine weighting function (SIN), the STD increases in all configurations. It could be preferred to not use this weighting function, although it gives better results than the uniform function (CST) only in the case of a  $10 \text{ mm h}^{-1/2}$  random walk on the ZWD and  $10^\circ$  cut-off angle. On the other side, the square-root of a sine weighting function (SQRTSIN) gives significantly better results on all configurations, and thereby should be favored. A choice of a  $10 \text{ mm h}^{-1/2}$  random walk on the ZWD systematically gives a worse STD on the difference between PANO and Brest tide gauge than the lower random walk values. Indeed, the decrease of STD compared to the worst resulting STD of the study is mostly lower of 5%, and until 10%, than when using a random walk of  $3 \text{ mm h}^{-1/2}$  or  $5 \text{ mm h}^{-1/2}$ . These two random walk parameters are decreasing the STD of 10 to 14% compared to the worst STD.

With a  $10^\circ$  cut-off angle, the STD of the difference is high in most cases, except when applying a  $3 \text{ mm h}^{-1/2}$  random walk on ZWD. However, this case does not provide a STD as good as the best parameterization that results in a STD of 3.6 cm. Then, the parameter  $3 \text{ mm h}^{-1/2}$  random walk on ZWD might also be left out when used with both previous ones:  $10 \text{ mm h}^{-1/2}$  random walk on the ZWD and  $10^\circ$  cut-off angle.

The three parameters  $10^\circ$  cut-off angle,  $10 \text{ mm h}^{-1/2}$  random walk on the ZWD and sine weighting function,

provide a STD of the height difference at most 12% better than the worst STD of the difference on height between PANO and the Brest tide gauge. On the contrary, using the other parameters always provide a STD of the height difference at least 12% better than the worst case.

Finally, three parameterizations seem to provide a better height estimation. Indeed, it appears that by favoring the square-root of a sine weighting function, both  $3 \text{ mm h}^{-1/2}$  and  $5 \text{ mm h}^{-1/2}$  random walk on the ZWD are giving relevant results with a  $3^\circ$  cut-off angle. Both random walk values are still relevant with a  $7^\circ$  cut-off angle, even if here the choice of  $5 \text{ mm h}^{-1/2}$  random walk on the ZWD gives a slightly poorer result with  $-12\%$  of STD of the height difference against  $-14\%$  in the three other configurations, compared to the worst case. These couples of parameters must be chosen according to the situation as they give really similar results.

### 3.2 Comparison Between PANO and BRST IWV

The shipborne GNSS IWV are compared to the ground GNSS IWV from BRST station. For each configuration, the Root Mean Squared error (RMS) on the difference between the IWV of stations PANO and BRST is computed, as well as the RMS on the difference between the height of the station PANO corrected from the air draft of the vessel, and the tide gauge.

The resulting bias on the IWV is between  $0.03 \text{ kg m}^{-2}$  in the best case and  $0.51 \text{ kg m}^{-2}$  in the worst situation, and the STD is between  $0.52 \text{ kg m}^{-2}$  and  $0.99 \text{ kg m}^{-2}$ . Although these results are already good regarding to the expectations of  $2 \text{ kg m}^{-2}$ , the purpose of the study is to settle whether a parameterization is better than the others. To this end, statistical tests have been purchased, showing that the biases and the variances are significantly different between each processing configuration. The contribution of each configuration is assessed by computing the decreases of RMS with respect to the worst RMS value of  $1.01 \text{ kg m}^{-2}$ . The resulting

percentages are shown in Fig. 2 (right). Actually, the IWV estimation is improved when the height is well estimated in the PPP processing. This was expected because of the strong correlation of ZWD and height estimates in the analysis.

On the one hand, the best resulting RMS on the difference of the IWV is of  $0.53 \text{ kg m}^{-2}$ . It was obtained with a configuration of  $3^\circ$  of cut-off angle, square-root of a sine weighting function of the elevation of the satellites, and  $3 \text{ mm h}^{-1/2}$  random walk on the ZWD. A RMS higher of maximum  $0.15 \text{ kg m}^{-2}$  than this best parameterization is a lowly significant change. The parameters used to provide such a satisfying RMS on the difference of the IWV are chosen among the following:

- cut-off angle of  $3^\circ$  or  $7^\circ$ ;
- uniform or square-root of a sine weighting function;
- random walk on the ZTD of 3 or  $5 \text{ mm h}^{-1/2}$ .

On the contrary, the worst resulting RMS is of  $1.01 \text{ kg m}^{-2}$ , with a configuration of  $10^\circ$  cut-off angle, uniform weighting function of the elevation, and  $10 \text{ mm h}^{-1/2}$  random walk on the ZWD. Figure 2 shows that choosing the sine function for the elevation weighting or  $10^\circ$  of cut-off angle systematically degrades the RMS on the differences of the IWV as well as the differences of the height. The  $10 \text{ mm h}^{-1/2}$  of random walk on the ZWD does not give suitable results either on the RMS of the IWV and the height, except when the chosen cut-off angle is  $3^\circ$  and the weighting function is square-root of a sine.

Moreover, by choosing one of these parameters ( $10^\circ$  cut-off angle,  $10 \text{ mm h}^{-1/2}$  random walk on the ZWD and sine weighting function), the RMS on the difference of the IWV higher of  $0.15 \text{ kg m}^{-2}$  than the best RMS on the difference of IWV between PANO and BRST. This is significantly higher

than the best resulting RMS of  $0.53 \text{ kg m}^{-2}$  with respect to the other configurations introduced above. These parameters are therefore to be avoided to process ZWD from shipborne GNSS antennas.

Finally, three parameterizations seem to provide a globally better water vapor column estimation by shipborne GNSS PANO with respect to ground GNSS station BRST. Indeed, it appears that by favoring square-root of a sine weighting function as for the height estimation, both  $3 \text{ mm h}^{-1/2}$  ( $-48\%$  of RMS) and  $5 \text{ mm h}^{-1/2}$  ( $-45\%$  of RMS) random walk on the ZWD are giving relevant results with a  $3^\circ$  cut-off angle. Both random walk values are still relevant with a  $7^\circ$  cut-off angle, even if the choice of  $3 \text{ mm h}^{-1/2}$  random walk on the ZWD gives a better result with an improvement of  $45\%$  of RMS here. As previously, these couples of parameters give really similar results, so they can be chosen according to the situation.

### 3.3 Comparison of PANO IWV with ERA5 Reanalysis and Radiosonde

The best computed IWV after Sect. 3.2 is the parameterization  $3^\circ$  cut-off angle, square-root of a sine function for elevation weighting, and  $3 \text{ mm h}^{-1/2}$  random walk on the ZWD. The corresponding IWV dataset is compared to the ERA5 reanalysis and the radiosonde of Brest-Guipavas. Superimposing these timeseries with the BRST one provides the top chart in Fig. 3.

This graph reveals a succession of wet (more than  $20 \text{ kg m}^{-2}$ ) and dry (less than  $10 \text{ kg m}^{-2}$ ) episodes for the region. These events are well described by the different

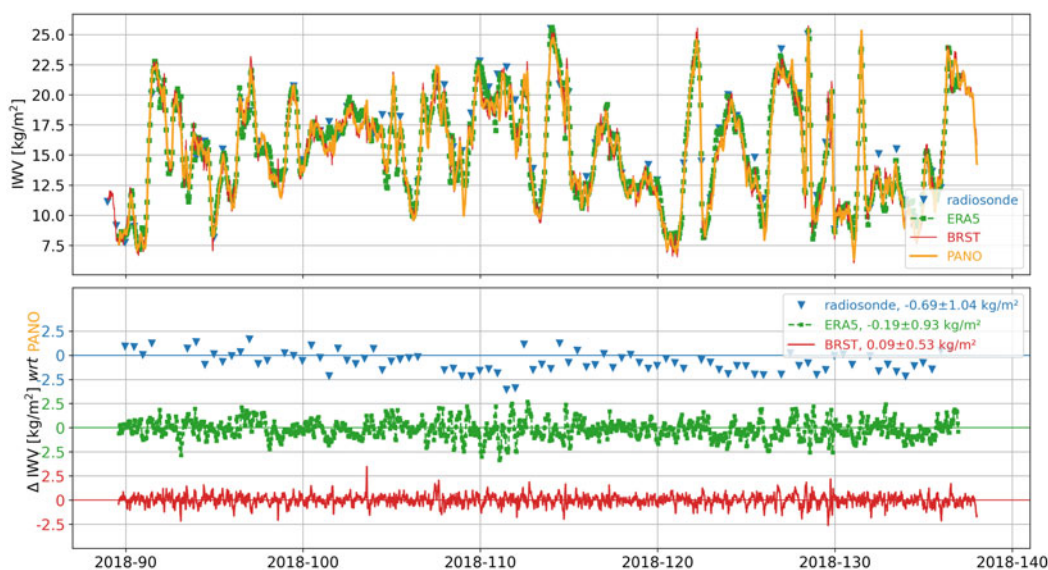


**Fig. 3** Timeseries of the different IWV datasets (top) and differences between the PANO configuration giving the best RMS, and each reference (bottom). Numerical values in bottom figure indicate bias  $\pm$  standard deviation

techniques studied: radiosonde, ERA5 reanalysis from the ECMWF, BRST GNSS permanent station and PANO GNSS station. All over the period of study of nearly 50 days from April to May 2018, these IWV show a very good agreement with each other. The bottom chart on Fig. 3 shows the differences between the IWV estimated with the best PANO processing parameters and the radiosonde of Brest-Guipavas (blue), the ERA5 reanalysis (green) and the BRST GNSS station (red). The mean bias is inferior to  $1 \text{ kg m}^{-2}$  in all cases, but it is negative for ERA5 and radiosonde comparisons. The STD of differences with ERA5 and radiosonde are about  $1 \text{ kg m}^{-2}$ . The difference between PANO and ERA5 is varying from  $2.4 \text{ kg m}^{-2}$  to  $-3.1 \text{ kg m}^{-2}$ . The difference between PANO and the radiosonde is varying from  $1.7 \text{ kg m}^{-2}$  to  $-3.6 \text{ kg m}^{-2}$ . These results are consistent with those presented in recent works (Bossler et al. 2021; Wang et al. 2019) and highlights the potential of retrieving IWV estimates from shipborne GNSS antennas.

## 4 Conclusion

GPS measurements from a shipborne GNSS receiver have been used in order to highlight an adequate parameterization of PPP processing for the improvement of shipborne IWV retrieval. The measurements take place in the harbour of Brest, during 50 days in the second quarter of 2018.

The three processing parameters we focused on here are the cut-off angle for the satellite elevation, the random walk on the ZWD, and the use of different weighting function on the observation phase of the signal. These parameters are commonly modulated to mitigate multipath effects on the signal or correlation between height and ZTD estimates during the analysis.

A best parameterization to process the IWV appears to be  $3^\circ$  cut-off angle with  $3 \text{ mm h}^{-1/2}$  of random walk on the ZWD and square-root of a sine elevation weighting function on the observation phase, in our study. This parameterization provides an IWV difference between the shipborne GNSS antenna and the reference station GNSS antenna of  $0.09 \text{ kg m}^{-2} \pm 0.53 \text{ kg m}^{-2}$ . The comparison of this IWV result with ERA5 and radiosonde provides a difference of  $-0.19 \text{ kg m}^{-2} \pm 0.93 \text{ kg m}^{-2}$  and  $-0.69 \text{ kg m}^{-2} \pm 1.04 \text{ kg m}^{-2}$  respectively. These differences are good according to the literature. GNSS dynamical height computed in the better parameterization case has also been compared to the Brest tide gauge, providing here a difference of  $3.4 \text{ cm} \pm 3.6 \text{ cm}$ . Some parameterizations should be avoided because they systematically give worst results than other parameterizations. Then, the parameters  $10^\circ$  of cut-off angle,  $10 \text{ mm h}^{-1/2}$  of random walk on the ZWD, or sine function of the elevation applied on the phase observation has to be left out of the PPP processing.

In the future, simulations will be conducted for further insight into the role of the parameterization. It will mostly permit to assess whether the use of a sine function for the elevation weighting is systematically degrading the IWV estimation. Results need also to be confirmed with datasets acquired in a broader range of sea states and on a longer period.

**Acknowledgements** We would like to thank the CNRS for supporting this work through the projet GEMMOC in the LEFE/INSU program. We are also grateful to the Fondation Van Allen and Région Bretagne for their financial support, and ENSTA Bretagne for hosting the project.

## Conflict of Interest

The authors declare that they have no conflict of interest.

## Availability of Data and Material

The datasets generated during and/or analysed during the current study are available from the corresponding author on request. Authors' contributions: AP carried out the GNSS data analysis and the comparisons. AP, PB analysed the results and co-wrote the article with contributions from AK.

## References

- Bengtsson L (2010) The global atmospheric water cycle. *Environ Res Lett* 5(2):Article 025202. <https://doi.org/10.1088/1748-9326/5/2/025202>
- Bertiger W, Desai SD, Haines B, Harvey N, Moore AW, Owen S, Weiss JP (2010) Single receiver phase ambiguity resolution with GSP data. *J Geodesy* 84:327–337. <https://doi.org/10.1007/s00190-010-0371-9>
- Bevis M, Bussinger S, Herring TA, Rocken C, Anthes RA, Ware RH (1992) GPS Meteorology: remote sensing of atmospheric water vapor using the Global Positioning System. *J Geophys Res* 97:15787–15801
- Bock O, Keil Ch, Richard E, Flamant C, Bouin M-N (2005) Validation of precipitable water from ECMWF model analyses with GPS and radiosonde data during the MAP SOP. *Q J Roy Meteorol Soc* 131(612):3013–3036. <https://doi.org/10.1256/qj.05.27>
- Bock O, Bossler P, Bourcy T, David L, Goutail F, Hoareau C, Keckhut P, Legain D, Pazmino A, Pelon J, Pipis K, Poujol G, Sarkissian A, Thom C, Tournois G, Tzanos D (2013) Accuracy assessment of water vapour measurements from in situ and remote sensing techniques during the DEMEVAP 2011 campaign at OHP. *Atmos Meas Tech* 6(10):2777–2802. <https://doi.org/10.5194/amt-6-2777-2013>
- Bock O, Bossler P, Pacione, R, Nuret, M, Fourrié N, Parracho A (2016) A high-quality reprocessed ground-based GPS dataset for atmospheric process studies, radiosonde and model evaluation, and reanalysis of HyMeX special observing period. *Quart J Roy Meteorol Soc* 142:56–71. <https://doi.org/10.1002/qj.2701>
- Bock O, Bossler P, Flamant C, Doerflinger E, Jansen F, Fages R, Bony S, Schnitt S (2021) IWV observations in the Caribbean Arc from a

- network of ground-based GNSS receivers during EUREC<sup>4</sup>A. *Earth Syst Sci Data*. <https://doi.org/10.5194/essd-2021-50>
- Boehm J, Schuh H (2013) Atmospheric effects in space geodesy. Springer atmospheric sciences. Springer, Berlin, Heidelberg. <https://doi.org/10.1007/978-3-642-36932-2>
- Bosser P, Bock O (2021) IWV retrieval from ground GNSS receivers during NAWDEX. *Adv Geosci* 55:13–22. <https://doi.org/10.5194/adgeo-55-13-2021>
- Bosser P, Bock O, Thom Ch, Pelon J, Willis P (2010) A case study of using Raman lidar measurements in high-accuracy GPS applications. *J Geodesy* 84:251–265. <https://doi.org/10.1007/s00190-009-0362-x>
- Bosser P, Bock O, Flamant C, Bony S, Speich S (2021) Integrated water vapour content retrievals from ship-borne GNSS receivers during EUREC<sup>4</sup>A. *Earth Syst Sci Data* 13(4):1499–1517. <https://doi.org/10.5194/essd-13-1499-2021ff>
- Elosegui P, Davis JL, Jaldehag RTK, Johansson JM, Niell AE, Shapiro II (1995) Geodesy using the Global Positioning System: The effects of signal scattering on estimates of site position. *J Geophys Res* 100:9921–9934
- Haase J, Ge M, Vedel H, Calais E (2003) Accuracy and variability of GPS tropospheric delay measurements of water vapor in the western Mediterranean. *J Appl Meteor* 42:1547–1568. [https://doi.org/10.1175/1520-0450\(2003\)042](https://doi.org/10.1175/1520-0450(2003)042)
- Hersbach H, Bell B, Berrisford P, Hirahara S, Horányi A, Muñoz-Sabater J, Nicolas J, Peubey C, Radu R, Schepers D, Simmons A, Soci C, Abdalla S, Abellan X, Balsamo G, Bechtold P, Biavati G, Bidlot J, Bonavita M, De Chiara G, Dahlgren P, Dee D, Diamantakis M, Dragani R, Flemming J, Forbes R, Fuentes M, Geer A, Haimberger L, Healy S, Hogan RJ, Hólm E, Janisková M, Keeley S, Laloyaux P, Lopez Ph, Lupu C, Radnoti G, de Rosnay P, Rozum I, Vamborg F, Villaume S, Thépaut J-N (2020) The ERA5 global reanalysis. *Q J Roy Meteorol Soc*. Accepted Author Manuscript. <https://doi.org/10.1002/qj.3803>
- Kealy J, Foster J, Businger S (2012) GPS meteorology: An investigation of ocean-based precipitable water estimates. *J Geophys Res Atmospheres Am Geophys Union (AGU)* 117(D17). <https://doi.org/10.1029/2011jd017422>
- Lyard F, Lefevre F, Letellier T, Francis O (2006) Modelling the global ocean tides: insights from FES2004. *Ocean Dynamics* 56:394–415
- Mahfouf JF, Ahmed F, Moll P, Teferle NF (2015) Assimilation of zenith total delays in the AROME France convective scale model: a recent assessment. *Tellus A* 67:26106. <https://doi.org/10.3402/tellusa.v67.26106>
- Männel B, Zus F, Dick G, Glaser S, Semmling M, Balidakis K, Wickert J, Maturilli M, Dahlke S, Schuh H (2021) GNSS-based water vapor estimation and validation during the MOSAiC expedition. *Atmos Meas Tech* 14:5127–5138. <https://doi.org/10.5194/amt-14-5127-2021>
- Ning T, Wang J, Elgered G, Dick G, Wickert J, Bradke M, Sommer M, Querel R, Smale D (2016) The uncertainty of the atmospheric integrated water vapour estimated from GNSS observations. *Atmos Meas Tech* 9(1):79–92. <https://doi.org/10.5194/amt-9-79-2016>
- Petit G, Luzum B (2010) IERS 2010 conventions, technical report, IERS, Frankfurt-am-Main, Germany
- Saastamoinen J (1972) Atmospheric correction for the troposphere and stratosphere in radio ranging of satellites, in the use of artificial Satellites for geodesy. *Geophysical Monograph* 15, 16:247–251
- Smith SR, Alory G, Andersson A, Asher W, Baker A, Berry DI, Drushka K, Figurskey D, Freeman E, Holthus P, Jickells T, Kleta H, Kent EC, Kolodziejczyk N, Kramp M, Loh Z, Poli P, Schuster U, Steventon E, Swart S, Tarasova O, de la Villéon LP, Vinogradova-Shiffer N (2019) Ship-based contributions to global ocean, weather, and climate observing systems. *Front Marine Sci* 6(434). doi:10.3389/fmars.2019.00434
- Wang J, Wu Z, Semmling M, Zus F, Gerland S, Ramatschi M, Ge M, Wickert J, Schuh H (2019) Retrieving precipitable water vapor from shipborne multi-GNSS observations. *Geophys Res Lett* 46(9). <https://doi.org/10.1029/2019GL082136>
- Zumberge JF, Heflin MB, Jefferson DC, Watkins MM (1997) Precise point positioning for the efficient and robust analysis of GPS data from large networks. *J Geophys Res* 102:5005–5017

**Open Access** This chapter is licensed under the terms of the Creative Commons Attribution 4.0 International License (<http://creativecommons.org/licenses/by/4.0/>), which permits use, sharing, adaptation, distribution and reproduction in any medium or format, as long as you give appropriate credit to the original author(s) and the source, provide a link to the Creative Commons license and indicate if changes were made.

The images or other third party material in this chapter are included in the chapter's Creative Commons license, unless indicated otherwise in a credit line to the material. If material is not included in the chapter's Creative Commons license and your intended use is not permitted by statutory regulation or exceeds the permitted use, you will need to obtain permission directly from the copyright holder.







# Application of the Total Variation Method in Near Real-Time GNSS Tropospheric Tomography

Zohreh Adavi and Robert Weber

## Abstract

GNSS tomography is an all-weather remote sensing technique to capture the spatiotemporal behavior of the atmospheric water vapor using the standing infrastructure of GNSS satellites and networks. In this method, the troposphere is discretized to a finite number of 3D elements (voxel) in horizontal and vertical directions. Then, the wet refractivity in these voxels is reconstructed using the Slant Wet Delay (SWD) observations in the desired tomography domain by means of the discrete inverse concept. Due to the insufficient spatial coverage of GNSS signals in the voxels within the given time window, some of the voxels are intersected by a few signals or plenty of signals, and others are not passed by any signals at all. Therefore, the design matrix is sparse, and the observation equation system of the tomography model is mixed-determined. Some constraints have to be applied or external data sources should be added to the tomography problem in order to reconstruct the wet refractivity field. Moreover, the GNSS tomography is a kind of discrete ill-posed problem, as all singular values of the structure matrix ( $A$ ) in the tomography problem decay gradually to zero without any noticeable gap in the spectrum. Hence, slight changes in the measurements can lead to extremely unstable parameter solutions. In consequence, the regularization method should be applied to the inversion process and ensure a stable and unique solution for the tomography problem. In this research, the Total Variation (TV) method is suggested to retrieve a regularized solution. TV is a nonlinear technique, which resists noise and efficiently preserves discontinuities in the model. This method can also reconstruct the wet refractivity field without any initial field in a shorter time span. For this purpose, observation data from the EPOSA (Echtzeit Positionierung Austria) GNSS network located in the eastern part of Austria is processed within the period DoYs 232-245 in 2019. Then, the TV method is performed in six different tomography windows (10–60 min) with a time step of 10 min by focusing on near-real-time applications. Finally, radiosonde measurements in the area of interest are utilized to compare the estimated wet refractivity field in order to obtain the accuracy of the proposed method.

## Keywords

GNSS · Tomography · Total variation method

## 1 Introduction

The most important key element of the troposphere is water vapour. This parameter is highly variable both temporally and spatially and therefore remains challenging for modelling. GNSS tomography is one of the promising and devel-

Z. Adavi (✉) · R. Weber (✉)  
Department of Geodesy and Geoinformation, TU Wien, Vienna,  
Austria  
e-mail: [zohreh.adavi@tuwien.ac.at](mailto:zohreh.adavi@tuwien.ac.at); [robert.weber@tuwien.ac.at](mailto:robert.weber@tuwien.ac.at)

oping methods that can provide 4D spatiotemporal information of water vapour in all-weather conditions with an almost reasonable spatial resolution. The principle input data for GNSS tomography is the GNSS ray path and the tropospheric signal delay. Using these observations, water vapour can be modeled in terms of temporal variation and spatial distribution. For this purpose, the troposphere is discretized into a finite number of 3D elements, named voxels and then an intended parameter (here, wet refractivity  $N_w$ ) can be retrieved. One of the main challenges of the GNSS tomography is ill-posedness since all singular values of the structure matrix ( $A$ ) decay gradually to zero without no obvious gap in the spectrum (Aster et al. 2013; Hansen 1998; Menke 2012). During the last two decades, a number of methods have been developed that mainly focus on the regularization techniques and methodology to solve or avoid ill-posedness in the GNSS tomography. In this regard, in 2000, Hirahara successfully conducted a 4D tropospheric tomography experiment based on the damped least-square method due to the singularity of the observation equation system of the tomography problem (Hirahara 2000). Braun and Rocken (2003) and Braun (2004) used the extended sequential batch filter to overcome the sensitivity of the GNSS tomography model as well as updating the tomography solution. Rohm and Bosy (2011) applied the Moore–Penrose pseudo inverse to invert the observation equation system of the tomography model. Bender et al. (2011) implemented several members from the algebraic reconstruction techniques (ART) to reconstruct the wet part of the troposphere. According to their result, the multiplicative techniques (MART) could establish the tomography solution with higher accuracy in least processing time in comparison to other iterative techniques in the ART family. In the year 2013, Xia et al. presented a combined iterative and non-iterative reconstruction algorithm (CRA) using GPS observations and COSMIC profiles (Xia et al. 2013). Rohm et al. (2014) proposed a new GNSS tomography model named TOMO2. TOMO2 applies a robust Kalman filtering technique to solve the unconstrained tomography model. In the year 2015, Adavi and Mashhadi-Hossainali used a hybrid regularization method to compute a reconstructed tomography solution. This method is combined of the Least-Square QR (LSQR) and the Tikhonov regularization techniques which benefits from the advantages that both the non-iterative and iterative techniques are independent of an initial field (Adavi and Mashhadi Hossainali 2015). Guo et al. (2016) proposed for GPS troposphere tomography an optimal weighting method to determine the optimal weights for three types of equations, namely the observation equation, the horizontal constraint equation, and the vertical constraint equation. Ghaffari Razin and Voosoghi (2020) used artificial neural networks (ANNs) to model the wet refractivity of the troposphere. In their method, the objective function is calculated using the squared difference between SWD from

GNSS (SWDGPS) and SWD from ANN (SWDANN). Then, the ANN network is trained by a hybrid PSO (particle swarm optimization) -BP (backpropagation) algorithm to obtain the minimum of the objective function as well as optimize the network weights. Using the calculated objective function, the model wet refractivity can be reconstructed with high accuracy. Sá et al. (2021) implemented a simultaneous algebraic reconstruction technique (SART) to accelerate estimation solutions using tropospheric tomography. According to their results, the processing time is significantly reduced even for large datasets by applying parallel algebraic reconstruction techniques like SART. In the year 2022, Adavi et al. investigated the accuracy of the retrieved solution using ART techniques (ART, MART, and Landweber) and the Total Variation (TV) method based on single-frequency (SF) and dual-frequency (DF) observations. Their results proved a reasonable performance for all ART techniques+ Numerical weather model (NWM) in both SF and DF schemes compared to the TV and TV+ART techniques. Moreover, the accuracy of the refractivity profiles retrieved by the tomography solution using ART methods+ TV was between 6.11 and 8.99 ppm for the SF scheme. For the DF scheme, the accuracy of the wet refractivity field ranged from 4.86 to 7.84 ppm, and ART+TV had a superior performance in comparison to the other ART techniques +TV (Adavi et al. 2022).

In spite of all of these efforts and attainments, there are still some challenges that stand in GNSS tomography. One of these challenges is the dependency of the accuracy of the retrieved wet refractivity structure on the quality of the a priori field used in some of the solution strategies like ART methods. Therefore, the retrieved tomography field may be very similar to the a priori field instead to reflect the real physical conditions if the chosen regularization parameter was not suitable. Another challenging task in the GNSS tomography is to reconstruct a reasonable near-real-time solution, especially when the number of rays is low and the area covered by the voxel model is large.

In this research, we apply the Total Variation (TV) regularization method to reconstruct the spatiotemporal structure of the wet refractivity field. This method is a non-linear technique and independent from an initial field. Moreover, this method can resolve the tomography field when the number of rays is low, and therefore, this could be a step forward towards near-real-time tomography. In this paper, we investigate the feasibility of the TV method in order to reconstruct the wet refractivity in a short tomography window. Therefore, six different temporal resolutions (10–60 min) with a time step of 10 min are defined and then the wet refractivity field is estimated using the TV method. Moreover, one of the well-known iterative methods named Landweber is also applied to retrieve the wet refractivity solution to provide a better interpretation of the TV results.

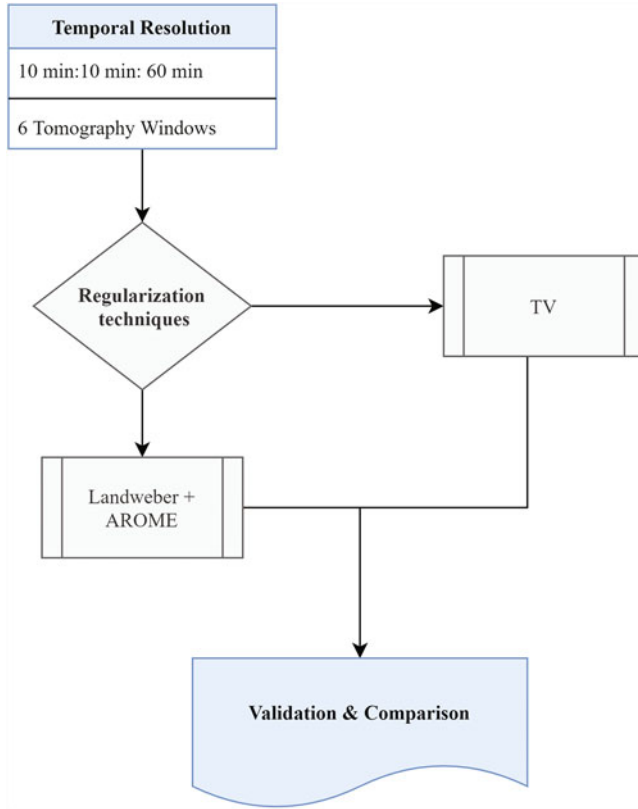


**Fig. 1** Main strategy of this research

This method needs an initial field and therefore in this study we have employed the AROME (Applications of Research to Operations at MEsoscale) model (Seity et al. 2011). The main strategy of this research is presented in Fig. 1. Test computations are based on observations of the twenty-one multi-GNSS stations from the EPOSA network which are mostly located in the eastern part of Austria. Moreover, the experimental period covers fourteen different rainy days in summer 2019.

In the following parts, first, the fundamental principle of GNSS tomography is described. Next, the notable mathematical concepts and formulas in TV and Landweber regularization techniques are presented. After that, the case study in this research is defined. Then, the obtained results using the TV and Landweber method in different temporal resolutions in comparison to radiosonde observations are investigated. Finally, conclusions based on the outcome of this research are drawn.

## 2 Methodology

In this section, the principle of GNSS tropospheric tomography is explained. Then, the TV and Landweber techniques are described in order to reconstruct the wet refractivity field.

### 2.1 Tropospheric Tomography Concept

In order to reconstruct the wet refractivity ( $N_w$ ) [unit: ppm] structure, the wet part of troposphere discretizes to 3D voxels. Then, the spatiotemporal behaviour of the wet part of the refractivity is retrieved by analyzing the impact of the wet part of the troposphere on GNSS signals with an assumption that  $N_w$  is constant in the individual model elements. For this purpose, a large number of Slant Wet Delays (SWD) [unit: mm] are integrated in the GNSS tomography according to Eq. (1) (Flores et al. 2000; Heublein 2019):

$$SWD_i = 10^{-6} \cdot \sum_{j=1}^m N_{wj} \cdot d_{ij} \quad (1)$$

whereby,  $d_{ij}$  is the length of  $i^{\text{th}}$  signal inside the  $j^{\text{th}}$  model element [unit: km]. According to Eq. (1), the total slant wet delay observation of each satellite ( $SWD_i$ ) can be defined as a summation over voxels intersected by the GNSS signals. In GNSS data processing, SWD can be estimated as below:

$$SWD = VMF1_w(elv) \cdot ZWD + MF_{az}(elv) \times [G_{N_w} \cos az + G_{E_w} \sin az] \quad (2)$$

$elv$  and  $az$  are the elevation and azimuth angle of the satellite signal.  $G_{N_w}$  and  $G_{E_w}$  are the wet horizontal gradients in the north-south and east-west directions, respectively.  $VMF1_w$  and  $MF_{az}$  are the Vienna Mapping Function 1 (VMF1) and Chen-Herring mapping function (see (Böhm et al. 2006; Chen and Herring 1997) for more details). Furthermore, the Zenith Wet Delay (ZWD) is the delay in zenith direction caused by the wet part of the troposphere. This parameter can be calculated by subtracting the Zenith Hydrostatic Delay (ZHD) from the estimated Zenith Total Delay (ZTD) as follows:

$$ZWD = ZTD - ZHD \quad (3)$$

Here, the Bernese GNSS software was employed in baseline mode to estimate  $ZTD$  and horizontal gradients (Dach et al. 2015). Moreover, the hydrostatic Saastamoinen model was applied (Saastamoinen 1973) to calculate the dry part of  $ZTD$ , namely  $ZHD$ . After that,  $SWD$  was calculated by substituting Eq. (3) in Eq. (2). Please refer to (Adavi et al. 2022) for more details.

Equation (1) can be presented in matrix form as noted below (Flores et al., 2000):

$$SWD = A N_w \quad (4)$$

here,  $SWD [m \times 1]$  and  $N_w [n \times 1]$  are the vectors of observations and unknown parameters, respectively. Moreover,  $A [m \times n]$  is a structure matrix which links the observation

space to the model space and can be demonstrated as (Rohm and Bosy 2009):

$$\mathbf{A} = \begin{bmatrix} d_{11} & 0 & 0 & 0 & \cdots & d_{1n} \\ d_{21} & d_{22} & d_{23} & 0 & \cdots & d_{2n} \\ \vdots & \vdots & \vdots & \vdots & \ddots & \vdots \\ d_{m1} & d_{m2} & 0 & d_{m4} & \cdots & d_{mn} \end{bmatrix} \quad (5)$$

where  $d_{ij}$  is the length of ray  $i$  inside the voxel  $j$ . According to Eq. (5), the coefficients of the design matrix  $\mathbf{A}$  can be defined as follows:

$$A_{ij} = \begin{cases} d_{ij} & \text{if ray } i \text{ crosses voxel } j \\ 0 & \text{otherwise} \end{cases} \quad (6)$$

As shown in Eq. (4), matrix  $\mathbf{A}$  is a mapping matrix governed by the geometry of the tomography model, the geometry of the measurements, the distribution of the GNSS receivers as well as the time window of integration (Bender et al. 2011; Lutz 2008; Troller 2004). Due to insufficient spatial coverage of the voxels by GNSS rays within the tomography window, some of the voxels are intersected by a small number or a plenty number of signals and others are not passed at all. Therefore, the design matrix  $\mathbf{A}$  is a sparse, and Eq. (4) is mixed-determined (Menke 2012). Hence, the model null space of the design matrix is non-trivial, which causes the partly ill-conditioned tomographic inversion system. Therefore, in order to reconstruct the wet refractivity field using Eq. (4), some constraints or external data sources should be added to the tomography problem as well as some inversion techniques must be applied. In this research, horizontal and vertical constraints were added to Eq. (4) to obtain a unique solution. For more information, please refer to (Adavi and Weber 2019). Moreover, two different regularization techniques, TV and Landweber, were also applied to reconstruct the wet refractivity field that are described in more detail in the next part.

## 2.2 Regularization Technique

The purpose of this section is to describe two different regularization techniques (TV and Landweber) to solve the equation system of the tomography model (Eq. (4)). The main characteristic of this problem is that all singular values of the structure matrix ( $\mathbf{A}$ ) decay gradually to zero without any noticeable gap between non-zero and zero singular values (Aster et al. 2013; Hansen 1998; Menke 2012). Therefore, regularization techniques should be applied in order to reconstruct the wet refractivity field. From a general perspective, two classes of regularization methods can be

used to produce a stable inverse solution. The first class of methods covers the direct methods like the TV technique and the second class of algorithms covers iterative methods like Landweber.

In the following, first, the TV regularization technique is described. This method is a nonlinear technique, which resist noise and effectually preserves discontinuities in the model (Abbasbandy 2006; Aster et al. 2013; Lee et al. 2007; Yao et al. 2019). Afterwards, the Landweber method is described which is generally appropriate for the tomography reconstruction problems (Aster et al. 2013).

**TV** TV method is a direct and nonlinear technique that is independent of the initial field. In recent years, this technique has been successfully applied in CT (Computer Tomography) and ionospheric tomography (Lee et al. 2007; Sidky et al. 2006; Tang et al. 2015). The objective function ( $J$ ) of the TV regularization technique can be defined as follows (Jensen et al. 2012; Lohvithee 2019; Persson et al. 2001; Rudin et al. 1992):

$$J(\mathbf{N}_w) = \underset{\mathbf{N}_w}{\operatorname{argmin}} \left( \tau \|\mathbf{N}_w\|_{TV} + \frac{1}{2} \|\mathbf{A} \mathbf{N}_w - \mathbf{SWD}\|_2^2 \right) \quad (7)$$

whereby,  $\tau > 0$  and  $\|\mathbf{N}_w\|_{TV}$  are a regularization parameter and TV norm, respectively. In order to estimate the TV norm ( $\|\mathbf{N}_w\|_{TV}$ ), Eq. (8) can be applied (Persson et al. 2001):

$$\|\mathbf{N}_w\|_{TV} = \left\| \vec{D} \mathbf{N}_w \right\|_1 = \sum_{i,j,k} \|D_{i,j,k} \mathbf{N}_{w_{i,j,k}}\| \quad (8)$$

here  $D_{i,j,k} \mathbf{N}_{w_{i,j,k}}$  is the discrete gradient of  $\mathbf{N}_w$  at the model element  $[i, j, k]$ . In this study, the augmented Lagrangian algorithm to minimize the TV norm is chosen as shown below (Li 2009):

$$\begin{aligned} L_A(w_{i,j,k}, \mathbf{N}_w) &= \sum_{i,j,k} (\|w_{i,j,k}\| - V_{i,j,k}^T (D_{i,j,k} \mathbf{N}_w - w_{i,j,k}) + \frac{\beta_{i,j,k}}{2} \\ &\times \|D_{i,j,k} \mathbf{N}_w - w_{i,j,k}\|_2^2) - \lambda^T (\mathbf{A} \mathbf{N}_w - \mathbf{SWD}) + \frac{\mu}{2} \\ &\times \|\mathbf{A} \mathbf{N}_w - \mathbf{SWD}\|_2^2 \end{aligned} \quad (9)$$

with  $w_i$  defined according to (Li 2009):

$$\begin{aligned} w_i = \max \left\{ \left\| D_{i,j,k} \mathbf{N}_w - \frac{v_{i,j,k}}{\beta_{i,j,k}} \right\| - \frac{1}{\beta_{i,j,k}}, 0 \right\} \\ \times \frac{(D_{i,j,k} \mathbf{N}_w - v_{i,j,k}/\beta_{i,j,k})}{\left\| D_{i,j,k} \mathbf{N}_w - v_{i,j,k}/\beta_{i,j,k} \right\|} \end{aligned} \quad (10)$$

During the minimization procedure of Eq. (9),  $v_{i,j,k}$  and  $\lambda$  is continuously updated in each iteration. These parameters can

be defined as follows (Li 2009; Li et al. 2010):

$$\begin{aligned} \tilde{v}_{i,j,k}^{iter+1} &= v_{i,j,k}^{iter} - \beta_{i,j,k} (D_{i,j,k} N_w^* - w_{i,j,k}^*) \quad \text{for all } i, j, k \end{aligned} \quad (11)$$

$$\tilde{\lambda}^{iter+1} = \lambda^{iter} - \mu (A N_w^* - SWD) \quad (12)$$

In Eqs. (11) and (12),  $N_w^*$  and  $w_{i,j,k}^*$  refer to an approximate solution for Eq. (9) (Li 2009). In addition, the sparsity level of the exact solution and the noise level of the observations is used in order to define a reasonable barrier parameter  $\mu$  (Li et al. 2010). However, obtaining the noise level of the observation (here SWD) is quite challenging without the availability of an exact solution. As claimed by experience,  $\mu$  varies from  $2^4$  to  $2^{13}$  and the best value is defined based on the *RMSE* of the retrieved solution and the value of  $\beta_{i,j,k}$  is also selected within the range of  $[2^4, 2^{13}]$  (Li 2011).

**Landweber** The Landweber method belongs to the Simultaneous Iterative Reconstruction Technique (SIRT) family (Hansen 1998; Kaltenbacher et al. 2008). To retrieve the wet refractivity field using this technique, as shown in Eq. (13), all rows of the coefficient matrix  $A$  are used in one iteration. This implies that the system of observation equations is solved simultaneously. The wet refractivity field in iteration  $k+1$  can be retrieved according to (Landweber 1951):

$$N_w^{k+1} = N_w^k + \lambda_k A^T (SWD - A N_w^k) \quad (13)$$

hereby  $\lambda_k$  is a relaxation parameter which can be optimally determined in a range of  $0 < \lambda_k < 2/s_{max}^2$  where  $s_{max}$  denotes the largest eigenvalue of matrix  $A^T A$  (Aster et al. 2013; Elfving et al. 2014; Elfving et al. 2010; Hansen 1998). However, this strategy, named optimal choice, needs beforehand knowledge of the real solution (Elfving et al. 2010). Other strategies to determine the relaxation parameter  $\lambda_k$  are line search,  $\psi_1$ -based relaxation strategy,  $\psi_2$ -based relaxation strategy, and modified  $\psi_1$  and  $\psi_2$  strategies (Aster et al. 2013; Elfving et al. 2010; Hansen 1998). In this work, the modified  $\psi_2$ -based relaxation strategy is used that takes advantage of better damping of the noise propagation and also faster convergence (Elfving et al. 2012; Elfving et al. 2010).

The relaxation parameter in the modified  $\psi_2$ -based relaxation strategy is defined as below (Elfving et al. 2010):

$$\lambda_k = \begin{cases} \frac{\sqrt{2}}{s_{max}^2} & \text{for } k = 0, 1 \\ \tau_k \frac{2}{s_{max}^2} (1 - \xi_k) & \text{for } k \geq 2 \end{cases} \quad (14)$$

where  $\xi_k \in (0, 1)$  is the unique root in (Elfving et al. 2010):

$$g_{k-1}(\xi_k) = \left[ (2k-1)(\xi_k)^{k-1} \right] - \frac{1 - (\xi_k)^{k-1}}{1 - \xi_k} = 0 \quad (15)$$

Moreover,  $\tau_k \in (0, (1 - \xi_k)^{-1})$  is normally chosen as a constant value  $\tau_k = \tau$ . If  $\tau > 1$  then the convergence is accelerated (Elfving et al. 2010).

### 3 Case Study

EPOSA is the GNSS network operated by Energie Burgenland AG, ÖBB Infrastruktur AG, and Wiener Netze GmbH which consists of thirty-eight permanent GNSS stations. Observation files of reference stations contain phase and code observations with a rate of 1 second for GPS and GLONASS satellites. Therefore, this network has considerable potential for tropospheric tomography modelling and other meteorological studies. In this research, only twenty-one permanent GNSS reference stations of the EPOSA network are considered due to the availability of their observations for a period of interest. Therefore, the area of interest extends from  $13.40^\circ$  to  $17^\circ$  in longitude, and  $46.5^\circ$  to  $48.5^\circ$  in latitude according to the location of selected GNSS permanent stations. Figure 2 demonstrates the distribution of the multi GNSS stations as well as the location of the radiosonde station RS11035.

In this network, the heights of the GNSS sites vary from 220 m to 860 m with a mean interstation distance of about 60 km. In addition, observations on days 232–245 in the year 2019 have been selected due to the unstable weather conditions with different amounts of precipitation in the experimental period. In Fig. 3 the observed relative humidity (RH) calculated from the radiosonde data and variations of precipitation reported by the AROME model are shown. Furthermore, it should be noted that the required a priori field for the Landweber method was calculated from the AROME model at midnight and noontime.

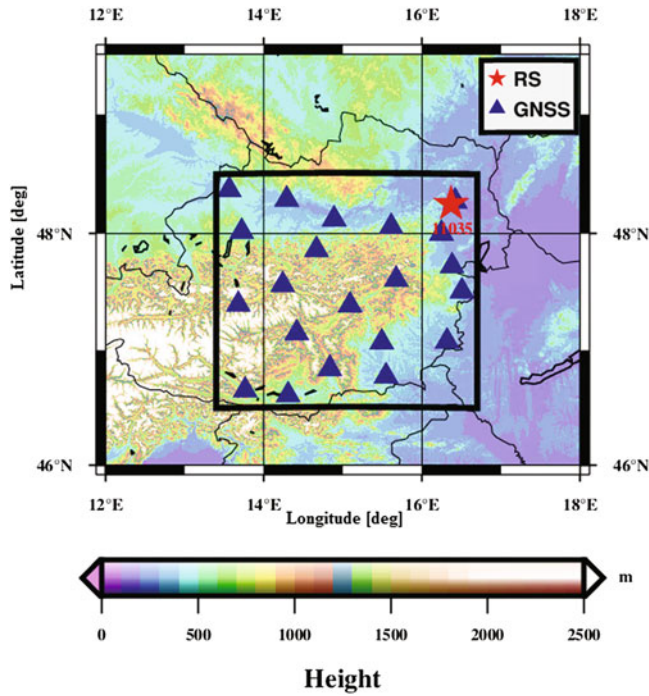


**Fig. 2** Distribution of GNSS stations in the area of interest

#### 4 Numerical Results

To evaluate the efficiency of the TV regularization method to retrieve the wet refractivity field without any initial field and in a short time span, an estimated tomography profile in different temporal resolutions was compared to radiosonde measurements located at Vienna airport (RS11035) for midnight and noontime. Figure 4 shows examples of the reconstructed wet refractivity profile in comparison to the RS for three days of the study period with different performances on DoYs 232, 237, and 244. Figure 4(a) and (b) present the results for midnight and noontime, respectively. For shorter tomography windows of up to 40 min, the agreement

between the reconstructed profiles and the RS profile at midnight is less than 5 and 7.6 ppm, for DoYs 232 and 237, respectively. However, on DoY 244, the performance of the TV method is almost poor at midnight. For temporal windows of more than 40 min, the quality of the reconstructed profiles using the TV method is quite good for all sample days at midnight and noontime. In the following, the efficiency of the TV method is demonstrated by Mean Absolute Error (MAE [unit: ppm]), Root Mean Square Error (RMSE [unit: ppm]), Bias [unit: ppm], and Standard deviation (Std [unit: ppm]) calculated over the whole period. The mentioned statistical tools can be computed as below (Guerova 2003; Xiaoying et al. 2014):

$$Bias = \frac{1}{n_l} \sum_{i=1}^{n_l} (N_{wtomoi} - N_{wobsi}) \quad (16)$$

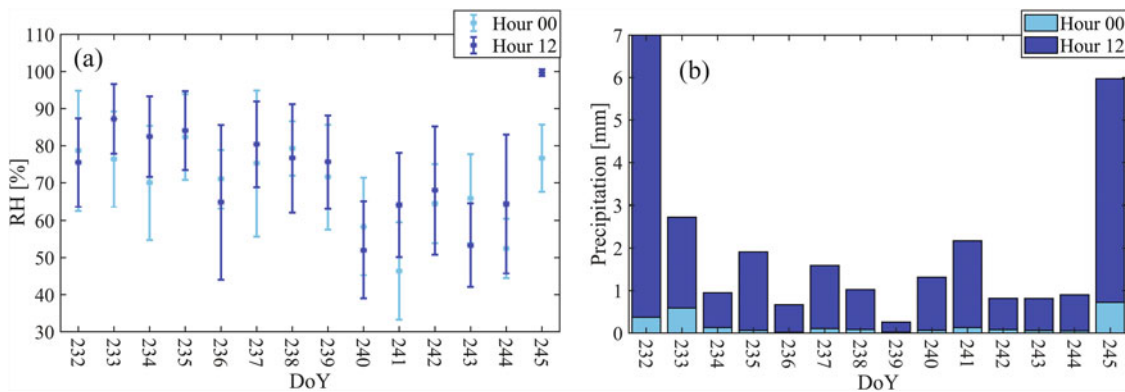
$$RMSE = \sqrt{\frac{1}{n_l} \sum_{i=1}^{n_l} (N_{wtomoi} - N_{wobsi})^2} \quad (17)$$

$$Std = \sqrt{RMSE^2 - Bias^2} \quad (18)$$

$$MAE = \frac{1}{n_l} \sum_{i=1}^{n_l} |N_{wtomoi} - N_{wobsi}| \quad (19)$$

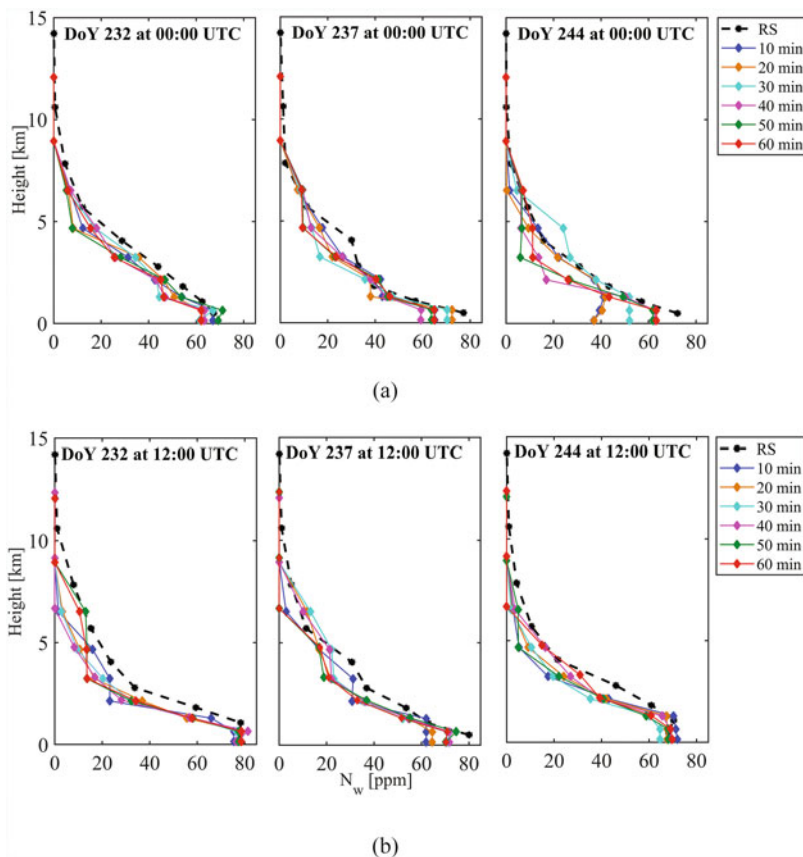
whereby,  $N_{wobs}$  and  $N_{wtomo}$  are the computed wet refractivity field obtained from the radiosonde profiles and the tomography model, respectively. Moreover,  $n_l$  represents the number of vertical levels, here  $n_l = 9$ .

Figure 5 presents the average MAE over the experimental period for the reconstructed wet refractivity in different temporal resolutions. According to the obtained results, for the lower layers, the inconsistency between the retrieved field and RS wet refractivity is mostly better of noontime in comparison to midnight. Moreover, the discrepancy between the tomography solution and the RS profile is decreasing with extending the tomography time window. For the upper layers from 2 km to 6 km, the obtained

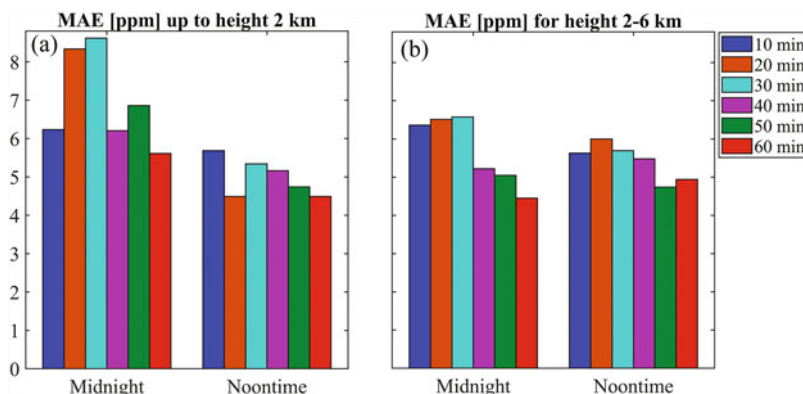


**Fig. 3** Variation of RH up to 4 km (a), and average of precipitation within the whole area (b) at midnight and noontime

**Fig. 4** Comparison of tomographic refractivity profiles of different tomography windows to the profile calculated from RS11035 data at midnight (a), and noontime (b) for DoYs 232, 237, and 244



**Fig. 5** Average MAE of the reconstructed wet refractivity field for heights up to 2 km (a), and 2 to 6 km (b) at midnight and noontime at RS11035 location



results for noontime and midnight are comparable. Additionally, the discrepancy of reconstructed wet refractivity with respect to the RS profile generally amounts to 7 ppm or less for spans longer than 40 min for both studied height layers.

In the next step, RMSE, Std, Bias and MAE were calculated for the reconstructed wet refractivity field using the TV method during the entire study period at midnight and noontime. Table 1 reports the average value over all 14 days of these statistical parameters for different temporal resolutions at midnight (see Appendix A for daily RMSE at midnight). The numbers shows that the performance of the tomography

model, calculated with high temporal resolution, is comparable with longer time setups. As expected, the RMSE, Std and MAE of the tomography solution with 60 min temporal resolution are slightly better than for other schemes. By looking at Table 1, it becomes clear the average Bias for the temporal resolutions of 20 and 30 min are averagely larger than 10 min. As shown in Table A.4 (see Appendix A), this is due to the three problematic days (DoYs 242-244) with the highest inconsistency with respect to the RS profiles, which most probably returns to the weak performance of the tomography model in the lower layers (see Fig. 5). The main factors for this inconsistency could be related to the low

**Table 1** Average RMSE, Std, and Bias over the experimental period for all different temporal resolutions (epoch 00:00 UTC, location: RS11035)

Midnight	RMSE [ppm]	Std [ppm]	Bias [ppm]	MAE [ppm]
10 min	6.77	6.46	0.33	1.70
20 min	7.72	7.26	-0.28	2.11
30 min	7.46	6.95	-0.61	1.93
40 min	5.80	5.30	-0.41	1.86
50 min	6.05	5.70	-0.97	1.58
60 min	5.26	5.02	-0.71	1.19

amount of water vapour in the troposphere (see Fig. 3(b)) and the lack of proper definition of the regularization parameter for the TV technique. For shown Bias values in Table 1, there is no general judgment due to the different behaviour of this quantity by extending temporal resolution. This could return to the various signs ( $\pm$ ) of Bias and the affectability of this statistical parameter from the systematic errors in the GNSS observations, meteorological measurements (here pressure), and the instability of the retrieved solution using the TV method. However, it is worth mentioning that a sensor Bias is usually removed by the meteorologists before assimilation in the NWM models based on test periods. So in case the parameter retrieval ‘environment’ is stable, also the bias should be kept stable and can be absorbed before assimilation. Furthermore, according to the reported Bias in Table 1, it turns out that the wet refractivity solutions calculated in tomography windows of more than 10 min are averagely underestimating RS wet refractivity over the experimental period.

Table 2 presents the statistical evaluation of retrieved wet refractivity using the TV method at noontime (see Appendix A for daily RMSE results). From this table, it becomes obvious that the performance of the TV technique at noontime is slightly better than for midnight. This is generally because of the low accuracy of the retrieved wet refractivity for DoYs 242-244. For other days, the accuracy of the tomography solution is comparable at midnight and noontime. Additionally, the amount of water vapour is higher at noontime in comparison to midnight. This variation of water vapour is a crucial factor for the TV performance. Furthermore, the estimated tomography profiles using the TV method are generally underestimating the wet refractivity of the reference RS profile similar to midnight according to the reported values of Bias.

In the next step, in order to evaluate the similarity of the reconstructed wet refractivity with the RS profile, the average correlation was calculated over the experimental period at midnight and noontime. According to the reported values in Table 3, it can be stated that the behaviour of the

**Table 2** Average RMSE, Std, and Bias over the experimental period for all different temporal resolutions (epoch 12:00 UTC, location: RS11035)

Noontime	RMSE [ppm]	Std [ppm]	Bias [ppm]	MAE [ppm]
10 min	5.72	5.24	-0.46	1.91
20 min	5.47	5.05	-0.90	1.77
30 min	5.81	5.29	-0.74	1.98
40 min	5.50	5.04	-0.003	1.79
50 min	4.98	4.58	-0.07	1.58
60 min	4.82	4.54	-0.30	1.18

**Table 3** Average correlation coefficient [%] over the entire study period between the retrieved wet refractivity profile and RS profile for different temporal resolution

	10 min	20 min	30 min	40 min	50 min	60 min
Midnight	96.40	95.12	95.61	97.38	97.23	97.98
Noontime	97.84	97.88	97.69	98.03	98.37	98.48

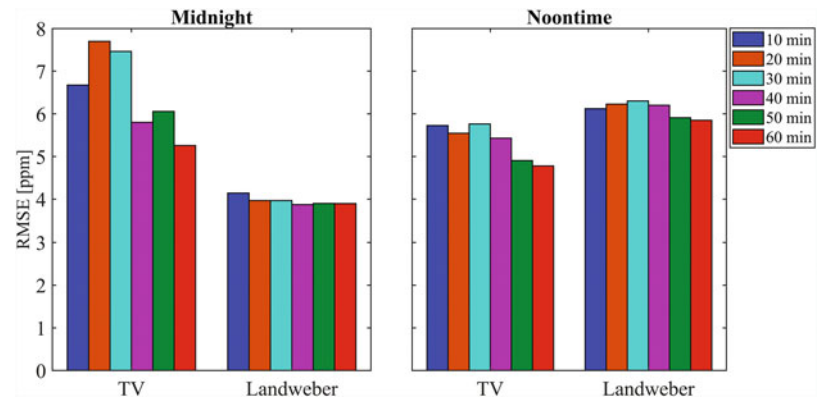
retrieved profile is considerably close to the RS profile with a correlation of more than 95% and 97% for all tomography windows at midnight and noontime, respectively. In addition, the correlation between the tomography solutions and RS wet refractivity is slightly higher at noon than for midnight. As expected, the correlation of the tomography solution with the RS profile increases with extending the tomography time window.

In order to gain a better interpretation of the obtained results, the wet refractivity field was also reconstructed using the Landweber technique by considering the AROME model as an a priori field. According to Fig. 6, the RMSE of the Landweber method is smaller than for the TV method in all temporal resolutions. However, the quality of the reconstructed field using the Landweber method technique extremely depends on the initial field, and it does not change significantly with varying the tomography window. In comparison, the accuracy of retrieved wet refractivity by the TV method is clearly increased by extending the temporal window up to 60 min. It should also be highlighted that the TV technique has provided a more reliable tomography solution than the Landweber method for all temporal resolutions at noontime.

According to the obtained results, the TV technique reconstructed the wet refractivity field with an accuracy of less than 8 ppm and 6 ppm at midnight and noontime, respectively. In addition, the accuracy of this method was comparable with the accuracy of the Landwber method even in a short tomography window at noontime and windows of at least 40 min at midnight. Thereby, the TV method would be a good choice to estimate the tomography solution, especially when there is no access to the (reliable) initial field.



**Fig. 6** Average of RMSE over the entire study period for TV and Landweber methods at midnight and noontime



## 5 Conclusions and Remarks

Processing high quality tomography models without any initial field in a short time span is one of the challenges in the GNSS tropospheric tomography. Here, the TV method is investigated in order to retrieve a regularized solution. This method is independent of an initial field and also resists noise. Accordingly, the TV method was applied in six different tomography windows (10 min to 60 min) with a time step of 10 min by focusing on near-real-time applications. Moreover, the wet refractivity field was also retrieved using the Landweber technique by considering the AROME model as the initial field to better judge the potential of the TV method. Finally, radiosonde measurements located at Vienna airport (RS11035) have been utilized at midnight and noontime to evaluate the estimated wet refractivity field. According to our results, the accuracy of the retrieved wet refractivity field in all tomography windows using the TV method at noontime was slightly better than for midnight. In addition, the correlation between the tomography solution and RS profiles for all temporal resolutions was higher than 95%. Moreover, the inconsistency between the reconstructed wet refractivity field and the reference profile was less than 8.6 ppm at midnight and 5.7 ppm at noontime for lower layers. For upper layers, the discrepancy between the tomography solution and the reference solution was maximally about 6.6 ppm and 6 ppm at midnight and noontime, respectively. Further investigations were also performed to compare the estimated tomography solutions using the TV method with the Landweber technique. Based on the obtained results, the accuracy of the retrieved field using the Landweber method was generally better than for the TV technique at midnight. At noontime, the performance of retrieving wet refractivity by the TV method, especially for spans longer than 40 min, was comparable to the Landweber technique or even better. Therefore, reconstructing the tomography model

using the TV method is advantageous in case of no access to a (reliable) initial field even for a short tomography window if the condition number of the design matrix is not very large and also the amount of water vapour in the troposphere is considerable high. However, it should be noted that considering the short tomography window is not always applicable due to various weather conditions during a day. Therefore, further investigations are encouraged to assess the plausibility of the TV method in other case studies located in different climate zones and over further time periods. Furthermore, assessing the TV method in comparison to other regularization techniques, which are independent of an initial field, may provide better judgment about the quality of the retrieved wet refractivity field using this method. It is also worth mentioning considering a more complete GNSS constellation, i.e. GPS-GLONASS-GALILEO-BeiDou may lead to a better satellite geometry and thus to a better spatial distribution of observations.

**Acknowledgment** The authors would like to thank EPOSA (Echtzeit Positionierung Austria) for providing GNSS observation and appreciate ZAMG (Zentralanstalt für Meteorologie und Geodynamik) for supplying Numerical weather model data, AROME. They would also acknowledge the IGS and CDDIS (Crustal Dynamics Data Information System) for supplying satellite products and ionosphere maps.

## Appendix A RMSE of Reconstructed Wet Refractivity Field in Different Temporal Resolutions Using TV and Landweber Techniques

Here, the detailed RMSE for all studied tomography windows in comparison to RS profile is reported for the entire experimental period at midnight and noontime (Tables A.1, A.2, A.3, A.4).

**Table A.1** RMSE of the wet refractivity field for different temporal resolutions during the entire study period using TV technique at hour 00:00 UTC for RS11035

Time-Res	10	20	30	40	50	60
DOY						
232	1.94	3.52	4.88	3.67	3.40	3.62
233	6.88	6.65	7.83	6.04	7.78	6.00
234	6.41	5.51	4.55	4.30	3.48	3.61
235	5.57	7.01	7.41	4.98	4.77	3.31
236	7.02	7.83	5.00	4.27	5.24	4.40
237	6.68	6.76	7.57	7.12	6.98	6.75
238	5.95	5.19	5.30	4.28	4.99	5.21
239	5.39	8.51	6.96	6.06	6.05	4.76
240	5.65	5.52	5.71	5.81	5.84	6.48
241	5.53	4.50	5.22	4.73	6.18	5.80
242	7.28	<i>12.32</i>	<i>12.71</i>	<i>12.54</i>	<i>12.03</i>	9.27
243	8.98	<i>14.10</i>	<i>13.66</i>	4.84	7.03	4.96
244	<i>13.57</i>	<i>13.30</i>	<i>10.06</i>	6.64	5.84	4.64
245	8.02	7.44	7.60	5.91	5.13	4.80
Mean	6.77	7.72	7.46	5.80	6.05	5.26

Italic values show worst cases during the experimental period

**Table A.2** RMSE of the wet refractivity field for different temporal resolutions during the entire study period using Landweber technique at hour 00:00 UTC for RS11035

Time-Res	10	20	30	40	50	60
DOY						
232	2.92	2.67	3.07	2.78	2.96	3.02
233	4.18	4.15	4.39	3.76	3.68	3.49
234	4.21	4.05	3.57	3.17	3.60	4.02
235	3.04	3.49	3.33	3.12	2.89	2.87
236	2.00	2.57	2.53	2.44	2.40	2.30
237	7.11	5.99	6.41	6.90	6.76	6.71
238	3.50	3.70	3.74	3.78	3.82	3.84
239	7.74	7.82	7.76	7.74	7.73	7.74
240	2.96	2.27	2.12	2.14	2.21	2.28
241	5.36	4.35	4.06	4.12	4.37	4.72
242	3.42	3.62	3.66	3.63	3.62	3.57
243	3.46	3.47	3.44	3.38	3.18	2.88
244	2.62	2.61	2.59	2.59	2.58	2.61
245	5.46	4.81	4.89	4.66	4.77	4.52
Mean	4.14	3.97	3.97	3.87	3.90	3.90

**References**

Abbasbandy S (2006) Numerical solutions of the integral equations: homotopy perturbation method and Adomian decomposition method. *Appl Math Comput* 173:493–500

Adavi Z, Mashhadi Hossaini M (2015) 4D-tomographic reconstruction of water vapor using the hybrid regularization technique with application to the North West of Iran. *Adv Space Res* 55:1845–1854. <https://doi.org/10.1016/j.asr.2015.01.025>

Adavi Z, Weber R (2019) Evaluation of virtual reference station constraints for GNSS tropospheric tomography in austria region. *Adv Geosci* 50:39–48. <https://doi.org/10.5194/adgeo-50-39-2019>

Adavi Z, Weber R, Glaner MF (2022) Assessment of regularization techniques in GNSS tropospheric tomography based on single- and

**Table A.3** RMSE of the wet refractivity field for different temporal resolutions during the entire study period using TV technique at hour 12:00 UTC for RS11035

Time-Res	10	20	30	40	50	60
DOY						
232	4.82	3.64	3.00	4.83	3.90	3.57
233	2.84	2.62	5.52	6.18	4.77	4.45
234	4.11	4.10	6.62	6.95	6.25	5.37
235	7.39	8.93	11.31	7.93	5.52	5.08
236	5.60	8.02	4.53	4.09	3.77	3.45
237	7.25	6.67	6.58	6.21	6.97	6.12
238	6.47	7.92	6.07	6.38	6.61	6.64
239	6.79	7.66	7.06	6.48	5.64	5.83
240	7.85	5.91	7.94	7.08	7.03	6.86
241	7.26	3.39	4.30	3.85	3.29	3.08
242	3.93	4.51	4.23	3.81	3.42	3.28
243	6.85	5.44	5.48	5.30	5.50	5.63
244	4.19	2.96	4.39	3.70	2.81	4.43
245	4.79	4.83	4.27	4.26	4.20	3.65
Mean	5.72	5.47	5.81	5.50	4.98	4.82

**Table A.4** RMSE of the wet refractivity field for different temporal resolutions during the entire study period using Landweber technique at hour 12:00 UTC for RS11035

Time-Res	10	20	30	40	50	60
DOY						
232	5.19	5.38	6.00	5.83	4.28	5.13
233	4.10	4.67	4.87	4.82	4.77	4.69
234	6.87	7.52	8.46	8.58	7.40	7.24
235	5.67	5.66	5.63	5.60	5.57	5.56
236	3.33	3.38	3.33	3.31	3.48	3.30
237	11.40	11.72	11.70	11.04	10.49	10.37
238	9.17	9.18	9.10	8.67	8.76	8.73
239	10.15	9.97	9.43	8.97	8.66	8.01
240	3.08	3.14	4.19	4.30	4.17	4.01
241	7.50	7.12	7.29	7.20	6.45	6.34
242	3.40	4.33	3.46	3.84	4.31	4.50
243	4.49	3.93	4.15	4.50	4.46	4.21
244	7.95	7.72	7.39	7.02	6.86	6.79
245	3.38	3.47	3.24	3.14	3.03	2.99
Mean	6.12	6.23	6.30	6.20	5.91	5.85

dual-frequency observations. *GPS Solutions* 26. <https://doi.org/10.1007/s10291-021-01202-2>

Aster R, Borchers B, Thurber C (2013) Parameter estimation and inverse problems. In: Aster R, Borchers B, Thurber C (eds) *International geophysics*, 2nd edn. Academic Press, 360 pp

Bender M, Dick G, Ge M, Deng Z, Wickert J, Kahle H-G, Raabe A, Tetzlaff G (2011) Development of a GNSS water vapour tomography system using algebraic reconstruction techniques. *Adv Space Res* 47:1704–1720. <https://doi.org/10.1016/j.asr.2010.05.034>

Böhm J, Werl B, Schuh H (2006) Troposphere mapping functions for GPS and very long baseline interferometry from European Centre for Medium-Range Weather Forecasts operational analysis data. *J Geoph Res* 111. <https://doi.org/10.1029/2005JB003629>

Braun J (2004) Remote sensing of atmospheric water vapor with the global positioning system, Ph.D., Department of Aerospace Engineering Sciences, University of Colorado, 137 pp

- Braun J, Rocken C (2003) Water vapor tomography within the planetary boundary layer using GPS. International Workshop on GPS Meteorology, Tsukuba, Japan, 3-09-01-04
- Chen G, Herring TA (1997) Effects of atmospheric azimuthal asymmetry on the analysis of space geodetic data. *J Geophys Res* 102:20489–20502. <https://doi.org/10.1029/97JB01739>
- Dach R, Andritsch F, Arnold D, Bertone S, Fridez P, Jäggi A, Jean Y, Maier A, Mervart L, Meyer U, Orliac E, Ortiz-Geist E, Prange L, Scaramuzza S, Schaer S, Sidorov D, Susnik A, Villiger A, Walser P, Baumann C, Beutler G, Peter H, Gäde A (2015) In: Dach R, Lutz S, Walser P, Fridez P (eds) Bernese GNSS Software Version 5.2. Astronomical Institute, University of Bern
- Elfving T, Nikazad T, Hansen PC (2010) Semi-convergence and relaxation parameters for a class of SIRT algorithms. *Electr Transact Numer Anal* 37:321–336
- Elfving T, Hansen PC, Nikazad T (2012) Semi-convergence and relaxation parameters for projected SIRT algorithms. *J Sci Comput* 34:A2000–A2017
- Elfving T, Hansen PC, Nikazad T (2014) Semi-convergence properties of Kaczmarz's method. *Inverse Probl* 30
- Flores A, Ruffini G, Rius A (2000) 4D tropospheric tomography using GPS slant wet delays. *Annales Geophys* 18:223–234. <https://doi.org/10.1007/s00585-000-0223-7>
- Ghaffari Razin M-R, Voosoghi B (2020) Estimation of tropospheric wet refractivity using tomography method and artificial neural networks in Iranian case study. *GPS Solut* 24:65. <https://doi.org/10.1007/s10291-020-00979-y>
- Guerova G (2003) Application of GPS derived water vapour for Numerical Weather Prediction in Switzerland, PhD. Dissertation. Institute of Applied Physics, University of Bern
- Guo J, Yang F, Shi J, Xu C (2016) An optimal weighting method of global positioning system (GPS) troposphere tomography. *IEEE J Select Top Appl Earth Observ Remote Sens* 9:5880–5887. <https://doi.org/10.1109/JSTARS.2016.2546316>
- Hansen PC (1998) Rank-deficient and discrete ILL-posed problems: numerical aspect of linear inversion. edited by: SIAM, Society for Industrial and Applied Mathematics, 264 pp
- Heublein M (2019) GNSS and InSAR based water vapor tomography: a compressive sensing solution, PhD. Dissertation. Institute of Photogrammetry and Remote Sensing, Karlsruhe Institute of Technology, Germany, 134 pp
- Hirahara K (2000) Local GPS tropospheric tomography. *Earth Planets Space* 52(11):935–939
- Jensen TL, Jørgensen JH, Hansen PC, Jensen SH (2012) Implementation of an optimal first-order method for strongly convex total variation regularization. *BIT Numer Math* 52:329–356. <https://doi.org/10.1007/s10543-011-0359-8>
- Kaltenbacher B, Neubauer A, Scherzer O (2008) Iterative regularization methods for nonlinear ill-posed problems
- Landweber L (1951) An iteration formula for Fredholm integral equations of the first kind. *Am J Math* 73:615–624
- Lee, J. K., Kamalabadi, F., and Makela, J. J. (2007) Localized three-dimensional ionospheric tomography with GPS ground receiver measurements. *Radio Sci* 42, <https://doi.org/10.1029/2006RS003543>
- Li C (2009) An efficient algorithm for total variation regularization with applications to the single Pixel Camera and compressive sensing, MSc. Dissertation. Rice University
- Li C (2011) Compressive sensing for 3D data processing tasks: applications, models and algorithms, PhD. Dissertation. Rice University
- Li C, Yin W, Zhang Y (2010) TVAL3: TV minimization by augmented Lagrangian and alternating direction algorithms. In: Rice University
- Lohvithee M (2019) Iterative Reconstruction Technique for Cone-beam Computed Tomography with Limited Data, Ph.D. Dissertation. Department of Electrical and Electronic Engineering, University of Bath
- Lutz SM (2008) High-resolution GPS tomography in view of hydrological hazard assessment, Ph.D. Dissertation. ETH Zurich, 219 pp
- Menke W (2012) Geophysical data analysis: discrete inverse theory (MATLAB edition). Academic Press, New York
- Persson M, Bone D, Elmqvist H (2001) Total variation norm for three-dimensional iterative reconstruction in limited view angle tomography. *Phys Med Biol* 46:53–866
- Rohm W, Bosy J (2009) Local tomography troposphere model over mountains area. *Atmosph Res* 93(4):777–783. <https://doi.org/10.1016/j.atmosres.2009.03.013>
- Rohm W, Bosy J (2011) The verification of GNSS tropospheric tomography model in a mountainous area. *Adv Space Res* 47:1721–1730. <https://doi.org/10.1016/j.asr.2010.04.017>
- Rohm W, Zhang K, Bosy J (2014) Limited constraint, robust Kalman filtering for GNSS troposphere tomography. *Atmos Meas Techniq* 7:1475–1486. <https://doi.org/10.5194/amt-7-1475-2014>
- Rudin LI, Osher S, Fatemi E (1992) Nonlinear total variation based noise removal algorithms. *Physica D* 60:259–268
- Sá A, Rohm W, Fernandes RM, Trzcina E, Bos M, Bento F (2021) Approach to leveraging real-time GNSS tomography usage. *J Geodesy* 95, <https://doi.org/10.1007/s00190-020-01464-7>
- Saastamoinen J (1973) Contributions to the theory of atmospheric refraction. Part II: refraction corrections in satellite geodesy. *Bull Geod* 107:13–34
- Seity Y, Brousseau P, Malardel S, Hello G, Bernard P, Bouttier F, Lac C (2011) The AROME-France convective-scale operational model. *Monthly Weather Rev* 139:976–991. <https://doi.org/10.1175/2010MWR3425.1>
- Sidky EY, Kao CM, Pan X (2006) Accurate image reconstruction from few-views and limited-angle data in divergent-beam CT. *J X-Ray Sci Technol* 14:119–139
- Tang J, Yao Y, Zhang L, Kong J (2015) Tomographic reconstruction of ionospheric electron density during the storm of 5-6 August 2011 using multi-source data. *Sci Rep* 5:13042. <https://doi.org/10.1038/srep13042>
- Troller M (2004) GPS based determination of the integrated and spatially distributed water vapor in the troposphere, Ph.D. Dissertation. ETH Zurich, 189 pp
- Xia P, Cai C, Liu Z (2013) GNSS troposphere tomography based on two-step reconstructions using GPS observations and COSMIC profiles. *Ann Geophys* 31:1805–1815. <https://doi.org/10.5194/angeo-31-1805-2013>
- Xiaoying W, Ziqiang D, Enhong Z, Fuyang KE, Yunchang C, Lianchun S (2014) Tropospheric wet refractivity tomography using multiplicative algebraic reconstruction technique. *Adv Space Res* 53:156–162
- Yao Y, Xiin L, Zhao Q (2019) A new tropospheric tomography model combining the pixel-based and function-based models. *Ann Geophys Discuss* 89–100, <https://doi.org/10.5194/angeo-2018-34>

**Open Access** This chapter is licensed under the terms of the Creative Commons Attribution 4.0 International License (<http://creativecommons.org/licenses/by/4.0/>), which permits use, sharing, adaptation, distribution and reproduction in any medium or format, as long as you give appropriate credit to the original author(s) and the source, provide a link to the Creative Commons license and indicate if changes were made.

The images or other third party material in this chapter are included in the chapter's Creative Commons license, unless indicated otherwise in a credit line to the material. If material is not included in the chapter's Creative Commons license and your intended use is not permitted by statutory regulation or exceeds the permitted use, you will need to obtain permission directly from the copyright holder.





# Comparison of the Effective Isotropic Radiated Power Parameter in CYGNSS v2.1 and v3.0 Level 1 Data and Its Impact on Soil Moisture Estimation

Paulo T. Setti Jr. and Tonie van Dam

## Abstract

The effective isotropic radiated power (EIRP) is the measured radiated power of an antenna pointed in a specific direction. For the Global Positioning System (GPS), the EIRP is a function of the transmitted power and the gain of the transmitting antenna. It is a fundamental observation used for estimating surface reflectivity that can be used to estimate near-surface soil moisture. Most investigations of GPS EIRP for soil moisture used level 1 version 2.1 data from the eight satellites of the Cyclone Global Navigation Satellite System (CYGNSS) mission. The newer version 3.0 introduces a dynamic EIRP calibration algorithm with the variations in GPS transmit power being tracked using the direct signal power measured by the navigation receivers. In this paper we compare the estimated EIRP from versions 2.1 and 3.0 for the year of 2020. We correlate the estimated surface reflectivity with reference soil moisture observations from the Soil Moisture Active Passive (SMAP) mission provided on a 9x9 km grid using the bistatic radar equation for coherent reflections. The correlation of CYGNSS with SMAP is slightly improved using version 3.0 versus 2.1 with average of 0.10 and maximum of 0.30. The advantage of version 3.0 was most noticeable in areas where soil moisture retrieval is challenging, such as the arid and densely vegetated regions of the world.

## Keywords

CYGNSS · EIRP · GNSS-R · Soil moisture

## 1 Introduction

Near-surface (0–5 cm) soil moisture information is of great scientific and socioeconomic relevance. As an essential climate variable, soil moisture influences interactions between land surface and atmosphere through the exchange of water,

energy and biogeochemical fluxes. Monitoring soil moisture is also important in applications such as agriculture, vegetation change detection, and drought and flood forecasting and monitoring (Entekhabi et al. 1996; Ochsner et al. 2013; Peng et al. 2021).

L-band microwave satellite remote sensing has been used to retrieve soil moisture at the global scale due to its ability to penetrate clouds and part of overlying vegetation. The Soil Moisture Active Passive (SMAP) L-band mission (Entekhabi et al. 2010) has been providing soil moisture data since 2015 with two- or three-day global revisit times. The retrievals have spatial resolution of about 40 km.

Spaceborne Global Navigation Satellite Systems (GNSS) Reflectometry (GNSS-R) represents an alternative for retrieving soil moisture with a relatively high spatial resolution, having a footprint on the order of hundreds of meters to few

P. T. Setti Jr. (✉)

Faculty of Science, Technology and Medicine, University of Luxembourg, MNO, Luxembourg  
e-mail: paulo.setti@uni.lu

T. van Dam

Department of Geology & Geophysics, University of Utah, Salt Lake City, UT, USA

Interdisciplinary Center for Security and Trust, University of Luxembourg, Esch-sur-Alzette, Luxembourg

kilometers, with daily or even subdaily repeat observations (Garrison et al. 2020). GNSS-R is a bistatic remote sensing technique that relies on the reception of signals that have reflected or scattered from the Earth's surface. These signals of opportunity are used to infer properties of the reflecting surface itself. GNSS-R was initially designed for ocean altimetry, however, its application has been extended to land surface remote sensing (Zavorotny et al. 2014).

The Cyclone Global Navigation Satellite System (CYGNSS) is a spaceborne GNSS-R mission (Ruf et al. 2013) with a constellation of eight low-Earth satellites at an orbital inclination of 35°. Its main objective is to estimate wind speed over the oceans to track and monitor hurricanes and tropical cyclones. Measurements consist of reflected Global Positioning System (GPS) L1 C/A signals. Reflections over a land depend on the surface reflectivity and can be used to infer information about soil moisture (Ruf et al. 2018; Chew and Small 2020).

One of the parameters necessary to convert CYGNSS observations to surface reflectivity is the GPS effective isotropic radiated power (EIRP). The EIRP defines the power density incident on the Earth's surface and is a product of transmitted power and antenna gain (Steigenberger et al. 2019). In CYGNSS version 2.1 (v2.1) level 1 data, available since March 2017, the EIRP is computed assuming a static value for the power level of the L1 signal transmitted by the GPS satellites. In version 3.0 (v3.0) level 1 data, available since August 2018, a dynamic EIRP calibration algorithm was introduced, where the variations in the GPS transmitted power started being tracked using the direct signal power measured by the navigation receivers (Wang et al. 2021b). Most of the published research on soil moisture estimation (Chew and Small 2020; Clarizia et al. 2019; Dong and Jin 2021; Eroglu et al. 2019; Senyurek et al. 2020a,b; Yueh et al. 2020) use CYGNSS v2.1 data to take advantage of a longer time series or because the study was conducted before v3.0 was made available. In this paper we compare the estimated EIRP from CYGNSS v2.1 and v3.0 considering the different GPS satellite blocks. Through a comparison with SMAP data based on the correlation coefficient, we also analyze how these differences can impact estimates of soil moisture.

## 2 GNSS-R for Soil Moisture

The magnitude of the received power  $P_r^r$ , considering the bistatic radar equation for coherent reflections, can be written as (Garrison et al. 2020):

$$P_{rl}^r = \frac{P_r^t G^t}{4\pi(R_{ts} + R_{sr})^2} \frac{G^r \lambda^2}{4\pi} \Gamma_{rl}, \quad (1)$$

where:

- $P_r^t$  is the transmitted Right-Hand Circularly Polarized (RHCP) power;
- $G^t$  is the gain of the transmitting antenna;
- $R_{ts}$  is the distance between the transmitter and the specular reflection point;
- $R_{sr}$  is the distance between the specular reflection point and the receiver;
- $G^r$  is the gain of the receiving antenna;
- $\lambda$  is the wavelength; and
- $\Gamma_{rl}$  is the effective surface reflectivity.

The effective surface reflectivity,  $\Gamma_{rl}$  in Eq. 1, depends on soil moisture content, vegetation attenuation, surface roughness, and incidence angle. The soil moisture content is linked to the surface reflectivity through the relative complex permittivity (Zavorotny et al. 2014), which is also a function of soil type. The measured reflected signal can be converted to surface reflectivity if the calibration parameters in Eq. 1 are known, with the surface reflectivity being proportional to the soil moisture.

## 3 EIRP Variations

The EIRP, given by  $P_r^t G^t$  in Eq. 1, is an important calibration parameter when converting the reflected power to surface reflectivity as it defines the incident power density. Precisely estimating EIRP is very challenging for various reasons (Wang et al. 2021b, 2020): the unique transmit power of each GPS satellite; the need to have the GPS transmit antenna gain pattern; pattern asymmetry, and spacecraft yaw maneuvers that cause antenna gain uncertainty in the direction of the specular reflection; and variations of the GPS transmit power over time and across different regions of the globe.

In v2.1 data, EIRP for the GPS satellites and varying incidence angles are statically estimated based on a lookup table (LUT). These values are determined based on some given assumptions. (1) The effective GPS transmit power is considered as a static value through a GPS power monitoring system; (2) the GPS antenna gain in the direction of the specular reflection represents an averaged estimate of the GPS transmitters (Wang et al. 2021b). The limitations of this method include, among other things, the flex transmit power of GPS satellites from blocks IIR-M and IIF, and errors in the estimated transmit power.

To overcome these limitations, the v3.0 data introduced a dynamic EIRP calibration algorithm. In this method, variations in GPS transmit power are tracked by the direct signal power measured by the navigation receiver zenith antenna. Using this approach, it is possible to detect transmit power fluctuations in a GPS satellite and minimize the error caused by the GPS antenna gain pattern azimuthal asymmetry (Wang et al. 2020).

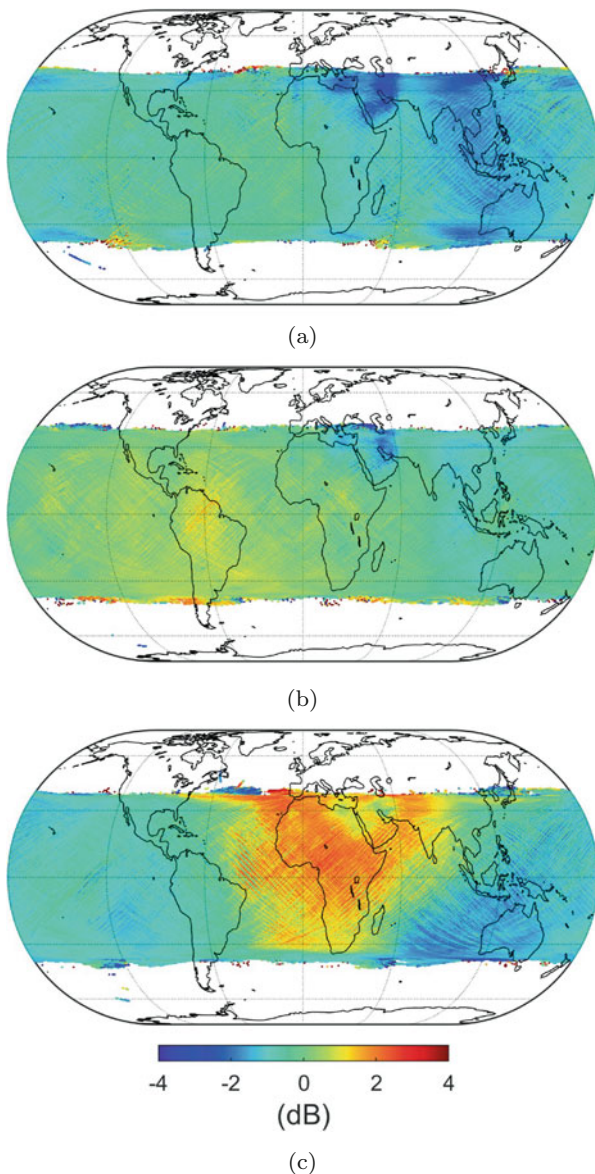


**Fig. 1** Difference between estimated EIRP in v2.1 and v3.0 for 5 satellites from blocks (a) IIR (PRN 19, 20, 21, 23 and 28), (b) IIR-M (PRN 07, 12, 17, 29 and 31), and (c) IIF (PRN 01, 08, 09, 24 and 30)

To compare the EIRP estimates in versions 2.1 and 3.0, Fig. 1 shows global maps of the average difference between the EIRP for five GPS satellites of blocks IIR, IIR-M and IIF as observed by all eight CYGNSS satellites. The observations are binned in 9×9 km grid cells, considering all specular incident angles and data from January 2020. For this period, we note that, for blocks IIR (top panel of the figure) and IIR-M (middle panel), the difference between the two versions is generally below 2 dB. For block IIF, however, the difference depends on the location on the globe. This variability is caused by a geographically driven flex power mode that was implemented in block IIF GPS satellites,

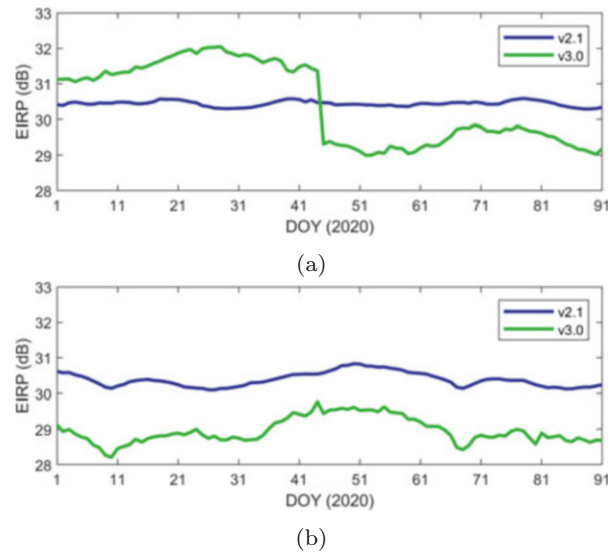


**Fig. 2** v2.1 and 3.0 GPS EIRP parameter for the first three months of 2020, observations from block IIF GPS satellites over (a) Africa and (b) Australia

which can redistribute the L1 C/A power for certain regions with every orbit and is used for increased protection against jamming (Steigenberger et al. 2019). The difference reaches almost 4 dB over Africa and western Asia.

To better understand the behavior of the flex power mode in block IIF GPS satellites, Fig. 2 shows the daily average of the EIRP over Africa and Australia, two regions with different EIRP variations (Fig. 1c), for the first three months of 2020. For v2.1, it can be seen that the EIRP assumes a static value for the whole globe, with very similar behavior in both regions. In fact, the EIRP are not flat because all incidence angles were considered, which causes slight variations in the daily EIRP averages. Over Australia (bottom panel in the figure), v2.1 EIRP is larger by more than 1 dB than v3.0. Over Africa, we observe that the power varies not only geographically but also with time. A jump of more than 2 dB occurs when the flex power mode changes on 14 Feb. 2020 (DOY 45/2020).

#### 4 Impact on Soil Moisture Estimation

EIRP determine estimates of surface reflectivity (Eq. 1). Figure 3 shows, for the first three months of 2020, the average surface reflectivity from v2.1 and v3.0 estimated day by day considering only the observations reflected over land from all GPS blocks and satellites over the whole globe. We observe that when the flex power mode was changed in mid-February, the average reflectivity dropped by almost 1 dB when using the EIRP parameter from v2.1. This jump is essentially unnoticeable when using v3.0 data. This variation

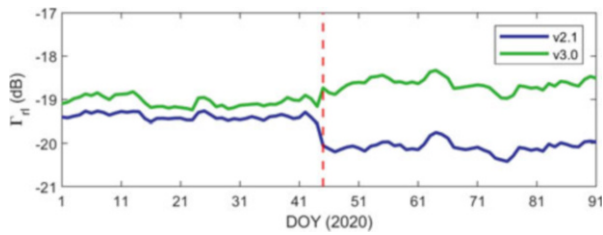


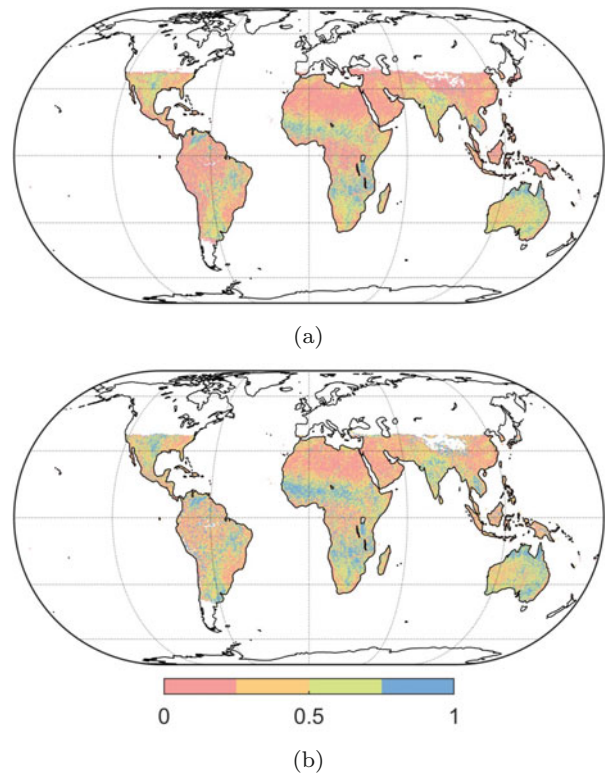
**Fig. 3** Surface reflectivity averaged over the whole globe for the first three months of 2020. The vertical dashed red line indicates the day when the flex power mode for block IIF GPS satellites was changed

can directly influence soil moisture retrieval, as the model could assume that the difference in reflectivity was caused by a change in the soil moisture content when in fact it was caused by a change in the power of some of the transmitting GPS satellites.

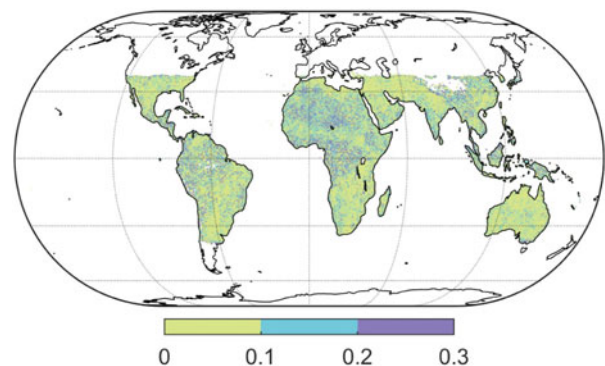
To assess the real impact of the EIRP parameter from both versions in soil moisture estimation, we compare the CYGNSS surface reflectivity with the soil moisture data from SMAP (O'Neill et al. 2020). The correlation assumes, as proposed by Chew and Small (2020), that surface reflectivity can be linearly related to soil moisture, varying spatially but not over time. Surface reflectivity was estimated using Eq. 1, with data covering the whole of 2020. The received power is considered as the peak value of the delay-Doppler maps (DDM), corrected from the noise floor (measurement) (Clarizia et al. 2019). We used the same quality flags and incidence angle correction method as proposed by Chew and Small (2020). Reflections over inland water bodies were removed using as reference the Global Surface Water Explorer (GSWE) product described in Pekel et al. (2016). The observations were gridded into  $9 \times 9$  km grid cells based on their specular reflection location and correlated to the soil moisture data from SMAP enhanced L3 radiometer global daily 9 km product.

Figure 4a, b shows the correlation between CYGNSS surface reflectivity and SMAP soil moisture for v2.1 and v3.0 datasets, respectively. Soil moisture retrieval is very challenging in regions with high vegetation density (e.g. Amazon and Congo rainforests) due to the signal scattering. Soil moisture retrieval is also challenging in arid regions (e.g. Sahara desert) where the soil moisture is essentially constant throughout the year. The CYGNSS noise significantly affects the correlation coefficient, and the slope of a linear regression would be closer to zero. In wetter regions CYGNSS seems to work well on retrieving soil moisture information.

The slight improvement in correlation between CYGNSS v2.1 to v3.0 surface reflectivity and SMAP soil moisture can be seen in Fig. 5. The improvement is not very significant in regions where the correlation between CYGNSS and SMAP



**Fig. 4** Correlation between CYGNSS surface reflectivity and SMAP 9 km-grid soil moisture data for the year of 2020, (a) v2.1 and (b) v3.0



**Fig. 5** Improvement from v2.1 to v3.0 in the correlation coefficient between CYGNSS surface reflectivity and SMAP soil moisture

is moderate/strong, such as most of the Australian territory, the Sahel region, and the southeastern Africa and South America. However, those regions where the correlation was originally low are benefited from the EIRP estimates of v3.0. In arid areas, where the CYGNSS noise really influences the surface reflectivity values, more realistic estimates of the EIRP can improve the correlation coefficient. The average correlation was 0.47 for v2.1, and increased to 0.51 in v3.0. The average improvement in correlation was of 0.10, reaching up to 0.30 in some regions.

## 5 Summary and Future Work

In this paper we compared the EIRP parameters from two CYGNSS level 1 data versions: 2.1, where EIRP is estimated based on a static LUT, and v3.0, where it is dynamically calibrated and estimated based on the direct signals tracked by the navigation receivers. We found that the power transmitted by the GPS satellites varies depending on the GPS satellite block, locations on the globe and time. Through the correlation coefficient between the CYGNSS surface reflectivity and SMAP soil moisture, our results showed that in some parts of the globe replacing v2.1 to v3.0 may not be very relevant, but in regions where soil moisture retrieval is very challenging the improvement in the correlation coefficient can go as high as 30%.

In the future work, we will include an analysis of the impact of soil moisture retrieval using both version not only based on the correlation coefficient, but also on the RMSE of the estimation using a linear regression or other models proposed in the literature. The version 3.1 of CYGNSS level 1 data is due to be released soon (Wang et al. 2021a), bringing new updates on the characterization of the antenna gain patterns. A future analysis could include this new data.

**Funding** This research received no external funding.

**Conflicts of Interest/Competing Interests** All authors certify that they have no affiliations with or involvement in any organization or entity with any financial interest or non-financial interest in the subject matter or materials discussed in this manuscript.

**Availability of Data and Material** The CYGNSS data are publicly available at <https://podaac-tools.jpl.nasa.gov/drive/files/allData/cygnss/L1>, and the SMAP data at <https://nsidc.org/data/smap/smap-data.html>.

## References

- Chew C, Small E (2020) Description of the UCAR/CU soil moisture product. *Remote Sensing* 12(10):1558. <https://doi.org/10.3390/rs12101558>
- Clarizia MP, Pierdicca N, Costantini F, Floury N (2019) Analysis of CYGNSS data for soil moisture retrieval. *IEEE J Sel Top Appl Earth Observ Remote Sens* 12(7):2227–2235. <https://doi.org/10.1109/JSTARS.2019.2895510>
- Dong Z, Jin S (2021) Evaluation of the land GNSS-reflected DDM coherence on soil moisture estimation from CYGNSS data. *Remote Sensing* 13(4):570. <https://doi.org/10.3390/rs13040570>
- Entekhabi D, Rodriguez-Iturbe I, Castelli F (1996) Mutual interaction of soil moisture state and atmospheric processes. *J Hydrol* 184(1–2):3–17. [https://doi.org/10.1016/0022-1694\(95\)02965-6](https://doi.org/10.1016/0022-1694(95)02965-6)
- Entekhabi D, Njoku EG, O'Neill PE, Kellogg KH, Crow WT, Edelstein WN, Entin JK, Goodman SD, Jackson TJ, Johnson J, Kimball J, Piepmeier JR, Koster RD, Martin N, McDonald KC, Moghaddam M, Moran S, Reichle R, Shi JC, Spencer MW, Thurman SW, Tsang L, Van Zyl J (2010) The soil moisture active passive (SMAP) mission. *Proc IEEE* 98(5):704–716. <https://doi.org/10.1109/JPROC.2010.2043918>
- Eroglu O, Kurum M, Boyd D, Gurbuz AC (2019) High spatio-temporal resolution CYGNSS soil moisture estimates using artificial neural networks. *Remote Sensing* 11(19):2272. <https://doi.org/10.3390/rs11192272>
- Garrison J, Zavorotny VU, Egido A, Larson KM, Nievinski F, Moll-fulleda A, Ruffini G, Martin F, Gommenginger C (2020) GNSS reflectometry for earth remote sensing. In: Morton YJT, Diggelen F, Spilker JJ, Parkinson BW, Lo S, Gao G (eds) *Position, navigation, and timing technologies in the 21st century*, 1st edn. Wiley, pp 1015–1114. <https://doi.org/10.1002/9781119458449.ch34>
- Ochsner TE, Cosh MH, Cuenca RH, Dorigo WA, Draper CS, Hagimoto Y, Kerr YH, Larson KM, Njoku EG, Small EE, Zreda M (2013) State of the art in large-scale soil moisture monitoring. *Soil Sci Soc Am J* 77(6):1888–1919. <https://doi.org/10.2136/sssaj2013.03.0093>
- O'Neill PE, Chan S, Njoku EG, Jackson T, Bindlish R, Chaubell MJ (2020) SMAP enhanced L3 radiometer global daily 9 km EASE-grid soil moisture, version 4. <https://doi.org/10.5067/NJ34TQ2LFE90>, type: dataset
- Pekel JF, Cottam A, Gorelick N, Belward AS (2016) High-resolution mapping of global surface water and its long-term changes. *Nature* 540(7633):418–422. <https://doi.org/10.1038/nature20584>
- Peng J, Albergel C, Balenzano A, Brocca L, Cartus O, Cosh MH, Crow WT, Dabrowska-Zielinska K, Dadson S, Davidson MW, de Rosnay P, Dorigo W, Gruber A, Hagemann S, Hirschi M, Kerr YH, Lovergine F, Mahecha MD, Marzahn P, Mattia F, Musial JP, Preuschmann S, Reichle RH, Satalino G, Silgram M, van Bodegom PM, Verhoest NE, Wagner W, Walker JP, Wegmüller U, Loew A (2021) A roadmap for high-resolution satellite soil moisture applications – confronting product characteristics with user requirements. *Remote Sens Environ* 252:112162. <https://doi.org/10.1016/j.rse.2020.112162>
- Ruf C, Unwin M, Dickinson J, Rose R, Rose D, Vincent M, Lyons A (2013) CYGNSS: Enabling the future of hurricane prediction [remote sensing satellites]. *IEEE Geosci Remote Sens Mag* 1(2):52–67. <https://doi.org/10.1109/MGRS.2013.2260911>
- Ruf CS, Chew C, Lang T, Morris MG, Nave K, Ridley A, Balasubramanian R (2018) A new paradigm in earth environmental monitoring with the CYGNSS small satellite constellation. *Scientific Reports* 8(1):8782. <https://doi.org/10.1038/s41598-018-27127-4>
- Senyurek V, Lei F, Boyd D, Gurbuz AC, Kurum M, Moorhead R (2020a) Evaluations of machine learning-based CYGNSS soil moisture estimates against SMAP observations. *Remote Sensing* 12(21):3503. <https://doi.org/10.3390/rs12213503>
- Senyurek V, Lei F, Boyd D, Kurum M, Gurbuz AC, Moorhead R (2020b) Machine learning-based CYGNSS soil moisture estimates over ISMN sites in CONUS. *Remote Sensing* 12(7):1168. <https://doi.org/10.3390/rs12071168>
- Steigenberger P, Thöert S, Montenbruck O (2019) Flex power on GPS Block IIR-M and IIF. *GPS Solutions* 23(1):8. <https://doi.org/10.1007/s10291-018-0797-8>
- Wang T, Ruf C, Gleason S, McKague D, O'Brien A, Block B (2020) Monitoring GPS Eirp for Cygnss Level 1 calibration. In: *IGARSS 2020 - 2020 IEEE international geoscience and remote sensing symposium*. IEEE, Waikoloa, HI, USA, pp 6293–6296. <https://doi.org/10.1109/IGARSS39084.2020.9324491>
- Wang T, Ruf C, O'Brien A, Gleason S, McKague D, Russel A (2021a) The important role of the antenna pattern characterization in the absolute calibration of gnss-r measurements. In: *IGARSS 2021 - 2021 IEEE international geoscience and remote sensing symposium proceedings*, p. 3
- Wang T, Ruf CS, Gleason S, O'Brien AJ, McKague DS, Block BP, Russel A (2021b) Dynamic calibration of GPS effective isotropic radiated power for GNSS-reflectometry earth remote sensing. *IEEE Trans Geosci Remote Sens*, 1–12. <https://doi.org/10.1109/TGRS.2021.3070238>



- Yueh SH, Shah R, Chaubell MJ, Hayashi A, Xu X, Colliander A (2020) A semiempirical modeling of soil moisture, vegetation, and surface roughness impact on CYGNSS reflectometry data. *IEEE Trans Geosci Remote Sens*, 1–17. <https://doi.org/10.1109/TGRS.2020.3035989>
- Zavorotny VU, Gleason S, Cardellach E, Camps A (2014) Tutorial on remote sensing using GNSS bistatic radar of opportunity. *IEEE Geosci Remote Sens Mag*, 38

**Open Access** This chapter is licensed under the terms of the Creative Commons Attribution 4.0 International License (<http://creativecommons.org/licenses/by/4.0/>), which permits use, sharing, adaptation, distribution and reproduction in any medium or format, as long as you give appropriate credit to the original author(s) and the source, provide a link to the Creative Commons license and indicate if changes were made.

The images or other third party material in this chapter are included in the chapter's Creative Commons license, unless indicated otherwise in a credit line to the material. If material is not included in the chapter's Creative Commons license and your intended use is not permitted by statutory regulation or exceeds the permitted use, you will need to obtain permission directly from the copyright holder.





# Cross-polarization Correction for Soil Moisture Retrieval Using GNSS SNR Data

M. Han, D. Yang, B. Zhang, X. Hong, and F. Wang

## Abstract

The Global Navigation Satellite System – Interferometric Reflectometry (GNSS-IR) technique utilizes the GNSS Signal-to-Noise Ratio (SNR) data to retrieve soil moisture. In this study, the physical SNR model incorporating antenna's cross-polarization component is re-derived to a more intuitive and straightforward degree, which is based on the work of V. U. Zavorotny et al. 2009. Then this model is used in combination with the signal reconstruction method we proposed before to correct the cross-polarization effect when retrieving soil moisture. Both simulation and experiment data were used for validation purpose. The results showed that the mean retrieval error could be reduced by about  $0.16\text{cm}^3\cdot\text{cm}^{-3}$  after cross-polarization correction.

## Keywords

Cross-polarization correction · GNSS-IR · SNR · Soil moisture

## 1 Introduction

Soil moisture monitoring using Global Navigation Satellite System – Interferometric Reflectometry (GNSS-IR) technique has gain wide interests in recent years (Edokossi et al. 2020; Zavorotny et al. 2014). It utilizes the interference phenomenon happened between the direct signal and the reflected signal which is also called the multipath signal. K. M. Larson et al. found for the first time that the multipath signal would cause the Signal-to-Noise Ratio (SNR) data routinely recorded by the GNSS receiver to show a cosine-like variation pattern especially when the satellite elevation

angle is low ( $\sim 30^\circ$ ) (Larson et al. 2008), and further proposed a two-step fitting model to extract three metrics including the amplitude, frequency and initial phase from the SNR data (Chew et al. 2014). In the first step, a low-order polynomial fitting model is used to de-trend the SNR data, and in the second step a standard cosine function model is fitted with the de-trended SNR data. However, the standard cosine function can not accurately model the amplitude variation of the SNR data. Therefore, we proposed a semi-empirical fitting model to address this problem in 2018 (Han et al. 2018). By directly fitting this model with the raw SNR data, it is possible to estimate the power of the direct and reflected signal. Then, the reflection coefficient of soil is calculated, which can be regarded as a better replacement for the amplitude metric. Finally, theoretical model is used to retrieve soil moisture from the reflection coefficient instead of the empirical model commonly used for the amplitude metric (Chew et al. 2014, 2015; Small et al. 2016). However, the correction of antenna cross-polarization effect was not considered in our previous study due to the lack of through understanding of the physical mechanism behind the scene, which caused large soil moisture retrieval errors sometimes.

This work is supported by the National Natural Science Foundation of China (No. 42104031) and the Post Doctoral Innovative Talent Support Program (No. BX20200039).

M. Han (✉) · D. Yang · B. Zhang · X. Hong · F. Wang  
School of Electronic and Information Engineering, Beihang University, Beijing, China  
e-mail: [hanmutian@buaa.edu.cn](mailto:hanmutian@buaa.edu.cn); [edkyang@buaa.edu.cn](mailto:edkyang@buaa.edu.cn);  
[bozhang@buaa.edu.cn](mailto:bozhang@buaa.edu.cn); [joyce\\_hong2008@yeah.net](mailto:joyce_hong2008@yeah.net);  
[wangf.19@163.com](mailto:wangf.19@163.com)

Earlier in 2009, V. U. Zavorotny et al. built a physical model of the total GPS received power using the direct signal and the reflected signal as input, where the cross-polarization leakage of GNSS antenna was considered for the first time (Zavorotny et al. 2009). Complex notation of the signals were used in the model derivation, which is mathematical concise. However, the model has not been derived to a final usable form, therefore, can not be directly used for correction purpose. Hence, in this study, we re-derived the physical model from the receiver point of view using real signal representations, which is easier to understand. We further derived the model to a final form and showed how this model was used in combination with the retrieval method we proposed before to achieve cross-polarization correction for the first time. Both simulation and experiment data were used for validation purpose.

## 2 The Polarization-Mixing SNR Model

SNR is defined as the ratio of the signal power to the noise power. Since the noise power is normally considered as constant, only the signal power is concerned in GNSS-IR technique. From the receiver point of view, the total signal captured by GNSS antenna is first down-converted to intermediate frequency (IF). By ignoring the modulation of the navigation data and pseudo-random code, the IF signal can be expressed as:

$$s(t) = \sqrt{2P_d} \cos(\omega_{IF}t + \varphi_d) + \sqrt{2P_{rr}} \cos(\omega_{IF}t + \varphi_d + \Delta\varphi_p + \Delta\varphi_{rr}) + \sqrt{2P_{rl}} \cos(\omega_{IF}t + \varphi_d + \Delta\varphi_p + \Delta\varphi_{rl}) \quad (1)$$

where  $\omega_{IF}$  is the intermediate angular frequency;  $P_d$  is the direct signal power;  $P_{rr}$ ,  $P_{rl}$  are the power of the RHCP and LHCP component of the reflected signal, respectively;  $\varphi_d$  is phase of the direct signal;  $\Delta\varphi_p$  is the additional phase delay experienced by the reflected signal due to the excess propagation path relative to that of the direct signal;  $\Delta\varphi_{rr}$ ,  $\Delta\varphi_{rl}$  are the phase shift happened upon reflection corresponding to the RHCP and LHCP component, respectively. The additional Doppler frequency on the reflected signal is neglected since it is very small under ground-based applications.

Next, the IF signal is sent to the receiver's acquisition and tracking module to de-spread and recover the signal that is embedded in the noise. After that, the power of the signal can be measured. Assuming perfect carrier frequency and code phase tracking, the signal processing architecture can be simplified as illustrated in Fig. 1.

In Fig. 1, the input signal is first down-converted to baseband by multiplying with two quadrature local carrier

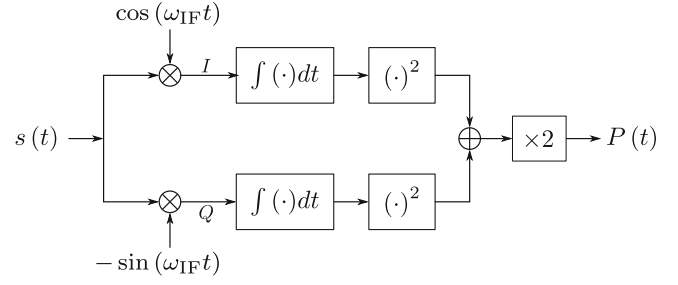


Fig. 1 Simplified receiver signal processing

forming two signal processing branches, namely,  $I$  branch and  $Q$  branch. Then each branch is integrated, squared, and finally summed together to calculate the signal power  $P(t)$ .

$$P(t) = P_d + P_{rr} + 2\sqrt{P_d P_{rr}} \cos(\Delta\varphi_p + \Delta\varphi_{rr}) + P_{rl} + 2\sqrt{P_d P_{rl}} \cos(\Delta\varphi_p + \Delta\varphi_{rl}) + 2\sqrt{P_{rr} P_{rl}} \cos(\Delta\varphi_{rr} - \Delta\varphi_{rl}) \quad (2)$$

The first line of Eq. (2) resembles the well-known SNR model seen in the literature. The additional terms are related to the cross-polarization, which complicates the SNR model and makes it difficult to be applied at this current state. Note that the two cosine functions that contain  $\Delta\varphi_p$  can be combined through further trigonometric manipulation. Then, the remaining terms are grouped appropriately, which leads to a compact expression as shown in Eq. (3).

$$P(t) = P_d + P_r + 2\sqrt{P_d P_r} \cos(\Delta\varphi_p + \Delta\varphi_r) \quad (3)$$

where  $P_r$  and  $\Delta\varphi_r$  are the total reflected signal power and the total phase change upon reflection, respectively, which are expressed as:

$$P_r = P_{rr} + P_{rl} + 2\sqrt{P_{rr} P_{rl}} \cos(\Delta\varphi_{rr} - \Delta\varphi_{rl}) \quad (4a)$$

$$\Delta\varphi_r = \arctan\left(\frac{\sqrt{2P_{rr}} \sin(\Delta\varphi_{rr}) + \sqrt{2P_{rl}} \sin(\Delta\varphi_{rl})}{\sqrt{2P_{rr}} \cos(\Delta\varphi_{rr}) + \sqrt{2P_{rl}} \cos(\Delta\varphi_{rl})}\right) \quad (4b)$$

Without loss of generality, Eq. (3) is the top-level representation of the interference power between the direct signal and the reflected signal. Note that Eq. (4a) resembles Eq. (3) since the total reflected signal results from the interference between the RHCP and LHCP component of the reflected signal. However,  $\Delta\varphi_p$  does not appear in Eq. (4a) since there is no path delay between the two components. And  $\Delta\varphi_{rr} - \Delta\varphi_{rl}$  in Eq. (4a) is similar to  $\Delta\varphi_r$  in Eq. (3). Also note that whether the cross-polarization

component presents or not does not affect the top-level model.

Now assume that the transmission power of the navigation satellite is  $C$ . Then,  $P_d$ ,  $P_{rr}$ , and  $P_{rl}$  is expressed as:

$$P_d = C \cdot G_R(\theta) \quad (5a)$$

$$P_{rr} = C \cdot |\Gamma_{rr}|^2 \cdot G_R(-\theta) \quad (5b)$$

$$P_{rl} = C \cdot |\Gamma_{rl}|^2 \cdot G_L(-\theta) \quad (5c)$$

In Eq. (5),  $\Gamma_{rr}$  and  $\Gamma_{rl}$  are the RHCP-to-RHCP and RHCP-to-LHCP reflection coefficient, respectively;  $G_R(\cdot)$  and  $G_L(\cdot)$  are the RHCP and LHCP antenna gain pattern, respectively;  $\theta$  is the satellite elevation angle; the “-” sign means that the reflected signal enters the antenna from the bottom direction.

Finally, by substituting Eq. (5) into Eq. (4a), the polarization-mixing reflection coefficient taking account the cross-polarization effect can be expressed as:

$$|\Gamma| = \sqrt{\frac{P_r}{P_d}} = \sqrt{\frac{|\Gamma_{rr}|^2 \frac{G_R(-\theta)}{G_R(\theta)} + |\Gamma_{rl}|^2 \frac{G_L(-\theta)}{G_R(\theta)} + 2 \sqrt{(|\Gamma_{rr}| |\Gamma_{rl}|)^2 \frac{G_R(-\theta) G_L(-\theta)}{G_R^2(\theta)}}}{\times \cos(\varphi_{rr} - \varphi_{rl})}} \quad (6)$$

$\Gamma_{rr}$  and  $\Gamma_{rl}$  in Eq. (6) can be calculated from the horizontal and vertical linear polarization reflection coefficient (Zavorotny et al. 2009), which are directly given here.

$$\Gamma_{rr} = \frac{(\varepsilon_r - 1) \cos^2 \theta}{(\varepsilon_r \sin \theta + \sqrt{\varepsilon_r - \cos^2 \theta}) (\sin \theta + \sqrt{\varepsilon_r - \cos^2 \theta})} \quad (7a)$$

$$\Gamma_{rl} = \frac{(\varepsilon_r - 1) \sin \theta \sqrt{\varepsilon_r - \cos^2 \theta}}{(\varepsilon_r \sin \theta + \sqrt{\varepsilon_r - \cos^2 \theta}) (\sin \theta + \sqrt{\varepsilon_r - \cos^2 \theta})} \quad (7b)$$

where  $\varepsilon_r$  is the complex relative dielectric constant.  $\varepsilon_r$  is mainly determined by soil moisture, which can be described by well-established dielectric models at microwave frequencies such as Hallikainen’s model (Hallikainen et al. 1985).

### 3 Materials and Methods

#### 3.1 A Review of the Experiment Data

The experiment data used here was collected by N. Roussel et al. at a bare farmland at Lamasquère, France in 2014 (Roussel et al. 2016). The soil contains 41% of clay mineral and 18% of sand by weight. The SNR data on L1 C/A channel

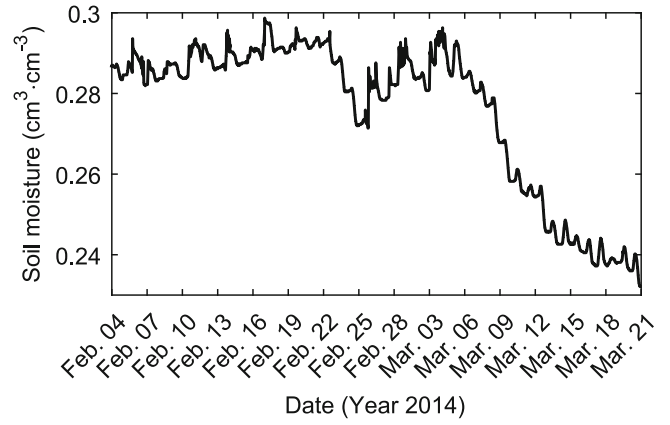


Fig. 2 In-situ soil moisture variation

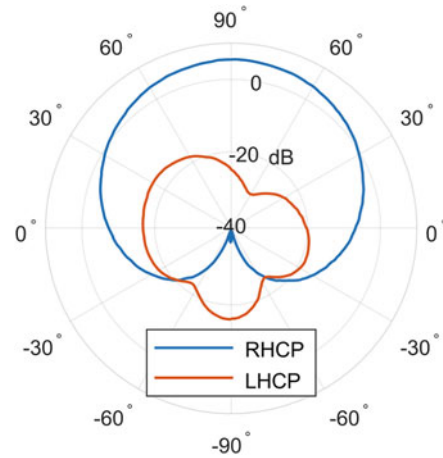


Fig. 3 The antenna gain pattern

were acquired at 1Hz frequency. The 5-cm soil moisture varied between  $0.2321 \sim 0.2987 \text{ cm}^3 \cdot \text{cm}^{-3}$  as shown in Fig. 2, which was measured by a probe. In that experiment, the cross-polarization component of reflected signal leaked into receiver through the antenna causing cosine-like SNR variation at high elevation angles (above  $30^\circ$ ), which was noticed for the first time. The antenna gain measurement is shown in Fig. 3. The maximum RHCP antenna gain was pointed to the zenith direction. The angles shown in Fig. 3 represent the satellite elevation angles. The minus elevation angle indicates the antenna’s bottom direction. As shown in the figure, the antenna’s LHCP gain is comparable to the RHCP gain at the bottom direction, therefore, the effect of the cross-polarization can not be ignored in soil moisture retrieval.

#### 3.2 A Review of the Semi-empirical SNR Model

The semi-empirical SNR model works as a new fitting model, which is aimed at improving the goodness of fit

(Han et al. 2018). From the conventional viewpoint, the SNR model shown in Eq. (3) is grouped into two terms: the very low frequency trend term  $P_d + P_r$  and the remaining high frequency term. And they are regarded as independent of each other and treated differently. While in our opinion, the basic components of the Eq. (3) should be  $P_d$  and  $P_r$ . Since  $P_r$  shows higher order variation than  $P_d$  does, we thus proposed to use a low-order polynomial and a high-order polynomial to approximate the power variation of the direct and reflected signal in Eq. (3), respectively. Therefore, a new SNR fitting model was obtained, which can be expressed as:

$$S = c_0 \left[ \begin{array}{l} 10^{\frac{p^{n_0}(\sin \theta)}{10}} + 10^{\frac{p^{n_1}(-\sin \theta)}{10}} \\ + 2\sqrt{10^{\frac{p^{n_0}(\sin \theta) + p^{n_1}(-\sin \theta)}{10}}} \cos(2\pi c_1 \sin \theta + c_2) \end{array} \right] \quad (8)$$

where  $p^{n_0}(\cdot)$  is a  $n_0$ -th order polynomial describing the direct signal power variation, and  $p^{n_1}(\cdot)$  is a  $n_1$ -th order polynomial describing the reflected signal power variation. Each polynomial is placed at the exponential position to ensure that the signal power is always positive. These two polynomials have  $n_0 + n_1 + 2$  coefficients to be estimated in total.  $c_1$  and  $c_2$  represent the frequency and initial phase to be estimated, respectively.  $c_0$  accounts for the noise power.

### 3.3 Data Processing and Soil Moisture Retrieval Method

- (1) Convert the SNR data from logarithmic scale to linear scale through  $10^{\frac{(\cdot)}{10}}$  rather than through  $10^{\frac{(\cdot)}{20}}$ .
- (2) Calculate the satellite elevation angle using broadcast ephemeris and antenna's position.
- (3) Select SNR data whose corresponding elevation angle is below  $30^\circ$ .
- (4) Fit the SNR data with Eq. (8) to obtain all the undetermined coefficients. In this paper,  $n_0$  and  $n_1$  in Eq. (8) was set to 2 and 4, respectively.
- (5) Substitute the corresponding coefficients back into  $p^{n_0}(\cdot)$  and  $p^{n_1}(\cdot)$ . The other coefficients are ignored.
- (6) Calculate the reflection coefficient under a certain elevation angle  $\theta$  using Eq. (9):

$$|\hat{\Gamma}| = \sqrt{\frac{10^{\frac{p^{n_1}(-\sin \theta)}{10}}}{10^{\frac{p^{n_0}(\sin \theta)}{10}}}} = 10^{\frac{p^{n_1}(-\sin \theta) - p^{n_0}(\sin \theta)}{20}} \quad (9)$$

- (7) Substitute all the known system parameters into Eq. (6) under the same satellite angle used in Step (6). Then solve Eq. (10) for soil moisture.

$$|\hat{\Gamma}| - |\Gamma| = 0 \quad (10)$$

## 4 Results and Discussions

### 4.1 Forward Simulation

Following Eq. (3) to Eq. (7), how cross-polarization affects SNR variation can be simulated as shown in Fig. 4. The actual SNR variation of GPS PRN No. 4 satellite is used as a reference (black line), which is significantly affected by the cross-polarization effect during the satellite's ascending phase. Its key feature is that significant interference phenomenon is observed at elevation angles above  $30^\circ$ . As a comparison, the blue line shows the SNR simulation without considering the antenna's LHCP gain. No significant oscillation is observed at high elevation angles, which is in accordance with previous studies (Larson et al. 2010; Larson and Nievinski 2013; Larson 2016). The red line shows the simulated SNR variation taking account the antenna's LHCP gain, which is nearly in accordance with the actual SNR variation. The effect of the cross-polarization on the interference is bidirectional: it will weaken the interference at low elevation angles, and at the same time, reinforce the interference at high elevation angles. There is a transition region where the interference is smallest as highlighted by the pink box. This region is near the co-angle of the Brewster's angle (Brewster 1815) which is a determined by the soil moisture. The above simulation shows that the cross-polarization is able to have a significant effect on the interference pattern. How does this affect soil moisture retrieval will be discussed next.

### 4.2 Soil Moisture Retrieval

Figure 5 shows the soil moisture retrieval results with and without correcting the cross-polarization effect using the ascending phase of GPS PRN No. 4 for example. The retrieval

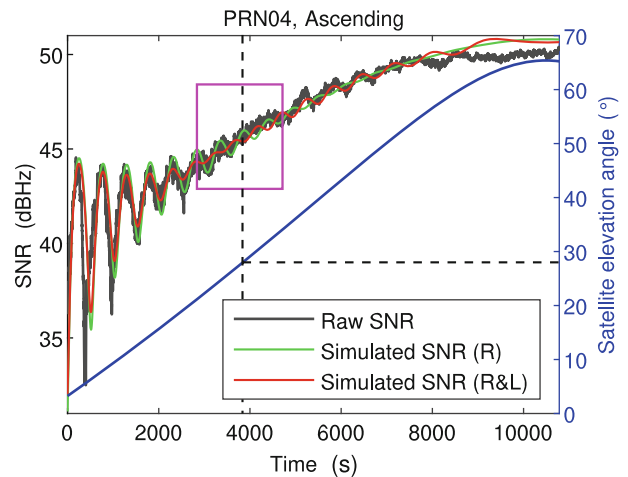


Fig. 4 SNR simulation

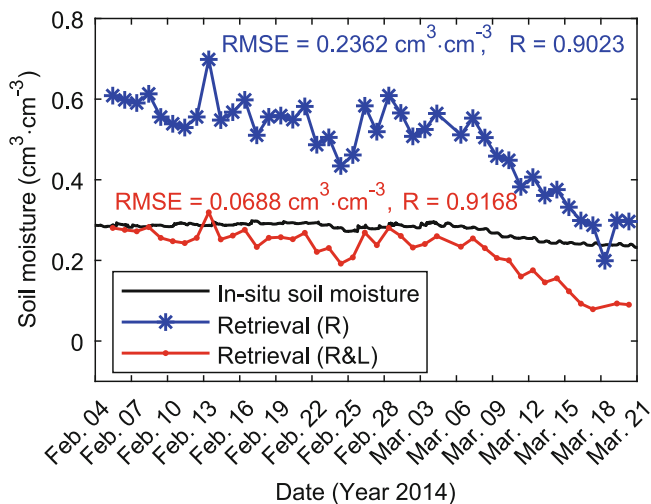


Fig. 5 Soil moisture retrieval results of GPS PRN04

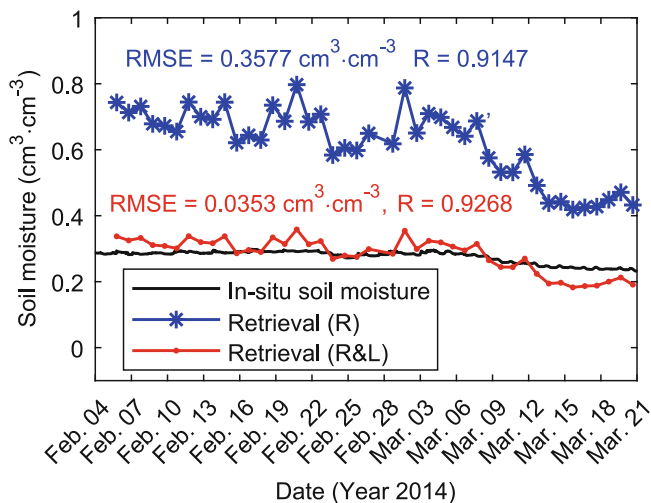


Fig. 6 Soil moisture retrieval results of GPS PRN08

is carried out at 10° elevation angle here and hereafter. The reason of this choice will be discussed later. Since PRN No. 4 satellite passes overhead one time each day, there is only one retrieval at 10° elevation angle during the ascending phase each day. The blue line shows that, without considering the cross-polarization, the retrieval shows good correlation ( $R > 0.9$ ) with the in-situ soil moisture. However, the Root Mean Square Error (RMSE) of the retrieval is also very large (above  $0.2 \text{ cm}^3 \cdot \text{cm}^{-3}$ ). After cross-polarization correction, as shown by the red line, the RMSE is reduced significantly by about  $0.16 \text{ cm}^3 \cdot \text{cm}^{-3}$  and the correlation coefficient increases slightly.

Figure 6 shows another example where the data of PRN No. 8 satellite was used. Similar degree of error reduction is achieved. Both of the two examples show that the ignorance of cross-polarization will cause significant over-estimation of the soil moisture.

Table 1 Overall retrieval results

PRN	Status	Without correction		With correction	
		ME	R	ME	R
2	Asc.	0.2373	0.6463	-0.0477	0.5911
4	Asc.	0.2178	0.9023	-0.0541	0.9168
5	Asc.	0.2011	0.7104	-0.0641	0.7379
14	Asc.	0.2240	0.7751	-0.0526	0.8006
17	Asc.	0.2610	0.3467	-0.0300	0.3388
28	Asc.	0.2400	0.7660	-0.0425	0.7920
3	Desc.	0.1870	0.5927	-0.0689	0.5964
7	Desc.	0.3923	0.8535	0.0272	0.8754
8	Desc.	0.3458	0.9147	<b>0.0077</b>	<b>0.9268</b>
21	Desc.	0.4163	0.8500	0.0371	0.8694
22	Desc.	0.2771	0.8316	-0.0240	0.8451
28	Desc.	0.2877	0.8401	-0.0281	0.8915

As shown in Fig. 3, the antenna’s LHCP gain is not symmetrical in azimuth direction, therefore not all the satellites’ data suffer from obvious cross-polarization problem. Table 1 summarizes all the retrievals that should perform cross-polarization correction, where Asc. and Desc. represent the ascending and descending phase of the satellite, respectively. Mean Error (ME) are used as the error metric instead of RMSE to expose the sign of the error, where positive value means that the retrieved soil moisture is larger than the in-situ measurement on average. Before correction, much of the mean retrieval error is larger than  $0.2 \text{ cm}^3 \cdot \text{cm}^{-3}$ . After correction, the mean error is within  $0.07 \text{ cm}^3 \cdot \text{cm}^{-3}$ . The best result is highlighted in the table, whose mean error is less than  $0.01 \text{ cm}^3 \cdot \text{cm}^{-3}$  and correlation coefficient is higher than 0.92.

### 4.3 Error Analysis

Ideally, three-dimensional antenna gain pattern should be used for accurate correction purpose instead of the one-cut antenna gain pattern as shown in Fig. 1, which is the main error source. Other error sources are relatively small, which includes: (1) the limited modelling capability of the polynomials in the semi-empirical SNR model; (2) the ignorance of soil roughness; (3) the inaccuracy of the soil dielectric model.

However, the final retrieval error depends not only on the magnitude of the error sources but also on how the error propagates through the retrieval process, namely, the error sensitivity of the retrieval. Figure 7 shows how the polarization-mixing reflection coefficient varies with soil moisture under different satellite elevation angles. As shown in the figure, the relationship between the polarization-mixing reflection coefficient and soil moisture is different under different satellite elevation angles. The difference mainly exists on the slope and the monotonicity of the curve. The slope determines the error sensitivity. The greater the

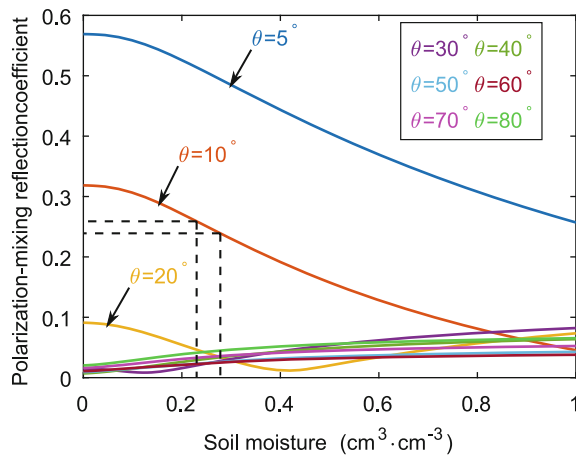


**Fig. 7** Polarization-mixing reflection coefficient simulation

absolute value of the slope is, the less error-sensitive the retrieval is.

The sign of the slope determines the sign of the retrieval error relative to the sign of the reflection coefficient estimation error. Negative slope means that an overestimation of the reflection coefficient will cause an underestimation of the soil moisture. The error sources mentioned above is equivalent to the reflection coefficient estimation error directly or indirectly. For example, according to Eq. (6) and Fig. 4, under the condition of  $\theta = 10^\circ$ , an underestimation of the cross-polarization gain ( $G_L(-\theta)$ ) is equivalent to an overestimation of the reflection coefficient in the forward modelling, which is equivalent to an underestimation of the reflection coefficient in the retrieval/inversion process. Since the slope is negative, the underestimation of the reflection coefficient will result in an overestimation of soil moisture. This explains why the retrieved soil moisture is much larger than the in-situ measurement without considering the cross-polarization.

Finally, the monotonicity determines uniqueness of the retrieval/solution. Additional information is needed to help determine the true solution once the non-monotonic relationship is used such as the case of  $\theta = 20^\circ$ .

Based on the above analysis, the relationship under the condition of  $\theta = 10^\circ$  was chosen for retrieval due to its low error sensitivity and monotonicity.

One should note that Fig. 7 is generated according to Eq. (6), therefore, the quantitative relationships shown are dependent on the specific antenna gain pattern.

## 5 Conclusions

(1) The final expression of the polarization-mixing SNR model was given in a compact and hierarchical form including a top level expression and a series of lower-

level expressions. The model shows clearly that the cross-polarization affects only the low-level model but not the top level model.

- (2) The effect of the cross-polarization on the interference pattern is bidirectional. It will weaken the interference at low satellite elevation angles ( $\sim 30^\circ$ ) while reinforce the interference at high elevation angles.
- (3) Ignorance of the cross-polarization effect will lead to a significant overestimation of the soil moisture when carrying out retrieval using the estimated reflection coefficient under low satellite elevation angle cases.
- (4) The polarization-mixing reflection coefficient determines the error propagating performance. It varies with satellite elevation angle and the antenna gain pattern.
- (5) In the case where the antenna gain pattern is not omnidirectional, it is better to use three-dimensional antenna gain pattern for correction purpose.

**Acknowledgements** The authors would like to thank F. Baup and K. Boniface for collecting the meteorological data, and N. Roussel and F. Frappart for collecting GNSS observation data, and J. Darrozes for providing the data.

**Author Contributions** M. Han proposed the idea and drafted the manuscript. D. Yang proposed the idea and organized the architecture of the paper. B. Zhang carried out the simulations. X. Hong processed the data. F. Wang contribute to the revision and language usage checking. All of the authors contributed to the discussions.

**Conflict of Interest** The authors declare that they have no conflict of interest.

## References

- Brewster D (1815) On the laws which regulate the polarisation of light by reflexion from transparent bodies. *Phil Trans R Soc Lond* 105:125–159
- Chew CC, Small EE, Larson KM, Zavorotny VU (2014) Effects of near-surface soil moisture on GPS SNR data: Development of a retrieval algorithm for soil moisture. *IEEE Trans Geosci Remote Sens* 52(1):537–543
- Chew CC, Small EE, Larson KM, Zavorotny VU (2015) Vegetation sensing using GPS-Interferometric Reflectometry: Theoretical effects of canopy parameters on Signal-to-Noise Ratio data. *IEEE Trans Geosci Remote Sens* 53(5):2755–2764
- Edokossi K, Calabria A, Jin S, Molina I (2020) GNSS-reflectometry and remote sensing of soil moisture: A review of measurement techniques, methods, and applications. *Remote Sens* 12(4):614
- Hallikainen MT, Ulaby FT, Dobson MC, El-Rayes MA, Wu LK (1985) Microwave dielectric behavior of wet soil-part 1: Empirical models and experimental observations. *IEEE Trans Geosci Remote Sens* 1:25–34
- Han M, Zhu Y, Yang D, Hong X, Song S (2018) A semi-empirical SNR model for soil moisture retrieval using GNSS SNR data. *Remote Sens* 10(2):280
- Larson KM (2016) GPS Interferometric Reflectometry: Applications to surface soil moisture, snow depth, and vegetation water content in

- the Western United States. *Wiley Interdisciplinary Reviews: Water* 3(6):775–787
- Larson KM, Nievinski FG (2013) GPS Snow sensing: Results from the earthscope plate boundary observatory. *GPS Solut* 17(1):41–52
- Larson KM, Small EE, Gutmann E, Bilich A, Axelrad P, Braun J (2008) Using GPS multipath to measure soil moisture fluctuations: initial results. *GPS Solut* 12(3):173–177
- Larson KM, Braun JJ, Small EE (2010) GPS multipath and its relation to near-surface soil moisture content. *IEEE J Sel Top Appl Earth Obs Remote Sens* 3(1):91–99
- Roussel N, Frappart F, Ramillien G, Darrozes J, Baup F, Lestarquit L, Ha MC (2016) Detection of soil moisture variations using GPS and GLONASS SNR data for elevation angles ranging from 2 to 70. *IEEE J Sel Top Appl Earth Obs Remote Sens* 9(10):4781–4794
- Small EE, Larson KM, Chew CC, Dong J, Ochsner T (2016) Validation of GPS-IR soil moisture retrievals: Comparison of different algorithms to remove vegetation effects. *IEEE J Sel Top Appl Earth Obs Remote Sens* 9(10):4759–4770
- Zavorotny VU, Larson KM, Braun JJ, Small EE, Gutmann ED, Bilich AL (2009) A physical model for GPS multipath caused by land reflections: Toward bare soil moisture retrievals. *IEEE J Sel Top Appl Earth Obs Remote Sens* 3(1):100–110
- Zavorotny VU, Gleason S, Cardellach E, Camps A (2014) Tutorial on remote sensing using GNSS bistatic radar of opportunity. *IEEE Geosci Remote Sens Mag* 2(4):8–45

**Open Access** This chapter is licensed under the terms of the Creative Commons Attribution 4.0 International License (<http://creativecommons.org/licenses/by/4.0/>), which permits use, sharing, adaptation, distribution and reproduction in any medium or format, as long as you give appropriate credit to the original author(s) and the source, provide a link to the Creative Commons license and indicate if changes were made.

The images or other third party material in this chapter are included in the chapter's Creative Commons license, unless indicated otherwise in a credit line to the material. If material is not included in the chapter's Creative Commons license and your intended use is not permitted by statutory regulation or exceeds the permitted use, you will need to obtain permission directly from the copyright holder.







## Correction to: Dilution of Precision (DOP) Factors for Evaluating Observations to Galileo Satellites with VLBI

Helene Wolf, Johannes Böhm, Matthias Schartner, Urs Hugentobler,  
Benedikt Soja, and Axel Nothnagel

**Correction to:**  
**Chapter “Dilution of Precision (DOP) Factors for Evaluating Observations to Galileo Satellites  
with VLBI” in: H. Wolf et al., International Association of Geodesy Symposia,**  
[https://doi.org/10.1007/1345\\_2022\\_165](https://doi.org/10.1007/1345_2022_165)

In the published chapter, double vertical lines were missing for  $L_2$  in Eq. (2). This has now been added to read as,

$$\begin{aligned} \begin{pmatrix} \frac{\partial \Delta \tau}{\partial x} \\ \frac{\partial \Delta \tau}{\partial y} \\ \frac{\partial \Delta \tau}{\partial z} \end{pmatrix} &= \frac{1}{c} \left[ \frac{L_2}{\|L_2\|} - \frac{L_1}{\|L_1\|} \right] - \frac{1}{c^2} \left[ \dot{\omega}_2 - \frac{L_1}{\|L_1\| \|L_2\|} (L_2 \cdot \dot{\omega}_2) \right. \\ &\quad \left. + \|L_1\| \frac{L_2}{\|L_2\|^3} (L_2 \cdot \dot{\omega}_2) - \frac{\|L_1\|}{\|L_2\|} \dot{\omega}_2 \right], \end{aligned} \quad (2)$$

The updated original version of this chapter can be found at [https://doi.org/10.1007/1345\\_2022\\_165](https://doi.org/10.1007/1345_2022_165)

---

## Associate Editors

Bogusz, Janusz  
Gikas, Vassilis  
Jäggi, Adrian  
Kealy, Allison  
Kotsakis, Christopher  
Novák, Pavel  
Reguzzoni, Mirko

---

## List of Reviewers

Amiri-Simkooei, Ali Reza  
Anastasiou, Dimitrios  
Balidakis, Kyriakos  
Barriot, Jean-Pierre  
Barzaghi, Riccardo  
Bloßfeld, Mathis  
Boehm, Johannes  
Bolkas, Dimitrios  
Bucha, Blažej  
Bui, Luyen  
Caporali, Alessandro  
Carraz, Olivier  
Chao, Ben  
Chatzinikos, Miltiadis  
Claessens, Sten  
Collilieux, Xavier  
Dabove, Paolo  
Dammalage, Thilantha  
Danezis, Chris  
Darrozes, José  
Dawidowicz, Karol  
Dawson, John  
Delikaraoglou, Demitris  
Delva, Pacôme  
Encarnação, João  
Erol, Bither  
Forsberg, Rene  
Fukuda, Yoichi  
Gabela, Jelena  
Gallon, Elisa  
Geng, Jianghui  
Gianniou, Michael  
Gikas, Vassilis  
Glaser, Susanne  
Greiwe, Ansgar  
Hippenstiel, Ryan  
Hsu, Li-Ta  
Kallio, Ulla  
Kaplon, Jan  
Khodabandeh, Amir  
Kosek, Wieslaw  
Kowalczyk, Kamil  
Kutterer, Hansjörg  
Legrand, Juliette  
Liwosz, Tomasz  
Loomis, Bryant D.  
Lösler, Michael  
Marti, Urs  
Masiero, Andrea  
Meyer, Ulrich  
Middlemiss, Richard  
Migliaccio, Federica  
Ming, Feng  
Mueller, Juergen  
Naranen, Jyri  
Nikolaidou, Thalia  
Nilsson, Tobias  
Nothnagel, Axel  
Novák, Pavel  
Otsubo, Toshimichi  
Pail, Roland  
Pavlis, Erricos C.  
Pavlov, Dmitry  
Paziewski, Jacek  
Pikridas, Chris  
Polcari, Marco  
Psychas, Dimitrios  
Rajavarathan, Jenan  
Retscher, Guenther  
Rivera, Jullian  
Roberts, Craig  
Ruotsalainen, Laura  
Ryszard Karsznia, Krzysztof  
Sánchez, Laura  
Seitz, Manuela  
Sjöberg, Lars E.  
Soja, Benedikt  
Sosnica, Krzysztof

Stanaway, Richard  
Süsser-Rechberger, Barbara  
Titov, Oleg  
Veryaskin, Alexey  
Wanninger, Lambert  
Wielgosz ,Pawel  
Wieser, Andreas

Woppelmann ,Guy  
Wziontek, Hartmut  
Wöske, Florian  
Yigit, Cemal Ozer  
Zajdel, Radoslaw  
Zaminpardaz, Safoora

---

## Author Index

### A

Abrykosov, O., 203–211  
Adavi, Z., 405–414  
Albo-Castaño, C., 77–81  
Alcaras, E., 139–144  
Allahviridi-Zadeh, A., 377–383  
Amoroso, P.P., 139–144  
Ampatzidis, D., 25–29  
Andritsanos, V.D., 165–170  
Angermann, D., 111–119  
Aoki, Y., 155–162  
Arnold, D., 183–188, 191–199  
Azcue, E., 95–103  
Azcue-Infanzón, E., 77–81

### B

Bachmann, S., 3–12  
Balidakis, K., 253–257  
Beaufils, Q., 213–219  
Belda, S., 253–257  
Beltrán-Martínez, F.J., 77–81  
Bettadpur, S., 175–180  
Bilinskis, I., 39–43  
Biskupek, L., 259–264  
Bloßfeld, M., 3–12  
Böhm, J., 305–311  
Bossler, P., 397–402  
Brack, A., 15–22  
Bradke, M., 279–285  
Bramante, B., 147–151  
Brcic, R., 289–300  
Breva, Y., 333–342, 345–356

### C

Chatzinikos, M., 67–74, 83–94, 289–300  
Christofe, A., 289–300  
Christoforou, M., 289–300  
Courde, C., 105–108  
Crowley, J.W., 123–128

### D

Danezis, C., 83–94, 289–300  
D'Aoust, B., 123–128  
Dawidowicz, K., 321–331  
del Pino, J., 39–43

de Vicente-Abad, P., 77–81  
de Vicente, P., 95–103  
Dodo, J.D., 269–277

### E

Eineder, M., 289–300  
El-Mowafy, A., 377–383  
Eschelbach, C., 57–64, 105–108

### F

Falchi, U., 139–144  
Fathulhuda, M.S., 147–151  
Ferreira, J.S., 77–81  
Flechtner, F., 203–211  
Flohner, C., 245–251  
Foroughi, I., 131–136  
Förste, C., 203–211  
Fotiou, K., 289–300

### G

García-Asenjo, L., 105–108  
García-Castellano, A., 77–81  
Geisser, L., 183–188  
Gerstl, M., 111–119  
Gipson, J., 3–12  
Girdiuk, A., 245–251  
González-García, J., 77–81  
Grigoriadis, V.N., 165–170  
Grombein, T., 191–199  
Gross, R., 111–119  
Gruber, T., 111–119  
Guillory, J., 105–108

### H

Hadjimitsis, D., 289–300  
Han, M., 423–428  
Hedekvist, P.O., 105–108  
Heinkelmann, R., 111–119, 253–257  
Heki, K., 111–119  
Hellmers, H., 3–12, 245–251  
Hong, X., 423–428  
HosseiniArani, A., 213–219, 221–230  
Huang, J., 123–128  
Hugentobler, U., 111–119, 305–311

- I**  
 Icking, L., 359–365  
 Ince, E.S., 203–211  
 Ioannou, G., 289–300
- J**  
 Jäggi, A., 183–188, 191–199
- K**  
 Kakoullis, D., 289–300  
 Kallio, U., 45–54, 105–108  
 Kang, Z., 175–180  
 Kersten, T., 321–331, 333–342, 345–356  
 Khenchaf, A., 397–402  
 Kingdon, R., 131–136  
 Kitpracha, C., 253–257  
 Klügel, T., 45–54, 57–64, 105–108  
 Knabe, A., 213–219, 221–230  
 Kotsakis, C., 67–74, 83–94, 289–300  
 Krawinkel, T., 313–319  
 Kröger, J., 333–342, 345–356  
 Krzan, G., 321–331  
 Kyriakides, N., 289–300
- L**  
 Lasser, M., 191–199  
 Le, N., 387–395  
 Lengert, L., 245–251  
 López-Fernández, J.A., 77–81  
 López-F, J.A., 95–103  
 López-P, J.A., 77–81, 95–103  
 López-Ramasco, J., 77–81  
 Lösler, M., 57–64
- M**  
 Mähler, S., 45–54  
 Männel, B., 15–22, 269–277, 279–285, 387–395  
 Mansur, G., 15–22  
 Marila, S., 45–54  
 Martinec, Z., 131–136  
 Martínez, E., 95–103  
 Marti, U., 111–119  
 Melillos, G., 289–300  
 Meyer, U., 183–188, 191–199  
 Modiri, S., 3–12, 253–257  
 Müller, J., 213–219, 221–230, 259–264
- N**  
 Nakamura, Y., 31–37  
 Natsopoulos, D., 165–170  
 Neyezhmakov, P., 105–108  
 Nguyen, C.T., 387–395  
 Nikolaidis, M., 289–300  
 Nothnagel, A., 305–311
- P**  
 Pahlevi, A.M., 147–151  
 Panetier, A., 397–402  
 Parente, C., 139–144  
 Pavão, S., 77–81
- Pavlic, G., 123–128  
 Pekri, M., 289–300  
 Pereira dos Santos, F., 213–219  
 Pesce, D., 105–108  
 Pham, H.T., 387–395  
 Pilidou, S., 289–300  
 Pinto, F., 233–240  
 Pisani, M., 105–108  
 Pollinger, F., 105–108  
 Poutanen, M., 45–54  
 Prijatna, K., 147–151  
 Puente, V., 95–103
- R**  
 Raut, S., 253–257  
 Ries, J., 175–180  
 Rodríguez, J.C., 95–103  
 Ruwisch, F., 359–365
- S**  
 Saari, T., 45–54  
 Sakic, P., 15–22, 269–277, 387–395  
 Salmins, K., 39–43  
 Sánchez, L., 111–119  
 Sánchez Sobrino, J.A., 95–103  
 Santos, L.R., 77–81  
 Santos, M., 131–136  
 Save, H., 175–180  
 Schartner, M., 305–311  
 Schilling, M., 213–219, 221–230  
 Schöne, T., 279–285  
 Schön, S., 221–230, 313–319, 321–331, 333–342, 345–356, 359–365, 367–375  
 Schuh, H., 15–22, 111–119, 253–257, 269–277, 279–285, 387–395  
 Schüler, T., 45–54  
 Sehnal, M., 111–119  
 Seitz, M., 3–12  
 Seo, N., 31–37  
 Seppä, J., 105–108  
 Setti, P.T. Jr., 417–421  
 Singh, V.V., 259–264  
 Soja, B., 305–311  
 Sprogis, V., 39–43  
 Steigenberger, P., 111–119  
 Su, J., 367–375  
 Suurmäki, H., 45–54  
 Suzuki, A., 31–37
- T**  
 Tanaka, Y., 155–162  
 Tapley, B., 175–180  
 Tennstedt, B., 221–230  
 Thaller, D., 3–12, 25–29, 245–251  
 Themistocleous, K., 289–300  
 Thomas, M., 111–119  
 Tzouvaras, M., 289–300
- U**  
 Ueshiba, H., 31–37  
 Underwood, R., 105–108  
 Usifoh, S.E., 269–277

**V**

Valdés, M., 95–103  
Vancíček, M., 131–136  
van Dam, T., 417–421  
Vaquero, B., 95–103  
Vaquero-Jiménez, B., 77–81  
Véronneau, M., 123–128

**W**

Wallenstein, F.M., 77–81  
Wang, F., 423–428  
Wang, K., 377–383  
Wang, L., 25–29  
Watanabe, S., 31–37

Weber, R., 405–414  
Wezka, K., 105–108  
Wiśniewski, M., 105–108  
Wolf, H., 305–311  
Wu, H., 213–219, 221–230

**Y**

Yang, D., 423–428  
Yokota, Y., 31–37

**Z**

Zhang, B., 423–428

# Subject Index

- A**  
Absolute antenna calibration, 333–335, 337–341  
Accuracy, 4, 16, 32, 41, 46, 57, 68, 78, 90, 97, 107, 112, 124, 132, 140, 147, 156, 165, 175, 193, 205, 217, 222, 234, 247, 257, 260, 271, 279, 290, 306, 315, 322, 333, 345, 360, 370, 380, 388, 399, 406, 423  
Air refractivity compensation, 106, 107  
Allan deviation, 314, 317, 318  
Atom interferometry, 214, 218, 221–230
- B**  
BPS inventory, 112, 119  
Bundle adjustment, 58–64  
Bureau of Products and Standards (BPS), 111–119
- C**  
Chronometric leveling, 155, 156, 158, 160, 161  
Classical heights, 132, 136  
Climate, 4, 102, 112, 115, 175, 184, 191, 222, 321, 322, 368, 371, 373, 387, 395, 413  
Closed-loop simulation, 214, 216–219, 239  
Close range photogrammetry, 46, 57–64, 108  
Codephase center corrections, 333–342  
Cold atom interferometer accelerometry, 214, 222–223  
Co-location, 31–37, 46, 47, 49, 53, 54, 58, 108, 306  
Combination at the normal equation level, 246, 250  
Combination of normal equations, 4, 6, 7  
Combined weekly coordinate solutions, 67–74  
Continuously operating reference stations (CORS), 84, 290–293, 295, 297  
Coordinates, 4, 16, 31, 40, 46, 58, 67, 86, 98, 106, 112, 134, 140, 160, 167, 183, 236, 247, 260, 270, 280, 290, 307, 314, 322, 336, 347, 360  
Corner reflectors (CRs), 290–295, 299  
Correlations, 7, 12, 25–29, 59, 61–64, 68, 71–73, 89, 141, 142, 167, 184, 185, 195, 246, 254, 255, 260–263, 289, 306, 329, 347–349, 354, 368, 390, 391, 393, 394, 398, 399, 401, 402, 412, 413, 418, 420, 421, 427  
Covariance projection, 68  
Cross-polarization correction, 423–428  
Crustal deformation, 156  
CubeSats, 377–383  
CYGNSS, 417–421  
CYPOS, 83–85, 90, 93, 94  
Cyprus, 83–94, 289–300
- D**  
Datum definition, 7, 10, 12, 26, 86, 93, 186  
Datum problem, 45–54, 108  
Dilution of Precision (DOP) factors, 305–311  
Dispersion force engineering, 233–240  
Doppler Orbitography and Radiopositioning Integrated by Satellite (DORIS), 4, 26–29, 32, 46, 47, 50, 51, 112, 246, 270  
Double difference (DD), 85, 89, 297, 298, 322, 325, 327, 329, 378
- E**  
Earth Gravitational Model (EGM), 123–128, 140, 147, 148, 150, 151, 167, 168, 203, 210, 223, 379  
Earth orientation parameters (EOPs), 4–8, 11, 12, 100, 101, 114, 245–251, 254, 260, 261, 264, 281, 306  
Earth rotation parameters (ERPs), 9–12, 16, 26, 85, 183–188, 259–264, 271, 281  
Earth rotation phase, 260, 261  
Effective isotropic radiated power (EIRP), 417–421  
El-Niño, 253–257  
Empirical mode decomposition, 333–342  
Enhanced (augmented) gravity field models, 203–211  
EPN-repro2, 16, 17, 68, 73, 74  
Error bounding, 367–375  
EUREF/EPN, 67, 73, 85  
EUREF permanent network (EPN), 67–74, 84–86, 90, 93, 94, 97, 98, 291, 294, 297, 299, 321, 346
- F**  
Frame parameter accuracy, 68–71, 73, 74  
Frequency transfer (FT), 313–318  
Future satellite gravity missions, 213–219, 221–230
- G**  
Galileo, 16–22, 85, 97, 98, 102, 248, 281, 305–311, 314, 315, 318, 334, 337–341  
Generic patterns, 326–329  
Geodesy, 4, 37, 78, 84, 96, 111, 131, 149, 183, 203, 239, 247, 257, 290, 314  
Geodetic products, vi, 102, 111–119  
Geoid height, 124, 133, 139–143, 148–151, 159–161, 170, 193–195  
Geoid modeling, 34, 51–54, 124–127, 133, 140, 141, 143, 147–151, 157, 161, 167, 168, 170  
GeoMetre, 46, 47, 51, 54, 58, 59, 64, 105–108  
Geopotential, 124–127, 134, 135, 148, 149, 166, 168, 183–188  
GGOS website, 112, 114–119



- Global Geodetic Observing System (GGOS), vi, 40, 46, 49, 52, 54, 57, 61, 64, 78, 80, 81, 96, 111–119, 204
- Global geodetic reference frame, 32, 57, 81, 245
- Global Navigation Satellite System–Interferometric Reflectometry (GNSS-IR), 423
- Global navigation satellite systems (GNSS), 4, 16, 31, 39, 46, 67, 77, 83, 96, 107, 112, 133, 140, 147, 156, 166, 184, 191, 204, 246, 254, 261, 270, 280, 290, 306, 313, 321, 333, 345, 377, 417
- GNSS data processing, 33–34, 69, 70, 74, 84–89, 97, 271–272, 280, 298, 325, 327, 329, 407
- GNSS reflectometry (GNSS-R), 99, 417–418
- GPS-based gravity field recovery, 191–193, 199
- GRACE, 101, 156, 159, 161, 162, 175–180, 184, 191–199, 213, 215–218, 222–224, 226, 228, 229
- GRACE-FO, 156, 159, 161, 175–180, 184, 191–199, 215, 216, 222–224, 226–229
- Gravitational potential, 155–162, 217
- Gravity field coefficients, 176, 177, 184–187, 193, 195, 196, 199, 217
- Gravity field combination, 195
- Gravity network, 165–170
- Greece, 166, 167
- Group delay variations (GDV), 334
- H**
- Helmert's second condensation, 147–151
- Helmert transformation parameters, 10, 25–29, 90
- High resolution global gravity field modelling, 203–211
- Hybrid accelerometer, 214, 217–219, 221–230
- I**
- IGN, 77, 80, 95–103, 140
- Image similarity metrics, 345–356
- Integrated water vapor (IWV), 321–323, 329, 398–402
- Integrity, 367–369
- International GNSS Service (IGS), 15–22, 32, 35, 39, 67, 69–71, 78–80, 84, 85, 97, 100, 118, 247, 280, 281, 284, 285, 291, 293, 298, 299, 323, 334, 346, 368, 370, 371, 374, 375, 388–391, 393
- International Height Reference System (IHR), 123–128, 204
- International Terrestrial Reference Frame (ITRF), 3–12, 16, 25–29, 31–35, 37, 39–41, 46, 47, 53, 54, 57, 58, 67, 68, 70–72, 74, 83–94, 100–120, 125, 183, 248, 261, 272, 276, 277, 281, 306
- International VLBI Service for Geodesy and Astrometry (IVS), 3–12, 78, 80, 100, 102, 118, 246, 247
- Interpolation, 106, 139–144, 148, 215, 247, 255, 336, 371, 389
- Interval analysis, 367–375
- ITRF2020, 3–12, 16, 32, 37, 47, 54, 101, 102, 108, 183
- K**
- Kinematic orbits, 191–199, 380
- Kriging, 139–144
- L**
- LAGEOS, 35, 101, 176, 177, 183–187
- LARES, 176, 177, 183–188
- Length of day (LOD), 8, 101, 185, 245–249, 253–257, 260
- Local geoid, 34, 51, 140, 143, 151
- Local tie metrology, 106, 108
- Local ties, 32–37, 39–43, 45–54, 57, 58, 64, 78–80, 106, 108, 295
- Local ties stability, 43
- Local tie survey, 32–37, 45–54
- Long-arc computation, 184, 185, 188
- Low Earth Orbiting (LEO) satellites, 183, 187, 191–193, 196, 199, 378
- Lunar laser ranging (LLR), 112, 259–263
- M**
- Machine learning (ML), 387–395
- Meteorology, 48, 98, 161, 293, 294, 321–323, 368, 370–375, 397, 409, 412
- Molodensky heights, 131–136
- Multi-GNSS processing, 346
- Multilateration systems, 107
- Multipath, 293, 315, 334, 341, 359–365, 367, 378, 379, 398, 399, 402, 423
- N**
- Network adjustment, 33–35, 51, 53, 68, 85, 88–90, 156, 160, 165, 167, 296, 297, 299
- Normal heights, 131, 133–136
- Novel accelerometers, 217, 234
- O**
- Optical lattice clock (OLCs), 156, 158
- Optimal forecast model, 388–390
- Orbit combination, 16, 19
- Orientation, 4, 26, 33, 46, 47, 49, 51–54, 58, 59, 63, 68–70, 72, 100, 108, 114, 115, 228, 236, 254, 260, 294, 295, 306, 311, 321
- Orthometric heights, 49, 132–136, 139, 140, 147, 151, 156, 157, 161
- P**
- Phase centre corrections (PCC), 85, 298, 322–329, 333–342, 345–355
- Plate tectonics, 77, 270, 277
- Precise orbit determination (POD), 19, 176, 177, 192, 306, 311, 377–383
- Precise Point Positioning (PPP), 35, 269, 271, 272, 277, 293, 313, 325, 333, 398–402
- Q**
- Quantum technology for geodesy, 240
- Quasigeoid, 49, 50, 54, 131–133, 135, 136
- R**
- Radiotelescope, 77, 78, 80, 96, 100, 306, 308
- Ray-tracing, 359–365, 374
- Receivers and GNSS, 39–41, 77, 80, 85, 96, 99, 166, 191, 271, 293, 313–319, 377, 402, 423, 424
- Reference point determination, 57–64, 108
- Regional network densification, 84, 93–94
- Relativistic geodesy, 314
- Repro3, 15–22, 271, 280, 281, 284
- Residual tropospheric error, 367–375
- S**
- SAR, 290, 291, 294–296, 299
- Satellite gravimetry, 175, 222, 226, 230
- Satellite laser ranging (SLR), 4, 8, 16, 19, 21, 25–27, 29, 31–37, 39–43, 46, 50, 51, 53, 58–60, 64, 78, 80, 96, 100–102, 106, 108, 175–180, 183–188, 222, 246, 251, 306, 380
- Scale, 4, 9–12, 18, 25–27, 29, 46, 48, 49, 51, 54, 57, 60, 61, 64, 68–72, 74, 90, 102, 105–108, 113, 148, 151, 155–162, 168, 178,

- 179, 192, 199, 204, 214, 222, 233–240, 255, 277, 281, 310, 321, 322, 337, 346, 350, 351, 371, 417, 426
- Sea level, 4, 99, 102, 112, 114, 117, 118, 139, 157, 254, 279, 280, 284, 285, 387, 399
- Shipborne GNSS, 397–402
- Signal-to-noise ratio (SNR), 377–382, 423–428
- Singular value decomposition (SVD), 346, 350–356
- SI traceability, 106
- Soil moisture, 99, 272, 417–421, 423–428
- Space-geodetic techniques, 4, 7, 8, 12, 31, 32, 46–48, 50, 54, 57, 64, 68, 106, 108, 118, 306
- Standards and conventions, 111, 112, 119
- Station coordinate, 4, 5, 7–12, 16, 19, 67, 68, 80, 86, 100–102, 183–187, 247, 248, 261, 270, 271, 281, 282, 298, 322
- Statistical test, 389, 393, 400
- Stokes, 125, 147–151
- Swarm, 191–199, 406
- T**
- TEC forecast, 387–395
- Terrestrial reference frame (TRF), v, 5, 7, 8, 12, 25–29, 99, 115, 116, 245–248
- Tide gauge, 96, 99, 133, 279–285, 399, 400, 402
- Tide Gauge Benchmark Monitoring Pilot Project (TIGA), 280
- Tides, 4, 52, 85, 96, 99, 114, 124, 133, 156, 158–162, 166, 184, 217, 218, 279–285, 298, 299, 398, 400, 402
- Time-variable gravity, vi, 117, 183, 191, 192, 197–199, 213
- Tomography, 405–414
- Topographic gravity field, 123–128, 203–211
- Topographic gravity field model (TGFM), 123–128, 203–211
- Total variation (TV) method, 405–414
- TRF assessment, 25–29
- U**
- Urban GNSS, 359–365
- V**
- Variance components estimation (VCE), 7, 11, 12, 15–22, 169, 188, 192, 196–199
- Velocity field, 94, 269–277
- Vertical land motion, 279–285
- Very Long Baseline Interferometry (VLBI), 4, 7–12, 26–29, 31–32, 46, 47, 49, 50, 52–54, 78, 80, 96, 100, 102, 108, 245–254, 260, 263, 305–311
- VieSched++, 306–307, 311
- VLBI Global Observing System (VGOS), 4, 6, 12, 49, 77–80, 96, 100, 108, 309, 311
- VLBI intensives, 100, 245–251
- VLBI rapid sessions, 245–251
- W**
- Weighting model, 377–383
- Z**
- Zenith tropospheric delays (ZTD), 98, 100, 322, 370, 398
- Zero difference (ZD), 271, 322, 325, 327, 329